



11th International Conference on
Heavy Ion Accelerator Technology
June 8-12, 2009 - Venezia (Italy)

Organized by:



Laboratori Nazionali di Legnaro

Under the auspices of:



**UNIVERSITÀ
DEGLI STUDI
DI PADOVA**



Heavy Ion Accelerator Technology

June 8-12, 2009 - Venezia (Italy)

<http://hiat09.lnl.infn.it> – e-mail: hiat09@lnl.infn.it

Scientific Advisory Committee

Jeff Ashenfelter, *Yale University, USA*
Walter Assmann, *Ludwig-Maximilians-Universität München, Germany*
James R. Beene, *Holifield Radioactive Ion Beam Facility, ORNL, USA*
Giovanni Bisoffi, *INFN-LNL, Italy*
Robin Ferdinand, *GANIL, France*
Oliver Kester, *Gesellschaft für Schwerionenforschung, Germany*
Robert Laxdal, *TRIUMF, Canada*
Francis Osswald, *Institut de Recherches Subatomiques, Strasbourg, France*
Richard Pardo, *Argonne National Laboratory, USA*
Roland Repnow, *Max-Planck-Institut für Kernphysik Heidelberg, Germany*
Danilo Rifuggiato, *INFN-LNS, Italy*
Amit Roy, *Inter-University Accelerator Centre, India*
Kimikazu Sasa, *University of Tsukuba, Japan*
Dannie Steski, *Brookhaven National Laboratory, USA*
Suehiro Takeuchi, *Japan Atomic Energy Agency, Japan*
Bernard Waast, *Institut de Physique Nucléaire d'Orsay, France*
David Weisser, *Australian National University, Australia*
Guan Xialing, *China Institute of Atomic Energy, China*

Local Organizing Committee

Giovanni Bisoffi, *INFN-LNL, Italy (Chairman)*
Daniele Ceccato, *Padova Univ. and INFN-LNL, Italy*
Anna D'Este, *INFN-LNL, Italy (Secretary)*
Juan Esposito, *Consorzio RFX and INFN-LNL, Italy*
Augusto Lombardi, *INFN-LNL, Italy*
Vincenzo Palmieri, *INFN-LNL, Italy*
Piero Antonio Posocco, *Consorzio RFX and INFN-LNL, Italy*

Organizing Secretariat

Elena Borin, *INFN-LNL, Italy*
Anna D'Este, *INFN-LNL, Italy*

Correspondence Address

HIAT 2009
INFN - Laboratori Nazionali di Legnaro
Viale dell'Università 2, 35020 Legnaro (Padova) ITALY
phone: +39 049 8068 310 - Fax: +39 049 8068 829
E-mail: hiat09@lnl.infn.it
Conference web page: <http://hiat09.lnl.infn.it/>

Conference Address

Centro Culturale Don Orione Artigianelli
Zattere Dorsoduro 909/A
30123 Venezia (Italy)
Phone: +39 041 5224 077 - Fax +39 041 528 6214
E-mail: info@donorione-venezia.it



Heavy Ion Accelerator Technology

June 8-12, 2009 - Venezia (Italy)

<http://hiatog.lnl.infn.it> – e-mail: hiatog@lnl.infn.it

LIST OF PARTICIPANTS

Alessi	James	Brookhaven National Laboratory	Upton, NY	USA
Alpat	Ali Behcet	INFN - Perugia	Perugia	ITALY
An	Dong Hyun	Korea Institute of Radiological and Medical Sciences	Seoul	KOREA
Andrighetto	Alberto	INFN - Laboratori Nazionali di Legnaro	Legnaro	ITALY
Ashenfelter	Jeff	Yale University	New Haven, CT	USA
Baelde	Jean-Louis	GANIL	Caen	FRANCE
Battistella	Andrea	INFN - Laboratori Nazionali di Legnaro	Legnaro	ITALY
Beck	Ludwig	Maier-Leibnitz-Laboratorium Beschleunigerlabor	Garching	GERMANY
Becker	Reinard	IAP, Universität Frankfurt	Frankfurt/Main	GERMANY
Bedau	Jürgen	Bruker Biospin SA	Wissembourg	FRANCE
Bignami	Gaetano	Oltrebase srl	Milano	ITALY
Bisoffi	Giovanni	INFN - Laboratori Nazionali di Legnaro	Legnaro	ITALY
Bollen	Georg	Michigan State University	East Lansing	USA
Bongiovanni	Stefano	Strumenti Scientifici CINEL srl	Vigonza	ITALY
Borisov	Oleg	Joint Institute for Nuclear Research (JINR)	Dubna	RUSSIA
Bousonville	Michael	GSI, Darmstadt	Darmstadt	GERMANY
Burgun	Gérard	Bruker Biospin SA	Wissembourg	FRANCE
Canella	Stefania	INFN - Laboratori Nazionali di Legnaro	Legnaro	ITALY
Carletti	Enrico	Ion Beam Applications SA	Louvain-la-Neuve	BELGIUM
Carlucci	Davide	INFN - Laboratori Nazionali di Legnaro	Legnaro	ITALY
Cavenago	Marco	INFN - Laboratori Nazionali di Legnaro	Legnaro	ITALY
Chautard	Frédéric	CNRS	Caen	FRANCE
Cherenshchykov	Sergiy	NSC KIPT, Kharkov	Kharkov	UKRAINE
Corniani	Giorgio	Ettore Zanon SpA	Schio	ITALY
Cossutta	Ludovico	Università di Padova	Padova	ITALY
Dahl	Ludwig	Gesellschaft für Schwerionenforschung mbH	Darmstadt	GERMANY
Deambrosio	Silvia M.	INFN - Laboratori Nazionali di Legnaro	Legnaro	ITALY
Dobrescu	Serban	IFIN-HH	Magurele-Ifov	ROMANIA
Doleans	Marc	NSCL, Michigan State University	East Lansing	USA
Duppich	Jürgen	Paul Scherrer Institut	Villigen	SWITZERLAND
Dupont	Claude	Ion Beam Applications SA	Louvain-la-Neuve	BELGIUM
Ene	Daniela	Commisariat à l'Énergie Atomique	Gif-sur-Yvette	FRANCE
Esposito	Juan	INFN - Laboratori Nazionali di Legnaro	Legnaro	ITALY
Fagotti	Enrico	Consorzio RFX & INFN - Laboratori Nazionali di Legnaro	Legnaro	ITALY
Festa	Mauro	Ettore Zanon SpA	Schio	ITALY
Furukawa	Takuji	National Institute of Radiological Sciences	Chiba-city	JAPAN
Galata'	Alessio	INFN - Laboratori Nazionali di Legnaro	Padova	ITALY
Grespan	Francesco	Università di Milano and CERN		ITALY
Grieser	Manfred	Max-Planck-Institut für Kernphysik Heidelberg	Heidelberg	GERMANY
Gulbekyan	Georgij	JINR, Dubna	Dubna	RUSSIA
Gupta	Anit Kumar	Tata Institute of Fundamental Research	Mumbai	INDIA
Hahn	Garam	Korea Institute of Radiological and Medical Sciences	Seoul	KOREA
Hatanaka	Kichiji	Osaka University, Research Center for Nuclear Physics	Ibaraki, Osaka	JAPAN
Hegelich	B. Manuel	LANL, USA and LMU Munich	Munich	GERMANY
Hofmann	Ingo	GSI, Darmstadt	Darmstadt	GERMANY
Hottenbacher	Johannes	RI Research Instruments GmbH	Bergisch Gladbach	GERMANY
Hug	Eugen	Paul Scherrer Institut	Villigen	SWITZERLAND
Inaniwa	Taku	National Institute of Radiological Sciences	Chiba	JAPAN
Ito	Seiji	Dept. of Nuclear Engineering and Management, Tokyo University	Tokyo	JAPAN
Ivanenko	Ivan	JINR, Dubna	Dubna	RUSSIA
Kamigaito	Osamu	Nishina Center, RIKEN	Wako-shi, Saitama	JAPAN



Heavy Ion Accelerator Technology

June 8-12, 2009 - Venezia (Italy)

<http://hiat09.inl.infn.it> – e-mail: hiat09@inl.infn.it

LIST OF PARTICIPANTS

Kanjilal	Dinakar	Inter-University Accelerator Centre (IUAC)	New Delhi	INDIA
Kato	Yushi	Osaka University	Suita-shi, Osaka	JAPAN
Kester	Oliver	NSCL, Michigan State University	East Lansing	USA
Kinross-Wright	John	Diversified Technologies, Inc.	Bedford, MA	USA
Koivisto	Hannu	University of Jyväskylä Department of Physics	Jyväskylä	FINLAND
Krauth	Helmut	BRUKER	Hanau	GERMANY
Kravchuk	Leonid	Institute for Nuclear Research RAS	Moscow	RUSSIA
Kulevoy	Timur V.	Institute for Theoretical and Experimental Physics	Moscow	RUSSIA
Lagniel	Jean-Michel	GANIL	Caen	FRANCE
Lamy	Thierry	LPSC - UJF, Grenoble	Grenoble	FRANCE
Laxdal	Robert	TRIUMF	Vancouver	CANADA
Lechartier	Michel	GANIL	Caen	FRANCE
Leitner	Daniela	Lawrence Berkeley National Laboratory	Berkeley	USA
Leitner	Matthaeus	Lawrence Berkeley National Laboratory	Berkeley	USA
Letourmel	Michel	Vivirad SA	Handschuheim	FRANCE
Libralato	Mirko	INFN - Laboratori Nazionali di Legnaro		ITALY
Liu	Yong	Institute of Modern Physics Chinese Academy of Sciences	Lanzhou	CHINA
Lombardi	Augusto	INFN - Laboratori Nazionali di Legnaro	Legnaro	ITALY
Maggiore	Mario	INFN - Laboratori Nazionali del Sud	Catania	ITALY
Malyshev	Oleg	ASTeC, STFC Daresbury Laboratory	Daresbury	UNITED KINGDOM
Manzolaro	Mattia	INFN - Laboratori Nazionali di Legnaro	Legnaro	ITALY
Moisio	Maria Francesca	INFN - Laboratori Nazionali di Legnaro	Legnaro	ITALY
Montaño	Jacobo	INFN - Laboratori Nazionali di Legnaro	Legnaro	ITALY
Mustafin	Edil	GSI, Darmstadt	Darmstadt	GERMANY
Naab	Fabian	University of Michigan	Ann Arbor	USA
Nanal	Vandana	Tata Institute of Fundamental Research	Mumbai	INDIA
Napoli	Daniel Ricardo	INFN - Laboratori Nazionali di Legnaro	Legnaro	ITALY
Noda	Akira	Institute for Chemical Research, Kyoto University	Uji-city	JAPAN
Noda	Koji	National Institute of Radiological Sciences	Chiba	JAPAN
Nolen	Jerry	Argonne National Laboratory	Argonne	USA
Osa	Akihiko	Japan Atomic Energy Agency	Tokai, Ibaraki	JAPAN
Osswald	Francis	IPHC (CNRS/IN2P3/Strasbourg University)	Strasbourg	FRANCE
Ostroumov	Peter	Argonne National Laboratory	Argonne	USA
Palancher	Hervé	CEA-Cadarache Department for Fuel Studies	Saint Paul lez Durance	FRANCE
Palmieri	Antonio	INFN - Laboratori Nazionali di Legnaro	Legnaro	ITALY
Pardo	Richard C.	Argonne National Laboratory	Argonne	USA
Parravicini	Anna	Fondazione CNAO	Pavia	ITALY
Pasini	Matteo	CERN	Geneve	SWITZERLAND
Perrot	Luc	IN2P3-CNRS, Institut de Physique Nucléaire	Orsay	FRANCE
Pisent	Andrea	INFN - Laboratori Nazionali di Legnaro	Legnaro	ITALY
Porcellato	Anna Maria	INFN - Laboratori Nazionali di Legnaro	Legnaro	ITALY
Posocco	Piero Antonio	INFN - Laboratori Nazionali di Legnaro	Legnaro	ITALY
Prete	Gianfranco	INFN - Laboratori Nazionali di Legnaro	Legnaro	ITALY
Puglierin	Gabriele	INFN - Laboratori Nazionali di Legnaro	Legnaro	ITALY
Repnov	Roland	Max-Planck-Institut für Kernphysik, Heidelberg	Heidelberg	GERMANY
Rifuggiato	Danilo	INFN - Laboratori Nazionali del Sud	Catania	ITALY
Roncolato	Carlo	INFN - Laboratori Nazionali di Legnaro	Legnaro	ITALY
Rossato	Dimitri	ECOR Research		ITALY
Roy	Amit	Inter-University Accelerator Centre	New Delhi	INDIA
Sakamoto	Naruhiko	Nishina Center, RIKEN	Wako, Saitama	JAPAN
Sasa	Kimikazu	Tandem Accelerator Complex, University of Tsukuba	Tsukuba, Ibaraki	JAPAN
Sauge	Xavier	SDMS la Chaudronnerie Blanche	St Romans	FRANCE
Scarpa	Fabio	INFN - Laboratori Nazionali di Legnaro	Legnaro	ITALY
Schippers	Jacobus Maarten	Paul Scherrer Institut	Villigen	SWITZERLAND



Heavy Ion Accelerator Technology

June 8-12, 2009 - Venezia (Italy)

<http://hiat09.inl.infn.it> – e-mail: hiat09@inl.infn.it

LIST OF PARTICIPANTS

Senecal	Gilles	GANIL	Caen	FRANCE
Schmidt	Thomas	FuG Elektronik GmbH	Rosenehim	GERMANY
Shen	Hong tao	China Institute of Atomic Energy	Beijing	CHINA
Spingler	David	Florida State University	Tallahassee	USA
Stark	Sergey	INFN - Laboratori Nazionali di Legnaro	Legnaro	ITALY
Synal	Hans-Arno	ETH Zurich	Zurich	SWITZERLAND
Syresin	Evgeny	JINR, Dubna	Dubna	RUSSIA
Tabacaru	Gabriel	Cyclotron Institute, Texas A&M University	College Station	USA
Tamura	Jun	Tokyo Institute of Technology	Tokyo	JAPAN
Tarvainen	Olli	University of Jyväskylä, Department of Physics, Accelerator Laboratory	Jyväskylä	FINLAND
Tranquille	Gerard	CERN	Geneva	SWITZERLAND
Variante	Vincenzo	INFN - Bari	Valenzano (BA)	ITALY
von Hahn	Robert	Max-Planck-Institut für Kernphysik, Heidelberg	Heidelberg	GERMANY
Vondrasek	Richard	Argonne National Laboratory	Argonne	USA
Watanabe	Tamaki	RIKEN, The Institute of Physical and Chemical Research	Wako-shi, Saitama	JAPAN
Weisser	David	Australian National University	Canberra	AUSTRALIA
Wenander	Fredrik	CERN	Geneva	SWITZERLAND
Yamada	Kazunari	Nishina Center, RIKEN	Wako, Saitama	JAPAN
Yaramyshev	Stepan	GSI, Darmstadt	Darmstadt	GERMANY
Yim	Heejoong	Korea Institute of Radiological and Medical Sciences	Seoul	KOREA
Zhabitsky	Vyacheslav	JINR, Dubna	Dubna	RUSSIA
Zinkann	Gary	Argonne National Laboratory	Argonne, Illinois	USA
Zschornack	Günter	Technische Universität Dresden, Institute of Applied Physics	Dresden	GERMANY



11th International Conference on
Heavy Ion Accelerator Technology
June 8-12, 2009 - Venezia (Italy)

Scientific Program

SUNDAY 07 June 2009

SALA PALLADIO

17:00 – 19:00 **Registration**

MONDAY 08 June 2009

AULA MAGNA

Session GENERAL TOPICS

Chair: G. Bisoffi

09:00 – 09:30 **Opening**

09.30 – 10:00 **Nuclear Physics Perspectives with next-generation RNB Facilities** 5
G. Bollen, Michigan State University, USA

Session RADIOACTIVE ION BEAMS FACILITIES

Chair: G. Bisoffi

10:00 – 10:30 **Complementarity of new RNB Facilities and their Technological Challenges** 5
J. Nolen, Physics Division, Argonne National Laboratory, USA

10:30 – 11:00 **Coffee break - Sala Vivaldi**

Session RADIOACTIVE ION BEAMS FACILITIES

Chair: R. Laxdal

11:00 – 11:30	The RI beams from the Tokai Radioactive Ion Accelerator Complex (TRIAC)	6
	A. Osa, Japan Atomic Energy Agency, Japan	
11:30 – 11:50	ReA3, the new reaccelerated beam facility at MSU/NSCL	6
	M. Doleans, National Superconducting Cyclotron Laboratory, USA	
11:50 – 12:10	First Beam Tests of the ²⁵²Cf CARIBU Project	7
	R. Pardo, Argonne National Laboratory, USA	
12:10 – 12:30	Operational experience with the EXCYT facility	7
	D. Rifuggiato, INFN/LNS, Italy	
12:30 – 12:50	The SPES project: an ISOL facility for exotic beams	8
	G. Prete, INFN/LNL, Italy	
12:50 – 13:10	The SPES Project: research and development for the multi-foil direct target	8
	M. Manziolaro, INFN/LNL, Italy	
13:10 – 14:40	Lunch - San Trovaso Restaurant	

Session RADIOACTIVE ION BEAMS FACILITIES

Chair: O. Kester

14:40 – 15:10	Radiological safety aspects of the design of the RNB facilities	9
	D. Ene, CEA, IRFU/SPhN, France	
15:10 – 15:30	Progress on the commissioning of Radioactive Isotope Beam Factory at RIKEN Nishina Center	9
	K. Yamada, RIKEN Nishina Center, Japan	
15:30 – 15:50	Intensity-upgrade plans of RIKEN RI-beam factory	10
	O. Kamigaito, RIKEN Nishina Center, Japan	
15:50 – 16:10	The refinement of REX-ISOLDE	10
	F. Wenander, CERN, Switzerland	
16:10 – 16:30	Building design for high beam-power facilities, the example of SPIRAL2	11
	J.M. Lagniel, GANIL, France	
16:30 – 17:00	Coffee break - Sala Vivaldi	
17:00 – 18:30	POSTER SESSION – Cloister	
19:00 – 21:00	Welcome Reception – Cloister	

TUESDAY 09 June 2009

AULA MAGNA

Session ELECTROSTATIC ACCELERATORS

Chair: F. Osswald

- 09:00 – 09:30 **Present and Future of Electrostatic Accelerators** 12
D. Weisser, *Department of Nuclear Physics, Research School of Physics and Engineering, Australian National University, Australia*
- 09:30 – 09:50 **Upgrade of the Bucharest FN Tandem Accelerator** 12
S. Dobrescu, *National Institute for Physics and Nuclear Engineering (IFIN-HH), Romania*
- 09:50 – 10:10 **Development Activities at BARC-TIFR Pelletron Accelerator Facility** 13
A.K. Gupta, *Nuclear Physics Division, BARC, India*
- 10:10 – 10:30 **Maier-Leibnitz-Laboratorium - Tandem operation and experiments** 13
L. Beck, *Maier-Leibnitz-Laboratorium / Beschleunigerlabor, Germany*

10:30 – 11:00

Coffee break - Sala Vivaldi

Session ELECTROSTATIC ACCELERATORS

Chair: D. Rifuggiato

- 11:00 – 11:20 **"DIANA" - a new, deep-underground accelerator facility for astrophysics experiments** 14
M. Leitner, *Lawrence Berkeley National Laboratory, USA*
- 11:20 – 11:40 **Progress of an accelerator mass spectrometry system on the TSUKUBA 12UD Pelletron Tandem accelerator** 14
K. Sasa, *University of Tsukuba, Japan*

Session CIRCULAR ACCELERATORS

Chair: D. Rifuggiato

- 11:40 – 12:10 **Operation status of High Intensity Ion Beams at GANIL** 15
F. Chautard, *CNRS, France*
- 12:10 – 12:30 **Status report and future development at FLNR JINR heavy ions accelerator complex** 15
G. Gulbekian, *JINR, Russia*
- 12:30 – 12:50 **RCNP cyclotron facility** 16
K. Hatanaka, *Research Center for Nuclear Physics, Osaka University, Japan*
- 12:50 – 13:10 **RF Sytem for Heavy Ion Cyclotrons at RIKEN RIBF** 16
N. Sakamoto, *Nishina Center, RIKEN, Japan*

13:10 – 14:40

Lunch - San Trovaso Restaurant

Session CIRCULAR ACCELERATORS

Chair: A. Noda

14:40 – 15:00	<i>A novel design of a cyclotron-based accelerator system for multi-ion-therapy</i> 17 J. M. Schippers, <i>Paul Scherrer Institute, Switzerland</i>
15:00 – 15:20	<i>Design study of the medical cyclotron SCENT300</i> 17 M. Maggiore, <i>INFN/LNS, Italy</i>
15:20 – 15:50	<i>HIRFL-CSR Commissioning Status</i> 18 Y. Liu, <i>Institute Modern Physics, Chinese Academy of Sciences, China</i>
15:50 – 16:10	<i>Acceleration, Deceleration and Bunching of Stored and Cooled Ion Beams at the TSR, Heidelberg</i> 18 M. Grieser, <i>Max Planck Institut für Kernphysik, Germany</i>
16:10 – 16:30	<i>Status of the Cryogenic Storage Ring</i> 19 R. Von Hahn, <i>Max Planck Institut für Kernphysik, Germany</i>
16:30 – 17:00	Coffee break - Sala Vivaldi

WEDNESDAY 10 June 2009

AULA MAGNA

Session APPLICATIONS AND ANCILLARY SYSTEMS

Chair: I. Hofmann

09:00 – 09:30	<i>Medical application of Hadrontherapy</i> 20 E. Hug, <i>Center for Proton Therapy at Paul Scherrer Institute, Switzerland</i>
09:30 – 10:00	<i>Review on HI Accelerators for Hadrontherapy</i> 20 K. Noda, <i>National Institute of Radiological Sciences, Japan</i>
10:00 – 10:30	<i>New and Improved AMS Facilities</i> 21 H.A. Synal, <i>Laboratory of Ion Beam Physics, ETH Zurich, Switzerland</i>
10:30 – 11:00	Coffee break - Sala Vivaldi

Session APPLICATIONS AND ANCILLARY SYSTEMS

Chair: R. Pardo

11:00 – 11:20	<i>The radiation assurance test facility at INFN-LNS Catania</i> 21 A. B. Alpat, <i>INFN/Perugia Section, Italy</i>
11:20 – 11:40	<i>Development of beam current monitor with HTS SQUID and HTS current sensor</i> 22 T. Watanabe, <i>The Institute of Physical and Chemical Research, Japan</i>

Session ION SOURCES

Chair: R. Pardo

- 11:40 – 12:10 **Latest developments in ECR Charge Breeders** 22
T. Lamy, *Laboratoire de Physique Subatomique et de Cosmologie, UJF Grenoble 1, CNRS/IN2P3, INPG, France*
- 12:10 – 12:30 **Initial Results of the ECR Charge Breeder for the ²⁵²Cf Fission Source Project (CARIBU) at ATLAS** 23
R. Vondrasek, *Argonne National Laboratory, USA*
- 12:30 – 12:50 **Ion beam cocktail development and ECR ion source plasma physics experiments at JYFL** 23
O. Tarvainen, *University of Jyväskylä, Department of Physics, Accelerator Laboratory, Finland*
- 12:50 – 13:10 **Metal ion beam and beam transmission development at JYFL** 24
H. Koivisto, *University of Jyväskylä, Department of Physics, Accelerator Laboratory, Finland*

13:10 – 14:40 **Lunch - San Trovaso Restaurant**

Session ION SOURCES

Chair: R. Repnow

- 14:40 – 15:00 **Superconducting ECR ion source development at LBNL** 24
D. Leitner, *Lawrence Berkeley National Laboratory, USA*
- 15:00 – 15:30 **A High-Performance Electron Beam Ion Source** 25
J. Alessi, *Collider-Accelerator Department, Brookhaven National Laboratory, USA*
- 15:30 – 15:50 **Acceleration of heavy ions generated by ECR and EBIS** 25
R. Becker, *IAP, Universität Frankfurt, Germany*
- 15:50 – 16:10 **Dresden electron beam ion sources: latest developments** 26
G. Zschornack, *Technische Universität Dresden, Institute of Applied Physics, Germany*
- 16:10 – 16:30 **Ion Sources at the Michigan Ion Beam Laboratory: Capabilities and Performance** 26
F. Naab, *University of Michigan, USA*

16:30 – 17:00 **Coffee break - Sala Vivaldi**

17:00 – 18:30 **POSTER SESSION – Cloister**

19:00 – 20:30 **Visit to St. Mark's Basilica**

AULA MAGNA

Session LINACS

Chair: D. Weisser

09:00 – 09:30	Heavy Ion Superconducting Linacs: new machines and new upgrades 27 R. Laxdal, TRIUMF, Canada
09:30 – 09:50	Commissioning of the ATLAS Upgrade Cryomodule 27 P. Ostroumov, Argonne National Laboratory, USA
09:50 – 10:10	Frequency Tuning and RF Systems for the ATLAS Energy Upgrade SC Cavities 28 G. Zinkann, Argonne National Laboratory, USA
10:10 – 10:30	Performances of the ISAC Heavy Ion Linacs 28 M. Marchetto, TRIUMF, Canada

10:30 – 11:00 **Coffee break - Sala Vivaldi**

Session LINACS

Chair: A. Roy

11:00 – 11:20	HIE-ISOLDE LINAC: Status of the R&D activities 29 M. Pasini, CERN, Switzerland
11:20 – 11:40	Development of heavy ion accelerator and associated systems 29 D. Kanjilal, Inter University Accelerator Centre (IUAC), India
11:40 – 12:00	Operational experience of the superconducting LINAC booster at Mumbai 30 V. Nanal, Tata Institute of Fundamental Research, India
12:00 – 12:20	Multiple charge state ion beam acceleration with an RFQ LINAC 30 J. Tamura, Tokyo Institute of Technology, Japan
12:20 – 12:40	Upgrade of the HIT Injector LINAC-Frontend 31 S. Yaramyshev, GSI, Germany
12:40 – 13:00	Status of linac beam commissioning for the Italian Hadron Therapy Center CNAO 31 P. A. Posocco, Consorzio RFX – INFN/LNL, Italy

13:00 – 14:30 **Lunch - San Trovaso Restaurant**

14:30 – 19:30 **Conference Tour - Venetian Islands**

19:30 – 22:30 **Conference Banquet - Locanda Cipriani**

FRIDAY 12 June 2009

AULA MAGNA

Session LINACS

Chair: O. Kamigaito

09:00 – 09:30	The GSI UNILAC Upgrade Program to Meet FAIR Requirements 32 <i>L. Dahl, GSI, Germany</i>
09:30 – 09:50	Status of Construction and Commissioning of the GSI HITRAP Decelerator 32 <i>O. Kester, NSCL, Michigan State University, USA</i>
09:50 – 10:10	Improved on line performance of the installed ALPI Nb sputtered QWRs 33 <i>A. M. Porcellato, INFN/LNL, Italy</i>
10:10 – 10:30	Operational experience in PIAVE-ALPI complex 33 <i>E. Fagotti, Consorzio RFX – INFN/LNL, Italy</i>
10:30 – 11:00	Coffee break - Sala Vivaldi

Session GENERAL TOPICS

Chair: J.M. Lagniel

11:00 – 11:30	Towards GeV Laser-driven ion acceleration 34 <i>B. M. Hegelich, Los Alamos National Laboratory, USA and Ludwig- Maximilian Universität München, Germany</i>
11:30 – 11:50	Laser accelerated ions and their potential use for therapy accelerators34 <i>I. Hofmann, GSI, Germany</i>
11:50 – 12:20	Heavy Ion Irradiation of Nuclear Reactor Fuel 35 <i>H. Palanchar, CEA, France</i>
12:20 – 12:40	HIAT09 Outlook <i>A. Roy, Inter – University Accelerator Centre, India</i>
12:40 – 13:00	Closing
13:00 – 14:30	Lunch - San Trovaso Restaurant
14:30 – 19:30	Visit to INFN - Laboratori Nazionali di Legnaro

LIST OF POSTER CONTRIBUTIONS

SESSION A: GENERAL TOPICS

- A 1 REFERENCE SIGNAL GENERATION WITH DIRECT DIGITAL SYNTHESIS FOR FAIR 39**
M. Bousonville
GSI, Germany
- A 2 OVERVIEW OF AR BEAM INDUCED DESORPTION FROM DIFFERENT MATERIALS
AT TSL 39**
O. Malyshev¹, M.C. Bellachioma², M. Bender³, H. Kollmus², A. Kraemer²,
H. Reich-Sprenger², M. Leandersson⁴, E. Hedlund⁵, L. Westerberg⁵, A. Krasnov⁶ and
B. Zajec⁷
¹ ASTeC, STFC Daresbury Laboratory, UK, ² GSI, Germany, ³ Ludwig-Maximilians-Universität
München, Germany, ⁴ KTH Physics, Sweden, ⁵ Uppsala University, Sweden, ⁶ BINP, Russia,
⁷ "Jozef Stefan" Institute, Svolenia
- A 3 PREPARATION OF THE IRRADIATION TEST AT CAVE HHD OF GSI DARMSTADT 40**
A. Plotnikov¹, E. Mustafin¹, E. Floch¹, E. Schubert¹, T. Seidl¹, A. Smolyakov² and
I. Strasik¹
¹ GSI, Germany, ² ITEP, Russia
- A 4 IRRADIATION OF SUPERCONDUCTING MAGNET COMPONENTS FOR FAIR 40**
E. Mustafin¹, L. Latysheva², E. Floch¹, A. Plotnikov¹, E. Schubert¹, T. Seidl¹,
A. Smolyakov³ and I. Strasik⁴
¹ GSI, Germany, ² INR RAS, Germany, ³ ITEP, Russia, ⁴ STU, Slovakia
- A 5 DEPTH-PROFILING OF THE RESIDUAL ACTIVITY INDUCED BY HIGH-ENERGY
URANIUM IONS IN THIN STAINLESS STEEL TARGET 41**
I. Strasik^{1*}, E. Mustafin¹, E. Floch¹, T. Seidl¹, A. Plotnikov¹, E. Schubert¹ and
A. Smolyakov¹
¹ GSI, Germany *on leave from FEI STU Bratislava, Slovakia

SESSION B: ELECTROSTATIC ACCELERATORS

- B 1 CURRENT STATUS REPORT OF RAPID, THE UNIVERSITY OF TOKYO 41**
S. Ito, A. Morita and H. Matsuzaki
*Department of Nuclear Engineering and Management, School of Engineering, The
University of Tokyo, Japan*

SESSION C: LINACS

- C 1 CONCEPTUAL DESIGN OF A RADIO FREQUENCY QUADRUPOLE FOR THE HEAVY-
ION MEDICAL FACILITY 42**
G. Hahn and D.H. An
Korea Institute of Radiological and Medical Science, Korea
- C 2 COMMISSIONING OF THE CNAO LEBT AND SOURCES 42**
A. Parravicini¹, S. Alpegiani¹, D. Bianculli¹, E. Bressi¹, G. Bazzano¹, J. Bossler¹,
G. Burato¹, G. Butella¹, M. Caldara¹, E. Chiesa¹, L. Falbo¹, A. Ferrari¹, M. Ferrarini¹,
F. Generani¹, F. Gerardi¹, L. Lanzavecchia¹, R. Monferrato¹, V. Mutti¹, M. Nodari¹,
G. Balbinot¹, M. Pezzetta¹, A. Portalupi¹, C. Priano¹, M. Pullia¹, S. Rossi¹, M. Scotti¹,

M. Spairani¹, E. Vacchieri¹, S. Vitulli¹, L. Frosini², G. Venchi², C. Biscari³, C. Sanelli³, L. Celona⁴, G. Ciavola⁴, S. Gammino⁴, F. Maimone⁴, C. Roncolato⁵, A. Reiter⁶ and B. Schlitt⁶

¹ CNAO Foundation, Italy, ² Dipartimento di Ingegneria Elettrica, Università di Pavia, Italy,

³ INFN/LNF, Italy, ⁴ INFN/LNS, Italy, ⁵ INFN/LNL, Italy, ⁶ GSI, Germany

C 3	BEAM DIAGNOSTICS IN THE CNAO INJECTION LINES COMMISSIONING	43
	G. Balbinot ¹ , J. Bosser ² , C. Biscari ³ , M. Caldara ¹ , E. Bressi ¹ , L. Lanzavecchia ¹ , M. Pullia ¹ , <u>A. Parravicini</u> ¹ and M. Spairani ¹	
	¹ CNAO Foundation, Italy, ² CERN, Switzerland, ³ INFN/LNF, Italy	
C 4	NDCX-II, A NEW INDUCTION LINEAR ACCELERATOR PROJECT FOR WARM DENSE MATTER RESEARCH	43
	<u>M. Leitner</u> ¹ , F. Bieniosek ¹ , A. Friedman ² , E. Gilson ³ , J. Kwan ¹ , G. Logan ¹ and W. Waldron ¹	
	¹ Lawrence Berkeley National Laboratory, USA, ² Lawrence Livermore National Laboratory, USA, ³ Princeton Plasma Physics Laboratory, USA	
C 5	DECELERATING HEAVY ION BEAMS USING THE ISAC DTL	44
	<u>M. Marchetto</u> , F. Yan and R. Laxdal	
	<i>TRIUMF, Canada</i>	
C 6	FABRICATION OF SUPERCONDUCTING NIOBIUM RESONATORS AT IUAC	44
	P.N. Potukuchi, K.K. Mistri, S.S.K. Sonti, J. Zacharias, A. Rai, D. Kanjilal and <u>A. Roy</u>	
	<i>Inter-University Accelerator Centre, India</i>	
C 7	UPGRADE OF THE CONTROL SYSTEM FOR THE ALPI CRYOGENIC DISTRIBUTION PLANT	45
	<u>S. Canella</u> , A. Beltramin, A. Calore, T. Contran, P. Modanese and F. Poletto	
	<i>INFN/LNL, Italy</i>	
C 8	WIDE BANDWIDTH, LOW COST SYSTEM FOR CAVITY MEASUREMENTS	45
	S. Stark	
	<i>INFN/LNL, Italy</i>	
C 9	DESIGN OF THE MEBT REBUNCHERS FOR THE SPIRAL 2 DRIVER	46
	M. Lechartier	
	<i>GANIL, France</i>	

SESSION D: CIRCULAR ACCELERATORS

D 1	DESIGN OF THE CENTRAL REGION OF THE NEW MULTI-PURPOSE CYCLOTRON U400R	46
	I. Ivanenko	
	<i>JINR, Russia</i>	
D 2	EXTRACTION OF THE HEAVY ION BEAM FROM THE CYCLOTRONS BY STRIPPING	47
	O. Borisov	
	<i>JINR, Russia</i>	
D 3	DESIGN STUDY OF THE INJECTION SYSTEM OF K120 SUPERCONDUCTING CYCLOTRON	47
	<u>D.H. An</u> , J. Kang and Y.S. Kim	
	<i>Korea Institute of Radiological and Medical Science, Korea</i>	

D 4	GANIL HIGH INTENSITY TRANSPORT SAFETY SYSTEM	48
	<i>G. Senecal, C. Jamet, P. Anger, T. Andre, J.L. Baelde, C. Doutressoulles, B. Ducoudret, E. Petit and E. Swartvagher GANIL, France</i>	
D 5	ELECTRON COOLING OF PB⁵⁴⁺ IONS IN LEIR	48
	<i>G. Tranquille Beams Department (BE), CERN, Switzerland</i>	
D 6	APPROACH TO 2 DIMENSIONAL LASER COOLING AND ITS OPTICAL OBSERVATION SYSTEM	49
	<i>A. Noda¹, M. Grieser², H. Souda³, H. Tongu³, M. Nakao³, A. Smirnov⁴, T. Shirai⁵ and K. Jinbo⁶ ¹ Institute for Chemical Research, Kyoto University, Japan, ² Max-Planck-Institute für Kernphysik, Germany, ³ ICR, Kyoto University, Japan, ⁴ JINR, Russia, ⁵ National Institute of Radiological Sciences, Japan, ⁶ Institute for Advanced Energy, Kyoto University, Japan</i>	
D 7	LATTICE STUDY OF A COMPACT SYNCHROTRON FOR CARBON THERAPY	49
	<i>H. Yim Korea Institute of Radiological and Medical Science, Korea</i>	
D 8	BEAM STABILITY IN SYNCHROTRONS WITH DIGITAL FILTERS IN THE FEEDBACK LOOP OF A TRANSVERSE DAMPER	50
	<i>V. Zhabitsky JINR, Russia</i>	
D 9	SIMULATION AND DESIGN OF THE COMPACT SUPERCONDUCTING CYCLOTRON C400 FOR HADRON THERAPY	50
	<i>E. Syresin¹, Y. Jongen², M. Abs², A. Blondin², W. Kleeven², S. Zarembo², D. Vandeplassche², V. Alexandrov¹, S. Gyrsky¹, G. Karamysheva¹, N. Kazarinov¹, S. Kostromin¹, N. Morozov¹, V. Romanov¹, N. Rybakov¹, A. Samartsev¹, E. Samsonov¹, G. Shirkov¹, V. Shvetsov¹ and A. Tusikov¹ ¹ JINR, Russia, ² Ion Beam Application, Belgium</i>	

SESSION E: ION SOURCES

E 1	FORMATION OF HIGH INTENSIVE RADIOACTIVE CARBON ION BEAMS IN THE ELECTRON STRING ION SOURCE	51
	<i>E. Syresin, D. Donets, E.D. Donets, E. E. Donets, V. Salnikov and V. Shutov JINR, Russia</i>	
E 2	SIMULATION AND DESIGN OF TUBULAR ELECTRON STRING ION SOURCE	51
	<i>E. Syresin¹, V. Drobin¹, D. Donets¹, E.D. Donets¹, E. E. Donets¹, A. Shabunov¹, Y. Shishov¹, A. Dubinov², R. Garipov² and I. Makarov² ¹ JINR, Russia, ² All-Russian Institute of Experimental Physics, Russia</i>	
E 3	LARGE BORE ECR ION SOURCE WITH CYLINDRICALLY COMB-SHAPED MAGNETIC FIELDS CONFIGURATION	52
	<i>Y. Kato, F. Sato and T. Iida Osaka University, Japan</i>	

E 4	NOVEL MODES OF VACUUM DISCHARGE IN MAGNETIC FIELD AS THE BASE FOR EFFECTIVE ION GENERATION	52
	S. Cherenshchikov <i>Institute of High Energy Physics and Nuclear Physics of National Science Center "Kharkov Institute of Physics and Technology", Ukraine</i>	
E 5	UPGRADE AND COMMISSIONING OF THE PIAVE-ALPI ECR INJECTOR AT LNL	53
	A. Galatà, M. Sattin, L. Bertazzo, S. Contran, A. Dainese, A. Lombardi, D. Maniero, M. Poggi, F. Scarpa and A. Facco <i>INFN/LNL, Italy</i>	
E 6	HIGH CURRENT ION SOURCES, BEAM DIAGNOSTICS AND EMITTANCE MEASUREMENT	53
	M. Cavenago ¹ , M. Comunian ¹ , E. Fagotti ¹ , T. Kulevoy ^{1,2} , S. Petrenko ^{1,2} and M. Poggi ¹ ¹ INFN/LNL, Italy, ² ITEP, Russia	

SESSION F: RADIOACTIVE ION BEAM FACILITIES

F 1	A SECONDARY RADIOACTIVE BEAM LINE SECTION FOR THE SPIRAL 2 PROJECT: FIRST STEP, THE DESIGN STUDY	54
	F. Osswald and A. Khouaja <i>CNRS/IN2P3, Uni. Strasbourg, France</i>	
F 2	HOLLOW CATHODE E-GUN FOR EBIS IN CHARGE BREEDING EXPERIMENT	54
	V. Variale ¹ , V. Valentino ¹ , M. Batasova ² , G. Kusnetsov ² , T. Clauser ³ and A. Rainò ³ ¹ INFN/Bari Section, Italy, ² BINP, Russia, ³ Bari University, Physics Department, Italy	
F 3	STUDY AND TEST ON THE 1+ ION SOURCE OF THE SPES PROJECT	55
	M. Libralato ¹ , M. Manzolaro ¹ , A. Andrighetto ¹ , L. Biasetto ¹ , G. Meneghetti ² , S. Carturan ¹ , D. Scarpa ¹ , P. Colombo ² and G. Prete ¹ ¹ INFN/LNL, Italy, ² University of Padua, Italy	
F 4	THE LIGHT ION GUIDE CB-ECRIS PROJECT AT THE TEXAS A&M UNIVERSITY CYCLOTRON INSTITUTE	55
	G. Tabacaru ¹ , H. L. Clark ¹ , G. Kim ¹ , D.P. May ¹ , F. Abegglen ¹ , G. Chubaryan ¹ , G. Souliotis ¹ , J. Arje ² ¹ Cyclotron Institute, Texas A&M University, USA, ² JYFL, Finland	
F 5	IRRADIATION CONTROL OF THE "SPIRAL1" TARGET BY MEASURING THE ION BEAM INTENSITY: "CICS" PROJECT	56
	P. Anger, J.L. Baelde, C. Doutressoulles, M. Ozille, J.F. Rozé, J.C. Deroy, B. Jacquot, M. Dubois, S. Faure, F. Bucaille and C. Mauger <i>GANIL, France</i>	

SESSION G: APPLICATIONS

G 1	A NEW ACCESS CONTROL UNIT FOR GANIL AND SPIRAL 2	56
	J.L. Baelde, C. Berthe and J.F. Rozé <i>GANIL, France</i>	

G 2	STATUS OF THE CAVIAR DETECTOR AT LISE-GANIL	57
	<u>L. Perrot</u> ¹ , S. Grévy ² , C. Houarner ² , R. Hue ² , C. Marry ² , S.M. Lukyanov ³ and R. Astabatyan ³	
	¹ IPN-IN2P3-CNRS, France, ² GANIL-IN2P3-CNRS, France, ³ JINR, Russia	
G 3	HEBT LINES FOR THE SPIRAL2 FACILITY	57
	<u>L. Perrot</u> ¹ , P. Bertrand ² , J.L. Biarrotte ¹ and D. Uriot ³	
	¹ IPN-IN2P3-CNRS, France, ² GANIL-IN2P3-CNRS, France, ³ SACM/IRFU/DSM/CEA, France	
G 4	DEVELOPMENT OF RASTER SCANNING SYSTEM AT NIRS-HIMAC	58
	<u>T. Furukawa</u> , T. Inaniwa, S. Sato, N. Saotome, T. Shirai, Y. Takei, S. Fukuda, S. Mori, A. Nagano, Y. Iwata, S. Minohara and K. Noda	
	National Institute of Radiological Sciences, Japan	
G 5	STATUS OF ELECTRON BEAM ION SOURCES FOR PARTICLE THERAPY	58
	<u>G. Zschornack</u> ¹ , V. Ovsyannikov ² , F. Grossmann ² , F. Ullmann ² , A. Schwan ² , E. Tanke ³ and P. Urschuetz ³	
	¹ Technische Universitaet Dresden, Institute of Applied Physics, Germany, ² DREEBIT GmbH Dresden, Germany, ³ Siemens AG Erlangen, Germany	
G 6	DEVELOPEMENT OF TREATMENT PLANNING SOFTWARE FOR CARBON-ION SCANNING AT HIMAC	59
	<u>T. Inaniwa</u> , T. Furukawa, S. Sato, S. Mori, N. Kanematsu, K. Noda and T. Kanai	
	National Institute of Radiological Sciences, Japan	
G 7	RESEARCH ON MEASUREMENT OF THE FISSION PRODUCT NUCLIDE ¹²⁶SN BY AMS	59
	<u>H. Shen</u> ¹ , S. Jiang ¹ , M. He ¹ , K.J. Dong ¹ , X. Wang ¹ , C. Li ¹ , G. He ¹ , D. Zhang ² , G. Shi ² , C. Huang ² , S. Wu ¹ , J. Gong ¹ , L. Lu ¹ , S. Li ² and S. Wu ¹	
	¹ China Institute of Atomic Energy, China	
	² College of Physical Science and Engineering Technology, Guangxi university, China	
G 8	ACCELERATOR MASS SPECTROMETRY FOR LONG-LIVED HEAVY ION ²³⁶U AT CIAE	60
	X. Wang, <u>H. Shen</u> , S. Wu, S. Jiang, M. He, Y. Bao, X. Guan, Y. Hu, Q. You, C. Li and W. Wang	
	China Institute of Atomic Energy, China	

THE RI BEAMS FROM THE TOKAI RADIOACTIVE ION ACCELERATOR COMPLEX (TRIAC)

A. Osa, S. Abe, T. Asozu, S. Hanashima, T. Ishii, N. Ishizaki, H. Kabumoto, K. Kutsukake, M. Matsuda, M. Nakamura, T. Nakanoya, Y. Otokawa, H. Tayama, Y. Tsukihashi, Japan Atomic Energy Agency (JAEA), Tokai, Japan
 S. Arai, Y. Fuchi, Y. Hirayama, N. Imai, H. Ishiyama, S.C. Jeong, H. Miyatake, K. Niki, M. Okada, M. Oyaizu, Y.X. Watanabe,
 High Energy Accelerator Research Organization (KEK), Tsukuba, Japan

Abstract

Tokai Radioactive Ion Accelerator Complex (TRIAC) is an ISOL-based radioactive nuclear beam (RNB) facility, connected to the ISOL in the tandem accelerator at Tokai site of Japan Atomic Energy Agency (JAEA). At JAEA-tandem accelerator facility, we can produce radioactive nuclei by means of proton induced uranium fission, heavy ion fusion or transfer reaction. Since TRIAC was opened for use in 2005, we have provided RNBs of fission products and ^8Li . For the production of ^8Li , we chose ^{13}C (^7Li , ^8Li) neutron transfer reaction by ^7Li primary beam and a 99% enriched ^{13}C sintered disk target. The release time of Li ions from the ^{13}C sintered target was measured to be 3.2 s. We are developing the RNB of ^9Li ($T_{1/2}=178$ ms) but the long release time caused a significant loss of the beam intensity. A boron nitride target which has fast release of Li is developed for ^9Li beam with intensity of 10^4 ions/s after separation by JAEA-ISOL.

INTRODUCTION

The tandem accelerator of Japan Atomic Energy Agency (JAEA-Tandem accelerator) has been operated since 1982 for studies of nuclear physics, nuclear chemistry, atomic/molecular physics, solid state physics and material science. A superconducting linac was built as a booster in 1994 to advance these studies. Since 2005, we have been operating an ISOL-based radioactive nuclear beam facility, Tokai Radioactive Ion Accelerator Complex (TRIAC), connected to the ISOL in JAEA-Tandem accelerator (JAEA-ISOL).

The total operational time of these accelerators for FY2008 (From April 1, 2008 to March 31, 2009) was 210 days. The total experimental proposal and the usage of the beam times for FY2008 are summarized in Table 1 and Table 2, respectively.

RNBs of fission products and ^8Li were supplied to TRIAC experiments for 23 days. Typical experiments are as follows:

- Measurement of Li diffusion coefficients in Li ionic conductors
- Search of highly excited state of ^{10}Be using deuteron elastic reaction to ^8Li
- R&D for JAEA-ISOL and TRIAC.

This report presents the upgrade of JAEA-Tandem facility and status of TRIAC, especially target-ion source system of JAEA-ISOL.

Table 1: Experimental Proposal

Proposals accepted by the program advisory committee:	
In house staff proposals	13
Collaboration proposals	33
Number of experiment proposed	60
Total numbers of scientists participating in research:	
from out side	258
in-house	251
Number of institutions presented	33

Table 2: Usage of Beam Times in Different Research Fields

Research field	Beam time	
	days	%
Nuclear physics	96	45.7
Nuclear chemistry	22	10.5
Atomic physics and material science	73	34.8
Accelerator development	19	9.0
total	210	

UPGRADE OF JAEA-TANDEM FACILITY

In recent years, we have maintained and upgraded some apparatus of the tandem accelerator and the booster. Main upgrade works are as follows:

- Replacement of acceleration tubes with compressed ones. These tubes were treated by high-pressure water jet rinse to improve the high-voltage performance [1]. At this time, we provide ion beams at the maximum terminal voltage of 18 MV.
- Replacement of 180-degree analysing magnet at the high-voltage terminal. We also realigned all beam optical devices in the terminal and have improved the transmission efficiency of ion beams to 2-3 times

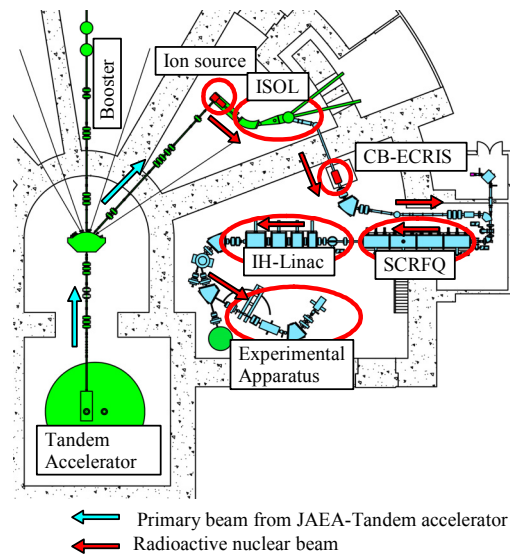


Figure 1: Layout of TRIAC.

and very close to 100 % for ions lighter than mass of about 40.

- Replacement of in-terminal ion source [2] to a permanent-magnet type 14.5 GHz ECR ion source, SUPERNANOGAN. Beam intensities were increased 3-5 times compared to the previous 10-GHz one. We have even accelerated Xe^{30+} from the high-voltage terminal.
- Treatment of degraded superconducting resonators by using high-pressure water jet rinse to recover acceleration electric fields (E_{acc}). The average of E_{acc} at RF power of 4.0 W improved from 4.96 MV/m to 6.53 MV/m.
- We fabricated a prototype low beta superconducting twin quarter wave resonator and carried out off-line test.

STATUS OF TRIAC

The layout of TRIAC is given in Figure 1. TRIAC is based on an isotope separator on line (ISOL) and the radioactive nuclei are produced via proton-induced fission of ^{238}U or heavy-ion reactions with the primary beams from the JAEA-Tandem accelerator. The produced radioactive nuclei are singly charged and mass-separated with the JAEA-ISOL. They are fed to the 18GHz electron cyclotron resonance ion-source for charge-breeding (CB-ECRIS), where the singly charged ions are converted to multi-charged ions. The charge-bred radioactive ions, usually with a mass to charge-state ratio of around 7 ($A/q \sim 7$), are extracted again and fed to the linear-accelerator (linac) complex for re-acceleration. The linac complex consisting of two linacs, a split-coaxial radio-frequency quadrupole (SCRFQ) linac and an interdigital-H (IH) linac, can accelerate the RNB to the energy necessary for experiments. The acceleration of the RNBs charge-bred by CB-ECRIS was the first time over the world and the overall efficiency of transmission of ISOL to experimental hall was about 2%. The basic parameters of TRIAC are summarized in Table 3.

Radioactive Ion Beam Facilities

Table 3: Basic Parameters of TRIAC

Primary Beam	Ion (energy/intensity)	p (34 MeV / 1 μ A) 7Li (68 MeV/300 p nA) ^{19}F (78 MeV/100 p nA), etc.
Prod. target		UCx, BN, Mo, etc.
ISOL	Ion source Mass resolution	FEBIAD, SI type 1200
Charge Breeder	Ion source Freq. / power	ECRIS 18 GHz / 1 kW
Linac Complex	Injection energy Output energy (var.)	2.1 keV/u 0.14-1.09 MeV/u
SCRFQ linac	Frequency output energy duty cycle	25.96 MHz 178.4 keV/u ($A/q \leq 28$) 100% ($A/q \leq 16$), 30% ($A/q = 28$)
IH linac	Frequency output energy duty cycle	51.92 MHz 0.14-1.09 MeV/u ($A/q \leq 9$) 100% ($A/q \leq 9$)

ISOTOPE SEPARATOR ON-LINE

Target-Ion Source System

Originally, the JAEA-ISOL is utilized for the study of decay properties of nuclei far from stability. To supply an intense RNB to the CB-ECRIS, we have developed two types of ion sources, surface ionization type ion source for ionization of alkali, alkaline earth and rare-earth elements and FEBIAD type one for ionization of gaseous and volatile elements. Additionally, we have developed a target-ion source system to produce medium-heavy neutron rich RNBs with proton-induced fission of ^{238}U and a thin-window ion source system for heavy-ion reaction products for each type. Using these ion sources, more than 100 isotopes of 21 elements have been ionized and mass-separated. [3]

A glassy graphite fiber was chosen as a base material for making a uranium carbide target for the target-ion source system. A typical uranium carbide target was prepared at a uranium density of 600-mg/cm² U. A target container was filled with glassy graphite fiber ($\phi = 11 \mu m$, GC-20, Tokai Carbon Co.) as the base material and uranyl nitrate solution was impregnated. After drying-out, the target was out-gassed and converted to oxide form at 600 °C in argon atmosphere before insertion into the ion source. The target is loaded to the ion source system and sintered as uranium carbide.

The surface ionization type target-ion source system was used for the production of neutron rich Rb, Sr, In, Cs and Ba ion beams. The uranium carbide target was bombarded with a 33-MeV proton beam (25 MeV on target) with intensity of about 1 μ A. A typical separation yield with this ion source was 1.8×10^7 ions/s for ^{93}Rb , 6×10^7 ions/s for ^{94}Sr , 2.5×10^6 ions/s for ^{143}Cs and 3×10^6 ions/s for ^{143}Ba ; the value was normalized to the uranium-target

thickness of 1 g/cm^2 and $1 \mu\text{A}$ primary proton beam current. Particular application of this ion source was separation of neutron rich ^AEu isotopes around $A \sim 160$. New isotopes $^{163,164,165,166}\text{Eu}$ have been identified with this ion source.

The forced electron beam induced arc-discharge (FEBIAD) ion source type-B2 with a uranium target container was used for the production of neutron rich Kr, Xe and volatile elements ion beams. A typical separation yield with this ion source was 1.4×10^6 ions/s for ^{91}Kr , 2.6×10^6 ions/s for ^{138}Xe , 5.2×10^6 ions/s for ^{123}In and 2.5×10^5 ions/s for ^{132}Sn ; the condition of normalization is same as the surface ionization type one.

Safety Handling System of Target-Ion Source Modules

In the ion sources, 2.6-g/cm^2 of ^{238}U is loadable maximum. We plan to produce the neutron-rich RNB by proton-induced fission with an intensity of $3 \mu\text{A}$ proton. After an irradiation for 5 days in this condition, the dose equivalent rate is estimated to be 40 mSv/h at 1 m from the ion source. Therefore, we have built a system of carrying and storing target-ion source in safety.

At the convenience of handling, the target-ion source system is united into one module with the irradiation vacuum housing. The target-ion source module is designed to a vacuum-tight by itself.

- The primary beam entrance port is sealed with $5\text{-}\mu\text{m}$ thick HARVAR foil.
- On the RNB extraction side of the housing, a pneumatic valve is installed and closed before carrying the module.
- Electric feed-throughs, gas and water connections are coupled to quick connectors.

This module could be handled by a remote carrying device and stored in a shielding cell to cool residual radioactivity. By use of this handling system, we can carry and store the target-ion source module without radioactive contamination around the irradiation area.

Development of Target-Ion source System

A short-lived isotope beam, ^9Li ($T_{1/2}=178 \text{ ms}$), is required with intensity of more than 5×10^3 ions/s on the target at the end of TRIAC to the study of highly-excited state of ^{11}Be . For the production of ^8Li ($T_{1/2}=838 \text{ ms}$), we have chosen ^{13}C (^7Li , ^8Li) neutron transfer reaction by ^7Li primary beam and a 99% enriched ^{13}C sintered disk target. The 99% enriched ^{13}C thick graphite disk was mounted to the catcher position of the surface ionization type ion source with $3\text{-}\mu\text{m}$ thick tungsten-window. The target was bombarded with a 67-MeV $^7\text{Li}^{3+}$ beam with intensity of about 100 pA . In this condition, the separation yield of ^8Li was evaluated to be 1×10^6 ions/s. However, the separation yield of ^9Li ($T_{1/2}=178 \text{ ms}$) was reduced to 10^2 ions/s. We thought that the long release time caused a significant loss of the ^9Li beam intensity. A release profile of Li from the target/catcher/ion-source system was measured using the heavy ion implantation

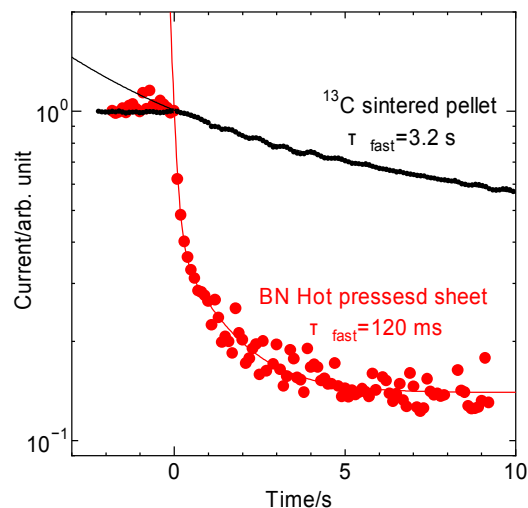


Figure 2: Release profile of Li from the surface ionization type ion source.

technique [6]. As shown in Figure 2, the fast component of release profile of Li ions from the ^{13}C sintered target was 3.2 s . In a search for high-temperature-resistant target material for the production of ^9Li , we found out that boron nitride (BN) has a short release time of Li; as shown in Figure 2, the fast component release profile was 120 ms . With a hot pressed BN sheet target, we obtained a ^9Li beam with an intensity of 10^4 ions/s after separation by JAEA-ISOL.

The FEBIAD-B2 type target-ion source has separation efficiencies of about 8% for long-lived In isotopes. However, the efficiencies depend strongly on the half-lives and decrease to about 0.4% for $^{129\text{m}+g}\text{In}$ ($T_{1/2}=1.29/0.59 \text{ s}$). This result consists with the long release time of In, $\tau = 7 \text{ s}$, at the target-ion source temperature of $1550 \text{ }^\circ\text{C}$. It is expected to accelerate diffusion, adsorption and effusion processes by raising the temperature of the target-ion source system; a short release time of In, $\tau=1.7 \text{ s}$, was achieved by the surface ionization type one at the temperature of $2100 \text{ }^\circ\text{C}$. [4] In the FEBIAD-B2 type, the target container is connected to a top of the target heating cathode capsule; the temperature reaches $1550 \text{ }^\circ\text{C}$. For the separation of short-lived isotopes around ^{132}Sn , the FEBAID-E type ion source [5] with a uranium target container has been newly developed [3]; the FEBIAD-E type ion source is operated at the temperature of $1700\text{-}2000 \text{ }^\circ\text{C}$. To raise the temperature of the target to $2000 \text{ }^\circ\text{C}$, it is heated by an electron bombardment from a couple of tungsten filaments surrounding the target container. An on-line test and preliminary separation yield search is performed. Measurements of release profiles of several elements are in progress.

OUTLOOK

Continuous upgrade enabled JAEA-Tandem facility to deliver a variety beams for experiments. Until now, TRIAC facility provides relatively weak intensity and low energy RNBs. However, we have produced good results

by using ^8Li beam which is a specialty of TRAIC facility. It is expected to allow further applications and progresses especially by use of the RNBs of medium-heavy neutron-rich isotopes. Development of the target-ion source system is one of the highest priority issues on operation of RNB facility. We will carry on the development for the facility.

REFERENCES

- [1] S. Takeuchi, T. Nakanoya, H. Kabumoto and T. Yoshida, Nucl. Instrum. and Methods A 513 (2003) 429.
- [2] M. Matsuda, C. Kobayashi and S. Takeuchi, Proc. of 8th Inter. Conf. on Heavy Ion Accelerator Technology, p.65-76 (1998).
- [3] A. Osa, S. Ichikawa, M. Matsuda, T.K. Sato and S.C. Jeong, Nucl. Instrum. Methods B 266 (2008) 4394.
- [4] A. Osa, S. Ichikawa, M. Matsuda, T.K. Sato and S.C. Jeong, Nucl. Instrum. Methods B 266 (2008) 4373.
- [5] R. Kirchner, K. H. Burkard, W. Hüller and O. Klepper, Nucl. Instrum. and Methods 186 (1981) 295.
- [6] R. Kirchner, Nucl. Instrum. Methods. B 70 (1992) 186.

OPERATIONAL EXPERIENCE WITH THE EXCYT FACILITY

D. Rifuggiato, L. Calabretta, L. Celona, F. Chines, L. Cosentino, G. Cuttone, P. Finocchiaro, A. Pappalardo, M. Re, A. Rovelli
 Istituto Nazionale di Fisica Nucleare, Laboratori Nazionali del Sud, Catania, Italy

Abstract

The EXCYT project has successfully come to conclusion at the end of 2006. As a consequence a new facility for production and acceleration of radioactive ion beams is now available at Laboratori Nazionali del Sud, Catania. This facility is based on the ISOL method: in particular the primary beam is delivered by a Superconducting Cyclotron, while the secondary beam is post-accelerated by a Tandem. A low energy radioactive beam is also available at the exit of the pre-injector. The main features of the commissioning of the facility will be described. Details will be given on the characteristics of the diagnostic devices. Future development activities are related both to the operative features of the new facility and to the improvements and upgrading that are planned to be introduced in the near future. All of these subjects will be extensively discussed.

INTRODUCTION

The layout of the INFN-LNS with the scheme of the EXCYT facility is shown in Fig. 1.

The EXCYT facility is able to produce beams with high purity, but the role of the Tandem as a post-accelerator implies that the recoils produced in the reaction between the primary beam and the target must be ionized negatively in order to be accelerated by the Tandem.

The commissioning of the EXCYT facility started in the first months of 2005 and a detailed description of the facility together with the commissioning phases are extensively reported in [1].

For the commissioning case, the production of the radioactive ions is performed by injecting a $^{13}\text{C}^{4+}$ primary beam of 45 AMeV on a graphite target up to a beam power of 150 W, while the ionisation of ^8Li is achieved by a Tungsten positive surface ioniser. For such a kind of ion beam, the highest extraction efficiency from the TIS is obtained by positive ionisation. Then the post-acceleration with the Tandem is possible only after a charge exchange cell (CEC) to obtain negative ions. The CEC consists of a cell containing Cesium vapours, which interact with the ^8Li beam converting its charge from +1 to -1 by a two step reaction. The Li^+ beam has been produced at different energies to cross-check the transmission efficiency together with the charge exchange efficiency.

The maximum ^{13}C primary beam intensity was 1 μA which corresponds to a beam power of 147W leading to a production yield of 9×10^6 pps of ^8Li . Table 1 summarizes the production yields at the entrance of the first stage of isobaric separation. The yields of ^9Li and ^{21}Na are also reported even if measured in not optimized conditions.

Table 1: ^8Li , ^9Li and ^{21}Na Measured Yields at the Entrance of First Stage of Isobaric Separation

Beam	Beam Power	Intensity
^8Li	147 W	$9 \cdot 10^6$ pps
^9Li	82 W	$3.4 \cdot 10^5$ pps
^{21}Na	82 W	$3.7 \cdot 10^5$ pps

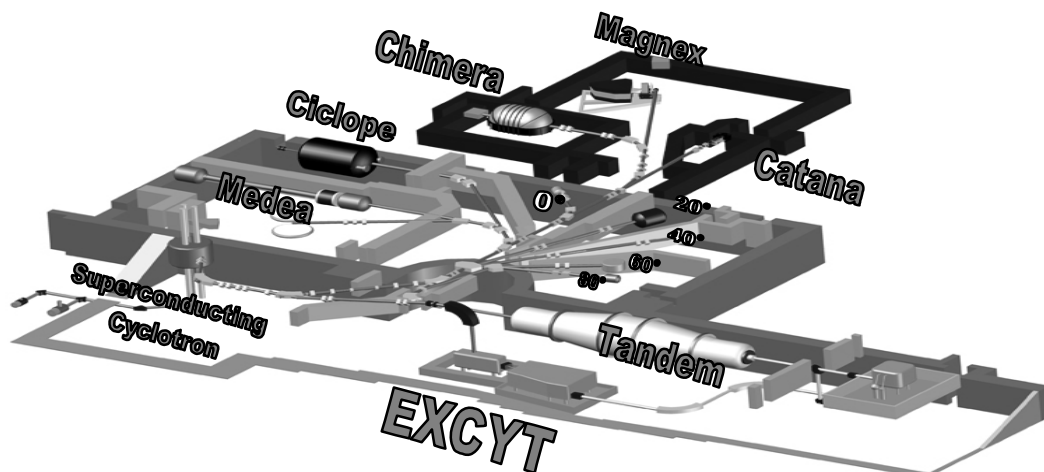


Figure 1: The layout of INFN-LNS with the Excyt facility for the production of radioactive beams.

THE PRIMARY DRIVER

The LNS Superconducting Cyclotron is the primary accelerator of EXCYT. It is a three sectors compact machine with a typical extraction efficiency of 30-50%. The high intensity operations have been made possible by some modifications of the electrostatic deflectors and beam diagnostics.

The first modification was the installation of a cooling circuit on the first electrostatic deflector, Fig. 2, assembled in the rear part of the housing, which provided indirect cooling of the septum, the ground element where a big part of the accelerated beam is lost.

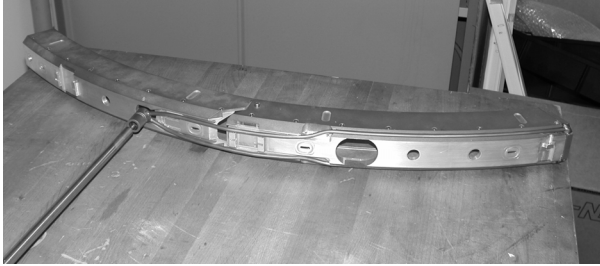


Figure 2: Water cooling circuit assembled in the rear part of the deflector housing.

At the same time, it was necessary to upgrade also the main probe, so as to have a diagnostic device able to measure intense beams. The original probe, designed for not intense beams, was replaced by a water cooled one.

With this equipment, it was possible to extract a $^{13}\text{C}^{4+}$ 45 AMeV beam with a power of 100 watt.

To go beyond 100 watt, it was decided to introduce further modifications to the electrostatic deflector in order to improve its reliability: a new housing was realized with a new cooling circuit, allowing the septum to be directly cooled, as shown in Fig. 3. Moreover the septum material was changed from tantalum to tungsten, which ensures a better thermal exchange. Finally, the septum thickness was increased from 0.15 to 0.3 mm, which ensures a better mechanical stability under thermal stresses. With these modifications, an extraction efficiency of 63% was obtained and a 150 watt beam was extracted in a quite reliable way.

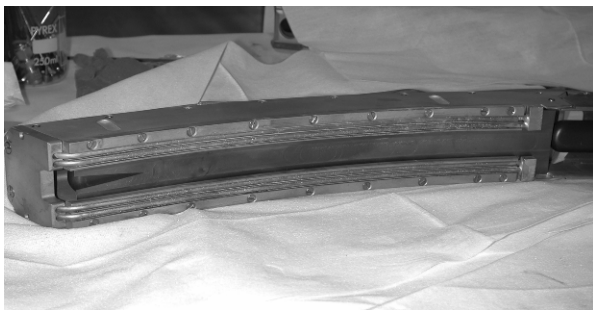


Figure 3: New deflector provided with direct cooling of the septum.

In order to reach the objective set by EXCYT, namely a beam power of 500 watt, it is wise to search for an

Radioactive Ion Beam Facilities

increased extraction efficiency. This could be achieved by improving the beam formation at the source exit and realizing a better matching between the source and the cyclotron. The immediate result would be an increased injection efficiency, allowing for the possibility of cutting particles out of the machine acceptance. Beam tests will soon be accomplished to study the problem.

STATUS OF THE EXCYT FACILITY

The production yield of the radioactive nuclear beam (RNB) depends on many factors such as: primary beam parameters (element, energy, intensity), target material (nuclear cross-section, operating temperature), target structure (diffusion mechanism), container geometry (effusion to the ionizer), ionizer type (ionization mechanism and efficiency), charge exchange efficiency, transport efficiency, isobaric separation and post-acceleration efficiency.

Target Ion Source Complex

The graphite made target is enclosed in a Ta container and heated by a surrounding electrical heater. The recoils produced in the target will effuse through the transfer tube to the ionizer, where they are ionized by an ISOLDE-type ion source and then extracted by an acceleration voltage up to 50 kV. The sources available for the TIS are the Hot Plasma Ion Source (HPIS), which is suitable to ionize positively many elements, included noble gases with an efficiency of about 1%, and the surface ionization type sources for positive and negative ion production. The positive one (PIS) is particularly suitable for alkaline ions for which it is highly selective and efficient, while the negative one (NIS) is indicated for halogens with exception of fluorine. The source presently used is the PIS (efficiency measurements indicate a ionization rate around 70% for Lithium beam) [2].

The selection of our target material has been done following the criteria of high porosity, small grain size, high thermal conductivity, high chemical purity, high melting point and low vapour pressure.

Experimental results indicate the UTR146 graphite from XYCarb as the best target material for our facility [3]. Taking into account the Superconducting Cyclotron (CS) operational diagram, the ^8Li demand and the target material, we selected $^{13}\text{C}^{4+}$, 45 AMeV ion as a primary beam. In this energy range $^{8,9}\text{Li}$ are essentially produced both by target and projectile fragmentation: EPAX code simulations indicate the nuclear cross-section for $^{8,9}\text{Li}$ production to be 3.41 mb and 4.25 mb respectively [4].

The first target prototype used for the preliminary test at SPIRAL in Ganil and at LNS during March 2006 is shown in [5].

It consists of two parts: the upper tablet and the lower part which acts also as mechanical support. The transfer tube to the ionizer is located in between these two parts. Sizes were chosen to maximize the Li collection.

At the operating temperature of 2600 K, many diffusion mechanisms are active inside the target: Li particles will mainly diffuse through interstices in graphite. Once the

particle reaches the grain boundary it can diffuse in a neighbour grain or effuse in the target porosity.

Moreover at this temperature, after the effusion process through the porosity, the probability of re-diffusion inside a grain is quite high. For this reason we performed some computer simulations using a very simple, mono-dimensional modified form of Fick's law to reproduce the ^8Li production efficiency measured at LNS. It turned out a large value of the diffusion coefficient, thus confirming the good features of this target.

In particular the simulations suggest that only the ^8Li particles produced within the first hundreds of microns are able to reach the target surface before their decay, ^8Li atoms produced deeper will decay during their path inside the target and will never be collected.

These considerations led the decision to modify the target design by employing ten, uniformly spaced, 1 mm thick, graphite disks (see Fig. 4). An increase of a factor 6 on the ^8Li production yield was then expected.

An increment of a factor 3.6 has been found, which is not far from the foreseen factor 6, this reduction being probably due to a different temperature distribution in the new target design. These values are very promising for the future when the beam power will be increased up to 500 W. Further investigations are planned to better understand the Li release mechanism from the target. Other target candidate materials such as fibres, felts and nano-structured materials are taken into consideration.

Charge Exchange Cell

The charge exchange cell (CEC) is a vacuum chamber containing cesium vapours at a variable temperature, in which Li^+ ions, extracted from the ion source, are transformed into negative ones by interaction with the Cesium atoms.

The CEC device and the efficiency measurement procedure have already been described [6]. The charge exchange consists of a two step process, the first of which is energetically supported (exothermic) while the second is not (endothermic). Cesium was chosen because of its low ionization energy. Other alkaline elements exhibit bigger values reducing the CEC efficiency. The CEC efficiency strongly depends on the energy of the Li^+ extracted from the TIS: the lower the Li energy the higher the CEC efficiency. The maximum efficiency in this case lies at about 5 keV [6].

The beam optics elements have been originally designed to operate at a typical extraction energy of 15-20 keV. Strong efforts were dedicated to improve the beam transmission at the lowest suitable RNB extraction energy. This value was fixed at 8-10 keV as a good compromise between a good transmission and CEC efficiency. On-line measurements confirm the expectations: the CEC efficiency for ^8Li at 10 keV is 3.4%, very close to the expected value of 3.6%.

Diagnostics

The facility is equipped with beam diagnostics, allowing to acquire in real time all necessary beam



Figure 4: New target geometry.

parameters (the beam position, the shape and the intensity) for the tuning, and also to identify the transported radionuclides. Along the beam pipe before the Tandem, we have installed the LEBI (Low Energy Beam Imager/Identifier) devices, that allow to visualize the 2D profile of radioactive and stable beams, to measure the beam intensity and to perform the nuclear identification. The sensitivity is high enough, in order to work with very low intensity beams (down to 10^3 pps). The high sensitivity scintillating screen for the beam monitoring is made of Cesium Iodide doped with thallium, $\text{CsI}(\text{Tl})$. Such a screen is covered for a half of its surface, by a very thin ($6\ \mu\text{m}$) aluminized mylar tape, that can be wound in front of it. In case of stable beam monitoring, the beam hits the screen directly, while the radioactive beam hits the tape, in order to avoid the contamination of the screen. In such a case the light spot is produced by the radioactive decay of the radionuclides implanted inside the tape. In order to measure the beam intensity and to perform the identification, LEBI also lodges a plastic scintillator BC408 coupled with a photomultiplier (Hamamatsu R1924A), in order to detect the beta particles emitted by the radionuclides decay. The detection efficiency has been calculated by the Montecarlo code Penelope, and for the ^8Li nuclei it is 0.45. A couple of germanium detectors, positioned at a relative angle of 90° , can detect gamma rays emitted in the decays, thus allowing a more accurate identification of the particles. In Fig. 5 two profiles for a stable (left) and unstable ^8Li beam (right) are shown.

For the accelerated beams, the diagnostic devices that we have used up to now to measure the beam intensity consist of $3 \times 3\ \text{cm}^2$ silicon detectors.

Radioactive Ion Beam Facilities

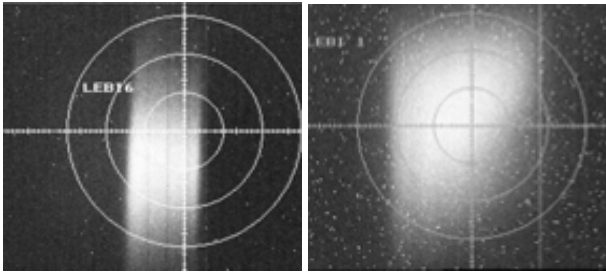


Figure 5: Beam profiles acquired with LEBI for a stable (left) and a radioactive beam (right). The intensities are below 1 pA.

However, such devices are not suitable to work over 10^4 pps, because of radiation damage, therefore we have decided to install plastic scintillators BC408 coupled with pmt for such purpose. A position sensitive (PSD) silicon detector ($50 \times 50 \text{ mm}^2$) has been adopted as a beam profile monitor. This is able to reconstruct the impact position of each particle, by reading the signals produced at the four vertex of the detector. In the telescope configuration, it also allows to identify the Z and A of each particle. In Fig. 6, the reconstructed coordinates of alpha and beam particles, crossing a mask with several holes, are shown.

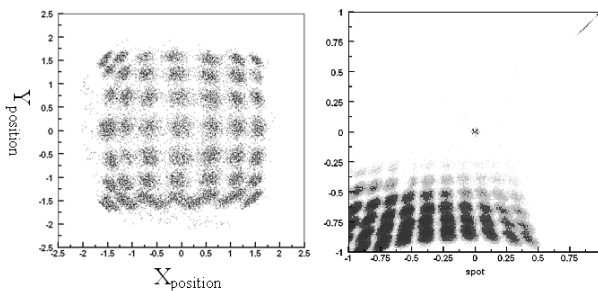


Figure 6: Mask profiles acquired with alpha particles (left) and ^8Li beam (right), using the silicon PSD. The scale axes are different.

In order to manage all the installed devices (10 LEBI's, 15 PMT and 15 PSD) a suitable software platform based on LAB VIEW have been designed. An easy user interface allows the operators to control the main functions of the devices and to acquire all the data useful for the beam transport.

PRESENT CAPABILITIES AND PROSPECTS OF THE EXCYT FACILITY

With the successful production and post-acceleration of ^8Li , the commissioning of the EXCYT facility has been completed and the beam delivered to the first experiments approved by the LNS Scientific Committee. The RNB production is sufficient to deliver to the users a good

beam quality in terms of stability, purity and intensity for the experimental program already approved by the LNS PAC. This is an important achievement, considering that the facility is installed in the accelerator area, most of the time not accessible during the routine operation of the LNS accelerators with stable beams.

Using a primary beam of 100 W, $5.4 \cdot 10^6$ pps of $^8\text{Li}^+$ are produced. After the CEC, $1.5 \cdot 10^5$ pps of $^8\text{Li}^+$ are transported through the mass separator until the Tandem entrance. The transport efficiency through the two stages of the isobaric mass separation is close to 100% as expected. The acceleration transmission at the Tandem is of the order of 50%, lower than with Li stable beams, therefore some improvements are planned in the injection line of the Tandem, possibly the installation of a new quadruplet. The final intensity of ^8Li on target is $5 \cdot 10^4$ pps.

Further improvements are needed to make the facility more reliable and performing. Different activities are under way to achieve this goal: a factor three is requested from the Superconducting Cyclotron and a lot of efforts are focused on the optimisation of the TIS assembly. Actually the CEC efficiency is the major bottleneck to overcome. The TIS extraction voltage reduction has given a successful improvement on the RNB yield, however several alternative solutions are taken into account to directly produce negative Li ions.

This overall optimisation process involves several key points of the facility (CS, TIS, CEC, Tandem), but it will permit a significant increase of the beam intensity on target. In particular a ^8Li intensity up to $5 \cdot 10^5$ pps can be expected at the experimental point in the future.

Finally, the installation of a different source type is planned in the near future: the aim is to start developing a new radioactive beam, different from ^8Li , that can be of scientific interest for users. A possible choice might be ^{15}O .

REFERENCES

- [1] G.Cuttone et al., Nucl. Instrum. Methods, B 261, (2007) 1040.
- [2] R. Kirchner, Nucl. Instrum. Methods, A292,(1990) 203.
- [3] D. Rifuggiato, L. Calabretta, G. Cuttone, Proc. of the XVII International Conference on Cyclotrons and their Applications, Tokyo, Japan, (2004) 118.
- [4] M. Re, D. Garufi, M. Menna, G. Raia, G. Cuttone, LNS activity report 2003, (2004) 170.
- [5] M. Re, M. Menna, F. Chines, G. Cuttone, E. Messina, D.W. Stracener, Proc. of the Particle Accelerator Conference 2005, Knoxville,(2005) 898.
- [6] G. Cuttone et al., LNS activity report 2004, (2005) 175.

THE SPES PROJECT: AN ISOL FACILITY FOR EXOTIC BEAMS

G. Prete, A. Andrighetto, L. Biassetto, F. Gramegna, A. Lombardi, M. Manziolaro,
INFN Laboratori Nazionali di Legnaro, viale dell'Università, 2-35020 Legnaro, Italy
L. Calabretta, INFN Laboratori Nazionali del Sud, via Santa Sofia, 62 – 95125 Catania, Italy
and SPES collaboration, www.lnl.infn.it/~spes

Abstract

SPES (Selective Production of Exotic Species) is an INFN project to develop a Radioactive Ion Beam (RIB) facility as an intermediate step toward EURISOL. The SPES project is part of the INFN Road Map for the Nuclear Physics development in Italy and is supported by LNL and LNS the INFN National Laboratories of Nuclear Physics in Legnaro and Catania.

The Laboratori Nazionali di Legnaro (LNL) was chosen as the facility site due to the presence of the PIAVE-ALPI accelerator complex, which will be used as re-accelerator for the RIBs. The SPES project is based on the ISOL method with an UCx Direct Target and makes use of a proton driver of at least 40 MeV energy and 200 μ A current. Neutron-rich radioactive beams will be produced by Uranium fission at an expected fission rate in the target in the order of 10^{13} fissions per second. The key feature of SPES is to provide high intensity and high-quality beams of neutron rich nuclei to perform forefront research in nuclear structure, reaction dynamics and interdisciplinary fields like medical, biological and material sciences.

The exotic isotopes will be re-accelerated by the ALPI superconducting linac at energies up to 10 A MeV for masses in the region of $A=130$ amu with an expected rate on target of 10^9 pps.

PHYSICS CASE

Starting from a nucleus on the stability line and adding successively neutrons one observes that the binding energy of the last neutron decreases steadily until it vanishes and the nucleus decays by neutron emission. The position in the nuclear chart where this happens defines the neutron drip line. It lies much farther away from the valley of stability than the corresponding drip line associated with protons, owing to the absence of electrical repulsion between neutrons. The location of the neutron drip line is largely unknown as we have experimental data only for nuclei with mass up to around 30.

The interest in the study of nuclei with large neutron excess is not only focused on the location of the drip line but also on the investigation of the density dependence of the effective interaction between the nucleons for exotic N/Z ratios. In fact, changes of the nuclear density and size in nuclei with increasing N/Z ratios are expected to lead to different nuclear symmetries and new excitation modes. While in the case of some very light nuclei a halo structure has been identified, for heavier nuclei the formation of a neutron skin has been predicted.

The evolution of nuclear properties towards the neutron drip line depends on how the shell structure changes as a function of neutron excess. This evolution has consequences on the ground state properties (spin, parity, and electromagnetic moments) and on the single-particle and collective excitations. In particular, studies of neutron-rich nuclei beyond doubly magic ^{132}Sn are of key importance to investigate the single-particle structure above the $N=82$ shell closure and find out how the effective interaction between valence nucleons behaves far from stability.

New modes of collective motion are also expected in connection with the formation of a neutron skin, namely oscillations of the skin against the core, similar to the soft dipole mode already identified in the case of very light halo nuclei. Presently, neither the thickness nor the detailed properties of the neutron skin of exotic nuclei are known. This information is needed to enable a quantitative description of compact systems like neutron stars, where exotic nuclei forming a Coulomb lattice are immersed in a sea of free neutrons, a system which is expected to display the properties of both finite and infinite (nuclear matter) objects.

Despite the large number of experimental studies, so far it is not yet possible to predict reliably the limits of nuclear stability or the behaviour of the Nuclear Equation of State (NEOS) at low and high baryon densities.

In particular, the asymmetry term in the NEOS is largely unknown but in the region close to saturation. However, it is just this energy which plays an important role in setting the stability limits. For this reason, it is quite challenging to investigate the behaviour of nuclear matter far from stability. Although the SPES energy range is somewhat limited for studies of this kind, the neutron-rich ion beams of SPES will allow one to further extend the investigation of the NEOS along the isospin coordinate, in a region where it is largely unknown at low as well as high excitation energy.

FACILITY DESCRIPTION

The basic elements of the ISOL facilities are: the primary accelerator, the production target coupled to the ion source (TIS), the charge booster, the beam transport system and the re-accelerator. According to the requirements of the experimental needs a High Resolution Mass Spectrometer (HRMS) can be part of the transport system.

The SPES design is based on a cyclotron as primary accelerator able to supply at least 40 MeV 0.2 mA proton beam onto a UCx direct target to produce a fission rate of about 10^{13} fission/s. Thus, a total beam power of 8 kW

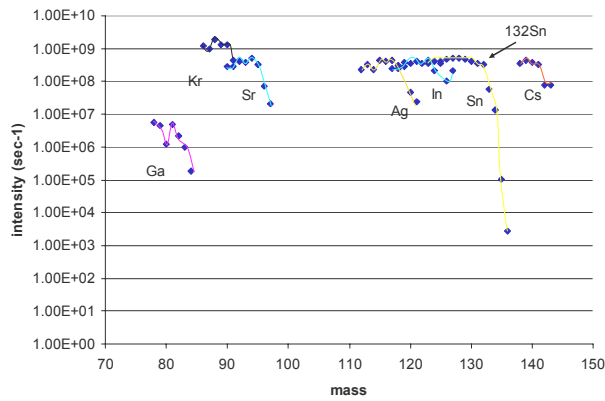


Figure 1: Expected on-target intensities calculated considering emission, ionization and acceleration efficiencies (see text) for different isotopes.

has to be managed. A surface ionization source will be used with the possibility to add a laser device to improve the purity of the ionized exotic species. For this purpose a HRMS with a mass resolution $1/20000$ is also planned. To reach the charge state and ion velocity that fit the requirement for injection into the PIAVE-ALPI acceleration system a charge breeder and 2 high voltage platforms (HV~250kV) will be used. The first platform will host the TIS and first stage mass separator, the second the charge breeder. The description of the facility is reported in the Technical Design Report on the LNL web site [1].

As the facility will handle radioactive species, special care is devoted to the radiation protection safety and several systems are added to prevent radiation hazards. A control system will integrate in a homogeneous architecture the many subsystems necessary for the operation of the facility: from the accelerator control to the radiation and safety survey.

Several factors have to be considered to determine the intensities and the ion species available for experiment in an ISOL facility. The production of isotopes inside the primary target is the first ingredient but a crucial point, as we are dealing with radioactive species, is the target release time, i.e. the time needed by the reaction products to reach the ionization source from inside the target grains, where they are produced. The in-target beam intensity at SPES has been determined starting from the fission fragment production yield calculated with the MCNPX [2] transportation Monte Carlo code in which the target geometry is included. The following diffusion and effusion of the exotic species inside the target was evaluated with both GEANT4 [3] and RIBO [4] Monte Carlo codes. The calculations have been tuned using the available experimental data from ISOLDE, ORNL and PNPI and the complete geometry of our target has been included. Finally, source ionization and extraction, charge breeding, beam transport and reacceleration efficiencies have to be considered. Following the literature, we assumed $1+$ and $N+$ (charge breeder) ionization efficiencies equal to 90% ($1+$) and 12% ($N+$) for Kr and

Xe, 30% ($1+$) and 4% ($N+$) for Zn, Sr, Sn, I and Cd. The typical Linac ALPI transmission efficiency is 50%.

The final estimated beam currents for the SPES facility are shown in Figure 1 for some interesting species.

Proton Driver

A proton driver based on a cyclotron with energy 40-50 MeV and current 0.2 mA fulfils the requirements for the SPES project as the direct target is actually designed for 8 kW power.

A commercial cyclotron, with characteristics which fulfils the needs for the SPES project, was recently developed by IBA: the Cyclone® 70 (C70). It is in operation at the ARRONAX (Accélérateur Recherche Radiochimie Oncologie Nantes) project [5]. C70 delivers 750 μ A current of protons at 70 MeV.

Another commercial solution is the T40 from ACSI which is able to supply up to 1.2mA at 40 MeV energy.

The use of a cyclotron as proton driver is very interesting from the point of view of a multi-user proton facility as, accelerating H^- , they are normally equipped with two exit ports with stripper extraction, allowing for dual proton beam operation which can supply two end-users at the same time.

The SPES project is designed with two target stations for RIB production. Alternatively the second beam will be used for the development of applied physics based on 70 (40) MeV proton beam and current as high as 0.5 (1) mA according to the adopted cyclotron.

Target System

The UCx target is made by 7 disks (each ~1 mm thick and 4 cm diameter) to optimize power dissipation and release time of the fission products. The gaps between the disks allow an efficient cooling of the system by thermal radiation. The total amount of the U fissile material is only 28 g.

A detailed study has been performed to evaluate the thermo-mechanical behaviour with two codes: ANSYS [6] and a code provided by ENEA [7] used for nuclear power design. Experimental tests of the target principle were performed at the HRIBF facility (ORNL-USA). The main result is that, in the adopted configuration, the target does not melt and to reach the operating temperature it is necessary to supply external power.

A strong R&D program is under development on the Direct Target subjects for material, characterization techniques and prototyping. The possibility to produce disks of carbides with the right dimensions has been proved developing and characterizing LaC and UCx pellets.

Collaborations with ISOLDE (CERN) and HRIBF (ORNL) have been established as well as participation to the EURISOL-DS Task3. A detailed discussion of the target status in [8].

Beam Transport and Reacceleration

The secondary beam line transport system will handle the radioactive beam from the output of the ionization

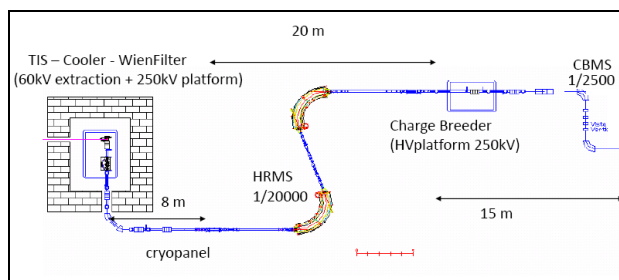


Figure 2: Scheme of the transport line for the SPES exotic beams. For details see the text.

source to the low-energy experimental area and to the re-accelerator complex. One of the main problems to operate an ISOL facility is the beam purification since the extracted species are transported according to their A/q value. Due to the low rigidity of the beam, electrostatic quadrupoles can be used to focus and transport the beam. This guarantees a reliable beam handling and a very simple procedure to set the beam transport line.

The beam, extracted from the source with 60 kV extraction potential, will go through a first stage of A/Z purification, which allows trapping the largest amount of radioactive contaminant. According to other facilities, and to satisfy the previous constraint, we plan to use a small Wien filter, placed on the first HV platform just beyond the source. Furthermore a small magnetic dipole, like in the EXCYT design, can be also used. A mass resolving power ($M/\Delta M$) of 300 for this “analytical” magnet is acceptable. It will be followed by a 1/20000 High Resolution Mass Spectrometer (HRMS) which allows the isobar selection. To improve selection capability the HRMS shall operate at an input energy in the order of 200 keV. To fulfil this requirement the HV platform, where both target and first mass separator are mounted, is operated at 200 kV supplying 1+ beam at total energy of 250 keV.

To optimize the reacceleration, a charge breeder will be developed to increase the charge state to $N+$ before the injection of the exotic beam in the PIAVE Superconducting RFQ’s, which represent the first re-acceleration stage before the final injection in ALPI.

The charge breeder acts as a trap where the 1+ ions are stopped and re-extracted with increased charge state. To fulfil these requirements the charge breeder is mounted on a second HV platform operated at 250 kV; this allows to stop the incoming ions and to give the right energy to the out-coming ones. The scheme of the transport line is shown in Figure 2.

The reacceleration of the exotic species will be performed by the acceleration complex PIAVE-ALPI. The PIAVE injector is in regular operation at LNL since fall 2006. It is based on an ECR Ion Source (placed on a 350 kV platform), and on super-conducting RFQ’s able to accelerate ions with $A/q \leq 8.5$ up to 1.2 AMeV. For the

SPES beams a transfer line from the charge breeder will be added. No main difficulties are expected as the ions coming from the charge breeder have similar characteristics as that ones produced in the present ECR.

The ALPI acceleration capability allows to push the RIBs energy up to 10 AMeV for masses in the region of $A=130$ amu. Refer to the FR-03 and FR-04 papers in this conference for a detailed description of ALPI characteristics.

Summary and Conclusions

The SPES project is one of the main Nuclear Physics developments in Italy for the next years. It is organized as a wide collaboration among the INFN Divisions, Italian Universities and international Laboratories. The SPES collaboration allows covering all the specific aspects of the project, also those outside the main competences available inside INFN. A strong link and support was established with ISOLDE (CERN, CH) and HRIBF (ORNL, USA). With SPIRAL2 (GANIL, F) there is a collaboration in the frame of LEA (Laboratorio Europeo Associato) which aims to share the technical developments and the scientific goals in the field of Nuclear Physics with exotic beams. Specific collaboration for target and charge breeder was opened with KEK (IPNS, Japan)

SPES is an up-to-date project in this field with a very competitive throughout representing a step forward to the European project EURISOL. The relevance of the project is not only related to nuclear physics research but also to Astrophysics and Applied Physics: mainly for Nuclear Medicine, material research and nuclear power energy.

The first exotic beam at SPES is expected in 2014.

REFERENCES

- [1] G. Prete and A. Covello, "SPES Technical Design Report", INFN-LNL 223 (2008); http://www.lnl.infn.it/~spes/TDR2008/tech_design08_index.htm.
- [2] Denise B. Pelowitz (Editor), "MCNPXTM User’s manual", Version 2.5.0, LA-CP-05-0369 (2005).
- [3] "GEANT4: Geant_detector description and simulation tool", CERN Program Library W5013.
- [4] M. Santana Leitner, PhD. Thesis, UPC-ETSEIB / CERN (2005); <http://ribo.web.cern.ch/rib>.
- [5] "Proceedings of the 18th Int. Conf. on Cyclotrons and their Applications", 2007; <http://accelconf.web.cern.ch/accelconf/c07/>.
- [6] <http://www.ANSYS.com>.
- [7] S. Cevolani, "FIS-P815-022" (ENEA report).
- [8] A. Andrighetto, C.M. Antonucci et al., "Eur. Phys. Journal. S.T.", 150 (2007)273 and A. Andrighetto et al. "Proceedings Zakopane Conference on Nuclear Physics", Sept 1-7 2008, to be published in Acta Physica Polonica.

THE SPES PROJECT: RESEARCH AND DEVELOPMENT FOR THE MULTI-FOIL DIRECT TARGET

M. Manzolaro, A. Andrichetto, L. Biassetto, S. Carturan, M. Libralato, G. Prete, D. Scarpa,
LNL-INFN, Viale dell'Università 2, Legnaro, Italy

G. Meneghetti,

University of Padova, Department of Mechanical Engineering, Via Venezia 1, Padova, Italy
P. Colombo,

University of Padova, Department of Mechanical Engineering, Via Marzolo 9, Padova, Italy

P. Zanonato, University of Padova, Department of Chemistry, Via Marzolo 8, Padova, Italy

P. Benetti, University of Pavia, Department of Chemistry and INFN, Via Taramelli 12, Pavia, Italy

M. Guerzoni, INFN, Viale Berti Pichat 6/2, Bologna, Italy

I. Cristofolini, B. Monelli,

University of Trento, Department of Mechanical Engineering, Via Mesiano 77, Trento, Italy.

Abstract

SPES is a facility to be built at National Institute of Nuclear Physics (INFN-LNL, Legnaro, Italy) intended to provide intense neutron-rich Radioactive Ion Beams (RIBs) [1] directly hitting a UCx target with a proton beam of 40 MeV and 0.2 mA; RIBs will be produced according to the ISOL technique and the new idea that characterize the SPES project is the design of the production target: we propose a target configuration capable to keep the number of fissions high, the power deposition low and the release of the produced isotopes fast. In this work we will present the recent results on the R&D activities regarding the multi-foil direct UCx target.

INTRODUCTION

The SPES project is focused on the production of neutron-rich radioactive nuclei by ISOL technique, employing the proton induced fission on a direct target of UCx; the fission rate expected with a proton beam of 40 MeV and 0.2 mA is 10^{15} fissions/s. The main goal of the SPES facility [1] is to provide an accelerator system to perform forefront research in nuclear physics by studying nuclei far from stability, in particular neutron-rich radioactive nuclei with masses in the range of 80–160. The final RIB energy on the experimental target will be up to 11 MeV for $A = 130$, with an intensity in the range 10^7 – 10^9 pps, depending on the extracted ion species. The bombarding energy achieved allows to overcome the Coulomb barrier in most systems and opens up new possibilities for experimental studies of neutron-rich nuclei, employing different reaction mechanisms such as Coulomb excitation, inelastic scattering, single and multiple nucleon transfer, fusion reactions, etc.

In an ISOL facility the working core is constituted by the production target and the ion source [2]: they have to be designed and optimized carefully in order to obtain the desired RIB production rate (see Fig. 1). In the SPES project, the RIBs extracted from the ion source (coupled to the production target by means of the transfer line) will

go through a first stage of A/Z purification, which allows to trap the largest amount of radioactive contaminant.

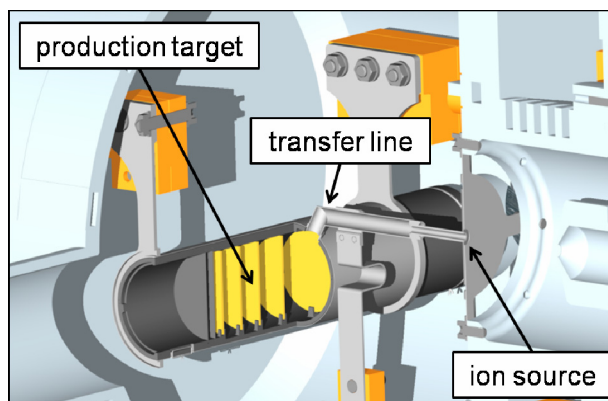


Figure 1: The SPES production target and the ion source.

A small Wien filter will be placed in the platform just beyond the source; it will be followed by a 1/20000 isobar mass separator. To optimize the reacceleration, a charge breeder will be developed to increase the charge state to $N+$ before the injection of the exotic beam in the PIAVE Superconducting RFQ, which represents the first reacceleration stage; the second and final reacceleration step will take place in the ALPI superconducting linear accelerator: as reported above, the final RIBs energy on experiments will be up to 11 MeV.

THE TARGET SYSTEM

In the production target - ion source complex for ISOL based facilities, many physical phenomena occur: power deposition, fission, atomic diffusion-effusion, ionization, extraction. In the SPES project, the primary proton beam is stopped in the target, dissipating its power and generating by fission exotic nuclei in the intermediate mass range ($80 < A < 160$) [1]. The desired exotic species must be extracted from the target, ionized and accelerated to make a RIB. This process is time demanding and usually unsuitable for atoms having half lives lower than

a few tens of ms. Dealing with a target - ion source system, the intensity of the radioactive beam available at the source output, is usually described by the following equation:

$$I = \sigma \cdot \Phi \cdot N \cdot \varepsilon_1 \cdot \varepsilon_2 \cdot \varepsilon_3 \quad (1)$$

where σ stands for the production cross section, Φ the proton beam intensity, N the target thickness, ε_1 the release efficiency from the target up to the source, ε_2 the ion source efficiency and ε_3 the delay transfer efficiency due to the radioactive decay losses. The SPES target design has been optimized in order to maximize the release efficiency and to exploit, at the same time, devices (basically the ion sources) developed in other laboratories (mainly at CERN, Switzerland). The energy deposited in the target material by the electromagnetic and nuclear interactions has to be removed, and because of the low pressure of the environment, the target can be only cooled by thermal radiation towards the container box surrounding it. In order to optimize the heat dissipation along with the fission fragments evaporation, the SPES target consists of multiple thin disks housed in a cylindrical graphite box [1]. In this way the cooling of the target is strongly simplified: in fact, due to the vacuum environment, the heat dissipation is fully entrusted to thermal radiation: radiative heat transfer is directly proportional to the body surface and in our case the use of 7 thin UCx disks, 40 mm in diameter and 1.3 mm thick each, increases the total surface and allows for a better cooling. It is fundamental to underline that the radiative cooling is supported also by the high temperature level of the target during the working conditions, approximately equal to 2000°C. In this configuration only the protons with higher fission cross-section are exploited in the UCx target discs, while the outgoing lower energy, less than about 15 MeV, is driven towards a passive graphite dump; as a consequence, the power deposited in the UCx is lowered considerably and at the same time the number of fission reactions is maintained high. In the selection of the beam profile, a uniform distribution of the beam has been chosen in order to flatten the power deposition inside the disks as much as possible and consequently to reduce temperature gradients and thermal stresses.

The architecture proposed for the SPES target represents an innovative solution in terms of capability to sustain the primary beam power; the design is carefully oriented to cool the target by thermal radiation, taking advantage of the high operating temperature. The thermal analyses performed [1] show the capability of thermal radiation to cool the disks with a reasonable margin below the material limiting temperature. The release from the target has been carefully studied by means of dedicated computational codes: simulations show that the SPES multi-foil direct target presents a good isotope extraction behavior up to intermediate masses.

The ideal target material for RIBs production should combine different properties which sometimes cannot be fully maximized in a single material: low density, good

release properties, good mechanical stability, high thermal conductivity and emissivity, and limited ageing at high temperature under intense irradiation. Such materials must operate for extended periods of time with constant performance and efficiently dissipate the incoming beam power.

The preparation of the SPES UCx disks is based on the carbon-thermal reduction of UO_2 powders in excess of graphite. The powders are mixed and grinded in order to obtain a homogeneous mixture (2 wt.% of phenolic resin is added as binder); these powders are uniaxially cold pressed at 75 MPa for 1 h. Finally the heat treatment is performed in a dedicated vacuum furnace, built at LNL-INFN. The bulk density of the disks turns out to be about 3 g/cm^3 , while the atomic ratio of the uranium compared to the carbon is assumed to be U:C=1:4. In Fig. 2 a picture of the first 13 mm UCx pellet is reported.



Figure 2: The first UCx pellet for the SPES project.

THE ION SOURCE SYSTEM

The hot-cavity ion source chosen for the SPES project was designed at CERN (ISOLDE) [3]. The source has the basic structure of the standard high temperature RIB ion sources employed for on-line operation. The ionizer cavity is a W tube (34 mm length, 3 mm inner diameter and 1 mm wall thickness) resistively heated to near 2000°C. The isotopes produced in the target diffuse in the target material and after that will effuse through the transfer tube (its length is approximately equal to 100 mm) into the ionizer cavity where they undergo surface or laser ionization. The Surface ionization process can occur when an atom comes into contact with a hot metal surface. In the positive surface ionization, the transfer of a valence electron from the atom to the metal surface is energetically favorable for elements with an ionization potential lower than the work function of the metal. Ideally that atoms should be ionized +1, then extracted and accelerated to 60 keV and after that injected into the

transport system. For alkalis and some rare earth elements high ionization efficiencies can be achieved using the surface ionization technique. For most part of the others elements, the laser resonant photo-ionization, using the same hot cavity cell, is the powerful method to achieve a sufficient selective exotic beams. This technique will be implemented in collaboration with the INFN section of Pavia. The aim is to produce a beam as pure as possible (chemical selectivity) also for metal isotopes, as shown in Fig. 3.

Light Metals		Heavy Metals									
GROUP	Is	Is	Is	IVa	Va	VIa	VIIa	VIIIa	IXa	Xa	XIa
1	H	He									
2	Li	Be									
3	B	C	N	O	F	Ne					
4	Na	Mg	Al	Si	P	S	Cl	Ar			
5	K	Ca	Sc	Ti	V	Cr	Mn	Fe	Co	Ni	Cu
6	Rb	Sr	Y	Zr	Nb	Mo	Tc	Ru	Rh	Pd	Ag
7	Cs	Ba	La	Hf	Ta	W	Re	Os	Ir	Pt	Au
8	Fr	Ra	Lr	Rf	Db	Sg	Bh	Hs	Mt		

Figure 3: The main isotopes that will be ionized and extracted in the SPES project.

The laser ion source has been investigated in the past at Pavia University, as a spin-off of the atomic vapor laser isotope separation. As first step for the R&D of the photo-ionization process for SPES, dye laser will be used to generate resonant light source. These lasers are in turn pumped by the second harmonic of Nd-Yag laser. All these devices are already present in the Pavia laboratory. The main work in the last months has been to bring back into use either the Nd-Yag, a Quanta System model, and a dye laser, manufactured by Lambda Physik. The spectral characterization of the laser beam is underway. The final goal is the set-up a system composed of three tunable lasers, an atomic beam and a time of flight mass spectrometer. This system is intended for a full diagnostic of LIS applied to the chemical elements belonging to the fission fragments selected by the SPES group.

THE SPES TARGET PROTOTYPE

Recently a full scale target prototype, based on a series of SiC thin disks, was developed and tested off-line (without the presence of the proton beam) at INFN-LNL (see Fig 4). In this prototype seven SiC disks are contained in a cylindrical graphite box, and closed inside the heating system. The present SPES heating system (see Fig. 4) is composed of a thin Tantalum tube, with an average length of 200 mm, an external diameter and a thickness of 50 and 0.35 mm, respectively; it is welded at its edges to two Tantalum wings; they are directly connected to Copper clamps (see Fig. 4) and thanks to them a 10 kW power supply ($I_{MAX} = 1000 A / \Delta V_{MAX} = 10 V$) is able to provide the electric current necessary to dissipate by Joule Effect the “proton beam – independent” heating power.

Radioactive Ion Beam Facilities

A coupled electrical-thermal Finite Element model of the target and its heating system was defined using the FE code ANSYS®; it is able to reproduce the electrical and thermal behavior of the target and its heating system. The model was validated by temperature and potential difference measurements; it will be used to optimize the target in a virtual environment, with a great profit in terms of time and money.

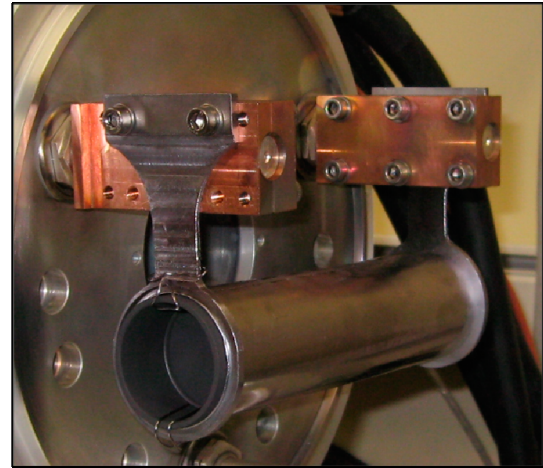


Figure 4: The SPES target prototype.

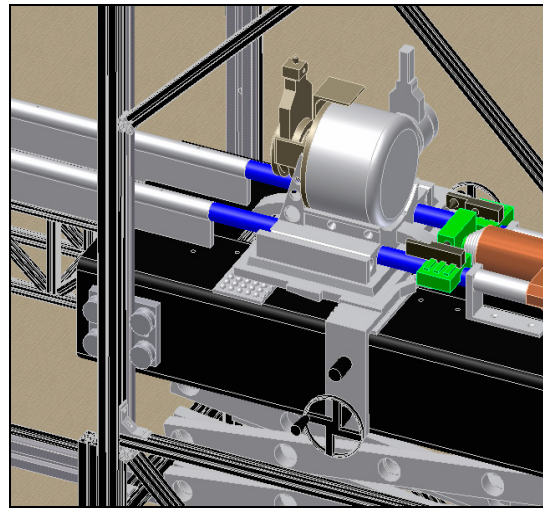


Figure 5: The target chamber handling.

THE TARGET CHAMBER HANDLING

Another important aspect of the R&D for the SPES project is the remote handling of the target vacuum chamber. The chamber used to contain the SPES target and the ion source in vacuum is designed for easy connection and removal from the beam extraction and transport system; it is coupled to the RIB line and to the proton beam channel by means of two quick connectors and two pumping ports which can be sealed off with high vacuum valves moved by pneumatic actuators. Standard industrial components were used to design the chamber handling system, in order to have high reliability, rapid

maintenance and limited costs. An image of the designed handling system is reported in Fig. 5.

CONCLUSIONS

The SPES project is one of the main Nuclear Physics development in Italy for the next years. It is organized as a wide collaboration among the INFN Divisions, Italian Universities and international laboratories. SPES is an up to date project in the field of Nuclear Physics and in particular in the field of RIBs, with a very competitive know how and representing an important step in the direction of the European project EURISOL.

Before starting the construction, the R&D program will continue mainly focusing in the target and in the ion source development and optimization.

ACKNOWLEDGEMENTS

Authors wish to thank M. Lollo, E. Brezzi, L. Costa and M. Giacchini from INFN-LNL for their precious technical support

REFERENCES

- [1] A. Andrighetto, C.M. Antonucci, S. Cevolani, C. Petrovich and M. Santana Leitner Eur. Phys. J., A30 (2006) 591.
- [2] Jim Al-Khalili, Ernst Roeckl, The Euroschool Lectures on Physics with Exotic Beams, Vol. II, Springer (2006).
- [3] J. Lettry, Proceedings of the 1999 Particle Accelerator Conference, New York, 1999.

PROGRESS ON THE COMMISSIONING OF RADIOACTIVE ISOTOPE BEAM FACTORY AT RIKEN NISHINA CENTER

K. Yamada*, T. Dantsuka, M. Fujimaki, T. Fujinawa, N. Fukunishi, A. Goto, H. Hasebe, Y. Higurashi, E. Ikezawa, O. Kamigaito, M. Kase, M. Kobayashi-Komiyama, H. Kuboki, K. Kumagai, T. Maie, M. Nagase, T. Nakagawa, J. Ohnishi, H. Okuno, N. Sakamoto, Y. Sato, K. Suda, M. Wakasugi, H. Watanabe, T. Watanabe, Y. Watanabe, Y. Yano, S. Yokouchi, RIKEN Nishina Center, Wako, Saitama 351-0198, Japan

Abstract

The Radioactive Isotope Beam Factory at RIKEN Nishina Center is a next generation facility which is capable of providing the world's most intense RI beams over the whole range of atomic masses. Three new ring cyclotrons have been constructed as post-accelerators for the existing facility in order to provide the intense heavy-ion beam for the RI beam production by using a in-flight separation method. The beam commissioning of RIBF was started in July 2006 and we succeeded in the first beam extraction from the final booster cyclotron, SRC, by using 345 MeV/A aluminum beam on December 28th 2006. The first uranium beam with energy of 345 MeV/A was extracted from the SRC on March 23rd 2007. Various modifications for equipments and many beam studies were performed in order to improve the transmission efficiency and to gain up the beam intensity. Consequently, the world's most intense 0.4 pnA ²³⁸U beam with energy of 345 MeV/A and 170 pnA ⁴⁸Ca beam with energy of 345 MeV/A have been provided for experiments.

OVERVIEW OF RI BEAM FACTORY

The Radioactive Isotope Beam Factory (RIBF) [1] at RIKEN Nishina Center was proposed in order to produce the world's most intense radioactive isotope (RI) beams over the whole range of atomic masses. The powerful RI beams allows us to expand our nuclear world on the nuclear chart into presently unreachable region and opens up new possibilities for the unified understanding of nuclear structure, for the elucidation of elemental synthesis, and for new scientific discoveries and applications. Figure 1 shows the entire layout of RIBF accelerator complex. The existing facility has a K540-MeV separate-sector cyclotron (RIKEN ring cyclotron, RRC) [2] and a couple of different types of the injectors: one is a linear accelerator complex that consists of a folded-coaxial radio-frequency quadrupole [3], a variable-frequency heavy-ion linac (RILAC) [4], and a energy-booster linac [5]; and the other is a K70-MeV AVF cyclotron (AVF) [6]. Three new ring cyclotrons with K=570 MeV (fixed-frequency ring cyclotron, fRC [7]), 980 MeV (intermediate-stage ring cyclotron, IRC [8]), and 2600 MeV (the world's first superconducting ring cyclotron, SRC [9]), respectively, have been constructed for the RIBF as post-accelerators, which

can boost energies of beams up to 440 MeV/A for light ions and 345 MeV/A for very heavy ions extending to uranium. These energetic heavy-ion beams are converted into intense RI beams via the projectile fragmentation of stable ions or the in-flight fission of uranium ions by a superconducting in-flight fragment separator, BigRIPS [10]. The goal of the available beam intensity is set to be 1 pμA.

FIRST BEAM AND INITIAL EXPERIMENT

The beam commissioning of RIBF was started in July 2006 in parallel with constructing the rest of equipments for latter-stage accelerator. At first, the beam acceleration test of fRC, which is the first booster among the new cyclotrons, was performed with uranium beam in the intervals of experiment at the existing facility. For the uranium beam acceleration, the beam from linac complex is fed to the cascade of RRC, fRC, IRC, and SRC, where the accelerators are used at fixed-energy mode with the rf frequency of 18.25 MHz and its harmonics. The first uranium beam with energy of 50 MeV/A was successfully extracted from the fRC on September 29th 2006. The beam study of fRC was performed at total seven times until November in order to improve the beam emittance and the transmission efficiency. After the completion of the beam line to IRC, beam commissioning of IRC began on November 21st by using ⁸⁴Kr³¹⁺ beam. For the ions not heavier than krypton can be accelerated by a variable-energy mode up to at least 345 MeV/A without using the fRC. The first beam was extracted from IRC on November 25th, only 110 minutes were required from the injection to the extraction of IRC.

Because of the serious trouble on the heat insulating vacuum of helium cooling system, four acceleration resonators and one flat-top resonator were installed on the SRC at June 24th 2006 at last, which was five-months behind to initial plan. Installation of the power amplifiers and low-level controls was made from July to October 2006. After the resonators were carefully aligned, they were connected with the sector magnets to make a vacuum chamber for ion beams. The two vacuum chambers, which enclose the electrostatic channel or phase pickups, were installed in the two valley regions where no resonators fill the space. Evacuation pumps and beam diagnostics were also installed. Initial pumping of the beam chamber started from September

* nari-yamada@riken.jp

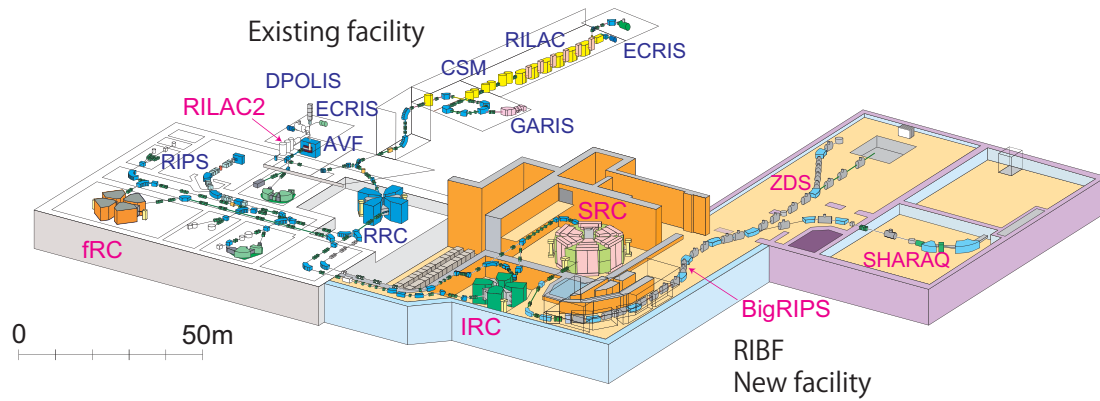


Figure 1: Bird's-eye view of RIBF at RIKEN Nishina Center.

29th. After the leak hunt, cryopumps were turned on and the vacuum pressure reached to 5.0×10^{-6} Pa at the end of October, which is the designed value. The power test of RF system was started on 13th November. On 27th November, the first resonator became operational in cw mode with a magnetic field of the sector magnets. The beam diagnostics were also installed to the SRC during this period. The superconducting coils were fully excited several times to check whether the installed components could work properly under stray fields from the sector magnets. Many local magnetic shields made of iron were put to the parts which did not work properly under the stray fields.

The beam commissioning of SRC started on December 17th 2006 with using $^{27}\text{Al}^{10+}$ beam from the IRC. The beam tuning of SRC was hard work as compared with fRC and IRC. The first beam extraction was finally accomplished at 16:00 on December 28th 2006. After the various modification of hardware and the conditioning of rf resonator, the first RI beam production at RIBF was achieved by the fragmentation of 345 MeV/A $^{86}\text{Kr}^{31+}$ beam on March 15th 2007. Following the delightful event, the uranium beam acceleration of SRC was performed immediately because the uranium beam was the top priority for RIBF. The first $^{238}\text{U}^{86+}$ beam with energy of 345 MeV/A was successfully extracted from the SRC on March 23th 2007. After passing the facility inspection, the beam became possible to utilize the experiment on April 2007. The initial experiment at the RIBF was carried out from mid-May to early in June by using the uranium beam, and a new isotopes ^{125}Pd and ^{126}Pd was successfully discovered [11]. A beam current of up to 30 pA for 345 MeV/A $^{86}\text{Kr}^{34+}$ was attained on November 10th 2007 at the exit of SRC.

IMPROVEMENT OF PERFORMANCE

The total transmission efficiency of the accelerator complex for uranium beam was only 2 % in July 2007, where the charge stripping efficiency is not taken into account. The poor transmission efficiency was mainly caused by insufficient beam tuning due to the inappropriate beam diagnostics for uranium beam. For the uranium beam, huge

number of secondary electrons disturbed the radial beam pattern on main differential probe (MDP) and boosted the apparent beam current on Faraday cups. In addition that, the stray field from the flat-top (FT) acceleration resonator overrode on the differential probe and the radial beam pattern was collapsed. The instability of rf voltage on four resonators in the RILAC, these resonators were controlled by old low-level gain controllers, complicated the adequate beam tuning during the commissioning. Another reason of low transmission for uranium beam was the emittance growth caused by the rough uniformity of the charge stripper carbon foils, which are required at the downstream of RRC and fRC for the uranium beam acceleration.

Modification of Beam Monitors

In order to improve the transmission efficiency of cyclotrons, an accurate adjustment of rf voltage and phase is required, especially for the FT resonator. If the phase of FT resonator is shifted at only one degree, turn separation deteriorates drastically as shown in Fig. 2. It is desired to observe the proper information of radial beam pattern by using the MDP because the information gives a criterion for the adjustment of rf. The radial beam pattern is measured by a differential electrode mounted on behind an integral electrode with 0.5 mm overhang. Only the beam reached to the "0.5 mm" is counted at each radius. However, a lot of secondary electrons emitted from the sidewall of integral electrode due to hitting the uranium beam had a great influence on the detection of differential signal and the radial beam pattern could not be constructed properly. In order to overcome the problem, the differential electrodes were modified for fRC, IRC, and SRC to shift away from the integral electrode. In the case of SRC, new differential electrode of 0.3 mm \times 3 mm tungsten ribbon was attached in front of the integral electrode at intervals of 10 mm. Another problem we had in the MDP was that the beam signal was disturbed by the electromagnetic radiation from the FT resonator: the rf frequency is high enough for the electromagnetic wave to travel through the vacuum chamber. A schematic drawing of the MDP in the chamber is shown in

Fig. 3. The driving shaft of the MDP is grounded by the metallic wheel on the chamber in the original configuration. Since the electromagnetic wave is TE01 mode, this asymmetric configuration allows the electric field to penetrate into the narrow gap between the shaft and the chamber, which induces the electric charge in the head of the probe. Therefore, we put an electric contact on the upper side of the shaft, as shown in Fig. 3, in order to suppress the electric field around the probe head. For the SRC, a pantograph structure was adopted for the contact because the chamber face was not seamless. An adjustment for balance of the vertically located movable shorts in the FT is required simultaneously in order to reduce the leakage of microwaves. These modifications enabled us to measure the radial beam pattern for entire region of the MDP with using the FT resonator as shown in Fig. 2.

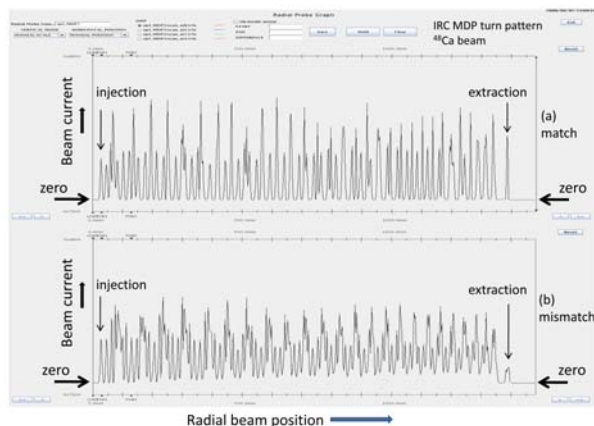


Figure 2: Radial beam pattern of ^{48}Ca beam measured by MDP on IRC. FT resonator was activated. The rf phase of FT is matching in the upper panel, whereas the phase is shifted at only one degree in the lower panel.

Accurate measurement of beam current is essential for the elaborate tuning to reduce the beam loss in the injection and extraction channels of cyclotrons and in the beam transport lines. Newly designed Faraday cups and separated-type electron suppressor with 70 mm thickness were adopted to overcome the problem that the beam intensity was overestimated by a factor of two or three due to the insufficient suppression of secondary electrons. This new Faraday cup replaced the one mounted at the key point of accelerator complex. Faraday cup located at the exit of SRC is based on a special design, that consists of a fixed main-suppressor electrode, a fixed long-cylindrical electrode, and a cup bottom movable with respect to the beam axis. The beam stops on the cup bottom and the emitted secondary electrons are captured by the cylindrical electrode. Residual electrons are returned by the electrostatic field provided by the main-suppressor electrode. The sub-suppressor electrode is used to trap the electrons escaping from the aperture between the cup bottom and the cylindrical

Radioactive Ion Beam Facilities

cal electrode. The cup bottom is made of oxygen-free copper with $\phi 62$ mm inner diameter, and the bottom is 23 mm thick and cooled by water. This thickness is designed to fit beams from argon to uranium accelerated by the SRC.

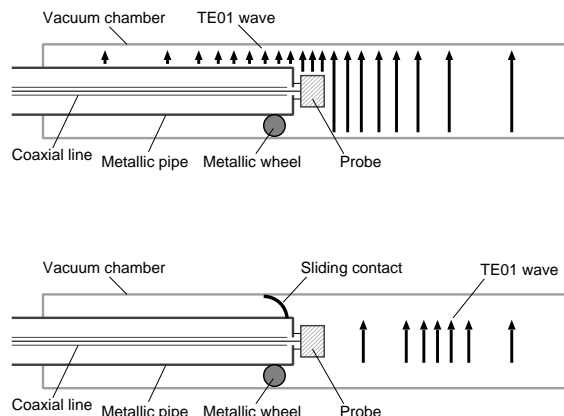


Figure 3: Effect to disturb the propagation of TE01 microwave.

Problem of Helium Cryogenic System

Helium cryogenic system of SRC met the serious problem that the flow rate in the system had decreased gradually, the temperature of 80 K stage adsorbers had increased, and the inlet pressure of the first turbine had fallen. We had to stop the helium refrigerator every two months to warm it up to room temperature and transpire the impurity. By the long term investigation, the source of the problem was found that the lubricant oil of screw compressors had passed through the cascade of four-stage oil separators and polluted the first heat exchanger, 80 K adsorbers, first and second turbine, and their inlet filters in the refrigerator. This oil had frozen and degraded the flow rate of helium gas in the refrigerator. To rinse out the impurity, heat exchangers were taken out from the refrigerator and were washed away by using HCFC solvent. The charcoal in the adsorber was also replaced with the new one. Additional 1.5th and 5th oil separators were installed in parallel with the reconstruction of helium refrigerator to enhance the ability of oil elimination. This trouble delayed the steady operation of SRC from December 2007 until September 2008. The recooldown of SRC started at once and the superconducting coils were ready to operate in October 2008.

Present Performance

A series of studies were performed without the SRC by using ^{48}Ca and ^{238}U beam during the reconditioning of helium cryogenic system. In this period, the monitoring system for the RF pick-up and beam phase pickup signal using lock-in amplifiers (SR844) was developed [12] and the long-term stabilities were clarified as described above. After solving the problem of helium cryogenic system, the acceleration of ^{238}U was performed for the commissioning

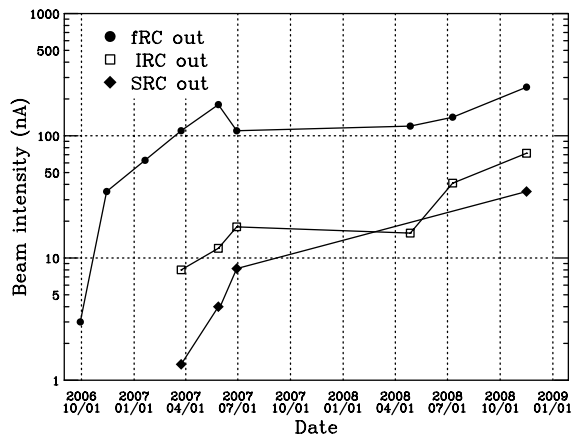


Figure 4: Evolution of maximum intensity for uranium beam during the commissioning.

of the Zero-Degree Spectrometer and following new isotope search experiment at BigRIPS in November 2008. The beam intensity from the SRC grew up to 0.4 pA, which was ten times higher than the one in 2007. More than twenty candidates of new isotopes were discovered within a week.

Table 1: Transmission efficiencies from the ion source to the exit of each accelerator. Note that the observed currents include 20–30 % errors.

	^{86}Kr	^{238}U	^{48}Ca
RILAC	47 %	40 %	54 %
RRC	28 %	30 %	50 %
fRC	Not used	35 %	Not used
IRC	20 %	23 %	48 %
SRC	9 %	16 %	35 %

Following that, the first acceleration of ^{48}Ca on the SRC was carried out in December 2008 for a series of day-one experiment. The modifications performed in past two years and elaborate tuning of accelerators realized the world's most intense ^{48}Ca beam that reached up to 170 pA at the exit of SRC. Figure 4 indicates the evolution of the maximum intensity for uranium beam during the commissioning. The degradation of intensity on fRC in July 2007 corresponds to the adoption of new Faraday cups. The transmission efficiencies from the ion source to the exit of each accelerator are summarized in Table 1. The efficiency of 82 % for the SRC corresponds to about 500 W loss for 170 pA ^{48}Ca beam. In most cases, the major beam loss in cyclotron take place on the septum of electrostatic deflector (EDC). For the acceleration of kilowatt beams such as the ^{48}Ca , large beam loss causes the serious thermal damage on the hardware and that restricts the maximum beam intensity effectively. For the protection during the ^{48}Ca beam acceleration, type-E thermocouple gauges were mounted on the EDC septum to measure the temperature and switch off

Radioactive Ion Beam Facilities

the beam if the maximum heat-up exceeded the criterion, which was set to 5 degrees in December 2008. The temperature clearly responded to the beam loss and that was available to improve the extraction efficiency via tuning as decreasing the temperature.

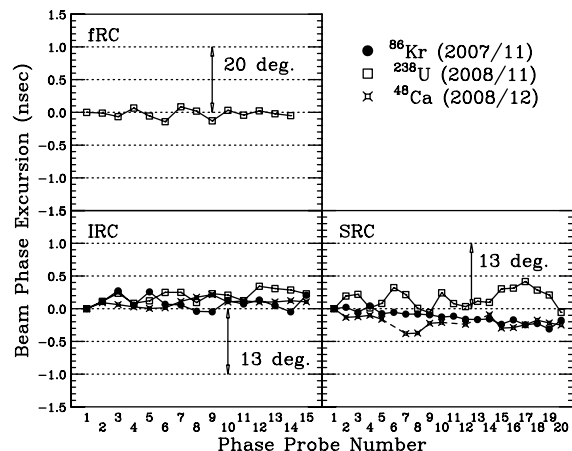


Figure 5: Isochronous condition of new cyclotrons. Data point of SRC phase probe no.6, 11, 13 in the case of ^{48}Ca is not plotted because the probe was troubled by FT stray field.

The accurate isochronism is the significant condition for the cyclotron to make capable for providing the intense beam with high transmission efficiency. Figure 5 describes the excursion of periodic arrival time for revolving beam in each cyclotron as a function of phase pickups located along the radius vector. Signals were detected by the pairs of phase pickups which are radially mounted on the orbital region of cyclotron, and analyzed by the lock-in amplifier. The result of krypton beam indicates that the isochronous condition of the magnetic field is attained to the acceptable level for each cyclotron as the booster in the RIBF accelerator complex. The isochronous condition of uranium beam for the SRC is not as good as the others since the intensity of uranium beam in the SRC is not enough to obtain the data set with high signal to noise ratio.

In the case of ^{48}Ca , the transverse emittance of beam at the entrance of SRC was evaluated to be $1.7\pi\text{-mm-mrad}$ [13] in both the horizontal and vertical directions. This indicates no distinct emittance growth. However, it was found that the emittance grew by a factor of three from the RRC to the fRC for the uranium beam. That is caused by a emittance mismatch during the injection to fRC and by a dispersion mismatch at a rebuncher placed between the RRC and fRC.

LIGHT ION ACCELERATION

The new acceleration mode using AVF-RRC-SRC combination can provide the extremely light ions such as deuteron and nitrogen with the energies of 250–440 MeV/A. For the acceleration mode, a new beam transport line bypassing the IRC was constructed in the fiscal

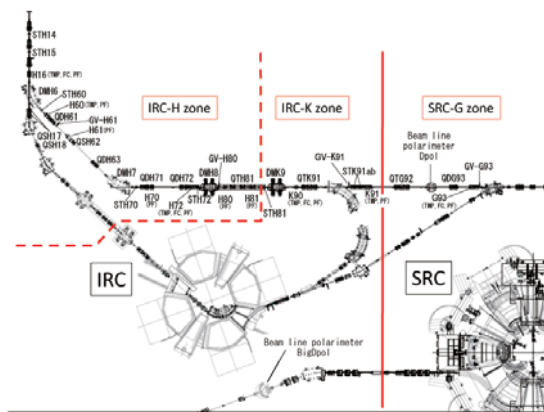


Figure 6: Schematic layout of IRC-bypass beam line used for relatively light-particle acceleration.

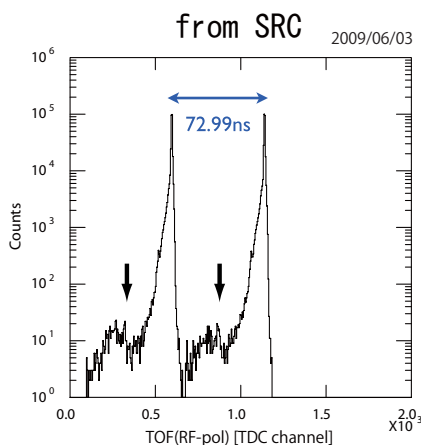


Figure 7: Longitudinal beam structure of polarized deuteron beam at the downstream of SRC. The down arrows indicate the mixture of different turn.

year 2008 [14]. The schematic layout of the beam line is described in Fig. 6. This acceleration mode was tested with a 250 MeV/A nitrogen beam in February 2009. New high-resolution spectrometer SHARAQ [15] was successfully commissioned by using the 250 MeV/A nitrogen beam in March 2009. This beam was also used for additional test experiment of SHARAQ and another experiment at BiGRIPS in May 2009.

A 250 MeV/A polarized deuteron beam was accelerated to study the nuclear three-body force in April 2009. For the deuteron beam acceleration, special beam diagnostic devices were mounted on the SRC because the existing devices could not stop the deuteron beam in themselves. The elaborate beam tuning was performed because the single turn extraction was required for the polarized deuteron beam experiment. Figure 7 shows the longitudinal beam structure of the polarized deuteron beam downstream of SRC measured by a plastic scintillator. The time-of-flight spectrum indicates that the single turn extraction of SRC was remarkably actualized.

Radioactive Ion Beam Facilities

OUTLOOK

Several modifications are organized in order to increase the beam intensity further more. New injector linac system [16] will be constructed in the fiscal year 2009. Combining with a new superconducting ECR ion source [17], we expect the uranium beam intensity to increase up to 100 times. The injector enables the independent and simultaneous operation between the RILAC and the RIBF accelerator complex. The old low-level circuits for RILAC will be replaced to the new stable ones. In order to reduce the disadvantage to the beam quality, thinner carbon foils will be employed for the stripper between the RRC and fRC. The power supplies of fRC magnet have to be modified since the charge state of uranium beam will be shifted from 71^+ to 69^+ . The most difficult problem is regarding to the lifetime of stripper foil. Although various types of stripper are tested, excellent answer has not been obtained yet.

REFERENCES

- [1] Y. Yano, Nucl. Instr. Meth. B 261, 1009 (2007).
- [2] Y. Yano, Proc. 13th Int. Cyclo. Conf., 102 (1992).
- [3] O. Kamigaito et al., Rev. Sci. Instrum. 70, 4523 (1999).
- [4] M. Odera et al., Nucl. Instr. Meth. A 227, 187 (1984).
- [5] O. Kamigaito et al., Rev. Sci. Instrum. 76, 013306 (1999).
- [6] A. Goto et al., Proc. 12th Int. Cyclo. Conf., 51 and 439 (1989).
- [7] T. Mitsumoto et al., Proc. 17th Int. Conf. on Cyclotrons and Their Applications, 384 (2004).
- [8] J. Ohnishi et al., Proc. 17th Int. Conf. on Cyclotrons and Their Applications, 197 (2004).
- [9] H. Okuno et al., Proc. 17th Int. Conf. on Cyclotrons and Their Applications, 373 (2004).
- [10] T. Kubo et al., Nucl. Instr. Meth. B 204, 97 (2003).
- [11] T. Ohnishi et al., J. Phys. Soc. Jpn Vol.77, No.8, 083201 (2008).
- [12] R. Koyama et al., Proc. EPAC08, 1173 (2008).
- [13] N. Fukunishi et al., Proc. 23rd Int. Conf. on Particle Accelerators (PAC09), in print.
- [14] Y. Watanabe et al., RIKEN Accel. Prog. Rep. 42, to be published.
- [15] T. Uesaka et al., Nucl. Instr. Meth. B 266, 4218 (2008).
- [16] O. Kamigaito et al., Proc. of PASJ3-LAM31, WP78, (2006).
- [17] T. Nakagawa et al., Rev. Sci. Instrum. 79, 02A327 (2008).

INTENSITY-UPGRADE PLANS OF RIKEN RI-BEAM FACTORY

O. Kamigaito*, S. Arai, M. Fujimaki, T. Fujinawa, H. Fujisawa, N. Fukunishi, A. Goto, Y. Higurashi, E. Ikezawa, T. Kageyama, M. Kase, M. Komiyama, H. Kuboki, K. Kumagai, T. Maie, M. Nagase, T. Nakagawa, J. Ohnishi, H. Okuno, N. Sakamoto, Y. Sato, K. Suda, H. Watanabe, T. Watanabe, Y. Watanabe, K. Yamada, H. Yamasawa, Y. Yano, S. Yokouchi, RIKEN Nishina Center for Accelerator-Based Science, Wako-shi, Saitama 351-0198 Japan

Abstract

In 2008, the RIKEN RI-Beam Factory (RIBF) succeeded in providing heavy ion beams of ^{48}Ca and ^{238}U with 170 pA and 0.4 pA, respectively, at an energy of 345 MeV/u. The transmission efficiency through the accelerator chain has been significantly improved owing to the continuous efforts paid since the first beam in 2006. From the operational point of view, however, the intensity of the uranium beam should be much increased. We have, therefore, constructed a superconducting ECR ion source which is capable of the microwave power of 28 GHz. In order to reduce the space-charge effects, the ion source was installed on the high-voltage terminal of the Cockcroft-Walton pre-injector, where the beam from the source will be directly injected into the heavy-ion linac by skipping the RFQ pre-injector. The test of the ion source on the platform has started recently with an existing microwave source of 18 GHz. This pre-injector will be available in October 2009. We will show further upgrade plan of constructing an alternative injector for the RIBF, consisting of the superconducting ECR ion source, an RFQ, and three DTL tanks. An RFQ linac, which has been originally developed for the ion-implantation application will be reused for the new injector. Modification of the RFQ as well as the design study of the DTL are under progress. The new injector, which will be ready in FY2010, aims at independent operation of the RIBF experiments and super-heavy element synthesis.

INTRODUCTION

The accelerator complex of the RIKEN RI-Beam Factory (RIBF)[1] is schematically shown in Fig. 1. It consists of a heavy-ion linac (RILAC) [2], which is used as an injector, and four booster cyclotrons (RRC [3], fRC [4], IRC [5] and SRC [6]) in a cascade. The fRC is exclusively used for very heavy ions such as uranium and xenon, where the rf frequency of the RILAC is fixed to 18.25 MHz and the beam energy at the exit of the SRC is 345 MeV/u. For medium-mass ions such as calcium and krypton, the fRC is skipped; it is possible to tune the final energy in this variable-frequency mode. There is another acceleration mode in the RIBF, where the light ions such as deuteron and carbon are injected through the AVF cyclotron (K70 MeV) [7] and boosted by the RRC and SRC.

The RILAC plays another important role of providing intense beams for the synthesis of super-heavy elements

(SHE) using the GARIS spectrometer [8]. Combined with the energy booster [9], medium-mass nuclei such as iron and zinc are accelerated to the maximum energy of 5.8 MeV/u.

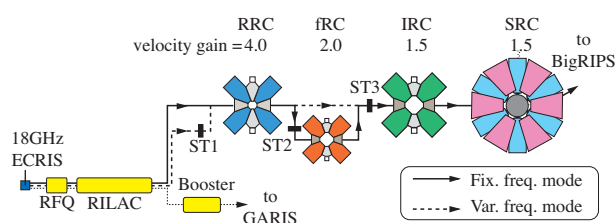


Figure 1: Conceptual layout of the accelerator chain of the RI-Beam Factory (RIBF). A linac injector (RILAC) is followed by the booster cyclotrons: RRC (RIKEN Ring Cyclotron, K540 MeV), fRC (fixed-frequency Ring Cyclotron, K570 MeV), IRC (Intermediate-stage Ring Cyclotron, K980 MeV), and SRC (Superconducting Ring Cyclotron, K2600 MeV). The charge strippers are indicated by ST1 - ST3.

As already reported [10], the intensities of the extracted beams from the SRC reached 170 particle-nano-ampere (pA) and 0.4 pA for ^{48}Ca and ^{238}U , respectively, at an energy of 345 MeV/u. The transmission efficiency through the accelerator chain has been significantly improved so far: the efficiency from the exit of the RILAC to the exit of the SRC has exceeded 60 % in the calcium acceleration. Using the uranium beam in the BigRIPS spectrometer [11], more than twenty candidates of new radioactive isotopes were discovered within a week in November 2008. Thus the exploration into the nuclear extremes was started. The intensity of the calcium beam is coming closer to our final goal of 1000 pA, as mentioned above. It is clear that, however, we need more beams from the ion source for the very heavy ions such as uranium. In order to meet the demand, a new superconducting ECR ion source has been constructed, which is capable of the microwave power of 28 GHz. We are planning to upgrade the intensity in two steps with different injection schemes as shown below.

* kamigait@riken.jp

NEW PRE-INJECTOR FOR RILAC

Superconducting ECR ion source[12, 13]

The main features of the ion source are as follows. First, the size of ECR surface is large. It has as large plasma volume as 1100 cm^3 . Second, the field gradient and surface size at ECR zone can be changed independently to study these effects on the ECR plasma.

Six sets of solenoid coils and hexapole coil are used for making the magnetic field. The inner solenoid coils are used for introducing a flat magnetic field region between the mirrors. The maximum magnetic field of RF injection side, that of beam extraction side, and radial magnetic field at the surface of the plasma chamber are 3.8, 2.4 and 2.1T, respectively.

A photograph of the coil system is shown in Fig. 2. The coils use a NbTi-copper conductor and are bath-cooled in liquid helium. The hexapole field in the central region is increased by using iron poles, which is same structure as the VENUS ion source at LBNL [14]. The excitation test of the coil system was successfully performed in October 2008. After assembling the cryostat, the ion source was brought to RIKEN in December 2008. The source has been installed on the high-voltage platform as illustrated below.

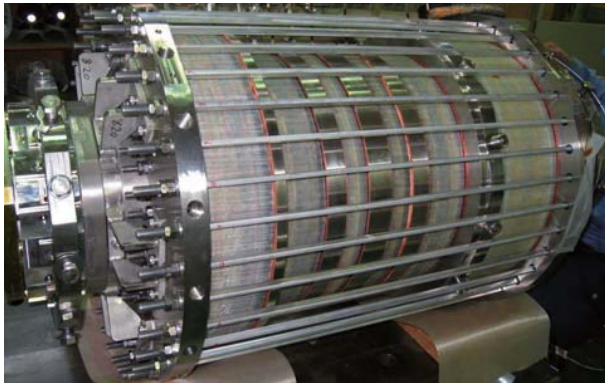


Figure 2: Superconducting coil of the ECR ion source.

Beam Line

In the fixed-frequency operation of the RIBF shown in Fig. 1, the uranium beam starts with 35+ from the ion source. Low frequency operation of the RFQ pre-injector [15] at 18.25 MHz requires, however, such low extraction voltage as 5.7 kV for the uranium beam. High power beams of 5.7 kV surely grow up due to their space charge forces in the low-energy beam-transport (LEBT) line. On the other hand, the RILAC requires such low injection energy as 127 kV for this beam. Therefore, we decided to put the superconducting ECR ion source on the high-voltage terminal of the original Cockcroft-Walton pre-injector so that extracted beam from the source can be directly injected to the RILAC, skipping the RFQ, as shown in Fig. 3. We expect that the emittance growth can be suppressed in the beam

Radioactive Ion Beam Facilities

transport system. In addition, the extraction voltage of the ion source can be set as high as 27 kV, which will help us to obtain higher beam currents.

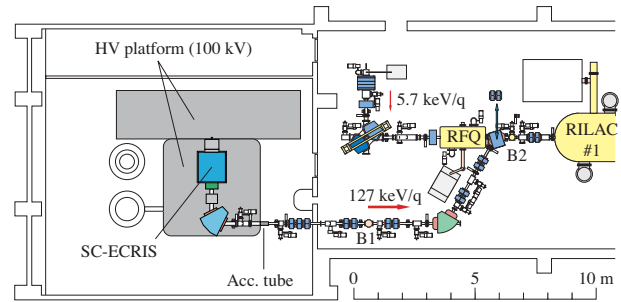


Figure 3: Configuration of the new pre-injector for the RILAC. B1 and B2 denote the bunchers operated at the fundamental frequency.

On the platform, an LEBT system including an analyzing magnet and beam monitors are settled. The analyzing magnet has been constructed according to the design of the LBNL [16]. The large pole gap of 180 mm leads to beam aberration due to fringing fields. Corrective measures have been taken by shaping the pole faces in such a manner as to introduce aberration countering sextupole moments to the beam. The original power generator of 50 kVA will be used for the devices on the platform as well as an additional power transformer of 50 kVA. At the end of the platform, an accelerating tube with ten gaps is placed, which was confirmed to withstand the high DC voltage of 120 kV.

The beam from the high-voltage terminal goes through a medium-energy beam-transport (MEBT) line consisting of two bending magnets of 60° , one quadrupole triplet, four quadrupole doublets, and a buncher system before joining the beam line from the RFQ. Existing devices will be reused for all these components: for example, the bending magnets used here are the ones that were once removed from the beam line from the Cockcroft-Walton in 2003. The base plate of the second bending magnet was designed so that dipole can be quickly replaced by a quadrupole doublet for the variable-frequency operation and the GARIS experiments where the RFQ pre-injector is used.

The MEBT line, which has a feature of achromatic transport, was designed mainly based on the TRANSPORT code [17]. Detailed simulations have also been performed using the TRACK code [18] including the space charge effects [19].

The vacuum is another key issue for the transport system. In order to keep the beam loss in the MEBT line below 5 %, it was estimated that the vacuum level should be lower than 2×10^{-6} Pa [20]. We will use four TMPs of 220 l/s and two cryogenic pumps of 750 l/s in the MEBT line to realize this vacuum level. In addition, surface treatment was applied to almost all the vacuum components: the beam pipes made of aluminum alloy and the vacuum chamber in the second dipole have been chemically polished, and the chamber in the first dipole adopted electric polishing.

Current Status

The ion source and the LEBT system have been fully assembled on the platform. Excitation test of the superconducting coils and vacuum test were successfully performed so far. We also confirmed that the devices on the terminal work perfectly with the high voltage being applied. The first plasma was ignited on May 11 with an existing microwave power source of 18 GHz. Since a small problem was found in the cooling channel of the plasma chamber, the rf power is limited to 50 W at present. A new plasma chamber will be ready in June and the generation of uranium ions will be started in this summer.

The installation and alignment of the MEBT line will be completed in June. The evacuation of the beam line will be started in June, and the beam will be acceptable in July. In October, the accelerator complex of the RIBF will have a configuration shown in Fig. 4: the expected beam current of uranium is 5 pA after the SRC. The medium-mass ions are still to be delivered from the original 18-GHz ECR ion source. This injection scheme with two ion sources will make it possible to reduce the switching time of the beam which is necessary for changing the ion species.

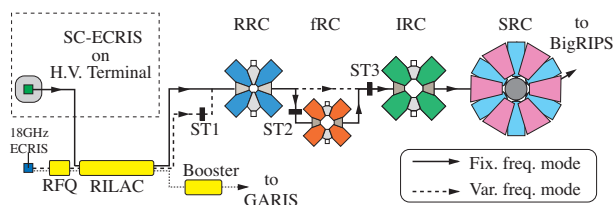


Figure 4: Expected configuration of RIBF at the middle of FY2009. Heavy ions such as uranium and xenon will be supplied from the superconducting ECR ion source on the high-voltage terminal of the Cockcroft-Walton generator.

NEW LINAC INJECTOR FOR RIBF

Outline

The recent success in the synthesis of SHE [8] using the GARIS spectrometer in the RILAC facility strongly encourages us to pursue the search for the heavier elements and to study the physical and chemical properties of SHEs more extensively. This compels us to provide a longer beam time for these experiments. However, the SHE research and RIBF conflict with each other, because both of them use the RILAC. Therefore, a new additional injector linac to the RRC has been proposed and designed [21], which will make it possible to conduct the SHE research and RIBF independently, as shown in Fig. 5. The new injector, which will be placed in the AVF-cyclotron room, will be used exclusively in the fixed-frequency operation of the RIBF.

The injector is designed to accelerate ions with a mass-to-charge ratio of 7, aiming at heavy ions such as $^{136}\text{Xe}^{20+}$

Radioactive Ion Beam Facilities

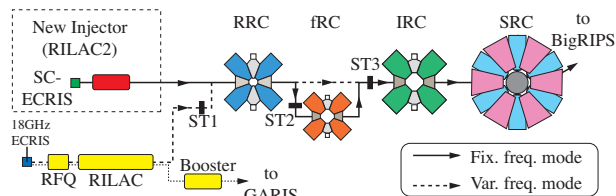


Figure 5: Expected configuration at the end of FY2010. Heavy ions such as uranium and xenon will be supplied by the new injector. Independent operation of RIBF and SHE research will be realized.

and $^{238}\text{U}^{35+}$, up to an energy of 680 keV/u in the cw mode. The output beam will be injected to the RRC without charge stripping. The injector consists of an ECR ion source, an LEBT system including a pre-buncher, an RFQ linac based on the four-rod structure, and three DTL tanks based on the quarter-wavelength resonator (QWR). There is a rebuncher resonator between the RFQ and the first tank of the DTL. The rf resonators excluding the pre-buncher are operated at a fixed rf frequency of 36.5 MHz, whereas the pre-buncher is operated at 18.25 MHz. Strong quadrupole magnets will be placed in the beam line between the rf resonators.

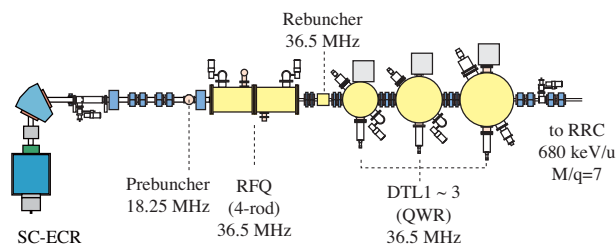


Figure 6: Schematic drawing of the new injector.

Construction of the new injector has started since the budget was fortunately approved at the end of FY2008. In order to save the cost, we decided to use the superconducting ECR ion source mentioned above for the injector: they will be moved to the AVF-cyclotron room in summer 2010. Moreover, we will reuse an RFQ linac which was constructed fifteen years ago, as shown below, and modify a decelerator resonator developed for Charge-State-Multiplier system[22] for the last tank of the DTL.

RFQ Linac

In November 2007, an RFQ system including two post accelerators and their rf amplifiers was transferred to RIKEN through the courtesy of Kyoto University. This RFQ system was originally developed by Nissin Electric Co., Ltd. in 1993 [23]. Since the termination of its acceleration tests in the company, the system has been maintained in the Advanced Research Center for Beam Science, Kyoto University for several years.

The RFQ linac, based on a four-rod structure, accelerated heavy ions of $m/q = 16$ up to an energy of 84 keV/u in the cw mode with an rf frequency of 33.3 MHz. When the RFQ resonator is modified so as to have a resonant frequency of 36.5 MHz, it becomes possible to accelerate ions of $m/q = 7$ to 100 keV/u without changing the vane electrodes.

The main parameters of the RFQ after the modification is listed in Table 1, that were obtained by scaling the original parameters. The required rf power for the intervane voltage of 42.0 kV is 11 kW according to the original shunt impedance of 77.9 k Ω [24]. The RFQ has been reassembled in the RIBF building and high power tests was successfully performed in October 2008 using the original amplifier at 33.3 MHz. No significant problem was detected even at the input power of 14 kW.

Table 1: Main Parameters of RFQ

Frequency (MHz)	36.5
Duty	100 %
Mass-to-charge ratio (m/q)	7
Input energy (keV/u)	3.28
Output energy (keV/u)	100
Input emittance (mm·mrad)	200 π
Vane length (cm)	222
Intervane voltage (kV)	42.0
Mean aperture (r_0 : mm)	8.0
Max. modulation (m)	2.35
Focusing strength (B)	6.785
Final synchronous phase	-29.6°

In order to modify the resonant frequency, we are planning to put a block tuner into every gap between the posts supporting the vane electrodes. The size of the tuner was optimized by Microwave Studio, and the rf measurement using test pieces made of aluminum was started as shown in Fig. 7. High power tests at 36.5 MHz will be done in October.

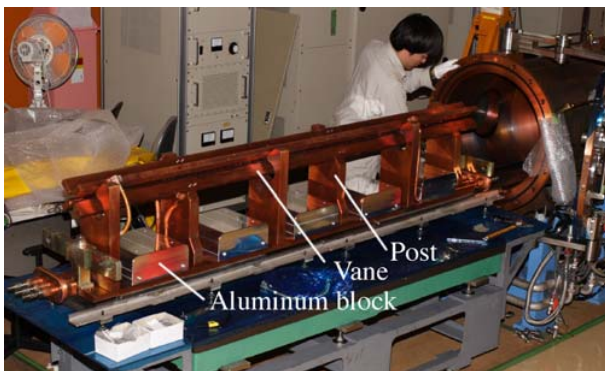


Figure 7: RFQ electrodes in preparation for the rf measurements with block tuners made of aluminum.

Drift Tube Linac

Initial parameters of the DTL were determined by optimizing the beam dynamics and rf characteristics of the resonators. A computer program, developed for the design of the RILAC booster [9], was used for the beam tracking simulation, whereas Microwave Studio was used to estimate of the rf-power consumption. The beam calculations have also been checked by the TRACK code.

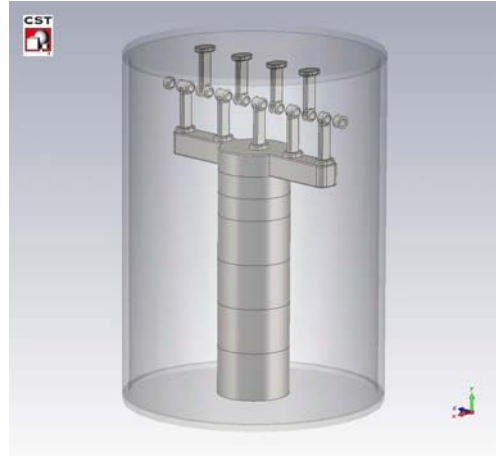


Figure 8: Schematic drawing of the DTL resonator.

The structure of the DTL tanks is designed based on the quarter-wavelength resonator, which is similar to that of the RILAC booster. The inner diameter of the resonators ranges from 0.8 to 1.3 m, depending on the beam energy. The maximum electric field on the drift tubes is kept below 1.2 Kilpatrick. Table 2 shows the main parameters of the DTL.

Table 2: Design parameters of DTL

Resonator	DTL1	DTL2	DTL3
Frequency (MHz)	36.5	36.5	36.5
Duty	100 %	100 %	100 %
Mass-to-charge ratio (m/q)	7	7	7
Input energy (keV/u)	100	220	450
Output energy (keV/u)	220	450	680
Length (= Diameter: m)	0.8	1.1	1.3
Height (m)	1.3	1.4	1.9
Gap number	10	10	8
Gap voltage (kV)	110	210	260
Gap length (mm)	20	50	65
Drift tube aperture (a : mm)	17.5	17.5	17.5
Peak surface field (MV/m)	8.2	9.4	9.7
Synchronous phase	-25°	-25°	-25°
Power (for 100% Q : kW)	5.1	13.4	15.4

The power losses estimated with Microwave Studio range from 5 to 15 kW. In order to save the construction cost and space for the equipments, direct coupling scheme has been adopted for the rf amplifier. Detailed design of the amplifier is under progress.

Beam Line

Design study of the LEBT section from the analyzing magnet to the RFQ is almost completed, as shown in Fig. 6, using TRANSPORT and TRACK. A quadrupole quartet has been introduced to help the beam matching with the solenoid coil placed before the RFQ. The position of the pre-buncher was optimized so that enough bunching effect could be obtained for the expected beam current of 200 μA of $^{238}\text{U}^{35+}$.

The DTL requires compact quadrupole magnets with very high magnetic-field gradients (0.4 T/cm), to obtain sufficient transverse focusing as well as to prevent the phase width of the accelerated beam from spreading widely. Two types of quadrupole magnets have been designed: short quadrupoles (Q_S) with an effective length of 6 cm and long quadrupoles (Q_L) with an effective length of 10 cm. These quadrupole magnets will be used as quadrupole doublets ($Q_S + Q_S$) and quadrupole triplets ($Q_S + Q_L + Q_S$). The maximum beam width estimated with the optical calculations is 45 mm, as shown in Fig. 9, and the bore diameter was chosen to be 50mm. Therefore, the pole-tip field should be approximately 1 T, which is close to the limit of the conventional normal-conducting magnets. Another difficulty in the design is that the space allowed for the coils is as small as 4 cm on each side in the beam direction. It was finally confirmed using the TOSCA code that a field gradient of 0.41 T/cm is excited by 11900 ampere turns per pole for the long quadrupole magnet, which corresponds to an overall current density of 6 A/mm².

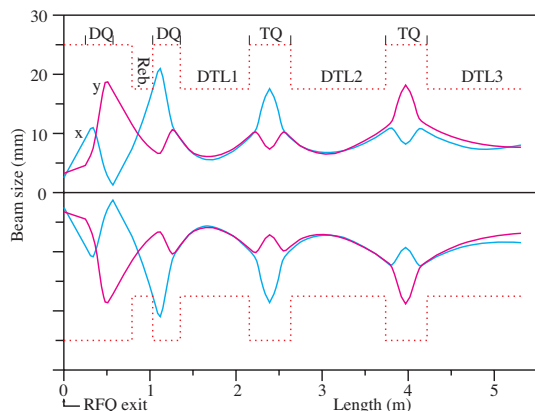


Figure 9: Calculated beam envelopes in the DTL. The emittance ellipses were assumed to be 0.6π mm-mrad (normalized) in both of the transverse planes.

One of the post accelerators of the ion implantation system [24] will be reused for the rebuncher between the RFQ and the DTL. It is based on a spiral loaded resonator with three gaps. The drift tubes and the beam chamber are now under fabrication. Another post accelerator will also be modified and used for a rebuncher in the high-energy beam-transport (HEBT) section between the DTL and RRC.

Radioactive Ion Beam Facilities

Outlook

The RFQ and DTL including the MEFT line will be installed in the AVF-cyclotron room in March 2010. The superconducting ECR ion source will be moved to the new injector in summer 2010, and we hope to deliver the uranium beam of 50 - 100 pA from the SRC by using this injector.

REFERENCES

- [1] Y. Yano, Nucl. Instrum. & Methods B261 (2007) 1009.
- [2] M. Odera et al., Nucl. Instrum. & Methods 227 (1984) 187.
- [3] H. Kamitsubo, Proc. 10th Int. Conf. on Cyclotrons and their Applications, East Lansing, MI, USA, 1984, p. 257 (1984).
- [4] N. Inabe et al., Cyclotrons'04, Tokyo, Oct. 2004, 18P15, p. 200 (2004), T. Mitsumoto et al., *ibid*, 20P12, p. 384, <http://www.JACoW.org>.
- [5] J. Ohnishi et al., Cyclotrons'04, Tokyo, Oct. 2004, 18P14, p. 197 (2004), <http://www.JACoW.org>.
- [6] H. Okuno et al., IEEE Trans. Appl. Supercond. 17 (2007) 1063.
- [7] A. Goto et al., Proc. of 12th Int. Conf. on Cyclotrons and their Applications, Berlin, Germany, p. 51 (1989).
- [8] K. Morita et al., J. Phys. Soc. Jpn. 78 (2009) 064201.
- [9] O. Kamigaito et al., Rev. Sci. Instrum. 76 (2005) 013306.
- [10] N. Fukunishi et al., PAC'09, Vancouver, May 2009, MO3GRI01.
- [11] T. Kubo et al., Nucl. Instrum. & Methods B204 (2003) 97.
- [12] T. Nakagawa et al., Rev. Sci. Instrum. 79 (2008) 02A327, ECRIS'08, Chicago, Sep. 2008, MOCO-B01, p. 8 (2008), <http://www.JACoW.org>.
- [13] J. Ohnishi et al., EPAC'08, Genoa, Jun. 2008, MOPC153, p. 433 (2008), <http://www.JACoW.org>.
- [14] D. Leitner et al., Cyclotrons'07, Giardini Naxos, Sep. 2007, p. 265 (2007), <http://www.JACoW.org>.
- [15] O. Kamigaito et al., Rev. Sci. Instrum. 70 (1999) 4523.
- [16] M. Leitner, et al., Proc. 15th Inter. Workshop on ECR Ion Sources, June 12-14, 2002, Jyväskylä, Finland.
- [17] PSI Graphic Transport Framework by U. Rohrer based on a CERN-SLAC-FERMILAB version by K.L. Brown et al.
- [18] P. N. Ostroumov, V. N. Aseev, and B. Mustapha., Phys. Rev. ST. Accel. Beams 7 (2004) 090101.
- [19] H. Okuno, HB2008, Nashville, Aug. 2008.
- [20] G. Auger et al., GANIL R 01 02, Sep. 2001, p. 50 (2001).
- [21] O. Kamigaito et al., PASJ3-LAM31, Sendai, Aug. 2006, WP78, p. 502 (2006).
- [22] O. Kamigaito et al., LINAC'98, Chicago, Aug. 1998, TU4085, p. 603 (1998), <http://www.JACoW.org>.
- [23] H. Fujisawa, Nucl. Instrum. Methods A345 (1994) 23.
- [24] H. Fujisawa et al., Proc. 7th Int. Symp. on Advanced Energy Research, Takasaki, Mar. 1996, p. 436 (1996).

PRESENT AND FUTURE OF ELECTROSTATIC ACCELERATORS

David C. Weisser, Department of Nuclear Physics, Research School of Physics and Engineering,
College of Science, Australian National University, Canberra, Australia

Abstract

Electrostatic accelerator laboratories were the nurseries for the heavy ion physics research of today and the accelerators this research needed. The first conference, of what has evolved into the HIAT series, was the “International Conference on the Technology of Electrostatic Accelerators” hosted by the Daresbury Laboratory in 1973. While some of the founding labs of this series have ceased doing accelerator based physics, electrostatic accelerators still inject beams into present day heavy ion boosters. Electrostatic accelerators also continue to provide beams for nuclear and applied physics in laboratories with and without boosters.

The development of electrostatic accelerators remains active and will continue in the next few years. The improvements have been spurred by injection beam requirements of boosters as well as the special transmission and stability needs of accelerator mass spectrometry.

The survey of the electrostatic accelerator community presented here, has identified a broad range of improvements and uses as well as future technical directions for electrostatic accelerators.

INTRODUCTION

The present and future cannot be understood without at least a glance to the past. The evolutionary tree of nuclear physics separated into the electrostatic branch and the circular accelerator branch in the 1930s. Both branches nurtured nuclear physics research and developed their respective technologies right through the 1970s.

The first conference of the HIAT series was at Daresbury Laboratory and titled the “International Conference on the Technology of Electrostatic Accelerators”. After a small alteration, the title “International Conference on Electrostatic Accelerator Technology” served for the next two conferences in Strasbourg in 1977 and Oak Ridge in 1981. These three conferences concentrated on the technology central to the new large machines in the three hosting laboratories: the Daresbury 20-30 MV machine, the 20-30 MV Vivitron and the Oak Ridge 25 URC. The maximum voltage aspired to became more conservative over time. Only the 25 URC still exists and now runs above 24 MV. None of the participants in the first conference is here today.

The striving for higher voltages in large machines went along with the development of booster RF machines. These developments were in response to the desire of

nuclear physics researchers for ever higher energies to explore reactions with heavier targets well above the Coulomb barrier using light ions. This voltage push was soon subsumed into the budding of research with heavy ion beams. The booster efforts and successes lessened the impact on research of the failure of the electrostatic machines of the 1970s to reach the 20+ MV terminal voltages. The competition of the booster concept acted as a spur to Daresbury and Strasbourg but also contributed to their eclipse.

This eclipse was gradual as reflected in the evolution of the conference title to “International Conference on Electrostatic Accelerator Technology and Associated Boosters” for the next three conferences; the 1985 conference in Buenos Aires, the 1989 conference in Strasbourg-Heidelberg and the 1992 conference in Padua (Legnaro). Even at these transitional conferences, the boosters allowed were LINACs rather than the barely tolerated cyclotron booster at Munich. The linear-circular divide was alive but faltering.

Reality finally seeped into the title as the “International Conference on Heavy Ion Accelerator Technology” for the conferences in Canberra (1995), Argonne (1998), New Delhi (2002), Brookhaven (2005) (a combined conference with SNEAP), and now in Venice (2009) Legnaro. This change reflected proper focus on the broad topic of heavy ion accelerators and an open-minded acceptance of combined linear and circular machines. The linear and circular accelerator tree branches have now coalesced and are stronger for it.

Survey

Questions about their facilities were sent to staff at many laboratories with electrostatic accelerators and broadcast on the Symposium of North Eastern Accelerator Personnel bulletin board. I apologize to those at some facilities who have been inadvertently left out. The generous input of the colleagues who have contributed is gratefully acknowledged as the basis of this report. They represent the full gamut of electrostatic accelerators ranging from small ion implanters, neutron generators and ion beam analysis facilities to radioactive ion beam accelerators and injectors with straight nuclear physics and accelerator mass spectrometry machines in the middle.

Table 1 summarizes input. Labs are abbreviated by three letters so that the relative involvement in various areas is clearer in Table 2.

Table 1: Survey of Electrostatic Accelerators

Lab	Abbreviation	Respondents	e-mail address
Albuquerque	San	Barney Doyle	"Doyle, Barney L" <bldoyle@sandia.gov>
Argonne	ANL	Richard Pardo	Richard pardo <pardo@phy.anl.gov>
Beijing	CIA	Guan Xia Ling	Guan XiaLing <guanxl@ihep.ac.cn>
Brookhaven	BNL	Dannie Steski, Chuck Carlson	Dannie Steski <steski@bnl.gov> Charles Carlson <ccarlson@bnl.gov>
Catania	LNS	Danilo Rifuggiato	Danilo Rifuggiato <rifuggiato@lns.infn.it>
Geel	IRM	Göran Lövestam	Goeran.LOEVESTAM@ec.europa.eu
Heidelberg	MPI	Roland Repnow	repnow <repnow@mpi-hd.mpg.de>
Legnaro	LNL	Davide Carlucci	davide.carlucci@lnl.infn.it
Lucas Heights	ANS	David Garton	"GARTON,David" <dbg@ansto.gov.au>
Melbourne	Mel	Roland Szymanski	Roland Szymanski <ras@unimelb.edu.au>
Michigan	Mic	Ovidiu Toader	"Toader, Ovidiu" <ovidiu@umich.edu>
Middleton	NEC	Greg Norton	NEC <nec@pelletron.com>
Mumbai	TIF	Raj Pillay	Raj Pillay <pillay@tif.res.in>
Munich	MLL	Ludvig Beck	Ludwig.Beck@physik.uni-muenchen.de
New Delhi	IUA	Amit Roy	Amit Roy <roy@iuac.res.in>
Oak Ridge	ORN	Martha Meigs	Martha Meigs <meigsmj@ornl.gov>
Purdue	Pur	Tom Miller	"Miller, Thomas Edward" <millerte@purdue.edu>
São Paulo	USP	Alinka Lépine-Szily	alinka.lepine@dfn.if.usp.br
Strasbourg	VIV	Michel Letournel	Michel LETOURNEL <mletournel@vivirad.fr>
Tallahassee	FSU	Ingo Wiedenhoever	Ingo Wiedenhoeve<ingo@nucmar.physics.fsu.edu>
Tel Aviv	Wei	Yourm Lasser	Yoram Lasser <yoraml@ariel.ac.il>
Tokai	JAE	Matsuda Makoto	Matsuda Makoto <matsuda.makoto@jaea.go.jp>
Tokyo	HFI	Todoa Iwai	Takeo Iwai <iwai@nuclear.jp>
Woods Hole	NOS	Karl von Reden	Karl von Reden <kvonreden@whoi.edu>
Yale	Yal	Jeff Ashenfelter	Jeff Ashenfelter <ash@riviera.physics.yale.edu>
Zurich	ETH	Lukas Wacker	Lukas Wacker <wacker@phys.ethz.ch>

THE PRESENT

The members of the electrostatic accelerator family share many traits but display interesting differences in the same way as siblings and cousins do. They each have started with a technical inheritance from either High Voltage Engineering Corporation, HVEC, or from National Electrostatics Corporation, NEC. Each suite of stating equipment was somewhat different and each evolved in response to the strengths of their individual staffs, host laboratories and scientific-political environment.

Keys to Success

In my view, all successful labs have in common three essential traits. First is the excellence of their technical staff characterized by their competence, commitment and innovative spirit. The second is the quality of the scientific staff. Their status in the international physics community is based on productivity built upon the competence of their home accelerator facilities. They are also notable for nimble response to changing science priorities and clever exploitation of the strengths in local equipment and personnel. This scientific competence provides the political strength that protects and nurtures their home accelerators. Thirdly, the best labs profit from close collaboration between the scientific and technical staff.

Table 2: Activities and Plans

Category	Past	Next	Wish
Power supplies & Vac Eq	Yal, MPI, ANS, TIF, BNL, ANU, ORN, FSU, MLL	Yal, ANS	Yal, MPI, ANS
Accel Tubes HVEC VIVIRAD	FSU, IRM, Mic		LNS, LNL
Accel Tubes NEC	JAE, MPI		ORN
Voltage grading	LNL, MPI, TIF, San	USP, IUA	MPI, TIF, IUA
Computer control upg	ANS, MLL, MPI, ANS, TIF	FSU, ANU, IRM, Pur	BNL
Beam pulsing	IUA	TIF, FSU, USP, ANU, Yal	
Positive ion source	ANL, LNL, BNL	ANL, LNL, BNL	
ECR Terminal	JAE	JAE, IRM,	Yal, Mel, HFI
High vlotage deck	HMI, CIA, ANS, MPI	HMI, CIA	
LINAC expand	CIA	CIA	FSU, San, JAE
Replace/Add El Accel		ANS	Mel, Mic, NOS, IRM
Pellet chains	San, Yal		Wei, IUA
RIB accelerator	LNS, ORN, CIA	LNS, ORN, CIA	Yal, JAE
RIB recoil	FSU, Pur	FSU, Pur, ANU	Yal

Consolidation

The present focus of most labs is on consolidation of existing facilities exemplified by the replacement of old electronic control and vacuum equipment. This has the largest numbers of entries in Table 2. Effort also is directed at improving reliability of control equipment and power supplies.

Other important areas for attention to shortcomings are in voltage grading systems in the Sao Paulo 8UD and the replacement of accelerator tubes in the Florida State FN. Computer control systems are being modernized in several labs reflecting the normal life trajectory of computer equipment.

Reliability at the Brookhaven MPs has been greatly improved by the adoption of laser ablated carbon stripper foils bought from Peter Maier-Komor in Munich. Since these foils last about three times longer than the locally made arc discharge foils, the frequency of tank openings has decreased and the beam is more consistent in intensity as the foil ages. Laser ablated foils from Peter Maier-Komor, are also in use for heavy beams at ANU and New Delhi.

The change of role for large electrostatic machines to injecting boosters has lessened the need to achieve the highest possible terminal voltage which results in much more reliable operation at Heidelberg and Brookhaven. Facility reliability is enhanced by the redundancy of having two MPs at Brookhaven and the choice of injectors at ANL and Heidelberg.

The successful marriage of DC electrostatic machines to RF boosters depends upon efficient beam pulsing

systems. This is a center of current interest in Mumbai, Sao Paulo and Florida State. Competent pulsing systems are also a valuable tools for the basic nuclear physics tasks of measuring nuclear lifetimes and time of flight particle identification. Beam pulsing is convenient for AMS facilities providing flexibility to reduce the intensity stable beams.

Areas of Use

The range of science being performed is still dominated by nuclear physics in many labs but is no longer done at facilities concentrating on ion beam analysis like the labs at Michigan, Tel Aviv, Tokai-Mura and Sandia. Dedicated AMS facilities like Lucas Heights, Woods Hole and Purdue also do no nuclear physics. There is a nuclear physics component for the MPs at Brookhaven serving as injectors for the Relativistic Heavy Ion Collider, RHIC, or for the NASA Space Radiation Laboratory, NSRL, as well as providing for some stand alone users. The Heidelberg MP, on the other hand, is an injector for the heavy ion storage ring and other facilities dedicated to atomic physics research.

Many labs spend 75% or more of their effort on nuclear physics. These include Florida State, Geel, Oak Ridge, Legnaro, Catania, Yale and Canberra. The competing uses include AMS, single event upset of electronic devices, materials analysis and atomic physics. This is the case for JAERI, Brookhaven, New Delhi and Munich.

Innovation

The focus of development has shifted in several labs from the accelerator to novel and demanding

Electrostatic Accelerators

experimental equipment. The introduction of light radioactive ion beams at Florida State, Notre Dame, Sao Paulo and Canberra has driven work on high intensity lithium beams used to bombard beryllium targets. The later three labs are exploiting superconducting solenoids to filter and focus the radioactive beam on secondary targets. While at FSU, a superconducting resonator homogenizes the energy of the radioactive beam impinging on the secondary target. The resulting small energy spread facilitates analysis of the reaction.

AMS continues to be an incubator for novel electrostatic accelerator development. NEC has developed a new type of "accelerator" that exploits their realization that the molecules of $^{12}\text{CH}_2$ and ^{13}CH , which would interfere with ^{14}C detection, can be dissociated in stripper gas at only 250 keV and not requiring the MeV terminals of the past. They are now building 500 kV tandems that are small versions of the standard 1.7 MV machines. But they have also taken the audacious step of eliminating the accelerator tank completely. This is accomplished in the Single Stage AMS facilities. [1] in which the ion source is near ground potential with the analysis devices and detectors on a 200 kV voltage deck. Since an accelerator tube is still used, this still qualifies as an electrostatic accelerator.

Exploitation of hundreds of kilovolts rather than millions of volts for molecule dissociation also features in an extremely novel ^{14}C AMS device from ETH Zurich [2]. This machine does away with gas insulation and uses high vacuum insulation instead. It also does away with graded accelerator tubes and replaces them with gap lenses. Basically, it resembles a 200 kV Einzel lens in which the central electrode contains a differentially pumped gas stripper canal. The hollow ceramic insulator supporting the electrode is connected to a turbo pump at ground potential. The stripper gas that escapes through a pair of pumping impedances, at the entrance and exit of the electrode, is pumped by another pair of turbo pumps. The high voltage comes from an external commercial high voltage power supply through another vacuum feed through. This accelerator confronts most of the challenges of electrostatic accelerator technology. These features include conditioning electrodes at extremely high surface electric fields in vacuum. A special challenge is maintaining vacuum good enough for insulation which is in conflict with the flow of stripper gas through pumping impedances. These need to be small to ensure good vacuum but large to allow 100% beam transmission. Careful beam optics is demanded to ensure excellent transmission through small stripper assemblies. As well, there are the usual problems with 200 kV across ungraded ceramic insulators and the x-rays inherent in such equipment.

THE FUTURE

Research topics, at most facilities, for the next two years or so are expected to be more of the same with marginal shifts in emphasis. This is less the case where

the electrostatic machines are in competition with positive ion injectors especially at Legnaro and Brookhaven. Although the Argonne FN injector, has been expected to be displaced by the positive ion injectors for the last ten years, it continues to be relied on for light ion beams and providing respite time for work on the other injectors. It is likely, that this strength-through-diversity will also keep the electrostatic injectors operating at Legnaro and Brookhaven longer than now anticipated.

Just about the full gamut of accelerator devices are on the agenda in Beijing. This lab stands out for vigorous expansion of its accelerator facility to cater for radioactive ion beam work as well as AMS. The Beijing Radioactive Ion-beam Facilities, BRIF, will have a 100 MeV, 200 μA proton cyclotron coupled to isotope separator. The MP will accelerate the radioactive ion beam and be coupled to a superconducting LINAC using quarter wave resonators.

The development of reliable electron cyclotron resonance, ECR, ion sources along with the improvement in spark protection in the terminals of machines, has enabled the return of terminal ion sources as important capabilities. This is being pursued in JAERI, a long exploiter of a terminal ECR ion source and in Geel. Reliable terminal ion sources avoid the limitations of terminal stripper foils with their limited lifetime to say nothing of the potential for increased beam intensity that positive ion sources offer. There is interest in terminal ECR sources from other facilities with single ended machines such as the 5U in Melbourne.

SUMMARY

The future of electrostatic accelerators lies in their continued use as flexible, reliable injectors, as stand alone nuclear physics facilities and in applied accelerator technology.

It is somewhat ironic that electrostatic accelerator technology is returning to terminal ion sources. Their displacement by the tandem concept was one of the tandem's great selling points. The solution of spark protection in large machines has been essential in allowing terminal ion sources to provide reliably the advantages of high intensity and noble element beams.

Large tandems were also the foundation facilities at which AMS was established. The electrostatic technology developed there informs the extrapolation to lower terminal voltage of the new compact AMS machines. The cross fertilization of technical ideas in AMS is evident in the careful beam optics needed for 100% beam transmission, beam chopping systems, differentially pumped strippers and electrostatic design.

The menu of possible improvements to electrostatic machines is now quite bare. Even the most exciting innovation in cleaning the inside of NEC accelerator tubes with high pressure water by Takeuchi [3], is from 2003. NEC has now adopted high pressure cleaning to deal with alumina particulates during the manufacturing process. The cross fertilization from superconducting

LINAC technology to electrostatics, exemplified by the high pressure cleaning, has not been able to be more thoroughly exploited because of the difficulty in maintaining class 10 cleanliness in large electrostatic machines during tube installation, alignment and maintenance. Thus the Takeuchi's tactic of cleaning the inside of the tube after assembly is superior to the pre-cleaning adopted by NEC.

The high gradient tubes from NEC still maintain the historic 30 kV per 1.25 cm insulation gap and achieve total voltage increase by extending into the dead sections. Extended tubes were introduced many years ago by Michel Letournel in Strasbourg and have long been standard in large HVEC machines.

The aspirations of some leading edge electrostatic accelerator laboratories are moderated by the completion for resources from LINACs and positive ion injectors.

The resources are not only financial but the interest and enthusiasm of young accelerator personnel. The strong interest shown in HIAT 2009 suggests that these essential ingredients to accelerator technology are still vibrant and perhaps sufficiently widespread to nurture our diverse technologies.

REFERENCES

- [1] J. B. Schroeder, T. M. Hauser, G. M. Klody, G. A. Norton, R. L. Loger, R. L. Kitchen and M. L. Sundquist, Nucl. Instr. and Meth. B240 (2005) 463-467.
- [2] H. Synal, M. Stocker, M. Suter, Nucl. Instr. and Meth B 259 (2007) 7-13.
- [3] S. Takeuchi, T. Nakanoya, H. Kabumoto, T. Yoshida, Nucl. Instr. and Meth. A 513(2003)429-438.

UPGRADE OF THE BUCHAREST FN TANDEM ACCELERATOR

S. Dobrescu, I. Branzan, C. V. Craciun, G. Dumitru, C. Florea, D. Ghita, G. Ion, G. Mihon, D. Moisa, D. V. Mosu, G. Naghel, C. Paun, S. Papureanu and T. Sava
National Institute for Physics and Nuclear Engineering "Horia Hulubei"
77125 Magurele-Ilfov, Romania

Abstract

The Bucharest FN Tandem Accelerator was put in operation in 1973 and upgraded a first time in 1983 to 9 MV. In the period 2006-2009 a second program of the tandem upgrade was performed aiming to transform this accelerator in a modern and versatile facility for atomic and nuclear physics studies as well as for different applications using accelerated ion beams. The upgrade was achieved by replacing the main components of the tandem by new ones and by adding new components.

The old HVEC belt of the Van de Graaff generator was replaced by a "pelletron" system, the old inclined field stainless steel electrodes accelerator tubes were replaced by titanium spiral field tubes, the old HICONEX 834 sputter negative ion source was replaced by a new SNICS II sputter source and all old electronic equipment including NMR and Hall probe gauss meters as well as low voltage and high voltage power supplies for the magnets, lenses and ion sources were replaced by new ones.

The new equipment added to the tandem consists of a helium negative ion source, a new injector based on a multi-cathode ion source 40 MC-SNICS II for AMS applications, a new GVM, a new pulsing system in the millisecond range and a new chopper and bunching system for pulsing the ion beam in the nanosecond range. Now the tandem is currently operated in very stable conditions up to 9 MV on a basis of about 4000 hours/year accelerating a broad range of ion species.

INTRODUCTION

The Bucharest FN tandem accelerator (made by High Voltage Engineering Corp. – HVEC, USA) was commissioned in 1973 as a major Romanian facility for atomic and nuclear physics researches using accelerated ion beams. After a first upgrade in 1983 (installation of a sputter negative ion source [1] and increase of the terminal voltage from 7.5 MV to 9 MV by installing inclined field stainless steel tubes and adding SF₆ to the tank gas) the tandem delivered up to now in average 3500 hours/year a large range of accelerated ion species. This long period was marked in 1977 [2] and 1986 by two major damages of the tandem column due to strong earthquakes. In 1990 an original protection system of the tandem tank against earthquakes was installed [3, 4].

The main original tandem equipment still in use in 2006 was in very poor condition due to physical and moral wear and some of the necessary spare parts were no longer available on the market. After an analysis of the opportunity to invest in this old tandem accelerator, it was

decided to change most of the equipment and to upgrade the tandem so that to convert the Bucharest tandem into a modern and versatile machine. The main motivations of this decision were: 1) such a facility is still important for specific atomic and nuclear physics researches; 2) a tandem accelerator is a very good tool for applications such as ion beam analysis – IBA (PIXE, RBS) and accelerator mass spectrometry – AMS; 3) a tandem accelerator laboratory is important for the education of young generations of physicists; 4) the preparation at the tandem accelerator of experiments at large scale facilities - LSF where the access is very limited is important; 5) last but not least, the Bucharest tandem accelerator is the single facility of this type not only in Romania but also in the south-east Europe, so that by its upgrade it may become a facility of regional importance.

Following this decision, a plan of upgrading the Bucharest tandem accelerator was started in 2006, the plan spreading over three and a half years. This long period is partially due to the limited and gradual financing but also to the decision to do the implementation of the new equipment with minimum interruptions of the tandem operation and delivery of accelerated ion beams.

The upgrade of the Bucharest tandem consisted of the following actions:

- modification of the Van de Graaff generator by installation of a "pelletron" system instead of the HVEC belt which is no more produced;
- installation of a new set of accelerator tubes in the tank;
- renewal and development of the tandem injector by installing a new SNICS II sputter negative ion source, development and installation of a new source for negative helium ions and installation of a dedicated injector for AMS based on a sputter negative ion source (MC-SNICS II);
- development and installation of a millisecond ion beam pulsing system;
- installation of a nanosecond pulsing system of the ion beam;
- replacement of all electrical equipment (low voltage and high voltage power supplies, fluxmeters, GVM) by new ones;
- refurbishment of the vacuum system by installing new vacuum pumps, new vacuum valves and a new vacuum measurement system.
- improvement of auxiliary equipment.

The upgrade program was started in order to diversify the available ion beam species, to enhance the quality of the accelerated beam and to make the accelerator much more reliable and stable, covering so the requirements of

modern research and applications with ion beams delivered by an accelerator. The general configuration of the tandem was conserved. That means the HVEC 3 legs, 20⁰ inflection magnet for the injector, the 90⁰ analyzing magnet of the accelerated ion beam (1 m radius of beam curvature) and the 7 legs switching magnet that deflect the beam toward two experimental rooms remained in position.

Some of the works performed in the frame of this upgrade program were previously reported [5]. Here are outlined all the aspects of this program and are given more details.

DESCRIPTION OF THE MAIN WORKS FOR THE TANDEM UPGRADE

Pelletron System Installation

The “pelletron®” system made by National Electrostatic Corporation - NEC, USA for the Van de Graaff generator of an FN tandem accelerator consists of two chains installed on the left outer side of the column in the tank. On the right side of the column are installed the accelerator tubes. Pelletron chains are made of metal pellets connected by insulating nylon links and are charged by an induction scheme [6]. In order to be able to install the pelletron chains, a new location of the terminal voltage resistive divider installed since 1990 on the left outer side of the column had to be found keeping in the same time the advantages of the screwed system [7]. As the space between the two column sections became accessible by the removing of the old HVEC belt, the resistive divider was installed in this space. For this a set of 384 frames, one for each column plate, made of chromium plated 5 mm thick steel band were made, on each frame being mounted by screws the two Wellwin 300 M Ω resistors corresponding to a column gap (Fig. 1).



Figure 1: The new terminal voltage resistive divider installed between the column sections.

These frames with resistors were installed in the space between the column sections by securing them with screws on the upper side of the column steel plates. The pelletron system installed in 2007 proved so far to be reliable and to offer a stable operation of the tandem up to 9 MV. A further advantage offered by the pelletron

Electrostatic Accelerators

system is that it uses electrical motors of lower power than the HVEC belt system. As a result we could remove from the tank the water cooled heat exchanger that had given us in time much trouble due to microscopic, undetectable water leaks. By renouncing to the heat exchanger the dryness of the tank gas (90% N₂ and 10% SF₆) was significantly improved. On the other hand, the tank gas has to be more frequently recirculated through the gas dryer with alumina in order to eliminate the fluorine compounds formed at surges in the tank. These compounds may drastically shorten the lifetime of the pelletron chains. The alumina in the dryer has to be changed yearly.

Installation of a New Set of Accelerator Tubes

Until 2008 the Bucharest tandem accelerator used a set of HVEC stainless steel, inclined field accelerator tubes. After more than 50,000 hours, the tubes began to produce high levels of X-radiation and prevented the raise of the voltage over 5 MV. It was decided to change them with a new set of titanium, spiral field accelerator tubes we had as spare parts since 1993. The new tubes, carefully conditioned mainly by monitoring the X-ray level of emission outside of the tank, behaved normally up to the maximum terminal voltage of 9 MV.

Renewal and Development of the Tandem Injector

The upgrade of the tandem injector consisted in the installation of three new negative ion sources:

- A new sputter negative ion source model SNICS II made by NEC [8], replacing the old HICONEX 834 source, was installed on one leg of the 20⁰ inflection magnet. New power supplies and a computer control system with optical fibers using a Labview software were installed. The old preaccelerator tube is still in use allowing an input in the tandem of ion beams with energies up to 100 keV. This ion source proved to be stable and easy to operate. It produces ion beams for all elements which form a stable negative ion. The ion beams have a good match to the accelerator tube admittance.

- A helium negative ion beam source based on a duoplasmatron ion source followed by a lithium vapor charge exchange unit was developed in our laboratory and installed on the opposite 20⁰ leg of the inflection magnet; it provides helium negative ion beams of intensities up to 5 μ A at 80 keV.

- A dedicated injector for AMS based on a 40 cathode sputter negative ion source (model MC-SNICS II made by NEC [8]) followed by a 90⁰ analyzing magnet and a short accelerator tube was installed on the 0⁰ leg of the inflection magnet. This injector shares the high voltage platform and preacceleration power supply with the SNICS II ion source.

The ion optics of the injector, of the low energy (LE) beam transport system and of the overall transmission through the tandem accelerator were checked with the SIMION code.

The Millisecond Beam Pulsing System

For some experiments a millisecond pulsing of the accelerated ion beam is necessary. This system was home developed and installed on the low energy (LE) beam transport line, just after the inflection magnet. The system consists of a chopper system fed with rectangular pulses by a pulse generator followed by a power amplifier. The pulse generator gives TTL-pulses with a period between 5 ms and 2×10^4 s (very long periods are required in some activation experiments). The power amplifier provides on the chopper plates pulses with an amplitude up to 1 kV and a rise-time less than 50 ns. The pulse duration may be changed between 3% and 50 % of the period. The two rectangular chopper plates are 500 mm long with a distance of 50 mm between them allowing to use a pulse amplitude limited between 100 V and 200 V for any particles accelerated by the Bucharest tandem accelerator.

The Nanosecond Beam Pulsing System

This system, made by NEC and recently installed, consists of a chopper system and a buncher. The 2.5 MHz sweep (chopper) system produces 5 MHz pulse rate and is

combined with a countdown system allowing repetition rates of 5 MHz, 1.25 MHz, 625 kHz and down to 19.53 kHz. This system is installed right downstream the preacceleration tube of the negative ion beam delivered by the SNICS II sputter source. The chopper system is completed by a model 63-50 (63 mm aperture, 50 kV) Einzel lens for a better beam matching to the tandem. The buncher is installed just in front of the first tandem accelerator tube and consists of two tubes of different lengths to match injected ion beams from mass 1 (protons) up to mass 40 u. The beam pulse duration is in the range of 1-3 ns with a packing efficiency of 25% This system will be very soon tested and commissioned.

In Fig. 2 the layout of the injector and the LE beam transport of the tandem accelerator is given, including the three negative ion sources and both beam pulsing systems described above.

Fig. 3 is a picture of the millisecond beam pulsing system and of the buncher of the nanosecond beam pulsing system, which are installed in front of the tandem tank.

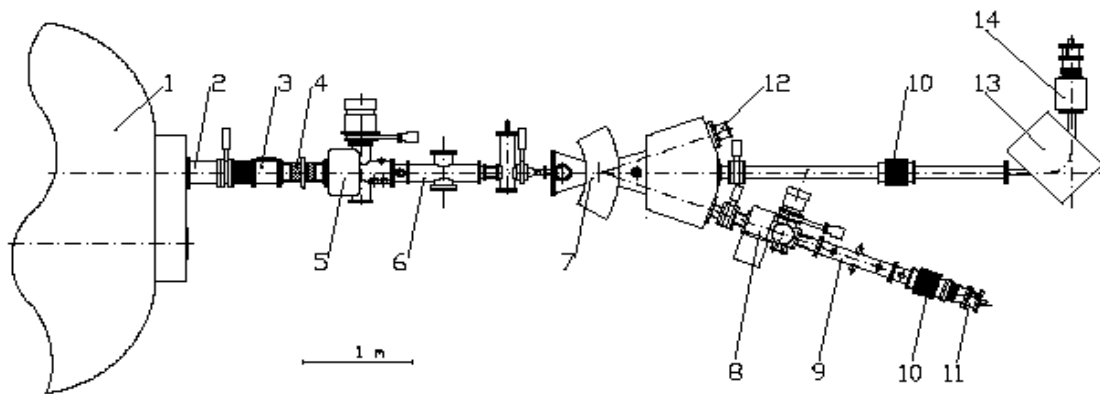


Figure 2: Layout of the tandem injector and of the LE beam transport line: 1 - Accelerator tank; 2 - LE steerer; 3 - Faraday cup; 4 - Einzel lens; 5 - Buncher of the ns pulsing system; 6 - ms pulsing system; 7 - 20° Inflection magnet; 8 - Einzel lens and chopper of the ns pulsing system; 9 - Steerer; 10 - Preaccelerator tube; 11 - Negative ion source (SNICS II); 12 - Duoplasmatron of the He negative ion source; 13 - 90° Analyzing magnet; 14 - Negative ion source (40MC-SNICS II) for AMS.

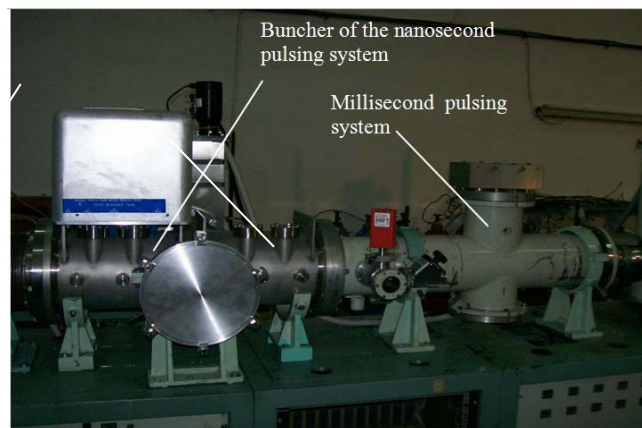


Figure 3: Beam pulsing systems installed on the LE beam transport line.

The replacement of the electrical equipment of the Bucharest tandem accelerator was a must of the upgrade program because it was very old, obsolete and unstable if not defective. This situation was due to the fact that for many years no funds were available for renewing the tandem equipment. Now most of the very old electrical devices were replaced by new ones, reliable and capable to support a computer control system. Several categories of devices were replaced:

- The old HVEC power supplies of low voltage and high power for the three beam deflection magnets: inflection magnet (1 kW), analyzing magnet (12 kW) and switching magnet (20 kW) were replaced by new Danfysik power supplies having a long term current stability of 10 ppm; these power supplies significantly contributed to improve the ion beam stability.

- The old power supplies for the magnetic quadrupole doublet lenses that focus the ion beam on the HE line and in front of experiments were replaced by Sorensen, USA power supplies which have a long term current stability of 100 ppm and contribute also to improve the ion beam stability.

- The high voltage power supplies for the ion injectors and for the Einzel lens on the LE ion beam line were replaced by Glassman, USA power supplies that proved to be reliable and stable in operation.

- The fluxmeters for measuring the magnetic field in the inflection magnet gap and in the analyzing magnet gap were replaced by a Hall probe fluxmeter made by Group3, New Zealand and respectively by a NMR fluxmeter made by Metrolab, Switzerland; these flux meters proved to be accurate, reliable and easy to use.

- The instability of the old HVEC generating voltmeter (GVM) led us first to decide its replacement with a new one. But after a careful inspection, we observed some misalignment between the fixed and the rotating disks of the old GVM as the major cause of this instability. After fixing this misalignment the old GVM output allowed a much improved stability of the terminal voltage, in the range of 4 kV at 9 MV, so it was decided to keep it in operation. This accuracy combined with the terminal voltage low ripple given by the pelletron charging system is enough to maintain a stable ion beam spot on target even in the absence of the slit stabilization for most experiments at terminal voltages over 5 MV. At lower terminal voltages the GVM output is too small and the noise is affecting the beam stability, so the slit stabilization has to be used. Nevertheless, in some experiments, as is the AMS application, the terminal voltage must be stabilized even in the absence of a measurable beam that usually allows to use the slit stabilization. Such applications require a very accurate GVM. For this purpose a new GVM developed at the Technical University Munich, Germany was installed on an available port of the tandem tank beside the old GVM (Fig. 4). The tandem may work with either of the two GVM's, the change consisting only in the change of the signal cables to the common amplifier. The new GVM has definite geometrical and technical improvements,

described in [9], that determine higher performances (terminal voltage stability of 1 kV or even better at a terminal voltage of 9 MV with GVM stabilization).



Figure 4: The two generating voltmeters installed on two neighbor ports of the tandem tank.

Refurbishment of the Vacuum System

Until recently the Bucharest tandem accelerator was still using the original vacuum equipment supplied by HVEC in 1973, mainly based on diffusion oil pumps using SANTOVAC 5 oil. The vacuum was in the range of $1-4 \times 10^{-6}$ mbar. The actual requirements for a clean vacuum in the range of 10^{-7} mbar determined us to replace all the oil diffusion pumps by turbomolecular pumps and all the fore vacuum pumps by modern ones provided with oil sucking back protection and filters. Some of the gate valves were also changed with new ones. The old vacuum measuring system was doubled by a new one more accurate and that give the possibility to automatically record the readings.

Improvement of Auxiliary Equipment

The main improvement consisted in the installation of a high power (250 kVA) on-line, dual UPS (Uninterruptible Power Supply) providing to the entire building that houses the tandem accelerator electrical power of 3×400 V, 50 Hz. The UPS was necessary due to the very frequent interruptions, in general of short duration, of the electricity that caused the general shutdown of the accelerator and incidentally damage of the equipment. The stable and uninterrupted feed with electrical power had a benefic effect on the tandem operation. Other improvements consisted in the increase of the thermal capacity of the refrigeration system that cools down the distilled water used as cooling agent by the tandem accelerator and the installation of new distilled water pumps and air compressors.

CONCLUSIONS

The upgrade program of the Bucharest FN tandem accelerator developed in the period 2006-2009 had as a

main result the transformation of this 36 years old accelerator into a modern, performing and reliable facility, offering stable beams of a large range of ion species: protons (2-18 MeV), helium (3-27 MeV) and a broad range of heavy ions that may be produced by the SNICS II sputter negative ion source (energies up to 100 keV or even somewhat higher depending on the ion atomic number). The beam intensities range from nA to μ A depending on the electron affinity of the elements, parameter which determines the ion source efficiency to producing negative ions. The accelerated beam may be pulsed in the millisecond range (pulse period adjustable between 5 ms and 2×10^4 s, pulse duration adjustable between 3% and 50% of the period) and in the nanosecond range (pulse duration in the range of 1-3 ns and repetition rates of 5 MHz, 1.25 MHz, 625 kHz and down to 19.53 kHz). The tandem is currently operated in very stable conditions up to 9 MV on a basis of about 4000 hours/year.

The performances and versatility of the upgraded Bucharest FN tandem accelerator combined with a strong scientific research program [10] and with high level results show the possibility for this facility to become an active part of the European Infrastructure in Nuclear Physics.

ACKNOWLEDGEMENTS

The upgrade of the Bucharest FN tandem accelerator was possible due to the financial support of the Romanian National Agency for Scientific Research.

The permanent interest and help of N. V. Zamfir, Director General of IFIN-HH, were determinant in realizing this program.

The good and competent advise and help of G. Pascovici, A. Dewald and R. Steinert from the Nuclear

Physics Institute of the Cologne University, Germany are warmly acknowledged.

Last but not least are acknowledged the competence and hard work of the technical team of the Bucharest tandem accelerator: V. Batraneanu, C. Popescu, L. Povariu, C. Ghitescu, P. Dima, S. Cojocar, N. Preda.

REFERENCES

- [1] S. Dobrescu and L. Marinescu, AIP Conference Proceedings Vol. 287, (1993) Particles and Field Series 53, Editors J. G. Alessi and A. Herscovitch, BNL, pp. 474-483.
- [2] S. Dobrescu, Nucl. Instr. and Meth. 184, 103 (1981).
- [3] L. Marinescu, G. Pascovici, V. Zoran, R. Dumitrescu, T. Sireteanu, E. Iordachescu, I. Filimon and A. Winkler, Nucl. Instr. and Meth. A328, 90 (1993).
- [4] S. Dobrescu and L. Marinescu, in "Electrostatic accelerators", editor R. Hellborg, Springer Verlag, 2005, pp. 374-377.
- [5] S. Dobrescu, D. V. Mosu, D. Moisa and S. Papureanu, AIP Conference Proceedings, Vol. 1099, (2009), Editors F. D. McDaniel and B. L. Doyle, pp. 51-54.
- [6] <http://www.pelletron.com/charging.htm>
- [7] S. Dobrescu, L. Marinescu, G. Dumitru, Gh. Cata-Danil, Rom. Reports Phys. 55, 4 (2003).
- [8] <http://www.pelletron.com/negion.htm>
- [9] L. Rohrer and H. Schnitter, in "Electrostatic accelerators", editor R. Hellborg, Springer Verlag, 2005, pp. 152-160.
- [10] D. Bucurescu, G. Cata-Danil and N. V. Zamfir, Nuclear Physics News, 17, 5 (2007).

DEVELOPMENTAL ACTIVITIES AT BARC-TIFR PELLETRON ACCELERATOR FACILITY

A. K. Gupta, P. V. Bhagwat and R. K. Choudhury, BARC, Mumbai 400085, India

Abstract

The 14 UD Pelletron Accelerator Facility at Mumbai has recently completed two decades of successful operation. The accelerator is mainly used for basic research in the fields of nuclear, atomic and condensed matter physics as well as material science. The application areas include accelerator mass spectrometry, production of track-etch membranes, radioisotopes production, radiation damage studies and secondary neutron production for cross section measurement etc. Over the years, a number of developmental activities have been carried out in-house that have helped in improving the overall performance and uptime of the accelerator and also made possible to initiate variety of application oriented programmes. Recently, a superconducting LINAC booster has been fully commissioned to provide beams up to A~60 region with E~5 MeV/A. As part of Facility augmentation program, it is planned to have an alternate injector system to the LINAC booster, consisting of 18 GHz superconducting ECR ion source, 75 MHz room temperature RFQ linac and superconducting low-beta resonator cavities. The development of an alternate injector will further enhance the utilization capability of LINAC by covering heavier mass range up to Uranium. The ECR source is being configured jointly with M/s Pantechnik, France, which will deliver a variety of ion beams with high charge states up to $^{238}\text{U}^{34+}$. This paper will provide detailed presentation of developments being carried out at this facility.

INTRODUCTION

The accelerator development in the Department of Atomic Energy set out in the fifties. One MeV Cockroft-Walton accelerator was commissioned at Tata Institute of Fundamental Research (TIFR), Mumbai in 1953. In early sixties a 5.5 MV Van de Graaff accelerator manufactured by High Voltage Engineering Corporation (HVEC), was installed at the Bhabha Atomic Research Centre (BARC), Mumbai that provided much-needed boost in accelerator based research in the country. In the late seventies, the only accelerator facility in medium energy range available in the country was indigenously developed Variable Energy Cyclotron at Kolkata. In order to meet the diverse requirements of nuclear physics community, a Medium Energy Heavy Ion Accelerator (MEHIA) project was conceived to accelerate ions right from proton to highest possible mass at intermediate energies. In 1982, the project MEHIA started, where a 14 UD Pelletron Accelerator was purchased from M/s NEC, USA and installed at Tata Institute of Fundamental Research campus, Mumbai. This accelerator was commissioned on 30th December 1988 and since then it has been serving as

a major facility for heavy ion accelerator based research in India.

Since its inception, the accelerator has been continuously working with progressively increased efficiency (see Fig. 1) [1]. The accelerator upgradation was done by implementing following features; the original NEC accelerator has voltage grading based on corona needles that were replaced by resistances, a new terminal potential stabilizer was installed, two turbo-molecular pumps are introduced in the terminal to improve performance of gas stripper, development of negative ion beams for a wide range of species, a double harmonic drift buncher was introduced in the low energy injection path of the accelerator to obtain pulsed beam with a typical width of 1.5 ns, separation of 100 ns and a bunching efficiency of ~ 60%. The dark beam current between the beam bunches is swept away by a RF parallel plate sweeper situated at the exit of the accelerator, a Linux based control system consisting of a scanner and an operation interface (OIF) has been developed.

This paper will be providing an overview of the developmental tasks executed already (enabling the success of various application oriented programmes) at this facility, as well as the ones that are currently underway.

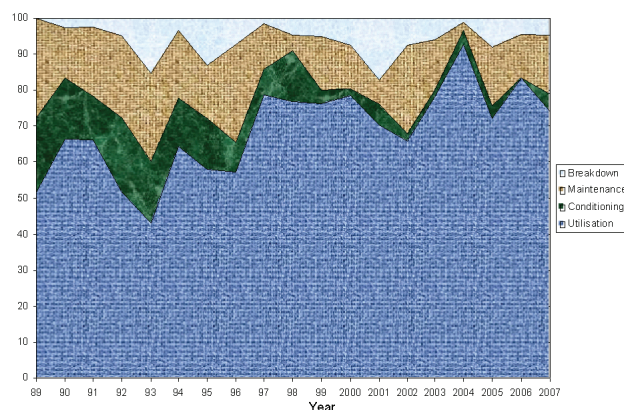


Figure 1: Performance Curve.

DEVELOPMENTAL ACTIVITIES AND ASSOCIATED APPLICATIONS

Resistor Grading

An important consideration in high voltage design of an electrostatic accelerator is the potential grading system used to divide the terminal potential equitably (or as required) across the column or tube electrode gaps. Solid carbon or carbon film resistors were used in the early HVEC accelerators. These were bogged down with problems of frequent resistor failures either due to

sparkling damage or changes in the resistance values under application of high electric fields. However, development of very high values ceramic metal resistor technology has been found to be most suitable for use in high voltage grading chains. We have designed resistance chain to install 2 G Ω per gap in the column and 1 G Ω per gap in the accelerating tube (1 G Ω resistors; 1008 in columns and 924 in accelerating tubes). There are two charging chains in Pelletron Accelerator and each chain can transport more than 100 μ A current, which is sufficient to go to 14 MV terminal voltage. The operation of accelerator, henceforth, became very stable particularly at lower terminal voltages, and it is now possible to deliver beam even at as low voltage as 2 MV.

New Terminal Potential Stabilizer

Onwards of 1995, a thrust was given to various application programs. Needless to say, Accelerator Mass Spectrometry program was on top of our agenda. At that point of time, accelerator beam used to be stable only in slit control mode and not in generating volt meter (GVM) mode. To attain the requisite terminal voltage stability, a new Terminal Potential Stabilizer (TPS) was procured from NEC, USA, especially for this programme. This has helped in a smoother control of the terminal potential in the Generating Voltmeter (GVM) mode, too. Accelerator Mass Spectrometry program took a leap forward and by 2005, ^{36}Cl based measurements could be performed, successfully. As the interfering isobar in the ^{36}Cl detection is ^{36}S , a segmented gas detector was developed in-house to circumvent the rather intense isobaric interference. The ratio obtained for standard sample is in agreement with the value specified by the Prime Lab within a statistical error of 12%. Such a good agreement obtained for direct measurement of ratio indicates that transmission for Cl isotopes through the accelerator is well optimized. Estimated detection limit is $\sim 7 \times 10^{-14}$ [2]. We are planning to extend this programme for ^{129}I in near future.

Recirculating Terminal Gas-Stripper

Gas pressure has a major role in getting intense and highly stripped ions, but at the same time bad vacuum conditions in accelerator tube causes loss of beam transmission due to charge exchange and scattering. The gas stripper system was originally installed with Titanium Sublimation pumps in high voltage terminal section. These pumps require periodic replacement of cartridges and pumping speed of these pumps used to come down with time. A new recirculation gas stripper system from NEC has been installed, consisting of two Turbo Pump (Varian make V 301 Navigator) in place of sublimation pumps. Our new installation of turbo pump is based on existing stripper housing (see Fig. 2). Table 1 shows vacuum condition inside accelerating tube at different canal pressure.

Recently BeO $^+$ beam was injected in our accelerator and by using turbo based gas stripper system Beryllium $^9\text{Be}^{+n}$

beam was given to users [3]. Results are in displayed in Table 2.

Table 1: Vacuum across Accelerating Tube

	Base Vacuum	Terminal Turbo Pump on	@ 280 micron	@640 micron
IP-02-1	2.4×10^{-8}	2.4×10^{-8}	2.4×10^{-8}	2.5×10^{-8}
IP-D1-1	6.5×10^{-9}	5.9×10^{-9}	2.1×10^{-8}	1.8×10^{-7}
IP-T-1	5.5×10^{-9}	4.8×10^{-9}	8.2×10^{-8}	1.8×10^{-6}
IP-D2-	2.2×10^{-8}	1.8×10^{-8}	3.8×10^{-7}	6.8×10^{-7}
IP-03-1	5.2×10^{-8}	5.2×10^{-8}	5.4×10^{-8}	6.3×10^{-8}

Table 2: Be Beam Stripping Fraction

	Beam Current With Foil Stripper	Beam Current with Gas & Foil Stripper
Tank Top BeO $^+$ yield	220 nA	220nA
Tank Bottom Be $^{+n}$, O $^{+n}$ total yield	400 nA	610 nA
Be $^{+3}$ analyzed yield	10nA	35 nA

@ Terminal Voltage – 10 MV, Beam Energy- 33.6 MeV ; Gas stripper Pressure 240 Micron

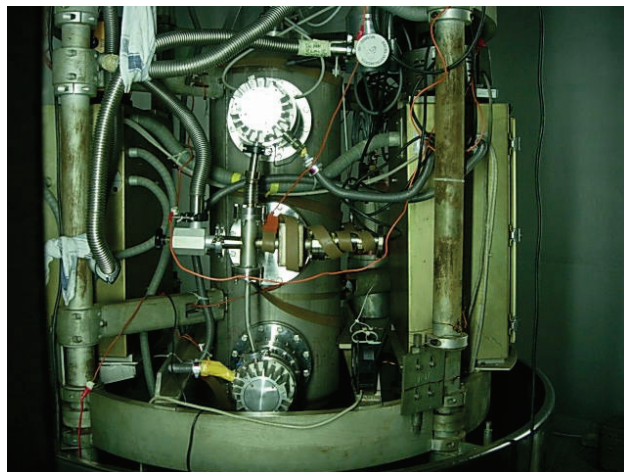


Figure 2: Terminal Gas Stripper System.

A Linux based Control System

A new Linux based control and monitoring software has been written for the Pelletron Accelerator. This software has a graphical User Interface (GUI) through which the operator can interact and control the accelerator. The GUI incorporates features like software assignable meters and slider controls. This will obviate the need for shaft encoders and assignable meters that

were in use for the past twenty years. The control system software is relatively more reliable and user friendly compared to the old system that is DOS based and has been in use for twenty years.



Figure 3: FPGA based CAMAC ADC module.

The Pelletron control system hardware is CAMAC based. The CAMAC interface modules are more than twenty years old and are now facing end-of-life issues. To ensure continuity of the CAMAC platform, general purpose FPGA based CAMAC modules like ADC/DAC modules and digital input/output modules have been designed and developed at the Pelletron accelerator (see Fig. 3). All the modules have been tested [4]. Of these, a 16 channel, 12 bit CAMAC ADC module has been installed and is currently in continuous use.

Beam Profile Monitor

In order to facilitate measurement and monitoring of position and focusing parameters during beam tuning, beam profile monitors (BPM) are used at various places in the accelerator. A two channel, PCI based FPGA compatible BPM digitizer along with the associated GUI has been designed and developed at the accelerator (see Fig. 4).

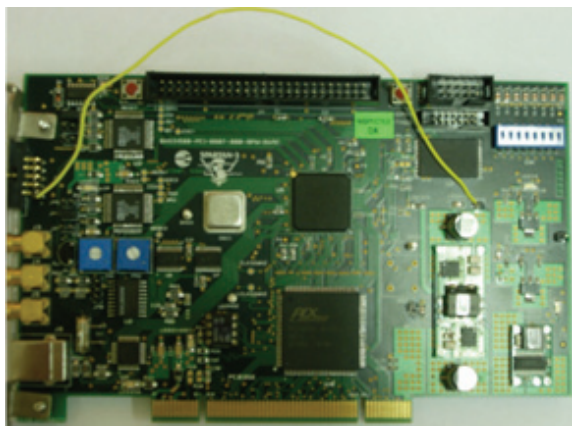


Figure 4: BPM digitizer.

Electrostatic Accelerators

The digitizer can display two BPM waveforms simultaneously. These waveforms can also be filtered and archived. Data archival helps in comparison and monitoring of the BPM waveform and aids the beam tuning process. The digitizer card can also function as a general purpose platform for testing various FPGA based designs. It can also function as a general purpose PCI interface card. The card has been tested [5].

Ion Source and Beam Development

To produce a wide range of negative ions, sources such as SNICS (Source of Negative Ions by Cesium Sputtering) and Alphatross are commonly used in tandem accelerator facilities. An ion source test bench was set up to meet the increasing demand of intensity and quality of beams at Pelletron Accelerator Facility. The sputter-characteristics of the cathodes are optimized using the ‘cooking systematics’ generated in our lab. Different types of composite-sputter cathodes, gas feed-sputter cathodes and disc covered-gas feed-sputter cathodes have been developed and tested at our test bench, with particular emphasis given to the elements of user’s interest [6,7]. Composite-sputter cathodes development has led to a significant reduction in the down time of the accelerator by eliminating the beam changeover delays and enhanced ion source lifetime. Gas feed-sputter cathodes provide molecular negative ions of low electron affinity elements. Disc covered-gas feed-sputter cathodes are developed to generate negative ions of the rare earth elements without impairing the ionization efficiency of ionizer. Over the years, various versions of high intensity negative ion sources based on cesium sputtering i. e. SNICS, Gas feed-SNICS, MC-SNICS (Multi Cathode-Source of Negative Ions by Cesium Sputtering) have been developed, in house [8, 9]. Recently, ^9Be beam has been accelerated through Pelletron Accelerator Facility, successfully. Given to the toxicity of beryllium, a dedicated ion source was used and stringent safety requirements were followed as recommended by the Particle Accelerator Safety Committee (PASC), BARC, at different levels of production, acceleration, and utilization [10].

Track Etch Membrane Set Up

Microporous membranes with well defined and uniform pore size and pore density, uniform thickness, high tensile strength and inertness to toxic environments are in good demand for growing number of scientific and technological applications. Heavy ion accelerators provide greater flexibility to produce Track Etch Membrane (TEM) of a wide range as they can provide various heavy ions of different atomic number (Z), kinetic energy (E) and particle flux. Pore densities of the order of 10^6 to 10^8 pores/cm² and pore size of the order of 0.2 to 1.0 micron are required for many applications. A magnet was used to scan the heavy ions from the accelerator in horizontal direction and the polymer film was moved in vertical direction using a roller mechanism. The scanner magnet gives a peak magnetic field of 1.35 Kgauss [11].

To get larger deflection higher charge states of the desired ions are produced using post stripper. The deflection, at the exit of the scanner is few centimeters, which is then widened using a horn chamber of one metre length. At the end of the scanner deflection up to 25 cm is achieved. The film is wound on a perspex shaft of 19 mm diameter and is continuously unwound on to another roller that is driven by a D.C motor from outside the chamber. Coupling is done using a vacuum rotary feedthrough. The linear speed of the film is kept at 60 cm/min. The beam is defocused in vertical direction to get almost uniform particle distribution. These membranes are being used by Radiation Medicine Centre, Mumbai to immobilize antibodies against specific analyte and are also used for purification of gases, in separating various Actinides and metals.

High Current Irradiation Set Up

Drift space above analyzing magnet is modified to accommodate a Proton Beam Irradiation Setup at 6 meter level at this facility (see Fig. 5). This setup is capable of delivering proton beam in the energy range of 2 MeV to 26 MeV and current in μA range. The shielding at this level is such that radiation is within permissible limit when proton beam with high energy and high current is accelerated. In order to study radiation effects on metals at a higher temperature a hot target assembly is developed which can go up to 500°C . Radionuclides such as ^{52}Mn , ^{67}Ga , ^{96}Tc , and ^{236}Pu are produced for radio-pharmaceutical applications.



Figure 5: Irradiation Setup.

Radiation Biology Set Up

A thin window ($20\mu\text{m}$) of Titanium is placed at 30°N beam line to bring out ion beam in air. Various users have used this facility. A large area proton beam of size 25 mm to 40 mm diameter in air was made available to Indian Space Research Organization for testing their on-line electronic devices.

FUTURE PROGRAMME

ECR-RFQ based Positive Ion Injector

An alternate injector system (see Fig. 6) comprising of a superconducting ECR (Electron Cyclotron Resonance) source, room temperature RFQ (Radio Frequency Quadrupole) and superconducting low-beta resonator cavities is planned, to enhance the utilization capability of LINAC booster, enabling the study of reactions above the Coulomb barrier even for very heavy system like U+U [12]. Prior to injection into Superconducting LINAC, the ion beam needs to be accelerated to 12-14 MV/q.

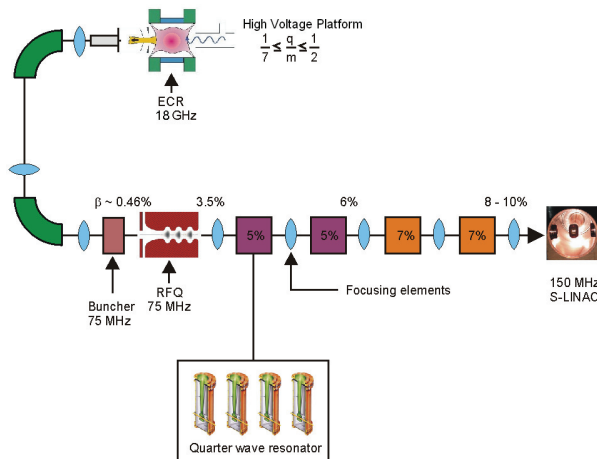


Figure 6: Alternate Injector Layout.

The superconducting ECR ion source (ISIS) operating at 18 GHz frequency is being configured jointly with M/s Pantechnik, France, which will deliver a variety of ion beams with high charge states including up to $^{238}\text{U}^{34+}$ with emittance $<1\pi$ mm-mrad and beam current up to $3\mu\text{A}$. The ECR will be mounted on a 300 kV platform with mass selection feature on it. This source will also have an arrangement of varying the B_{min} via an independent third coil. It is proposed to operate the ion-source in two modes. In one mode it will inject ions at 10 keV/A into the RFQ. In the other mode, it will be a stand-alone facility, directly delivering ions, right from protons (at 300 keV) to U^{34+} (at 10.2 MeV), to users for experiments in atomic physics, material science, etc.

The RFQ will be operating at 75 MHz and will accelerate ions up to 575 keV/u ($\beta \sim 3.5\%$). The beam dynamics studies were performed using LIDOS [13] and the resonant structure design was carried out by employing SOPRANO module of OPERA 3D [14]. The Table 3 summarizes the final RFQ parameters.

Recently, the RFQ vanes, stems and base plate are machined from ETP (Electrolytic Tough Pitch) copper (see Fig. 7). The prototype RFQ is undergoing RF tests, currently. The physics design of superconducting low-beta resonator cavities have also been initiated.

Table 3: RFQ Parameters

q/m	1/7, U ³⁴⁺
Ein / Eout, keV/u	10 / 575
Frequency, MHz	75
Kilpatrick Factor	1.4
Focussing Parameter (B)	4.26
Intervane Voltage, kV	16*m/q
Mean Aperture Radius(r_0)	8.0 mm
Minimum Aperture (a), mm	8.0-4.51
Current (I), mA	0.1
ϵ (input, norm.) π mm mrad	1.0
Modulation (m)	1.0 - 2.3
Synchronous Phase (ϕ_s)	-90 ⁰ to -20 ⁰
Number of cells (n)	167
Length, m	4.62
RMS Long. Emitt., keV/u*ns	0.3
Transmission	87%

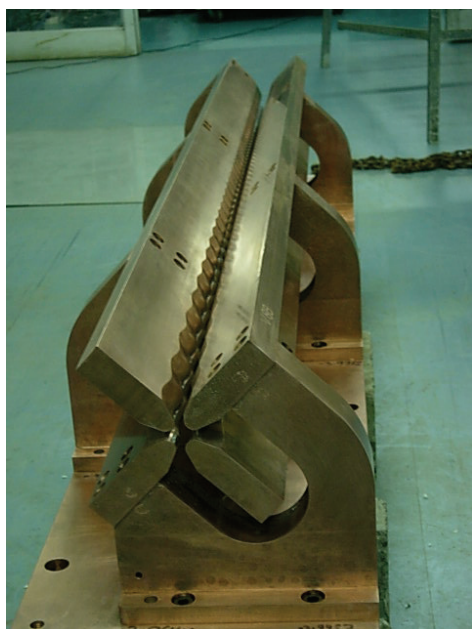


Figure 7: RFQ Assembly.

CONCLUSIONS

Developmental work carried out over the past two decades has resulted into increased uptime as well as enhanced utilization of the Pelletron Accelerator Facility. Pelletron Accelerator stand-alone and the ECR based injector shall cover elements across periodic table to meet

the requirements of research in basic science and applications of departmental interest, essentially.

ACKNOWLEDGEMENT

The authors thank their colleagues of Pelletron Accelerator Facility for their contribution. We are also thankful to Dr S. Kailas for his keen interest and constant support for the accelerator based programmes.

REFERENCES

- [1] P. V. Bhagwat, Pramana-Journal of physics, Vol 59, pp 719-724 (2002).
- [2] P. Surendran, A. Shrivastava, A. K. Gupta, R. M. Kale, J. P. Nair, M. Hemalatha, K. Mahata, M. L. Yadav, H. Sparrow, R. G. Thomas, P. V. Bhagwat, S. Kailas, Nucl. Inst. & Meth. Phys. Res. B 267 (2009) 1171.
- [3] S. C. Sharma, N.G. Ninawe, M.L. Yadav, M. Ekambaram, Ramjilal, U.V. Matkar, Q. N. Ansari, R. L. Lokare, Ramlal, A. K. Gupta, R. G. Pillay and P. V. Bhagwat, Indian Particle Accelerator conference (Inpac-2009), Feb. 10-13, 2009, RRCAT, Indore.
- [4] S. G. Kulkarni, J. A. Gore, A. K. Gupta, P. V. Bhagwat, R. K. Choudhury, Indian Particle Accelerator conference (Inpac-2009), Feb. 10-13, 2009, RRCAT, Indore, India.
- [5] J. A. Gore, S. G. Kulkarni, A. K. Gupta, P. V. Bhagwat, R. K. Choudhury and S. Kailas, Indian Particle Accelerator conference (Inpac-2009), Feb. 10-13, 2009, RRCAT, Indore, India.
- [6] A. K. Gupta, N. Mehrotra, R. M. Kale, D. Alamelu, and S. K. Aggarwal, DAE Symposium on Nuclear Physics, Dec. 2003.
- [7] A. K. Gupta, N. Mehrotra, R. M. Kale, D. Alamelu, and S. K. Aggarwal, DAE-BRNS 50th Symposium on Nuclear Physics, BARC, Mumbai, Dec. 12-16 (2005).
- [8] A. K. Gupta, P. Ayyub, European Physical Journal D 17 (2001) 221.
- [9] S. C. Sharma, R. M. Kale and A. K. Gupta, DAE symposium on Nuclear Physics, Dec. 21-25, (1998).
- [10] A. K. Gupta, R. M. Kale, N. Mehrotra, P. N. Bhat, S. Soundararajan, A. Shanbag, D. D. Thorat, P. V. Bhagwat, R. K. Choudhury, Indian Particle Accelerator conference (Inpac-2009), Feb. 10-13, 2009, RRCAT, Indore, India.
- [11] J.P. Nair et al. Indian Particle Accelerator conference (Inpac-2005), VECC, Kolkata.
- [12] N. Mehrotra et al., Design Study of Alternate Injector at Pelletron Accelerator Facility, EPAC-2008, Genoa, Italy, June 2008, THPP034, pp. 3443-3445.
- [13] LIDOS.RFQ.DESIGNER™ Version 1.3, <http://www.ghga.com/accelsoft/>.
- [14] OPERA-3D/SOPRANO v11.0 ©Vector Fields Limited, Oxford OX51JE, U.K., <http://www.vectorfields.com/>

MAIER-LEIBNITZ-LABORATORIUM TANDEM OPERATION AND EXPERIMENTS

L. Beck, Maier-Leibnitz-Laboratorium, Am Coulombwall 6, Garching, Germany

Abstract

The Tandem accelerator of the Maier-Leibnitz-Laboratorium (MLL), the former “Beschleunigerlabor der LMU und TU München” was running very reliable during the last years. The status of the Tandem accelerator will be presented and some technical problems of the past years of operation will be discussed.

The MAFF project (Munich Accelerator for Fission Fragments) was suspended due to missing funding. MAFF was planned to be the successor of the Tandem accelerator. In the next years the Tandem accelerator will be useful for experiments in the framework of the two clusters of excellence “Origin and Structure of the Universe” and MAP (Munich Centre for Advanced Photonics). The Tandem ion beams are applied for experiments in the field of nuclear astrophysics, AMS with astrophysical implication, for irradiation of cells, tissue and finally animals for cancer therapy studies.

STRUCTURE OF THE MLL

The former “Beschleunigerlabor der Ludwig-Maximilians Universität und der Technischen Universität München” has since July 2008 now officially the name “Maier-Leibnitz-Laboratorium (MLL)”. The person Heinz Maier-Leibnitz is associated with the old research reactor FRM. This reactor started its operation in 1957 until it was shut down in 2000. The research field of Heinz Maier-Leibnitz was nuclear physics and especially the physics with neutrons. In the framework of the MLL physicists of both Munich universities and the Universität der Bundeswehr (University of armed forces) are in close collaboration in the field of nuclear and particle physics. The Ultra Cold Neutrons (UCN) working group is developing a new source for UCN which will be installed at the new research reactor FRM-II in the next years. This new source promises a much higher neutron density as all now existing sources. The last year was the first full year in which the MLL groups have performed most of their work with the additional support of the clusters of excellence “Origin and Structure of the Universe” and “Munich Centre for Advanced Photonics (MAP)”. In the MAP cluster the use of laser beams for cooling, production and acceleration of ions or electrons is one of the main research fields. Both clusters are also performing a lot of experiments at the Tandem accelerator. Some of these experiments are presented later.

TANDEM OPERATION

In 2008 the tandem accelerator (MP-8 from HVEC) was running 6600 hours for experiments. For maintenance each week 6-8 hours were scheduled but not used always. In Table 1 the beam on target time in the

past years is shown. With an average of 7000 h the operation of the accelerator was very reliable.

Table 1: Beam on Target

Year	Beam on target [h]
2008	6600
2007	7000
2006	6800
2005	7000
2004	7200
2003	7600
2002	7200
2001	6600

Fig. 1 shows the operating statistics for 2008 in detail. In July and August we had a 3 week routine maintenance period for cleaning the whole machine and check of all components. The maximum terminal voltages for experimental use were all the year around 13 MV as is shown in Fig. 2. The accelerated ions range from hydrogen to heavy ions like gold. The light ions (partially polarized) are mostly used for nuclear physics experiments and the heavy gold ions for material analysis with ERDA. The distribution of beam time to the different ions is shown in Table 2.

Table 2: Beam Time in percent of total available Beam Time for 2008 (The isotopes marked with an * were measured with AMS studies. The ion source for polarized protons and deuterons delivered about 70% of all protons and deuterons in a running time of about 800h)

Ion	%	Ion	%
1H	14.4	36Cl*	0.9
2H	2.5	41Ca*	2.2
3He	0.7	53Mn*	2.9
4He	5.0	58Ni	2.3
7Li	0.9	59Ni*	0.9
11B	5.2	63Ni*	1.8
12C	4.3	127I	23.4
16O	9.0	197Au	12.4
26Al*	0.9	Others	10.0

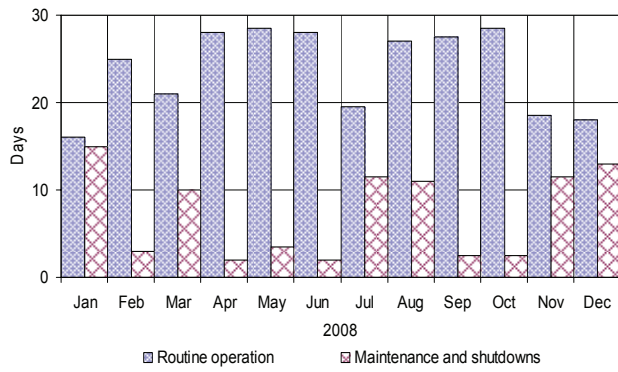


Figure 1: Operation statistics.

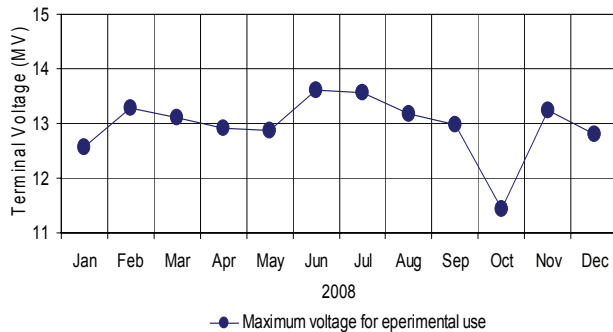


Figure 2: Terminal voltage.

Replacement of Charging Chains

In April 2009 the set of 3 charging chains at the high energy (HE) side was replaced. These chains were running since September 1990. With an average running time of 7000 h per year they reach about 130 000 h of total operation time. In the past years all chains reached operation times of 100 000 h or more. Unexpectedly we had also to replace the chains at the low energy (LE) side in May 2009 after 24 000 h of operation. These chains were installed in August 2005. With these chains we had a problem which never before occurred. The spacers in each link of the chain became very brittle and many of them were broken. It is probably a problem with the material of the spacers. In 1993 NEC changed the material from originally nylon to delrin (polyoxymethylene). The chains we installed in 2005 were purchase 1998 as spare chains for the tandem accelerator in Heidelberg. The new chains (purchased in 2005) we have installed have also delrin spacers with purple colour. We hope that this problem will not occur here. Inside our tank delrin was used for example for high voltage feedthroughs or gearwheels. The material also became brittle after a few years. Maybe there is a problem when using delrin in a dry SF₆ atmosphere. NEC assumes the reason for the problem in the SF₆ break down products, but it also may be caused by the missing humidity. NEC will investigate the problematic spacers in their laboratory.

Electrostatic Accelerators

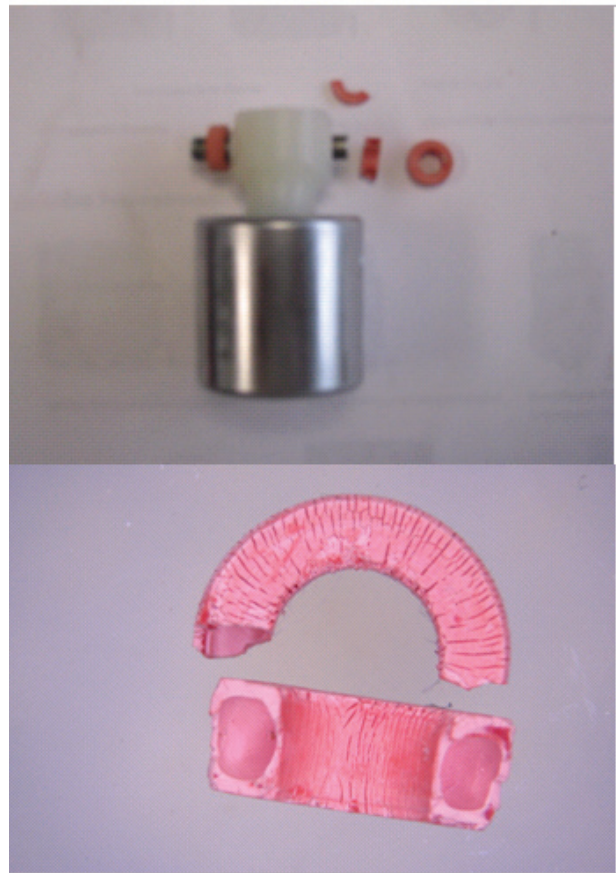


Figure 3: Chain link and spacer.

Repair of a Quadrupole Lens

The ion beam since a long time seemed to leave the accelerator with an angle in y-direction. Therefore a steering magnet was used for y-correction. But last year the problem became worsened. A correction was not possible anymore. First there was the suspicion that there is something wrong with the beam optics in the accelerating tubes which would have been fatal. But the reason for the problem was the quadrupole doublet lens located close to the exit of the accelerator. The magnetic field of one pole was significantly lower than at the other three poles. In this incorrect field of the quadrupole lens the beam was deflected in y-direction. All four coils of one doublet were replaced. There is bad experience in the SNEAP-community with replacement of only the defective coil. Replacement coils with nominally the same number of turns produced significantly different fields than the original ones. Although we do not understand why a coil with supposedly the same number of turns should produce a different field, we decided that we had to use them in sets of 4 in a quad singlet rather than replace just one. The set of four spare coils we have gotten from the tandem accelerator in Heidelberg. What was the reason for failure? The resistance of all four coils was about 0.4Ω . But a measurement of the inductance showed a significant difference between the coils. The good coils had 800 μH but the bad one only 150 μH . The

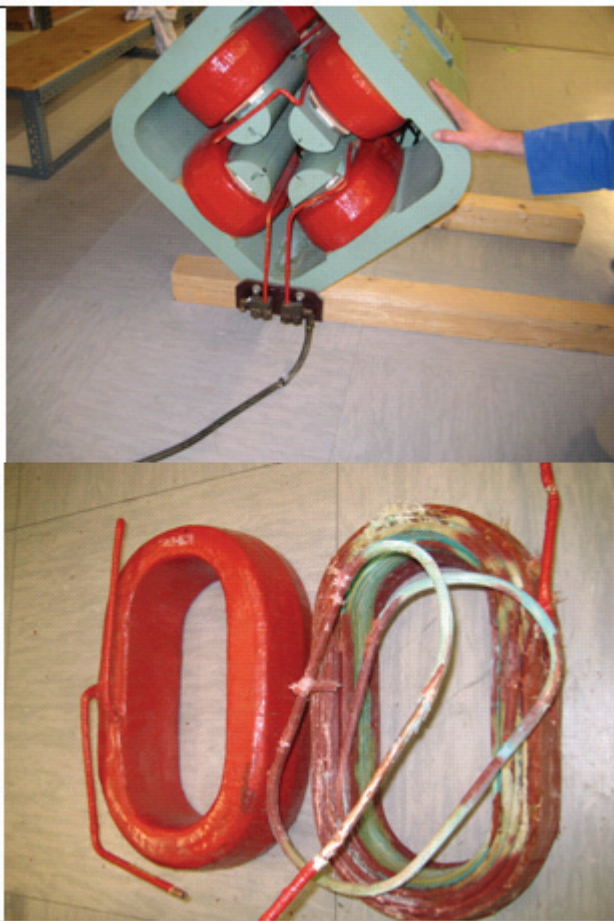


Figure 4: Quadrupole lens at the exit of the accelerator and the defective coil.

reason was found when opening this coil. Inside we found the coil filled with water and a lot of corrosion products of copper. This mixture of water and corrosion products was certainly highly conductive and produced a kind of short circuit in the coil.

With the new coils the beam is perfectly horizontal after the lens and no steering is necessary anymore.

Storage of Idle Wheels

We had in the past years a problem with our spare idle wheels. The rubber like material of the wheels showed a consistency like chewing gum, not elastic as rubber. The problem here is the moisture of the air. Therefore we now store the spare idle wheels at both ends inside the accelerator in dry SF₆ atmosphere. Our experience in the past three years shows that the problem vanished.

Electrostatic Accelerators

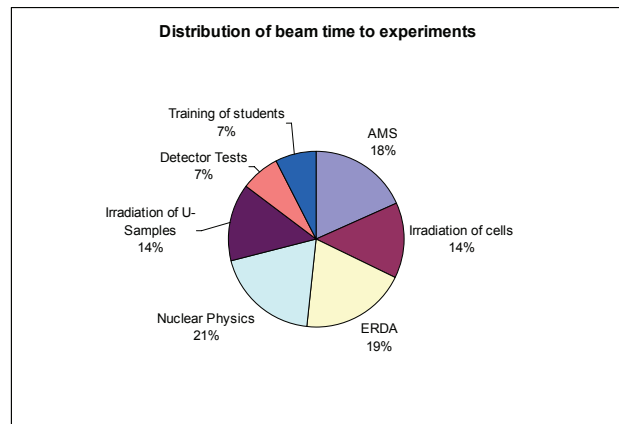


Figure 6: Distribution of beam time to experiments.

EXPERIMENTS

When the Tandem accelerator started in 1970 almost all experiments were in the field of fundamental nuclear physics. But with the years the methods used in the beginning for nuclear physics led to a lot of applications for example in AMS or materials analysis with ERDA.

Today only 21 percent of beamtime are in the field of nuclear physics. Many of these experiments have astrophysical relevance and were performed in the excellence cluster Origin and Structure of the Universe. A project in the MAP cluster is the irradiation of living cells with single ions. These experiments were carried out with the microbeam facility called SNAKE. The laboratory can offer some 20 experimental places. The instrument most frequently used is the magnetic spectrograph Q3D. About 22% of available beam time was there. The experiments here are in the field of high resolution nuclear spectroscopy and material analysis with ERDA. About 18% account for the gas filled analysing magnet GAMS. The microprobe SNAKE accounts for 13% of beamtime. Especially in the last year the irradiation of Uranium-samples demanded about 14% of available beam time. The goal of these studies is the development of a new reactor fuel element with lower enrichment for the research reactor FRM-II. More information about the experiments can be found in the annual report of the laboratory (<http://www.bl.physik.uni-muenchen.de/ml1-jb.html>).

Future perspective of the Tandem Accelerator

In the next years a high demand for beam time at the Tandem accelerator is expected. Many groups of very different fields will use the versatile experimental places at the beam lines.

“DIANA” – A NEW, DEEP-UNDERGROUND ACCELERATOR FACILITY FOR ASTROPHYSICS EXPERIMENTS*

M. Leitner[#], D. Leitner, A. Lemut, P. Vetter, LBNL, Berkeley, CA 94720, U.S.A.
M. Wiescher, University of Notre Dame, Notre Dame, IN 46556, U.S.A.

Abstract

The DIANA project (Dakota Ion Accelerators for Nuclear Astrophysics) is a collaboration between the University of Notre Dame, University of North Carolina, Western Michigan University, and Lawrence Berkeley National Laboratory to build a nuclear astrophysics accelerator facility 1.4 km below ground. DIANA is part of the US proposal DUSEL (Deep Underground Science and Engineering Laboratory) to establish a cross-disciplinary underground laboratory in the former gold mine of Homestake in South Dakota, USA.

DIANA would consist of two high-current accelerators, a 30 to 400 kV variable, high-voltage platform, and a second, dynamitron accelerator with a voltage range of 350 kV to 3 MV. As a unique feature, both accelerators are planned to be equipped with either high-current microwave ion sources or multi-charged ECR ion sources producing ions from protons to oxygen. Electrostatic quadrupole transport elements will be incorporated in the dynamitron high voltage column. Compared to current astrophysics facilities, DIANA could increase the available beam densities on target by magnitudes: up to 100 mA on the low energy accelerator and several mA on the high energy accelerator. An integral part of the DIANA project is the development of a high-density super-sonic gas-jet target which can handle these anticipated beam powers. The paper will explain the main components of the DIANA accelerators and their beam transport lines and will discuss related technical challenges.

INTRODUCTION

Nuclear Astrophysics is concerned with the origin of elements in stars and stellar explosions through charged particle, neutron, and weak interaction induced nuclear processes. The field, at the intersection of nuclear physics, astrophysics, and observational astronomy, explores the origin of the elements in our universe. Experimental Nuclear Astrophysics is characterized by four major directions, *nucleosynthesis processes in stars*, which is studied with very low energy accelerator experiments similar to the proposed DIANA facility, *explosive nucleosynthesis processes*, which requires measurements far of stability with radioactive beams, *neutron-induced nucleosynthesis in late stellar evolution*, which is pursued at reactor and neutron spallation facilities, and finally *neutrino-induced nucleosynthesis processes*, which is still largely confined to theoretical prediction and observation.

Measuring nuclear synthesis cross sections at energies (temperatures) relevant to processes in stars is extremely difficult, because of the vanishing small signal rates in comparison to the large background rates associated with cosmic ray-induced reactions, background from natural radioactivity in the laboratory environment, and the beam-induced background on target impurities. By placing the experiment into an underground location, the cosmic-ray induced background is reduced by several orders of magnitude and the measurements can be pushed to far lower energies than would be possible over ground. The natural shielding provided by the rock has allowed pushing solar cross section measurements to far lower energies than previously possible. This has been clearly demonstrated at the 50 keV LUNA-I and 400 keV LUNA facility located in the Gran Sasso National Laboratory [1].

The “DIANA” project addresses the need for a next generation low energy underground accelerator facility. It is proposed to be part of the integrated suite of experiments of the proposed Deep Underground Science and Engineering Laboratory (DUSEL) in South Dakota, USA.

DIANA will provide much enhanced capabilities in terms of ion beam intensity (which will be more than one order of magnitude higher than in LUNA), ion species, and energy range. This will enable measurements of solar burning cross-sections at lower energies with higher precision. The higher energy capability of DIANA (up to 3 MeV using singly charged ions, or beyond 3 MeV using multiple charged ions) will widen the physics reach of the facility to more complex reaction mechanisms during late stellar burning. In particular, the experimental objectives include the study of low energy capture and fusion reactions with ^{12}C , which are key for the chemical evolution in the universe and production rates of neutrons needed to synthesize elements heavier than iron.

To accomplish these ambitious science goals, we propose to design two complementary, high-current accelerators for installation and operation 1.4 km underground. Substantial R&D is necessary to design such high-intensity beams. A dense gas-jet target will offer well-controlled systematic uncertainties. However, engineering ingenuity will be required to integrate the highest achievable jet target densities with the high ion beam current beamline and the nuclear detection instrumentation. The accelerators should be capable of providing very intense ion-beams (10 to 100 mA) continuously, for periods up to several weeks, on high-density targets (up to 10^{18} atoms/cm²). The design work is underway for both, the accelerator and gas-jet target.

* This work was supported by the U.S. Department of Energy under Contract No. DE-AC02-05CH11231.

[#]MLeitner@lbl.gov

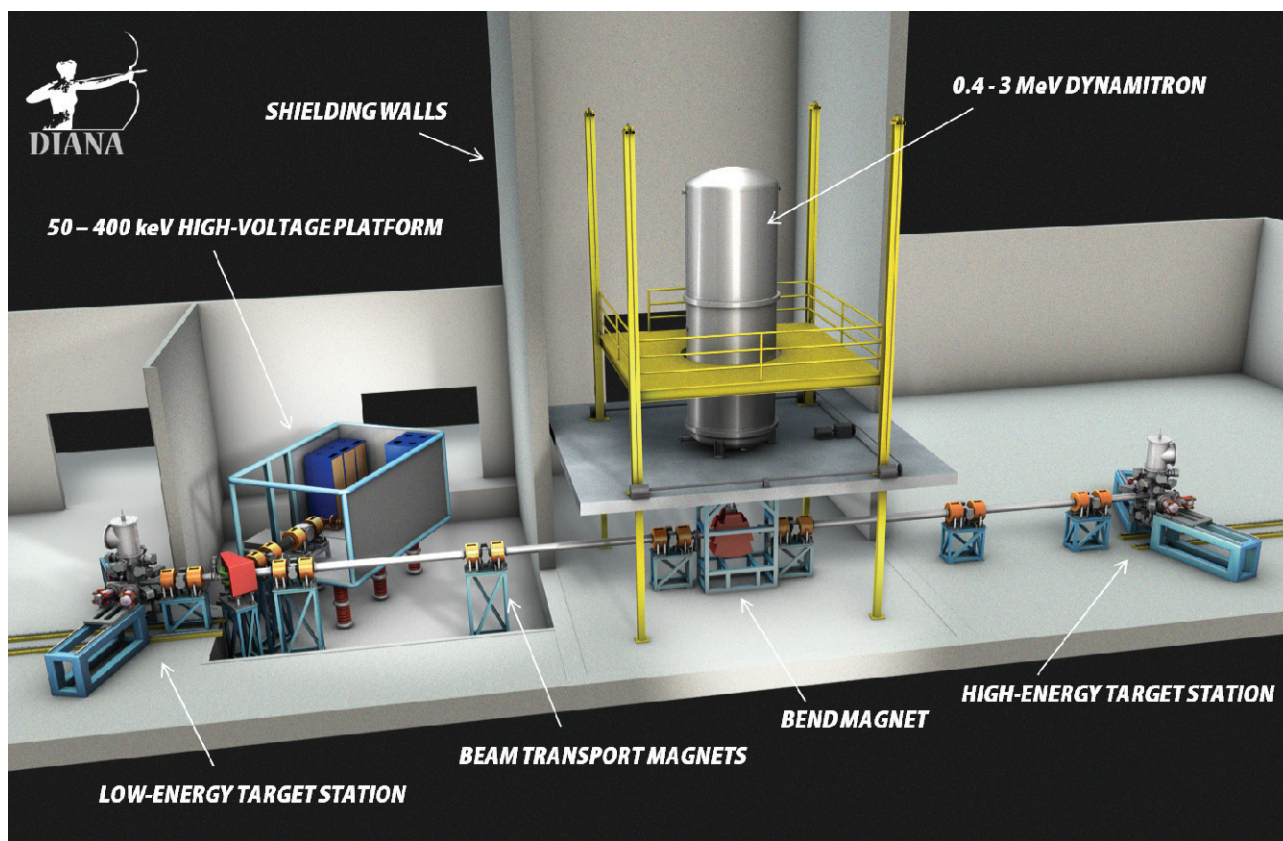


Figure 1: The DIANA facility will consist of two accelerators that will cover a wide range of ion beam energies and intensities.

TECHNICAL DESIGN CONCEPT

Key novel features of DIANA compared to existing nuclear astrophysics experiments will be:

- (1) The DIANA facility will consist of two accelerators (see Fig. 1) that will cover a wide range of ion beam energies and intensities.
- (2) The 400 keV low energy accelerator will be a major technological advance with regard to ion beam intensity on target in order to address the low count rates close to the Gamow window energies.
- (3) The 3 MeV accelerator will substantially extend the physics reach over what is presently feasible (which is limited to 400 keV at the LUNA facility in Gran Sasso [1]).
- (4) The proposed accelerators will have sufficient energy overlap to allow the study of nuclear reaction over a wide range and to consistently connect the results to measurements above ground.
- (5) The facility will feed the low energy target from both the low and the high energy accelerators. This will allow a particular reaction to be measured at both accelerators in complementary energy ranges with identical target and detector set-ups.
- (6) Both accelerators will feed the same gas target station, but an additional, independent target station is planned for the 3 MeV accelerator for conducting two experimental campaigns simultaneously or preparing the next experimental campaign. This feature will greatly enhance the ability to timely and efficiently carry out the planned science program, and addresses one of current limitations at the LUNA facility (which has only one target station available) since the experimental set-ups are difficult and time consuming.
- (7) Both accelerators are designed to be able to incorporate highly-charged Electron Cyclotron Resonance (ECR) ion sources to increase the beam energy or to vary the accelerated ions (from hydrogen to heavier elements). This unique feature will allow expansion of the scientific goals in the future.
- (8) Advanced target and detector technology will be developed in order to take advantage of DIANA's high beam currents.

THE 400 keV ACCELERATOR

The low energy accelerator (see Fig. 2) will have an accelerator voltage capability from 50 kV to 400 kV. To allow for easy access and maximum flexibility, the low energy accelerator has been designed as a 400 kV open-air high-voltage platform. The design criteria for the accelerator are high beam currents (up to 100 mA for singly charged ions, two orders of magnitude higher than current state of the art accelerators) with tight focus (< 1 cm) and a narrow beam energy distribution (~ 0.1% of the beam energy). Development of a stable power supply for the whole energy and beam current

Electrostatic Accelerators

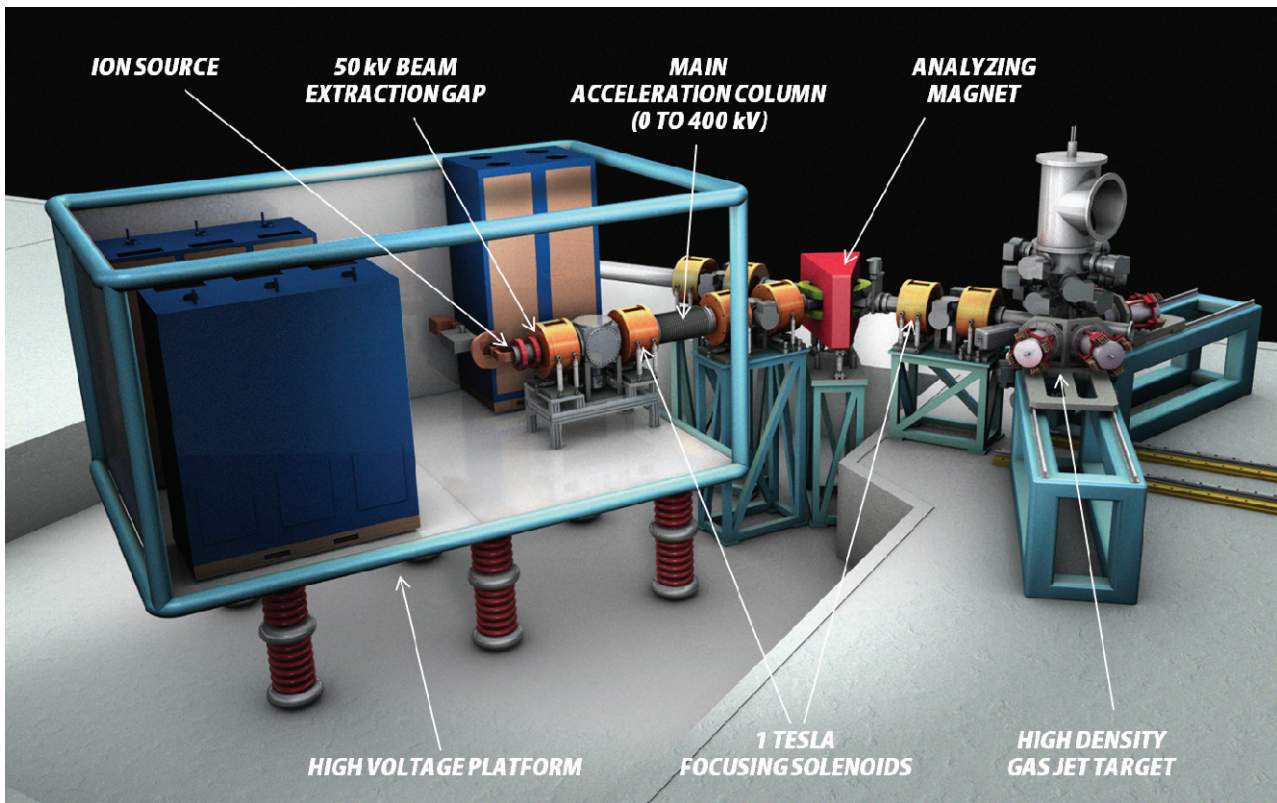


Figure 2: The DIANA low energy accelerator will have an accelerator voltage capability from 50 kV to 400 kV. The design criteria for the accelerator are high beam currents (up to 100 mA for singly charged ions) with tight focus (< 1 cm) and a narrow beam energy distribution ($\sim 0.1\%$ of the beam energy).

range will be important. A company (Kaiser Systems, Inc., Beverly, MA) capable of developing such a supply has been contacted.

Ion Sources for the 400 keV Accelerator

Two types of ion sources are planned for the high voltage platform. High intensity singly charged ions will be produced by a microwave ion source [2]. More than 100 mA of proton beam intensity and 20 mA of helium beam have been demonstrated under continuous operation [3, 4]. In addition, a permanent magnet ECR ion source [5] can be used to extend the energy range of the accelerator for helium to 800 keV up to several hundred μA , for nitrogen to 2 MeV, and for carbon up to 1.6 MeV at beam intensities of up to a hundred μA . The maximum energy specification will depend on a cost/benefit analysis between maximum energy necessary and beam line magnet costs.

Ion Beam Optics for the 400 keV Accelerator

The ion beam will be extracted with up to 50 kV extraction voltage and passed through two solenoid lenses. These lenses will convert the diverging ion beam to a near-parallel beam that is passed through the main acceleration gap that defines the final energy of the ion beam. The transport of high current of low energy ion-beams is made difficult by rapid beam expansion due to space charge forces. As the ion beam is transported along the beam line it will ionize the residual background gas,

and the electrons liberated will be radially confined by the ions therefore compensating the space charge forces. The actual acceleration gap length will be adjustable (see Fig. 3) to allow for minimizing the non-neutralized transport section for the lower energies and thus enabling transporting high intensity beams at the lowest beam energy. A similar concept of a movable high voltage gap has been demonstrated at the GSI facility (Gesellschaft für Schwerionenforschung, Darmstadt Germany) and has been the basis of the present design [6]. Two more solenoid lenses will prepare the beam for the transport

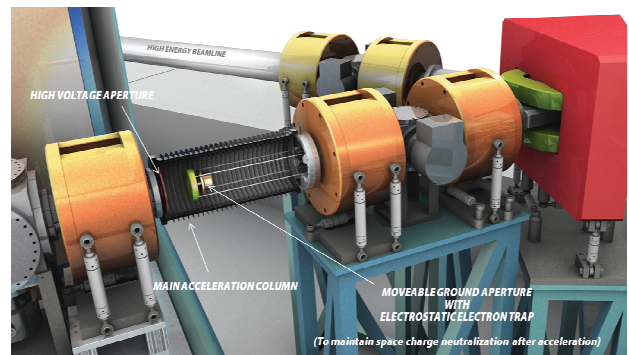


Figure 3: The acceleration gap length will be adjustable to allow for minimizing the non-neutralized transport section for the lower energies and thus enabling transporting high intensity beams at the lowest beam energy.

Electrostatic Accelerators

through the dipole magnet, which isolates the beam of interest from impurity ions. A fourth solenoid will provide the final focus onto the gas jet target [7]. An additional focusing element after the target will be required to focus the beam into the beam dump to reduce beam-induced background.

Preliminary Simulation Results

Fig. 4 shows simulations of the entire DIANA low energy beam transport line using the particle-in-cell code WARP [8]. The bottom plot of Fig. 4 displays the simulated beam edge in both, horizontal (X) and vertical direction (Y) versus beam direction, for a ${}^3\text{He}^+$ ion beam with 50 keV extraction energy without post acceleration. The top plot displays the same information for a ${}^3\text{He}^+$ ion beam with 50 keV extraction energy with 250 keV post acceleration (final beam energy 300 keV). In both cases, neutralization factors of 90% and a beam current of 100 mA have been assumed. Both figures show that a beam diameter less than 1 cm can be achieved at the target station to fit within the gas-jet-target entrance and exit collimators.

THE 3 MeV ACCELERATOR

The second accelerator (Fig. 5) has a maximum acceleration voltage capability of 3 MV. One of the options under consideration is a commercially available dynamitron accelerator supplied by IBA Industrial (formerly Radiation Dynamics Inc.). It has the advantage of supporting relatively high ion currents (several mA) over the whole voltage range with good energy resolution and tuneability.

Ion Sources for the 3 MeV Accelerator

Again, the use of two different types of ion sources is currently planned for the dynamitron. A permanent-magnet, microwave ion source will be used for producing several mA of singly charged ions in a reliable manner. In addition, a small permanent magnet ECR ion source will be incorporated to produce up to 30 μA of low charged ions with a total extracted ion beam intensity of 1-2 mA. A key R&D and engineering item of the project will be the design of the high voltage terminal to accommodate the microwave and the ECR ion sources. The use of ECR sources in connection with electrostatic accelerators has been demonstrated, but remains a technical challenge, in particular, the pumping at the extraction region. Successful examples are the BECRIS, a 5 GHz ECR source mounted at the terminal of the CN Van de Graaff of the Hahn-Meitner Institute in Berlin, and a 10 GHz Nanogun (PANTECHNIK, IBA Group) mounted on a 3 MeV single-ended electrostatic UH-2 Pelletron accelerator (National Electrostatics Corp.).

Ion Beam Optics for the 3 MeV Accelerator

Two options for the high voltage column design are currently being considered. The first option would use standard, commercially available accelerator rings. Alternatively, a unique combination of accelerator rings and electrostatic quadrupoles that would provide additional focusing for high intensity beams will be considered similar to ion beam transport systems developed in the heavy ion fusion program at LBNL. After the electrostatic accelerator, the beam will pass through an analyzing magnet that will permit alternatively feeding both target stations. The maximum bending power of the beam elements is proposed to be 1.4 Tm, which will allow bending up to 6 MeV ${}^{20}\text{Ne}$.

TARGET AREA

In order to minimize the background radiation for each experiment, the accelerator halls will be separated by low level activity concrete shielding walls, and the two target halls will be pointed in opposite directions.

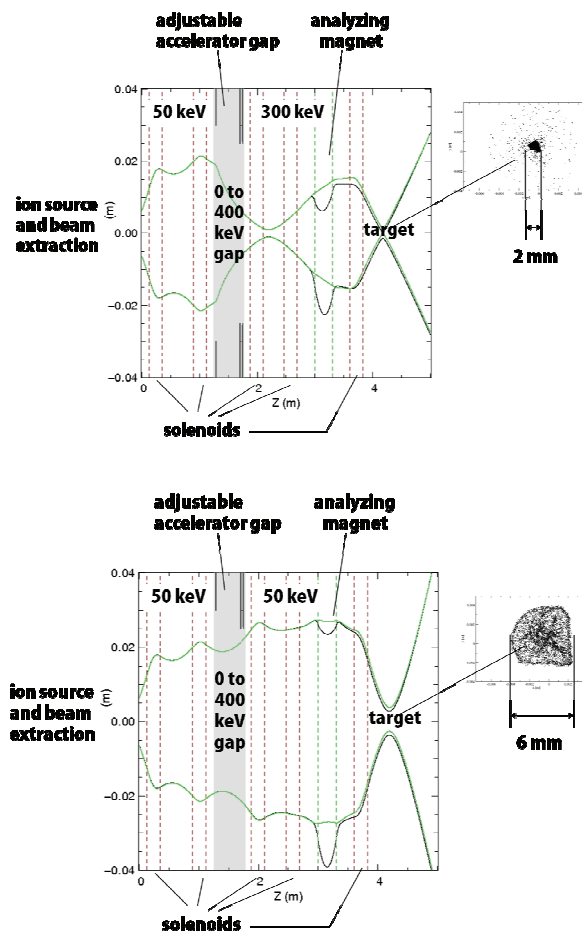


Figure 4: Simulations of the entire DIANA low energy beam transport line using the particle-in-cell code WARP. See text for description.

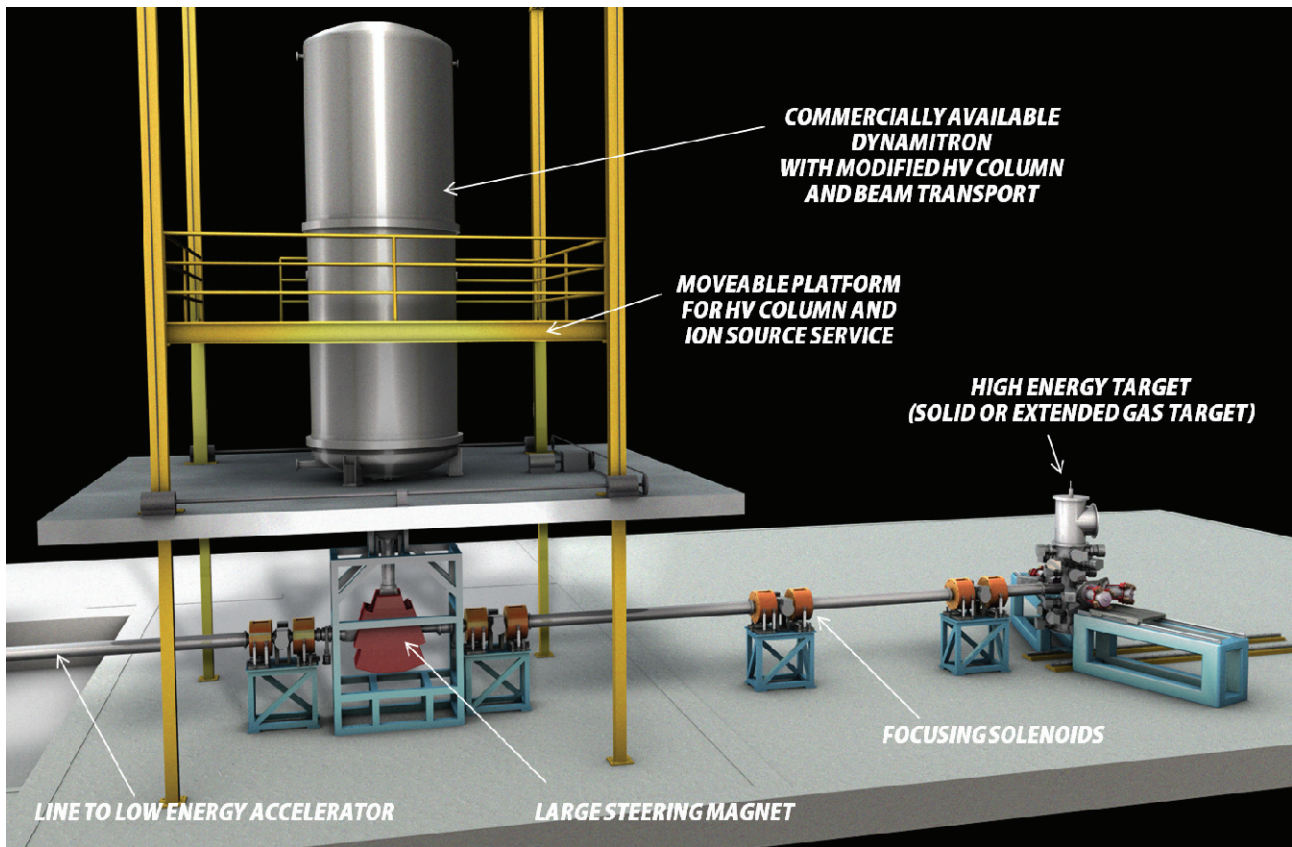


Figure 5: The second DIANA accelerator has a maximum acceleration voltage capability of 3 MV. One of the options under consideration is a commercially available dynamitron accelerator supplied by IBA Industrial.

Initial shielding calculations have already been performed, and results indicate that – even for high intensity ion beam experiments – less than 1 m thick concrete walls will be sufficient. Other DUSEL experimental halls will be separated by distances of approximately 100 meters in rock, so that significant reduction of any gamma or neutron field is expected by local shielding and distance. Further reduction in thermal neutron flux can be made with local placement of boron-loaded water elements immediately around target detectors and beam stops. More complex simulations involving secondary scattering from surrounding materials will be performed in the future to characterize beam-induced background in more detail.

A critical necessity for the low energy experiments using high intensity beams will be R&D on target systems that can withstand high beam currents without significant deterioration. Because of the nearly point-like gas zone, a supersonic gas-jet-target is an ideal target configuration for many investigations of nuclear reactions. Moreover, the power dissipated by an intense ion beam in a solid target could heat the material up to its melting temperature, making it difficult or impossible to operate for several weeks. Furthermore, the purity of the backing material of a solid target should be kept as high as possible to avoid parasitic nuclear reactions contaminating the spectra. Most of these problems could be solved using a gas target, where the target purity can

be better controlled. The gas jet target being considered for DIANA should be able to provide target areal densities up to 10^{18} atoms/cm². Because of the low energy of the reactions to be studied, corresponding to very small stopping ranges of ions in matter, a windowless gas target should be used to prevent beam energy resolution degradation. Thus a differentially pumped windowless gas jet target type, with four pumping stages is under design for DIANA.

REFERENCES

- [1] A. Formicola, G. Imbriani, M. Junker, et al., NIMA 507 (2003), 609
- [2] T. Taylor and J. S. C. Wills, NIMA 309 (1991), 37
- [3] R. Gobin, O. Delferriere, F. Harrault, et al., in ECRIS'08 (Pardo, Chicago, IL USA, 2008).
- [4] R. Gobin, P.-Y. Beauvais, D. Bogard, et al., RSI 73 (2002)
- [5] D. Hitz, M. Delaunay, A. Girad, et al., in 16th International Workshop on ECR Ion Sources, edited by M. Leitner (AIP, Berkeley, 2006), Vol. 749
- [6] P. Spadtke and B. H. Wolf, Vacuum 34 (1984), 73
- [7] D.S. Todd, D. Leitner, M. Leitner, et al., NIMB 261 (2007), 544
- [8] A. Friedman, D. P. Grote, and I. Haber, Phys. Fluids B. 4 (1992), 2203.

PROGRESS OF AN ACCELERATOR MASS SPECTROMETRY SYSTEM ON THE TSUKUBA 12UD PELLETRON TANDEM ACCELERATOR*

K. Sasa[#], T. Takahashi, Y. Nagashima, Y. Tosaki, K. Sueki, T. Amano, Y. Yamato, N. Kinoshita, UTTAC, University of Tsukuba, Tsukuba, Japan
 H. Matsumura, K. Bessho, RSC, KEK, Tsukuba, Japan
 Y. Matsushi, MALT, The University of Tokyo, Tokyo, Japan.

Abstract

The 12UD Pelletron tandem accelerator was installed at the University of Tsukuba in 1975. In recent years, the main research field of the 12UD Pelletron tandem accelerator has shifted to accelerator mass spectrometry (AMS) research from nuclear physics. AMS is an ultra-sensitive technique for the study of long-lived radioisotopes, and stable isotopes at very low abundances. The high terminal voltage is an advantage in the detection of heavy radioisotopes. It is important for sensitive measurements of heavy radioisotopes that background interference of their stable isobars are suppressed by AMS measurements. With the multi-nuclide AMS system at the University of Tsukuba (Tsukuba AMS system), we are able to measure long-lived radioisotopes of ¹⁴C, ²⁶Al, ³⁶Cl and ¹²⁹I by employing a molecular pilot beam method that stabilize the terminal voltage with 0.1% accuracy. Much progress has been made in the development of new AMS techniques for the Tsukuba AMS system. As for ³⁶Cl AMS, ³⁶Cl⁹⁺ at 100 MeV is used for AMS measurements. The standard deviation of the fluctuation is typically ± 2%, and the machine background level of ³⁶Cl/Cl is lower than 1 × 10⁻¹⁵. This report presents the overview and progress of the Tsukuba AMS system.

INTRODUCTION

The 12 UD Pelletron tandem accelerator was manufactured by National Electrostatic Corp. (NEC), USA and was installed at the University of Tsukuba, Tandem Accelerator Complex (UTTAC) in 1975 [1]. A maximum terminal voltage of 12 MV is available for various ion beam applications. Figure 1 shows a layout of the 12UD Pelletron tandem accelerator facility. In its early stages, the 12 UD Pelletron tandem accelerator was principally used for nuclear physics research. In recent years, the focus of nuclear physics research has shifted to high energy accelerators. The beam time for accelerator mass spectrometry (AMS) research has increased to about 42% of the total operation time. Figure 2 shows a percentage of the experimental beam time for one year on the 12UD Pelletron tandem accelerator. At present, AMS research projects are conducted on more than 50 days per annum. The Tsukuba AMS system has been continually developed since 1993 [2] and it is currently capable of measuring environmental levels of long-lived

radioisotopes of ¹⁴C, ²⁶Al, ³⁶Cl and ¹²⁹I.

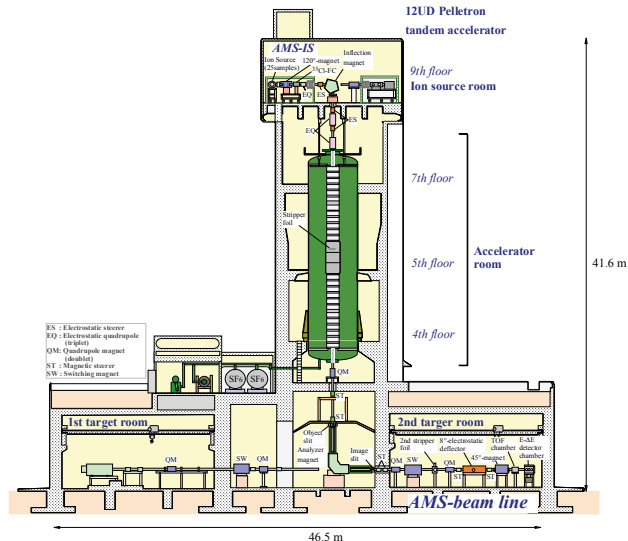


Figure 1: Layout of the 12UD Pelletron tandem accelerator facility at the University of Tsukuba.

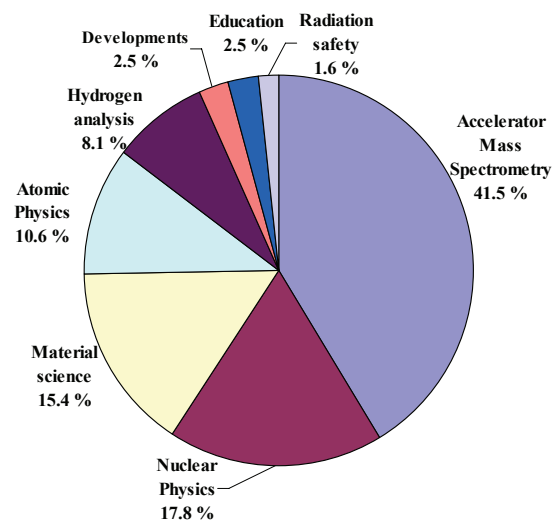


Figure 2: Percentage of the experimental beam time for the 12UD Pelletron tandem accelerator.

DESCRIPTION OF THE TSUKUBA AMS SYSTEM

Figure 3 shows a schematic diagram of the Tsukuba AMS system. The AMS beam line is equipped with a 25-sample sputter ion source and a 120° mass separator on the low energy side and a spectrometer consisting of a 90°

*Work supported by Grants-in-Aid for Scientific Research Programs of the Ministry of Education, Culture, Sports, Science and Technology, Japan.

[#]ksasa@tac.tsukuba.ac.jp

analyzing magnet ($\rho = 1.28$ m, $ME/q^2 = 200$ MeV amu, $p/\Delta p = 7.9 \times 10^3$), a second stripper foil, a 45° magnetic momentum analyzer, an 8° electrostatic analyzer ($\rho = 10$ m, $E/q = 10$ MeV), TOF and a gas $\Delta E - \text{SSD E}$ detector on the high energy side. The beam currents of the major stable nuclei are measured by offset Faraday cups just behind the 120° mass separator. The terminal voltage of the 12UD Pelletron tandem accelerator is controlled by a slit current feedback system in which the slit current is generated by a pilot beam. This method enables the terminal voltage to be kept stable within $\pm 0.1\%$ [3, 4]. A $5 \mu\text{g}/\text{cm}^2$ carbon foil with a diameter of 16 mm is used to strip the ions at the terminal. A second stripper carbon foil of $11 \mu\text{g}/\text{cm}^2$ with a diameter of 20 mm is used to eliminate the pilot ions from the mass separator beam line.

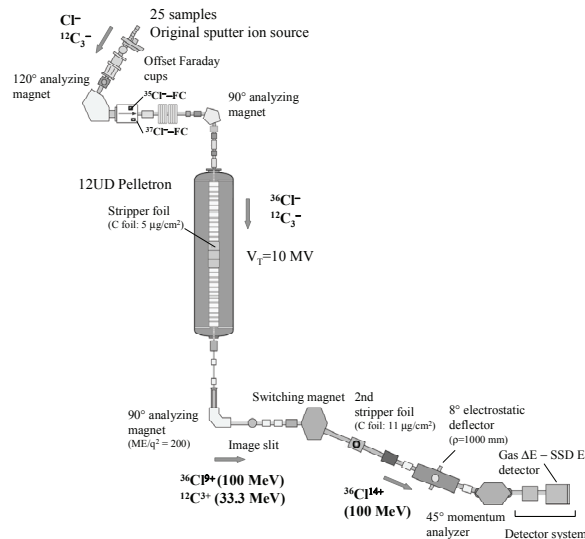


Figure 3: Schematic diagram of the Tsukuba AMS system. Labels indicate the main components along the AMS beam line and the experimental setup for AMS measurements of ^{36}Cl .

In the case of ^{36}Cl -AMS, a $^{12}\text{C}_3^-$ pilot beam is used for the slit current feedback system. The experimental setup for ^{36}Cl measurements is also indicated in Figure 1. $^{36}\text{Cl}^{9+}$ at 100 MeV and $^{12}\text{C}^{3+}$ at 33.3 MeV have the same mass energy product ME/q^2 after acceleration with a terminal voltage of 10 MV. The beam current of the $^{12}\text{C}^{3+}$ ions measured by the image slit is applied for slit current feedback to stabilize the terminal voltage. After the second stripper carbon foil, $^{36}\text{Cl}^{14+}$ and interference ions are selected and detected by the gas $\Delta E - \text{SSD E}$ detector, which consists of two gas ΔE sections [4]. For our AMS system, a standard sample is measured prior to measuring an unknown sample to reduce the system uncertainties.

RECENT PROGRESS OF THE TSUKUBA AMS SYSTEM

AMS Ion Source

A dedicated AMS sputter ion source with 25 sample cathodes has been developed at the University of Tsukuba. The AMS ion source is installed on a 100 kV platform and is controlled remotely by a computer through fiber optic links. We converted the Cs ionizer to a spherical type manufactured by NEC. A focused electrode was also installed to focus the Cs beam in front of the target. As a result, we can precisely control the focusing of the Cs beam onto a 1-mm-diameter sample holder. The Cs beam spot is evenly distributed on the target. The maximum beam current from the ion source is $50 \mu\text{A}$ for $^{35}\text{Cl}^-$.

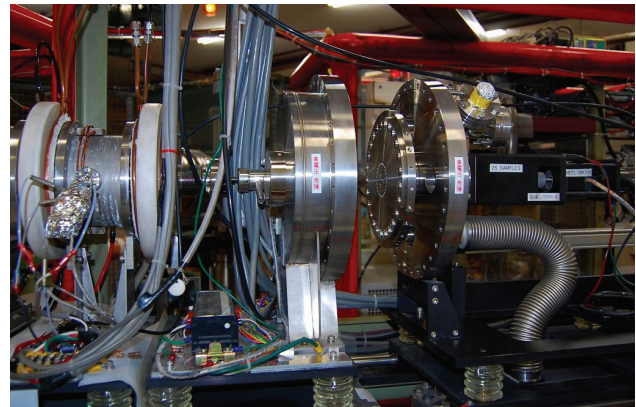


Figure 4: A 25-sample holder of an original Cs sputtering ion source for AMS.

AMS Data Integration System

Major stable beam currents are measured on the low energy side of our AMS system. Two offset Faraday cups are installed behind the 120° mass separator, as shown in Figure 3. A data integration system for AMS was developed that consists of a new beam-current monitoring system and a new data acquisition system (DAQ). The beam-current monitoring system for the offset Faraday cups can record the currents of multiple beams and automatically transfer the current integrated data into a spreadsheet. The DAQ is formed by the NIM ADCs and the CAMAC crate controlled by a FreeBSD operating system. The data integration system is combined with the DAQ in the beam-current monitoring system, which includes start and stop functions for AMS measurements. AMS analysis software has been developed at the University of Tsukuba and it permits AMS spectra to be displayed and analyzed on the same PC control system. Figure 5 shows a display of the data integration system for the Tsukuba AMS system.

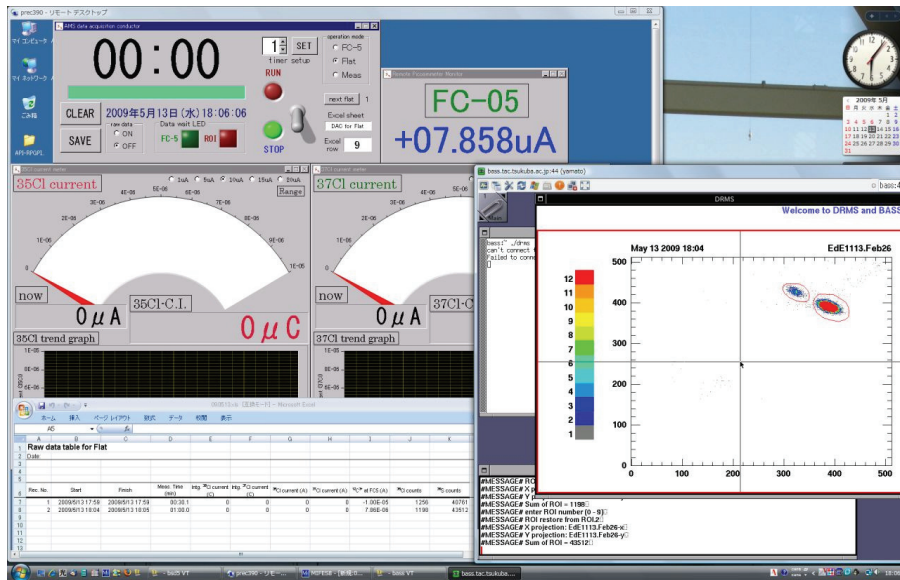


Figure 5: A display on the monitor of the data integration system for the Tsukuba AMS system. Beam current monitor system of the offset-Faraday cups located on the low energy side. The screen displays the diagrammatic representation of AMS spectrum by the PC control system.

New Gas ΔE – SSD E Detector

We developed a new gas ΔE – SSD E detector which consists of two gas ΔE sections and an ion-implanted silicon surface-barrier detector with a 45 × 45 mm² active area (Hamamatsu Photonics K.K.). The tail of the isobaric interference in the detector was reduced by introducing two ΔE gates. A 4 μm aramid film (Toray Industries, Inc.) is used as the entrance window of the detector. Pure iso-butane gas with a pressure of 670 Pa is applied in the gas section for the AMS measurement. Figure 6 shows a cross sectional view of the new detector.

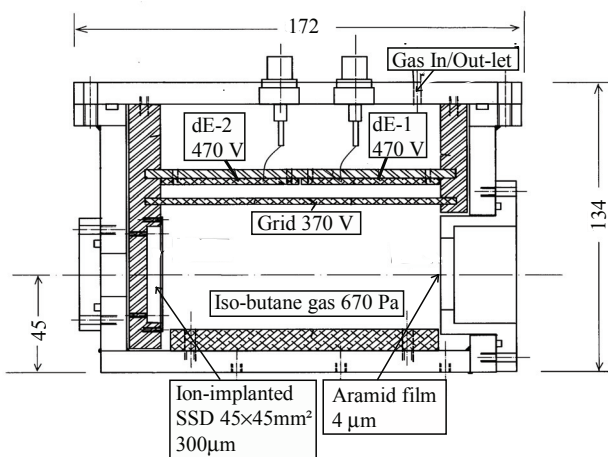


Figure 6: A new gas ΔE – SSD E detector.

PERFORMANCE OF THE TSUKUBA AMS SYSTEM

Table 1 gives a summary of the AMS performance for multiple nuclides. We have developed the pilot beam

method for various nuclides. Over the last three years, we have improved the performance of ³⁶Cl-AMS in order to measure low ³⁶Cl concentrations in the Dome Fuji ice core [5].

¹⁴C-AMS

A terminal voltage of 7 MV is selected and 35 MeV ¹⁴C⁴⁺ is accelerated with a ⁷Li² pilot beam. After the second stripper foil, 35 MeV ¹⁴C⁵⁺ is detected by the gas ΔE – SSD E detector. The measurement precision was approximately ± 2% [6].

²⁶Al-AMS

We use AIO⁻ molecular ions instead of Al⁻. In the pilot beam method, the target sample is prepared as an Al₂O₃ powder mixed with silver and enriched ²⁶MgO₂. ²⁶MgO⁻ molecular ions are used as the pilot beam to control the stability of the terminal voltage by the slit current feedback system. The maximum beam current of AIO⁻ extracted from Al₂O₃ samples was more than 1.5 μA. The beam current of ²⁷Al¹⁶⁻ is measured by an offset Faraday cup simultaneously while measuring ²⁶Al counted by the gas ΔE – SSD E detector. The accelerator is operated at a terminal voltage of 10.2 MV, and ²⁶Al⁷⁺ and ²⁶Mg⁷⁺ ions with energies of 78 MeV are selected by the 90° analyzing magnet. The pilot beam current of ²⁶Mg⁷⁺ is measured at the image point of the 90° analyzing magnet. ²⁶Al⁷⁺ ions are fully stripped to ²⁶Al¹³⁺ ions by a second carbon stripper foil and then ²⁶Al and ²⁶Mg are clearly separated by the subsequent spectrometer. The beam transmission of fully stripped Al¹³⁺ ions from AIO⁻ is up to 10%. The detection limit for the ²⁶Al/²⁷Al ratio is lower than 1 × 10⁻¹⁵ [4].

Table 1: Summary of ^{14}C , ^{26}Al , ^{36}Cl and ^{129}I AMS by the Tsukuba AMS System.

Trace isotope	^{14}C ($T_{1/2}= 5,730$ yr)	^{26}Al ($T_{1/2}= 7.20\times 10^5$ yr)	^{36}Cl ($T_{1/2}= 3.01\times 10^5$ yr)	^{129}I ($T_{1/2}= 1.57\times 10^7$ yr)
Target material	C+Li ₂ O	Al ₂ O ₃ + $^{26}\text{MgO}_2$ + Ag	AgCl + C ₆₀	AgI+MoO ₂ +Nb
Injection ion	$^{14}\text{C}^-$	$^{26}\text{AlO}^-$	$^{36}\text{Cl}^-$	$^{129}\text{I}^-$
Pilot beam	$^7\text{Li}_2^-$	$^{26}\text{MgO}^-$	$^{12}\text{C}_3^-$	$^{97}\text{MoO}_2^-$
Reference ion	$^{12}\text{C}^-$	$^{27}\text{AlO}^-$	$^{35}\text{Cl}^-$ & $^{37}\text{Cl}^-$	$^{127}\text{I}^-$
Typical current of reference ion	10 μA	1.5 μA	~ 20 μA & 5 μA	10 μA
Injection energy	103 keV	115 keV	103 keV	103 keV
Terminal voltage	7 MV	10.2 MV	10 MV	9.68 MV
Particle energy	35 MeV ($^{12}\text{C}^{4+}$)	78 MeV ($^{26}\text{Al}^{7+}$)	100 MeV ($^{36}\text{Cl}^{9+}$)	125.8 MeV ($^{129}\text{I}^{12+}$)
Detected ion	$^{12}\text{C}^{5+}$	$^{26}\text{Al}^{13+}$	$^{36}\text{Cl}^{14+}$	$^{129}\text{I}^{26+}$
Background	$^{14}\text{C}/^{12}\text{C} < 2 \times 10^{-14}$	$^{26}\text{Al}/^{27}\text{Al} < 1 \times 10^{-15}$	$^{36}\text{Cl}/\text{Cl} < 1 \times 10^{-15}$	$^{129}\text{I}/^{127}\text{I} < 1 \times 10^{-13}$
Typical precision	$\leq 2\%$	5 – 10 %	$\leq 2\%$	$\leq 8\%$

^{36}Cl -AMS

The performance of ^{36}Cl -AMS was enhanced by improving the AMS technique and system, including modifying the sample preparation technique [7], upgrading the ion source and installing a new data acquisition system. Beam currents of $^{35}\text{Cl}^-$ and $^{37}\text{Cl}^-$ could be measured by the offset Faraday cups with the beam-current monitoring system (see Figure 5). A typical beam current for $^{35}\text{Cl}^-$ was up to 20 μA . $^{36}\text{Cl}^{14+}$ with an energy of 100 MeV is detected by the gas ΔE – SSD E detector.

In 2007, we changed the standard reference sample to the KN standards [8] instead of using internal standards. Figure 7 shows ^{36}Cl spectra for the KN standard of $^{36}\text{Cl}/\text{Cl} = 1.60 \times 10^{-12}$ and a halite sample from the Himalayas, which was mined from a layer that was several hundreds of million years old, to confirm the system background level. The ^{36}Cl spectrum of the KN standard sample exhibits complete separation from ^{36}S in

the detector. The AMS system achieved complete discrimination between ^{36}Cl and ^{36}S up to a counting rate of ~ 5 kHz. The background level measured for the halite sample was lower than 1×10^{-15} for the $^{36}\text{Cl}/\text{Cl}$ ratio, as shown in Figure 7(b). The precision for the ^{36}Cl -AMS system was typically $\pm 2\%$ which was determined from the reproducibility of standard sample measurements.

^{129}I -AMS

A $^{97}\text{Mo}^{16}\text{O}_2$ molecular pilot beam is applied to ^{129}I -AMS [9]. $^{127}\text{I}^-$ ions are measured by the offset Faraday cup simultaneously while measuring ^{129}I ions in the detector. An electric beam deflector has been installed in front of the offset Faraday cup at the 120° magnet. The purpose of this installation is to increase the separation between the $^{129}\text{I}^-$ ion trajectory and the $^{127}\text{I}^-$ ion trajectory. We anticipate that the $^{127}\text{I}^-$ current can be measured more precisely using this deflector and consequently more

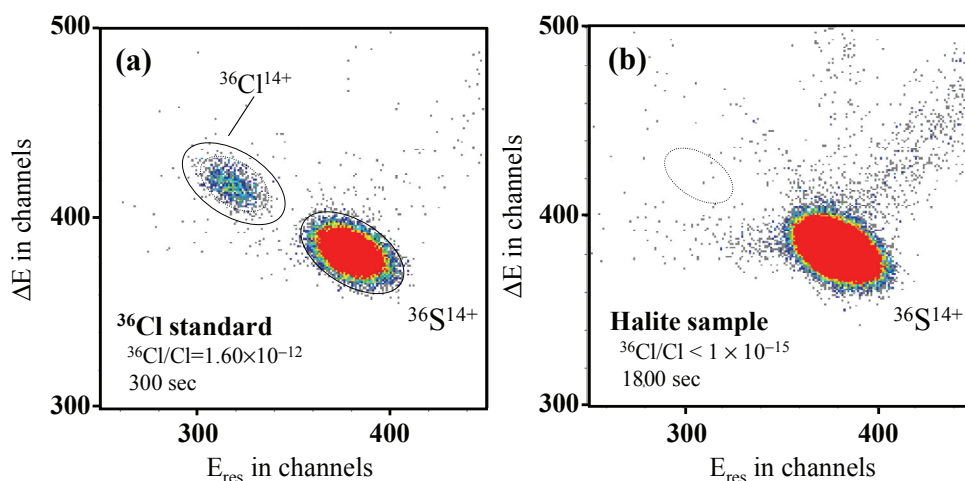


Figure 7: (a) ^{36}Cl spectrum of a standard sample for $^{36}\text{Cl}/\text{Cl} = 1.60 \times 10^{-12}$. (b) ^{36}Cl spectrum of a halite sample for the system background check. Total 3 counts of ^{36}Cl are detected for 30-minute measurement. The background level is lower than $^{36}\text{Cl}/\text{Cl} = 1 \times 10^{-15}$.

accurate measurement should be realized. $^{129}\text{I}^-$ and $^{97}\text{Mo}^{16}\text{O}_2^-$ ions are accelerated concurrently and $^{129}\text{I}^{12+}$ and $^{97}\text{Mo}^{9+}$ ions can pass through the 90° analyzing magnet. $^{97}\text{Mo}^{9+}$ ions pass through about 5 mm from the image point of the magnet and produce the slit current for the slit current feedback used to stabilize the terminal potential. After passing through the second stripper foil, $^{129}\text{I}^{26+}$ is selected as the detection particle. $^{129}\text{I}^{26+}$ ions are clearly detected by a silicon surface barrier detector. The terminal voltage is set to 9.68 MV. The background level of $^{129}\text{I}/^{127}\text{I}$ is lower than 1×10^{-13} .

SUMMARY

In recent years, the 12 UD Pelletron tandem accelerator is principally used for accelerator mass spectrometry (AMS) research. The Tsukuba AMS system is currently capable of measuring environmental levels of long-lived radioisotopes of ^{14}C , ^{26}Al , ^{36}Cl and ^{129}I . Especially for the ^{36}Cl -AMS, the machine background level of $^{36}\text{Cl}/\text{Cl}$ has been achieved lower than 1×10^{-15} .

We replaced the old point-to-plane corona needle system with a resistor-based potential grading system manufactured by NEC in the spring of 2009. The replacement is expected to improve the stability of the terminal voltage. We have developed a GVM control system for the terminal voltage. A second injection beam line has been designed for the AMS system. The 40-sample multiple cathode MC-SNICS manufactured by NEC was installed at the UTTAC in 2008. The new injection beam line with a high current ion source will

enhance the ability to efficiently perform routine AMS measurements.

REFERENCES

- [1] S. Seki, K. Furuno, T. Ishihara, Y. Nagashima, M. Yamanouchi, T. Aoki, T. Mikumo, J. Sanada, Nucl. Instr. and Meth. 184 (1981) 113.
- [2] Y. Nagashima, H. Shioya, Y. Tajima, T. Takahashi, T. Kaikura, N. Yoshizaki, T. Aoki, K. Furuno, Nucl. Instr. and Meth. B 92 (1994) 55.
- [3] Y. Nagashima, R. Seki, T. Takahashi, D. Arai, Nucl. Instr. and Meth. B 172 (2000) 129.
- [4] K. Sasa, Y. Nagashima, T. Takahashi, R. Seki, Y. Tosaki, K. Sueki, K. Bessho, H. Matsumura, T. Miura, M. He, Nucl. Instr. and Meth. B 259 (2007) 41.
- [5] H. Motoyama, Sci. Drill. 5 (2007) 41.
- [6] Y. Nagashima, R. Seki, T. Baba, N. Funaya, N. Miyazaki, T. Takahashi, T. Kaikura, T. Aoki, K. Furuno, Nucl. Instr. and Meth. A 382 (1996) 321.
- [7] Y. Tosaki, N. Tase, G. Massmann, Y. Nagashima, R. Seki, T. Takahashi, K. Sasa et al., Nucl. Instr. and Meth. B 259 (2007) 479.
- [8] P. Sharma et al., Nucl. Instr. and Meth. B 52 (1990) 410.
- [9] Y. Nagashima, R. Seki, K. Sasa, et al., Nucl. Instr. and Meth. B 259 (2007) 241.

OPERATION STATUS OF HIGH INTENSITY ION BEAMS AT GANIL

F. Chautard, G. Sénécal, GANIL, Caen, France

Abstract

The Grand Accélérateur National d'Ions Lourds (GANIL, Fig. 1) facility (Caen, France) is dedicated to the acceleration of heavy ion beams for nuclear physics, atomic physics, radiobiology and material irradiation. The production of stable and radioactive ion beams for nuclear physics studies represents the main part of the activity. Two complementary methods are used for exotic beam production: the Isotope Separation On-Line (ISOL, the SPIRAL1 facility) and the In-Flight Separation techniques (IFS). SPIRAL1, the ISOL facility, is running since 2001, producing and post-accelerating radioactive ion beams. The running modes of the accelerators are recalled as well as a review of the operation from 2001 to 2008. A point is done on the way we managed the high intensity ion beam transport issues and constraints which allows the exotic beam production improvement.

- Additionally, the cyclotron CIME (SPIRAL post-accelerator) delivers stable beams for detector tests for example.

During radioactive beam production, no more than three experiments are working simultaneously.

Intense Primary Beams

The facility delivers a wide spectrum of high intensity ion beams ranging from ^{12}C to ^{238}U accelerated up to 95MeV/A as a function of their masses. The acceleration scheme lies on the use of three cyclotrons in line. One compact (C01 or C02, K=30) and two separated sector cyclotrons (CSS1 and CSS2, K=380). Those accelerators and beamlines have been adapted to transport intense ion beams. More than 10 beams are available at a power exceeding 1 kW (Table 1) over 50 stable beams available from the GANIL sources [1]. The beam losses detectors, beam transformers and control system allow the transport of intense stable beams with power exceeding 3 kW in routine operation.

Table 1: Some of the GANIL High Intensity Beams, the main Limitation Come now from the Target Ability to Withstand the High Power Density

Beams	I_{max} [μAe]	10^{13} [pps]	E_{max} [MeV/A]	P_{max} [W]	Used with Spiral
$^{12}\text{C}^{6+}$	18	1.9	95	3 200	
$^{13}\text{C}^{6+}$	18	2.	80	3 000	X
$^{14}\text{N}^{7+}$	15	1.4	95	3 000	
$^{16}\text{O}^{8+}$	16	1	95	3 000	X
$^{18}\text{O}^{8+}$	17	1	76	3 000	X
$^{20}\text{Ne}^{10+}$	17	1	95	3 000	X
$^{22}\text{Ne}^{10+}$	17	1	79	3 000	
$^{36}\text{S}^{16+}$	6.4	0.25	77.5	1100	X
$^{36}\text{Ar}^{18+}$	16	0.55	95	3 000	
$^{40}\text{Ar}^{18+}$	17	0.6	77	3 000	
$^{48}\text{Ca}^{19+}$	4-5	0.13	60	600-700	X
$^{58}\text{Ni}^{26+}$	5	0.12	77	860	
$^{76}\text{Ge}^{30+}$	5	0.12	60	760	
$^{78}\text{Kr}^{34+}$	7.5	0.14	70	1200	X
$^{124}\text{Xe}^{46+}$	2	0.03	53	300	

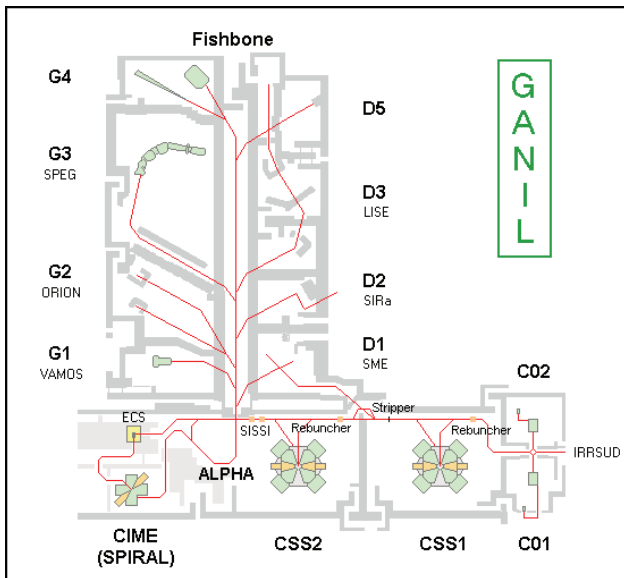


Figure 1: GANIL layout.

RUNNING MODES

Multibeam delivery is possible at GANIL. Using its 5 cyclotrons GANIL-SPIRAL is increasingly a multi-beam facility. Up to four experiments can be run simultaneously in different rooms with stable beams:

- Using the beam of C01 or C02, an irradiation beam line IRRSUD works with 1 MeV/A.
- Using one charge state of the ion distribution downstream CSS1 after the ion stripping, a line uses ion in the range 4-13MeV/A beams, for atomic physics, biology, solid states physics.
- A high-energy experiment.
- An auxiliary experiments sharing the CSS2 beam

Secondary Exotic Beams

Exotic beams are produced with two complementary methods. ISOL method with SPIRAL where the primary beam is fragmented in a thick carbon target. The

fragments produced are post-accelerated with the cyclotron CIME from 1.2 to 25 MeV/A (Table 2).

Table 2: Radioactive Beam Produced and Post-accelerated from 2001 to 2006. W in [MeV/A]

ions	W	[pps]	ion	W	[pps]
¹⁸ Ne	7	10 ⁶	³¹ Ar	1.45	1.5
⁸ He	15.5	10 ⁴	⁶ He	5	3.10 ⁷
⁸ He	3.5	10 ⁵	⁸ He	15.4	2.10 ⁴
²⁴ Ne	4.7	2 10 ⁵	⁸ He	3.9	8.10 ⁴
⁷⁴ Kr	4.6	1.5 10 ⁴	⁸ He	3.5	6.10 ⁵
⁸ He	15.4	1.5 10 ⁴	¹⁸ Ne	7	10 ⁶
⁸ He	15.4	9 10 ³	²⁴ Ne	10	2.10 ⁵
²⁴ Ne	10	2 10 ⁵	²⁶ Ne	10	3.10 ³
⁸ He	15.4	2.5 10 ⁴	⁴⁴ Ar	10.8	2.10 ⁵
¹⁵ O	1.2	1.7 10 ⁷	⁴⁶ Ar	10.3	2.10 ⁴
²⁴ Ne	7.9	1.4 10 ⁵	⁷⁴ Kr	2.6	1.5.10 ⁴
³³ Ar	6.5	3 10 ³	⁷⁶ Kr	4.4	6.10 ⁵
⁶ He	3.8	2.8 10 ⁷	⁷⁵ Kr	5.5	2 10 ⁵
⁸ He	15.4	2.5 10 ⁴	⁴⁴ Ar	3.8	3 10 ⁵
³⁵ Ar	0.43	4 10 ⁷	⁶ He ²⁺	20	5 10 ⁶
⁶ He	2.5	3.7 10 ⁷	⁶ He ¹⁺	Lirat	2 10 ⁸

And by the In flight method with SISSI (Superconducting Intense Source for Secondary Ions) [5] consisting of fragmenting the intense primary beams onto a rotating target. The exotic cocktail beam after the target is purified with the alpha spectrometer and sent to the experimental area.

Since October 1994, SISSI produces secondary radioactive beams. A 0.4mm diameter spot is created on a thick rotating target with a superconducting solenoid with a maximum field of 11 T. A second identical solenoid after the target improves the downstream beam line angular acceptance and thus increases the collection of the secondary exotic ions. The cooling system is provided by a circuit of liquid helium at 4.6 K. The target is a 2000 rpm rotating disk, so that the radiated heat is spread over a much larger area than the beam spot.

In June 2007, the second solenoid quenched and cannot be used. Therefore, a project have been launched to overview all possible solutions to produce secondary beams (alternative solutions, repairing) compatible with the operation schedule and resources. Meanwhile CLIM took over for physicists.

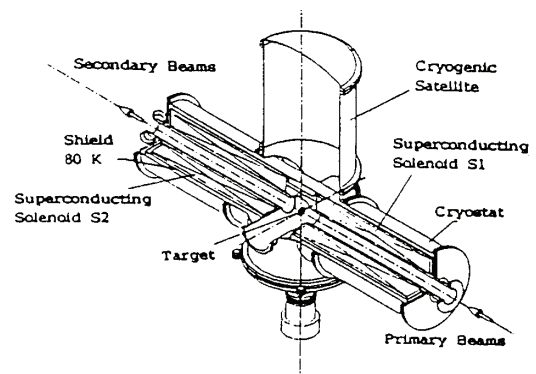


Figure 2: Schematic view of the cryostat of SISSI.

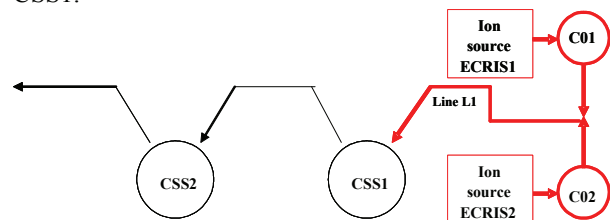
HIGH INTENSITY BEAM TRANSPORT

In 1995, a High Intensity Transport safety system (THI) was studied and validated in 1998 in order to allow sending a several kilowatt beam into the experimental rooms. The system protects equipment against the beam power loss. The safety regulation rules allow the GANIL to accelerate beam to a maximum of 2·10¹³ ions per second or 6 kW out of CSS2. Within those limits, uncooled or unshielded elements may melt very rapidly and must be protected by a safety system.

The machine tuning uses three modes to increase beam power transportation.

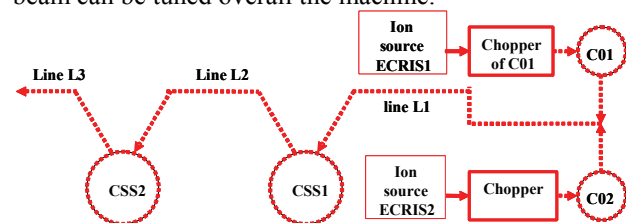
Injector Mode

This mode allows the acceleration of an ion beam with a maximum beam power < 400 W up to the injection of CSS1.



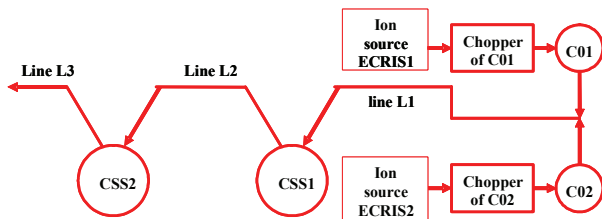
Tuning Mode

By using of a chopper to reduce the mean beam intensity (equipment protection) and keeping the crest intensity identical (space charge limitation) a 400 W beam can be tuned overall the machine.



Watching mode

The high power beam (up to 6 kW) is reached in this mode by reducing the chopping rate and monitoring the safety system controls beam losses presented in [3] and [4].



A 26 μ Ae (5 kW) for ^{36}Ar at 95 MeV/A has been successfully accelerated.

2001-2008 SPIRAL STATUS

For the production and acceleration of radioactive ions with the ISOL method, the stable heavy ion beams of GANIL are sent into a target and source assembly. The radioactive atoms produced by nuclear reactions are released from the target, kept at high temperature, into an ECR source. After ionisation and extraction from the source (extraction voltage < 34 kV), the multi-charged radioactive ions are accelerated up to a maximum energy of 25 MeV/A by the compact cyclotron CIME (K=265). The first SPIRAL beam delivered to the physics was ^{18}Ne in October 2001. Since, more than 30 radioactive beams were produced in 8500 hours of SPIRAL operation over 23600 hours of total beamtime delivered to nuclear physics experiments.

Fig. 3 shows the time repartition between SPIRAL and GANIL beams over 8 years.

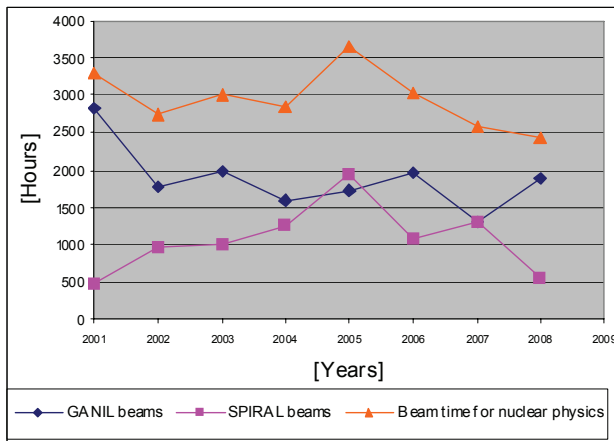


Figure 3: Beamtime shared over the years between GANIL beam (out of CSS) and SPIRAL1 beams (out of CIME).

Over the same period, the experience allowed reducing and optimizing the tuning time (Fig. 4) and meanwhile the number of tuned beams increased (Fig. 5).

A list of the radioactive beams [2] delivered is reported in Table 2.

More generally, the GANIL cyclotron delivers beam around 4000 hours a year (Fig. 6). The reduced time in 2008 is due to a shortened machine schedule of 4.5 weeks to allow technical staff to concentrate on SPIRAL2 construction.

Circular Accelerators

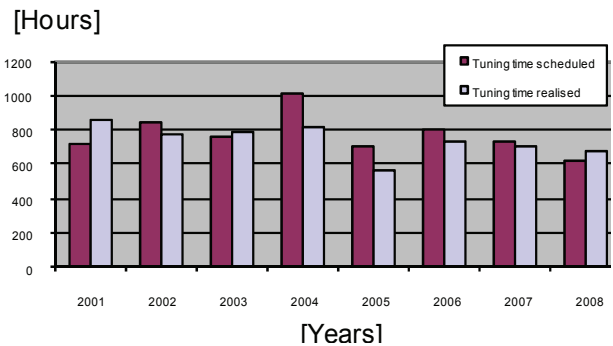


Figure 4: Tuning time.

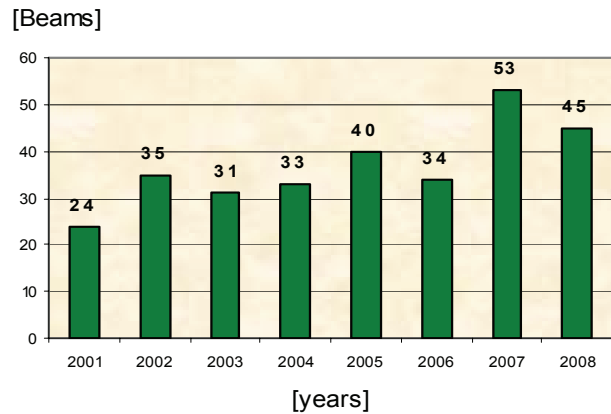


Figure 5: Number of beams tuned between 2001 and 2008.

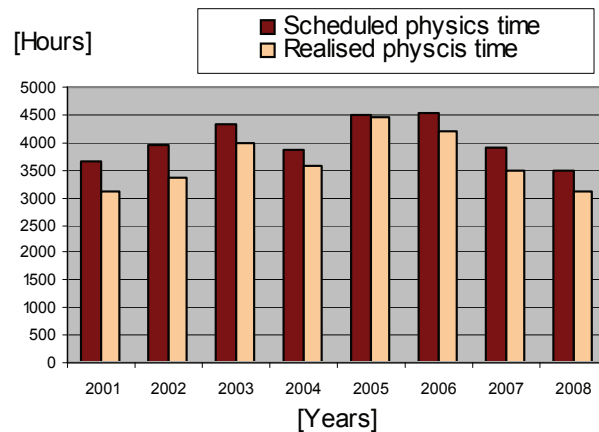


Figure 6: Schedule and realized machine running time.

FORSEEN MACHINE DEVELOPMENTS

The SPIRAL2 machine [7] will increase the capability of the GANIL. It is foreseen to some extent to use at the same time the new SPIRAL2 beams and the existing ones. Therefore, a GANIL 2015 committee was created to identify the strength and weakness of the actual facility for the close future [8]. One of the main recommendations of this committee is to extend the radioactive ion beam variety available from the SPIRAL1 facility. As the highest priority, the study of the modification needed for the insertion of a charge breeder out of the cave of SPIRAL1 is pointed out. Additionally, detailed studies to

allow the high intensity beams of SPIRAL2 into specifically identified caves have to be carried out with very specific constraints from the radioactive beams. In the following is reviewed the evolutions machine-side to take into account the committee recommendations.

Most of the ions produced in SPIRAL are gases (He, O, Ne, Xe, etc.). The 1+/N+ ion source actually used cannot extract other species with an acceptable yield. Therefore, a modification of the couple target-source should be studied. Moreover, any modification of the existing irradiation cave implies a safety report inducing a time delay in the construction. It has been decided to study new sources that fit in the existing environment (plugs, power supply connections, remote handling, etc.). In addition, it becomes obvious that the choice of the source type will be done between two types:

- Compact 1+/N+ : Alkali source
- 1+ source in the cave and a charge breeder (N+) outside of the cave.

Compact 1+/N: Alkali Source

In the framework of the production of radioactive ion beams by the isotope separator on-line (ISOL) method, a new system has been developed at GANIL/SPIRAL to produce multi-charged alkali ions. The principle, referred to as the “direct 1+/N+ method”, consists of a surface ionization source associated with a multi-charged electron-cyclotron-resonance ion source without an intermediate mass separator [6]. This new system has been tested on line using a ⁴⁸Ca primary beam at 60.3 MeV/A. The experimental evidence of the direct 1+/N+ process has been obtained for a potential difference between the two sources of 11 V, and with a 1+/N+ charge breeding efficiency of 0.04% for ⁴⁷K⁵⁺. This value is significantly lower than the value of 6% obtained for stable K ions with the standard 1+/N+ method.

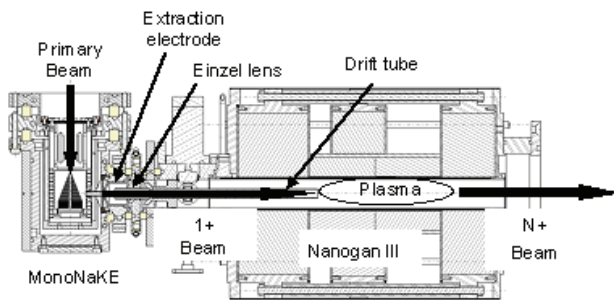


Figure 7: surface ionization source associated with a multi-charged electron-cyclotron-resonance ion source.

Charge Breeding for SPIRAL1

Another possibility to create new ion species and accelerate them through CIME cyclotron is to implement a 1+ source in the irradiation cave. The atom produced during the fragmentation of the primary in the carbon target of SPIRAL is ionized only once by an ion source. The final higher charge state necessary to accelerate it through the cyclotron is done via a so-called charge

Circular Accelerators

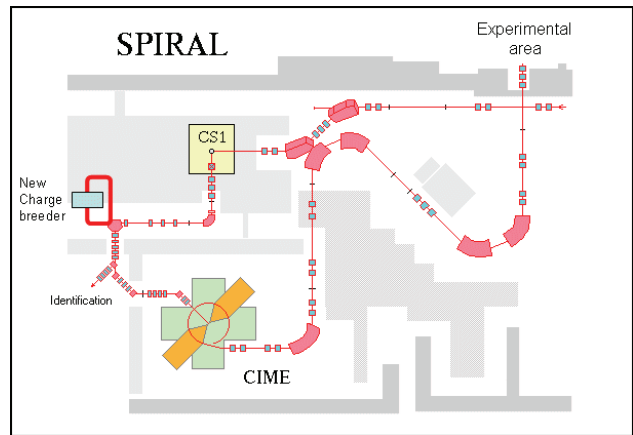


Figure 8: Possible SPIRAL1 low energy beam modifications to insert a new charge-breeder.

breeder outside the cave. The interest of such a solution is that the reduced source dimension compared to ECR source is kept compatible with the cave mechanical constraints due to their compactness.

Intensity Increase (primary and secondary Beams)

The increase of the ion beam intensities is still possible for the primary stable beams and the exotics beams as well. We recall the safety regulation limitations: 2·10¹³ ions per second or 6 kW out of CSS2 and 5·10¹¹ ions per second out of CIME. It appears that already few beams reach or are close to reach these limits, mostly light ion species (Table 1). Nevertheless, significant improvements are possible for heavy ions. A GANIL Test Source (GTS) exists and is under commissioning until the middle of 2010. Its installation on a machine platform is technically possible and will be decided then. The Table 3 recalls the gains expected along the acceleration chain by increasing the production at the source.

Table 3: Expected Intensity and Energy Gains by Implementing the GTS Source

Gains	Low energies	Middle energies (<13MeV/A)	High energies
Intensities			
Light Ions	1 to 2	1 to 2	1 to 2
Heavy Ions	2 to 4	2 to 4	2 to 4
Very heavy Ions	10	10	10
Max Energies			
Light Ions	1 MeV/A	13.6 MeV/A for all ions	No gain
Heavy Ions	for all ions		Possible gain
Very heavy Ions			

From the exotic beams point of view, the production is limited by the power that the carbon target can handle. Two target types exist: one for the ^{6,8}He production that

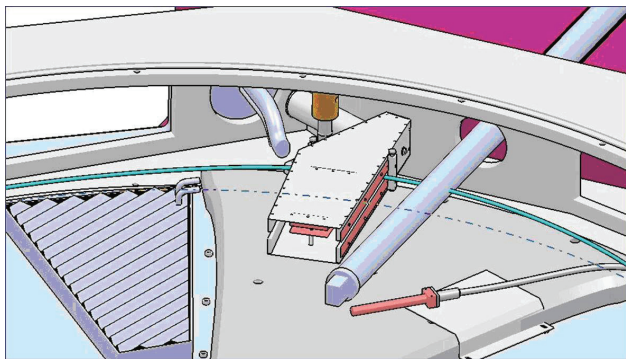


Figure 9: Electrostatic vertical deflector used to purify exotic beam from pollutant beam.

can handle 3kW beams and another limited to 1.5 kW for other ion species. The safety limitation to 6 kW beam shows a potential improvement of the production from 2 to 4. Nevertheless, preliminary study shows the increase of the target dimensions for higher power might reduce the diffusion of the created beam in the kernel target. The gain seems not to be linear with the power deposited. A working group is constituted to investigate this option.

Increase Beam Purity out of CIME

Even with a selective ECR source, the exotic ion beams created on SPIRAL1 might be polluted by ions with a ratio mass over charge close to the ion of interest and then be accelerated by the cyclotron CIME. The condition to eliminate an undesired ion corresponds at first order to:

$$\left[\frac{M_2}{Q_2} - \frac{M_1}{Q_1} \right] / \frac{M_1}{Q_1} > \frac{1}{2\pi H N_{turn}} \quad (1)$$

where N_{turn} is the number of turns. Hence the mass resolution of a cyclotron is defined as $R = 1/2\pi H N_{turn}$.

Depending on the harmonic, the mass resolution of CIME can reach $2 \cdot 10^{-4}$. But even with this resolution beam tail may exit. The intensity of such beams does not need to be necessarily high to penalize the physics experiment. A elegant solution is to insert an electrostatic vertical deflector around the 10 last trajectory paths of the beam in the cyclotron. The amplitude of the sinusoidal electric wave between the deflector plates will be zero for the beam of interest (isochronous) and increase with the mass/charge ratio difference. The efficiency of such a

device is measured and is able to reduce by a factor 10 beams $3 \cdot 10^{-4}$ far. This device will improve purity of the beam sent to the physics.

CONCLUSIONS

The first beam of GANIL was sent to an experimental room in 1983. Since then, the variety and intensity of the ion beams available always increased. Progresses in the source domain make possible to potentially transport of kW beams. The cyclotrons and the beam lines had to be upgraded to handle such a new constraint. In 2001, the first exotic beam of SPIRAL1 was produced with the existing cyclotron used as a driver. The exotic ion production was then depending on the target power resistance and the increase of the primary beam power. This leads to the developments of 3 kW target of SPIRAL1 and meanwhile increases the primary beam power within the safety rules (<6 kW).

The variety of the ion species is now the main concern at GANIL. The actual selective ECR ion source should be replaced by an alternative ion in order to access to metallic beams.

The great care given to the maintenance of the 25 year old machine allows us to still expect to increase its performances and be competitive until the SPIRAL2 arrival and afterwards.

REFERENCES

- [1] http://www.ganil.fr/operation/available_beams/available_beams_tabular.htm
- [2] http://www.ganil.fr/operation/available_beams/radioactive_beams.htm
- [3] C. Jamet et al., "THI safety system", Proceedings of DIPAC 2005, Lyon, France, p169 (2005), <http://www.JACoW.org>.
- [4] G. Sénécal et al., "GANIL high intensity transport safety system", poster HIAT09. This conference.
- [5] A. Savalle, et al., "The SISSI facility at GANIL", Sitges, June 1996.
- [6] C. Eléon et al., Proceedings of EMIS07, Deauville, FRANCE, 24th-29th June 2007.
- [7] J.M. Lagniel, "Building design for high beam power, the example of SPIRAL2", HIAT09, this conference.
- [8] Report on prospective for GANIL 2015. DIR_059_2009.

STATUS REPORT AND FUTURE DEVELOPMENT FLNR JINR HEAVY IONS ACCELERATOR COMPLEX

G. Gulbekyan, B. Gikal, I. Kalagin, N. Kazarinov,
 Joint Institute for Nuclear Research, FLNR, Dubna, Moscow region, Russia

Abstract

Four heavy ions cyclotrons are in operation at FLNR now. Heavy ion beams used for super heavy elements synthesis, RIB production and application. Plan for seven years accelerator development and operation are presented.

INTRODUCTION

At present time four isochronous cyclotrons: U400, U400M, U200 and IC100 are under operation at the JINR FLNR. Total operation time is about 10 000 hours per year. The U400M is a primary beam generator and U400 is as postaccelerator in RIB(DRIBs) experiments to produce and acceleration exotic nuclides as ^6He , ^8He , etc. The layout of FLNR accelerators complex is presented on Fig.1 [1].

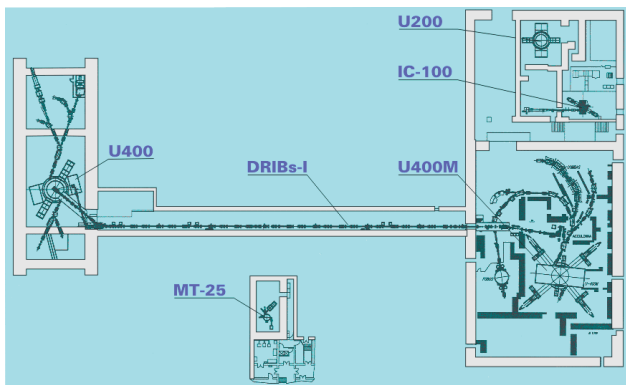


Figure 1: Layout FLNR JINR accelerator complex.

U400→U400R CYCLOTRON

The cyclotron U400 (pole diameter 4 m) has been in operation since 1978 [2], [3]. In 1996, the ECR-4M ion source (GANIL) was installed at the U400. The axial injection system with two bunchers (sin and linear) and spiral inflector was created to inject ions in cyclotron Fig.2. From 1997 to present time U400 had worked in total 64 000 hours. About 66% of the total time was used for acceleration $^{48}\text{Ca}^{5+,6+}$ ions for synthesis of new super-heavy elements. Within the mentioned period elements with $Z=113, 114, 115, 116, 118$ were synthesized. Chemical properties of $Z=112$ were studied. The ^{48}Ca beam intensity on the target is $8 \cdot 10^{12}$ pps ($1.2 \mu\text{A}$) at ^{48}Ca substance consumption of 0.4 mg/hour. Extraction efficiency of ^{48}Ca beam by stripping is on the level of 40% only. The U400→U400R modernization is planned to start in 2010 and finished in 2011. The aim of the modernization:

Circular Accelerators

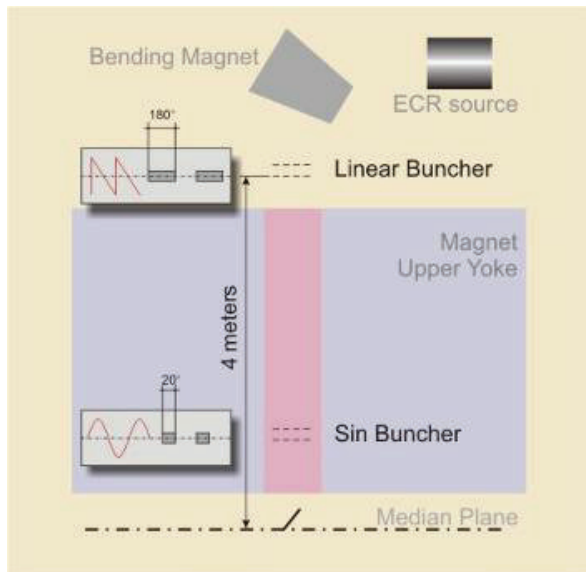


Figure 2: Scheme of the beam bunching system.

- increasing ^{48}Ca , ^{50}Ti , ^{54}Cr , ^{58}Fe , ^{64}N , beam intensity on the target up to $2.5 \div 3 \mu\text{A}$;
- providing the fluent ion beam energy variation at factor 5 by magnetic field variation from 0.8 up to 1.8 T instead $1.93 \div 2.1$ T now;
- improvement of the energy spread in the ion beam at the target up to 10^{-3} ;
- improvement of the ion beam emittance at the target up to $10 \pi \text{ mm} \cdot \text{mrad}$.

The project of modernization intends changing axial injection system, magnetic structure, vacuum system, RF system, power supply system, beam diagnostic system and additionally electrostatic deflector positioning. The main comparative parameters of U400 and U400R are presented in Table 1.

Table 1: Comparative Parameters of U400 and U400R

Parameters	U400	U400R
A/z range	5÷12	4÷12
Magnetic field	1.93÷2.1 T	0.8÷1.8 T
K factor	530÷625	100÷500
RF modes	2	2, 3, 4, 5, 6
Injection potential	10÷20 kV	10÷50 kV
Ion energy range	3÷20 MeV/n	0.8÷27 MeV/n
Number of sectors	4	4
Number of dees	2	2
Flat – top system	-	+
Beam extraction	stripping	Stripping, deflector
Power consumption	~1 MW	~0.4 MW

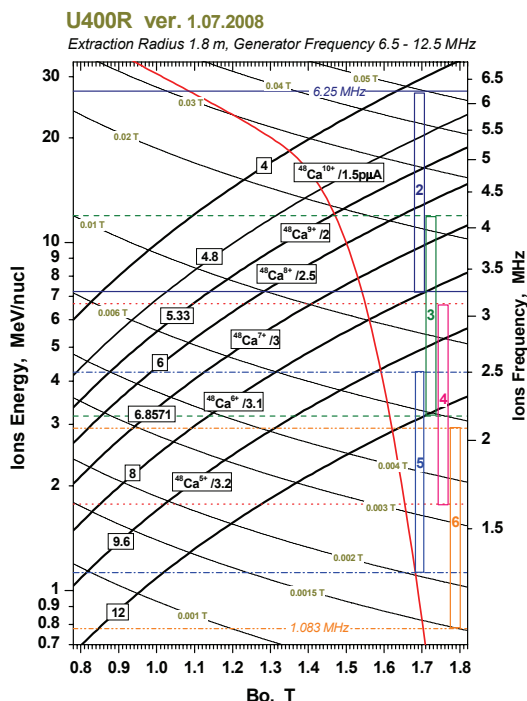


Figure 3: Operating chart of the U400R cyclotron.

Table 2: Parameters of U400 and U400R Typical Ion Beams

U400		
Ion	Ion energy [MeV/u]	Output intensity
⁴ He ¹⁺	-	-
⁶ He ¹⁺	11	3·10 ⁷ pps
⁸ He ¹⁺	7.9	-
¹⁶ O ²⁺	5.7; 7.9	5 μA
¹⁸ O ³⁺	7.8; 10.5; 15.8	4.4 μA
⁴⁰ Ar ⁴⁺	3.8; 5.1 *	1.7 μA
⁴⁸ Ca ⁵⁺	3.7; 5.3 *	1.2 μA
⁴⁸ Ca ⁹⁺	8.9; 11; 17.7 *	1 μA
⁵⁰ Ti ⁵⁺	3.6; 5.1 *	0.4 μA
⁵⁸ Fe ⁶⁺	3.8; 5.4 *	0.7 μA
⁸⁴ Kr ⁸⁺	3.1; 4.4 *	0.3 μA
¹³⁶ Xe ¹⁴⁺	3.3; 4.6; 6.9 *	0.08 μA
U400R (expected)		
Ion	Ion energy [MeV/u]	Output intensity
⁴ He ¹⁺	6.4 ÷ 27	23 μA **
⁶ He ¹⁺	2.8 ÷ 14.4	10 ⁸ pps
⁸ He ¹⁺	1.6 ÷ 8	10 ⁵ pps
¹⁶ O ²⁺	1.6 ÷ 8	19.5 μA **
¹⁶ O ⁴⁺	6.4 ÷ 27	5.8 μA **
⁴⁰ Ar ⁴⁺	1 ÷ 5.1	10 μA
⁴⁸ Ca ⁶⁺	1.6 ÷ 8	2.5 μA
⁴⁸ Ca ⁷⁺	2.1 ÷ 11	2.1 μA
⁵⁰ Ti ¹⁰⁺	4.1 ÷ 21	1 μA
⁵⁸ Fe ⁷⁺	1.2 ÷ 7.5	1 μA
⁸⁴ Kr ⁷⁺	0.8 ÷ 3.5	1.4 μA
¹³² Xe ¹¹⁺	0.8 ÷ 3.5	0.9 μA

Circular Accelerators

The working diagram of the U400R cyclotron with ⁴⁸Ca beams intensities is presented in Fig. 3.

Parameters of U400 and U400R typical ion beams presented in Table 2.

Scheme of the ion beam extraction from U400R by stripping foils in two opposite directions A and B and by deflector in direction A are presented in Fig. 4.

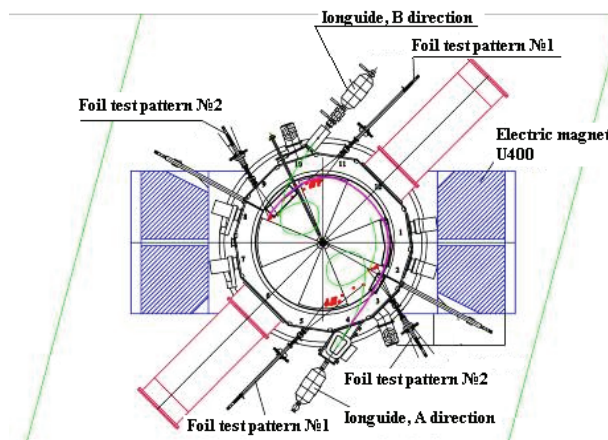


Figure 4. Scheme of the beam extraction in two selected directions.

U400M CYCLOTRON

The 4 sector and 4 dees cyclotron U400M has been in operation since 1991 [3]. The cyclotron was originally intended for ion beam acceleration with A/z = 2÷5 at energies of 20÷100 MeV/n. The ion beams is extracted from cyclotron by stripping with stripping ratio Z₂/Z₁= 1.4÷1.8 and why energy range of extracted beams from 30 up to 50 MeV/n. The light ion beams from U400M are used for radioactive beams production. The intensity of light ion beams as ⁷Li or ¹¹B on the targets 3÷5·10¹³ pps. Tritium ions are accelerated as molecular (DT)¹⁺ with intensity 6·10¹⁰ pps and energy 18 MeV/n. The generation of (DT)¹⁺ ion is in special RF ion source. In 2008 the U400M possibilities have beam intended by addition ion beams with A/z =5÷10 at energies of 4.5÷20 MeV/n. This low energy ion as ⁴⁸Ca will be used too for synthesis and study of new elements.

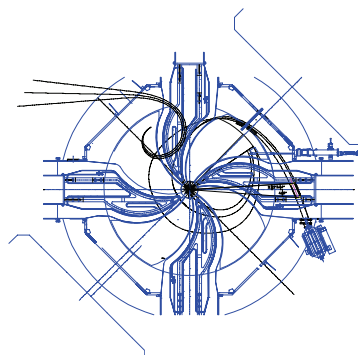


Figure 5: Scheme of beam extraction from U400M.

Scheme of low and high energy beam extraction from U400M in two opposite direction are presented in Fig. 5.

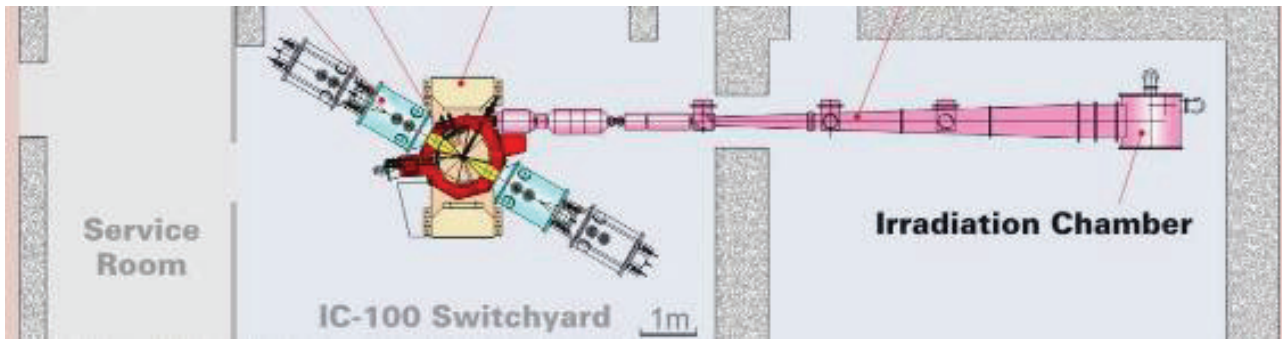


Figure 6: Plan of a specialized complex for applied research based on the IC100 cyclic implanter.

U200 CYCLOTRON

The 2 m, 4 sectors and 2 dees U200 cyclotron has been in operation more than 40 years. At present accelerator is used for isotope production with 36 MeV ^4He beam.

In the next year we are going to install ECR ion source at U200.

IC-100

The 1 m pole diameter, 4 sector, 2 dees cyclotron equipment with SC ECR ion source. The cyclotron was designed to accelerate ions with a fixed energy 1.2 MeV/n. The range of accelerated ions goes from C up W. The IC-100 is used for polymer film irradiation (200x600 mm) and solid matter investigation. The $^{132}\text{Xe}^{23+}$ beam intensity, for example, is 0.2 μA at the target. Layout of IC-100 is presented in Fig. 6.

The DRIBs (Dubna RIB) project has been running at the Lab since 2002 (Fig. 1) [3]. The primary ion beams (^7Li or ^{11}B) from U400M are used for production nuclides as ^6He , ^8He at the target (Be or C). The produced radionuclides are transported from the hot catcher into an ECR (2.45 GHz) ion source where they are ionized. Then, the radioactive ions are extracted, separated and transported through a 120 m transport line into the U400, where they are accelerated. At present, $^6\text{He}^{2+}$ ions at energy of 11 MeV/n are available for physical experiments. DRIBs possibilities will be extended after carrying out U400→U400R modernization (see Table 2).

DUBNA ECR (DECRIS) ION SOURCE AND INJECTION SYSTEMS [4]

For the last 15 years 6 units room temperature 14 GHz ECR sources have been developed in the Lab. Two SC ECR (DECRIS-SC) have been developed too for IC-100 and U400M cyclotrons. Three permanent magnet 2.45 GHz ECR have been developed in Lab for generation single-charge stable and radioactive ions. For increasing beam capture efficiency from the ECR source by the accelerator, axial injection systems have been developed too. For example, the scheme of U400R axial injection channel is shown in Fig. 7. The results of the capture

efficiency for $^{40}\text{Ar}^{4+}$ are presented in Fig. 8. The reasons of the decreasing efficiency in the regime with bunchers can be the influence of space-charge effects. In the future, we are planning to increase the injection voltage from 13÷20 up to 50÷100 kV what means shift of the space charge limits for factor 6÷20.

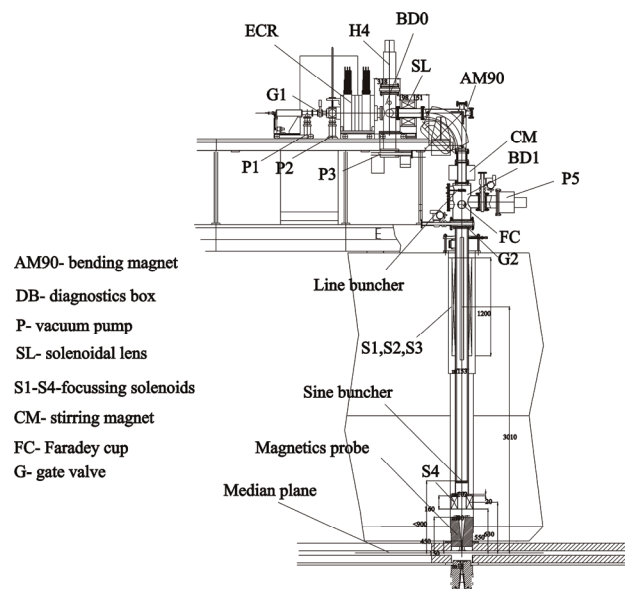


Figure 7: Scheme of U400R axial injection system.

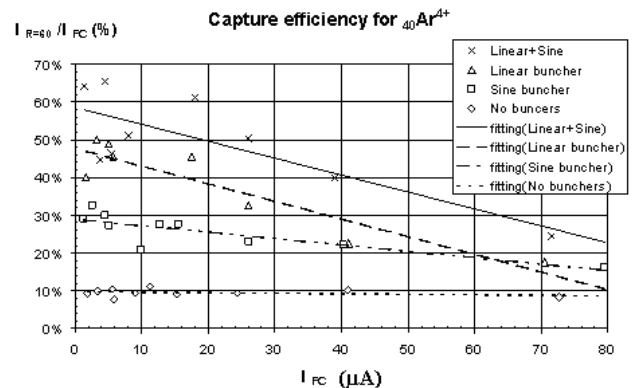


Figure 8: The efficiency of capture versus injecting beam current and bunchers.

NEW FLNR ACCELERATOR

In order to improve efficiency of the experiments for the next 7 years it is necessary to obtain the accelerated ion beams with following parameters.

Energy	4÷8 MeV/n
Masses	10÷100
Intensity (up to 48Ca)	10 μ A
Beam emittance	less than 30 π mm·mrad
Efficiency of beam transfer	>50%
ECR frequency	18÷28 GHz

Now two variants are under consideration here: SC linac or specialized cyclotron.

Variant 1 – SC LINAC

The proposed superconducting linac structure includes RFQ and 26 QuarterWave Resonators (QWR). The total length is close to 46 m, total power consumption 350 kW, average accelerating gradient (along all QWR) near 1.5 MV/m.

Variant 2 – DC200 high-current Cyclotron [7]

Main parameters and goals DC200 cyclotron are presented in Table 3.

Table 3: Main Parameters and goals DC200 Cyclotron

Parameter DC200	Goals
1. High injecting beam energy (up to 100 kV)	Shift of space charge limits for factor 30
2. High gap in the center	Space for long spiral inflector
3. Low magnetic field	High starting radius. High turns separation. Low deflector voltage
4. High acceleration rate	High turns separation.
5. Flat-top system	High capture. Single turn extraction. Beam quality.

Main parameters of the DC200 cyclotron are presented in Table 4.

Table 4: Main Parameters of the DC200

Injecting beam potential	Up to 100 kV
A/Z range	4÷7
Magnetic field level	0.65÷1.15 T
K factor	200
Gap between plugs	250 mm
Valley/hill gap	350/240 mm/mm
Magnet weight	470 t
Magnet power	170 kW
Dee voltage	2x130 kV
RF power consumption	2x30 kW
Flat-top dee voltage	2x14 kV
Beam turns separation	10 mm
Radial beam bunch size	3 mm
Efficiency of beam transferring	60%
Total accelerating potential	up to ~ 40 MV

The DC200 plan view presented in Fig. 9.

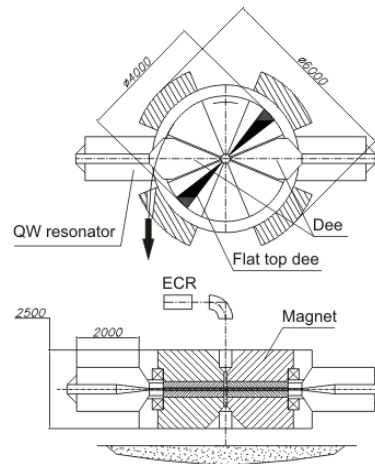


Figure 9: Scheme of the DC200.

The working diagram of DC200 presented in Fig. 10.

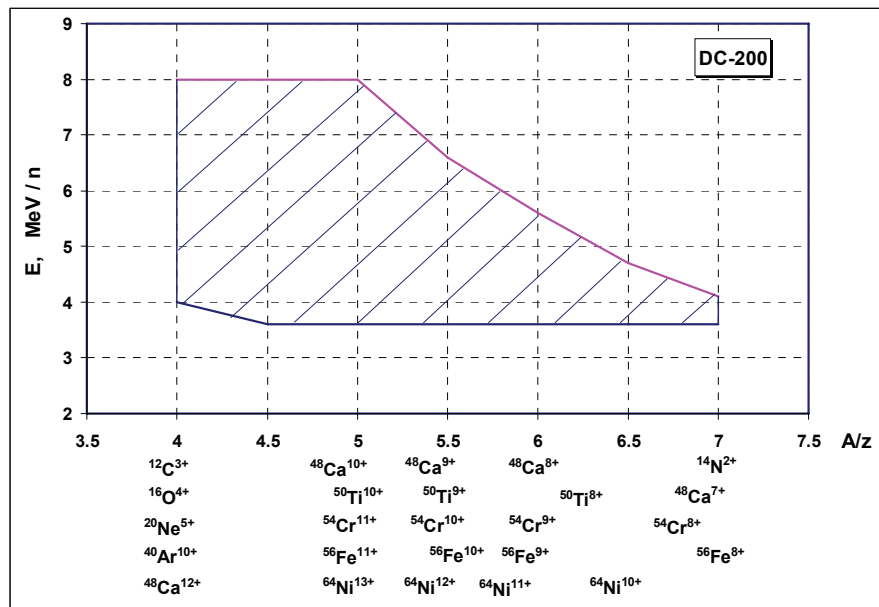


Figure 10: Cyclotron DC200 working diagram.

REFERENCES

- [1] Gulbekian G. and CYCLOTRONS Group, “Status of the FLNR JINR Heavy Ion Cyclotrons” in Proc. of 14th Int. Conf. On Cyclotrons and Their Applications, Cape Town, South Africa, pp. 95-98, 1995.
- [2] Yu. Ts. Oganessian, G.G. Gulbekyan, B.N. Gikal, I.V. Kalagin et al., “Status report of the U400 cyclotron at the FLNR JINR”, in Proc. of APAC2004, Gyeongju, Korea, pp.52-54, 2004.
- [3] B.N. Gikal, S.L. Bogomolov, S.N. Dmitriev et al., “Dubna cyclotrons- status and plans”, in Proc. of Cyclotron04 Int. Conf., Tokyo, Japan, 2004. accelconf.web.cern.ch/accelconf/c04/data/CYC2004_papers/20A1.pdf.
- [4] Efremov A.A., Bekhterev V.V., Bogomolov S.L. et al., “Status of the ion source DECRIS-SC”, Review of Scientific Instruments, V. 77, P.235–239, No.03A320, 2006.
- [5] B.N.Gikal et al., “U200 cyclotron operating experience and upgrade”, JINR preprint, 9-83-311, Dubna, 1983.
- [6] B.N.Gikal, S.N.Dmitriev et al., “IC-100 Accelerator Complex for Scientific and Applied Research”, ISSN 1547-4771, Physics of Particles and Nuclei Letters, Vol. 5, No. 1, pp. 33–48. © Pleiades Publishing, Ltd., 2007.
- [7] N.Yu. Kazarinov. “Non-linear distortion of multi-component heavy ion beam emittance caused by space charge fields”, Proceedings of the 14th International Conference on Ion Sources, Dubna, Russia, 2003, Review of Scientific Instruments, 75, 1665, (2004).

RCNP CYCLOTRON FACILITY

K. Hatanaka*, M. Fukuda, T. Yorita, T. Saito, H. Tamura, M. Kibayashi, S. Morinobu, K. Nagayama
 RCNP, Osaka University, 10-1 Mihogaoka, Ibaraki, Osaka 567-0047, Japan

Abstract

The Research Center for Nuclear Physics (RCNP) cyclotron cascade system has been operated to provide high quality beams for various experiments. In order to increase the physics opportunities, the Azimuthally Varying Field (AVF) cyclotron facility was upgraded recently. A flat-topping system and an 18 GHz superconducting Electron Cyclotron Resonance (ECR) ion source were introduced to improve the beam's quality and intensity. A new beam line was installed to diagnose the characteristics of the beam to be injected into the ring cyclotron and to bypass the ring cyclotron and directly transport low energy beams from the AVF cyclotron to experimental halls. A separator is equipped to provide RI beams produced by fusion reactions at low energy and by projectile fragmentations at high energy. Development has continued to realize the designed performance of these systems.

INTRODUCTION

The Research Center for Nuclear Physics (RCNP) is a national users facility founded in 1971 and is the major research institute for nuclear physics in Japan. RCNP, as a national laboratory, is open to all users in Japan and from abroad. The cyclotron facility is its major facility and consists of an accelerator cascade and sophisticated experimental apparatuses. Research programs cover both pure science and applications. Demands for industrial applications have been growing more and more.

A schematic layout of the RCNP cyclotron facility is shown in Fig. 1. The accelerator cascade consists of an injector Azimuthally Varying Field (AVF) cyclotron ($K=140$) and a ring cyclotron ($K=400$). It provides ultra-high-quality beams and moderately high-intensity beams for a wide range of research in nuclear physics, fundamental physics, applications, and interdisciplinary fields. The maximum energy of protons and heavy ions are 400 and 100 MeV/u, respectively. Sophisticated experimental apparatuses are used like a pair spectrometer, a neutron time-of-flight facility with a 100-m-long tunnel, a radioactive nuclei separator, a super-thermal ultra cold neutron (UCN) source, a white neutron source, and a RI production system for nuclear chemistry. Such ultra-high-resolution measurements as $\Delta E/E=5 \times 10^{-5}$ are routinely performed with the Grand-Raiden spectrometer by utilizing the dispersion matching technique. The UCN density was observed to be 10 UCN/cc at the experimental port at a beam power of 400 W. The white neutron spectrum was calibrated and the flux was estimated to be 70% of that obtained at Los Alamos Neutron Science Center (LANSCE) in the USA.

Neutrons are used for the radiation effect studies on integrated circuits and so on.

User's demands on the beam characteristics are expanding rapidly: ultra-high resolution, high intensity, a variety of heavy ions, and so on. Since there are no slits or collimators in the beam lines after the ring cyclotron, the beam quality on targets is determined by the characteristics of the beam from the AVF cyclotron. The injector upgrade program for these items is in progress [1-3]:

1. a new acceleration system with a flat-top system,
2. an 18 GHz Electron Cyclotron Resonance (ECR) ion source to produce highly charged heavy ions,
3. a polarized Li^{3+} ion source,
4. a beam line to diagnose the beam characteristics from the AVF cyclotron and to deliver low energy beams to the experimental halls,
5. renewal of power supplies of 13 trim coils and magnetic channels,
6. renewal of 100-kW power supplies for the analyzing magnet and the switching magnet
7. renewal of the accelerator control system by using a PC-based distributed system with a network.

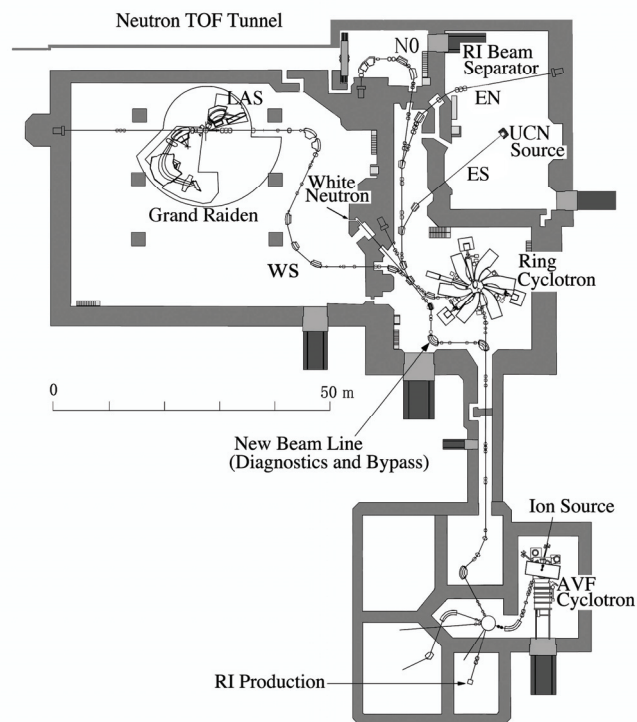


Figure 1: Layout of the RCNP cyclotron facility.

*hatanaka@rcnp.osaka-u.ac.jp

ECR ION SOURCE

An 18 GHz superconducting ECR ion source was installed in order to increase beam currents and to extend the variety of ions, especially for highly-charged heavy ions, which can be accelerated by RCNP cyclotrons. The production development of several ions beams and their acceleration by the AVF cyclotron has been performed since 2006.

Fig. 2 shows a cross sectional view of the source. The source was designed based on RAMSES [4] at RIKEN, but the inner diameter of the hexapole magnet and of the plasma chamber were extended to 90 and 80 mm, respectively, due to the experience with their development. The mirror magnetic field is produced with four liquid-helium-free superconducting coils, which are cooled by two Gifford-McMahon refrigerators and which are installed in a cryostat chamber covered by iron magnetic shields. Upstream coil 1 (U1) and downstream coil (D) are of the same size and are excited in series by using a common power supply. Central coil (C) and upstream coil 2 (U2) are excited by using independent power supplies, and the mirror magnetic field distribution is controlled quite flexibly. Typical simulated (by TOSCA) magnetic field inductions created on the axis by each coil are shown in Fig. 3. Typical operating currents are 36.3 A, 36.9 A, and 60.5 A for the U1+D, C, and U2 coils, respectively. The maximum current for each coil is 66 A.

The permanent magnet hexapole is of the Halbach type, with 24 pieces of NEOMAX-44H material. The radial field strength is 1.0 T on the stainless-steel plasma chamber's inner diameter. The diameter and the length of the plasma chamber are 80 mm and 380 mm, respectively.

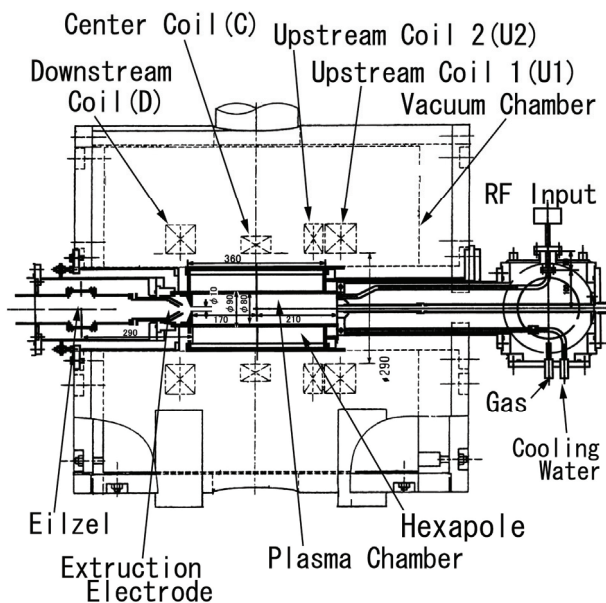


Figure 2: Cross-sectional view of a liquid-helium free 18 GHz superconducting ECR ion source.

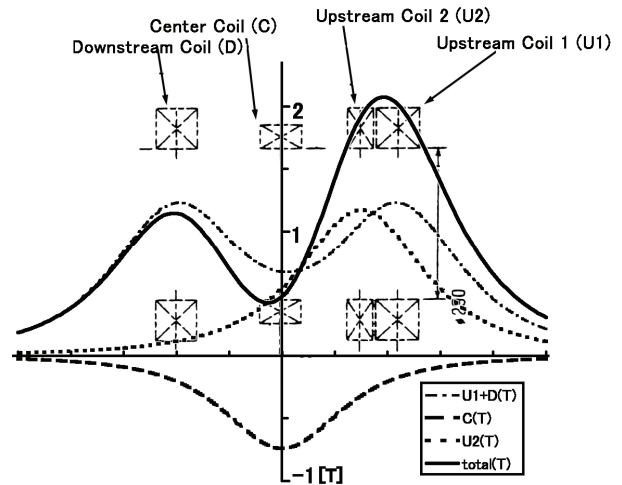


Figure 3: Simulated magnetic field distribution.

In order to improve the performances of the source, a liner was inserted. Tests have been performed with two different thicknesses and materials (1 and 3.5 mm; pure aluminium and aluminium coated with Al_2O_3). In the latter case, it was difficult to get stable operation due to discharge or degassing from the liner.

A bias probe was installed on the beam axis on the injection side. The maximum applicable voltage is -500 V relative to the plasma chamber, and the probe position is variable between 120 and 220 mm from the center of the C coil. The optimum position is located at 170-190 mm, which corresponds to the position of the maximum mirror field. The extraction system is composed of two electrodes and can be moved along the beam axis. An einzel lens is placed downstream of the extraction electrode.

The ion beams extracted from the source are analyzed by using a dipole magnet (AM) and are measured in a Faraday cup (FC) placed at the image focal point of the analyzing magnet. Fig. 4 shows the typical charge-state distribution of ^{86}Kr ions obtained by using oxygen as a gas mixing. Table 1 summarizes the performance of the source. $^{86}\text{Kr}^{21+, 23+}$ ions were accelerated for the first time by using the AVF cyclotron and were delivered to user's experiments.

In order to produce metallic boron-ions, a test by using the MIVOC (Metal Ion from Volatile Compounds) method [5] was performed using o-carborane ($\text{C}_2\text{B}_{10}\text{H}_{12}$). Its vapor pressure was around 1-2 Torr at the room temperature. The stable flow of the vapor from the o-carborane powder to the plasma chamber enabled us to produce a stable boron-ion beam. The o-carborane was put in a glass vessel directly connected to the plasma chamber via a buffer tank. A helium support gas was used as the mixing gas. Different support gases were tested to optimize the $^{11}\text{B}^{5+}$ intensity. With oxygen, we were not able to produce $^{11}\text{B}^{5+}$; with hydrogen, the current was divided by three with respect to the current for helium.

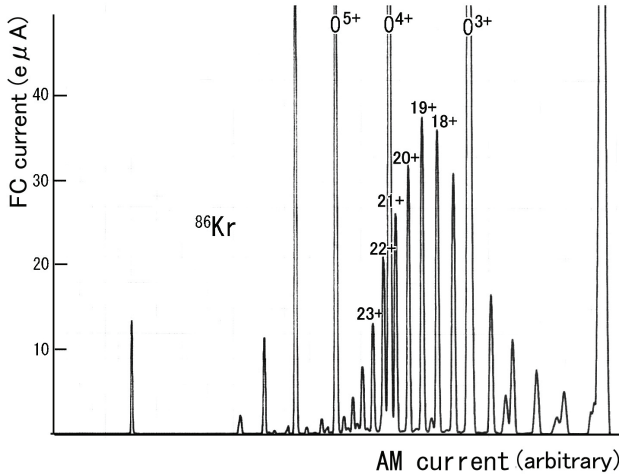


Figure 4: Charge state distribution of ^{86}Kr ions with a 700-W RF power and oxygen mixing.

Table 1: Ion Currents (μA) Obtained by the RCNP 18 GHz ECR Ion Source

	RF						RF
	2+	3+	4+	5+	6+	7+	(W)
^{11}B	1.3	4.1	9.3	8.2			400
^{12}C			410	115			500
^{15}N		167	477	725	117		500
^{16}O	10	178		779	517	27	500
^{18}O		88	235	475	673	39	500
	11+	12+	13+	14+			
^{40}Ar	188	70	17	3			500
	20+	21+	22+	23+	24+	25+	
^{86}Kr	32	26	21	13	8.1	4.5	600
	28+	29+	30+	31+	32+	33+	
^{136}Xe	11.3	10.6	8.8	6.2	4.2	2.3	770

FLAT-TOPPING ACCELERATION SYSTEM

A schematic layout of the main and the flat-top resonators of the AVF cyclotron is shown in Fig. 5. An additional flat-top cavity of a coaxial movable-short type is capacitively coupled to the main resonator on the opposite side of the main power feeder for fundamental-voltage production. The flat-top cavity has a length of 700 mm and an outer diameter of 170 mm. A full stroke of the shorting plate of the flat-top cavity is 100 mm. The coupler electrode and the inner conductor of the flat-top cavity are shown in Fig. 5. The gap between the coupler electrode and the inner tube of the main cavity can be changed from 0 to 155 mm. Fine adjustment for 50 Ω impedance matching is accomplished by using a tuner with a full stroke of 40 mm.

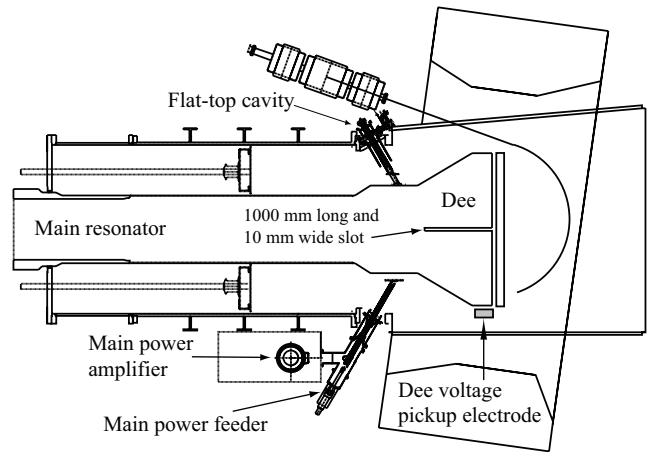


Figure 5: Layout of the RCNP AVF Cyclotron.

A flat-topped dee voltage waveform can be generated by superimposing a harmonic voltage on the fundamental one [6]. The main parameters of the RF system are listed in Table 2. The RF power from a 10-kW transistor amplifier is transmitted to the flat-top resonator through a coaxial waveguide (WX39-D). The input impedance is adjustable by changing the capacitance of the feeder capacitor between 5 and 250 pF. Impedance matching of the 50- Ω transmission line from the flat-top cavity to the main resonator is optimized by adjusting the positions of the coupler, the shorting plate, the tuner, and the feeder capacitor. Impedance matching can be achieved over a wide range of harmonic frequencies from 50 to 80 MHz. Hence, the fifth, seventh, and ninth harmonic modes are available for production of the flat-topped voltage waveform. Such higher order harmonic modes have an advantage of saving power for the harmonic voltage production, because the n -th harmonic voltage required for flat-top waveform production is $1/n^2$ of the fundamental one [7].

A parasitic resonance mode is known to exist originally around 76 MHz. This resonance is generated in the transversal direction of the dee electrode axis. There is some possibility of the parasitic resonance's interference with the fifth harmonic voltage production for the flat-top acceleration of higher energy protons. In order to shift the transversal resonance frequency to around 55 MHz, we replaced the original dee electrode with a new one with a 1000-mm-long and 10-mm-wide slot along the electrode axis, as shown in Fig. 5.

New dee-voltage pickup electrodes were installed near the acceleration gap of the dee electrode. The four pickup electrodes were mounted on a copper block facing the side of the dee electrode. Two pickup electrodes were designed to have a pickup signal level ratio of $1/10^4$ and are used for fundamental voltage regulation and RF reference signal supply to users and control systems of a beam buncher and a beam chopper. The pickup signal with a ratio of $1/10^5$ is used for monitoring the flat-top voltage waveform at the console in the operating room.

Other pickup electrodes provide a harmonic signal for the low-level control of the flat-top resonator.

Table 2: Main Parameters of the RF System

Fundamental frequency	6 - 18 MHz
Maximum acceleration voltage	60 kV peak
Flat-top: harmonic number	5, 7, 9
Flat-top: harmonic frequency	54 - 80 MHz
Flat-top: maximum harmonic voltage	5 kV peak
Flat-top maximum Q-value of resonator	2000
Flat-top: maximum RF power	10 kW
Flat-top: maximum voltage of resonator	80 kV peak
Flat-top: maximum current density	50 A/cm

The performance of the flat-top acceleration system was investigated in power tests using the following fifth harmonic frequencies: 77.084 MHz for 53 MeV protons (to be accelerated up to 300 MeV by using the ring cyclotron), 50.582 MHz for 44 MeV deuterons (200 MeV), 58.250 MHz for 88 MeV $^3\text{He}^{2+}$ (420 MeV), and 50.720 MHz for 87 MeV $^4\text{He}^{2+}$ (400 MeV). We have also succeeded in generating the seventh and the ninth harmonic voltages at 71.008 MHz for 87 MeV $^4\text{He}^{2+}$ (400 MeV) and 60.750 MHz for 19 MeV deuterons (80 MeV), respectively. An example of a flat-top voltage waveform observed at 77.084 MHz is shown in Fig. 6.

Development of a flat-top accelerated beam is now in progress. In order to obtain a high-quality beam with an energy spread of less than $\Delta E/E = 5 \times 10^{-4}$, a beam phase width has to be defined within several RF degrees by using two pairs of phase defining slits placed in the center region of the AVF cyclotron, which causes a sharp decrease in the beam intensity. In the case of fundamental acceleration, the beam phase width must be reduced to 4 RF degrees or less. The beam phase acceptance can be increased to more than 10 RF degrees by the flat-top acceleration within the limits of the phase acceptance of the ring cyclotron. In both cases, the beam buncher installed in the injection beam line plays a significant role in increasing the beam intensity. The flat-top acceleration and single-turn extraction from the AVF cyclotron are indispensable for producing a high-quality beam from the ring cyclotron.

The 300 MeV proton beam, accelerated using the injection beam of flat-top-accelerated 53 MeV protons, was transferred to a gold target in an achromatic mode, and the energies of elastically-scattered particles were analyzed with the Grand-Raiden spectrometer for a beam-quality evaluation. The energy resolution of the elastic peak was estimated to be $\Delta E/E = 1 \times 10^{-4}$. The beam intensity of the high quality proton beam was remarkably increased by a factor of four.

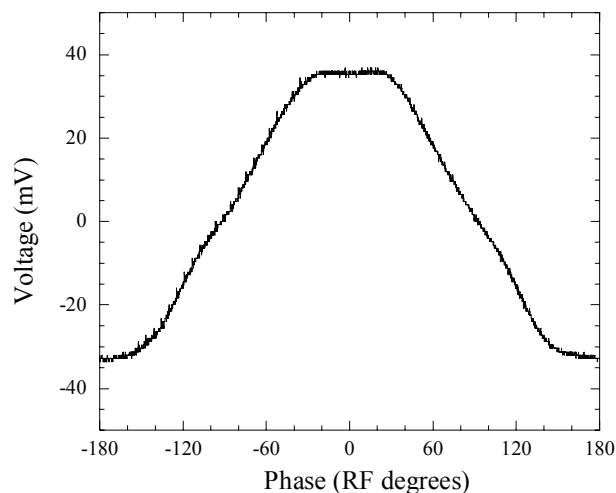


Figure 6: Example of the flat-top voltage waveform observed at 77.084 MHz with the dee voltage pickup electrode.

DIAGNOSTIC AND BYPATH BEAM LINE

A new beam line was installed to bypass the ring cyclotron and to directly deliver low-energy, high-intensity beams from the AVF cyclotron to the experimental halls, where sophisticated apparatuses are available. It is expected to increase research opportunities at the cyclotron facility. The schematic layout of the beam line is shown in Fig. 7. In addition, the part from the “source point” in the figure to the “focus point” serves to diagnose the quality of the beam injected into the ring cyclotron. As mentioned above, the quality of the beam on target from the ring cyclotron is primarily determined by the characteristics of the injected beam from the AVF cyclotron. However, there were no available diagnostic devices to precisely measure the emittance and energy

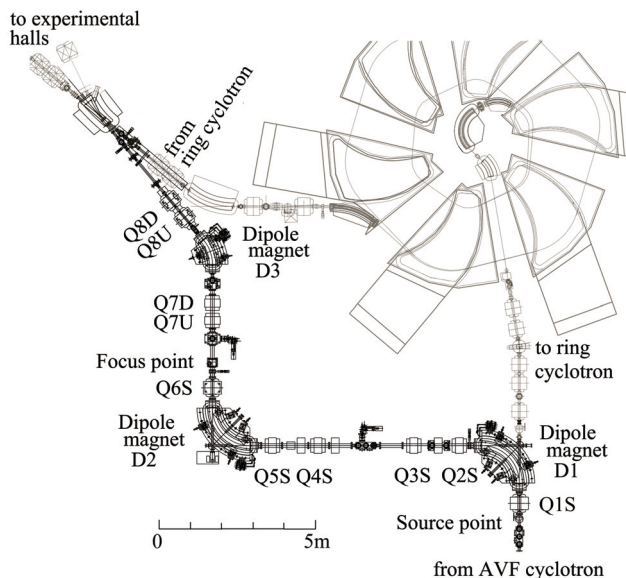


Figure 7: Schematic layout of the beam line to analyze the quality of the beam from the AVF cyclotron and to directly deliver low-energy, high-intensity beams to the experimental halls of the ring cyclotron.

spread before injection. Two 90-degree dipole magnets have a bending radius of 1200 mm. They have round pole faces to reduce the ion optical second-order aberrations. The momentum dispersion of the analyzing section is designed to be 12.6 m. The parameters of the AVF cyclotron and the transfer beam line to the ring cyclotron can be optimized by referring to the measured beam characteristics.

SUMMARY

The upgrade of the RCNP cyclotron cascade has been successfully started and is being continued. The beam quality and the intensity of 300 MeV protons have been improved by using flat-top acceleration in the AVF cyclotron. Developments are being performed to apply the system to other beams. An 18 GHz superconducting ECR ion source has been commissioned to increase the beam intensity of highly-charged heavy ions; a 7.5 MeV/u $^{86}\text{Kr}^{23+}$ beam was delivered to experiments. A new beam line has been installed to diagnose the beam characteristics from the AVF cyclotron and to help match it to the acceptance of the ring cyclotron. It also makes 10÷400 MeV protons and 1÷100 MeV/u heavy ions available for a variety of research in nuclear physics, fundamental physics, and interdisciplinary studies.

REFERENCES

- [1] K. Hatanaka, T. Itahashi, M. Itoh, M. Kibayashi, S. Morinobu, K. Nagayama, S. Ninomiya, T. Saito, Y. Sakemi, K. Sato, A. Tamii, H. Tamura, and M. Uraki, Proceedings of the 17th International Conference on Cyclotrons and their Applications, Tokyo, Japan, pp. 115-117 (2004).
- [2] M. Fukuda, H. Tamura, T. Saito, T. Yorita, and K. Hatanaka, Proceedings of the 18th International Conference on Cyclotrons and their Applications, Giardini Naxos, Italy, pp. 470-472 (2007).
- [3] K. Hatanaka, M. Fukuda, M. Kibayashi, S. Morinobu, K. Nagayama, H. Okamura, T. Saito, A. Tamii, H. Tamura, and T. Yorita, Proceedings of the 18th International Conference on Cyclotrons and their Applications, Giardini Naxos, Italy, pp. 125-127 (2007).
- [4] T. Nakagawa, T. Aihara, Y. Higurashi, M. Kidera, M. Kase, Y. Yano, I. Arai, H. Arai, M. Imanaka, S. M. Lee, G. Arzumanyan, and G. Shirkov, Rev. of Sci. Instru. 75, 1394 (2004).
- [5] H. Koivisto, E. Kolehmainen, R. Seppala, J. Arje, and M. Numia, Nucl. Instr. Meth. Phys. Res. B117, 186 (1996).
- [6] J. L. Conradie, A. H. Botha, J.J.Kritzinger, R. E. F. Fenemore, and M. J. Van Niekerk, Proceedings of the 14th International Conference on Cyclotrons and their Applications, Cape Town, South Africa, pp. 249-251 (1995).
- [7] M. Fukuda, S. Kurashima, S. Okumura, N. Miyawaki, T. Agematsu, Y. Nakamura, T. Nara, I. Ishibori, K. Yoshida, W. Yokota, K. Arakawa, Y. Kumada, Y. Fukumoto, and K. Saito, Rev. Sci. Instru., 74, 2293 (2003).

RF SYSTEM FOR HEAVY ION CYCLOTRONS AT RIKEN RIBF

N. Sakamoto*, M. Fujimaki, A. Goto, M. Kase, O. Kamigaito, R. Koyama, K. Suda, K. Yamada, and S. Yokouchi, Nishina Center, RIKEN, Wako, Saitama, 351-0198 Japan

Abstract

At RIKEN RIB-factory(RIBF) an accelerator complex as an energy booster which consists of superconducting ring cyclotron (SRC), intermediate-stage ring cyclotron (IRC) and fixed-frequency ring cyclotron (FRC) provides very heavy ion beams like uranium with an energy of 345 MeV/u [1]. The total beam power obtained up to now at the SRC is as high as 3 kW in the case of ^{48}Ca with an intensity of 170 pA. Recently we have succeeded in achieving stable and reliable operation of rf system for new cyclotrons. In this paper the present performance of the rf system and a recent development is reported.

OVERVIEW OF THE CYCLOTRON COMPLEX AS AN ENERGY BOOSTER

Acceleration Scheme of the Accelerator Complex

Three cyclotrons have been designed and built to boost the energy of the beam accelerated by RIKEN Ring Cyclotron (RRC) [2] for RI-Beam production. There we have three acceleration modes.

1. *very heavy ion ($A > 40$) mode*
RILAC \Rightarrow RRC \Rightarrow IRC \Rightarrow SRC
2. *high energy (uranium 345 MeV/u) mode*
RILAC \Rightarrow RRC \Rightarrow FRC \Rightarrow IRC \Rightarrow SRC
3. *light heavy ion ($A \leq 40$) mode*
AVF \Rightarrow RRC \Rightarrow SRC

The conceptual design of the cavities was described in ref. [3] and their construction and commissioning were reported in ref. [4] and [5]. In the end of 2006, ^{27}Al was accelerated in the mode 1 with an energy of 345 MeV/u as the first beam from the SRC. After that ^{238}U acceleration test in the mode 2 was performed extensively and the beam current of 0.4 pA was provided to a new-isotope search experiment. A high intensity beam of ^{48}Ca was accelerated in the mode 1 with a beam power of 3 kW. In the mode 3, ions whose mass number A is less than 40 can be accelerated with an energy of 440 MeV/u to the maximum. This year ^{14}N and polarized deuteron beams have been accelerated with an energy of 250 MeV/u in this mode. In Table 1 parameters for rf system for the new cyclotrons together with the RRC are summarized.

Table 1: Parameters of the RF System

item	RRC	FRC	IRC	SRC
freq. [MHz]	18~45	54.75	18~42	18~42
<i>mode 1</i>	$f_o^*(9^{**})$	-	$2f_o(7)$	$2f_o(6)$
<i>mode 2</i>	18.25(9)	54.75(12)	36.5(7)	36.5(6)
<i>mode 3</i>	$f_o(5)$	-	-	$f_o(5)$
# of cav.	2	2	2	4
# of gap	2	1	1	1
V_{gap} [kV]	300	500	650	650
$P_{\text{w.l.}}$ [kW]	150	100	150	150
FT cav.	none	1	1	1
Harmonics	-	3	3 or 4	3 or 4
$P_{\text{w.l.}}$ [kW]	-	20	20	60

*: f_o is a frequency of master oscillator.

**:(#) denotes a harmonic number $H=f_{\text{rf}}/f_{\text{beam revolution}}$

Requirements

Heavy ion cyclotrons have not only a wide acceptance of charge to mass ratio but also a wide energy ranges according to the purposes of physics experiments. The frequency range for new cyclotrons, SRC and IRC, are $18 \div 42$ MHz to meet that of the RRC. The FRC has been designed with a fixed frequency of 54.75 MHz to aim at an uranium acceleration with an energy of 345 MeV/u, while in the mode 1 the maximum energy of the uranium is 150 MeV/u.

In the acceleration modes 1 and 2, charge conversions getting a higher charge state are necessary to accept the beam due to the limitation of the magnetic rigidity of the succeeding cyclotrons. The conversion is made by using charge stripper (carbon foil) at the sacrifice of longitudinal emittance growth. Therefore the flattopping systems in the cyclotrons are essential. The rf third harmonic make the longitudinal acceptance as large as $\pm 16^\circ$.

In the operational aspect, stability of the acceleration field is a key issue and trouble-free is desirable. With stable rf system it is possible to make fine tuning of the accelerator cascades and to maintain the beam quality and the intensity during a long term physics experiment. To obtain much more reliability, improvement of the rf system has been made by fixing the problems turned out since the commissioning as described below.

CHARACTERISTICS OF THE RF SYSTEM

Here, the rf system for the SRC(K2600) is mainly described because the rf systems for other cyclotrons are basically the same and because it is the most severe case from the point of view of tolerance for rf stability providing a

* nsakamot@ribf.riken.jp

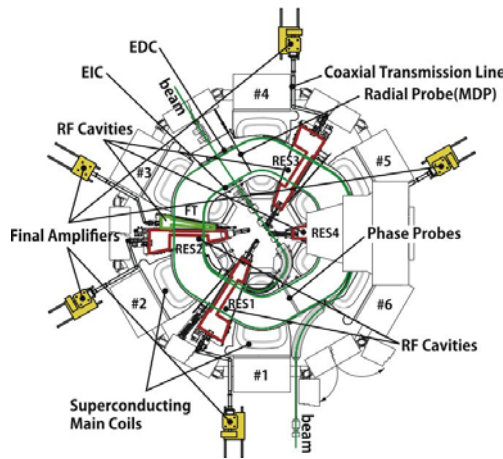


Figure 1: Schematic of the Superconducting Ring Cyclotron (SRC) as a final stage booster.

high beam current. The SRC consists of six superconducting separate-sector magnets with four acceleration cavities and one flattopping cavity (Fig. 1).

Acceleration Cavities

As shown in Table 1 the newly built cyclotrons have various harmonics (the ratio of the rf frequency to the beam revolution frequency); the single-gap structure is suitable. The resonant frequency of the cavities varies 18÷42 MHz by moving a pair of large capacitor-panels which rotate from 0° to 90° (see Fig. 2). The panel are supported by rotating shafts and are electrically connected to the cavity wall with copper sheets with a thickness of 0.2 mm. The tuner panels are adjusted symmetrically so as to make the leakage of rf field from beam aperture minimum. The maximum current density is 80 A/cm at the end part of the dee electrode of the machine center side. Sliding contacts which are attached between the cavity wall and the rotating shaft which supports the tuner panels have the maximum current density of 60 A/cm. The contacts are made of silver plated BeCu and their finger tips are made of sil-

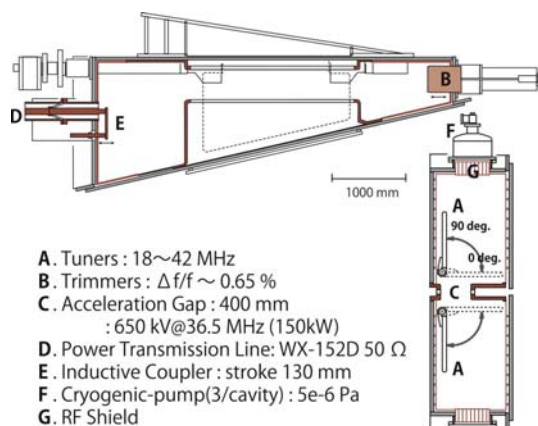


Figure 2: Schematic of the acceleration cavity for the SRC.

Circular Accelerators

ver blended with carbon. The chassis of the cavity consists of two parts. One is stainless steel wall with a thickness of 40 mm to prevent collapsing under the pressure of the atmosphere and one is a copper sheet with a thickness of 4 mm inside the stainless steel chassis on which the water pipes are soldered in back side. The total amount of the cooling water is 300 l/min per cavity supposing the wall losses by rf currents amount to 150 kW. Without rf power the vacuum of the cavity reaches 1×10^{-6} Pa with three cryogenic pumps (10000 l/min via N₂) and with rf input of 100 kW the vacuum pressure is nominally 5×10^{-6} Pa which has been improved by fixing the heating problem of the rf shield (G in Fig. 2) attached in front of cryogenic-pump.

Flattopping Cavity

One flattopping cavity provides a harmonic field with a decelerating phase to make the longitudinal acceptance larger. The cavity is a single-gap resonator with a set of shorting plate to tune the resonant frequency. The frequency range is set from 72 MHz to 132 MHz so as to make the cavity compact. The harmonic of flattopping is 3 for the fundamental frequency range of 24÷42 while the harmonic 4 is adopted for lower frequencies. The maximum power dissipation is 60 kW. Since cutoff frequency of the beam aperture is 75 MHz, the set of shorting plates must be placed at the electrical symmetry positions, otherwise the beam probes (MDP and PP) and/or high voltage electrostatic channels (EIC, EDC) got damaged by rf heat loads.



Figure 3: Photo of installing the accelerating cavity(RES2) and the flattopping(FT) cavity to the valley area between the sector #2 and #3.

Amplifiers

The main rf amplifier is based on a tetrode THALES (SIEMENS) RS2042SK coupled with a tetrode THALES (SIEMENS) RS2012CJ with a grounded-grid circuit. Four power-amplifiers are installed and then the four acceleration cavities were excited by individual amplifiers driven by the same master oscillator. For the flattopping cavity, a newly developed amplifier which is based on a THALES (SIEMENS) RS2058CJ tetrode is adopted and excited using a tripled rf signal from a frequency multiplier. The

transmission coaxial lines between the amplifier and the cavity is about 15 m. Each lines was equipped with a sliding mechanism with a stroke of 1 m which makes possible to avoid exciting parasitic modes of the transmission line and output circuit by changing the total length of the transmission line [5]. The stray field of the superconducting sector magnet at the position of power tube is as large as 100 G with an excitation current of 5000 A for $^{238}\text{U}@345$ MeV/u. The power tubes worked well without any problem.

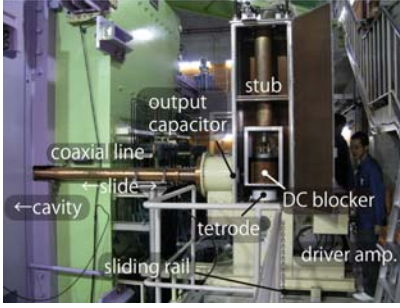


Figure 4: Photo of the main amplifier.

Tolerances

Here tolerances for rf amplitude and phase are considered. The rf system for the SRC consists of four acceleration cavities and one third-harmonic flattopping cavity. Then the energy gain per turn is denoted as

$$E_g = \sum_{i=1}^4 V_i \cdot \cos(\phi + \alpha_i) + V_{ft} \cdot \cos(3 \cdot \phi + \alpha_{ft})$$

Here ϕ is a beam phase, V_i, V_{ft} are gap voltages, α_i, α_{ft} are phase errors. According to the criterion in Ref.[7] by W. Joho, the error of the energy gain $\Delta E_g/E_g$ should be 10 times smaller than number of turns (i.e. $|\Delta E_g|/E_g < 1/10N$). In our case, the number of turns is about 350 on the average, and the amplitude of flattopping cavity is about 13% of the sum of the four acceleration cavities. The phase acceptance is set as $\pm 16^\circ$. Then tolerances for amplitude and phase were obtained as

$$\begin{aligned} \text{amplitudes : } & \quad |\Delta V_i|/V_i < 3/10000 \quad (i = 1..4), \\ & \quad |\Delta V_{ft}|/V_{ft} < 2/1000, \\ \text{phase : } & \quad |\Delta \alpha_i| < 0.03^\circ. \end{aligned}$$

Note that the cavities are excited by individual amplifiers as mentioned, though the deviation due to the instability of the power line (i.e. 50 Hz, 300 Hz) occurs coherently. The errors due to the thermal deformations and the mechanical vibrations of the cavities and due to the electrical noise have no correlation with each other cavity. Those random errors are averaged over cavities and then are reduced by factor $\sqrt{4}$.

Circular Accelerators

RF CONTROL

Low Level System

A block diagram of the RF control system is shown in Fig. 5. The reference signal from master-oscillator is multiplied if needed and divided by a power divider to deliver for each cavity. The phase of the cavity is detected by auto-phase-lock utilizing super-heterodyne and locked by frequency modulator (VCO). The amplitude is stabilized by auto-gain-control. The forward power and the reflected power at the feeder-line were detected to tune the resonant frequency of the cavity by a servo system. The main parts of the electric circuit of the feedback control are packed in a temperature controlled aluminum box so that the circuit works stably under a constant temperature with the temperature coefficient of $\Delta T_{\text{box}}/\Delta T_{\text{room}} < 0.03$ and is electrically well shielded. The measured temperature at the room where the rf controls are installed is typically $24.5 \pm 0.5^\circ\text{C}$ for 24 h.

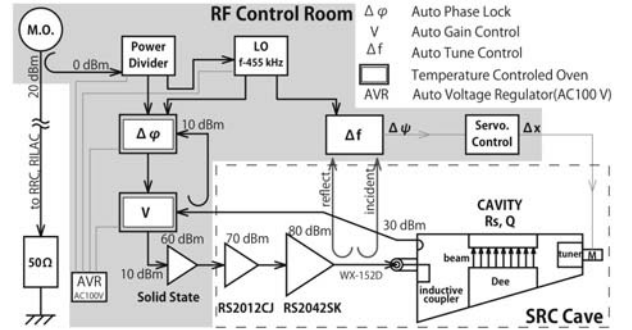


Figure 5: Block diagram of the rf system.

Monitoring System

Since the commissioning of the new facility, it has been pointed out that the monitoring of all rf of the cavities and the beam timing is crucial to handle the accelerator complex which employs 25 rf cavities. In the old facility the vector voltmeter (HP8508A) was used for a rf monitor. The HP8508A was discontinued more than 10 years ago and its accuracy and resolution were not enough. For the new system the amplitude and the phase resolutions of $\sim 0.01\%$ and $\sim 0.01^\circ$ are needed. A Lock-in amplifier is an instrument which extracts a component of a particular frequency of reference sinusoidal signal and calculates the amplitude and the phase, or I/Q component. The RF Lock-in Amplifier SR844 manufactured by Stanford Research Systems [8] has a bandwidth of $25 \text{ kHz} \div 200 \text{ MHz}$ which is suitable for our operational rf frequency range from $18 \div 165 \text{ MHz}$. A feasibility test was made [6] and we finally decided to introduce the instrument as a replacement of the vector voltmeter. The amplitude- and the phase-resolution of the SR844 are evaluated as better than $|\Delta V/V| \sim 10^{-4}$ and $|\Delta \phi| \sim 0.03^\circ$.

ACHIEVEMENTS

Ripples

Modulations of voltage and phase is caused mainly by a ripple of d.c. power supplies adopted to the amplifier. The ripples of power supplies (its main frequency component is 300 Hz) appear as an amplitude modulation and a phase modulation. The modulation of rf signal can be observed as a side-band spectrum by using a spectrum analyzer. For example, an amplitude modulation of $\pm 5 \times 10^{-4}$ and a phase modulation of $\pm 0.1^\circ$ correspond to the spectrum levels of -72 dBc and -61 dBc, respectively. Such a fast modulation can be removed/minimized by tuning a feed back loop (i.e. choosing a gain and a time constant) observing a strength of side-band spectrum. Finally the level better than -70 dBc at 300 Hz side-band has been obtained.

Long Term Stability

By using the newly introduced monitoring system, deviation of amplitudes and phases of the SRC cavities were measured. A block diagram of the measurement was shown in Fig. 6. During the measurement, rf parameters were not changed while the beams were provided to users. The beam was polarized deuteron with an energy of 250 MeV/u in the mode 3 and the frequency of the master oscillator was 13.7 MHz which was provided for an injector AVF and was doubled by frequency multiplier for the RRC and the SRC. The pickup signals of 27.4 MHz from the four acceleration cavities (RES1~4) were switched with an interval of 5 s and compared with the reference signal from the master oscillator by using a doubler mode of SR844. Note that the used pickups were outside the feedback loop so as to obtain the net deviation of the rf of the cavity. As a reference for the pickup signal of the flattopping cavity, the same signal as the signal from the frequency tripler for the excitation of the flattopping cavity. The measured voltage deviation and phase drift were plotted in Fig. 7 for 24 hours. The voltages stayed fairly within $\pm 0.03\%$. The phases were almost within ± 0.03 deg. (0.09 deg. for flattopping cavity) but the common drift of about $+0.05$ deg. was observed. The drift was thought to originate from the phase drift of the frequency doubler. The obtained stability was satisfactory for a precise experiment using a polarized deuteron beam.

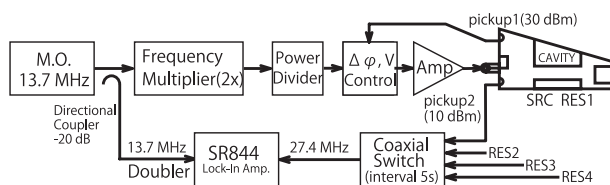


Figure 6: Block Diagram of RF amplitude and phase measurement for SRC.

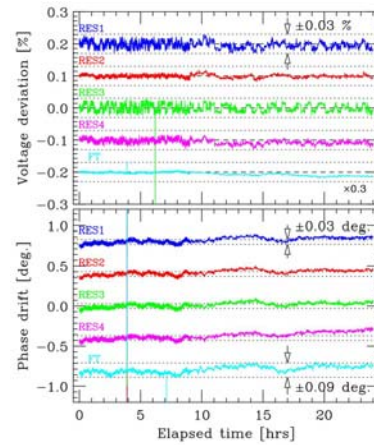


Figure 7: Amplitude and phase measured for 24 hrs.

Single Turn Extraction

RIBF has another aspect of a unique facility which handles the deuteron spin freely. The polarized ion source [9] provides polarized deuteron and its spin direction is rotated into horizontal plane by using a Wien Filter installed downstream of the ECR ionizer. Then the direction of the polarization axis on target can be selected freely as long as single-turn extraction is realized for the three cyclotrons in the mode 3. Single-turn acceleration is essential since the spin-precession ratio (g-factor) is not an integer so the spin direction varies turn by turn.

Here the protocol of the rf tuning is described: turn off the flattopping cavity and get an isochronous field observing by phase probes and make the beam-turn-pattern well-centered; set the phases of the acceleration cavities accelerating phase; change the voltage of the electrostatic injection channel to get off-centering; turn on the flattopping cavity and choose the phase and the amplitude of the flattopping cavity to make the beam profile as sharp as possible as shown in Fig. 8. The contamination of the turns was less than 0.01 %, though the transmission efficiency of the SRC itself was as low as 50 %.

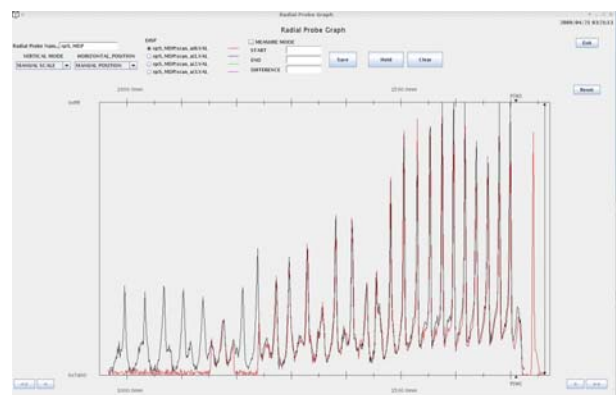


Figure 8: The turn pattern of polarized deuteron beam at 250 MeV/u.

OPERATION EXPERIENCES

Multipactor

In the initial stage of the commissioning of the SRC, the acceleration cavities were very difficult to be switched on due to a strong multipactor with the presence of the magnetic stray fields of the sector magnets. For the FRC and the IRC the multipactor was cleared by using a pulse excitation technique to pass through the voltage levels of multipactor, following dashed lines in Fig. 9. For the SRC the multi-

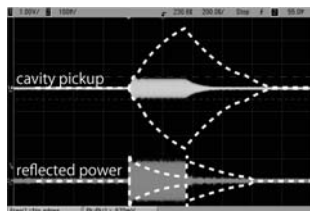


Figure 9: Profiles of the pickup signal from a cavity and the reflected power.

pactor was much more severe and it took more than one day to overcome it. In order to make the startup time shorter, conditioning with low power cw wave (cw) was tested instead of pulse and it turned out the new method works very well. By observing the level of the cavity pickup, the reflected power and the vacuum pressure, the level of the rf power is increased step by step until the cavity voltage becomes around 100 kV. Usually it takes only a few hours. It is enough to take 12 h for a careful conditioning. After the conditioning the cavity will be excited by a cw/pulse mode which recovers the voltage breakdown automatically turning the cw rf power to pulse mode to recover instantly in the case of voltage breakdown. If we see Fig. 7 carefully, sporadic losses of gap voltage are observed together with a breakdown of phase lock. It was caused by rf breakdowns in the cavity and automatically recovered within a few seconds.

The statistics of such breakdowns was counted and listed in Table 2. The number in round bracket counts the long loss when a manual recovery was needed. Until the 7th day after the initial conditioning the count per day was small.

Table 2: Summary of RF Breakdowns during an Experiment from May 1 to May 7(27.4 MHz. 100 kW/cavity)

day	RES1	RES2	RES3	RES4	FT	all
5th	0	0	1	0	2	3
6th	0	0	0	1	0	1
7th	0	0	0	1(1)	1	2
8th	1	2(1)	2	1	3	9
9th	3(1)	3	1	2	1	10
10th	0	2	1	5(1)	1	9
11th	2	8(1)	1	4	2	17
total	6	15	6	14	10	51(5)

From the 8th day the counts increased extraordinarily and finally, after 11 days, it was required to have a cw conditioning for three hours. This is one of the major problem with the SRC cavities which disturbs providing beams for an experiment longer than 2 weeks.

Other Troubles

- The temperature of the fins of the rf shield for cryogenic pump was increased up to 300 °C and the temperature of the final stage of cryogenic-pump was increased to about 50 K. This trouble has been proved by installing a direct cooling with a water pipe and then the vacuum pressure has been improved by factor 2.
- The contact fingers attached between the cavity wall and the shaft which supports the capacitive tuner were burned out. The gap size where the contact fingers were inserted became larger when the capacitive tuner was opened at larger angles. This problem has been fixed by adjusting the shape of the contact fingers to fit the gap size.

ACKNOWLEDGMENT

The authors are grateful to the staff members of Sumitomo Heavy Industry for construction of the rf system for RIBF. They thank Sumitomo Accelerator Service operators for making continuous efforts to make the system work with designed performance. They would like to thank Dr. Y. Chiba(Liniac Lab, RIKEN), Dr. T. Saito(RCNP, Osaka Univ.) and Dr. Jacques Cherix(PSI) for valuable comments on the rf system.

REFERENCES

- [1] N. Fukunishi et al., "Operating experience with the RIKEN radioactive isotope beam factory", Proc. 23rd Int. Conf. on Particle Accelerators(PAC09), Vancouver, Canada, (2009), in print.
- [2] Y. Yano, Nucl. Instr. Meth. B261(2007)1009.
- [3] N. Sakamoto et al., "Design of the rf resonators for the new booster ring cyclotrons in the RIKEN RI Beam factory", Proc. 15th Int. Conf. on Cyclotrons and their applications, Caen, France, (1998) p.223.
- [4] N. Sakamoto et al., "Construction of the rf-resonators for the RIKEN superconducting ring cyclotron", Proc. 16th Int. Conf. on Cyclotrons and their applications, Tokyo, Japan, (2001) p.342.
- [5] N. Sakamoto et al., "RF-system for the RIBF superconducting ring cyclotron", Proc. 17th Int. Conf. on Cyclotrons and their applications, Giardini Naxos, Italy, (2007) p.223.
- [6] R. Koyama et al., "Proc. of the 5th Ann. Meeting of Particle Acc. Soc. of Japan", (2008) p.318.
- [7] W. Joho, "Tolerances for the SIN RING-CYCLOTRON", SIN REPORT TM-11-4(1968).
- [8] <http://www.thinkSRS.com>.
- [9] H. Okamura et al.,AIP Conf. Proc. 293(1993) p.84.

A NOVEL DESIGN OF A CYCLOTRON BASED ACCELERATOR SYSTEM FOR MULTI-ION THERAPY

J.M. Schippers, A. Adelman, W. Joho, M. Negrazus, M. Seidel, M.K. Stam,
 Paul Scherrer Institut, Villigen, Switzerland
 H. Homeyer, Berlin, Germany

Abstract

A cyclotron based system for hadron therapy is developed, which allows a phased installation: start with protons and Helium ions and add Carbon ions later. The concept is based on an accelerator system of two coupled cyclotrons. The first cyclotron provides protons or He-ions that can be used for the full spectrum of treatments and “low energy” C-ions, with a range of 12.7 cm in water for a subset of tumours and radiobiological experiments. For treatments at all tumor sites with C-ions, the C-ions can be boosted subsequently up to 450 AMeV in a separate sector cyclotron, consisting of six sector magnets with superconducting coils and three RF cavities. First studies of the separate sector cyclotron indicate a relatively robust design with straight forward beam dynamics. This system is smaller than corresponding synchrotrons and possesses the typical advantages for therapy applications of a cyclotron. Present efforts to optimize the design of the super conducting sector magnets indicate that the introduction of a radial gradient in the sector would have many advantages.

motivation to use carbon ions for radiation therapy is based on the ballistic properties (heavy, thus limited scatter) and the expected advantages of a higher Radio Biological Effect (RBE, the ratio of the dose given with ⁶⁰Co gamma rays to the dose given with the Carbon ions, for the same cell killing). Until now all clinical carbon therapy facilities are using an injector linac coupled to a synchrotron (typically Ø=25 m) to accelerate particles. The advantage is the selectable energy, but the pulsed beam structure (the spills) and the relatively large fluctuations of the beam intensity during the slow extraction process prevent the application of fast pencil beam scanning methods. Such methods are suggested [1] to deal with organ motion and tumour motion during the administration of the irradiation dose. A cyclotron, however, offers a DC (actually CW) beam with a very stable beam intensity (also at kHz bandwidth [2]), fast (<80 ms) energy change (external energy degrader), fast (kHz) beam intensity control with an accuracy of a few percent, high extraction efficiency and no intensity problems. Since building a synchrotron does not allow for a phased approach, a solution based on two cyclotrons is proposed here, where the second cyclotron is coupled to the first one in the second installation phase of the project. Furthermore, this concept exploits the advantages typical for cyclotrons as mentioned above.

INTRODUCTION

Hospitals considering radiation therapy with protons, Helium or Carbon ions, often desire a phased approach: start with protons and add Carbon ions later. The

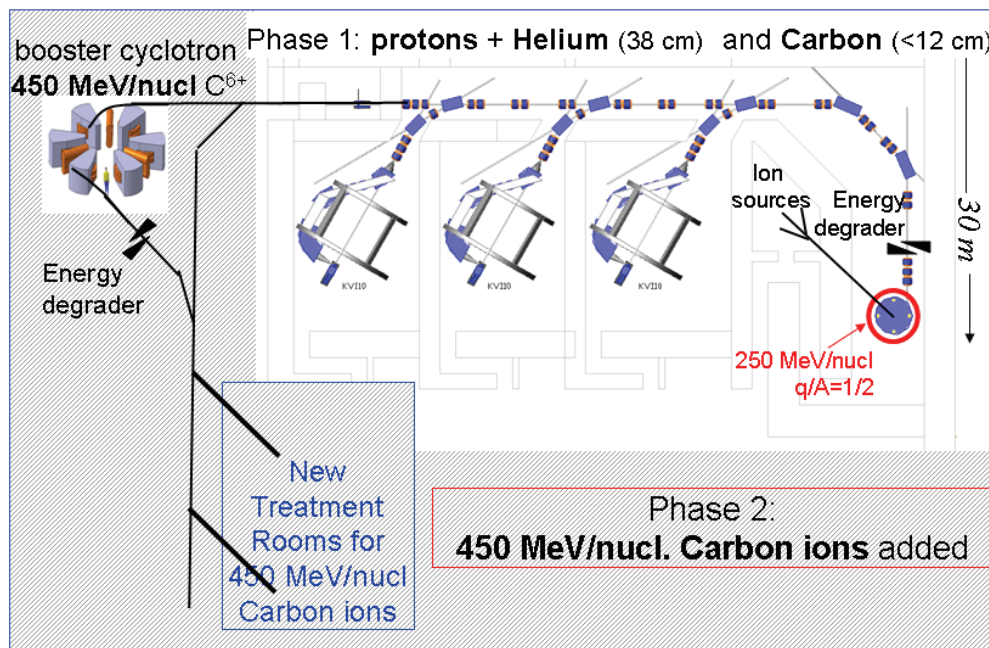


Figure 1: Possible layout for a multi-ion facility, based on two coupled cyclotrons, built in two phases.

Protons (H_2^+), He^{2+} , or C^{6+} -ions of 250 MeV/nucl will be accelerated in the first cyclotron, which is compact and has superconducting coils. Protons can be used for the full spectrum of treatments and the Helium ions, having the same water equivalent range of ~ 38 cm as the protons, also allow a full scale medical program, as well as radiobiology research with moderate RBE particles. For a subset of treatments, with a maximum water equivalent depth of ~ 12.7 cm, the “low energy” C-ions can be used for therapy, but also enable a sophisticated research program in radiobiology.

In the second phase of the project (Fig. 1), one can extend the treatment possibilities with C-ions to all sites (depth of 33 cm) by boosting the energy to 450 AMeV in the second cyclotron. For this booster we a separate sector cyclotron is proposed, consisting of six sector magnets with superconducting coils and three or four RF cavities.

In this paper the specifications of the total cyclotron system will be described first, followed by a detailed discussion of several design possibilities of the separated sector cyclotron.

SPECIFICATIONS AND GLOBAL DESIGN OF THE CYCLOTRON SYSTEM

Ion Sources and Injection

ECR sources for Helium and Carbon ions and a cusp source or ECR source for H_2^+ ions will be mounted in a separated vault (quick access) in close vicinity to the injector cyclotron. A typical injection energy is about 25 kV. A fast laminated switching magnet is used to select the ion source within a few seconds. The beam intensity can be switched off by means of a fast electrostatic deflector in the beam line to the axial injection system of the first cyclotron. Using a slit system down stream of the deflector, this system can be used for beam intensity modulation with kHz speed.

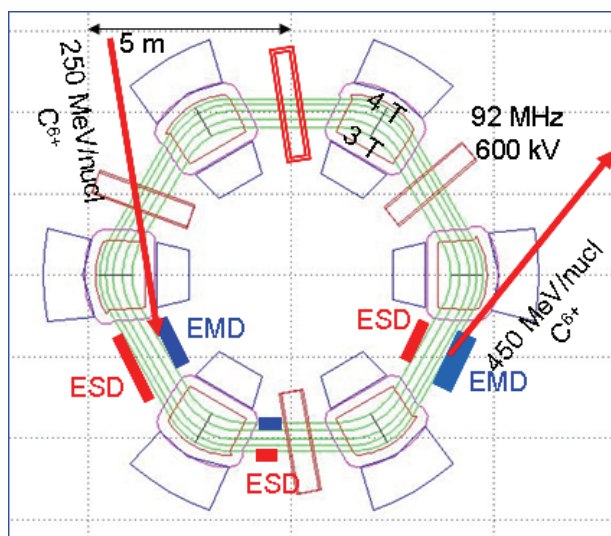


Figure 2: Injection and extraction in a 3(4) cavity layout of the 450 MeV/nucl booster cyclotron.

Injector Cyclotron

The choice of a superconducting “compact” cyclotron is based on the advantageous properties of and good experience with the COMET cyclotron [3] currently in use at PSI’s Center for Proton Therapy [4]. The optimal value for the beam energy must be found in the range 230-250 AMeV, with simplicity of the design as major criterion. Extraction of the Carbon ions will be by means of electrostatic elements. The extraction of the H_2^+ ions, however, could be done by stripping the ion and extracting the protons. The stripper option will give almost 100% extraction efficiency, but will most probably require a dedicated extraction channel and stripping foil technology. With the COMET 250 MeV proton cyclotron, the extraction efficiency is $>80\%$, resulting in a relatively low radioactivity in the cyclotron [3]. To achieve at least a similar extraction efficiency, is an important specification for the injector cyclotron.

Switching the setting of the cyclotron between different particles requires a slight ($\sim 0.8\%$) change of the RF-frequency and a small change of the magnetic field shape. Field changes can be made by using trim rods or correction coils. It is to be investigated how this can be done fast and reproducibly, also in view of the extraction method.

A possible candidate for the injector cyclotron could be the existing design of a cyclotron for 250 AMeV, made by the Catania group [5]. This design operates at 92 MHz, has a diameter of 4.9 m and a weight of 320 tons. However, an up scaling of the COMET cyclotron will also be considered.

Separated Sector Cyclotron

The application of superconducting magnets in a sector cyclotron has been demonstrated at the K2500 cyclotron at Riken (Japan) [6]. This cyclotron enables acceleration of many different isotopes in the radioactive beam facility at Riken. Since this is not needed in our case, this will strongly simplify the magnet. In order not to complicate the design of the superconducting coils, the beam dynamics of the cyclotron must be chosen such that no concave coil shapes are needed.

DESIGN STUDY OF THE BOOSTER: SEPARATED SECTOR CYCLOTRON

The first design studies presented here, have been confined to a six sector machine, using 92 MHz (12th harmonic) cavities with a peak voltage of 600 kV. A four sector machine would need larger magnets and may offer less flexibility and a more complicated injection or extraction.

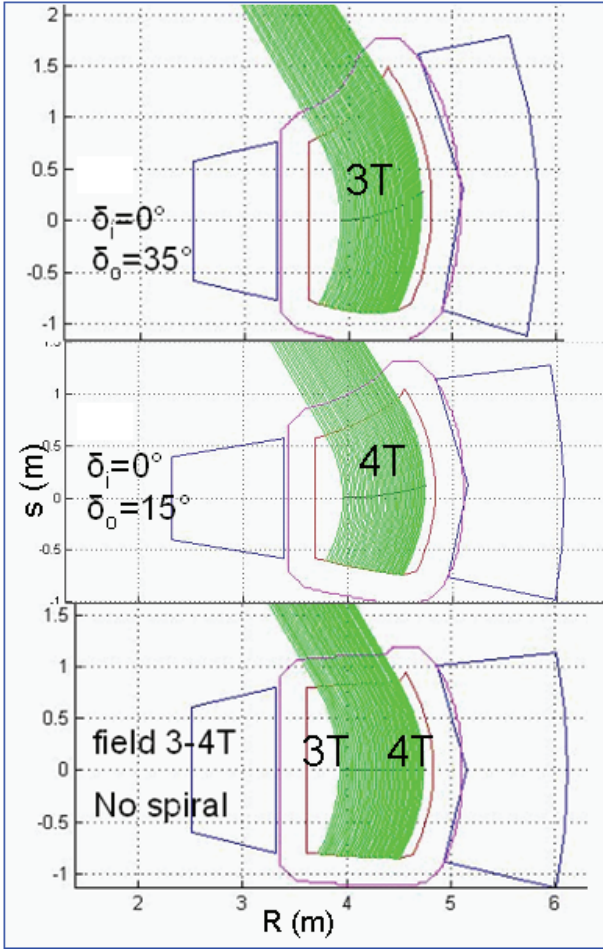


Figure 3: Magnet shapes and equilibrium orbits in the 3T, 4T and 3-4T designs, and their spiral angle at injection and extraction $\delta_{i,o}$.

Designs (see Table 1) with different magnetic fields in the sector magnets have been compared: 3 T, 4 T and one with a field varying from 3 T at injection to 4 T at extraction. Working at a lower harmonic number (e.g. 10 or 8) would reduce the magnet dimensions considerably. However, the space between the magnets would not allow enough room for the RF cavities or injection/extraction elements. Furthermore, a spiral angle up to 40° would be needed, which will be extremely difficult to construct in a 4 T magnet.

In the current design (Fig. 2) three single-gap RF cavities are foreseen. Depending on the layout of the injection and extraction channels, it may be an option to use four cavities. In some layout options (e.g. in the one shown in Fig. 2) the symmetry in the cavity locations is distorted, which needs further study of the consequences for the beam dynamics. However, experiences with the 590 MeV proton ring cyclotron at PSI have shown, that this need not be a problem. Also the potential of having a redundancy in the RF cavities, is an interesting feature for therapy. The injection and extraction paths cover two or three sectors and can be performed with electrostatic deflectors and septa (ESD, ~ 100 kV/cm) and magnetic deflectors (EMD, ~ 0.4 T).

Circular Accelerators

Table 1: Design Options for a Six Sector Cyclotron

Field in sector magnet:	3 T	4 T	3-4 T
Harmonic number (f_{RF}/f_{turn})	12	12	12
Weight 1 sector magnet (tons)	88	93	94
Diameter(m)	12	12	12
Spiral angle inj/extr (degr)	0/35	0/15	0/0
Orbit separation inj/extr (mm)	3.0/2.5	3.0/2.5	3.0/2.5

Beam Dynamics

The tune diagram has been calculated with a computer program employing analytical methods, which allow a review of different designs in rather short time. The effect of the magnetic field has been approached by a first order beam transport formalism in which a sector magnet is modeled by a transport matrix, which includes fringe field approximations and pole face rotations at entrance and exit of the magnet. At a series of radii between those of injection energy and extraction energy, the transport matrices of the magnet are calculated. Within the sector magnet a circular trajectory is assumed. At each radius the length along the arc of the trajectory and the spiral angle have been calculated, thus yielding the geometrical shape of the pole. In this way also a curved pole face and/or a radial gradient in the field could be taken into account. For the fringe field calculation several methods have been explored, all assuming more or less ‘‘classical’’ magnet field boundaries with a parameterization proposed by Kato [7]:

$$B(s) = \frac{B_{\max}}{2} \left[1 - \frac{(s/g) - a}{\sqrt{((s/g) - a)^2 + b^2}} \right]^n.$$

Here s is the distance from the magnet’s effective field boundary and a is the distance of $B_{\max}/2$ from the field boundary, b the softness of the edge, g the magnet gap and n the inverse of the tail extension. The effect of the fringe field is approximated as a correction ψ on the pole face rotation angle β , having only effect in the vertical plane [8]. In an alternative approach, giving almost the same results, the fringe field was approximated as a product of transport matrices, each representing a slice with thickness Δs of the fringe field.

From the beam transport matrix $M_{r,z}$ of a sector magnet and following drift space to the next sector magnet, the betatron frequencies in the radial and vertical plane have been calculated using

$$v_{r,z} = \frac{n_{\text{sec}}}{2\pi} \mu_{r,z}, \quad \mu_{r,z} = \arccos\left(\frac{1}{2} \text{trace}(M_{r,z})\right),$$

where $\mu_{r,z}$ is the phase advance in the section (one out of n_{sec}). Fig. 3 shows the thus obtained tune diagrams of the three designs.

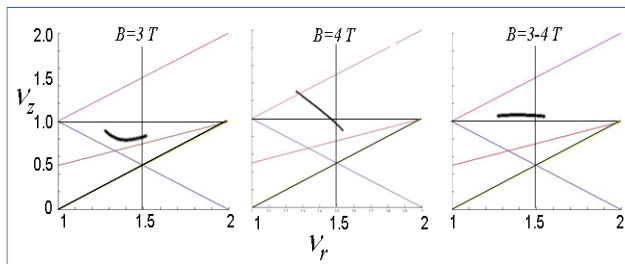


Figure 3: Tune diagrams and some resonances for the three design options.

Using the model described above, sensitivity calculations were performed to study the effect of the fringe field and the spiral angle. Variations of ν_z were typically within a range of 0.22, when varying the fringe field between “clamped Rogowsky” and very soft edge magnets. Similar variations were observed when varying the pole face rotations from 14 to 20 degree at injection and 30 to 35 degree at extraction radius. These “free” parameters can be used to force the vertical tune into a convenient value between 1.0 and 1.5. As can be seen in Fig. 3, such an adjustment (e.g. by slightly rotating the sector magnets along their vertical axis) is needed in the 3-4 T design to avoid the $\nu_z=1$ resonance.

In the horizontal plane, ν_r is about 1.3 at injection and 1.5-1.7 at extraction. The approximate phase advance of 100° and 80° per sector respectively, can be exploited in the extraction and at the extraction to increase the orbit separation (see Fig. 2).

The tune diagram needs to be confirmed in more detail by tracking calculations. As Fig. 3 shows, dangerous resonance crossings are not expected, but optimizations are still needed for the vertical focusing (e.g. move away from $\nu_z=1$, prevent concave sector magnet boundaries) and to establish the injection and extraction trajectories more accurate.



Figure 4: 150 MHz test cavity (single gap). A 92 MHz cavity is approx 1.5 times higher.

RF Cavities

We have chosen four single gap RF-cavities. A 1.5 times larger version of the existing test cavity (150 MHz) for the 590 MeV ring cyclotron at PSI could be used (see Fig. 4). The advantages with respect to a dual gap system are the relatively small space needed in the azimuthal direction and the small volume to be pumped. Based on the experience with this test cavity, a gap voltage of 600 kV can be expected, so that at extraction radius an orbit separation of 2.5 mm can be achieved, not taking the additional effect of the $\nu_r=1.5$ resonance into account. A fourth cavity could be added, ensuring redundancy but also allowing operation with lower power per cavity. Here some trade-off studies must be made.

Superconducting Sector Magnets

The main motivation for a super conducting coil is the possibility to achieve fairly strong magnetic fields. The advantages are the reproducibility of the magnetic field and the relative independence of the field from small artifacts in the iron. A study has been started to design the super conducting sector magnet. An advantage of the currently chosen size of the cyclotron is the possibility to use H-magnets. Fig. 5 shows the result of preliminary TOSCA calculations of a simplified 4 T magnet with a 3 cm gap. The coil has been modeled such that there are no concave sections. Compared to the original estimate, the size of the magnet has been increased to 215 tons, to limit the field in the yoke to 2.3 T. Using a separate iron layer with air gaps will allow a weight reduction. The totally stored energy is 24 MJ and radial forces of 150-300 tons are acting on the coil. In the model the poles are flat but have a concave shape at one end. Fig. 5 clearly shows that quite some shimming is needed.

Forces on coils in tons

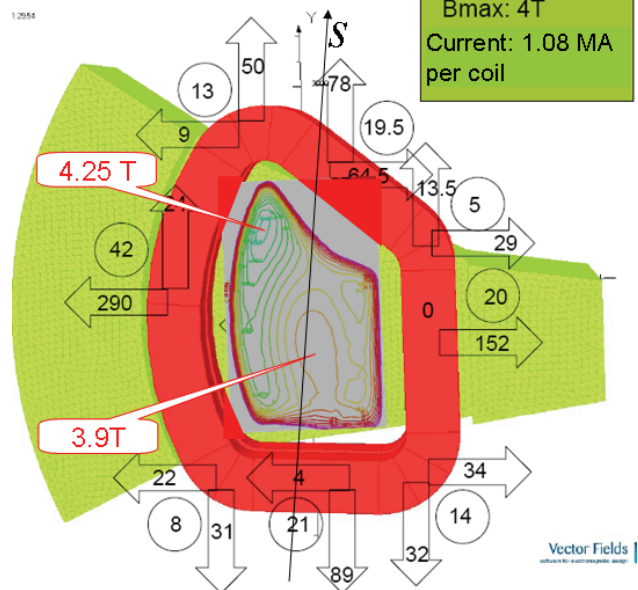


Figure 5: Magnetic forces and iso-field lines in a model of the 4T sector magnet, calculated with TOSCA.

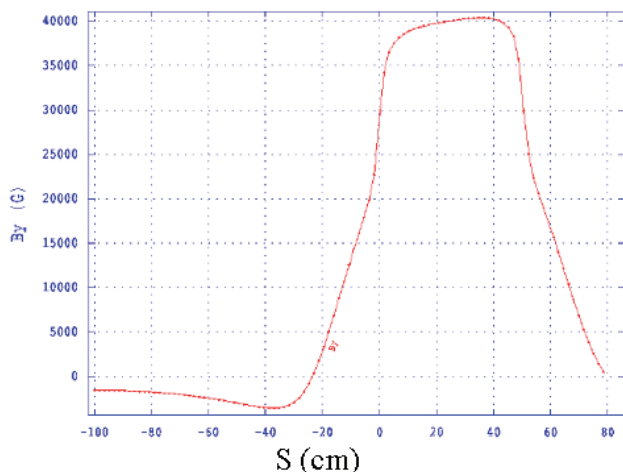


Figure 6: Magnetic field of one sector magnet along a line in the azimuthal direction, calculated with TOSCA.

The shape of the magnetic field is largely determined by the field from the coil. The vertical and horizontal position of the coils can thus be optimized to help the field shaping. In the magnet with the gradient an optimized coil location and orientation will be of major importance. The larger distance of the coil to the inner trajectories (3 T) compared to the coil distance to the outer trajectories (4 T) may be used advantageously. A design with a tilted coil is under investigation. The profile of the magnetic field along the line in Fig. 5 in the azimuthal directions shows some interesting features. First of all the top is not flat and the edges are not sharp due to saturation of the iron. Between -20 and 0 cm the slope of the field is shallow due to the coil field. The coil field is apparently so strong that a negative field of 0.2 T exists between the sector magnets. Although this makes the design sensitive for iron in the direct environment of the magnet, it may also be an advantage, since it increases flutter and thus focusing.

CONCLUSIONS

The study of various design options of a separated sector cyclotron for the acceleration of 250 AMeV C^{6+} ions until 450 AMeV indicated that the version with the radial gradient offers very favourable characteristics and advantages for the magnet engineering. The magnet can be rotated slightly in the horizontal plane to increase the vertical focussing. Furthermore its length is short enough to allow ample space for injection/extraction elements and

RF cavities. Beam dynamics studies indicate a relatively robust design with straight forward beam dynamics.

Present efforts to optimize the design of the superconducting sector magnets indicate no principal problems. However, work still needs to be done on minimizing the amount of iron, shaping of the field and the design of the coil.

The concept of two cyclotrons presented here, indicate that the proposed solution may turn to become an excellent solution for a combined - light and heavy particle - therapy machine for the following reasons:

- the robust and simple design allows a machine with a high reliability,
- it has the advantage of a CW cyclotron ion beam,
- the external ion source simplifies fast beam current variations necessary for optimal scanning and organ motion synchronization,
- the concept of two cyclotron offers an attractive two-phase realization. In the first step protons and helium ions are available for the full range. In particular helium ions have less angular spreading, which is important for deep seated tumors. Carbon ions with a range of up to 12.7 cm are attractive for cases where extreme localization is necessary. In a second stage the booster cyclotron can be added and the corresponding treatment rooms can be dedicated to heavy ion treatment.

REFERENCES

- [1] E. Pedroni et Al., Zeitschrift fur Medizinische Physik, Vol. 14, Issue 1,03-2004, pag. 25.
- [2] M. Schippers et al., Proc. 18th Int. Conf. Cyclotrons and Appl., Catania, Italy, 1-5 October 2007, pp 300-302.
- [3] Stefan Adam et al., PSI Scientific Report 2008, pp 92-95.
- [4] J.M. Schippers et al., Nucl. Instr. and Meth. B 261 (2007) 773-776.
- [5] L. Calabretta et al., Nucl. Instr. And Meth. A, 557 (2006) 414-420.
- [6] J. Ohnishi et al., Proc. 18th Int. Conf. Cyclotrons and Appl., Catania, pp 429-431.
- [7] S.Kato, Nucl. Instr. And Meth. A540 (250) 1-13.
- [8] D. C. Carey, The optics of charged particle beams, Harwood academic publishers, 1987.

DESIGN STUDY OF MEDICAL CYCLOTRON SCENT300

M. Maggiore, L. Calabretta, M. Camarda, G. Gallo, S. Passarello, L.A.C. Piazza,
LNS-INFN, Catania, Italy

D. Campo, D. Garufi, R. La Rosa, University of Catania, Dept of Physics and Engineering, Italy

Abstract

The study of the Superconducting Cyclotron named SCENT300 [1] was carried out by the accelerator R&D team of Laboratori Nazionali del Sud (LNS-INFN) of Catania in collaboration with the University of Catania and supported by IBA (Belgium).

Combining the compactness of a superconducting cyclotron, with the advantage of this kind of machine as its continuous beam and its very good current control, the accelerator R&D group of LNS, by its ten-year of experience with this kind of machine, has developed a concept for a multiparticle therapy cyclotron which is described in the following report.

INTRODUCTION

Beams of hadrons, such as protons and carbon ions, offer an important advantage over traditional radiotherapy: minimum damage to healthy tissue around a tumour. While dedicated facilities based on the proton therapy are well established around the world, most of the hadron-therapy ones are currently in operation at large particle-physics laboratories. In Europe, two dedicated facilities are under construction (CNAO in Italy and HIT in Germany) and many projects based on light ion therapy are at different stages of the approval and financing path [1]. These centres are based on synchrotron accelerators, due to the high energy of light ions (400 AMeV for ^{12}C) needed to reach the whole deep-seated tumours.

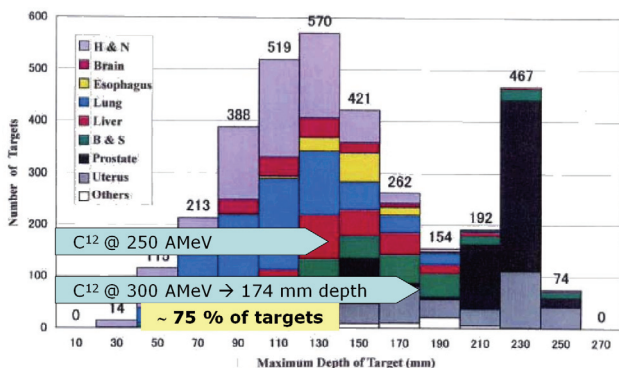


Figure 1: The plot shows the number of targets (for different tumours highlighted on the left square) as function of the depth inside the human body. The arrows indicate the depth limits of the carbon beams at two different energy. These data are provided by HIMAC (Japan) concerning the treated patients from 1995 to 2001 [2].

Today IBA and INFN are involved to study the possibility to use the cyclotron accelerator to get both the protons and the carbon ions for the therapy. IBA, in

Circular Accelerators

collaboration with JINR laboratories, is carrying out the project of C400, a compact cyclotron able to accelerate the carbon ions up to the energy of 400 AMeV and protons up to 270 AMeV [3]. The INFN is accomplishing the design study of a superconducting cyclotron to deliver 300 AMeV of carbon ions and protons of 260 AMeV [4]. The choice to get the energy of 300 AMeV for the carbon ions is due to the higher number of tumours reachable inside the human body using the carbon beams, as shown in the Fig. 1. On the other hand, the extraction energy of protons of 260 AMeV guarantees to treat the whole targets.

MAIN PARAMETERS

SCENT300 is a four-fold symmetry superconducting cyclotron optimized to accelerate both the fully stripped carbon ion and the H_2^+ with a charge to mass ratio of 0,5 for the hadrontherapy application. The carbon beam is extracted at the maximum energy of 300 AMeV by two electrostatic deflectors (ED) and a set of passive magnetic channels. The ionised hydrogen molecule H_2^+ is extracted at the inner radius of 122 cm, by the stripping process at the energy of 260 AMeV, delivering the proton beam with the same energy, by a different extraction channel through the iron yoke.

Table 1: Main Parameters of SCENT300

Parameters	Values
Particles	H_2^+ , $^{12}\text{C}^{6+}$
Injection Energy	25 AkeV
Extraction Energy	$^{12}\text{C}^{6+}$ @ 300 AMeV, H_2^+ @ 260 MeV
K bending	1200 MeV
Number of Sectors	4
Pole Radius	132.5 cm
Mean Magnetic Field	3.15 T ÷ 4.2 T
Peak Magnetic Field	4.95 T
Injection scheme	Axial + external ion sources
Extraction	Carbon by 2 ED, H_2^+ by stripping
Size	Diameter= 5 m, Height= 3 m
Weight	~ 350 tons
Coils	2 superconductors
Max Current density	47 A/mm ²
Energy Stored	35 MJ
Number of Cavities	4
Operating RF harmonic	4
RF frequency	~ 98 MHz
Estimated power losses	50 kW/cavity

The machine is a relatively compact cyclotron (5 m in diameter) and most of operating parameters, as the operating RF frequency are fixed (see Table 1).

MAGNETIC FIELD DESIGN

The study was carried out by an intensive use of FEM code in order to get a full parameterization and a better accuracy for the magnetic fields calculation.

The minimum requirements to satisfy for the magnetic field design, are the following:

- Vertical and radial beam dynamic stability ($Q_r > 0$; $Q_z > 0$);
- Isochronism $|\Delta\omega/\omega| < 1 \cdot 10^{-4}$ in order to keep the phase slip calculated in static mode, within acceptable values $|\Delta\phi| < 20$ deg;
- Minimization of the current density of the coils to keep right margins of reliability and safety of the cryogenic systems;
- Minimization of harmful effects on the beam quality due to the resonances crossing;

The main magnetic field was refined in order to deliver the fully stripped Carbon ions up to the maximum energy of 300 AMeV. A special care was done to bring the last orbit accelerated as close as possible to the edge of the pole in order to make the extraction process by the ED easier.

The average magnetic field varies from the value of 3.15 T at the injection up to 4.2 T at the extraction radius of 129.5 cm. The 4 fold symmetry and the spiral shape of the sectors (82° of maximum spiral angle) provide the needed axial focusing of the beam.

To validate the properties of the magnetic field, the preliminary analysis of the beam dynamic in static mode was done by means of dedicated code. The first calculations were done, setting two different values of constant voltage: 70 kV and 120 kV in order to check the phase behaviour, being the effective voltage included within these values. In the plot shown in Fig. 2, it can be seen that the phase value, thanks to the good isochronization, oscillates within a range of $\pm 10^\circ$ RF.

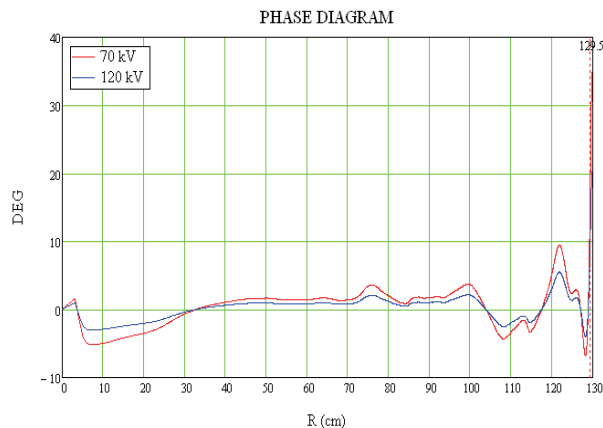


Figure 2: Two different phase behaviours depending on the voltage value set for the calculation in static mode.

CENTRAL REGION DESIGN

The proposed cyclotron will be equipped with an external ECR ion source producing both H_2^+ and fully stripped Carbon ions. A solution with two separated sources to reduce the switching time between proton and carbon treatment is also considered. Ions at the energy of 25 AkeV are delivered axially, through an injection line, into the machine, where an electrostatic inflector, operating with an electric field of 23 kV/cm, bends the beam by 90° from its axial path to the cyclotron median plane.

An optimal configuration could be able to transport a beam emittance of 30π mm mrad in phase shift of 20 RF deg to the acceleration region with a few millimetres of off-center and a good vertical focusing.

The accelerating structure consists of a set of specially-shaped electrodes attached to the Dees of the cavities: the position and size of each RF electrodes and of ground are optimized to accelerate the beam along a well centered path with a reasonable energy gain of the beam (see Fig. 3). The Dees have been shaped using all the available space between two different magnet hills and reaching the maximum angular amplitude, but in the first 5 cm from the machine centre, where the beam trajectory covers the first turn, the Dee tips and electrodes have to be inserted along the reference trajectory, in order to provide the vertical focusing. The introduction of two channels for each Dee improves the effect of the accelerating electric field and confines it close the gaps.

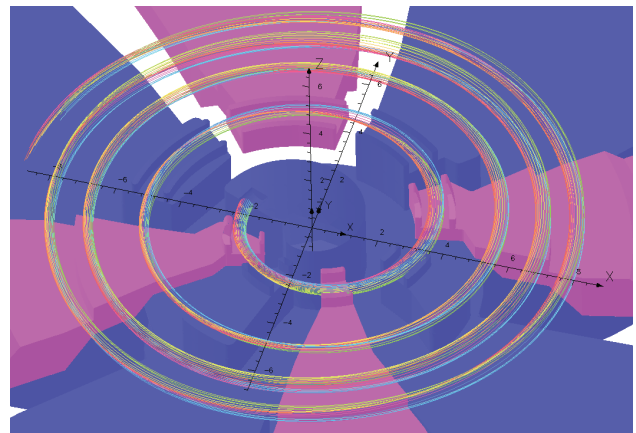


Figure 3: The figure shows the central region configuration. The dee-electrodes are highlighted in magenta, while the ground surfaces in blue. A set of particle trajectories from the housing (where the inflector is located) to first turns.

RF SYSTEM DESCRIPTION

The RF system, working in the fourth harmonic, is based on four cavities operating at 97 MHz. These cavities, copper made and water cooled, are entirely installed inside the free valley regions. The multi-stem cavity configuration [5] needed to reach the high resonant frequency, found out by means of 3D electromagnetic codes. The aim is to obtain a cavity with a voltage

distribution going from 70 kV in the injection region to a peak value of 120 kV in the extraction region, and a low power consumption (60-70 kW per cavity). The cavities operate at the phase, and the power is fed by an inductive coupler for each cavity. A trimmer capacitor per cavity will be used for the fine tuning of the resonant frequency. The RF system is powered by four amplifiers.

In a general cavity structure, the stems give the main contribution on the inductance of the cavity and give mechanical stability being the connection between the dee and the liner. As regards the cavities we expect to use in SCENT300, in order to attain the high resonant frequency, we have been forced to insert at least three stems. Thus, we have chosen to have higher electrode voltages on the inner and outer extremities and to keep a lower voltage in most of the DEE, in order to optimise the shunt impedance. By applying the above-described method, we have obtained the resonator shown in Fig. 4. The large central stem (low inductance) concentrates the currents coming from most of the electrode, while the two lateral ones (high inductance) resonate with the much smaller capacitances of the DEE extremities.

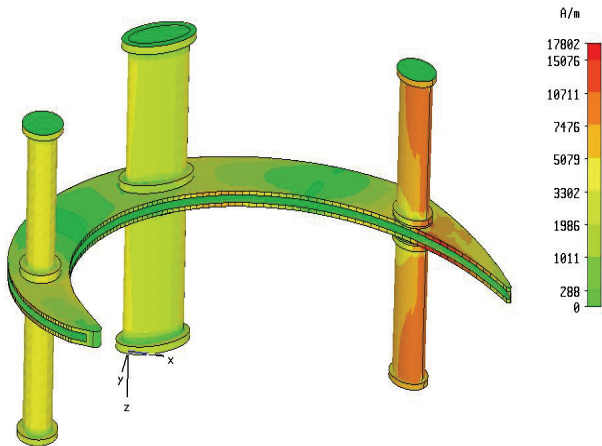


Figure 4: The three stems configuration of a single cavity without the liner is shown. The current density on the surfaces of the DEE and stems is also plotted. The peak value is 142 A/cm.

BEAM DYNAMIC STUDY

In the following section the beam dynamics of Carbon ions, taking into account the acceleration effects on the beam envelop, is discussed. The working diagram of the machine is shown in Fig. 6.

As first step, we verified the accelerated equilibrium orbit AEO of a single particle, in order to check the phase slip using the varying voltage profile. The starting conditions for the AEO, i.e. the radius, the radial momentum and the phase, are given by the equilibrium orbit data. From the dynamics calculations, a very small excursion of phase is reached. The maximum value corresponds to 44.4° at 303.4 AMeV (130.42 cm of radius). The energy gain varies from 0.2 AMeV/turn to 0.47 AMeV/trun, being almost 1100 turns needed to get the final energy.

Circular Accelerators

The beam envelop behaviour during the acceleration is analyzed. The transverse beam dynamic on phase space (r,r') and (z,z') is carried out. Two values of radial amplitude A_r of displacement from the AEO have been studied: +0.1 cm and +0.2 cm.

The twice crossing of the dangerous structural resonance $Q_r=4/3$, respectively at 120.6 cm (246 AMeV) and 127.9 cm (293 AMeV), does not cause a significant growth of the beam size with an initial amplitude $A_r=0.1$ cm. The harmful effect instead is quite evident on the radial envelop of particles delivered with the initial amplitude of 0.2 cm, as shown in Fig. 5.

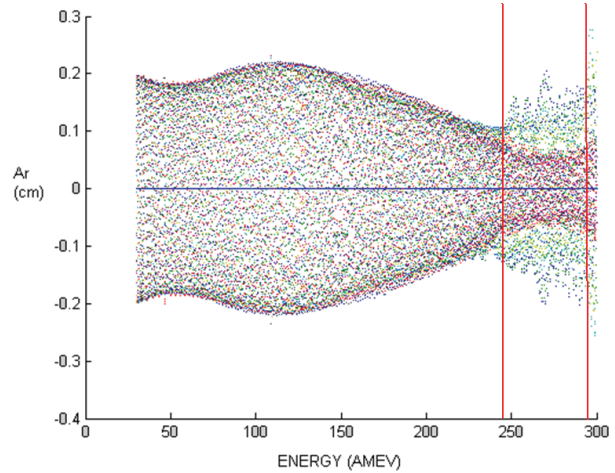


Figure 5: Radial beam envelop versus energy of the accelerated orbit with $A_r=0.2$ cm of initial amplitude. The effect of the crossing of the $Q_r=4/3$ (signed by the red lines) on the size of the beam is evident.

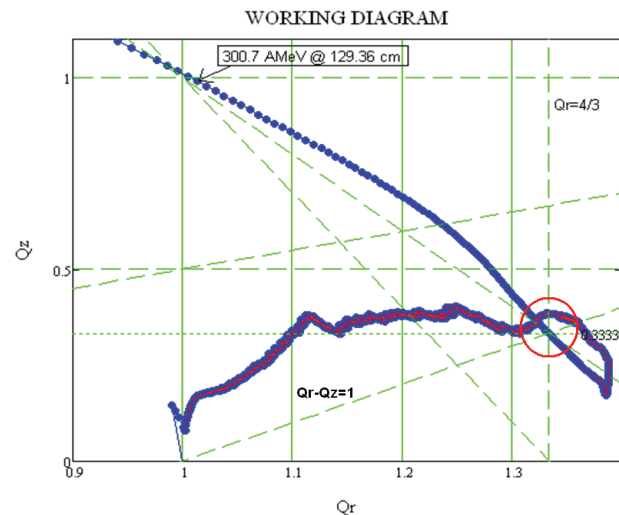


Figure 6: Working point diagram of Carbon ion. Lines of most important resonances are shown. The point where the beam passes through 2 dangerous resonances is highlighted.

Despite the first crossing does not get an excessive growth, the second one, even if faster, could become capable to doing harm on the beam quality.

On the other hand, since the beam passes through both the coupling ($Q_r-Q_z=1$) and structural ($Q_r=4/3$) resonances at the same point on the working diagram (see Fig. 6), it could be possible to introduce a local $B_{1r}(r)$ perturbation (max 10 G) in order to reduce the impact on the radial growth at expense of the vertical one.

TRIMMING OF THE MAGNETIC FIELD

The SCENT300 machine is designed to get carbon ions and protons for hadrontherapy use. Despite the charge to mass ratio of both ion species is similar ($Q/A=0.500137$ for $^{12}\text{C}^{6+}$; $Q/A=0.4966345$ for H_2^+), the magnetic field has to be changed in order to compensate the de-synchronization due to the mass discrepancies between the two beams.

There are two ways to do that:

- changing only the main magnetic field (+0.78% constant along the radius) and keeping constant the RF cavity frequency;
- changing both the main magnetic field (from 0% at injection to -0.5% at extraction) and the RF cavity frequency by about 0.78%;

The first solution allows simplifying the cavity design but it requires a larger tuning of the magnetic field as shown in Fig. 8; the second one requires a small variation of the magnetic field but it needs to design a RF system working at two different frequencies.

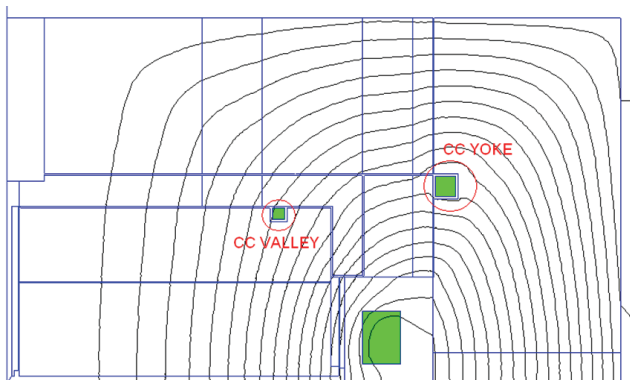


Figure 7: side view of the cyclotron with the coils position highlighted.

We decided to keep constant, within few hundreds of Hertz, the RF frequency, changing the whole magnetic field by almost 0.78%. To do that, in addition to the main coils current setting, we suggest to insert two pair of correction coils (CC) operating at room temperature as shown in Fig. 7. The position and the size of the coils were chosen to best fit the needed magnetic field and, at the same time, to minimize the current and the power losses of the resistive coils (see Table 2). The found out solution allows shaping the magnetic field with a precision of ± 3 G respect to the ideal one as shown in Fig. 8. The small magnetic spread ensures for the H_2^+ dynamics, a phase excursion within ± 10 RF deg both in static and acceleration mode.

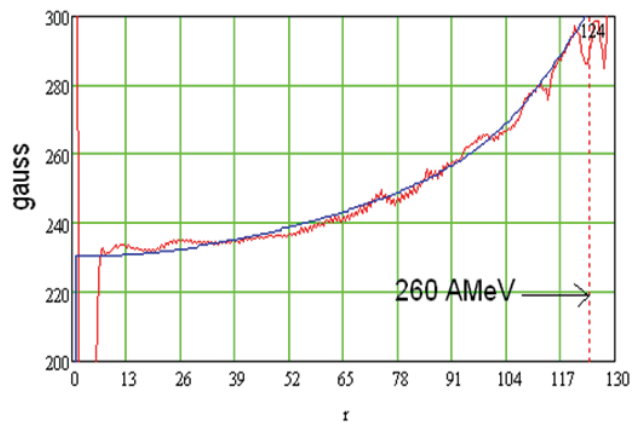


Figure 8: Comparison between the average magnetic field needed to accelerate the H_2^+ (red line) and the best fit achieved by tuning the main coil current and by adding on two resistive correction coils.

Table 2: Different Coils Setting for C and H_2^+ Acceleration

	MAIN COIL	CC VAL	CC YOKE
SIZE mm ²	150x210	80x80	50x40
C setting A/mm ²	45.86	0	0
H_2^+ setting A/mm ²	45.86+0.53	4	1.1
Power losses kW/coil	SC	3.24	1.32

EXTRACTION STUDIES

The extraction of a fully stripped ion $^{12}\text{C}^{6+}$ requires the use of electrostatic deflectors (ED). The choice to install the 4 RF cavities inside the valleys implies to put two electrostatic deflectors (E1 and E2 in Fig. 9) in two hills, where the gap is deep enough (5 cm). The electrostatic deflectors operate at 50 kV and the maximum electric field on the gap is 120 kV/cm. The protons are extracted by stripping of the H_2^+ . The carbon foil is positioned at the internal radius of 120-122 cm, in order to intercept the accelerated beam at the energy of 260 AMeV as shown in Fig. 9. The protons leaves the cyclotron by a single turn without interfering with the central region device and the inner wall of the cryostat. The two beams exit from two different yoke apertures. A set of passive magnetic channels (MP and MC in Fig. 9) are needed to make the extraction both the carbon and the protons easy. Such magnetic channels compensate the defocusing effect on the radial plane due to the fall-off of the magnetic field close the outer edge of the poles.

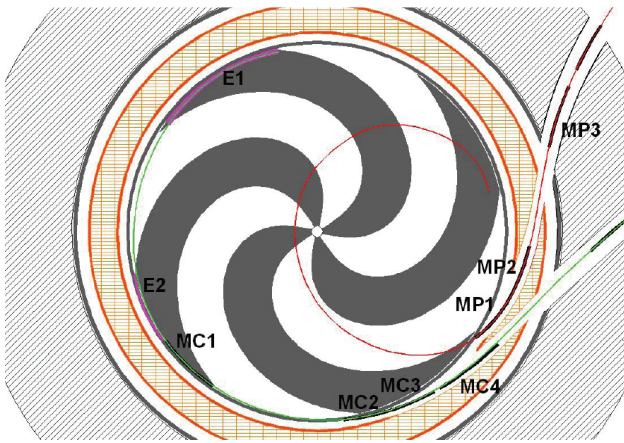


Figure 9: The two extraction paths are shown in figure. The red line corresponds to the proton trajectory, and the blue one to the carbon beam. The position of the different passive magnetic channels (MP used for the protons and MC for the carbon) is shown.

FINAL CONSIDERATIONS

The magnetic field trimming system is the key point of this cyclotron. Since SCENT300 operates in 4th harmonic mode, the average magnetic field has to match with high precision the isochronous one to accelerate both on species. We think that the described system could become useful during the cyclotron commissioning to provide for eventually fine tuning for the Carbon magnetic field too. Indeed some imperfection due to the iron cast and the mechanical assembly has to be taken into account during

the building of the machine. Their effect on the magnetic field is seldom negligible and it may require at later stages, extensive modifications could be impractical or difficult, because of the freezing meanwhile of other parameters.

While the use of both superconducting (K250 SC by VARIAN-ACCEL GmbH) and conventional cyclotrons (C235 RT by IBA) in protontherapy centers is today consolidated, this cyclotron is an interesting option for the facilities dedicated to the treatments of tumours with ions and protons too.

REFERENCES

- [1] S. Rossi, "Developments in proton and light ion therapy", EPAC'06, Edinburgh, Scotland, June 2006, p. 3631.;
- [2] Y. Hirao, "Results from HIMAC and other therapy facilities in Japan", Cyclotrons 2001, East Lansing, USA, May 2001, p. 8.;
- [3] Y. Jongen et al., "Current Status of the IBA C400 cyclotron project for hadron therapy", EPAC 2008, Genova, Italy, July 2008, p 1806;
- [4] M. Maggiore et al., "SCENT300, a superconducting cyclotron for hadron therapy", EPAC'08, Genova, July 2008, TUPP123, (2008);
- [5] M. Maggiore et al., "Conceptual design of the RF accelerating cavities for a superconducting cyclotron", Nuclear Instruments and Methods A 557 (2006) p 441-420.

HIRFL-CSR COMMISSIONING STATUS AND FUTURE UPGRADE*

J.W. Xia, Y.J. Yuan, Y. Liu[#], X.D. Yang, J. C. Yang, L.J. Mao, D. Y. Yin, X. Chen, P. Li, H. Jia, IMP, CAS, Lanzhou, 730000, P.R. China

Abstract

CSR is a new ion cooler-storage-ring system in IMP, Lanzhou, China, which consists of a main ring (CSRm) and an experimental ring (CSR_e) with two previous cyclotrons SFC (K=69) and SSC (K=450) as the injectors. The main construction of CSR was completed in 2005. It was being commissioned in the following two years. In 2008 the main purposes of CSR was focused on the primary ⁷⁸Kr beam with kinetic energy up to 500MeV/u for precise mass spectroscopy at CSR_e at isochronous mode. The cancer therapy phase-II in IMP with 100-250MeV/u carbon beam from CSRm was tested and 6 patients with tumors in the heads were treated successfully.

INTRODUCTION

HIRFL-CSR (Heavy Ion Research Facilities in Lanzhou, Cooler Storage Ring) consists of a main ring (CSRm), an experimental ring (CSR_e) and RIB production and transfer line (RIBLL2) in between [1][2], shown in Fig. 1. The two previous cyclotrons SFC (K=69) and SSC (K=450) of the HIRFL are used as the injectors, offering lighter ion beams like ¹²C⁴⁺ at maximum 7 MeV/u with SFC, or heavier or higher-energy ion beams with SFC+SSC combination. The heavy ion beams from the cyclotrons are injected first into CSRm for accumulation with e-cooling, consequently accelerated, and finally either fast-extracted via RIBLL2 into CSR_e for internal-target experiments or mass measurements of radioactive ion beams (RIBs), or slow-extracted for external-target experiments or cancer therapy.

In 2005 the main construction of CSR was completed. It was being commissioned in the following two years. Main features of CSR were realized and examined by the national testing team, including the stripping injection (STI), electron-cooling with hollow electron beam, carbon beam stacking with the combination of STI and e-cooling, the wide energy-range acceleration from 7 MeV/u to 1000 MeV/u with the RF harmonic-number changing at the mid-energy, the multiple multi-turn injection (MMI) and the beam accumulation with MMI and e-cooling for heavy-ion beams of C, Ar and Xe, the fast and slow extraction from CSRm, the commissioning of CSR_e with two lattice modes and testing RIB mass spectroscopy at CSR_e at isochronous mode with time-of-flight (ToF) method.

In 2008 the main commissioning purposes was focused on the primary ⁷⁸Kr beam with maximum kinetic energy up to 500MeV/u for production of proton-rich drip-line nuclei and precise mass spectroscopy at CSR_e at

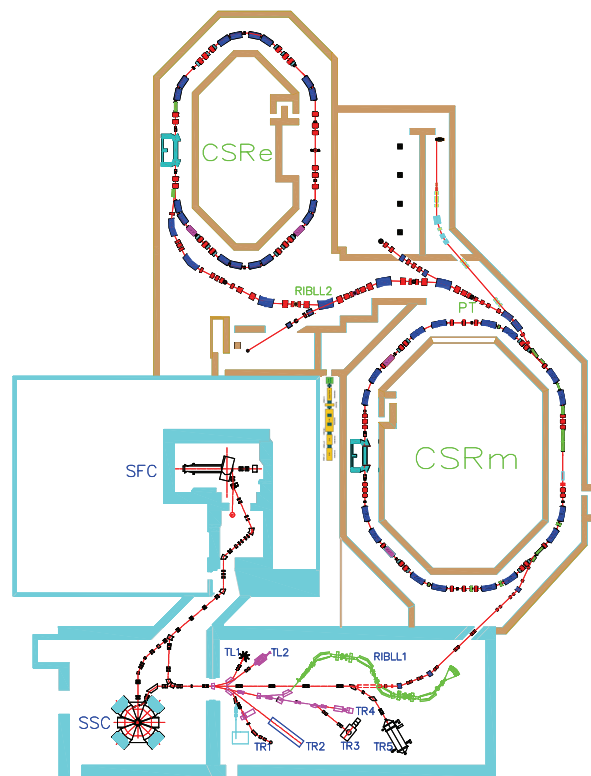


Figure 1: Layout of present HIRFL-CSR.

isochronous mode. Great effort was made to accumulate injected $\delta 600 \text{ nA } ^{78}\text{Kr}^{28+}$, which was actually hard to see at the ring at first, to the ultimate current $80 \mu\text{A} (1 \times 10^8)$.

The cancer therapy phase-II in IMP with 100-250 MeV/u stepped by 5 MeV/u with carbon beam from CSRm was performed and 6 patients with tumors in the heads were treated successfully. Stripping injections with and without accumulation with e-cooling were tested for the possible miniaturization of this type of cancer-therapy machine-complex.

COMMISSIONING AND TEST EXPERIMENT

The first stored beam in CSRm was obtained with charge stripping injection for carbon beam ($\text{C}^{4+} \rightarrow \text{C}^{6+}$) in Jan. 2006, with much effort due to the low injected beam current of only a few μA and still improving beam diagnostics and control system at the very beginning of commissioning. Later on the remote control system and tune measurement [3] were available, which assured the commissioning on the right way.

Successful acceleration of injected $^{12}\text{C}^{6+}$ at 7 MeV/u (0.76T m/0.1 T) to 1GeV/u (11.3T m/1.5 T) with a beam intensity of 2.8×10^8 pps was achieved in Oct. 2006. It

*Work supported by NSFC project 10635090

[#]y.liu@imp.cas.cn

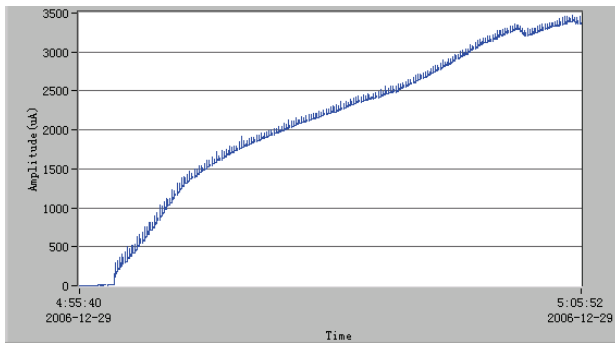


Figure 2: Measured beam current of $^{12}\text{C}^{6+}$ at 7MeV/u, with stripping injection and accumulation with electron cooling.

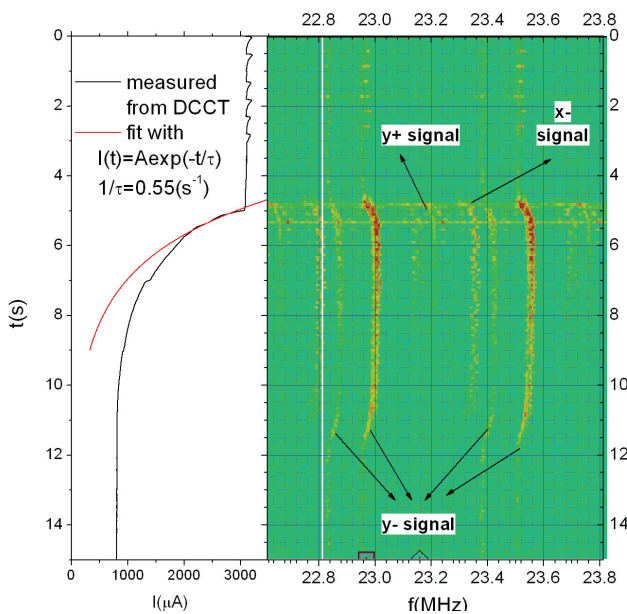


Figure 3a: Measured beam current and longitudinal spectrum of cooled $>2.5\text{mA}$ $^{12}\text{C}^{6+}$ beam at 7MeV/u during the beam break-up.

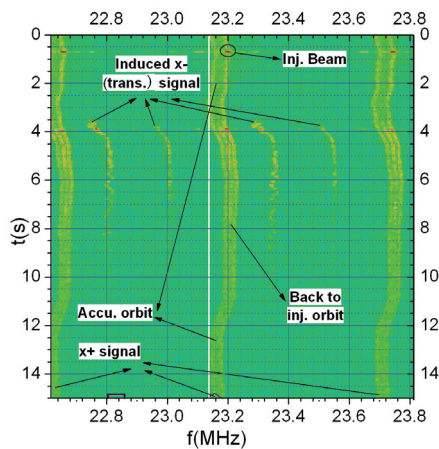


Figure 3b: Measured transverse spectrum during the beam break-up.

relied on the techniques of modification of ramping curve against systematic error in the measured magnet-field data, and with the high-efficiency harmonic-transfer RF-acceleration. The latter is to divide the acceleration into

Circular Accelerators

two or more ramping parts, each with different RF-harmonics. The RF-harmonics transfer is applied in most of the CSRm operations, shown in Figs. 7 and 11 at about 3.5 s and 2.5 s respectively. It is of great importance for CSR because the lower-energy $^{12}\text{C}^{4+}$ beam from SFC beam is thus acceptable for CSRm to be accelerated to 1GeV/u. So the efficiency of carbon beam is greatly enhanced with the absence of SSC.

As a key point for the accumulation of ion beam, the electron cooler system at CSRm was in function by the end of 2006 [4]. The availability of beam current monitor DCCT helped to realize the accumulation of stripping-injected carbon beam with electron-cooling. The new generation of electron cooler system with adjustable electron-beam distribution dramatically improved the $^{12}\text{C}^{6+}$ beam intensity with normal accumulation time of 10 seconds to 7×10^9 pps at 1GeV/u in Sep. 2007 [3].

Experiments were made for the no-time-limit accumulation of carbon beam with stripping injection. With injected C^{4+} beam of 10 μA , a saturated maximum current of 3.4 mA of C^{6+} beam was achieved, i.e. 1.6×10^{10} at CSRm, which is a factor of ~ 300 , in 8 minutes, as was shown in Fig. 2.

Instabilities and beam break-up were observed for such long-stored cooled beam, as shown in Fig. 3. When the beam current reached a certain level, ~ 2.5 mA in this case, and when the coming of “hot” injected beam was stopped, the injection-cooling-decay balance would be broken. Then the stored beam got more deeply cooled until certain resonances were met.

Coherent modes were developed and after about 2 s the beam loss began. A new equilibrium was reached at last with a remained current of ~ 0.8 mA.

The mechanism behind is related to the angle between electron-beam and ion-beam. Perturbation or the incoming “hot” beam can maintain the equilibrium.

From the above results it is clear that the stripping injection proved to be so successful to make the planned RF-stacking no more necessary at CSRm.

However, the stripping injection is not fit for elements heavier than argon, for which multiple multi-turn injection (MMI) scheme is required. The MMI was first realized in Apr. 2007 with carbon beam. Soon after the first beams of argon (4×10^8 pps) and xenon (1×10^8 pps) were successfully accumulated and accelerated at CSRm [3].

In Aug. 2007 the first fast extraction from CSRm was carried out. After struggling with the beam line the first beam was stored in CSRe in October, with the stored beam of 7×10^9 pps for $^{12}\text{C}^{6+}$ and 1.2×10^8 pps for $^{36}\text{Ar}^{18+}$ after optimization.

A last testing experiment was performed to exam the CSR overall ability and readiness. Operation with the combination of SFC+SSC+CSRm+RIBLL2+CSRe was applied, for primary $^{36}\text{Ar}^{18+}$ beam at 368 MeV/u up to 400 MeV/u, producing RIB fragments with mass of $A=2Z$ and $A=2Z-1$, respectively, at transition energy of CSRe at 368 MeV/u, i.e. $\gamma_{tr} = 1.395$, at isochronous mode. The resolution of mass was better than 10^{-5} .

The first slow extracted beam was seen on detector in Jan. 2008, but the 50 Hz ripple of power supply was obvious, estimated to be around 5×10^{-4} . Efforts were made to improve it after this test, shown in Fig. 8.

FIRST OPERATION OF CSR FOR MASS SPECTROSCOPY EXPERIMENT

The first operation of CSR for mass spectroscopy was similar to the testing experiment, with the primary beam of $^{78}\text{Kr}^{28+}$, aiming at proton-rich drip-line nuclei of germanium, arsenic and selenium with the life-time of ~ 100 ms. The experiment was taken in two time periods in 2008.

The resolution and even the feasibility of the mass spectroscopy at CSRe at isochronous mode are highly dependent on the relevant reproducibility, efficiency and stability and ripple of power supplies of the combination of SFC+SSC+CSRm+RIBLL2+CSRe, with iteratively changing and testing the energy settings, as shown in Table 1.

The real challenge was the weak injected beam from SSC. The most critical point is to see the very first storage of the beam to tune the machine. In this case the maximum injected $^{78}\text{Kr}^{28+}$ beam current was ~ 600 nA. It is difficult for the DCCT at CSRm to distinguish the small current below $1 \mu\text{A}$. It is also difficult for BPM which requires rebunching the first weak stored beam.

During the first period in the middle of 2008 $^{78}\text{Kr}^{19+}$, $^{78}\text{Kr}^{29+}$ and $^{78}\text{Kr}^{28+}$ were tested for several times to ensure the ring status and to pursue the best chance. Finally the first storage was found by averaging the long-time DCCT data. After this breaking point the accumulation was just consequence with the powerful electron cooling. Maximum currents of $55 \mu\text{A}$ (7×10^7) and $80 \mu\text{A}$ (1×10^8) at injection level were achieved respectively for the two periods. The experiment succeeded to count enough events of aimed-nuclei for reliable mass spectroscopy measurements. Some of the results are shown in Fig. 5 for a measurement of signal with only one particle, and Fig. 6 for the total event-counts.

Table 1: Energy Setting Steps for Mass Spectroscopy at CSRe at Isochronous Mode with primary $^{78}\text{Kr}^{28+}$ Beam

Ext. Energy from CSRm (MeV/u)	Bp Conditions	RIBLL2 settings
198.98	$B\rho(^{78}\text{Kr}^{28+}) = B\rho(^{63}\text{Ge}^{32+} _{\text{iso}})$	Passing through
~ 371.71	$B\rho(^{78}\text{Kr}^{36+}) = B\rho(^{63}\text{Ge}^{32+} _{\text{iso}})$	Energy degrader
~ 450.86	$B\rho(^{78}\text{Kr}^{36+}) = B\rho(^{63}\text{Ge}^{32+} _{\text{iso}})$	Energy degrader +Target
~ 499.78	$B\rho(\text{RIB}) = B\rho(^{63}\text{Ge}^{32+} _{\text{iso}})$	Energy degrader +Target

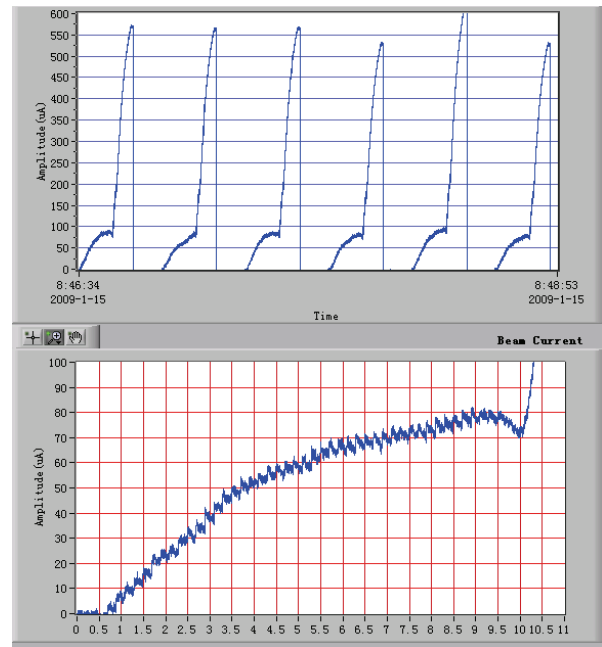


Figure 4: Accumulation, zoomed in the lower graph, and acceleration of $^{78}\text{Kr}^{28+}$ at CSRm.

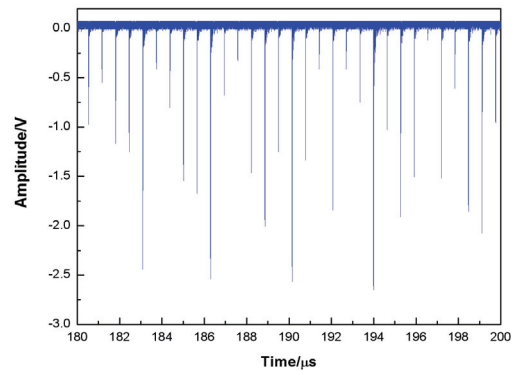


Figure 5: Single particle signal at ToF detector with isochronous mode in CSRe.

FIRST OPERATION OF CSR FOR CANCER THERAPY

The first operation of CSR for cancer therapy was carried out in Mar. 2009. In the treatment phase the stripping injection of carbon beam accumulated with e-cooling was applied for more insurance of current and stability of slow-extracted carbon beam of $\sim 1 \times 10^9$ at CSRm with energy ranged from 100 MeV/u to 250 MeV/u. At the treatment terminal the scan magnets was used for expansion of beam profile, offering an enough field of $\pm 5 \text{ cm} \times \pm 5 \text{ cm}$ with uniformity better than 95% at the multi-leaf collimator. Beam energy was changed passively with energy degrader.

The main results were shown in Fig. 7 for the beam-current measurement from accumulation to slow-extraction, Fig. 8 for extracted beam measured at scintillation detector at the beam line, Fig. 9 for the expansion uniformity of the irradiation field. Fig. 10 shows the 3D and 2D irradiation field distribution.

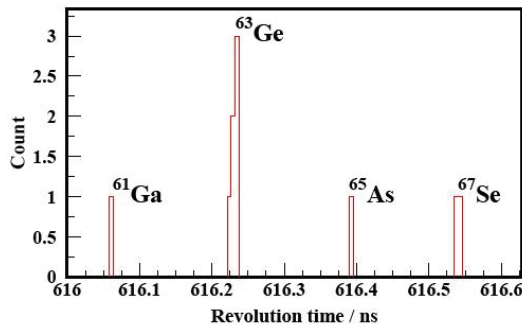


Figure 6: Experiment counts of the aimed target nuclei ^{63}Ge , ^{65}As , ^{67}Se .

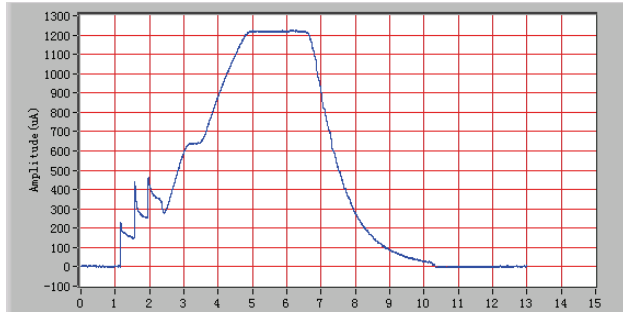


Figure 7: DCCT measurement at CSRm for cancer-therapy operation.

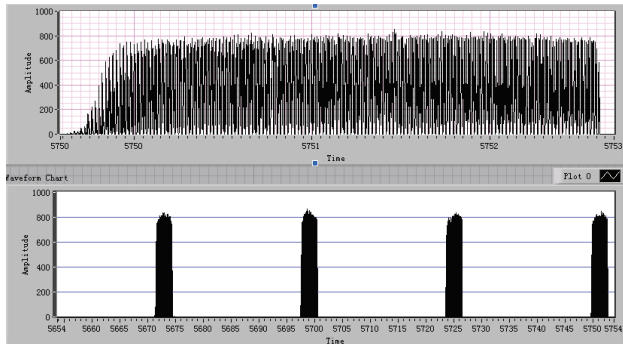


Figure 8: Extracted beam measured at beam line with scintillation detector.

In this operation 6 patients, who were all suffering from recrudescence after normal treatments, with focus-depth of 3-10 cm, were treated and the preliminary clinic results indicated the success of the therapy.

After the treatment several issues were tested. Beam delivering with energy actively changed by CSRm was successfully tested.

The other issue is if the single stripping injection without e-cooling can be enough, efficient and stable for cancer therapy. Fig. 11 shows the positive tested results after optimization. CSR m settings for single stripping injection differ from accumulation mode which requires large accumulation space with dipole magnet fields ~0.5% higher.

CONCLUSIONS AND PROSPECTS

Present commissioning and operation status of HIRFL-CSR were listed in Table 2. From the commissioning and

first operations experiences were gained and concluded as follows.

The first one is the extraordinary performance of stripping injection, especially for our cases with low injection current. Optimized “gain” factors of 25, 150 and 300 were achieved for stored beam with operation modes of single stripping injection, 10 s and no-limit accumulation, respectively, for carbon beam with injection of ~10 μA , which managed to meet the current and emittance requirements of cancer-therapy and other applications.

For cyclotrons the CW-mode is normally not a problem. So it is really flexible to inject and accumulate to the ring at desired repetition rate, depending on the chopper and the injection bumpers. It was also shown a scheme with single stripping injection from a cyclotron like SFC can offer carbon beam with 10^9 pps in a relevant small synchrotron, which can be a possible miniaturized candidate for cancer-therapy.

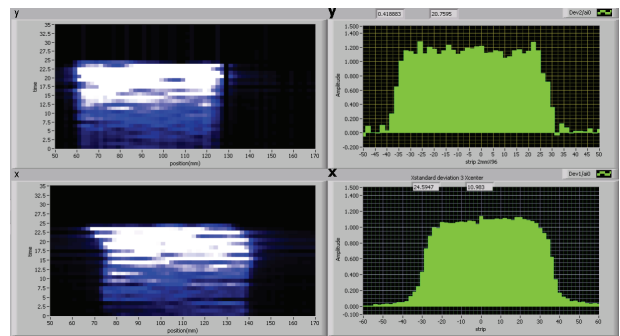


Figure 9: Contour historical (left) and total counts (right) plots for horizontal (up) and vertical (down) scanning for expansion of irradiation field.

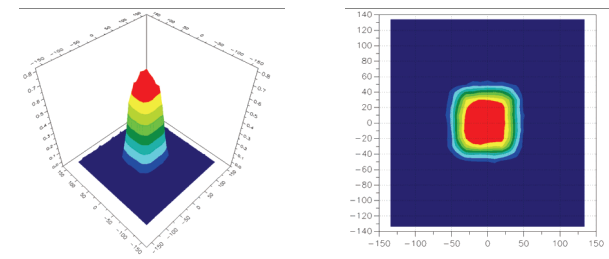


Figure 10: The measured 3D and 2D irradiation field distribution.

Table 2: CSR Commission and Operation Status

Ion	$^{12}\text{C}^{6+}$, $^{36}\text{Ar}^{18+}$, $^{78}\text{Kr}^{28+}$, $^{129}\text{Xe}^{27+}$
Energy	1 GeV/u for C & Ar in CSRm
Intensity	10mA (7×10^9) for C-660MeV/u in CSRm
	1.2mA (4×10^8) for Ar-368MeV/u in CSRm
	0.6mA (1×10^8) for Kr-480MeV/u in CSRm
	0.5mA (1×10^8) for Xe-235MeV/u in CSRm
	15mA (8×10^9) for C-660MeV/u in CSRc
Experiment	RIBs mass-measurement, isochronous mode of CSRc, $\Delta M/M \sim 10^{-6}$

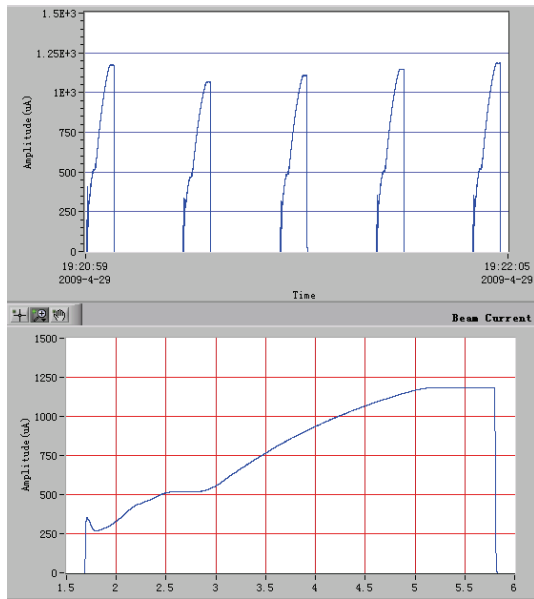


Figure 11: Testing of optimized single stripping injection.

It is shown the RF harmonic-transfer scheme can be applied with high efficiency to simplify the RF of the ring.

It is also clear that if there is a new and more powerful injector besides the present cyclotron injection system the performance of CSR will be great enhanced. Cooperation has been started with IAP, University of Frankfurt, for a dedicated heavy-ion LINAC injector for CSR [5], the first part of which consists of an RFQ and IH-DTLs. Heavy ions with charge to mass ratio from 1:3 to 1:8.5 are to be accelerated to 3.5 MeV/u. In the future it is planned to extend the LINAC to beam energies of up to 10 MeV/u. The main parameters are listed in Table 3, and the layout is shown in Fig. 12. In the HIRFL layout, the position of the new injector can be found in the small hall beside the CSRm cooler, as shown in Fig. 1.

With the new LINAC scheme it is prospected that the injected beam for $^{12}\text{C}^{4+}$ will be increased by 50-100 times. It is hoped that the previous 8-minute accumulation can be shortened to within 5 s. Furthermore, the increased injection current will for sure improve the accumulated beam current. For heavier ions with ~ 1000 times more current will offer much more possibilities at CSR with the new injector. The HIRFL will also gain much flexibility with the multi-injector system.

ACKNOWLEDGEMENTS

The authors wish to thank the international advisory committee members of CSR: N. Angert, V.V. Parkhomchuk, D. Reistad, Y. Yano, T. Katayama, A. Goto, M. Steck, A.N. Skrinsky, J. Xu, S.Fang, and the institutions in cooperation and with much help, among which are the GSI Darmstadt and the BINP Novosibirsk.

Many thanks also to the HIAT committees and the community for giving this opportunity to the CSR commission group.

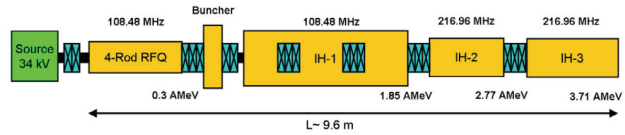


Figure 12: Preliminary LINAC layout.

Table 3: Briefed Parameters of CSR New Injector Scheme

Ion source	Parameters
Super-Conducting 28 GHz ECR	$^{12}\text{C}^{4+}$, $^{40}\text{Ar}^{12+}$, $^{129}\text{Xe}^{27+}$, $^{208}\text{Pb}^{27+}$, $^{238}\text{U}^{28+}$
Beam Current (emA)	0.5 - 1.0
Emittance(π mm mrad)	0.4 - 0.8 (normalized, 90%)
Extraction Voltage (kV)	25 - 40
RFQ	Parameters
Inj. Energy (keV/u)	3 - 5
Ext. Energy (keV/u)	300
Charge-Mass Ratio(q/A)	1/8.5 - 1/3
RF Frequency (MHz)	108.48
Max. RF Power (kW)	250
Ext. emittance (π mm mrad)	< 0.8 (normalized, 90%)
IH-DTL	Parameters
Inj. Energy (keV/u)	300
Ext. Energy (MeV/u)	3.5
Charge-mass Ratio (q/A)	1/8.5 - 1/3
RF frequency (MHz)	108.48/216.96
Ext. Emittance (π mm mrad)	0.8 (normalized, 90%)
Ext. momentum Spread (%)	< ± 0.15

REFERENCES

- [1] J.W. Xia et al, "The heavy ion cooler-storage-ring project (HIRFL-CSR) at Lanzhou", NIMA, 2002, vol. 488, no1-2, pp. 11-25.
- [2] J.W. Xia et al, "Construction and Commissioning of the HIRFL-CSR", Proceedings of APAC 2007, Indore, India, pp.534-538.
- [3] Y. J. Yuan et al, "Present status and future improvement of HIRFL-CSR", Proceedings of EPAC08, Genoa, Italy, pp.388-390.
- [4] X.D.Yang, V.V. Parkhomchuk et al, Proceedings of COOL 2007, Bad Kreuznach, Germany, pp.59-63.
- [5] H. Podlech, U. Ratzinger, A. Schempp, Arbeitsnotiz Nr: IAP-ACCC-090209.

ACCELERATION, DECELERATION AND BUNCHING OF STORED AND COOLED ION BEAMS AT THE TSR, HEIDELBERG

M. Grieser, R. Bastert, K. Blaum, H. Buhr, R. von Hahn, M. B. Mendes, R. Repnow, A. Wolf
 Max-Planck-Institut für Kernphysik, D-69029 Heidelberg, Germany

Abstract

Several experiments at the heavy ion storage ring TSR have shown the feasibility of wide range, efficient acceleration and deceleration. The newly developed method of mass selective acceleration enables an effective separation of ion species with relative mass differences of $\frac{\Delta m}{m} = 3.7 \cdot 10^{-4}$. Parabola shaped short bunch lengths were measured for an electron cooled 50 MeV $^{12}\text{C}^{6+}$ ion beam in the space charge limit. To overcome the space charge limit the TSR was operated at a momentum compaction of $\alpha = 1.57$.

RF ACCELERATION

The heavy ion storage ring TSR, installed at the Max-Planck-Institut für Kernphysik, is used for accelerator, atomic and molecular physics experiments. The TSR storage ring has a circumference of 55.42 m and can receive heavy ions from a 12 MV tandem van-de-Graaff and a normal conducting RF linac combination. Light positive and negative ions with mass to charge ratio $\frac{A}{|q|} \leq 9$ are provided by the high current injector. Heavy positive molecules are available from the Pelletron. Up to now the TSR is mainly used for experiments performed at injection energy. The widely tunable range of the TSR resonator opens up the possibility to accelerate and decelerate ions. Recent experiments have shown the feasibility of acceleration and deceleration. For ramping the magnetic fields the newly developed DAC cards as well a DSP driven synthesizer card were used. The generated functions to ramp the magnets can be directly calculated from the rigidity, taking into account the measured saturation effects of the TSR magnets. The user front end used for the ramp calculation is written in Mathematica. Only with the calculated functions for the power-supply currents and the calculated rf frequency it was possible to accelerate a $^{12}\text{C}^{6+}$ beam from 73.3 MeV to 362 MeV. The measured ion current during this acceleration process is shown in fig. 1. The ion current rises as the revolution frequency is increased during the ramp. From the final rf frequency and the stored ion current at the final energy an efficiency of 98% for the acceleration process can be calculated. The efficiency is the ratio of the ion number reaching the final energy, to the injected ion number. In these tests a record magnetic rigidity for an ion beam in the TSR of 1.57 Tm was achieved, significantly above the rigidity of 1.4 Tm realized in any previous beam time. The ramping time of 7s in the present case was limited by the voltage induced in the correction windings on the iron

Circular Accelerators

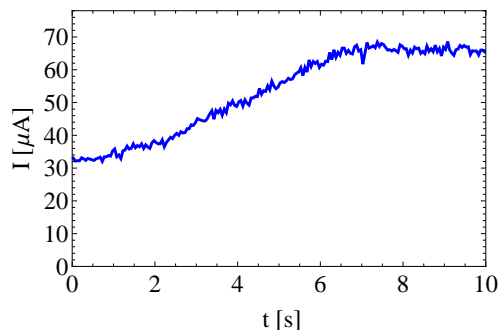


Figure 1: Ion current during acceleration of $^{12}\text{C}^{6+}$ ions from 73.3 MeV to 362 MeV. After 7 s the maximum rigidity of 1.57 Tm was reached.

cores of the TSR main magnets, which had to kept below 6 V for proper operation of the power supplies presently in use. The high efficiency was achieved by pre-cooling the ion beam with the electron cooler before starting the ramp.

Mass Selective Acceleration

Acceleration of molecular ions has been applied in experiments bringing, among others, D_3O^+ beams from 2 MeV at injection to final energies of 4.2 MeV within 2.5 s. Singly charged molecules are produced in a Penning ion source located at the 2 MV terminal of the Pelletron. Besides heavy singly charged molecules, like DCND^+ , the ion source produces several other ion species such as N_2D^+ , DCO^+ etc., with equal masses of 30 u. Due to the fact that the relative mass difference of two neighboring ion species, like DCND^+ and N_2D^+ , is only $\Delta m/m = 3.7 \cdot 10^{-4}$, the desired molecule ions (DCND^+) can neither be separated with the separation dipole of the ion source nor with the magnets of the transferline guiding the ion beam to the TSR ring. The Schottky spectrum of the injected molecular ion beams, taken at the 44th harmonic of the revolution frequency, is shown on fig. 2. The peaks in the spectra correspond to the different ion species. Because the energy of each ion type is the same, given by Pelletron voltage and the ion charge, the frequency splitting $\Delta f/f$ can be calculated, in the non-relativistic approach, with following formula: $\frac{\Delta f}{f} = -\frac{1}{2}(1 + \alpha)\frac{\Delta m}{m}$, where α is the momentum compaction of the storage ring, describing the change of the closed C_0 orbit length by variation the momentum p of the ions: $\alpha = \frac{\Delta C_0/C_0}{\Delta p/p}$. In the standard mode of the TSR the momentum compaction factor $\alpha = 0.1$ results in

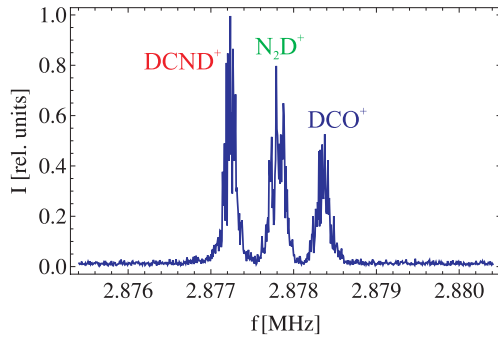


Figure 2: Measured Schottky Spectrum of a molecular ion beam, consisting of three ion species with a mass of 30 u.

a frequency splitting of 581 Hz at $f=2.878$ MHz, shown in fig. 2. The width of each peak in the spectrum is determined by the momentum spread ($\sigma_p/p \approx 3 \cdot 10^{-5}$) of the injected beam, which is quite small, yielding in a clear separation of the mass peaks. With mass selective acceleration the desired ion species, for example DCND^+ , can be separated from the other type of ions. The procedure is explained in fig. 3. Mass selective acceleration can be described in the longitudinal phase space, defined by the frequency deviation $\Delta f_0 = f_0 - f_s$ and phase deviation $\Delta\phi = \phi - \phi_s$ of an ion, with a revolution frequency f_0 and rf phase ϕ . The revolution frequency of the synchronous particle is given by f_s and its rf phase is ϕ_s . After multiturn injection, which takes place at a resonator voltage of $U = 0$, three frequency bands are formed in the phase space (fig. 3 a). The width of each frequency band is given by the measured momentum spread of the injected beam. After injection the resonator

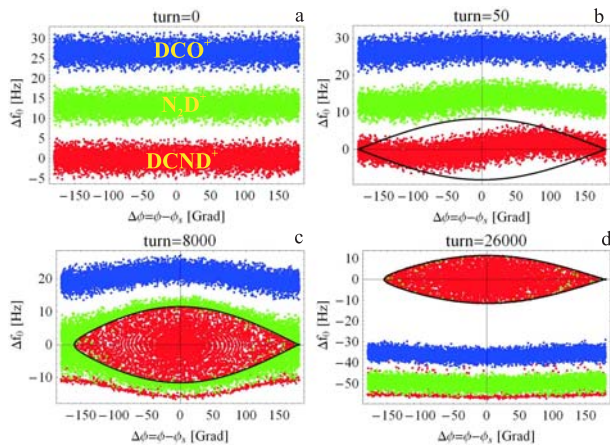


Figure 3: Illustration of mass selective acceleration in the longitudinal phase space. The size of the separatrix given by the resonator voltage and synchronous phase is shown as a black curve.

voltage was increased linearly in 1.5 ms to $U = 10$ V, capturing the stored ion beam into the rf bucket, enclosed by the separatrix (compare fig. 3 b). To accelerate the ions, the synchronous phase was increased from 0° to 1° . In

Circular Accelerators

the calculation a time of 200 ms was used to simulate the shift of the synchronous phase. In the experiment the same shift was carried out in 0.5 s, by changing the derivative of the rf frequency $\frac{df}{dt}$ from 0 to 0.45 MHz/s, following the magnetic rigidity $B\rho$ of the DCND^+ ion beam. The longitudinal phase space during the synchronous phase shift is displayed in fig. 3 c. At turn=26000 displayed in fig 3 d the synchrotron phase is already 1° . The ions outside the bucket, created in the bunching process (fig 3 b), taking place during the first 1.5 ms, are not accelerated and keep their energy. In fig. 3 c the rf bucket, filled with DCND^+ ions, moves through the N_2D^+ ion beam without capturing a N_2D^+ ion. There are only a few N_2D^+ ions inside the DCND^+ bucket, caused by the bunching process taking place in the first 1.5 ms. To avoid a trapping of any undesired ions, the resonator voltage has to be slightly decreased. Due to the small energy spread of the injected ion beam a reduction of the resonator voltage is possible. However, a small energy drift of the Pelletron will cause an energy error that cannot be balanced by the bucket size if the resonator voltage is decreased. In fig. 3 c,d it can be seen that some DCND^+ ions are not captured in the bucket, because the resonator voltage was increased too fast. For that low ion beam velocity $\beta = 0.012$ a slower voltage increase (≥ 5 ms instead of 1.5 ms) would be more adequate. During the acceleration process the energy difference of the ion bucket to the non accelerated undesired ions is increasing with time. Since the magnetic field of the storage ring is matched to the DCND^+ ions, the false ions will hit the vacuum chamber of the storage ring during the acceleration process, due to the limited momentum acceptance of the storage ring. After 2 s acceleration time a pure DCND^+ ion beam reaches the final energy of $E=3$ MeV. At this energy the neutral reaction products from collisions

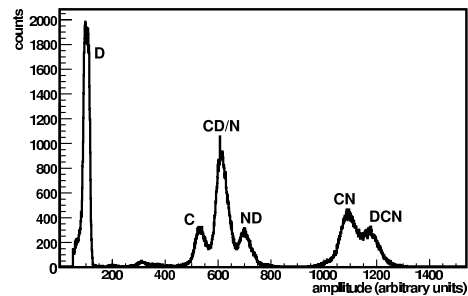


Figure 4: Pulse height spectrum of a finely segmented surface barrier detector for neutral fragments from reactions of DCND^+ with residual gas. The spectrum shows peaks corresponding to mass 2, 12, 14, 16, 26 and 28. Coincident pulses yield a sum of up to mass 30 (DCND).

of DCND^+ with residual gas (mostly H_2) were observed using a finely segmented, energy-sensitive surface barrier detector. These collisions lead to dissociation into neutral and charged or only neutral fragments. The corresponding pulse height spectrum is shown in fig. 4. Changing the rf

start frequency to an integer multiple of the revolution frequency of the simultaneously stored N_2D^+ or DCO^+ beam allows to separate also N_2D^+ or DCO^+ ions.

Deceleration

In a first test devoted to the deceleration of highly charged ions, a reduction of the beam energy by a factor of > 6 , from 73.3 MeV to 11.8 MeV (1 MeV/u), could be achieved readily with an efficiency of 68%, corresponding to a rigidity decrease from 0.71 Tm to 0.28 Tm. Formerly deceleration tests using the rf-booster were much more difficult and resulted in beam losses of several order of magnitudes. This feature now considerably widens the operating range with highly charged ions, produced at the MPIK accelerators, for new stored ion beam experiments planned at the TSR.

SHORT ION BUNCHES

For efficient ion beam deceleration small initial longitudinal bunch lengths, obtained by bunched beam electron cooling, are required. Even smaller longitudinal bunch lengths are necessary for experiments with a reaction microscope in a storage ring. Tests therefore were performed with 50 MeV $^{12}C^{6+}$ ion beams using the 6th harmonic for bunching. A bunched ion beam profile obtained with simultaneous electron cooling, measured with a capacitive pick-up, is shown in fig. 5. The intensity of the $^{12}C^{6+}$ ion beam with $E = 50$ MeV used for this measurements was $I = 45 \mu A$. The resonator voltage was set to 795 V. Also shown in fig. 5 is a parabola fit function (red line),

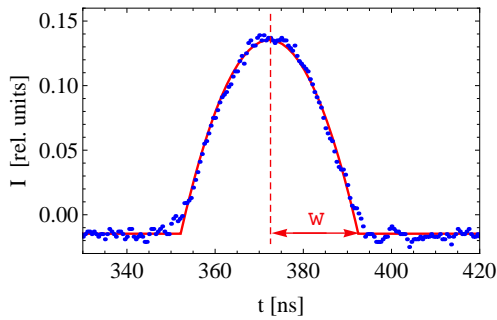


Figure 5: Measured electron cooled longitudinal ion beam ($^{12}C^{6+}$, $E = 50$ MeV) profile. The width of the parabola profile is defined by w .

which represents the data very well. A bunch length, defined in fig. 5, of $w = 20$ ns can be obtained from the fit. This bunch length is space charge limited. In the space charge limit the voltage of the resonator $U_i(\Delta\phi) = U \sin(\Delta\phi + \phi_s)$ each ion is passing through is compensated by the longitudinal space charge voltage of the ion beam. For bunching, in the TSR standard mode, where the slip factor $\eta = \frac{\Delta f_0/f_0}{\Delta p/p}$ is positive, the synchronous phase

Circular Accelerators

used for bunching is $\phi_s = 0$, where f_0 is the revolution frequency of an ion and p describes its momentum. Because the synchrotron oscillation is a very slow process compared to the revolution time, the longitudinal electrical field $E_{||}(\Delta\phi)$, seen by one ion, can be assumed to be constant during one turn and the space charge voltage can be defined by $U_s(\Delta\phi) = E_{||}(\Delta\phi) \cdot C_0$, where C_0 denotes the circumference of the storage ring. The ion phase $\Delta\phi$ is related to the longitudinal position s in the bunch: $\Delta\phi = -\omega \frac{s}{v_s}$, where ω is the angular position frequency of the resonator and v_s the velocity of the synchronous particle, located in the center of the bunch at $s=0$. Ions in front of the synchronous particle ($s > 0$) arrive at the resonator gap earlier than the synchronous one, therefore there is a negative sign in the formula. The longitudinal electrical field $E_{||}(s)$ can be calculated from the charge line density $\lambda(s)$ of the bunch by the following formula [1]:

$$E_{||}(s) = -\frac{1 + 2 \ln(\frac{R}{r})}{4\pi\epsilon_0\gamma^2} \frac{\partial\lambda(s)}{\partial s}. \quad (1)$$

The constant ϵ_0 is the absolute permittivity and γ is the relativistic mass increase (for TSR energies $\gamma = 1$). R denotes the radius of the beam tube ($R = 0.1$ m) and r is the average beam radius, defined by twice the two σ_r value ($r = 2\sigma_r$) of the transverse beam width. A parabola density profile is the only longitudinal charge line distribution, for an electron cooled ion beam with $\Delta\phi \ll 2\pi$ ($\sin(\Delta\phi) = \Delta\phi$), which compensates the resonator voltage $U_i(\Delta\phi)$ for each ion, independent of its phase $\Delta\phi$. The parabola charge line density $\lambda(s)$ can be calculated from the number N_B of particle in the bunch:

$$\lambda(s) = \frac{3N_B Q}{4w_s} \left(1 - \frac{s^2}{w_s^2}\right) \quad (2)$$

for $|s| \leq w_s$, with $\int_{-w_s}^{w_s} \lambda(s) ds = N_B \cdot Q$. The charge of an ion is Q and w_s describes the bunch length in meters, related to the bunch length w in seconds, $w_s = v_s \cdot w$, defined in fig. 5. If $U_i(\Delta\phi)$ is completely compensated by the space charge voltage $U \cdot \sin(\Delta\phi + \phi_s) + E_{||}(\Delta\phi) \cdot C_0 = 0$, the synchrotron oscillation of each particle in the bunch is frozen. This condition leads finally to the longitudinal space charge limit. For a beam, having a parabola longitudinal charge line density, the space charge limit is given by following formula:

$$w = C_0 \sqrt[3]{\frac{3(1 + 2 \ln(\frac{R}{r}))I}{2^4 \pi^2 c^4 \epsilon_0 \gamma^2 h^2 \beta^4 U}}. \quad (3)$$

The bunch length w in formula (3) is determined by the beam intensity I , the resonator voltage U , the number of bunches h in the ring and the beam velocity β in units of the speed of light c . If the space charge voltage $|U_s(\Delta\phi)|$ of the ion beam were larger than $|U_i(\Delta\phi)|$, the magnitude $|\Delta\phi|$ of each ion would increase by the repelling space charge force, resulting in an increase of the bunch length. On the

other hand a larger bunch has a smaller space charge voltage $|U_s(\Delta\phi)|$, thus the ion starts to oscillate. These oscillations $\Delta\phi$ will be damped by the electron cooler, bringing back the beam to the space charge limit. Therefore an electron cooled ion bunch in the space charge limit is stable. With an average transverse beam size $\sigma_r=1$ mm, the bunch length w can be calculated. Fig. 6 shows the measured bunch length w as a function of resonator voltage U as well the theoretical prediction (red curve). As it is shown in fig. 6 the calculated function agrees very well with the fit to the data ($w \sim U^{-0.34}$), blue line. At the

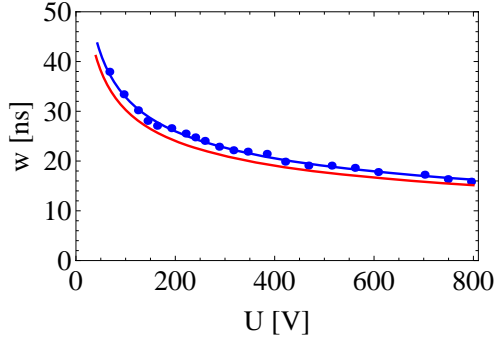


Figure 6: Measured bunch length w for an electron cooled $^{12}\text{C}^{6+}$ ion beam ($E = 50$ MeV, $I = 20$ μA) as a function of the resonator voltage. The red curve is a calculation, where formula (3) was used.

same number of bunches $h = 6$, the bunch length w was measured as a function of the beam intensity, shown in fig.7. The resonator voltage used in these measurements was $U = 795$ V. A fit through the data, blue curve, gives an exponent of 0.31, which is slightly less than the predicted value of $1/3$. Furthermore the bunch length w was

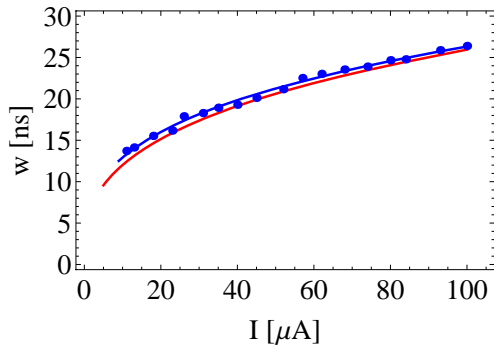


Figure 7: Measured bunch length for an electron cooled $^{12}\text{C}^{6+}$ ion beam as a function of the ion intensity. The resonator voltage used in this measurement was $U = 795$ V. The red curve is a calculation using formula (3).

measured as a function of the rf frequency for a $^{12}\text{C}^{6+}$ ion

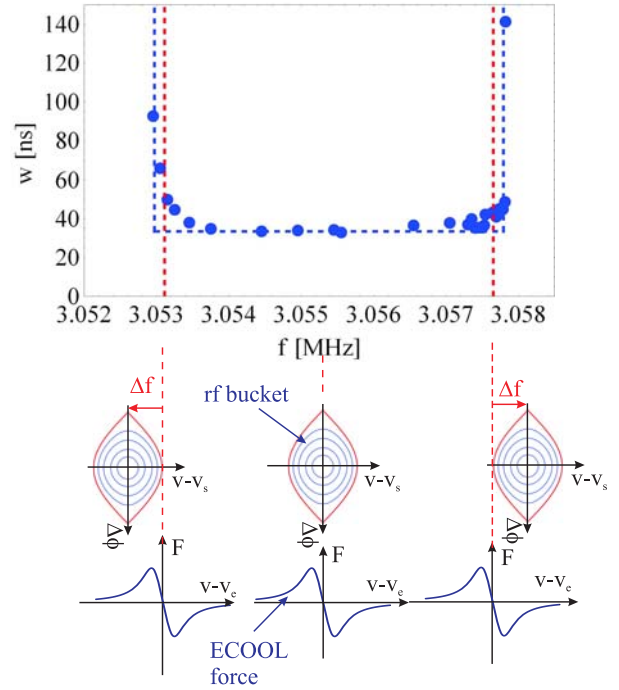


Figure 8: Measured bunch lengths for an electron cooled $^{12}\text{C}^{6+}$ ion beam as a function of the rf frequency f . Also shown is the explanation of the bunch length increase at large frequency shifts.

beam with $E = 50$ MeV. The result of these measurements are displayed in fig. 8. The voltage used in this measurement was $U = 96$ V and the ion current was $I = 20$ μA . As it can be seen in fig. 8 the bunch lengths are constant, around $w = 33$ ns, in a relatively wide frequency range. On the borders the bunch lengths are increasing rapidly. There is a deviation from the parabola bunch shape if the bunch length is larger than $w = 90$ ns. Outside the boundaries, blue marked vertical lines in fig. 8, there are no observed ion bunches. This behavior can be explained also with fig. 8. If the rf frequency f is changed, the velocity v_s and the revolution frequency f_s of the synchronous particle, which has to fulfill the equation $f = h \cdot f_s$, is modified. This means that the rf bucket, where the synchronous particle is sitting in the center ($v = v_s$), is shifted with respect to the velocity v_e of the electron beam. The cooling force of the electron cooler tries to shift the ion velocity v to the electron velocity v_e . If the electron velocity v_e comes to the outside of the rf bucket no bunching is possible, due to the missing closed orbits in the longitudinal phase space around the synchronous particle. The experimental values found for the two limits are $\Delta f_l = \pm 2.37$ kHz, which is close to the bucket height $\Delta f_b = 2.27$ kHz calculated with: $\Delta f_b = \frac{1}{C_0} \sqrt{\frac{2|\eta|hQU}{\pi m}}$, where m is the mass of an ion. In fig. 8 the bucket size (red lines) are also shown. The small frequency difference between the vertical blue and red dashed lines can be explained by the momentum

spread of the stored ion beam.

Bunch Lengths at Negative η

The ion bunch length can be decreased by increasing the resonator voltage U or by decreasing the intensity I of the stored ion beam. But for both quantities there are practical limits. The intensity limit is given by the experimental requirements, whereas the voltage is limited by the maximum voltage of the resonator, which should not exceed in our case 5 kV. To decrease the bunch length further the space charge limit has to be overcome. Because the synchrotron frequency f_{sy} fulfills the following relation: $f_{sy} \sim \sqrt{\eta \cos(\phi_s)}$, bunching is done at $\phi_s = \pi$ for $\eta = \frac{\Delta f_0/f_0}{\Delta p/p} < 0$, to obtain a real synchrotron frequency. If the beam is bunched at $\phi_s = \pi$, the voltage $U_i(\Delta\phi)$, seen by one ion, has the same sign as the space charge voltage, thus the space charge of the ion beam $U_s(\Delta\phi)$ cannot compensate $U_i(\Delta\phi)$. A negative η parameter means that particles with larger momentum than the central particle need more times T ($T = 1/f_0$) for one turn compared to the central one. A negative slip factor η can be achieved by increasing the length of the closed orbit for an ion having a positive momentum deviation. The length of the closed orbit C_0 can be described by the momentum compaction α of the storage ring, defined in the subsection mass selective acceleration. To avoid the space charge effect, the TSR was set to $\alpha=1.57$, which is consistent with $\eta = -0.57$, for 50 MeV $^{12}\text{C}^{6+}$ ions. An α parameter of 1.57 results in an average dispersion $\bar{D}_x = 13.8$ m in the TSR main dipole magnets. At this setting bunch length measurements for an electron cooled 50 MeV $^{12}\text{C}^{6+}$ ion beam were performed. A longitudinal ion bunch profile taken at a beam intensity of $I = 1.3 \mu\text{A}$ and at a rf frequency $f=3.053$ MHz is shown in fig. 9. In contrast to the profile measured at the space

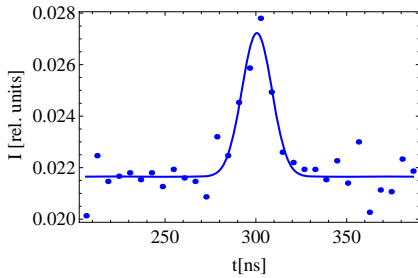


Figure 9: Measured ion bunch profile ($I = 1.3 \mu\text{A}$) at $\eta = -0.57$. A resonator voltage of 10 V was selected.

charge limit, this profile can be described with a Gaussian distribution. At the intensity of $I = 1.3 \mu\text{A}$ a beam width $\sigma=8$ ns was determined. The measured beam widths σ as a function of the rf frequency f for different resonator voltages U are shown in fig. 10. After the measurements at resonator voltages of $U=10$ V and $U=19$ V the electron energy was increased slightly, resulting in a shift of the red

Circular Accelerators

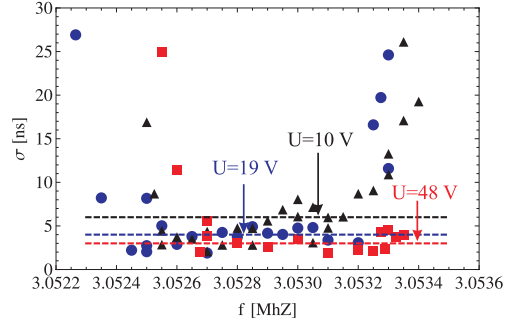


Figure 10: Measured bunch length as a function of the rf frequency f at $\eta = -0.57$. The beam intensity was between 0.5-1.5 μA .

data points to higher frequencies compared to the measurements at 10 V and 19 V. As it can be seen in fig. 10 the bunch length σ decreases with the applied resonator voltage U . At $U=48$ V bunch lengths of $\sigma \approx 3$ ns were measured. To compare this Gaussian bunch length σ with the parabola bunch length w obtained at the space charge limit, the parabola bunch length has to be converted to a corresponding length σ_w of a Gaussian distribution, having the same half width. A parabola and a Gaussian distribution have the same half width if the relation: $\sigma_w = \frac{w}{2\sqrt{\ln(2)}}$ is fulfilled. For 50 MeV $^{12}\text{C}^{6+}$ ions the space charge limit is given by: $w[\text{ns}] = 62.1 \frac{I[\mu\text{A}]^{0.31}}{U[\text{V}]^{0.34}}$. This equation gives for $I = 0.5 \mu\text{A}$ and $U=48$ V a corresponding Gaussian bunch length $\sigma_w=8$ ns, which is a factor 2.7 larger than the measured bunch length ($\sigma \approx 3$ ns) at $\eta = -0.57$.

CONCLUSION AND OUTLOOK

Ramping of the TSR storage ring is now routinely used to accelerate a stored ion beam to the rigidity limit of the storage ring. With the method of mass selective acceleration simultaneously stored ion species with relative mass differences down to $\frac{\Delta m}{m} = 3.7 \cdot 10^{-4}$ can be separated. For a bunched electron cooled ion beam ($^{12}\text{C}^{6+}$, $E = 50$ MeV), a bunch length of $w = 3.1$ ns at $h = 6$ and $I = 0.1 \mu\text{A}$ can be anticipated in the TSR standard mode ($\eta > 0$), sufficient for the experiments with an internal gas jet target and a reaction microscope. To overcome the space charge limit the TSR was operated at a momentum compaction of $\alpha = 1.57$. In this mode shorter bunch lengths compared to the standard mode were achieved, if the same intensity and resonator voltage U are used. But currently the maximum voltage which can be applied to the beam, at $\eta = -0.57$, was limited to approximately $U \approx 50$ V. At higher resonator voltages almost no storage of a cooled bunched ion beam was possible. To improve this situation further investigations are necessary.

REFERENCES

- [1] A. Hofmann, CERN yellow report, CERN 77-13, page 143 (1977).

REVIEW ON HI ACCELERATOR FOR HADRONTHERAPY

K. Noda

National Institute of Radiological Sciences, Chiba, 263-8555 Japan

Abstract

Heavy-ion beams have attractive growing interest for cancer treatment owing to their high dose localization at the Bragg peak as well as high biological effect there. Recently, therefore, heavy-ion cancer treatments have been successfully carried out at various facilities and several construction projects for the facility of the heavy-ion therapy have also been progressing in the world, based on the development of accelerator technologies.

INTRODUCTION

Heavy-ion beams are very suitable for treatment of deeply seated tumours, because of the excellent physical dose localization and a high LET characteristic around the Bragg peak, which was supported by the prospective results of heavy-ion research work at LBNL [1]. The National Institute of Radiological Sciences (NIRS) decided to carry out heavy-ion therapy based on the 20 years experience of radiotherapy with protons and neutrons. The HIMAC project [2] had been progressed since 1984, as one of the major projects of "Comprehensive 10 years Strategy for Cancer Control" promoted by Japanese government. The HIMAC facility was completed in October 1993 as the world's first heavy-ion accelerator dedicated to medical use. Since June 21, 1994, at NIRS, more than 4,500 patients have been treated, and the clinical efficiency of carbon-ion radiotherapy has been demonstrated for various diseases. With stimulating results of the HIMAC treatment, therefore, various facilities in the world have carried out the heavy-ion cancer therapy, and several projects have also been progressing. This report reviews the heavy-ion accelerator facility for the cancer therapy and the related development of accelerator and beam-delivery technologies.

PROGRESS OF HIMAC

We have continuously developed the accelerator and beam-delivery technologies for the cancer therapy and the related research fields.

Development of Beam-Delivery Method

Respiration-gated irradiation

Damage to normal tissues around tumour was inevitable in treatment of a tumour moving along with respiration of a patient. A respiration-gated irradiation system with the broad-beam method [3], therefore, which can respond quickly to irregular respiration, was developed. In this system, the irradiation-gate signal is generated only when target is at the design position and the synchrotron can extract a beam. The beam is

delivered by the RF-KO extraction method [4], according to the gate signal. This method has been applied to liver, lung and uterus cancers since February 1996. Fig. 1 shows the view of irradiation gated with respiration.

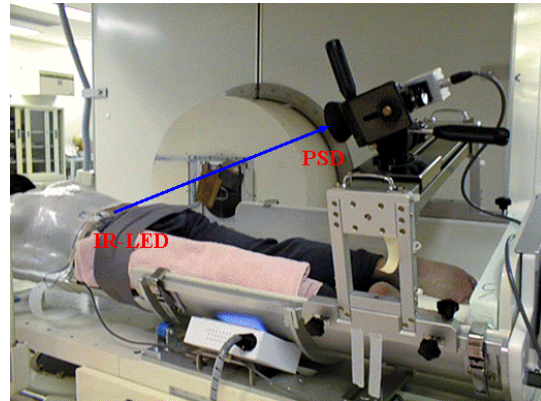


Figure 1: The view of irradiation gated with respiration using the horizontal irradiation port.

Layer-stacking Irradiation

In a conventional broad-beam method, the fixed SOBP (Spread-Out Bragg Peak) produced by a ridge filter results in undesirable dosage to the normal tissue in front of target, because the width of an actual target varies within the irradiation field. In order to suppress the undesirable dosage, thus, the layer-stacking irradiation method was proposed [5] and experimentally verified [6,7], which has been routinely utilized.

This method is to conform a variable SOBP to a target volume by controlling dynamically the conventional beam-modifying devices. The target volume is longitudinally divided into slices, and the small SOBP with several mm in WEL, which is produced by a single ridge filter, is longitudinally scanned over the target volume in a stepwise manner. Changing an aperture of the MLC (Multi Leaf Collimator) dynamically, on the other hand, a lateral dose distribution of each slice is conformed according to a cross-sectional shape of each slice.

Development of Accelerator Technology

RF-KO Slow-Extraction Method

We developed the RF-KO slow extraction method for a respiration-gated irradiation system. The RF-KO method has a huge ripple of kHz order in time structure of the extracted beam (spill) due to the coherency in its extraction mechanism. However, the huge spill ripple has never disturbed the dose distribution in the beam-wobbling method, while it disturbs in the beam-scanning

Applications and Ancillary Systems

method, because the disturbance magnitude depends on the difference between the ripple and wobbling frequencies. Thus we developed the dual FM method and separated function methods [8] in order to significantly suppress the spill ripple. Furthermore, we have also developed the method to suppress a fluctuation of Hz order in the time structure by optimizing AM function of the RF-KO system [9].

A beam-spill control system has been developed [10], based on the improvement of the time structure in the spill as mentioned above. The core part of this system requires the following functions: 1) calculation and output of AM signal according to request-signals from an irradiation system, 2) real-time processing with a time resolution less than 1ms, and 3) feed-forward and feedback controls to realize the extracted intensity as requested. This system allows us to control dynamically the beam intensity almost as required, as shown in Fig. 2.

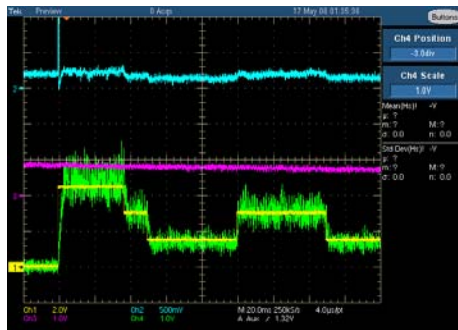


Figure 2: Time structure of extracted beam obtained by the spill control system. Spill time structure (green) can be modulated by request signal (yellow).

Control of Beam Profile and Position

In order to deliver the beam with the desired profile and positions at a target through a beam-transport line, it has been essential to match the beam-optical parameters with those at an extraction channel of the ring. For the optical matching, thus, we developed an accurate prediction method of the optical parameters at the extraction channel through an outgoing-separatrix estimated by a rod-monitor measurement [11]. As a result of the experiment, it was verified that the predicted beam-optical parameters was in good agreement with the measured ones.

Intensity Upgrade

In order to increase the delivered beam intensity, the optical-parameter matching in the vertical direction was carried out in a flat-base of the synchrotron-operation cycle. As a result, the vertical emittance was decreased to 15 from 33 π -mm-mrad before matching. Increasing the beam intensity in the ring, we observed a large beam loss due to the space-charge effect. Since the vertical tune of 3.13 is close to an integer resonance due to the incoherent tune-shift under high ion density after bunching, we changed it to 3.23. Even in this tune,

however, the 3rd-order coupling resonance ($Q_x + 2Q_y = 10$) caused a large beam loss. We thus tested the resonance correction by using four sextupoles. After the correction, the beam lifetime was increased by more than 5 times under $(Q_x, Q_y) = (3.74, 3.23)$. An un-tuned RF-cavity, further, having a Co-based amorphous core, has been developed so as to make multi-harmonics operation possible for reducing the longitudinal space-charge effect [12]. By the multi-harmonics operation, the beam intensity was increased by 40% [13]. As a result of studies mentioned above, more than 2×10^{10} carbon ions can be delivered to the iso-center with one operation cycle of the ring.

New Treatment-Facility Project

New 3D Scanning for Both Moving and Fixed Targets

For further development of the HIMAC treatment, we have developed a 3-D scanning method for a moving target as well as a fixed one. As a feasible solution, we found the respiration phase controlled rescanning (PCR) [14]. In the PCR method, the rescanning completes the irradiation on one slice during one gated period. Since the movement of the target is close to “zero” on average, thus, we can obtain the uniform dose distribution even under the irradiation on the moving target. The PCR method has required mainly two technologies: 1) Intensity-modulation technique for a constant irradiation time on each slice having a different cross section, and 2) Fast-scanning technique for completing several-times rescanning within a tolerable irradiation time [14].

Design of new treatment facility

Based on the development of the PCR method, the new treatment facility has been designed and being constructed, as shown in Fig. 3. The facility is connected with the upper synchrotron of HIMAC. In the treatment hall, placed underground of the facility, three treatment rooms are prepared in order to treat more than the present number of patients at the existing HIMAC treatment. Two of the treatment rooms are equipped with both horizontal and vertical fixed beam-delivery systems, and the other one is equipped with a rotating gantry. Two treatment-simulation rooms are also equipped for obtaining CT-image for a treatment planning and for patient positioning as a rehearsal. Furthermore, there are six rooms devoted for patient preparation before irradiation.

In the new treatment facility, the maximum ion energy is designed to be 430 MeV/n in the fixed beam-delivery system in order to obtain the residual range of around 30 cm in a ^{12}C beam and more than that 22 cm in an ^{16}O beam. The maximum lateral-field and SOBP sizes are 25 cm \times 25 cm and 15 cm, respectively, so as to cover almost all treatment needs with the HIMAC [15]. On the other hand, the rotating gantry system has a maximum energy of 400 MeV/n, a maximum lateral-field of 15 cm

× 15 cm and a maximum SOBP size of 15 cm, in order to downsize the rotating-gantry size and weight.

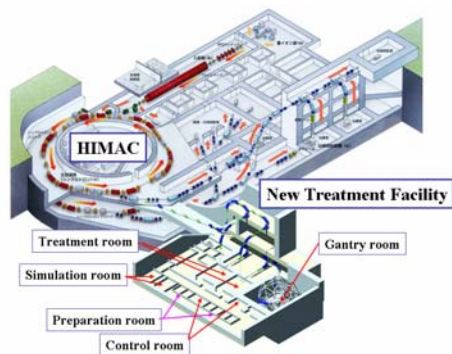


Figure 3: Schematic view of the new treatment facility.

A rotating gantry employs also the PCR method [16] in order to increase significantly treatment accuracy for a tumour located close to a critical organ through the multi-field optimization method [17]. Further, the rotating gantry can reduce considerably patient stress due to the face-downward attitude while the patient is positioned. It is important for the gantry design to avoid any change of the beam size depending on the rotation angle. Thus, we will adapt a compensation method of the asymmetric phase-space distribution [18]. This method is based on multiple scattering by a thin foil placed at the position with the optimum beam-optical parameters in the BT line. Further, the final dipole magnet is divided into 30° and 60° magnets, and two scanners are placed between the two dipole magnets in order to extend the effective length from the scanners to the iso-center. The total weight of the rotating-gantry system is around 350 tons.

HEAVY ION FACILITY IN THE WORLD FOR CANCER TREATMENT

Asia

Hyogo Ion Beam Medical Center

This facility has treated 2,339 patients to October 2008 from May 2001, with both proton and carbon beams. A utilization ratio of proton and carbon are 82% and 18%, respectively. An accelerator complex consists of two ECR ion sources, an injector linac cascade (RFQ and Alvarez linacs) and a separated function synchrotron, which was designed based on the HIMAC one. Output energy is variable and the maximum values are 230 MeV and 320 MeV/n for protons and carbon ions, respectively. A residual range in water is 30 cm for protons and 20 cm for carbons. There are two rotating gantries for protons, and three treatment rooms are prepared for carbons; a horizontal, a vertical and a 45° beam lines for each room.

Applications and Ancillary Systems

Gunma University Heavy Ion Medical Center

For the purpose of widespread-use of carbon-ion radiotherapy in Japan, the NIRS designed a standard type of carbon-ion radiotherapy system [15] so as to reduce the construction cost. Based on the design study, the Gunma University has been constructing the standard-type facility since 2006 and the first patient will be treated in FY2009. This facility consists of an ECR ion source, an RFQ and an APF-IH linac, a synchrotron ring, three treatment rooms and one experimental room for basic researches. In this facility, a C⁴⁺ beam, which is generated by the compact 10 GHz ERC source, is accelerated to 4 MeV/n through the injector linac cascade. After fully stripped, the C⁶⁺ beam is injected to the synchrotron by the multi-turn injection scheme and is accelerated to 400 MeV/n at maximum. All the magnets in the beam transport lines are made of laminated steel in order to change the beam line quickly within one minute. The beam-delivery system employs a spiral beam-wobbling method [19] for forming a uniform lateral dose distribution with a relatively thin scatterer. The facility size is downsized to be one-third of the HIMAC facility. An image view of the Gunma-University facility with installed equipments is shown in Fig. 4.

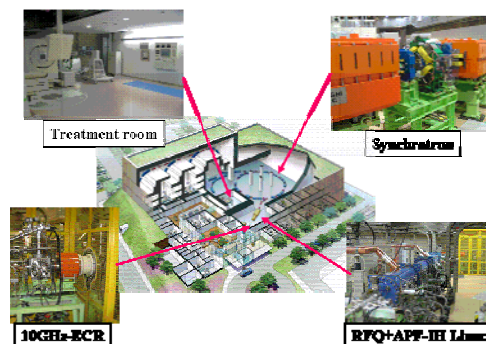


Figure 4: An image view of Gunma facility with installed equipments.

Institute of Modern Physics in China

The Institute of Modern Physics (IMP) in China, using a carbon beam with 100 MeV/n from a tandem of heavy-ion cyclotrons (SFC and SSC) [20], has already treated 103 patients with superficially-placed tumours since Nov. 2006. As a good result of these treatments, the treatment of deeply-seated tumour started successfully since March 2009, with a carbon beam having 400 MeV/n from CSR (Cooling Storage Ring). A C⁴⁺ beam with 7 MeV/n from the cyclotron is injected to CSR [20] by the charge-exchange injection method. After being stacked by the cool-stacking method, the beam is accelerated to a desired energy. The CSR can accelerate a C⁶⁺ beam to 1000 MeV/n at maximum and deliver to the beam intensity of 2×10⁹ pps at maximum.

Other projects in Asia

China has several projects of the heavy-ion therapy, except for the IMP. One of them is the Shanghai project,

which will construct the Siemens machine as described in the later section. The EMIT (Energy Modulation Ion Therapy) facility, which has rapid cycle proton and carbon synchrotron rings, was designed by IHEP group. Taiwan also has a plan to construct the standard-type carbon facility in Japan, collaborating with the NIRS.

In Japan, the Saga and Kanagawa projects were approved by their prefectural governments and they started the conceptual design based on the standard-type carbon-therapy facility.

Europe

In Europe, the EULIMA (European Light Ion Medical Accelerator) project was started in 1987 by the European Commission and proposed carbon-ion radiotherapy with the different 400 MeV/n accelerators: a superconducting cyclotron and a synchrotron ring [21]. Unfortunately, this project has never been realized. The GSI pilot project has begun in 1993 and carries out fixed target treatments since 1997. The GSI pilot project brought the construction of the HIT (Heidelberg Ion Therapy) facility. On the other hand, the PIMMS (Proton and Ion Medical Machine Study) project was also started in 1996. Based on the modified PIMMS design by the PMMS/TERA project, the construction of the CNAO (Centro Nazionale di Adroterapia Oncologica) facility is being constructed since 2003.

GSI/HIT Project

Since 1997, the GSI has successfully carried out the cancer treatments of around 400 patients with a ^{12}C beam from SIS with applying the intensity controlled raster-scanning method. Based on the developments and experiences of the GSI, the HIT facility, which is a hospital based light ion accelerator facility for the clinic in Heidelberg, has been proposed and been being constructed [22]. In the HIT project at the present, almost all beam commissioning has been successfully completed, and the first patient will be treated this autumn.

The HIT facility consists of two ECR ion sources, a RFQ and IH linac cascade, a synchrotron ring and two treatment rooms with a horizontal beam-delivery system and one rotating gantry. Light ions (p, He, C, O) generated by ECR sources are accelerated to 7 MeV/n by the RFQ and IH linac cascade and are injected to the synchrotron. The ions slowly extracted by the RF-KO method are delivered to each treatment room. The residual range of C^{6+} ions is designed to be 30 cm at maximum, which corresponds to 430 MeV/n. The main characteristics of this facility are the application of the raster-scanning method with active variation on intensity,

energy and beam-size both in two treatment rooms and in the rotating gantry. The facility layout is schematically shown in Fig. 5.

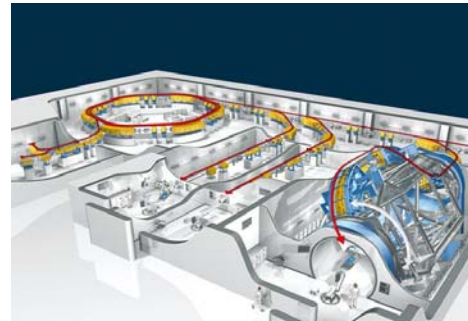


Figure 5: Layout of the HIT facility.

The developed technologies have been transferred to Siemens. Siemens has carried out a cost-reduction program, while keeping its performance, and has constructed the complete therapy unit in both Marburg and Keil Universities, Germany. Further, Siemens has already made a contract with the Shanghai project. In these projects, 45° beam line is employed, instead of a rotating gantry.

CNAO Project

The Italian hadron-therapy centre CNAO is presently under construction in Pavia, Italy. The CNAO project will be devoted to the treatment of deeply-seated tumours with proton and carbon beams and to clinical and radiobiological research [23]. The CNAO accelerator is designed based on the modified PIMMS. The facility consists of two ECR ion sources, a 7 MeV/n injector linac cascade designed by GSI and a 400 MeV/n synchrotron ring. The CNAO synchrotron consists of two symmetric achromatic arcs connected by two dispersion free straights and has a circumference of approximately 78 m. The maximum energy of the ions is 400 MeV/u. The extraction scheme employs both the acceleration-driven and RF-KO methods under the third-order slow extraction condition. In the final phase the CNAO project will have 5 treatment rooms (3 rooms with fixed beams and 2 rooms with gantries) and one experimental room. In the first phase, three treatment rooms will be equipped with 4 fixed beams, three horizontal and one vertical line. As a beam-delivery method, the CNAO will employ the active scanning that has been developed at GSI. At present, the commissioning of the injector part has been carried out. A schematically view of the CNAO facility is shown in Fig. 6.

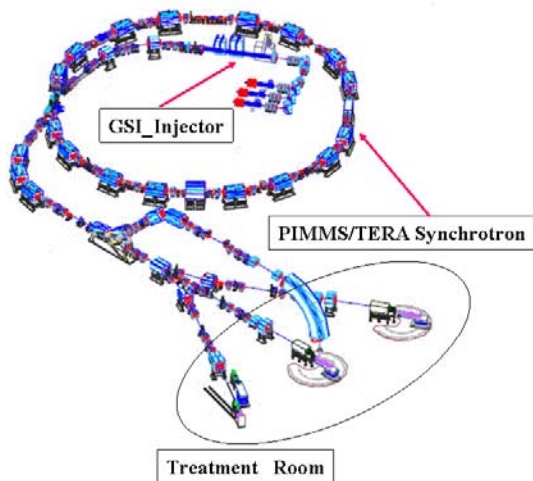


Figure 6: Schematic view of CNAO facility.

Other Projects in Europe

The construction of ETOILE [24] has been approved by the French ministries of health and research in May 2006. The basic design of an accelerator system is similar to that of CNAO and the active scanning method will be also employed.

The Med-Austron project [25] has designed a synchrotron based facility for both proton and carbon radiotherapy, based on the modified PIMMS design. The delivered energy of carbon and of proton are variable from 120 to 400 MeV/n and from 60 to 220 MeV, respectively.

ARCHADE project [26] has designed superconducting carbon cyclotron, cooperating with IBA. This cyclotron is designed to deliver 400 MeV/n carbon and 250 MeV proton. 400 MeV/n Carbon beam is extracted through an electrostatic deflector, and 265 MeV proton beam is obtained by a stripping extraction of H_2^+ .

INFN has designed a superconducting cyclotron for both proton and carbon radiotherapy [27]. Acceleration energy is 300 MeV/n. A proton beam with 260 MeV is obtained by H_2^+ stripping method.

SUMMARY

With stimulating through remarkable results of the carbon therapy with HIMAC, various facilities have carried out the heavy-ion therapy and several projects have also been being progressed. With improving both the beam-delivery and accelerator technologies of

HIMAC, on the other hand, the NIRS designed the standard-type carbon therapy facility in Japan, which has been constructed at Gunma University. The new treatment facility, further, has been designed for further development of the HIMAC treatment, since 2006. The construction of the facility building has been carried out since February 2009, which will be completed at March 2010.

REFERENCES

- [1] W. T. Chu et al., Rev. Sci. Instr. 64 (1993) 2055.
- [2] Y. Hirao et al., Nucl. Phys. A538 (1992) 541c.
- [3] S. Minohara et al., Int. J. Rad. Oncol. Bio. Phys. 47, 1097-1103 (2000).
- [4] K. Noda et al., Nucl. Instr. Meth. A 374 (1996) 269.
- [5] T. Kanai et al., Med. Phys. 10, 344 (1983).
- [6] Y. Futami et al., Nucl. Instr. Meth. A 430 (1999) 143.
- [7] T. Kanai et al., Med. Phys. Med. Phys. 33, 2989 (2006).
- [8] K. Noda et al., Nucl. Instr. Meth. A 492 (2002) 253.
- [9] T. Furukawa et al., Nucl. Instr. Meth. A 522 (2004) 196.
- [10] S. Sato et al., Nucl. Instr. Meth. A 574 (2007) 226.
- [11] T. Furukawa et al., Nucl. Instr. Meth. A 515 (2003) 861.
- [12] M. Kanazawa et al., Nucl. Instr. Meth. A566 (2006) 195.
- [13] C. Ohomori et al., Nucl. Instr. Meth. A 547 (2005) 251.
- [14] T. Furukawa et al., Med. Phys. 34, 1085 (2007).
- [15] K. Noda et al., J. Rad. Res., 48 (2007) A43.
- [16] T. Furukawa et al., Nucl. Instr. Meth. B 266 (2008) 2186.
- [17] A. Lomax, Phys. Med. Biol. 44:1219 (1999).
- [18] T. Furukawa and K. Noda, Nucl. Instr. Meth. A 565 (2006) 430.
- [19] S. Yonai et al., Med. Phys. 35, 927 (2008).
- [20] Y. J. Yuan et al., Proc. EPAC08, pp.388-390.
- [21] P. Mandrillon et al., EPAC92, pp.179-181.
- [22] H. Eickhoff et al., Proc. EPAC04, pp.290-294.
- [23] S. Rossi, Proc. EPAC06, 2006, pp.3631-3635.
- [24] F. Meot et al., Proc. EPAC02, 2002, pp.2745-2747.
- [25] E. Griesmayer et al., Nucl. Instr. Meth. B 258 (2007)134.
- [26] Y. Jongen et al., Proc. EPAC08, pp.1806-1808.
- [27] M. Maggiore et al., Proc. PAC07, pp.2748-2750.

NEW AND IMPROVED AMS FACILITIES

Hans-Arno Synal, ETH Zurich, Laboratory of Ion Beam Physics, Switzerland

Abstract

Accelerator Mass Spectrometry (AMS) provides instrumentation originally developed by nuclear physicists more than 30 years ago to measure long lived cosmogenic radionuclides such as ^{10}Be , ^{14}C , ^{26}Al , ^{36}Cl , ^{41}Ca , ^{129}I , U, Pu and Pa at natural levels. In the past ten years impressive progress in the measurement technique has been made and with the appearance of compact low energy radiocarbon AMS systems, a new category of AMS instruments has been introduced [1,2,3]. This has resulted in a boom of new AMS facilities with more than 20 new installations over the last five years. But low energy AMS is not limited to radiocarbon only and there is a great potential for ^{10}Be , ^{26}Al , ^{129}I and actinides measurements at compact AMS systems. The latest developments towards the low energy limit of AMS resulted in two new types of systems, the NEC [4] Single Stage AMS (SSAMS) and ETH mini carbon dating system (MICADAS) operating with terminal voltages of about 200 kV only. In addition, systems like the HVEE [5] 1 MV Tandetron or the compact ETH 600 kV system are capable to extend the range of applications at compact systems beyond radiocarbon. These systems will have enormous impact, not only on the use of AMS in biomedical research and on radiocarbon dating but also for research applications with ^{10}Be , ^{26}Al , ^{129}I and actinides.

THE EARLY DAYS OF AMS

The fundamental principles of AMS as they were developed in 1977 in connection with tandem accelerators [6, 7] are still the basis of state-of-the-art AMS instrumentation. In the early days, three different concepts had been applied: first, a dedicated spectrometer generation based on 2.5 MV Tandetron accelerators from General Ionex Corporation was introduced by Kenneth Purser (Arizona, Oxford, Gif-sur-Yvette); second, transformation of medium sized tandem accelerators such as High Voltage EN type into dedicated AMS spectrometers (e.g. Zurich, Utrecht, Uppsala, Erlangen) and third, the gentle modification of large sized tandem facilities to accommodate the needs of AMS experiments (e.g. Rochester, Munich, Canberra). Triggered by the need of highly precise radiocarbon dates and a tremendous measurement capacity in connection with the World Ocean Circulation Experiment WOCE in the early 1990's an AMS-system based on a 3 MV Tandetron accelerator was proposed by Kenneth Purser and installed in 1991 at the Woods Hole Oceanographic Institution [8]. Followed by similar systems in Groningen, Kiel, Nagoya, JEARI, Seoul, Jena and Oxford, this kind of instrumentation became the benchmark for high precision radiocarbon analysis over many years.

Applications and Ancillary Systems

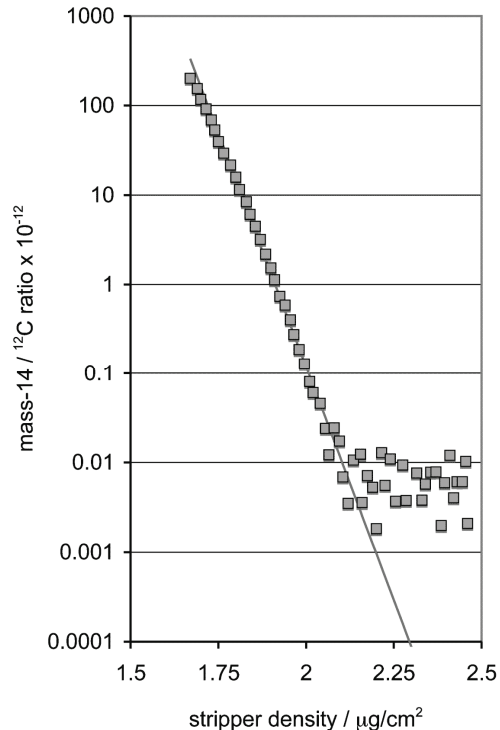


Figure 1: Intensity of molecules of mass 14 amu. At sufficient density the interference can be eliminated and radiocarbon dating measurements become possible.

COMPACT ^{14}C AMS INSTRUMENTS

To measure long-lived radionuclides at natural concentrations mass interferences have to be filtered out. In several cases isobaric nuclides can be suppressed already in the ion source and only remaining molecular ambiguities have to be removed. These interferences are eliminated exploiting the stripping process inside the tandem accelerator. There are no bound states of small molecules with charge state 3+ and higher, and thus, such molecules simply decompose as soon as they lose their binding electrons in collisions with gas atoms or molecules. To reach sufficient charge state yields, the ions require relatively high energies, e.g. the maximum yield for 3+ and 4+ is reached for ^{14}C ion at 2.5 MeV and 6.5 MeV respectively in Ar stripper gas. Consequently, quite large accelerator systems are required to provide ions in the necessary energy range.

However, there is a certain probability of molecular ions to decompose in collisions process with stripper gas even if there are bound states. Consequently, the intensity of the molecular component of an ion beam will decrease exponentially with increasing area density of the stripping medium and the interfering molecular component of the ion beam can be reduced down to a level where isotope

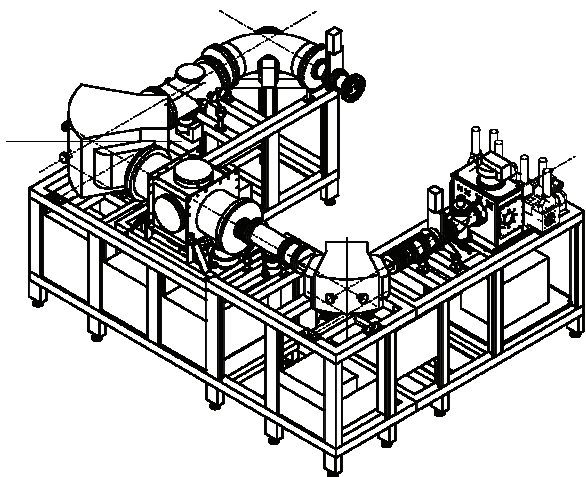


Figure 2: Design view of the next generation AMS spectrometer for radiocarbon dating and for biomedical research. The overall dimensions of the are 2.5 m x 3 m.

ratio measurements at natural concentrations become possible. This new way to eliminate molecular interferences has the great advantage that the maximal yield for ^{14}C in charge exchange to 1+ can be reached at energies of about 500 keV. Consequently, AMS systems based on this principle are more compact with smaller accelerators and can be produced and operated at much lower cost than traditional systems. The development of compact AMS systems for radiocarbon was undertaken at ETH in collaboration NEC. NEC has used these developments to commercialize AMS systems based on the new technology. The obvious advantages of the compact systems have also been realized by HVEE which now has proposed its own compact AMS system based on a 1 MV Tandatron accelerator [9]. The first instrument of this type was installed at University of Seville in Spain in 2005 [10]. In contrast to the compact NEC systems, which are optimized for radiocarbon, the compact HVEE system has the option to analyze beams up to plutonium.

Next Generation of Compact Systems

Shortly after proof of principle of the new method to eliminate molecular interferences, the question of the low energy limit of AMS arose. Detailed measurements of molecule dissociation cross sections revealed that even at energies as low as 200 keV, the cross sections are sufficiently high to achieve suppression of molecular interference down to levels where dating measurements can be performed. Stripping yields for the 1+ charge state are still approximately 50% and thus high enough for efficient radiocarbon detection. Traditional accelerator systems are not necessary anymore to obtain ion energies in these ranges. At ETH we have designed a vacuum insulated high-voltage platform in a tandem configuration fed from a commercial high voltage power supply and hosting a charge exchange channel that provides sufficient area density of a stripper gas to eliminate molecular interferences. Based on initial tests of this

Applications and Ancillary Systems

device, a prototype dedicated radiocarbon dating system (MICADAS, Fig. 2) was built and became operational in 2004 [11]. The MICADAS type system has a footprint of $2.5 \times 3 \text{ m}^2$ only and is therefore the smallest AMS instrument capable of high performance radiocarbon measurements.

Frontiers of Radiocarbon Dating

Measurements at the 1‰ level require counting statistics beyond 1 million ^{14}C events per sample. Even with modern high current ion sources this requires long measurement times. In general, the measurement system must provide stable and reproducible measurement conditions over much longer times because appropriate normalization procedures and assessment of machine internal variability should be evaluated in parallel with the high precision measurements of samples.

The ETH MICADAS system is based in its design more on a conventional mass spectrometer than a traditional AMS system. This should be a good qualification to achieve highly precise $^{14}\text{C}/^{12}\text{C}$ measurements. At the MICADAS system, we have measured homogenized material of oxalic acid I standard material. A set of four standard cathodes was analyzed together with blank samples in a 24 h measurement, where for each standard cathode the total measurement time was 2.5 h resulting in 600'000 detected ^{14}C events equivalent to 1.3‰ statistical precision. The $^{14}\text{C}/^{12}\text{C}$ ratios of the 120 runs are shown in Fig. 3. Note that none of the total 1200 data blocks taken during the 24 hours of measurement have been discarded. The scatter of the individual measurements is consistent with their internal uncertainty based on counting statistics. The relative standard uncertainty of each of the four standards is between 1.12‰ and 1.35‰ and is reproduced at sub-per mil level. This shows that MICADAS-type systems, in general, are capable to provide measurement conditions necessary for ultra-high precision measurements.

AMS system for Biomedical Research

Despite the great potential to use AMS in connection with biomedical research a widespread biomedical use of AMS had been impeded by the complexity of the measurement technology and the related high cost of the

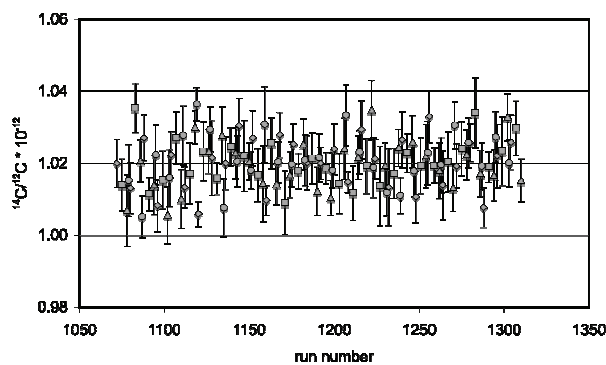


Figure 3: $^{14}\text{C}/^{12}\text{C}$ measurements of different targets over 24h of operation.

analyses. Biomedical applications have, compared to radiocarbon dating, different demands. Analytic accuracy of typically 5% is sufficient, a much wider dynamic range (1000 Modern to a few % Modern) must be covered and a high sample throughput is required for the efficient use of the installations and for a significant reduction in effective cost for the analyses. In order to provide the advantages of latest type of AMS systems for biomedical research, we have developed at ETH a dedicated biomedical system based on the MICADAS concept (BioMICADAS) in collaboration with Vitalea Science, a commercial service provider for biomedical AMS services. In particular, the sample handling and the capability to digest huge counting rates of the rare isotope have been improved. The present system has the capability to analyze more than 20000 samples per year under conditions, as they are required in biomedical research projects. In parallel, NEC has invented a single stage AMS system that can fit the needs of biomedical research as well. Thus, the latest developments in AMS with advent of compact and more recently of SSAMS as well as the dedicated BioMICADAS systems substantially pushed forward the use of AMS in biomedical research. This should be kept in mind in connection with changes in government regulations regarding the concept of micro-dosing where the new systems enable novel and very attractive applications with pharmaceutical drug developments.

MULTI-PURPOSE AMS SYSTEMS

There has always been the question of which type of accelerator would be optimal for dedicated AMS systems. A pure radiocarbon dating system has different requirements than a multi-purpose AMS system covering a range of AMS nuclides for which substantial isobar suppression capabilities are needed. FN accelerators reaching terminal voltages of 10 MV seemed to be well suited as basis of versatile multi-purpose AMS systems. At Lawrence Livermore National Laboratory, at Purdue University and at the Australian Nuclear Science and Technology Organisation AMS facilities were built around FN tandems. Large Pelletron and MP tandem accelerators with terminal voltages ranging from 14 to 25 MV (Canberra, Munich, Oakridge) are still used for AMS measurements, predominantly for heavier nuclides which suffer from abundant nuclear isobar interferences. In general, the effort to operate and maintain such large accelerator facilities is too high to justify it with an AMS program.

During the early times of AMS the Toronto group has pioneered the analysis of heavy nuclides at fairly small Tandatron based AMS systems and the AMS system in Vienna has demonstrated that a versatile multi-purpose AMS instrument can be built around a 3 MV accelerator. But more recently, AMS systems based on larger accelerators show quite a renaissance. A number of new facilities have been installed recently or are under construction/commissioning. With these systems measurements of ^{36}Cl are possible because at higher beam

Applications and Ancillary Systems

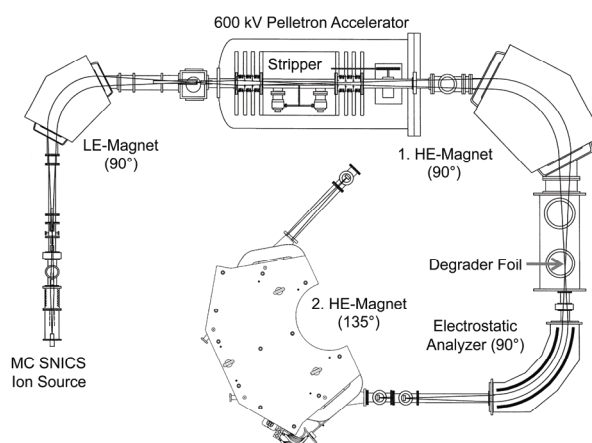


Figure 4: Extension of the high-energy spectrometer of the ETH 600 kV AMS system. By adding a second magnetic spectrometer to the beam line interferences from scattered ions causing background events can be reduced significantly.

energies the interfering isobar ^{36}S can be suppressed sufficiently using dE/dx energy loss difference of ions with different nuclear charge.

Possibilities of Compact Multipurpose AMS Systems

Compact AMS facilities are not limited to radiocarbon only. In particular, ^{10}Be can be sufficiently separated from its isobaric counterpart ^{10}B and identified at terminal voltages well below 1 MV [12, 13]. This has become possible because of significant improvements in the detection technique of low energetic ions with gas ionization detectors [14] due to the use of i) the now available very thin and homogenous SiN detector windows [15] and ii) due to the improved detector resolution of the detector electronics by using CoolFET preamplifiers [16] reducing the contribution of the electronic noise to the resolution of the detector signals. Applying the degrader foil technique [12, 17, 18] at beam energies as low as 700 keV and eliminating background from scattered molecular fragments yields competing performance with larger AMS systems. Detection limits for $^{10}\text{Be}/^9\text{Be}$ ratios in the range of a few times 10^{-15} and ^{10}Be transmission efficiencies of about 8 % have been demonstrated [19]. The total potential for ^{26}Al at compact AMS facilities has not yet been sufficiently explored. Performance measurements at the Zurich compact AMS system using 1+ have shown 25% overall beam transmissions and background levels of the order of 10^{-14} [20]. Further improvements seem possible with the upgrade of the high-energy mass spectrometer (Fig. 4) and the expected higher suppression of scattered molecular fragments.

^{41}Ca measurements are interfered by the atomic isobar ^{41}K and are therefore predominantly performed at larger AMS systems e.g. PRIME Lab [21], CAMS/LLNL [22]. However, the performance achievable at compact systems has been demonstrated to be sufficient for biomedical

studies [23] and due to the reduced analysis cost at smaller AMS systems, these systems can be regarded as a viable alternative for those applications. With systems having about 5 MV terminal voltage, a much better sensitivity of a few times 10^{-14} can be reached [23] due to the quite impressive potassium suppression of optimized gas ionization detectors. A similar performance has been reached at the VERA system with 3 MV terminal voltage for CaF_2 samples and of 10^{-15} and below using CaH_2 [24].

Actinides like U, Pu and Pa are not interfered by stable atomic isobars and the atomic isobar of ^{129}I does not form negative ions. Therefore, these nuclides can be measured with low energy AMS systems, if molecular isobars can be eliminated. In the case of ^{129}I , Zhao et al. [25] have shown that using 3+ with stripping efficiency of 10% at 1 MeV $^{129}\text{I}/\text{I}$ ratios as low as 10^{-14} can be measured. This is sufficient for almost all applications of ^{129}I . At the Zurich compact AMS system, ^{129}I measurements have been made using the 4+ charge state [26]. More recently, the performance of these measurements could be increased using 3+ at 500 kV terminal voltage [27]. Because charge state 3+ is used, the stripper density does not have to be increased beyond the equilibrium region, but molecular fragments in charge state 2+ with the same m/q ratio as ^{129}I can survive the stripping process and can under unfavorable circumstances limit proper identification of ^{129}I ions. Apart from these minor obstacles, the performance of compact AMS for ^{129}I will fit the needs of the applications and these systems can be regarded as true alternatives to systems with larger accelerators.

Ultra-sensitive detection of plutonium isotopes have been demonstrated at an accelerating voltage of 300 kV at the Zurich compact AMS system [28]. The observed transmission efficiencies were surprisingly high (15% for Th) and detection levels competitive to larger systems have been demonstrated. Detection limit for $^{236}\text{U}/\text{U}$ of 10^{-9} have been shown [29] and further progress can be expected adopting better high-energy spectrometers with improved suppression capabilities against scattered molecular fragments. AMS of ^{231}Pa measurements became possible with a performance comparable to modern mass spectrometers [30] and thus a new radionuclide was introduced into the AMS world of compact AMS systems. The HVEE 1 MV compact AMS system in Seville has also demonstrated impressive capabilities of actinide measurements [31]. As pointed out by Fifield [32], the much better transmission efficiency at low energies make compact systems very attractive for actinide measurements. Further improvements of the mass spectrometer at the high-energy end of these systems, in particular an improved rejection of scattered molecular fragments will make future compact systems even better suited for actinide AMS.

CONCLUSIONS

AMS has evolved to a powerful analytic technique. Worldwide more than 80 AMS facilities contribute to a wide variety of research fields. Whereas during the early

days of AMS research laboratories optimized their accelerator systems and advanced the technology, today, the two competing companies NEC and HVEE provide a wide variety of AMS instruments with acceleration stages from 0.2 MV to 6 MV terminal voltage. Practically, all the new installations of AMS facilities over the last five years were equipped with instrumentation already available or especially tailored to the intended application program by these two companies. Despite the fact that the collaborative efforts between commercial AMS providers and various research groups has fruitfully improved the available AMS instrumentation, the ultimate goal of having available AMS instruments as compact and as easy to operate and maintain as conventional mass spectrometers has not yet been reached. Thus, there is still a strong need for independent technological and methodical developments at universities and research institutions to advance AMS instrumentation to meet future requirements and to promote a more widespread use of AMS. The availability of small and compact AMS systems has already launched a boom of new laboratories with AMS capabilities. During the past 5 years more than 20 new facilities became operational using accelerators systems with terminal voltages of 1 MV or less. Low energy systems do have the capability to provide competitive performance not only for radiocarbon, but also for other important AMS nuclides such as ^{10}Be , ^{129}I and actinides, although this potential has not been fully exploited yet. In addition, concentrated efforts should be made to sustain the capabilities of AMS of more exotic nuclides requiring large accelerator system and high beam energies.

REFERENCES

- [1] M. Suter, S. Jacob, H.A. Synal, Nucl. Instr. and Meth. B 123 (1997) 148.
- [2] H.A. Synal, S. Jacob, M. Suter, Nucl. Instr. and Meth. 161-163 (2000) 29.
- [3] H.A. Synal, S. Jacob, M. Suter Nucl. Instr. and Meth. B 172 (2000) 1.
- [4] National Electrostatics Corporation, Middleton, WI, USA.
- [5] High Voltage Engineering Europa B.V., Amersfoort, The Netherlands.
- [6] C.L. Bennett, R.P. Beukens, M.R. Clover, H.E. Gove, R.B. Liebert, A.E. Litherland, K.H. Purser, W.E. Sondheim, Science 198 (1977) 508.
- [7] D.E. Nelson, R.G. Korteling, W.R. Stott, Science 198 (1977) 507.
- [8] K.H. Purser, T.H. Smick, R.K. Purser, Nucl. Instr. and Meth. B 52 (1990) 263.
- [9] M.G. Klein, D.J.W. Mous, A. Gott dang, Nucl. Instr. and Meth. B 249 (2006) 764.
- [10] E. Chamizo, J.M. Lopez-Gutierrez, A. Ruiz-Gomez, F.J. Santos, M. Garcia-Leon, C. Maden, V. Alifimov, Nucl. Instr. and Meth. B 266 (2008) 2217.
- [11] H.-A. Synal, M. Stocker, M. Suter, Nucl. Instr. and Meth. B 259 (2007) 7.

- [12] M. Grajcar, M. Döbeli, P.W. Kubik, H.-A. Synal, L. Wacker, M. Suter, Nucl. Instr. and Meth. B 259 (2007) 173.
- [13] A.M. Müller, M. Christl, M. Döbeli, P.W. Kubik, M. Suter, H.-A. Synal, Nucl. Instr. and Meth. B Proceedings of the AMS-11 Conference (2009).
- [14] M. Suter, M. Döbeli, M. Grajcar, A. Müller, M. Stocker, G. Sun, H.-A. Synal, L. Wacker, Nucl. Instr. and Meth. B 259 (2007) 165
- [15] M. Döbeli, C. Kottler, M. Stocker, S. Weinmann, H.-A. Synal, M. Grajcar, M. Suter, Nucl. Instr. and Meth. B 219-220 (2004) 415.
- [16] Amptek, Inc., D.A. Drive, M.U.S.A. Bedford.
- [17] G.M. Raisbeck, F. Yiou, D. Bourles, J. Lestringuez, D. Deboffe, Nucl. Instr. and Meth. B 5 (1984) 175.
- [18] W. Kutschera, W. Henning, M. Paul, R.K. Smither, E.J. Stephenson, J.L. Yntema, D.E. Alburger, J.B. Cumming, G. Harbottle, Physical Review Letters 45 (1980) 592.
- [19] A.M. Müller, M. Christl, M. Döbeli, P.W. Kubik, M. Suter, H.A. Synal, Nucl. Instr. and Meth. B 266 (2008) 2207.
- [20] M. Stocker, M. Döbeli, M. Grajcar, M. Suter, H.-A. Synal, L. Wacker, Nucl. Instr. and Meth. B 240 (2005) 483.
- [21] G.S. Jackson, D. Elmore, F.A. Rickey, S.M. Musameh, P. Sharma, D. Hillemonds, L. Coury, P. Kissinger, Nucl. Instr. and Meth. B 172 (2000) 899.
- [22] M.L. Roberts, et al., Nucl. Instr. and Meth. B 123 (1997) 57.
- [23] T. Schulze-König, C. Maden, E. Denk, S.P.H.T. Freeman, M. Stocker, M. Suter, H.-A. Synal, T. Walczyk, Nucl. Instr. and Meth. B Proceedings of the AMS-11 Conference (2009).
- [24] A. Wallner, O. Forstner, R. Golser, G. Korschinek, W. Kutschera, A. Priller, P. Steier, C. Vockenhuber, Nucl. Instr. and Meth. B Proceedings of the AMS-11 Conference (2009).
- [25] X.L. Zhao, A.E. Litherland, W.E. Kieser, C. Soto, Nucl. Instr. and Meth. B 259 (2007) 265.
- [26] M. Stocker, M. Döbeli, M. Grajcar, M. Suter, H.-A. Synal, L. Wacker, Nucl. Instr. and Meth. B 240 (2005) 483.
- [27] V. Alfimov, H.A. Synal, Proceedings of the AMS-11 Conference (2009).
- [28] L.K. Fifield, H.A. Synal, M. Suter, Nucl. Instr. and Meth. B 223-224 (2004) 802.
- [29] L. Wacker, E. Chamizo, L.K. Fifield, M. Stocker, M. Suter, H.A. Synal, Nucl. Instr. and Meth. B 240 (2005) 452.
- [30] M. Christl, L. Wacker, J. Lippold, H.-A. Synal, M. Suter, Nuclear Instruments and Methods in Physics Research Section B: Beam Interactions with Materials and Atoms 262 (2007) 379.
- [31] E. Chamizo, S.M. Enamorado, M. García-León, M. Suter, L. Wacker, Nuclear Instruments and Methods in Physics Research Section B: Beam Interactions with Materials and Atoms 266 (2008) 4948.
- [32] L.K. Fifield, P.P. Pavel, Radioactivity in the Environment, Elsevier, 2008, pp. 263.

THE RADIATION ASSURANCE TEST FACILITY AT INFN-LNS CATANIA

B. Alpat, M. Menichelli, A. Papi, INFN Sezione di Perugia, Italy
 F. Bizzarri, D. Caraffini, M. Petasecca, F. Renzi, MapRad S.r.l., Perugia, Italy
 R. Harboe-Sorensen, ESA/ESTEC, Noordwijk, The Netherlands
 P. Cirrone, F. Ferrera, P. Figuera, P. Finocchiaro, M. Lattuada, D. Rifuggiato,
 INFN Laboratori Nazionali del Sud, Catania, Italy
 H. Denizli, Abant İzzet Baysal Universitesi, Bolu, Turkey
 O. Amutkan, Ortadogu Teknik Universitesi, Ankara, Turkey

Abstract

This paper describes the beam monitoring system that has been developed at the Superconducting Cyclotron at INFN-LNS (Istituto Nazionale di Fisica Nucleare, Laboratori Nazionali del Sud, Catania, Italy) in order to monitor the beam parameters such as energy, flux, beam profile, for SEE (Single Event Effects) cross-sections determination and DD (Displacement Damage) studies.

In order to have an accurate and continuous monitoring of beam parameters we have developed fully automatic dosimetry setup to be used during SEE (with heavy ions) and DD (with protons of 60 MeV/u) tests of electronic devices and systems.

The final goal of our activity is to demonstrate how operating in air, which in our experience is easier than in vacuum, is not detrimental to the accuracy on controlling the beam profile, energy and fluence delivered onto the DUT (Device Under Test) surface, even with non relativistic heavy ions.

We have exposed during the same session, two beam calibration systems, the "Reference SEU monitor" developed by ESA/ESTEC and the beam monitoring and dosimetry setup developed by our group. The results are compared and discussed here.

INTRODUCTION

The LNS Superconducting Cyclotron (CS), is a compact, strong focusing three-sector machine. The pole radius is 90 cm and the magnetic field at the center ranges from 2.2 to 4.8 T. This is obtained with superconducting Nb-Ti coils cooled down to 4.2 K in an LHe bath. The expected maximum energies of the machine are of 20 MeV/u for the heaviest ions, like $^{238}\text{U}^{38+}$, and 100 MeV/u for fully stripped light ions as given respectively by the bending limit $K_b=800$ and by the focusing limit $K_f=200$.

The measurement of beam flux and uniformity is one of the ingredients for the calculation of SEE cross-section. According to the ESA standard ESCC-25100 these measurements should be done with an accuracy of $\pm 10\%$.

The relatively high energy of the beams (for this study 20 MeV/u) allows the irradiation of components in air which is used also as a degrader. The selection of the ion species we use in SEE studies is done by taking into

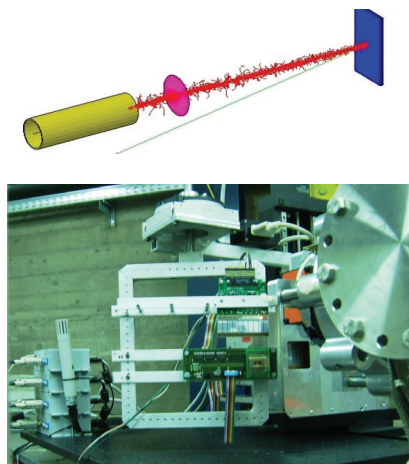


Figure 1: Upper: Geant4 simulation of setup representing, from left to right, vacuum pipe, thin scintillator and silicon detector or DUT. Lower: The beam dosimetry setup. The DS microstrip silicon detector, 3-D stage and rotator to which the DUT holder is attached are shown.

account the easiness of beam changing operation and at the same time the necessity to cover as large a LET interval as possible. Hence, four gaseous beams (^{20}Ne , ^{40}Ar , ^{84}Kr , ^{129}Xe) all with 20 MeV/u energy are selected.

A careful evaluation of energy loss in air end of the energy spread at DUT surface is carried out through a full Monte Carlo simulation of the test setup and comparing the results with data.

The DD studies are performed using 60 MeV/u protons instead.

BEAM MONITORING SYSTEM

At LNS we perform extraction of ion beams in air, where our flux and dosimetry setup resides; additionally we use air as a degrader in order to adjust LET values. A basic schematic of the dosimetry measurement setup is shown in Fig. 1. The upper part of the figure shows the particles getting into air from beam pipe, crossing a thin scintillator and then reaching the DUT or silicon detector surface. The air thickness between beam exit and thin scintillator is fixed while the one between thin scintillator and DUT (or Si detector) is variable (respectively, A1 and A2 in Table 1).

Table 1: Typical Set of LET(Si) Values and corresponding Ion Species, Ranges and Air Thicknesses

Ion	E (MeV/u)	A1 (cm)	A2 (cm)	Impact Angle (°)	Scintillator Thickness (μm)	Ek Tot (MeV)	Ek at Si Surf. (MeV)	Range in Si (μm)	LET in Si (MeV/mg/cm ²)
²⁰ Ne	20	5	5	0	50	400	341	402	3,66
²⁰ Ne	20	5	30	0	50	400	259	254	4,39
⁴⁰ Ar	20	5	5	0	50	800	617	252	10,56
⁴⁰ Ar	20	5	30	0	50	800	347	105	14,26
⁸⁴ Kr	20	5	5	0	50	1680	1074	150	30,76
⁸⁴ Kr	20	5	15	0	50	1680	751	93	34,69
¹²⁹ Xe	20	5	5	0	50	2580	1473	109	57,99
¹²⁹ Xe	20	5	15	0	50	2580	923	70	56,62

The setup consists in a thin scintillator counter (NE102A of 50 or 100 μm thickness) read by a photomultiplier just after the beam exit into air, an XYZ stage with submicron absolute position resolution. The scintillator is inserted into a metallic box with variable size beam hole to allow the adjustment of the beam size. The DUT is placed onto a supporting frame (DUT holder) which is held by a rotator fixed to the positioning stage. On the same structure close to DUT holder a double sided, 1.5 mm thick microstrip detector (500 μm readout pitch and 3x3 cm² active area) is mounted for energy, fluence and beam profile measurements. Because of its thickness the silicon detector behaves like a calorimeter to the above mentioned ion species in non relativistic regime, containing all their energy: the stopping range in silicon is, for all ions we use, at least 30 μm , in accordance to the minimum penetration depth required by the ESA standard ESCC-25100.

The dosimetry setup includes two additional important features. A laser device, which is used to measure the

distances in Z (beam) direction with 200 μm position accuracy. Such level of accuracy in measurement of the relative distances (i.e. silicon detector surface to delidded DUT surface, DUT surface to beam exit in air, etc.) is important to achieve as small as possible overall systemic error on LET value in silicon. The other feature of the setup is a custom module (SELDP) built specifically to monitor the current drawn on power line of a DUT. The SELDP cuts the power supply to DUT for an adjustable time duration whenever the current drawn by DUT exceeds a preset current limit. This both protects DUT from burnout because of Single Event Latchup (SEL) effect and registers the number of SEL occurred by incrementing a counter.

The overall configuration of beam setup is given in the block diagram below. The two PCs indicated inside the red frame are located in the beam, while all the rest of the boxes are representing tasks carried out by a single laptop in the control room communicating via TCP-IP with the PCs inside the beam area.

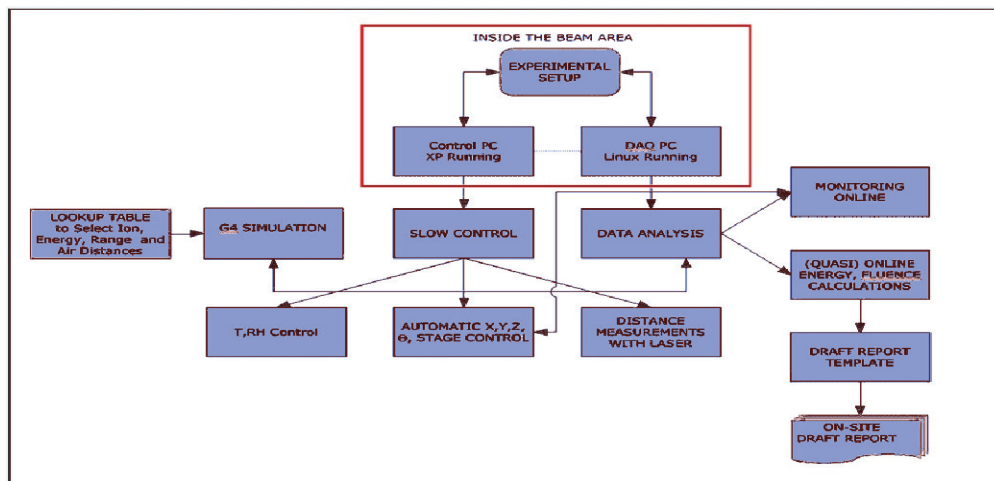


Figure 2: The configuration of DAQ and control PCs (inside the beam area) and laptop in control room. The tasks carried out by each computer are also shown.

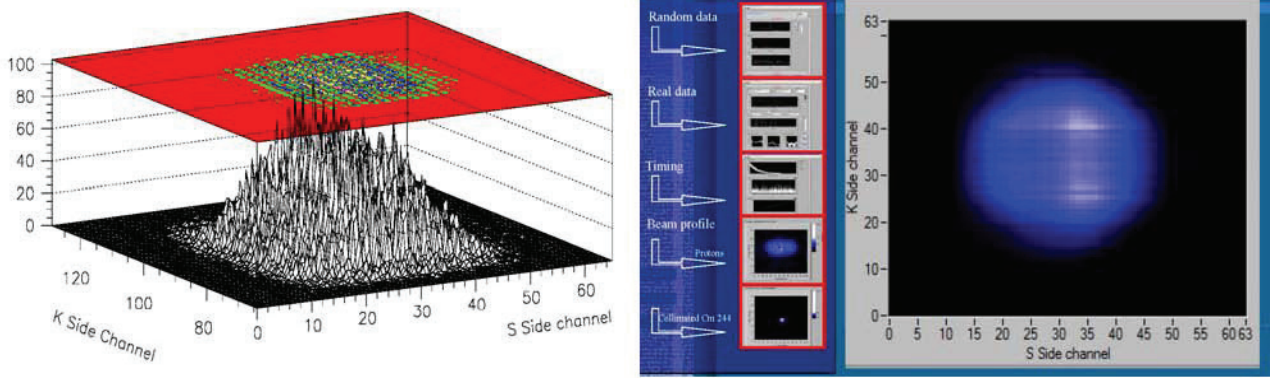


Figure 3: The online monitoring of beam parameters with silicon detector. Left: The beam profile is shown in 3D. Each channel corresponds to 0.5 mm (strip pitch of double sided silicon detector). Right: The beam profile reconstructed from data.

PERFORMING SEE AND DD MEASUREMENTS

Prior to go to LNS for a test period, all dosimetry system including DUT mounting and performance is tested in MAPRAD laboratories (REF) onto a mock-up mechanical system of the beam setup which includes also a pulsed IR laser source. All mechanical parts necessary are produced and tested on this mock-up, as well as electronics parts which are tested under the pulsed laser beam to verify the behaviour of the entire DAQ system.

Test Procedure for SEE Studies

A full Geant4 Monte Carlo description of the setup has been done and run for the four different ion species in use to prepare a detailed look-up table. This table includes, among others, the range and LET values achieved for each experimental configuration differing by 1 mm increments of air thickness between thin scintillator and DUT surface.

For each device to be tested several LET values over an agreed LET range are selected and corresponding parameters are extracted from the table. A typical set of LET values and corresponding air thicknesses are listed in Table 1. The effective LET values larger than 100 MeV/mg/cm² can be obtained by altering the beam impact angle on the DUT, since $LET_{eff} = LET_{(0)}/\cos(\Theta)$.

The SEE test procedure consists in following steps;

- For each ion, we memorize on the control PC the data taking positions (see A1 and A2 distances and impact angles given in Table 1).
- Start with the beam profile on the silicon detector to get the beam shape and position with respect to DUT, so that it can be automatically moved under the beam.
- Start data acquisition by monitoring; the flux measured by thin scintillator and DUT parameters. The beam parameters (energy, profile, flux, time tag) measurement is done by moving silicon detector under the beam for short periods without stopping the run (see Fig. 3). A possible alternative procedure is to keep the silicon detector off-beam close to DUT

Applications and Ancillary Systems

and monitor continuously the tail of the beam. A calibration run with thin scintillator “on” and silicon detector “on/off” beam will provide normalization factors to achieve the real flux.

The steps described above, are repeated for different DUT distances (air thicknesses) or impact angles, to obtain various LET values using the same ion species.

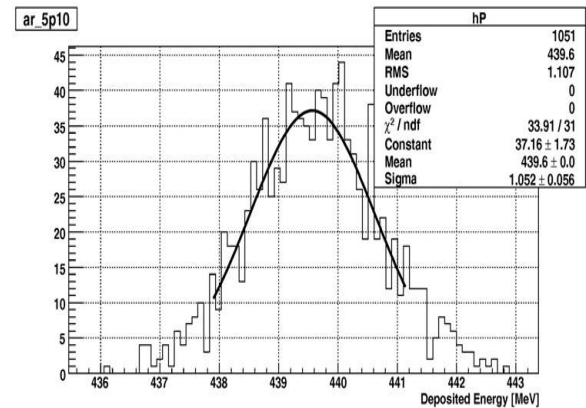


Figure 4: For ⁴⁰Ar beam at 10 cm air thickness (A2) Distribution of energy deposited in silicon simulated by Geant4.

Systematic Error Evaluation

A careful evaluation of systematic errors is necessary to estimate overall error introduced on LET and on fluence values. Definition of LET and cross section is given in Eq. 1 where ρ is silicon density.

$$LET(\text{MeV} \cdot \text{cm}^2 / \text{mg}) = \frac{dE}{dX} \cdot \frac{1}{\rho}; \quad \sigma(\neq / \text{cm}^2) = \frac{N_{SEE}}{\text{Fluence} \cdot \text{Cos}\theta}; \quad (1)$$

Systematic errors on LET values are;

- Distance (air thickness) measurements. This is done with a 200 μm accuracy laser system only once during the initial calibration phase. All other positions are relative to that point with submicron precision 4-D stage (X,Y,Z, Theta)

- Fragmentation in air. It is negligible (i.e. $<10^{-4}$ for 20 MeV/u ^{40}Ar after 15 cm of air) according to Geant4 simulation performed using “binary light ion cascade” and “Wilson abrasion” models.
- The determination of energy deposited and range in DUT by Geant4 simulation; the energy distribution from Monte Carlo has less than 3% error at FWHM (see Fig. 4), and there is a good correlation with the charge measured by the silicon detector, which provides the possibility to convert the charge values to deposited energy. The correlation between charge collected in silicon and simulated energy for different air thicknesses for ^{40}Ar is given in Fig. 5.
- Positioning of beam spot to the center of DUT and correction of non uniformity of beam over the beam spot. Fig. 6 shows a typical beam spot and DUT dimensions. This error includes a 180 μm contribution from the silicon detector spatial resolution, as well as a $\sim 300\ \mu\text{m}$ one from the accuracy of the DUT mounting on the holder frame; the two contributions are summed in quadrature since they are independent.

The detailed analysis of errors have shown that the overall error, on determination of both fluence and LET, is less than 4% which is well below the upper limit (10%) required by ESCC-22500. Table 2 lists the overall systematic errors on LET values for different ion species at 10 cm of A2.

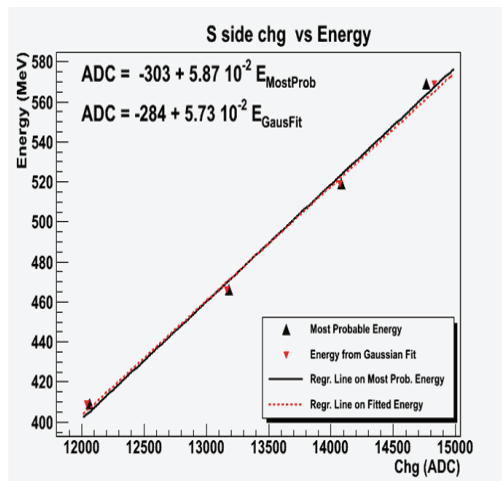


Figure 5: Correlation curves between charge deposited in silicon (ADC counts) and simulated energy release (MeV). The two data sets and curves refer to different ways to estimate energy from Monte Carlo distribution: black triangles use the most probable value taken from energy histogram; red upside-down triangles use the mean from a gaussian fit.

Comparison of Results with SEU Monitor

The reference SEU (Single Event Upset) monitor system [1] was developed specifically for inter-site calibrations to address the issue that in different

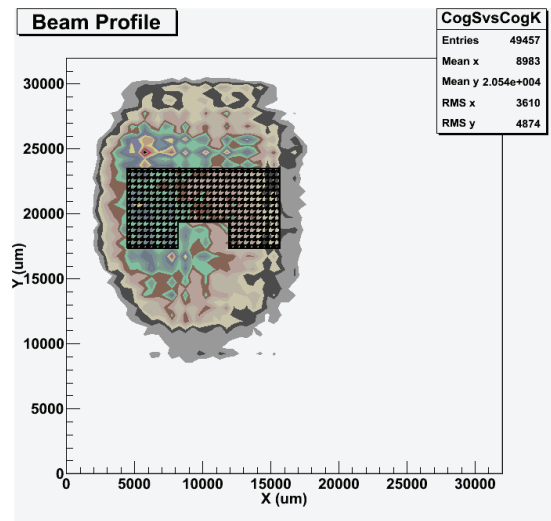


Figure 6: Beam spot is centred over the DUT surface. From this profile one can extract the real fluence distribution over DUT surface. The beam spot positioning accuracy is at most 400 μm .

irradiation facilities the user usually has no means of checking suspicious beams and of discovering data discrepancies on-site.

In order to minimize test errors because of faulty beams a simple reference system allowing beam re-checking capabilities was necessary. The reference SEU monitor system was developed for this purpose by using a SRAM (Atmel AT60142F) as active detector.

We have used in LNS reference SEU monitor pre-calibrated with heavy-ions, protons and neutrons, provided by ESA/ESTEC to check the quality of the dosimetry systems we described above, as well as the beam quality of LNS site. After each irradiation of the SEU monitor, the user has to supply the measurements for LET and fluence from his own dosimetry system to the SEU monitor own software, which carries out the calculation of cross section independently of the operator and adds a new data point to a comparison plot. The results are given in Fig. 7. The blue points are data points for LNS site which are in good agreement with calibration points obtained in two other irradiation facilities (HIF in Belgium and RADEF in Finland).

Table 2: LET(Si) values and corresponding systematic errors for different ion species at the 10 cm of Air (A2) thickness experimental configuration

Ion	LET(Si) (MeV/mg/cm ²)	Error on LET(Si) (MeV/mg/cm ²)
^{20}Ne	3.7	0.1
^{40}Ar	13.1	0.2
^{84}Kr	30.6	0.7
^{129}Xe	52.9	0.8

Applications and Ancillary Systems

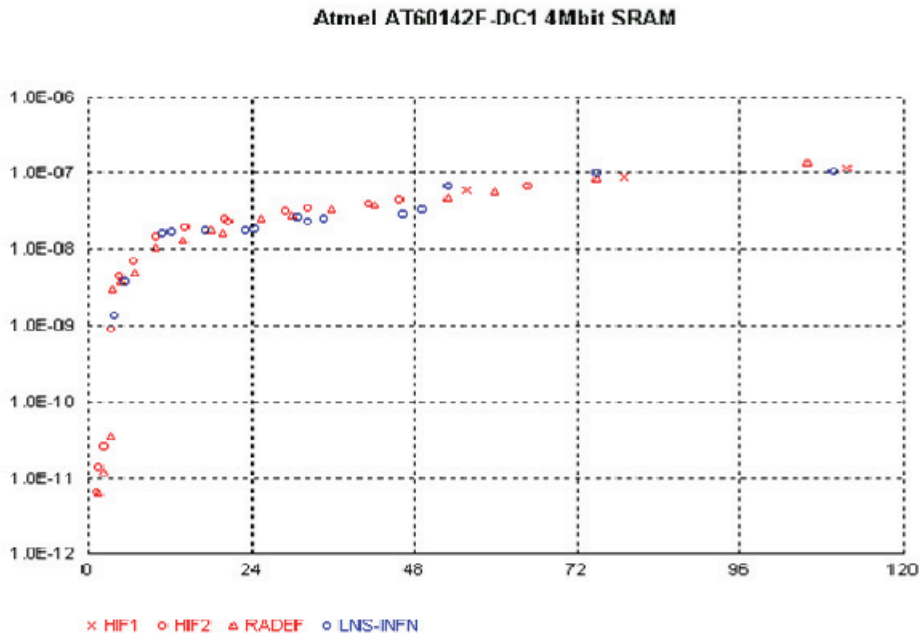


Figure 7: Comparison of cross section versus LET for the SEU monitor from different sites: the blue points are data points for LNS site, the red points are series obtained previously by ESA at other facilities (HIF in Belgium and RADEF in Finland) as calibration points. The measurements taken at LNS are in good agreement with the ESA calibration.

Test Procedure for DD Studies

The displacement damages are non ionizing effects caused mostly by protons and neutrons on silicon lattice structure by dislodging or displacing the atoms from their lattice sites. The DD studies at LNS are carried out using 60 MeV protons. Here the testing procedure is simpler than that of SEE since tests are realised at a fixed A1 and A2 distances. The DUTs under proton irradiation are usually unbiased (unless otherwise requested). The critical parameters of DUT are tested before and after irradiations. The test points are after different dose values delivered to the DUT, which are calculated as:

$$Dose(rad(Si)) = LET(SiO_2) \cdot Fluence \cdot 1.6 \cdot 10^{-5} \quad (2)$$

In this kind of test, the main problem is that test equipment materials do activate after prolonged exposition to the proton beam. For this reason we designed the supporting frame so that only the DUT and a minimal amount of test board is directly under the beam, in order to reduce activations as much as possible. To avoid putting the silicon detector under the beam for long times, it is possible to use it to monitor the intensity of the beam tails after an initial intercalibration phase with a gas chamber put in front of the beam outlet; the chamber can then be removed during actual DUT irradiation. The electrical connections of the DUT’s pins to power supply,

bias line and measurement apparatus must be designed so that it is possible to (dis)connect them remotely to avoid getting close to a possibly activated DUT.

CONCLUSIONS

In Europe there is a limited number of accelerator sites whose delivered ion beams fulfil the requirements of ESCC standards for SEE testings. We have developed a fully automatic dosimetry system to demonstrate the validity of beam characteristics of LNS sites for SEE and DD tests as well as to accurately measure the parameters relevant to perform detailed SEE and DD studies. With energies available at LNS and with four selected gaseous beams it is possible to perform SEE studies from few up to 110 MeV/mg/cm² of LET.

The beam changing time is relatively short (few hours) and beam size and fluence are stable in time. Furthermore, the presence of air gives possibility to reach “fine-tuned” LET values by adjusting the air thickness accordingly. Last but not least, operating the setup in air has the obvious advantages of reducing setup time and complexity.

REFERENCES

[1] R. Harboe-Sorensen, F.-X. Guerre and A. Roseng, Design, Testing and Calibration of a "Reference SEU Monitor" System. Proceedings of RADECS 2005.

DEVELOPMENT OF BEAM CURRENT MONITOR WITH HTS SQUID AND HTS CURRENT SENSOR

T. Watanabe*, N. Fukunishi, M. Kase, Y. Sasaki and Y. Yano

RIKEN Nishina Center for Accelerator-Based Science, Wako-shi, Saitama 351-0198 Japan

Abstract

A highly sensitive beam current monitor with an HTS (High-Temperature Superconducting) SQUID (Superconducting Quantum Interference Device) and an HTS current sensor, that is, an HTS SQUID monitor, has been developed for use of the RIBF (RI beam factory) at RIKEN. Unlike other existing facilities, the HTS SQUID monitor allows us to measure the DC of high-energy heavy-ion beams nondestructively in real time, and the beam current extracted from the cyclotron can be recorded without interrupting the beam user's experiments. Both the HTS magnetic shield and the HTS current sensor were dip-coated to form a $\text{Bi}_2\text{-Sr}_2\text{-Ca}_2\text{-Cu}_3\text{-O}_x$ (Bi-2223) layer on 99.9% MgO ceramic substrates. In the present work, all the fabricated HTS devices are cooled by a low-vibration pulse-tube refrigerator. These technologies enabled us to downsize the system. Prior to practical use at the RIBF, the HTS SQUID monitor was installed in the beam transport line of the RIKEN ring cyclotron to demonstrate its performance. As a result, a $20 \mu\text{A } ^{40}\text{Ar}^{15+}$ beam intensity (63 MeV/u) was successfully measured with a 500 nA resolution. Despite the performance taking place in an environment with strong gamma ray and neutron flux radiation, RF background and large stray magnetic fields, the measurements were successfully carried out in this study. This year, the HTS SQUID monitor was upgraded to have a resolution of 100 nA and was reinstalled in the beam transport line, enabling us to measure a $4 \mu\text{A } ^{132}\text{Xe}^{20+}$ (10.8 MeV/u) beam and a $1 \mu\text{A } ^{132}\text{Xe}^{41+}$ (50.1 MeV/u) beam used for the accelerator operations at RIBF.

Hence, we will report the results of the beam measurement and the present status of the HTS SQUID monitor.

INTRODUCTION

The RIBF project to accelerate all elements from hydrogen to uranium up to an energy of 440 MeV/u for light ions and 350 MeV/u for heavy ions started in April 1997 [1]. Fig. 1 shows a schematic layout of the RIBF facility. These research activities in the RIBF project make extensive use of the heavy-ion accelerator complex, which consists of one linac and four ring cyclotrons, i.e., a variable-frequency linac (RILAC), the RIKEN ring cyclotron (RRC), a fixed-frequency ring cyclotron (fRC), an intermediate-stage ring cyclotron (IRC) and a superconducting ring cyclotron (SRC). Energetic heavy-ion beams are converted into intense RI beams via the projectile frag-

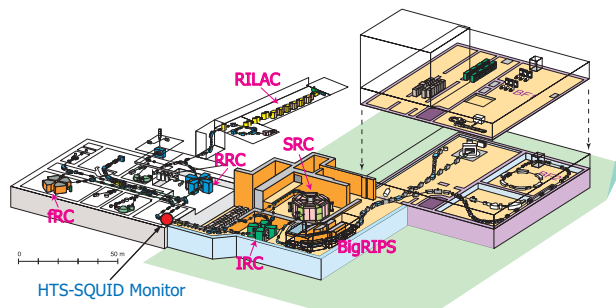


Figure 1: Schematic bird's-eye view of the RIBF facility.

mentation of stable ions or the in-flight fission of uranium ions using a superconducting isotope separator, BigRIPS [2]. The combination of these accelerators and BigRIPS will greatly expand our knowledge of the nuclear world into the presently inaccessible region on the nuclear chart. We succeeded in accelerating a uranium beam to 345 MeV/u in March 2007, and a new RI, a neutron-rich palladium isotope, ^{125}Pd , was discovered in July 2007 [3, 4].

Hence, it is essential to keep the beam transmission efficiency as high as possible, because the production of the RI beam requires an intense primary beam during the beam commissioning. Furthermore, activation produced by beam loss, in particular, should be avoided. In this facility, to evaluate the beam transmission efficiency, Faraday cups are used. When an accelerated particle collides with the surface of a Faraday cup, secondary electrons are always generated. If these electrons escape from the insulated cup area, the reading of the beam current is wrong by the number of lost electrons. Thus, the suppression of secondary electrons is very important for measuring the beam current precisely. Usually, this can be done by applying a high negative voltage close to the entrance of the cup. However, since the electrical field on the beam axis is lower than that on the edge, it is difficult to completely suppress the high-energy secondary electrons that are produced by high-energy heavy-ion beams such as uranium beams. To evaluate how many secondary electrons are generated by a beam, a high positive voltage was used for suppression. A measurement result obtained by applying the suppression voltage for a $10.7 \text{ MeV/u } ^{238}_{92}\text{U}^{72+}$ beam is shown in Fig. 2. From this result, the current generated by the secondary electrons was found to be eight times stronger than that of the uranium beam.

To resolve this technical issue, a study of the HTS SQUID monitor has been started at RIKEN [5, 6, 7].

*wtamaki@riken.jp

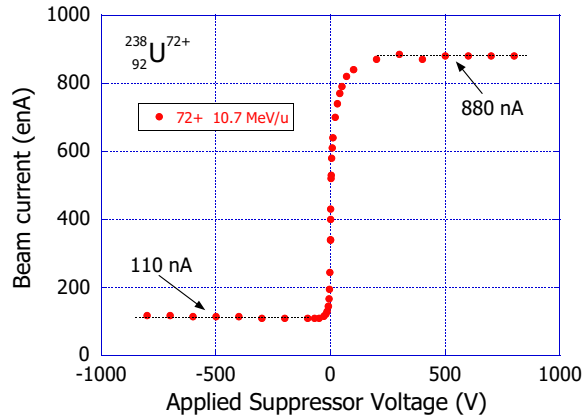


Figure 2: Measurement result obtained applying suppression voltage for 10.7 MeV/u $^{238}_{92}\text{U}^{72+}$ beam. To evaluate how many secondary electrons are generated by the beam, a positive high voltage was used for suppression.

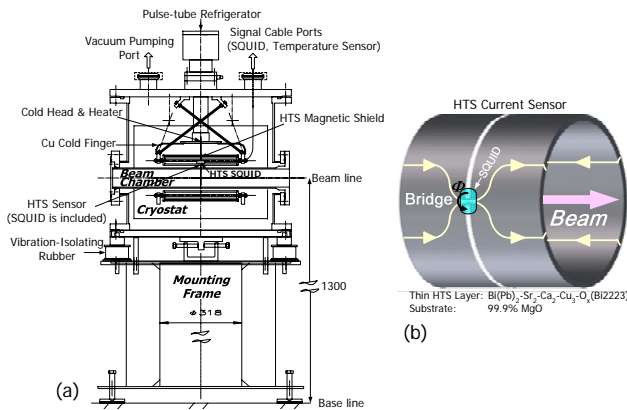


Figure 3: Schematic drawing of the HTS SQUID monitoring system (a) and the current sensor (b).

HTS SQUID MONITOR SYSTEM

A schematic drawing of the HTS SQUID monitor system is shown in Fig. 3(a). This system consists of two vacuum chambers completely separated from each other: one for a cryostat in which the HTS SQUID, an HTS magnetic shield and an HTS current sensor are cooled, and the other the chamber that a beam passes through. In the present work, all these fabricated HTS devices are cooled by a low-vibration pulse-tube refrigerator with a refrigeration power of 11 W at a temperature of 77 K. The operation temperature can be set in the range of 64 K to 90 K (the critical temperature of the HTS SQUID) using a heater, since the pulse-tube refrigerator is capable of cooling the system to temperatures lower than liquid-nitrogen temperature. Furthermore, it is possible to stabilize the temperature of the HTS SQUID with an accuracy of 5 mK using a PID feedback controller, which has four thermometers and a heater. The PID controller calculation involves three separate pa-

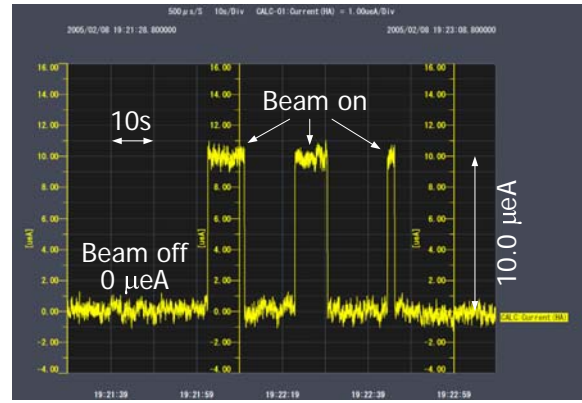


Figure 4: A $10\ \mu\text{A}$ $^{40}\text{Ar}^{15+}$ beam intensity (63 MeV/u) was successfully measured in real-time with a 500 nA resolution when a $1\ \mu\text{A}$ beam produced a magnetic flux of $6.5 \times 10^{-6} \Phi_0$ at the input coil of the HTS SQUID.

rameters; the Proportional, the Integral and Derivative values. The temperature of the cold head was measured as a function of time. Consequently, the deviation of the temperature over a period of 18 h was controlled within 3.4 mK (1σ) [5]. Both the HTS magnetic shield and the HTS current sensor were fabricated by dip-coating a thin $\text{Bi}_2\text{-Sr}_2\text{-Ca}_2\text{-Cu}_3\text{-O}_x$ (Bi-2223) layer on 99.9% MgO ceramic substrates. The HTS SQUID system (Model BMS-G manufactured by Tristan Technologies) contains a low-noise HTS SQUID gradiometer ($\text{Y-Ba}_2\text{-Cu}_3\text{O}_{7-\delta}$) and a controller [5]. When a charged particle (ion or electron) beam passes along the axis of the HTS tube, a shielding current produced by the Meissner effect flows in the opposite direction along the wall of the HTS tube so as to screen the magnetic field generated by the beam. Since the outer surface is designed to have a bridge circuit (Fig. 3(b)), the current generated by the charged particle beam is concentrated in the bridge circuit and forms an azimuthal magnetic field Φ around the bridge circuit. The HTS SQUID is set close to the bridge circuit and can detect the azimuthal magnetic field with a high S/N ratio.

EXPERIMENTAL RESULTS

Prior to the beam measurements in the RRC hall, preliminary measurements were successfully carried out as follows: (1) the first beam test of the HTS SQUID monitor in the beam transport line for the electron cyclotron resonance (ECR) ion source in the CNS experimental hall and (2) the second beam measurement at the E1 experimental hall in RIKEN to measure the current of the high-energy heavy-ion beam. Aiming at practical use for accelerator operations, the authors installed the HTS SQUID monitor system in the beam transport line in the RRC hall (Fig. 1).

However, the SQUID electric circuit, which has a dynamic range of 100 dB (from $1\ \mu\text{A}$ to 0.1 A) and a frequency range from DC to 25 kHz, did not function normally owing to the following reasons: (1) an RF back-

ground was caused by the high-power RF cavities of the RRC, which can produce a total power of 0.6 MW; (2) a large stray magnetic field was induced by the main magnetic field of the RRC (max. 1.67 T); (3) there was a neutron radiation dose of 25.5 Sv/year and a gamma radiation dose of 3.0 Sv/year. The radiation doses of neutrons and gamma rays were measured using an ionization chamber and a ^3He proportional counter, respectively. The actual radiation doses where the HTS SQUID monitor is installed should be higher than the above values, because both dosimeters are located 4 m above the HTS SQUID monitor. These data gave tentative criteria from the judgment of safety for radiation damage. After overcoming these difficulties by reinforcing the RF shield and surrounding the flux-locked loop (FLL) circuit with lead and concrete blocks, there were no more problems with the beam current measurement. As a result, a $10\ \mu\text{A}\ ^{40}\text{Ar}^{15+}$ beam intensity (63 MeV/u) was successfully measured with a 500 nA resolution, as shown in Fig. 4, where a $1\ \mu\text{A}$ beam produced a magnetic flux of $6.5 \times 10^{-3} \Phi_0$ at the input coil of the HTS SQUID.

Futhermore, a prolonged recording 4 h of the Ar beam current extracted from the RRC without interruption of the beam user's experiments was achieved, as shown in Fig. 5(a). In this recording, several dips in beam intensity due to ECR ion source discharge can be observed at irregular intervals of 10 s to 60 min. Fig. 5(b) shows a magnified

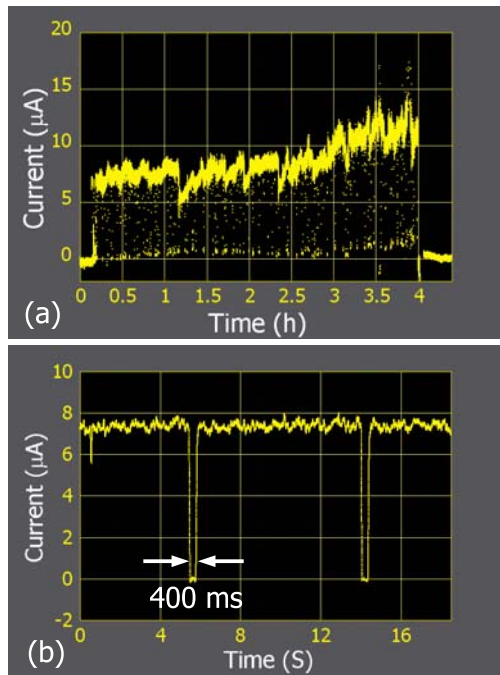


Figure 5: (a) Measurement of 63 MeV/u Ar beam extracted from RRC, which could be recorded for approximately 4 h without interrupting the beam user's experiments. (b) Magnified image of (a) showing dips in current caused by ECR ion source discharge, which recovered within 400 ms.

Applications and Ancillary Systems

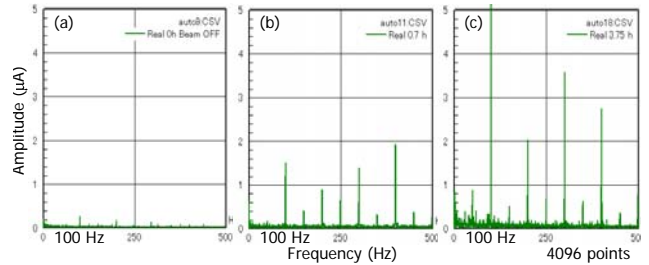


Figure 6: Results analyzed by fast Fourier transform (FFT) of measurements shown in Fig. 5 (a) at 0 h (beam off) (a), 0.7 h (b) and 3.75 h (c).

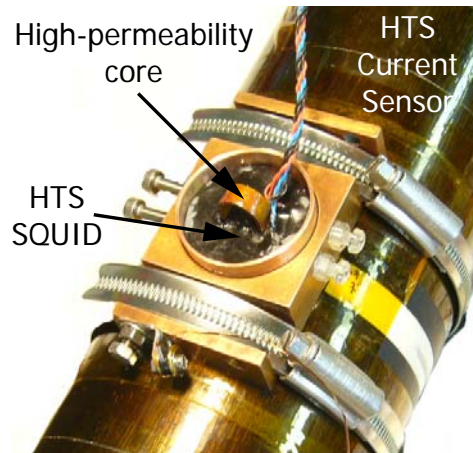


Figure 7: Photograph of new HTS SQUID with two holes containing high-permeability cores.

image of Fig. 5(a), which indicates that the dips in current caused by ECR ion source discharge recovered within 400 ms. The current signals were analyzed by a fast Fourier transform (FFT) in a frequency domain and the results are shown in Fig. 6. The amplitudes of ripples in the modulated beam current increased with beam current. All recording and control systems were connected to a PC-based data acquisition system. Through the Ethernet, these systems were linked to a laptop in the main control room located 200 m from the RRC hall. The sampling time for data acquisition was $500\ \mu\text{s}$, and 100 data points were averaged to improve the signal-to-noise ratio.

PRACTICAL USE OF HTS SQUID MONITOR FOR RIBF

Upgrade and Measurement Results

Aiming at practical use for accelerator operations at the RIBF, we developed a new HTS-SQUID with a high-permeability core that is installed in the two input coils of the HTS-SQUID to improve sensitivity [7]. Fig. 7 shows a photograph of the new HTS SQUID with two holes containing high-permeability cores. The core is composed of

80% Ni and Mo, Re and Fe. The output voltage of the HTS SQUID controller as a function of the simulated beam current is plotted in Fig. 8. From these measurement results, the calibration equation is obtained as

$$\begin{aligned} V_s &= S_{co} \times I_b \times G/500 \\ &= 46.60 \times I_b \times G/500, \end{aligned}$$

where S_{co} , I_b , V_s and G are the coupling efficiency (mV/ μ A), the beam current (μ A), the output voltage of the SQUID controller (mV) and the gain, respectively. A test using a simulated beam current showed a 2-fold improvement in gain, because the coupling efficiency S_{co} of the HTS SQUID monitor when it was not equipped with the magnetic core was 22.8 mV/ μ A [5]. The transfer of the magnetic field produced by the simulated beam current to the SQUID is thus improved. The HTS SQUID monitor was upgraded with the new HTS SQUID and the magnetic core, following which the HTS SQUID monitor was re-assembled. For the purpose of canceling the environmental magnetic noise, the previous mounting frame made of iron was replaced with one made of aluminum with a relative permeability of 1. Fig. 9 shows the HTS SQUID monitor equipped the Al mounting frame and the noise cancellation system, which was installed in the transport line between the fRC and the IRC (Fig. 1). Fig. 10 shows the results of the cooling processes; the temperatures of the cold head, the thermal anchor and the Cu block holding the SQUID were recorded for over 30 h using silicon diode thermometers. The temperature of the HTS SQUID was found to reach the temperature of liquid nitrogen (77 K) after 16.5 h. This year, we were able to measure a 3.6 μ A $^{132}\text{Xe}^{20+}$ (10.8 MeV/u) beam (Fig. 11) and a 1 μ A $^{132}\text{Xe}^{41+}$ (50.1 MeV/u) beam for use in the accelerator operations at RIBF as a result.

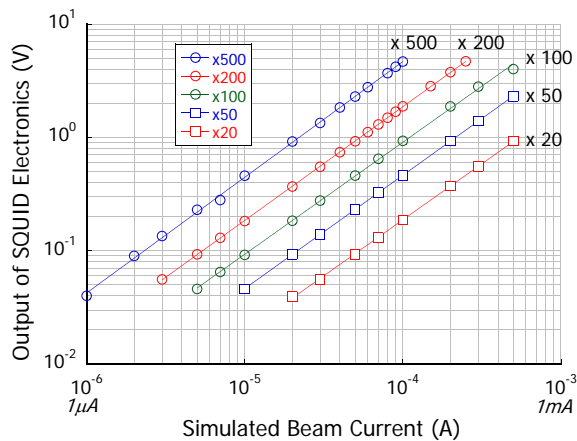


Figure 8: Plot of output voltage of the HTS SQUID controller as a function of simulated beam current.

Applications and Ancillary Systems

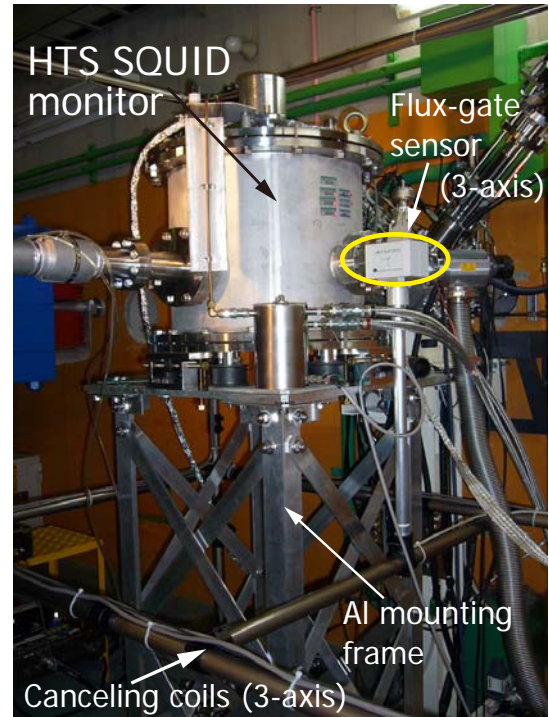


Figure 9: HTS SQUID monitor equipped with the Al mounting frame and the noise cancellation system, which was installed in the transport line between the fRC and the IRC (Fig. 1).

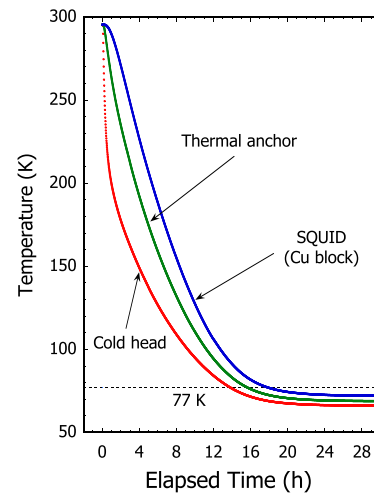


Figure 10: Cooling processes recorded for over 30 h using silicon diode thermometers.

Noise Reduction

To obtain a better resolution for the measurement, we paid close attention to the reductions of noise. A noise-cut transformer, which is completely isolated from the power circuit and not affected by AC source noise, was introduced to remove normal-mode and common-mode noises. In line noise, the noise that flows along one line of leading wires

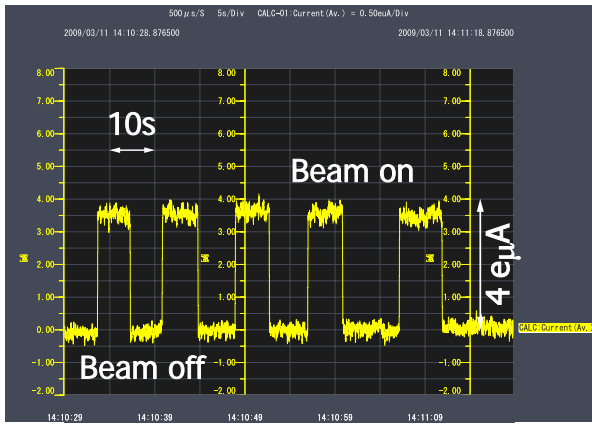


Figure 11: This year, we were able to measure a $3.6 \mu\text{A}$ $^{132}\text{Xe}^{20+}$ (10.8 MeV/u) beam.

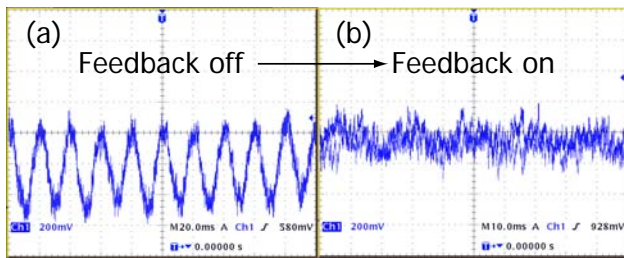


Figure 12: Effect of removed environmental noise by introducing the noise cancellation system.

in one direction and then another line in the return journey is called normal-mode noise, and the noise that flows along both lines in the outward journey and to earth in the return journey is called common-mode noise. Furthermore, all instruments are fixed on a large aluminum plate and the grounds of the instruments are connected to the plate. The signal cables were wired carefully to reduce unnecessary loops as much as possible and all AC lines were covered by braided wires.

The design of noise cancellation system is based on a three-axis Helmholtz cage and feedback control engineering. Three-axis flux-gate sensors are placed near the equipment. A signal is fed through the proprietary controller to a compensation coil, producing precisely calibrated electromagnetic fields. The preliminary result in Figs. 12 (a) and (b) shows the effect of the removal of environmental noise by introducing the noise cancellation system.

The data acquisition and control program, being written in LabVIEW (National Instruments, Ltd.), is almost complete, but some modifications are necessary.

The authors are grateful to E. Nemoto of JEOL DATUM, Ltd., for cooperation regarding the noise cancellation system.

REFERENCES

- [1] Y. Yano, Nucl. Instrum. and Meth. (2007) B 261 p. 1009.
- [2] T. Kubo et al., IEEE Trans. Appl. Supercond. 17 (2003) p. 97.
- [3] Y. Yano, Proc. Int. Nuclear Physics Conf. (INPC2007), Tokyo, Japan, June 2007; Proc. 22nd Particle Accelerator Conf. 07 (PAC07), Albuquerque, New Mexico, U.S.A., June 2007.
- [4] T. Ohnishi et al., J. Phys. Soc. Jpn. 77 No.8 (2008) p. 1069.
- [5] T. Watanabe T et al., Supercond. Sci. Technol. 17 (2004) S450.
- [6] T. Watanabe et al., J. Phys. 43, (2006) p. 1215.
- [7] T. Watanabe et al., J. Phys. 97, (2008) p. 012248.

LATEST DEVELOPMENTS IN ECR CHARGE BREEDERS

T. Lamy, J. Angot, C. Fourel

Laboratoire de Physique Subatomique et de Cosmologie UJF-CNRS/IN2P3-INPG
53, rue des Martyrs 38026 Grenoble CEDEX, France

Abstract

The basic principles of the ECR charge state breeder (CSB) are recalled, special attention is paid to the critical parameters allowing the optimization of the ECR charge breeders characteristics (efficiency yield, charge breeding time, capture potential ΔV). An overview is given on the present ECR charge breeders situation and results worldwide. Possible means to increase the $1+$ ion beam capture for light ions is presented. In the context of radioactive environment, possible technological improvements and/or simplifications are suggested to facilitate the maintenance and to reduce the human intervention time in case of a subsystem failure.

INTRODUCTION

The Electron Cyclotron Resonance (ECR) charge breeding, developed at Laboratoire de Physique Subatomique et de Cosmologie in Grenoble has been studied and setup (or is under development) in many laboratories worldwide (CERN/ISOLDE - Switzerland, KEK TRIAC - Japan, TRIUMF - Canada, Argonne National Laboratory - United States of America, Texas A&M University - United States of America, SPIRAL2 - France). These developments allow the cross check of the different experimental results and allow improvements of the method and of the technologies.

BASIC PRINCIPLES OF ECR CHARGE BREEDERS

An ECR charge state breeder (CSB) is a classical ECRIS where the injection side is opened in order to inject a $1+$ beam. The $1+$ beam is suitably decelerated in order to optimize its capture by the ECRIS plasma where the multi ionization process takes place before the extraction (Fig. 1).

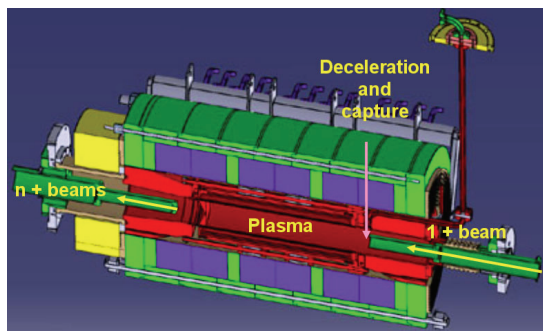


Figure 1: Cut view of the PHOENIX ECR charge breeder.

The main characteristics of an ECR charge breeder for a radioactive ion beam facility are efficiency, fastness, purity and quality of the beams delivered, tuning

Ion Sources

possibilities, reliability and easy maintenance. The critical parameter for the capture efficiency is the final energy of the decelerated beam that should be equal to the energy of the ions of the plasma (a few eV). Different behaviours can be seen for gaseous and non gaseous ions on the ΔV plots which show the $n+$ ion intensity evolution when varying the potential of the ECR charge breeder (Fig. 2). At too low energies (right side of the curves), the beam is reflected by the plasma, then, when decreasing the voltage of the charge breeder, the $1+$ beam begins to get captured and multi ionized; at too high energies (left side of the curves), the metallic ions go to the wall and are lost, the gaseous ones are still available for the multi ionization process because they can be reflected by the walls.

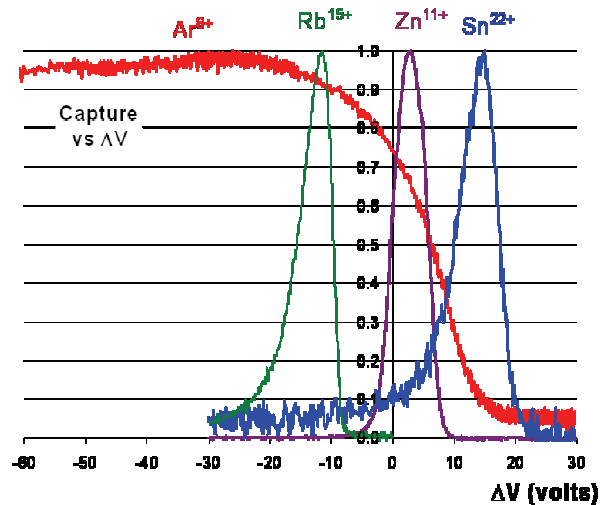


Figure 2: Normalized ΔV plots for various elements and $1+$ sources.

EXPERIMENTAL AND OPERATIONAL ECR CHARGE BREEDERS WORLDWIDE

CERN-ISOLDE

The LPSC-PANTECHNIK PHOENIX charge breeder bought by CRLC Daresbury has been installed at ISOLDE as an experiment (IS397) just after the General Purpose Spectrometer. The purpose was to investigate the charge breeding process with $1+$ beams produced by a realistic and well known ISOL facility. This experiment has been unfortunately stopped in 2008 due to insufficient manpower; however, it has produced a lot of interesting and/or preliminary results detailed in [1]. To summarize, stable and radioactive ions have been injected, the efficiency yields measured are within the range of the results obtained at LPSC, the charge breeding times are

roughly 10 ms/charge which is consistent with the ones obtained at LPSC. The injection of a cocktail of radioactive beams delivered by one ion source, like: ^{142}Xe ($T_{1/2} = 1.22\text{s}$) + ^{142}Cs ($T_{1/2} = 1.689\text{s}$) + ^{142}Ba ($T_{1/2} = 10.6\text{min}$) + ^{142}La ($T_{1/2} = 91.1\text{min}$), show when analysing the gamma rays emitted by the n^+ ions, that the xenon and the caesium ions are present with their own ΔV plots giving the evidence of the capture process explained in the previous paragraph. The injection of molecules has been performed (i.e., LaO^+) and it has been experimentally proven that these molecules are broken in the charge breeder (an efficiency of 3.5 % has been measured for the production of $^{139}\text{La}^{23+}$ with such process).

KEK – TRIAC

The KEK-TRIAC ECR charge breeder [2] is basically of the same kind as the LPSC one but with a higher injection magnetic field (1.6 T with respect to 1.2 T). The efficiency yields obtained on one charge, for a 18 GHz operation, are typically in the range 7-10% for gaseous elements, and 1-2 % for non-gaseous ones. A promising treatment method of the plasma chamber walls [3] has been proposed in order to decrease the background superimposed with the low level radioactive n^+ beams. To understand the low efficiencies observed with non gaseous ions better, a very interesting study has been performed to measure the repartition of the remaining activity in the plasma chamber. It shows that the main part of the activity is isotropic at the extraction side of the source [4].

TRIUMF - ISAC

At TRIUMF, many experiments have been performed on a test stand with a modified LPSC-PANTECHNIK PHOENIX charge breeder including two steps deceleration and extraction systems. The source operates at 14.5 GHz, helium is used as buffer gas. For alkali ions the efficiencies obtained are nominal, for gaseous ones a bit lower than in other laboratories certainly due to the n^+ transmission that was not fully optimized. The charge breeding times are much higher than the ones usually observed, it could be due to the use of helium as buffer gas [5]. n^+ impurities have been significantly decreased by the setup of an additional electrostatic bender just after the magnetic separation [6]. The ECR charge breeder has been setup on the ISAC facility and a first radioactive ion beam (^{80}Rb) has been charge bred and accelerated [7]. Additional results will be presented at the 2009 International Conference on Ion Sources at Gatlinburg (Tennessee-USA).

ANL - CARIBU

In the frame of the ATLAS superconducting linear accelerator upgrade, the CARIBU project will permit the production and the charge breeding of neutron rich ions. The ECR charge breeder has been designed and setup by modifying an existing ECR ion source. Stable Rubidium and caesium 1^+ ion beams have been successfully charge

bred with good efficiencies. It has been recently shown that the vacuum improvement of the ECR charge breeder shifts the charge state distribution towards higher charge states and improves the efficiency yields. Let us note that very good results have been obtained on this project within a tight schedule. For more details see [8].

Texas A&M University

In the frame of the upgrade of the K500 superconducting cyclotron facility, in order to reaccelerate radioactive ion beams by 2011, an ECR charge breeder has been designed and built by Scientific Solutions (San Diego, USA) [9]. It is a 'classical' ECR charge breeder based on the AECR-U magnetic configuration [10], but innovative concepts have been applied with respect to other charge breeders: the 1^+ beam injection is performed through a little hole, the microwaves are injected axially into an almost closed plasma chamber leading to an expected better HF coupling. A first plasma test has been performed into the device, charge breeding experiments are planned by the end of year 2009.

CHARGE BREEDING SIMULATION

Some theoretical work has been and is still performed with more or less sophisticated methods.

At the Laboratori Nazionali di Legnaro, M. Cavenago has developed a 3D model of the full process in the PHOENIX ECR charge breeder (axial and radial magnetic fields and ambipolar potential including pre-sheath and hexapolar distortion). It is based on a 3D Monte Carlo simulation where random kicks, at each time step, simulate the collision from the background, including ionization and recombination models [11], [12].

At Institute of Particle and Nuclear Studies - KEK, S. C. Jeong has calculated the stopping efficiency [13] for a 10 eV incident Ar^+ ion beam injected into a uniform plasma of N^{2+} ($n_i = 5 \times 10^{11}/\text{cm}^3$, $T_i = 1\text{eV}$), the model includes ion-ion collisions and magnetic field.

At FAR-TECH Inc., J. S. Kim is developing a suite of codes modelling successively the capture process, the physics of the ECR plasma leading to the charge state distribution, and then the extraction. Each code is based on a specific model like Monte Carlo simulations for capture, Fokker-Planck equation resolution for ECR physics and a specific mesh less method for the extraction (Particle In Cloud Of Points) [14, 15].

All these theoretical works can help to a better understanding of the processes and may permit to improve the characteristics of the method.

ECR CHARGE BREEDER IMPROVEMENTS

Efficiency Increase

The efficiency of a ECR charge breeder (CSB) for a specific charge state n^+ is the ratio of the ionic current of this n^+ ion beam relative to the 1^+ beam current injected.

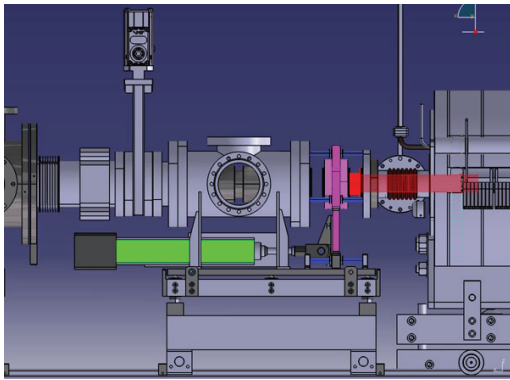


Figure 3: Mechanical setup for the movement of the grounded tube.

Depending on the tuning of the device, the charge state distribution can be peaked on different charge states. The efficiency, generally given on the most abundant charge state, is about 10 % for gaseous elements and a factor 3 less for metallic or alkali ones. Due to the electrostatic configuration of a CSB, with a grounded tube on the injection side, a proportion of the $n+$ ions are extracted in the backward direction. In order to confidently compare different CSB setups, one should first control the transmission of the $n+$ line (ratio of the sum of the $n+$ ion beam currents measured after the analysis device with respect to the total current extracted measured just after the extraction of the source). This must be performed as a preliminary stage of the characterization of a CSB, closing it at the injection side as a normal ECRIS (equipotential).

Deceleration of the $1+$ ion beam is considered as a critical phase of the process that should lead to the optimal velocity of the $1+$ ions entering the plasma in order to maximize their capture. Even if theoretical studies have been performed in order to better understand this process, 3D magnetic field, decelerating electric field, plasma sheath, and final slowing down of the $1+$ ions have to be included in such simulations, the ECR semi-empirical experimental method is often preferred for the optimization. The decelerating optics has been optimized by a two electrode system at TRIUMF and a multi electrode one has been setup at the KEK [16] charge breeder without obvious efficiency increase with respect to the direct deceleration taking place at the extremity of the grounded tube in the LPSC charge breeder. This tube, acting like an extraction system on the injection side and establishing the decelerating electric field, may be of crucial importance for the interface between the $1+$ ion beam and the ECR plasma. Specifically, light ions ($A < 40$), which have a higher speed than heavier ones in the CSB, are difficult to capture and their charge breeding efficiency is lower. The best result obtained at LPSC for sodium is an efficiency of 1.4 % for $^{23}\text{Na}^{6+}$ (using He gas) with a charge breeding time of 50 ms. In such conditions, it has been shown that the injection of NaO^+ , available from the thermo ionization source producing the Na^+ beam, permitted to immediately increase the efficiency to 1.9 %, showing that the plasma capture may effectively

depend on the speed of the $1+$ ions during deceleration. At LPSC, we have developed a system permitting to move the decelerating tube, like as shown in Fig. 3, with the idea that for light ions a higher deceleration distance would be needed.

The green part is a hydraulic jack moving the pink part guided by the blue tubes and supporting the grounded tube in red. The available range is 40 mm.

Simulations of the $1+$ ion trajectories have been performed with SIMION for different positions. The simulation includes the full 3D magnetic field calculated with RADIA [17]. On Fig. 4, two sets of trajectories are shown. On the first one, the grounded tube ends in front of the HF power input, on the second one, the grounded tube is moved backward by a distance of 30 mm. The initial conditions for the $1+$ ions have been reconstructed from the emittance measurement of a real rubidium beam extracted from a thermo-ionization source, supposing a Gaussian beam. The blue vertical line is the entrance of the hexapole, the green one is the axis of the HF wave guide. These plots show that when moving the tube, the focus point of the $1+$ beam is moved along the axis and that the interface between the $1+$ beam and the plasma can be drastically changed. This movement can be an additional tuning to the classical double Einzel lens optics and may help to adapt the $1+$ beam to the plasma entrance, especially for light ions which are too fast to be efficiently captured.

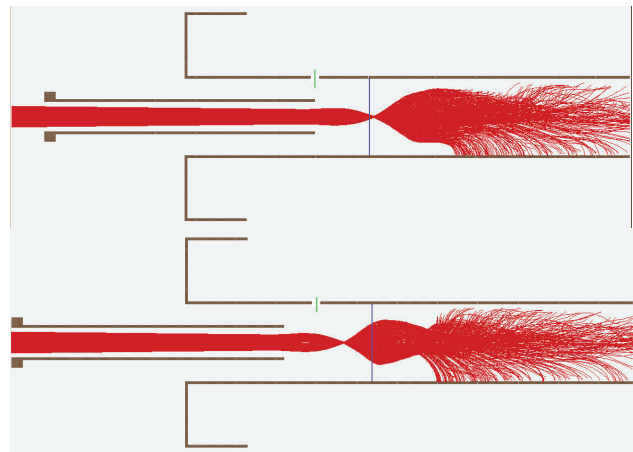


Figure 4: $1+$ trajectories during deceleration for two positions of the grounded tube.

Suppression of the Grounded Tube

In a radioactive environment, especially when using high intensities, one should facilitate the maintenance of the system in order to limit potential contamination and personal exposition to radiations. Due to the configuration of the ECR charge breeder, with the grounded tube at the injection and the puller electrode at the extraction which are supported by the injection and extraction vacuum chambers, it is not easy to find the best mechanical design and an easy procedure to remove the booster from the beam line, unless the two tubes are motorized and axially moveable. The best solution at the injection would be to

fix the grounded tube into the body of the booster itself, but due to the high voltage configuration, the ground has to be brought from the injection vacuum chamber. However, if the 1+ beam were able to enter the charge breeder without a grounded tube, it would be extremely interesting. Without the red grounded tube of Fig. 3, it would be possible to partially close the CSB. A disk (with a hole permitting the injection of the 1+ beam) can be inserted into the plasma chamber at the entrance of the hexapole, the present HF injection (perpendicular to the grounded tube) could be modified to an axially injection in a fully equipotential plasma chamber like in standard ECR ion sources (see Fig. 5).

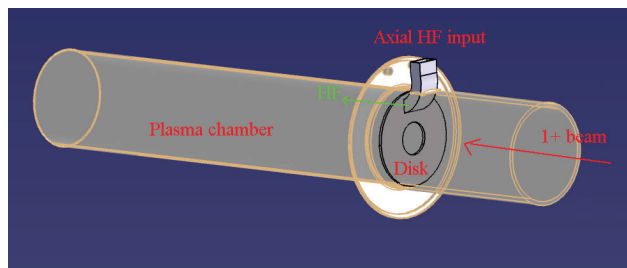


Figure 5: HF and 1+ beam injections in the plasma chamber without decelerating tube.

The benefits of such configuration are:

- The decrease of the HF leaks towards the injection side
- A more efficient coupling of the HF to the plasma
- The disappearance of the extraction of n+ beams towards the injection side

Depending on the optical characteristics of the 1+ beam entrance in the charge breeder, the charge breeding efficiency may be increased significantly. Simulations of the 1+ trajectories have been performed for such a configuration, and show that modifying the double Einzel lens tunings, thanks to the magnetic field, it is possible to enter the charge breeder despite the deceleration at its entrance. The mechanics of this concept is rather simple and is planned to be designed and tested at LPSC.

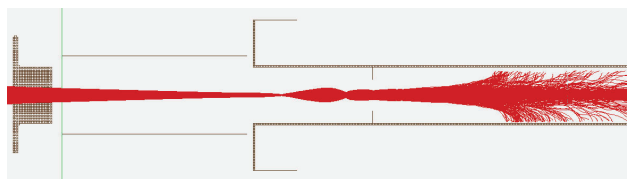


Figure 5: 1+ trajectories without decelerating tube.

Charge Breeding Time Decrease

Efficiency, when charge breeding radioactive ions, is not the only parameter to improve. Depending on the half-life of the isotope, a compromise should be found between the efficiency and the charge breeding time, in fact, each radioactive ion beam should have its specific tuning depending on its half-life. For example, we have published in [18] an efficiency of 5.5 % with a charge

breeding time of 225 ms ('slow charge breeding'). Recently, we could find a different tuning, lowering the confinement magnetic field, leading to a lower efficiency (3.6 %) but with a much lower charge breeding time of 70 ms ('fast charge breeding'). If we apply these results to the charge breeding of ^{74}Rb ($T_{1/2} \approx 64.9$ ms), and ^{82}Rb ($T_{1/2} \approx 76$ sec), the final number of ions available for physics will be higher when using the fast charge breeding tuning (but lower efficiency) for the ^{74}Rb , when it will be the opposite for the ^{82}Rb . In order to further improve the method, the reproducibility and the parameters influencing the charge breeding time should be better theoretically and experimentally characterized.

REFERENCES

- [1] M. Marie-Jeanne, PhD Thesis Université Joseph Fourier – Grenoble 1, "Investigation of the performance of an ECR charge breeder at ISOLDE: a study of the $1+ \rightarrow n+$ scenario for the next generation ISOL facilities", February 6th, 2009.
- [2] S. C. Jeong et al., Nucl. Instr. Meth. B Vol. 266, Issues 19-20, pp 4411-4414.
- [3] N. Imai et al., Rev. Sci. Instr. 79, 02A906, (2008).
- [4] M. Oyaizu et al., Proceedings of the 6th Japan-Italy Symposium on Heavy-Ion Physics, AIP Conf. Proc. Vol. 1120, pp. 308-312 (May 2009).
- [5] F. Ames et al., Rev. Sci. Instr. 79, 02A902 (2008).
- [6] F. Ames et al., Rev. Sci. Instr. 77, 03B103 (2006).
- [7] F. Ames et al., Proc. of the PAC09, Vancouver - Canada, May 2009, "Acceleration of charge bred radioactive ions at TRIUMF".
- [8] R. Vondrasek et al., these proceedings, "Initial Results of the ECR Charge Breeder for the ^{252}Cf Fission Source Project (CARIBU) at ATLAS".
- [9] Wayne D. Cornelius, Proc. of ECRIS08, Chicago, Illinois - USA, WECO-B01, "Design of a Charge-Breeder Ion Source for Texas A&M University".
- [10] <http://ecrgroup.lbl.gov/aecr-u.htm>
- [11] M. Cavenago, Proc. Of the PAC'05, Knoxville, Tennessee - USA, "Simulations of beam injection and extraction into ion Sources".
- [12] M. Cavenago et al., Rev. Sci. Instr. 73 (2), 537-540 (2002).
- [13] S. C. Jeong et al., Rev. Sci. Instrum. 73 (2), 803-805 (2002).
- [14] J.S. Kim et al., Rev. Sci. Instrum. 79, 02B906 (2008)
- [15] J.S. Kim et al., Proc. of ECRIS08, Chicago, Illinois-USA, TUCO-C04, "Status of far-tech's electron-cyclotron-resonance charge-breeder simulation toolset: MCBC GEM and IONEX".
- [16] S. C. Jeong et al., Rev. Sci. Instrum. 75 (5), 1631-1633 (2005).
- [17] O. Chubar, P. Elleaume and J. Chavanne, J. Synchrotron Rad. 5, 481-484 (1998).
- [18] Lamy T. et al., Rev. Sci. Instrum. 73 (2), 717-719 (2002).

INITIAL RESULTS OF THE ECR CHARGE BREEDER FOR THE ^{252}Cf FISSION SOURCE PROJECT (CARIBU) AT ATLAS*

R. Vondrasek[#], R. Scott, J. Carr, R. Pardo, Argonne National Laboratory, Argonne, IL 60439, U.S.A.

Abstract

The construction of the Californium Rare Ion Breeder Upgrade (CARIBU), a new radioactive beam facility for the Argonne Tandem Linac Accelerator System (ATLAS), is nearing completion. The facility will use fission fragments from a 1 Ci ^{252}Cf source, thermalized and collected into a low-energy particle beam by a helium gas catcher. In order to reaccelerate these beams, the existing ATLAS ECR1 ion source was redesigned to function as an ECR charge breeder. The helium gas catcher system and the charge breeder are located on separate high voltage platforms. An additional high voltage platform was constructed to accommodate a low charge state stable beam source for charge breeding development work. Thus far the charge breeder has been tested with stable beams of rubidium and cesium achieving charge breeding efficiencies of 5.2% into $^{85}\text{Rb}^{17+}$ and 2.9% into $^{133}\text{Cs}^{20+}$.

INTRODUCTION

The Californium Rare Ion Breeder Upgrade (CARIBU) [1] will utilize fragments from fission of ^{252}Cf to provide nuclei which will be thermalized in a helium gas-catcher, mass separated and injected into an ECR charge breeder (ECRCB) to raise their charge state for subsequent acceleration in the ATLAS superconducting linear accelerator.

The 1Ci ^{252}Cf source will be mounted in a heavily shielded cask assembly attached to a helium gas catcher/RFQ ion guide which will thermalize the fission fragments. After a 50 kV acceleration, the fission fragments will be delivered to an isobar separator with a mass resolution of 1:20000. The entire system will be on a high voltage platform located in a new building addition allowing isolation from the rest of the ATLAS facility.

After analysis by the isobar separator, the mass analyzed beam will be delivered to the ECRCB through an electrostatic beam transport system. The ECRCB is based on the redesign of an existing ATLAS stable-beam 10.5 GHz ECR source (ECR1) [2] and is mounted on a separate 350 kV high voltage platform to provide the necessary velocity to match the velocity profile of the first resonator of the Positive Ion Injector (PII) linac. A small high voltage platform was constructed next to the existing ECRCB platform to house a stable beam source. The source provides stable low charge state beams to the ECRCB for system configuration, accelerator tuning, and development work. The overview of the charge breeder system is shown in Fig. 1.

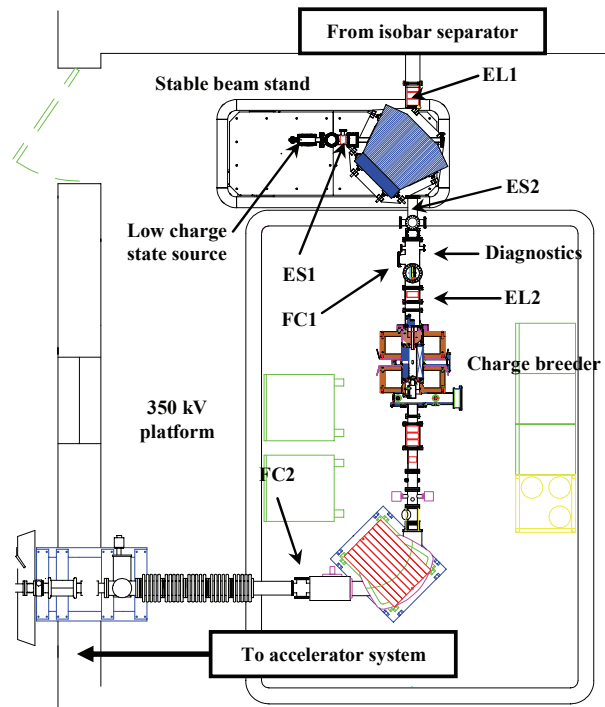


Figure 1: Floor plan of the charge breeder system showing the stable beam stand and surface ionization source, the electrostatic steerers (ES1 and ES2), the einzel lenses (EL1 and EL2), the Faraday cups (FC1 and FC2), the diagnostics location (emittance), and the ECR charge breeder.

CHARGE BREEDER

The modifications required for the ECR1 ion source to function as a charge breeder were extensive, with the details given in [3]. In summary, the charge breeder is a room temperature ECR ion source with an open structure permanent magnet hexapole with a wall field of 0.84 T. The source is capable of accepting multiple frequencies with the RF launched through the hexapole radial slots. This scheme allows a large amount of iron to be retained on the injection side of the source resulting in a higher magnitude and symmetric axial field. The low charge state ions are introduced into the plasma through a stainless steel tube which is mounted on a linear motion stage, thus allowing the deceleration point to be adjusted on line. A new deceleration tube constructed of 1008 iron is being fabricated in order to increase the magnetic mirror ratio as well as test the theory that a better defined magnetic center field will improve the ion capture. For the isobar separator to achieve the required resolution of 1:20000, beam extraction from the gas catcher must occur

*Work supported by the U.S. Department of Energy, Office of Nuclear Physics, under Contract No. DE-AC02-06CH11357.

[#]vondrasek@anl.gov

at 50 kV. Hence, the high voltage isolation of the source was upgraded to allow 50 kV operation.

Stable Beam Source

Stable beams for development and set up of the charge breeder are currently provided by two sources – a surface ionization source which can provide beams up to 1 μA (Li, Na, Mg, K, Ca, Rb, Cs, Ba, and Sr) and an RF discharge source which can provide beams up to 2 μA (O, Ne, Ar, Kr, and Xe). To date the RF discharge source has only been tested off line. The stable source is mounted on a high voltage platform adjacent to the charge breeder platform. The optics of the stable beam system were designed such that the beam coming from the stable beam source matches the optics condition of the beam coming from the isobar separator. In this way, minimal tuning should be necessary when switching over from the stable guide beam, used to set up the charge breeder and linac system, to the radioactive beam of interest.

CHARGE BREEDING METHODOLOGY

The charge breeding efficiency is determined by measuring the ‘background’ beam (at FC2 in Fig. 1) coming from the ECR charge breeder when the system is tuned for a particular beam species but the 1+ beam is not yet being introduced into the breeder. The 1+ beam intensity is measured before the charge breeder (at FC1 in Fig. 1) and once introduced into the charge breeder, the measurement at FC2 is repeated. The efficiency is the ratio of the particle current of the charge bred n^+ beam (corrected for background) and the particle current of the incoming 1+ beam. Critical to an accurate efficiency measurement is reliability of the beam current measurement system (both 1+ and n^+) and the measurement of the background coming from the steady state ECR plasma.

The first charge bred beam of ^{133}Cs was achieved in May 2008 and resulted in an apparent breeding efficiency of 9.0% for $^{133}\text{Cs}^{20+}$. The previous best result for charge breeding of cesium was achieved by TRIUMF using a PHOENIX ECR ion source and resulted in a 2.7% efficiency into $^{133}\text{Cs}^{18+}$ [4]. The large disparity in results prompted a systematic investigation of the charge breeder system as well as the technique used to determine the breeding efficiency.

Beam Current Measurement

The first path of investigation was the accuracy of the beam current measurement of the incoming 1+ beam. The calibration of the picoammeter used to measure the beam currents was checked and found to be accurate. A small Faraday cup (Fig. 2), with 300 V suppression and ground rings, was constructed and inserted into the upstream end of the transfer tube (insulated from tube with a thin walled Vespel sleeve). This method allowed a direct comparison of the two Faraday cup readings under the same running conditions and also served as a check of the acceptance of the transfer tube since its diameter (Φ 19

mm) is smaller than that of the ‘standard’ Faraday cup (Φ 25 mm).

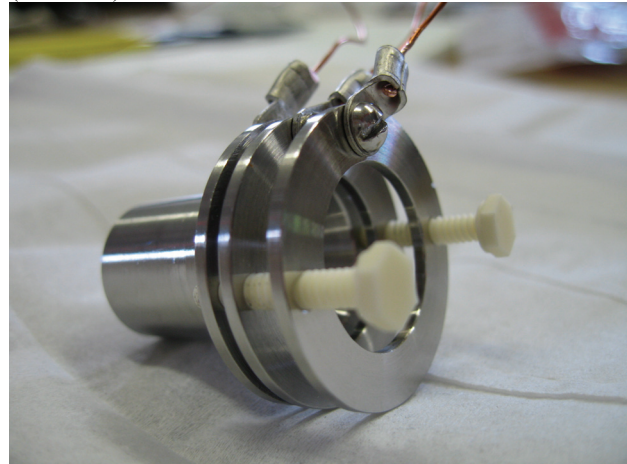


Figure 2: Small Faraday cup which was inserted into the transfer tube. The cup has an isolated ground ring, suppressor ring at -300 V, and isolated collector. The cup acceptance (Φ 19 mm) matches that of the transfer tube.

Resetting the system to the same parameters as those that produced the 9.0% breeding efficiency, it was observed that the ‘standard’ Faraday cup measured 34 enA while the ‘transfer tube’ Faraday cup measured 125 enA. The tantalum charge collector from the ‘standard’ Faraday cup was removed and testing with a multimeter showed that portions of the charge collector surface were covered with an insulating layer. With a beam energy of only 10 keV, the 1+ ions were unable to penetrate this layer, thus resulting in an erroneous beam current measurement. The charge collector was replaced with a new one fabricated from stainless steel. The series of measurements with the cesium beam were repeated and the two cup readings were found to be in agreement.

Background Measurement

The n^+ background level is determined by measuring the beam intensity with the transport system tuned for the ion species of interest without injecting the 1+ beam into the charge breeder. The measurement is repeated after the 1+ beam is introduced into the breeder and the difference in beam intensities represents the charge bred beam ‘ n^+ ’.

The initial technique used to stop introduction of the 1+ beam was to insert FC1. To check the validity of this technique, observations were made of the spectrum from the ECR source with the 1+ beam stopped with FC1, stopped with the electrostatic steerer just after the surface ionization source (ES1), and finally with the surface source turned off. Fig. 3 shows the disparity in background levels for these various techniques using a rubidium beam (saturating ES1 and turning off the surface source were equivalent in their effect).

A direct comparison of the techniques demonstrates the effect. With $^{133}\text{Cs}^{20+}$ under the same conditions, the calculated charge breeding efficiency using the FC1 technique was 6.5%, using the ES1 saturation technique resulted in an efficiency of 2.6%. The ultimate source of

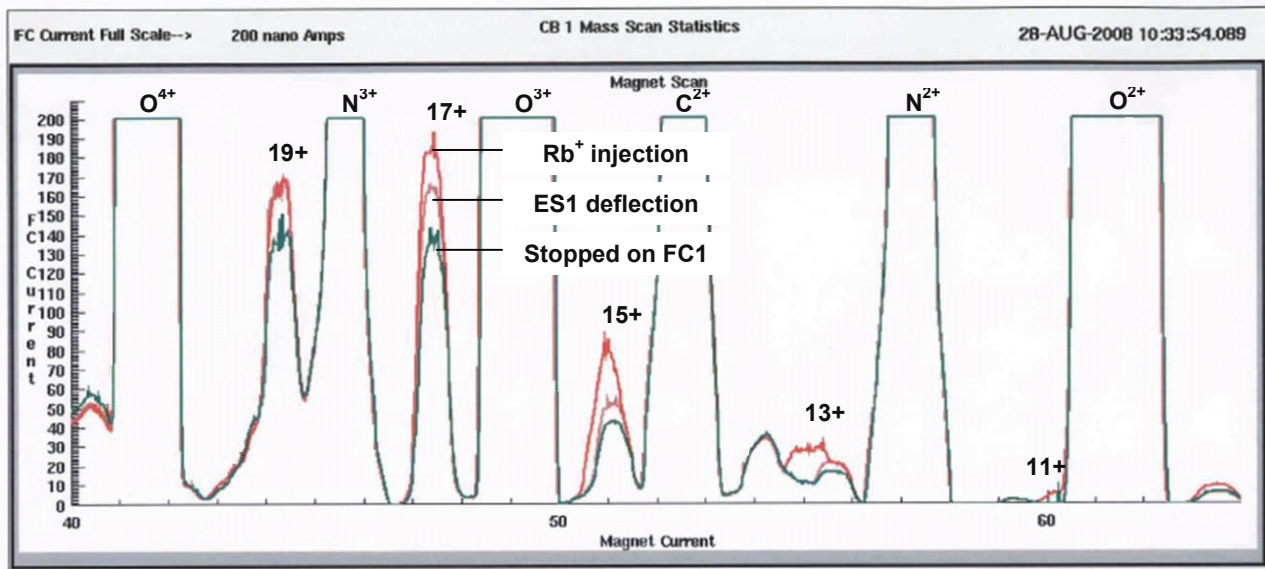


Figure 3: The top trace is with Rb⁺ injection. The middle trace is with Rb⁺ stopped using the electrostatic steerer (ES1) just after the 1+ source but before the analyzing magnet (saturating the steerer generates the same background spectrum as shutting off the 1+ source). The bottom trace is with the Rb⁺ stopped using the Faraday cup (FC1). The rigidity of ⁸⁵Rb¹⁵⁺ is similar to that of ⁴⁰Ar⁷⁺ and the rigidity of ⁸⁵Rb¹⁷⁺ corresponds to that of ⁴⁰Ar⁸⁺.

the discrepancy was traced to outgassing in the 1+ injection line which was not present when FC1 was inserted. With FC1 removed from the line, the n+ beam coming out of the injection side of the ECR source would generate outgassing in the upstream 908 analyzing magnet. The gas would diffuse into the ECR plasma, be ionized and raise the background level. The rigidity of ¹³³Cs²⁰⁺ corresponds to that of ⁴⁰Ar⁶⁺. Similar results were obtained with ¹³³Cs²³⁺ corresponding to ⁴⁰Ar⁷⁺.

CHARGE BREEDING RESULTS

After resolving the problems discussed above, a series of studies of the effect of various parameters on charge breeding was undertaken.

Cesium Results

¹³³Cs charge breeding tests were performed using oxygen support gas and an RF power level of 250 W at 10.44 GHz. Optimizing on ¹³³Cs²⁰⁺ resulted in a breeding efficiency of 2.4%. The Cs⁺ beam current was 62 enA. This test was also conducted using helium as the base plasma resulting in a decreased breeding efficiency of 1.8%. At the time of these tests, the alumina insulators on the surface ionization source were beginning to break down due to surface contamination. Thus, the optics of the source could not be fully optimized, resulting in a poorly matched beam condition. It is believed that this limited the achieved breeding efficiency.

Rubidium Results

The surface ionization source was disassembled and cleaned, and the rubidium sample was installed at this

time to test the rubidium breeding efficiency. The source was run on oxygen support gas with 270 W at 10.44 GHz and optimized on ⁸⁵Rb¹⁵⁺ resulting in a breeding efficiency of 3.8%.

After the initial series of tests, the charge breeder remained idle and under vacuum for a seven month period while work on other aspects of the CARIBU project was undertaken. During this time the source vacuum improved resulting in an operating pressure of 7.5·10⁻⁸ Torr with plasma. The charge breeding results with rubidium improved as well, with a shift in the peak of the charge state distribution from 15+ to 17+ and a factor of 2 improvement in the charge breeding efficiency for 17+ and above. The full results are shown in Table 1.

Table 1: Charge breeding results for rubidium and cesium with single and two frequency heating

Species	Single Frequency Efficiency (%)	Two Frequency Efficiency (%)
¹³³ Cs ¹⁶⁺	0.9	1.4
¹³³ Cs ¹⁸⁺	1.0	1.5
¹³³ Cs ²⁰⁺	2.4	2.9
¹³³ Cs ²³⁺	0.5	1.1
⁸⁵ Rb ¹³⁺	0.8	-
⁸⁵ Rb ¹⁵⁺	3.8	-
⁸⁵ Rb ¹⁷⁺	5.2	-
⁸⁵ Rb ¹⁹⁺	3.2	-
⁸⁵ Rb ²⁰⁺	2.9	-

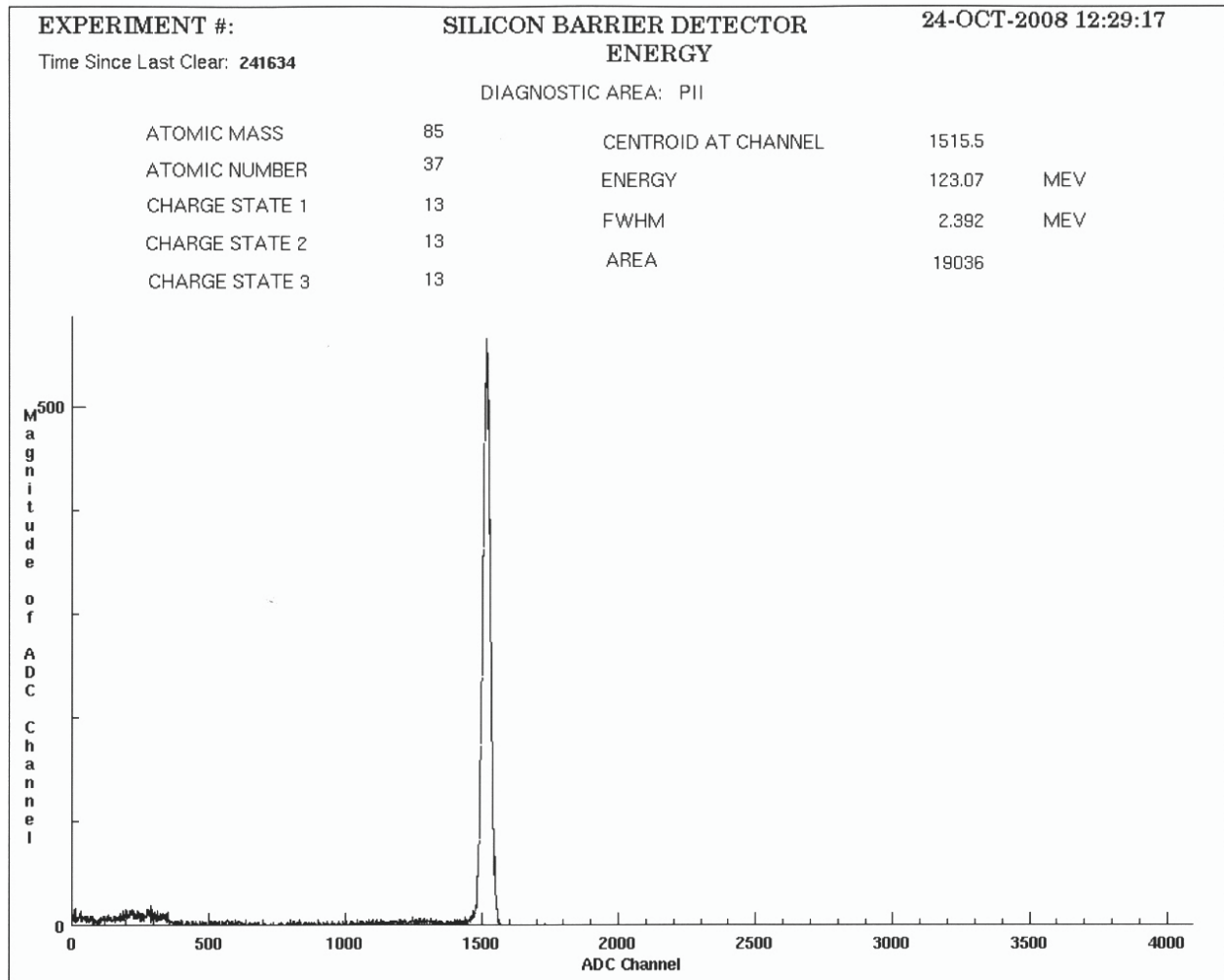


Figure 4: Energy Spectrum of charge bred $^{85}\text{Rb}^{13+}$ after acceleration through the Positive Ion Injector Linac of ATLAS showing an exit energy of 123.07 MeV(1.45 MeV/u).

Acceleration of Charge Bred Rubidium Beam

As a proof of principle, a charge bred beam of $^{85}\text{Rb}^{13+}$ was accelerated off of the ECRCB high voltage platform and injected into the first section of superconducting linac (PII). A beam energy of 129 MeV was measured at the linac exit with a silicon barrier detector (Fig. 4) with an incident beam intensity of 0.62 enA.

Two Frequency Heating

Multiple frequency heating was employed during the cesium tests in an effort to improve the breeding efficiency. A travelling wave tube amplifier (TWTA) was used to provide RF between 11-13 GHz in addition to the 10.44 GHz from the klystron. The total RF power was kept constant to serve as a direct comparison of the two RF injection schemes.

With the source running on an oxygen plasma and the RF divided between the two transmitters - 175 W at 10.44 GHz and 75 W at 12.27 GHz - the charge breeding efficiency for $^{133}\text{Cs}^{20+}$ increased from 2.4% to 2.9%, a modest but meaningful improvement. For $^{133}\text{Cs}^{23+}$ the

efficiency increased from 0.5 to 1.1%, a doubling of efficiency at the same total RF power level.

Time has not allowed similar tests to be carried out with the rubidium, but these tests are planned for the coming months. In addition, previous testing with the ECR1 ion source [5] has shown that the addition of a third frequency further enhances the source performance. The next series of tests will include this aspect of operation.

FUTURE PLANS

Emittance Measurement System

Previous groups have observed that the breeding efficiency increases when the beam emittance is reduced [6]. This same effect was observed with our tests using a set of 4-jaw slits immediately downstream of the surface ionization source as a means of controlling the beam emittance. At the time of the test, however, an emittance measurement system was not installed and change in beam emittance could not be quantified. An emittance measurement system has now been constructed and is ready for installation. The system consists of a mask which has 20 μm laser drilled holes, 0.5 x 0.5 mm

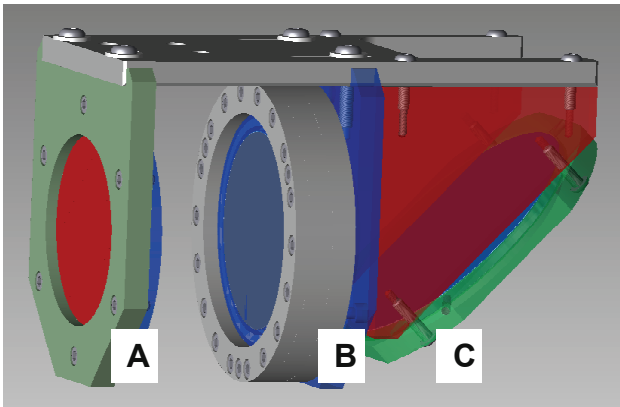


Figure 5: Schematic of the pepper pot emittance device constructed for the 1+ and charge bred beams. Item A is the mask, B is the CsI crystal and C is a mirror.

spacing, on a Φ 40 mm tantalum disk. Behind the mask is a CsI crystal (Φ 40 mm). This scintillator has been tested with a 300 enA, 10 kV beam Cs^+ beam to demonstrate its sensitivity at low energies and intensities. For the much weaker beam currents expected from the CARIBU system, improved sensitivity is possible using a higher lux camera, signal averaging, or the addition of a micro channel plate/phosphor assembly. The capability to add all of the above mentioned options is built into the present system.

Improved Vacuum

The low charge state injection line and charge breeder have base pressures of $2.0 \cdot 10^{-8}$ Torr with no plasma present. The injection line pressure increases to $1.0 \cdot 10^{-7}$ Torr with plasma, and increases further to $3.0 \cdot 10^{-7}$ Torr when the beam extracted from the injection side of the ECR source impacts the surfaces of the analyzing magnet. As this pressure increases, the charge breeding efficiency decreases by $\sim 30\%$. To combat this problem, the chamber that houses the transfer tube has been modified to accept an additional turbo pump. The analyzing magnet chamber is scheduled to be removed, cleaned, and baked out to reduce the outgassing. A set of beamline collimators will also be installed to inhibit gas flow from the low charge state line into the ECR source, an important condition when the RF discharge source is used. The turbo pump locations are such that the placement of the collimators will provide a differential pumping arrangement.

50 kV Operation

For the isobar separator to achieve the required resolution of 1:20000, beam extraction from the gas catcher must occur at 50 kV. Hence, the high voltage isolation of the source was upgraded to allow 50 kV operation. To date, the source has only operated at 30 kV due to drain current issues with the high voltage power supply. However, all aspects of the ECR source were tested to 65 kV without plasma present. A new power supply has been purchased and testing to 50 kV operation will take place in the coming weeks.

Charge Breeding Tests

The main issue with the injection of metallic beams is that once an incoming low charge state ion strikes the wall, that ion is lost to the plasma. In an attempt to combat this problem, a hot tantalum liner has been constructed for the ECR charge breeder. Charge breeding efficiencies with and without the liner in place will be compared to determine the effectiveness of this technique. Attention has to be paid to the hold up time of the atoms on the wall. If the hold up time becomes too great, the breeding efficiency of the shorter lived radioactive species will not be improved.

Up to now, only alkali metals from the surface ionization source have been used for charge breeding. The RF discharge source, which has been tested off line, will soon be moved on line to test the breeding efficiency with gases.

REFERENCES

- [1] R. Pardo, Guy Savard, Sam Baker, Cary Davids, E. Frank Moore, Rick Vondrasek, Gary Zinkann, NIM-B 261, Issues 1-2, 965 (2007).
- [2] D. Moehs, R. Vondrasek, R. H. Scott, R. C. Pardo, J. M. Montgomery, Rev. Sci. Instrum. 73, 576 (2002)
- [3] R. C. Vondrasek, R. Scott, J. Carr, R. C. Pardo, Rev. Sci. Instrum. 79, 02A901 (2008).
- [4] F. Ames, R. Baartman, P. Bricault, K. Jayamanna, M. McDonald, P. Schmor, T. Spanjers, D. H. L. Yuan, T. Lamy, Rev. Sci. Instrum. 79, 02A902 (2008).
- [5] R. C. Vondrasek, R. Scott, R. C. Pardo, Rev. Sci. Instrum. 77, 03A337 (2006).
- [6] P. Sortais, J. F. Bruandet, J. L. Bouly, N. Chauvin, J. C. Curdy, R. Geller, T. Lamy, P. Sole, and J. L. Vieux-Rochaz, Rev. Sci. Instrum. 71, Number 2, 617 (2000).

ION BEAM COCKTAIL DEVELOPMENT AND ECR ION SOURCE PLASMA PHYSICS EXPERIMENTS AT JYFL*

O. Tarvainen[#], T. Kalvas, H. Koivisto, T. Ropponen, V. Toivanen, J. H. Vainionpää, A. Virtanen and
J. Ärje, JYFL, 40500 Jyväskylä, Finland

Abstract

The accelerator based experiments at JYFL (University of Jyväskylä, Department of Physics) range from basic research in nuclear physics to industrial applications. A substantial share of the beam time hours is allocated for heavy ion beam cocktails, used for irradiation tests of electronics. Producing the required ion beam cocktails has required active development of the JYFL ECR ion sources. This work is briefly discussed together with the implications of the beam cocktail campaign to the beam time allocation procedure. The JYFL ion source group has conducted experiments on plasma physics of ECR ion sources including plasma potential and time-resolved Bremsstrahlung measurements, for example. The plasma physics experiments are discussed from the point of view of beam cocktail development.

INTRODUCTION

The JYFL accelerator laboratory has been operational since 1992 in its present location. The heart of the facility is the K-130 isochronous cyclotron [1] with annual operation time exceeding 6000 hours since already more than ten years. The ion beams for the cyclotron are produced with two electron cyclotron resonance ion sources (ECRIS) [2,3] for heavy, highly charged ions and with a negative filament-driven multicusp ion source for H⁻ and D⁻ [4]. Due to the intense use of the cyclotron, the development work of the accelerator systems has concentrated on the ECR ion sources and the available selection of ion beams.

A substantial share of the beam time hours at JYFL is allocated for heavy ion beam cocktails, used for irradiation tests of electronics at RADEF-facility [5]. The users of the facility range from privately owned companies to large scale institutions, e.g. the European Space Agency. The irradiation tests of electronic components are nearly indispensable for the JYFL accelerator laboratory from the economic point of view. This is reflected in the annual distribution of accelerated ions. The share of heavy ion cocktails has grown gradually from < 5 % in 2002 to > 25 % in 2009 (January - June).

HEAVY ION BEAM COCKTAILS AT JYFL

For efficient irradiation tests of single event effects (SEE's) in semiconductors with the cyclotron three requirements have to be met by the ion beam cocktails.

First of all, the linear energy transfer (LET) value of the ions has to be varied in order to study the sensitivity of the component. This is done by varying the mass of the ions. Secondly, the penetration depth of the projectile has to be sufficient to reach the sensitive area of the component from the reverse side (due to assembly technique). The penetration depth, and more importantly the location of the Bragg peak, is determined by the beam energy. Finally, the mass to charge ratio (m/q) of the ion beams has to be virtually constant to allow fast transitions between different ion species. However, the variation of the m/q value, $\Delta(m/q)$, has to be greater than 0.03 % to resolve different species with the JYFL K-130 cyclotron. Properties of the high penetration cocktail used by the RADEF-facility are listed in Table 1.

Table 1: Properties of the 9.28 MeV/u Ion Beam Cocktail

Ion	Energy [MeV]	Penetration depth [μm]	LET [MeV/(mg/cm ²)]	$\Delta(m/q)$ [%]
¹⁵ N ⁴⁺	139	202	1.7	0.0
³⁰ Si ⁸⁺	278	130	6.0	-0.09
⁵⁶ Fe ¹⁵⁺	523	97	18	-0.56
⁸² Kr ²²⁺	768	94	30	-0.71
¹³¹ Xe ³⁵⁺	1217	89	53	-0.26

Reaching adequate beam currents of ¹³¹Xe³⁵⁺ with the JYFL 14 GHz ECRIS has required extensive development work. The most significant improvement during the recent years has been the implementation of multiple frequency plasma heating [6], which typically more than doubles the extracted beam currents of the highest charge states.

It would be desirable to increase the energy of the heaviest component of the beam cocktail even further to ensure that the Bragg peak of the energy transfer curve is well within the sensitive area of the component. In practice the performance of the ion source has to be increased to reach even higher charge states of xenon. The properties of a proposed (upgraded) beam cocktail are listed in Table 2. In order to reach Xe³⁸⁺ with the JYFL 14 GHz ECRIS a new hexapole (plasma chamber) has been designed and is foreseen to be installed by the end of 2009. With the new hexapole the simulated radial field on the magnetic pole at the plasma chamber wall reaches 1.07 T in comparison to the presently used hexapole with field strength of 0.93 T. The improvement of the magnetic field strength on the poles has been obtained by changing the magnetization angle of the permanent magnet blocks and moving them radially. The

*This work has been supported by the Academy of Finland under the Finnish Centre of Excellence Programme 2006-2011 (Nuclear and Accelerator Based Physics Programme at JYFL).

[#]olli.tarvainen@jyu.fi

new design follows the proven upgrade of the 14 GHz ECRIS at Argonne National Laboratory [7].

Table 2: Suggested 10.77 MeV/u Ion Beam Cocktail

Ion	Energy [MeV]	Penetration depth [μm]	LET [MeV/(mg/cm ²)]	$\Delta(m/q)$ [%]
¹⁴ N ⁴⁺	151	242	1.6	0.0
³⁵ Cl ¹⁰⁺	377	138	8.3	-0.11
⁵⁶ Fe ¹⁶⁺	603	117	17	-0.14
⁸⁰ Kr ²³⁺	862	108	29	-0.74
¹³² Xe ³⁸⁺	1422	106	52	-0.85

Introducing the new plasma chamber has profound implications on the beam time allocation procedure at JYFL. It has been decided that the experiments with ion beam cocktails at RADEF-facility, requiring highest possible performance of the ion source, will be carried out in campaigns lasting 3-6 months. The new hexapole will be used during these runs while the old plasma chamber will be installed for nuclear physics experiments requiring metallic ion beams. In particular, employment of the MIVOC-method [8] with the new chamber is to be strictly avoided as the inevitable carbon contamination degrades the performance of the ion source by reducing secondary electron emission from the plasma chamber walls (see section 3). Following this procedure minimizes the maintenance time of the ion sources.

ECRIS PLASMA PHYSICS EXPERIMENTS AT JYFL

In order to gain understanding on the ECR ion source parameters and different techniques, e.g. biased disc and multiple frequency heating, affecting the production of highly charged ions, a series of plasma physics experiments has been carried out at JYFL in recent years. These experiments include plasma potential measurements [9-11] and time-resolved measurements of bremsstrahlung emission, ion currents [12,13] and bias disc current [14]. One objective of the experiments is to study the feasibility of pulsed operation mode for the production of highly charged ions for the beam cocktails for which the time structure of the beam is almost irrelevant. In this section we review some of the results obtained in these experiments.

Plasma Potential Measurements

The plasma potential measurements with the JYFL ECR ion sources have been performed with a retarding field analyzer [9]. Fig. 1 shows the results obtained with the JYFL 6.4 GHz ECRIS with different ion species namely hydrogen, deuterium, helium, nitrogen, oxygen, neon, argon and krypton. The vertical range represents the effect of the ion source tuning parameters i.e. neutral gas pressure, microwave power and magnetic field configuration within their typical limits. The plasma potential clearly depends on the ion mass. The difference

between electron and ion mobilities increases with increasing ion mass. Higher plasma potential is consequently required to balance the loss rates of positive and negative charges. The plasma potential of the JYFL 14 GHz ECRIS, exhibiting a similar mass dependence, is typically about 50 % lower than the plasma potential of the 6.4 GHz ion source.

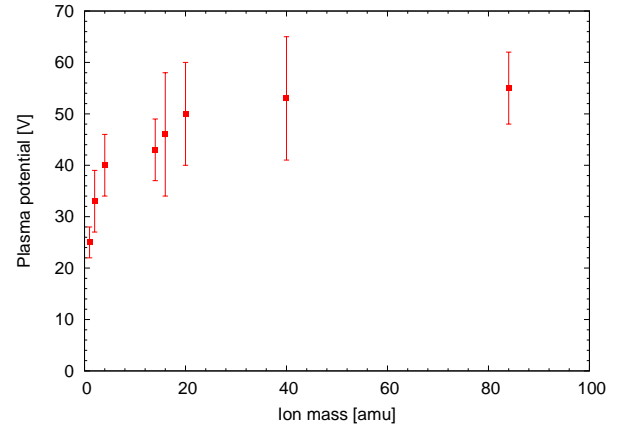


Figure 1: Plasma potential of the JYFL 6.4 GHz ECRIS as a function of ion mass. Vertical range corresponds to the variation of ion source parameters within typical limits.

One of the most important findings with the retarding field analyzer has been the effect of carbon contamination on the plasma potential and energy spread. Fig. 2 shows data curves measured with O⁷⁺ under different contamination levels i.e. before and after a 2 week MIVOC-run (Ti). The plasma potential values associated with each case are given in the figure label. The corresponding beam currents (optimized tune) were 160 μA and 48 μA before and after the MIVOC-run, respectively.

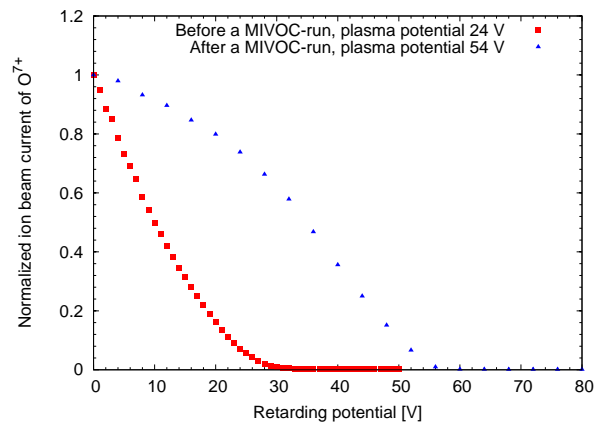


Figure 2: Normalized “plasma potential curves” with a clean aluminium plasma chamber and under heavy carbon contamination due to a MIVOC-run.

The increase of the plasma potential is believed to be due to reduced secondary electron emission from the walls of the aluminium plasma chamber under heavy carbon contamination. Restoring the performance of the

ion source to the original level after a serious carbon contamination by the means of plasma cleaning (with oxygen) takes typically more than 100 hours [15]. Therefore, the only viable option compatible with the beam time schedule at JYFL is mechanical cleaning of the plasma chamber. It has been observed that production of metal ion beams with evaporative oven or sputtering technique also affects the performance of the ion source. A layer of deposited metal lowers the secondary electron emission from the chamber walls resulting to a slight increase of the plasma potential. Another indication suggesting that the loss rate of electrons (net flux of electrons) defines the value of the plasma potential and affects the ion losses is the observation that the negative voltage applied to the biased disc reduces the plasma potential up to 20 % [9].

Time-resolved Plasma Diagnostics Experiments

The focus of the ECRIS plasma physics studies at JYFL has recently been time-resolved diagnostics of Bremsstrahlung emission [12,13] and plasma breakdown [14]. For these experiments both JYFL ECR ion sources have been operated in pulsed mode. The goal of the studies is to gain understanding on the electron heating mechanism resulting into electron energies of hundreds of keV. The contribution of these so-called runaway electrons to the production of (highly charged) ions is minimal since the ionization cross section typically peaks at electron energies below a few keV. High energy electrons create problems as they produce Bremsstrahlung, which gives rise to unnecessary heating of the cryostat of superconducting ECR ion sources [16] and poses a radiation hazard for the laboratory personnel.

In the measurements with several noble gases it has been observed that the ion currents of different charge states appear and saturate well before the Bremsstrahlung emission reaches steady state. As an example Fig. 3a and 3b present time-resolved ion currents of different charge states of neon, plotted together with the integrated (over the energy range > 30 keV) Bremsstrahlung count rate. The rf pulse length was set to 1.76 seconds with off time of 5.9 seconds and the Bremsstrahlung was recorded in radial direction from a magnetic pole as described in detail in Ref. 12. The rf power is applied at $t=0$.

Reaching steady state Bremsstrahlung emission count rate takes 200-300 ms while the ion currents saturate in 50-150 ms depending on charge state. Fig. 3b highlights the preglow effect [17] observed with low charge states. The preglow effect is much more pronounced than the afterglow observed only with highest charge states. Under the given ion source settings the plasma breakdown time is 8-10 ms. The step-wise nature of the ionization process is also clearly visible in Fig. 3b i.e. ion currents of high charge states appear a few milliseconds after the breakdown. It can also be seen that the decay of the ion currents takes several hundreds of milliseconds.

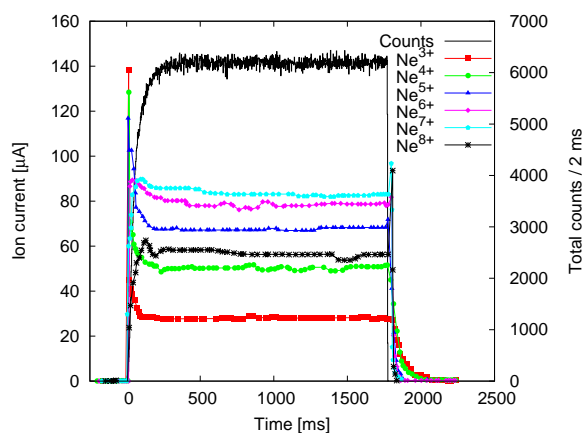


Figure 3a: Time-resolved ion currents of neon and corresponding Bremsstrahlung count rate.

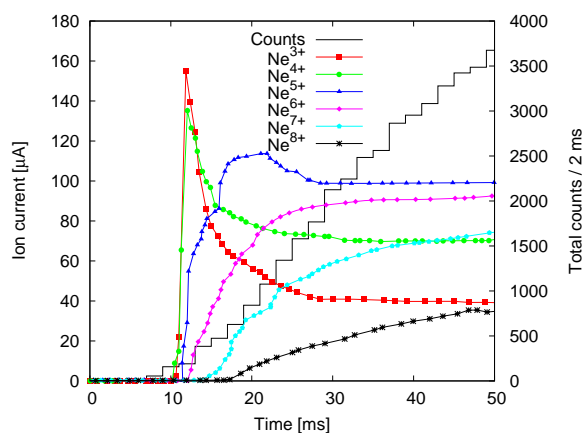


Figure 3b: Time-resolved ion currents of neon and corresponding Bremsstrahlung count rate in the beginning of the rf pulse.

It has been observed at JYFL that the shape of the preglow signal (FWHM) depends on the ion beam optics, namely dipole magnet and solenoid settings. The effect of the dipole magnet could be explained by variation of the plasma potential during the transient. This will be investigated in near term future by measuring the time evolution of the plasma potential. The influence of the solenoids could be related to variations of focusing properties under evolving space charge compensation by electrons from ionized residual gas. This is also a subject of a further study.

The formation of the preglow has been thoroughly discussed in [17]. During the initial stage of the plasma breakdown the plasma density is very low and the electron collision time is much longer than the interaction time between the electron and the rf in the resonance region. Essentially all free electrons are heated very efficiently since the total power absorbed by the plasma is less than the power provided by the rf amplifier. This is due to low electron density and stochastic heating limit resulting from the lack of phase randomization in consecutive resonance crossings [18]. Under these conditions the electron energy distribution function is superadiabatic [17] i.e. the average electron energy is

very high but limited to a certain threshold value. As the electron density increases with the preceding ionization cascade, the absorbed rf power becomes insufficient to maintain the superadiabatic EEDF. As a consequence the average electron energy collapses [17] and eventually becomes bi-Maxwellian described by cold and hot populations [19]. As this shift between the breakdown stages takes place, a sudden increase of ion currents (preglow) is observed due to exponentially increasing plasma density and surge of cold electrons escaping the confinement. The length of the preglow pulse is related to the depletion of neutrals and proceeding step-wise ionization towards the steady-state charge state distribution.

In order to test the validity of this qualitative description we measured the Bremsstrahlung count rate with rf pulse length of 50 ms with a pulse separation of 500 ms. The pulse pattern was chosen in order to have enough electrons absorbing the rf during the superadiabatic stage (seed electrons remaining from the previous pulse as discussed later). Sufficient electron density is required to obtain a detectable Bremsstrahlung count rate during the initial stage of the breakdown. On the other hand the initial electron density has to be low enough to reach the superadiabatic EEDF. The recorded Bremsstrahlung count rate and corresponding time-resolved biased disc current (for details of the measurement see [12-14]) in the case of helium plasma are plotted in Fig. 4.

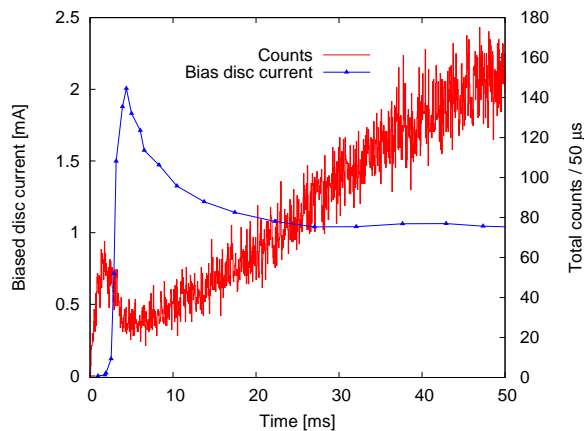


Figure 4: Comparison of time-resolved biased disc current and bremsstrahlung count rate. Rf pulse pattern: 50 ms on / 500 ms off.

The data presented in the figure show that the Bremsstrahlung count rate at energies above 30 keV decreases abruptly to about 50 % when the plasma breakdown occurs. The observation supports the “superadiabatic model” claiming that initially a substantial portion of the electrons is heated to high energies followed by a sudden shift of the EEDF (collapse of average energy). The saturation time scale of the biased disc current is believed to be due to neutral depletion [14].

Fig. 4 brings up another interesting issue, namely the density of “seed electrons”, affecting the plasma breakdown time and the characteristics of the preglow transient. It has been observed that the rf pulse duration and pulse separation affect the time required for the plasma breakdown. This can be explained by the (hot) electrons from the preceding pulse remaining confined in the magnetic field structure of an ECRIS and thus acting as a source of “seed electrons”. It has been observed that it can take up to 10 seconds to erase the influence of the previous rf pulse indicating that the (hot) electron confinement time can be on the order of seconds [14]. The effect of the seed electrons is seen by comparing the rise times of Bremsstrahlung count rates presented in Figs. 3 and 4 with long and relatively short rf pulse separations, correspondingly. In the case of Fig. 4 the rf pulse pattern is adequate to maintain certain density of seed electrons resulting into immediate detection of Bremsstrahlung and short plasma breakdown time.

The effect of the seed electrons on the plasma breakdown time and preglow has been studied further by sustaining low density plasma with a TWTA operated at very low power in cw mode and pulsing the klystron simultaneously. It was observed that the seed electrons cause the charge state distribution during the preglow transient to shift towards higher charge states. This is demonstrated in Figs. 5a and 5b comparing the preglow in the case of helium with and without the seed electrons provided by the TWTA at 11.56 GHz. The 14 GHz rf power is applied at $t=0$. In this “forced preglow” mode the steady state charge state distribution is reached faster as the plasma breakdown shifts towards the leading edge of the rf pulse from the klystron. The maximum rf power from the TWTA was set to 10 W, matching the maximum power of cheap commercial units at 11-13 GHz. Thus, the “forced preglow” could offer an inexpensive technique to optimize the preglow characteristics (ionization time, pulse rate, charge state distribution). Similar behavior i.e. faster ionization and shift of the charge state distribution was also observed with neon.

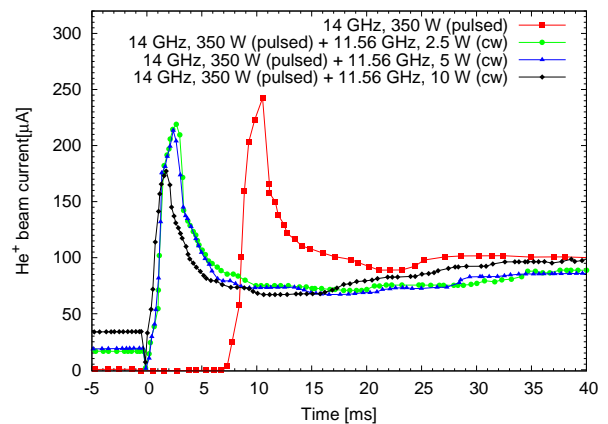


Figure 5a: Time-resolved ion beam currents of He^+ with and without seed electrons provided by TWTA.

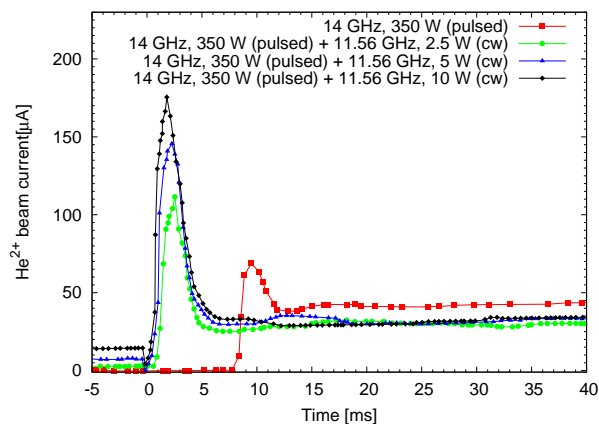


Figure 5b: Time-resolved ion beam currents of He^{2+} with and without seed electrons provided by TWTA.

DISCUSSION

The ECRIS plasma physics experiments have provided insight for the development of new beam cocktails with higher penetration depth i.e. higher energies. If the new plasma chamber with higher radial field proves not to be sufficient for producing enough Xe^{38+} , for example, operating the JYFL 14 GHz ECRIS in afterglow mode becomes a considerable option. Pulsed time structure of the beam is perfectly tolerable from the point of view of the irradiation tests as long as the time averaged flux of ions can be measured. However, it would be desirable to maximize the integrated number of ions by maximizing the repetition rate of the rf pulses (in the afterglow mode). In order to reach high charge states in shorter times, techniques to speed up the ionization process are being sought. It has been shown that seed electrons provided by a TWTA operated in cw mode at low rf power level result in faster ionization of high charge states. A future goal of this ongoing project is to study the feasibility of “forced preglow” to maximize the pulse repetition rate for the production of extremely high charge states in afterglow mode. Instead of operating the ion source in the classical afterglow mode, the recently discovered regime, so-called “micropulsed beam mode” [20] could be used. In this mode the rf pulse length is shortened to (sub)millisecond level, producing afterglow transients with highly charged ions current exceeding the classical afterglow currents by a large factor [20]. Explaining this observation is another goal of the plasma breakdown studies at JYFL.

The time-resolved plasma diagnostics provide valuable information for development of codes modeling e.g. electron heating [21]. The time-resolved Bremsstrahlung experiments have clearly demonstrated that ions are produced faster than it takes to reach steady state electron energy distribution. Therefore, it might be possible to control the EEDF by pulsing the rf with (sub)microsecond pulses and optimize the production of highly charged ions.

REFERENCES

- [1] E. Liukkonen, 13th Intl. Conf. on Cyclotrons, Vancouver, (1992), p. 22.
- [2] P. Suominen, O. Tarvainen and H. Koivisto, Rev. Sci. Instrum. 77, (2006), 03A332.
- [3] H. Koivisto, P. Heikkinen, V. Hänninen, A. Lassila, H. Leinonen, V. Nieminen, J. Pakarinen, K. Ranttila, J. Ärje and E. Liukkonen, Nucl. Instr. and Meth. in Phys. Res. B, 174, (2001), p. 379.
- [4] T. Kuo, R. Baartman, G. Dutto, S. Hahto, J. Ärje, and E. Liukkonen, Rev. Sci. Instrum. 73, (2002), p. 986.
- [5] H. Kettunen, R. Harboe-Sørensen, I. Riihimäki, A. Javanainen, A. Pirojenko, K. Ranttila, A. Virtanen, Proc. of RADECS 2006 Workshop, (2006), Athens.
- [6] H. Koivisto, P. Suominen, O. Tarvainen, A. Virtanen, and A. Parkkinen, Rev. Sci. Instrum. 77, (2006), p. 03A316.
- [7] R. C. Vondrasek, R. Scott and R. C. Pardo, Rev. Sci. Instrum. 75, (2004), p. 1532.
- [8] H. Koivisto, J. Ärje and M. Nurmi, Nucl. Instr. and Meth. in Phys. Res., B94, (1994), p.291.
- [9] O. Tarvainen, P. Suominen, and H. Koivisto Rev. Sci. Instrum. 75, (2004), p. 3138.
- [10] O. Tarvainen, P. Suominen, T. Ropponen, T. Kalvas, P. Heikkinen, and H. Koivisto, Rev. Sci. Instrum. 76, (2005), 093304.
- [11] O. Tarvainen, P. Suominen, T. Ropponen, and H. Koivisto, Rev. Sci. Instrum. 77, (2006), 03A309.
- [12] T. Ropponen, O. Tarvainen, P. Jones, P. Peura, T. Kalvas, P. Suominen, H. Koivisto and J. Ärje, Nuclear Inst. and Methods in Phys. Res. A, 600, (2009), p. 525.
- [13] T. Ropponen, O. Tarvainen, P. Jones, P. Peura, T. Kalvas, P. Suominen and H. Koivisto, Submitted to IEEE Transactions on Plasma Science.
- [14] O. Tarvainen, T. Ropponen, V. Toivanen, J. Ärje and H. Koivisto, Submitted to Plasma Sources Sci. T.
- [15] O. Tarvainen, P. Suominen, H. Koivisto and I. Pitkänen, Rev. Sci. Instrum. 75, (2004), p. 1523.
- [16] D. Leitner, J. Y. Benitez, C. M. Lyneis, D. S. Todd, T. Ropponen, J. Ropponen, H. Koivisto and S. Gammino, Rev. Sci. Instrum. 79, (2008), 033302.
- [17] I.V. Izotov, A.V. Sidorov, V.A. Skalyga, V.G. Zorin, T. Lamy, L. Latrasse, T. Thuillier, IEEE Transactions on Plasma Science, 36, 4, Part 2, (2008), p. 1494.
- [18] K. Wiesemann Rev. Sci. Instrum. 79, (2008), 02B506.
- [19] A. Girard, D. Hitz, G. Melin and K. Serebrennikov, Rev. Sci. Instrum. 75, (2004), p. 1381.
- [20] L. Maunoury et al., Rev. Sci. Instrum. 79, (2008), 02A313.
- [21] T. Ropponen, O. Tarvainen, P. Suominen, T.K. Koponen, T. Kalvas and H. Koivisto, Nucl. Instr. and Meth. in Phys. Res. A, 587, 1, (2008), p. 115.

DEVELOPMENT OF METAL ION BEAMS AND BEAM TRANSMISSION AT JYFL*

H. Koivisto[#], T. Ropponen, O. Tarvainen, V. Toivanen, O. Steczkiewicz, M. Savonen, JYFL, Jyväskylä, Finland

Abstract

The activities of the JYFL ion source group cover the development of metal ion beams, improvement of beam transmission and studies of Electron Cyclotron Resonance Ion Source (ECRIS) plasma parameters. The development of metal ion beams is one of the most important areas in the accelerator technology. The low energy beam injection for K-130 cyclotron is also studied in order to improve its beam transmission. It has been noticed that the accelerated beam intensity after the cyclotron does not increase with the intensity extracted from the JYFL 14 GHz ECR ion source, which indicates that the beam transmission efficiency decreases remarkably as a function of beam intensity. Three possible explanations have been found: 1) the extraction of the JYFL 14 GHz ECRIS is not optimized for high intensity ion beams, 2) the solenoid focusing in the injection line causes degradation of beam quality and 3) the focusing properties of the dipoles (analysing magnets) are not adequate. In many cases a hollow beam structure is generated while the origin of hollowness remains unknown.

INTRODUCTION

The research at the JYFL accelerator laboratory focuses on the research in nuclei under extreme conditions, on accelerator based material physics and on the accelerator based applications in industry. The main tool for the studies is the isochronous K-130 cyclotron [1] equipped with two ECR ion sources [2,3] for heavy ion beams and a filament driven multicusp-type light ion source for negative ions. Typical energy needed for the nuclear physics programme is about 5 MeV/nucleon. This requirement is met with the q/A -ratio of about 0.2.

The requirements towards the use of heavier projectile elements and higher ion beam intensities have increased. These demands require the work for improving the performance of the ion sources, beam transport and methods for the production of metal ion beams. The efficient development of ion sources requires plasma studies in order to improve the understanding of plasma ignition and plasma-wave interaction, for example. In this R&D work the good availability of ion sources and different tests benches at JYFL plays an important role.

METAL ION BEAMS

At JYFL the solid ion beams are produced mainly by

*This work has been supported by the Academy of Finland under the Finnish Centre of Excellence Programme 2006-2011 (Nuclear and Accelerator Based Physics Programme at JYFL).

[#]Hannu.Koivisto@phys.jyu.fi

Ion Sources

the MIVOC method [4] and with ovens. As a latest approach the sputter technique [5] has been adopted. Table 1 shows the solid elements available from the JYFL ECR ion sources, the method usually used and the intensity for the charge state giving the q/A -ratio of at least 0.2. In some cases the intensity shown in the table does not correspond to the maximum performance of the ion source, instead the value corresponds to intensity, which is high enough to meet the requirements set by nuclear physics experiment.

Table 1: Solid Ion Beams by the JYFL ECRIS's

Element	Method	Intensity [μ A] ($q/m \approx 0.2$)	Note
B	MIVOC	235	($C_2H_{12}B_{10}$)
C	CO ₂	195	
F	SF ₆	19	6.4 GHz
Mg	MIVOC	12	6.4 GHz
Al	Oven	9.5	6.4 GHz
Si	SiH ₄	124	
S	SF ₆	22	6.4 GHz
Cl	TiCl ₄	23	6.4 GHz
Ca	Oven	75	CaO + Zr
Ti	MIVOC	45	($(CH_3)_5C_5Ti(CH_3)_3$)
V	MIVOC	10	V(C_5H_5) ₂
Cr	Ind. oven	20	
Mn	Oven	22.5	
Fe	MIVOC	115	Fe(C_5H_5) ₂
Co	MIVOC	12	Co(C_5H_5) ₂
Ni	MIVOC	55	Ni(C_5H_5) ₂
Cu	Oven	7.5	
Zn	Sputter	5.5	6.4 GHz
Sr	Oven	30	ZrO + Zr
Y	Foil oven	5	
Zr	Sputter	12	
Ru	MIVOC	9.1	Ru(C_5H_5) ₂
Ag	Oven	5.8	
Au	Oven	15	

The Beams have been produced with 14 GHz ECRIS if not mentioned otherwise.

MIVOC Method

The MIVOC method is based on the fact that some compounds including metal element have relatively high saturated vapour pressure already at room temperature. For example Fe(C_5H_5)₂ has the vapour pressure of about

10^{-3} mbar, which can easily give the feed rate of several mg/h for iron into the ECRIS plasma chamber if the conductance of feed line between the sample and plasma chamber is adequate. The MIVOC method can provide very intensive ion beams for some elements as is shown in Table 1. In addition the consumption rate of metal element is usually very small, which is very important factor in the case of enriched materials. However, compounds from enriched materials are not commercially available, which means that the user has to have a know-how to synthesize the compound of interest (for example $\text{Fe}(\text{C}_5\text{H}_5)_2$). The lack of convenient compound including the element of interest also gives a limitation for the use of the method. The other drawback is the carbon existing in the compound causing the contamination of the plasma chamber. Often the ECRIS plasma chamber is made out of aluminium, which behaves as a good source of secondary electrons strongly increasing the intensity of highly charged ions. Consequently, the carbon contamination on the surface of the plasma chamber decreases the performance of the ECRIS. However, similar effect is seen with some other metal elements like Zr for example.

JYFL Evaporation Ovens

The MIVOC method was not able to provide all metal ion beams needed for the cyclotron. Consequently evaporation ovens were chosen to increase the variety of available metal ion beams. Presently, three different evaporation ovens are available for the metal ion beam production at JYFL: miniature oven, foil oven and inductively heated oven. The use of the most appropriate oven is chosen according to requirements.

JYFL Miniature Oven

The miniature oven has been used at JYFL for the metal ion beams since 1997. It is a modified copy of the MSU design [6] and layout of one version is shown in Fig. 1. The oven has been tested up to 1400°C without any signs of failure. The limitations come from the maximum temperature for the surface-to-surface stability between the tungsten filament and Al_2O_3 insulator ($T_{\text{max}} \approx 1700^\circ\text{C}$). In addition, the vapour pressure of Al_2O_3 is about $1\text{E-}5$ mbar at 1763°C [7]. The oven has successfully been used - especially with the JYFL 6.4 GHz ECRIS [2] - for the production of several metal ion beams like Al, Ca and Cu. However, the capability of the oven was not adequate for the production of metal ion beams needing evaporation temperature significantly higher than 1400°C . This excluded several metal ion beams needed for the nuclear physics program at JYFL. Consequently, an active development work has been performed to develop both the resistively and inductively heated ovens. The most difficult problem concerning the oven development work comes from the surface-to-surface interaction of different materials, which limits the maximum usable temperature [7].

Ion Sources

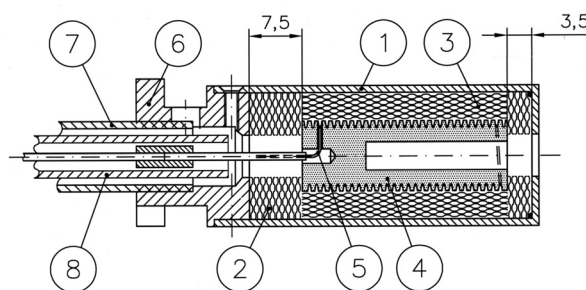


Figure 1: The JYFL miniature oven. 1) outer Mo body (OD = 20 mm), 2 and 3) Mo radiation shielding, 4) Al_2O_3 inner body, 5) W/Re filament, 6 and 7) stainless steel parts, 8) Al_2O_3 insulation.

JYFL foil Oven

The structure of the foil oven is presented in Fig. 2. It is capable of operating close to temperature of 2000°C . The current is conducted through the copper stem (1) and Mo crucible (2) to Ta heater foil (3), which thickness is $25\ \mu\text{m}$. The current of close to 80 A is needed to reach the temperature of $1900\text{--}2000^\circ\text{C}$. The heater foil is pressed using parts (4) and (5) which can cause temperature variation of even 50°C depending on the contact of the foil. The material to be evaporated is inserted into the crucible, which is heated by the heat radiation from the heater foil. The current loop is closed via Mo-body (8) and stainless steel tube (9). The inner part is electrically insulated from the outer part by Al_2O_3 insulator (7).

The foil oven has been tested for the production of Au, Y and Ti ion beams. Especially in the case of Y and Ti evaporation a strong surface-to-surface reaction was seen (depends only on the materials in contact). The drawback of the foil oven is a difficult handling because it has to be disassembled when the evaporated material is changed.

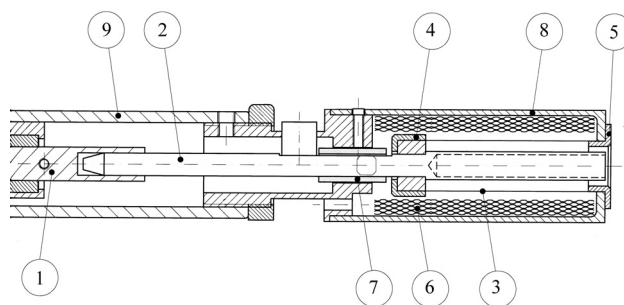


Figure 2: Resistively heated foil oven: 1) Cu rod, 2) Mo crucible, 3) Ta heater foil 4-5) Mo foil holder, 6) Ta radiation shielding, 7) Al_2O_3 insulator, 8) Mo body, 9) stainless steel outer tube.

JYFL Inductively Heated Oven

An inductively heated oven is very efficient for the production of metal ion beams requiring high temperature. Fig. 3 clarifies the operation principle of the final version of the home-made control unit, which makes the oscillation of the circuit at resonance frequency possible. The gate voltage of the transistor is controlled

with the integrated signal generator at the resonant frequency of the circuit. Proceeding this way the voltage of the circuit provided by -50 V power supply is changed. The amplitude of the oscillation is controlled by the voltage of the power supply. The oven has intensively been tested at the test bench up to 2000°C. No failure of the oven - including control unit – have occurred during the tests of several days. The oven has been used for the production of Cr and Ti ion beams. The structure of the oven is shown in Fig. 4.

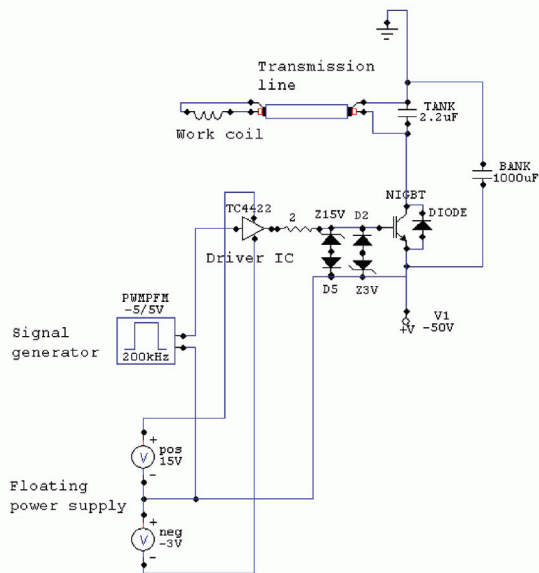


Figure 3: Control unit layout of the inductively heated oven at JYFL.

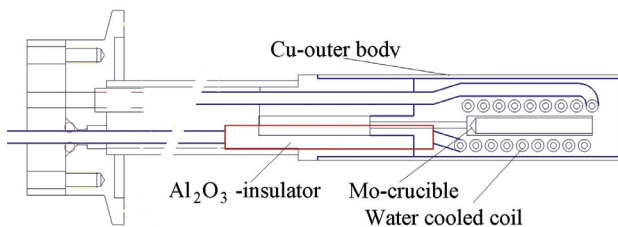


Figure 4: The JYFL inductively heated oven.

Sputter Technique

The sputter technique is beneficial especially for elements requiring very high temperatures to be vaporized. In this method the surface of the material is bombarded by the ions originating from the ECRIS plasma to give an extra energy to the atoms at the crystal lattice of the material. With the aid of the adequate energy the atoms of the target material are removed from the bulk material. The erosion of the material is measured by the sputtering yield, which is defined as $(\text{removed atoms})/(\text{projectile atom})$. The yield depends on the properties of the target material, the mass and the energy of projectile atoms and the angle of incidence (with respect to the normal of the bombarded surface). Information about the sputter yields can be found for

example from ref. [8]. There it can be seen that Ag, Au, Cu and Pd are among the most easily sputtered materials.

The sputter technique was adopted because some of the elements cannot be evaporated by the ovens (like Mo, W, etc). The most of the information and know-how needed was received from ANL ion source group. Fig. 5 shows the sputter device at the JYFL 14 GHz ECRIS. The sample to be sputtered is inserted through a radial pumping slot (width ≈ 6 mm) of plasma chamber. The face of the sample is approximately at the level of plasma chamber surface and its position can be adjusted. The ion beam production is very sensitive to the position of the sample – even the movement of less than 0.5 mm can have a drastic effect. The stem of the sputter sample is insulated from the plasma chamber wall by Al_2O_3 tube.

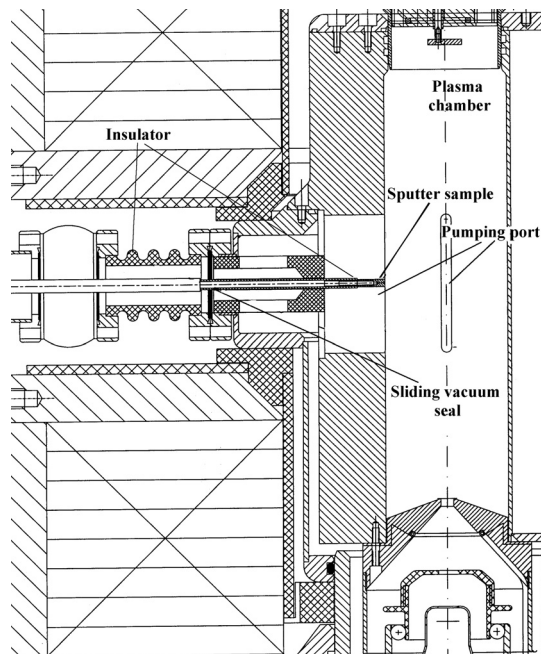


Figure 5: Radial sputter device at the 14 GHz ECRIS.

The development work concerning the sputtering was carried out with zirconium, which has relatively low sputter yield. In the first tests the diameter of the sputter sample was 5 mm, but due to frequent sparking and short-circuits (happened after few hours operation) the width of the sample was reduced to 3.5 mm. The new sample geometry increased the operation hours but vacuum seal failures started to appear as a new problem. This happened especially when the beam intensity was maximized. It was expected that failure took place because of excessive heat load, which damages the sealing. However, the problem did not disappear when the cooling for the sputter stem was added. The problem disappeared when an adequate tantalum radiation shielding for the sliding vacuum seal was provided. The zirconium beam has successfully been used for nuclear physics experiments and the intensity varied between 4-8 μA (14 GHz ECRIS). The consumption rate has been about 1 mg/h. The sputter voltage of about 1.3 kV is required with the sputter current of 1-1.5 mA.

BEAM TRANSMISSION

Ion beam transmission plays a crucial role in the operation of cyclotron facility. For example in the operation of the JYFL K-130 cyclotron facility it was noticed that in some cases no positive effect in the accelerated beam intensity was seen when the extracted beam intensity from the JYFL 14 GHz ECR ion source was increased. In some cases the ion beam intensity after the cyclotron even started to decrease. The behaviour indicates that the beam quality decreases from the ECR ion source or/and the beam quality degrades by the inadequate properties of the beam line in the case of high ion beam intensities. Several experiments to understand the behaviour have been performed.

Beam Transmission of Different Beam Line Sections

The injection line from the JYFL 14 GHz ECRIS to cyclotron has been divided into two different sections for the studies: injection line from the 1) extraction of JYFL 14 GHz ECRIS to the analysing magnet and 2) first Faraday cup after analysing magnet (FC2) to the last Faraday cup before the cyclotron. The first section has been studied only by simulations because the transmission of total ion beam including all charges cannot be measured due to inadequate bending capability in the case of low charge states. Fig. 6 shows the simulated beam behaviour from the JYFL 14 GHz ECRIS to the analysing magnet with two different Ar^{8+} intensities. The simulations have been performed by TRANSPORT-code using the extraction voltage of 10 kV and initial emittance of $200 \pi \text{ mm mrad}$. The code can include only one charge state and consequently, the measured charge state distribution was converted to Ar^{8+} beam, in such a way that equivalent beam potential is obtained (corresponds to 1.5 mA of Ar^{8+}). As the figure shows such beam intensity cannot be transported through the analysing magnet at 10 kV, which is a typical injection voltage for the K-130 cyclotron. The intensity has to be decreased to the value of 0.6 mA before the transmission of 100 % through the section 1 is obtained. The highest Ar^{8+} intensity measured after the analysing magnet of the JYFL 14 GHz ECRIS at 10 kV is about $350 \mu\text{A}$. The results indicate that the available beam intensity for the cyclotron is strongly limited by the first section of the injection line.

The beam behaviour in section 2 was studied experimentally by measuring the intensity in several locations. Fig. 7 shows the behaviour between the analysing magnet after 14 GHz ECRIS and the last Faraday cup before the cyclotron. As the figure shows the transport efficiency of section 2 decreases dramatically when the beam intensity from the ion source increases. The further measurements demonstrated that behaviour is seen only in the last part of section 2.

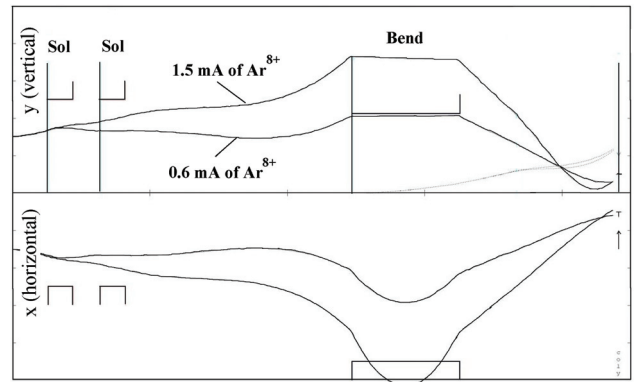


Figure 6: Beam transport simulations from the extraction to the bending magnet using two different Ar^{8+} intensities.

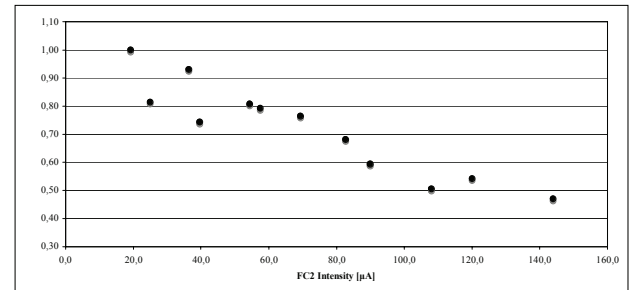


Figure 7: The normalized transmission of Ar^{8+} ion beam as a function of beam intensity from the JYFL 14 GHz ECRIS after the first dipole to the last FC before the cyclotron (i.e. section 2).

Asymmetric Beam Shape

The beam viewers have shown that the ion beam profile after the analysing magnet is elliptical as is shown in Fig. 8. The aberration can come for example from the wrong entrance-exit angle of the analysing magnet, which causes different focusing properties in different planes. The elliptical beam can have remarkable difference in the Twiss parameters in different planes, which will result in high value of mismatch factor. This will increase 2D emittance in solenoid focusing as is shown by Eq. (1)

$$\varepsilon_x^2 = \varepsilon_x \left[\left(1 + \frac{\Delta\varepsilon}{\varepsilon_x} \sin^2 \theta \right)^2 + \frac{M}{4} \left(1 + \frac{\Delta\varepsilon}{\varepsilon_x} \right) \sin^2 2\theta \right] \quad (1),$$

where $\Delta\varepsilon = \varepsilon_y - \varepsilon_x$ is the difference in the 2D emittances between the two transverse phase spaces and $M = \beta_x \gamma_y + \beta_y \gamma_x - 2\alpha_x \alpha_y - 2$ [9]. The rotation angle is close to 45° in the case of JYFL solenoids giving the highest effect on emittance increase.



Figure 8: Asymmetric Ar⁹⁺ beam after the dipole magnet.

Hollow Beam Structure and Space Charge Compensation

Probably the most severe transport problem at JYFL is related to the hollow beam structure, most evident with low and medium charge states (see Fig. 9). This makes the beam transport difficult and increases beam losses. Possible reasons for the hollowness include strong solenoid focusing and consequent space charge effects between the ECR ion source and analyzing magnet, the spatial charge state distribution inside ECR plasma and possible flaws in the ion source extraction geometry.



Figure 9: A hollow Ar⁸⁺ ion beam after dipole.

Studies by L. Celona et. al. [10] with Caprice ion source have revealed that the shape of the beam profile is dependent on the microwave frequency, i.e. on the mode structure, which can cause the hollowness of the beam. Similar behaviour has recently been measured with the JYFL 14 GHz ECRIS [11]. This indicates that at least part of the hollowness can be due to plasma phenomena inside the ECR ion source. It has also been noticed, that with high beam currents the beam becomes increasingly hollow. Increasing the acceleration voltage of the ion source reduces the effect and strongly improves the beam transmission. These indicate that the at least part of the hollow beam structure is generated inside the beam line due to space charge effect. Recent studies have also shown that the beam shape has strong dependence on the pressure at the beginning of the beam line. This can be due to space charge neutralization effects and thus is an indication of space charge problem.

The beam compensation with the residual gas is a well-known method in the light ion source community to

decrease the space charge effect. This has been tested at JYFL with highly charged Ar ion beams (Ar⁶⁺ - Ar¹¹⁺) by feeding nitrogen into the beam line upstream from the analysing magnet where all beam components are still included. It was observed that the hollow beam structure started to disappear and emittance decreased as a function of beam line pressure. The brightness of the beam reached the maximum value around the pressure of $5 \cdot 10^{-6}$ mbar [12]. Later different residual gases will be tested and the results will be confirmed with the cyclotron. As a consequence of lower emittance and higher brightness it is assumed that the beam transmission efficiency will increase substantially in the case of high beam intensities.

FUTURE PLANS

New metal ion beams will be required with the inductively heated oven and with the aid of sputter technique (especially Ti, Gd, Mo, and W). The improvement of beam quality will be continued by testing different residual gases in the beam line and as a next step to use a filament to introduce extra electrons for the beam neutralization. The possibility to have the first section of the beam line at high voltage (including analysing magnet) with adequate electron traps will be studied.

REFERENCES

- [1] E.Liukkonen, 13th. Intern. Conf. on Cyclotrons, Vancouver, (1992), p. 22.
- [2] P. Suominen, O. Tarvainen and H. Koivisto, Rev. Sci. Instrum. 77, (2006), p. 03A332.
- [3] H. Koivisto, P. Heikkinen, V. Hänninen, A. Lassila, H. Leinonen, V. Nieminen, J. Pakarinen, K. Ranttila, J. Ärje and E. Liukkonen, Nucl. Instr. and Meth. in Phys. Res., B174, (2001), p. 379.
- [4] H. Koivisto, J. Ärje and M. Nurmia, Nucl. Instr. and Meth. in Phys. Res., B94, (1994), p.291.
- [5] R. Harkewicz, P.J. Billquist, J.P. Greene, J.A. Nolen and R.C. Pardo, Rev. Sci. Instrum. 66 (4), June 1995, p. 2883.
- [6] R. Harkewicz, Rev. Sci. Instrum. 67 (6), June 1996, p. 2176.
- [7] K.J. Ross and B. Sonntag, Rev. Sci. Instrum. 66 (9), Sept. 1995, p. 4409.
- [8] <http://www.angstromsciences.com/reference/material-properties/index.html?ID=4>
- [9] M. Doleans, W. Hartung, G. Machicoane and E. Pozdeyev, "Beam Experiments and Measurements at the NSCL" US Particle Accelerator School, MSU, East Lansing, MI, 2007.
- [10] L. Celona, et. al., Rev. Sci. Instrum. 79, (2008), p. 023305.
- [11] L. Celona, V. Toivanen, O. Steczkiewicz, O. Tarvainen, T. Ropponen and H. Koivisto, to be published.
- [12] V. Toivanen, O. Steczkiewicz, O. Tarvainen, T. Ropponen and H. Koivisto, to be published.

SUPERCONDUCTING ECR ION SOURCE DEVELOPMENT AT LBNL*

D. Leitner[#], S. Caspi, P. Ferracin, C.M. Lyneis, S. Prestemon, G.L. Sabbi, D. Todd, F. Trillaud
Lawrence Berkeley National Laboratory, Berkeley, CA 94720, U.S.A.

Abstract

The development of the superconducting 28 GHz ECR ion source VENUS at the Lawrence Berkeley National Laboratory (LBNL) [1] has pioneered high field superconducting ECR ion sources and opened a path to a new generation of heavy ion accelerators. Because of the success of the VENUS ECR ion source, superconducting 28 GHz ECR ion sources are now key components for proposed radioactive ion beam facilities. This paper will review the recent ion source development program for the VENUS source with a particular focus on the production of high intensity uranium beams.

In addition, the paper will discuss a new R&D program started at LBNL to develop ECR ion sources utilizing frequencies higher than 28 GHz. This program addresses the demand for further increases of ion beam intensities for future radioactive ion beam facilities. The most critical technical development required for this new generation of sources is the high-field superconducting magnet system. For instance, the magnetic field strengths necessary for 56 GHz operation produce a peak field in the magnet coils of 12-14 T, requiring new superconductor material such as Nb₃Sn. LBNL has recently concluded a conceptual, comparative design analysis of different coil configurations in terms of magnetic performance and has developed a structural support concept compatible with the preferred magnetic design solution. This design effort concludes that a sextupole-in-solenoid ECR magnet structure (VENUS type) is feasible with present Nb₃Sn technology, but that an inverted geometry (solenoid-in sextupole) exceeds the capability of Nb₃Sn superconductors and can be ruled out as candidate for a 56 GHz ECR ion source.

INTRODUCTION

Electron Cyclotron Resonance (ECR) ion sources are an essential component of heavy-ion accelerators. Their ability to produce any low to high charge state ion beam from hydrogen to uranium has made them the injector of choice for many applications. Over the last few decades advances in magnet technology and an improved understanding of the ECR ion source plasma physics have led to remarkable performance improvements of ECR ion sources. At the same time, the demand for increased intensities of highly charged heavy ions continues to grow. The path for further improving the ECR ion source performance includes the use of higher magnetic fields and

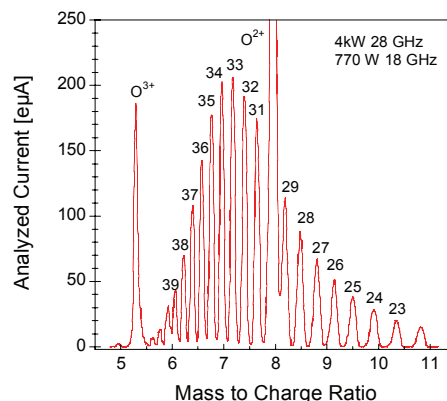


Figure 1: Uranium charge state distribution for a high intensity medium charge state tune optimised for 33 to 34+.

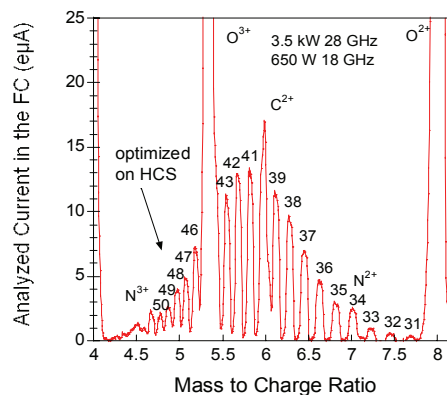


Figure 2: High charge state (HCS) Uranium beam distribution.

higher heating frequencies as formulated in Geller’s famous ECR scaling laws [2]. Following these guidelines several generations of ECR ion sources have been developed. Qualitatively, if the microwave heating frequency is doubled, the ion beam intensities are enhanced by a factor of four on average and even more for the highest charge state ions. When the ECR heating frequency is increased the magnetic confinement field has to be scaled accordingly. The magnetic confinement structure used for ECR ion sources utilizes a combination of solenoid fields for axial and multipole fields (typically sextupole) for radial confinement. ECR ion sources that utilize normal conducting electromagnetic coils in combination with a permanent hexapole are limited to operating frequencies of up to about 20 GHz due to the maximum achievable field strength. Beyond these frequencies only fully superconducting magnetic confinement structures can reach the field strengths required for optimum performance.

*This work was supported by the Director, Office of Energy Research, Office of High Energy and Nuclear Physics, Nuclear Physics Division of the U.S. Department of Energy under Contract DE AC03-76SF00098.

[#]dleitner@lbl.gov

Table 1: Recently Extracted VENUS Ion Beam Intensities in eμA

VENUS 28 GHz or 18 GHz +28 GHz							
CS	¹⁶ O	⁴⁰ Ar	CS	⁸⁴ Kr	¹²⁹ Xe	²⁰⁹ Bi	²³⁸ U
6 ⁺	2850		25 ⁺	223		243	
7 ⁺	850		26 ⁺			240	
8 ⁺			27 ⁺	88		245	
12 ⁺		860	28 ⁺	25	222	225	
13 ⁺		720	29 ⁺	5	168	203	
14 ⁺		514	30 ⁺	1	116	165	
16 ⁺		270	31 ⁺		86		
17 ⁺		36	33 ⁺		52		205
18 ⁺		1	34 ⁺		41		202
			35 ⁺		28.5		175
			37 ⁺		12		
			38 ⁺		7		
			41 ⁺			15	
			42 ⁺				.4
			47 ⁺			2.4	5
			50 ⁺			.5	1.9

VENUS ECR ION SOURCE PERFORMANCE

Table 1 shows a summary of the VENUS ion source performance. The source can be operated with two frequencies. In addition to 28 GHz, 18 GHz can be injected either as a second frequency for double frequency heating or used alone for single frequency heating. The VENUS ECR ion source has been developed with two applications in mind. First as a prototype ECR ion source for the Facility for Rare Isotope Beams (FRIB) the emphasis of the R&D is the production of medium high charge states such as U³³⁺ (Fig. 1). Second as an injector into the 88-Inch Cyclotron the emphasis is on the production of high charge state ions, in particular U⁴⁷⁺ (Fig. 2). Uranium beams are especially challenging to produce because of the chemical properties of uranium and the high temperature required to evaporate enough feeding material for the plasma. In addition, chemical reactions (between the oven, the crucible and uranium or uranium compounds) at higher temperatures complicate operation [3].

At LBNL, Uraniumdioxide (UO₂) is currently pursued as feed material. It is an ideal compound since it is chemically stable and sublimates. In addition, its oxygen component serves as an ideal mixing gas for the plasma [3]. The only drawback is the high oven temperature required. UO₂ has a vapour pressure of about 1·10⁻² mbar at 2000°C. Therefore, the VENUS oven has to be operated at temperatures between 1900 and 2100°C in

order to provide enough vapour flow into the plasma through the 2.6 mm² aperture area. Building a furnace within the restricted space of an ECR injection flange that can reliably reach such high temperature is a major challenge. Over the last years LBNL has developed compact high temperature ovens to meet these temperature requirements in the presence of the high axial magnetic field at the oven position. The latest is a coaxial design which allows the heater current flow to be parallel with the axial magnetic field thus eliminating any IxB forces that might limit the lifetime of the hot oven. Testing of this new oven concept will be the focus of the near term R&D program.

MAGNETIC FIELD REQUIREMENTS

Over the last few decades clear guidelines have been established for the optimum confinement field strength for a given microwave heating frequency. The recommended field relationships between the confining fields at the injection end (B_{inj}), extraction end (B_{ext}), and in the radial direction (B_{rad}) and the resonant heating field (B_{ECR}) are summarized in table 2. The resonant heating field is related to the microwave frequency f_{rf}, by B_{ECR}=2πf_{rf}m/e, where m the electron mass, and e the electron charge. For example, the corresponding resonant magnetic field for 28 GHz heating is 1 Tesla.

The VENUS ECR ion source at LBNL [1] has been optimised for operation at 28 GHz by following the guidelines given in table 2. Its magnetic field values for the axial mirror field created by three solenoid coils and the radial sextupole fields are shown in Fig. 3.

In terms of confinement and heating an important feature of the superimposed solenoidal and hexapolar magnetic fields is the magnitude of the last closed surface created within the plasma chamber. For high performance ECR ion source a typical value for the last closed surface is about two times B_{ECR}, which corresponds to 2 Tesla in the case of VENUS. Beyond this value (for example three or four times B_{ECR}) the gains due to the enhancement of the magnetic confinement are much less than the gains achievable by using higher frequencies with a closed surface of 2 B_{ECR} instead.

As an example, the magnetic iso-surfaces of the VENUS ECR ion source are shown in Fig. 4 in an axial cut through the plasma chamber. The number 2 indicates the two Tesla line, the number 1 indicates the one Tesla line which corresponds to the 28 GHz resonance zone.

Table 2: Typical Magnetic Field Ratios for high performance ECR Ion Sources

B _{inj} /B _{ecr}	~ 4
B _{ext} /B _{ecr}	~ 2
B _{min} /B _{ecr}	~ 0.5 to 0.8
B _{rad} /B _{ecr}	≥ 2
B _{ext} /B _{rad}	≤ 0.9 to 1

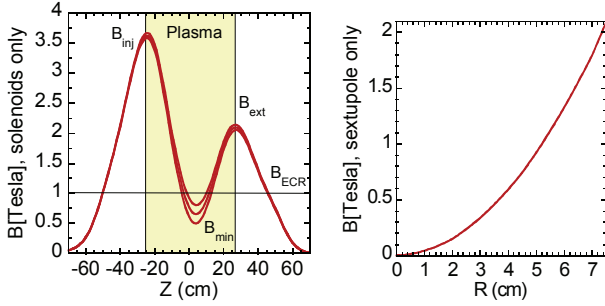


Figure 3: The axial and radial fields of the VENUS ECR ion source. The minimum B field using the middle solenoid coil.

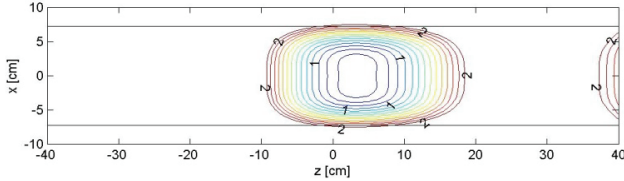


Figure 4: The closed magnetic field surfaces inside the VENUS plasma chamber in 10% increments of the ratio between B/B_{ECR} . The axial field peaks are roughly at $z = -24$ cm and at $z = 26$ cm.

When the optimum magnetic field values inside the plasma chamber are achieved, the peak fields on the conductor will be much higher. For example, to achieve a sextupole field of 2 T on the plasma chamber wall the maximum field on the sextupole conductor is 6 to 7 T in the case of the VENUS ECR ion source. The maximum field that can be produced in a superconducting magnet is limited by processes that drive the superconductor into the normal-conducting state (magnet quench). To avoid quenching, the magnet design must keep the current densities and local magnetic fields at the coils below the short sample critical current in the superconductor, which depends on the type of superconductor used, the local magnetic field and the temperature. All modern superconducting ECR ion sources use NbTi superconducting wires. The performance of NbTi magnets is limited by its upper critical field of about 10 T at 4.2 K, which limits these ion sources to maximum microwave frequencies between 20 and 30 GHz (see Fig. 5).

Table 3: Magnetic Field Requirements for a 28 GHz and a 56 GHz ECR Ion Source

Magnetic Design		28 GHz	56 GHz
Max solenoid field	on the coil	6 T	12 T
	on source axis	4 T	8 T
Max sextupole field	on the coil	7 T	15 T
	on plasma wall	2.1 T	4.2 T
Superconductor		NbTi	Nb₃Sn

Ion Sources

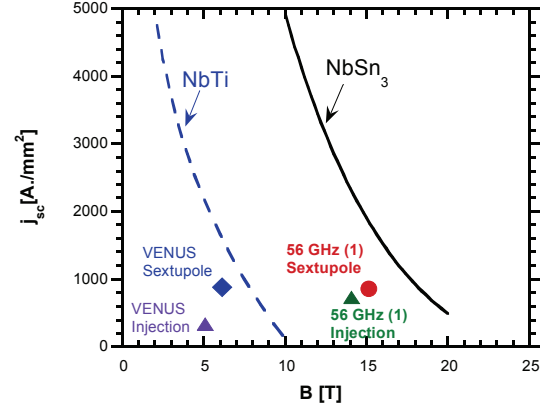


Figure 5: Critical current density in a NbTi and a Nb₃Sn superconductor wire (A/mm^2) vs. total magnetic field (T). The operating points for the VENUS ECR and the proposed 56 GHz ECR ion source (sextupole-in solenoid) for the sextupole magnet and the injection solenoid are indicated. The current density j_{sc} is quoted inside the superconductor and is not the engineering current densities through the total cross section of the wire or cable.

To extend ECR ion sources to frequencies well above 28 GHz, new superconductor technology will be needed in order to fabricate the magnet structure. Presently, the most advanced material for high-field applications is Nb₃Sn, for which the upper critical field limit increases to about 20 T at 4.2 K. The critical current densities for both materials (NbTi and Nb₃Sn) are shown in Fig. 5 for a temperature of 4.2 K.

Table 3 summarizes the magnetic field requirements for a 28 GHz and a 56 GHz ECR ion source. In addition, to the maximum field inside the plasma chamber, the peak field on the conductors is shown.

SUPERCONDUCTING MAGNET R&D

Two very distinct options can be pursued to design a fully superconducting ECR ion source magnet structure: The sextupole coils can be placed inside the solenoids (sextupole-in solenoid, geometry 1 in Fig. 6) or outside the solenoids (solenoid-in-sextupole, geometry 2 in Fig. 7). Both design options have been pursued for third generation ion sources. The VENUS source follows the sextupole-in-solenoid design concept [4], the SECRAI source in Lanzhou [5, 6] follows the solenoid-in-sextupole design concept. There are advantages to each design concept.

Both options have been analysed as possible design solution for a 56 GHz Nb₃Sn magnet structure [7]. To compare the two geometry options specific field requirements at different spatial locations were imposed as summarized in Table 2.

Table 4 summarizes the dimensions used for the models. These dimensions were chosen following the design of the existing ECR ion sources VENUS and SECRAI. A detailed description of the magnetic analyses and the structural magnet implications can be found in Ferracin et al. [8] and Prestemon et al [7].

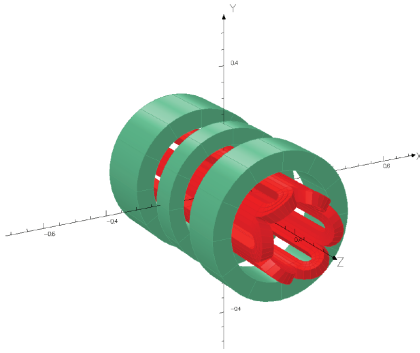


Figure 6: VENUS: Sextupole-in-Solenoid Geometry (1). The sextupole-in-solenoid VENUS geometry leverages proximity of the sextupole to the plasma chamber, minimizing peak fields in that coil.

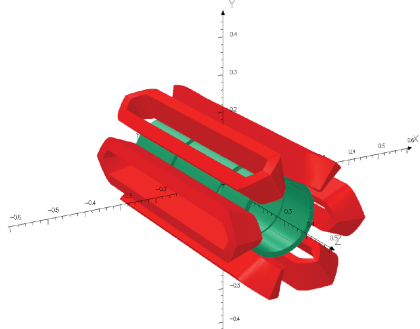


Figure 7: SECRAL Solenoid-in-Sextupole Geometry (2). The solenoid-in sextupole geometry minimizes the influence of the solenoid on the sextupole field, at the expense of significantly higher field on the sextupole magnet surface due to the larger radius of the coils.

The magnetic analyses show, that the solenoids in configuration 2 (Solenoid-in-Sextupole) are subjected to large sextupole fields, resulting in high peak fields in all coils for that configuration. These high current densities in the solenoids stem from the need to minimize the radius of the sextupole and exceed the capabilities of the Nb_3Sn superconductor. In addition, the sextupole field generates a large radial field on the solenoid that alternates sign azimuthally; the resulting Lorentz force distribution leads to sizable shear stresses within the solenoid coils. Based on the magnetic analysis, the solenoid-in-sextupole configuration can be ruled out as a candidate for a Nb_3Sn 56GHz ECR source.

For configuration 1 (Sextupole-in-Solenoid), there are two limits to consider: the peak field at the conductor and the location of the maximum force. The peak field on the sextupole occurs in the middle of the injection coil. However, at this location the solenoid field contributes predominantly a B_z field component on the sextupole, which is parallel to the sextupole current flow. Therefore this field component contributes less to the maximum (critical) field strength at which the superconductor quenches. In order to be more conservative, the total field strength was used for this analysis and for the operation point indicated in Fig. 5. The operation points of the VENUS ECR ion source are also shown as a reference. The maximum for-

ces are located at the sextupole ends. A solution for this issue is to lengthen the sextupole coils which results in the extended sextupole structure typical for superconducting ECR ion sources.

It can be concluded from the magnetic analysis that the design is challenging, but feasible, with current Nb_3Sn technology. The design operates at about 86% of the current limits corresponding to a temperature margin of about 2.5K.

Table 4: Radial Dimensions (ID and OD) for the two Geometry Options (sextupole-in-solenoid and solenoid-in-sextupole) used

Sextupole-in-Solenoid (geometry 1)				
	Sext.	Inj.	Middle	Extr.
r_1/r_2	100/162	194/253	194/244	194/253
$J_{sc}[\text{A}/\text{mm}^2]$	860	727	-542	595
peak fields	15.1	13.35	8.57	10.31
Solenoid-in-Sextupole (geometry 2)				
	Sext.	Inj.	Middle	Extr.
r_1/r_2	106 /146	92/106	101/106	92/106
$J_{sc}[\text{A}/\text{mm}^2]$	1083	1924	-227	1657
peak fields	16.9	16.5	13.97	15.25

OTHER CHALLENGES FOR SUPERCONDUCTING ECR ION SOURCES

Besides the size and weight of the high field superconducting ECR ion source cryostat, the energy stored in the magnet, the quench protection system and cryogenic engineering challenges, other issues in connection with the operation of the ECR ion source plasma have to be considered in the design.

Plasma Chamber

The required microwave power densities injected into the plasma constitutes a major challenge for the design of the plasma chamber cooling circuits. The superconducting structure implies a relatively large plasma volume and this requires a large amount of microwave power to achieve sufficient plasma heating. In addition, as the frequency is increased, more power can be coupled into the plasma without causing instabilities. Taking VENUS as a reference, this source has been operated so far with up to about 9 kW of RF power (about 1 kW/l) and is clearly not yet at the power saturation point of the ion source. The main danger for the high power source operation is local melting of the plasma chamber due to the inhomogeneous heating distribution onto the plasma chamber walls due to localized particle losses. The weakest regions of the magnetic confinement field are three local magnetic field minima at the inner edge of the injection and extraction solenoid, where the large gradient in the solenoid field

produces a radial component that partially cancels the radial field produced by the sextupole. At these spots the plasma confinement is weakest and localized heating of the plasma chamber walls occurs which can lead to local melting of the plasma chamber. Therefore, the engineering design of the plasma chamber cooling needs to be carefully optimised to withstand this localized heat load. As an example, the VENUS plasma chamber is made out of aluminium and has been optimised to maximize the water flow around the plasma chamber. A similar or more advanced design will be needed for the 4th generation ECR ion sources.

Ion Beam Extraction

Transport of the high intensity, space charge dominated, heavy ion beam extracted from the outlet aperture located at the peak of the mirror field is also a major challenge. As the extracted beam is accelerated through this decreasing magnetic field, an axial rotation is introduced due to canonical angular momentum conservation, which results in transverse emittance growth. Therefore, as the extraction field is increased to operate the source at higher frequency, some emittance growth will be observed. However, since the highly charge state ions are believed to be concentrated near the source axis the actual, this emittance growth is less than what could be expected from the increase in the magnetic field [9]. In VENUS, the average emittance growth for the same charge state produced with 18 GHz fields and 28 GHz fields is about 20%, while the simple field extrapolation would predict 40%. In addition, due to the size of the cryostat, the beam has to be extracted from a long channel (at least 0.5m) before the first focusing element can be placed.

X-Ray Heat Load and Bremsstrahlung from the Plasma

Finally, the x-ray load from the plasma adds a sizeable heat load to the cryostat. X-rays that are produced by the hot plasma electrons colliding with the plasma walls are particularly troublesome for SC ECR ion sources. The x-rays produced by electron-ion collisions or electrons colliding with the plasma chamber walls can penetrate through the plasma chamber wall and are the cause of x-ray radiation in the vicinity of ECR ion sources. The x-rays can add a substantial heat load to the cryostat and cause localized heating in the superconducting coils (particular at the location of the three magnetic field minima) that may lead to quenches. In addition, they can lead to the degeneration of the synthetic high voltage insulator located between the warm bore of the cryostat and the plasma chamber [10]. During the development of the VENUS ECR ion source it had been recognized that it is crucial to add x-ray shielding in between the cryostat and the plasma chamber to reduce the heat load. A 2 mm Ta cylinder was added between the plasma chamber and the cryostat, which reduced the x-ray flux roughly by a factor of 10. However, it can be expected that the electron temperature will increase significantly when the heating frequency is doubled from 28 GHz to 56 GHz. A

comparison of the axial x-ray energy spectra at 18 GHz and 28 GHz in VENUS clearly shows that the high energy tail of the x-ray spectrum which is difficult to shield increases substantially at the higher microwave frequency [11], as shown in Fig. 8.

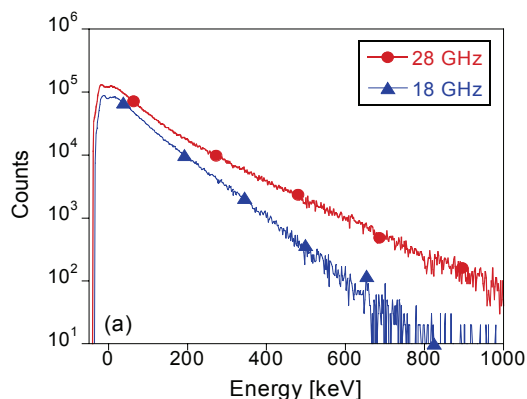


Figure 8: Comparison of the bremsstrahlung spectra for 28 GHz heating to 18 GHz heating using scaled (28/18) magnetic fields [11]

In addition, preliminary measurements on the LBL ECR suggest a higher radial energy component of the x-ray energy spectrum. This observation is not surprising and can be qualitatively understood by the transverse ECR heating process. However, it has important implications for the design of future superconducting ECR ion sources and it will be crucial to characterize the frequency scaling of the x-ray emission and its angular dependence.

REFERENCES

- [1] D. Leitner, C. M. Lyneis, T. Loew, et al., Rev. Sci. Instrum. 77, 03A303 (2006).
- [2] R. Geller, Electron Cyclotron Resonance Ion Source and ECR Plasmas (Bristol, Institut for Physics Publishing, 1996).
- [3] D. Leitner, M L Galloway, T. J. Loew, et al., RSI 79 (2008).
- [4] C. E. Taylor, S. Caspi, M. Leitner, et al., IEEE Transactions on Applied Superconductivity 10, 224 (2000).
- [5] H. W. Zhao, L. T. Sun, X. H. Guo, et al., High Energy Physics and Nuclear Physics 31, 8 (2007).
- [6] H. W. Zhao, L. T. Sun, X. H. Guo, et al., in CYCLOTRONS 2007, Giardini Naxos, Italy, (2008).
- [7] S. Prestemon, F. Trillaud, S. Caspi, et al., IEEE Trans. Appl. Supercon 19 (2009).
- [8] P. Ferracin, S. Caspi, H. Felice, et al., in PAC'09, Vancouver, 2009).
- [9] D. Leitner, J.Y. Benitez, M L Galloway, et al., in CYCLOTRONS 2007, Giardini Naxos, Italy, (2008).
- [10] C. M. Lyneis, D. Leitner, O. Tarvainen, et al., Rev. Sci. Instrum. 77, 1 (2006).
- [11] D. Leitner, C.M. Lyneis, H. Koivisto, et al., RSI 79, 033302 (2008).

A HIGH-PERFORMANCE ELECTRON BEAM ION SOURCE*

J. Alessi[#], E. Beebe, S. Bellavia, O. Gould, A. Kponou, R. Lambiase, R. Lockey, D. McCafferty, M. Okamura, A.I. Pikin, D. Raparia, J. Ritter, L. Snyderstrup, BNL, Upton, Long Island, New York

Abstract

At Brookhaven National Laboratory, a high current Electron Beam Ion Source (EBIS) has been developed as part of a new preinjector that is under construction to replace the Tandem Van de Graaffs as the heavy ion preinjector for the RHIC and NASA experimental programs. This preinjector will produce milliamper-level currents of essentially any ion species, with $q/A \geq 1/6$, in short pulses, for injection into the Booster synchrotron. In order to produce the required intensities, this EBIS uses a 10 A electron gun, and an electron collector designed to handle 300 kW of pulsed electron beam power. The EBIS trap region is 1.5 m long, inside a 5 T, 2 m long, 8" bore superconducting solenoid. The source is designed to switch ion species on a pulse-to-pulse basis, at a 5 Hz repetition rate. Singly-charged ions of the appropriate species, produced external to the EBIS, are injected into the trap and confined until the desired charge state is reached via stepwise ionization by the electron beam. Ions are then extracted and matched into an RFQ, followed by a short IH Linac, for acceleration to 2 MeV/A, prior to injection into the Booster synchrotron. An overview of the preinjector is presented, along with experimental results from the prototype EBIS, where all essential requirements have already been demonstrated. Design features and status of construction of the final high intensity EBIS is also be presented.

INTRODUCTION

A new heavy ion preinjector is presently under construction at Brookhaven. This preinjector will replace two existing Tandem Van de Graaff accelerators and an 800 m transport line, as the heavy ion preinjector for both the Relativistic Heavy Ion Collider (RHIC) and NASA Space Radiation Laboratory (NSRL). The front end of the preinjector is shown in Fig. 1. Following the IH linac, there is a 37 m long beam transport line matching the beam into a Booster synchrotron. A key component of this preinjector is a high-performance EBIS source, which is based on the successful performance of the prototype BNL Test EBIS. Other key elements of this preinjector include an RFQ and IH linac.

The preinjector is designed to deliver milliamper currents of any ion species in $\sim 10 \mu\text{s}$ pulses, to allow single-turn injection into the Booster. Species from EBIS can be changed on a pulse-to-pulse basis, by changing the 1+ ion injected into the EBIS trap from the external ion sources. The switching time for the magnets in the beam

transport line following the linac will be 1 second. Table 1 shows high-level parameters for the preinjector. In addition to it being a modern replacement for the aging Tandems, and its ability to produce any ion species rather than only those starting as negative ions, it also eliminates the need for any stripping foils before Booster injection, which will result in more stable beams.

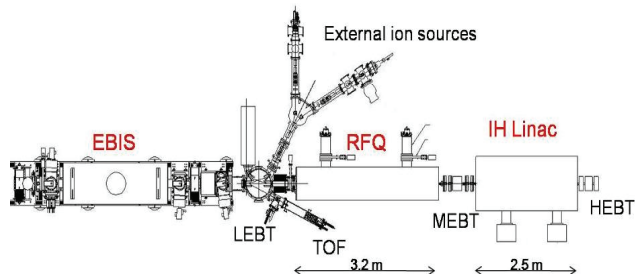


Figure 1: Layout of the EBIS Preinjector.

Table 1: Preinjector Parameters

Ions	He – U
Q / m	$\geq 1/6$
Current	$> 1.5 \text{ emA}$
Pulse length	$10 \mu\text{s}$ (for 1-turn injection)
Rep rate	5 Hz
Final energy	2 MeV/u
Time to switch species	1 s

PREINJECTOR SYSTEMS STATUS

The EBIS source will be covered in detail in the later sections. Here, a brief status of the remaining components is presented.

RFQ

A 100 MHz, 4-rod RFQ will accelerate the beam from an input energy of 17 keV/A, to 300 keV/A. Some RFQ parameters are given in Table 2. The RFQ was built by A. Schempp, et al. at the Institute of Applied Physics at the University of Frankfurt [1], with most of the fabrication by NTG [2]. The RFQ is now at Brookhaven (Fig. 2). Beams from the Test EBIS have been used for initial testing of the RFQ [3]. In early tests, we have accelerated He, Ne, and Cu beams, and while exact measurements of performance are complicated by the presence of multiple charge states entering the RFQ, results to date are consistent with the calculated performance.

*Work supported under the auspices of the US Department of Energy and the National Aeronautics and Space Administration.

[#]alessi@bnl.gov



Figure 2: The EBIS RFQ at BNL.

Table 2: Parameters of the RFQ

Input Energy	17 keV/A
Output energy	300 keV/A
Q / m	> 1 / 6
Frequency	100.625 MHz
Length	3.2 m
Power (with beam loading)	~ 200 kW

Medium Energy Beam Transport

Following the RFQ, there is a ~1 m matching section which consists of four pulsed magnetic quadrupoles for transverse matching, and one rebuncher cavity for longitudinal matching into the linac. The rebuncher cavity was built by IAP, Frankfurt, and is now ready for installation.

IH Linac

The IH Linac is being built by U. Ratzinger, et.al. at IAP, Frankfurt. Linac parameters are given in Table 3. The linac is designed for a beam current of up to 10 mA. Fabrication of the cavity by PINK [4] is complete, and the cavity is now at GSI for copper plating. The internal quadrupole triplet is being built by Bruker [5]. Linac drift tubes are complete, and the structure was assembled (with a dummy drift tube for the internal quadrupole triplet) for low level rf measurements, as shown in Fig. 3. The linac is scheduled for delivery in the fall of 2009.

Table 3: Parameters of the IH Linac

Input energy	300 keV/A
Output energy	2 MeV/A
Q / m	> 1 / 6
Frequency	100.625 MHz
Cavity Length	2.46 m
Power (with beam loading)	~ 300 kW

Ion Sources



Figure 3: IH linac during initial rf testing.

High Energy Beam Transport

Following the linac, there is a 37 m long transport line to match beam into the Booster Synchrotron. This line consists of one pulsed quadrupole triplet, seven quadrupole singlets, and two 73 degree magnetic dipoles. Two debuncher cavities in the line reduce the beam energy spread going into Booster. The dipoles, made by Sigmaphi [6], have been installed in the Booster tunnel, as shown in Fig. 4.



Figure 4: Dipoles installed in the Booster tunnel.

SOURCE REQUIREMENTS

The source requirements are shown in Table 4. An EBIS is well suited for meeting RHIC requirements. An EBIS can produce any type ions - from gas, metals, etc., and is easy to switch species, even pulse-to-pulse, when feeding the trap by injection of singly charged ions from external sources. One has precise control over the charge state produced, and it is easy to produce a distribution peaked at intermediate charge states such as Au^{32+} or U^{45+} . One has control over pulse width, extracting a fixed charge, so one can better match synchrotron requirements. EBIS produces a narrow charge state distribution ($\geq 20\%$ in the desired charge state), so there is less of a space charge problem in the extraction and transport of the total current. Finally, the source is reliable, has excellent pulse-to-pulse stability, and long lifetime.

Table 4: Source Requirements for the RHIC Preinjector

Species	He to U
Output (single charge state)	$\geq 1.1 \times 10^{11}$ charges
Ion output (Au^{32+})	3.4×10^9 particles/pulse
Q/m	$\geq 1/6$, depending on ion
Pulse width	10 - 40 μs
Max rep rate	5 Hz
Beam current (single charge state)	1.7 - 0.42 mA
Output energy	17 keV/A
Species switching time	1 second

TEST EBIS RESULTS

The Test EBIS was built to demonstrate all essential features of an EBIS meeting RHIC requirements. This half-trap length (half-yield), full power electron beam prototype is described in detail in [7]. The following are some key results:

- Electron beam currents greater than 10 A have been propagated through the Test EBIS with losses less than 1mA.
- Au^{32+} has been produced in less than 35 ms, Ne^{8+} in 18ms, N^{5+} in 4ms, and Cu^{15+} in 15 ms. Charge state vs. confinement time agrees with calculations. A sample result for Ne is shown in Fig. 5, 6.
- With external ion injection, 3.5×10^{11} charges/pulse of Au ions, and $\geq 2 \times 10^{11}$ charges/pulse of Ne, N, and Cu have been achieved. In all cases our goal of extracting charge of 50% of the trap capacity has been exceeded (Fig. 7). (“Trap capacity” is the total number of electrons beam charges in the trap region, i.e. full space charge neutralization of the electron beam in the trap by ions).
- The above yields can be extracted in pulses of 10-20 μs FWHM, resulting in extracted currents for these ions of several mA’s.
- Emittance = 0.1 π mm mrad (rms normalized) has been obtained for a 1.7 mA beam extracted from the EBIS after Au injection, while lighter beams have emittances up to $\sim 0.3 \pi$ mm mrad. (Since there is no separation of beam components, the emittance of all charge states were measured; individual charge state emittance could be smaller).
- The EBIS has operated on the pulsed high voltage platform at > 100 kV, producing the required 17 keV/A. The EBIS only has to be at high voltage during the < 50 μs ion extraction time, so pulsing of the high voltage reduces the likelihood of breakdowns, and allows the external ion sources and injection lines to sit at laboratory potential.

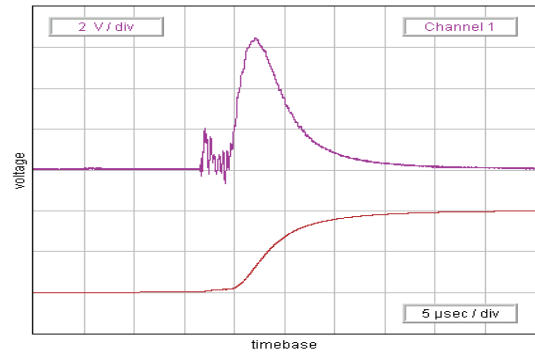


Figure 5: Neon beam pulse, 6.3 mA peak (upper) and integrated charge, 2.4×10^{11} (lower). $I_c=6.8$ A.

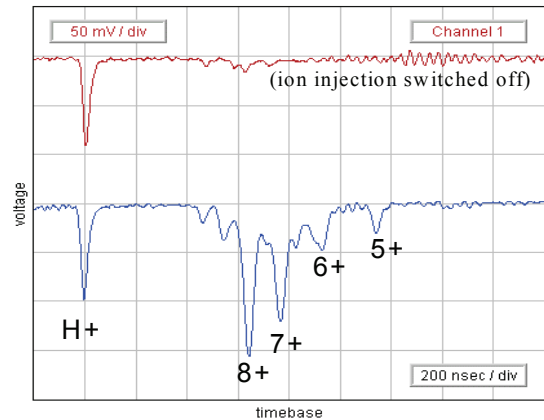


Figure 6: Ne time-of-flight spectra without and with ion injection (upper and lower), for 14 ms confinement time.

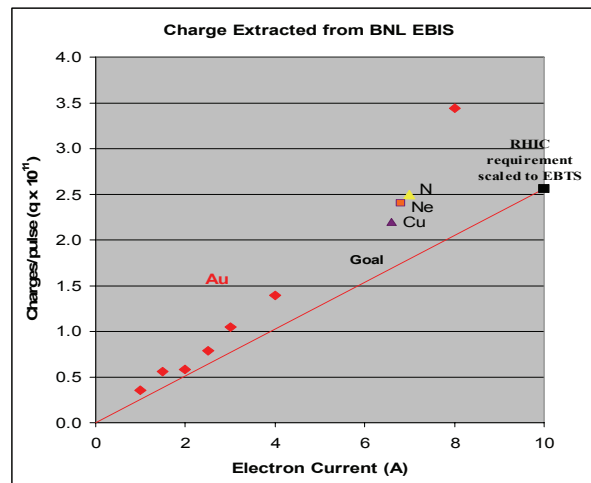


Figure 7: Ion yield vs. electron beam current, for various species.

- Extracted beam has been matched into the RFQ with a LEBT including a gridded einzel lens and pulsed magnetic solenoid after the HV acceleration.

RHIC EBIS

The design of the RHIC EBIS is very similar to the prototype Test EBIS. For the RHIC EBIS, a straightforward doubling of the trap length by installing a

longer superconducting solenoid is required, in order to double the ion output. Linear scaling of output with trap length has been shown on the Test EBIS over a range of 35-107 cm.

The design value of the electron beam current of 10 A is the same as run on the Test EBIS. The source is shown schematically in Fig. 8, and some key parameters are given in Table 5. All EBIS subassemblies have been fabricated, and have either already been tested, or are in the final assembly stages.

Table 5: RHIC EBIS Source Design Parameters

Electron gun current	10 A
Solenoid field	5.5 T
Trap length	1.5 m
Pressure in the trap region	low 10^{-10} Torr
Total extracted charges per pulse	5×10^{11} (80 nC)
Total current per pulse (all charge states)	~ 8 mA in 10 μ s
Output energy	17 keV/A

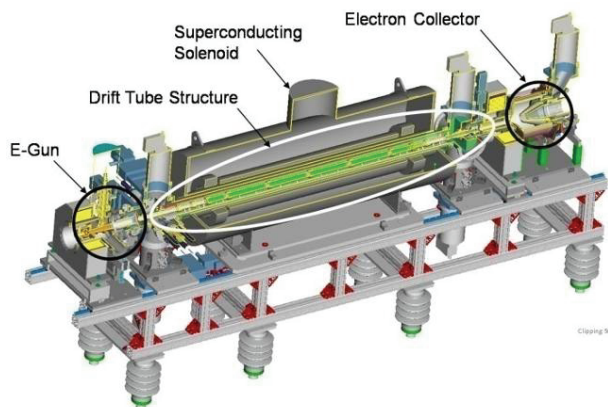


Figure 8: Drawing of the RHIC EBIS.

Electron Gun

The performance required for the RHIC EBIS can be achieved with the 10 A electron gun originally used on the Test EBIS. Nevertheless, it was desirable to have a safety margin with electron beam current for EBIS operation at 10 A plus some prospects for increase of output ion intensity in the future. The electron gun cathode is a 9.2 mm diameter IrCe unit, made for BNL by BINP [8], and with this IrCe cathode one has the possibility of increasing emission and producing an electron current up to 20 A. To reach electron current of $I_{ej}=20$ A with existing 40 kV anode power supplies the perveance of the gun is doubled relative to our earlier gun, to $\sim 2.5 \cdot 10^{-6}$ A/V^{3/2}. The IrCe cathode can provide emission current density 40 A/cm², with an expected lifetime at this density of several thousand hours [9]. At 15 A/cm² required for 10A operation, the estimated lifetime is >20,000 hours. The design is based on the inverted magnetron geometry of our first electron gun of Novosibirsk design, which

produces a laminar electron beam, allowing operation in a wide range of electron current, potential and magnet field distributions. It also allows substantial deceleration of the electron beam in the ion trap and electron collector regions. The cathode is immersed in a magnetic field of approximately 0.14 T.

The final electron gun has been successfully tested to 10 A on the Test EBIS, and has been in routine use there for ~ 6 months. It is shown schematically in Fig. 9.

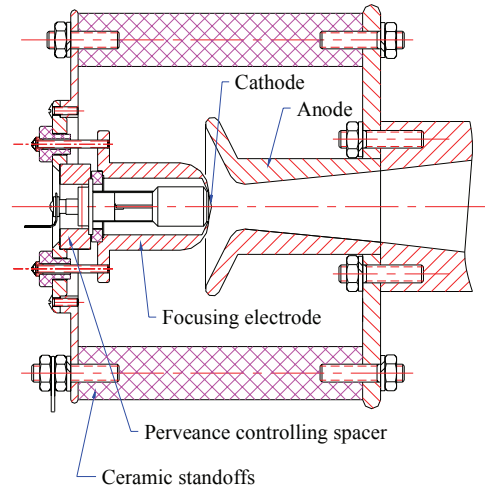


Figure 9: Schematic of the 20 A Electron Gun.

Electron Collector

The electron collector is designed to handle a nominal electron beam of 20 A, 15 kV dc, i.e. 300 kW, but since ionization times are typically < 50 ms, the electron beam can be pulsed at a duty factor < 25%, for a lower average power. The maximum heat load on the inner surface is ~ 350 W/cm² during the pulse, and averaged over the area being hit, is ~ 200 W/cm² during the pulse. A collector fabricated from a Zr-Cr-Cu alloy is completed and has been in use on the Test EBIS, although the duty factor is low on Test EBIS due to power supply limitations. A second, spare collector has been completed which is identical, except that it is made from a high conductivity Be-Cu (Hycon3 HP). This should have somewhat better thermal fatigue lifetime. The collector is shown in Fig. 10.

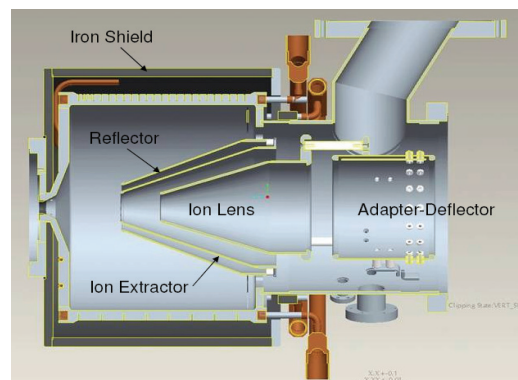


Figure 10: Schematic of the Electron collector.

Ion Sources



Figure 11: The 5 T, 2 m long EBIS solenoid at BNL.

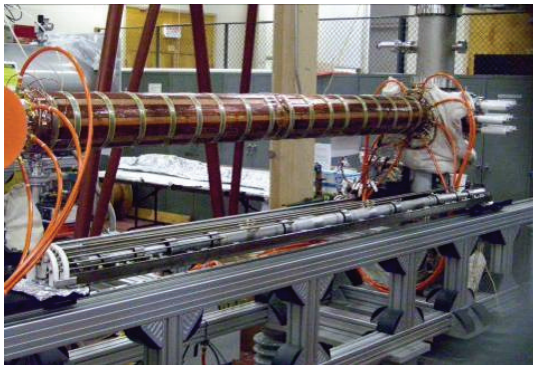


Figure 12: EBIS drift tube structure (below) and central vacuum chamber (above) where it will be inserted.

Superconducting Solenoid

The superconducting solenoid for the EBIS is 2 m long, with a 5 T field, and field uniformity sufficient to allow a 1.5 m trap length. The solenoid has a 204 mm diameter warm bore, to allow sufficient space for the vacuum pipe, which also has heating rods and water cooled shield for baking of the central trap region. The solenoid was fabricated by ACCEL Instruments [10], and following a failure during a quench test in 2007, it was repaired and passed factory acceptance testing in January, 2009. Some damage during shipping to Brookhaven has now been repaired, and the magnet has passed all acceptance tests. It is shown at BNL in Fig. 11.

Central Trap

The central trap region consists of six cylindrical electrodes of ~ 42 mm diameter. The electron beam radius in the trap is ~ 0.8 mm ($J_e \sim 500$ A/cm²). There is NEG material running the length of the central vacuum pipe to provide extra pumping in this region. A pressure of $\sim 10^{-10}$ Torr is required in this region to minimize contaminant ions. This inner trap electrode assembly is complete, and is shown in Fig. 12. Also shown in Fig. 12 is the outer vacuum chamber, with heating elements for baking, an outer cooling jacket, and steering coils. This unit has been successfully tested, reaching a central drift tube temperature in excess of the required 450 °C, while maintaining the outer skin at room temperature.

Ion Sources

EXTRACTION AND TRANSPORT TO THE RFQ

The entire EBIS and its power supplies sit on a voltage isolated platform, and can be pulsed at up to ~ 100 kV to provide 17 keV/A for any ion species at $Q/m > 1/6$. This platform is pulsed to high voltage for only ~ 100 μ s, during ion extraction. Matching into the RFQ is via one gridded einzel lens, and one pulsed magnetic solenoid. This matching section has been installed and operated on Test EBIS, to verify the performance of this LEBT. Emittance measurements are complicated by the presence of multiple charge states, but generally are consistent with expectations (rms values of $\sim 0.1 - 0.3 \pi$ mm mrad at the RFQ entrance location, depending on species).

EXTERNAL ION SOURCES

We rely on external ion injection to provide most ion species. In this manner, the EBIS functions purely as a charge state multiplier. One can easily change species and charge state on a pulse to pulse basis, and there is virtually no contamination or memory effect. To date, we have operated the EBIS successfully with external ion injection from a Metal Vapor Vacuum Arc Source, a Hollow Cathode Ion Source, and a Liquid Metal Ion Source. Injected 1+ ion currents of 10's to 100's of microamperes are required for seeding the EBIS trap, and these ions are transported to the EBIS at ~ 15 kV. In addition, for beams such as helium, we have used standard gas injection.

For the RHIC EBIS, we are building two ion sources plus injection lines, as can be seen in Fig. 1, which can be selected on a pulse-to-pulse basis. There is also a third port where 1+ ions from a laser ion source may be injected in the future [11], which offers the possibility of producing almost any desired 1+ beam from a single ion source.

REFERENCES

- [1] M. Vossberg, et.al., "The new EBIS RFQ for BNL", Proc. of Linac 2008, Victoria, BC, Canada.
- [2] NTG GmbH, Gelnhausen, Germany.
- [3] M. Okamura, et.al., "Beam Commissioning of the RFQ for the RHIC-EBIS Project", PAC 2009.
- [4] PiNK GmbH, Wertheim, Germany.
- [5] Bruker Biospin S.A., Wissenbourg, France.
- [6] Sigmaphi, Vannes, France.
- [7] E.N. Beebe, et.al., Rev. Sci. Instr. 73 (2002) 699.
- [8] G. Kuznetsov, Nuclear Instrum. & Meth. In Physics Res. A 340, 1994, p. 204.
- [9] G.I. Kuznetsov, Journal of Phys.: Conf. Series 2 (2004) 35-41.
- [10] ACCEL Instruments GmbH, Bergisch Gladbach, Germany.
- [11] T. Kanesue, et. al., "Measurement of ion beam from Laser Ion Source for RHIC EBIS", EPAC 2008, Genoa, Italy. p. 421.

ACCELERATION OF HEAVY IONS GENERATED BY ECR AND EBIS

R. Becker, Goethe-Universität, Frankfurt, Germany
 O. Kester, NSCL/MSU, East Lansing, MI, USA

Abstract

ECR and EBIS have become well-known ion sources for most heavy ion accelerator projects. The basic difference arises from the method, how energy is provided to create dense energetic electrons: An ECR uses microwave heating of a magnetically confined plasma, while in an EBIS the energy comes from a power supply to accelerate an electron beam and focus it to high density in a strong solenoidal magnetic field. Basically ECR sources are dc sources of heavy ions but the afterglow extraction also provides intense mA pulses in ms. In contrast to this EBIS sources provide an intense ion pulse in 1÷100 μ s and therefore find application in feeding synchrotrons. This determines most of the accelerator applications: ECR sources have very successfully extended the range (and life) of cyclotrons, while EBIS has found application at high energy facilities. For radioactive beam facilities, both kind of sources are in use. ECR sources in the trapping mode (ECRIT) perform the ionization (charge breeding) of high intensity primary beams, while EBIS can reach higher charge states at lower emittance, which provides an improved signal to noise ratio for rare isotopes.

INTRODUCTION

In the beginning of EBIS (1967) and ECR (1971) development both sources have been important to improve the charge to mass ratio over that available from Penning sources, which so far had been used exclusively for cyclotrons and linacs. Today both sources (including the electron beam ion trap, EBIT) are seen as charge breeding devices, which can put the burden for the production of delicate singly charged ions to specialized ion sources. This also includes accelerators for rare isotope production using the ISOL or the fragmentation method with subsequent gas stopping [1].

The production of highly charged ions is governed in both sources by the same physical collision processes: sequential ionization by successive electron impact, heating of ions by small angle Coulomb collisions, cooling of ions by ion-ion-collisions, and internal loss of highly charged ions by charge exchange and radiative recombination as well as losses to the wall of the ionisation chamber. Both sources differ very much from each other in construction and in the mix of collision and loss processes, which makes it worth to have a closer look on common and differing features. EBIS as well as ECR ion sources may be purchased from companies today, nevertheless for sophisticated applications in cutting edge research, ECRIS and EBIS devices are still being developed. In particular for heavy ion accelerators, high performance devices are in construction. In case of ECRIS, those devices use super-conducting (SC-)

magnets and operate with 28 GHz Microwave frequency [2]. In case of EBIS/T, high performance devices use multi ampere electron beams, strong magnetic fields from SC- magnets and high electron beam current densities [3].

BASICS OF ION PRODUCTION IN EBIS/T AND ECRIS

The sequential ionization needs – depending on the charge state to be reached and the density of ionizing electrons – a certain time to evolve. Therefore the ions require a confinement. In EBIS/T the trapping is electrostatic by the negative space charge of the electron beam, which cannot be exceeded by the ionic space charge. This limits the yield of extracted ions but simple laws then allow to design an EBIS with a required ion yield straightforward (BNL [4]). In ECR sources the trapping mechanism is not so clear. Some people in the past have favoured a magnetic trapping, but also an electrostatic trapping is possible by the ECR-zones, where electrons are heated up and have similar density as nearby but a higher energy. These ECR-zones therefore are regions with more ionic than electronic space charge, causing the electrostatic potential to form a barrier for ions. This has been well proven by trapping measurements with an ECRIT, although another explanation has been given by the authors at that time. Accepting the electrostatic barrier then immediately explains the after-glow operation by opening this barrier after switch-off of the rf and the action of the biased disk by using the space charge of an axially oscillating electron beam to lower the barrier in the reflection zone of these electrons. It also explains the cooling of trapped ions by collisions with ions from the mixing gas, as explained later.

The ionizing collisions of electrons, however, are at the same time Coulomb collisions. In spite of the fact that the electron mass is negligible with respect to the mass of heavy ions, many Coulomb collisions transfer energy from the electrons to the ions. Therefore the ions are heated considerably, in particular the highly charged ones, which are bombarded during the whole confinement time. By setting the ionization time equal to the heating time, an unique relation is obtained for the ionic energy in dependence of the ionic mass A , the cross sections for stepwise ionization $\sigma_{i-1 \rightarrow i}$, and the electron energy E_e :

$$E_i \approx \frac{10^{-18}}{AE_e} \sum_i^q \frac{i^2}{\sigma_{i-1 \rightarrow i}} \quad (1)$$

For energies much higher than the ionization energy cross sections in Eq. (1) are falling with $1/E_e$ and electron

heating of ions becomes independent of electron energy. The dependence on the ionic mass is consistent with the “isotope effect” found by Drentje [5]. The result of Eq. (1) for 3 keV electrons and for noble and residual gases is shown in Fig. 1. For higher charge states than Ne^{9+} , Ar^{16+} , Kr^{27+} , and Xe^{35+} the ion energy by electron heating exceeds 10 eV which will correspond to a transverse energy of extracted ions of the same order.

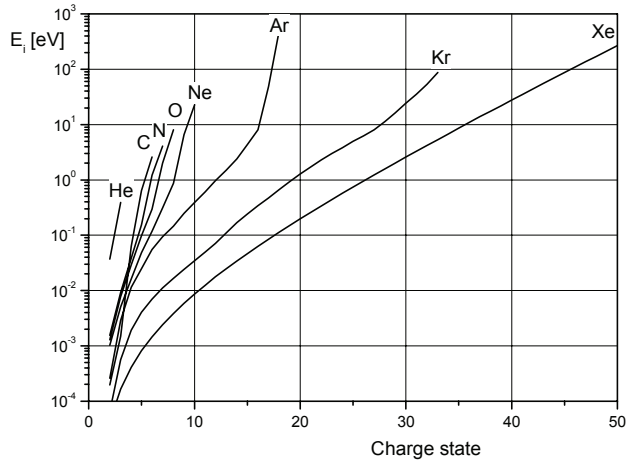


Figure 1: Ion energies by Coulomb collisions with 3 keV electrons during stepwise ionization.

While EBIS/T traps are deep enough to confine much hotter ions, this becomes a problem for the shallow trap of an ECR. In any case, this transverse energy will require attention for ion beam extraction and transport, which will be explained later. While charge exchange can be suppressed strongly in EBIS/Ts, which are essentially UHV-devices, it cannot be avoided in ECRs, due to the required high support gas pressure in the range of 10^{-8} - 10^{-7} mbar for the generation of the plasma. Charge exchange with neutrals has two distinct effects on the resulting charge distribution. The charge spectrum is wider and becomes limited to higher charge states.

This is well demonstrated in Fig. 2 for a charge breeding simulation of lead without and in Fig. 3 including charge exchange at a residual gas pressure of 10^{-8} mbar. The simulation in Fig. 2 shows an interesting feature when mono-energetic electrons are used for ionization, which is not possible for ECRs. The ionization energy of Pb^{54+} is at 5026 eV. Providing only 5025 eV inhibits the ionization of Pb^{54+} resulting in a maximum abundance of this ion. This shell effect is most pronounced at closed subshells of the ions, like for Pb^{54+} , which is alike nickel.

Including charge exchange shows in Fig. 3 that at a given instant, say $j \cdot \tau = 100$, the charge state distribution contains 12 instead of 7 different charge states at the same time. Also the highest charge state is less than Pb^{54+} . These results become even more important, when considering the classical procedure in ECRs and EBIS/T, to cool the heated ions by ion-ion collisions.

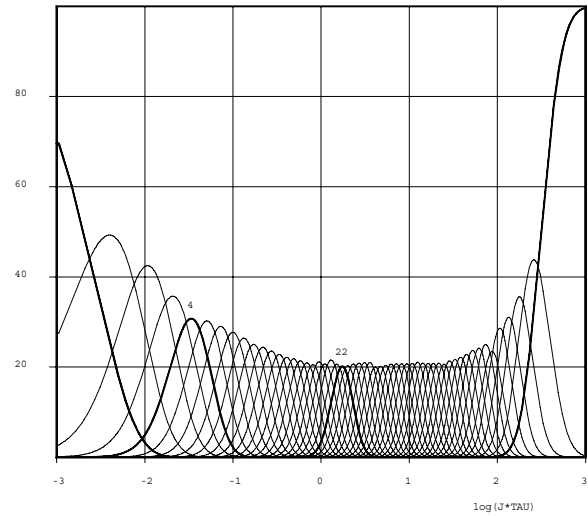


Figure 2: Charge breeding of lead at 5025 eV electron energy, without radiative recombination and without charge exchange.

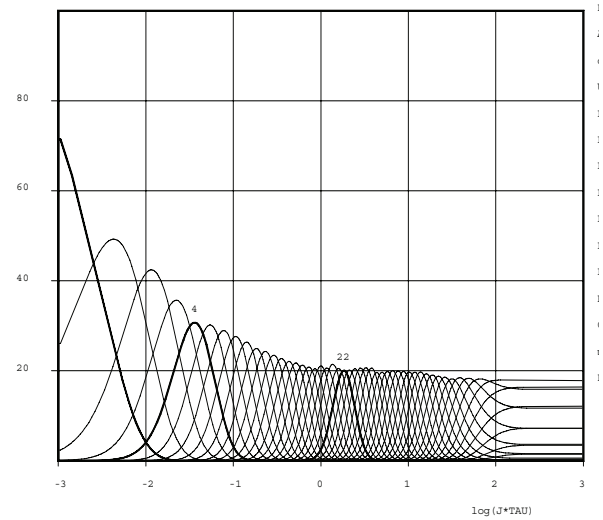


Figure 3: Charge breeding of lead at 5025 eV electron energy including charge exchange at a pressure of 10^{-8} mbar.

In order to create cold ions inside the source, an additional gas species must be fed in (gas mixing). The ions from this gas are absorbing energy by Coulomb collisions from the wanted ions. Then the competition starts, which kind of ion can survive in the potential trap and which one will be evaporated out. It is therefore important that the cooler ions cannot be ionized to the same high charge state as the wanted ones. Only then the trapping potential is less for the cooler ions than for the wanted ones. In literature this is quite often confused by referring to the ion mass. This is not wrong, because the ion mass is also an indicator for the highest possible charge state, but it is hiding the underlying physical effect.

MAGNETIC EMITTANCE

Busch's theorem in electron (and ion) optics reflects the conservation of the angular momentum of a charged particle, when moving through solenoidal magnetic fields. This has noticeable effects for ions generated in high magnetic fields and extracted to almost vanishing fields. By the conservation of the angular momentum each ion will have a skew trajectory, increasing the 2D subsections of the transverse emittances. The following formulation of the "magnetic" (caused) emittance has been given [6], which can well dominate the emittances caused by thermal effects and by aberrations

$$\varepsilon = \frac{\pi}{4} \sqrt{\frac{2eq}{M}} \frac{B_z r^2}{\sqrt{U_0}} \quad [m] \quad (2)$$

Here B_z is the magnetic field at the birth place of the ion, q and M are the charge and mass, and U_0 is the extraction voltage of the ion. For ECRs and EBIS the magnetic fields are now in the region of a few T, even higher for EBITs. The extraction voltage is also quite the same – a few 10 kV. Therefore the main parameter influencing the magnetic emittance is r , the radius of the ion at B_z , which is typically 5×10^{-3} m for ECRs and $10^{-5} \div 10^{-4}$ m for EBIS. This is the reason, why ECRs have a much larger magnetic emittance than EBIS devices. In ECRs the magnetic emittance usually dominates, while in EBIS the emittance by transverse velocities and by aberrations is the dominating part. Ion-ion cooling has led to an interesting effect in ECRs which is similar to the effect observed in EBIS/T devices: highly charged ions concentrate near the axis and therefore have a reduced magnetic emittance to lower charged ones in contradiction to Eq. 2. This has been proved by emittance measurements done at ECRIS [7].

BEAM TRANSPORT AND INJECTION INTO THE HEAVY ION ACCELERATOR

The transport and charge state separation of extracted ions in particular for ECRIS devices is a matter of ongoing discussions, although some solutions have been found, which seem to be satisfactory [8,9,10]. One has to distinguish between high current sources for beam production at high performance driver linacs and sources used for charge state boosting of ions prior to their acceleration. In the latter case the purification especially of weak secondary beam or rare isotopes from residual gas contamination is an issue. In case of intense beams of highly charged ions for injector and driver linacs, the space charge of the extracted beams leads to a significant beam spreading.

Transport of Beams of Charge Bred Ions

Usually an achromatic mass and charge state separator is used downstream an EBIS/T to select the required charge state and isotope prior to the injection into the

subsequent accelerator [11]. The principle of such a Nier-type achromatic separator is shown in Fig. 4. Typical for this application, a mass resolving power of $R \sim 100$ for beams of emittances of as high as 0.6 mm-mrad normalized is adequate for most beams of interest. Emphasis is given to obtain achromatic mass separation since the electron impact processes in EBIT type breeders tend to create beams of non-negligible energy spreads [12]. Usually the intensity of charge bred exotic ions is several orders of magnitude lower than the intensity of the rest gas contaminants, even in the EBIS/T case. Hence the maximum overlap with a residual gas peak should not exceed 0.01% of the ion in the corresponding charge state. Therefore the achromatic system compensates the energy dependence of the magnets resolving power and is a velocity filter that purifies the spectrum from ions which did undergo charge exchange and have therefore the wrong kinetic energy.

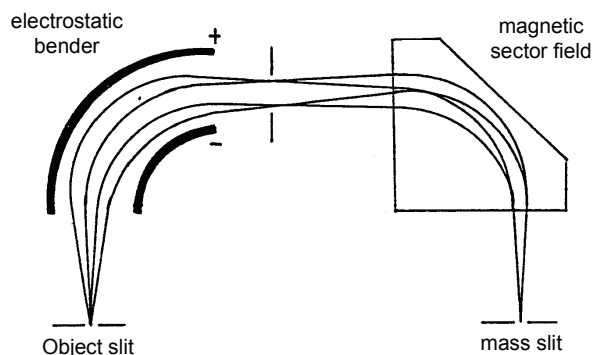


Figure 4: Principle of an achromatic Q/A-separator or a separated function velocity filter.

Even in case of an ECR charge state breeder, the extracted beam intensity is several mA and therefore the beams are space charge dominated, because a certain plasma density is required, which can only be delivered by the support gas. The intensity of typical secondary beams is much lower and does not contribute significantly to the space charge of the extracted ion beams. Here the usual approach is a triode extraction system to allow for space charge compensation, a short drift through a pumping station and a subsequent double focusing magnet for charge state and mass selection [13,14]. In case of ECRs used as charge state breeder, the intensities of the rare isotopes are even lower than the constant background of ions produced by charge exchange in the extraction region. The intensity of this background can be several nanoamperes [15]. Therefore the use of a combination as shown in Fig. 4 used as velocity filter reveals a significant cleaning of the spectrum from scattered and charge-exchanged ions as shown in ref. [16].

The time structure of the extracted beams is another important topic, which determines the duty cycle of the following post accelerator and is of relevance for the experiments served. EBIS/T devices allow for a huge

variation of the pulse length of several orders of magnitude, ranging from a few microseconds to several ten milliseconds by pushing the ions slowly over the collector barrier. However, while ions are extracted from an EBIS/T, ions cannot be injected into the device. Hence macro pulses cannot be avoided. ECRs allow continuous injection of singly charged ions and extraction of highly charged ions at the same time. In case of the ECRIT mode of operation, a pulsed extraction using the after glow mode is applied. The length of the extracted ion bunches is usually a few milliseconds.

The longitudinal matching of the highly charged ions to the subsequent accelerator can be done with a multi harmonic buncher [17] or a Radio Frequency Quadrupole (RFQ) accelerator with shaper and adiabatic buncher section [18]. Both schemes, sketched in Fig. 5, are used in present radioactive ion beam facilities and have certain benefits.

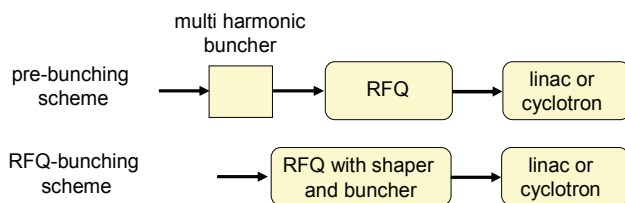


Figure 5: Schemes of micro bunching of the ion beams extracted from EBIS/T and ECRIS devices using an external buncher-RFQ combination or an RFQ with shaper and buncher section.

Pre-bunching of the ion beams with a multi harmonic buncher (up to three harmonics or a double drift buncher) reduces the longitudinal emittance significantly (up to a factor of five) compared to the bunching in an RFQ. The number of cells and therefore the length of the RFQ can be reduced as well, which is mandatory for linacs operating at lower frequency (<50 MHz) and large A/q acceptance (up to 50) like the ISAC RFQ at TRIUMF. The matching with a three harmonic buncher system has an efficiency of about 80%. Using just an RFQ without a separate pre-buncher instead allows for highest transmission close to 100%, as demonstrated with the REX-ISOLDE linac.

Transport of intense Beams of highly charged Ions

For the transport of intense beam of highly charged ions in the order of several milliamperes usually solenoid lenses are used for beam focusing. These magnetic lenses have the advantage of keeping space charge compensation of the beam and axial symmetry. However, these lenses couple the phase space in both lateral directions and the focusing strength depends on the charge state of the ion species.

The most common approach of a LEBT in case of ECRs is a solenoid lens in front of the separator magnet and one lens downstream the separator magnet. In case of the injection of ions from RHIC EBIS into the RFQ a

solenoid lens is used too [19], because pulses from RHIC EBIS can reach several mA of peak current. No separation is done, as in RHIC EBIS the background pressure is so low, that any contamination of the beam can be neglected and different charge states of the required ion species are singled out in the linac and prior to injection into the AGS booster.

REFERENCES

- [1] G. Bollen, et al., Nucl. Instr. and Meth. B 266 (2008) 4442.
- [2] C. Lyneis, D. Leitner, D.S. Todd, G. Sabbi, S. Prestemon, Rev. Sci. Instrum. 79 (2008) 02A321
- [3] S. Schwarz et al., Nucl. Instr. and Meth. B 266 (2008) 4466
- [4] J. Alessi et al., "High Performance EBIS for RHIC", Proceedings of the PAC07, Albuquerque, NM, USA, FRYAB02, p.3782
- [5] A.G. Drentje, Rev. Sci. Instrum. 63 (1992) 2875.
- [6] W. Krauss-Vogt et al., Nucl. Instrum. Meth. A268 (1988) 5.
- [7] M.A. Leitner, D.C. Wutte, C.M. Lyneis, Proc. PAC-2001, MOPB004 (2001) and D. Wutte et al., Physica scripta T92 (2001) 247.
- [8] D.S. Todd et al., Rev. Sci. Instrum. 77 (2006) 03A338.
- [9] P. Spädtke et al., Rev. Sci. Instrum. 79 (2008) 02B716
- [10] D. J. Warner et al., "CERN heavy-ion facility design report", (1993), CERN-93-01.
- [11] M. Portillo, "An Achromatic Mass Separator Design for Ions from the EBIT Charge Breeder at the NSCL", proceedings of the PAC09, Vancouver, Canada, FR5PFP015.
- [12] O. Kester et al., J. of Physics: Conf. Series 2 (2004) p.107.
- [13] M. Machicoane, "Performance Investigation of the NSCL 18 GHz Superconducting ECR Ion Source SUSI", Proc. of the PAC09, Vancouver, Canada, MO6RFP035.
- [14] P. Delahaye et al., Rev. Sci. Instrum. 77 (2006) 03B105
- [15] S. C. Jeong et al., Rev. Sci. Instrum. 75 (2004) 1631.
- [16] F. Ames et al., Rev. Sci. Instrum. 77 (2006) 03B103.
- [17] Q. Zhao et al., "Design and Test of the Triple-Harmonic Buncher for the NSCL Reaccelerator", Proc. of the LINAC08, Victoria, Canada, THP069 (2008).
- [18] M. Pasini et al., "Beam Dynamics Studies for the Low Energy Section at MAFF", Proc. EPAC2004, Lucerne, Switzerland, TUPLT034.
- [19] J. Alessi et al., "Design and Performance of the Matching Beam Line Between the BNL EBIS and an RFQ", proc. of the PAC07, Albuquerque, New Mexico, USA, p.1844, TUPAS083

ION SOURCES AT THE MICHIGAN ION BEAM LABORATORY: CAPABILITY AND PERFORMANCE

F. Naab and O. Toader, MIBL, University of Michigan, MI 48109, U.S.A.

Abstract

The Michigan Ion Beam Laboratory (MIBL) at the University of Michigan has instruments equipped with ion sources capable of generating a wide variety of ions. The 1.7 MV Tandem accelerator can operate with three different sources: a Torvis source, a Duoplasmatron source and a Sputter source. The 400 kV ion implanter is equipped with a CHORDIS source that can operate in three different modes (gas, sputter, and oven) and is capable of producing ion beams for most of the elements in the periodic table. In this work, we discuss the principle of operation of each source, their performances and the latest applications and projects conducted at MIBL using these sources.

INTRODUCTION

The Michigan Ion Beam Laboratory is located in Ann Arbor, Michigan, and is part of the Department of Nuclear Engineering and Radiological Sciences at the University of Michigan. The laboratory is equipped with two major instruments: the 1.7 MV tandem accelerator (General Ionex Corporation) and the 400 kV ion implanter (National Electrostatic Corporation).

The accelerator is a solid-state gas insulated high frequency device, capable of operation between 0.4 and 1.7 MV (see Fig. 1). It can operate with three different ion sources: the Torvis source (National Electrostatic Corporation), the 358 Duoplasmatron source (General Ionex Corporation) and the PS120 Sputter source (Peabody Scientific). The accelerator has two ion injection beamlines attached to the low-energy bending magnet, each one at 30° to the accelerator beamline direction. The Torvis source is installed in one of this injection beamlines and in the other one is installed either the Duoplasmatron or the Sputter source. After the bending magnet at the high energy end of the accelerator there are two beamlines: the 15° beamline for ion beam modification (ion implantation, ion mixing and radiation damage), and the 30° beamline for ion beam analysis.



Figure 1: Picture of the 1.7 MV tandem accelerator and the area where the ion sources are located.



Figure 2: 400 kV ion implanter.

The ion implanter is air-insulated (see Fig. 2) and is designed to produce high current and high brightness ion beams. The implanter's ion source is a CHORDIS source model 921 made by Danfysik. The source can provide beams for most of the elements in the periodic table. The design of the implanter allows for obtaining implantation energies between 10 and 400 kV.

In the next sections we describe in more detail each of the ion sources mentioned including their principle of operation, performance in producing different ion beams and applications to current research projects.

TORVIS SOURCE

TORVIS stands for TORoidal Volume Ion Source. Fig. 3 shows a schematic of the Torvis source. This source is used in MIBL to create negative ion beams using H₂ and D₂ gases.

Principle of Operation

The gas is leaked into the source volume and the molecules are ionized by electrons emitted from a tungsten filament to form a plasma of charged particles.

The body of the source is formed by the upstream and downstream flanges and a cylinder between these two flanges. Inside the flanges and cylinder there are concentric rings of magnets in which the poles of the magnets alternate by ring (see Fig. 3). This magnet assembly produces cusp fields that surround the entire plasma chamber. In addition, the source incorporates a conical magnetic filter field to separate the plasma into two distinct regions. In the outer toroidal region, the abundant fast electrons produce highly vibrationally excited molecules in the gas discharge. The conical magnetic dipole field separating the toroidal region from the axial region prevents fast electrons from entering the axial region, while allowing the excited hydrogen molecules to enter. This filtering prevents the fast electrons from destroying the negative atomic ions which are subsequently formed in the axial region by dissociative attachment of slow electrons. This complicated magnetic field is the critical feature of the source [1].

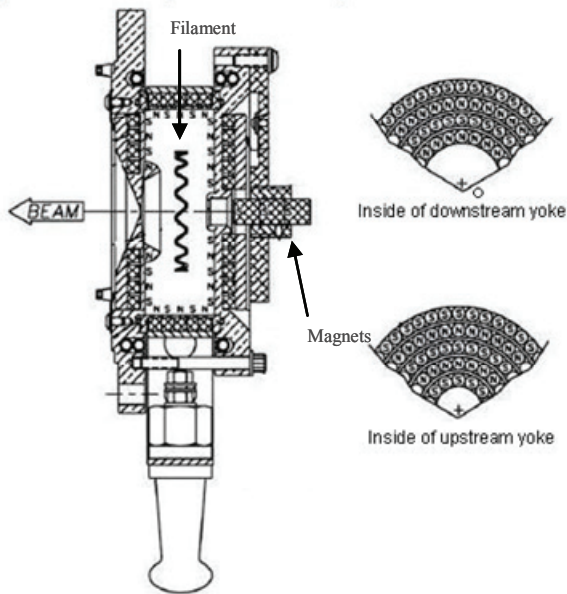


Figure 3: Torvis source schematic.

Maintenance

The most frequent service is the replacement of the tungsten filament after ~1000 hours of usage. When this task is done, the inside volume of the source is cleaned to remove a thin tungsten layer deposited on the walls due to sputtering of the filament by the plasma.

Performance and Applications

The Torvis source is used to produce H^- and D^- ion beams. Current of ~100 μA can be easily obtained for each ion on the target after a ~50% ion transmission through the accelerator.

MeV-proton (H^+) beams are used to study the effects of irradiation on materials, with emphasis on material issues related to the nuclear power industry: materials degradation and design for advanced reactor systems [2]. These experiments run at proton beam currents of ~65 μA on the sample. The beam is scanned continuously on the sample 24 hours a day (with no beam interruption) over an area of 24 mm \times 16 mm. The irradiation times range between 1 to 10 days. The damage rate accumulated on the sample surface is ~1 DPA (displacement per atom) per day.

MeV-deuterium ion (D^-) beams are used to do nuclear reaction analysis (NRA). Recent measurements were done using the $^{12}C(d,p)^{13}C$ and $^{14}N(d,\alpha)^{12}C$ nuclear reactions to obtain the depth profile distributions of C and N in different samples. Also, deuterium beams were used to do NRA-ion channelling to measure the substitutional fraction of N in GaAs samples [2].

DUOPLASMATRON SOURCE

This source, as the Torvis source, produces ion beams using gases. Both sources can be configured to extract either positive or negative ions. Negative ions coming out of the source can be injected directly into a tandem

accelerator without using a charge-exchange system. At MIBL, the Duoplasmatron source is configured to extract positive ions. In this case, the charge-exchange system uses sodium vapor to form negative ions. Fig. 4 shows a schematic diagram of the source.

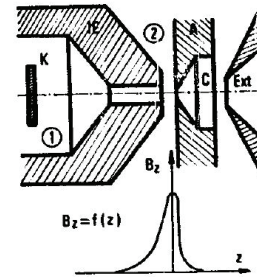


Figure 4: Schematic diagram of the Duoplasmatron source. (1) Cathode region. (2) Anode region. K: hot cathode. IE: intermediate electrode. A: anode. C: expansion cup. Ext: extractor. Below the schematic is the plot of the magnetic field intensity along the axial direction [3].

Principle of Operation

A gas is leaked into the source and the molecules are ionized by electrons emitted from the filament to create a discharge. The arc has a dual compression: geometrically and magnetically. The ions are axially extracted from the plasma of the low pressure arc between a hot cathode K and an anode A. In the case of positive ion extraction the emission aperture is bored in the anode on the discharge axis. In order to obtain an enhanced plasma density and a high ionization degree in front of the anode aperture, the discharge is strongly concentrated successively by the focusing action of the intermediate electrode IE and the effect of a strong axial magnetic field between IE and A. The dense arc plasma protrudes through the anode aperture. The form of the emissive surface of this "expansion ball" maybe shaped in order to improve the ion beam optical properties if the diffusion processes in an "expansion cup" placed just behind the anode are adequately controlled [3].

Maintenance

At MIBL the filament of the source is done with a platinum mesh (gauge 52, 0.1-mm diameter wire) with dimensions of 1" \times 4" rolled up as a scroll. The mesh is coated with high calcium triple carbonate (Ba-Sr-Ca CO_3). The most frequent service on this source is to recoat the filament after ~80 hours of operation. A less frequent task is to reload sodium in the charge-exchange system.

Performance and Applications

We use this source to produce helium ion beams to do ion beam analysis: Rutherford Backscattering Spectrometry (RBS), Elastic Recoil Detection Analysis (ERDA), and RBS-ion channelling [2]. Typical He^{++}

current on the target ranges from ~5 to ~50 nA depending upon the sample composition and the detector count rate. The helium ion transmission through the accelerator is ~15% for both +1 and +2 charge states.

SPUTTER SOURCE

Sputter sources are adequate for a wide variety of nuclear experiments but some exceptions do occur particularly with elements having small electron affinities. Sputter sources have found broad application in areas such as ion implantation, radiation damage studies and accelerator mass spectrometry. Fig. 5 shows the schematic of the Sputter source at MIBL which has a cylindrical ionizer.

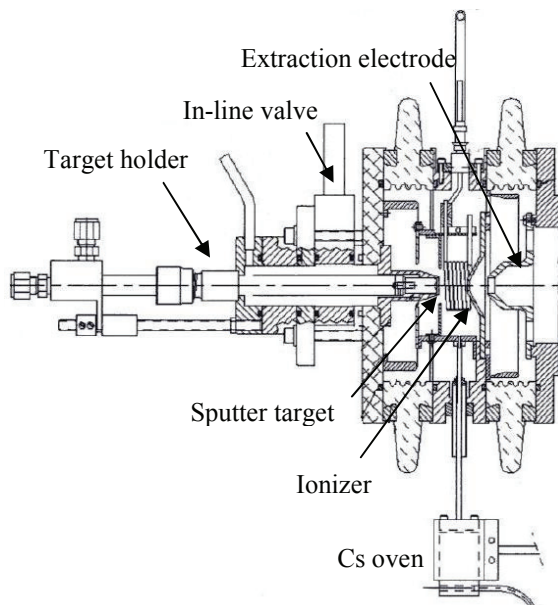


Figure 5: Sputter source schematic.

Principle of Operation

Cesium is heated in the Cs oven and the resulting vapor enters the source region which contains the ionizer assembly. The ionizer and chamber are at the same voltage while the sputter target is held in an insulated holder assembly at a voltage negative compared to the ionizer. Cesium ions are formed by surface ionization and are then attracted to the sputter target holder assembly. This beam of cesium sputters the target with a large fraction of the sputtered components being negative ions of the target material [4]. These negative ions are extracted up to 40 keV. The ionizer and source chamber can be biased up to 30 kV and the sputter target up to 10 kV. To change the sputter target, the target holder is retracted through the rear plate and the in-line valve is closed to preserve vacuum in the source.

Maintenance

The main maintenance task done on this source is to reload the cesium oven and change the sputter target.

Ion Sources

Performance and Applications

The PS120 sputter source has been recently acquired by MIBL. Our experience with it is still limited. So far we have produced Si and Fe beams. The Si beam was produced to test the source after its installation. We obtained ~110 μA after the 30° bending magnet located 2 m from the source. The only optical element between the source and the magnet was a 5"-diameter gridded lens located 1.4 m from the source and 0.5 m from the magnet. We are particularly interested in producing iron beams to study the effects of irradiation on materials as in the case of proton beams produced with the Torvis source. The Fe beam has the advantage of a much higher damage rate on the sample surface than the proton beam. A 5 MeV Fe^{++} beam at a current of ~1 μA scanned over the same area than the proton beam will accumulate a damage dose of ~100 DPA per day. We have produced Fe beams using two different cathode target materials: Fe_3O_4 and pure metallic Fe. In the first case we obtained in the Faraday cup after the 30° bending magnet a maximum ($^{56}\text{Fe}^{16}\text{O}^-$)-molecular-ion beam current of ~22 μA , and in the second case ~10 μA of Fe^- ions.

By installing an Einzel lens immediately after the sputter source the beam currents after the 30° bending magnet have increased by a factor of ~2 for the same source parameters. Also, the installation of the Einzel lens improved the transmission of the Fe beam through the tandem accelerator by a factor of ~2.

In the latest test we obtained a current of ~1.5 μA of 2.7 MeV Fe^{++} ions after the analyzing magnet in the high energy end of the accelerator.

CHORDIS SOURCE

CHORDIS stands for Cold or Hot Reflex Discharge Ion Source. The Model 921A ion source is designed for the production of high current and high brightness ion beams for applications in particle accelerator injection, ion implantation, isotope separation, ion beam mixing, sputtering, fusion plasma diagnostics, etc.

Principle of Operation

A schematic of the CHORDIS source is shown in Fig. 6. The primary ionizing electrons are emitted from tungsten-filament cathodes. The source chamber walls form the anode for the discharge. The plasma is confined radially by an array of permanent magnets that form a multicusp field and axially by two biased reflector electrodes. The front reflector forms the first electrode of the extraction system. Particles are fed through the rear electrode in the form of gases to produce different ion beam [5,6].

Alternatively, ion beams can be produced by mounting a metal disk inside the discharge chamber in front of the outlet hole. The disk may be biased to a negative potential with respect to the cathode. With an argon gas discharge in the source, sputtered atoms from the disk will be ionized and mixed with the discharged plasma, causing the extracted beam to contain a large fraction of them.

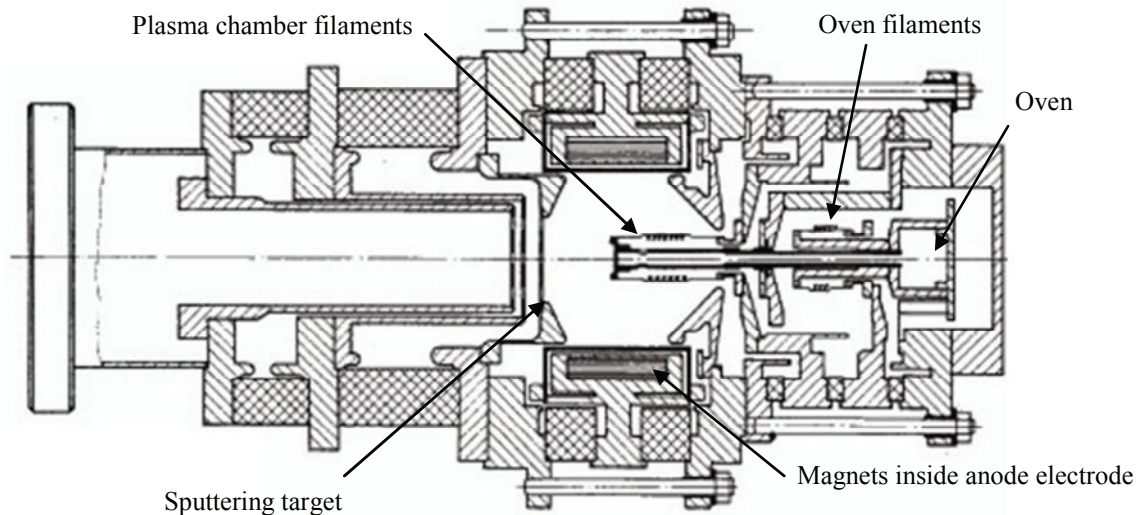


Figure 6: Schematic of the CHORDIS source.

The sputter version is particularly well suited for producing ions of medium and high melting point materials. Elemental materials as well as alloys and sintered mixtures may be used for the sputter disks.

The CHORDIS source in MIBL is also equipped with an internal oven which makes it ideal for production of pure ion beams from elements with low melting point and at least 2 Torr vapour pressure at 1000 °C. The oven temperature is regulated independently of the other operating parameters, and condensation of charge materials is avoided by making all other internal source parts hotter than the oven itself. The charge can be introduced from the rear end, with the source mounted in operating position. Auxiliary gas (e.g. argon) may be used to stabilize the discharge. The oven version is suitable for materials like the alkalines and earth-alkalines, aluminium, indium, thallium, tin, lead, antimony, and bismuth.

Maintenance

The most frequent maintenance task is the replacement of the filaments in the plasma chamber. The lifetime of the filaments depends upon the intensity of the plasma and beam currents needed. On average in MIBL we replace the filaments every ~100 hours.

Every time a new ion beam is required the source has to be opened to either change the gas bottle, the sputtering target, or the material in the oven to be evaporated into the plasma chamber.

Performance and Applications

The 400 keV implanter was installed in MIBL two years ago. Since then we have produced 19 different ion-type beams to do ion implantation for a wide variety of

research projects in material science and medical applications [2]. The implanted species using gases are: H, He, and N; using a sputtering target: B, Si, Cr, Fe, Co, Cu, Pd, Ag, In, Ce, Er, Yb, Ta, and Au; and using the oven: Sn and Bi. Other ion beams have been produced: Be⁺, C⁺, O⁺, O⁺⁺, Ne⁺, Ar⁺, Ar⁺⁺, Ni⁺, Sm⁺, and W⁺.

SUMMARY

The Michigan Ion Beam Laboratory was established for the purpose of advancing the understanding of ion-solid interactions by providing unique and extensive facilities to support both research and development in the field. Every year the laboratory activities involve about thirty research projects including research groups in the University of Michigan, other universities in USA and around the world, and private companies. All of these activities are related with the use of ion sources. These facts show how important it is to understand the basic principles of operation of ion sources and achieve a good performance for each of them.

REFERENCES

- [1] M.L. Sundquist, J.R. Adney, R.C. Schmidt, Nucl. Instr. and Meth. 99 (1995) 684.
- [2] <http://www-ners.engin.umich.edu/research/Mibl/Research.html>
- [3] C. Lejeune, Nucl. Instr. and Meth. 116 (1974) 417.
- [4] R. Middleton, Nucl. Instr. and Meth. 215 (1983) 139.
- [5] R. Keller, F. Nöhmayer, P. Spädtke, M-H. Schönenberg, Vacuum 34 (1984) 31.
- [6] R. Keller, P. Spädtke, H. Emig, Vacuum 36 (1986) 833.

COMMISSIONING OF THE ATLAS UPGRADE CRYOMODULE*

P. N. Ostroumov[#], J.D. Fuerst, S. Gerbick, M. Kedzie, M. P. Kelly, S.W.T. MacDonald, R.C. Pardo, S.I. Sharamentov, K. Shepard, G. Zinkann, Physics Division, ANL, Argonne, IL 60439, U.S.A.

Abstract

The ongoing energy upgrade of the heavy-ion linac ATLAS at ANL includes a new cryomodule containing seven 109 MHz $\beta=0.15$ quarter-wave superconducting cavities [1] to provide an additional 15 MV voltage. Several new features have been incorporated into both the cavity and cryomodule design. For example, the cryomodule separates the cavity vacuum space from the insulating vacuum [2-4], a first for TEM cavities. The cavities are designed in order to cancel the beam steering effect due to the RF field [5]. Clean techniques have been applied to achieve low-particulate rf surfaces and are essential for reliable long-term high-gradient operation. The sealed clean subassembly, consisting of cavities, beam spools, beam valves, couplers, vacuum manifold, and support frame, has been attached to the top plate of the cryomodule outside the clean room. Initial commissioning results are presented. The module was designed and built as a prototype for the Facility for Rare Isotope Beams (FRIB) driver linac, however, a similar design can be effectively used in the front-end of SC proton linacs based on TEM-class SC cavities.

INTRODUCTION

Like the Positive Ion Injector at Argonne's ATLAS heavy ion linac, a rectangular cryomodule design has been developed [2-4] that is simple to assemble and maintain. This latest design is also consistent with the requirements for high performance superconducting rf surfaces. Features include separation of the cavity and the cryogenic vacuum systems, and top-loading of the cavity-string subassembly which enables assembly and hermetic sealing of the cavity string in the clean room. The cryomodule assembly includes three stages: (1) clean-room subassembly of the cavity-string, (2) installation of cryogenics, RF and mechanical systems outside of the clean room, (3) installation of the final assembly into the cryostat to form a completed module. The design of the cryomodule and cavities reflects the current state-of-the-art in SRF technology and incorporates several new features with respect to other recently commissioned SC ion linacs [6, 7]. As a result, substantially higher accelerating fields and cavity voltages are possible as compared to other TEM cavity linacs around the world.

The off-line cryogenic and RF commissioning of the cryomodule has been completed and the cryomodule is installed in the ATLAS tunnel. Subsystem testing is being performed in order to start beam commissioning within several weeks.

*This work was supported by the U.S. Department of Energy, Office of Nuclear Physics, under Contract No. DE-AC02-06CH11357.

[#]ostroumov@anl.gov

CRYOMODULE DESIGN

The ATLAS energy upgrade cryomodule (Table 1) consist of 7 $\beta_G=0.15$ QWRs operating at 109.125 MHz and one 9 T SC solenoid. There is presently one empty slot that will accommodate an additional resonator. Primary design and fabrication technology of the cryomodules, cavities and sub-systems have been reported in several papers [8-10].

Table 1: Main Parameters of the Cryomodule

Parameter	Value	Units
Cryomodule dimensions	1.0×2.0×4.62	m
Average acc. gradient	8.4	MV/m
Cavity eff. length	25	cm
Total heat load (4.5K)	<100	W

RF Couplers

Six cavities are equipped with adjustable inductive couplers as reported in ref. [9, 10]. We have also developed an adjustable capacitive coupler which is installed on one of the cavities. This coupler was a simple modification of the other “loop” antennas. In this application as a bottom mounted coupler on QWR cavities, the cold tests show that the capacitive coupler is less susceptible to the RF heating in overcoupled operation than the loop coupler. The cavities will be operated with $Q_{EXT}=2 \cdot 10^8$ at average accelerating gradient of roughly 8.4 MV/m determined largely by the maximum VCX switching power.

Slow and Fast Tuners

Large frequency excursions are corrected using a pneumatically actuated mechanical slow tuner which compresses the cavity along the beam axis. The VCX fast tuner is similar to those that is used on existing ATLAS cavities, and was modified slightly to support independent cavity and cryogenic vacuum spaces and to facilitate clean assembly.

CRYOMODULE ASSEMBLY

A primary design goal was to minimize the number and complexity of the parts requiring clean assembly. This is achieved by limiting class-100 clean-room assembly to a minimum number of components. These include a pumping manifold to evacuate the cavity rf volume and the seven dressed cavities, each with coupler, VCX fast tuner and rf pickup installed. The cavity string is supported on an anodized aluminum strong-back. A pair of beam-line gate valves (one is visible in Fig. 1) and a large right-angle valve are installed on the pumping

manifold to seal the cavity vacuum system before it is removed from the clean room. Following the DESY developments, we have implemented low particulate pump down and venting scheme [11] for the cavity string. Final course tuning adjustments were made by “one-shot” squeezing the cavities along the beam axis, and preliminary alignment of cavities was performed in the clean room prior moving the cavity string (Fig. 1) out of the clean area for further assembly.



Figure 1: The cavity string assembly in the clean area is complete, including complete, sealed cavity vacuum system.

The cavity string is suspended from the box cryostat lid outside the clean room. Installation of liquid nitrogen and helium systems, complete assembly of couplers, local thermal shielding, RF pick-up cables, solenoid current leads, thermometry, etc have been performed outside the clean room. After leak checking of LHe and LN systems, the assembly (Fig. 2) was loaded into the cryostat vacuum-box and sealed. Final leak checks of the insulating vacuum, LN and LHe systems were performed after cool down to LN and LHe temperatures respectively. The cryomodule was cooled down to 77K and warmed up twice due to a cold leak in the LN system, found to be in a commercial flexible metal hose in the cryostat thermal shield circuit.



Figure 2: Cavity string suspended from the lid, with all cryogenic plumbing assembled and leak-checked, ready to drop into the box vacuum vessel.

Linacs



Figure 3: The main RF rack containing 109 MHz amplifiers and control modules.

RF SYSTEM

The RF system of each resonator includes a 250 W water-cooled solid-state power amplifier, an I&Q type LLRF controller, slow and fast tuner controllers and a stepping motor controller for the variable coupler. The I&Q controller includes amplitude, frequency and phase feedback loops. The amplitude feedback loop regulates RF field amplitude by changing the input drive power of the power amplifier. The frequency feedback loop provides stabilization of the resonator central frequency via a slow tuner control system. The phase stabilization loop controls the phase of the RF field in the resonator by means of VCX. The main RF rack (Fig. 3) includes eight RF power amplifiers with three GEN30-50 (30V, 50A) power supplies, 6U euro crate with eight LLRF controllers, 3U euro crate with eight slow tuner controllers, frequency counter and RF patch panel. The VCX PIN-diode pulsers are located in a separate rack in the accelerator tunnel. The RF control module provides phase scan and RF field amplitude adjustments from the control room. All electronic modules have been developed in the Physics Division and built at ANL.

OFF-LINE COMMISSIONING

We have installed 38 diodes to monitor temperatures in various locations during the cool down. The LHe cool down of the cavities is performed sequentially by manually opening valves in each LHe line of the cavity to provide fast transition through the “Q-disease” temperature range. Fig. 4 shows cool down of the 7 cavities and solenoid as a function of time.

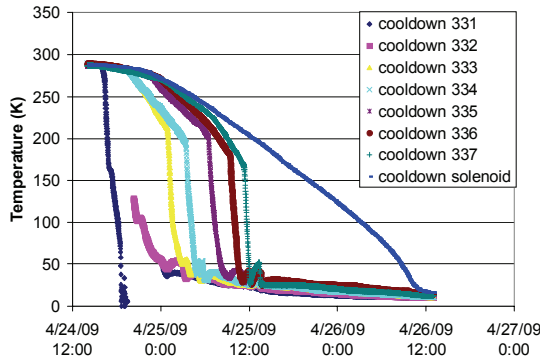


Figure 4: Temperature of the cavities and solenoid as a function of time.

As soon as temperature stabilized near 4.5K, resonant frequencies of all 7 cavities were measured. The operational frequency is 109.125 MHz with the slow tuner at its middle position or 109.135 MHz before activation of the slow tuner. As discussed in ref. [12] all cavities have very similar frequencies and warm-to-cold frequency shift. Slow tuners were cold tested in the pressure range from 0 to 24 psi. The tuning range is 36 kHz for the six production cavities and 55 kHz for the prototype cavity due to the geometry difference. Fast tuners have been tested by manually switching bias voltage on the pin-diodes. The fast tuner frequency window is 35-45 Hz depending from the cavity number [12]. Microphonics measurements have been made and one sigma rms frequency shifts are ~1 Hz for all cavities.

Cold Test of Cavities

The fast tuning of the cavity is provided by a VCX. The latter consumes considerable RF power (about 60 W at 8.4 MV/m accelerating gradient) that dissipates into the LN system. Therefore, the Q of the cavity system in normal operation mode is much lower than with a bare cavity without VCX as shown in the Q-curves in Fig. 5 for the prototype cavity.

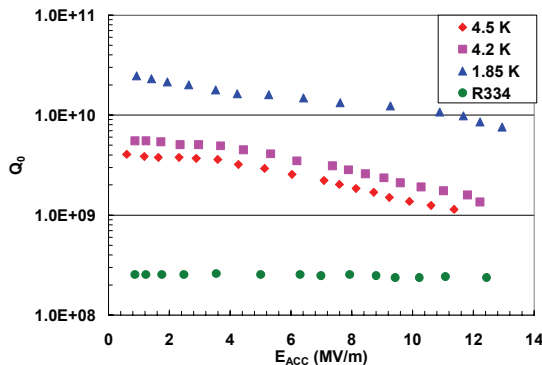


Figure 5: Q-curves measured for the prototype cavity before the installation of the VCX at 4.2K, 4.5K and 1.85K. The green dots show recent measurements with the VCX diodes are on.

The latter has been tested several times in the test cryostat [1] before the installation of the VCX. Measured

maximum accelerating gradients for all cavities are shown in Fig. 6. Due to the project schedule constraints we had a limited time for the RF conditioning of the cavities (3-4 hours per cavity). Despite of this, all cavities tested in the cryomodule have shown as good or better performance than in the test cryostat. This fact can be explained by the superior handling techniques and low-particulate pumping system available for the full cavity string assembly. The RF conditioning results of fully-dressed cavities are discussed in detail in ref. [12]. The operational accelerating gradients will be limited by the VCX to an average of 9.38 MV/m.

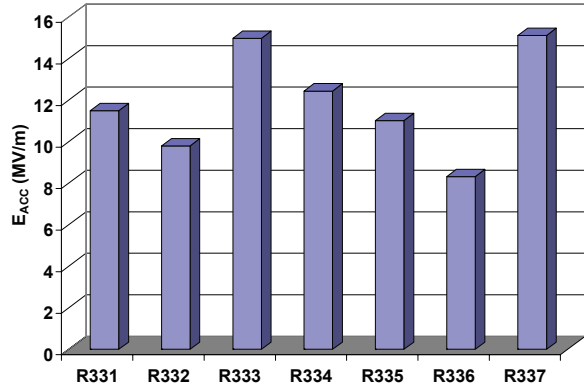


Figure 6: Measured maximum accelerating gradients ($L_{EFF} = 0.25$ cm).

Static Cryogenics Losses

The static heat leak of the box cryomodule has been measured by the boil-off rate of gaseous helium. The static load is (17 ± 2) W. In addition, the liquid nitrogen static load is 100 W.

ALIGNMENT

The cryomodule box, lid and strongback have been fiducialized to establish fit and repeatability of the cryomodule assembly and to facilitate final alignment of the cryomodule in the beamline. The resonators and solenoid have been preliminarily aligned in the clean room with respect to the strongback. The small welded blocks located at the top and bottom of the resonators serve as fiducial reference points. Fixtures have been built and installed to transfer the cavity aperture center to the resonator fiducial points. More accurate alignment of the cavities and solenoid have been performed outside the clean room using optical tooling instruments. At this stage, the ± 100 μ m accuracy of beam port alignment in both lateral and vertical directions with respect to the strongback has been achieved. However, measurements taken after the resonator flange connections and loading cavity string into the cryostat, indicate the final positions of the beam ports were closer to ± 0.5 mm. The aperture diameter of the cavities is 30 mm and it is larger by 5 mm than the aperture of any accelerating and focusing devices in the existing ATLAS. Therefore, we have decided to

accept present ± 0.5 mm alignment results and proceed with the installation of the cryomodule in the tunnel.

To monitor movement of the cavities and solenoids during the cooldown and pumping out, we have installed 6 cross-hair targets attached to the solenoids and cavities. Targets are visible through optical viewports on the ends of the cryomodule. Up cooldown shift of (1.58 ± 0.25) mm in vertical position of the targets was measured and is very close to the calculated value of 1.5 mm.

Final alignment of the entire cryomodule will be performed in the tunnel. We plan to verify the alignment procedures by turning on each resonator sequentially and measuring beam center.

BEAM DYNAMICS

The new 7-cavity cryomodule contains only one 9 T SC solenoid. However, beam optics calculations show that an additional SC solenoid is required between the existing F-cryostat of ATLAS and new cryomodule for the focusing of ion beams with lowest $q/A \approx 1/7$. Therefore we have decided to develop and build a new cryostat to house 9 T SC solenoid which was available as an ATLAS spare. Fig. 7 shows assembled cryostat with the SC solenoid inside.



Figure 7: New solenoid in an individual cryostat.

The new cryomodule will routinely provide 14.8 MV accelerating voltage which is calculated assuming 90% of the demonstrated maximum accelerating voltage with VCXs in operation. Energies of all ion beams available at the ATLAS facility will be increased as is shown in Table 2. The simulation of the energy gain of each ion beam has been performed with the code TRACK taking into account available voltages from the existing cavities and new cryomodule.

Table 2: Ion Beam Energies in the upgraded ATLAS

Ion	Q1*	W (MeV/u)	Q1/Q2*	W (MeV/u)
^{12}C	4	19.3	4/6	23.9
^{16}O	6	20.9	6/8	24.3
^{28}Si	9	18.8	7/14	23.1
^{50}Ti	13	16.2	12/21	20.8
^{64}Ni	14	14.3	14/25	19.7
^{84}Kr	15	12.2	15/31	18.5
^{92}Mo	21	14.7	21/34	19.2
^{127}Xe	25	13.2	25/40	17.1
^{178}Hf	31	12.0	31/50	15.7
^{208}Pb	36	11.9	36/55	15.1
^{238}U	34	10.0		

*Q1 is the charge state selected after the ECR, Q2 is the charge state after the stripping downstream of the Booster.

INSTALLATION

After high-power RF testing of all cavities, the box cryomodule was moved into the ATLAS tunnel. The new SC 9 T solenoid in the individual cryostat will be installed upstream of the cryomodule. A cold trap with the total length of ~ 60 cm was built and will be installed downstream of the cryomodule. Both the cold trap and solenoid cryostat will help to isolate the cavity space in the upgrade cryomodule from the rest of ATLAS vacuum space which is not maintained as a clean, oil free and low particle environment. A photograph of the cryomodule installed and roughly aligned to the ATLAS beamline is shown in Fig. 8.



Figure 8: Photo of the cryomodule in the tunnel.

CONCLUSION

A new state-of-the-art cryomodule for TEM-class SC cavities has been successfully assembled and commissioned. The initial performance of SC cavities exceeds the design goal of $E_{ACC}=8.4$ MV/m. The cryomodule was installed into the ATLAS tunnel and beam commissioning will be started in several weeks.

REFERENCES

- [1] M.P. Kelly, et al., Proc. of the LINAC-04, Lubeck, Germany, p. 605.
- [2] J.D. Fuerst, and K.W. Shepard, Proc. of the 19th Inter. Cryogenic Engineering Conf. (ICEC19), Grenoble, France, 22-26 July 2002.
- [3] K.W. Shepard, et al., Proc. of the PAC-03, Portland, Oregon, 2003, p. 1297.
- [4] J.D. Fuerst, et al., Proc. of the SRF-03, Travemunde, Germany, 8-12, September 2003.
- [5] P. N. Ostroumov and K. W. Shepard, Phys. Rev. ST Accel. Beams 4, 110101 (2001).
- [6] B. Laxdal, Proc. of the PAC-07, Albuquerque, NM, p. 2593.
- [7] A. Nagler, Proc. Of the LINAC-08, paper MO203.
- [8] J.D. Fuerst, et al. Proc. of the SRF 2005, Ithaca NY, 10-15 July 2005.
- [9] J.D. Fuerst, et al., TUP75, SRF-2007, Beijing, 2007.
- [10] M.P. Kelly, et al., Paper THP025, Proc. of the LINAC08, p. 823.
- [11] K. Zapfe, Proc. Of the SRF-2007, paper WEP74.
- [12] G. Zinkann, et al., Paper TH3, These Proceedings.

FREQUENCY TUNING AND RF SYSTEMS FOR THE ATLAS ENERGY UPGRADE SC CAVITIES*

G. P. Zinkann[#], J. D. Fuerst, S.M. Gerbick, M.P. Kelly, M. Kedzie, S. Macdonald, P.N. Ostroumov, R.C. Pardo, S. Sharamentov, Argonne National Laboratory
 K.W. Shepard, Techsource, Inc.
 Z. Conway, Presently at Cornell University

Abstract

A new cryomodule with seven low-beta superconducting radio frequency (SRF) quarter wave niobium cavities has been designed and constructed as an energy upgrade project for the ATLAS accelerator at Argonne National Laboratory [1]. The technology developed for this project is the basis for the next generation superconducting heavy ion accelerators. This paper will discuss the methods employed to tune the cavities eigenfrequency to match the accelerator master oscillator frequency and the development of the RF systems used to both drive the cavity and keep the cavity phase locked during operation.

INTRODUCTION

The ATLAS Energy Upgrade Project includes a new cryomodule containing seven 109 MHz, $\beta=0.15c$ quarter-wave superconducting cavities to provide an additional 15 MV voltage to the existing superconducting linac. The cavities are constructed so that there are no demountable joints. Due to the fact that all of the manufactured sections of the cavity are electron beam welded into the final cavity configuration, the dimensions of the parts prior to welding must be properly sized in order to achieve the final eigenfrequency demanded by the accelerator’s Master Oscillator system. Also, in order to phase lock to the accelerator’s Master Oscillator, two other systems are employed; a slow tuner system [2] is used to compensate for frequency shifts due to pressure changes, and a fast tuner system [3] is used to compensate for frequency shifts due to microphonics.

CAVITY TUNING DURING CONSTRUCTION

The individual cavity parts are formed and then electron beam (e-beam) welded into four sections. These four sections are illustrated in Fig. 1. They are the housing, the toroid, the center conductor and the dome. All four sections are manufactured with their length longer than needed. They will all be trimmed to length in increments so that in the end, the proper frequency will be achieved. The first step is to trim the dome and the toroid once, using Electrical Discharge Machining (EDM). This trim cut is to establish a square edge that will facilitate alignment to the housing and center conductor.

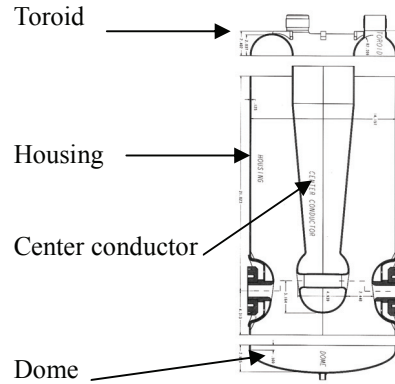


Figure 1: Four main cavity sections.

Several parameters must be known to determine what length the housing and center conductor will be trimmed to. For example, when the individual pieces are e-beam welded together, shrinkage of the niobium occurs that results in a frequency shift. This frequency shift must be accounted for in the sizing of the cavity parts. In addition, when the parts are electro-polished [4] the removal of the niobium results in a frequency shift which also must be accounted for. Table 1 lists the desired frequency at 4.5K and other parameters that must be known to achieve the final sizing results.

The four sections are assembled in a fixture which keeps them aligned and clamped together. indium wire is compressed between each clamped joint of this assembly.

Table 1: Development Parameters

Master Oscillator Frequency (for $B = .15c$)	109125.0	kHz
Slow Tuner Half-range	+20	kHz
1-shot hydraulic tuning	+/-20	kHz
Δ Freq / Δ Electro-Polish (uniform)	282.2	kHz/mm
Δ Freq / Δ EP(Dome & Toroid)	1078.9	kHz/mm
Δ Freq / Δ Pressure (Helium Jacket)	-9	kHz/atm
Δ Freq / Δ AIR (20C, 740 Torr, 40% Humid)	-34	kHz
Δ Freq / Δ T(293K - 4K)	-156	kHz
Δ Freq / Δ Indium wire .010" thick	-26	kHz
Δ Freq / Δ Length (center conductor)	-132	kHz/mm
Δ Freq / Δ Length (distance to dome)	30	kHz/mm

*This work was supported by the U.S. Department of Energy, Office of Nuclear Physics, under Contract No. DE-AC02-06CH11357.
[#]zinkann@anl.gov

The indium is necessary to reduce the joint losses at RF frequencies. Fig. 2 shows the individual sections clamped together in the “birdcage” for a frequency measurement.



Figure 2: Parts clamped in *birdcage* for a frequency measurement.

Once the initial frequency is measured a calculation is made to determine how much to shorten the center conductor and the housing. The center conductor and the housing are assembled with a second jig that aligns the beam hole in each piece and centers the top of the center conductor in the housing. The assembly is then put on an EDM machine and one cut is made to both pieces simultaneously. Fig. 3 shows the results of several trim cuts.



Figure 3: Trim cuts by EDM.

The process of clamping together all of the sections in the *birdcage* is repeated and then another trim cut is made to the center conductor and housing. This process is repeated until the desired, room temperature-clamped together frequency is achieved. Then the parts are electropolished and e-beam welded together to form a single assembled unit. Table 2 follows the frequency progression, working backwards from the cold frequency,

to achieve the desired room temperature-clamped together frequency.

Table 2: Frequency Progression

Master Oscillator Frequency (for B =.15c)	109125.0	kHz
Final cold frequency (4.3K) +20 kHz for 1/2 Slow Tuner Range	109145	kHz
At room temperature under vacuum	108989	kHz
Vented to air	108966	kHz
Before EP (125 microns base, 187 DT&Nose)	108728	kHz
Before welding (.58 mm shrink/weld)	108669	kHz
Clamp-up state (including .010 thick crushed indium wire)	108643	kHz

This tuning method was applied to all seven cavities. The results are listed below in Table 3.

Table 3: Final tuning Results for all seven Cavities

	293K	4.5K
*1	109016.0	109165.9
2	108953.1	109137.0
3	108952.0	109137.7
4	108952.5	109142.9
5	108954.6	109137.2
6	108952.0	109136.3
7	108955.1	109140.8

*Note: cavity number 1 below, is a different design from the other six. Its slow tuner range is double that of the others so its resulting frequency is higher in order to bring it into the middle of the slow tuner.

Fig. 4 shows the slow tuner range for a cavity at 4.5 K. The red line indicates the frequency of the accelerator’s Master Oscillator.

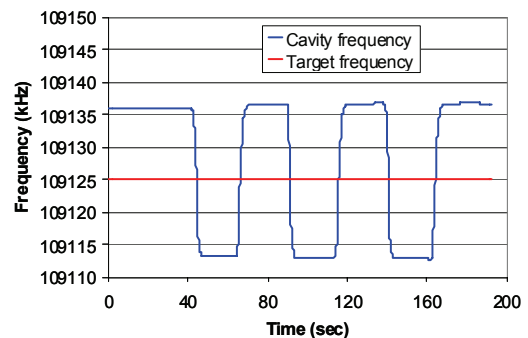


Figure 4: Typical slow tuner range measured at 4.5K.

RF POWER COUPLERS

Two types of RF power couplers were designed and tested on the quarter wave cavities. One coupler is an inductive coupler and the other is a capacitive coupler. Both coupler designs have a variable coupling strength with a stroke of about three inches. Fig. 5 shows a picture of each coupler.

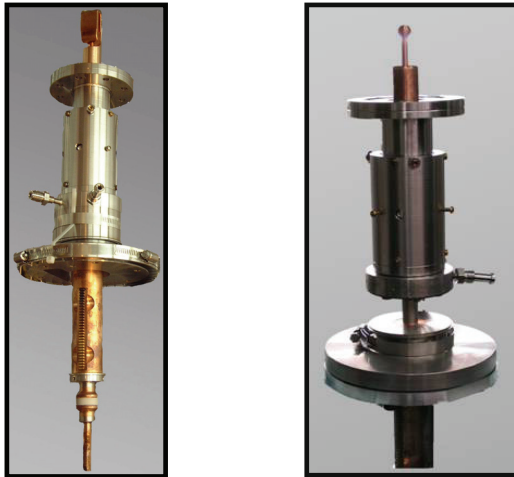


Figure 5: Inductive coupler on the left and a capacitive coupler on the right.

The coupler design for both types of couplers are very similar, the main difference being the probe tip. Fig. 6 is a cut-away diagram of the capacitive coupler and its features.

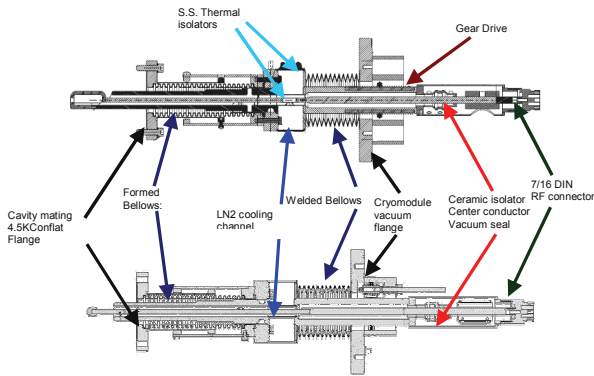


Figure 6: Design features.

Two tests were done on each probe. The two test conditions were the following. Test 1: the RF probe was fully inserted into the cavity resulting in an over coupled condition. Then approximately 600 Watts of RF power was applied to the coupler. Test 2: it was performed with each RF coupler in the critically coupled position. Then the field level of the cavity was set to approximately 9 MV/m. It must be noted that the coupling port on the

cavity is located in an electric field region. To measure the power dissipation into the helium system for each coupler, a thermometer and a resistive heater were placed on the 4.5 K mating flange of the coupler and cavity. Thermometers were also placed on the 77 K intercept point and room temperature sections of the couplers. The test results show for the 600 W over coupled condition, that for both couplers the heating at the 77 K and 290 K sections were negligible. Measurements on the 4.5 K mating flange for each coupler was significantly different. Fig. 7 illustrates the heating results for all conditions. As expected the power into the helium system for the inductive probe was high. For the capacitive coupler in the critically coupled position the power into the helium system was in the 100's of milliwatts.

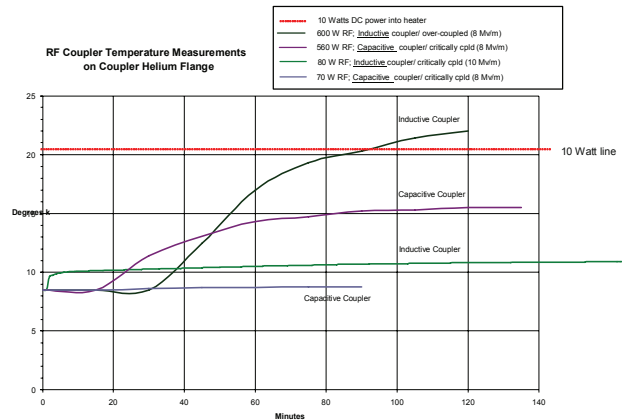


Figure 7: RF Coupler heating at the 4.5K flange.

CRYOMODULE 4.5K TESTS

Seven cavities were assembled in a clean room following clean assembly techniques. The cavity assembly was then mounted in the box cryomodule. The cavities were cooled down to 4.5K and the cavity subsystems were tested. Six of the seven cavities were brought up to high field levels, the seventh cavity was tested at low power only. Measurements were take on the slow tuner ranges, the fast tuner windows, cavity frequencies, microphonics, and peak accelerating fields. All subsystems functioned as designed and were within the specified performance parameters.

The frequency deviation due to microphonics is defined by a gaussian distribution. The measured sigma value for the frequency deviation on the cavities was measured at 1.05 Hz RMS. In order to phase lock a SC cavity a control window of at least 80 is required. The fast tuner windows measured 35 to 45 Hz. This is well over the 80 that is needed. Fig. 8 shows a plot of the the frequency deviation of a typical cavity and a plot of the fast tuner range as measured in a cavity.

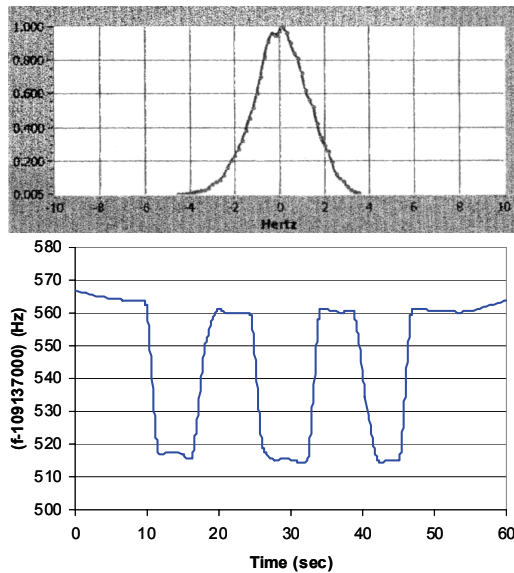


Figure 8: Top, measured frequency deviation from microphonics. Bottom, measured fast tuner window.

The field levels achieved are shown in Fig. 9 along with the field levels for each cavity as tested after production in an off-line test cryostat. Each cavity was High Pressure Rinsed (HPR) [5] after the initial off-line test, just prior to the cryomodule assembly. The HPR and more stringent clean assembly techniques accounts for the improvement of some of the cavities in the cryomodule tests displayed in Fig. 9.

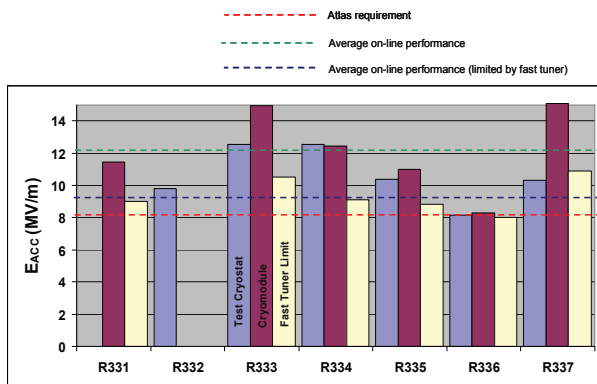


Figure 9: Field level results.

CONCLUSIONS

The parameters that were developed and used to calculate the cavity sizing were successful. All of the 4.5 K cavities frequencies were correct.

The RF power couplers performed well, their coupling strengths were within the design specifications. The power dissipation tests demonstrated that the capacitive coupler is the preferable design for use on this type of cavity, though the inductive coupler will also work.

The microphonics as measured with the cryomodule operating on the helium refrigerator system is low. The fast tuner window is more than adequate to phase lock the cavities.

Finally, the field level performance is above the 8 MV/m operational requirement. The average field level of the six cavities is 12.1 MV/m, but when the fast tuner is employed the average field level is lowered to 9.2 MV/m. This limitation of the fast tuner is a subject for future development. We are planning to develop a new system to replace the reactive power fast tuner that is presently in use.

REFERENCES

- [1] M. Kelly, et al., Proc. of the LINAC-04, Lubeck, Germany, p. 605.
- [2] G P. Zinkann, S. Sharamentov, Proc of the PAC 2005, Knoxville, Tennessee, USA.
- [3] N. Added, et al, Proc of the 16th International Linear Accelerator Conference, 1992, Ottawa, Ontario.
- [4] Gerbick, S.M. et al, "A New Electropolishing System at ANL for Superconducting Quarter-Wave Resonators," SRF 2007, Beijing, China.
- [5] M. Kelly, et al., Proc. of the SRF 2001, Tsukuba, Japan, PT017.

PERFORMANCES OF THE ISAC HEAVY ION LINACS

M. Marchetto, TRIUMF, Vancouver, BC V6T2A3, Canada

Abstract

ISAC is the TRIUMF facility for the production and post acceleration of Rare Isotope Beams (RIBs). The post acceleration section includes two normal conducting linacs, an RFQ injector and a variable energy IH-DTL, and a superconducting linac composed of five cryomodules each containing four quarter wave bulk niobium resonators. All three machines operate CW. The RFQ and DTL deliver beam since 2000 to a medium energy area with energies variable between 150 keV/u and 1.8 MeV/u. The superconducting linac, with an effective voltage of 20 MV started delivering in 2007 with performances exceeding design specifications reaching final energies up to 11 MeV/u for lighter particles. The linac gradients show no average degradation in performance. Well established operational and tuning procedures allow reliable operations. Schemes have been developed to effectively deliver the very low intensity (as low as few hundred particles per second) radioactive ion beams. The superconducting linac will be upgraded with the addition of twenty more cavities (boosting the acceleration voltage to 40 MV) by the end of 2009 making the reliability quest more challenging. In this paper we present past, present and planned operations with the ISAC linacs.

INTRODUCTION

The delivery of radioactive ion beams (RIBs) is challenging because it requires many components to perform properly at the same time. The TRIUMF facility for isotope selection and acceleration (ISAC) uses the isotope separation on line (ISOL) method [1]. ISAC has three main components: the driver, the target station and the post accelerators. This delivery chain can use also a charge state booster (CSB) to increase the charge state of the single charged ions coming from the target.

A group of physicists, with different area of expertise, is present in TRIUMF in order to maintain high standard of reliability and productivity in the beam delivery field. This group covers many aspects of the delivery beyond the basic production and post acceleration processes. In particular it relates with the experimental groups in order to facilitate the installation of the experiments itself and to adapt the best tuning strategy for each individual need. Each expert follows during the runs the performance of its own section to maximize the output of the experiment. This is done not only fine tuning each components of the delivery chain but also training and supporting the operation group on a 24/7 basis. The group evaluates the success of each experiment based on well defined metrics. This is necessary to keep track of the performances quantitatively.

Linacs

In this context the ISAC post accelerators are the last component of the delivery chain. Since the beginning of operation (back in 2000) they have a dedicated expert and therefore a well established operational and tuning procedures that allow them to be quite reliable. Maintaining the reliability of the linacs is a major goal above all in view of the ISAC-II superconducting linac upgrade.

ISAC RIB PRODUCTION FACILITY

The driver of the ISAC facility is the TRIUMF cyclotron [2](see Fig. 1). The cyclotron accelerates H^- ions up to an intensity of $250 \mu A$ to a maximum energy of 500 MeV. The H^- are then stripped and protons are extracted in three different beam lines at different energies. One of these beam line is dedicated to the ISAC radioactive beam production. In this case the beam is extracted at 500 MeV and up to $100 \mu A$. The simultaneous extraction of multiple beams with stable delivery is challenging. Nevertheless a 90% availability of the proton beam for the ISAC facility is regularly achieved.

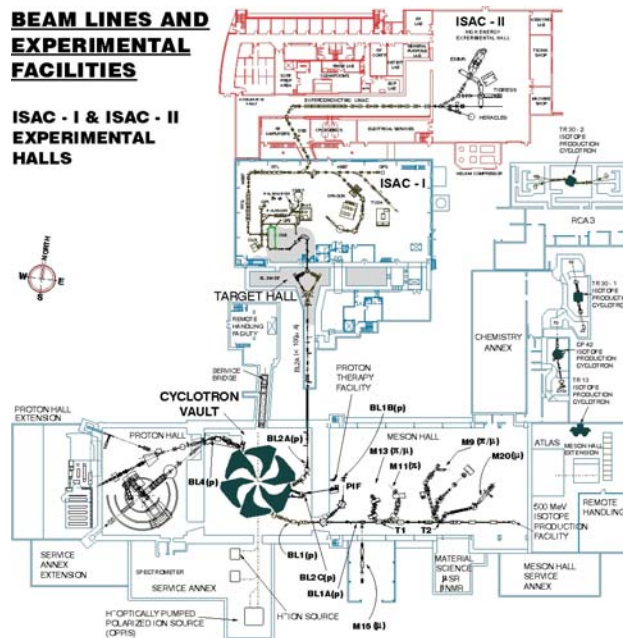


Figure 1: Overview of the TRIUMF site. The main machine is the H^- 500 MeV cyclotron used also as driver of the ISAC facility.

The ISAC facility has two independent underground target stations that can be fed with proton one at the time. This allows service on one target station while producing and delivering radioactive beams with the other. The neu-

tral isotopes produced in the target can be ionized using different sources available at ISAC.

The ionized isotopes are then selected in the mass separator and sent to ground level where the experimental areas and the post accelerators are located. After selection it is also possible to boost the charge state of the radioactive ions by diverting them through an electron cyclotron resonance ion source (ECRIS). This charge breeder allows the post acceleration of masses $A > 30$.

ISAC POST ACCELERATORS

The RIBs can be delivered to three experimental areas as represented in Fig. 2: a low energy area where the ions are accelerated at source potential (up to 60 kV), a medium energy area ($\beta = 1.8\% \rightarrow 6\%$) or a high energy area ($\beta = 6\% \rightarrow 15\%$) where the ions are post accelerated with linacs.

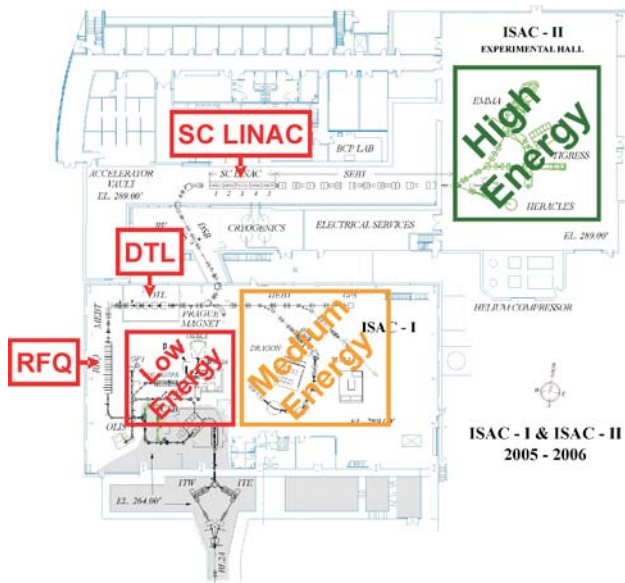


Figure 2: Overview of the ISAC facility at TRIUMF. The ISAC II linac is superconducting while in ISAC I the RFQ and the DTL are room temperature machines.

The first stage of acceleration uses a radio frequency quadrupole (RFQ, top left Fig. 3) acting as an injector [3]. The RFQ boosts the energy from 2 keV/u to 150 keV/u. It can accelerate mass to charge ratio of $3 \leq A/Q \leq 30$. The RFQ is a room temperature CW machine operating at 35.36 MHz. In order to achieve a high quality output longitudinal emittance the beam is prebunched at the entrance by means of a three harmonics electric buncher, the fundamental being 11.78 MHz. Part of the beam transmitted but not accelerated is dumped into a fixed collimator installed at the exit port of the RFQ. The particles transported into the downstream medium energy beam transport (MEBT) line is 75-80% of the injected. This configuration produces an estimated longitudinal emittance after the RFQ of 0.22π keV/u·ns [4].

Linacs

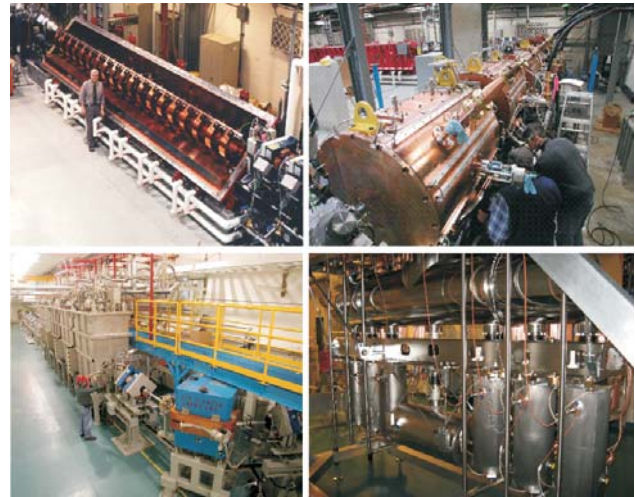


Figure 3: The ISAC accelerators: the RFQ (top left), the DTL (top right), the medium beta section of SC linac (bottom left) and the high beta section future upgrade of the SC linac (bottom right).

After the RFQ the charge state of the ions is increased by stripping through a thin carbon foil ($4 \mu\text{g}/\text{cm}^2$). As a general rule the most populated charge state is selected using magnetic benders as long as the mass to charge ratio is within $2 \leq A/Q \leq 6$ set by the second stage of acceleration, the drift tube linac (DTL, top right Fig. 3). The efficiency of the stripping foil depends on the mass of the stripped ions; in most of the cases it ranges between 30% to 50%. In order to maintain a good beam quality after stripping in terms of both transverse and longitudinal emittances, the beam is focused in the transverse directions and in time at the foil location.

The DTL [5] is a variable energy machine covering the entire range of design energies $150 \text{ keV/u} \leq E \leq 1.5 \text{ MeV/u}$. These design boundaries are indeed overtaken pushing the limit in both directions [6] (see Fig. 4). The DTL is a separated function machine composed of five IH interdigital structure accelerating tanks and three split ring bunchers located between the first four tanks. This layout produces good beam quality for each deliverable energy. After the fourth tank the beam quality is already good enough that no buncher is required. The resonance frequency of the tanks and bunchers is 106.08 MHz. They operate at room temperature in CW mode. Transverse focus through the linac is provided by quadrupoles triplets between each tank. The transmission of this linac is greater than 95%. The DTL is also used as an injector for the ISAC II superconducting (SC) linac.

The present installation (medium beta section, bottom left Fig. 3) of the SC linac [7] is composed of five cryomodules. Each cryomodule houses four superconducting cavities and one superconducting solenoid. The superconducting cavities are bulk niobium quarter wave resonators at 106.08 MHz operating at 4K. The linac is now operating for two years at an average gradient of 35 MV/m peak

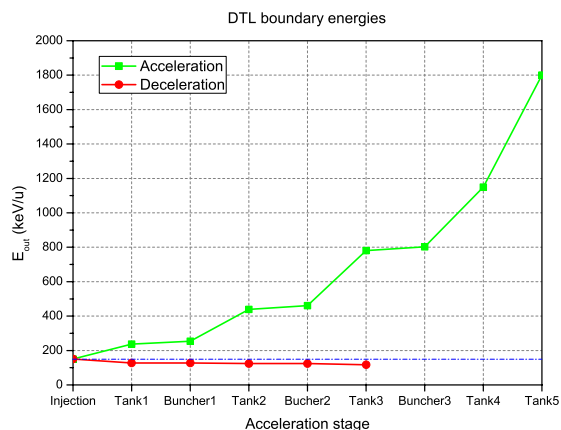


Figure 4: The boundary energies of the DTL: the design energy range is 0.15-1.5 MeV/u.

surface field (7 MV/m of acceleration) at 7W exceeding the specification of 30 MV/m at 7W. During this period there is on average no significant degradation in the cavities performance. Each cavity is independently phased at -25° synchronous phase. The transmission through the SC linac is 100%.

An upgrade (top right Fig. 3) of the SC linac is underway [8]. The upgrade (high beta section) consists of twenty more cavities housed in three cryomodules installed downstream of the existing section. The new superconducting cavities are quarter wave bulk niobium resonators operating at the higher frequency of 141.44 MHz. The first two cryomodules house six superconducting cavities and one superconducting solenoid while the last one has eight superconducting cavities and one superconducting solenoid. This upgrade increases the ISAC II linac voltage capability to 40 MV. This voltage will boost the beam energy above the Coulomb barrier for all masses. Since the SC linac always operates at the maximum possible voltage for stable operation, the final energy depends on the mass to charge ratio of the accelerated species. We anticipate an energy of 22 MeV/u for $A/Q=2$ and 8 MeV/u for $A/Q=6$. The cryomodules are scheduled for installation and commissioning by the end of 2009.

BEAM DELIVERY OPERATION

Post Accelerators Tuning

ISAC is design to produce and to post accelerate radioactive beams but we also deliver stable ion beams (SIBs). The low intensity of the radioactive beam, ranging typically between 10^3 and 10^6 particle per second, makes not possible to tune the beam lines and the accelerators. The post accelerator sections are tuned using a SIB as pilot beam with intensities of the order of enA. The stable beam used has the same mass to charge ratio of the RIB.

The stable ions are produced in an off line ion source

Linacs

(OLIS). OLIS is composed of three sources: a surface, a microwave and an electron cyclotron resonance (ECR) source. This last source produces multi charged isotopes that match the beams coming from the CSB.

The switchover procedure from the pilot beam to the radioactive is straightforward. The transmission of the RIB is checked using several low intensity detectors (like silicon detector, photodiode or channeltron) distributed along the beam line.

Beam Delivery Strategy

As already mention the main challenge of delivering radioactive beam is the complexity of the delivery chain. The single failure of a facility component (driver, target or accelerators) results in no particle at the user end. In order to complete successfully a scheduled experiment is essential that every components work properly.

The strategy adopted by TRIUMF to guarantee this success is to have a group of physicists (beam delivery group) experts in different section of the facility. This group of physicists is ultimately responsible to ensure high standard of reliability and productivity. These two concepts are defined quantitatively using two metrics.

The reliability is defined with the following Eq. 1 (metric1):

$$reliability = \frac{beamhoursdelivered}{beamhourspromised} \quad (1)$$

where the beam hours promised represent the availability of the system. The availability is defined as the number of hours (in a year) we commit to deliver beam to the experiments. For each experiment the availability is well defined in a pre-run meeting where all the sources of downtime (procedural time, maintenance, development, shutdown activities, extra activities...) are removed in the terms of hours from the total amount of time the experiment is scheduled to run.

The reliability lowers when a single components doesn't work. As example if the cryogenic system of the superconducting linac fails the linac goes off and the beam is not delivered. This is a source of unscheduled downtime and as consequence the reliability (in this example of the linac) goes down. The source of downtime can also be due to extra unscheduled procedural time. On the post accelerator side well defined tuning procedures allow us to schedule the right amount of time needed. One of the future goals is to increase the availability by reducing the tuning time without reducing the reliability. For the DTL we already established a new way to tune the machine that can be further developed toward a more automated tuning procedure [9]. In general we want to implement high level software application to tune the beam lines; this should increase the availability of the system.

The productivity is defined with the following Eq. 2 (metric2):

$$productivity = \frac{actualintegratedcountstouser}{promisedintegratedcounts} \quad (2)$$

where the promised integrated counts are calculated based on a minimum yield that the experiment needs in order to achieve publishable results. This minimum yield is also based on the historic yield produced for a given isotopes. This minimum has to be satisfactory both for the experiment and the beam delivery group. As far as the experiment is concerned the higher the minimum the better, while on the beam delivery side it is important to promise what is reasonably achievable. The productivity is most related to the target production. The target behavior can be influenced by many factors: the quality of the target itself, mechanical failure of the target or the target station, failure of the ionizing source.

In some way the productivity can be influenced also by the post accelerators performances with particular reference to the transmission. Considering all the linac (and the stripping foil efficiency) we typically have a transmission of 20-40% depending on the accelerated isotopes. If this transmission dropped below 20% then the productivity lowers due to poor performance of the accelerators.

The metrics used to grade an experiment success are an important resource to understand which area needs more development. The beam delivery group takes advantage of

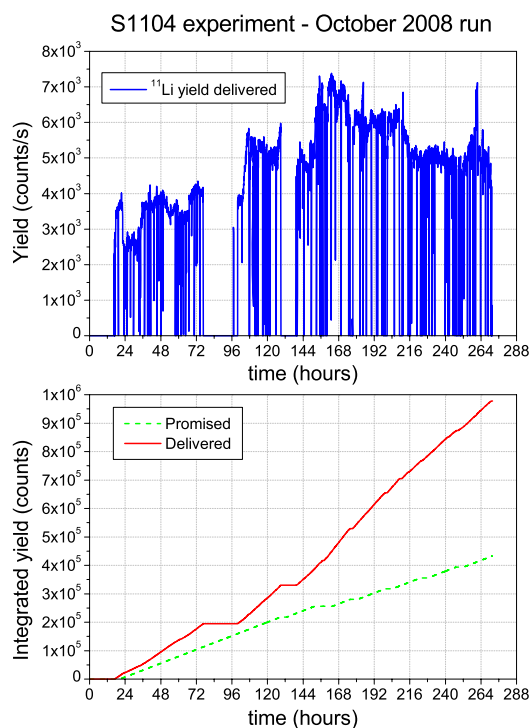


Figure 5: The top plot represents the delivered yield to the experiment S1104 in the ISAC-II experimental hall TIGRESS facility. The bottom plot represents the integrated curves of promised (green dotted line) and delivered (red line) yield.

Linacs

this analysis process to improve the quantity and quality of the beam delivered.

Beam Delivery Performance

The amount of delivered beam to an experiment is recorded during each run. These data allow to calculate the reliability and productivity during the experiment. The goal is to reach a reliability higher than 75% and a productivity higher than 100%.

The top chart of Fig. 5 represents the yield of ^{11}Li delivered during experiment S1104 at the TIGRESS facility. This facility belongs to the ISAC-II experimental. The bottom chart of Fig. 5 represents integrated yield for the same experiment. The dotted green curve is the promised integrated yield while the red curve is the actual delivered one. The metrics of this experiment score a 92% reliability and a 226% productivity.

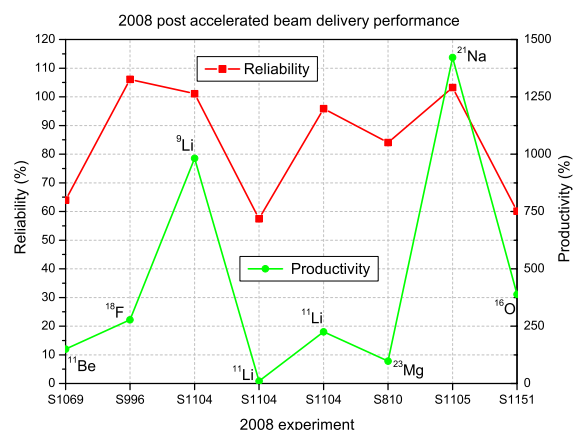


Figure 6: The plot represents the 2008 reliability (red squared line) and productivity (green circled line) curves.

The 2008 performance of post accelerated beam experiments are summarized in Fig. 6. These performance includes all the components of the delivering chain. As far as the linacs are concerned in 2008 they reach a reliability of 97%. The performance of the linacs in term of transmission has always been inside the expected values.

CONCLUSION

In order complete successfully an RIB experiment all the delivery chain components have to work properly at the same time. This makes the delivery task a challenge that at ISAC is approached with a group of physicists experts in different areas of the delivery chain. The group has two well define metrics to grade reliability and productivity of the ISAC facility. The delivery performance are collected and analyzed run by run in order to improve where necessary. In this scenario the ISAC post accelerators performed a reliability of 97%. The future goal is to maintain or to

improve the reliability of the linacs and possibly increase the availability. This leads to an overall increase of beam counts at the experimental targets and therefore a potential increase in the output of the science produced.

REFERENCES

- [1] M. Marchetto, "ISAC-II operation and future plans", LINAC08, Victoria, British Columbia, CANADA, September 2008.
- [2] I. Bylinskii et al., "TRIUMF 500 MeV Cyclotron Refurbishment", Cyclotrons and Their Application, Giardini Naxos, ITALY, September 2007, p. 143.
- [3] R.L. Poirier et al., "CW Performance of the TRIUMF 8 Meter Long RFQ for Exotic Ions", LINAC2000, Monterey, California, USA, August 2000, p. 1023.
- [4] S. Koscielniak et al., "Beam Dynamics Studies on the ISAC RFQ at TRIUMF", PAC'97, Vancouver, British Columbia, CANADA, May 1997, p. 1102.
- [5] R.E. Laxdal et al., "Beam Commissioning and First Operation of the ISAC DTL at TRIUMF", PAC2001, Chicago, Illinois, USA, June 2001, p. 3942.
- [6] M. Marchetto et al., "Decelerating Heavy Ion Beams Using the ISAC DTL", this conference proceedings.
- [7] R.E. Laxdal, "Commissioning and Early Experiments with ISACII", PAC07, Albuquerque, New Mexico, USA, June 2007, p. 2593.
- [8] R.E. Laxdal et al., "ISAC II Superconducting Linac Upgrade - Design and Status", LINAC08, Victoria, British Columbia, CANADA, September 2008.
- [9] M. Marchetto et al., "Upgrade of the ISAC DTL Tuning Procedure at TRIUMF", EPAC08, Genoa, July 2008, p. 3440.

HIE-ISOLDE LINAC: STATUS OF THE R&D ACTIVITIES

M. Pasini, CERN, Geneva, CH and Instituut voor Kern- en Stralingsfysica, K.U.Leuven, Leuven, BE
 S. Calatroni, J-C. Gayde, G. Lanza, C. Lasseur, M. Lindroos,
 C. Maglioni, R. Maccaferri, D. Parchet, P. Trilhe, CERN, Geneva, CH
 A. D'Elia, CERN, Geneva, CH and Cockcroft Institute, Warrington, UK
 M. A. Fraser, CERN, Geneva, CH and Cockcroft Institute, Warrington and U. of Manchester, UK

Abstract

For the post-accelerator of radioactive ion beams at CERN a major upgrade is planned to take place in the next 4-5 years. The upgrade consists in boosting the energy of the machine from 3 MeV/u up to 10 MeV/u with beams of mass-to-charge ratio $2.5 < A/q < 4.5$ and in replacing part of the existing normal conducting linac. The new accelerator is based on two gap independently phased 101.28 MHz Nb sputtered superconducting Quarter Wave Resonators (QWRs). Two cavity geometries, “low” and “high” β , have been selected for covering the whole energy range. A R&D program has started in 2008 looking at the different aspects of the machine, in particular beam dynamics studies, high β cavity development and cryomodule design. A status report of the different activities is given here.

INTRODUCTION

The ISOLDE facility at CERN (see Fig. 1) is object of a general upgrade in view of an extended demand of the physics program with accelerated radioactive ion beams (RIBs). In particular, nuclear physics experiments request for higher energy, up to 10 MeV/u, for higher intensity, and for better beam quality, in terms of purity and smaller emittances [1]. In order to match the higher energy requirement a modular superconducting linac based on quarter wave resonators (QWRs) is planned to be installed downstream the present normal conducting linac. In the short term the new accelerator modules will boost the energy up to 5.5, 8 and 10 MeV/u, while in the longer term, part of present normal conducting linac will be replaced by new superconducting cavities in order to allow the full energy variability between 1.2 and 10 MeV/u [2].

Concerning the higher beam intensity, ISOLDE will profit from the ongoing upgrade of the proton injectors chain at CERN [3] which will allow the beam power on target to be doubled and for which new target stations, targets and their associate handling system will need new development. Moreover, an upgrade of the REX trap and charge breeder is planned to cope with the increased intensity.

Finally in order to improve the quality of the beam a new mass separator with higher resolution is under study and new targets and ion sources are under development.

Because of the limited resources available the whole upgrade project has been split in two parts, namely HIE-ISOLDE 1, and HIE-ISOLDE 2. In the former it is aimed

Linacs

at the design and construction of the SC linac up to at least 8 MeV/u and also a design study of the intensity upgrade. In the latter it is envisaged a further extension of the energy up to 10 MeV/u and the construction of higher power targets with their adequate handling system and a high intensity charge breeder.

The highest priority of the project is the construction of the superconducting linac. In particular the R&D effort has focused so far on the the development of the high β cavity ($\beta = 10.3\%$), for which it has been decided to adopt the Nb sputtered on Cu substrate technology. Other R&D activities are related to the beam dynamics studies which seek to define a very compact accelerating lattice and consequently the shortest possible machine, a design of the SC solenoids with limited fringe fields, and the design of the cryomodule concept.

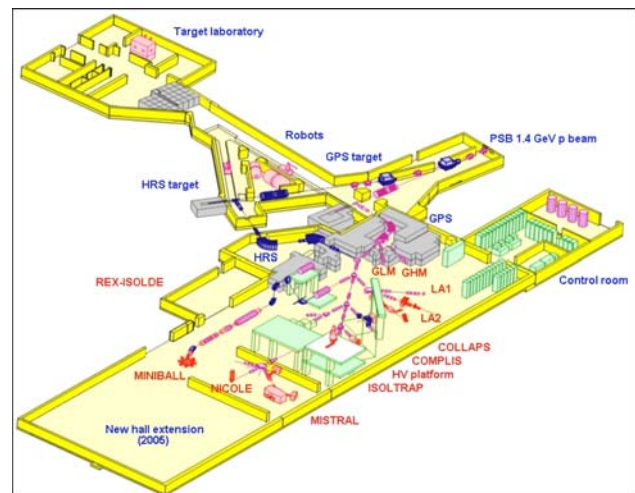


Figure 1: The ISOLDE facility.

As mentioned above the first part of the SC linac that will be installed is the high energy section. The first high β cryomodule will be installed at his final position so that when the low β cryomodule will be installed no further modifications and/or displacements of the cryomodules needs to be done. This is of high importance since it allows to minimize the down time of the machine and the installation can be done during the usual maintenance period in the winter. Fig. 1 shows also the new extension hall that was built in 2005 in order to house the extension of the linac.

A study covering all the issues of the infrastructure and

first cavity and as soon as the beam picks more velocity the kick becomes rapidly negligible.

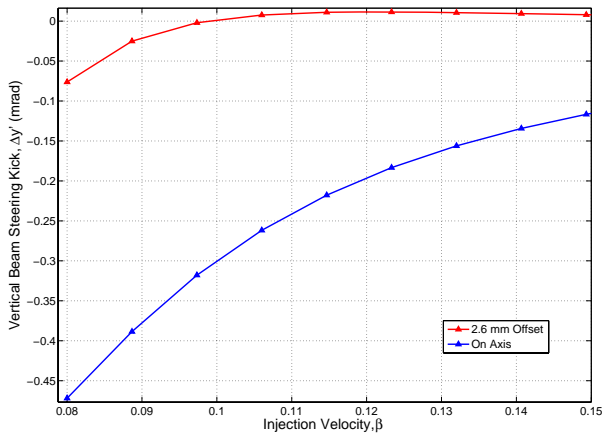


Figure 4: Divergence of the beam in case of a compensated (red) and not compensated (blue) case for a synchronous phase of -20 as a function of the incoming beam velocity.

Figure 5 shows the result of the beam dynamics study of the high energy section in case of a beam with $A/q=4.5$ and with a transversed matched beam coming from the present NC machine.

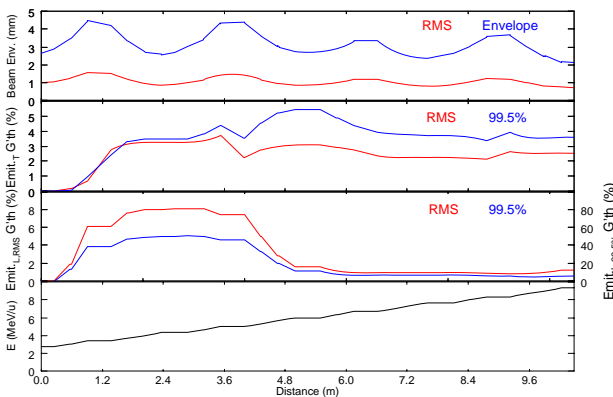


Figure 5: Beam dynamic of $A/q=4.5$ in the case of the high energy section only.

The beam dynamics study is now focused on the error study, considering longitudinal fast error (RF jitter) and static error as well as static transverse misalignment. It is found that the longitudinal emittance in the high energy section of the machine increases by a factor 1.9 if the RF jitter is limited at 0.5% in amplitude and at 0.5 in phase for a beam with $A/q=4.5$.

SC Solenoid

The employment of the SC solenoids as unique focusing elements allows to increase the transverse acceptance of the beam with respect to the un-matched beam condition and allows a great reduction of the tuning knobs, hence

making the tuning and operation of the machine easier. The magnetic and mechanical specifications of the solenoid are summarized in Table 1.

Table 1: Solenoid Specifications

Magnetic Integral $\int B^2 dz$	16.2 T ² m
Mechanical Length	0.4 m
Fringe field at 23 cm from center	< 0.2 G
Inner Diameter	30 mm

A 2D electromagnetic study of the solenoid has been performed: the specifications are met with 570A Nb₃Sn coils which produces a peak field in the center of the solenoid of 120kG. The return yoke is made by high quality iron. The fringe field is cut by two additional coils in reversed sign. These coils, at this moment of the design, are powered independently from the coils that build the main field, but a solution to have a unique power supply is under study. Fig. 1 show a schematic of the mechanical assembly of the solenoid.

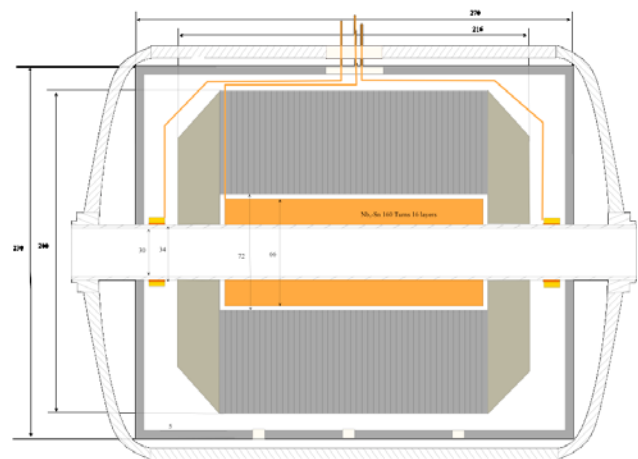


Figure 6: Solenoid schematics.

HIGH β CAVITY MANUFACTURING

The construction of a high β cavity prototype started in the middle of 2008 and the copper body which makes the substrate for the Nb sputtering was completed in April 2009. During the same period a new sputtering chamber was constructed and is now under commissioning. The cavity manufacturing process has been reported in [9] and now the critical fabrication steps have been identified. In details the long longitudinal full penetration electron beam weldings have shown the creation of some porousness that could harm the Nb deposit. This defect could be removed by passing the electron beam in smoothing mode from the inside of the cavity - this operation would require the use of a special electron beam welding machine with a miniaturized head - but at this time it was not felt as a immediate action to take. Moreover it is possible that the chemi-

cal etching needed for the surface preparation for coating could solve the problem by enlarging the pocket enough so that no acid is trapped and released afterwards, for example, during the sputtering. The most critical and also time-consuming step was the direct extrusion of the beam port. This step requires high precision in mounting and remounting the different tools and particular care in handling the cavity since for the production of the beam ports, the cavity needs to undergo to eight heat treatments which locally soften the copper. Finally the construction of the prototype suffered a couple of accidents which are related to human errors. For this reason a strong QA procedure needs to be in place for the series production. The cavity has been checked also with a series of RF measurement, especially the variation of the resonance frequency during the several manufacturing steps and all the measurements are in line with the prediction. Fig. 7 shows an advanced status during manufacturing of the copper substrate.



Figure 7: Cavity copper substrate towards final machining steps.

In parallel to the copper cavity a dummy cavity made in stainless steel was built. The purpose of this dummy cavity is to use it as samples holder for the characterization of the plasma inside the chamber, to test the assembly procedure of the sputtering chamber itself and to serve also as a training tool for the handling operation during the chemical treatment.

The sputtering chamber is now operational and the first plasma has been produced. The vacuum level of the chamber after baking reached the low 10^{-8} mbar level and minor adjustments should push the vacuum level another order of magnitude lower. This is of course of great importance as the vacuum level is directly linked to the quality of the Nb films produced. All subsystems have been checked and a characterization of the plasma and hence of the Nb deposit quality is ongoing as a function of the different gas pressure level, cathode voltage and bias voltage. First Nb deposit on the copper cavity is expected towards the end of July. Fig. 8 shows on the left a moment during the installation of the dummy cavity inside the sputtering chamber and on the right the sputtering chamber closed.



Figure 8: On the left the dummy cavity during mounting for the first sputtering. On the right the sputtering chamber closed.

Coupler

An adjustable power coupler has been designed with an extreme dynamic range. In fact the Q_{ext} can be adjusted between 10^4 up to 10^9 so that it is possible to reach critical coupling at room temperature and a moderate under-coupling when the cavity is superconducting. This feature allows to perform some preliminary room temperature conditioning that should help in cleaning the multipacting barrier at low field level and allow to fine tune the coupling needed for the field and phase stabilisation loops. From the mechanical point of view the sliding mechanism concept is dust free as the contact points are reduced to the minimum (see Fig. 9). This should avoid any seizure of the moving parts and guarantees the functionality of the system. A first prototype is under construction and expected to be delivered by the end of July.

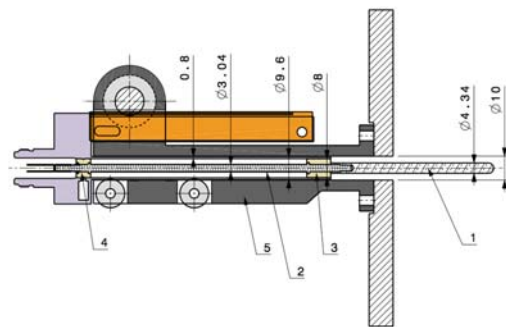


Figure 9: Coupler schematics.

Tuner

The tuning system chosen for the HIE-ISOLDE cavities take advantage from the experience developed at TRIUMF [10]. An *oil-can* shaped diaphragm of CuBe has been hydroformed with a pressure up to 120 bar. All radial slot necessary for the elongation and contraction of the diaphragm are performed with a laser beam. The same plate can be mounted directly on the low β cavity or welded to

a flange in the case of the high β cavity. The actuator is designed to have no backlash. A coarse frequency tuning range of 220 kHz is expected. The first prototype of the tuner is available and the internal surface should be sputtered by the end of June.

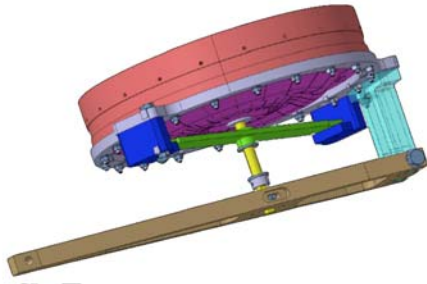


Figure 10: 3D view of the tuner with the lever actuator.

CRYOMODULES

An initial study of the cryomodule concept was reported in [11]. Specifically, in that report the choice for a single vacuum system with an active thermal shield was shown to best fit the requirements of the new machine. In the last months, work has continued at a level of a concept study and a series of major choices have been taken concerning the dimensions, accessibility, assembly procedure and maintenance of the cryomodule, the holding system for the cavities and for the solenoid, and the alignment system.

One of the general considerations that set the pathway to the concept of the HIE-ISOLDE cryomodule was the maintenance service. In order to minimize cost and downtime of repairs it is clear that the maintenance should take place at CERN and that at this point one needs to consider the available infrastructure such as clean rooms. All the clean rooms at CERN are quite limited in height but they are quite large and long. As a consequence the dismantling of the cryomodule can occur only if the access is from the lateral side (see Fig. 11). Starting from this consideration a study concerning the stability of a mechanical structure with two openings on the side has been performed and found that this structure is feasible. The mounting and pre-alignment of the cavities will be externally in the support girder which, with the help of a special forklift, can be positioned inside the cryomodule and hooked to the support stems. Given the recent result in the error study it has been decided to have a separate frame for the support of the solenoid which can be adjusted from outside even when the system is cold.

Concerning the alignment system, it is under study the possibility to use a BCAM system [12]. Such a system consists of a calibrated laser source that can track changes in the position with an accuracy in the order of few tens of μm with a rather large span in distances. The advantage of such system is that the active part of the alignment system is kept outside the vacuum envelope and that it is possible

to perform a continuous survey so that in case of accident one can retrace the position of the different elements just before the accident.

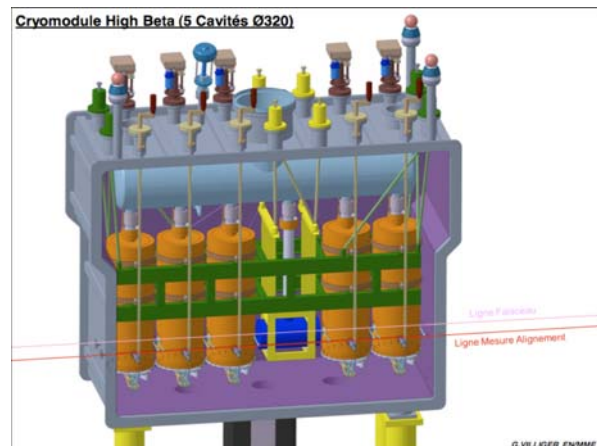


Figure 11: Cryomodule schematics.

ACKNOWLEDGMENTS

The authors wish to thank all the designers and technicians that have worked and continue to work in this project. Their commitment and dedication has been greatly appreciated.

REFERENCES

- [1] HIE-ISOLDE: the scientific opportunities, CERN Report 2007-08.
- [2] M. Pasini et al., "A SC upgrade for the REX-ISOLDE accelerator at CERN", Linac'08, Victoria, Canada, Sept. 2008.
- [3] <http://linac4.web.cern.ch/linac4/>.
- [4] M. Pasini et al., "Beam Dynamics Studies for the SCREX-ISOLDE linac at CERN", Linac'08, Victoria, Canada, Sept. 2008.
- [5] M. A. Fraser et al., "Beam Dynamics Studies for the HIE-ISOLDE Linac at CERN", Pac'08, Vancouver, Canada, May 2009.
- [6] <http://www.cst.com>.
- [7] P. Ostroumov et al., <http://www.phy.anl.gov/atlas/TRACK/>
- [8] P. Ostroumov and K. Shepard, Phys. Rev. ST. Accel. Beams 11, 030101(2001).
- [9] M. Pasini et al., "SC Nb sputtered QWRs for the REX-ISOLDE accelerator at CERN: prototype design and manufacturing", Linac'08, Victoria, Canada, Sept 2008.
- [10] T. Ries et al., "A mechanical Tuner for the ISAC-II Quarter Wave Superconducting Cavities", PAC'03, Portland, USA, May 2003.
- [11] V. Parma et al., "Concept Design Studies of the REX-ISOLDE cryomodules at CERN", Linac'08, Victoria, Canada, Sept. 2008.
- [12] <http://alignment.hep.brandeis.edu/Devices/BCAM/>.

DEVELOPMENT OF HEAVY ION ACCELERATOR AND ASSOCIATED SYSTEMS

D. Kanjilal, Inter University Accelerator Centre, New Delhi 110067, India

Abstract

A 15 UD Pelletron electrostatic accelerator is in regular operation at Inter-University Accelerator Center (IUAC). It has been providing various ion beams in the energy range from a few tens of MeV to 270MeV for scheduled experiments. A superconducting linac booster module having eight niobium quarter wave resonators has been made operational for boosting the energy of the heavy ion beams from the Pelletron for experiments at higher energies. A new type of high temperature superconducting electron cyclotron resonance ion source (HTS-ECRIS) was designed, fabricated and installed. It is in regular operation as a part of an alternate high current injector (HCI) system being developed for injection of highly charged ions having higher beam current in to the superconducting linac. A radio frequency quadrupole (RFQ) accelerator is being developed to accelerate highly charged particles ($A/Q \sim 6$) to an energy of 180 keV/A. The beam will then be accelerated further by drift tube linacs (DTLs) to the required velocity for injection of the beams to the linac booster. Details of various developmental activities related to the heavy ion accelerators and associated systems are reported.

ACCELERATOR AND RELATED SYSTEMS

Pelletron

The 15UD Pelletron electrostatic accelerator [1, 2] having compressed geometry tubes for 16MV terminal potential, is in regular operation at IUAC since 1990. It has been upgraded by using resistor grading of accelerating columns and support posts, two turbo molecular pumps based re-circulating gas stripper along with a foil stripper system at high voltage terminal, multi harmonic buncher, multi-cathode sputtered negative ion source, external chiller for cooling the re-circulating SF₆ gas and accelerator mass spectrometry beam line having off-set Faraday cup and Wien filter. One of the unique features of the Pelletron at IUAC is the incorporation of the off-set quadrupole triplet (see Fig. 1) after the Gas/Foil Stripper system for selection of ions having desired positive charge state inside the terminal before acceleration by high energy section after the terminal. A matching quadrupole triplet after the off-set quadrupoles is used to match the selected ions to the high energy section of the Pelletron. This helps in decrease in loading of the charging system by reducing the number of charge states to be accelerated after the terminal to one charge state selected by the off-set quadrupole triplet followed by matching quadrupoles triplet inside the high voltage

terminal. It also makes the analysis of the charge states of ions stripped of electrons again at higher energy by the next foil stripper in the high energy dead section located after six of the fifteen units from the terminal simplifier. The 15 UD Pelletron has been operational round the clock seven days a week maintaining high uptime and delivering a variety of beams to users from all over India and abroad. All types of problems faced during its operation since 1990 are solved successfully by the accelerator personnel of IUAC. The integrated beam pulsing systems have been in regular use for various experiments and for accelerating beams through LINAC. The AMS facility has been tested successfully and user experiments have been carried out regularly.



Figure 1: Off-set quadrupoles after strippers in terminal.

Superconducting Linac Booster

The basic design and development of the superconducting linear accelerator (linac) which started in early ninties at IUAC is based on niobium technology. Later a collaboration to design and fabricate a suitable superconducting linac structure was developed in early 1992 with Argonne National Laboratory (ANL) [3]. Quite a few novel features were incorporated in the new design. Instead of niobium bonded to copper which was used in ANL's split-ring resonator, a niobium quarter wave resonator (QWR) jacketed in a stainless steel outer vessel was developed [4]. The linac system at IUAC consists of one superbuncher cryostat having one QWR, three linac modules and one rebuncher cryostat containing two QWRs. Each linac module consists of a cryostat holding eight QWRs and one superconducting solenoid magnet (see Fig. 2). Twelve resonators were fabricated in collaboration with ANL [5]. Another three resonators have been fabricated indigenously and tested. Two of them are used in the first linac module and rebuncher.

Bulk production of fifteen more QWRs for second and third linac modules are nearing completion.

All the problems observed during acceleration of beam through the first linac module have been analyzed systematically and rectified successfully. Some of the major problems encountered during earlier beam tests were: 1) inadequate cooling of the niobium resonators by liquid helium for attaining higher accelerating fields, 2) requirements of high RF power (150-300 W) to operate the resonators leading to cable melting, metal coating on the niobium surface and increased cryogenic losses, 3) cold leak in the tuner bellows from the vacuum seal and/or from the electron beam welded joints of the niobium bellows convolutions of the tuner, and 4) exposure of brass rack and pinion mechanism of the drive coupler causing zinc coating on the inside surface of the RF power port of the niobium resonator. These problems were systematically analyzed and solved for further beam tests and regular operation of linac (see Fig. 2) for scheduled experiments.

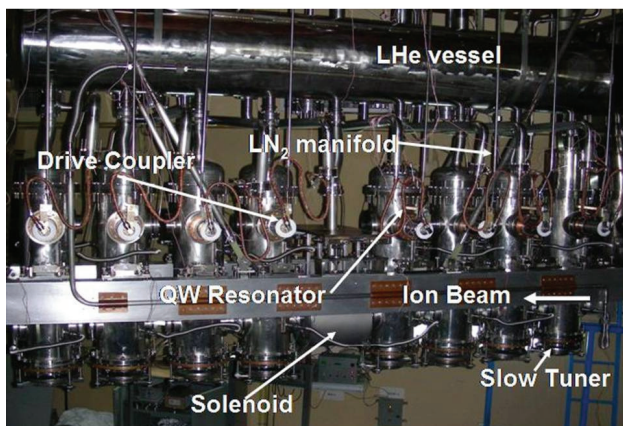


Figure 2: First linac having eight QWRs and superconducting solenoid.

Hemispherical dome structure on each of the eight Nb QWRs was incorporated to avoid accumulation of bubbles below the top flat flange. In addition to the stoppage of formation of bubbles near the top Nb surface by moving them upward, the dome structure provided a buffer volume for liquid helium near the top Nb surface where current is maximum. After this, all resonators performed very well and an average field of about 4 MV/m could be achieved regularly. The requirements of forward RF power was reduced by a factor of about half by using a novel technique of damping the mechanical modes of the resonator [6]. For this purpose eighty polished stainless steel balls of 4 mm diameter were inserted in the central conductor. With the new damping mechanism, a forward power of less than 100 W was found to be sufficient for each of the resonators to lock it at maximum achievable fields (up to 5 MV/m) at ~ 6 W of power going into liquid helium (LHe). An improved slow tuner fixture was designed to avoid entry of helium gas inside niobium bellows for controlling the capacitance. The slow tuner is controlled by flexing

stainless steel (SS) bellows which pulls or pushes Nb bellows by a SS-shaft. The problem of helium leakage from slow tuner disappeared after incorporation of this new design. Modified drive couplers are designed and fabricated to avoid exposure of brass made rack and pinion mechanism. The problem of coating on the niobium surface near RF power port is eliminated. The superconducting niobium resonator fabrication facility was commissioned at IUAC. The facility consists of an electron beam welding machine, surface preparation laboratory for ultrasound cleaning, electropolishing, high vacuum furnace for heat treatment/annealing, high pressure rinsing and a test cryostat. Initially a single QWR was fabricated and tested successfully. It is being used in the rebuncher cryostat of the linac. Later two completely indigenous QWRs were fabricated. One of them is installed in the first linac module for regular operation of linac. Production of fifteen more QWRs for the 2nd and 3rd linac modules is at the final stage of completion. In addition to the in-house programs of indigenous fabrication of resonators and associated components, IUAC has taken up a project to construct two niobium single spoke resonators for Project-X at Fermi National Accelerator Laboratory (FNAL), USA. Raja Ramanna Centre for Advanced Technology (RRCAT), India has started fabrication of a Tesla-type single cell niobium cavity in collaboration with IUAC.

For acceleration through linac the ion beam from negative ion source is bunched by multiharmonic buncher placed before entrance to the 15UD Pelletron accelerator. The high energy sweeper after the analyzer magnet is used to remove the background of the pulsed beam pre-accelerated by the 15 UD Pelletron. The typical pulse width available is about 1 ns. The beam is further bunched to 150 to 200 ns by adjusting amplitude and phase of the superbuncher (one QWR) before the entrance of the first linac module. Each of the linac modules consists of total eight QWR resonators with a superconducting solenoid placed at the centre of the module as shown in Fig. 2. After optimizing the phase and amplitude of every resonator the beam is accelerated to the required energy to conduct scheduled experiments. The energy focus or time focus at the target in the experimental chamber is optimized by adjusting the superbuncher having two QWRs [7]. Time focus of about 400 ps is achieved.

During various beam acceleration experiments through linac, the transmission of more than 90% was achieved through the niobium QWR resonators. A series of tests were conducted systematically before regular operation of SC-LINAC booster for scheduled experiments started. All the resonators in the linac cryostat have been performing satisfactorily. An average accelerating field of ~ 4 MV/m is obtained at 6 W of input power. All the cavities were phase locked with ~ 100 W of forward power from the amplifier. The average locking field was ~ 3.8 MV/m.

Beams of carbon, oxygen (isotopes $A=16$ and $A=18$), fluorine, silicon, titanium and silver have been accelerated by the linac.

High current Injector

A high current injector (HCI) system is being developed for injection of highly charged ions having higher beam current in to the superconducting linac. A high temperature superconducting ECR ion source (HTS-ECRIS) PKDELIS[8] requiring simpler single-stage cryostat and air-cooled cryo-cooler has been designed, developed and installed successfully (see Fig. 3). The performance of the source is as per the design goal. Analysed beam current of more than one milli-Ampere for nitrogen, neon, argon are obtained from this source. The HTS coils have been operational for more than 27000 hours without any problem. A radio frequency quadrupole (RFQ) accelerator is being developed to accelerate highly charged particles ($A/Q \sim 6$) to an energy of 180 keV/A. The beam will then be accelerated further by drift tube linacs (DTLs) to the required velocity for injection of the beams to the linac booster.

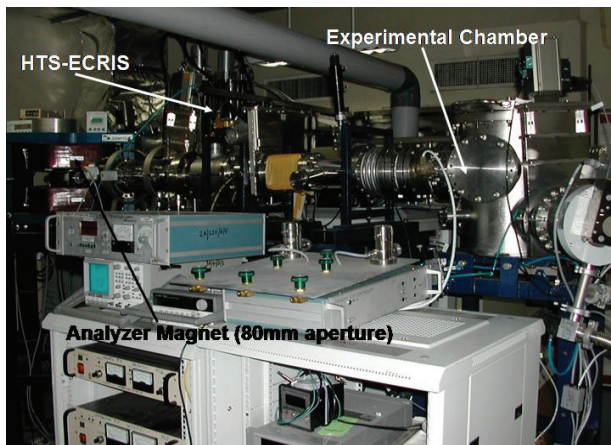


Figure 3: The HTS-ECRIS with analyzing magnet.

The cryogen-free HTS-ECRIS is very suitable for operation on a high voltage platform as required for our HCI program. The two axial coils are cooled by single-stage Gifford McMahon type refrigerators to 23K for optimum operation. The performance of HTS-ECRIS is found to be excellent. The power and cooling requirements of this type of ECRIS is decreased by a factor of 10 compared to conventional ECRIS using copper coils.

To reduce the loading of the high voltage power supply biasing the high voltage platform and the accelerating tubes across the platform and ground due to space charge of multi-charged ions from ECR, a large acceptance analysing magnet having 80 mm pole gap is placed on the high voltage platform to pre-select ions from the ECR source before acceleration from the high voltage platform. The main design goals for the analysing magnet are large acceptance, minimum weight, air-cooling and reasonable mass resolution. The geometrical aberrations due to

higher order terms are minimized by incorporating multipole field components. The vertical focussing is obtained by incorporating increasing sextupole field components at the entrance and exit of the magnet. This is achieved by having cylindrical pole shape at entrance and exit with negative radius of curvature. The horizontal focussing is achieved by introducing decreasing sextupole field component in the radial plane at the middle of the magnet.

A prototype unmodulated 48.5 MHz radio frequency quadrupole (RFQ) was developed initially to have a detailed understanding of the various issues involved in the mechanical design, beam optical design and tests. The electrodes are in the form of four-rod structure. The bore radius and length of the electrodes are 4 mm and 1.17 meters respectively. A fully automated bead puller system is used to test the performance of the prototype RFQ. The prototype is a full scale model of the final design. The design parameters like RF frequencies, shunt impedance, water cooling, tunability, mechanical vibrations and stability are being investigated with this prototype. After successful bead pull tests of unmodulated prototype RFQ, modulated vanes are fabricated (see Fig. 4).

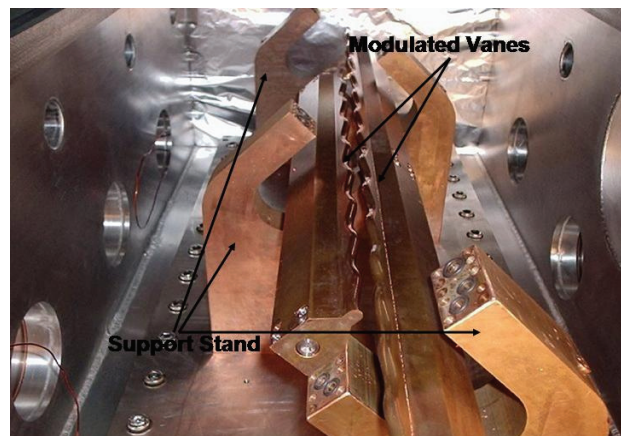


Figure 4: Modulated vanes of RFQ in the chamber.

Six Inter-digital H type RF resonators operating at 97 MHz are being designed and developed to accelerate ions from 180 keV/u to 1.8 MeV/u. A bead pull test was carried out to measure the voltage profile across the gaps of the first prototype cavity (see Fig. 5). The voltage profile is found to be reasonably good. The prototype cavity having an inner diameter of 85 cm and length of 38 cm is fabricated using SS304 material. The vacuum test is completed successfully. The machining of the ridges, stems and drift tubes has been carried out at IUAC using the in-house vertical machining centre (VMC) and associated facilities. Water cooling channels have been made in each of the stems as well as the end walls of the cavity.

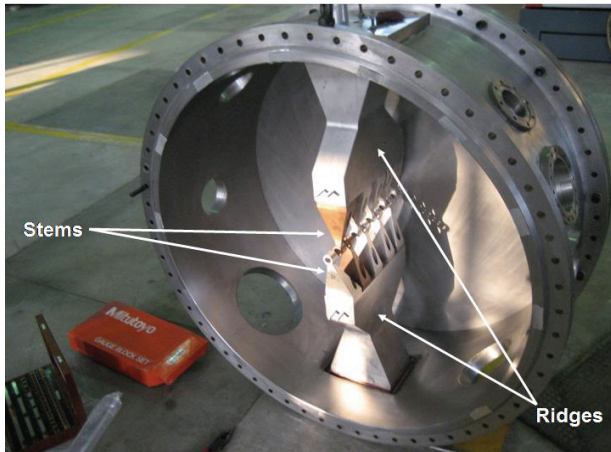


Figure 5: Prototype DTL cavity with stems and ridges.

CONCLUSION

The 15 UD Pelletron has been in regular operation round the clock seven days a week. It has been upgraded at various stages for improved performance. It has been delivering various beams from proton to gold in a wide range of energy from tens of MeV to hundreds of MeV. The first module of the superconducting linac booster is fully operational. Various beams have been accelerated using this linac module. Average accelerating field achieved was more than 3.5 MV/m. A cryogen free high temperature superconducting ECR ion source (HTS-ECRIS) PKDELIS for alternate high current injector for the superconducting linac has been developed for production of various ion beams at higher charge states. Its superconducting axial coils have been under regular

operation at 23K for more than 27000 hours. This high performance HTS-ECRIS requires much less power and cooling water making it ideal ion source for operation on a high voltage platform for future high current alternate injector. The RFQ and DTL are being developed as a part of the high current injector program. Development of other superconducting resonators as collaborative projects are taken up.

ACKNOWLEDGEMENTS

The author is grateful to A. Roy, Director, IUAC for planning and executing the futuristic programs in development of accelerators and associated systems. The contributions of the colleagues at IUAC involved in these developmental projects are highly appreciated.

REFERENCES

- [1] D.Kanjilal et al, Nucl. Instr. Meth. A 328 (1993) 97.
- [2] S. Chopra et al, Nucl. Instr. and Meth A 550, 70 (2005) 70.
- [3] D. Kanjilal, DAE-BRNS Symp on Nucl. Phys., 47A (2004) 21.
- [4] A. Roy, Current Science 76 (1999) 149.
- [5] P. N. Prakash et al, Pramana 59 (2002) 849.
- [6] S. Ghosh et al, Phys. Rev. ST Accel. Beams 10 (2007) 42002.
- [7] S. Ghosh et al, Phys. Rev. ST Accel. Beams, 12, Phys. Rev. ST Accel. Beams 12, (2009) 40101.
- [8] D. Kanjilal et al, Rev. Sci. Instr. 77 (2005) 1.

OPERATIONAL EXPERIENCE OF THE SUPERCONDUCTING LINAC BOOSTER AT MUMBAI

Vandana Nanal[#], R.G. Pillay, J. N. Karande, S. S. Jangam, P. Dhumal
 M.S. Pose, C. Rozario, S.K. Sarkar, R.D. Deshpande and S.R. Sinha

Department of Nuclear and Atomic Physics, TIFR, Mumbai – 400005

B. Srinivasan, S.K. Singh, Nuclear Physics Division, BARC, Mumbai – 400085

Abstract

The superconducting LINAC booster, indigenously developed to boost the energy of the heavy ion beams from the 14 MV Pelletron accelerator at TIFR, Mumbai, has been fully operational since July 2007. The LINAC consists of seven modular cryostats, each housing four lead plated quarter wave resonators, designed for an optimum velocity $\beta_0=0.1$ at an operating frequency of 150 MHz. In order to maintain a stable phase and amplitude of the electric field in the cavity, the RF controller cards based on a self-excited loop (SEL) with phase and amplitude feedback have been developed indigenously. The cryogenic system for the LINAC has been designed for a typical power dissipation of 6 W in each resonator. Initial beam trials have yielded average energy gain of 0.4 MV/q per cavity corresponding to 80% of the design value. Operational experience of the LINAC, namely, empirically devised procedures for the acceleration of different beams and RF settings, and associated developments are presented.

isochronous mid-bend magnet system (QD-MD-QD-QD-MD-QD). A compact longitudinal phase space is essential for acceptance in Phase II after the mid-bend and for optimization of the beam quality at target position. During the acceleration and beam transport, it is also important to preserve the longitudinal phase space over the length of the LINAC. The empirically devised procedures for the acceleration of different beams and RF settings are described in this paper. Different subsystems and associated developments are also presented.

QUARTER WAVE RESONATOR

The LINAC consists of seven modular cryostats, each housing four accelerating cavities. The RF cavity is a Quarter Wave Resonator (QWR), an open-ended $\lambda/4$ coaxial transmission line. The resonator is made out of OFHC copper (outer diameter 200 mm, 640 mm long) and is designed for an optimum velocity $\beta_0=0.1$, at an operating frequency of 150 MHz (Fig. 2) [2,3]. Typically, $Q \sim 1-2 \times 10^8$ is obtained at an average accelerating field of 2-2.5 MV/m.

INTRODUCTION

A superconducting linear accelerator, indigenously developed to boost the energy of heavy ion beams delivered by the Pelletron accelerator at Mumbai, has been operational since July, 2007 [1]. A schematic layout of the LINAC booster is shown in Fig. 1.

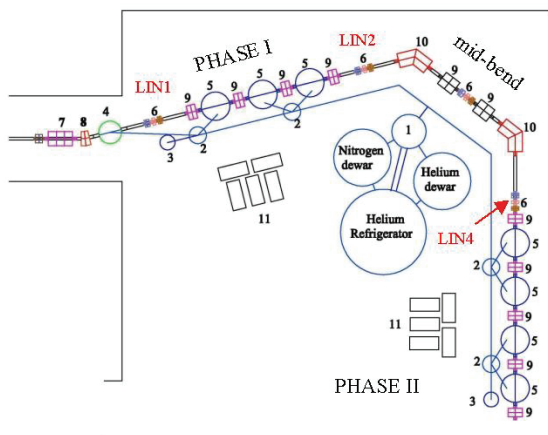


Figure 1: A schematic layout of the LINAC.

The LINAC Phase I (superbuncher + 3 modules) and Phase II (4 modules) are connected by an achromatic,

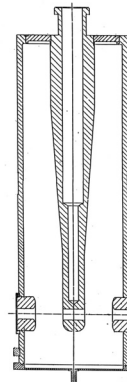


Figure 2: The Quarter Wave Resonator.

The fabrication and the e-beam welding of the QWR were carried out by the Centre for Design & Manufacture (CDM), BARC. The brazing of the two side beam ports to the outer conductor was carried out in a hydrogen furnace at SAMEER, Mumbai. The porosity present in the e-beam welded joint on the inner surface, at the junction of the shorting plate and the outer can, has been the single major manufacturing hurdle. We have designed a burnishing tool to repair some of the minor defects at this welding zone and have successfully refurbished several resonators. The QWRs were plated with Lead, approximately 2 μm thick, using a commercially available

[#]nanal@gmail.com

MSA (Methyl Sulfamic Acid) plating bath in a laboratory specially set up for this purpose at TIFR.

CRYOGENICS

The heart of the cryogenic system for the heavy ion superconducting LINAC booster is a custom-built liquid helium refrigerator Linde TCF50S. The Refrigerator is rated for 300 Watts at 4.5 K with a dual JT (Joule-Thomson valve) at the final cooling stage, which allows simultaneous connections to the cryogenic loads (the LINAC module cryostats) and to a liquid helium storage dewar (1000 l). The two-phase helium at 4.5 K produced at the JT stage in the refrigerator is delivered to the cryostats through a cryogenic distribution system. The phase separation is achieved in the individual cryostats and the cold (4.5 K) helium gas is returned, by the distribution system, back to the helium refrigerator. The four quarter wave cavities inside each cryostat are gravity-fed from a horizontally mounted liquid helium vessel. The total mass at 4.5 K in each of the modules is close to 250 kg.

The cryogenic distribution system for the LINAC is designed to deliver both liquid helium and liquid nitrogen to the cryostats [4]. The system consists of a main junction box, distribution trunk lines, remote filling stations, triaxial transfer tubes and loop back end boxes.

A 300 l dewar is used as a source of the liquid nitrogen to the main junction box. The boiled off nitrogen gas returned from the cryostats is used for thermal shielding of the distribution line and let out to the atmosphere at the main box.

The cryostat has a helium vessel of 40 l capacity connected to the recovery system via a manual valve and a relief valve (set at 0.7 bar), and two blow off valves set at 1.7 bar for over-pressure safety. In addition, the He vessel has a pressure transducer and a liquid He level sensor. Silicon diodes are mounted on the relief valve ports and are used for remote monitoring of the temperature in the neck zone to trigger an audio-visual alarm in the control room. This over-pressure warning has resulted in a failsafe and efficient operation of the cryogenic system.

The cold gas after the JT stage in the cold box is used for the cool down of the modules starting from ambient temperature. An empirical procedure has been evolved to make a smooth switchover on different return paths in the cold box. The entire LINAC comprising all 8 cryostats is cooled simultaneously and a complete cool down is typically achieved in 3-4 days. The plant is designed to work automatically and the control is based on a Siemens SIMATIC S7-400 PLC system. We have developed a control system for the remote operation of the plant from the accelerator control room using the Siemens visualization software platform, WINCC.

Table 1 gives details of estimated and measured heat load. Actual total heat load of 180 W was observed for the whole system without RF power. Therefore, the available cooling power for RF load is only 120 W, which

is not adequate. Hence during the user cycle, the refrigerator was operated with liquid nitrogen precooling. The refrigeration power can be enhanced by a maximum of 150 W with a full precool.

Table 1: Estimated and Actual Heat Load

	Estimated Heat load		Actual Heat load
	Phase I	Phase II	
Distribution box, main box, and Trunk line	16W	16W	50W
Transfer tube and cryostat	4x12W=48W	4x12W=48W	130W
RF power load (SB + Modules)	12x6W=72W 1 x 4W =4W	16x6W=96W	172W
Total (Phase I+II)	300W		352W

RF POWER AND PHASE SETTINGS

In order to maintain a stable phase and amplitude of the electric field in the cavity, Electronics Division, BARC has developed the RF controller cards based on a self-excited loop (SEL) with phase and amplitude feedback [5]. The RF power is fed to each resonator using this controller card with a solid state 150 MHz, 150 W RF power amplifier. It is essential to calibrate the RF output power as a function of the controller card settings. Fig. 3 gives a schematic representation of the calibration procedure. A reference signal at 0 dBm is given to the input of the controller card and by varying the RF level from the controller, the output power of the amplifier is measured at the resonator end terminated with a 50 Ω load. The output power is measured by an in-line power meter and at the side port of a calibrated directional coupler.

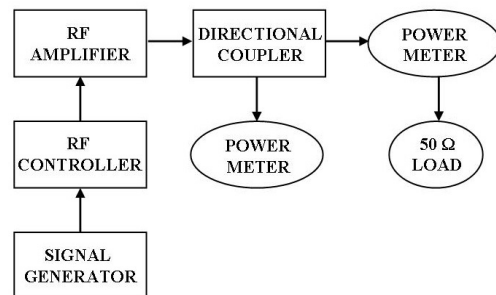


Figure 3: Power setting procedure for the QWR.

The voltage pickup for each resonator at the desired power setting (6 W) is recorded under critical coupling condition. These pickup values are monitored during the accelerator operation. The quiescent power from the amplifier is set to 50 W and the variable power coupler is adjusted to achieve the necessary over-coupling and the field amplitude in the cavity as measured for the critical coupling at 6 W setting.

Synchronous Phase Settings

As the phase of the electric field in each of the cavities can be set independently, it is possible to accelerate a variety of ions (Q , M) over a wide range of velocities (β). Furthermore, to maintain a periodic time focusing of the bunched beam over the length of the LINAC, the accelerating cavities need to be set at synchronous phase angles (Φ_{res}) corresponding to time focusing or defocusing.

The reference phase setting of the controller (Φ_{ref}) for each individual resonator needs to be determined as a function of Q , M and β of incident ions. In order to set these phases, it is necessary to measure the phase offsets (Φ_0) for each resonator. The phase offset for each resonator control circuit is independent of the beam and depends only on the hardware. The phase of the RF field in each resonator can be expressed as:

$$\Phi_{\text{res}} = \omega t + \Phi_{\text{ref}} - \Phi_0 \quad (1)$$

where ω is the RF frequency and $t = l/\beta$ is the arrival time of the beam after the drift length l from the preceding cavity. The Φ_0 can be extracted from Φ_{ref} values corresponding to zero energy gain, namely at $\Phi_{\text{res}} = 0$,

$$\Phi_{\text{ref}} = \Phi_0 - \omega t \quad (2)$$

Both the $\Phi_{\text{res}} = 0$ (time focusing) and $\Phi_{\text{res}} = \pi$ (time defocusing) correspond to zero energy gain and were measured for different beams (C, O and Si) over a wide range of velocities ($\beta \sim 0.05$ to 0.12) to extract the phase offsets for all cavities.

We have developed a program to optimize the longitudinal phase space ($\Delta E - \Delta t$) at the target position based on a complete non-linear algebra using the measured resonator field values. The program tracks the evolution of the longitudinal phase space for all 2^N configurations corresponding to both time focusing (-20°) and time defocusing ($+20^\circ$) of N resonators. The LINAC Phase I (Superbuncher and M1 to M3) and Phase II (M4 to M7) are computed sequentially. For the Phase I, the starting 2D Gaussian distribution with $\sigma_t \sim 0.375$ ns, $\sigma_e \sim 0.05$ MeV, is taken from longitudinal phase space measurements of the bunched beam at the injection of the LINAC. For the Phase II, the starting phase space is taken as a bounding 2D Gaussian distribution describing the output of the Phase I. Fig. 4 shows the calculated phase space for a distribution of 1024 rays at various points during the acceleration in the Phase I.

From the outputs corresponding to all 2^N configurations, a subset of solutions satisfying criteria of a compact phase space throughout the accelerating length (minimum ΔE and ΔT) is chosen. For any of these configurations, the given set of Φ_{res} is used to calculate the reference phase settings (Φ_{ref}) for all resonators using Eq. 1. A final configuration corresponding to an optimal phase space at target (determined by measurement of the

transmission and the time structure) is then selected from this subset.

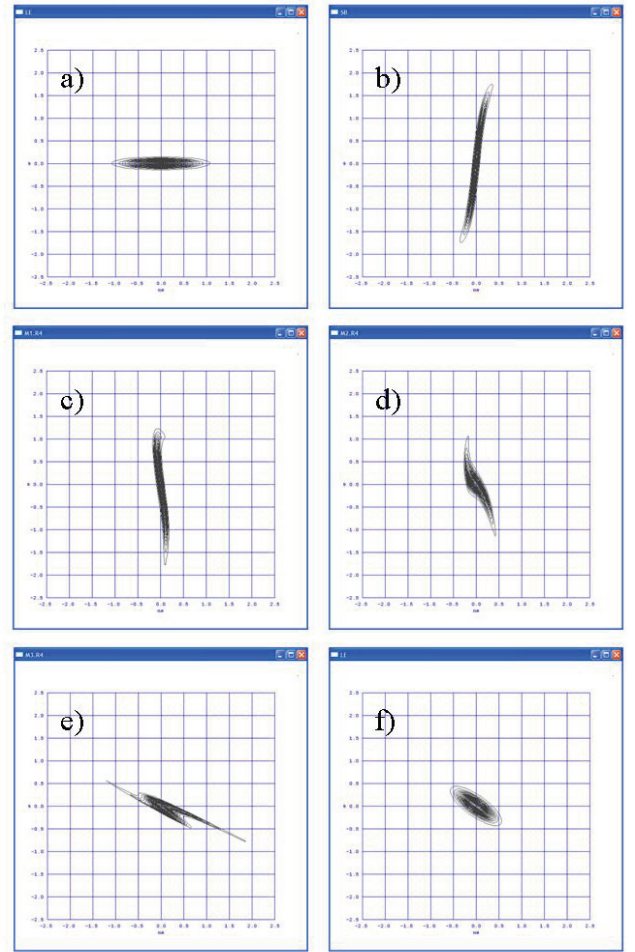


Figure 4: Longitudinal phase space (see text for details): a) at LINAC injection, b) after Superbuncher, at the entry of M1, c) after M1, at the entry of M2, d) after M2, at the entry of M3, e) after mid-bend, at the Phase II entry, f) equivalent distribution for the Phase II corresponding to (e).

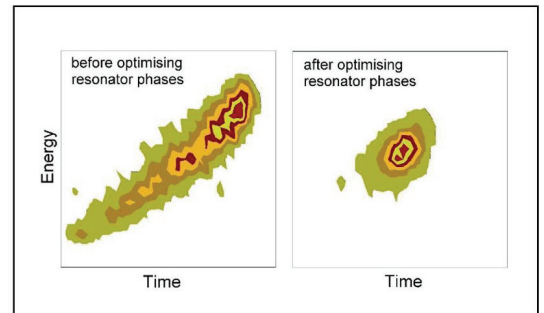


Figure 5: Longitudinal phase space across the mid-bend.

As a part of initial diagnostic tests, detailed measurements were carried out using microsphere plate, BaF₂ detector and Silicon detector. Fig. 5 shows the longitudinal phase space measured for scattered Si beam

from a thin Au target at the entrance of the LINAC Phase II [6].

This procedure described above has been established with several beam trials and eases the setting up of beam acceleration for routine operation.

RF Stability

A stable operation over a period of several days is essential to deliver the beam for experiments. This necessitates very high stability for the RF control system. The control circuit is designed with a phase stability better than 0.1 and amplitude stability better than 0.1% [5]. At startup, typically 30 minutes are required for the stabilization of the controller circuits and the power amplifier. Detailed stability tests were carried out over the period of several days, where both amplitude and phase errors were recorded for each controller card and amplifier. The high power devices employed in the RF amplifier and the controller cards are prone to drift as a function of the ambient temperature. However, this does not adversely affect the acceleration as the phase and amplitude in the controller circuit is derived from a low power section of the circuit, which is fairly independent of the ambient temperature.

CONTROL SYSTEM

A CAMAC based accelerator control system based on a master-slave configuration has been developed [7]. A local control station (LCS) consisting of a PC interfaced to CAMAC crates with analog and digital modules and the RF electronics controls up to eight cavities (i.e. two modules). These LCS in the accelerator hall are interconnected via Ethernet to the main control station (MCS) located in the control room. This system allows simultaneous setting up of parameters for the different LINAC modules with the MCS enabling overall control during the beam tuning. The control software developed using JAVA operating on Linux OS, consists of two layers, namely, a scanner and a graphical user interface (GUI). The scanner acts as a TCP/IP server and directly accesses the CAMAC crates, while GUI connects to the scanner via TCP/IP.

INSTRUMENTATION

Interface and control electronics has been developed for various cryogenic parameters and beam line devices. The MCS in the control room communicates to different addressable local control stations (μ C based) via Ethernet to serial link.

A local multi-channel, multiplexed cryo-control station, controls and monitors the cryogenic valves, level sensors for both LHe and LN₂, pressure and temperature of each cryostat. Two such cryo-control stations, catering to four cryostats each, have been installed.

A large number of locally developed Faraday Cups and beam profile monitors (BPM) have been installed in the beam lines. A 24 channel multiplexed, control and

readout unit with a 12 bit ADC has been developed for Faraday cups as well as for BPMs.

A magnetic X-Y steerer designed using a standard motor stator with sin-cos windings to provide a uniform magnetic field over a ~ 50 mm diameter and length ~ 100 mm have been installed at several locations. All the power supplies for magnetic elements like steerers, quadrupoles and dipoles are individually controlled from the MCS via the ethernet to serial link.

ACCELERATOR OPERATION

Carbon, Oxygen and Silicon beams were accelerated and delivered at various experimental stations in user hall I (Table 2). Energy of the accelerated ions was measured by the magnetic field of the bending magnet. The number of resonators used for acceleration is varied as per the user requirement. The field in each resonator was also similarly measured using energy gain of the DC beam. Initial beam trials have yielded average energy gain of 0.4 MV/q per cavity corresponding to 80% of the design value. Beam transmission from entry to exit of LINAC was found to be 80%, without using any beam steerers. Timing detectors are provided at injection of the LINAC, at entry of the Phase II and after the switching magnet in user beamlines. Typically, beam transmission at target after collimation was found to be $\sim 50\%$ of that at the entry to the LINAC. The beam timing measured at target was found to be excellent $\sigma \sim 250$ ps (see Fig. 6).

Table 2: Beams accelerated through LINAC

Beam	E_{pell} (MeV)	E_{LINAC} (MeV)	E_{total} (MeV)
¹² C	82.5	37.5	120.0
¹⁶ O	93.6	22.1	115.7
¹⁹ F	94.0	50.2	144.2
²⁸ Si	90-100	48-109	138-209

With the procedure described in the preceding section, typically 6-8 hours are needed for tuning the beam to the experimental station.

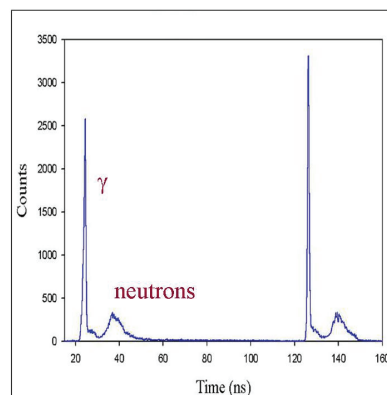


Figure 6: Time spectrum with BaF₂ detector at target position ($\sigma_{\text{beam}} \sim 250$ ps).

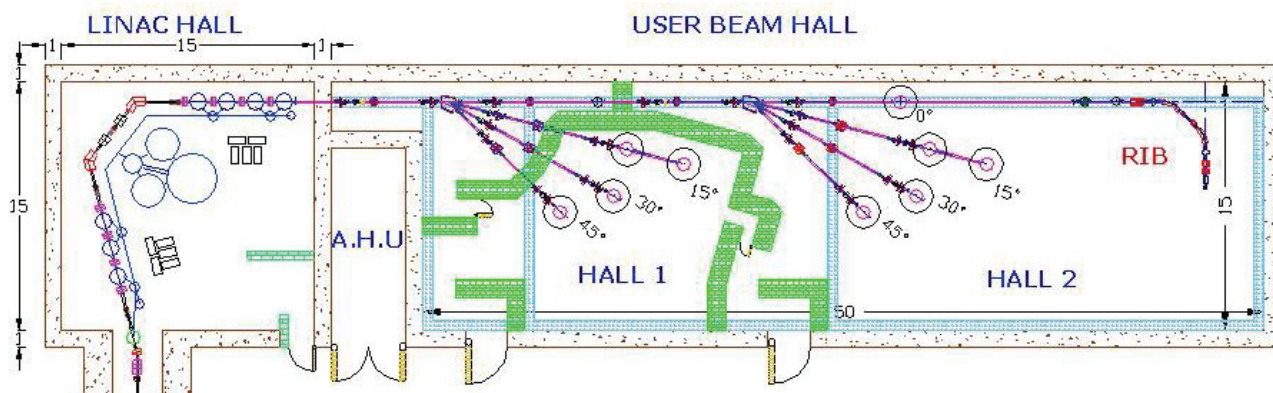


Figure 7: A Schematic layout of the experimental facilities.

EXPERIMENTAL FACILITIES

The complete layout of experiment halls together with LINAC is shown in Fig. 7. A total of 7 beam lines are planned in two separate user areas. The research programmes cover a wide span of disciplines like Nuclear Physics, Atomic, Molecular and Cluster Physics, and Condensed Matter Physics. Several new experimental facilities are planned. For example, BGO/NaI multiplicity filters, BaF₂ array for high energy gamma ray studies, 1 x 1 m² plastic scintillator array for neutron spectroscopy have already been installed. The Indian National Gamma Array (INGA) a 24 element Clover array for high resolution in-beam gamma spectroscopy, will be commissioned at PLF, Mumbai in near future. A Momentum Achromat for light Radioactive Ion experiments (MARIE) and a large solid angle, modular, segmented array of 50 detectors (Si+CsI) are under development.

CONCLUSION

The superconducting LINAC booster at PLF, Mumbai is fully operational. For acceleration of different beams, an algorithm for RF power and phase settings of the individual resonators has been devised. We plan to extend routine operations to heavier beams (up to Ni). The development of digital RF controller cards and improvements to GUI are being planned for better performance. We also propose to upgrade the cryogenics system so that LINAC can be operated without LN₂ precool.

ACKNOWLEDGEMENT

We would like to thank Electronics Division and CDM, BARC, Central Workshop and Low Temperature Facility, TIFR, and the Pelletron-LINAC staff for their dedication, hard work and support.

REFERENCES

- [1] R.G. Pillay, "Superconducting LINAC at BARC-TIFR heavy ion accelerator facility", Proceedings of DAE symposium on Nuclear Physics, 52, 182 (2007).
- [2] B. Srinivasan et. al., *Pramana*, 57, 651 (2001).
- [3] M.B. Kurup, *Pramana*, 59, 811 (2002).
- [4] M.K. Pandey and R.G. Pillay, *Indian Journal of Pure and Applied Physics* 35, 168 (1997).
- [5] G. Joshi et. al., "Resonator Controller for the Superconducting LINAC", Proceedings of Symposium on Intelligent Nuclear Instrumentation 2001, p. 105 (2001).
- [6] B. Srinivasan et. al., "Longitudinal phase space of LINAC beam" Proceedings of DAE Symposium on Nuclear Physics, 46B, 450 (2003).
- [7] S.K. Singh et. al., "Experiences with RF control system for BARC TIFR LINAC", Proceedings of DAE Symposium on Nuclear Physics, 47B, 486 (2004).

MULTIPLE CHARGE STATE ION BEAM ACCELERATION WITH AN RFQ LINAC

J. Tamura, Tokyo Institute of Technology, Tokyo and RIKEN, Saitama, Japan
 T. Hattori, N. Hayashizaki, T. Ishibashi, T. Ito
 Institute of Technology, Tokyo, Japan
 T. Kanetsue, Kyushu University, Fukuoka, Japan
 H. Kashiwagi, Japan Atomic Energy Agency, Gunma, Japan
 M. Okamura, Brookhaven National Laboratory, New York, USA

Abstract

We are investigating space charge dominated beam dynamics in a Radio Frequency Quadrupole (RFQ) linac. In some accelerator systems, desired ions with different charge state ions are simultaneously injected into an RFQ linac. To describe the evolution of the multi charge beam inside the RFQ, we did particle simulation by using Particle-Mesh (PM) method. Here the high-intensity carbon beam made up of C^{4+} , C^{5+} and C^{6+} was applied to the simulation (C^{5+} was set to the designed ion). The space charge contributions to the transverse emittance growth and to the transverse and longitudinal particle motions are presented.

INTRODUCTION

The beam current from recent heavy ion sources are high enough that the self fields cannot be neglected in comparison to the applied fields. Some of the heavy ion sources are being developed to generate highly ionized particles. In these kinds of sources, desired ions with different charge state and contaminating particles are generated and extracted. In some heavy-ion accelerator systems, such as Electron Beam Ion Source (EBIS) Project at Brookhaven National Laboratory (BNL) [1] and Direct Plasma Injection Scheme (DPIS) [2], ions, which have close charge to mass ratio, are simultaneously injected into an RFQ linac with desired species.

In the EBIS-based pre-injector for Relativistic Heavy Ion Collider (RHIC) at BNL, which consists of EBIS, RFQ and Inter-digital H mode Drift Tube Linac (IH-DTL), the designed ion is Au^{32+} . However Au ions with different charge state are generated and extracted in the EBIS and transported through the Low Energy Beam Transport (LEBT) and injected into the RFQ linac.

The DPIS is the new method combining a Laser Ion Source (LIS) and an RFQ linac without an LEBT. In the DPIS, multiple charge state ions are extracted from the laser-produced plasma at the entrance of the RFQ. Therefore simultaneous injection of different charge state ions is unavoidable.

It is necessary to consider how the other charge state ions affect the condition of the desired ions especially in high-current accelerator systems. To evaluate the multi-charge effect, here we focus on the RFQ acceleration with numerical simulation using Particle-Mesh (PM) method [3] [4].

Linacs

SIMULATION METHOD

Particles are forced by an external RF field of RFQ and internal space charge field. In this simulation, the external field was defined as two-term potential function [5] and the space charge field was obtained by solving three-dimensional Poisson equation inside the calculation box. This enables us to directly calculate the space charge field caused by the distribution of multiple charge ions. At each step in time, the simulation solves for the fields generated by the particles, and then produces particle motion.

RFQ Electric Field

The electric field is obtained from the gradient of the two-term potential function. The potential function is decided by the RFQ electrode parameters of intervene voltage, cell length, minimum radial aperture and modulation factor. Here, the parameters of our RFQ linac were used for the simulation. The RFQ linac (100MHz, 4-rod type, 118cell) was designed to accelerate high-intensity C^{4+} beam from an input energy of 20 keV/u to 100 keV/u (Fig. 1 and Fig. 2).

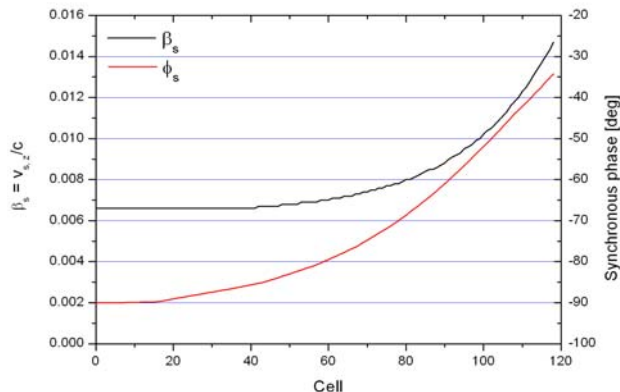


Figure 1: Normalized velocity of the synchronous particle and the synchronous phase at each cell of the RFQ. The cell length is equal to $\beta_s \lambda / 2$ (λ is the wavelength of the RF).

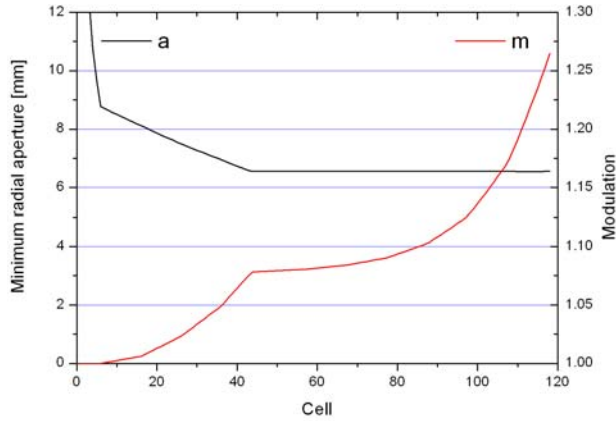


Figure 2: Minimum radial aperture and modulation factor at each cell of the RFQ.

Space Charge Electric Field

The space charge field is calculated inside the three-dimensional calculation box. The size of the box is transversely fixed to $20\text{mm} \cdot 20\text{mm}$ and longitudinally set to $\beta\lambda$. This was decided by averaging β of the surviving, desired ions. This box was partitioned to $40 \cdot 40$ volumes transversely and 80 volumes longitudinally.

To calculate the charge density on the discrete grid points from the continuous particle positions, the electric charges of the macro-particles were assigned to the grid points by first-order weighting. The space charge potential on the grid points was obtained by solving Poisson equations using successive overrelaxation method. The boundary conditions of the calculation box is Dirichlet ($u = 0$) in the transverse direction and periodic in the longitudinal direction. The potential at the grid points inside the RFQ electrodes were set to zero ($u = 0$). The iteration was stopped when the maximum absolute value of the change rate became smaller than 0.001 ($(u_{\text{new}} - u_{\text{old}})/u_{\text{new}} \leq 0.001$) with the overrelaxation parameter of 1.8. The space charge field at the grid points was calculated by the central difference of the potential. The space charge field at the particle positions were obtained by linearly interpolating the space charge field at the nearest grid point as in the charge assignment.

Integration of the Equation of the Motion

The macro-particles are moved by both external RFQ field and space charge field described above. The equation of motion was integrated by using the leapfrog method. Then Δt was set to one RF cycle divided by 16 (10/16 ns). This means that 994 computational steps in time are needed for 118 cells of the RFQ electrode.

Conditions for Particle Simulation

In this simulation, multiple charge state carbon beam made up of C^{4+} , C^{5+} and C^{6+} was injected into the RFQ linac with same normalized emittance of $0.5 \pi \text{ mm-mrad}$. The C^{5+} beam have the designed input energy of 20 keV/u while C^{4+} and C^{6+} beam have the energy of 16 keV/u and 24 keV/u due to the same extraction voltage. The particles were randomly distributed inside the four-dimensional

ellipsoid defined by the Twiss parameters. 1 macro-particle represents about 2500 particles.

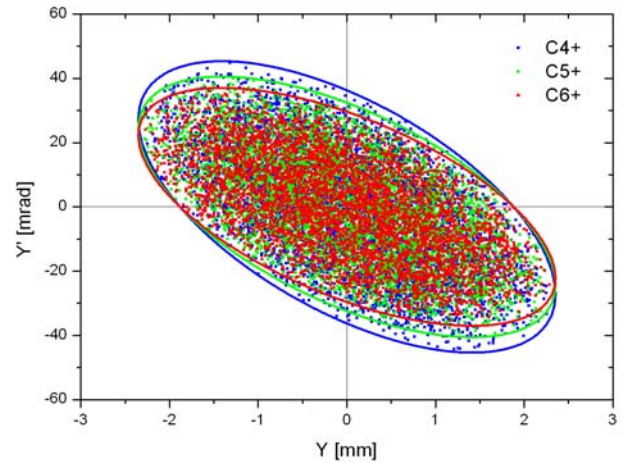


Figure 3: Initial distribution of the particles on the vertical phase space.

Table 1: Twiss Parameters for Initial Ellipse

	α	β (mm/mrad)	ϵ (mm-mrad)
C^{4+}	0.750	0.0648	85.310
C^{5+}	0.750	0.0725	76.301
C^{6+}	0.750	0.0794	69.658

The applied intervane voltage is 96 kV, which is the designed voltage to accelerate C^{5+} with input energy of 20keV/u to the designed output energy of 100 keV/u.

When a particle hits the electrode or goes transversely out of the calculation box, the particle is eliminated from the calculation. When a particle goes longitudinally out of the box, the particle comes back to the box from opposite side keeping the same x , v_x , y , v_y , v_z . Particles which have energy difference of more than 250k eV are excluded from the velocity and rms averaging.

RESULTS

For the beam dynamics simulation, a multi-charge state ion beam (shown in Table 1) was injected into RFQ linac.

Table 2: Beam Current of each Charge State injected into RFQ

Total (mA)	C^{4+} (mA)	C^{5+} (mA)	C^{6+} (mA)
3.0	0.8	1.0	1.2
12.0	3.2	4.0	4.8
21.0	5.6	7.0	8.4
30.0	8.0	10.0	12.0

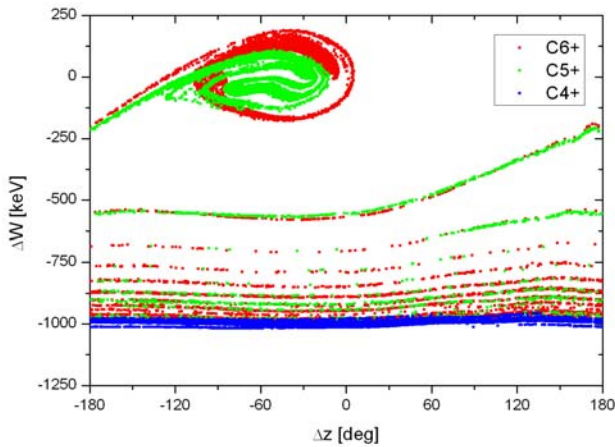


Figure 4: Longitudinal phase space at the last cell. The beam currents of each charge state are 3.2 mA, 4.0 mA and 4.8 mA for C⁴⁺, C⁵⁺ and C⁶⁺.

Transmission Efficiency

Fig. 4 shows the multi charge beam with the total current of 12.0 mA on the longitudinal phase space at the last cell. In this case, about 90% of C⁵⁺ ions can be accelerated, while all the C⁴⁺ ions are not accelerated and maintain the initial velocity due to the insufficient injection energy and intervane voltage. Due to the high injection energy, about half of the C⁶⁺ ions are not accelerated and accelerated C⁶⁺ ions are not distributed at the center of the longitudinal bucket.

Table 3 shows the transmission efficiency (both transversely and longitudinally survived) of each charge state. The transmissions of C⁵⁺ and C⁶⁺ decrease with increasing beam current.

Table 3: Transmission Efficiencies of each Charge State

Total (mA)	C ⁴⁺	C ⁵⁺	C ⁶⁺
0.0	0%	96%	70%
3.0	0%	94%	52%
12.0	0%	91%	53%
21.0	0%	90%	50%
30.0	0%	83%	47%

Transverse Emittance Growth

Fig. 5 shows the transverse rms-emittance growth of C⁵⁺. The C⁵⁺ emittance growth of single charge beam (C⁵⁺) was plotted in black and red (horizontal and vertical). The C⁵⁺ emittance growth of multi charge beams (C⁴⁺, C⁵⁺, C⁶⁺) was plotted in green and blue (horizontal and vertical). The ellipse parameters of injected beam are matched in beam current of 0 mA case. Therefore this figure includes a space charge effect not only from the particle distribution but from radial mismatching.

If the total current is same, single charge beam has larger emittance growth than multi charge beam. One reason can be considered that each charge state beam has

its own oscillations both transversely and longitudinally. The period of these oscillations depend on the charge to mass ratio. This results in a smaller space charge effect to the desired particles than in a single charge beam.

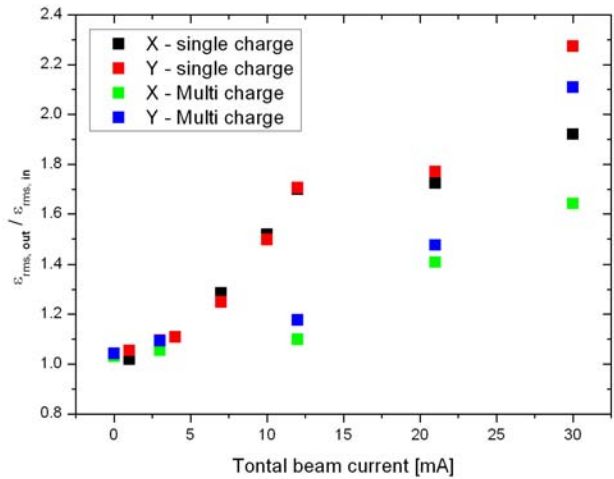


Figure 5: Transverse rms-emittance growth of C⁵⁺ beam.

We can see the longitudinal example in Fig. 6 and Fig. 7. These are the longitudinal phase space at the 18th cell. Both have the same total current of 12 mA. At the 18th cell, synchronous phase is to -89.4 deg for C⁵⁺ acceleration. The width of the separatrix is almost 360 deg. Particles inside the separatrix are successively accelerated by longitudinal restoring forces. This forces produce phase and energy oscillations about the synchronous particle. Due to the different initial energy and the different bucket shape, each charge state ion moves differently on the longitudinal plane. From these figures, we can see that space charge density in multi charge beam is less localized than in single charge beam because C⁴⁺ and C⁶⁺ ions are distributed in the longitudinal direction with uniformity. In Fig. 6, C⁵⁺ ions can rotate around the synchronous particle (center of the phase space), while in Fig. 7, C⁵⁺ ions bounce at the center by the strong space charge repulsion force.

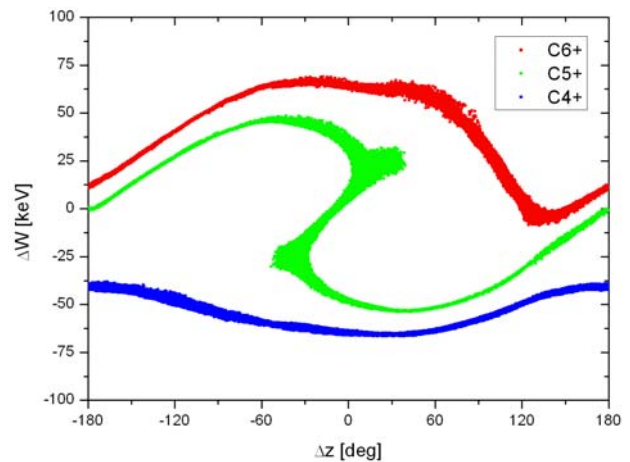


Figure 6: Longitudinal phase space of multi charge beam with total beam current of 12 mA at 18th cell.

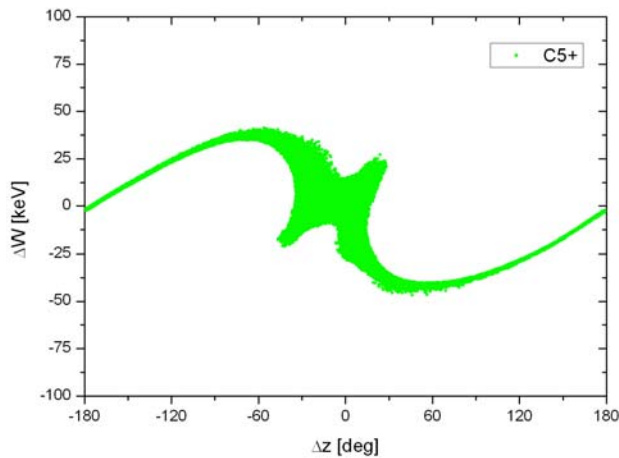


Figure 7: Longitudinal phase space of single charge beam with beam current of 12 mA at 18th cell.

CONCLUSION

To describe the evolution of the beam inside the RFQ, we simulated the multiple charge state ion beam acceleration. Due to the different charge to mass ratio, each charge state beam oscillates differently in both transverse direction and longitudinal direction, influencing each other. As an example, we saw the difference in how the beam is bunched even under the same total beam current. This can affect the transverse motion of particles. In high current RFQ acceleration like DPIS, to estimate the effect to the desired ions from the

other ions will be more important. We need to continue this study by considering the charge distribution, particle distribution and beam matching of the injected beam.

ACKNOWLEDGMENTS

I would like to thank H. En'yo of Radiation Laboratory, RIKEN for support of this presentation, J. Alessi and D. Raparia of Collider-Accelerator Department, Brookhaven National Laboratory for valuable advice and encouragement and R. Dabrowski of City College of New York for reading the manuscript.

REFERENCES

- [1] J. Alessi et al., "Status of the Ebis Project at Brookhaven", Proceedings of LINAC 2006, Knoxville, Tennessee USA, p. 385.
- [2] M. Okamura et al., "Direct plasma injection scheme in accelerators", Rev. Sci. Instrum. 79, 02B314 (2008).
- [3] R. W. Hockney and J. W. Eastwood, "Computer Simulation Using Particles", (Taylor & Francis Group, New York, 1988).
- [4] C. K. Birdsall and A. B. Langdon, "Plasma Physics via Computer Simulation", (Taylor & Francis Group, New York, 2005).
- [5] Thomas P. Wangler, "RF Linear Accelerators", (WILEY-VCH, Weinheim, 2008).

UPGRADE OF THE HIT INJECTOR LINAC-FRONTEND

S. Yaramyshev, W. Barth, M. Maier, A. Orzhekhovskaya, B. Schlitt, H. Vormann, GSI, Darmstadt
 R. Cee, A. Peters, HIT, Heidelberg

Abstract

The Therapy Linac in Heidelberg (HIT) was successfully commissioned in 2006. Required beam parameters were reached except for the beam intensity. The achieved particle transmission for C^{4+} (design ion) is significantly lower than design. Particle losses are mainly observed in the RFQ. One critical point is the matching section of the RFQ electrodes - Input Radial Matcher (IRM). The original design requires too rigid and narrow beam Twiss-parameters at the RFQ entrance. Also the measured emittance is about twice higher compared to the design. Numerically and experimentally it was proven that the solenoid, used for the beam matching to the RFQ, is not able to provide for the necessary beam size and convergence. As it was shown by beam dynamics simulations using the code DYNAMION, a minor modification of the IRM allows for an improvement of the beam transmission (up to 50%). The proposed measure was realized for an advanced HIT-RFQ-layout, which is recently under test stage. The same modification is already proposed for the linac frontend at Italian Hadrontherapy Center (CNAO, Pavia).

INTRODUCTION

The Heidelberg Ion-Beam Therapy Centre (HIT) is the first in Europe dedicated clinical synchrotron facility for cancer therapy using high energy proton and ion beams (C, He, and O) [1]. The accelerator comprises a 7 MeV/u, 217 MHz injector linac and a 430 MeV/u synchrotron. Installation and commissioning of the linac were performed in three phases: ion sources and LEBT, 400 keV/u RFQ, and 20 MV IH-type drift tube linac (Fig. 1). The commissioning of the linac was successfully finished in December 2006 [2].

To provide for the designed intensities, a linac upgrade program has been initiated. Yet the overall achieved transmission through the injector linac is about 30% (C^{4+} design ions), mainly due to a mismatch of the beam at the RFQ entrance. Thus a detailed upgrade program has been started to exchange the RFQ with a new radial matcher design, to correct the misalignment and to optimize beam transition to the IH-DTL. The aim is to achieve a sufficient overall linac transmission above 60% [3,4].

The main goal of the beam dynamics study with the DYNAMION code [5] was to estimate the maximum possible transmission for the HIT linac front-end system, namely for the matching solenoid and the RFQ. The commissioning results before the matching solenoid showed good coincidence with previous design calculations. As a first step, an adequate description of the linac elements was carried out. Specifications of the RFQ [6] and of the solenoidal field, available from the measurements or external calculations, were used for the simulations. Additionally, the measured misalignments of the linac elements were taken into account.

Emittance Measurements

During commissioning emittance measurements were performed behind the LEBT (without installation of the RFQ). The distance from the solenoid to the RFQ entrance is only about 10 cm; the emittance measurement device (slit-grid) was positioned 50 cm behind the solenoid. The magnetic field of the solenoid was varied in the range from 40% to 60% of the nominal value to provide for a reasonable beam size at the slit position. The measured horizontal total beam emittance (Fig. 2) is about 300 mm·mrad for 90% level of intensity ($^{12}C^{4+}$; 200 μA). The measured vertical emittance is similar.

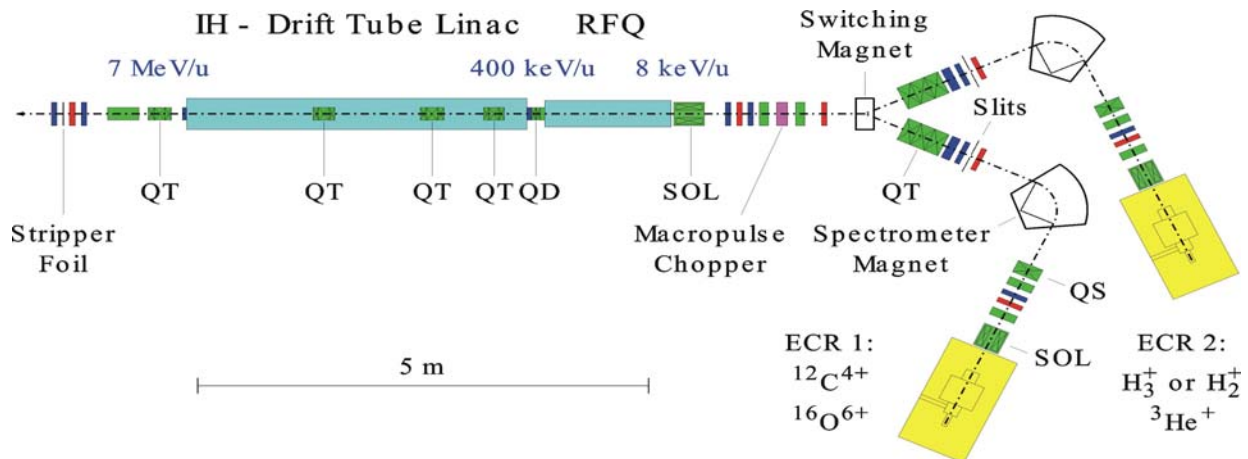


Figure 1: Layout of the HIT Injector Linac; SOL - solenoid, QD - quadrupole doublet, QT - quadrupole triplet.

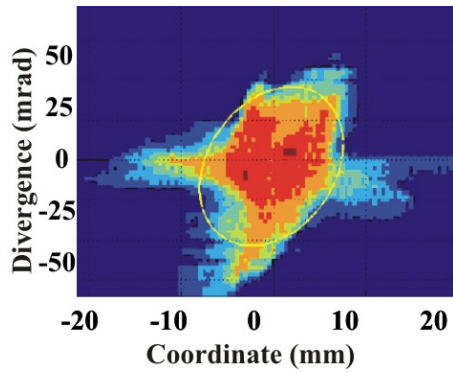


Figure 2: Measured beam emittance in the horizontal phase plane behind the matching solenoid ($^{12}\text{C}^{4+}$, 200 μA).

Input Macroparticle Distribution

A dedicated procedure for the reconstruction of the particle distribution, based on emittance measurements, was developed (Fig. 3).

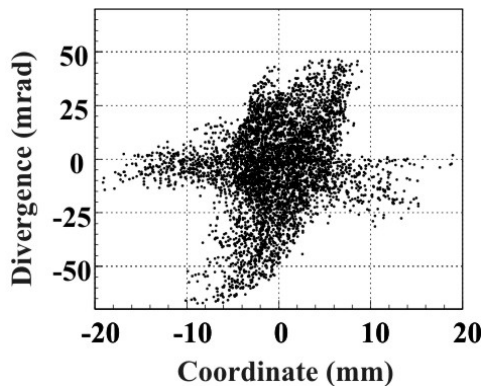


Figure 3: Macroparticle distribution based on the measured emittances ($^{12}\text{C}^{4+}$, 200 μA).

Magnetic Field of the Solenoid

Data of the magnetic field measurements along the matching solenoid were used for the reconstruction of the complete solenoidal field. As measurements were done only for dedicated points along the axis, a relaxation scheme was implemented to interpolate the magnetic field at each node of 3D field mapping. A dipole component in the field distribution was observed (Fig. 4). During commissioning the solenoid was transversally tilted to compensate the influence of the dipole component (steering) on the particle motion. Taking into account the measured displacement of the solenoid and the measured non-uniformity of the field, the particle motion was simulated backward through the solenoidal B-field as it was set during the measurements.

In 2007 the matching solenoid was replaced by a new one with improved quality of the magnetic field distribution. Nevertheless, earlier calculations of the HIT front-end particle transmission did not show an essential difference between ideal (axis-symmetrical) and real solenoidal field (with recent settings of the machine). It can be assumed that the dipole field component in the real solenoid is partly compensated by its tilt.

Linacs

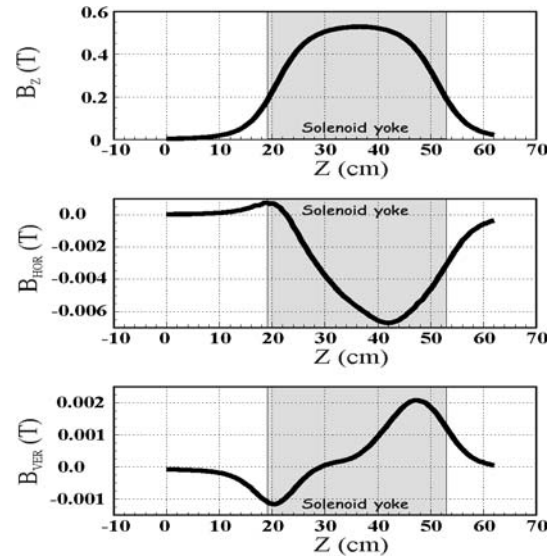


Figure 4: Measured magnetic field of the solenoid; longitudinal (top), horizontal (middle) and vertical (bottom) component on axis.

Representation of the RFQ

Available geometrical data from the specifications (cell length, aperture, width and rounding of the electrodes) were used for an advanced RFQ description. Dedicated subroutines of the DYNAMION code precisely calculate the 3D electrical field, solving the Laplace equation for the potential:

- RFQ Input Radial Matcher (IRM): The area for the grid is formed by the surface of electrodes / flange of the tank. 3D mapping of electrical field is calculated and used for the simulations.
- RFQ regular cells: The area for the grid for each cell is formed by the surface of the modulated electrodes; the potential is approximated with a classical 8-term series assuming the quadrupole symmetry; coefficients of the series are introduced into calculations as input data; 3D electrical fields are calculated as corresponding derivatives of the potential.
- DTL gaps (rebuncher section): The area for the grid is formed by the surface of the tubes; the potential and the 3D electrical fields for each gap, including the slack of the field into tubes, are approximated with 30-term series assuming an axial symmetry; coefficients of the series are introduced as input data.

RFQ ACCEPTANCE

A normalized acceptance V_k for each regular RFQ cell can be calculated from the solution of the Floquet equation as $V_k = v_f (a^2 / \lambda)$, where v_f is the minimum of the phase advance μ on the focusing period, a - aperture of the cell, λ - wave length of the operating frequency [7]. The local acceptance along the HIT-RFQ for C^{4+} beam is shown on Fig. 5. The minimum value (dashed line)

corresponds to 327 mm·mrad (total, unnormalized) at the RFQ input energy of 8 keV/u.

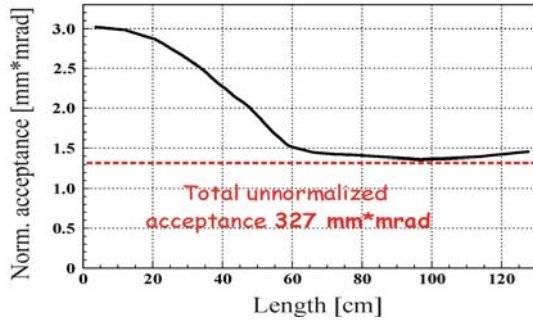


Figure 5: Local acceptance along the HIT-RFQ; the dashed line shows the unnormalized total RFQ acceptance related to the input energy.

The orientation of the acceptance at the RFQ entrance was calculated by a dedicated code [8]. It provides for backward transformation of the beam envelopes, matched at the first regular RFQ cell, taking into account the given shape of the Input Radial Matcher.

Alternatively, the RFQ acceptance can be obtained from the beam dynamics simulations using a wide four-dimensional grid in the transverse phase space as an input particle distribution. In the DYNAMION code each particle has a unique ID-number. The particles, accelerated to the final RFQ energy, are selected in the input distribution and represent the acceptance at the RFQ entrance (Fig. 6).

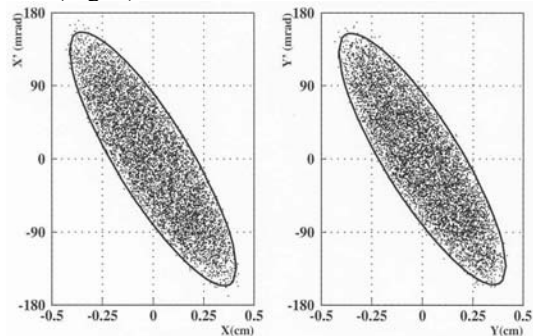


Figure 6: Simulated horizontal and vertical RFQ acceptance; ellipses correspond to 99% of intensity.

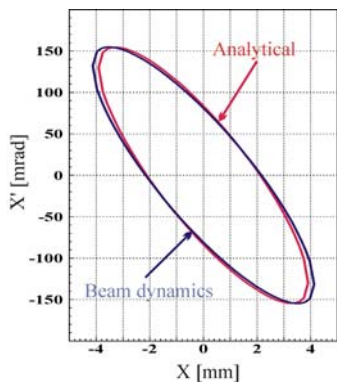


Figure 7: The horizontal acceptance at the HIT-RFQ entrance calculated analytically and obtained from beam dynamics simulations.

The "simulated" acceptance for both transverse planes is about of 330 mm·mrad, what corresponds well to the analytical calculations of the minimum local acceptance along RFQ (Fig. 7).

THE RFQ TANK DEFORMATION

During commissioning the alignment of the electrodes has been checked and a strong bending due to mechanical stress on the structure was observed. Such deformation is measured also for the CNAO RFQ [9]. A new robust tank design with thicker walls (6 mm instead of 4 mm), extra supports and 3 instead of 4 fixation points should solve this problem. The electrodes measured of the CNAO-RFQ have a maximum vertical misalignment of 0.8 mm. Dedicated beam dynamics simulations were performed assuming a sinusoidal shape of electrodes $d = 0.8 \sin(\pi z/L)$, where L is the length of the electrodes.

For the simulations the regular electrodes are represented by a set of 10 linear parts; each part (also IRM) has a vertical shift and tilt (Fig. 8).

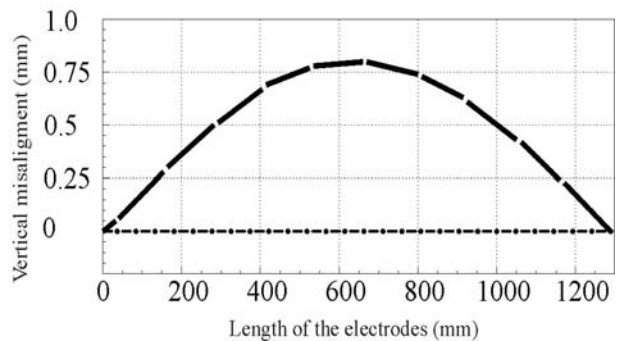


Figure 8: Representation of the HIT-RFQ misalignment, assumed for beam dynamics simulations.

Applying the above described procedure, the acceptance of the deformed RFQ was calculated using the results of beam dynamics simulations (Fig. 9). For the normal case an RFQ acceptance is about 330 mm·mrad for both transverse planes, while in case of the deformed electrodes it is about 180 mm·mrad only.

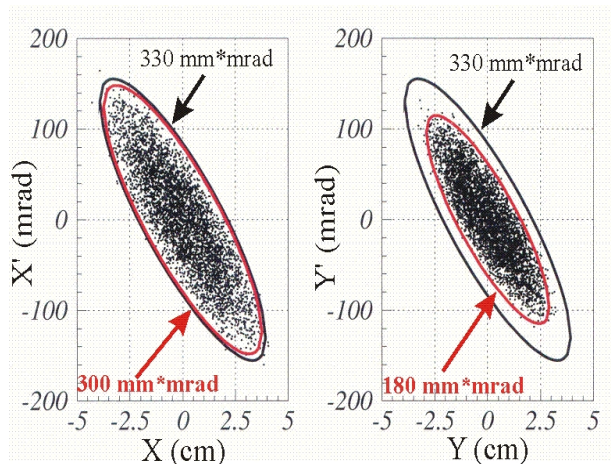


Figure 9: The horizontal and vertical RFQ acceptances with ideal (black) and deformed (red) electrodes.

FRONT-END BEAM DYNAMICS SIMULATIONS

Forward simulations through the matching solenoid with the measured field (design value), the measured tilt and using the reconstructed particle distribution were performed. An ideal alignment of the electrodes was assumed for this study. The calculated horizontal macroparticle distribution at the RFQ entrance is shown on Fig. 10; vertical one is similar. The ellipse represents the RFQ acceptance.

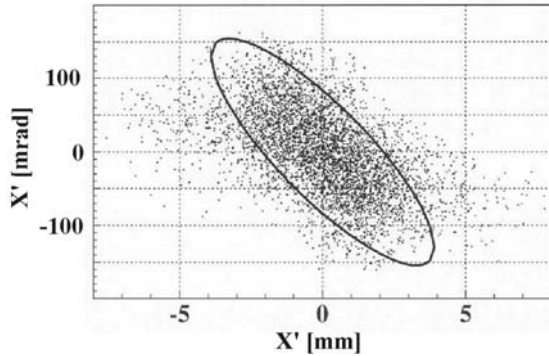


Figure 10: The calculated horizontal macroparticle distribution at the RFQ entrance.

A significant number of particles are outside the acceptance even with similar values of beam emittance and RFQ acceptance. This mismatch was illustrated by simulations of the RFQ transmission with C^{4+} ions varying the magnetic field of the solenoid (Fig. 11).

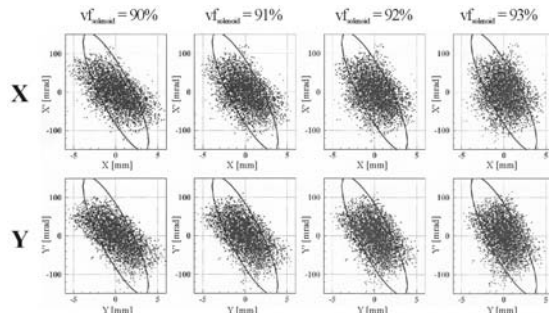


Figure 11: The horizontal (top) and the vertical (bottom) macroparticle distribution at the RFQ entrance for different values of the solenoidal B-field; 100% corresponds to the design value.

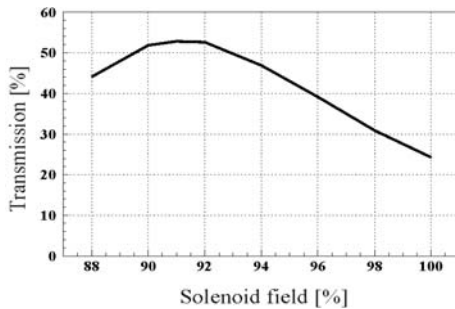


Figure 12: Calculated RFQ transmission as a function of the solenoidal B-field; 100% corresponds to the design value.

A maximum particle transmission (Fig. 12) of about 50% was calculated; the measured one is about 30%.

The matching solenoid is already placed as close as possible to the RFQ. Due to the technical limitations this distance can not be decreased. With recent machine settings the only magnetic field of the solenoid can be optimized for a beam matching to the RFQ. The beam spot and the convergence (95% and 90% level of intensity) in dependence on the magnetic field of the solenoid are presented on Fig. 13. The dashed lines show the beam parameter required by the design of the RFQ Input Radial Matcher. Obviously the necessary beam spot is reached at B-field about of 91% of the design, while the obtained angle is far away from the necessary value.

Generally, the beam can be matched to the RFQ with significantly higher B-field and simultaneously shorter distance from the solenoid to the RFQ. For the HIT-frontend it is not possible due to the technical reasons: field is already high; distance is already as short as possible.

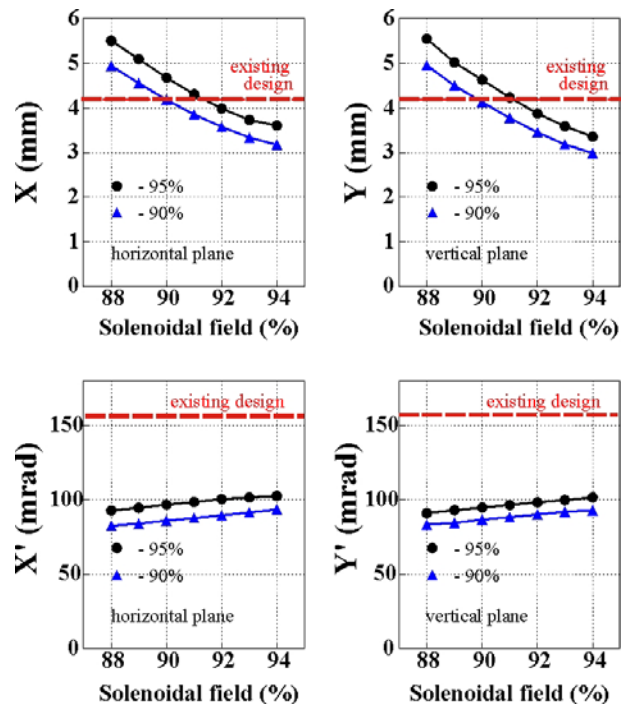


Figure 13: Beam spot and convergence at the RFQ entrance as a function of the solenoidal B-field; dashed lines represent the design requirements.

NEW INPUT RADIAL MATCHER DESIGN

Generally, the particle transmission for the whole front-end system can be significantly increased by changing the matching conditions at the RFQ entrance. It requires minor modifications at the beginning of the RFQ electrodes. Such optimization was proposed for the design of the HSI-RFQ at GSI [10]. An upgrade of the IRM was successfully realized in 2004. The calculated gain in the particle transmission was experimentally verified [11].

To improve the transition of the HIT front-end the IRM was redesigned. Originally the length of the electrodes

with changing aperture was only 8 cells ($8\beta\lambda/2$). The following 8 cells were designed with a small modulation (amplitude less than $\pm 2\mu\text{m}$) not influencing the longitudinal particle motion. The aperture along the new increased IRM (16 cells) follows a special law to provide for improved beam matching (Fig. 14, right), not in accordance with the classical model. The length of the modified IRM is about 4.5 cm. The total length of the electrodes (128 cm) is not changed.

The improved orientation of the acceptance at the RFQ entrance (Fig. 14, left) was calculated using the DYNAMION code and dedicated semi-analytical algorithms. The new IRM design requires for about 50% lower beam convergence ($\alpha = 0.7$, $\beta = 0.058$ mm/mrad) compared to the old design ($\alpha = 1.6$, $\beta = 0.047$ mm/mrad). With the same particle distribution and an optimum solenoidal field a significantly higher transmission was obtained: 75% instead of 50%.

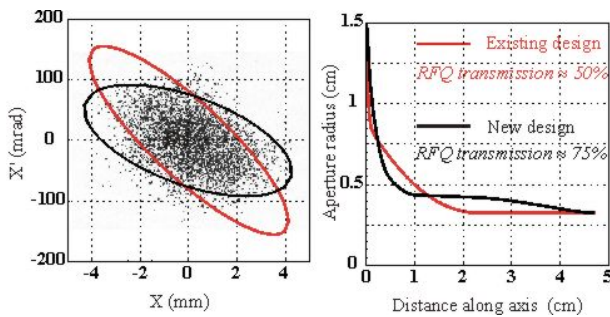


Figure 14: Comparison of the new (black) and the old (rod) design of the IRM: acceptance and calculated particle distribution at the RFQ entrance (left) and the aperture along the IRM-section (right).

The newly fabricated electrodes were installed into the new HIT-RFQ. After a first measurements campaign in Risoe (Denmark) [12] the RFQ was transported to IAP (UNI-Frankfurt, Germany) for further alignment of the electrodes and the rebuncher section. The new design of the IRM is also realized for a second generation RFQ which is recently under commissioning at Marburg Therapy Center (Germany). A substitution of the electrodes for the CNAO-RFQ is already proposed.



Figure 15. Plastic model (GSI construction department) and copper test piece of the RFQ Input Radial Matcher (NTG Neue Technologien GmbH).

CONCLUSION

Advanced beam dynamics simulations by means of the DYNAMION code with C^{4+} design ions demonstrate a low particle transmission of about 50% for the HIT front-end system with recent machine settings. The measured transmission is about 30% only. The most serious reasons are beam mismatch at the RFQ entrance and a significant tank deformation. Minor modification of the RFQ Input Radial Matcher allowed for the increase of calculated transmission up to 75% with the same machine settings.

This measure was realized for the new HIT-RFQ (recently under test stage) and for the RFQ which is now commissioned at Marburg Therapy Center.

REFERENCES

- [1] H. Eickhoff et al., "HICAT - The German Hospital-Based Light Ion Cancer Therapy Project" Proc. EPAC 04, p. 290, 2004.
- [2] M. Maier et al., "Commissioning of the linac for the Heidelberg heavy ion cancer therapy centre (HIT)" PAC 07, Albuquerque, New Mexico, USA, 2007.
- [3] B. Schlitt, "Commissioning and operation of the injector linacs for HIT and CNAO" LINAC 08, Victoria, BC, Canada, pp. 708-712, 2008.
- [4] R. Cee et al., "Intensity upgrade programme for the HIT injector LINAC", EPAC 08, Genoa, Italy, 2008.
- [5] S. Yaramishev et al, "Development of the versatile multi-particle code DYNAMION" Nuclear Inst. and Methods in Physics Research A, Vol 558/1 pp. 90-94, 2005.
- [6] A. Bechtold et al., "Beam dynamics of an integrated RFQ drifttube combination" LINAC 06, Knoxville, Tennessee USA, 2006.
- [7] I. M. Kapchinsky, "Theory of Resonance the linear accelerators" Harwood Academic Pub, 1985
- [8] Balabin A. I. "Numerical field calculation in RFQ structure with special shape of electrodes" Preprint ITEP Nr: 107, Moscow, 1981.
- [9] H. Vormann et al., "Status of the linac components for the Italian hadron therapy centre CNAO" EPAC 08, Genoa, Italy, 2008.
- [10] W. Barth et al., "Upgrade Program of the High Current Heavy Ion UNILAC as an Injector for FAIR" Nuclear Inst. and Methods in Physics Research, A, 577(1), pp.211-214, 2007.
- [11] S. Yaramishev et al., "Upgrade of the high current heavy ion front-end system of the GSI UNILAC" Prob. Atomic Sci. Technol. No 4, pp. 64-66, 2006.
- [12] M. Maier et al. "Linac front-end upgrade at the cancer therapy facility HIT" LINAC 08, Victoria, BC, Canada, pp. 208-210, 2008.

STATUS OF LINAC BEAM COMMISSIONING FOR THE ITALIAN HADRON THERAPY CENTER CNAO

P. A. Posocco, A. Pisent, C. Roncolato, INFN/LNL, Legnaro, Italy
 C. Biscari, INFN/LNF, Frascati, Italy

L. Celona, G. Ciavola, S. Gammino, INFN/LNS, Catania, Italy

G. Clemente, C. M. Kleffner, M. Maier, A. Reiter, B. Schlitt, H. Vormann, GSI, Germany

G. Balbinot, E. Bressi, M. Caldara, A. Parravicini, M. Pullia, E. Vacchieri, S. Vitulli,
 CNAO Foundation, Pavia, Italy

Abstract

The CNAO (Centro Nazionale di Adroterapia Oncologica), located in Pavia (Italy), is a dedicated clinical synchrotron facility for cancer therapy using high energy proton and Carbon beams. The 400 MeV/u synchrotron is injected by a 216.8 MHz 7 MeV/u linac composed by a low energy beam transport (fed by 2 ion sources), a 400 keV/u 4-rod type RFQ and a 20 MV IH-DTL. The commissioning of the two ECRIS ion sources and the low-energy line was successfully completed at the end of January 2009 reaching the proper beam conditions for injection into the RFQ. After installation and conditioning, the RFQ was commissioned with beam by the GSI-CNAO-INFN team in March 2009. The beam tests results are presented and compared to the design parameters.

INTRODUCTION

The CNAO [1] (Centro Nazionale di Adroterapia Oncologica) is the Italian center for deep hadrontherapy. It will deliver treatments with active scanning both with proton and Carbon ion beams. The accelerator complex (Fig. 1) is based on a 25 m diameter synchrotron capable of accelerating carbon ions up to 400 MeV/u and protons up to 250 MeV. Four treatment lines, in three treatment rooms, are foreseen in the first stage. In one of the three rooms a vertical and a horizontal fixed beam line are provided, while in the other two rooms the treatment will be administered with horizontal beams only.

The injection chain is based on a copy of the linac already working at HIT center [2, 3, 4], whereas the upstream components are similar but not identical. The linac was designed by GSI and IAP Frankfurt. At CNAO GSI also delivered technical support for installation, commissioning and integration of all technical systems, including control system [5, 6].

The injector is positioned inside the synchrotron ring itself, to save space and to better exploit the two non-dispersive regions in the synchrotron.

The Injector

The linac injector (Fig. 2) comprises the two ECR Ion Sources (ECRIS), the Low Energy Beam Transfer lines (LEBT) at 8 keV/u, a 400 keV/u Radio Frequency Quadrupole (RFQ) accelerator [7], and a 20 MV IH-type Drift Tube Linac (IH-DTL) [8] to reach the synchrotron

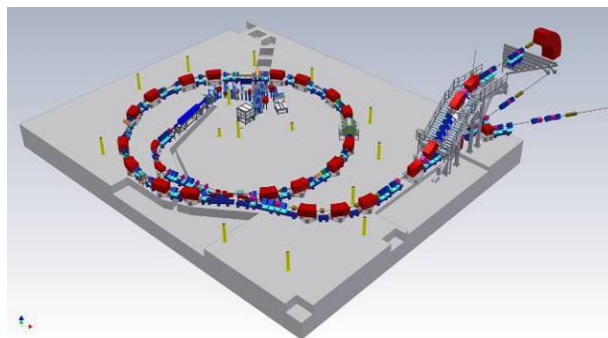


Figure 1: Bird's eye view of the CNAO complex.

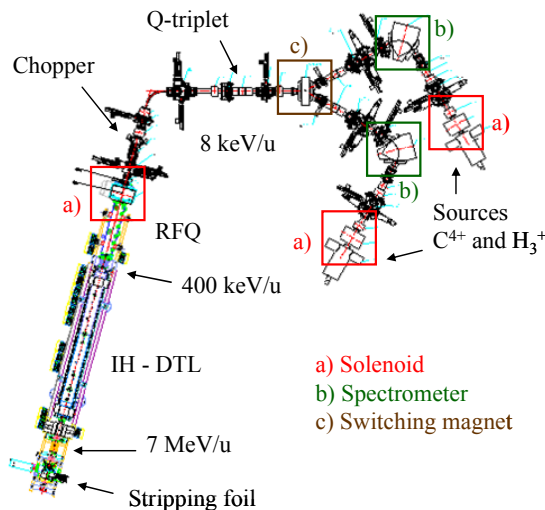


Figure 2: Layout of the CNAO injector.

injection energy (7 MeV/u). Both RFQ and IH-DTL are operated at 216.8 MHz; their overall length is 5.4 m. Beam pulses are $\leq 300 \mu s$ long at a repetition rate ≤ 5 Hz. At the end a stripping station breaks up H_3 molecules into protons or strips electrons from the Carbon ions. The total injector length is about 19 m.

Two ECRIS of the Supernanogan family have been built by Pantechnik [9] under the supervision of INFN/LNS and they were optimized for H_3^+ and C^{4+} extracted beams ($A/q = 3$, $V_{ext} = 24$ kV). Triggered by previous experiences gained at INFN/LNS, further R&D was carried out on the optimization of the extraction gap distance [10] and on the use of a tuneable signal generator that drives the main travelling wave tube amplifiers. As a result, it was possible to extract steadily a current of

1.1 mA of H_3^+ and 250 μA of C^{4+} , much more than the requested values (see Tab. 1). For this reason it was decided to reduce the plasma electrode hole diameter to 6 mm resulting in a smaller total normalized emittance, namely 0.5π mm mrad..

Table 1: Injector Main Parameters

Sources Specifications	
Extraction Voltage	24 kV
Current H_3^+	>700 μA
Current C^{4+}	>200 μA
Transv. norm. emitt. (95%)	< 0.75π mm mrad
LINAC Parameters	
Operating frequency	216.816 MHz
Final beam energy	7 MeV/u
Beam pulse length	$\leq 300 \mu s$
Beam rep. rate	≤ 5 Hz
Transv. norm. emitt. (95%)	0.8π mm mrad
Exit energy spread	$\pm 0.3\%$
Total injector length	~ 19 m

COMMISSIONING PHASES

The buildings construction started in autumn 2005 and now it has been completed along with the installation of the accelerator infrastructure (water cooling systems, cables, etc.). Installation of the CNAO accelerator started in May 2008 after the ECRIS commissioning [11] and by January 2009 the full characterization of the LEBT was performed. At the end of January the RFQ was installed, RF conditioned and commissioned with beam in March [12]. The IH-DTL was installed in April and at the moment it is under RF conditioning (see Table 2).

Table 2: CNAO Commissioning Milestones

	From	To	Section	Activity
2008	May	July	Source I	Test Source, LEBT installation and test
	September	Jan. 09	Source II LEBT+TB0	Commissioning with beam
2009	February	March	RFQ+TB2	Installation
	25 th Feb.	12 th Mar.	RFQ	RF Conditioning and test
	12 th Mar.	3 rd April	RFQ	Commissioning with beam
	April	May	IH+TB3	Installation
	18 th May	17 th June	IH	RF Conditioning and test
	18 th June	15 th July	IH	Commissioning with beam

Linacs

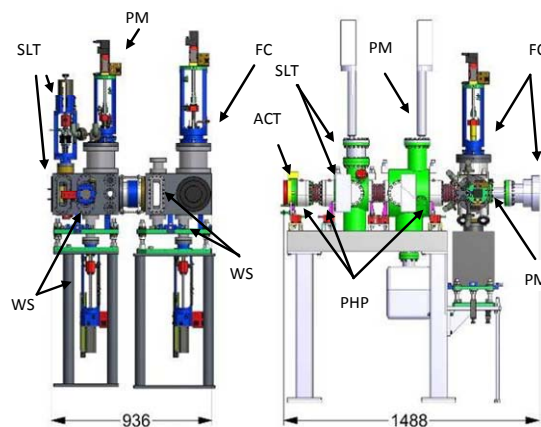


Figure 4: TB0 and TB2 layout. The beam enters from the left. Legend: ACT = Alternate Current Transformer, FC = Faraday Cup, PM = Profile Grid, PHP = Phase Probe, SLT = Emittance Slit, WS = Wire Scanner.

The Test Benches

Three modular beam diagnostics test benches (TB) were designed in order to measure the beam parameters (current, profiles and transverse emittance) behind the 3 different injector sections LEBT (TB0), RFQ (TB2) and IH-DTL (TB3). After installation of each section, the diagnostics bench is placed at its end and then removed only once the machine tests have been completed; the subsequent section is installed and the test bench is mounted in a new configuration.

In TB0 (Fig. 4) DC devices designed by CNAO and AC diagnostics from GSI are installed in order to measure the characteristics of both DC and chopped beam, whereas in TB2 and TB3 only AC devices are mounted. Thanks to the use of a Wire Scanner (WS) the emittance measurement system of TB0 has large angular acceptance (± 150 mrad) and allows the beam measurements at nominal field of the last LEBT solenoid at the RFQ matching point. In TB2 and TB3 three phase probes (PHP) were included to measure the beam energy with the time-of-flight (TOF) technique. To preserve the experimental resolution at higher beam energy for both emittance and TOF measurements, TB3 setup comprises a longer drift between the diagnostics boxes respect to TB2 (2 m instead of 0.7 m).

LEBT COMMISSIONING

CNAO has commissioned the LEBT very carefully to obtain consistent and reproducible beam parameters at the entrance of the linac [13]. Optimisation of the ECRIS sources was carried out in collaboration with INFN/LNS. The beam diagnostics instrumentation including the very compact emittance chamber has been presented in [14, 15].

A further big effort was spent as well to define a theoretical model of the line providing simulations coherent with the measurements. Overall LEBT transmission was always larger than 90% and for special optics reached even up to 97%.

Solenoid Effect

Once the whole linac is installed, the effect of the last LEBT solenoid on RFQ injection can be seen only in the diagnostics downstream the IH-DTL as an effect on the linac transmission. Since the solenoid acts on beam focalization, steering and transverse planes mixing, it was important to check the behaviour of the beam under various solenoid settings at TB0.

Since it was already known that the solenoids provided by SigmaPhi to HIT showed a poor geometric to magnetic axis alignment [4], a field distribution measurement campaign on the three CNAO solenoids was carried out in autumn 2006 [16]. The aim was to choose the best one among the three to be installed in front of the RFQ.

The beam positions of Fig. 5, measured 290 mm behind the solenoid exit, show that the steering is well predictable by a 1st order approximation. No significant emittance growth was measured.

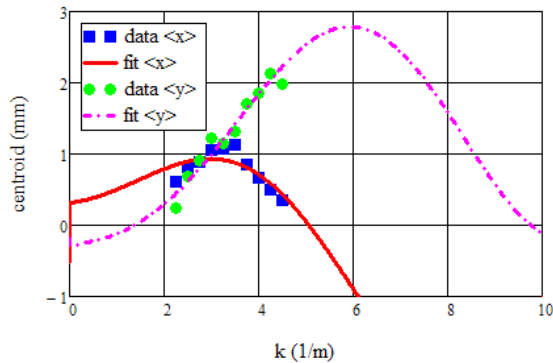


Figure 5: Beam centroid displacement at TB0 as function of the solenoid focal length. The best fit is given with $x=-1.3$ mm, $x'=2.8$ mrad, $y=-0.1$ mm, $y'=-0.3$ mrad as initial conditions before the magnet.

Matching Conditions

The nominal Twiss parameters necessary for a correct matching at the RFQ entrance are $\beta_{x,y}=0.035$ m and $\alpha_{x,y}=1.3$ with the nominal geometrical emittance of 180π mm mrad. Due to the design of TB0, it was possible to measure the distribution in Fig. 6a/b at the RFQ matching point, just 48 mm behind solenoid exit: more than 90% of the beam is included in the yellow ellipse, which represents the theoretical RFQ acceptance (180π mm mrad).

The H_3^+ ‘Probe-Beam’

Thanks to the high current of H_3^+ and to the LEBT design it was possible to prepare what is called a ‘probe-beam’ [17], which is a beamlet of much smaller emittance compared to nominal beam ($5 \div 10 \pi$ mm mrad versus 45π mm mrad RMS) but still with reasonable current ($\sim 120 \mu A$): using the slits of the two LEBT emittance meters [14] the beam is cut both in width and divergence and the final Twiss parameters are close to the matching ones. The resulting small physical dimensions of the beam compared to the RFQ electrodes aperture allow to

Linacs

decouple longitudinal and transverse effects along the acceleration in such a way that it is possible to investigate the linac transverse acceptance experimentally.

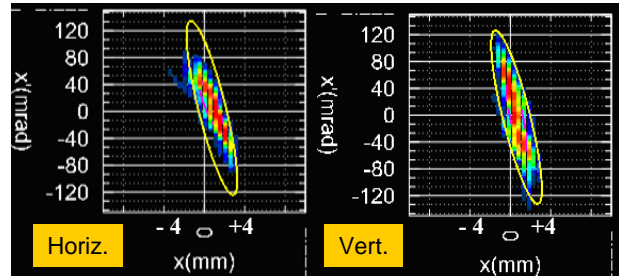


Figure 6a: H_3^+ at 8 keV/u emittance (TB0).

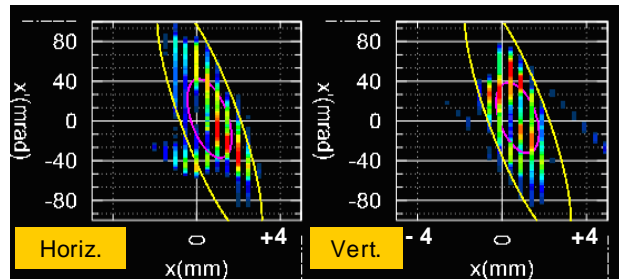


Figure 6b: C^{4+} at 8 keV/u emittance (TB0).

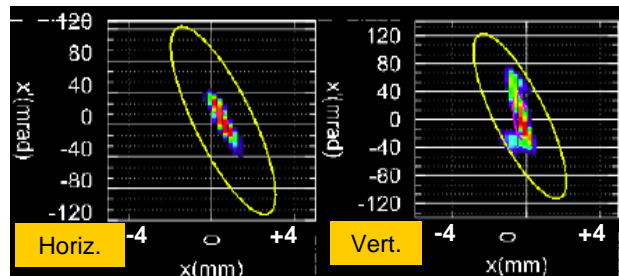


Figure 7: H_3^+ ‘probe-beam’ at 8 keV/u emittance (TB0).

RFQ COMMISSIONING

The RFQ was designed, assembled and RF tuned at IAP Frankfurt. After first beam tests, the final low level tuning of the field flatness was performed successfully at GSI. Prior to the commissioning at CNAO a proton beam test bench had been set up at GSI [18] in order to verify the RFQ output beam energy by TOF measurements and to check the correct function of the two-gap rebuncher drift tube set-up integrated into the RFQ cavity [19].

Installation and Alignment

The RF conditioning of the RFQ was initially carried out in parallel to LEBT commissioning, before the cavity was moved to its final position in the beam line together with the inter-tank matching (ITM) section. This section consists of a quadrupole doublet and a steerer to match the RFQ beam to the IH-DTL. At its end a phase probe monitors the bunch signals and allows adjustment of the phase between bunch and the RF amplifier for the IH-DTL. Finally TB2 was installed and all components were aligned.

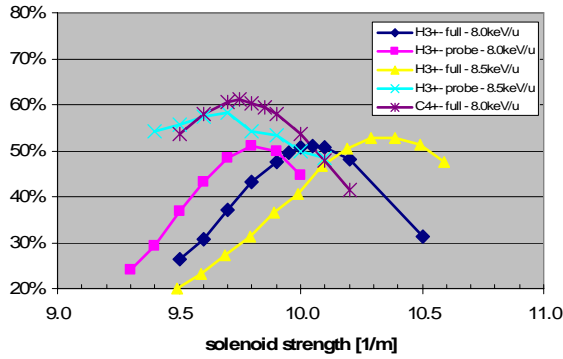


Figure 8a: RFQ transmission as function of the solenoid strength (RFQ tank voltage 5.1 V).

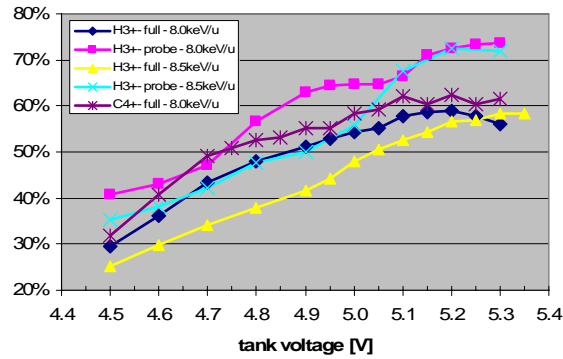


Figure 8b: RFQ transmission after optimization as function of the scaled tank voltage.

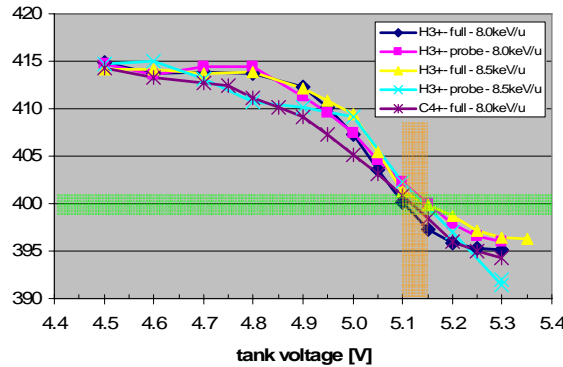


Figure 8c: RFQ output energy [keV/u] after optimization as function of the scaled tank voltage.

Commissioning Procedure

The RFQ commissioning was supported by INFN/LNL and GSI throughout the beam time. During working periods CNAO operated the ion sources continuously to maintain a constant beam quality. LEBT settings and beam parameters were carefully documented, at least once a day, before RFQ measurements were carried out.

For a given ion species (H_3^+ or C^{4+}), beam energy (7.5, 8.0 or 8.5 keV/u), input emittance (‘probe’ or ‘full-beam’) and LEBT setting, the optimization procedure foresaw to fine adjust the solenoid strength (Fig. 8a) to reach the best transmission at nominal RFQ tank voltage (5.1 V) and ITM settings. Then the RFQ beam was characterized as function of the tank voltage measuring the transmission

Linacs

(Fig. 8b), the steering effect, the output energy (Fig. 8c), and the transverse emittance (Fig. 9). Once the right energy for IH-DTL injection (~ 400 keV/u) was found, the transmission was further optimized by means of the quadrupole triplet or the last two LEBT steerers, defining the new nominal LEBT operation parameters.

The optimization of the ITM quadrupoles was tried afterwards in order to verify whether an increase of the transmission was still possible and to investigate the matching with the IH-DTL.

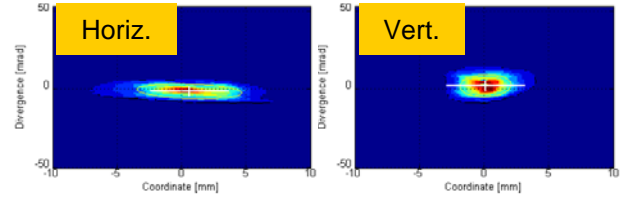


Figure 9a: H_3^+ at 8.0 keV/u emittance (TB2).

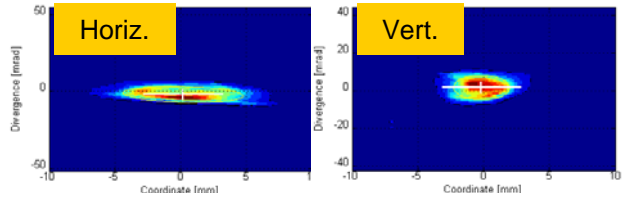


Figure 9b: H_3^+ at 8.5 keV/u emittance (TB2).

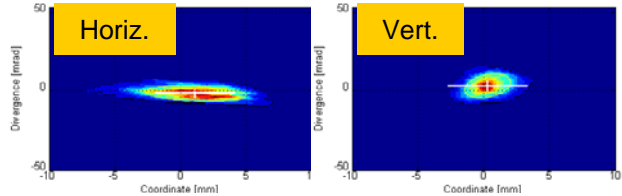


Figure 9c: C^{4+} at 8.0 keV/u emittance (TB2).

Table 3: RFQ Commissioning Results

Ion	H_3^+			C^{4+}
E (keV/u)	7.5	8.0	8.5	8.0
Tank Volt. (V)	5.15	5.10	5.15	5.10
Max. transm. ‘full-beam’	4.6%	58%	59%	62%
Max. transm. ‘probe-beam’	3.4%	71%	69%	n.a.

Normalized transverse output emittance (π mm mrad)

Ion	RMS	H_3^+ 7.5	H_3^+ 8.0	H_3^+ 8.5	C^{4+} 8.0
	Hor.	95%	n.a.	1.02	1.02
Vert.	RMS	n.a.	0.10	0.11	0.09
	95%	n.a.	0.78	0.68	0.67

Commissioning Results

For H_3^+ beam (Tab. 3) three different injection energies were tried in order to determine the best RFQ working point. As expected, the lowest energy (7.5 keV/u) has

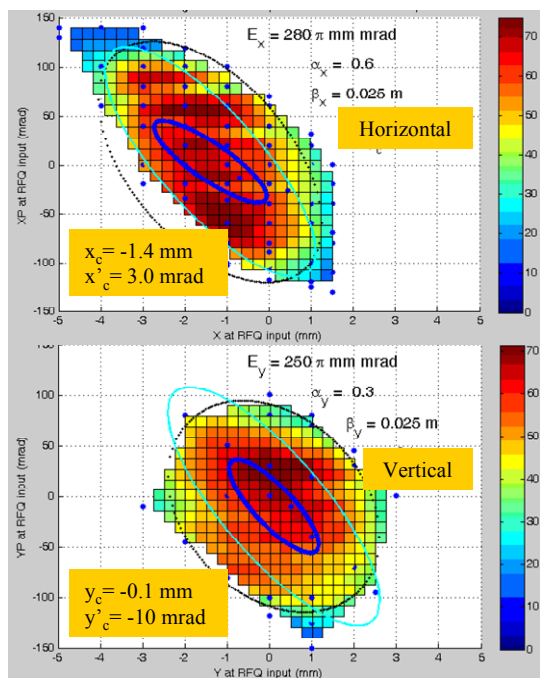


Figure 10: Horizontal and vertical RFQ acceptance measurement with H_3^+ ‘probe beam’ at 8.0 keV/u. The blue ellipse represents the RMS beam of Fig. 6, the azure one the 180π mm mrad matched ellipse and the black one the 90% acceptance fitting the experimental data.

very bad performances in terms of transmission, whereas the highest (8.5 keV/u) is equivalent to the nominal one (8.0 keV/u): The operating parameters may be adjusted later depending on the measured beam quality behind the IH-DTL. Very moderate steering effect was found and the use of the ITM steerers seems to be not required.

The RFQ transmission is though limited to $\sim 70\%$ for the ‘probe-beam’ whereas the design one is greater than 90% [20] for a ‘full-beam’ of 180π mm mrad emittance.

Measurement of RFQ Acceptance

A deformation of the RFQ electrodes (a longitudinal bump of ~ 0.5 mm) was observed for CNAO RFQ after installation by telescope measurements. A similar ‘banana-shape’ deformation had been detected during HIT RFQ commissioning [4] as well.

In order to check whether the acceptance is reduced by this ‘banana-shape’ causing the low transmission, by means of the steerers in the last LEPT section and their previously measured response matrix, it was possible to misalign the ‘probe-beam’ at the entrance of the RFQ up to ± 3 mm and ± 120 mrad starting from the setting of maximum transmission. The RFQ transmission as function of the misalignment is reported in Fig. 10 and shows that the vertical acceptance is reduced by more than 10% in divergence, which confirms that the simulations on HIT RFQ [21] describe the RFQ transverse behaviour with good approximation, but it does not explain why the transmission is limited to 70%.

The transverse emittance out of the RFQ seems also to be directly connected to the ‘banana-shape’: the reduced

vertical acceptance and the related losses causes the vertical emittance to be lower than the horizontal one by $\sim 50\%$ (Tab. 3). Given that the measured maximum beam transmission through the RFQ is limited to $\sim 70\%$ even for a very small and on axis beam (the axis is defined by the transmission map itself), it seems that the RFQ has a problem of longitudinal capture. Nevertheless the IH-DTL has a transverse acceptance twice as large as the RFQ output emittance and very likely the beam will be accelerated up to 7 MeV/u without additional losses.

CONCLUSIONS

After the source and LEPT optimization, the RFQ has been fully commissioned. The RFQ working point has been established and more than 500 μA of H_3^+ and 70 μA of C^{4+} are accelerated to 400 keV/u at 195 kW RF power. The design transmission could not be achieved (the maximum achieved is about 60%). The output beam is very stable and shows almost no steering. The measured transverse output emittances are well within the IH-DTL acceptance.

Measurements at 7.5, 8.0, and 8.5 keV/u RFQ injection energy delivered similar results for the two higher energies, but at 8.5 keV/u at a higher RFQ power level.

Finally, the ‘probe-beam’ data allowed to verify the RFQ acceptance experimentally, and to analyse and partly improve the performances for the ‘full-beam’.

ACKNOWLEDGEMENTS

The authors wish to thank all CNAO staff members for their vital support during LEPT and Linac commissioning. Further thanks to the numerous GSI staff who were involved in this linac project over the past years. Their efforts are greatly acknowledged.

REFERENCES

- [1] S. Rossi, FRYAPA01, EPAC 2006, p. 3631.
- [2] H. Eickhoff et al., FRYACH01, EPAC04, p. 290.
- [3] D. Ondreka et al., TUOCG01, EPAC08, p. 979.
- [4] B. Schlitt, WE205, LINAC08, p. 708.
- [5] B. Schlitt et al., GSI-AR2006, p. 383.
- [6] H. Vormann et al., TUPP131, EPAC08, p. 183.
- [7] A. Bechtold et al., TH480, LINAC02, p. 782.
- [8] B. Schlitt et al., TH479, LINAC02, p. 779.
- [9] [HTTP://WWW.PANTECHNIK.FR](http://www.pantechnik.fr)
- [10] G. Ciavola et al., MOPC145, EPAC08, p. 415.
- [11] M. Pullia et al., TUOCG02, EPAC08, p. 982.
- [12] E. Bressi et al., TU6PFP005, PAC09.
- [13] A. Parravicini et al., C02, HIAT09.
- [14] A. Parravicini et al., C03, HIAT09.
- [15] J. Bossert et al., TUPC013, EPAC08, p. 1071.
- [16] S. Vitulli et al., LNL-AR2006, p. 207.
- [17] E. Bressi, CNAO Internal Note.
- [18] C. M. Kleffner et al., THP089, LINAC06, p. 791.
- [19] A. Pisent et al., LNL-AR2006, p. 205.
- [20] A. Bechtold, PhD Thesis, Frankfurt Univ., Germany.
- [21] S. Yaramyshev et al., TH9, HIAT09.

THE GSI UNILAC UPGRADE PROGRAM TO MEET FAIR REQUIREMENTS

L. Dahl, GSI Helmholtzcenter for Heavy Ion Research, Darmstadt, Germany

Abstract

The GSI linear accelerator UNILAC and the synchrotron SIS18 will feed the future accelerator facility FAIR (Facility for Antiproton and Ion Research) with heavy ion beams. Several hardware measures at the UNILAC are necessary to meet the FAIR requirement, implicating a beam intensity of $3.2 \cdot 10^{11}$ of U^{28+} -particles within an UNILAC macro pulse of 100 μs length and defined emittance space at SIS18 injection.

The stripper gas jet density was strongly increased to get the equilibrium charge state even for the heaviest ions. A procedure matching the 6-D-phase space for proper Alvarez DTL injection and increase of the transverse phase advance in the Alvarez accelerators reduces emittance growth. In front of SIS18 injection a new separator provides an immediate selection of the desired charge state after stripping and therefore reduces space charge induced emittance growth.

The front-end of the high current injector includes several bottle necks. A compact solenoid channel is planned providing straight line injection into the 4-rod-RFQ. The RFQ will be equipped with new designed electrodes for increased acceptance and reduced emittance growth.

The contribution gives an overview of end-to-end simulations, the different upgrade measures, the particular beam investigations, and the status of beam development satisfying FAIR requirements.

INTRODUCTION

For Uranium (reference ion) the UNILAC has to inject $3.2 \cdot 10^{11}$ U^{28+} particles per 100 μs ($4.8 \cdot 10^{10}$ U^{73+}) with a repetition rate of 4 Hz into the synchrotron SIS18.

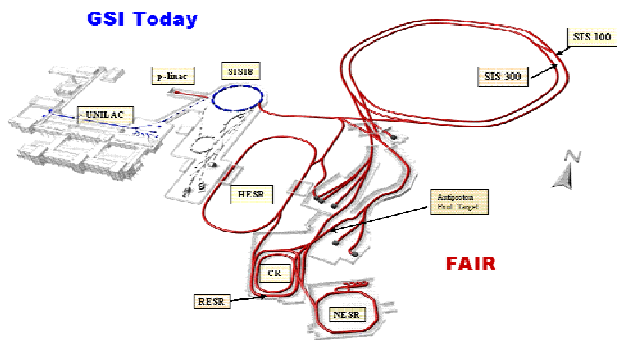


Figure 1: The existing GSI accelerators UNILAC and SIS18 and the future accelerator facility FAIR.

The low charge states for heavy ions (entering quadratic into the space charge limit SCL) enable intense beams. These are subsequently accelerated up to 1.5 GeV/u by the FAIR [1] synchrotron SIS100 for

radioactive beam production. Alternatively SIS100 accelerates intense proton beams up to 30 GeV for pbar-production. Heavy ion beams of energies up to 30 GeV/u will be provided by the FAIR synchrotron SIS300, using higher charge states and a slower cycling rate. SIS300 can also serve as a stretcher for radioactive beams, which will be injected, cooled, and stored in a system of rings with internal targets and in-ring experiments (Fig. 1).

GSI uses heavy ion sources of e.g. MUCIS or Mevva type which generate for a whole string of low charged ions beams of sufficient intensity. As the UNILAC was originally not designed for space charge dominated beams different measures are necessary to reduce beam losses and improve beam quality.

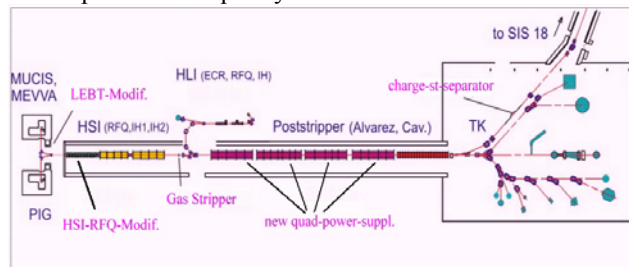


Figure 2: Schematic overview of the UNILAC, experimental area, transfer channel to SIS, and locations of upgrades.

The scheme of the UNILAC is presented in Fig. 2. The prestripper accelerator HSI (high current injector) comprises a 36 MHz RFQ and two IH-type drift tube DTLs for final energy of 1.4 MeV/u, suited for ions with mass to charge ratios up to 65. A gas stripper increases the charge states, e.g. U^{4+} delivered by the Mevva source is stripped to U^{28+} . Five 108 MHz Alvarez DTLs accelerate the ions up to 11.4 MeV/u. Finally a chain of ten single gap resonators allows exact adjusting of any energy between 3.6 and 12.4 MeV/u. A second injector HLI (high charge state injector) with an ECR source injects directly into the post stripper section. Finally, up to three different ion species can be accelerated interchangeably to different energies. Different experiments in any mixture on basis of a 50 Hz pulse-to-pulse switching mode can be accomplished. The transfer channel to SIS18 includes a foil stripper for another charge state increase.

BEAM DYNAMICS SIMULATIONS

Space Charge Parameter along the UNILAC

For the HSI commissioning end-to-end simulations for the entire UNILAC up to SIS18 injection were carried out with the multi particle codes PARMILA and PARMTRA. As result of these calculations the SCP (space charge

parameter) along the UNILAC was extracted (Fig. 3). The SCP is very high in the gas stripper area, but it decreases rapidly with particle separation. Another significant peak at the entrance of the Alvarez DTL appears due to the small size of the beam in all three dimensions, as required for beam matching. A further space charge affected area is situated behind the foil stripper device in the transfer channel to SIS18.

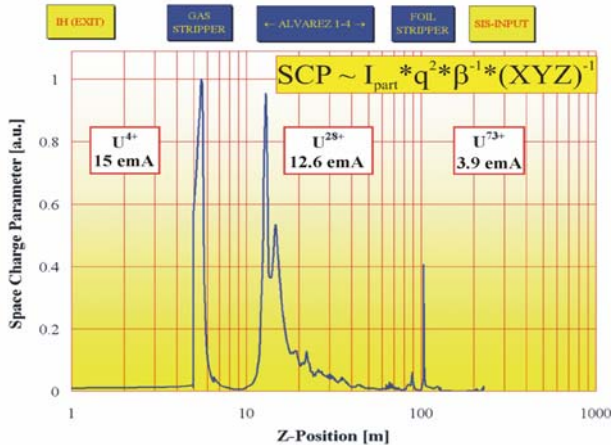


Figure 3: Space charge parameter along the UNILAC [2].

The separation of the required charge states behind both strippers and the beam matching to the DTL structure are taking place under extremely high space charge influence which are sources of emittance growth.

Matching Section for the Alvarez DTL

After the separation of the U^{28+} ions behind the gas stripper, the beam has to be matched to the periodic solution of the beta function of the first Alvarez DTL. The 6-D matching of the beam is carried out by a system comprising a 36 MHz rebuncher cavity, a quadrupole doublet and triplet, and a 108 MHz rebuncher cavity. In general the mismatched beam results in large beta function oscillations along the whole Alvarez DTL, which may cause emittance growth and beam losses (Fig. 4).

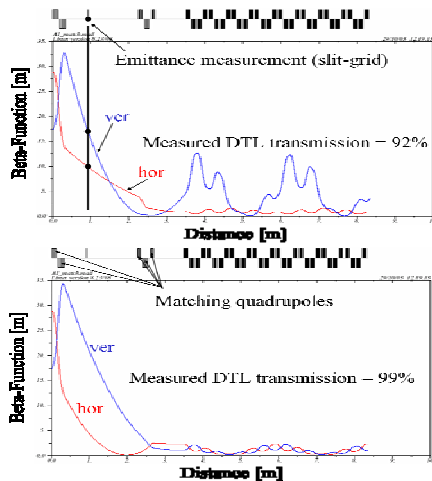


Figure 4: Horizontal and vertical beta-functions in the matching section and the first cells of the Alvarez DTL for mismatched (top) and matched (bottom) beam [2].

Linacs

Using the quadrupole settings in the first cells of the DTL the periodic solution for the first Alvarez tank is calculated. To match the periodic solution, a fitting routine involving the five quadrupoles and two bunchers is applied also considering space charge forces. The matched Twiss parameters decrease the measured losses along the Alvarez section from 8 % to less than 1 % [3].

Transverse Phase Advance in the Alvarez DTL

For U^{28+} beam the zero current transverse phase advance σ_0 in the Alvarez DTL is limited to 45° due to power supply currents. A $^{40}\text{Ar}^{10+}$ beam with less than half of the Uranium beam rigidity and the beam intensity of 7 emA is equivalent to the envisaged Uranium intensity. Therefore the influence of the phase advance on transverse emittance growth and transmission in the Alvarez DTL was investigated experimentally with a $^{40}\text{Ar}^{10+}$ beam up to σ_0 -values of 90° . As shown in Fig. 5, a value of $\sigma_0 = 60^\circ$ is required for an improved transverse brilliance for SIS18 injection. Transferred to Uranium, an increase of the maximum field gradients in the Alvarez DTL of 11% is necessary.

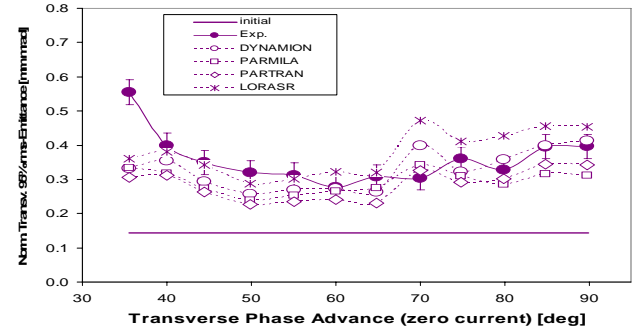


Figure 5: Transverse emittance at the exit of the Alvarez DTL calculated by different codes and measured as function of transv. phase advance. $\epsilon_{\text{norm}} = (\epsilon_x + \epsilon_y) / 2$ [3].

Charge State Separation behind Foil Stripper

Formerly charge state separation was accomplished 25 m behind the foil stripper in the TK (transfer channel) to SIS18. For FAIR beam quality requirements it became necessary to increase the resolving power for space charge reasons. A new compact charge state separator with four vertical dipole magnets of 35° deflection angle each was designed. Fig. 6 shows the vertical fully separated beam envelopes for the Uranium charge states $72+$, $73+$, and $74+$.

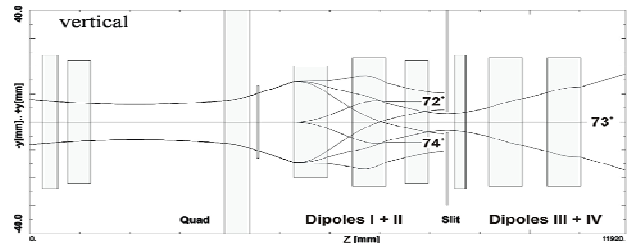


Figure 6: Beam dynamics layout of the charge state separator in the beam transfer line to SIS. Envelopes for Uranium charge states $72+$, $73+$, and $74+$ [6].

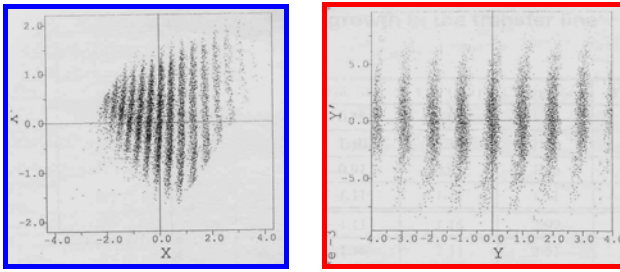


Figure 7: Multi particle calculations for high Uranium charge states in the dispersion plane for the old (left) and the new transfer channel charge state separator (right) [6].

The enormous progress of improved and direct charge state separation with evident impact on space charge forces reduction is pictured in Fig. 7. Measurements are reported below.

REALIZED UPGRADE MEASURES

Increase of Gas Stripper Pressure

To get charge state equilibrium and maximum exploitation of U^{28+} ions the nitrogen gas jet pressure was increased from 2,900 mbar to 4,500 mbar measured in front of the nozzle. The gas density is estimated as $1 \mu\text{g}/\text{cm}^2$. Besides the huge roots pump four 1,000 l/s turbo pumps were installed. The new stripper chamber with enlarged beam apertures is shown in Fig. 8. The measurements illustrated in Fig. 9 show the exploitation of different Uranium charge states depending on the gas pressure. Fig. 10 shows uranium charge state spectrum recorded behind the 15° analyzing and selecting magnet, proving the envisaged equilibrium.

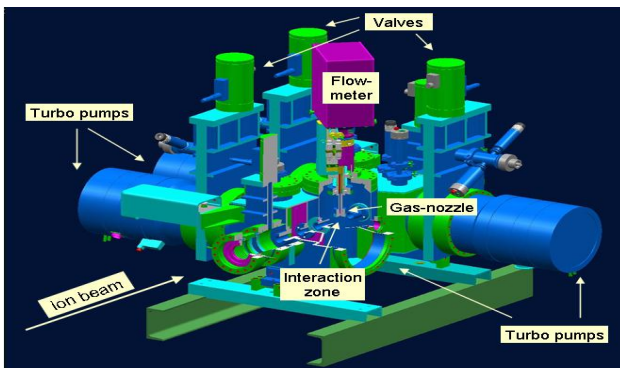


Figure 8: Improved nitrogen gas stripper chamber [4].

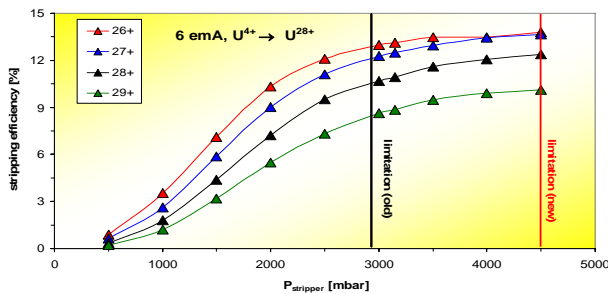


Figure 9: Yield of uranium charge states depending on nitrogen gas pressure [6].

Linacs

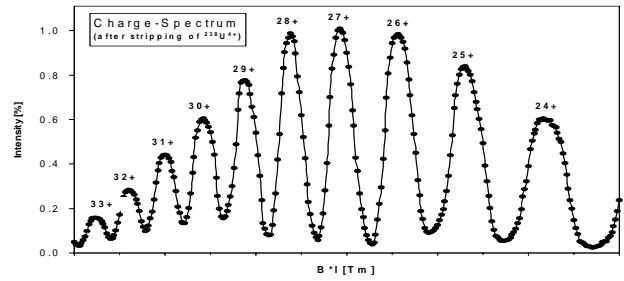


Figure 10: Uranium charge states after stripping [6].

Alvarez DTL Beam Brilliance Increase

As learned from the above described simulations, a sophisticated 6-D beam matching to the Alvarez DTL and an increased transverse phase advance of $\sigma_0 = 60^\circ$ promises a significant gain in beam brilliance.

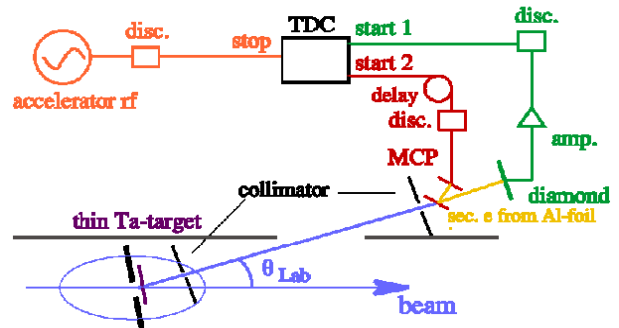


Figure 11: Scheme of the longitudinal bunch structure measurement device in front of the Alvarez DTL [5].

Additional to a slit-grid transverse emittance meter a TOF measurement of secondary electrons with Multi Channel Plate and a diamond detector (Fig. 11) was developed and installed in the matching section for the Alvarez DTL. On basis of MAD8-code the six measured phase space parameters are fitted to the Alvarez periodic FDDF focussing channel considering space charge power. The Alvarez magnetic quadrupole cooling allowed increasing the currents up to 20%. Therefore new power converters were ordered and partly already installed.

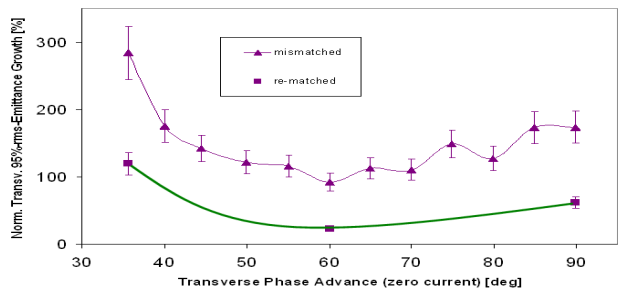


Figure 12: Measured emittance growth in the Alvarez DTL for mismatched and matched beam for different σ_0 [3].

After applying the procedure for matched beam injection and transverse phase advance of $\sigma_0 = 60^\circ$ for the Alvarez DTL a reduction of the transverse emittance growth from 100% to 20% was measured (Fig. 12) [3].

New Charge State Separator

In the transfer line to SIS18 the beam is stripped to higher charge states by a carbon foil, if high final energies from SIS18 are required. The TK is operated at 4 Hz pulse-to-pulse mode, with beams of different ion species and intensities, with or without stripping. An U^{28+} -beam of 15 emA has a power of 1.5 MW (100 μ s pulse length). After stripping, undesired charge states with 85 % of the beam power must be separated and dumped.

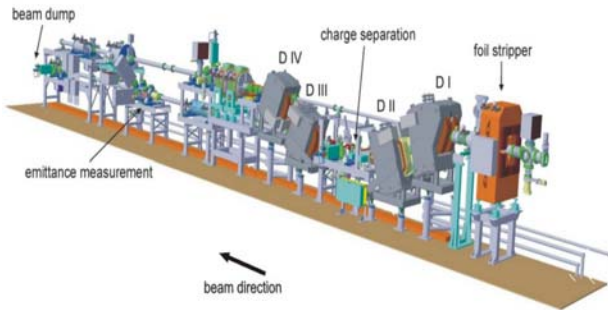


Figure 13: Charge state separator behind the foil stripper [6].

A stripper foil is loaded with 3 % of the beam power. To avoid evaporation in a single beam pulse, the beam is swept within 100 μ s over its width of 55 mm. Emittance growth in the TK is caused by small angle scattering in the stripper foil and by space charge forces. To minimize emittance growth, a beam of spotsize 4 mm · 20 mm is prepared, and the distance to the separator is kept as short as possible. Focused beams pass the stripper by use of a kicker or sweeper magnet horizontally off-axis and are bend back by a quadrupole magnet into the horizontally 90 mm wide gaps of the first two dipoles of the analyzing system. A second kicker or sweeper magnet realigns the beams on axis. Vertically the charge states are separated by the first dipole magnet. Pole face rotation angle of -20° focuses the beam into the analyzing slit. The charge resolution $q/\Delta q$ is about 100. The slot width is 10 mm; the dispersion is 7.5 mm/%. The complete system (Fig. 13) is designed achromatically [6].

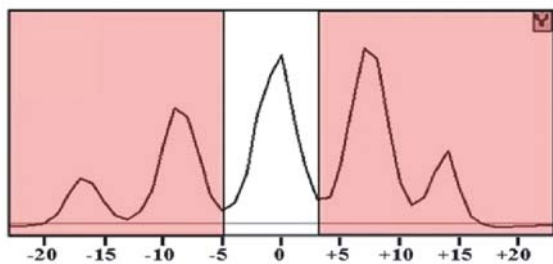


Figure 14: Measured uranium charge states 71 – 75+ [6].

The stripper foil device keeps ready 40 frames, each equipped with a small foil for kicker magnet operation and a large foil for sweeper or kicker magnet operation. The foil thicknesses are 200, 400, and 600 μ g/cm². E.g., 400 μ g/cm² provides equilibrium charge state distribution

Linacs

for an Ar beam. The 600 μ g/cm² foil serves for stripping of heavy ions, e.g. the U^{73+} yield reaches 15 % (Fig. 14).

Space charge forces act in the short region between stripper foil and charge separation only. The space charge influenced emittance growth is 10 % (hor.) and 20 % (vert.). The measured high current emittance potentially meets the requirement defined by the FAIR project.

ACHIEVED URANIUM INTENSITY

The revision of space charge dominated sections of the UNILAC implicated both an increase of beam intensity towards the goal of 15 emA of the design U^{28+} beam and 5 emA of the foil stripped U^{73+} beam, and significantly higher beam brilliance. As represented in Fig. 15 the measured normalized vertical emittance area is below the required limit for SIS injection of $\epsilon_{y,norm} = 2.5 \mu$ m whereas the horizontal emittance still exceeds the SIS18 limitation of $\epsilon_{x,norm} = 1.0 \mu$ m up to 60 % in terms of the total emittance area. As shown in Fig. 16 the absolute uranium beam intensities developed with the upgrade measures and sophisticated machine tuning towards 5.7 emA for U^{28+} beam and 2.7 emA for U^{73+} beam.

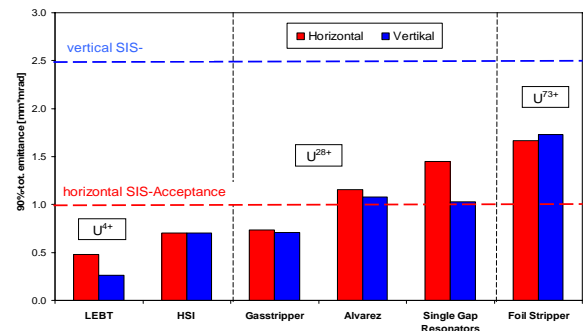


Figure 15: Normalized high current beam emittance measurements in June 2008 and SIS requirements [4].

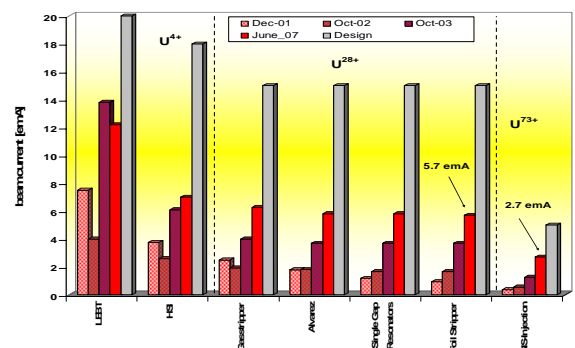


Figure 16: Improvement of the uranium beam intensities during the last years along the UNILAC [7].

ACTUAL UPGRADES

The Mevva ion source generates 37 emA of U^{4+} beam theoretically sufficient to meet the FAIR requirements. Nevertheless only 12 emA are calculated at the output of the HSI. There are two bottle necks in the front-end system: the LEBT and the 36 MHz RFQ. Currently the RFQ is reengineered.

RFQ Redesign

The ten HSI-RFQ modules are currently equipped with new electrodes comprising a new designed input radial matcher and a smooth gentle buncher (Table 1). Important is the enlarged normalized acceptance of $0.86 \mu\text{m}$. The maximum RF voltage grew from 125 to 155 kV. The U^{4+} beam output current and therefore the beam brilliance increases 40 % within an emittance of $20 \mu\text{m}$ (Fig. 17) [8]. After RF conditioning and beam commissioning the upgraded RFQ will go into routine operation in August 2009.

Table 1: Main RFQ Parameters

	New Design	Existing Design
Voltage, kV	155.0	125.0
Average radius, cm	0.6	0.52-0.77
Electrode width, cm	0.84	0.9-1.08
Maximum field, kV/cm	312.0	318.5
Modulation	1.012-1.93	1.012-2.09
Synch. Phase, degree	-90 to -28	-90 to -34
Aperture, cm	0.41	0.38
Min. transverse phase advance, rad	0.56	0.45
Norm. transverse acceptance, cm mrad	0.086	0.73
Output energy, MeV/u		0.120
Electrode length, mm		9208.4

Compact LEBT

Beam simulations on the existing LEBT demonstrate emittance filamentation and growth arising in the analyzing magnet, mismatch to the RFQ, and resulting significant beam loss in the front-end. In an upgrade I (see Fig. 18) foreseen in 2010, switching and quadrupole magnets will be substituted by magnets with enlarged apertures for proper beam matching to the increased RFQ acceptance. But this improves only partly the LEBT.

Simulation studies on alternative LEBT [9] show that a new straight line system based on sc solenoids (upgrade II in Fig. 18) provides the most efficient beam transport of the radial symmetric beam to the RFQ. The ions with wrong rigidity will be mainly lost in the LEBT. This system will be primarily used for mono isotopes and enriched heavy ion source material as it contains no charge analyzing section.

Together with the ongoing RFQ upgrade the compact LEBT enables an HSI output current of 20 emA U^{4+} beam meeting the FAIR requirement (see Fig. 16).

CONCLUSION AND OUTLOOK

The described sequence of upgrade measures of the UNILAC mainly applied to strong space charge influenced sections will fulfil the beam quality and quantity requirements at SIS injection. Nevertheless, it is

Linacs

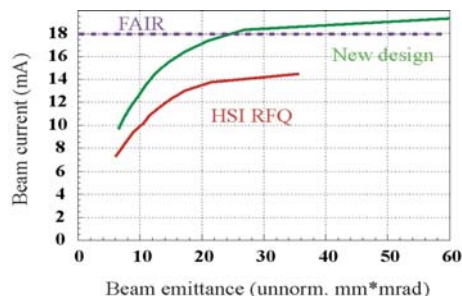


Figure 17: Simulation data of the modified HSI-RFQ (red: existing status, green: new design) [8].

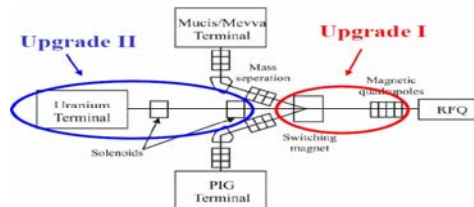


Figure 18: Modifications of the HSI LEBT system [9].

a challenge for the UNILAC to satisfy in multi ion pulse-to-pulse operation the requirements of the high duty factor (5 ms and 50 Hz) experiment program below 7.5 MeV/u and simultaneously the 4 Hz demand of high intensity 11.4 MeV/u beams in $100 \mu\text{s}$ pulses for FAIR. Both injectors, HSI and HLI, are modernized so far. But all beams are passing the 60 m long Alvarez DTL in operation since 1974 and fed by RF amplifiers with pulse power up to 1.6 MW. Long term plans are developed to separate these functions by a dedicated short 7.5 MeV/u sc linac and a substitution of the Alvarez DTL by IH and CH structures providing the beams for FAIR [7].

REFERENCES

- [1] FAIR Baseline Technical Report, Vol. 2, GSI Darmstadt, Germany, (2006).
- [2] S. Yaramishev, et al., Investigations of the beam matching to the GSI-Alvarez DTL under space charge conditions, LINAC2004, Lübeck, Germany, (2004).
- [3] L. Groening, et al., Benchmarking of measurement and simulation of transverse rms-emittance growth, Phys. Rev. Acc. and Beams 11, 094201, (2008).
- [4] W. Barth, The injector systems of the FAIR project, LINAC2008, Victoria (BC), Canada, (2008).
- [5] P. Forck, et al., Proceedings of the LINAC2000, Monterey, USA (CA), (2000).
- [6] W. Barth, Commissioning of the new GSI-charge state separator system for high current heavy ion beams, LINAC2008, Victoria (BC), Canada, (2008).
- [7] W. Barth, et al., A new high energy UNILAC as an high current heavy ion injector for the FAIR synchrotrons, PAC, Vancouver (BC), Canada, (2009)
- [8] A Kolomiets, Upgrade of the HSI-RFQ, LINAC2008, Victoria, Canada (BC), (2008).
- [9] L. Dahl, et al., A New LEBT and RFQ input radial matcher for the UNILAC front-end, LINAC2006, Knoxville, USA (TN), (2006).

STATUS OF CONSTRUCTION AND COMMISSIONING OF THE GSI HITRAP DECELERATOR*

O. Kester[#], NSCL, Michigan State University, East Lansing, MI 48824, USA

W. Barth, L. Dahl, P. Gerhard, F. Herfurth, M. Kaiser, H.-J. Kluge, S. Koszudowski, C. Kozhuharov,
G. Clemente, G. Maero, W. Quint, A. Sokolov, Th. Stöhlker, W. Vinzenz, G. Vorobjev, D. Winters
Helmholtzzentrum für Schwerionenforschung GSI, D-64291 Darmstadt, Germany

J. Pfister, U. Ratzinger, A. Sauer, A. Schempp
Goethe Universität, D-60438 Frankfurt, Germany

Abstract

The GSI accelerator facility provides highly charged ion beams up to U^{92+} at the energy of 400 MeV/u. These are cooled and decelerated down to 4 MeV/u in the Experimental Storage Ring. Within the Heavy Ion Trap facility HITRAP the ions are decelerated further down. The linear decelerator comprises a 108/216 MHz double-drift-buncher, a 108 MHz-IH-structure, a spiral-type rebuncher, and an RFQ-decelerator with an integrated debuncher providing energy spread reduction. Finally the beam is injected with the energy of 6 keV/u into a Penning trap for final cooling. The decelerator is installed completely and first sections have been successfully commissioned. For commissioning of the individual sections different ion species, e.g. $^{64}Ni^{28+}$, $^{20}Ne^{10+}$, $^{197}Au^{79+}$ were used. Each section was studied with comprehensive beam diagnostics to measure energy, emittance, intensity, transverse profiles, and bunch structure of the beam. The report gives an overview of the beam dynamics, the decelerator structures, and some results of the different commissioning runs.

INTRODUCTION

There are two possible methods to generate very highly charged heavy ions. One method employs an intensive and dense beam of electrons in electron beam ion source/trap (EBIS/T). It has been proved, that highly charged ions up to bare uranium could be generated in an EBIT, but only in minor quantities [1]. The other method uses a heavy ion accelerator that accelerates uranium ions to relativistic energies, where the uranium ions can be fully stripped with significant efficiency. In order to reach an efficiency of about 40%, uranium ions have to be accelerated above 400 MeV/u and sent through a copper target. World wide only the accelerator facility of GSI does accelerate uranium to this energy and can store a significant quantity ($\sim 10^8$) of the produced fully stripped uranium ions in the experimental storage ring (ESR) [2]. Heavy, highly-charged ions at very low, well defined energy are ideal systems for a number of precision experiments in different fields of physics. In case of production with an EBIS/T the ions are already at low kinetic energies, whereas in case of the stripping method the ions have to be decelerated. The highly charged heavy

ion trap facility (HITRAP) [3-5] issued in 2005, uses the storage ring in conjunction with an rf-linear accelerator for deceleration of the highly-charged ions down to the required energies in the keV/u range, where the ions can be caught in a special Penning trap. Deceleration in the storage ring allows for stochastic phase space cooling as well as cooling with electrons. This keeps the advantage of a small transverse emittance as well as a very small momentum distribution of the beam. Additionally, the linac can be extremely compact, using just an interdigital H-type drift tube structure for the main deceleration stage. The final deceleration and beam focusing is done by a 4-rod RFQ. The linac structures operate at the typical UNILAC rf-frequency of 108.408 MHz and run with a maximum duty cycle of 0.5%. The duty cycle is not defined by the beam structure, as the ESR provides a bunch of 1-3 μs length every 40 seconds, but by the need to keep the cavities on temperature level between the beam pulses.

STATUS OF THE HITRAP BEAM LINE

An overview of the HITRAP beam line system relevant for the beam commissioning is shown in Fig. 1. The transfer of ions from the ESR to the first structure of the linac, the double drift buncher (DDB), is done by using the beam optics elements available from the original re-injection line between ESR and SIS. A variety of diagnostics elements has been mounted in the beam diagnostics stations shown in Fig. 1. The diagnostics comprises Faraday cups (FC), grid-based beam profile monitors (BPM) and scintillation screens (SCS), where YAG crystals are used. Beam transport is provided by two bending magnets and two magnetic quadrupole singlets. Downstream the wall between the ESR and the HITRAP vault, a diaphragm is mounted, which has a length of 150 mm and an inner diameter of 12 mm. The diaphragm is required to decouple the ESR vacuum at a level of 10^{-11} mbar from the vacuum in the HITRAP linac of about 10^{-8} mbar. The transfer line is available since the first HITRAP beam time in 2007.

The HITRAP linac is installed in the vault of the re-injection line called the re-injection channel. Fig. 2 shows a view in beam direction into the re-injection channel with the DDB and IH-structure section. Since early 2009 the construction of all linac sections is completed. The first part of the HITRAP rf-linac the double drift buncher consists of two coaxial quarter wave resonators. The first

* Work supported by the BMBF

[#] Kester@nsl.msui.edu

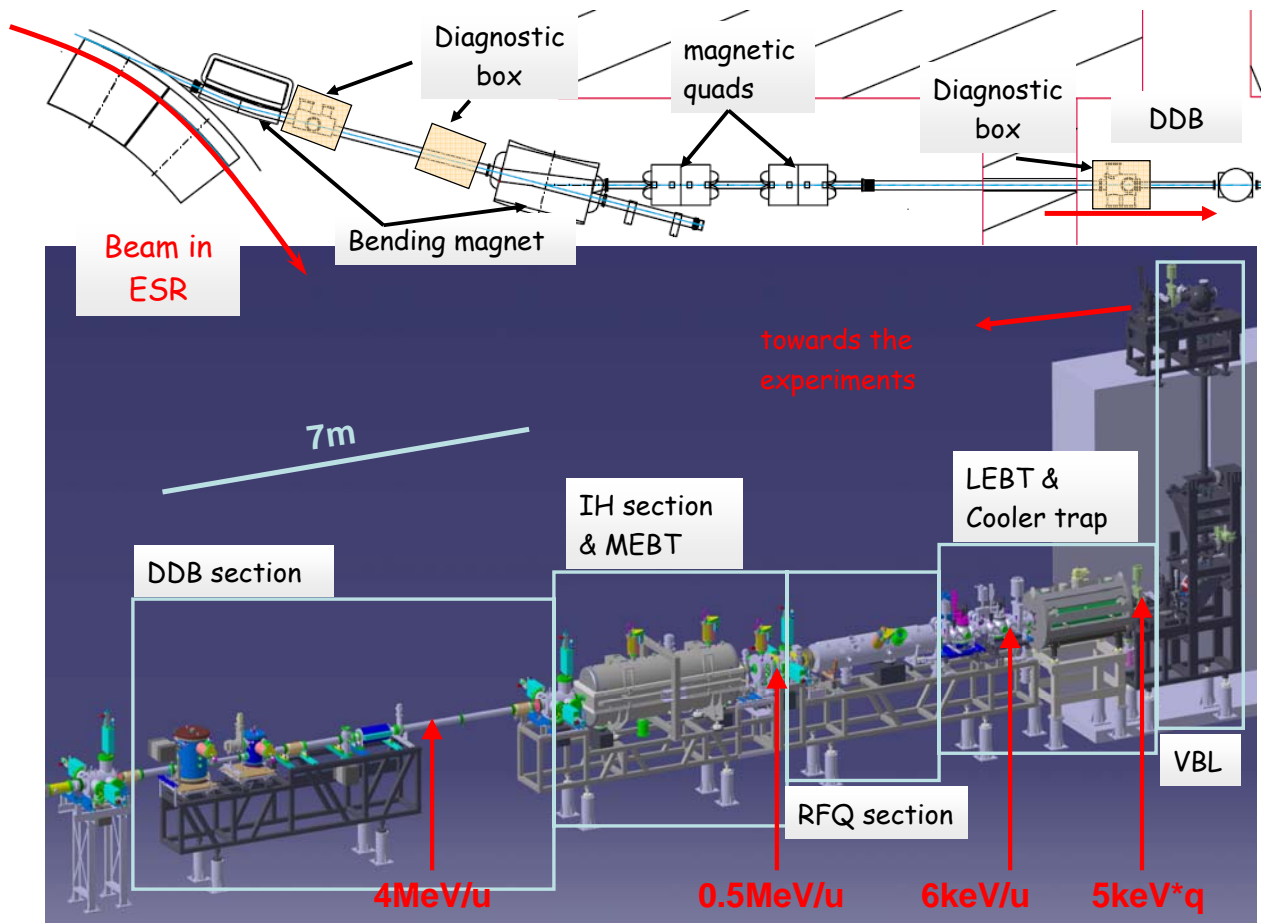


Figure 1: Overview of the ESR-HITRAP transfer line and of the HITRAP linac.

cavity has four gaps and operates at the first harmonic, whereas the second buncher resonator operates at the second harmonic and comprises two gaps. The main decelerating structure is the 25 gap interdigital H-type (IH) structure, shown in Fig. 3. The resonator is the main booster cavity, employing up to 10.5 MV effective voltage over 2.6 m inner tank length. The structure comprises one magnetic inner tank triplet lens and has been installed in 2008. Transverse matching of the beam from the DDB into the acceptance of the IH-structure is done with a magnetic quadrupole triplet lens as well. The intermediate section between IH-structure and the 4-rod radio frequency quadrupole structure (RFQ) has been installed in 2008, too. This section comprises two magnetic quadrupole doublet lenses and a two gap spiral re-buncher cavity. This inner tank section is required for the transverse and longitudinal matching of the beam coming from the IH-structure to the acceptance of the RFQ. The next section of the linear decelerator, the RFQ structure, was tested for vacuum leaks and conditioned at low rf power level in 2008. The space of the RFQ structure in the beam line has been used for beam diagnostic systems before [6]. The RFQ structure has finally been installed in early 2009.

Integrated in the RFQ tank is a short spiral buncher cavity [7]. Both are shown in Fig. 4. The spiral structure de-bunches the beam and reduces the energy spread of the

ions decelerated by the RFQ structure. This reduction of the energy spread is mandatory for an efficient injection of the ions into the strong magnetic field of the HITRAP cooler Penning trap. The low energy beam transport line (LEBT) that connects the RFQ to the cooler trap is installed since 2008. The beam line houses six Einzel lenses, two diagnostic boxes and two diaphragms for differential pumping purposes. The LEBT has to decouple the cooler trap vacuum in the order of



Figure 2: The re-injection channel in beam direction. The DDB structures appear on the left hand side and the IH-structure in pink are visible.



Figure 3: View into the HITRAP IH-structure from the low energy end of the resonator.

10^{-13} mbar from the typical RFQ vacuum of 10^{-8} mbar. In addition, the electrostatic beam focusing of the LEBT must cover a beam emittance of approximately 200 mm mrad, expected at the exit of the RFQ. The components of the LEBT have been baked and reached the specified pressure of 10^{-10} mbar. The LEBT beam line elements are operational and beam can be transported towards the HITRAP cooler trap.

The cooler Penning trap superconducting magnet has been tested and is being operational. The trap electrode structure is being assembled and ready to be installed in the SC-magnet. Most components for the transfer line to the experiments are available and ready for assembly in the re-injection channel, too. The SPARC-EBIT is being installed on top of the concrete shield of the re-injection channel. It will deliver highly-charged ions for offline commissioning of the cooler trap.

The status of the commissioning in the past two years has been described elsewhere [6, 8] in details. However, main purpose of the diagnostics used in the linac beam line is devoted to the determination of the transverse beam quality and of the beam energy of the ions. Measurements of the transverse beam emittance are done with a magnetic quadrupole lens scan and by using pepper pot emittance meter systems [9]. The beam energy is determined by deflecting the ions with a steerer magnet and by energy analysis using diamond detectors [10]. From the beam commissioning experiments done so far an urgent need of the ion beam energy analysis downstream the IH-structure has been concluded. A significant fraction of the ion beam which is transmitted by the IH-structure has higher kinetic energies than the expected 500 keV/u.

Linacs

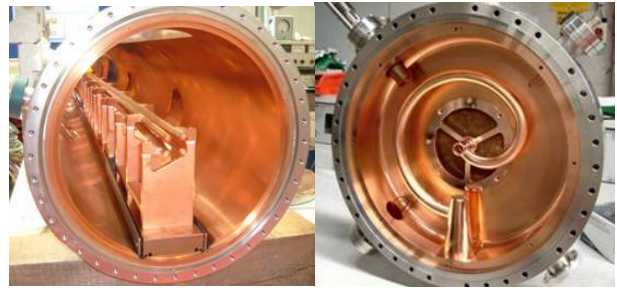


Figure 4: View into the HITRAP 4-rod RFQ and inside the de-buncher integrated into the RFQ tank.

HITRAP BEAM DYNAMICS

The beam dynamics of the HITRAP linac face several challenges due to the use of existing beam optics equipment and the reverse operation of the rf-accelerator structures. The rf-properties of the cavities determine essentially the overall beam dynamics from 4 MeV/u down to 6 keV/u. The main rf-parameters, such as effective shunt impedance, Q-value and the required effective acceleration voltage of the HITRAP linac structures are summarized in Table 1. The corresponding data have been taken into account for the beam optics simulations done for HITRAP.

The beam provided by the ESR is a bunch of 1-3 μ s length. No microstructure, which is matched to the rf-frequency of the linac structures, is available from the storage ring. Therefore the DDB does the longitudinal matching of the beam into the phase acceptance of the IH-structure. The principle is explained in Fig. 5. The phase or time window for deceleration of an ion down to 0.5 MeV/u is about 15° or 0.4 ns.

Table 1: Rf-Parameter of the HITRAP Linac Structures (QWR = quarter wave resonator)

Component (resonator type)	Z_{eff} [M Ω /m] or [k Ω ·m] (RFQ)	Q value	U_{eff} for A/q = 3 [kV]
DDB1 (4-gap QWR)	51.7	10950	220
DDB2 (2-gap QWR)	43	11100	70
IH-structure (25 gaps)	270	25800	11060
Re-buncher (spiral)	28.6	5300	105
RFQ (4-rod)	138	3700	77.5
De-buncher (2-gap spiral)	15.5	2700	0.4

A saw tooth like waveform of the buncher voltage is ideal for efficient bunching of a quasi continuous beam. However, it is difficult to generate it at the required rf-frequency and power level. In a harmonic buncher a saw tooth like voltage waveform is obtained by superposition of fundamental frequency ω with its various higher

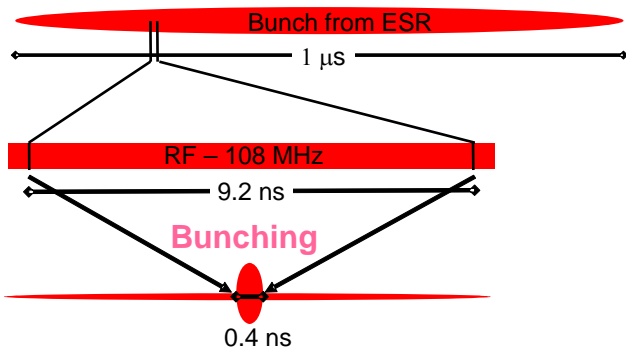


Figure 5: Bunching of the ion beam from the ESR.

harmonics 2ω , 3ω , 4ω etc. on a single gap. A double drift bunching system consists of two bunchers that are separated in space and are driven independently and phase locked together. The second buncher is driven at twice the frequency of the first. The phase adjustment is more flexible due to the long drift and the pre-bunching of the ions in the first cavity. A double drift buncher reveals the same bunching efficiency like a triple harmonic buncher of about 70% [11].

A comparison of the different systems is shown in Fig. 6. In this graphic the final phase distribution of the particles at the entrance of the IH-structure is plotted versus their initial phase at the entrance of the corresponding buncher. For the single harmonic buncher (red curve) about 40% of the ions can be bunched into the 15° phase interval, whereas the triple harmonic buncher and the DDB systems allow for about 70% of the particles focused into the phase acceptance. Note that the DDB has an even better bunching efficiency than the triple harmonic buncher.

The transverse focusing of the beam along the beam transport lines and in the linac is quite delicate, because the transverse emittance of the ions is very sensitive on the deceleration in the IH-structure. The beam dynamics design of the IH-structure has been done with the LORASR code [12]. This code has no fitting routines for the transverse beam matching with magnetic quadrupoles. Therefore an rf-gap routine has been developed for the COSY Infinity code [13], which incorporates the rf-defocusing in an acceleration gap. The COSY Infinity code has a couple of fit routines available, which can be used to match the beam in transverse direction to the IH-structure and to the RFQ further downstream. The results are shown in Fig. 7. Two panels show the two cases of beam dynamic with optimized settings. One covers the case that the beam is not decelerated (upper panel) and the other lower panel shows a perfectly decelerated beam down to 0.5 MeV/u. The brown box determines the location of the RFQ and of the beam measurement equipment in the commissioning runs. The 0.5 MeV/u beam is matched to the RFQ entrance conditions, whereas the 4 MeV/u beam is mismatched at the entrance of the RFQ and divergent. The goal is the reduction of particles with higher energies than 0.5 MeV/u at the entrance of the RFQ and to improve the signal to noise ratio of the decelerated ions.

Linacs

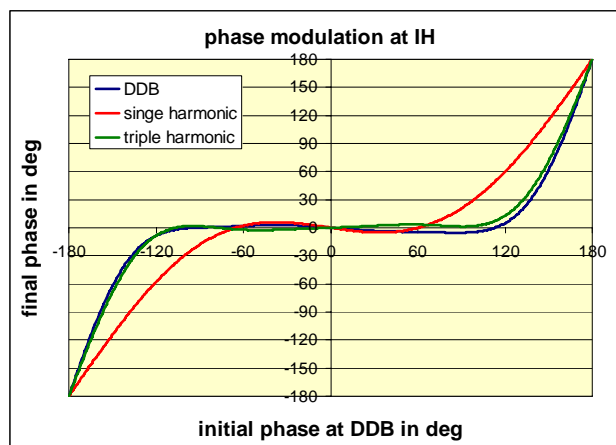


Figure 6: Bunching of the ion beam from the ESR for different buncher systems in comparison.

In addition to the transverse matching, the deceleration performance of the IH-structure is sensitive to the right phase setting and the injection energy [14]. Therefore the energy distribution of the ions at the exit of the IH-structure has been investigated with the LORASR code.

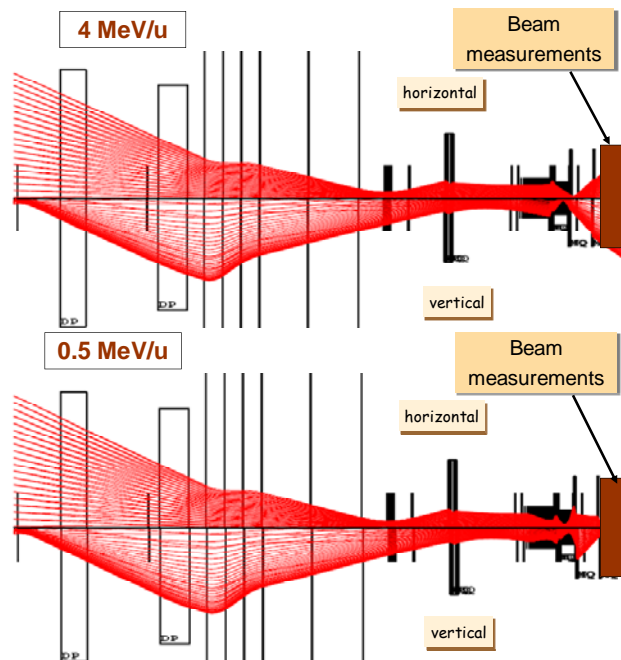


Figure 7: Transverse beam optics in the HITRAP beam line from ESR towards the RFQ for a matched beam tune calculated with COSY9. The upper panel shows the beam transport for a 4 MeV/u beam, the lower a decelerated beam that has 0.5 MeV/u downstream the IH-structure.

Fig. 8 demonstrates the dependence of the ion energy distribution on the phase setting of the IH-structure. For these simulation the assumption was made that all ions were bunched into a 20° phase interval at the entrance of the IH-structure. Even in this case, the ion energy distribution varies significantly with the phase setting of the IH-structure when it differs from the nominal phase setting of about 10° . At 40° the ion energy distribution

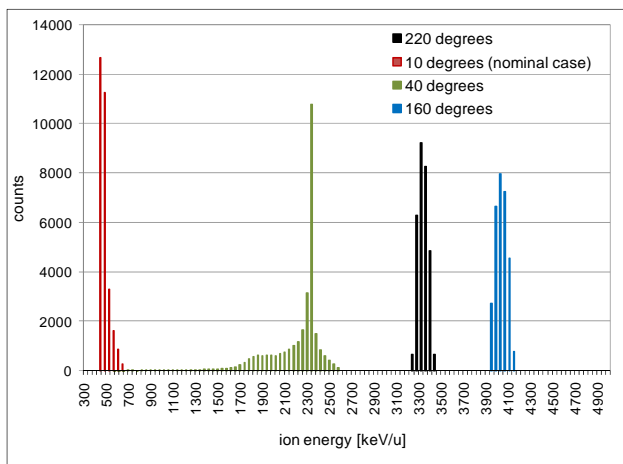


Figure 8: Energy distribution of the ions for different settings of the IH-resonators, assuming that all ions are pushed into a bunch of 20° phase length by the DDB.

reveals a maximum at an intermediate energy of about 2.3 MeV/u, which has been seen in the first commissioning run of the IH-structure in 2008. At 160° the ion energy distribution is peaked around 4 MeV/u, where the IH-structure has considerably high transport efficiency. In real life the situation is even worse, because the bunching efficiency of the DDB into the 20° phase interval is only about 75% and therefore 25% of the particles are distributed over the remaining 340° . Hence, these ions will populate the energy range between 1 MeV/u and 4.1 MeV/u.

Therefore we conclude that a single shot online analysis of the energy distribution of the ions is an important issue and a corresponding diagnostic has to be included in the HITRAP setup. However, decelerated ions with kinetic energy of 0.5 MeV/u could be detected and ions could be injected into the RFQ. The final energy of the ions downstream the RFQ requires a single shot energy analysis as well to find the right working points of the decelerator structures.

REFERENCES

- [1] R. E. Marrs et al., Phys. Rev. Lett. 72 (1994) 4082.
- [2] M. Steck et al., "Improved performance of the heavy ion storage ring ESR", EPAC04, Lucerne, Switzerland, July 2004, p. 1168.
- [3] F. Herfurth et al., "Highly charged ions at rest: The HITRAP project at GSI", AIP conference proceedings 793, 2005, p. 278.
- [4] F. Herfurth et al., Int. J. Mass Spectrom. 251 (2006) 266.
- [5] H.-J. Kluge, et al., "HITRAP: A facility at GSI for highly charged ions" in ADVANCES IN QUANTUM CHEMISTRY 53 (2008) 83.
- [6] F. Herfurth et al., "The HITRAP Decelerator Linac at GSI", Proc. of the PAC2009, Vancouver, Canada, 2008, WE4PBC05.
- [7] B. Hofmann et al., "An RFQ-decelerator for HITRAP", Proc. of the PAC07, Albuquerque, New Mexico, USA, 2007, p. 1437.
- [8] L. Dahl et al., "The HITRAP decelerator project at GSI – Status and commissioning report", Proc. of the LINAC2008, Victoria, Canada, 2008.
- [9] J. Pfister et al., "Commissioning of the HITRAP decelerator using a single-shot pepper-pot emittance meter", Proc. LINAC08, Vancouver, Canada, 2008, TUP074.
- [10] E. Berdermann et al., Diamond Relat. Mater 10 (2001) 1770.
- [11] V. S. Pandit et al., "Modification of a double drift beam bunching system to get the efficiency of a six harmonic buncher", in Proceeding of Cyclotrons and their applications 2001, East Lansing, USA, edited by F. Marti, AIP conference proceedings 600, 2001, p. 452.
- [12] R. Tiede et al., "LORASR Code Development", Proc. of the EPAC2006, Edinburgh, Scotland, 2006, WEPCH118, p. 2194.
- [13] K. Makino and M. Berz, COSY INFINITY version 9. Nucl. Instrum. and Meth. 258 (2005) 346.
- [14] G. Clemente, private communication.

IMPROVED ON LINE PERFORMANCE OF THE INSTALLED ALPI NB SPUTTERED QWRs

A.M. Porcellato, S. Stark, F. Stivanello, L. Boscagli, F. Chiurlotto, D. Giora, M. De Lazzari,
INFN- Laboratori Nazionali di Legnaro, Legnaro, Padova, Italy

Abstract

The average accelerating field of the ALPI 160 MHz sputtered QWRs has been improving with time up to reach, after the last conditioning cycle, the average accelerating field of 4.8 MV/m at 7 W. Such value can be effectively sustained in operation due to the intrinsic mechanical stability of the sputtered cavity whose frequency is practically not influenced by fluctuations in the bath He pressure.

The present average cavity performance approaches the maximum average accelerating field obtainable in the presently installed cavities, most of which were produced by replacement of Pb with Nb in the previously installed substrates. A higher average value can be obtained in ALPI replacing the less performing units; it is instead necessary to sputter on appropriately built substrates to produce QWRs which can reliably exceed 6 MV/m at 7W.

The cavity Q-curves, which were recently measured in ALPI, show a wide range of Q_0 and Q-drop, mainly associated with the substrate characteristics, but in some cases also influenced, as discussed in the paper, by cryostat assembling procedures and by cavity production and conditioning.

INSTALLATION OF SPUTTERED CAVITIES IN ALPI

ALPI initial project planned a large number of Pb plated Cu Quarter Wave Resonators (QWRs) of 3 different β . Only the 44 resonators of the medium β section ($\beta=0.11$, $f=160$ MHz) were built in this way. They were installed in 11 medium β cryostats (CR7-CR10; CR12-CR19) by 1994. Such resonators reached their maximum performance in 1996 when sustained 2.7 MV/m at 7W in average [1].

In parallel 80 MHz, bulk Nb, QWRs were developed for the low β ($\beta=0.056$) section. Twelve of these resonators were installed (in CR4-CR6) by 2000; the installation of further 4 cavities is planned this year in CR3. In spite of their high intrinsic performance, the operational accelerating field of these resonators in ALPI is still limited to a maximum average value of 3 MV/m, but a substantial increase in performance is foreseen by increasing the power management capability of both the coupler and cryostat RF input lines [2].

There are only two cryostats in ALPI high β section. As a matter of fact they are spare medium β cryostats in which we installed high β ($\beta=0.13$) QWRs produced by Nb sputtering. The first cryostat (CR20) was installed a first time in 1995, but it had its cavities replaced with new ones in 1998. The second cryostat (CR19) had its medium β resonators substituted by high β resonators in 2001.

A couple of medium β cavities are also installed in each of the 3 ALPI bunching cryostats (B2, B3, and B4).

The sputtering technology on QWRs was developed at Legnaro in parallel with the installation of ALPI medium β section. A usable high β resonator, suitable to be installed in a standard medium β cryostat, was produced by 1993. Two years later, 4 cavities of this type reached on line an average accelerating field of 4.2 MV/m at 7W, in spite of contamination occurred during the cryostat assembling [3]. In 1998 we substituted these cavities with new and more performing resonators obtained from new substrates [4]. These resonators are still in operation at an average field approaching 6 MV/m.

In the following years we applied the sputtering technology to the upgrading of the previously installed medium β QWRs. Both the cavity shape and other substrate characteristics limited the reachable accelerating field in these resonators; nevertheless a substantial increase in the ALPI performance was clearly possible, at negligible cost, substituting the Pb with Nb. Between 1999 and 2003, the need to uninstall the cryostats, to repair (or later to prevent) cryogenic leaks, gave us the opportunity to renew all the ALPI Pb on Cu accelerating cavities [5]. Initially, the lack of spare substrates prevented both to optimize the cavity production process and to reject the less performing resonators. Only in 2001, by replacing in CR19 the medium β cavities with high β ones previously installed in CR20, we had at hand a few more substrates which could be prepared in advance.

The first installed medium β cryostats (CR7, CR8, CR9, and CR10) had to be open to air again because of cryogenic leaks. For lack of time we fixed them without removing the resonators. Only in 2007/2008, when we repaired the cryostats CR8, CR9, CR10, and CR13 because of a new leak in the thermal shield, we could perform High Pressure Water Rinsing (HPWR) in the resonators. In that occasion we replaced also 6 resonators [6].

THE SUBSTRATES

The high β Resonators

All the high β resonators have a similar inner shape, a straight inner conductor ending in a hemisphere (Fig. 1). A shorting plate, having 30 mm curvature, joints the inner and the outer conductors. The beam ports are external and are connected to the cavity body by an In gasket. The cavities have a capacitive coupler, which is located on the outer conductor, in the plane perpendicular to the beam line, 10 mm lower than the inner conductor tip. The pick-up antenna is on the opposite side, in front of it. The

cavity is closed by a thin plate, about 7 cm apart from the inner conductor edge.

The cavities housed in the two high β cryostats are very different in the construction technology. The CR19 cavities (named HB) are made of Se-Cu and have a circumferential brazed joint in the outer conductor, about 14 cm apart from the shorting plate. Moreover they have both the cavity collar (in stainless steel) and the cavity supports, which are brazed to the cavity body. The CR20 resonators (named HB) are instead drilled out of OFHC 99.95%, certificated graded Cu billets and do not have any brazing joint, being the cavity collar screwed to the cavity body after the sputtering process and the cavity supports milled out of the outer conductor.

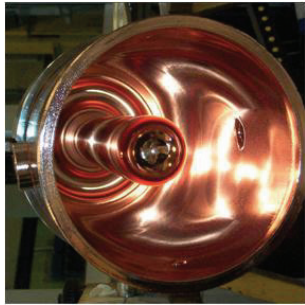


Figure 1: A high β cavity before being sputtered.

Medium β Resonators

Only 7 medium β substrates, labeled PP, are drilled out of OFHC copper billet. Most of the others are instead obtained by brazing a cylinder to a mushroom shaped preformed (FC). Two cavities, still in use, are prototypes built before starting the cavity series production. They do not have any label before the series number. Se/Cu and OFHC Cu were both used for FC series production, but, due to the low relevance of Cu composition for Pb plating, the composition of each prototype is not recorded. All the resonator types present many drawbacks which make the sputtering on them difficult. They have a flat shorting plate, where a hole, used during the plating process, is drilled. Moreover they have the coupler input in a high current region, nearby the cavity top. The PP series, but PP7, has moreover an extra similar aperture which further increases the rf losses.



Figure 2: An upgraded medium β cavity with its tuning plate.

Linacs

All the presently installed medium β resonators have both beam ports and the stainless still collar brazed to the resonator body; connection supports are similarly connected to it. The brazed joints, especially between different materials, can hide enclaves which can release contamination during the sputtering process. We found useful both to open the hidden volumes inside the joints and to make round the inner edges of the cavity apertures for improving the Nb film quality. A cylindrical spacer mounted outside the coupler hole and sputtered together with the resonator, helps reducing the rf losses. All these drawbacks are eliminated in the 4 new medium β cavities (Fig. 3), which have construction technology similar to the high β resonators while the beam ports are obtained by plastic deformation of the outer conductor [7].



Figure 3: A newly designed medium β cavity.

S.C. RESONATOR PRODUCTION

Surface Finishing and Chemical Treatments

Most of mechanical and chemical surface processes of the QWR substrates are described in detail in reference [8]. They have been practically unchanged during all the period of ALPI cavity production. The unique real innovation to be mentioned here is the cavity frequency adjustment, now performed by electro-polishing. Due to the mechanical and chemical treatments, the cavity frequency is modified by the upgrading processes. Now we set the cavity resonant frequency to the linac reference point ourselves, without waiting for access to the mechanical workshop. In the past, for saving time, we had to tolerate a higher discrepancy, which was later adjusted by deforming the tuning plate. The strength necessary to buckle the plate ended to stack the tuner mechanism in CR19-2, thus making that cavity unusable.

Nb Sputtering

We adopted the DC biased sputtering technology for producing the resonators. The process was performed in steps to limit the cavity temperature during discharge. We used cylindrical cathodes for both the high and the medium β cavities, lower in diameter in the second case. In 2003, after producing more than 50 medium β resonators, we had to replace with a new one the cathode, which had become too thin and started to lose fragments.

Stainless steel nets located in between the cathode and the inner and outer conductors provide grounding during the sputtering process, while the resonator body is

negatively polarized. An accurate alignment of the sputtering configuration is fundamental to avoid short circuits or sparks. Experience allowed reducing their occurrence although the cathode high voltage was increased from 700 V to 1 kV during the sputtering optimization process.

Vacuum spikes in the sputtering chamber during baking are often associated to lower resonator performance. In 1998 we used to produce cavities with Q-values very different. Later on, we systematically opened all the hidden volumes under the brazing joints reducing the differences in Q_0 values.

Initially the cavity bottom plates were coated one by one. Since 2001 we used a new system where it was possible to sputter up to 9 plates in the same cycle, thus making the resonator production cycle more efficient.

Evolution in Assembling Procedures

Due to both tight schedule of cryostat maintenance programme and lack of spare resonators, we could not risk any change in the cavity production processes until the installation of the upgraded resonators restored the previous ALPI gradient. Only in July 2001, on cavity FC41, we tried the effect of HPWR on a sputtered cavity, previously rinsed only with alcohol. We found Q_0 increasing from 2.5×10^8 to more than 5×10^8 . Since then we rinsed all the cavities after sputtering in this way.

In 2004 we succeeded in eliminating the In gasket, which assured the rf contact between the cavity body and the plate, by modifying the fixing flanges and the plate itself. The previous attempt to eliminate the gasket maintaining the old ones, resulted in the performance of cavity 2, still installed in CR15, which decreases its accelerating field when its plate is pulled out to reach the target frequency (from 3.7 to 2.8 MV/m at 7W). The absence of In gives the possibility to rinse the cavities just before their installation in the line cryostat, as we perform regularly nowadays. In future, hopefully, it will be also possible to rinse the resonators after each cryostat venting.

A further improvement would derive by performing the final rinsing after the cryostat alignment process which, for the medium and high β cryostats, has to be performed with the cavities installed and opened to air.

CONDITIONING

Not being assembled in a clean room, the cavities installed in ALPI usually present field emission. We process them in pulsed mode by 1 kW amplifier before using them for the first time. In many cases this treatment resulted sufficient to obtain a flat Q curve up the design operational power of 7 W, however we still have some cavities which would benefit from a few hours more high power conditioning. Up to now we devoted a limited time to this process, because we have to operate locally, one cavity at a time, limited by radioprotection and cryogenic limits.

The high power conditioning process is a little risky and, in two cases, CR19-1 and CR14-2, the rf input line

was not able to sustain the high power and failed. We should open the cryostats to put the cavities again in use.

Routinely, after either a thermal cycle to room temperature or a long inactivity period, we perform a couple of hours of He conditioning by the installed 100 W amplifiers. This is generally sufficient to restore in the cavity the previously reached accelerating field at the quoted power. If there is not enough time for that, it is possible to have an increase in the power consumption necessary to sustain the previously reached accelerating field. This is a rather rare event but it is the reason why the cavities, in which field emission is still active, are set at a slightly lower field than the value sustained at 7W.

CAVITY PERFORMANCE IN ALPI

We gathered the last measured Q-curves of the sputtered medium β accelerating field installed in ALPI in Fig. 4. Each plot collects the Q-curves of the cavities installed in two cryostats. A parallel graph, on the right side presents the accelerating field sustained by the cavities. Note that the legend of each Q-curve indicates the cavity position, resonator type and number, data of the first laboratory test (performed just after the cavity production). The further letter, present in cryostats CR8, CR9, CR10, CR13, indicates the treatment the cavity had when the relative cryostat was recently uninstalled for maintenance [9]. R means HPWR only, N stays for newly sputtered resonator. CR8, CR9, CR10 and also CR7 were opened to air before 2004, without substituting or rinsing the cavities.

As it is possible to notice, two cavities of CR15 present the worst performance. In 2000, when we had to repair that cryostat in emergency, we put inside the only cavities then available, whose performance were badly influenced by the substrate (PP1) from Cu quality and bad plate contact (2). A further cavity in CR15, FC03, was produced before the systematic opening of the volumes under the brazed joint. This also happened for the CR7 cavities. In both cases the film contamination during the sputtering process can be responsible for the results. All the CR8 resonators sustain accelerating fields of about 5 MV/m at 7 W, which were reached after the cavities were rinsed only in the last cryostat maintenance cycle (2008). Also the other medium β cryostats (CR10, CR12, CR13, CR18), which had their cavities HPW rinsed after sputtering, present now average accelerating fields at 7W of about 5 MV/m. Only CR9, which had to be vented after resonator rinsing, operates limited to 4.4 MV/m in average. The cavities of cryostats CR16, CR17 still present strong field emission: it limits their performance to 4.6 and 4.4 MV/m respectively. Both these cryostats were vented after having installed the resonators and surely this introduced contaminations difficult to process.

Notice that some cavities had further conditioning after the shown Q-curves. The performance at 7 W presently sustained can be found on the right plots together with the performance of the last years. Please note that in case of cavity substitution, the value refers to the resonator previously installed in that place.

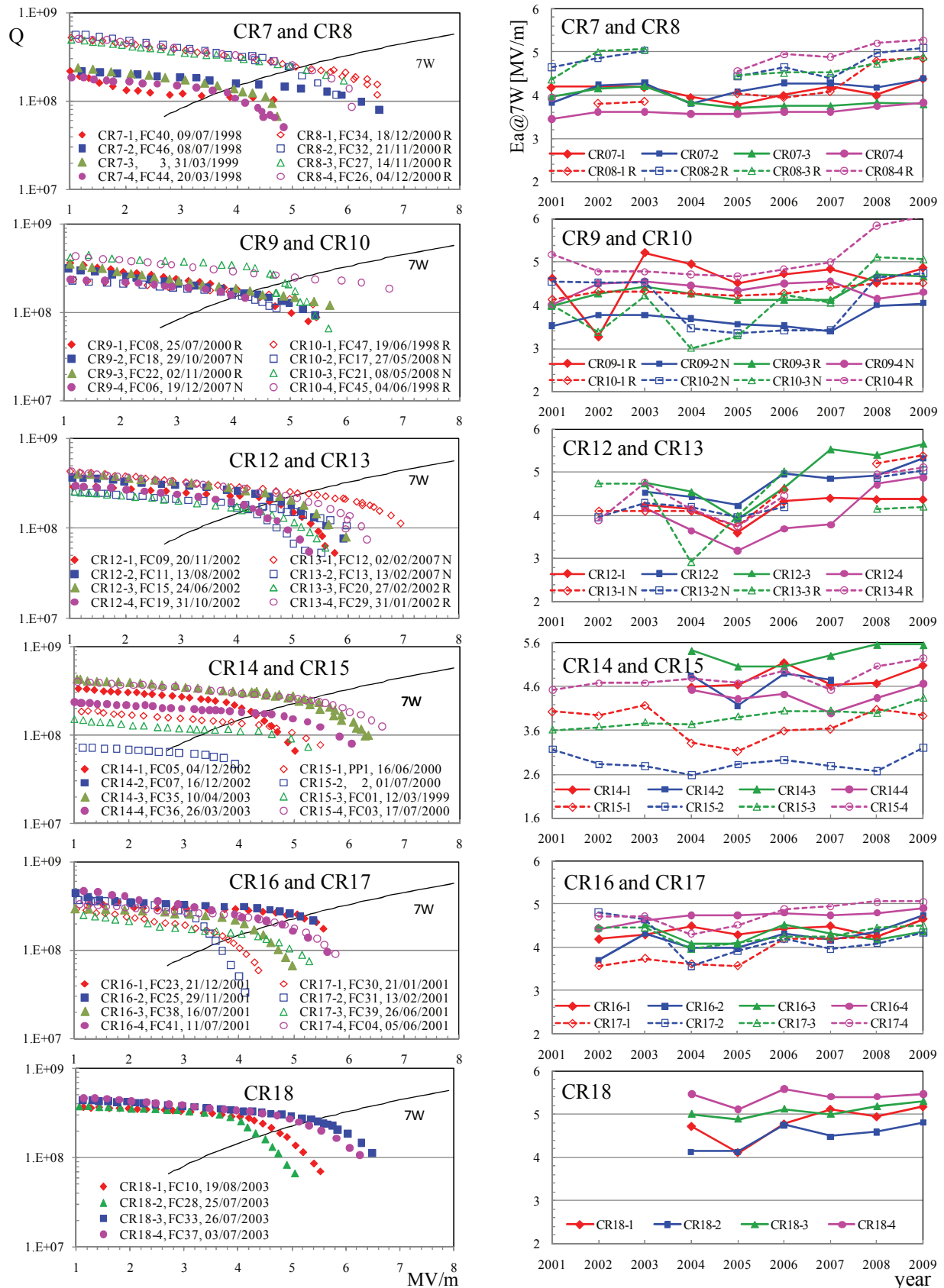


Figure 4: Q curves (left) and performance in the last years (right) of the medium β resonators installed in ALPI cryostats. See text for comments.

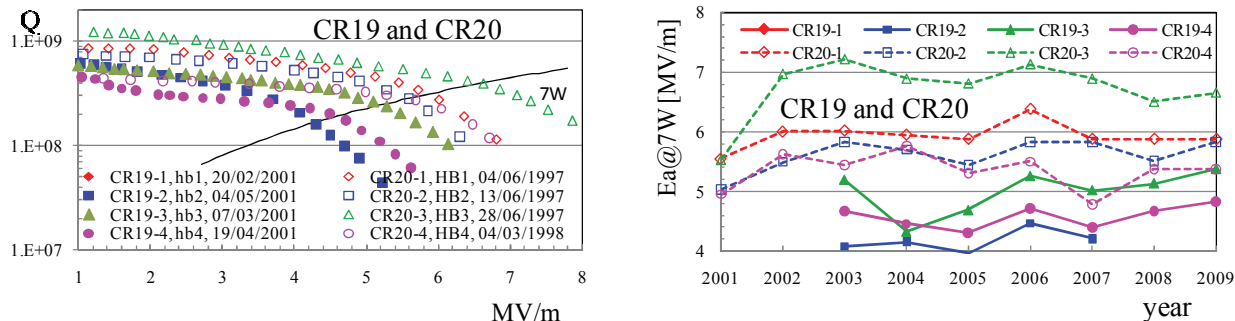


Figure 5: Q curves (left) and performance in the last years (right) of high β resonators installed in ALPI cryostats. See text for comments.

The Q-curves of the high β resonators are shown in Fig. 5. The cavities in CR20, built without any brazing joint, present better results than the cavities in CR19, whose construction technology is similar to the medium β resonators. The Q_0 value of CR20 cavities are about 1×10^9 , except HB4, whose Q-curve presents a Q-switch, not visible in the graph, which decreases the Q-value from 7×10^8 to 4×10^8 . The average accelerating field that they can presently sustain is about 6 MV/m at 7 W.

Cavities of CR19 have Q_0 around 5×10^5 and should reach accelerating fields higher than 5.5 MV/m when fully conditioned. However this is not the case because, as it happened also for the other high β resonators, they were often kept turned off, and not conditioned long enough, being their contribution not generally required for reaching the scheduled beam energy.

We are going to uninstall the CR19 both to repair the rf line of hb1 and to adjust the frequency of cavity hb2. In that occasion we plan to perform HPWR in the resonators which should reduce their field emission.

CONCLUSION

The sputtered high β cavities have been in operation for more than 10 years maintaining their performance and always showing high reliability [9].

The accelerating field of medium β resonators at 7 W is now approaching 5 MV/m, in average twice higher than the value they had when Pb plated [10]. The renewing of medium β resonators by Nb sputtering substantially increased the ALPI gradient and was performed without interfering with operation at a negligible cost. The cavities are still improving their performance, but they are now very close to the maximum value reachable by the old substrates. We could obtain accelerating field exceeding 6 MV/m also in medium β resonators only by sputtering on new substrates. Recently we had the possibility to develop and to sputter four of them and plan their installation in ALPI very soon [10].

The reliability and simplicity of operation of Nb sputtered cavities is clearly shown in ALPI where they steadily operate in spite of pressure instability in liquid He cooling bath [11].

REFERENCES

- [1] A. M. Porcellato, "Experience with the ALPI Linac resonators", Nucl. Instr. and Meth. A382 (1996) p. 121.
- [2] D. Zenere, A. Facco, F. Scarpa, "Progress in the ALPI-PIAVE low beta section upgrade", Proceeding of EPAC08, Genoa Italy.
- [3] Stark et al., "Niobium sputter-coated QWRs", Particle Accelerators, Vol.61 (1998) p. 383.
- [4] Palmieri et al., "Installation in LNL ALPI linac of the first cryostat with four niobium quarter wave resonators", Nucl. Instr. and Meth., A382 (1996), p. 112.
- [5] A. M. Porcellato, S. Stark, V. Palmieri, F. Stivanello, "Niobium Sputtered QWR", Proceedings of the 12th International Workshop on RF Superconductivity, Cornell University, Ithaca, NY 10-15 July 2005.
- [6] A. M. Porcellato et al., "Nb/Cu ALPI QWR Performance", LNL Annual Report 2008, in press.
- [7] S. Stark et al., "A Novel sputtered medium beta cavity for ALPI", Proceeding of the 13th International Workshop on RF Superconductivity, Beijing October 2007.
- [8] A.M. Porcellato et al., "Production Installation and test of Nb sputtered QWRs for ALPI", Pramana J. Phys. Vol. 59 p. 871 (2002).
- [9] A.M. Porcellato S. Stark, V. Palmieri, F. Stivanello, "Nb Sputtered Cu QWR: a 20 years experience from an idea to the routine beam acceleration", Proceedings of The International Workshop on Thin Films and new ideas for pushing the limits of RF superconductivity, Legnaro, October 30-31 2006.
- [10] S. Stark et al., "Production of new medium beta Nb sputtered ALPI cavities", LNL Annual Report 2008, in press.
- [11] G. Bisoffi et al., "ALPI QWR and S.RFQ operating experience", Proceedings of the 13th International Workshop on RF Superconductivity, Beijing October 2007.

OPERATIONAL EXPERIENCE IN PIAVE-ALPI COMPLEX

E. Fagotti, G. Bassato, A. Battistella, G. Bisoffi, L. Boscagli, S. Canella, D. Carlucci, M. Cavenago, M. Comunian, F. Chiurlotto, M. De Lazzari, A. Facco, A. Galatà, A. Lombardi, P. Modanese, M.F. Moiso, A. Pisent, M. Poggi, A.M. Porcellato, P.A. Posocco, C. Roncolato, M. Sattin, S. Stark, F. Scarpa, INFN-LNL, Legnaro, Padova, Italy.

PIAVE-ALPI is the INFN-LNL superconducting heavy ion linac, composed by an SRFQ (superconducting RFQ) section and three QWR sections for a total of 80 cavities installed and an equivalent voltage exceeding 70 MV. In the last years the SRFQ and the bulk niobium QWR came into routine operation, the medium energy QWR section was upgraded with a new Nb sputtered coating, ECR source was firstly improved by using water cooled plasma chamber and then replaced with a new one. The operation of the accelerator complex allowed acquiring a strong experience on many operational issues related to ECRIS, superconducting cavities and cryogenics, beam control and manipulation (with the new and higher accelerating gradient). The paper reports about operational experience, the present limitations and the future perspectives of the facility in view of the experimental campaign with the EU detector AGATA and of the use of PIAVE ALPI as RIB post-accelerator for SPES radioactive ion beam facility.

INTRODUCTION

The superconducting linac complex at LNL is composed by the PIAVE injector [1][2] and by the ALPI booster [3]. PIAVE injector is based on superconducting RFQs (SRFQs) [4][5], the first superconducting ones operational in the world. The SRFQs are followed by two cryostats of bulk Nb 80 MHz Quarter Wave Resonators ($\beta_0 = 0.047$). The beam, received from an ECR source on a 350kV platform [6], is first bunched between the ECR and the SRFQs and then re-bunched between PIAVE and ALPI by two normal conducting cavities [7]. The present PIAVE layout (Fig. 1) is very compact, with the SRFQ cryostat immediately followed by the two QWR cryostat periods with external doublet focusing. The period is kept as short as possible, especially to reduce the longitudinal phase advance.

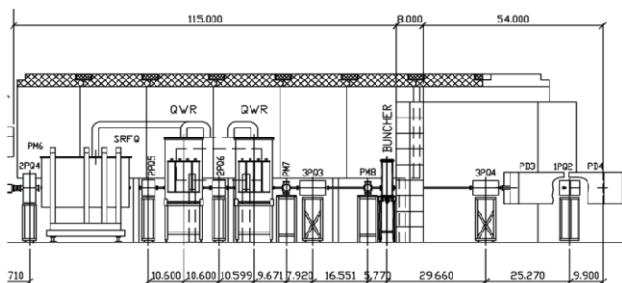


Figure 1: PIAVE layout.

ALPI booster consists, at the moment, in 3 cryostats of bulk Nb 80 MHz cavities ($\beta_0 = 0.056$) and 13 cryostats of Nb sputtered on copper base 160 MHz cavities ($\beta_0 = 0.11$

and $\beta_0 = 0.13$). The linac is composed by two branches connected by an achromatic and isochronous U-bend (Fig. 2). The linac period consists of one triplet and two cryostats (4 cavities per cryostat) with a diagnostic box in between.

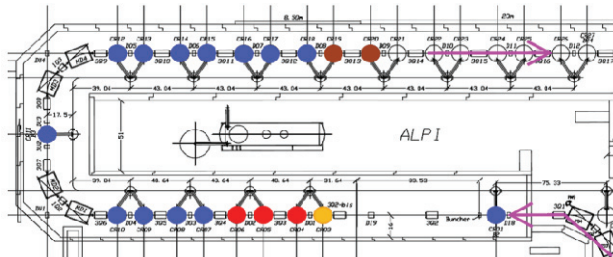


Figure 2: ALPI plan for 2009. The beam coming from PIAVE injector passes through the low- β (in orange and red), medium- β (blue) and high- β (brown) cavities.

In the total complex, there are 74 accelerating cavities and 6 bunchers with a maximum equivalent voltage of more than 70 MV (12 MV and 58 MV for PIAVE and ALPI respectively). However, the low beta cavities can be maintained at high gradient during operation only in exceptionally stable conditions of the Helium pressure. Practically, the maximum equivalent voltage reachable is limited to 64 MV (12 MV + 52 MV).

PIAVE injector commissioning started in November 2004 with a $^{16}\text{O}^{3+}$ pilot beam. In December 2005, after a long shutdown of the ALPI booster cryogenic plant, a very first ^{22}Ne test beam was accelerated by PIAVE and ALPI to the experimental apparatus PRISMA-Clara (final energy $\sim 6\text{MeV/A}$), where it provided stable beam-on-target conditions for around 50 hours, before the scheduled conclusion. In the period January-April 2006, tests with ^{22}Ne , ^{132}Xe , ^{40}Ar and ^{84}Kr beams were conducted. Final energy on target ranged between 5 and 8.25 MeV/A and beam currents extended between 5 and 15 pA. The required typical time for driving the beam through injector and booster to the experimental station was $\sim 2\text{-}3$ days. The period May-July 2006 was dedicated to maintenance on the SRFQ cryostat and the TCF50 cryogenic system. During the special maintenance, both fast and slow tuners of the superconducting RFQs were repaired and the distribution of temperature diodes was rationalized. By the end of July, the cryostat was closed and in September-October it was again prepared for beam operation. In November, the first official experiments with the PIAVE-ALPI combination started.

The ECR ion source Alice was also subject to a small but important upgrade at the end of 2006: the source

vacuum chamber was replaced with a water-cooled one. The immediate consequence of this operation was the shift of the distribution of the source charge state towards higher values. As an example, in the case of Xe beam, this allowed a 30% increase of the final energy on target.

In January 2007 a stripping station, equipped with carbon foils of different thickness, was placed before the ALPI U-bend, to test both the feasibility of acceleration and the transport of a charge enhanced beam. The acceleration was successful for Xe and Ar [8]. $^{136}\text{Xe}^{30+}$ was easily transported to the experiment with final energy of 1.1 GeV (8.1 MeV/A), a 20% more than the energy of the un-stripped beam (923 MeV). The beam current on target was greater than 1 pA. $^{36}\text{Ar}^{15+}$ was transported to the experiment with a final energy of 450 MeV, whereas the energy without stripping was 300 MeV.

In the mean time, an important upgrade of the ALPI low beta section started aimed to increasing the accelerating field up to 5.5 MV/m. After spring 2007, the overall machine availability was significantly affected by the replacement program of the old ECR ion source Alice with a new one (LEGIS, Supernanogan, Pantechnik S.A.), which was completed at the beginning of this year.

Commissioning of PIAVE injector with the new source was successful. New source guarantees a lower emittance allowing an increase in overall transmission.

PIAVE INJECTOR

The main components of the injector are the ECR ion source, installed on a 350 kV platform, the LEBT (Low Energy Beam Transport), the cryomodule housing two superconducting RFQs, the QWR linac section (two criomodules housing four cavities each) and the HEBT (High Energy Beam Transport) injecting into ALPI. The linac operates at 80 MHz, the bunching frequency is 40 MHz.

ALICE Source and Platform

Ion source beam, extracted with a typical $V_s = 11$ kV voltage, is mass separated (resolving power $m/\Delta m \sim 100$) and finally accelerated by an electrostatic column up to the nominal $\beta=0.00892$ for RFQ injection.

Stability of the platform voltage V_p confirmed being excellent (within $17 V_{pp}$) even at higher voltages. V_p was limited to 350 kV, but rarely more than 270 kV ($A/q=7.33$) were used. Injection into PIAVE was consistent with the high beam quality demonstrated by the previous emittance measurement (with a two slit scanner) for all tested beams. It is important to note that beam optics depends from the ratio V_p/V_s where V_s is the constant source voltage.

Among the beams delivered to PIAVE, ^{22}Ne was directly separated in the source from the natural gas. Also ^{132}Xe was obtained from natural mixture, while ^{136}Xe was prepared from enriched bottle allowing the proportional increase of the current so as to obtain the tuning simplification. Other important improvements for ^{136}Xe operation were:

- the development of a new cooled chamber (entirely designed and built in LNL workshop) for Alice which allowed the increasing of microwave power and consequently ion charge state q up to $23+$;
- the fine tuning of the frequency, from $f=14400$ MHz to $f=14363$ MHz, which increased the $^{136}\text{Xe}^{23+}$ current up to 1200 nA [9] (and up to 740 nA of $^{136}\text{Xe}^{24+}$). Frequency tuning is a laborious procedure since other source tunings must be optimized again at each f . A clear theoretical explanation of its effectiveness is missing, even if several mechanisms were proposed.

Even if operation of the ECR ion source Alice in the last years (up to 2008) was mainly devoted to produce beam for RFQ injection (up to ^{136}Xe), several test of induction ovens [10] for metallic beams up to element as refractory as vanadium and of other accessories, like sputter probes, were performed. Current in the order of 1 mA of V^{8+} was maintained for 3 days, after which the experiment was stopped because others were scheduled. Oven was operated up to about 2300 K for three weeks outside the ECRIS, with a gradual decay of the emitted flow. Results with Cr and Ti were similar. Experience proved that a very careful alignment of crucible and rf coil is necessary for reliable operation; moreover, some metals (for example tin) are much more difficult to maintain in the crucible than others (vanadium, silver, etc). For some materials, like iron, self consumable crucibles were also designed [10].

Superconducting RFQs

The RFQ part of PIAVE consists in two superconducting RFQ resonators. This original choice allows a very efficient acceleration (more than 2 MV/m for $A/q=8.5$) employing an innovative beam dynamics design [11]. The main specificity of a superconducting RFQ (SRFQ) is the possibility to employ an intense inter-vane voltage that allows achieving a large acceptance and acceleration. Moreover, in this case, the use of two separate structures, beside having clear construction advantages, allowed to further increase the voltage in the second SRFQ; the inter-vane voltage is 148 kV in SRFQ1 and 280 kV in SRFQ2 for $A/q=8.5$.

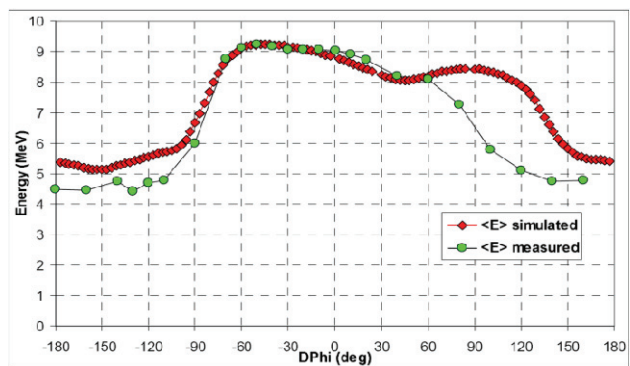


Figure 3: Average spectrum energy at RFQ exit as a function of phase difference between cavities.

The first tuning of the two PIAVE SRFQs was done with O^{3+} beam and the external buncher off, recording beam transmission (on FC) and energy spectrum (on Si detector) for different phases of SRFQ2 (Fig. 3). The nominal energies for oxygen are 5.45 MeV for SRFQ1 and 9.4 MeV for SRFQ2. Energy selection due to chromaticity effects of the doublet magnet next to RFQ are taken into account in the PAMTEQM [12] - PARMILA [13] simulations superimposed to the measurements in Fig. 3. Simulations and measurements match very well in the phase range in which the SRFQ1 beam falls within the separatrix of SRFQ2, allowing a precise determination of the nominal SRFQ2 phase.

After this, the buncher was switched on to the nominal voltages and adjusted in phase so to reach the maximum transmission. Transmission reached after a fast realignment of the LEBT with respect to SRFQ was 68%, as predicted by simulations.

QWRs and Bunchers

The PIAVE QWR section includes two cryostats, each containing 4 bulk niobium QWRs with $\beta=0.047$ working at 80 MHz. These large cavities, powered by 1 kW RF amplifiers, are equipped with mechanical dampers to reduce their sensitivity to ambient mechanical noise. QWRs reached off-line an accelerating field of ~ 7 MV/m ($E_s/E_a \sim 5$), while their nominal accelerating field in PIAVE is 5 MV/m. Beam dynamics considerations suggest scaling the accelerating field of QWRs with the A/q ratio as for the RFQ. Therefore, the maximum accelerating field used in operation is as high as 4.3 MV/m. Phase and amplitude locking asks for an enlargement of the resonant bandwidth on all cavities. This was achieved by over-coupling the SC cavity in a self-excited loop (SEL) mode (1 kW amplifiers were used). In addition to the QWRs, two room temperature bunchers are installed: the triple-harmonic low energy buncher and the high energy buncher, a high power, water-cooled $\beta=0.05$ QWR (a similar cavity was installed also in ALPI). The triple harmonic buncher, located upstream the first SRFQ, is used to match the beam in the SRFQ longitudinal acceptance ellipse. It guarantees a capture of 68 % in nominal conditions. The room temperature high energy buncher, together with the twin cavity located in ALPI, has the function to match the PIAVE 1.3 MeV/A beam to the ALPI line. A 10 kW amplifier powers this resonator.

ALPI BOOSTER

Low Beta Section

The ALPI low- β section includes, at present, three cryostats, each containing 4 bulk niobium QWR's with $\beta=0.055$ working at 80 MHz. Room for one more cryostat, named CR3, was left in the beginning of the line.

Resonators have an average gradient which is around 6 MV/m with the nominal 7 W power dissipation; this gradient, however, cannot be maintained in operation due to a too high sensitivity to the helium pressure fluctuation. The frequency sensitivity to pressure changes, in full Nb

QWRs, is about 1 Hz/mbar even though P_{He} occasionally fluctuates in ALPI at a rate of up to 100 mbar/min or more.

For long-term operation, to avoid cavity unlocking, the gradient is usually set at 3.5 MV/m. The RF system, originally dimensioned for this gradient, allows a steady forward power of about 50 W per cavity. The resulting value of the P/E_a^2 ratio gives the minimum RF bandwidth for safe operation in ALPI, i.e. about ± 15 Hz.

This limitation in accelerating fields together with the frequency jump after low beta section, make the transport in the ALPI U-bend extremely difficult especially for beam with high A/q . The beam behavior after frequency jump is highly non-linear due to the high gradients and strong Bessel components of the fields inside the medium beta cavities.

Medium Beta Section

ALPI medium beta section includes 44 superconducting resonators housed in 11 cryostats. The cavities are 160 MHz QWR with 0.11 optimum beta. Their original Pb superconductor layer was replaced with a sputtered Nb film in between 1999 and 2003 when a maintenance cryostat programme was set up for repairing cryogenic leaks developed in the cryostat cryogenic circuits. The cavity upgrading resulted in a substantial increase of ALPI average accelerating field, which rose from 2.7 MV/m (the best average value obtained with Pb) to 4.8 MV/m, at the available power of at 7W. The performance is still improving due to longer conditioning. The new performance was obtained without any further upgrading of both cavity equipment and control software.

Due to the mechanical stiffness, cavities are insensitive to changes in liquid He bath pressure. For this reason, they can be reliably phase locked at the accelerating field sustained by the available cryogenic power, fed by 100 W amplifier and without the necessity of continuous frequency tracking.

There are further 6 medium beta cavities in the bunching cryostats; only two of them, housed in the re-bunching unit, still maintain their original Pb layer. All the medium beta cavities are operational, but one (CR14-2) which has the rf input line damaged during high power conditioning.

The high β section consists of 2 cryostats only (CR19-20). These cavities maintain the medium β frequency of 160 MHz. The increase in their optimum beta ($\beta_0=0.13$) is obtained by moving the resonator beam port outside the resonator body. The cavities, housed in the two medium β cryostats, have the same inner shape, but different construction technology and copper quality. Cavities in CR20, designed to be sputtered and installed in 1998, reach 6 MV/m at 7 W in average, while the ones in CR19, which were later built similarly to the medium beta ones, present accelerating fields around 5.5 MV/m. At present two of these cavities are out of operation because of an rf line failure and a tuner stuck respectively. The high β cavity behavior is quite similar to the medium one; they maintain the same reliability and facility of setting [14].

PIAVE-ALPI UPGRADE

Many upgrades of the PIAVE-ALPI complex are concluded or very near to conclusion. Replacement of the ALICE source with the LEGIS one was completed last year. Injector commissioning with the new source started at the beginning of 2009 and was concluded at the end of May. Extremely good results have been obtained in terms of transmission and beam quality. In the meantime, an important upgrade of the ALPI low energy cryostats is in progress. This will guarantee an increase of the low beta cavity accelerating fields up to 5.5 MV/m.

The same accelerating field for the medium beta section will be guaranteed by sputtering on new copper bases.

LEGIS Source

The new ECR ion source, named LEGIS (LEGnaro ecrIS), is a product by Pantechnik [15] company. LEGIS is a full permanent magnet source working at 14.5 GHz. Good performance and low power consumption make it well suited for operation on a high voltage platform.

The source and its beam line are controlled via National Instruments FieldPoint modules that acquire all parameters and display them through a LabView interface.

Besides the production of ion beams from noble gases, it will be capable to produce metallic ion beam by two different methods:

- a resistive oven to produce metallic vapors from elements reaching a vapor pressure of 1 Pa for $T < 1500$ °C;
- plasma sputtering to produce metallic vapors from refractory elements.

Source installation was completed at the end of last year. It was housed in the old high voltage platform. All the line up to the accelerating tube was redesigned in order to have good flexibility and complete beam characterization. To this scope, two independent movable slits for beam selection and an emittance measurement device were installed (Fig. 4). Each slit consists of two water cooled tantalum plates, moved together by a stepper motor. Each plate has a current pickup for beam loss monitoring.

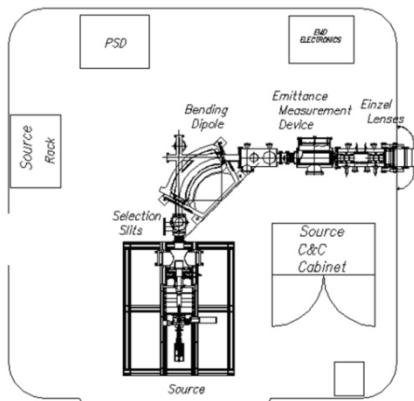


Figure 4: The complete beam line on the high voltage platform and its equipment.

Linacs

The emittance measurement device consists of a slit-grid system. The maximum stroke of the system is ± 30 mm while the maximum divergence that can be measured is more than 70 mrad.

The proof of good source performances with gaseous and metallic ion beams was given during acceptance tests at Pantechnik site (Table 1). For what concerns beam quality, the normalized 4-rms emittance was well below 0.3mm-mrad for oxygen, argon and gold beams.

Table 1: LNL Current Requests

	Ion	Current [μ A]
gaseous beams	O ⁶⁺	200
	Ar ⁹⁺	100
metals with oven	Ag ²¹⁺	3
	Au ²⁶⁺	10
	Au ³⁰⁺	1
metals with sputtering	Ta ²⁴⁺	1

Acceptance tests were partially repeated at LNL at the end of 2008 and will be completed within 2009.

PIAVE injector re-commissioning started in March 2009 with ⁴⁰Ar⁹⁺ beam. An important source alignment problem emerged in the first emittance measurements. We solved it, using the multi-polar corrector located on the dipole magnet in dipolar configuration and we added a new steerer to the line next to the accelerating tube. Emittances (normalized, rms) measured after the solution of the problem remain below 0.075 mm-mrad for all operating conditions. The best values that we measured are 0.059 mm-mrad for the x-plane and 0.048 mm-mrad for the y-plane. These low emittance values together with the use of an electrostatic triplets downstream of the accelerating tube allowed to reach very good performances in terms of transmission (Table 2).

Table 2: Comparison of Injector Transmissions (%) with ALICE Source (old PIAVE) and with LEGIS Source (new PIAVE)

	Old PIAVE	New PIAVE
Injector input	100	100
Injector output	63.3	70.3
Booster input	56.8	62.4

ALPI Low Beta Section Upgrade

At present, the equivalent voltage of the ALPI low- β section is around 7.5 MV, limited by the resonators RF system. In the view of the ALPI-PIAVE linac upgrade, that will lead to acceleration of ions of any mass above the Coulomb barrier energy this value must be doubled.

To set up the low- β section upgrade plan we profited from the experience developed at TRIUMF, where similar resonators [16] are operated above 7 MV/m by means of a more powerful RF system and cooled RF couplers [17].

The upgrade actions are the following:

- replacement of all the 150 W RF amplifiers with 1 kW units;
- replacement of all existing 80 MHz RF couplers with new ones cooled with liquid Nitrogen;
- modification of all low- β cryostats to allow use of the new couplers;
- replacement of cryostat rf input line;
- construction and installation in ALPI of one more cryostat hosting 4, $\beta=0.047$ resonators;
- installation of a liquid nitrogen distribution system in ALPI-PIAVE.

The upgraded cavities are expected to operate at least at 5 MV/m, giving an equivalent voltage of around 14.4 MV, as required. The average forward RF power required guaranteeing ± 15 Hz RF bandwidth at 6 MV/m is about 200 W, but up to 600 W are needed for safe long term operation and for pulsed power RF processing. At present, the new amplifiers are installed in the old cryostats. Before summer, a new cryostat, equipped with the new RF system and with the cooled couplers, will be installed in ALPI, becoming the test bench for the new equipment. In the next phase, all the cryostats will be modified and upgraded for coupler cooling.

ALPI Medium Beta Section Upgrade

The average accelerating field of cavities of medium beta section is still lower than the one of high beta section, due to the characteristics of recovered substrates. We expect to reach in medium beta cavities the same performance obtained in high beta cavities by sputtering on new, suitably built, bases.

Four cavities, produced by new substrates, were sputtered up to now. The laboratory test confirmed that they can reach in operation accelerating field in between 5.5 and 6 MV/m [14]. We plan that they will substitute the cavities presently housed in CR15 by this fall. The substitution of cavities in other cryostats would further increase ALPI energy, but it asks for devoted funding.

CONCLUSION

PIAVE and ALPI are working reliably, at present, fulfilling the experimental programme of INFN-LNL.

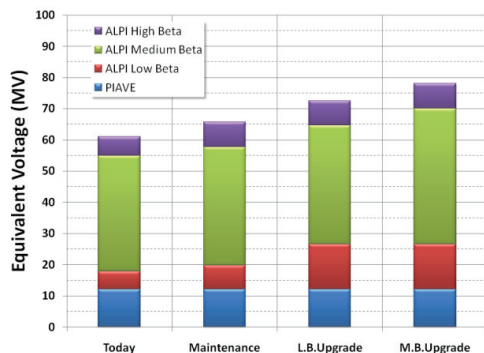


Figure 5: Equivalent Voltage increase with PIAVE-ALPI upgrade.

With maintenance of six cavities, (2 low- β , 1 medium- β and 2 high- β) and the completion of the low beta upgrade, the accelerator will reach an equivalent voltage of more than 70 MV. The funding of the medium beta upgrade would further pump up the equivalent voltage up to 78 MV (Fig. 5 and Fig. 6).

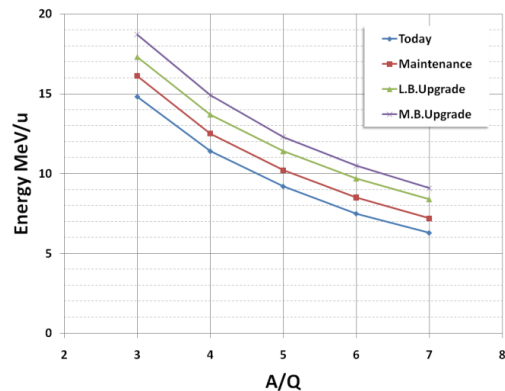


Figure 6: Expected final energies for the PIAVE-ALPI complex. Final energies for $A/Q=3$ could be slightly overestimated (beam dynamics imposes a decrease in the accelerating fields of low beta section cavities).

REFERENCE

- [1] A. Lombardi et al., Proc. of LINAC2000, Monterey, USA, 356.
- [2] A. Pisent and al., Proc. of LINAC2006, p. 227.
- [3] A. Dainelli and al., NIM A382 (1996), p. 100.
- [4] I. Ben-Zvi, A. Lombardi and P. Paul, Particle Accelerators, 1991, Vol. 35, pp. 177-192.
- [5] G. Bisoffi et al., Proc. of SRF 2001 Workshop, 123.
- [6] M. Cavenago et al., Rev. Sci. Instr. 71 (2000) 758.
- [7] A. Facco et al., Proc. of EPAC 2000, Vienna, Austria, 2037.
- [8] P. A. Posocco et al., MOP054, Proc. of LINAC08, Vancouver, Canada.
- [9] A. Galatà et al., LNL Annual Report 2007, 161.
- [10] M. Cavenago et al., Proc. of Epac 2008, Genova, Italy, 397.
- [11] A. Pisent, Proc. of HIAT 1998, AIP Conf. Proc. 473, 214 (1998).
- [12] K.R. Crandall et al. "RFQ Design Codes", LA-UR-96-1836, Revised January 16, 2005.
- [13] H. Takeda, "PARMILA", LA-UR-98-4478, Revised October 13, 2004.
- [14] A.M. Porcellato et al., Proc. of this conference.
- [15] <http://www.pantechnik.fr/joomla/>
- [16] A. Facco et al., Proc. of PAC 2001, Chicago, USA, June 18-22, 2001, 1092.
- [17] M. Marchetto et al., Proc. of PAC 07, Albuquerque, New Mexico, USA, 1392.

LASER ACCELERATED IONS AND THEIR POTENTIAL FOR THERAPY ACCELERATORS*

I. Hofmann, A. Orzhekhovskaya and S. Yaramyshev, GSI, Darmstadt, Germany
I. Alber, K. Harres and M. Roth, Technical University, Darmstadt, Germany

Abstract

The recent development in laser acceleration of protons and ions has stimulated ideas for using this concept as innovative and compact therapy accelerator. While currently achieved parameters do not yet allow a realistic conceptual study, we find that our simulation studies on ion collimation and transport, based on output data from the PHELIX experiment, already give useful guidance. Of particular importance are the chromatic aberrations of the first collimator as interface between the production target and a conventional accelerator structure. We show that the resulting 6D phase space matches well with the requirements for a hypothetical synchrotron injection.

INTRODUCTION

Proton or ion acceleration by irradiation of thin foils with very high power laser beams (typically 10^{19} W/cm²) has raised the question, if this principle can be the basis for a new type of compact ion accelerator with possible application to therapy, where the kinetic energy need is 50-250 MeV for protons, or up to 430 MeV/u for C⁶⁺ beams [1]. Successful acceleration of protons to energies around 50 MeV (see, for instance, Ref. [2, 3, 4, 5]) and theoretical predictions (see Ref. [6] and other references quoted there) of laser generated particle energies even up to the full energy needed in ion therapy warrant more detailed investigations. The acceleration of ions is predominantly discussed as “target normal sheath acceleration”, where a dense sheath of electrons is formed on the side of the target opposite to the incident laser, and ions are accelerated by the resulting quasi-static electric field of the order of 1000 GeV/m.

Some of the frequently quoted unique features of laser acceleration are: very high acceleration gradient, extremely small longitudinal and transverse emittances due to the short time duration (< 1 ps) and small source spot (few tens of μm) as well as a reasonably high yields of particles ($10^{12} - 10^{13}$ particles per shot). It is, however, not obvious how to take advantage of these features in order to compete with conventional accelerator technology.

The successful realization of ion accelerators for tumor therapy is based on more than half a century of accelerator development and relies upon a highly accurate control of intensity on the percent level as well as on well-defined energy, transverse spot size and timing controls for beam delivery on the tumor volume by 3D scans. Extreme reliability in all of these functions is a necessity for patient

treatment. Synchrotrons fulfil these requirements for all choices of ions from protons to carbon - yet with the disadvantage of large size and high capital cost.

Laser acceleration, on the other hand, is expected to be compact and cost effective. Early success in achieving impressive energies and particle yields led to considerable enthusiasm, which was responded by warnings not to overlook the yet large performance gaps [7]. The - more qualitative than quantitative - arguments in Ref. [7] have included concerns about the large production energy spread - at low energy up to 100% -, whereas $< 1\%$ is required for precise focusing on the tumor.

The scope of the present study is to quantify this discussion by evaluating primary beam characteristics starting from the actual source parameters. Here it seems useful to distinguish between two theoretical scenarios:

Case A: Laser acceleration as injector or pre-accelerator, with subsequent injection into a synchrotron (or FFAG). Currently achieved data are shown to be compatible with ring injection - irrespective of the low practical attractiveness of such a scenario in view of the remaining cost of a circular machine.

Case B: Laser acceleration to the full energy required for treatment. Such energies seem to be theoretically possible (see, for instance, Ref. [6]), but experimental data are still about a factor five below, thus most challenging questions remain open.

OVERVIEW ON PROTON DRIVERS

In this section we give a brief overview on parameters of several proton accelerators at the forefront of current development. The leading facility in terms of proton beam power is the Spallation Neutron Source (SNS) at Oakridge National Laboratory, which went into full operation in 2006 [8]. It consists of a linac accelerating the 1 ms long pulse train (of 38 mA peak current) of H⁻ from 2.5 MeV to 1 GeV with a bunch frequency of 402.5 MHz. The bunch train consists of $2.7 \cdot 10^5$ microbunches of $6 \cdot 10^8$ p each, hence a total of $1.6 \cdot 10^{14}$ ions. This pulse train is used to fill the storage ring at 60 Hz repetition using an H⁻ injection scheme, hence a total flux of 10^{16} p/s.

Another example is the injector linac (into the existing SIS18 synchrotron) planned for the FAIR antiproton facility at GSI [9]. It accelerates protons from a 325 MHz RFQ from 3 to 70 MeV at a peak current of 70 mA, hence $1.3 \cdot 10^9$ p/microbunch. A pulse train of 36 μs length delivers $7 \cdot 10^{12}$ p at 4 Hz, hence a total of $2.8 \cdot 10^{13}$ p/s.

* Work supported by EURATOM (IFE KiT Program)

A third example of interest in this context is the Heidelberg Ion Therapy Facility (HIT) allowing for an energy of 50-430 MeV/u for H, He, C and O ions [10]. A 216.8 MHz RFQ and subsequent IH-DTL accelerate ions up to 7 MeV/u. After acceleration in the synchrotron the beam is delivered by slow extraction, with a maximum ion number per spill of $4 \cdot 10^{10}$ and extraction times 1-10 s. A broader discussion of parameters for medical applications of accelerators is found in Ref. [1]

In Table 1 we summarize some of their parameters. Note that for the HIT-Therapy case the intensity per spill is assumed to be shared by typically 10^3 voxels (micropulses) for 3D scanning of the tissue. For C^{6+} energies of 430 MeV/u are needed, with reduced intensity. As a guidance it

Table 1: Proton driver examples

Facility	MeV	p/s	power (W)
SNS	1000	10^{16}	10^6
Fair p-linac	70	$3 \cdot 10^{13}$	100
HIT-Therapy	250	10^{10}	0.2

may be useful to compare the averaged proton beam power of Table 1 with the photon beam power of high rep rate Petawatt lasers. Top systems currently available are up to 5 Hz with a time averaged photon beam power of 150 W. A laser acceleration system up to full energy therefore requires a conversion efficiency of photons into “usable” protons of about 10^{-3} or higher.

BEAM QUALITY LIMITATIONS

Here we show that only a limited fraction of the proton or ion output is “usable” as a result of the transmission properties of the first collimator. Due to the relatively large production angle in current experiments it appears to be the most critical element. Options include a quadrupole focusing system [11], or a single pulsed solenoid as in the PHELIX experiment at GSI [12].

PHELIX experimental parameters

As data basis for our estimates we use results from the 2008 PHELIX laser acceleration experiments. These experiment have been carried out with a 170 TW laser beam of duration about 700 fs, which was focussed by a copper parabolic mirror on a beam spot of $12 \times 17 \mu\text{m}$ (FWHM). The specific power density was approximately $4 \cdot 10^{19}$ W/cm². The spectrum of p energies was up to almost 30 MeV, with a total yield of $1.5 \cdot 10^{13}$ protons over all energies. The energy specific measurements were carried out with a stack of radiochromic films, where each film is attributed to a specific p energy. At the reference energy of 10 MeV used in the following studies the yield per MeV slightly exceeds 10^{10} (Fig. 1). Protons are produced in a cone of 23° half angle for energies around 10 MeV. It is also important to note that the production opening angle

General Topics

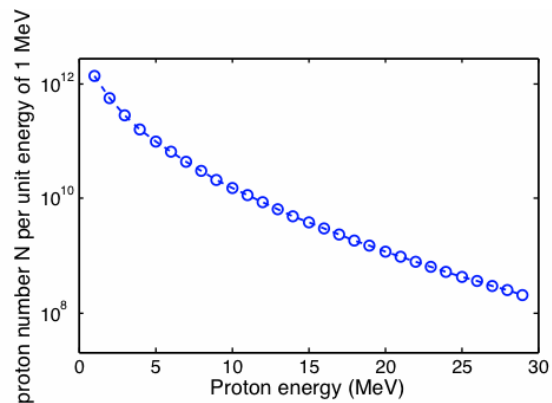


Figure 1: Dependence of differential particle yield on energy for PHELIX experiment (courtesy of M. Roth).

was found to decrease with increasing energy down to 8° half angle for 29 MeV.

Chromatic error in collimation and transport

The p yield per unit energy at given energy and production cone angle is a key parameters that limits the usable fraction of the total yield. In order to estimate this effect we take as example for a collimator a short solenoid comparable with the pulsed solenoid currently under experimental study at GSI. It has a length of 72 mm and maximum field strength of 16 T sufficient to parallelize protons at 10 MeV (Fig. 2). The distance target spot to solenoid edge is assumed to be 15 mm (likewise in all subsequent calculations).

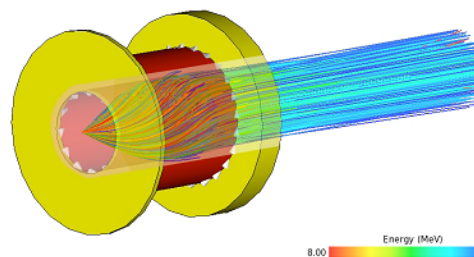


Figure 2: Solenoid collimator with CST calculated rays for PHELIX experiment.

To estimate the chromatic effect we use TRACE3D envelope simulations for a beam originating from a source spot of $30 \mu\text{m}$, and using an opening angle of 20° . The initial pulse duration is somewhat arbitrarily assumed here as 40 ps (while the experimental one is < 1 ps). As reference value for the initial energy spread we take $\Delta E/E = \pm 0.04$, which appears acceptable for subsequent bunch rotation. The initial short bunch length increases with debunching according to the assumed momentum spread. The large energy spread is reduced to a needed value below 1% by using a 550 kV / 108 MHz bunch rotation RF cav-

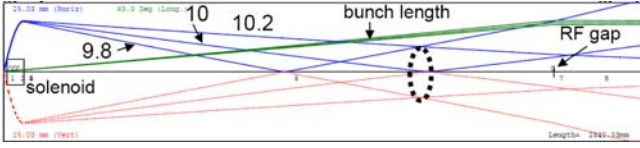


Figure 3: Envelopes for 9.8, 10 and 10.2 MeV (length scale 2.84 m; transverse scale 25 mm; bunch length scale 60°).

ity at about 2.35 m drift distance from the collimator. This drift distance allows the debunching process to expand the bunch to $\pm 40^\circ$ in the RF potential, which is matched to the assumed 550 kV voltage (with a weak space charge equivalent to 25 mA of current). The spread is thus coherent and a result of the correlation of energy and position along the bunch, while the local emittance is unchanged. Although TRACE3D considers only first order effects, we can easily estimate this chromatic effect by transporting beams of different central energy. According to Fig. 3 the energies displaced from the central value 10 MeV by the average values $\Delta E/E = \pm 0.02$ lead to large shifts of focal spots. This blows up the tiny mono-energetic focal spot to a much larger effective radius of 9 mm (shown by the dashed ellipse in Fig. 3) and results in an estimated effective rms emittance increase to 50π mm mrad. Hence, the tiny initial production emittance should be replaced by a *chromatic* emittance. For a given solenoid and spot radius, but varying opening angle x' and energy width, our TRACE3D simulations suggest a scaling (ignoring space charge)

$$\epsilon_{chrom} = \alpha_c (x')^2 \frac{\Delta E}{E}, \quad (1)$$

where α_c is specific to the collimator. A significant reduction either of the production cone angle x' or of the energy width is necessary to bring the effective emittance down to values competitive with beam quality in conventional accelerators. We have not examined an achromatic lens system, which is demanding and would have probably to include higher order focusing and bending magnets, likewise the suggestion of a laser-triggered micro-lens as novel type of collimation [13].

For a quadrupole channel, TRACE3D confirms the same functional dependence in the scaling law. The unsymmetric focusing, however, leads to much larger amplitudes behind the first defocusing magnet enhancing significantly the chromatic effect.

Full simulation results

In order to examine the behavior of the first collimator in a full simulation we have employed the DYNAMION code [14], which includes higher order effects in amplitudes and energy dependence as well as space charge effects. The latter are based on particle-particle interaction, which limits the space charge resolution. Starting again from an initial bunch duration of 40 ps the dynamics of the very early expansion phase of the proton cloud

General Topics

is ignored. This ignores the early charge de-neutralization phase, which is highly space charge sensitive - a problem beyond the scope of our study. Our simulations employ a transverse initial Gaussian distribution truncated at 2σ , and a uniform longitudinal distribution. Assuming again $\Delta E/E = \pm 0.04$ would cut out $8 \cdot 10^9$ protons from the full spectrum according to Fig. 1 assuming the full production cone angle. This is equivalent to 140 mA of “linac current”. Note that “linac current” is defined here as usual in linac notation with the (here fictitious) assumption that every bucket of a 108 MHz sequence of bunches is filled.

We start with the example of a (hypothetical) very compact 40 cm long quadrupolar focusing system consisting of 4 permanent magnet quadrupoles, with the first magnet again 15 mm away from the source and a 2 m long drift space following. We find that a production cone angle of 43 mrad (2.5°) is about compatible with a maximum field of 1.2 T. The 95% emittances along the focussing channel and subsequent drift space are shown in Fig. 4, where $\Delta E/E = \pm 0.04$ and space charge is ignored. Note that what is shown here are the effective *chromatic* values obtained by averaging over the full bunch length. The plot indicates an increase inside the quadrupole channel and an expected constant value in the drift section. The depen-

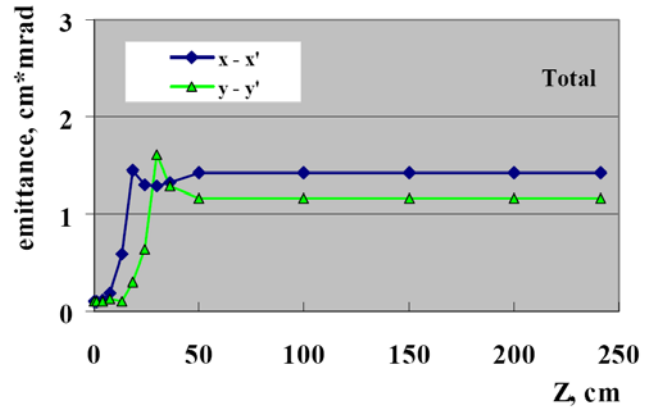


Figure 4: 95% chromatic emittances for quadrupole collimation and $\Delta E/E = \pm 0.04$ (43 mrad and no space charge).

dence on the energy width is shown in Fig. 5. The predicted linear behavior is well confirmed.

We also show in Fig. 5 results for a solenoid again 15 mm behind the laser spot. The solenoid 3D magnetic field has been obtained by direct integration [15] using the coil geometry of the experimental solenoid shown in Fig. 2. Chromatic aberration effects are much weaker than in the quadrupole case - we find an improvement by a factor five. This can be understood as result of the strong and symmetric solenoid focussing, which avoids large excursions as in the defocusing direction of the first quadrupole. Although DYNAMION tracking includes all amplitude dependent nonlinear effects like non-paraxial as well as geometric aberrations, we note that for vanishing energy width

the emittances practically approach the starting emittance value (marked by a red dashed line), hence these effects are negligible for the relatively small cone angles. Results

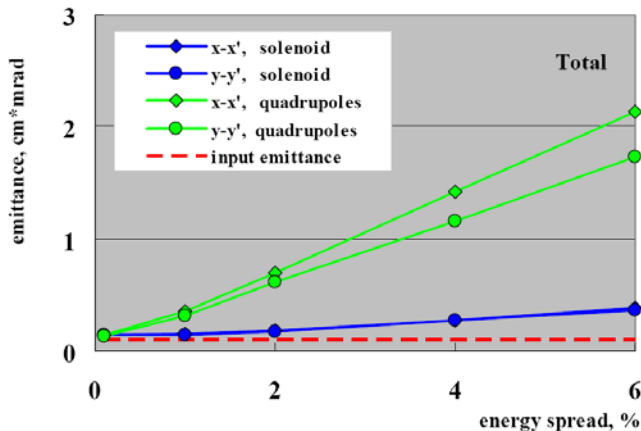


Figure 5: Final 95% emittances for quadrupole and solenoid collimation and variable $\Delta E/E$ (43 mrad and no space charge).

for the final emittances for different production cone angles up to 172 mrad (10°) are shown in Fig. 6. The quadratic dependence suggested in Eq. 1 is fully confirmed without space charge. For the chosen solenoid we find $\alpha_c \approx 0.04$ m/rad. For comparison we also show the result for $I=50$ mA. Here it is noted that the reduction of the production cone angle from 20° to $10/5/2.5^\circ$ should be accompanied by a quadratic reduction of the current (particle number) from the full cone value of 140 mA ($8 \cdot 10^9$) to 35/8.8/2.2 mA (or $20/5/1.25 \cdot 10^8$ particles) if a uniformly filled cone is assumed. Hence the tested maximum values of 50 mA are much higher than what is really transmitted in the respective production cones, and yet we see only moderate space charge effects. Next we compare in Fig. 7 the trans-

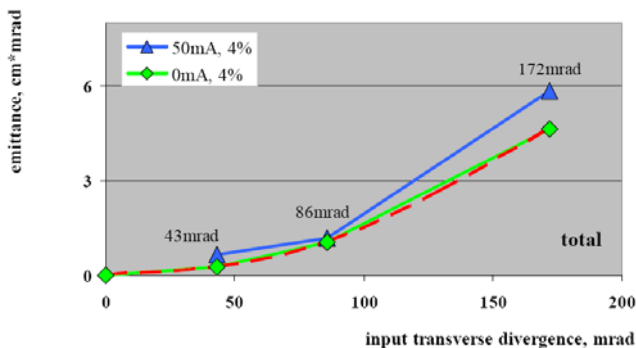


Figure 6: Emittance growth factors for different opening angles into solenoid ($\Delta E/E = \pm 0.04$; $I=0$ and $I=50$ mA).

verse and longitudinal emittance growth factors in solenoid collimation for large variations in energy widths as are typical for the experimentally obtained ensembles of particles. Assuming a constant energy spectrum we assume for the

General Topics

simulation that $I \propto \Delta E/E$ starting from 35 mA at 4%. It is noted from Fig. 7 that the growth of the longitudinal

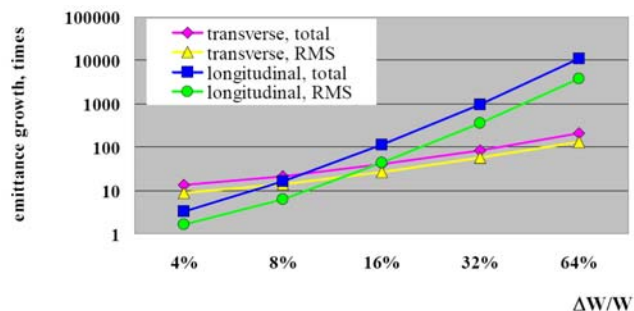


Figure 7: Solenoid collimation with increasing $\Delta E/E$ and current (172 mrad production cone).

emittance is much less pronounced than in the transverse case. For $\Delta E/E = \pm 0.04$ we find typically a doubling of the input value of 300 keV deg, whereas the transverse emittance increases by more than an order of magnitude.

Scaling to higher energy ions

For a first orientation results of the preceding sections based on 10 MeV protons can be scaled to higher energy protons or ions (with mass A and charge Z), if the magnetic rigidity scaling $B\rho \approx 3.13\beta\gamma A/Z$ is observed. Hence, using the same emittances and geometry of the magnetic focussing channel (ignoring space charge) one may expect identical chromatic aberration effects on the emittance growth. As an example, 150 MeV protons would reveal the identical behavior if the four times larger magnetic fields were adopted. In practice it is desirable to keep magnetic fields within technical limits, hence geometrical distances (starting from the distance source spot to collimator edge) need to be increased. This also increases transverse beam excursions and thus lens aberrations are inevitably enhanced. On the other hand, one may expect that production cone angles become smaller for higher energies, which helps reduce the aberrations.

Estimates for a reference bunch

We use above results to define a ‘‘reference bunch’’ of usable protons for hypothetical injection into a synchrotron (or other circular machine, like an FFAG). Both, energy spread and cone angle contribute to the bunch intensity and achievable emittance. Our data for solenoid focusing shown in Fig. 6 suggest to make use of the 4% energy spread and adopt the opening angle 10° (86 mrad), which suggests a final emittance of about 50π mm mrad and 35 mA ($2 \cdot 10^9$ particles).

Thus we suggest to define a reference bunch with $N_b \approx 2 \cdot 10^9$, $\Delta E/E = \pm 0.04$ and $\epsilon_{95} \approx 50 \pi$ mm mrad at the energy of 10 MeV. This corresponds to a ‘‘usable’’ fraction of $1.3 \cdot 10^{-4}$ of the total particle yield, or a $3 \cdot 10^{-5}$ energy fraction of the laser photon yield of 100 J. After reducing

the energy spread by a bunch rotation, this bunch could be used to fill a single bucket of a synchrotron.

IMPACT ON ACCELERATOR PARAMETERS

We discuss case A (laser acceleration as injector into a hypothetical synchrotron) and case B (full energy from laser) separately, noting that with the limited experimental data our conclusions can be only preliminary.

Case A: Here we assume that each laser shot provides a short bunch of the quality of the above defined reference bunch, which is to be transferred by bunch into bucket into a synchrotron at an injection energy of 10 MeV. We assume as example a radius of 16 m and harmonic $h = 25$ (10.8 MHz) for the stationary RF at injection. This gives a 50-60 ns long gap for switching of the injection kicker, which is technically acceptable. We assume a laser of 10 Hz repetition rate to deliver the 25 proton pulses with $5 \cdot 10^{10}$ protons for a spill cycle of 10 s. Currently available are PW lasers of 5 Hz, while 0.1 PW should be sufficient. A complete cycle would contain the following manipulations: (1) a drift section of 25 m (including transverse focusing) following the collimator for debunching of the beam to 20 ns duration ($\pm 40^\circ$ phase width of the RF); (2) a 10.8 MHz RF cavity with 550 kV for bunch rotation to match into the smaller ring momentum acceptance; (3) bunch into bucket transfer of the 10.8 MHz ring RF requiring < 100 kV (including space charge compensation) (4) after all 25 buckets are filled by repeated laser shots, rebunching to the harmonic of the acceleration cavities, acceleration and extraction as usual. It is important to note that the anticipated emittance of the reference bunch is consistent with a required space charge tune spread $\Delta Q \approx -0.1$ in the ring; a smaller value of the injection emittance would not be useful as nonlinear resonances would blow up the emittance and ΔQ correspondingly and lead to unacceptable beam loss during the long injection time of a few seconds. These parameters are independent of the ring radius, except that the RF period and the time window for kicker switching are proportional to the radius.

Case B: Assuming that the full energy needed for therapy applications can be provided by laser acceleration in the future, we can yet only make some very general statements here due to complete lack of experimental data. (1) a minimum of 10^3 ion pulses for 3D scanning within 10 s requires a 100 Hz rep rate laser system, probably exceeding 1 PW power; (2) the required $5 \cdot 10^7$ protons per pulse require a production cone angle of probably $< 2.5^\circ$ and a relative energy width of preferably $< \pm 0.01$; (3) for larger energy spread a several m long bunch rotation linac will be needed to provide the necessary voltage; (4) as the laser produced particle pulses directly hit the tumor the high demands of reproducibility in intensity and spot precision fall back on the laser-target system.

General Topics

CONCLUSIONS AND OUTLOOK

We have shown that a discussion of the performance of laser acceleration needs to include collimation and subsequent transport. The thus determined beam quality from PHELIX protons matches very well with injection requirements into a post-acceleration synchrotron, which can be filled by bunch into bucket transfer, although such a scenario may be more of a principle rather than practical interest. The low estimated “energy yield” of laser photons into “usable” protons of $3 \cdot 10^{-5}$ is a challenge to laser and target optimization, keeping in mind that therapy application should exceed 10^{-3} (for a 100 W average power laser, and following Table 1). The effect of charge neutralization in the very early expansion of the laser produced particle cloud needs to be addressed in the future. Further transport simulations should also include the complete production spectrum of particles in order to determine more accurately the usable part.

An experiment based on Fig. 3 including a 108 MHz bunch rotation cavity to verify the “reference bunch” prediction for PHELIX is under consideration at GSI. Currently studied upgrade options include injection into a 352 MHz CH-tank with post-acceleration from 11.5 to 21 MeV [16].

REFERENCES

- [1] H. Eickhoff and U. Linz, *Reviews of Accelerator Science and Technology* **1**, (2008) 143
- [2] R.A. Snavely *et al.*, *Phys. Rev. Lett.* **85** (2000) 2945.
- [3] P. McKenna, *Phys. Rev. E.* **70** (2004) 036405.
- [4] B.M. Hegelich *et al.*, *Nature (London)* **439** (2006) 441.
- [5] J. Fuchs *et al.*, *Phys. Rev. Lett.* **99** (2007) 015002.
- [6] Y.I. Salamin, Z. Harman and C.H. Keitel, *Phys. Rev. Lett.* **100** (2008) 155004.
- [7] U. Linz and J. Alonso, *PRST-AB* **10** (2007) 094801
- [8] M.A. Plum, *Proc. PAC’07*, Albuquerque, May 2007, p. 2603 (2009)
- [9] L. Groening *et al.*, *Proc. Linac’06*, Knoxville, August 2004, p.186 (2006)
- [10] H. Eickhoff *et al.*, *Proc. EPAC’04*, Luzern, July 2004 p. 290(2004)
- [11] M. Schollmeier *et al.*, *Phys. Rev. Lett.* **101** (2008) 55004.
- [12] F. Nuernberg *et al.*, *Proc. PAC’09*, Vancouver, May 2009, FR5RFP007 (2009)
- [13] T. Toncian *et al.*, *Science* **312**, (2006) 410
- [14] S. Yaramishev, W. Barth, L. Groening, A. Kolomiets and T. Tretyakova, *Nucl. Instr. Methods, A* **558**, 1 (2006).
- [15] M. Droba, private communication (2009).
- [16] U. Ratzinger, private communication (2009).

REFERENCE SIGNAL GENERATION WITH DIRECT DIGITAL SYNTHESIS FOR FAIR

M. Bousonville*, GSI, Darmstadt, Germany
 J. Rausch, Technische Universität Darmstadt, Germany

Abstract

In this paper, a method for the generation of RF reference signals for synchrotrons and storage rings will be presented. With these reference signals, the RF cavities in the Facility for Antiproton and Ion Research (FAIR) shall be synchronised. Digital frequency generators that work according to the DDS (direct digital synthesis) principle will be used as reference generators.

Via an optical network with star topology, these reference generators will be fed with two clock signals that show a certain correlation of frequency and phase. Due to delay measurements, their phases at different end points of the optical network are known. From these clock signals, reference signals with specific frequencies can be derived. The phases of these reference signals can be fine-tuned against the phases of the clock signals, allowing the phases of different reference signals to be synchronised.

With the commercially available DDS generators used in the prototype, phase steps of 0.022° are possible. At a reference signal frequency of 50 MHz, this corresponds to 1.22 ps.

The presentation describes the functionality of this method for reference signal generation and shows under which conditions the step size of the phase adjustment can be improved further.

INTRODUCTION

The method presented here for generating reference signals may be used in the future timing system for FAIR [1] (BuTiS – Bunch Phase Timing System [2]) as an alternative to other local reference synthesizers. Some aspects of this system, like the structure of the optical network and its noise characteristics, were already described in [3-4]. This article provides a more detailed description of the novel method for reference signal generation. To convey an appreciation for the system function of the reference generators used for this purpose, the basic principle of cavity synchronisation in FAIR is once again explained by way of introduction [3-5].

Cavity Synchronisation in FAIR

The objective is to synchronise the electrical fields of the cavities in the future FAIR (Fig. 1) [6] whose target frequencies (0.4 to 5.4 MHz) and target phase are defined by nearby signal generators (Fig. 2). The signal generators are frequency generators also that work according to the DDS (direct digital synthesis) principle.

To enable synchronous operation of the signal generators, these must be fed phase-synchronous reference clock signals. Reference Signal 1 (50 MHz) is

used by the signal generator for digital signal synthesis, and Reference Signal 2 (97.7 kHz) is used to enable frequency and phase shift commands to be carried out synchronously. In combination with data telegrams that are sent in the time window of Reference Signal 2, commands may be executed at an arbitrary slope of Reference Signal 1. Therefore, both reference signals together represent the reference time. The reference signals must have the same phase independent of the location where they are needed. In the concept presented here, the reference signals are generated by a DDS unit. This DDS unit requires a clock frequency at least two times higher than the output frequency. Therefore, the global clock signal of 200 MHz is defined by BuTiS [2]. As a conclusion, two system clocks (200 MHz and 97.7 kHz) are transmitted from a central point to the reference generators in order to generate the reference signals[†]. Due to the star distribution of these system clocks to different locations, they will be frequency-synchronous with one another but exhibit a phase displacement $\Delta\varphi$ that depends on the respective delay of the system clocks τ_n . To determine phase displacement, the delays are measured. With the help of this information, phase corrections are effected in the reference generators and in this way the phases of the reference signals φ_{Ref} are synchronised. Since the delays are time-variable due to environmental influences, they must be measured on a permanent basis.

The purpose of the system is to produce phase-synchronous and phase-stable reference signals at 13 spatially separate points of the facility.

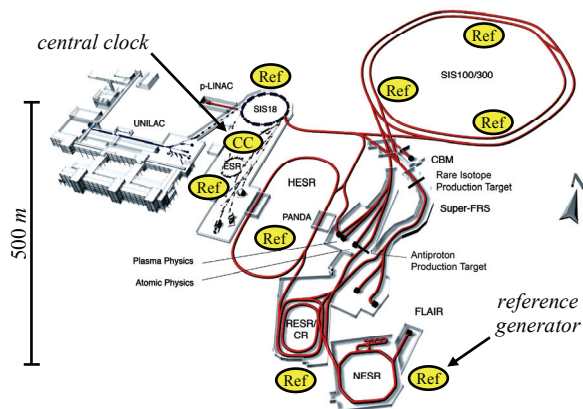


Figure 1: Facility for Antiproton and Ion Research.

[†] The system will be modified in future in such a way that the frequency 97.7 kHz for Reference Signal 1 and clock signal 1 is replaced by a frequency of 100 kHz.

*M.Bousonville@gsi.de

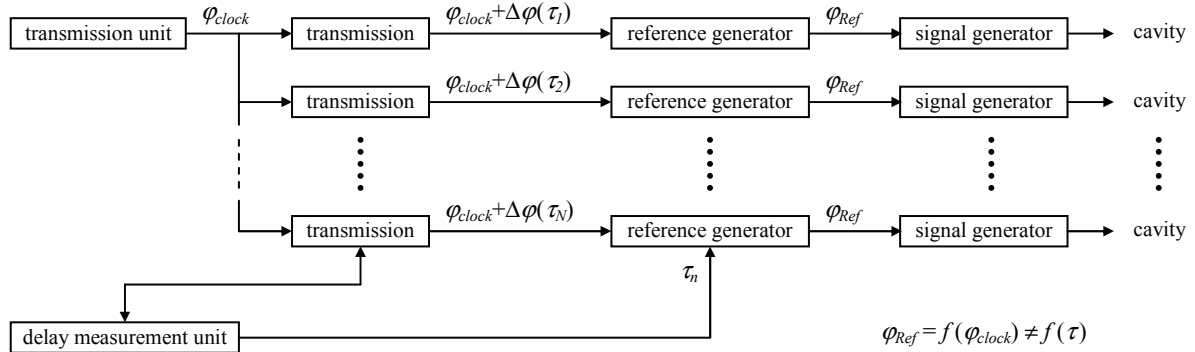


Figure 2: Basic principle of the cavity synchronisation.

State of Technology

In other systems, various techniques are used to shift the phase of the signal to be transmitted in such a way that the phase stabilises at the end of the transmission line. For phase shifting, the following are used: optical delays [7], optical phase shifters [8], fibre stretchers [9], compensation fibres in temperature cabinets [10-11], electrical delays and phase shifters [12-14]. For phase stabilisation this suffices to compensate the arising delay fluctuations. However, for synchronising the reference signals having a frequency of 97.7 kHz this is not sufficient because the phases have to be shifted by several microseconds. For this reason, a new method of phase correction was developed.

Not the phase of the system clocks are shifted, but new reference signals are created from these using digital frequency generators. The phase of the reference signals can be shifted in relation to the phases of the system clocks at the entry of the generator. In the following, the principle of direct digital synthesis (DDS) according to which the frequency generators operate and the resulting properties for the system are first described. After that the system parameters achieved in the prototype are presented, and lastly a way of enhancing performance even further is shown.

DIRECT DIGITAL SYNTHESIS

The structure of a DDS unit is shown in Fig. 3 [15, p. 25], [16, p. 21], [17, p. 1]. For the purpose of explaining the functioning principle, it is assumed that the phase register at the beginning contains the value 0. With the first clock pulse, the value of the FTW (frequency tuning word) is added to the content of the phase register. The adder at the same time performs the arithmetic operation modulo 2^M and the result is written into the phase register[‡], with M standing for the binary word length of the phase accumulator. The phase register can receive values between 0 and 2^M-1 which represent phases from 0 to nearly 2π . With the next clock the value of the FTW , which is constant in the application considered here, is added to the phase register. This process is repeated with

[‡] Actually, the phase register overflows at the value 2^M and starts again at 0.

each further clock, with the phase values accumulating in the phase register. In the bottom left of Fig. 3, this accumulation is represented for the first 8 clocks with an $FTW = 2^{M-3}$.

A phase shifter represents the next step of the DDS unit. Here, a phase displacement can be added to the current value of the phase register. The size of the phase displacement is predefined by the POW (phase offset word). Since its word length N as a rule is smaller than that of the phase accumulator, it has to be multiplied[§] by the factor 2^{M-N} to enable phase shifts of any size. However, this reduces the resolution of the phase displacement. The result of a displacement by 90° at the exit of the phase shifter can be seen in Fig. 3 below once again for the first 8 clocks. After that the phase values are normalised to 2π and in this way the phase signal is

$$\varphi_{DDS}(n) = \frac{2\pi}{2^M} \left[(nFTW + 2^{M-N} POW) \bmod 2^M \right] \quad (1)$$

obtained. The phase signal is fed to a phase-to-amplitude converter which via a look-up table assigns to each phase value $\varphi_{DDS}(n)$ an amplitude value $x(n)$ ^{**} and outputs the same. This gives rise to a time- and value-discrete signal

$$x(n) = a \cdot \sin \left[\frac{2\pi}{2^M} (nFTW + 2^{M-N} POW) \right], \quad (2)$$

with the amplitude a , which is then converted in the digital-to-analogue converter into an analogue signal

$$x(t = nT_{clock}) = a \cdot \sin \left[\underbrace{\frac{2\pi}{2^M T_{clock}} FTW \cdot t}_{\omega_{DDS}} + \underbrace{\frac{2\pi}{2^N} POW}_{\varphi_{DDS,off}} \right]. \quad (3)$$

The output signal of the DDS unit with $f_{clock} = 1/T_{clock}$ exhibits the frequency

$$f_{DDS} = \frac{FTW}{2^M} f_{clock} \quad (4)$$

[§] The multiplication is achieved by bit shifting of the binary POW .

^{**} In real systems, the phase normalising is also performed in this functional block.

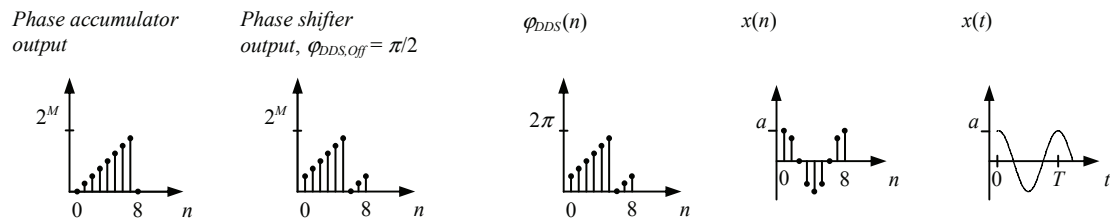
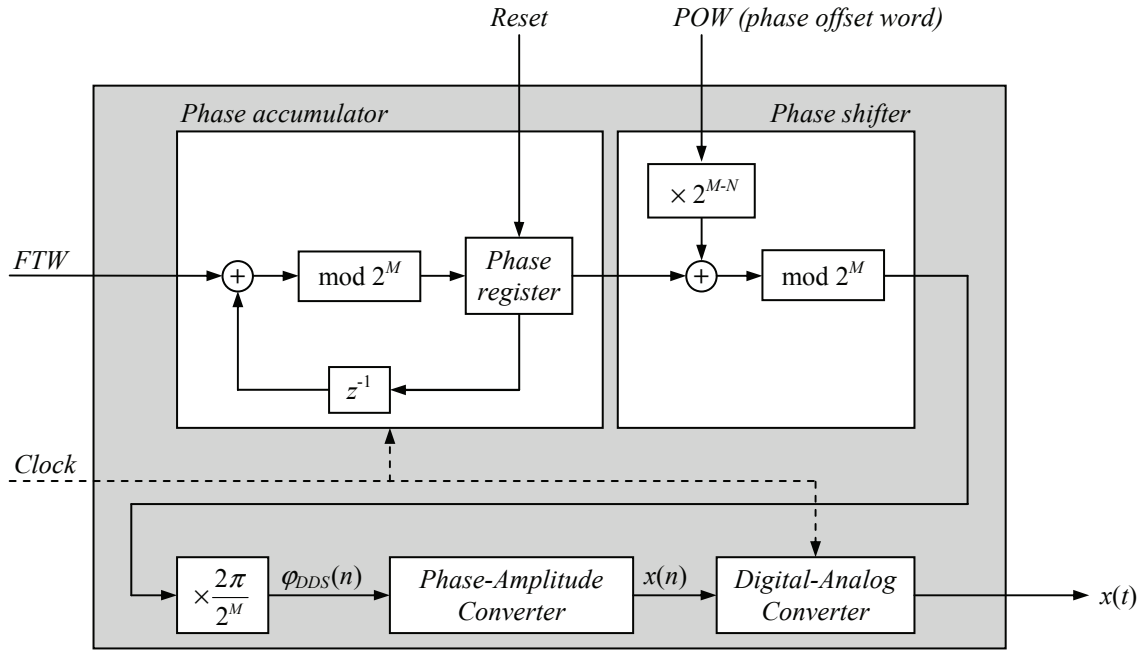


Figure 3: Direct digital synthesis principle.

and the phase displacement

$$\varphi_{DDS,off} = \frac{POW}{2^N} 2\pi. \quad (5)$$

REFERENCE SIGNAL GENERATION

Fig. 4 shows how two DDS units are used to generate the reference signals. Both were clocked by the system clock 1 at the frequency $f_{clock,1} = 200$ MHz. DDS_1 works at the $FTW_1 = 2^{M-2}$ and DDS_2 at the $FTW_2 = 2^{M-11}$, which is why according to Eq. (4) they generate the frequencies $f_{Ref,1} = 50$ MHz and $f_{Ref,2} = 97.65625$ kHz^{††}. The following integer relationships arise between the frequencies of the system clocks and reference signals which all have a uniform time reference:

$$\frac{f_{Ref,2}}{f_{clock,2}} = 1 \quad \frac{f_{Ref,1}}{f_{Ref,2}} = 2^9 \quad \frac{f_{clock,1}}{f_{clock,2}} = 2^{11}. \quad (6)$$

As a matter of principle, then, there is a constant phase relationship between the system clocks and the reference signals. However, this phase relationship is still

undefined, which is resolved by the possibility of setting the phase registers of both DDS units to zero. This is done by means of system clock 2. To initialise the reference generator, the phase registers of both DDS units are set to zero after the positive edge of system clock 2 to the next positive clock edge of system clock 1 and this value is output by the phase accumulator at initialisation time $n = 0$. The following phase accumulation is then once again similar to that of the example in Fig. 3. Now the phase displacement between the system clocks delivered to the reference generators at interface 2 and the reference signals is known (Fig. 4)^{††}. The last step for generating the reference signals consists in adjusting the phases at the exit of the reference generators by means of the phase shifters of the DDS units in such a way that they are synchronous at all reference points. For this purpose, a correction is made by calculating the phase values from the delays that were determined by the measurement unit which, after being converted into the binary form of the POW , are delivered to the DDS units which perform a corresponding phase shift.

^{††} As a matter of principle, the exact generation of 100 kHz for Reference Signal 2 is not possible according to Eq. (4).

^{††} In practice, the delays in the DDS unit still have to be taken into account.

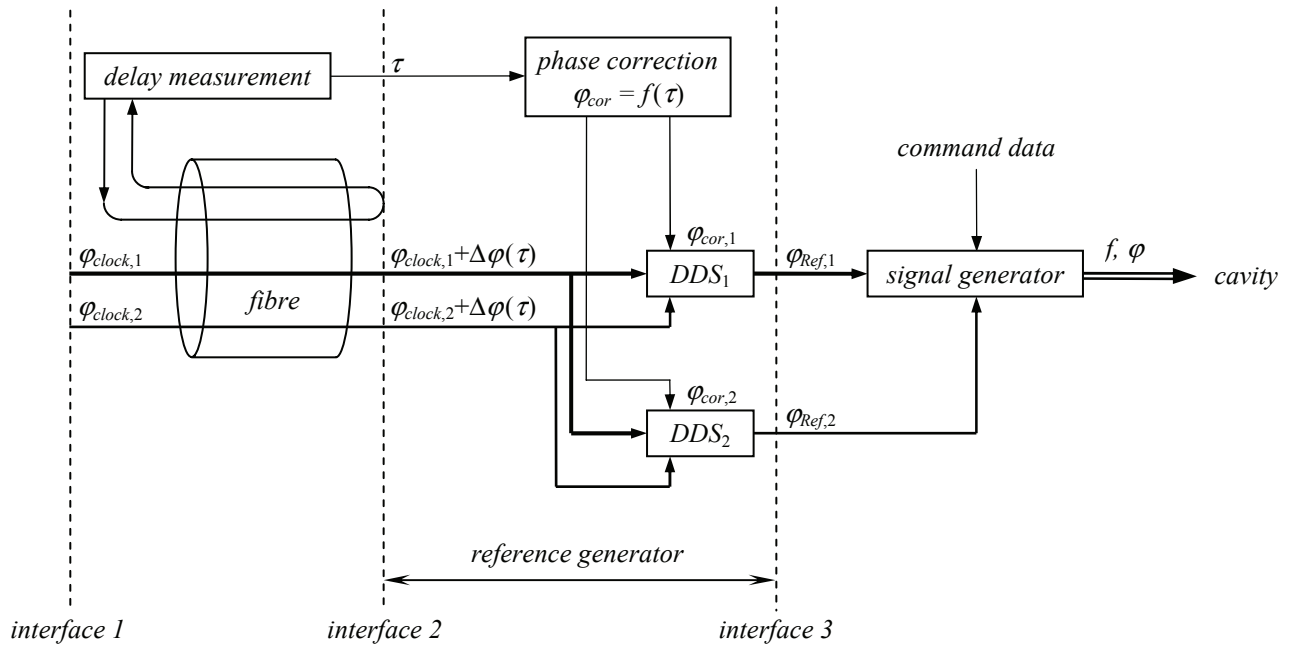


Figure 4: Generation of the reference signals.

PERFORMANCE

Now that the functioning principle of the reference generators has been explained, a description of the practical properties of the DDS units used (Fig. 5) will be provided. In Tab. 1 the values for the examined key values of the standard deviation of jitter, increment and precision of time adjustment are listed for each of the two reference signals. For the overall precision of the reference time, the quality of Reference Signal 1 is decisive.

Table 1: Quality of the Reference Signals

	Jitter	Increment	Precision
Reference Signal 1	7.56 ps	1.22 ps	< 7.5 ps
Reference Signal 2	140 ps	625 ps	527 ps

The jitter of Reference Signal 1 was measured directly at the generated sinusoidal oscillation, whereas Reference Signal 2 was converted prior to the measurement into a rectangular signal by means of a comparator^{**}. The latter facilitates further signal processing beyond interface 3 in the signal generators of the cavities. Moreover, phase relationships of Reference Signal 2 to the other signals can be measured significantly better given the higher edge steepness. The increment by which the time information of the reference signals can be shifted results from Eq. (5) in

$$t_{inc} = \frac{(\Delta\varphi_{DDS,off})_{min}}{2\pi} T_{DDS} = \frac{1}{2^N f_{DDS}} \quad (7)$$

^{**} The comparator is integrated into the DDS unit.

The *POW* of the DDS units used has a binary word length of 14 bits, resulting in an increment of 1.22 ps. To measure the precision of the time adjustment, two reference generators were connected via phase-stable, electrical components directly, i.e. without an optical network, to the system clock source. After that a phase synchronisation was performed and the extent to which the phases of both signals drifted apart was measured. Here, the phase displacement was always meaned over a time period of one second to suppress the influence of the jitter. Fluctuations occurred whose maximum amplitudes are recorded in Tab. 1. When the precision of Reference Signal 1 was measured, the difference between the minimum and maximum phase deviation over a time period of 7 hours was below the measurement precision of the oscilloscope of 15 ps. From this it is concluded that the precision is better than 7.5 ps.

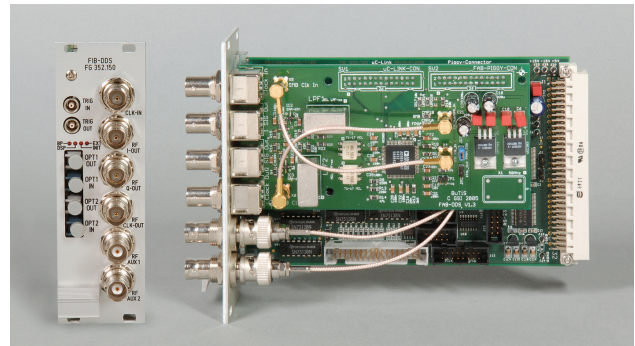


Figure 5: DDS unit.

All values for Reference Signal 2 in Tab. 1 are poorer due to the lower frequency, but perfectly adequate to satisfy the task of this signal of clearly identifying an edge of Reference Signal 1. The probability of an incorrect assignment approaches nil [5, p. 160]. This

ensures that commands to change the frequency and phase can be carried out synchronously in the different signal generators of the cavities (Fig. 2 and 4).

SUMMARY

A new method allowing for the generation of reference signals for synchronising cavities has been presented. This is done by means of digital frequency generators that work according to the direct digital synthesis principle (DDS). The phase of Reference Signal 1 (50 MHz) can be adjusted at increments of 1.22 ps and a precision of better than 7.5 ps. The jitter of the signal has a standard deviation of 7.56 ps.

All of the described values were subjected to practical examination.

A significant advantage compared with methods used to date to compensate for delay fluctuations in systems for distributing phase-stable signals is that the phase deviation is unlimited. The phases of the reference signals can be adjusted as desired and at small intervals.

OUTLOOK

The performance of the method presented can be enhanced even further by two measures. Firstly, the frequency of system clock 1 and of Reference Signal 1 must be increased (e.g. to 1 GHz, and 250 MHz, respectively) and, secondly, DDS units of a different type other than those of the prototype which can be clocked at such a high frequency must be used. Such DDS units are now available commercially and also bring further advantages in terms of precision [18]. The big advantage lies in the reduction of the jitter produced by the reference generator to a value of < 1 ps. Moreover, the increment is reduced by a *POW* having a large binary word length of 16 bit and the higher frequency of 250 MHz according to Eq. (7) to a value of 61 fs.

With these considerations it has to be kept in mind that developments in the area of frequency generators operating according to the DDS principle are advancing continually, and that in future even higher clock rates as well as larger word lengths of the *POW* and thus also even better properties for generating reference signals can be expected.

If combined with more effective temperature and delay stabilisation of the reference generators, this improvement will also enhance the precision with which the reference time can be adjusted.

The presented method can also be used in other systems to generate a stable reference signal if the DDS unit is capable of generating a frequency high enough for this.

REFERENCES

[1] FAIR Technical Design Report, 2008.

- [2] P. Moritz "BuTiS – Development of a Bunchphase Timing System", GSI Scientific Report, 2006.
- [3] M. Bousonville and J. Rausch "Universal Picosecond Timing System for the Facility for Antiproton and Ion Research", Physical Review Special Topics - Accelerators and Beams, Volume 12, Issue 4, 2009.
- [4] M. Bousonville and P. Meissner "RF Reference Signal Distribution System for FAIR", Proceedings of the European Particle Accelerator Conference, Genua, 2008.
- [5] M. Bousonville, Doctoral thesis, Technische Universität Darmstadt, Germany, 2009.
<http://tuprints.ulb.tu-darmstadt.de/1382>
- [6] H. Klingbeil "Overview on FAIR Synchrotron RF Control System Planning", Workshop on FAIR Synchrotron RF Control Electronics, 2008
- [7] T. Kobayashi et al. "RF Reference Distribution System for the 400-MeV Proton Linac of the KEK/JAERI Joint Project", Proceedings of the LINAC, 2002.
- [8] F. Lenkszus et al. "Timing and LLRF for the Argonne Short X-Ray Pulse Beamline", Low Level Radio Frequency Workshop, 2007.
- [9] A. Winter et al. "Femtosecond optical synchronization systems for XFELs", Low Level Radio Frequency Workshop, 2005.
- [10] J. Frisch et al. "A high stability, low noise RF distribution system", Proceedings of the Particle Accelerator Conference, 2001.
- [11] F. Lenkszus "Phase Reference System for the ILC", Low Level Radio Frequency Workshop, 2007.
- [12] F.R. Lenkszus and R.J. Laird "A Bunch Clock for the Advanced Photon Source", Proceedings of the Particle Accelerator Conference, 1997.
- [13] E. Peschardt and J.P.H. Sladen "Phase Compensated Fiber-optic Links for the LEP RF Reference Distribution", Proceedings of the Particle Accelerator Conference, Chicago, 1989.
- [14] T. Naito et al. "RF Reference Distribution Using Fibre-Optic Links for KEKB Accelerator", Proceedings of the Particle Accelerator Conference, 2001.
- [15] M. Kumm "FPGA-Realisierung eines Offset-Lokaloszillators basierend auf PLL- und DDS-Technologien", Diploma thesis, Technische Universität Darmstadt, 2007.
- [16] E. Schmid "DDS-Signalgeneratoren praktisch aufbauen und anwenden: Das Verfahren der direkten digitalen Synthese (direct Digital Synthesis- DDS) in der Praxis", Franzis Verlag, 2006.
- [17] Analog Devices "AD9854 - CMOS 300 MSPS Quadrature Complete DDS", data sheet, Rev. E, 2007.
- [18] Analog Devices "AD9912 - 1 GSPS Direct Digital Synthesizer with 14-Bit DAC", data sheet, Rev. A, 2008.

PREPARATION OF THE IRRADIATION TEST AT CAVE HHD OF GSI DARMSTADT

A. Plotnikov[#], E. Floch, E. Mustafin, E. Schubert, T. Seidl, I. Strasik,
 GSI FAIR AT, Darmstadt, Germany
 A. Smolyakov, ITEP, Moscow, Russian Federation.

Abstract

In the frame of the FAIR project in spring 2008 an irradiation test of superconducting magnet components was done at GSI Darmstadt. Cave HHD with the beam dump of SIS18 synchrotron was taken as the test area. The beam dump was reequipped to meet the irradiation test requirements. Thereby the first stage of preparation for the irradiation test was to investigate the radiation field around the reconstructed beam dump from the point of view of radiation safety. FLUKA simulations were performed to estimate the dose rate inside and immediate outside of the cave during the irradiation. The simulations showed safe level of the radiation field, and it was later confirmed by the measurements provided by the radiation safety group of GSI.

MOTIVATION

The Facility for Antiproton and Ion Research (FAIR) is planned to be finished in 2015 (Fig. 1). In the frame of the project among other accelerators two synchrotrons will be built: SIS100 and SIS300. The features of those machines are high intensity and energy of the proton and heavy ion beams. For SIS100 the energy is going to be 2.7 GeV/u for U^{28+} , and bunch compression to ~ 60 ns for $5 \cdot 10^{11}$ U ions. For SIS300 - 34 GeV/u for U^{92+} and slow extraction of $\sim 3 \cdot 10^{11}$ U-ions per sec [1].

The prospective beam loss during slow extraction is $1.5 \cdot 10^{10}$ particles per second. Thus, the slow extraction area is the region with the highest beam loss rate in the whole tunnel, accommodating the two synchrotrons.

At the present stage of SIS100/300 facility design, it is very important to investigate the lifetime of the materials which will be used in magnets and other equipment of the new facility. Since the superconducting magnets are the most important component of the synchrotrons, it is necessary to know as precisely as possible the radiation hardness of the most radiation fragile material used in the magnets – the insulators.

THE RADIATION TEST SET-UP

The significance of the presented irradiation test consists in the unique setup of the target. Main aim of the experiment was to reproduce the real beam-loss conditions during the operation of the synchrotron. All test samples were shielded by stainless steel plate which represented the wall of the vacuum chamber. Beams hit the surface of this plate at a tiny angle to reproduce the charge exchange losses and losses in the slow extraction

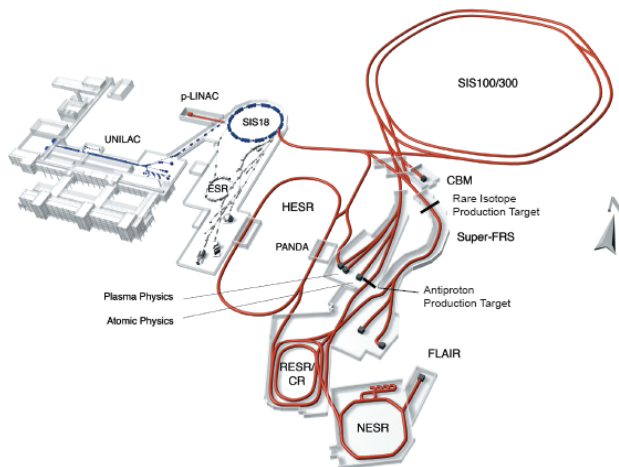


Figure 1: Schematic view on the existing GSI facility: UNILAC, SIS18, ESR (blue line) - and the planned FAIR facility on the right: the superconducting synchrotrons SIS100, SIS300, the collector ring CR, the accumulator ring RESR, the new experimental storage ring NESR, the rare isotope production target, the superconducting fragment separator Super-FRS, the proton linac, the antiproton production target, and the high energy antiproton storage ring HESR. Also shown are the experimental stations for plasma physics, relativistic nuclear collisions (CBM), radioactive ion beams (Super-FRS), atomic physics, and low-energy antiproton and ion physics (FLAIR).

area [2].

HHD Cave

Facility of the SIS18 contains a beam dump for the emergency dump of the high energy ion beam (Fig. 2). The beam dump is situated in the HHD cave. It is a massive iron cube with a cavity to accept the beam. This place was taken for the needs of the experiment. Part of the vacuum line 1.5 m long was removed to let us install a special transporter. This mechanism allowed moving the target in two horizontal dimensions of freedom. Thus one can remotely drive the target left-right in order to centre it relatively to the beam axis and also push-pull it in order to get the target inside the beam dump cavity or get it outside.

V target

All components of the target were installed on the so-called V-target (Fig. 3a). Each of the two arms of the V-target was a plate of stainless steel. All the samples under investigation were situated behind those plates, grouped

[#]a.b.plotnikov@gsi.de

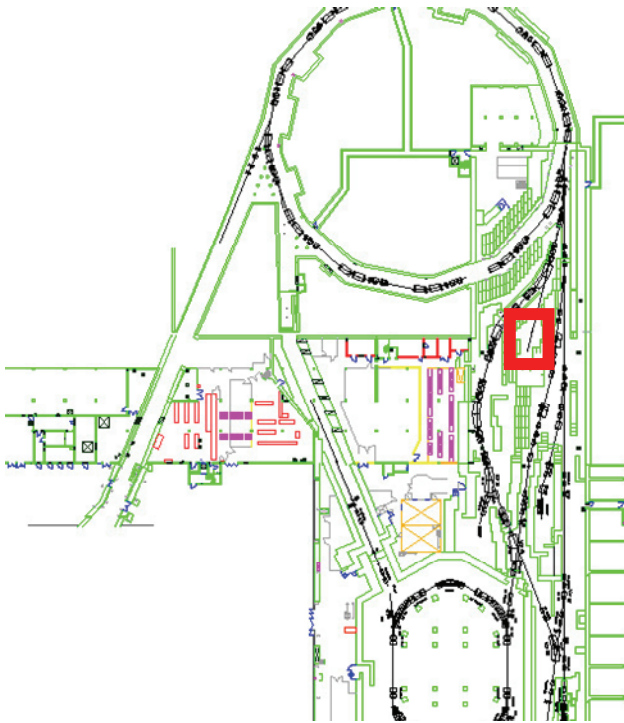


Figure 2: AutoCAD plot of the SIS18. The experimental area, cave HHD, is marked by red square.

in five identical modules (Fig. 3b). Last sixth module was empty. It was used for calibration of the ion flux. The beam of U^{28+} , 1 GeV/u passed the collimator and irradiated the surface of stainless steel plates. By using the method of scanning radiation treatment each single module absorbed different flux.

Samples

For the test the following samples of the equipment and materials were taken: S1 – stack of polyimide foils for thermal, mechanical, electrical tests and measurements by optical spectroscopy; S2 - kapton insulated wire; S3 – nuclotron cable; S4 - SIS300 cable; S5 – corrector conductor; S6 – SuperFRS conductor; S7 – voltage breaker; S8 – G11 rod for mechanical test in compression mode; S9 – G11 “dog bones” for tensile test; S10 – polyimide foils glued with Pixeo; S11 – G11 “sticks” for thermal conductivity test; S12 – G11 plate for high voltage tests; S13 – temperature sensors (Fig. 3b).

All of the samples were installed in the special holders and situated directly behind the stainless steel plates.

Radiation Safety in HHD

The beam dump was specially constructed to intercept safely high intensity heavy ion beams. The arbitrary changes of the beam dump set-up were not allowed according to the rules of radiation safety of the accelerator facility. Reconstruction of the beam line for the aims of the irradiation test dramatically changed geometry of the beam dump, thus the estimates of the dose rates in the cave and around it was necessary.

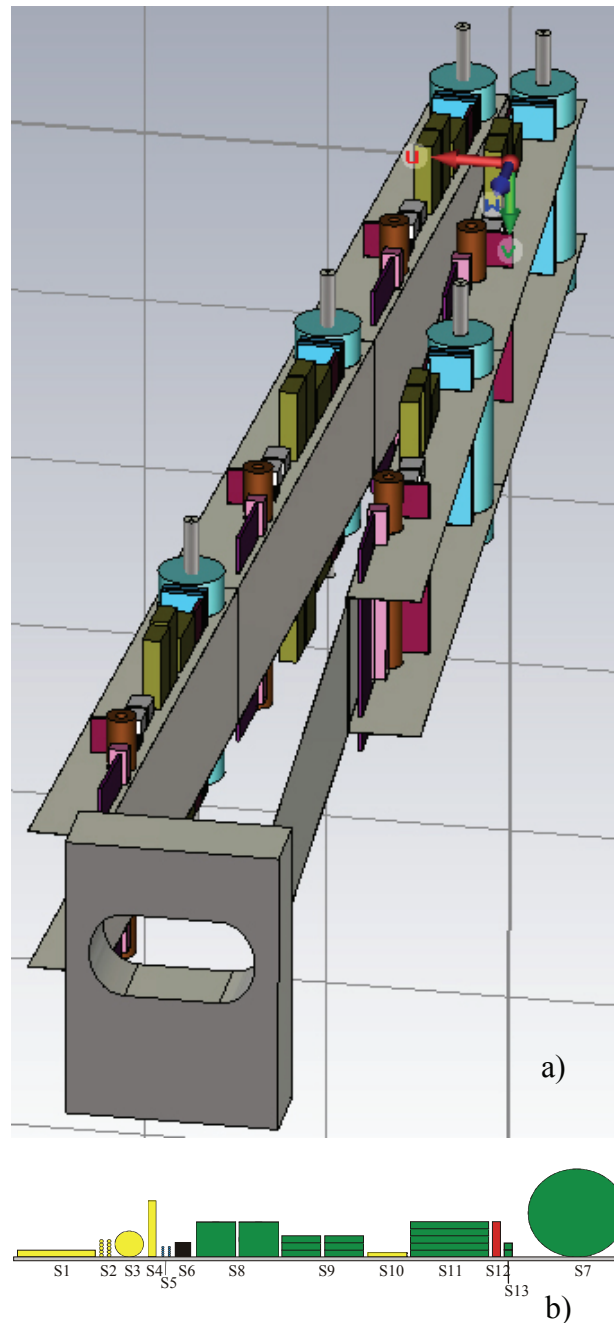


Figure 3: a) 3D virtual model of the V-target with the collimator and all samples installed; b) order and numbers of the samples in one single module of the V-target [3].

Originally the dumped heavy ion beams passed through the transportation channel from SIS18 to the 700 mm deep beam dump cavity. The cavity was directly connected to the vacuum pipe of the transport line.

New setup required the following changes: the vacuum chamber of the beam transport line were interrupted 1.5 m before the beam dump and was closed by a stainless steel vacuum window; the space between this vacuum window and the beam dump as well as the space inside the cavity of the beam dump were used to accommodate the rails of

the target set-up, the collimator, the sample holder, video-cameras and scintillating light targets.

In the reconstructed set-up of the beam dump the heavy ion beam would not hit the beam dump directly, but it would first pass through the target set-up with the irradiation samples. This would definitely increase the dose rate inside the cave. The aim of our simulation was to show how much the dose rate would increase outside the cave, and would that dose rate be below the safe level.

COMPUTER SIMULATION OF THE IRRADIATION TEST

To investigate this problem the FLUKA code was used. FLUKA is a general purpose tool for calculations of particle transport and interactions with matter, covering an extended range of applications spanning from proton and electron accelerator shielding to target design, calorimetry, activation, dosimetry, detector design, Accelerator Driven Systems, cosmic rays, neutrino physics, radiotherapy, etc. [4-6].

Simulation Setup

The entire HHD cave was simulated with the help of FLUKA, including beam dump details, shape and thickness of the concrete walls and geometry of the labyrinth. To obtain the high statistics without increasing the CPU time so-called BIASing was used. This feature of FLUKA allows multiplying the amount of particles on a border between regions with different BIAS coefficients.

The aim of the simulation was to get the level of the dose rates above the roof of the HHD cave, where the uncontrolled access area starts, and at the entrance to the HHD cave where the sluice is situated and controlled access area starts. Both places were the most problematic zones in sense of radiation safety.

Results of Numerical Estimation of the Dose Rate in the HHD Cave

Simulation with the help of the FLUKA code gave the results which allowed us to evaluate the dose rate in the whole volume of the HHD cave and in the surrounding area. The dose rate level in the spots of considerations is represented in Fig. 4.

This picture shows the dose rate in horizontal cross section of the cave at the 2 m height. Beam came from the top and absorbed in the beam dump (red flash in the centre of the picture). The left picture corresponds to the original construction of the beam dump and the right one shows the situation for the reconstructed cave.

For example, the dose rate near the entrance of the cave HHD (light blue area at the bottom of the plots on Fig. 4) is from 1 to 10 μ Sv/h. This level meets the requirements of the radiation safety.

In Fig. 5 the dose rate above the roof of the cave is shown. This is a horizontal cross section at the 0.5m distance above the roof of the HHD cave. The left plot corresponds to the original geometry, the right one to the

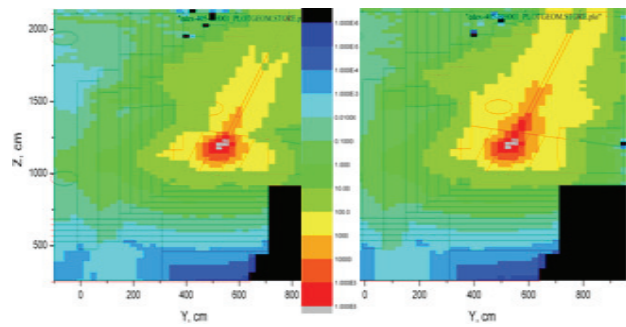


Figure 4: Dose rate map in the HHD cave (horizontal cross section): left – original geometry of the beam dump, right – after reconstruction. It the middle scale of the dose is situated, range in mSv/h.

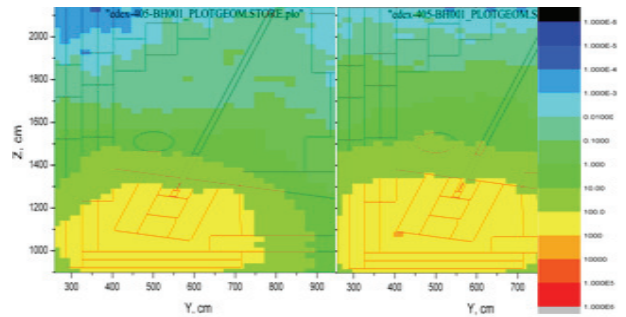


Figure 5: Dose rate map on the roof above HHD cave (horizontal cross section): left – original geometry of the beam dump, right – after reconstruction. At the right side scale of the dose is situated, range in mSv/h.

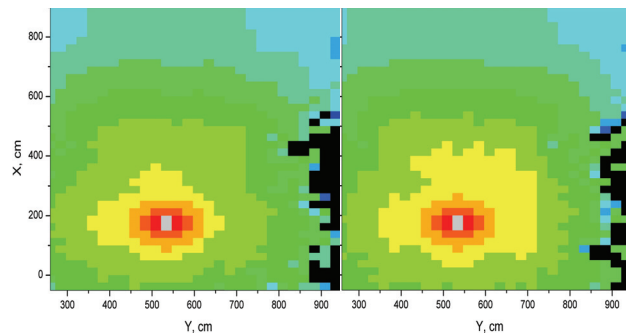


Figure 6: Dose rate map in the HHD cave (vertical cross section along the front of the beam dump): left – the original geometry of the beam dump, right – after reconstruction. The scale of the dose is the same as in Fig. 4 and 5.

new one. Most dangerous area lies exactly over the beam dump (the yellow spot at the bottom of the plots)

Thus we obtained the dose rate level on the roof of the cave of 10 – 30 μ Sv/h in both cases in the hottest point. One may conclude, the changes to the cave introduced with the experimental setup inside the cave did not change the dose rate above the test site.

At last in Fig. 6 one can see the dose rate in vertical cross section of the HHD cave which is perpendicular to the vacuum tube and lies on the front surface of the beam dump. The left plot shows the dose distribution in the original cave configuration, the right one shows the same

after the reconstruction. Those plots demonstrate that dose rate inside the cave is higher when the new experimental setup installed, but the doses outside the concrete walls are the same in both cases.

CONCLUSIONS

The experimental setup which was installed in the cave HHD for the purpose of the irradiation test changed the dose distribution inside the cave and in the area around this cave volume. The numerical estimation has been done by using the FLUKA code. Results showed that the average dose rates expected during the irradiation test become larger inside the cave. But the dose rates outside the HHD cave are the same as the dose rates one can expect from the original beam dump configuration. Thus all the safety requirements were preserved, and the experiment has got the permission. The measurements of the dose rates performed by the radiation safety group during the experiment (6.05.08 – 14.05.08) gave a good agreement with numerical estimations.

REFERENCES

- [1] H.H. Gutbrod, I. Augustin, H. Eickhoff, K.-D. Groß, W. F. Henning, D. Krämer, G. Walter, Baseline Technical Report Executive Summary, FAIR, Darmstadt, 2006.
- [2] E. Mustafin, O. Boine-Frankenheim, I. Hofmann, H. Reich-Sprenger, P. Spiller, “A theory of the beam loss-induced vacuum instability applied to the heavy-ion synchrotron SIS18”, Nuclear Instruments and Methods in Physics Research A 510 (2003) 199–205.
- [3] L. Latysheva, “Irradiation experiment in Cave HHD: numerical estimates of the energy deposition into the samples”, ACC_THEORY-note-2008-002, FAIR, Darmstadt, 2008.
- [4] A. Fassò, A. Ferrari, J. Ranft and P.R. Sala, “FLUKA: a multi-particle transport code”, CERN Yellow Report (2005), INFN/TC_05/11.
- [5] A. Fassò, A. Ferrari, S. Roesler, P.R. Sala, G. Battistoni, F. Cherutti, E. Gadioli, M.V. Garzelli, F. Ballarini, A. Ottolenghi, A. Empl and J. Ranft, “The physics models of FLUKA: status and recent developments”, Computing in High Energy and Nuclear Physics 2003 Conference (CHEP2003).
- [6] Official website of FLUKA: <http://www.fluka.org>
- [1] H.H. Gutbrod, I. Augustin, H. Eickhoff, K.-D. Groß, W. F. Henning, D. Krämer, G. Walter, Baseline

IRRADIATION OF SUPERCONDUCTING MAGNET COMPONENTS FOR FAIR

E. Mustafin[#], E. Floch, A. Plotnikov, E. Schubert, T. Seidl, GSI Helmholtzzentrum für Schwerionenforschung, Darmstadt, Germany

L. Latysheva, INR RAS, Moscow, Russia

A. Smolyakov, SSC RF ITEP, Moscow, Russia

I. Strasik, GSI Helmholtzzentrum für Schwerionenforschung, Darmstadt, Germany, on leave from FEI STU Bratislava, Slovak Republic

Abstract

In spring 2008 an irradiation test of superconducting magnet components was done at GSI Darmstadt in the frame of the FAIR project. Cave HHD with the beam dump of SIS synchrotron was used for irradiation. The irradiation set-up modeled a scenario of beam loss in a FAIR accelerator: U beam with energy of 1 GeV/u was used to irradiate a thin stainless steel bar at very small angle, so that the test samples situated behind the stainless steel bar were exposed to the beam of secondary particles created in the bar. The total number of U ions dumped on the target assembly was about $2 \cdot 10^{14}$. Presently, in spring 2009 some samples are still radioactive. In the paper we present the estimates of the energy deposition and secondary particle fluences in the test samples and also discuss some results of the irradiation campaign.

EXPERIMENTAL SET-UP

The layout of the experimental set-up is schematically shown in Fig. 1 [1, 3].

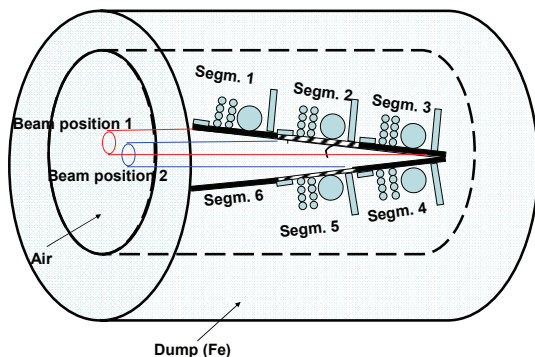


Figure 1: Layout of the experimental set-up.

The samples were organised into five identical segments. Each segment consisted of a 1 mm thick stainless steel plate and a set of thirteen samples. The arrangement of the samples in the segment is shown in Fig. 2. The segment 6 consisted of the stainless steel plate only and was used to study the residual activation induced in the plate [4]. Because of the expected high level of neutron flux during the irradiation campaign, the target assembly was accommodated inside the SIS-18

synchrotron beam dump in Cave HHD of GSI Darmstadt. Because of the expected high level of neutron flux during the irradiation campaign, the target assembly was accommodated inside the SIS-18 synchrotron beam dump in Cave HHD of GSI Darmstadt.

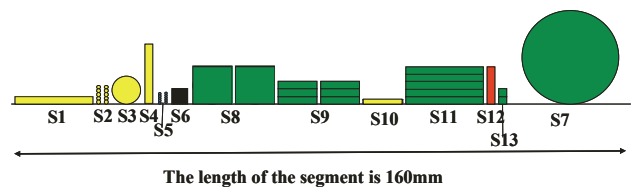


Figure 2: Layout of the samples in segments.

The following samples had been chosen for irradiation and were arranged in all five segments in identical way:

- S1 – stack of polyimide foils for thermal, mechanical, electrical tests and measurements by optical spectroscopy;
- S2 – pieces of kapton insulated wires;
- S3 – piece of nuclotron cable;
- S4 – piece of SIS300 cable;
- S5 – corrector conductor (piece of Cu-NbTi wire with enamel insulation);
- S6 – Super-FRS conductor;
- S7 – voltage breaker (sample S7 were present in Segments 2, 3, 4 and 5 only, it was absent in Segment 1);
- S8 – G11 rod for mechanical tests in compression mode;
- S9 – “dog-bone” shaped G11 plates for tensile tests;
- S10 – polyimide foils glued with Pixeo;
- S11 – G11 “sticks” for thermal conductivity tests;
- S12 – G11 plate for high voltage tests;
- S13 – temperature sensors

More detailed description of the samples (the geometry and the chemical composition) is given in [2].

The U beam of energy $E = 1$ GeV/u irradiated the stainless steel plates under the grazing incidence of 2.38° , so that the samples S1-S13 were not directly exposed to the primary U beam particles but to the products of the nuclear reaction of U ions with the nuclei of the stainless steel plates. In this way a realistic scenario of the beam loss into the inner surface of the accelerator vacuum chamber was modelled. In order to accumulate different radiation doses into the samples, the irradiation was done with two different positions of the U beam. In the first

[#]e.mustafin@gsi.de

position the beam irradiated Segments 1, 2 and 3 and in the second position the beam irradiated Segments 2, 3 and 4. The beam had about Gaussian transverse distribution with r.m.s. sizes of about 1 cm in horizontal direction and 0.5 cm in vertical. The Segment 5 was irradiated with the beam tails only. $1.06 \cdot 10^{14}$ ions were collected on the stainless steel plates in the first beam position and $1.17 \cdot 10^{14}$ ions in the second beam position.

COMPUTER MODELLING

There was no way to measure directly the energy deposited by the beam into the samples. The Monte-Carlo transport code SHIELD [5] was used to model the U beam interaction with the target assembly and to calculate the energy deposited into the samples.

The detailed dose distributions in the samples are given in [1] and [2]. Following [2], we show here the characteristic features of the dose distribution in two samples only: in samples S1 and S8.

Sample S1 is a stack of 10 layers of kapton foils. Each layer consists of 4 foils of different thicknesses: 0.012 mm, 0.025 mm, 0.05 mm and 0.1 mm. Computer simulation provides detailed estimates of energy deposited in the samples by different products of nuclear interaction of the U beam particles with the nuclei of the stainless steel plate. In Table 1 the energy deposition values are given for the first layer of samples S1 in the five different segments of the target assembly.

Table 1: Contribution of Ion Species to the Energy Deposition into the first layer of Sample S1 (in MGy)

ion	Seg.1	Seg.2	Seg.3	Seg.4	Seg.5
^1H	0.023	0.17	0.23	0.13	0.039
^2H	$3.3 \cdot 10^{-3}$	$4.3 \cdot 10^{-2}$	$5.8 \cdot 10^{-2}$	$2.7 \cdot 10^{-2}$	$8.1 \cdot 10^{-3}$
^3H	$1.5 \cdot 10^{-3}$	$2.7 \cdot 10^{-2}$	$3.7 \cdot 10^{-2}$	$1.7 \cdot 10^{-2}$	$5.6 \cdot 10^{-3}$
^3He	$2.4 \cdot 10^{-3}$	$4.8 \cdot 10^{-2}$	$6.3 \cdot 10^{-2}$	$2.8 \cdot 10^{-2}$	$9.7 \cdot 10^{-3}$
^4He	$3.0 \cdot 10^{-3}$	$7.7 \cdot 10^{-2}$	0.11	$4.6 \cdot 10^{-2}$	$1.5 \cdot 10^{-2}$
^7Li	$7.7 \cdot 10^{-5}$	$1.1 \cdot 10^{-2}$	$1.4 \cdot 10^{-2}$	$5.2 \cdot 10^{-3}$	$2.3 \cdot 10^{-3}$
^9Be	$3.5 \cdot 10^{-5}$	$3.9 \cdot 10^{-3}$	$5.9 \cdot 10^{-3}$	$2.3 \cdot 10^{-3}$	$2.3 \cdot 10^{-4}$
^{11}B	$9.9 \cdot 10^{-5}$	$9.4 \cdot 10^{-3}$	$9.0 \cdot 10^{-3}$	$5.1 \cdot 10^{-3}$	$1.6 \cdot 10^{-3}$
^{12}C	$9.2 \cdot 10^{-5}$	$3.8 \cdot 10^{-3}$	$3.2 \cdot 10^{-3}$	$1.5 \cdot 10^{-3}$	$3.9 \cdot 10^{-4}$
Z=7-20	$3.3 \cdot 10^{-4}$	0.12	0.19	0.051	0.021
Z=21-40	0.01	1.18	1.59	0.61	0.22
Z=41-60	0.032	2.65	3.38	1.54	0.43
Z=61-91	0	0.046	0	0	0
Total	0.078	4.45	5.74	2.49	0.77

One may notice, that the fragments with charge numbers from Z=21 to Z=40 and from Z=41 to Z=60 make the major part of the energy deposition. The fragments with Z heavier than 61 are practically absent in

the sample S1, because they are all stopped inside the stainless steel plate.

From the other hand one may notice in Table 2 that the number of heavy ion fragments penetrating into the first layer of samples S1 is negligibly small compared to the number of neutrons, protons and light fragments.

Table 2: Fluences of Ion Species Penetrating into the First Layer of Sample S1 (in $10^{13}/\text{cm}^2$)

ion	Seg.1	Seg.2	Seg.3	Seg.4	Seg.5
n	7.17	73.2	100	53.1	14.7
^1H	2.79	21.9	29.2	15.5	4.06
^2H	0.46	8.22	10.8	4.73	1.24
^3H	0.25	5.51	7.65	3.38	0.85
^3He	0.14	2.55	3.23	1.44	0.41
^4He	0.15	4	5.54	2.32	0.6
^7Li	$7.6 \cdot 10^{-4}$	0.25	0.33	0.12	$3.4 \cdot 10^{-2}$
^9Be	$3.1 \cdot 10^{-4}$	$4.8 \cdot 10^{-2}$	$5.8 \cdot 10^{-2}$	$2.8 \cdot 10^{-2}$	$8.9 \cdot 10^{-4}$
^{11}B	$5.6 \cdot 10^{-4}$	$6.5 \cdot 10^{-2}$	$7.1 \cdot 10^{-2}$	$4.1 \cdot 10^{-2}$	$8.5 \cdot 10^{-3}$
^{12}C	0	$1.7 \cdot 10^{-2}$	$1.3 \cdot 10^{-3}$	$5.6 \cdot 10^{-3}$	$1.3 \cdot 10^{-3}$
Z=7-20	$6.8 \cdot 10^{-4}$	0.13	0.26	0.075	0.026
Z=21-40	$3.3 \cdot 10^{-3}$	0.2	0.22	0.094	0.027
Z=41-60	$2.5 \cdot 10^{-3}$	0.17	0.23	0.11	0.024
Z=61-91	0	$5.6 \cdot 10^{-4}$	0	0	0

Comparing the numbers in Tables 1 and 2 one may conclude, that the number of heavy ion fragments penetrating into the first layer of sample S1 is less than 1% compared to the total number of the secondaries penetrating into the layer, but the contribution of this small number of heavy fragments into the energy deposition is above 80% of the total deposited energy. This is because of the Z^2 -dependence of the energy deposition on the charge number of the fragment.

The same picture one may observe looking into Tables 3 and 4, where the energy deposition and fluence values are given for the secondaries penetrating into the first layer (0.2 mm thick) of sample S8.

More detailed numbers for all samples are given in [1] and [2].

RESULTS OF IRRADIATION

The irradiation test was done in May 2008 and after the irradiation the target assembly was stored in a 'lead-brick castle' to allow the residual activity to 'cool-down' to the accessible level. First organic samples could be removed from the 'castle' after four month of 'cooling-down'. The samples with the metallic parts were removed after ten months after the irradiation. Some metallic parts are still in the 'castle' (one year after the irradiation) because they still show the residual dose rate at the level of $50 \mu\text{Sv/h}$.

Purely organic samples show at the moment much lower level of residual activity: about 0.5 $\mu\text{Sv/h}$ and less.

Table 3: Contribution of Ion Species to the Energy Deposition into the First Layer of Sample S8 (in MGy)

ion	Seg.1	Seg.2	Seg.3	Seg.4	Seg.5
^1H	0.068	0.15	0.19	0.12	0.045
^2H	$1.4 \cdot 10^{-2}$	$3.5 \cdot 10^{-2}$	$4.4 \cdot 10^{-2}$	$2.4 \cdot 10^{-2}$	$8.2 \cdot 10^{-3}$
^3H	$8.0 \cdot 10^{-3}$	$2.3 \cdot 10^{-2}$	$2.8 \cdot 10^{-2}$	$1.6 \cdot 10^{-2}$	$5.4 \cdot 10^{-3}$
^3He	$1.5 \cdot 10^{-2}$	$4.0 \cdot 10^{-2}$	$4.9 \cdot 10^{-2}$	$2.6 \cdot 10^{-2}$	$9.4 \cdot 10^{-3}$
^4He	$2.3 \cdot 10^{-2}$	$6.8 \cdot 10^{-2}$	$8.2 \cdot 10^{-2}$	$4.4 \cdot 10^{-2}$	$1.6 \cdot 10^{-2}$
^7Li	$2.3 \cdot 10^{-3}$	$8.4 \cdot 10^{-3}$	$1.2 \cdot 10^{-2}$	$5.4 \cdot 10^{-3}$	$2.0 \cdot 10^{-3}$
^9Be	$5.2 \cdot 10^{-3}$	$2.6 \cdot 10^{-3}$	$3.4 \cdot 10^{-3}$	$1.2 \cdot 10^{-3}$	$5.7 \cdot 10^{-4}$
^{11}B	$1.0 \cdot 10^{-3}$	$4.9 \cdot 10^{-3}$	$6.5 \cdot 10^{-3}$	$3.3 \cdot 10^{-3}$	$8.2 \cdot 10^{-4}$
^{12}C	$7.4 \cdot 10^{-3}$	$2.7 \cdot 10^{-3}$	$5.0 \cdot 10^{-3}$	$1.6 \cdot 10^{-3}$	$8.8 \cdot 10^{-4}$
Z=7-20	0.027	0.11	0.14	0.043	0.021
Z=21-40	0.37	0.78	0.88	0.45	0.16
Z=41-60	0.87	1.67	1.77	0.83	0.28
Z=61-91	0.0032	0	0.035	0	0
Total	1.4	2.94	3.31	1.60	0.56

Table 4: Fluences of Ion Species Penetrating into the First Layer of Sample S8 (in $10^{13}/\text{cm}^2$)

ion	Seg.1	Seg.2	Seg.3	Seg.4	Seg.5
n	26.5	67.1	88.9	53.8	20.7
^1H	8.97	20.3	25.5	15.7	5.68
^2H	2.69	7.15	8.84	4.54	1.61
^3H	1.7	4.97	6.26	3.05	1.13
^3He	0.81	2.19	2.71	1.35	0.54
^4He	1.18	3.62	4.43	2.19	0.811
^7Li	$4.7 \cdot 10^{-2}$	0.19	0.27	0.11	$4.5 \cdot 10^{-2}$
^9Be	$6.3 \cdot 10^{-3}$	$3.4 \cdot 10^{-2}$	$4.1 \cdot 10^{-2}$	$1.5 \cdot 10^{-2}$	$5.2 \cdot 10^{-3}$
^{11}B	$7.8 \cdot 10^{-3}$	$4.0 \cdot 10^{-2}$	$5.0 \cdot 10^{-2}$	$2.4 \cdot 10^{-2}$	$6.1 \cdot 10^{-3}$
^{12}C	$3.1 \cdot 10^{-3}$	$1.3 \cdot 10^{-2}$	$2.3 \cdot 10^{-3}$	$6.6 \cdot 10^{-3}$	$5.0 \cdot 10^{-3}$
Z=7-20	0.035	0.15	0.18	0.065	0.032
Z=21-40	0.057	0.11	0.14	0.068	0.026
Z=41-60	0.058	0.11	0.12	0.056	0.018
Z=61-91	$5.9 \cdot 10^{-5}$	0	$8.7 \cdot 10^{-4}$	0	0

In June 2009 first measurements of electrical and mechanical properties of the organic samples will start.

At the moment we may only report that the samples showed a visible sign of changes in dependence on the absorbed dose.

For example, in Fig. 3 photos of samples S8 are shown.

General Topics

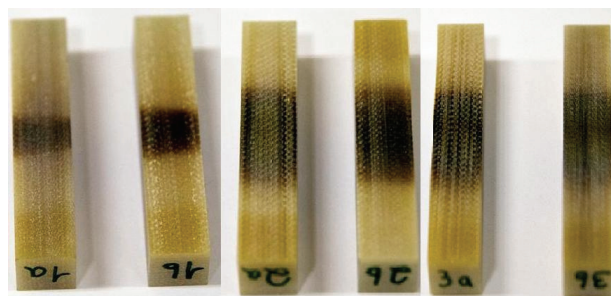


Figure 3: Photo of samples S8 from Segments 1, 2 and 3.

The burned areas on the samples correspond to the irradiated spots. One may see that the beam had an elliptical shape: the burned strip in Segment 1 is narrower than in Segments 2 and 3. According to the values in Table 3 samples S8 from Segments 1, 2 and 3 absorbed 1.4, 2.94 and 3.31 MGy respectively.

In Fig. 4 samples S1 from all five segments are shown.



Figure 4: Photo of samples S1 from Segments 1-5.

Kapton foils showed weaker colorization compared to samples S8 made of G11. One may notice strong change of colour of samples S1 from Segment 5. Segment 5 was not exposed to the beam directly, only the projectiles from tails of Gaussian distribution of the beam in position 2 hit this segment. But it was found after the irradiation, that there was a narrow opening between the stainless plates of Segments 5 and 6. So, the U beam particles from the tail of the distribution penetrated through that narrow opening and hit samples S1 of Segment 5 directly. This illustrates once that heavy ions damage the organics much heavier compared to light particles.

The dose distribution was different not only in different segments but it also depended on the position of the samples relative to the stainless steel plate: samples situated closer to the plate received higher dose. This may be illustrated taking as an example samples S11 and comparing their colorization in dependence on the segment number and on the position of the G11 plates relative to the stainless steel plate. S11 consisted of five G11 plates each of 1 mm thickness. In Fig. 5 calculated dose values are shown for each of five plates depending on the segment and their position relative to the stainless steel plate: sample number on the axis x corresponds to the distance of the G11 plates to the stainless steel plate, G11 plates with smaller number were situated closer to the stainless steel plate.

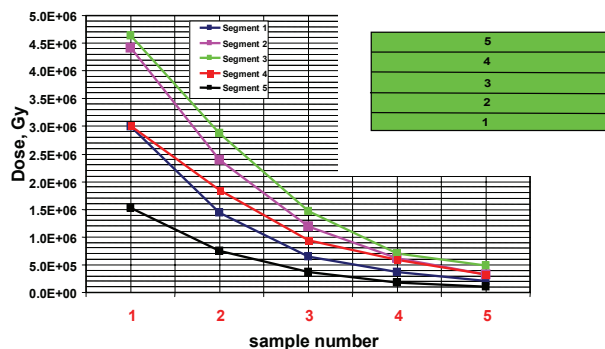


Figure 5: Calculated dose distribution in the center of samples S11 in different segments.

Dependence of the received dose on the distance from the stainless steel plate for samples S11 in one segment (Segment 2 in this case) is shown in Fig. 6.

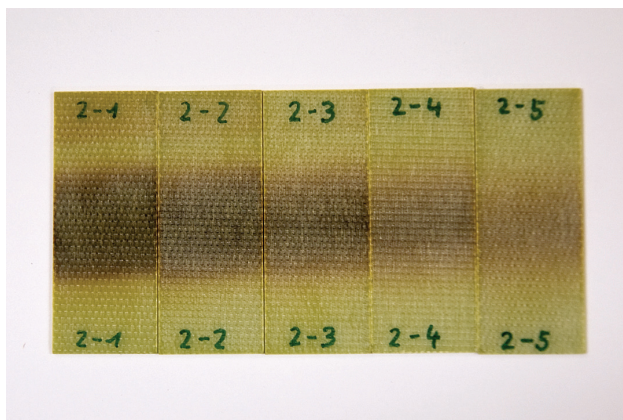


Figure 6: Dependence of the received dose on the distance of the samples from the stainless steel plate: first number on the G11 plate corresponds to the number of segment (Segment 2 in this case), the second number corresponds to the distance from the stainless steel plate (the G11 plate denoted as "2-1" was the closest to the stainless steel plate, and "2-5" was the most distant).

The dependence of the received dose on the segment is shown in Fig. 7. The most left G11 plate is a pristine one (non-irradiated sample).

CONCLUSION

High residual activation level does not allow yet measurement of changes in the electrical and mechanical properties of irradiated samples in dependence on the received dose. First electrical and mechanical measurements are planned for June 2009.

At the moment we may only report that the samples showed clearly visible sign of radiation damage, namely a strong colorization ('burning') of the irradiated layers of the organic materials.



Figure 7: Dependence of the received dose on the segment: "1-1" is the first G11 plate of samples S11 in Segment 1, "2" – first plate of S11 in Segment 2, and "3-1", "4-1", "5-1" – first plates of S11 in Segments 3,4,5.

Calculations showed that the samples received doses up to few MGy. The distribution of sample colorization is in agreement with the calculated distribution of radiation damage.

REFERENCES

- [1] L. Latysheva, "Irradiation experiment in Cave HHD: Numerical estimates of the energy deposition into the samples", GSI report DOC-2008-Nov-262-1, 2008.
- [2] L. Latysheva, "Contribution of the secondary particles to the dose distribution in samples S1 (1st layer) and S8 (1st part)", GSI report DOC-2009-Jan-47-1, 2009.
- [3] A. Plotnikov et al., "Preparation of the irradiation test at Cave HHD of GSI Darmstadt", poster contribution A3 to this conference.
- [4] I. Strasik et. al., "Depth-profiling of the residual activity induced by high-energy Uranium ions in thin stainless steel target", poster contribution A5 to this conference.
- [5] N.M. Sobolevskiy, "The SHIELD transport code: a tool for computer study of interaction of particles and nuclei with complex media", in: Proceedings of the Third Yugoslav Nuclear Society International Conference YUNSC 2000, Belgrade, October 2–5, 2000, The VINCA Institute, Belgrade, 2001, pp. 539–564.

DEPTH-PROFILING OF THE RESIDUAL ACTIVITY INDUCED BY HIGH-ENERGY URANIUM IONS IN THIN STAINLESS STEEL TARGET*

I. Strasik[#], GSI Helmholtzzentrum für Schwerionenforschung, Planckstrasse 1, 64291 Darmstadt, Germany, on leave from FEI STU Bratislava, Slovak Republic

E. Mustafin, E. Floch, T. Seidl, A. Plotnikov, E. Schubert, A. Smolyakov, GSI Helmholtzzentrum für Schwerionenforschung, Planckstrasse 1, 64291 Darmstadt, Germany

Abstract

In the frame of the FAIR project irradiation test of superconducting magnet components was performed at GSI Darmstadt in May 2008. As a part of the experiment stainless steel samples were irradiated by 1 GeV/u ^{238}U ions. In contrast to the previous experimental studies performed with thick cylindrical samples, the target was a thin plate irradiated at small angle. The target was constituted as a set of individual foils. This stacked-foil target configuration was foreseen for depth-profiling of residual activity. Gamma-ray spectroscopy was used as the main analytical technique. The isotopes with dominating contribution to the residual activity induced in the samples were identified and their contributions were quantified. Depth-profiling of the residual activity of all identified isotopes was performed by measurements of the individual target foils. The characteristic shape of the depth-profiles for the products of target activation and projectile fragments was found and described. Monte Carlo code FLUKA was used for simulations of the residual activity and for estimation of the number of ions delivered to the target and their distribution. The measured data are relevant for assessment of radiation situation at high-energy accelerators during the “hands-on” maintenance as well for assessment of the tolerable beam-losses.

INTRODUCTION

In recent years, the number of high-energy hadron accelerator facilities in operation, being commissioned, designed or planned has grown-up. Their parameters such as the beam energy, beam currents and intensities has significantly increased and given rise to new accelerator structure activation and radiation shielding aspects and problems. Residual activity induced in an accelerator structure generally depends on the primary beam losses (amount, energy and mass) as well as on the irradiated material [1] and may become a main source of exposure to personnel and a serious access-restriction for “hands-on” maintenance [2]. In the frame of the FAIR project (Facility for Antiproton and Ion Research) [3], extensive experimental studies [4, 5] and computer simulations [6-9] of the residual activity induced by high-energy heavy-ions in copper and stainless steel were performed at GSI Darmstadt. Copper and stainless steel have been chosen as the representatives of the most common materials for accelerator structures.

The computer simulations can be performed for several ion species and various targets, but the experiments have been so far focused mostly on cylindrical targets irradiated by uranium ions [4, 5]. In contrast to the computer simulations, activation experiments are much more demanding from the beam availability as well as analysis of the irradiated samples. It is practically impossible to carry out irradiation experiments for all primary ions, beam energies and targets of interest. The computer simulations are the only tool to provide this information. Various simulation codes like FLUKA [10], SHIELD [11], MARS [12] etc., are available. However, the computer simulations must be verified by experimental data and more check-points are necessary to validate the codes. That is why the irradiation experiments with cylindrical targets have recently been completed by another experiment with thin stainless steel target irradiated by 1 GeV/u uranium ions. Such kind of target represents thin accelerator structures like a beam pipe. The irradiated target were analysed by gamma-ray spectroscopy and depth-profiling of the partial residual activities of all identified isotopes was performed by measuring the activities of individual target foils.

The activation process is very complex. This is true especially for activation induced by heavy-ion beams. The radioactive nuclides are produced by nuclear reactions induced by primary ions (projectiles) as well as by secondary particles, mostly neutrons and protons, generated by interaction of the primary beam with the target material. On top of that, the projectiles are fragmented into many radioactive projectile-fragments that remain implanted in the target. However, their contribution to the total residual activity is negligible for high-energy projectiles [4, 5].

A summary of the radio-nuclides identified in common materials for accelerator structures irradiated by high energy charged particles is presented in Ref. [13]. Understanding of the activation process provides fundamental information that can be used in two ways: (1) to specify the tolerable beam losses in the machine and (2) to optimize the construction materials. The beam-losses distributed uniformly along the beam line on the level of 1 W/m (equivalent to 6.24×10^9 1 GeV protons/m/s) are presently accepted for high-energy proton machines as a threshold for “hands on” maintenance [14]. Tolerances for heavy-ion accelerators can then be specified by scaling the 1 W/m criterion for proton machines [6, 7, 15]. However, the scaling factors have to be obtained again by computer simulations, which

*Work is partially supported by project VEGA 1/0129/09.

[#]i.strasik@gsi.de

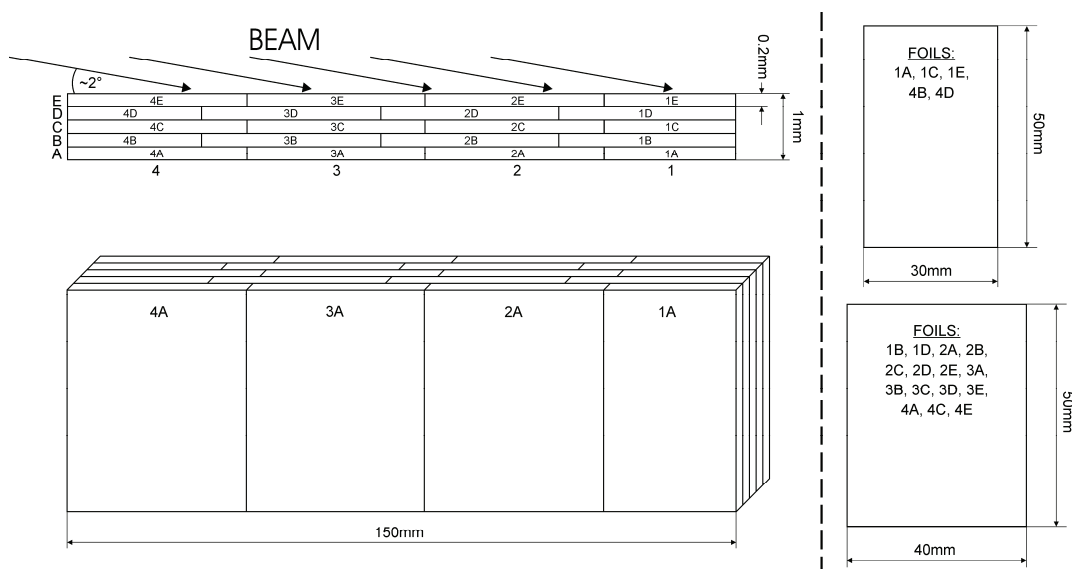


Figure 1: Target configuration and experimental setup. On the left are the parameters of the full-assembly target and on the right are the parameters of individual target foils. The foils are marked by numbers 1, 2, 3 and 4 (segments) and by characters A, B, C, D and E (layers).

brings back the necessity to validate the simulation codes and to collect experimental data.

EXPERIMENT AND METHOD

Target Configuration and Irradiation Conditions

Target configuration is shown in Fig. 1. The target was a plate with 1 mm of thickness \times 50 mm of width \times 150 mm of length. The target was assembled from twenty individual foils with 0.2 mm of thickness \times 50 mm of width \times 40 or 30 mm of length. The target was divided into five layers (A, B, C, D and E) and four segments (1, 2, 3 and 4). The stacked-foil target configuration was foreseen for depth profiling of residual activity. The target material was austenitic Cr-Ni stainless steel (density of 7.9 g/cm³) contained C (max 0.07 %), Mn (max 2.0 %), P (max 0.045 %), Si (max 1.0 %), Cr (17–19 %), Ni (8.5–10.5 %), N (max 0.1 %) and S (max 0.03 %) in addition to iron. Range of the primary ions was estimated by computer codes ATIMA [16], SRIM [17] and FLUKA [10] (Tab. 1). Detailed experimental and simulation study of the range of high-energy uranium ions in copper and stainless steel is presented in Ref. [18].

For the target irradiation the 1 GeV/u ²³⁸U beam from SIS-18 synchrotron at GSI-Darmstadt was used. Irradiation time was 30 minutes. The beam spot-size was about 2 cm in horizontal plane and 1 cm in vertical plane (checked visually on a scintillation screen before irradiation and measured by a profile-meter). The beam profile was approximately Gaussian according to the profile-meter. The glancing angle between the incident beam and surface of the target was about 2° (see Fig. 1). The beam intensity was monitored by a current transformer. Total number of ions registered by current transformer was 1.07×10^{12} , but only a part of the beam hit the target.

General Topics

Table 1: Range of 1 GeV/u ²³⁸U Ions in Stainless Steel

Computer code	ATIMA	SRIM	FLUKA
Range [mm]	15.21 ± 0.01	16.70 ± 0.59	16.06 ± 0.24

RESIDUAL ACTIVITIES

Isotope Identification and Activity Measurement

Results of isotope identification and their partial activities are summarized in Table 2. Partial activity represents the activity of each isotope with respect to the total target activity corresponding to the sum of all isotopes. The isotope identification was based on the energy and abundance of the gamma lines, half-life of the isotopes as well as on the experience from the previous experiments [4, 5]. The isotope characteristics were taken from the WWW Table of Radioactive Isotopes [19]. Half-life of the isotopes in Table 2 ranges from 58.6 h (^{44m}Sc) up to 2.6 y (²²Na). For all identified isotopes, the activity for each foil was obtained from the peak-net-areas (PNA) calculated by Genie2000. The measured activity was then extrapolated backwards in time to the end of the irradiation using the characteristic decay constant of a given isotope. Finally, the partial activity for each foil was summed-up to obtain the partial activity of each isotope induced in the whole target.

Generally, the activation products have several energy lines in the spectra but only the most pronounced lines or lines without an interference with the same or close energy lines of other isotopes were chosen for activity determination. Some isotopes that could be quantified in the early-measured spectra could not be quantified in the later measured spectra, because they decayed below minimum detectable activity (MDA) level. Determination of the activity of ⁸⁹Zr was not possible because its activity

decreased below minimum detectable activity before the measurement of all discs was completed. In the previous experiments performed with cylindrical targets irradiated by uranium beam [4, 5], on the basis of supporting information gained from depth-profiles two types of isotopes could clearly be distinguished: (1) products of target activation and (2) projectile fragments. Mass number of the target activation products ranged from 7 (⁷Be) up to 58 (⁵⁸Co), whereas mass number of the projectile fragments ranged from 89 (⁸⁹Zr) up to 237 (²³⁷U).

Table 2 indicates also partial RMS uncertainties of activities. The accuracy of the presented data is influenced by accuracy of the net-peak-areas and accuracy of the efficiency calibration of the detector. These two contributions are summed-up quadratically for each measured foil.

Depth Profiles of the Residual Activity

Depth-profile is the distribution of the activity as a function of depth in layers A, B, C, D and E of the target. The activity contributions for each foil of the pertinent layer were summed-up in order to get the overall activity of the isotope in the layer (e.g. activity of the foils 1A + 2A + 3A + 4A = activity in the layer A). It was found out in previous experiments [4, 5] that the profiles of the target activation products start at the sample surface and extend deeply beyond the range of primary ions. This is mainly due to large amount of secondary particles that have the range much longer compared to the range of the primary ions. In contrast to that, the depth-profiles of projectile fragments show no signal upstream of the range of primary ions. The profiles start at the range and occupy a region beyond the range from about few mm up to few cm depending on the mass of the fragment. The fragments with mass very close to the mass of the original projectile – ²⁰⁶Bi and, in particular, ²³⁷U – occupy a thin region well correlated to the range of primary ions (²³⁸U).

Figs. 2, 3 and 4 present a typical depth-profile for target activation product (⁵²Mn), light projectile fragment (⁹⁹Mo) and fragment with mass very close to the mass of the primary ion (²³⁷U), respectively. It can be seen in Fig. 2 that the target activation products have rather flat depth profiles. The depth profiles of the light fragments are characterized by a smooth peak in central layer C and comparatively lower values (more than factor of 2) in outer layers A and E (see Fig. 3). In contrast to the profiles of target activation products, the fragments with mass very close to the mass of the primary ion have a high maximum in central layer C and zero values in outer layers A and E (see Fig. 4). The profiles of the target activation products especially the high level of the activity in outer layers A and E compared to the profiles of the projectile fragments indicate strong scattering of secondary particles such as neutrons and protons causing the activation. The distribution of the ²³⁷U closely correlates to the distribution of primary particles because the ²³⁷U ions have almost the same depth profile as ²³⁸U.

Table 2: Identified Isotopes and their Activities

Isotope	Energy [keV]	A ₁ [Bq]	σ ₁ [%]	A ₂ [Bq]	σ ₂ [%]
⁷ Be	477.6	3.04E+2	2.14	3.25E+2	2.32
²² Na	1274.5	6.06E+0	6.75	4.71E+0	5.95
^{44m} Sc	271.1	8.30E+3	1.37	below MDA	
⁴⁶ Sc	889.3	3.18E+2	0.50	3.16E+2	0.56
⁴⁷ Sc	159.4	4.38E+3	1.72	below MDA	
⁴⁸ V	983.5	3.23E+3	0.30	3.21E+3	0.73
⁵¹ Cr	320.1	4.55E+3	0.38	4.59E+3	0.67
⁵² Mn	935.5	4.65E+3	0.45	below MDA	
⁵⁴ Mn	834.8	3.09E+2	0.48	3.06E+2	0.46
⁵⁶ Co	1238.3	1.49E+2	0.99	1.57E+2	0.81
⁵⁷ Co	122.1	8.12E+1	1.73	8.14E+1	1.69
⁵⁸ Co	810.8	1.35E+2	0.85	1.22E+2	0.96
⁸⁹ Zr	908.9	-	-	-	-
⁹⁵ Zr	756.7	2.23E+1	6.53	2.07E+1	5.84
⁹⁹ Mo	140.5	6.03E+2	2.74	below MDA	
¹⁰³ Ru	497.1	5.49E+1	1.61	4.68E+1	2.60
¹²¹ Te	573.1	1.59E+1	4.44	below MDA	
¹²⁶ Sb	414.8	1.71E+1	7.05	below MDA	
¹²⁷ Xe	202.9	1.60E+1	4.14	1.67E+1	7.43
¹³¹ Ba	216.1	7.72E+1	5.64	below MDA	
¹³¹ I	364.5	9.47E+1	3.16	below MDA	
¹⁴¹ Ce	145.4	1.80E+1	4.90	1.68E+1	9.28
¹⁴⁹ Gd	149.7	3.25E+1	5.28	below MDA	
²⁰⁶ Bi	803.1	4.37E+1	4.94	below MDA	
²³⁷ U	208.0	1.66E+3	0.85	below MDA	

A₁, A₂ – activity, σ₁, σ₂ – one standard deviation. Subscript “1” and subscript “2” is related to the spectra measured 8 – 28 and 66 – 91 days after the end irradiation, respectively.

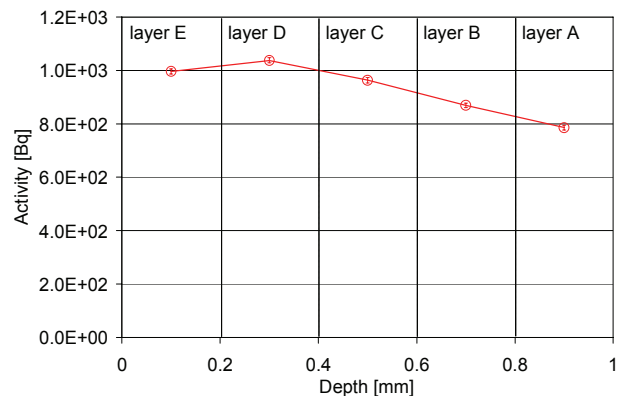
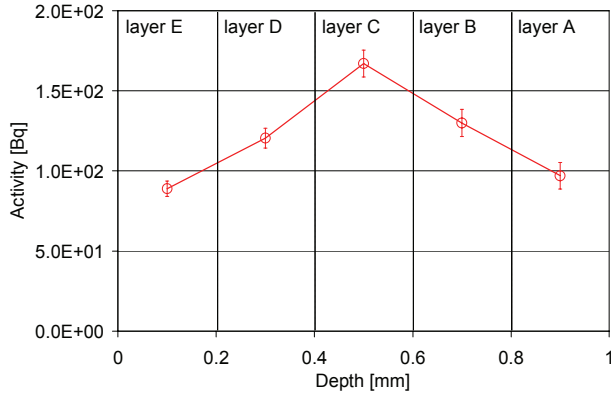
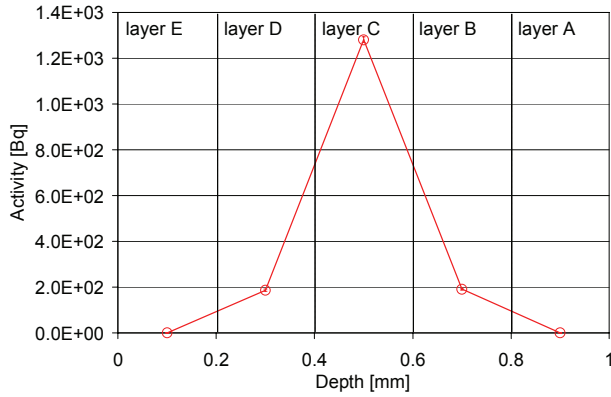


Figure 2: Depth profile of ⁵²Mn.

Figure 3: Depth profile of ^{99}Mo .Figure 4: Depth profile of ^{237}U .

DISTRIBUTION OF PRIMARY IONS

Monte Carlo particle transport code FLUKA was used for estimation of the number of ions delivered to the target and their distribution because the target was irradiated only by a part of the beam. In the simulation model the same experimental target configuration was applied and glancing angle between the incident beam and surface of the target was 2° (see Fig. 5). The distribution of the beam particles in simulation model was assumed to be uniform. The width of the beam cross-section in the plane parallel to the target surface was 10 mm across and 30 mm along to the target length (150 mm). Five independent irradiations were simulated for five different position of the beam from beginning up to the end along the target length (see Fig. 5).

The partial activities of each isotope in twenty foils (g_1, \dots, g_{20}) were calculated for five beam positions. The beam distribution was calculated using the formula:

$$\left(\sum_{j=1}^5 g_{ij} b_j - d_i \right) = \delta_i \text{ for } i = 1, 2, \dots, 20 \quad (1)$$

where g_{ij} is the activity per one incident ion [Bq/ion] in foil i for beam position j calculated by FLUKA, b_j is number of ions delivered to the target for beam position j and d_i is the experimentally measured activity [Bq] in foil i .

General Topics

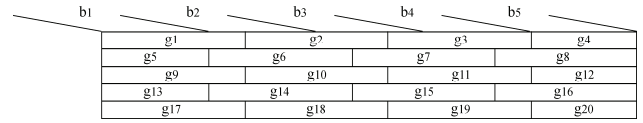


Figure 5: Model of the simulation.

The solution of Eq. 1 and unknown values of b_j were sought as follows:

$$\varphi(\mathbf{b}) = \sum_{i=1}^{20} \delta_i^2 = \sum_{i=1}^{20} \left(\sum_{j=1}^5 g_{ij} b_j - d_i \right)^2 \quad (2)$$

$$\frac{\partial \varphi}{\partial b_k} = \sum_{i=1}^{20} \frac{\partial \delta_i^2}{\partial b_k} = \sum_{i=1}^{20} 2g_{ik} \left(\sum_{j=1}^5 g_{ij} b_j - d_i \right) = 0 \quad (3)$$

for $k = 1, 2, 3, 4, 5$

$$\sum_{j=1}^5 \left(b_j \sum_{i=1}^{20} g_{ik} g_{ij} - \sum_{i=1}^{20} g_{ik} d_i \right) = 0 \quad (4)$$

$$\sum_{i=1}^{20} g_{ik} g_{ij} = G_{kj} \quad \sum_{i=1}^{20} g_{ik} d_i = D_k \quad (5)$$

for $k = 1, 2, 3, 4, 5$

$$\sum_{j=1}^5 (G_{kj} b_j - D_k) = 0 \quad (6)$$

for $k = 1, 2, 3, 4, 5$.

Finally we get the matrix:

$$\begin{aligned} j=1: & \quad j=2: \quad j=3: \quad j=4: \quad j=5: \\ k=1: & \quad G_{11}b_1 + G_{12}b_2 + G_{13}b_3 + G_{14}b_4 + G_{15}b_5 - 5 \times D_1 = 0 \\ k=2: & \quad G_{21}b_1 + G_{22}b_2 + G_{23}b_3 + G_{24}b_4 + G_{25}b_5 - 5 \times D_2 = 0 \\ k=3: & \quad G_{31}b_1 + G_{32}b_2 + G_{33}b_3 + G_{34}b_4 + G_{35}b_5 - 5 \times D_3 = 0 \\ k=4: & \quad G_{41}b_1 + G_{42}b_2 + G_{43}b_3 + G_{44}b_4 + G_{45}b_5 - 5 \times D_4 = 0 \\ k=5: & \quad G_{51}b_1 + G_{52}b_2 + G_{53}b_3 + G_{54}b_4 + G_{55}b_5 - 5 \times D_5 = 0 \end{aligned}$$

The distribution of the beam particles (b_1, b_2, b_3, b_4 and b_5) was calculated for the activity of the ^{51}Cr , ^{54}Mn , ^{99}Mo , ^{127}Xe and ^{237}U . The matrix was solved by Cramer rule and because the matrix is symmetric also by Cholesky decomposition. However results of the calculation showed that our approach failed because the negative values of the number of particles and big inaccuracy of the data were obtained. The reason could be that the calculated results using this method are strongly influenced by the inaccuracy of input data. It must be stressed that the discrepancies between measured and calculated values for individual isotopes induced in

stainless steel target irradiated by 1 GeV/u ^{238}U ions vary from factor of 0.19 to 6.23 [7].

CONCLUSIONS

Partial residual activities of the isotopes and their depth profiles in stainless steel target irradiated by 1 GeV/u ^{238}U beam were measured using a gamma-ray spectroscopy analysis of the stacked-foils target. The isotopes that dominate the residual activity from few days to several weeks after the end of irradiation were identified and their partial activities were quantified. The characteristic shape of the depth-profiles for target activation products and projectile fragments was found and described. The target activation products are present in all layers of the target in similar quantities. Such kind of activation is caused by neutrons, protons and lighter fragments. Projectile fragments have a maximum in the centre of the target and their activity in outer layers of the target decreases with increasing mass of the isotope. Experimental results and simulations performed with FLUKA code were used to calculate the distribution of the beam particles delivered to the target. However, our approach failed to give meaningful results of the number and distribution of the incident beam particles on the target surface, hence the method of the calculation must be improved.

REFERENCES

- [1] A.H. Sullivan, "A Guide to Radiation and Radioactivity Levels Near High Energy Particle Accelerators", Nuclear Technology Publishing, Ashford, Kent, United Kingdom (1992).
- [2] E. Mauro and M. Silari, "Radiation Protection Studies for a High-power 160 MeV Proton Linac" Nucl. Instr. and Meth. in Phys. Res. A, (2009) article in press.
- [3] P. Spiller, G. Franchetti, "The FAIR Accelerator Project at GSI", Nucl. Instr. and Meth. in Phys. Res. A 561 (2006) 305.
- [4] A. Fertman, E. Mustafin, R. Hinca et al., "First Results of an Experimental Study of the Residual Activity Induced by High-Energy Uranium Ions in Steel and Copper", Nucl. Instr. and Meth. in Phys. Res. B 260 (2007) 579.
- [5] I. Strasik, E. Mustafin, A. Fertman et al., "Experimental Study of the Residual Activity Induced by 950 MeV/u Uranium Ions in Stainless Steel and Copper", Nucl. Instr. and Meth. in Phys. Res. B 266 (2008) 3443.
- [6] I. Strasik, E. Kozlova, E. Mustafin et al., "Simulation of the Residual Activity Induced by High-Energy Heavy Ions", Nuclear Technology 168 (2009), article in press.
- [7] I. Strasik, E. Mustafin, E. Kozlova et al., "Residual Activity Induced by High-Energy Heavy Ions in Stainless Steel and Copper", EPAC08, Genoa, Italy, June 2008, p. 3551 (2008).
- [8] E. Kozlova, H. Weick, B. Achenbach et al., "Layout of the Super-FRS Target Hall", Nucl. Instr. and Meth. in Phys. Res. B 266 (2008) 4275.
- [9] H. Iwase, H. Weick, T. Radon et al., "Calculation of activation and dose spatial distributions induced by high intensity uranium beams at the Super-FRS fragment separator at FAIR", Nucl. Instr. and Meth. in Phys. Res. A 562 (2006) 972.
- [10] A. Fasso, A. Ferrari, J. Ranft et al., "FLUKA: a Multi-Particle Transport Code", CERN-2005-10 (2005), INFN/TC_05/11, SLAC-R-773.
- [11] A.V. Dementyev, N.M. Sobolevsky, "SHIELD - Universal Monte Carlo Hadron Transport Code: Scope and Applications", Radiation Measurements 30 (1999) 553.
- [12] <http://www-ap.fnal.gov/MARS/>
- [13] NCRP, "Radiation Protection for Particle Accelerator Facilities: Recommendation of the National Council on Radiation Protection and Measurements", NCRP Report No. 144, 2003.
- [14] N. V. Mokhov and W. Chou (Eds.), "Beam Halo and Scraping", the 7th ICFA Mini-Workshop on High Intensity High Brightness Hadron Beams, Wisconsin, USA, 13-15 September 1999, 3.
- [15] R. M. Ronningen, G. Bollen, and I. Remec, "Estimated Limits on Uncontrolled Beam Losses of Heavy Ions for Allowing Hands-on Maintenance at an Exotic Beam Facility LINAC", Nuclear Technology, 168 (2009), article in press.
- [16] <http://www-linux.gsi.de/~weick/atima>
- [17] <http://www.srim.org/>
- [18] A.A. Golubev, A.V. Kantsyrev, V.E. Luckjashin et al., "Measurement of the energy deposition profile for ^{238}U ions with specific energy 500 and 950 MeV/u in stainless steel and copper targets", Nucl. Instr. and Meth. in Phys. Res. B 263 (2007) 339.
- [19] <http://ie.lbl.gov/toi/>

ITEP HEAVY ION RFQ OUTPUT LINE UPGRADE FOR EXPERIMENTS OF REACTOR MATERIAL INVESTIGATION UNDER IRRADIATION

G.N. Kropachev, R.P. Kuibeda, A.I. Semennikov, A.A. Aleev, A.D. Fertman, T.V. Kulevoy,
 A.A. Nikitin, S.V. Rogozhkin, ITEP, Moscow, 117218, Russia
 M. Cavenago, LNL-INFN, Legnaro (PD), 35020, Italy

Abstract

Development of new materials for future energy facilities with higher operating efficiency is a challenging and crucial task. However, full-scale testing of radiation hardness of reactor materials is quite sophisticated and difficult as it requires long session of reactor irradiation; moreover, induced radioactivity considerably complicates further investigation. Ion beam irradiation does not have such a drawback, on the contrary, it has certain advantages. One of them is high speed of defect formation. Therefore, it provides a useful tool for modeling of different radiation damages. Improved understanding of material behavior under high dose irradiation will probably allow to simulate reactor irradiation close to real conditions and to make an adequate estimation of material radiation hardness.

Since 2008 in ITEP the ion beam irradiation experiments are under development at the ITEP heavy ion RFQ HIP-1. The main objectives of this work are to study primary damage, cascade formation phenomena, phase stability and self-organization under irradiation. This research is carried out by means of tomographic atom probe and transmission electron microscopy. This linac provides accelerated beams of Cu^{2+} , Fe^{2+} , Cr^{2+} ions with current up to 10 mA and energy 101 keV/u. The first experiments with ion beam at the linac injector demonstrated promising results. The linac output beam line is now under upgrade. The results of beam extraction line adjustment for experiments with reactor materials are presented. The construction of controllable heated target is presented as well.

INTRODUCTION

Precipitation hardening (PH) ferritic/martensitic steels are one of the most perspective structural materials for new generation fusion and fission reactors. Their higher heat- and radiation-resistance is the result of high number

density nano-sized precipitations that are formed during quenching with subsequent tempering. Development of such steels is based on optimization of macro-properties and micro structure of unpredicted material which requires considerable resources. At the same time, steel with adequate parameters in as-produced state can have miserable performance under irradiation. Thus, at the next step thorough investigation of nano-particles behavior under neutron flux is required. However, the main limiting factor for neutron irradiation is the time which is needed to achieve required displacements per atom (dpa) and to reduce induced radioactivity to the levels where micro structural study is allowed. Normally, it takes from several years for RAFM materials to decades or more for others, which makes such investigations practically impossible. So, the one of the closest way to predict material radiation resistance is to use heavy ion beams as a modeling irradiation. One of its advantages is high dose rates which are changeable in wide range and another is that no material activation occurs.

High potential of ITEP acceleration facility with unique possibilities of atom probe microscopy creates a powerful instrument for detailed study of materials degradation mechanism. As a demonstration of this potential, the first set of topographic atom probe data for EK-181 (RUSFER EK-181) steel were obtained [1]. This approach will be used in the program devoted to the study of radiation degradation of structural materials. The aim of this research program is to find out the laws, mechanisms and regularities of radiation degradation processes and to analyze nano-scale peculiarities in perspective materials for new generation power plants. This program covers a wide range of materials from pressure vessel steels to the active zone materials. It will provide useful information for adjusting and justification for full scale modeling by investigation of nano-scale changes in structural materials under modeling irradiation.

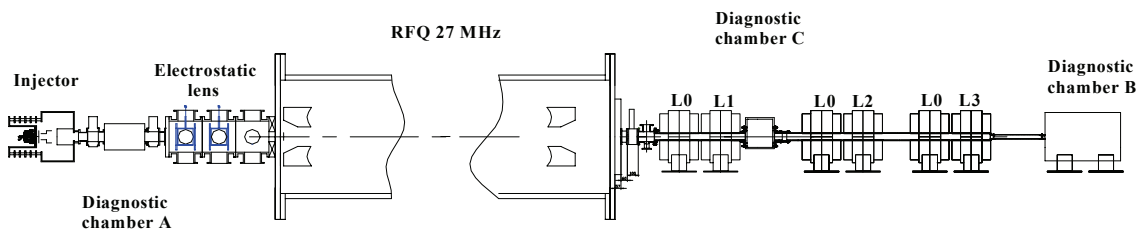


Figure 1: ITEP RFQ HIP-1. L1, L2, L3 – existing quadrupole lenses, L0- lenses needed for transportation of ions with specific mass of 60 amu (not installed).

To provide radiation resistance investigation of power plant vessel materials under high-dose irradiation, the imitational experiments with accelerated ion beam are developed in ITEP at the 27 MHz heavy ion RFQ HIP-1 (Heavy Ion Prototype). With neutron irradiation required doses (~ 100 dpa) could be achieved only in a few years even in fast breeding reactors. Heavy ion beams drastically increase defect generation speed preserving nature of cascade formation. As a result the high dpa can be reached in considerably lower time limits. The 27 MHz heavy ion RFQ provides acceleration of ions with mass to charge ratio up to 60 with energy of 101 keV/u [2]. The RFQ is the realization of proposed in ITEP new resonant structure [3]. The accelerator assembly consists of the 100 kV terminal with MEVVA ion source [4], low energy beam transport (LEBT) line with two electrostatic einzel lenses, diagnostic chamber A, 12 m long 27 MHz RFQ section and channel with 3 quadrupole lenses and two diagnostic station B and C at the output of the accelerator (see Fig. 1). The ion beam both with low energy ($45 \div 80$ keV/Z where Z – ion charge number at the injector output) and high energy (5.6 MeV for Fe beam) can be used for irradiation experiments.

The maximum of the radiation degradation dose is achieved at the end of ion track into the sample, so the beam ions are accumulated into the sample. The implanted particles must not change dramatically the chemical structure of the sample. Therefore the Fe and Cr ions are preferable for irradiation modeling experiments with reactor steels. Nevertheless, to enable the direct detection of ions implanted into the samples. the Al ion beam can be used for first test with the steels.

The status of the activity was presented at the IAEA meeting in May [5]. In this report the detailed results of the ion beam delivering to the target with maximum ion beam density in high energy experiments are presented. It was found that for routine linac operation the ion beam density at the target can be up to $3-4$ mA/cm². The ion beam pulse length is 140 μ s with repetition rate 1/4 pps,

therefore it allows to obtain total flux $\sim 10^{16}$ cm⁻² in 10 hours what corresponds with > 10 dpa. To increase the total flux, the mode with ion beam length of 450 μ s and repetition rate 1pps was successfully tested.

BEAM SIMULATION AT THE RFQ OUTPUT CHANNEL FOR IRRADIATION EXPERIMENT

To define the 1 cm² target position and quadruple lenses parameters corresponding to the maximum ion beam current density, the simulation of the beam dynamics throughout the output channel was carried out. The previous experimental program on the HIP-1 were carried out with accelerated Cu²⁺ ion beam [6]. This beam was taken for the initial work for beam line optimization for irradiation experiments. The following parameter limitations were used for output line optimization were used:

- Cu²⁺ ion beam with energy 101 keV/n.
- Beam current – 4, 6, 8, 10 mA.
- The initial Twiss beam parameters are defined at the RFQ output (from beam dynamics simulation with DYNAMION code) [7].
- Quadruple lenses L1, L2, L3 can be used in any combination. The lenses magnetic field gradient can be up to 8 T/m, effective length is 23.5 cm, distance between poles is 7 cm. The maximum gradient can reach even 12 T/m, but for stable routine operation it is better not to exceed 8 T/m.
- The distance from the last lens and the target should be less than 2 m.

Number of particles for simulation is 10^3 for tuning procedure and 10^5 for final simulations

The transverse dynamics of Cu²⁺ ion beam in the HIP-1 and its cross section are shown in Fig. 2 Twiss parameters for the beam at the linac output are shown as well.

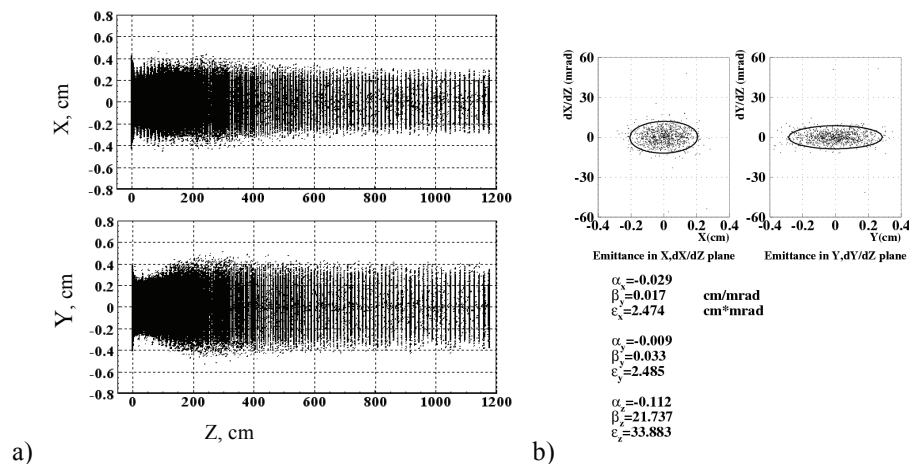


Figure 2: Result of Cu²⁺ ion beam simulation in the HIP-1 RFQ by DYNAMION code. a) Transverse plane of beam along linac; b) beam Twiss parameters at the output of linac.

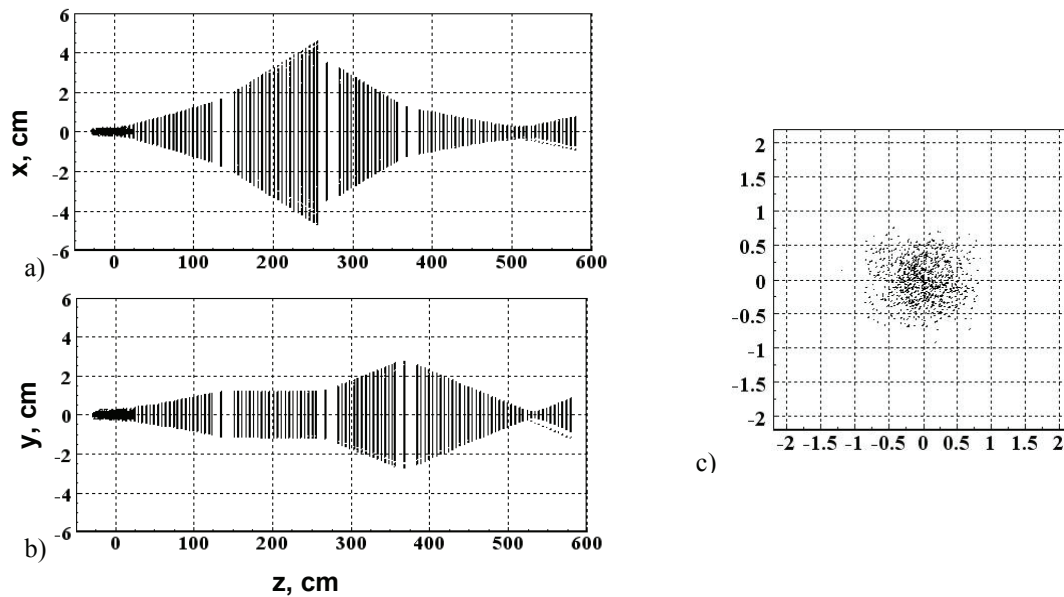


Figure 3: Result of Cu^{2+} ion beam dynamic simulation in HIP-1 output channel; a) vertical plane, b) horizontal plane c) beam cross section at the target plane.

It was very interesting to install the target in the diagnostics chamber one. In this case only lens L1 could be used. It is obvious that the beam profile is not axially symmetric from target point of view it can be even better because the set of samples can be installed in line. The simulation showed that the maximum beam density at the target installed into this chamber would not exceed 0.6 mA/cm^2 .

At the next step the different combination of two lenses were investigated and finally the mode when all three lenses operated together was investigated. Let's consider optimization problem to get maximal beam density at the target with cross-section of 1 cm^2 . Therefore our optimization criteria is beam density. The optimization procedure was following:

1. define the step of variation for distance after last lens;
2. fix the distance after last lens;
3. define the step of magnetic field variation for all lenses;
4. vary the magnetic field gradient at the one lens meanwhile all other are fixed;
5. make procedure 4 till the variation will not increase the beam density at the target;
6. change distance from last lens at carry out procedure 3, 4, 5.

The simulation showed that for two lenses the maximum beam density would not exceed the 0.77 mA/cm^2 . For three lenses operated mode it was found that the beam density at the target with cross section of 1 cm^2 can reach $j = 3.73 \text{ mA/cm}^2$ when the total beam current is 4 mA. The target should be located at the distance of 150 cm after the last lens and gradients at the lenses L1, L2, L3 should be 4, -7.5 and 7.9 T/m consequently. The transverse beam dynamics into the channel is given in Fig. 3. It is necessary to note that at the target plane the beam current density is about

uniform. Also it was found that this beam density can be obtained at the distance range of 130 – 170 cm from the last lens with small correction of lenses magnetic field gradients inside the above mentioned limits. The tolerance of magnetic field gradients for lenses L1 and L3 should be better than 5 % and for lens L2 it should be better than 2 %.

At the next step the Cu^{2+} ion beam with current of 6, 8 and 10 mA was transported throughout the channel. To define the input Twiss parameters for every beam current, the beam dynamics simulation into HIP-1 was carried out. Result of the simulation is given in Figure 4. One can see that for beam current 10 mA the density at the target can reach 7.97 mA/cm^2 .

As one can see from the Table 1 the beam density increases with total beam current. The increase of beam current can be obtained by upgrading of accelerator initial part (LEBT). Nevertheless, the simulation of ion beam dynamic into HIP-1 showed that the increase of input beam current in 3 times results just 30 % increase of accelerated beam current (see Table 1).

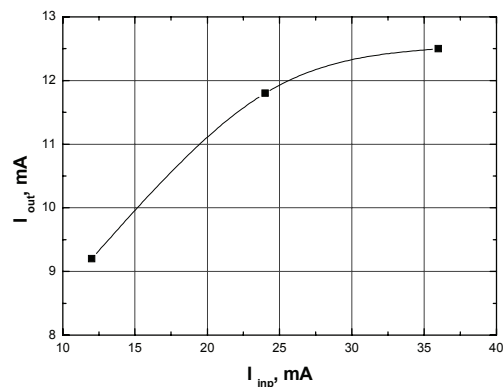


Figure 4: Beam current transmission throughout HIP-1 linac.

Table 1: Ion Beam Density at the Target for Different Accelerated Currents

beam current, mA	Beam current at the target of 1 cm ² , mA	% ion beam delivered to target
4	3.73	93.25
6	4.96	82.7
8	6.5	81.3
10	7.97	79.7

Table 2: Results of Ion Beam Simulation for Different Ions

Ion	Accelerated current, mA	Gradient at L1 T/m	Gradient at L2 T/m	Gradient at L3 T/m	Beam current density, mA/cm ²
Cu	4	4	-7.4	7.1	3.73
Fe	4	4	-6.7	6.8	3.62
Cr	4	4	-6.3	6.5	3.61

The results of simulation correlates with experimental results obtained at the linac during previous experiments. For stable linac operation the ion beam with current of 4 mA is preferable. Therefore the following simulation of Fe²⁺ and Cr²⁺ ion beam needed for irradiation experiments was carried out for this beam current. For these ion beams the same optimization procedure was carried out. With one exception – the position of target was fixed at 150 cm from the last lens. For both ion beams the Twiss parameters at the RFQ output were defined from beam dynamics simulation into HIP-1 RFQ. The magnetic field gradients and maximum beam density for all beams are shown in Table 2.

At the RFQ output the accelerated beam has pulse length of 140 μ s. The repetition rate is 1/4 pps. Therefore the total flux of 10^{16} on the target for Fe²⁺ ions can be obtained during 10 hours of accelerator operation. The flux of 10^{17} can be obtained if the pulse length is increased up to 450 μ s after 30 hours. To decrease the accelerator operation time needed for given flux, it is necessary to increase the repetition rate. Without any upgrade the repetition rate can be increased up to 1/3 pps. Further increasing of repetition rate requires the RF power system upgrade.

HEATED TARGET CHAMBER CONSTRUCTION

The construction of target assembly for high energy imitation experiments with controlled heated target is shown in Figure. 5. The cylindrical samples with diameter 3 mm and thickness 0.1 mm are used for investigations. Seven samples are fixed between two copper plates. The plate which looks at the beam has seven holes with diameter 2.9 mm – one at the axis and six at the radii 3.5 mm. Such sandwich is installed at the heated sample support made from copper. Copper is used to provide the temperature uniformity and stability for all samples. To prevent the vacuum vessel surface overheating, the water cooled screen around target assembly is used. The screen is manufactured from stainless steel. Two sets of 5 pillars with cross section 5x5 mm from stainless steel are used to keep the heated sample support inside the cooled screen. Stainless steel is chosen for both screen and pillars to provide the higher thermal gradient between screen and heated support.

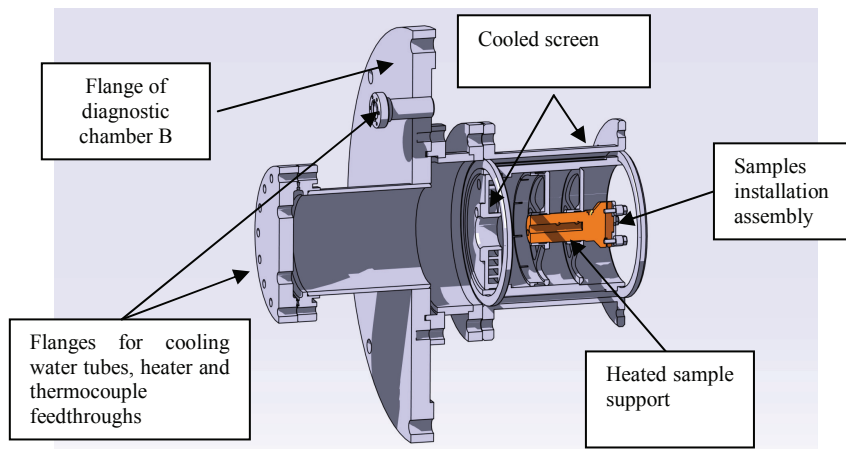


Figure 5: Design of target assembling for high energy ion beam irradiation experiments with controlled heated target.

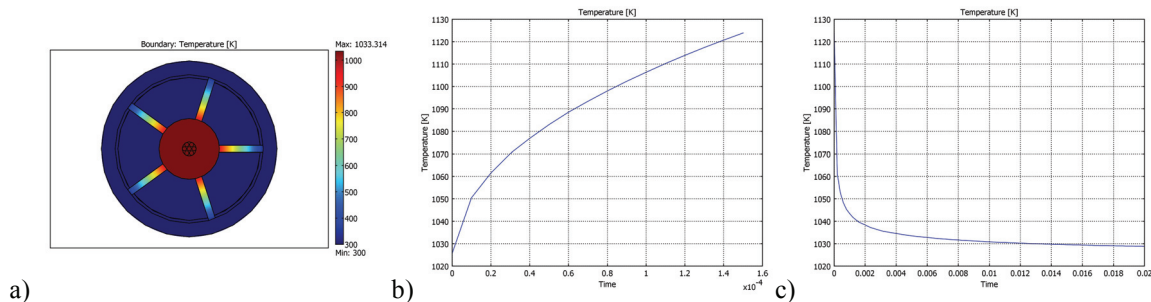


Figure 6: Temperature distribution at the target assembly. a) stationary solution before beam irradiation b) temperature of sample outside surface during the 4 mA beam irradiation, c) temperature of sample outside surface after beam.

The construction was investigated with COMSOL multiphysics code. Results of preliminary simulation are shown in Figure 6. The surface-to-surface radiative heat transfer was not yet taken into account for practical reasons. According to the simulation the temperature of heated samples without beam can be regulated in range from 25°C to 700°C with single heater of 250 W. During the irradiation by 4 mA beam with pulse length 0.14 ms the temperature of sample front side increases by 100°. The beam heating was added to the heat flow boundary condition. The temperature of sample inside surface connected to support surface increases by 30°. After irradiation the temperature of the sample reaches the initial stationary level in about 10 ms. The parts of target assembly are manufactured and now are under installation at the HIP-1. At next step the sample and its support surface radiation will be investigated with well known surface-to-ambient approximation. Moreover as a refinement, we plan to insert the actual beam energy loss distribution taken from SRIM simulation as a volume heat source (instead of the heat flux boundary condition term).

CONCLUSION

The nano-scale investigations of structure peculiarities and composition of structural materials that are used in power plants are carried on in ITEP. Such investigations are carried out in Russia for the first time with unique technique – tomographic atom probe. The ITEP 27 MHz heavy ion RFQ linac can be used as an effective experimental facility for the investigations. The experimental work can be carried on with Fe, Cr, Cu and Al ion beams with energy of 101 keV/u. As it was demonstrated in routine operation mode of the linac with 4 mA accelerated ion beam the beam current density at the target can reach 3.6 mA/cm². To reach this level, the target should be installed at 150 cm from the last quadruple lens of output linac channel and the gradients at the lenses less than 8 T/m. The precision of magnetic field gradients should be better than 5 % for first and last lens and better than 2 % for central one what can be easily provided. The total flux of 10¹⁶ – 10¹⁷ cm⁻² can be provided. The target assembly with heated samples for the experiments is under manufacturing. The simulation

showed that without irradiation the sample temperature can reach 700°C. The irradiation of ion beam with current density of 3.6 mA and pulse length of 0.14 ms provides the increase of target surface temperature of 100 °K. The temperature comes back to stationary level in 10 ms after beam irradiation.

ACKNOWLEDGES

This work was possible due to partial support of the Russian Foundation for Basic Researches (grant 08-02-01448-a).

REFERENCES

- [1] Rogozhkin, S.V., “Topographic atom probe study of RUSFER EK-181”, The Physics of Metals and Metallography, 2009 (to be published).
- [2] Kashinsky, D., et al., “Commissioning of ITEP 27 MHz Heavy Ion RFQ”, Proceedings of the Seventh European Particle Accelerator Conference. EPAC-2000, Vienna, 2000, p.p. 854-856.
- [3] Andreev, V.A., Parisi, G. “90°-apart-stem RFQ Structure for Wide Range of Frequencies”, Proc. of the 1993 Particle Acc. Conf., Washington DC. pp3124-3126.
- [4] Batalin, V., et al., “Report on ITEP MEVVA Development”, Proc. Workshop on Vacuum Arc Ion Sources, Berkeley, USA (1996). pp.37-39.
- [5] A.A. Aleev, et al., “ITEP Heavy Ion RFQ — Experimental Facility for Reactor Material Investigation under Irradiation”, Book of Abstracts, International Topical Meeting on Nuclear Research Applications and Utilization of Accelerators, 4–8 May 2009, Vienna, Austria, AP/P5_07, p.47.
- [6] M. Basko, et al., “Stopping Power Measurements for 100-keV/u Cu²⁺ Ions in Matter”, 32nd EPS Plasma Physics Conference, 27 June -1 July 2005, http://eps2005.ciemat.es/database/abstracts/packs/ABOOK_P1.pdf, P.1-146.
- [7] A. Kolomiets, et al. “DYNAMION - The Code for Beam Dynamics Simulation in High Current Ion Linac”. Proc. EPAC-98, Stockholm, Sweden, p.1201.

CURRENT STATUS OF RAPID, THE UNIVERSITY OF TOKYO

S. Ito, A. Morita, H. Matsusaki

Department of Nuclear Engineering and Management, School of Engineering,
University of Tokyo, Japan

Abstract

The 1.7 MV tandem accelerator RAPID (Rutherford Backscattering Spectroscopic Analyzer with Particle Induced X-ray Emission and Ion Implantation Developed), at the University of Tokyo has been dedicated to various scientific and engineering studies in a wide range of fields by the ion beam analysis availability, including RBS (Rutherford Backscattering Spectroscopy), PIXE (Particle induced X-ray emission) and ion implantation. Total accelerator operation time amounted to 9358 hours since its installation with the highest annual operation time recorded in 2007. RAPID-PIXE analysis system has been contributed to many environmental studies by analyzing elemental composition of water and sediments samples. It is also applied to the analysis of several cultural heritages such as a works of gilded frame from Renaissance in Italy. Recently, the low level ion irradiation system was also developed and applied for the study of CR-39 track detector with proton beam.

INTRODUCTION

RAPID (Rutherford Backscattering Spectroscopic Analyzer with Particle Induced X-ray Emission and Ion Implantation Developed) is an elemental analysis and the ion implantation system using ion beams accelerated by an electrostatic accelerator at the University of Tokyo, Japan. The system consists of a 1.7 MV tandem accelerator (Tandetron™, Model 4117-HC, provided by HVEE: High Voltage Engineering Europe corp., Netherlands), two negative ion sources (a Cs sputter solid ion source and “Duoplasmatron” gas ion source) and three beam lines (Fig. 1 and Table 1).

The 1.7 MV “Tandetron™” has Cockcroft Walton type charging system. The terminal voltage is monitored and stabilized by a Generating Volt Meter (GVM). Various ion species can be produced by the dual negative ion sources system. Totally 24 ion species, from Hydrogen to Gold, had been generated and accelerated. Especially it is one of specific features of RAPID that He⁻ ion is available by the “Duoplasmatron” gas ion source. PIXE detector system, RBS&ERDA detector system and Ion implantation chamber are equipped at the end of each beam line. PIXE chamber is mounted with three axis and one translation sample manipulator with Si(Li) detector. RBS chamber is mounted with three axis goniometer and silicon surface barrier detector. Recently ERDA system is also set up in the RBS chamber. The angle of Ion implantation line is fixed at -7° to the central axis of the accelerator. A target holder of ion implantation can be heated up to 800°.

RAPID was installed in 1994 at Research Center for Nuclear Science and Technology, The University of Tokyo at first and since then it has been used for various research fields using ion beams. As the Center was reorganized to be a department of School of Engineering in 2005, the educational utilization became an important mission of RAPID. Besides several application studies with PIXE analysis, environmental analysis (pond sediments and atmospheric SPM - Suspended Particulate Matter) is performed as a student experiment. Heavy metal elements analysis of gilded frames of art works from Florence, Italy is also one of recent topics. Another major topic is that a special beam irradiation system was developed to evaluate the response of CR-39 track detector to low level radiation.

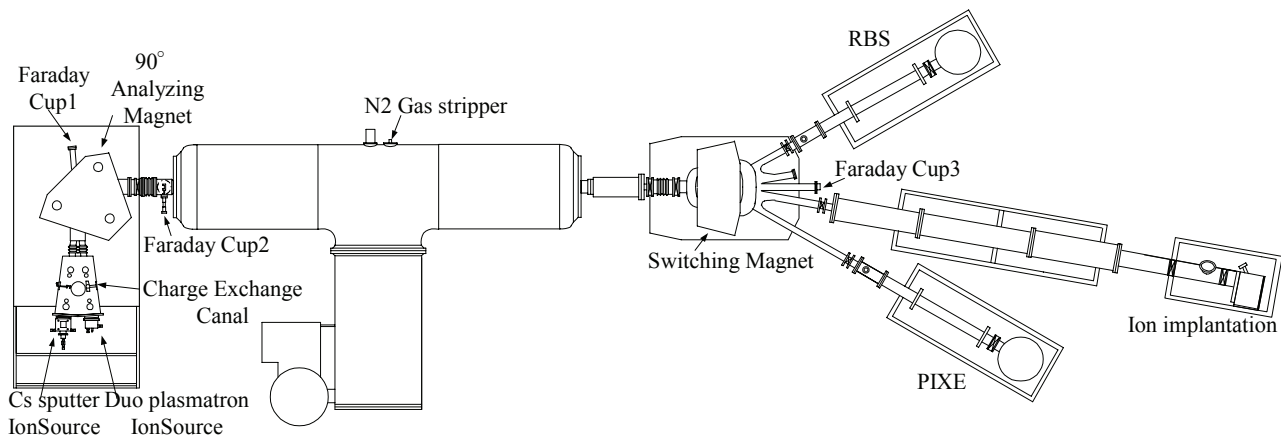


Figure 1: Schematic illustration of the 1.7 MV tandem accelerator system.

Table 1: Specification of RAPID

Negative ion Sources	
Cs sputtering Type	
Extraction Voltage	20kV
Duoplasmatron Type	
Extraction Voltage	20kV
Top Accelerator	
Available voltage range	0.1-1.7MV
Stability	< 80 Vrms
Ripple	< 30 Vrms
Produced beam current	
H ⁺	25 μA (3.4 MeV)
He ²⁺	2 μA (5.1 MeV)
Si ²⁺	140μA (5.1 MeV)
Au ²⁺	60 μA (5.1 MeV)
Cu ²	20 μA (5.1MeV)
N ²⁺	19μA (5.1 MeV)

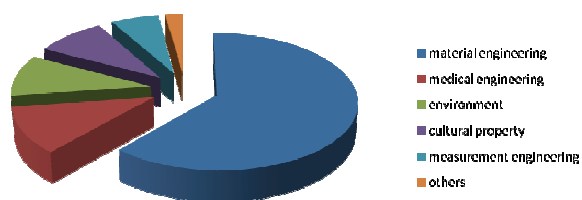


Figure 2: The percentage of various research fields in 2007.

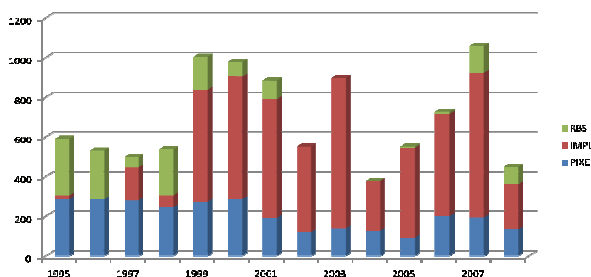


Figure 3: Yearly operation time for each beam line since 1995.

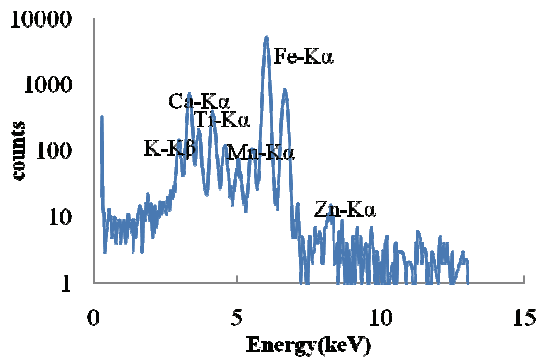


Figure 4: PIXE spectrum of pond sediment. This is that of “Sanshiro-ike” pond in the University of Tokyo.

Fig. 2 shows the percentage by which each application field occupies the RAPID machine time. Fig. 3 shows the yearly accelerator operation time of RAPID. Considerable drop in operation time in 2008 is due to the off-line development for low level irradiation system and new ERDA system. The total operation time has reached 9358 hours. Since RAPID has been operated carefully, it has never experienced a severe sparking nor a fatal discharging. That is why the main accelerator tank has never opened since the construction.

APPLICATIONS

PIXE Analysis of Pond Sediments and Air Dust

PIXE is a good example for understanding the basics of the IBA technique and is easily applied to the environmental study. Hence, a student experimental program was designed with PIXE analysis of environmental samples. Main subject of the program is simply the PIXE analysis of the pond sediments collected from the bottom of a “Sanshiro-ike” in the University of Tokyo, where various plants and creatures are living [1].

However, it contains from the field work, sampling, pre-treatment for the IBA, PIXE analysis itself and detailed analysis of the data. Students are expected to recognize the relationship between human and natural bio system as well as the acquisition of the PIXE technique through this program.

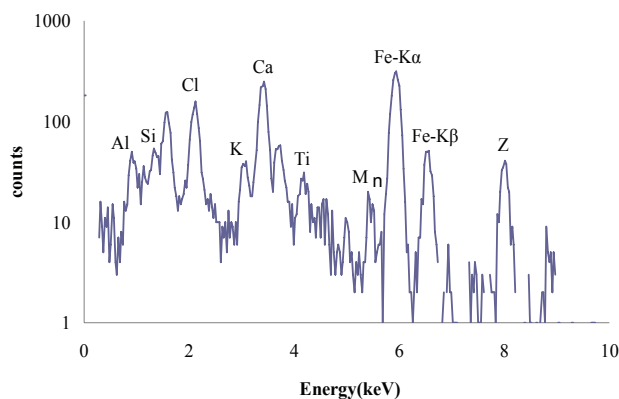


Figure 5: PIXE spectrum of SPM corrected in the campus of University of Tokyo.

Fig. 4 shows an example of the PIXE analysis spectrum of the pond sediments. Fortunately, pollutant metals such as Cd, As, Hg was not observed. In 2009, newly designed student experiment program was started which treats SPM (Suspended Particulate Matter) in the atmosphere. Atmospheric dust particles larger than 0.45 micro-m size were collected by a hand-made dust collector at the rooftop of the accelerator building. The main component of the dust around Tokyo area is 1) natural soil, 2) volcanic ash, 3) artificial origin dust due to such as the exhausted gas from the automobiles or factories, 4) Sea salt and 5) Yellow sand from Chinese continent.

The amount and the portion of these components varies with the seasons and the weather. For example, the

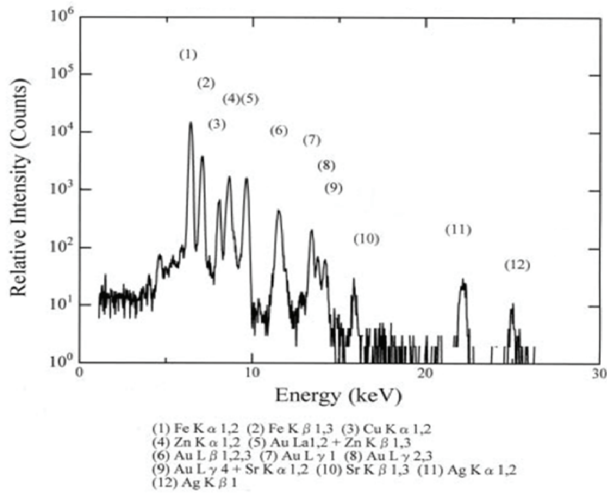
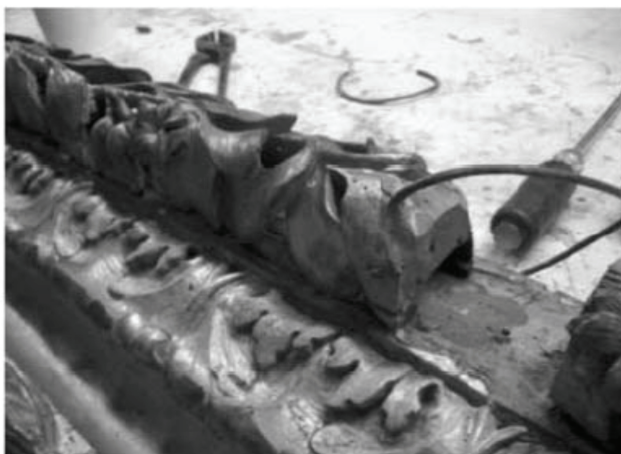


Figure 6: PIXE spectrum of the gilded frame of art works including one from Florence.

amount of the yellow sand arriving in Japan is greatly enhanced during the term from February to May. The PIXE spectrum of SPM collected at April 1st, 2009 is shown in Fig. 5. The main components of the yellow sand, Si, Al, are detected.

Analysis of Cultural Heritage

Cultural heritage is also an interesting target for PIXE analysis concerning the study of the history of “art”. Here, the analysis of the gilded frame at Florence, Italy is shown as an example. After the Renaissance era, the frame started to be used with paintings. Dr. Sumiko Hasegawa recognized the historical importance of this fact and considered that people of the Renaissance era began to recognize the importance of the frame. They found that a frame could enhance the fascination of the painting by the frame, i.e., excellent morphological design and coloring of the frame makes the painting more attractive. With such recognition, precious material such as gold came to be used (Figs. 6 and 7) [2].



Development of Low Level Irradiation Chamber

To evaluate the response of CR-39 track detector to low level irradiation, specially designed irradiation chamber system was developed and set at the ion implantation line of RAPID. If we receive accelerated proton beam directly, it is difficult to reduce the flux to less than 1×10^8 [ions/s·cm²]. Newly developed system uses the backscatter proton and enables to reduce proton dose significantly.

The backscatter angle is 45° [3]. The proton flux can be reduced to the degree of the backscattering cross section and the actual solid angle of the irradiation area. The geometry of the system is shown in Fig. 8. As a result, the dose was restricted to less than 10^7 [ions/s·cm²]. Initial proton flux is monitored by the faraday cup placed coaxially. The distance between the scattering target and the irradiated sample is 160 mm and the inner diameter of the aperture in front of the irradiated sample is 8 mm. Hence the actual solid angle for the scattered ion particles is as small as 0.063 sr so that the irradiation can be considered uniform. By the Silicon Surface Barrier detector placed behind the irradiated sample the energy spectrum of the back scattered ion particles is measured. The energy distribution of the scattered ion particles can be changed by changing the thickness and the materials of the scattered target film. Using this system the response of CR-39 to low level irradiation was investigated. Fig. 9 (a) is the result of direct irradiation of the initial proton beam to the CR-39 and Fig. 9 (b) is the result of the irradiation by the scattered ion particles. Obviously an appropriate dose rate to identify each ion track is the case of the scattered ion particle irradiation (Fig. 9 (b)). Each spot on the Fig. 9 (b) corresponds to a track. Concentrated spot means the concentrated energy deposit by the ion, a large energy loss near the end of the track. Track Spot A is more concentrated than track Spot B in Fig. 9 (b). Energy deposit for track Spot B is smaller which means that the ion had higher energy and the energy loss was smaller. Fig. 9 (c) shows the energy spectrum of the irradiated ion particles generated by the backscattering which was measured by a solid state detector.



Figure 7: A gilded frame being restored (left) and pieces of impress gold foil on (right).

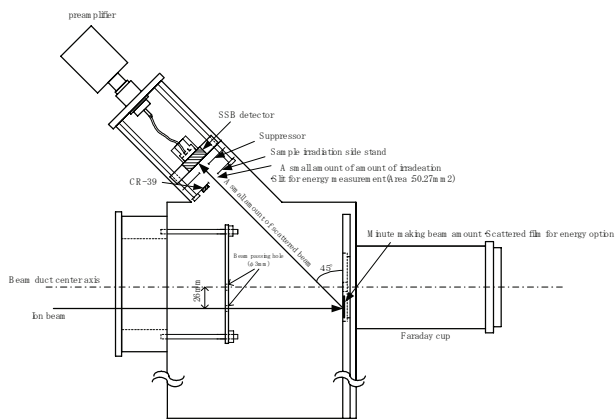


Figure 8: Schematic drawing of new irradiation system.

SUMMARY

RAPID, at the University of Tokyo, is a beam analysis and ion implantation system being used for various application studies. The range of application field extends not only in engineering but also to cultural heritages. Total accelerator operation time of RAPID amounts to 9358 hours since 1995. Recently environmental analysis (pond sediments and atmospheric dust) using PIXE was performed as a student experiment. A special irradiation chamber system was developed which enabled low level irradiation (less than 10^4 ions/s cm^2) by means of back scattering. The energy distribution of the back scattering beam is also variable by changing the thickness and materials of the scattered target. Using this system the response of CR-39 track detector to low level irradiation was investigated.

ACKNOWLEDGEMENT

The authors thank Kosako laboratory, the University of Tokyo, for providing CR-39 photos. The authors also express gratitude to Dr. Yosuke Miyairi, Ms. Yoko Tsuchiya and Mr. Chuichiro Nakano, the University of Tokyo for cooperation of student experiments. Dr. Fumitaka Nishiyama (Hiroshima University) and Mr. Masuchika Kohno (Kyoto University) are kindly provided useful advises about PIXE analysis. Mr. Masaru Yasumoto, the University of Tokyo fully helped the authors in developing the new irradiation chamber system. The authors appreciate all of them.

REFERENCES

- [1] S. A. E. Johansson, J. L. Campbell, "PIXE: A Novel Technique for Elemental Analysis", John Wiley & Sons, Ghichester (1988) 8.
- [2] S. Hasegawa, M. Kohno, H. Date, K. Kawamoto and M. Inoue, F. Nishiyama., S. Ito, A. Morita and H. Matsuzaki, "The Research for The Gilded frame at Florence", Proceeding of the 20th Meeting for Tandem Accelerators and their Associated technologies, (2008) 141 [in Japanese].
- [3] L. Bernardi, A. Cecchi, C. Gori, F. Lucarelli and R. Renzi "Studies of the response of CR-39 track detector to protons from a 3 MeV Van de Graaff accelerator", Nuclear Instruments and Methods in Physics Research B53 (1991) 61-66.

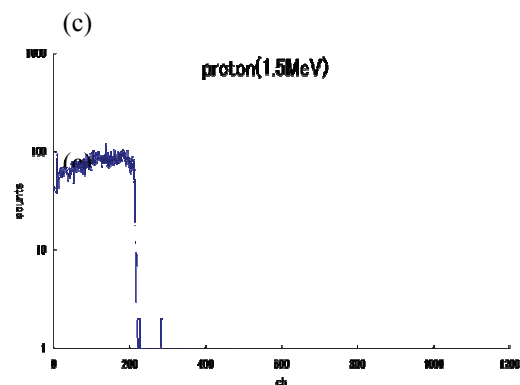
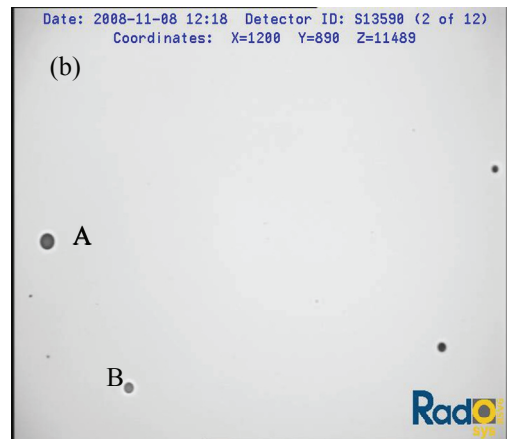


Figure 9: Photograph of the irradiated CR-39 by proton beam; (a) Direct irradiation (b) Backscattered irradiation (c) Energy spectrum of backscattered proton beam transmitting CR-39, which was obtained simultaneously with Fig. 9 (b). (Scatter target = 12.5 mm thick Al foil).

CONCEPTUAL DESIGN OF A RADIO FREQUENCY QUADRUPOLE FOR HEAVY ION MEDICAL FACILITY

G. Hahn, D. H. An, H. J. Yim, Y. S. Kim, KIRAMS, Seoul, South Korea

Abstract

Design of conventional 4-vane/rod type of RFQ (Radio Frequency Quadrupole) for the heavy ion medical facility has been studied. The RFQ is capable of accelerating C^{4+} ions from an initial energy of 10 keV/u to 300 keV/u. In this work, all the design parameters have been optimized to achieve stable structure and compactness. The 3D electromagnetic field distribution and RF analysis were obtained by CST Microwave Studio and the field was used in TOUTATIS for beam simulation. This paper shows the determined physical and mechanical design parameters of RFQ.

BEAM DESIGN

At least a set of four parameters, consisting in aperture, modulation, synchronous phase and end-to-end voltage difference of the adjacent tips is necessary to define a tip geometry and analytic potential map of RFQ. The tip can be divided into four sections named radial matching, shaper, gentle buncher and accelerator sections. Each section has its own function. Using this functionality, we defined a set of design parameters, keeping below the current limit condition ($<500 \mu A$), considered space charge effect, by applying smooth approximation. Fig. 1 shows the current limit condition and Fig. 2 shows the main design parameters. The output summary of the preliminary results is given in Table 1.

The aperture parameter was set from 4.1 mm to 3.1 mm to compensate the weakening focusing strength along the beam direction. Modulation and synchronous phase smoothly vary at the same time.

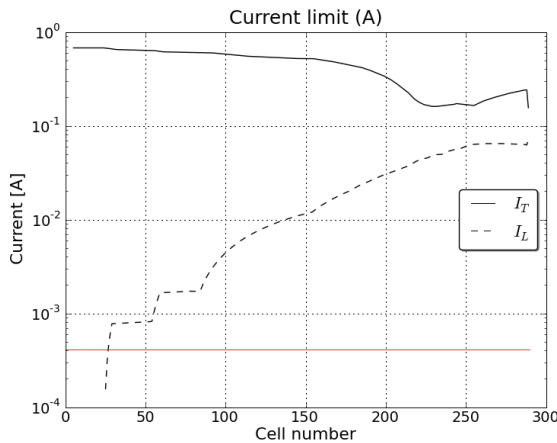


Figure 1: Current limit with smooth approximation line (I_T is transverse current limit and dashed line; I_L is longitudinal current limit)

Table 1: Design summary

Parameter	Value	Unit
Particle	C^{4+}	-
Input energy	10	keV/u
Output energy	300	keV/u
Peak current	410	μA
Input emittance x / y	1.43 / 1.41	π mm mrad (norm, rms, 90%)
Output emittance x / y	1.42 / 1.41	π mm mrad (norm, rms, 90%)
Energy deviation	0.86	%
Operating frequency	200	MHz
Duty	0.1	%
Pulse width	200	μs
Cavity length	1.6	m
Cavity diameter	28.2	cm
Peak power (4vane)	150	kW
Q (4rod / 4vane)	4200 / 10500	-
Average V0	96	kV
Transmission	98.9	%
Number of cells	283	-
Maximum surface field	1.6	Kilpatrick

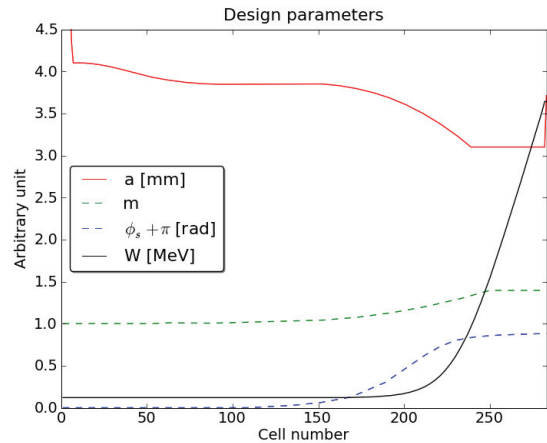
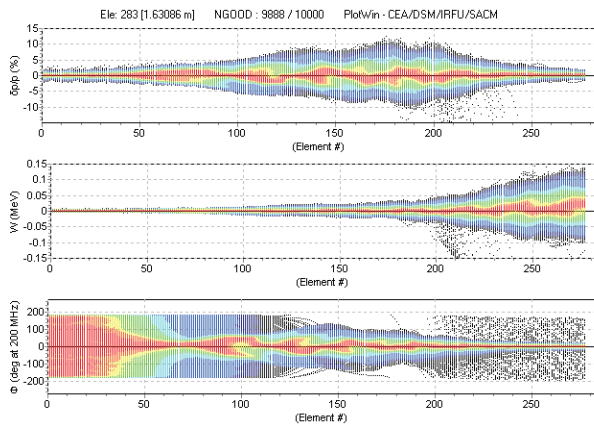
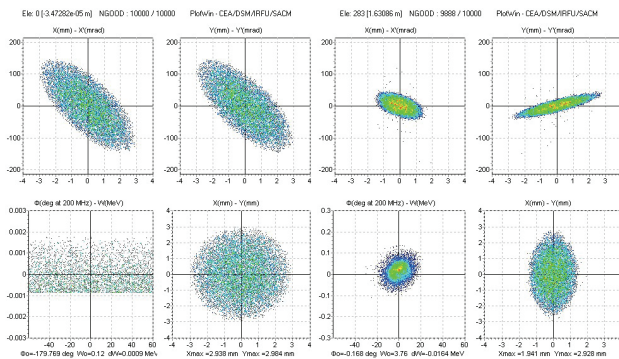


Figure 2: Main design parameters of RFQ consisting of a(aperture), m(modulation), phi(synchronous phase) and W(kinetic energy of synchronous particle)

garam@kirams.re.kr



(a) configuration plot



(b) input beam

(c) output beam

Figure 3: The figure (a) shows the configuration plot of the beam in the RFQ, the figure (b) shows input beams which have 4D water-bag distribution at cell zero and (c) shows the output beam profile at the last cell

Beam dynamics is calculated by TOUTATIS code. The transmission rate of this configuration reached 98.9% without emittance growth. The result is shown in Fig. 3(a) as a configuration plot and Figs. 3(b)(c) as the phase space plots.

CAVITY DESIGN

In the beam dynamics simulation, the vane tip voltage along the beam axis plays a key role. The focusing force mainly depends on the tip voltage difference between adjacent tips separated by a few millimeter. It means that the V_0 distribution is quite sensitive to aperture modulation of the tip. And the electric field near the beam axis is greatly affected by V_0 distribution which depends on geometrical cavity structure.

The absolute value of the voltage difference can be controlled by modulating the strength of stored power. But distribution of relative voltage value is determined by the geometrical structure of the cavity only. Therefore, the following procedure has been done.

- Adjust other parameters except V_0 (constant).
- Simulate the field by using the geometrical structure obtained from the output of the beam simulation.

- Applying V_0 distribution obtained from the above and proceed beam simulation again.

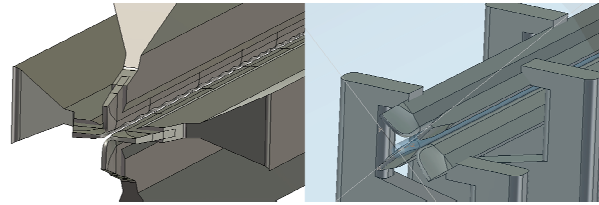


Figure 5: Two types of geometrical structure

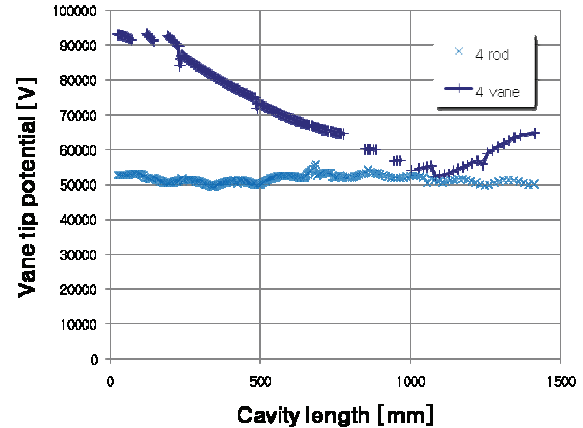


Figure 6: V_0 distributions of two RFQ structure

CONCLUSIONS

A simulation of RFQ for C^{4+} which is capable of accelerating up to 300 keV/u has been done by using TOUTATIS. To adjust resonance frequency and Q value, the geometrical structure was built and tested in MWS. As a result, design parameters of applied V_0 distribution was determined.

REFERENCES

[1] TOUTATIS, "A 3D RFQ Code", CEA
 [2] CST. Microwave Studio; <http://www.cst.com>

COMMISSIONING OF THE CNAO LEBT AND SOURCES

A. Parravicini, S. Alpegiani, G. Balbinot, G. Bazzano, D. Bianculli, J. Bossler, E. Bressi, G. Burato, G. Butella, M. Caldara, E. Chiesa, L. Falbo, A. Ferrari, F. Generani, F. Gerardi, L. Lanzavecchia, R. Monferrato, V. Mutti, M. Nodari, M. Pezzetta, A. Portalupi, C. Priano, M. Pullia, S. Rossi, M. Scotti, M. Spairani, E. Vacchieri, S. Vitulli, CNAO Foundation, Pavia, Italy
 A. Reiter, B. Schlitt, GSI, Darmstadt, Germany
 C. Biscari; C. Sanelli, INFN/LNF, Frascati, Italy
 C. Roncolato, INFN/LNL, Legnaro, Italy
 L. Celona, G. Ciavola, S. Gammino, F. Maimone, INFN/LNS, Catania, Italy
 M. Ferrarini, Politecnico di Milano, Milano, Italy
 L. Frosini, G. Venchi, Dipartimento di Ingegneria Elettrica -
 Università degli Studi di Pavia, Pavia, Italy

Abstract

The Centro Nazionale di Adroterapia Oncologica (CNAO) [1] is the Italian centre for deep hadrontherapy, namely an innovative type of radiotherapy using hadrons. The wide range of beam parameters (i.e. energy and intensity) at patient level together with the advantages of hadron-therapy with respect to traditional radio-therapy nourishes the hopes for more effective patient recovery. After the LEBT and the RFQ commissioning [2], the IH commissioning is now in progress. First patients are expected to be treated in 2010. The present paper summarizes and evaluates the Low Energy Beam Transfer (LEBT) line commissioning, which has been carried out between July 2008 and January 2009.

Particles are emitted by the sources at 8 keV/u, accelerated by the RFQ and the IH to 7 MeV/u, and then injected into the synchrotron. Extraction energy depends on treatment requirements: the deeper is the tumour to be irradiated, the higher is the required energy. Extraction energy can vary from 120 to 400 MeV/u for Carbon ions and from 60 to 250 MeV/u for protons. Extraction process nominally lasts one second.

Nominal beam intensity at patient level is 3.8 nA and 0.16 nA, for protons and Carbon ions, respectively. It can be reduced up to a factor 1000, by closing down LEBT slit plates, inserting pepper-pot filters in the MEBT line and extracting the beam with spills over a longer extraction time.

THE CNAO MACHINE

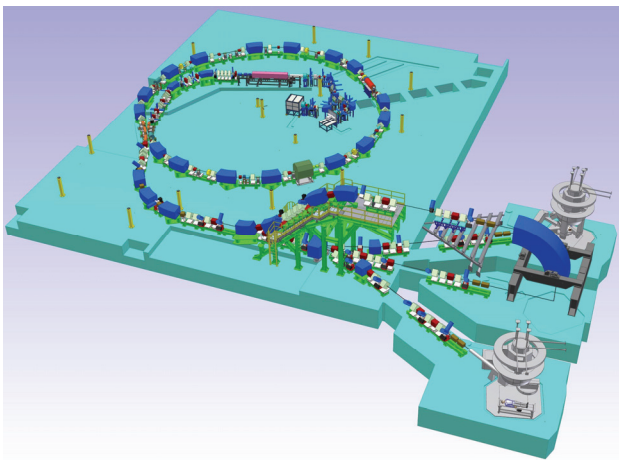


Figure 1: Sketch of the CNAO machine complex.

CNAO machine is depicted in Fig. 1. CNAO beam originates from one of the two Electron Cyclotron Resonance (ECR) sources, producing either C^{4+} or H_3^+ ions, it then travels along the LEBT line, the LINAC and the Medium Energy Beam Transfer (MEBT) line. It turns around a 25 m diameter synchrotron and, finally, is extracted into one of the four extraction lines, delivering either C^{6+} or proton beam to one of the three treatment rooms.

Linacs

THE LEBT LINE

The LEBT line (Fig. 2) begins with two ECR sources, both able to produce either H_3^+ and C^{4+} ions. A source produces a beam containing many ion species. Downstream each source, a 90° -dipole (also called Spectrometer) allows to select particles with different Z/A ratio and thus to separate H_3^+ and C^{4+} beams from other species. A switching dipole magnet merges the two source lines into one. After being bent by a 75° -dipole, the beam enters the RFQ.

Upstream the RFQ an electrostatic deflector, called Chopper, is installed. The beam is continuous from the sources to the Chopper, while it is pulsed (i.e., 50-100 us pulse, approximately every 2 s) behind it, if the Chopper is switched on.

Particles running along the LEBT cross many magnets and beam diagnostics monitors.

Three solenoids, four dipoles, eleven quadrupoles and eight correctors are used to focus, bend and steer the beam.

As far as Beam Diagnostics (BD) is concerned [3], vertical and horizontal wire scanners are used as profile monitors. Some Faraday cups and one Chopper Faraday cup measure beam intensity. Sets of four metallic plates, mounted on top, bottom, left and right tank ports, each one driven by a motor, altogether called Slit monitor, are used either to suppress beam halo, if positioned at beam

border, or to select thin beam slices, in case one plate is positioned close to the opposite one, making a slit. This last use allows both phase space distribution measurements, if beam profiles are measured behind the slit, and beam profile measurements at slit level, if beam intensity is measured downstream. Faraday cups and slit plates are cooled and can be polarized to capture secondary emitted electrons.

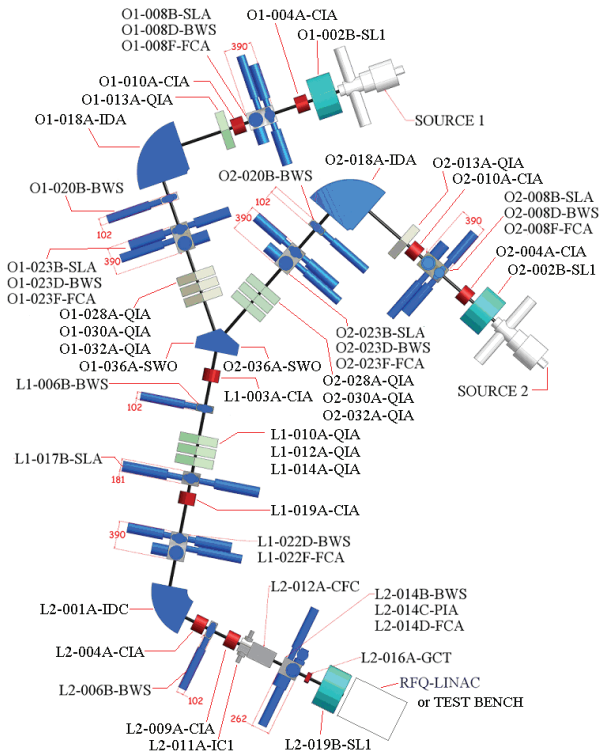


Figure 2: LEBT line layout. Sketch of magnets and beam diagnostics tanks, from the sources to the test bench installed at the end of the LEBT line. Legend: SLA= Slit monitor, FCA= Faraday Cup, BWS= Wire Scanner, CFC= Chopper Faraday Cup, GCT= AC- Current Transformer, PIA= Wires Harp, CIA= corrector, QIA= quadrupole, SL1= solenoid, SWO=switching magnet, IDA= 90° dipole, IDC=75° dipole, IC1= Chopper dipole.

In four positions along the line, a full set of BD monitors (i.e., four-plates slits, one horizontal and one vertical wire scanner, one Faraday cup) are installed in the same tank, 390 mm long [4]. In other two positions, this tank is installed, but not fully equipped.

This compact tank, equipped with all the monitors, was the main tool for most of the measurements here after reported. The high wire scanner spatial resolution and the comparatively large beam divergence allowed accurate emittance measurements in less than 150 mm, namely by using the instrumentation installed in a single tank.

COMMISSIONING MEASUREMENTS

Commissioning started with a coarse study of the first part of the LEBT line. Sources spectra were measured, the wished species (i.e., H_3^+ or C^{4+}) peak was selected and the resulting beam current intensity and ripples were studied versus source parameters, in order to obtain stable source operation and accurate ions species selection.

The beam is guided along the rest of the line. Optics parameters as dispersion, phase space distribution, beam width and barycentre position were measured along the full line. Their behaviour versus magnet settings was studied, as needed to define repeatable and reliable optics settings.

Beam current intensity was measured at Faraday cup levels to optimize beam transmission.

Finally, the LEBT line-end commissioning was performed, aiming to produce a beam matching with RFQ input requirements.

Ion Species Selection

Source spectra are measured by selecting a beam vertical slice with the slit downstream the spectrometer and changing spectrometer current, at the same time. The resulting beam current versus time pattern (Fig. 3) measured by the Faraday cup shows the different ion peaks and allows to select the required one.

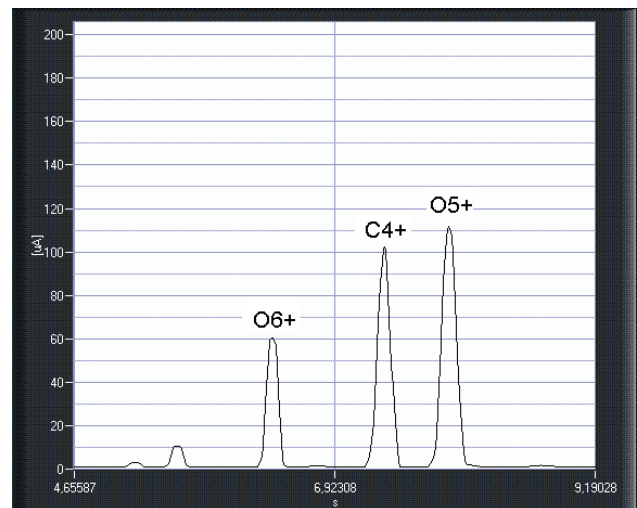


Figure 3: Source spectrum measured at the O2-023-FCA Faraday Cup, while ramping the O2-sector spectrometer from 30A to 60A. O2-023-SLA plates are positioned as follows: top and bottom plates fully out from beam path, left plate at -5 mm and right plate at +5 mm with respect to the vacuum chamber centre. One can notice the C^{4+} peak surrounded by other species peaks.

Emittance and Twiss Parameters Measurement

The same metallic plates, making vertical or horizontal thin slits, are used to perform vertical or horizontal emittance measurements (Fig. 4), respectively. Particles phase space distribution is derived step-by-step moving a slit from one side of the beam spot to the opposite one, and measuring beam profile with the wire scanner for each step. The distance between slit and wire scanner installed in the same 390 mm long tank is about 150 mm, that guarantees a good angular resolution. Spatial resolution is enhanced by increasing the number of steps, with the drawback that measurement time increases consequently. In L1-sector, slit and wire scanner distance is as large as 1 m and angular resolution is improved, accordingly.

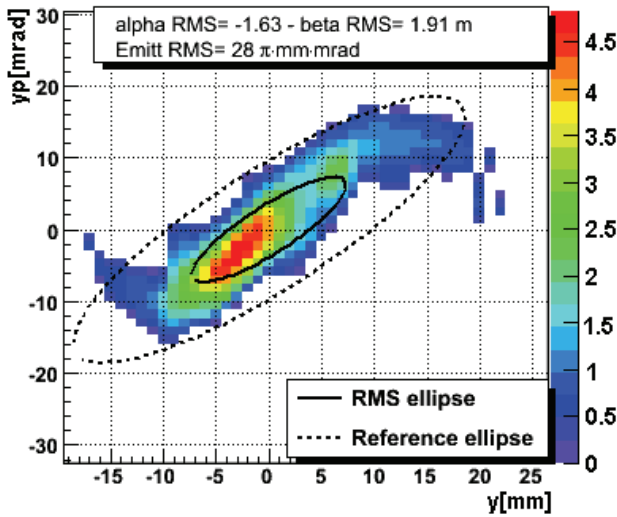


Figure 4: Phase space distribution at the level of O1-023-SLA, for the vertical plane. By using statistical emittance definition, we retrieve the RMS Twiss parameters and emittance value at 1σ . The corresponding ellipse is drawn on the plot with solid line. The dashed line ellipse uses alpha and beta parameters obtained from the measurement and a 180π mm mrad emittance. While vertical plates are moved from -30 mm to +30 mm, left and right plates are kept in place to select the ion species.

Table 1: Horizontal And Vertical Twiss Parameters At O1(O2)-023B-SLA

Twiss Parameters At O1(O2)-023B-SLA						
Species	Alpha		Beta [m]		Emitt RMS [π mm mrad]	
	Hor.	Vert.	Hor.	Vert.	Hor.	Vert.
H_3^+	-0.80	-1.21	0.49	1.49	28.05	21.03
C^{4+}	-0.04	0.78	0.16	1.17	40.90	34.04

Twiss parameters can be measured just downstream the spectrometers (Table 1) and behind the switching magnet

(Table 2), where slit monitors are available. Twiss parameters at source level have been derived as back-tracking of downstream parameters and used to check beam optics models and understand downstream beam behaviour.

Table 2: Horizontal and Vertical Twiss Parameters at L1-017B-SLA

Twiss Parameters At L1-017B-SLA						
Species	Alpha		Beta [m]		Emitt RMS [π mm mrad]	
	Hor.	Vert.	Hor.	Vert.	Hor.	Vert.
H_3^+	2.91	0.49	2.17	0.89	25.74	24.08
C^{4+}	3.51	2.18	2.94	2.05	33.80	37.10

Beam parameters along the line resulted consistent and reproducible. They are being employed to define a theoretical model of the line providing simulations coherent with the measurements, which will help line setting-up.

Meantime, an experimental response matrix for the full line was measured for each optics settings: it allows to steer the beam taking into account the actual effects of magnets changes on beam optics. That is a key-point for a fast and reproducible beam steering.

Dispersion

Horizontal and vertical dispersion was measured at some points along the line, everywhere a profile monitor is present. Table 3 collects some significant results.

From dispersion value at the selection slits (i.e. at O1(2)-023-SLA), spectrum peaks resolution is estimated, as well. Profile monitors layout gives the opportunity to measure dispersion at different points along a drift and dispersion derivative can be computed, consequently.

Table 3: Horizontal and Vertical Dispersion Values Along The LEPT Line

Dispersion Values for Carbon Ions [m]						
Species	O1(O2)-023D-BWS		L1-022D-BWS		L2-014B-BWS	
	Hor.	Vert.	Hor.	Vert.	Hor.	Vert.
C^{4+}	1.45	-0.01	-0.58	0.17	5.11	-0.12

Beam Transmission

Beam transmission was measured along the line by means of the Faraday cup monitors.

Overall transmission, from the species-selection level (i.e. behind the spectrometer) to the LEPT line-end, have been obtained up to 97%.

In order to guarantee the beam current intensities needed for treatments (i.e. $10E+10$ protons per spill and $4E+08$ C^{6+} ions per spill), the minimum intensities at the LEPT end must be of 600 μA and 200 μA for H_3^+ and C^{4+}

beams, respectively, if we assume 90% transmission along the LEBT.

During the LEBT commissioning, beams up to 1400 μA and up to 230 μA for H_3^+ and C^{4+} , respectively, have been measured.

End-Line Test Bench

Beam optics parameters in the last sector of the LEBT line were carefully adjusted so to maximize RFQ transmission and minimize damaging beam losses against the RFQ itself.

A test bench was installed in place of the RFQ during this commissioning phase. It consisted of two tanks of 390 mm-long type. The first one was equipped with one horizontal and one vertical slit for phase space distribution measurements; one horizontal and one vertical wire scanner for beam profiles when the beam is continuous; a wires harp for horizontal and vertical beam profiles dedicated to chopped beam, but used with continuous beam, too. A Faraday cup equipped with both, AC and DC electronics, was installed in the second tank. An end-Faraday cup was used to close the beam pipe and measure AC-beam intensity.

Test bench slit is not made by drawing-up two opposite plates, but is cut on the plate itself. It provides a fixed-amplitude slit, not changeable by the user, but more accurate and occupying a shorter longitudinal space. A rather complicated mechanical design was required to install slit plates exactly at the RFQ entrance level, because of the short available space. These slits resulted in a powerful tool to investigate particles distribution in the phase space, exactly at the matching point between LEBT and RFQ.

Table 4: Theoretical and Measured, Horizontal and Vertical Twiss Parameters at LEBT-End

Twiss Parameters @ Test Bench						
Species	Alpha		Beta [m]		Emitt RMS [π mm mrad] (*)	
	Hor.	Vert.	Hor.	Vert.	Hor.	Vert.
Theoretical	1.3	1.3	0.035	0.035	36	36
H_3^+	1.64	1.17	0.06	0.03	25	33
C^{4+}	0.56	0.49	0.03	0.03	37	32

(*) According to CNAO hypothesis on particles distribution, total emittance is given by 5 times the RMS emittance.

Beam trajectory was centred and aligned with respect to the RFQ entrance point and axis by using wire scanners and correctors of the last sector of the LEBT line (i.e. L2-sector), while beam emittance measurements performed with the test bench checked the actual position and divergence at the RFQ level. Test bench monitors were of

great help while preparing the beam for RFQ. RFQ acceptance was also investigated by means of a probe beam, defined by upstream slit plates, which is smaller than the full beam in position and divergence.

A cylindrical beam (Table 4) was produced at the test bench level. This was required as a pre-condition for starting the RFQ commissioning, in order to best fit with RFQ cylindrical symmetry and maximize the transmission. Indeed, beam transmission through the RFQ resulted above 60% for both the species.

CONCLUSIONS

Source and LEBT line commissioning took 15 weeks, alternated with installation periods.

BD monitors well fulfilled commissioning requirements, providing reproducible and reliable measurements. Wire scanner spatial resolution (nominally 0.1mm) resulted a great advantage to investigate particles angular distribution over short distances.

The use of a test bench measuring beam distribution in the phase space, exactly at the matching point between LEBT and RFQ, was very effective for preparing the beam outgoing the LEBT line.

Faraday cup and wire scanner CNAO-developed amplifier worked successfully, over a wide dynamic range and bandwidth.

Optics settings repeatability was poor initially since correctors share the same iron yoke and thus the two planes interfere with each-other. Then stabilization cycles were carefully defined and these effects minimized.

CNAO LEBT commissioning was carried on with satisfactory results. Measurements were good and their results allowed to define reliable and reproducible magnet settings for the line.

An experimental response matrix for the full line allows a fast and effective beam steering. Beam transmission over the full line is good (up to 97%) and beam intensities at the LEBT-end are larger than what required for treatments.

Beam parameters at test bench level well match with RFQ input beam requirements, resulting in a fast and fruitful RFQ commissioning.

LINAC commissioning is now in progress.

REFERENCES

- [1] S.Rossi, "Developments in protons and light-ions therapy", EPAC 2006.
- [2] E.Bressi et al, "Status report on the Centro Nazionale di Adroterapia Oncologica (CNAO)", PAC 2009.
- [3] A.Parravicini et al., "Beam Diagnostics in the CNAO injection lines commissioning", HIAT 2009.
- [4] J.Bosser et al, "A compact and versatile diagnostic tool for CNAO injection line", EPAC 2008.

BEAM DIAGNOSTICS IN THE CNAO INJECTION LINES COMMISSIONING

A. Parravicini, G. Balbinot, J. Bossler, E. Bressi, M. Caldara, L. Lanzavecchia, M. Pullia, M. Spairani, CNAO Foundation, Pavia, Italy
 C. Biscari, INFN/LNF, Frascati, Italy

Abstract

The Centro Nazionale di Adroterapia Oncologica (CNAO) [1] is the first Italian center for deep hadrontherapy, namely an innovative type of oncological radiotherapy using hadrons.

The CNAO machine installation is in progress and alternates with lines commissioning [2] [3], started in the Summer 2008.

The present paper reports about Beam Diagnostics (BD) choices, status and post-commissioning evaluation, as concerns the Low Energy Beam Transfer (LEBT) line monitors.

THE CNAO LEBT LINE

The CNAO Machine

The CNAO heart is made by a 25 m diameter synchrotron. One injection line, starting from one of the two available sources, brings the 8 keV/u ion (C^{4+} or H_3^+) beams to the RFQ-IH, that accelerates particles to 7 MeV/u, which is the energy of the Medium Energy Beam Transfer (MEBT) line beam. At the beginning of the MEBT line, electrons are stripped out from carbon or hydrogen ions, that become C^{6+} or protons, respectively.

The MEBT line brings particles into the synchrotron, where C^{6+} and protons can be accelerated up to 250 MeV/u and 400 MeV/u, respectively, according to the deepness of the tumour to be irradiated.

Finally, particles are extracted towards one of the four extraction lines (3 horizontal and 1 vertical), that deliver the beam to one of the three treatment rooms (i.e., the central treatment room is equipped with horizontal and vertical beam lines).

The LEBT Beam Diagnostics Layout

The CNAO beam originates from one of the two ECR sources, both able to produce C^{4+} or H_3^+ ion beam. The beam produced by a source contains many ion species. Downstream each source, a 90°-dipole (also called *spectrometer*) allows to select particles with different Z/A ratio and thus to separate H_3^+ and C^{4+} beams from the other species. A switching dipole magnet merges the two source lines into one, which is bent by a 75°-dipole and, finally, enters the RFQ (Fig. 1).

Ahead the RFQ, a Chopper magnet changes drastically the beam parameters: upstream the Chopper the beam is continuous; after the Chopper it is pulsed, with 50-100 μs long batches, every about 2 s. BD monitors for a continuous or a chopped beam are significantly different. The present paper mainly focuses on the BD monitors designed for a continuous beam, namely installed

upstream the Chopper, or downstream the Chopper but to be used when the Chopper is off.

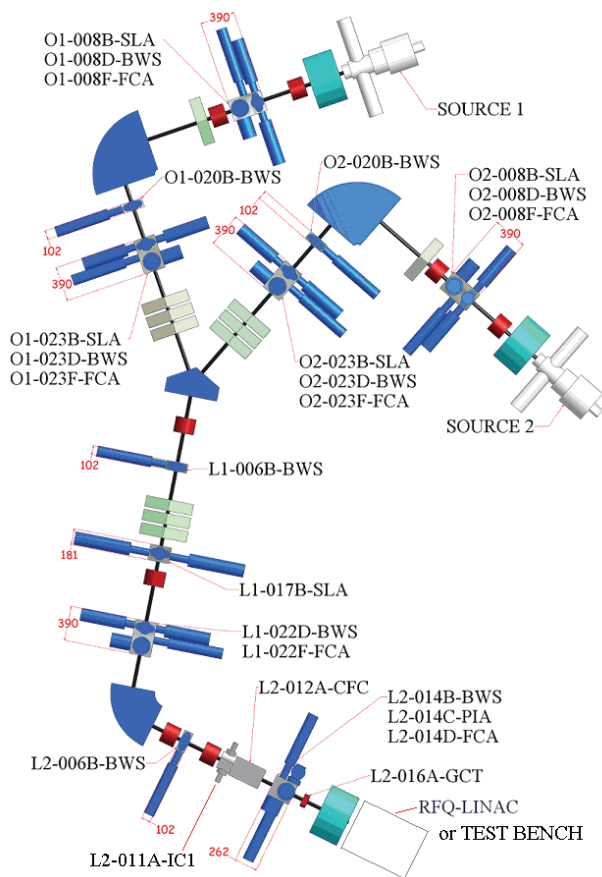


Figure 1: LEBT line layout. Sketch of magnets and beam diagnostics monitors, from the sources to the test bench installed at the end of the LEBT line, during LEBT commissioning, in place of the RFQ. Legend: SLA= Slit monitor, FCA= Faraday Cup monitor, BWS= Wire Scanner, CFC= Chopper Faraday Cup monitor, GCT= AC- Current Transformer, PIA= Wires Harp, IC1= Chopper magnet.

As concerns BD devices, vertical and horizontal wire scanners are used as profile and position monitors. Six Faraday cups and one Chopper Faraday cup measure beam intensity. Sets of four metallic plates, mounted on top, bottom, left and right tank ports, each one driven by a motor, altogether called slit monitor, are used either to suppress beam halo, if plates are positioned at beam border, or to select thin beam slices, in case one plate is positioned close to the opposite one, making a slit. This

last use allows both, phase space distribution measurements if beam profiles are measured behind the slit, and beam profile measurements at slit level, if beam intensity is measured downstream.

As a rule of thumb, two profile monitors (each made of one vertical and one horizontal wire) are installed along each straight sector, at least, in order to permit the measurement of beam profile and barycentre position at the beginning and at the end of the sector, and to determine the trajectory angle, in the vertical and the horizontal plane.

At the end of each straight sector, a beam current intensity monitor is usually installed.

Slit monitors are installed before and after each spectrometer, and a little before the 75°-dipole.

An additional full set of monitors (i.e., horizontal and vertical slit, horizontal and vertical wire scanner and one Faraday cup) was installed in the temporary test bench mounted at the end of the LEBT line, at commissioning time. In this case, a harp monitor, used for chopped beam profile measurements, is installed, too.

A standardization strategy was adopted in order to make monitors production cheaper, their maintenance easier, and to improve more quickly the experience about hardware problems and monitors behaviour. As a consequence of this strategy, a 390 mm long tank was designed [4], able to house four slit plates, one vertical and one horizontal wire scanner and a Faraday cup. Five tanks of this type are mounted along the LEBT line and two others made the temporary test bench installed at the end of the line itself, at commissioning time.

In the case longitudinal space is not a limitation, this tank was installed even if not all the monitors are required, closing down the unused tank ports with blind flanges. In few other cases, if not all the monitors are required and the available space was rather small, a shorter and dedicated tank was designed.

BD MONITORS IN THE LEBT COMMISSIONING

Wire Scanners Monitors

A wire scanner monitor is usually made by one vertical and one horizontal Tungsten wire, with 0.1 mm diameter. Each wire is driven perpendicularly to beam direction, by a brushless motor up to 250 mm/s (100 mm/s, typically). Wire position is measured by means of a linear potentiometer, with about 20 μm accuracy.

Wire scanners (Fig. 2) vacuum-side cables resulted very fragile and they often broke down, during the first period of commissioning. As soon as the problem appeared in all its seriousness, the design was revisited and the broken wires not only repaired, but also improved. Once all the wires have been reviewed, this kind of problem didn't occur any more.

During commissioning, the wire scanner spatial resolution (0.1 mm, nominally) with respect to a fixed-wires device (e.g., a multi-wires chamber) resolution was greatly appreciated. On the other hand, measurements

stressed out the importance of a careful alignment of the wires with respect to the beam reference path, that could be improved at CNAO.

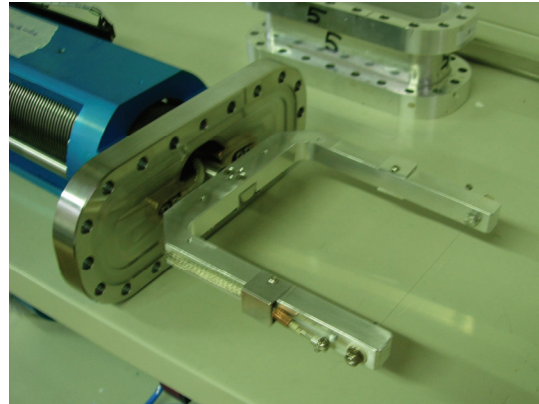


Figure 2: Picture of the Wire Scanner monitor wire, mounted on its fork. Wire fork is screwed to the brushless motor shaft that drives the wire IN /OUT the beam path.

The resolution obtained with the wire scanner was the key-element to allow emittance measurements (Fig. 3), within 150 mm only, namely by using slit and wire scanners housed in the same 390 mm long tank. Of course, a higher resolution in particles divergence measurement is reached behind the switching magnet, where slit (L1-017B-SLA, Fig. 1) and wire scanners (L1-022B-BWS, Fig. 1) are about 1 m away from each other.

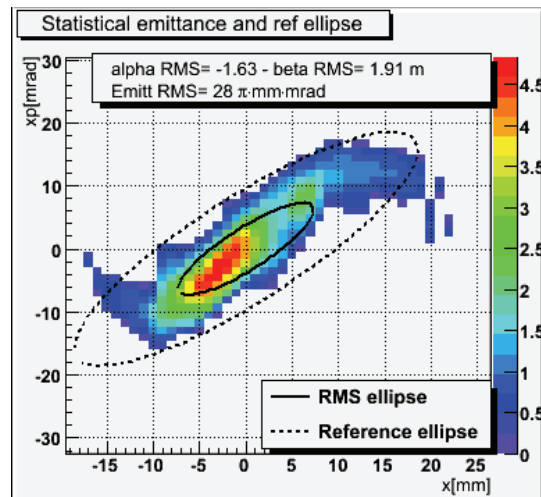


Figure 3: Phase space distribution at the level of O1-023B-SLA monitor, for the vertical plane. The measurement is performed moving the vertical plates from -30 mm to +30 mm, with 1 mm step, and keeping left and right plates at -5 mm and +25 mm, respectively, in order to select H_3^+ peak and stop all the other species. By using statistical emittance definition, we derive the RMS Twiss parameters and emittance value at 1σ . The corresponding ellipse is draft on the plot with full line. The dashed line ellipse is a reference ellipse the user can fix.

Wire scanner heating was tested leaving the wire on the beam spot for a long time. It never exceeded the 300°C temperature, which is far below the tungsten melting point (i.e., 900 °C). On the other hand, if wire temperature changes, its resistance changes, too. Despite that, beam profile measurements are not affected, since the wire scanner amplifier is a trans-conductance amplifier, whose output current does not depend on the wire resistance.

Wire scanner amplifier works from 1 nA to 1 mA, with five different gains (i.e., 10^4 to 10^8 V/A). It has a 400 Hz bandwidth that fully covers the 50 Hz bandwidth of the expected physical phenomena.

Faraday Cup Monitors

Commissioning operations showed up the good quality of the Faraday cup (Fig. 4) CNAO-developed front-end amplifier. It was designed in order to measure DC-beam current and to detect any ripples due to sources or power supplies, up to 15 kHz. It allowed to measure satisfactorily the chopped beam pulse, consequently, making the detector very versatile. Faraday cup amplifier works from 100 nA to 100 mA, with seven different gains (i.e., 10^2 to 10^8 V/A).

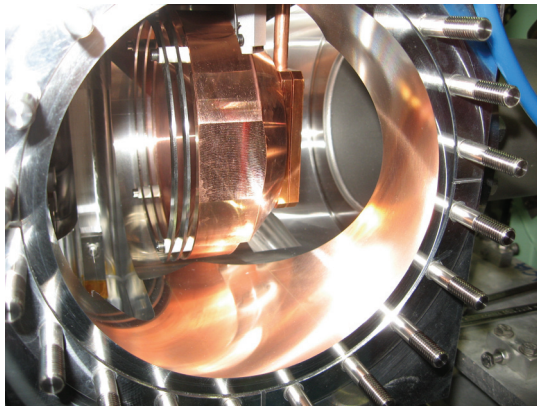


Figure 4: Faraday cup monitor installed on its tank and looked at from a side port (beam should come from the left). One can recognize the Copper cup, from its typical colour. Two stainless steel rings are mounted in front of the cup: the repeller ring (on the left), and the guard ring (on the right).

We could also appreciate the advantage of a large diameter (i.e., 135 mm) cup that can be used as beam stopper, as well, since it closes down the whole beam pipe section. Despite the large diameter, secondary emitted electrons are fully repelled when about -350 V are applied to the repeller ring. Repelling voltage can be set from 0 V to -1 kV.

Faraday cup vacuum-side insulators presented some troubles due to the fact that ions are deposited on them, they become conductive. This accident more often occurred at the Faraday cup monitors just behind the sources, where beam is larger and particles more scattered around the vacuum chamber. A shielding is under design

to protect the insulators from carbon ions and reduce the occurrence of this drawback.

A water-cooling system was designed to avoid overheating of the Faraday cup monitors left on the beam path for a long time, upstream the spectrometers, before ions selection, where the expected beam current was more than 10mA (i.e., about 360 W full beam power). To be conservative, the same cooling system was installed on all the Faraday cups of the LEBT line. It warranted monitors safety even in case they are used as beam stopper for an *infinite* time.

An additional monitor, belonging to the Faraday cup family is the Chopper Faraday Cup (CFC) (Fig. 5). It is installed just downstream the Chopper magnet.



Figure 5: Chopper Faraday cup body, that is the vacuum chamber section just behind the Chopper magnet. Thin metallic tabs are machined on the body itself, in order to enhance heat evacuation by air-convection.

It is an innovative monitor, developed at CNAO, and still under commissioning with beam. It is based on the Faraday cup principle, namely it aims to measure beam intensity by stopping the beam and measuring the collected charge. In fact, the “cup” stopping the beam to be measured is made by the 390 mm long vacuum chamber, installed just downstream the Chopper magnet and insulated from the rest of the LEBT beam pipe. An inner cylinder, opened on the side the beam is deviated towards by the Chopper, is grounded, while the “cup” can be polarized up to 1.25 kV, in order to capture secondary emitted electrons.

Differently from the usual Faraday cup, the CFC can be retained not destructive, since it measures the beam deviated by the Chopper magnet against the vacuum chamber and doesn't intercept the beam entering the RFQ.

Since the beam is deviated against the vacuum chamber by Chopper for 99.99% of the time, the CFC will allow a basically continuous beam current monitoring, without perturbing the beam delivered to the patients.

No water cooling is foreseen for the CFC: air cooling is retained sufficient, for the current intensities expected at the LEBT end. On the other hand, heat evacuation is enhanced by thin metallic tabs, machined all around the vacuum chamber acting as the cup.

Slit Monitors

Each one of the metallic plates (Fig. 6) used as halo suppressor or slit, is driven by a brushless motor up to 250 mm/s (100 mm/s, typically). Its position is measured by means of a potentiometer with about 20 μm accuracy, like for the wire scanner.

Care must be taken in manufacturing the plates with edge-angle borders, in order to avoid cutting the high-divergent particles: it was taken into account during plates design, but it was necessary increasing the angle, at commissioning time.

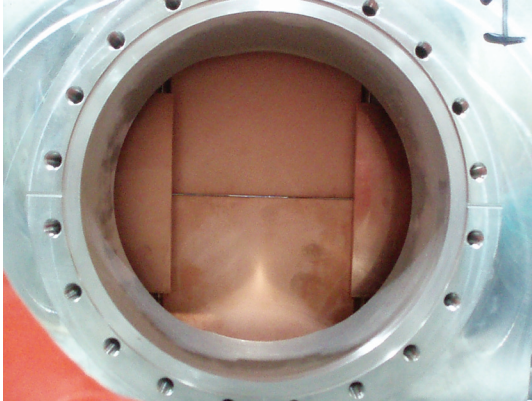


Figure 6: The four Copper plates, making one Slit monitor, installed on their tank. Left and right plates are positioned at beam border; top and bottom plates are making a very thin slit at about tank center.

Measurements (Fig. 7) with polarized (50 V) slit plates cancel the effect of the secondary electrons emitted by the plates hit by the beam, on the particles distribution, as seen by a wire scanner, downstream the slit plates. The effect is visible if the plates are grounded rather than polarized. Repelling voltage can be set from 0 V up to 1 kV.

Slit plates are equipped with the same water cooling system used on the Faraday cup monitors.

Watch-Dog Strategy

After commissioning, when CNAO machine will treat patients for most of the time, measurements perturbing the beam shall be avoided. The opportunity of monitoring beam parameters, without interfering with the beam, guided BD team at the time of monitors choice.

Wire scanners can be used in Watch-Dog mode, positioning a wire at beam spot border and measuring its current. If it suddenly increases or decreases, a warning is delivered to the user, since it could be due either to a beam transverse displacement or to a significant source current variation.

Similarly, slit plates will be used during treatments as beam halo suppressor, positioning the four plates at beam spot border.

Information about beam intensity without affecting the beam delivered to the patients is provided by the Chopper Faraday cup. As already discussed, it can monitor beam

current at the end of the LEBT line and warn the operator in case of significant changes, without intercepting the beam entering the RFQ.

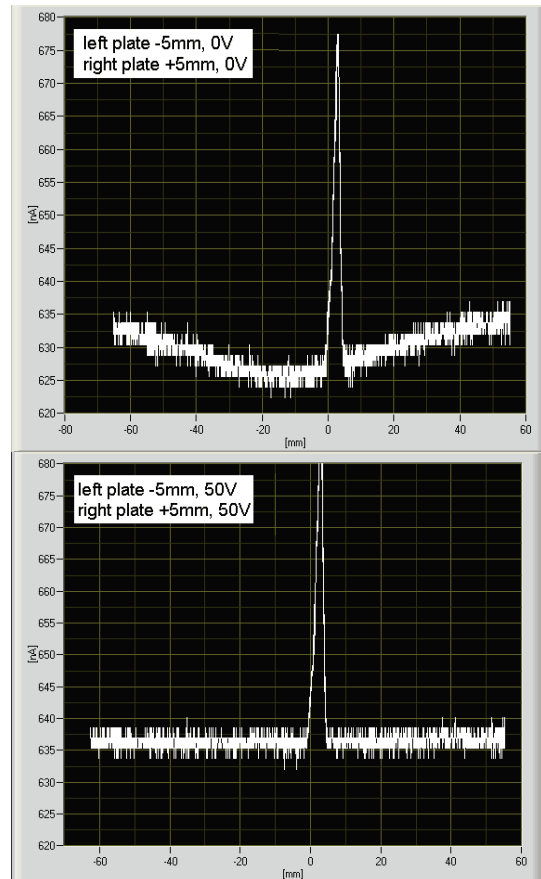


Figure 7: The two pictures show a horizontal beam profile, acquired with the O2-023D-BWS horizontal wire scanner, while upstream left and right slit plates (O2-023B-SLA) are placed at -5 mm and +5 mm, respectively. In the picture on the left, slit plates are grounded and we notice the profile baseline having a deformed shape, like a negative current is induced on the wire at beam peak sides. Secondary electrons produced by the beam impinging on plates border could be responsible for such a negative current. The effect disappears in the right picture, taken while slit plates are polarized at +50 V. Polarized slit plates re-capture their emitted secondary electrons and the wire doesn't detect a negative current at beam border, any more.

CONCLUSIONS

After some hardware wavers due to the innovative designs and the lack of pre-commissioning with beam, monitors installed in the CNAO LEBT line provided reliable and reproducible measurements.

The LEBT line commissioning was surely slowed down by the fact that monitors user's interface debugging was still in progress. On the other hand, the choice of monitor types and their layout along the line resulted well

fulfilling operation needs, in order to reach source and LEBT commissioning goals within 15 weeks.

Complicated mechanical designs were repaid by high-performing devices.

The CNAO-developed electronics comprising high voltage polarization, pneumatic actuator and brushless motor control, and interlock systems management worked successfully. The most deserving aspect surely concerns signals amplification and delivery, since it worked perfectly over a wide dynamic range (6 decades) and bandwidth (DC to 15 kHz for the Faraday cup and DC to 400 Hz for the wire scanner).

REFERENCES

- [1] S.Rossi, "Developments in proton and light-ion therapy", EPAC 2006.
- [2] E.Bressi et al, "Status report on the Centro Nazionale di Adroterapia Oncologica (CNAO)", PAC 2009.
- [3] A.Parravicini et al., "Commissioning of the CNAO LEBT and sources", HIAT 2009.
- [4] J.Bosser et al, "A compact and versatile diagnostic tool for CNAO injection line", EPAC 2008.

NDCX-II, A NEW INDUCTION LINEAR ACCELERATOR FOR WARM DENSE MATTER RESEARCH*

M. Leitner[#], F. Bieniosek, J. Kwan, G. Logan, W. Waldron, LBNL, Berkeley, CA 94720, U.S.A.
J.J. Barnard, A. Friedman, B. Sharp, LLNL, Livermore, CA 94550, U.S.A.
E. Gilson, R. Davidson, PPPL, Princeton, NJ 08543, U.S.A.

Abstract

The Heavy Ion Fusion Science Virtual National Laboratory (HIFS-VNL), a collaboration between Lawrence Berkeley National Laboratory (LBNL), Lawrence Livermore National Laboratory (LLNL), and Princeton Plasma Physics Laboratory (PPPL), is currently constructing a new induction linear accelerator, called Neutralized Drift Compression eXperiment NDCX-II. The accelerator design makes effective use of existing components from LLNL's decommissioned Advanced Test Accelerator (ATA), especially induction cells and Blumlein voltage sources that have been transferred to LBNL. We have developed an aggressive acceleration "schedule" that compresses the emitted ion pulse from 500 ns to 1 ns in just 15 meters. In the nominal design concept, 30 nC of Li^+ are accelerated to 3.5 MeV and allowed to drift-compress to a peak current of about 30 A. That beam will be utilized for warm dense matter experiments investigating the interaction of ion beams with matter at high temperature and pressure. Construction of the accelerator will be complete within a period of approximately two and a half years and will provide a worldwide unique opportunity for ion-driven warm dense matter experiments as well as research related to novel beam manipulations for heavy ion fusion drivers.

INTRODUCTION

Warm Dense Matter (WDM) Research

A US National Task Force [1] has identified exploration of fundamental properties of "warm dense matter" (WDM) as a major, future research area. Warm dense matter consists of extreme states of matter that are neither in a "cold, condensed-matter" state, nor in a "hot, plasma" state, but rather somewhere intermediate. Warm dense matter is typically a strongly-coupled, many-body charged particle system with energy density exceeding 10^{10} J/m^3 , conditions that are extremely difficult to study analytically and by numerical simulation. However, many astrophysical systems as well as common laboratory experimental conditions, where plasma is created quickly from a solid, fall into this regime. Because of the short timescales involved, attempts to isolate warm dense matter for study have proven to be a major challenge.

The U.S. Heavy Ion Fusion Science Virtual National Laboratory (HIFS-VNL) is currently developing an ion-

accelerator based driver system, including fast diagnostics, to experimentally probe WDM equations of state. In simplest terms, an equation of state attempts to describe the relationship between temperature, pressure, density, and internal energy for a given substance or mixture of substances. The HIFS-VNL plans experiments with targets in the density range between 10^{21} to 10^{23} ions/cm³ (solid aluminum density: $6 \cdot 10^{22}$ atoms/cm³) around a temperatures of 1 eV (11,000 K).

Heavy Ion-Driven WDM Research

Heavy ion beams have a number of advantages as drivers for warm dense matter experiments. First, heavy ions have a range exceeding the mean free path of thermal x-rays, so that they can penetrate and deposit most of their energy deep inside the targets. Second, the range of heavy ion beams in dense plasma targets is determined primarily by Coulomb collisions with the target electrons. The rate of energy loss in the target, dE/dx , is dependent on the energy of the incoming projectile and displays a pronounced peak, which occurs at higher energies for higher (atomic number) Z projectiles.

These properties make heavy ions an excellent candidate for warm dense matter physics studies, where thin (μm) target plasmas could be uniformly heated by locating the energy deposition peak ("Bragg peak") near the target center (see reference [2] for a more detailed description). To achieve the most uniform target heating volume (in contrast to non-uniform heating with laser or X-ray heating) the main strategy is to pick a target thickness and beam energy such that the ion beam enters the target slightly above ($\sim 1.5 E_{\text{peak}}$) the energy of maximum dE/dx , deposits most of its energy inside the thin target foil, and exits the target slightly below the dE/dx peak at $\sim 0.5 E_{\text{peak}}$. From an accelerator standpoint, the most cost-effective way of heating targets at the Bragg peak is to use lighter ion projectiles (e.g. Li^+) on low-mass target foils (e.g. aluminum) where the maximum dE/dx occurs at rather low energies. For NDCX-II, a combination of a Li^+ ion beam and an Aluminum target foil, the Bragg peak is located at 1.8 MeV, and the ion range is $\sim 5 \mu\text{m}$.

In summary, the advantages of such a low-range ion heating approach ("Bragg heating") are:

- The target is heated isochorically (uniformly).
- By placing the center of the target foil at the Bragg peak the heating uniformity is maximized and the accelerator beam energy is used most efficiently.
- Bragg heating requires low energy ($\sim \text{MeV}$) and thus much smaller accelerators.

* This work was supported by the U.S. Department of Energy under Contract No. DE-AC02-05CH11231.

[#]MLeitner@lbl.gov

However, this approach introduces also quite unique accelerator design challenges in different areas:

- Because of the low ion range, very thin targets are required ($\sim 3\text{-}5\ \mu\text{m}$ aluminium foil for NDCX-II).
- In order to reach sufficient energy densities, the target has to be heated fast enough compared to the hydro-expansion time of the target which is in the nanosecond range for micron thick foils. This requires accelerator technology, where $>30\ \text{A}$ of beam current has to be compressed to approx. $1\ \text{ns}$ ($\sim 1\ \text{cm}$ at approx. $3\ \text{MeV}$) long and $1\ \text{mm}$ diameter beam bunches.
- To reach $1\ \text{eV}$ target temperature, sufficient beam power (fluence $\sim 30\ \text{J}/\text{cm}^2$) is required. Because of the low-energy Bragg peak ($1.5\ \text{MeV}$), significant beam charge ($\sim 30\ \text{nC}$) has to be delivered on target. This is not possible without the HIFS-VNL invention of neutralized drift compression [3], where an ion beam is focused longitudinally within a space-charge neutralizing plasma channel and ultimately compressed radially by an $8\ \text{T}$ final focus solenoid within a high-density neutralizing plasma environment.

NDCX-I

Over the last few years the first phase of the Neutralized Drift Compression Experiment (NDCX-I, [3]), currently operating at LBNL, has successfully demonstrated simultaneous radial and longitudinal compression using the technique of imparting a velocity ramp on the ion beam, letting the beam drift through a

volumetric neutralizing plasma to offset space-charge forces, and applying a high solenoidal field before the target. To provide sufficient energy deposition over a time period less than the hydrodynamic expansion time, the neutralized drift compression technique has been developed to produce $\sim 1\ \text{ns}$, $\sim 1\ \text{mm}$ diameter beams from longer (μsec) beams with modest ($\sim 300\ \text{keV}$) energy. Experiments involving heating metal foils have begun on NDCX-I. The goal of the first phase of the experiment was to demonstrate the concept of using simultaneous neutralized drift compression in transverse and longitudinal direction. However, the goal of the second phase (NDCX-II) of the experiment is now to get uniform and efficient energy deposition for interesting WDM target experiments. For this purpose, Bragg peak heating will be employed at the center of planar targets in NDCX-II. To achieve the required higher target temperatures, higher ion energies and currents compared to the current NDCX-I will be necessary.

BASELINE DESIGN OF NDCX-II

Fig. 1 shows schematically the main components of NDCX-II [4], and table 1 summarizes the main parameters of this new accelerator facility. A short-pulse injector ($100\ \text{mA}$, $\sim 500\ \text{ns}$ pulse width) provides approx. $30\ \text{nC}$ of Li^+ ions. The ion beam has to be accelerated to approximately $3.5\ \text{MeV}$ by using an induction linear accelerator. In simplest terms, an induction cell is similar to a 1:1 transformer with ferrite material (to minimize losses because of the short pulse lengths involved) as transformer core. In the case of NDCX-II, a $200\ \text{kV}$

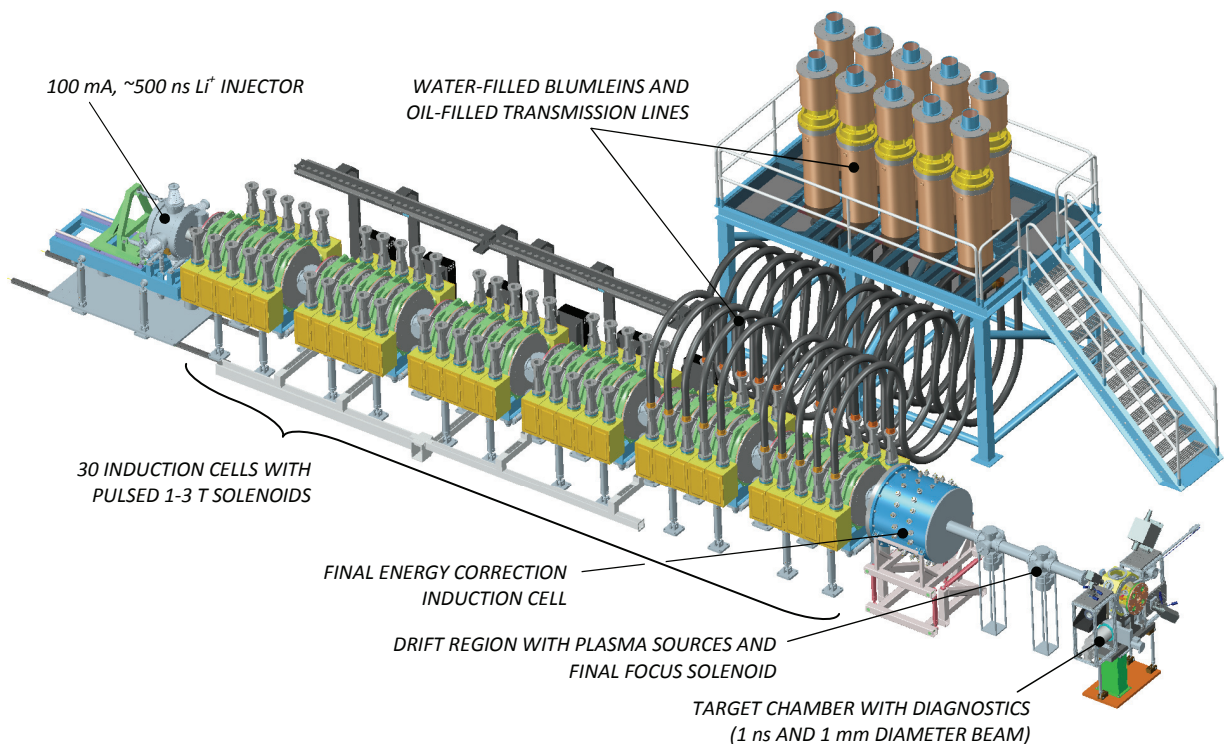


Figure 1: Schematic layout of the new NDCX-II facility. The accelerator is approx. 15 m long.

primary high voltage pulse is timed with the accelerating ion beam to develop the same high voltage across an insulating gap inside the accelerator beam pipe. Because of the short pulse length of the NDCX-II induction cell (70 ns), thousands of Amperes flow through the primary circuit of the induction core to develop the voltage. This requires substantial pulsed-power engineering, a specialty field in accelerator technology. Because of the high current flow, on the other hand, the induction cell is fairly insensitive to any beam loading, allowing to accelerate kilo-Amperes of beam. This is the primary advantage of induction accelerators compared to RF linacs. As with all linear accelerators the outside of the induction accelerator structure stays at ground potential.

Table 1: NDCX-I and NDCX-II Parameters

	Ion	Ion Energy [MeV]	Focal Diameter [mm]	Pulse Length [ns]	Peak Current [A]
NDCX-I	K ⁺	0.35	~2	2-4	~2
NDCX-II	Li ⁺	3.5	1	1	~30

As described in more detail further below, NDCX-II will rapidly compress the ion beam in longitudinal direction resulting in the transport of a high line-charge density ion beam at low energy. Magnetic solenoids have been chosen for the accelerator transverse focusing since they are efficient in transporting high beam currents at low energy. For NDCX-II, each accelerator cell requires a < 2 T pulsed solenoid for beam focusing.

A singly charged lithium beam has been chosen based on its modest Bragg peak energy of 1.8 MeV and existing expertise in fabricating alkali metal doped aluminosilicate ion sources. To get the total required charge of 30 nC from realistic Li⁺ ion sources and assuming a reasonable current density, the pulse at the injector is approx 500 ns. However, the original ATA pulsed power system to drive the induction cells was built for a 70 ns cell pulse. To make the most efficient use of the available hardware, the NDCX-II design implements an aggressive compression schedule to match the beam to this time structure of 70 ns or less as soon as possible [5]. The volt-seconds of the induction cells can then be used at the maximum acceleration gradient. The maximum repetition rate is limited by the charging power supplies and the pulsed transport solenoid cooling. The goal is to be capable of running at 0.2-1 Hz. In addition to the acceleration to 3.5 MeV, there is also an imparted velocity tilt in preparation for the longitudinal compression in the neutralized drift region.

A 50 kV ion source test stand (STS-50) at LBNL is being used to develop the capability of producing and/or characterizing the Li⁺ aluminosilicate ion sources. The preliminary injector design requires a 4-5 cm diameter ion source which can produce 1-2 mA/cm² current density.

In addition, a dedicated test stand has been built to evaluate the refurbished and modified ATA pulsed power

Linacs

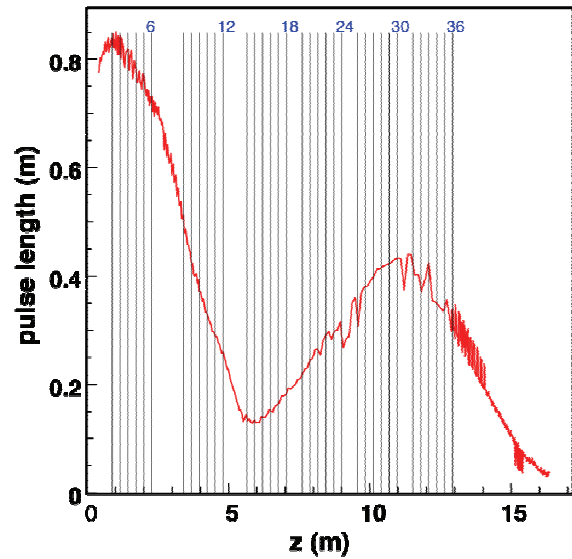


Figure 2: Beam pulse length evolution along the NDCX-II beamline. The unique, rapid beam compression in the first part of the accelerator, followed by a re-bounce and the final compression through the neutralizing section can be seen clearly. See text for a more detailed description.

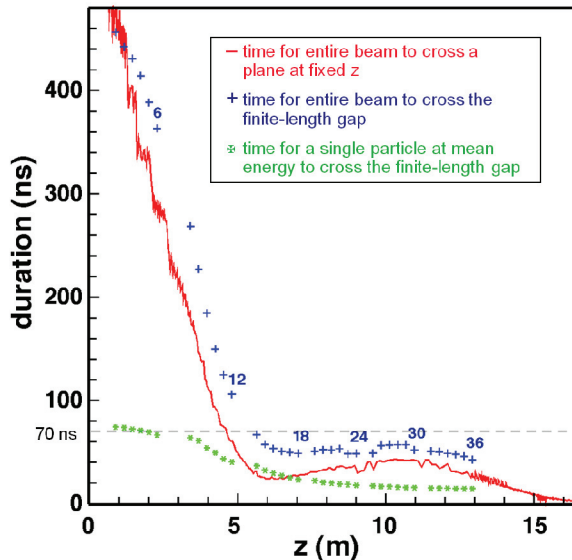


Figure 3: Beam pulse duration along the NDCX-II beamline. In the first part of NDCX-II the beam is compressed to fit within 70 ns, which corresponds to the pulse length of the main ATA acceleration cells. The beam is ultimately compressed to 1 ns on target.

and induction cell hardware. The refurbishing activities include disassembling the hardware, cleaning the parts, replacing seals and insulators, and reassembling. Since the ATA cells were originally used for the acceleration of an electron beam, the magnetic field strength of the focusing elements in the cells need to be upgraded from 3 kG DC solenoids to 2 T pulsed solenoids. This high pulsed magnetic field is a concern for the project as it may saturate some of the induction cell ferrites and reduce the available volt-seconds. An important task to be completed using the test stand will be to quantify the

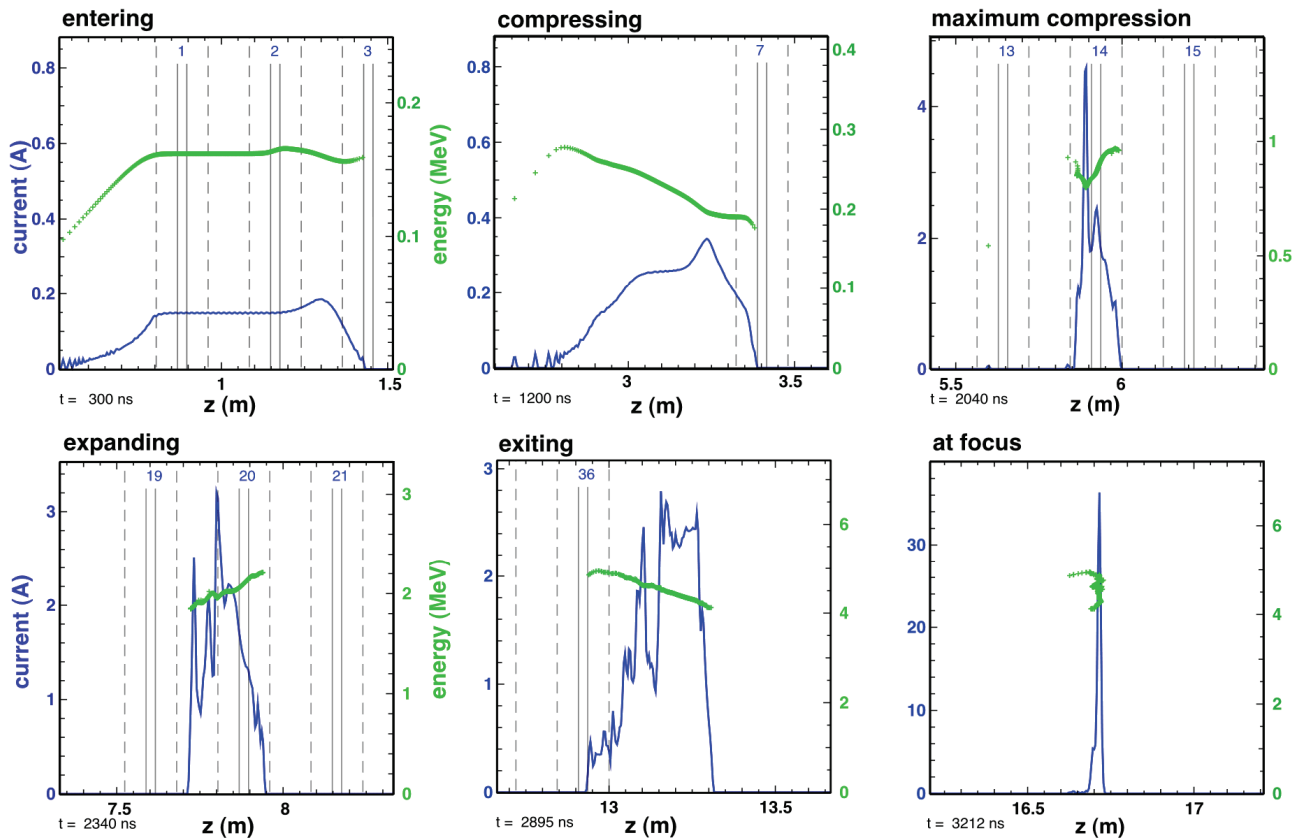


Figure 4: Evolution of the beam phase space and line-charge-density profile along NDCX-II. The second and third panels on the top illustrate the initial beam compression with subsequent beam expansion in the accelerator (panel 1 on bottom). At the exit of the accelerator (panel 2 on the bottom) the beam exhibits a superimposed velocity tilt which compresses the beam to the final pulse length on target of 1 ns with greater than 30 A peak current.

interaction between the high field pulsed solenoid and the ferrite cores, to verify voltage waveform tuning flexibility, and to characterize voltage holding and timing jitter.

In parallel, ongoing experimental tests on the existing NDCX-I include commissioning fast diagnostics, optimizing beam and target alignment methods, exploring techniques to increase the deposited energy density on target, and heating metal foil targets. Because NDCX-II will be able to provide up to 100 times greater energy deposition on target, a wider range of WDM equation of state experiments will be possible [6]. These experiments will concentrate on studying two-phase dynamics in metals, and identifying critical points and the liquid-vapor transition at temperatures near the critical point. Studies of the properties of high electron affinity targets and the behavior of porous targets are also planned.

ELEMENTS OF THE NDCX-II DESIGN

The arrangement of induction cells and applied accelerating waveforms for NDCX-II is novel, but the system is based on well-established technologies. It takes full advantage of available ATA induction cells and Blumlein high voltage pulsers. The system is compact, and relies heavily on passive circuit elements to provide the requisite waveform shaping. The adaptation from

ATA, which accelerated electrons is challenging, because of the need to aggressively compress the ion pulse from its initial ~ 500 ns duration to ~ 1 ns, as required for the WDM physics mission. The applied waveforms must simultaneously impose a head-to-tail velocity tilt, compensate for the beam space charge, and accelerate the beam. Using a 1-D particle-in-cell simulation code designed for this purpose, we developed an acceleration schedule employing thirty ATA cells (twenty driven by the ATA Blumleins, plus ten driven with special designed lower-voltage pulsed sources). To reduce the axial extent of the gap fringe fields, the 6.7 cm radius of the ATA beam pipe is reduced to 4.0 cm. This system accelerates a Li^+ beam (100 keV as injected, with a 67 mA flat-top) to 3.5 MeV at ~ 2 A, and imparts an 8% tilt. The beam then drifts for approximately 2 m through a neutralizing plasma channel (“neutralized drift compression”) until the 30 nC of beam are longitudinally compressed to less than 1 ns. The current of the compressed beam (averaged over that 1 ns window) is ~ 23 A, with a peak (averaged over a 0.1 ns window) of ~ 32 A, and a full-width at half maximum of ~ 1 ns.

A novel two-part strategy is employed to accelerate and compress the beam. In (roughly) the first half of the lattice, the pulse is rapidly compressed via “non-neutral drift compression.” The beam transit time through an

acceleration gap (including its axially extended fringe field) must be less than 70 ns for a high-voltage (up to ~200 kV) ATA Blumlein to be used as the pulser. Custom pulsers at lower voltage are required for longer pulses; to minimize the number of these, we use the volt-seconds of the first two cell blocks to impose a velocity tilt, with space between tilt cells for drift compression and longitudinal control. In the second half of the lattice, the beam is allowed to lengthen as it is accelerated, with only enough ramped pulses added to keep the duration under 70 ns. The initial compression is slowed by the increasing space-charge field; after the beam passes through a longitudinal waist, it begins to lengthen as a consequence of acceleration and space charge. Since the beam at the waist is shorter than the longitudinal extent of the gap fields, those fields cannot prevent this “bounce;” however, as the length increases, tilt cells can keep the beam duration from exceeding 70 ns. We find that two tilt cells in each block of five suffice. The modularity of these blocks is an attractive feature, since more can be added if a higher final kinetic energy is desired. A final block with five ramped pulses applies the tilt for neutralized drift compression onto the target; this is another attractive feature, since no high-voltage “tilt core” is required. Fig. 2 shows the evolution of the beam length, while Fig. 3 shows the evolution of the pulse duration. Fig. 4 shows the evolution of the beam phase space and line-charge-density profile; its final panel shows the beam when its centroid is at the “best longitudinal focus” plane.

BUDGET AND SCHEDULE

The construction of the accelerator is expected to be completed by October 2011. The estimated cost of constructing NDCX-II is 11 M\$. Re-using existing ATA hardware results in cost savings of approximately 10 M\$. This project is a pre-requisite for the Integrated Beam-High Energy Density Physics Experiment (IB-HEDPX), for which DOE has approved Critical Decision Zero (CD-0). IB-HEDPX would be a larger-scale user facility for heavy ion driven high energy density physics and IFE target physics in the future.

REFERENCES

- [1] National Task Force on High Energy Density Physics, “Frontiers for Discovery in High Energy Density Physics (Frontiers for Discovery in HEDP)”, Office of Science and Technology Policy, Washington DC, 2004.
- [2] L.R. Grisham, *Phys. of Plasmas* 11(2004), 5727
- [3] P.K. Roy, et al, *Phys. Rev. Lett.* 95 (2005), 234801
- [4] W.L. Waldron, et al., *Proc. of the 18th Topical Meeting on the Technology of Fusion Energy*, San Francisco, CA, Sept 28 to Oct 2, 2008, to be published in *Fusion Science and Technology*
- [5] A. Friedman, et al., *Nucl. Instr. And Meth. A* (2009), in print, <http://dx.doi.org/10.1016/j.nima.2009.03.189>
- [6] J.J. Barnard, et al., *Nucl. Instr. And Meth. A* (2009), in print, <http://dx.doi.org/10.1016/j.nima.2009.03.221>

DECELERATING HEAVY ION BEAMS USING THE ISAC DTL

M. Marchetto, R.E. Laxdal, Fang Yan TRIUMF, Vancouver, BC V6T2A3, Canada

Abstract

At the ISAC facility in TRIUMF radioactive ion beams (RIB) are produced using the ISOL method and post accelerated. The post accelerator chain consists of a radio frequency quadrupole (RFQ) injector followed by a drift tube linac (DTL) that accelerates the ions from 150 keV/u up to 1.8 MeV/u. A further stage of acceleration is achieved using a superconducting linac where the beam is injected using the DTL and the energy boosted with 20 MV of acceleration voltage (increased to 40 MV by the end of 2009). The possibility of decelerating the beam maintaining good beam quality using the DTL is investigated based on experimenters request to reach energies lower than 150 keV/u. The beam dynamics simulation using the LANA code are compared with on line measurements. In this paper we will report the results of the investigation that aims to establish the lowest energy we can deliver in the post accelerator section of the ISAC facility.

INTRODUCTION

ISAC is the TRIUMF facility (Fig. 1) to produce, mass select and post accelerate radioactive ion beams (RIB). The radioactive species are produced using the ISOL method.

The driver of the facility is the TRIUMF cyclotron that accelerates H^- up to 500 MeV. The electrons are then stripped from the hydrogen ions by means of a stripping foil and the protons extracted. In the present configuration the cyclotron has three operating extraction beam lines (with the possibility of recommissioning a fourth existing one). Each beam line is characterized by different energies and beam intensities. In ISAC beam line they are extracted at the maximum energy up to 100 μA making the ISAC the highest power driver beam (50 kW).

The proton beam is then directed to one of the two underground target stations. The beam loses part of its energy through the target material while producing the radioactive isotopes in a neutral state. These isotopes migrate into the source where they are ionized and extracted up to 60 kV towards the mass separator. The selected isotope charged 1+ can be sent through a charge state booster (CSB) to increase the charge state.

The radioactive beam is eventually transported at ground level where it can be directed to a low energy area or to the post accelerators. In the low energy are the experiments use the beam at source potential up to 60 kV. In the medium and high energy area the energies range typically between 150 and 5 MeV/u (the upper limit being restricted at present by license).

The goal of this paper is to investigate the feasibility of delivering beam with energies lower than 150 keV/u, this

Linacs

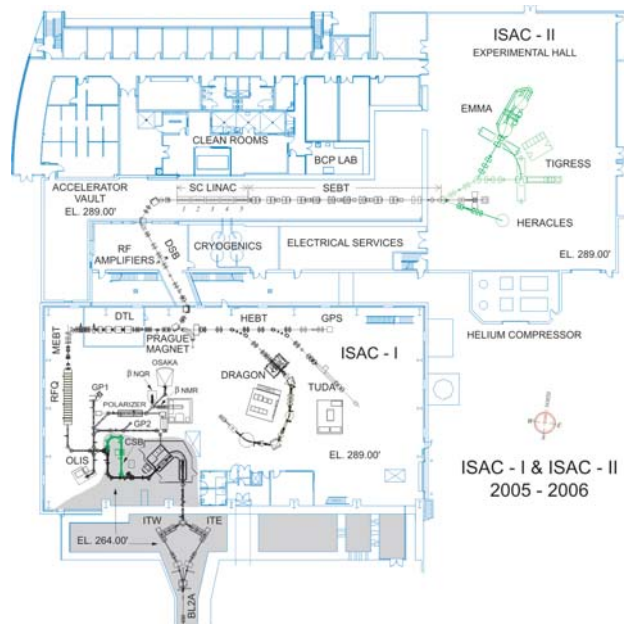


Figure 1: Overview of the ISAC facility at TRIUMF. The ISAC II linac is superconducting while in ISAC I they (RFQ and DTL) are normal conducting.

is mostly dictated by the request of TRIUMF experimentalists to have energies (in the post acceleration section) ideally as low as 100 keV/u. The result of this investigation sets the lowest limit for deliverable energies in the post acceleration section of ISAC facility.

THE POST ACCELERATORS

The post accelerator chain of the ISAC-I facility is composed of two room temperature linacs: a radio frequency quadrupole (RFQ) acting as injector for a drift tube linac (DTL). These two machines serve the medium energy experimental hall. In the ISAC-II facility the beam energy is boosted by a superconducting (SC) linac. This machine serve the high energy experimental hall.

The Radio Frequency Quadrupole

The RFQ has a nineteen split rings structure that support the four 7.6 m long electrodes [1]. It operates in continuous wave (CW) mode at a resonance frequency of 35.36 MHz. The beam is accelerated from 2 keV/u to 150 keV/u. Based on the available voltage (up to 74 kV) the RFQ is capable of accelerating isotopes with mass to charge ratio $3 \leq A/Q \leq 30$.

In order to obtain good longitudinal emittance after the

RFQ [2] the beam is prebunched at the entrance by means of an electric three harmonics buncher (Prebuncher) located ~ 5.5 m upstream of the RFQ entrance port. The fundamental harmonic of the prebuncher is 11.78 MHz. For the same purpose a percentage between 75-80% of the accelerated beam is transported downstream of the RFQ while the rest (tails of the longitudinal phase space) is dumped into fixed slits at the exit port of the machine.

The Drift Tube Linac

The DTL (see Figure 2) represents the second stage of acceleration in ISAC-I. This linac is composed of five accelerating modules (tanks); downstream of each one of the first three tanks there is a buncher. This layout [3] allows to accelerate all the energy between 150 keV/u and 1.8 MeV/u with a good beam quality.

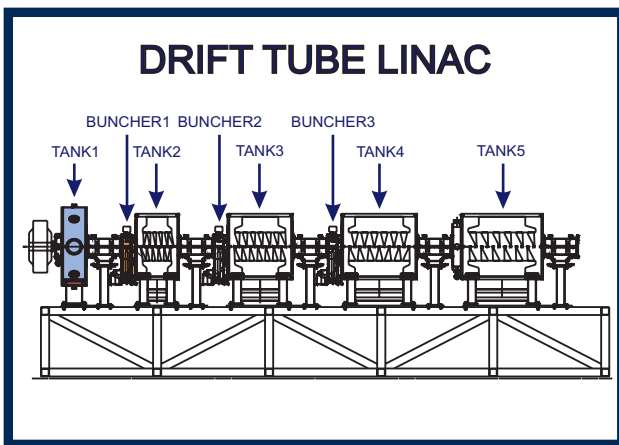


Figure 2: Side view of the ISAC DTL.

The DTL has an IH interdigital RF structure that resonates at 106.08 MHz. A triplet of quadrupoles is situated between tanks; these are necessary to maintain the transverse profile of the beam inside the 1.8 cm aperture of the drift tube.

The DTL design is optimized for mass to charge ratio $2 \leq A/Q \leq 6$. A stripping foil is present in the medium energy beam transport (MEBT) line that connects the RFQ to the DTL. The foil increases the charge state of the beam reducing the mass to charge ratio to a value inside the acceptance of the DTL. In order to minimize the transverse and longitudinal emittance growth during the stripping we focus transversally and bunch the beam in time at the foil location. The beam is also rebunched at the entrance of the DTL using a 35.36 MHz buncher (Rebuncher). Usually transmissions higher than 95% are achievable through the machine.

The DTL also inject the beam in the ISAC-II superconducting linac; in this case the beam is accelerated at 1.5 MeV/u.

Linacs

The Superconducting Linac

The third stage of acceleration is achieved with the ISAC-II superconducting (SC) linac [4]. The present installation of the SC linac is composed of five cryomodules each housing four superconducting bulk niobium quarter wave resonators (cavities) and one superconducting solenoid. These cavities resonate at 106.08 MHz. The cavity voltages are set to operate each at a fixed cryogenic power of 7 W, for a total of ~ 20 MV of acceleration. The twenty cavities are independently phased at -25° synchronous phase. The number of cavities turned on determines the final energy.

The ISAC II linac is going to be upgraded by the end of 2009 adding twenty more cavities housed in three cryomodules [5]. The new cavities have a resonant frequency of 141.44 MHz.

LANA SIMULATIONS

The ISAC DTL beam dynamics is designed using the LANA code [6]. In all DTL development studies this code is demonstrated to model quite accurately the machine [7]. In Figure 3 both the simulated and measured energy gain versus RF phase curve for DTL tank 1 are plotted.

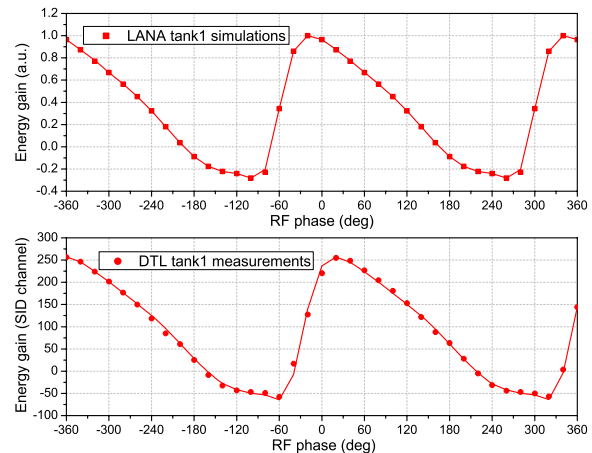


Figure 3: Simulated (top) and measured (bottom) energy gain versus RF phase curve.

Preliminary simulations show that a reasonable deceleration is possible using the first three tanks and two bunchers. In this simulation we use a longitudinal emittance of 1π keV/u·ns. This value differs from the design emittance being 1.5π keV/u·ns. The new value comes from an estimate done during a previous development run. The particle used in the simulation has an $A/Q=6$. The initial beam distribution, both transverse and longitudinal, is the same used in acceleration run.

The goal of the simulations is to check quality of the beam after deceleration. The operating voltage as well as the synchronous phase are used as free parameters to find

the optimum solution in term of maximum deceleration and minimum disruption of the longitudinal phase space (tails formation).

Since the DTL drifts are designed for an increasing beta it is necessary to verify which voltage gives more deceleration. Simulations show that the maximum deceleration happens at the maximum voltage. The acceleration rate is indeed very modest (see Table 1). In Figure 3 are plotted the Tank1 energy gain curves for different amplitude of the accelerating voltage. The amplitudes are given in term of the nominal voltage; the value 1 being the operational voltage that is used normally to accelerate a certain A/Q. This voltage scaled with the A/Q in order to reach always the final energy in term of keV/u. For reference the final maximum energy of Tank1 is 237 keV/u.

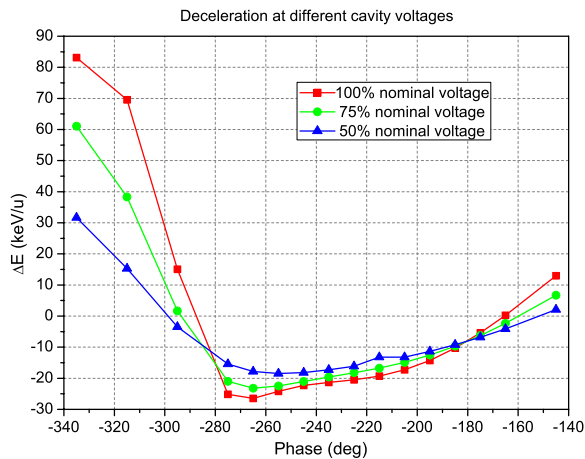


Figure 4: Energy gain versus RF phase curves for different nominal voltage amplitudes of DTL Tank1. The maximum deceleration happens using the maximum voltage.

The RF phases are set close (20° to 40°) to the decelerating peak for the tanks while the bunchers (1 and 2) are phased at -90° (bunching phase). It's evident from the Tank1 curves (Figure 3) that in the DTL case the fitting is more complex than a simple cosine function and the crest to valley distance is greater than 180° . As consequence even at 40° far from the peak the energy gain is still more the 90% with respect to the peak.

The simulations also show that at low energy some beam losses of the order of 10% are expected in the transverse plane. The possibility of reducing or minimizing such losses requires further studies varying the initial matching into the DTL. These studies are not object of this paper.

ON LINE MEASUREMENT

The on line deceleration measurements are done using $^{18}\text{O}^{4+}$ beam ($A/Q=4.5$). The beam energy profile and centroid (beam energy) are measured using a 90° analyzing magnet (PRAGUE magnet) located downstream of the

Linacs

DTL. This magnet is also used to phase this linac [7]. A second diagnostic consisting of a silicon detector (SID) is present downstream of the DTL; this gives information about energy and time structure of the accelerated beam. This can also be used to phase the linac.

The DTL is phased for deceleration following the LANA simulations using the PRAGUE magnet. The tank amplitudes are set to the same maximum value (nominal voltage) used for full acceleration of the same species ($A/Q=4.5$). The tanks are phase closed to the negative peak to maximize deceleration and minimize energy spread. The buncher amplitudes are set to 50% of the nominal voltage while they are phased in pure bunching mode (-90° synchronous phase).

The main result is that the deceleration is possible in the amount predicted by the simulations. In Table 1 the final simulated and measured (at the PRAGUE magnet) energies after each DTL RF device are listed.

Table 1: Final energies after each DTL RF device; the injection energy into the DTL is 150 keV/u.

DTL RF device	Simulated energy (keV/u)	Measured energy (keV/u)
Tank1	129	127.7±1
Buncher1	129	127.7±1
tank2	121	124±1
Buncher2	121	124±1
Tank3	115	117±1

Fig. 3 represents the final energy as measured at the PRAGUE magnet; the energy spread is in line with respect to what we typically deliver at such low energy.

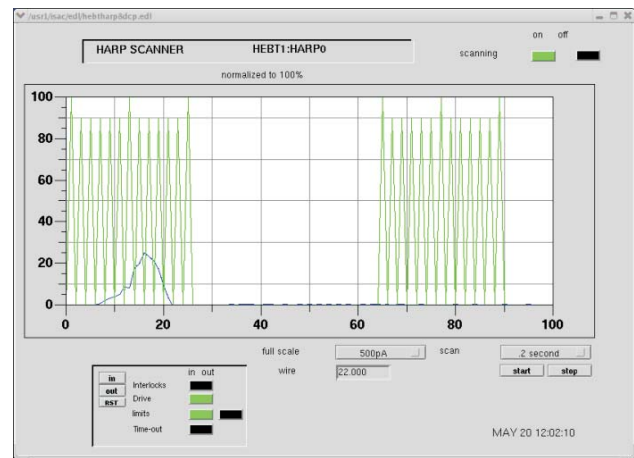


Figure 5: Simulated (top) and measured (bottom) energy gain versus RF phase curves for DTL Tank1.

Fig. 6 represents the time structure after DTL tank1 at the SID location (9.1 m downstream of tank1). The ISAC-I facility has two bunchers in the high energy beam transport (HEBT) line between the DTL and the ISAC-I experimen-

tal stations. One buncher operates at 11.78 MHz, the other at 35.36 MHz. These two bunchers (operating inside different velocity range) are normally used to compress the time (or the energy) down to 1 ns at the experiment. In the deceleration case, though, the beam is debunched so much that the phase spread at these buncher location is (in the best case) more than 100° for the lower frequency buncher. The HEBT bunchers can not be used with such a phase spread without forming tails in the longitudinal phase space. In term of time spread the beam is ~ 30 ns wide at the HEBT bunchers location; this time spread more or less doubles at any ISAC-I experimental station. Considering the beam bunches are spaced ~ 86 ns, it means that the beam is almost continuous at any ISAC-I experiment.

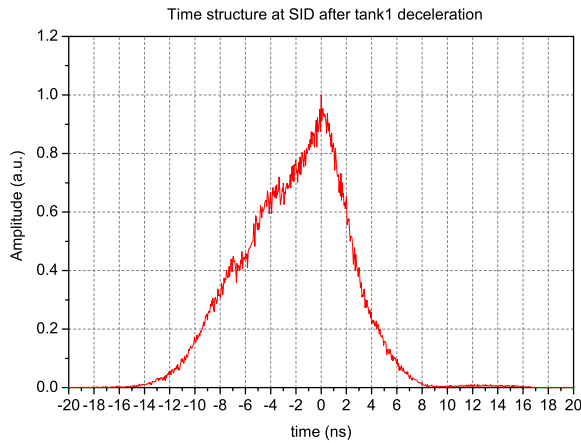


Figure 6: Time structure after DTL tank1.

SIMULATIONS VERSUS ON LINE MEASUREMENTS

Besides the final energy it is interesting to look at the energy and time spread after each DTL element and to compare them with the simulated value.

Table 2: Injection parameters used in the LANA simulations for different initial longitudinal emittances. The lower emittance simulation matches the measured values for time and energy spread.

ε_z (keV/u·ns)	α_z	β_z (ns/(keV/u))	ΔE (%)	ΔT (ns)
1	-0.2	0.053	± 3	± 0.23
0.35	-0.2	0.085	± 1.38	± 0.17

Fig. 7 and Figure 8 represent respectively the plot of the energy and the time spread versus each RF device. The measured energy spread is on average 45% of the simulated when using a longitudinal emittance of 1π keV/u·ns. The

Linacs

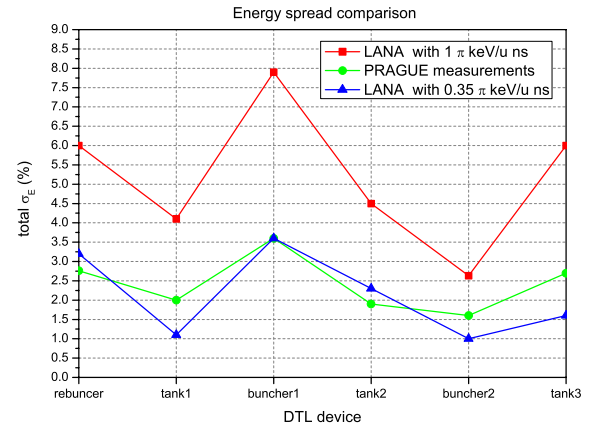


Figure 7: Simulated and measured energy spread after each DTL RF devices: the simulated data are for two different longitudinal emittances. The measured energy spread is as measured at the PRAGUE magnet.

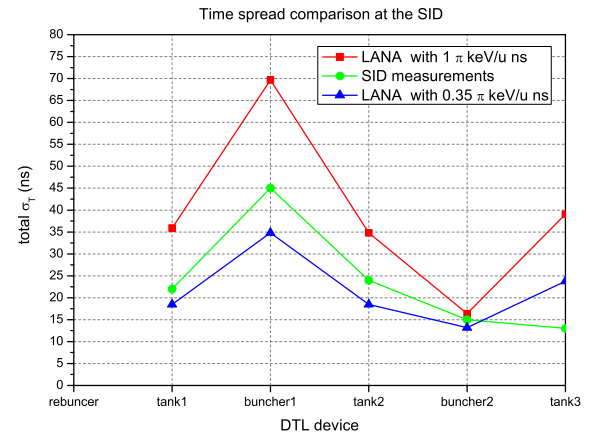


Figure 8: Simulated and measured time spread: in all cases the reported time spread is at the SID location.

measured time spread is on average 75% of the simulated when using the longitudinal emittance as above.

These lower values suggest the emittance of the real beam is smaller than 1π keV/u·ns. The asymmetry of the percentages can be interpreted as a different match in the longitudinal plane with respect to the simulations.

The results from a new set of simulations with a lower emittance match in a better way the measured energy and time spread (see Fig. 7 and Fig. 8). In this new simulations the longitudinal emittance and the Courant-Snyder parameter β are changed in order to reduce the energy and time spread respectively to $\sim 45\%$ and $\sim 75\%$ of the original value. In Table 2 the injection parameters for the two longitudinal emittances are listed.

The quality of the longitudinal emittance is determined

by the Prebuncher setting, the focusing of the beam at the stripping foil location and the stripping foil itself. Different longitudinal emittances inside some range are possible based on the different tuning configuration. This aspect requires further investigation.

CONCLUSION

The deceleration of the beam using the ISAC DTL is possible from 150 keV/u to 117 keV/u. The energy spread after deceleration is in line with the one reached for low energy accelerated beam. The time spread after deceleration is such that the beam has practically no time structure (continuous beam) at any ISAC-I experimental stations. The development leaves two open questions that need further investigation. The first issue is regarding the transmission through the DTL at such low energy. A better matching at injection can minimize the beam loss. The second issue is related to the size of the longitudinal emittance that seems to vary based on the quality of acceleration through the RFQ and the interaction with the stripping foil.

REFERENCES

- [1] R.E. Laxdal, "Beam Test Results with the ISAC 35 MHz RFQ", PAC'99, New York, New York, USA, March 1999, p. 3534.
- [2] S. Koscielniak et al., "Beam Dynamics Studies on the ISAC RFQ at TRIUMF", PAC'97, Vancouver, British Columbia, CANADA, May 1997, p. 1102.
- [3] R.E. Laxdal, "A Separated Function Drift Tube Linac for the ISAC Project at TRIUMF", PAC'97, Vancouver, May 1997, p. 1194
- [4] R.E. Laxdal, "Initial Commissioning Result From The ISAC II SC Linac", LINAC2006, Knoxville, Tennessee, USA, August 2006, p. 521.
- [5] R.E. Laxdal et al., "ISAC II Superconducting Linac Upgrade - Design and Status", Linac08, Victoria, British Columbia, CANADA, September 2008.
- [6] D.V. Gorelov et al., "Use of the LANA Code for the Design of a Heavy Ion Linac", PAC'97, Vancouver, British Columbia, CANADA, May 1997, p. 2621
- [7] M. Marchetto et al., "Upgrade of the ISAC DTL Tuning Procedure at TRIUMF", EPAC08, Genoa, July 2008, p. 3440

FABRICATION OF SUPERCONDUCTING NIOBIUM RESONATORS AT IUAC

P.N. Potukuchi, K.K. Mistri, S.S.K. Sonti, J. Zacharias, A. Rai, D. Kanjilal, A. Roy
 Inter-University Accelerator Centre, Aruna Asaf Ali Marg, New Delhi, India

Abstract

The facility for constructing superconducting niobium resonators indigenously was commissioned at the Inter-University Accelerator Centre in 2002. It was primarily setup to fabricate niobium quarter wave resonators for the superconducting booster linac. Starting with a single quarter wave resonator in the first phase, two completely indigenous resonators were successfully built, tested and installed in the cryomodules. Subsequently production of fifteen more resonators for the second and third modules began. Several existing resonators have been successfully reworked and restored from a variety of problems. In addition to building resonators for the in-house programs, a project to build two single spoke resonators for Project-X at Fermi Lab, USA has also been taken up. A Tesla-type single cell cavity is also being built in collaboration with RRCAT, Indore. This paper presents details of the fabrication, test results and future plans.

INTRODUCTION

The Superconducting Resonator Fabrication Facility (SuRFF) at the Inter-University Accelerator Centre (IUAC) consists of an electron beam welding machine, surface preparation laboratory for electropolishing, high vacuum furnace for heat treatment and annealing and a test cryostat [1]. The facility was primarily setup for constructing and testing niobium quarter wave resonators for the superconducting linear accelerator [2]. After the facility was commissioned a single niobium quarter wave resonator (QWR) was successfully fabricated and tested [3]. Subsequently it was installed in the rebuncher cryostat of the linac. In the second phase two completely indigenous QWRs were fabricated. Unlike the first QWR, all the fabrication for these two QWRs was done using local commercial vendors and the in-house SuRFF facilities. In Fig. 1, one of the resonators along with its niobium slow tuner bellows is shown. In Fig. 2, the performance of one of the indigenous resonator, which has now been installed in the first linac module for beam acceleration [4], is presented. Subsequently production of fifteen more QWRs for the 2nd and 3rd cryomodules began [5]. The resonator production is presently nearing its completion. In addition to the in-house programs IUAC has taken up a project to construct two niobium single spoke resonators for Project-X at Fermi National Accelerator Laboratory (FNAL), USA. More recently IUAC and Raja Ramanna Centre for Advanced Technology, India have jointly started the fabrication of a Tesla-type single cell cavity in niobium.



Figure 1: One of the indigenously built niobium quarter wave resonators along with the slow tuner bellows.

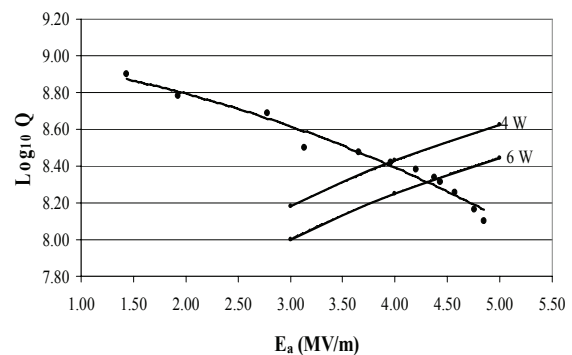


Figure 2: Offline performance of one of the indigenously built QWRs at 4.5 K.

QWR PRODUCTION

After the successful construction of the first two indigenous resonators, production of fifteen more QWRs for the 2nd and 3rd modules began. During the construction of the first two resonators itself we developed a local commercial vendor for doing the machining, sheet metal forming and fitting of the niobium components and assemblies. The idea was to avoid burdening the in-house workshop during the subsequent resonator production. The electron beam welding, electropolishing and heat treatment were done at IUAC using the SuRFF facilities.

Based on the operational experience with the existing resonators in the first module, several design changes were incorporated in the production QWRs. The original design had three coupling ports; one each for the drive coupler and RF pickup and a third port for the VCX fast tuner. However, the resonator control module was designed on the dynamic phase feedback control [6] which made the third port redundant. The production resonators therefore have only two coupling ports. In order to improve the cooling at the shorted end of the coaxial line, i.e. at the top end of the resonator where the magnetic field is highest, a separate hemispherical dome was incorporated in the first cryomodule [4]. The dome is attached to the resonator and the helium vessel using indium seals. The production resonators will not have a separate dome, rather the dome will be welded to the outer stainless steel vessel and it will attach to the helium vessel of the cryostat using a CF flange. This will also allow the resonators to be baked to a much higher temperature without breaking the vacuum seal. Two of the resonators built during the QWR production at Argonne National Laboratory (ANL), USA got punctured at the upper cap on the coaxial line (see details in the following section). The upper cap, which is formed in two steps, was made out of 1.6 mm thick niobium and the uniformity of the eventual wall thickness depended on the geometrical alignment of the blank and the forming dies. Subsequent heavy electropolishing further compromised with the wall thickness which finally resulted in the puncture at the thinnest region. In order to avoid this problem on the current production resonators, the upper caps (and end caps) on the Drift Tube of the coaxial line are made out of 3.2 mm thick niobium.

For the production work the electron beam welding fixtures were designed, wherever possible, to weld several pieces in a single pump down. Similarly multiple assemblies/parts were electropolished in a single setup to save time and effort. Although most of the tooling was available from the previous constructions, additional tooling and fixtures were made as required, or to replace those which had become unusable from wear and tear. In order to ensure that the QWRs were robust in construction several intermediate checks were incorporated in the process. For example, several electron beam welds, especially on critical components such as Drift Tubes, were radiographed to check porosity and other defects. Although during the welding parameter development we had gone through the procedure quite exhaustively, it was felt that randomly checking of a few components would be prudent. All the coupling and beam port bellows and subsequently, their assemblies were thermally shocked and pressure tested to ensure vacuum leak tightness, once they were installed and welded on the resonators. Leaks from the bellows on several of our existing resonators had been a major problem that prompted us to go through more stringent testing (see details in the following sections). Similarly the work hardened slow tuner bellows (without the Nb-Cu top disc) were stress relieved by vacuum annealing the convolutions at 800 °C.

The major niobium sub-assemblies of the QWR, i.e. the central conductor of the coaxial line, the outer cylindrical housing and the top flange (which joins together the other two sub-assemblies) were individually electropolished to remove 150 μm from the surface. The resonators were then frequency tuned and the sub-assemblies were welded together to complete the bare niobium resonator. Based on the frequency data they were electropolished in two different ways. Those resonators whose frequency was below or near the design value were fully electropolished to remove 50-100 μm from the surface depending on how far away their frequency was. The remaining resonators, whose frequency was higher than the design value, were first preferentially electropolished in the inductive region of the coaxial line to drop the frequency, followed by electropolishing of the full resonator to remove $\sim 50 \mu\text{m}$. The amount of preferential electropolishing was decided by how far away the frequency was compared to the design value. After all the electropolishing was completed each resonator was heat treated to 1100 °C in vacuum $< 5 \times 10^{-6}$ mbar. In Fig. 3(a), the bare niobium resonators with the Nb-SS flange welded at the open end and ready for the outer stainless steel jacketing are shown. In Fig. 3(b), the niobium slow tuner bellows are shown.



Figure 3: (a) Top-Bare niobium QWRs ready for the outer stainless steel jacketing. (b) Bottom-Slow tuner bellows.

RESONATOR REPAIRS

In addition to constructing new resonators for the linac, a variety of repairs on the existing QWRs have been successfully carried out. Two of the resonators built during the QWR production at ANL [7], got punctured at the upper cap on the central conductor of the coaxial line (Fig. 4). The upper cap is located where the capacitive drift tube joins the inductive loading arm. The resonators were cut open from the shorted end. All the formed components on the IUAC-QWR are made out of 1.6 mm or 3.2 mm thick niobium (except the slow tuner bellows). On the ANL built QWRs the upper caps had been formed out of 1.6 mm thick niobium. To avoid problems in future, we decided to form the upper cap as well as the end caps (located at the drift tube end) with 3.2 mm thick material. The punctured upper caps were cut and removed from the coaxial line, and after adjusting the drift tube length the new caps were welded in place. The length of the inductive loading arm also had to be adjusted in order to retain the overall length of the central conductor, thereby maintaining the RF frequency. The niobium outer housing length was also adjusted so that the beam ports on the central conductor could match the housing. The freshly inserted niobium parts on drift tube and loading arm were electropolished to remove 100 μm from the surface, and the entire drift tube and loading arm assemblies were further electropolished to remove 50 μm . They were then welded together and heat treated at 800 $^{\circ}\text{C}$ in vacuum $< 5 \times 10^{-6}$ mbar. The central conductor and outer housing (along with its stainless steel jacket) of a resonator after the repair, but before the closure welding, are shown in Fig. 5. After the repair was over both the resonators were lightly electropolished to remove 5 μm before the cold test. Since the resonators had been heavily electropolished in the past, we did not want to risk puncturing the original closure weld and decided for only light electropolishing. In cold tests at 4.5 K one of the resonators (QWR-6) performed as shown in Fig. 6. We believe that the slightly inferior performance of the resonator, as compared to the past [8], could be due to the very light final electropolishing.

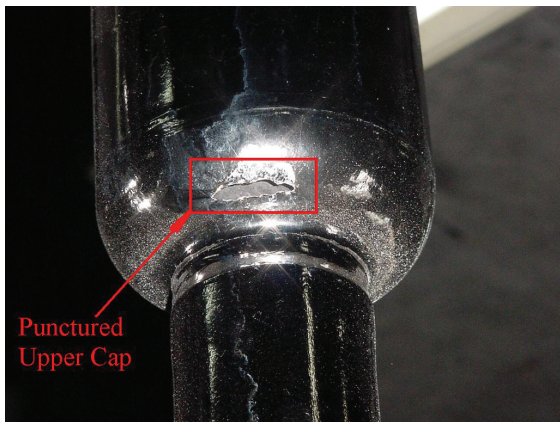


Figure 4: Punctured upper cap on the central conductor of the coaxial line.



Figure 5: Central conductor and outer housing, along with its stainless steel jacket, of the resonator after the repair.

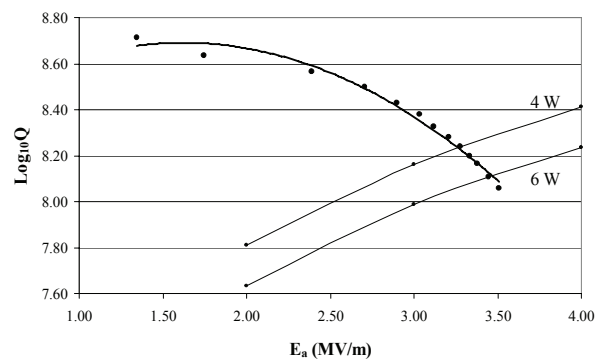


Figure 6: Offline performance of one of the repaired resonator QWR-6 at 4.5 K.

Several QWRs in the first cryomodule developed vacuum leaks through the coupling port transition flange bellows assembly. On all the resonators the leaking assemblies have been machined out and replaced with a newly designed assembly. The original design used niobium-stainless steel explosively bonded flange and welded SS bellows to provide the transition from niobium to stainless steel. An alternate assembly was designed using formed SS bellows, but retaining all the other features of the original assembly [3]. The formed bellows are commercially procured with appropriate end fittings and the Nb-SS flange is electron beam welded to it. Prior to welding to the flange, the bellows were thermally shocked from 300 to 77 K several times and pressure tested. After the bellows were welded to the flange, the assembly was again thermally shocked and pressure tested before welding to the resonator. The resonators were individually pressure tested and then lightly electropolished before mounting in the cryomodule. This entire effort has resulted in the cryostat vacuum improving from low 10^{-7} to high 10^{-9} mbar.

SINGLE SPOKE RESONATORS

Apart from constructing resonators for the in-house programs IUAC has taken up a project to build two niobium single spoke resonators designed for $\beta=0.22$ operating at 325 MHz, for Project-X at Fermi National Accelerator Laboratory (FNAL), USA [9]. An exploded view of the resonator is shown in Fig. 7.

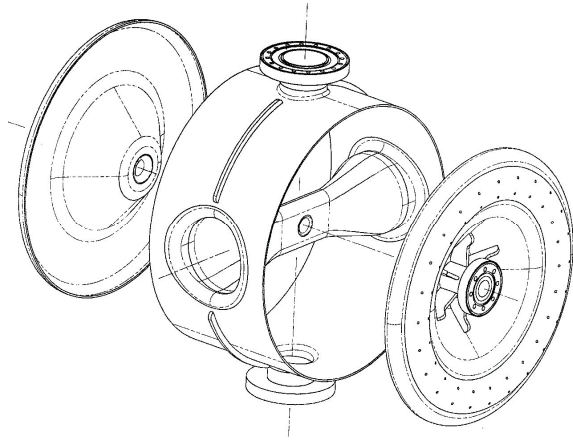


Figure 7: 325 MHz, $\beta=0.22$ Single Spoke Resonator. The outer shell diameter is 498 mm.

The single spoke resonator has three major sub-assemblies, namely the outer cylindrical shell, the spoke which is formed in two halves and welded together, and the end walls with its beam port, stiffening ribs and donut rib. The outer stainless steel jacketing of the resonator would be done at FNAL. Apart from the smaller dies required for forming the spoke to shell collar and the coupler port pullout, the major dies required are for forming the half spoke and the end wall, both of which are non-trivial. Therefore most of the initial effort was put into making these two large dies.

The dies for forming the half spoke and end wall have been developed and several trials were done on copper sheets. The half spoke is formed in two steps; first the central flat is formed followed by the loft and the circular ends. In Fig. 8(a), a half spoke formed in copper and after the edge machining is shown. The end wall is formed in three steps; the nose is formed in two steps using two different punches. This is followed by forming of the end radius (where the shell meets the end wall). In Fig. 8(b), an end wall formed in copper is shown. The edge has not been machined. In addition, the die for forming the spoke to shell collar has been developed and several trial pieces in copper have been formed. The coupler port pull out die is presently being developed. Apart from fabricating the dies several machining fixtures have also been designed and built. The brazed beam ports and coupler ports will be supplied by FNAL. At present the two outer shells have been rolled in niobium and they are being readied for the seam welding. The electron beam welding and electropolishing fixtures are also being designed. We plan to complete the fabrication by the end of this year.



Figure 8: (a) Left – Half Spoke formed in copper and after machining the edges and ends. (b) Right – End Wall formed in copper. The edge has not been machined.

TESLA TYPE SINGLE CELL CAVITY

IUAC in collaboration with Raja Ramanna Centre for Advanced Technology (RRCAT), India is fabricating a Tesla-type single cell cavity in niobium. In Fig. 9, a picture of the cavity being built is shown. All the dies, tooling and fixtures required for the fabrication have been developed and built by RRCAT. IUAC is extending its fabrication facilities and expertise and several fixtures have been designed based on its input. The first half cell that has been fabricated is shown in Fig. 10. We plan to complete the full single cell cavity in the next couple of months.

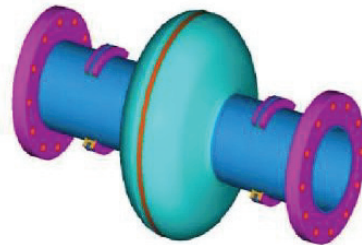


Figure 9: Tesla-type Single Cell cavity. The overall length is 392 mm.



Figure 10: Half cell of the Tesla-type single cell cavity.

CONCLUSIONS

The Superconducting Resonator Fabrication Facility at IUAC has been fully operational since July 2002. The facility is being primarily used for indigenously

constructing niobium quarter wave resonators for the linac project. IUAC has successfully fabricated quarter wave resonators which have been installed in the first cryomodule of the superconducting linac. Production of fifteen more resonators for the second and third modules is nearing completion. These two cryomodules will be commissioned by the end of this year. IUAC has also developed expertise in carrying out a variety of critical and challenging repairs on existing resonators. Two resonators have been successfully restored by repairing the punctured central coaxial line. While their present performance is inferior to the past, i.e. before they got punctured, it is still at an acceptable level. Several resonators have been repaired to fix recurring vacuum leaks from the coupling port bellows using an indigenously developed design. It has resulted in achieving better vacuum in the first linac module. In addition to building resonators for the in-house projects, construction of two single spoke resonators for Fermi Lab, USA has been taken up. Although this project has got slightly delayed, considerable progress has been made in the last six months in developing the tooling. IUAC in collaboration with RRCAT, India is also fabricating a Tesla-type single cell cavity in niobium, which should be ready for cold tests in the next few months.

ACKNOWLEDGEMENTS

The authors would like to thank the staff of Don Bosco Technical Institute, New Delhi for their help in machining and sheet metal work of the niobium components. The

authors thank the IUAC workshop, other members of the linac group and members of the cryogenics groups for their help. The authors are thankful to G. Apollinari, L. Restori, S.B. Roy, A.M. Puntambekar and their groups for the collaboration and technical interactions.

REFERENCES

- [1] P.N.Prakash et al., Proceedings of the Indian Particle Accelerator Conference - InPAC-2003, February 3-6, 2003, RRCAT, Indore, India, p148.
- [2] P.N.Prakash et al., PRAMANA, Journal of Physics, Vol. 59, No. 5, November 2002, p849.
- [3] P.N.Prakash et al., Proceedings of the Third Asian Particle Accelerator Conference - APAC-2004, March 22-26, 2004, Gyeongju, Korea, p684.
- [4] S.Ghosh et al., Phys. Rev. ST Accel. Beams 12, 040101 (2009).
- [5] S.S.K.Sonti et al., Proceedings of Indian Particle Accelerator Conference InPAC-2006, November 1-4, 2006, BARC & TIFR, Mumbai, p139.
- [6] G.Joshi et al., PRAMANA, Journal of Physics, Vol. 59, No. 6, December 2002, p1035.
- [7] P.N.Potukuchi et al., Proceedings of 1999 Particle Accelerator Conference, March 29 to April 02, 1999, New York, USA, p952.
- [8] P.N.Prakash et al., Proceedings of the Second Asian Particle Accelerator Conference - APAC-2001, September 17-21, 2001, Beijing, China, p115.
- [9] G.Apollinari, FNL, Private Communication.

UPGRADE OF THE CONTROL SYSTEM FOR THE ALPI CRYOGENIC DISTRIBUTION PLANT

S. Canella, A. Beltramin, A. Calore, T. Contran, P. Modanese, F. Poletto
INFN- Laboratori Nazionali di Legnaro, Viale dell'Università 2, 35020 Legnaro, Italy

Abstract

In the LNL Heavy Ion Accelerator Complex, ALPI is a superconducting linear accelerator (Linac), whose first runs date back to 1993. In more than 15 years the LNL ALPI Linac evolved from an initial small configuration of 5 cryostats and 16 resonators to the actual size of 20 cryostats and 74 resonators. The superconducting character of ALPI implies the availability of a large cryogenic plant and distribution system to supply the liquid helium necessary to keep the resonators at 4.2 K.

While the Linac structure has grown in the years and, in the mean time, the related cryogenic plant and distribution systems were enlarged and upgraded twice, the related control system remained largely unchanged in its main parts and it is now the first sub-system that urgently needs a deep renewing.

The challenge to renovate a working control system with limited shut-downs is the subject of this presentation.

INTRODUCTION

At LNL ALPI is a Linac (Fig. 1) now made up of 20 cryostats, each housing 2 or 4 RF superconducting resonators (80 and 160 MHz, either niobium bulk or niobium sputtered on copper) for a total number of 74 accelerating or bunching cavities. For all the ALPI resonators the temperature must be kept below the niobium superconductivity transition point (9.2 K), and they are therefore cooled down at about 4.2 K by liquid helium. Inside the cryostats high vacuum insulation is maintained and a cryogenic shield at 60-80 K is cooled by low-temperature gas Helium, to reduce thermal losses toward the external room temperature environment. A steel tank inside the cryostat (its capacity is about 100 l) is continuously refilled with liquid helium to keep the resonators below 9.2 K.

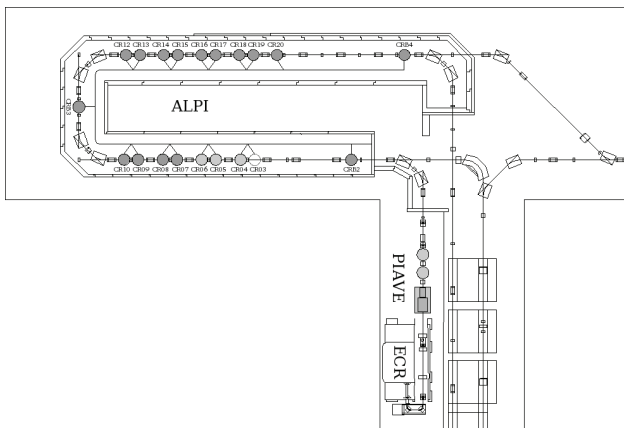


Figure 1: The ALPI linac layout.

The cryogenic plant necessary for ALPI [1] is a liquefier/refrigerator (Fig. 2) supplying both the liquid Helium at 4.2 and the 60-80 K gas Helium for the shields. The plant is composed by 2 screw cycle compressors (Mycom) housed in an external building and by a cold-box (Air Liquide - France) installed in the middle of the ALPI room, where the liquid helium is produced. A 2000 l dewar is directly connected to the cold-box for storage. The liquid helium line, the cold gas Helium line and the return lines (from the tanks and the shields) have a closed ring shape and are thermally insulated by means of Mylar and high vacuum. The cryostat tanks and shields are connected to the lines through valve boxes. In most cases one valve box feeds two cryostats, only for 3 cryostats in special positions (housing bunching or de bunching resonators) the valve box is sized for only one cryostat.



Figure 2: ALPI Cold-Box.

A good management of both the cryogenic plant (cycle compressors and cold-box) and of the distribution lines and cryostats tanks refilling system is essential to have stable and reliable working periods of the ALPI Linac.

THE ACTUAL CONTROL SYSTEM

The different parts of the ALPI cryogenic plant and distribution system are controlled by different PLC based systems. The communication among them, when present, makes use of common electrical signals or data exchange through serial lines.

The two cycle compressors are controlled by two local Schneider Twido PLCs, one for each compressor. These controllers have been already renewed some years ago. They have a limited hardware connection with the cold box control system (states, interlocks and a few common analogue signals of pressure) and no supervisory system.

Also the cold box control system was renewed some years ago and is now based on an Eurotherm PLC (PC3000), interconnected with the cycle compressors by interlocks and states and with the distribution control system through a serial line. This control system is supervised by a proprietary SCADA (Fig. 3), has a main control console, a second read-only monitor in the linac general console (for checks during the linac operation) and a separated logging system built on an OPC server with a Labview graphical user interface.

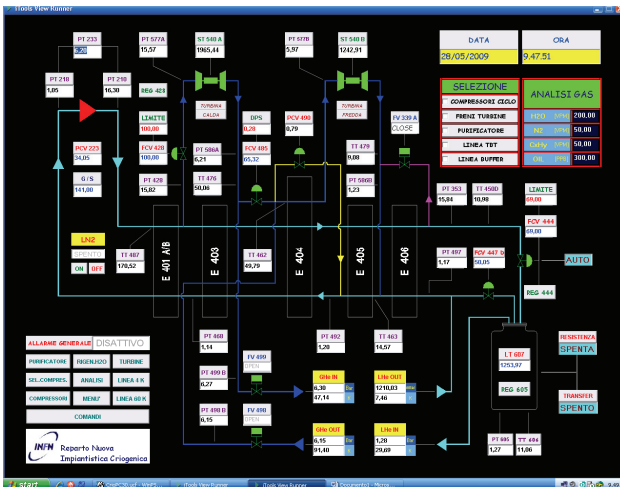


Figure 3: ALPI Cold-Box Supervisory Page.

The distribution system (cryogenic lines and cryostats) has its own control system dating back to 1992-1994. It is the biggest of the cryogenic control subsystems, with 20 PLCs a distributed topology and a large number of different instruments and actuators and the last one that needs to be renewed.

Hardware of the Distribution Control System

In the actual configuration the local thermal control of each cryostat and its tank refilling is demanded to a single Tecmint PLC model TPLC130C and its set of digital and analogue I/O cards and RS232 ports card (for cryogenic multi-sensors temperature monitors) (in Fig. 4 a rack for

two cryostats is shown). All the local PLC controllers are connected by RS485 ports to a central terminal server through 485/232 converters. In the same central terminal server a group of RS232 serial lines are reserved for some monitors of the temperatures and of the insulating vacuum instruments on the distribution ring lines. The central terminal server is located in the linac ALPI room and is connected to a local control PC and to the master PC by a proprietary network (ARCNET). A connection with the cold-box control system is present on one of the serial lines, to acquire some summary states. Another connection with the ALPI vacuum control system is present both at level of local Tecmint PLCs (states and interlocks) and on one of the RS232 ports of the master PC (cryostats temperatures are supplied to the vacuum system).

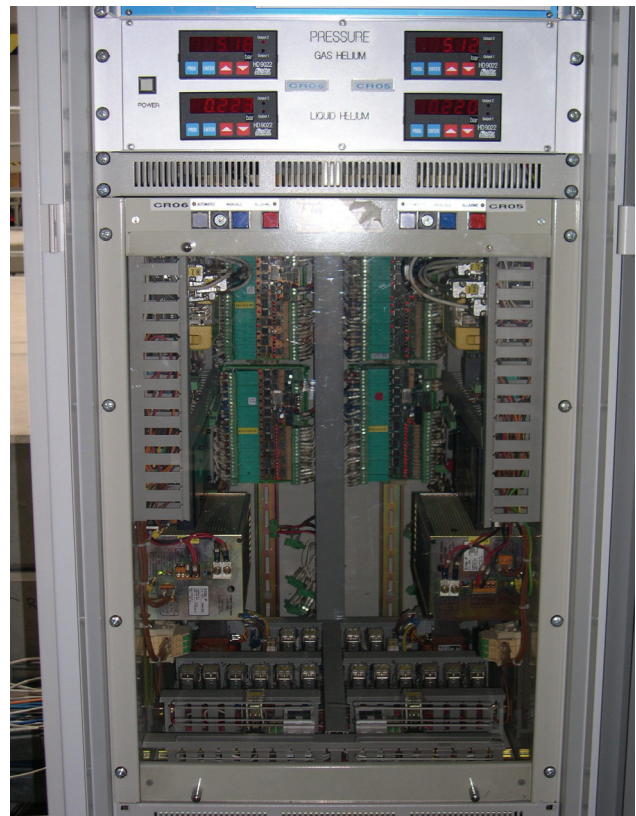


Figure 4: A rack for 2 PLCs of the Cryogenics Distribution System.

Software of the Distribution Control System

The total amount of signals that in each cryostat PLC have to be managed may be so grouped:

- 34 analogue inputs (but 24 of them come from 3 RS232 connected instruments);
- 3 analogue outputs;
- 24 digital inputs;
- 24 digital outputs.

Actually in the local control of each cryostat only some basic automation procedures, using these signals, are implemented:

- automatic management (switching on/off) of the probe for the liquid Helium level in the tanks;
- PID control of the liquid Helium level in the cryostat tanks, to maintain a given level set-point;
- baking on-off control of the resonators with one or two electrical warmer for each resonator.

All the local signals, controls and automation procedures are reported to the master PC where the supervisory system, in QNX environment, allows to monitor all measurements and states, to manually control all the valves, to start and stop the automation procedures. Several control windows are available.

An alarm management system is also included, together with a local logger. The actual master PC is shown in Fig. 5.



Figure 5: The master PC for the Cryogenics Distribution System.

THE REVAMPING PROJECT

The low-energy cryostat CR03 with 4 low-beta resonators is foreseen to be re-installed soon in the ALPI linac. This last module is a prototype with special features requiring a deep update of the cryostat cryogenic control:

more temperature sensors, a liquid nitrogen line to cool down the RF couplers and, related to it, one more local regulation loop to keep in a stable range the coupler temperatures, when fed with RF power. This facts and the hardware-software obsolescence of the whole distribution control system were the main reasons to plan the design of a new control prototype on a more modern PLC model and with up-to-date software development tools.

Hardware

Two families of middle size PLC were considered for the new control prototype, from Siemens and Schneider.

The present control topology will be maintained, with a single control PLC for each cryostat. In the new complete system a standard LAN network (doubled, if required, for a higher availability) will be used to connect local control PLCs to a main supervisory PC with a second PC as backup on the same network. A smooth and slow transition is foreseen between the old and the new control system after a complete test of the first cryostat prototype.

Software

Both for the control PLC programming and for the supervisory PC graphical user interface the advantages of the modern integrated development environments (IDEs) will help in a rapid software development. Only industrial commercial tools and IDEs will be used.

FUTURE PLANS

The different ALPI cryogenic control subsystems, for the compressors, the cold-box and the distribution lines (in future, the helium dryers might be also added) are now almost completely disjoint and have different, if they have, supervisory systems. In the future a general purpose SCADA is planned to be used as a common framework for the differently controlled subsystems, to have a unified and general control of the whole cryogenic plant.

CONCLUSIONS

The challenge to renovate a working control system with limited shut-downs is the subject of this presentation. A prototype with modern hardware and some necessary and some useful control improvements for a single cryostat is the way that will be followed to keep the system old alive while rejuvenating it.

REFERENCES

- [1] R. Pengo et al., "Cryogenics and related topics of the ALPI linac", Nuclear Instruments and methods in Physics research A328 (1993) p. 242-250 NH.

WIDE BANDWIDTH LOW COST SYSTEM FOR CAVITY MEASUREMENTS

S. Stark, A.M. Porcellato, INFN/LNL, Legnaro, Padova, Italy

Abstract

Recently we developed a novel measurement apparatus that simplified the tests of superconducting cavities. A few commercial electronic boards, mounted in a devoted chassis and controlled by a PC, operate most of the functions usually carried out by standard RF instrumentation. The set up allows the measurements of resonators in the 80-700 MHz frequency range and we used it to characterize resonators both in the ALPI vault and in off-line tests.

Upgraded control program carries out all the typical procedures, related to the cavity measurements in classical VCO-PLL system. It allows to adjust and to measure the RF forward power, to find and update the cavity resonant frequency, to calibrate the pick-up signal, to monitor the transmitted power, to adjust the coupler position. The implemented automatic procedures permit to measure the cavity decay time, to trace the Q-curve, to perform CW and pulse RF conditioning, to calibrate cables and measurement instruments.

The same software applies to the other two measurement systems routinely used at Legnaro to test resonators up to 6 GHz frequency.

INTRODUCTION

Our first experience was a PC based measuring system for 160, 1300, 1500 and 6000 MHz cavities [1, 2, 3] now used for the characterization of Tesla type cavities in the Superconductivity Laboratory at LNL.

Some years ago, we developed in house a second similar movable RF system covering 80, 160 and 350 MHz [4]. We extensively used it for the characterization of ALPI superconducting cavities produced by Nb sputtering at LNL and Superconducting RFQs. Both measuring systems showed over time to be reliable and easy to use.

Due to radioprotection access restriction, it was not so easy to move the system in and out the accelerator vault, thus making difficult to share it for Q-measurement in laboratory and on line.

Recently we found the way of setting up another system which consists mainly of old RF equipment already present in laboratory (RF generator, frequency counter, DC amplifier), integrated by a digital scope and by commercially available, low cost, electronic devices which make the functions of phase shifter, phase detector

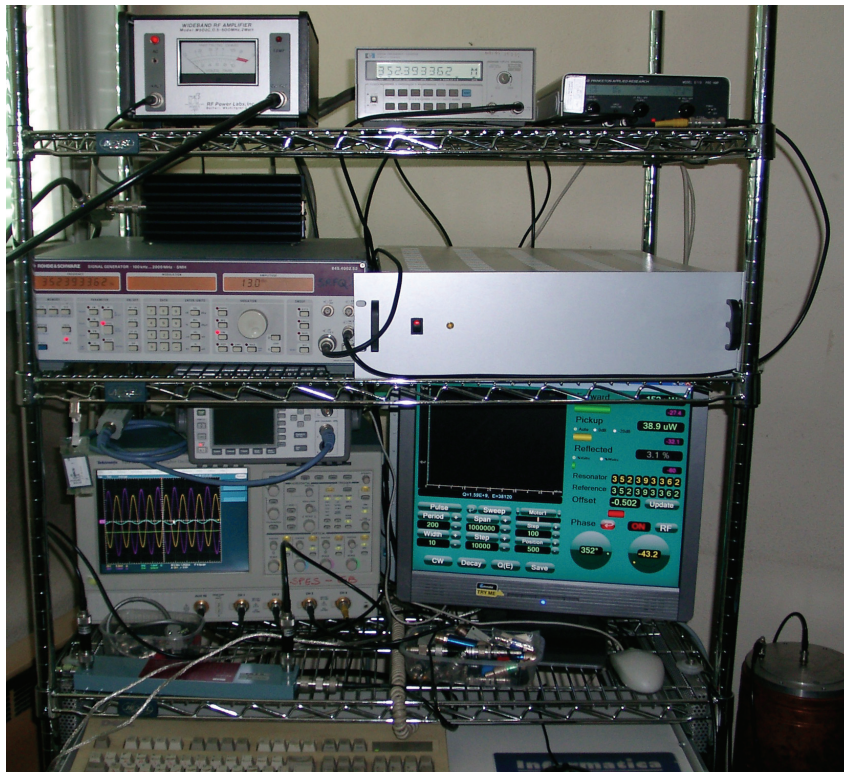


Figure 1: Measurement system for cavity characterization.

low frequencies to 2.7 GHz with dynamic range of 60 dB and provides the phase measurement over a 0 to 180 degree range scaled to 10 mV/degree. The applied input signal can range from -60 dBm to 0 dBm (50 Ω) [5].

Variable Gain Amplifier

We chose to use the AD8369 as variable gain amplifier. It is a 600 MHz, 45 dB, Digitally Controlled VGA. Its gain is controlled in 3 dB steps through either parallel or 3 wire serial control. It features high gain stability, flatness and low distortion [5].

SOFTWARE UPGRADE

We upgraded the original control program, developed in Visual Basic, to MS Visual Studio 2005 (Net 2.0). It covers the new apparatus and the previous measurement systems in order to use it for all of them.

The modular structure of the software permits a more flexible hardware configuration in the case of instrumentation substitution or upgrade.

The extended use of mouse wheel facilitates frequency, power and phase adjustment.

The main program window now contains the stepper motor control panel for the antennas and tuner movement.

The new tabbed options window permits to write the

measurement diary, to consult and to change setup parameters, to view the acquired data and to visualize the measuring systems hardware configuration. We are finishing the upgrade of the previously developed RF Calculator for computer assisted measurement and data verification and visualization to add it to the options window [4].

Fig. 3 presents the program main panel. There is a chart section to show the behavior of the variables of the activated automatic procedure.

The frequency sweep procedure gives the possibility of determining the cavity resonant frequency easily. It visualizes the phase detector output response that is an indication of the actual phase angle inside the PLL.

From panel menus, one can activate the semiautomatic procedures needed for forward/reflected and pickup RF lines calibration.

The decay procedure for cavity in both cold and warm condition gives the possibility of determining the cavity Q-value (Fig. 3). From it and from the measurements of forward, pickup (transmitted) and reflected power, presented on the panel to the right, it is possible to perform the pickup calibration. We use this procedure in warm condition for adjusting the pickup antenna.

The Q(E) procedure presents the resonator Q-curve as a function of the accelerating field (E_a). The E_a and the

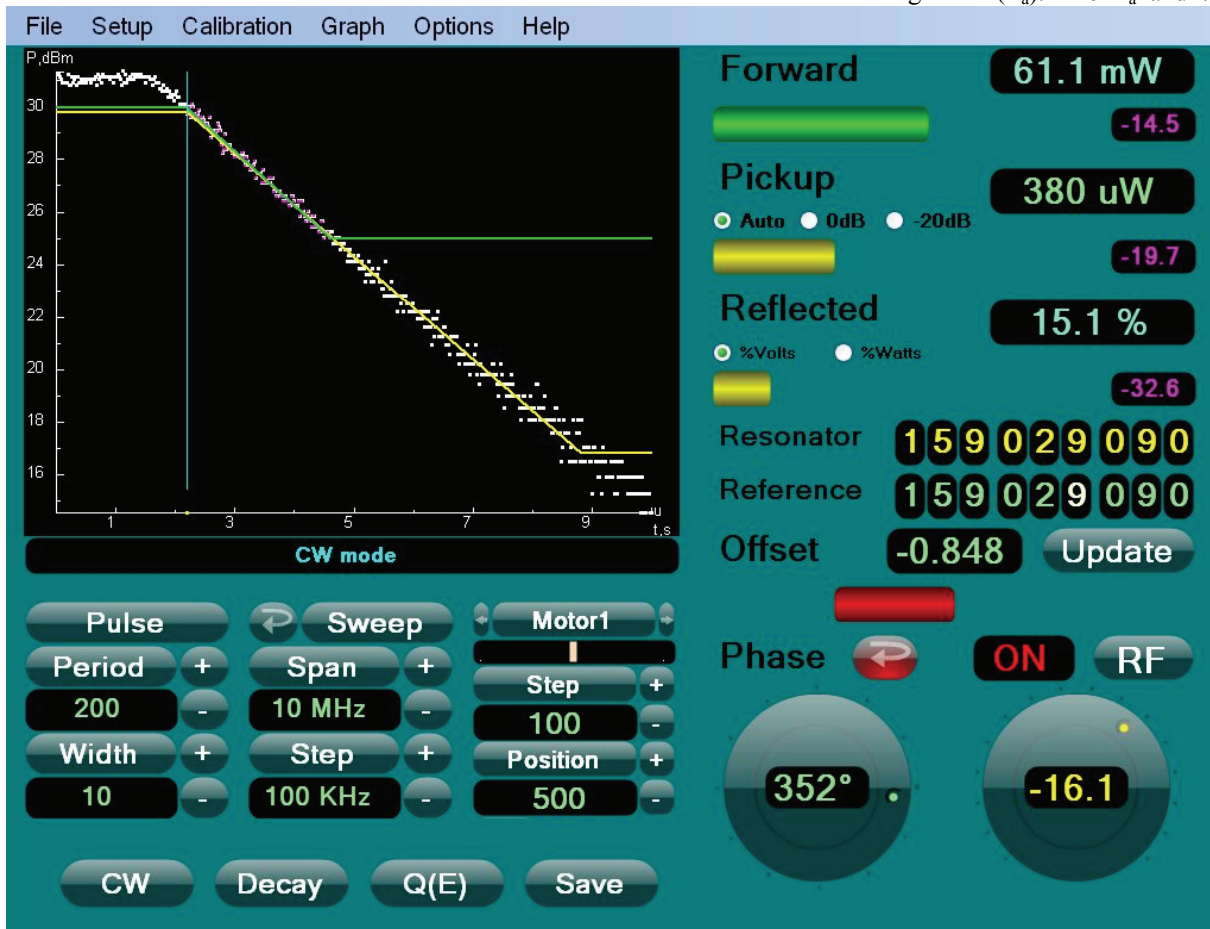


Figure 3: Control panel view during room temperature decay time measurement.



Figure 4. Options Window with RF Calculator panel.

corresponding Q value, as computed from the actual measured power values, are shown in the Q(E) plot and, if the case, saved by the Save button.

It is possible to adjust the coupling condition acting on the coupler stepping motor.

It is also possible to enter in the pulse mode using the Pulse panel on the left. We can choose both the pulse period and width for the cavity conditioning at high pick power. The chart in this case shows the reflected and transmitted power pulse envelopes for easy coupling adjustment.

A voltage-controlled attenuator, set by the knob on the left bottom side of the panel, regulates the forward power. Fast Down – Slow Up feature of this knob limits the risk of power overhead.

The cavity operates in phase lock loop. It is possible to adjust the phase in order to minimize the reflected power by moving the corresponding knob. The Phase button provides switching between the locked/unlocked conditions.

The panel gives the possibility to set the reference frequency manually. The frequency counter reading can also update the reference frequency automatically, thus making the reference frequency to follow the actual frequency of the locked resonator.

Semiautomatic procedure produces calibration tables for oscilloscope channels at different frequencies. The program can load and implement these curves using separate polynomial approximation for every vertical channel range of the scope.

Setup file including all the system parameters for a particular measurement is loaded at the software start. It

contains the hardware configuration settings, various measurement constants, calibration data and file references for calibration tables and stepper motors configuration. The panel menus visualize and permit modification of many of these parameters.

CONCLUSIONS

A new computer based mobile measuring system for laboratory and online characterization of superconducting cavities was set into operation at LNL. The system actually covers the frequency range up to 500 MHz with possible expansion to 700-750 MHz.

The use of conventional electronic components makes it possible to create low cost circuitry for laboratory and online cavity testing.

The upgraded software for cavity measurements was tested and put into operation. It smoothly covers three LNL cavity test systems with different frequency ranges and hardware configurations thus making the future development and hardware upgrades easier.

Availability, mobility and ease of use of the system permit the reliable evaluation of the state of ALPI cavities optimizing the conditioning time and consequently the operational performances.

REFERENCES

- [1] V. Palmieri, R. Parodi, A.M. Porcellato, V. Ruzinov, S. Stark, "Computer based measuring system for 160 and 1500 MHz resonators", LNL-INFN (REP)-81/94, p. 216.
- [2] C. Durand, V. Palmieri, A. Porcellato, S. Stark, "RF-Superconducting Cavity measurement", LNL-INFN (REP)-105/96, p. 300.
- [3] C. Durand, V. Palmieri, R. Preciso, S. Stark, F. Stivanello, W. Venturini, "RF Characterization of small scale cavities", Proceedings of the 8th workshop on RF Superconductivity, October 1997, Abano Terme, (Padua) V. Palmieri and A. Lombardi Eds, LNL-INFN (Rep) 133/98 p. 941.
- [4] S. Stark, G. Bisoffi, L. Boscagli, V. Palmieri, A.M. Porcellato, "New RF Measuring System for Cavity Characterization" Proceedings of EPAC 2004, Lucerne, Switzerland, p.692-694.
- [5] Analog Devices Documentation, www.analog.com.
- [6] A.M. Porcellato, S. Stark, F. Stivanello, F. Chiurlo, D. Giora, M. De Lazzari, "Improved on Line Performance of the installed ALPI Nb Sputtered QWRs" Proceedings of HIAT 2009, to be published.

DESIGN OF THE MEBT REBUNCHERS FOR THE SPIRAL 2 DRIVER

M. Lechartier, J.F. Leyge, D. Besnier, M. Michel, GANIL, Caen, France

Abstract

The Spiral 2 project [1] uses normal conducting rebunchers to accelerate high intensity beams of protons, deuterons and heavier ions. All cavities work at 88 MHz, the beta is 0.04 and 3 rebunchers are located in the MEBT line, which accepts ions with A/q up to 6. The paper describes the RF design and the technological solutions proposed for an original 3-gap cavity, characterised by very large beam aperture (60 mm) and providing up to 120 kV of effective voltage.

REBUNCHER REQUIREMENTS

- Operation: R1: 120 kV, R2: 60 kV, R3: 120 kV;
- injector commissioning: emittance measurements after RFQ R1: 190 kV, pulsed;
- short distance on the line.

RF DESIGN

- 3-gap structure;
- two opposing quarter-wave stems;
- two capacitive tuners;
- inductive coupler.

The Micro Wave Studio software was used to obtain the mechanical dimensions of the cavity and the radio frequency parameters. Tables 1 and 2 illustrate the RF design and the mechanical dimensions of the cavities.

These dimensions were imposed by the structure of the line. We control the resonance of the cavity with two movables panels. The first one is used to obtain a good resonance frequency range, the second to adjust the working frequency with the electric field.

The output radio frequency amplifier available is 5 kW for 60 kV and 10 kW for 120 kV.

Table 1: RF Design Parameters

Electrode voltage At 120kV (Veff)	80 kV
TTF	0,38
Q	7800
Rs (kV _{eff} ² / loss)	3680
Power loss (@120 kV)	4 kW
Max E field (pulsed)	11 MV/m
Max H field (pulsed)	17,4 A/m
Short circuit sensitivity	100. kHz/mm
Max trimmer sensitivity	140 kHz/mm

MECHANICAL STRUCTURE

The choice of a tank was made because it must be copper-plated.

Table 2: Mechanical Dimensions

Parameter	Mm
Beam diameter	60
Ring external diameter	90
Electrode ring length	32
Gap distances	13 .30 .13
Trimmer diameter	130
Trimmer stroke	15 to 45
Stem diameter	32 .40
Cavity central section sides	180x180
Cavity central section height	2*145
Cavity diameter	260
Cavity height	2*545
Flange to flange distance	280

MAGNETIC AND ELECTRIC FIELDS

Magnetic and electric fields were calculated with Micro Wave Studio.

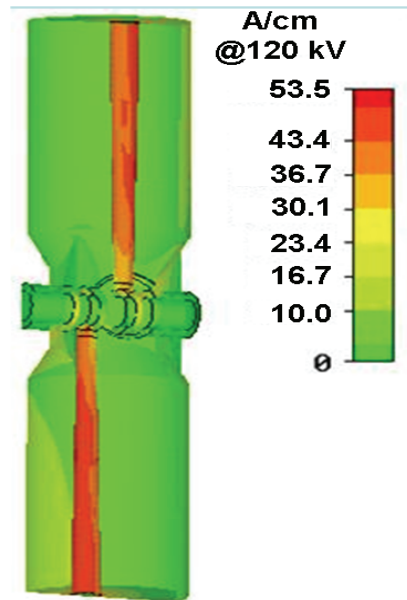


Figure 1: Stems current densities.

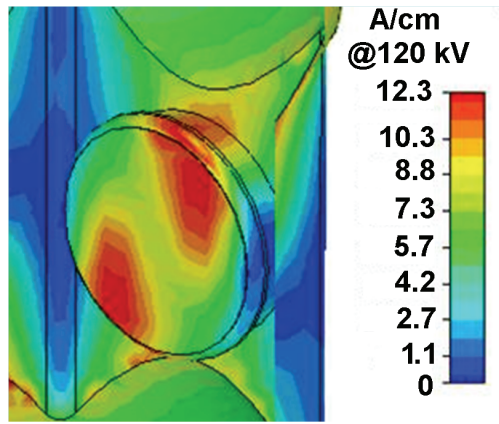


Figure 2: Movable panel densities.

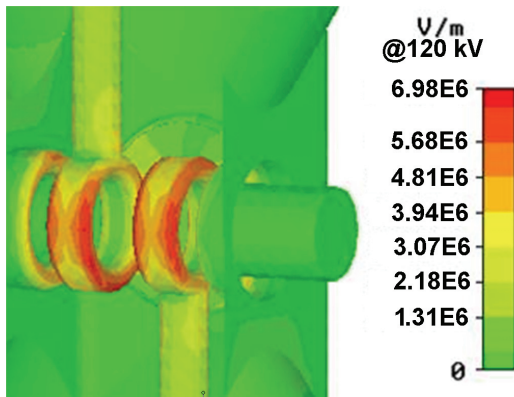
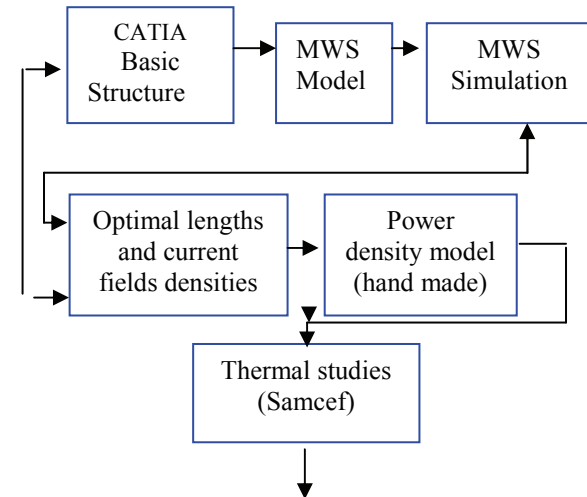


Figure 3 : Electric field on drift tubes.

The Study Process



The current density obtained by Figs. 1 and 2 give us the power density on the cavity.

With the software SAMCEF we estimated the temperature in all the surface of the cavity. (See Fig. 6).

MECHANICAL AND COOLING STUDIES

The external tank is made of copper-plated (70 μm) thick (5 mm) sheets, except for the central region which is milled in a solid block.

We use flexible belts as thermal and RF contact for the tuner.

The stems, beam ports, tuners, drift tubes are made of solid copper (Fig. 4).

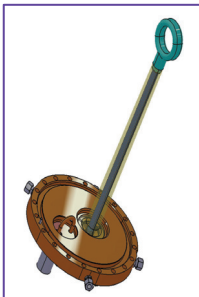


Figure 4: Stem.

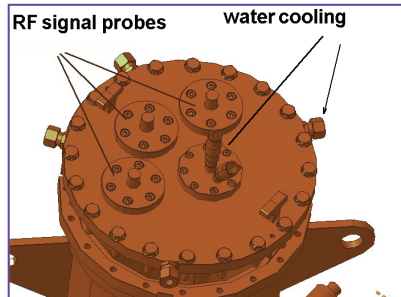


Figure 5: External tank.

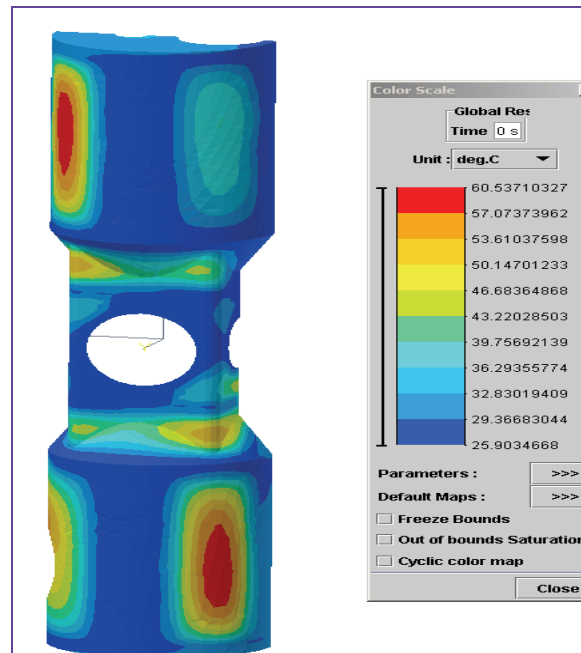


Figure 6: Copper-plated steel cavity temperature map.

The cooling system is realised with two circuits, one with a coupling loop with a flow of 2l/mn, and the second with the tank and feeder with a flow of 20 l/min.

Details of the power coupler with cooling system are shown in Fig. 7.

Drawing Office

In collaboration with the drawing office we calculated the cooling system. The goal was to obtain two cooling circuits. The maximum temperature input, output is fixed to 18°C .

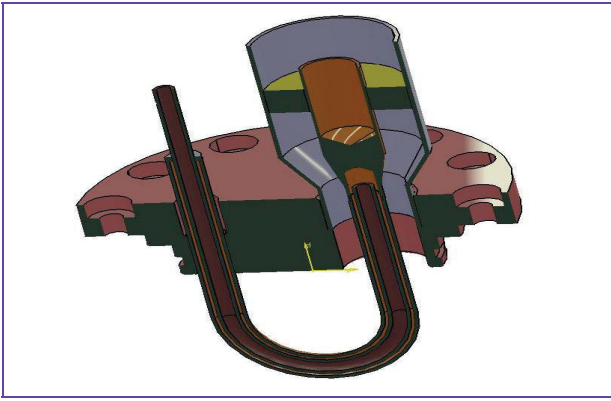


Figure 7: RF power coupler.

GENERAL DESIGN OF THE CAVITY

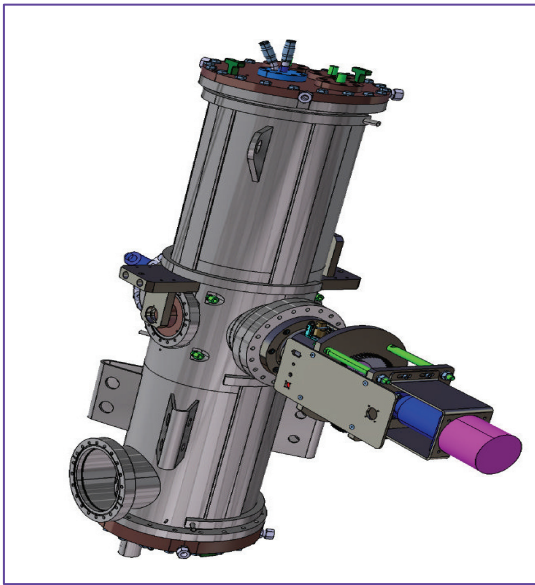


Figure 8: Cavity.

On the Stainless-steel tank we can see the cooling system. Observe the external tank made of cooper. The magnetic RF power coupler is under the cavity. On the right hand is the trimmer and its motorisation.

TRIMMER WITH FLEXIBLE BELTS

The general view is shown in Fig. 9.. We can see the tuner with the flexible belts.

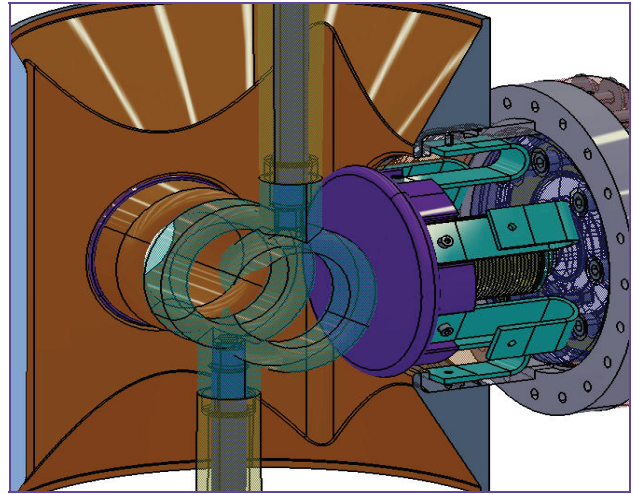


Figure 9: Movable panel.

The movable panel doesn't have any cooling system. The cooling is realised with the flexible belts in cooper.

MOTORISATION

The moving of the tuner is done by a walk-to-walk motor coupled to a reductor, see Fig. 10.

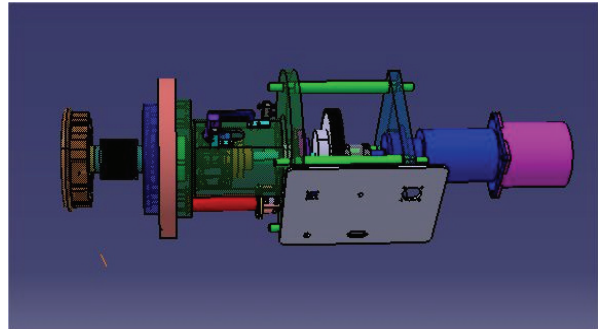


Figure 10: The motorisation.

CONTROL SYSTEM

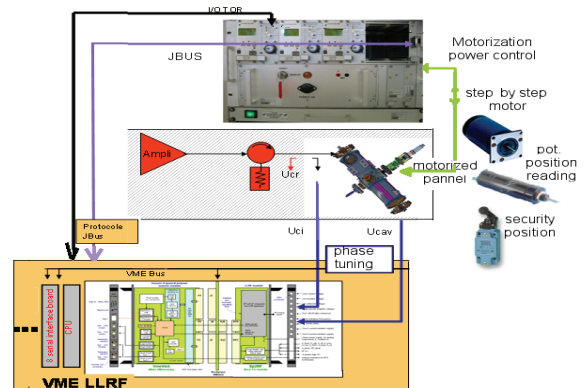


Figure 11: Control command for tuning.

Safety for the motor drive is obtained by electrical switches. A potentiometer gives a reading of the position of the trimmer.

We can move the motor either in MANUAL mode or via the control system.

CONCLUSION

An original RF structure has been designed to fit the SP2 requirement for the MEBT rebunchers. The proposed cavity has a high gradient, compactness along the beam axis and has tight alignment tolerances. The cavity design is now completed and the call for tender is in progress.

ACKNOWLEDGEMENTS

Many people have been involved in this work but we would particularly wish mention D. Uriot for beam

dynamics simulations, G. Le Dem for field-map macros, M. Malabaila and T. Dettinger for their explanations about the copper-plating process and M. Vretenar, H. Vormann and their teams at CERN and GSI for their help and comments on the overall design.

REFERENCES

- [1] T. Junquera et al., Proc. of EPAC 08, [2] MWS, Computer Simulation Technology, Darmstadt, Germany.

DESIGN OF THE CENTRAL REGION OF THE NEW MULTI-PURPOSE CYCLOTRON U400R

G. Gulbekian, I. Ivanenko, FLNR JINR, Dubna, 141980 Russia

Abstract

At the present time, the activities on creation of the new multi-purpose isochronous cyclotron U400R are carried out at the FLNR, JINR. The isochronous cyclotron U400R is intended for obtaining the beams of the accelerated ions from 4He^{1+} ($A/Z=4$, $W=27\text{MeV/u}$) up to $^{132}\text{Xe}^{11+}$ ($A/Z=12$, $W=3.5\text{MeV/u}$). The cyclotron magnetic field can be changed from 0.8T to 1.8T and allow the smoothly variation of the ion beam energy at the range $\pm 35\%$ from nominal. The cyclotron RF system keeps up $2 \div 6$ harmonic modes. The aim of the present work is to investigate the optimal geometry of U400R cyclotron center for the wide range of acceleration regimes. The computation of the beam acceleration is carried out by means of the computer code CENTR.

INTRODUCTION

The U400R cyclotron is an isochronous cyclotron with azimuthally varying field. It is designed as multipurpose machine and has to be able to accelerate wide range of the ion beams $^4\text{He}^{1+} \div ^{132}\text{Xe}^{11+}$ (mass to charge ratio range $4 \div 12$) up to the energy $W= 27 \text{ MeV/u} \div 3.5 \text{ MeV/u}$. The expected intensity of the beams has to be increased more then two times in comparison with U400 cyclotron. The cyclotron working diagram is presented in Fig. 1.

The cyclotron is equipped with an ECR ion source. The ions are extracted from the source, transported along the axial transport line and bent onto median plane by the spiral inflector. The magnet structure has the axial centre plugs and four pairs of 45° sectors. There are two 40° dees located at the opposite “valleys”. The RF generator frequency range $6.5 \div 12.5 \text{ MHz}$ gives the five modes of cyclotron operation, from 2nd to 6th RF harmonics. The main parameters of magnet and RF system at the central region are presented at the Table 1.

The wide range of ions, $A/Z = 4 \div 12$, and magnetic field variation, $0.8\text{T} \div 1.8\text{T}$, necessitate using more then one spiral inflector and a wide range of the RF harmonics. Moreover, the efficiency of the beams acceptance onto acceleration at the different RF harmonic modes required the different angular positions of the first acceleration gaps. In this case it is more convenient to separate U400R cyclotron working regimes in three groups with different spiral deflectors and RF harmonic modes:

- “A” – 2 and 3 RF harmonic modes,
- “B” – 3 RF harmonic mode,
- “C” – 4, 5 and 6 RF harmonic modes.

The construction of the central region has to be stationary and not separable for accelerating at the different RF harmonic modes. To do this the beams of “A” and “B” working regime groups are accepted onto

acceleration at the 1st dee puller, and the beams of the “C” group – at the opposite, 2nd dee puller.

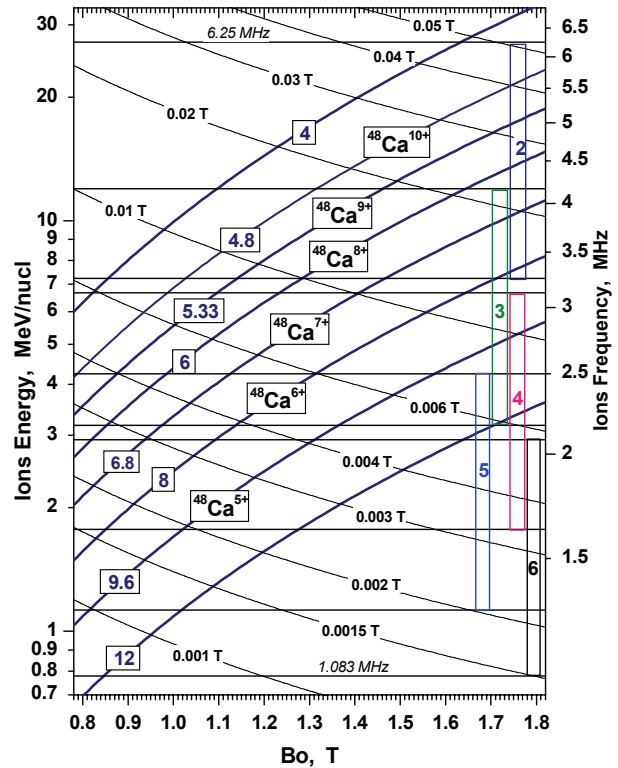


Figure 1: The working diagram of the U400R cyclotron.

Table 1: U400R Cyclotron Centre Main Parameters

Distance between centre plugs	82 mm
Centre plug radius (sectors inner radius)	100 mm
“Valley” (“hill”) gap	300(56) mm
Dee aperture at the centre and next	20(30) mm
Maximal dees voltage	80 kV
RF harmonic modes	2, 3, 4, 5, 6
Magnetic field operation range	0.8T÷1.8T
Extraction voltage of ion sources	≤ 22kV
Minimum width of acceleration gap	10 mm

According to the working diagram the ranges of RF harmonic modes intersect. So the same ion beam can be accelerated at different harmonic modes. The optimisation of the cyclotron centre region is carried out with CASINO, CENTR [1, 2, 3] and Relax3D computer codes. For beams dynamics calculation the 3D calculated magnetic field maps are used.

SPIRAL INFLECTORS

The limitation of the voltage of the axial injection and the wide range of the main magnetic field level leads to using three spiral inflectors with different magnetic radii R_m . These inflectors are used at the operation modes “A”, “B” and “C”. The main parameters of the inflectors are presented in Table 2.

Table 2: Spiral Inflectors for U400R Cyclotron

Mode	RF harmonic	R_m	A_e	Aperture	k'
A	2, 3	30 mm	35 mm	12 mm	0
B	3	39 mm	35 mm	12 mm	0
C	4, 5, 6	47 mm	35 mm	12 mm	0

The distance between the centre plugs and the possible dimension for the inflector box define the inflector geometric parameters, the inflector height A_e and aperture. The “A” and “B” mode inflectors transmit the beams at the 1st dee direction, Fig. 2. The “C” mode inflector transmits the beams at the 2nd dee direction, Fig. 6. To change the cyclotron operation mode the inflector exchange system is used. This system moves the inflector radially through the sluice at the side of the cyclotron vacuum chamber. The inflector exchange system provides the operative adjustment of the inflector position by rotation around z-axis at the angle $\pm 8^\circ$ and moving along R-direction ± 2 mm. The inflectors are shielded from RF at the central region by stationary placed ground box.

CENTRE REGION

The centre region of U400R cyclotron has to be optimized for the operating modes with the different RF harmonics modes from 2nd up to 6th. For design purpose the typical ion beams for different RF harmonics modes were chosen. At the calculations the aperture of the both dee pullers 20 mm and width of acceleration gaps 10mm were taken.

Table 3: The Typical Ion Beams

A/Z	Bo [T]	RF harmonic	U_{inj} [kV]	R_{start} [mm]	
$^4\text{He}^{1+}$	4	1.8	2	24	51
$^{48}\text{Ca}^{7+}$	6.86	1.5	3	24	62
$^{48}\text{Ca}^{5+}$	9.6	1.3	5	19	82

“A” and “B” modes, 2 and 3 RF harmonics

The “A” and “B” operation modes are intended to inject and accelerate the ion beams at 2 and 3 RF harmonics. The first accelerating gap for these modes is placed at the 1st dee, Fig. 2. From the calculations it was found that the optimal angle of the first gap position for both modes is 35° from the dee axes. The modes have different starting radii at the first accelerating gap.

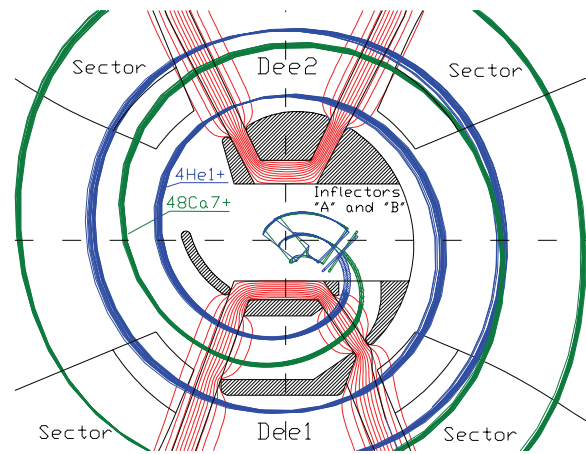


Figure 2: The first orbits of $^4\text{He}^{1+}$ and $^{48}\text{Ca}^{7+}$ ion beams at 2 and 3 RF harmonics respectively. In the figure “A” and “B” operation modes are combined.

For “A” operation mode the optimal starting radius is $R_{str}=51\text{mm}$, for “B” operation mode - $R_{str}=62$ mm. The test $^4\text{He}^{1+}$ ion beam, “A” operation mode, has a minimal increment of the radius and limits the centre dimension. In Figs. 3 and 4 the $^4\text{He}^{1+}$ ion beam emittance and the cyclotron radial and vertical acceptances for different initial phases are presented. The radial acceptance presents limitations of no more than 5 mm in centering the first one of the 5 beam orbits. In Fig. 3 the line of central particle position presents the possible displacement of radial emittance while inflector is rotated around z-axis. The changing of dee voltage up to 80 kV allows to tune radial acceptance position on RR’ plane.

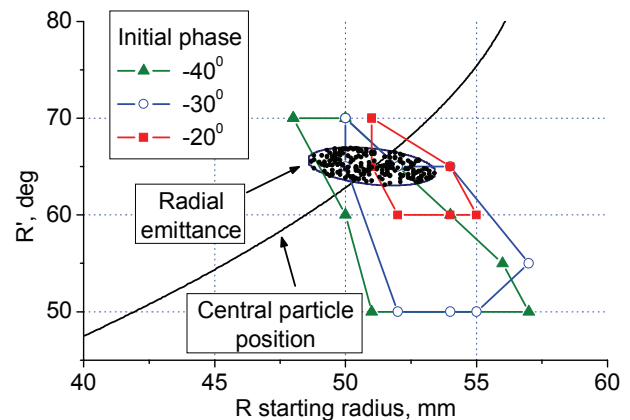


Figure 3: “A” operation mode. The cyclotron radial acceptance and $^4\text{He}^{1+}$ ions beam emittance.

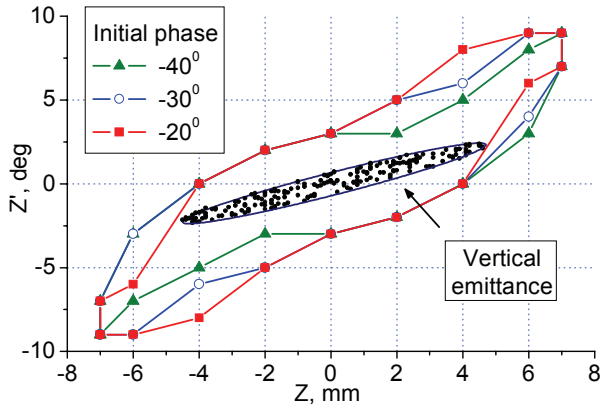


Figure 4: “A” operation mode. The cyclotron vertical acceptance and $^4\text{He}^{1+}$ ions beam emittance.

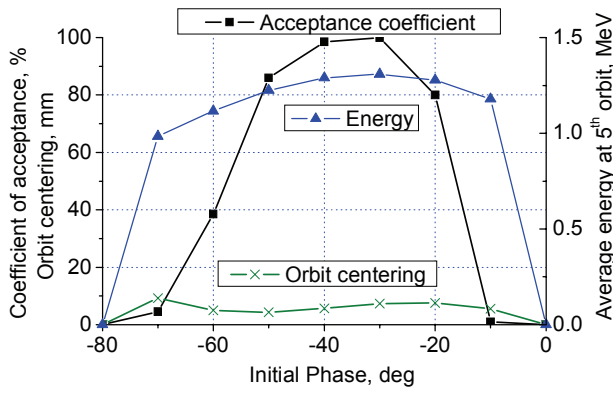


Figure 5: The efficiency, orbit centring and average energy of $^4\text{He}^{1+}$ ion beam at the central region.

The efficiency of $^4\text{He}^{1+}$ ion beam acceleration at the central region, for first five orbits, is presented in Fig. 5. The phase range of the effective acceptance into acceleration is about 50° . The calculation of test $^{48}\text{Ca}^{7+}$ ion beam of “B” operation mode has the similar results.

“C” mode, 4, 5 and 6 RF harmonics

The “C” operation mode combines the acceleration at 4, 5 and 6 RF harmonics and uses one spiral inflector with magnetic radius $R_m=47$ mm. A compromise angle position of the first accelerating gap is 25° from the dee axes was found. The beams of the “C” operation mode start into acceleration at the radius about 82 mm, Fig. 7. The “C” operation mode radial acceptance in Fig. 7 presents limitations of no more than 10 mm in centering the first one of the 5 beam orbits.

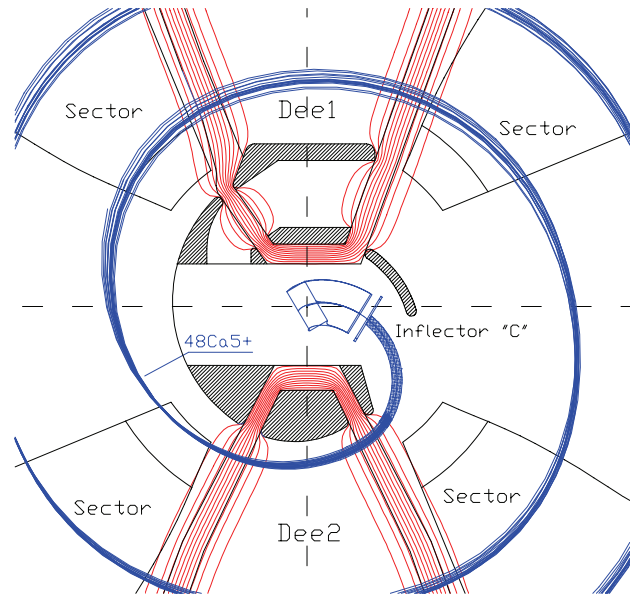


Figure 6: The first orbits trajectories of $^{48}\text{Ca}^{5+}$ ion beam at 5 RF harmonics, “C” operation mode.

The trajectories of ion beams, accelerated from 1st dee, prevent to place pillars to form first accelerating gap of the 2nd dee. That leads to RF field penetration inside the dummy-dee, and to increasing the gap effective length. As a result the acceptance efficiency a highest, 5 and 6 RF harmonics is decreased. The optimal angle positions of the first gap and the special form of the inflector box allow to minimize the action of RF deceleration phase on the sides of accelerating gap, Fig. 8, and provide the cyclotron acceptance with high efficiency.

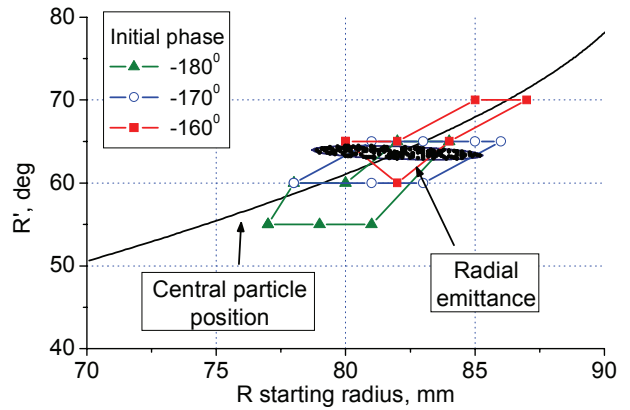


Figure 7: “C” operation mode. Radial acceptance and optimal position of the $^{48}\text{Ca}^{5+}$ ion beam emittance.

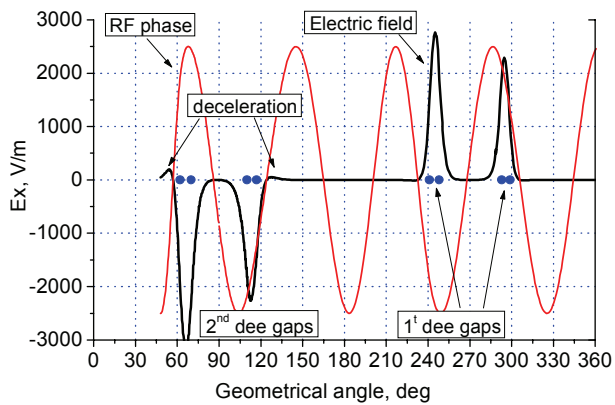


Figure 8: The RF phase and azimuth component of electric field acted on $^{48}\text{Ca}^{5+}$ central ion.

CONCLUSION

The design of the centre region of U400R multi-purpose cyclotron is carried out. The cyclotron operating modes are separated in three groups with different spiral deflectors and RF harmonic modes. The concept of

acceleration from the both 1st and 2nd dees let us to optimize the angular position of the first accelerating gap for 2 and 3 harmonic modes and for 4, 5 and 6 harmonic modes separately and use the stationary placed central region geometry. To change the cyclotron operation modes one needs only to exchange the spiral deflector.

REFERENCES

- [1] I. Ivanenko, "The central region of the U-400 cyclotron. The calculation of the accelerating beam dynamics for the first orbits after injection," 15th Conference on Cyclotrons, June 1998 France, p. 544.
- [2] I. Ivanenko, et. al., "The compensation of beam vertical defocusing after the spiral deflector by using passive magnetic channel," EPAC'2000, Vienna, June 2000, p. 1504.
- [3] G. Gulbekian, I. Ivanenko, "Beam injection and first orbits at 2 to 6 RF harmonic modes at the central region of DC-72 cyclotron" 17th Conference on Cyclotrons, October 2004, Tokyo, p. 459.

EXTRACTION BY STRIPPING OF HEAVY ION BEAMS FROM CYCLOTRONS

G.G. Gulbekyan, O.N. Borisov, V.I. Kazacha

Joint Institute for Nuclear Research, Dubna, Moscow region, Russia

Abstract

Accelerated heavy ions get a charge spectrum on passing a thin target. The charge dispersion and its maximum depend on the ion type, its energy, material, and the foil thickness. Change of the ion charge leads to change of the ion magnetic rigidity. Heavy ion beam extraction from the AVF cyclotrons by stripping in the thin targets is based on loss of the radial stability of the accelerated beam after its magnetic rigidity change. Property data of carbon foils used for the heavy ion beam extraction by stripping are given. Experience of using heavy ion beam extraction from the AVF cyclotrons of FLNR (Dubna) by stripping is considered.

INTRODUCTION

The method of heavy ion beam extraction from AVF cyclotrons was suggested in [1]. The sharp charge change of a heavy ion accelerated in the cyclotron when passing a thin target is the heart of this method. For that not completely stripped ions must be accelerated. As a result the charge and correspondingly magnetic rigidity of the ion change. And its orbit sharply differs from the closed one. Under correct radial and azimuthal position of the foil the ion orbit after the stripping can have a radial instability and the ion beam is extracted from the accelerator chamber practically freely. At FLNR the method of extraction of the accelerated heavy ions from AVF cyclotrons through the stripping foils is used as basic one in U200, U400, U400M cyclotrons.

The necessary thickness of the stripping foil is defined in the main by the accelerated ion velocity. The foil lifetime under low ion intensities depends on the dose density, ion type, and its energy. At very high power losses the foil lifetime is defined by thermal sublimation of the foil material. On the other hand, the stripping process has action upon the extracted beam.

The extraction efficiency of all charges after stripping almost always is close to 100%. The extraction efficiency of a separate charge from the spectrum amounts from 20 up to 100%.

The magnetic structure of AVF cyclotron affects on the possibility of the stripping method utilization. Evaluations of limits of the stripping method utilization for different magnetic structures are given below.

HEAVY ION EXTRACTION BY STRIPPING FROM AVF CYCLOTRONS OF FLNR

The method of heavy ion extraction from AVF cyclotrons suggested in [1] supposed placing the foil near

the valley-hill border. After stripping the ion orbit is in the region of one period of the cyclotron magnetic structure, that is the high magnetic field level between the sectors and low magnetic field level in the valley. Because of this the reference particle orbit has a strong radial drift with a step $(0.2 - 0.3) R_{ext}$ and the beam is extracted out of the cyclotron chamber.

The extraction method by stripping with utilization of only one magnetic structure period we identify as the method 1 (M1). For the first time method M1 was used at FLNR in the cyclotron U200 for extraction of ${}^2D^{1+}$, ${}^4He^{1+}$, ${}^{12}C^{3+}$, ${}^{16}O^{4+}$ beams with the extraction efficiency about 100%. The cyclotron U200 has the structure of four 45° sectors without spiralling with flatter equal to 0.1.

The U400 cyclotron weighing about 2000 ton has the maximum energy factor of 625. It has the mean magnetic field of 1.9 – 2.1 T and the flatter of four sector magnetic structure without spiralling equal to 0.1.

The energy range of the accelerated and extracted ion beams is from 3 up to 20 MeV/amu. Extraction by the stripping method 1 is the basic one for this cyclotron. We name the ratio Z_2/Z_1 (the ion charge after and before stripping) as the stripping coefficient.

One uses only one, two and three-turn beam extraction with stripping coefficient from 2.5 up to 4.5. The beam tuning is carried on in the center of the horizontal correcting magnet at the beam line input.

The extraction efficiency for sum of all charges is close to 100%. The extraction efficiency of a single charge corresponds to the charge dispersion after stripping. Parameters of U400 cyclotron extraction system for some ion beams are given in Table 1.

Table 1. U400 Beam Parameters of some Accelerated and Extracted Ions

Ion	W MeV/Amu	Z_1	Z_2	Z_2/Z_1	EXT _{eff} %	I _{target} pμA
7Li	8.6	1	3	3	100%	10
${}^{12}C$	16.6	2	6	3	95%	6
${}^{40}Ar$	5.1	4	16	4	50%	2
${}^{48}Ca$	5.2	5	18	3,6	45%	1,5
${}^{136}Xe$	5.3	15	42	2,8	25%	0,1

The example of two-turn extraction from U400 cyclotron for the ${}^{84}Kr$ ion beam spectrum is given in Fig. 1. One can see the angle and space dispersion of the beams at the accelerator output.

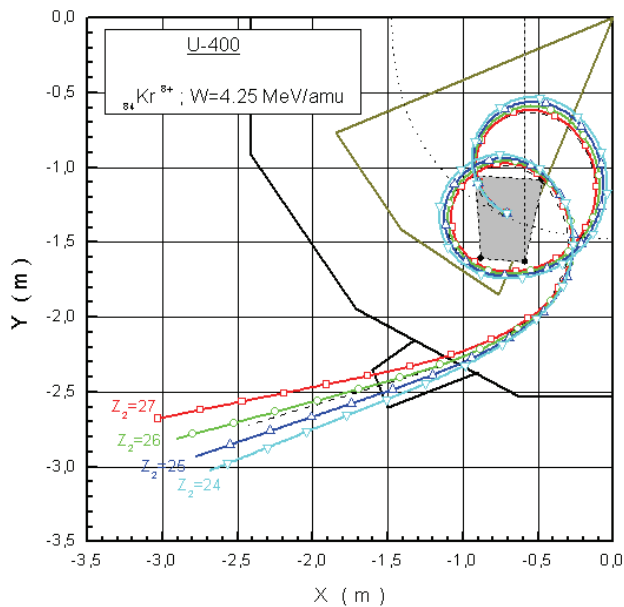


Figure 1: Two-turn extraction from U400 cyclotron.

This dispersion can be used for creation of a multichannel system for the ion beam lines or for irradiation of the large-format targets. The vertical dimension Δz of the extracted beam after stripping inside the cyclotron is less than 25 mm. The beam dimension at the distance of 1 m from the pole is $\Delta z \times \Delta x = 15 \times 50 \text{ mm}^2$.

Utilization of one, two and three-turn extraction allows one to vary the energy of the extracted beams gradually with the step of about 30% not changing the mode of operation of U400 cyclotron itself. The energy microadjust is made within the limits of 10% by little radial and azimuthal movements of the foil.

U400M cyclotron weighing about 2300 tons and having the pole diameter of 4 m was designed for the ion acceleration with energies from 4 up to 100 MeV/amu. The magnetic structure has four sectors with spiralling of 42° and flatter from 0.08 up to 0.12. The maximum energy factor is equal to 550. The light ions ${}^7\text{Li}^{2+}$, ${}^{11}\text{B}^{3+}$, ${}^{15}\text{N}^{5+}$ having energies from 35 up to 50 MeV/amu are accelerated most frequently for production of secondary radioactive nuclei. The stripping method is also used for extraction of such accelerated beams. But the stripping coefficient of such ion type is from 1.35 up to 2. The orbits of such ions after stripping go around the center of U400M cyclotron. There is no evident explanation of the reason of the closed orbit radial instability after stripping. We name this extraction method by stripping as a method 2 (M2).

The reference particle trajectories of the ions extracted from U400M cyclotron are shown in Fig. 2. The reference particle trajectory tuning at the matching point is made by little radial and azimuthal movements of the foil. In order to compensate the defocusing action of the stray magnetic field one uses two passive magnetic channels.

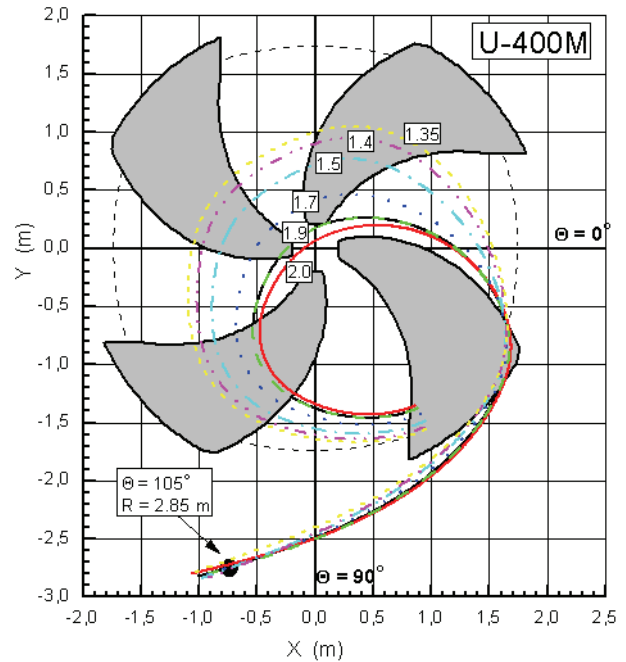


Figure 2: Reference particle trajectories of the ions extracted from U400M cyclotron by method 2.

The axial beam dimension Δz after stripping is less than 30 mm inside the accelerator.

Parameters of some ion beams extracted from U400M cyclotron by stripping method 2 are given in Table 2.

Table 2: U400M Beam Parameters of some Accelerated and Extracted Ions

Ion	W MeV/Amu	Z ₁	Z ₂	Z ₂ /Z ₁	EXT _{eff} %	I _{target} pμA
${}^7\text{Li}$	35	2	3	1.50	100	10
${}^{11}\text{B}$	32	3	5	1.66	100	10
${}^{15}\text{N}$	50	5	7	1.40	95	2
${}^{20}\text{Ne}$	43	7	10	1.43	90	1.5
${}^{40}\text{Ar}$	40	13	18	1.38	70	0.1

Trajectories of the low energy ion beams extracted from U400M cyclotron by method 1 are shown in Fig. 3. Tuning at the matching point (bending magnet) is carried out by changing the foil radius.

A combined extraction system for positive and negative (${}^1\text{H}^+$, ${}^2\text{D}^+$) ions was created for DC72 cyclotron. The reference particle trajectories are shown in Fig. 4.

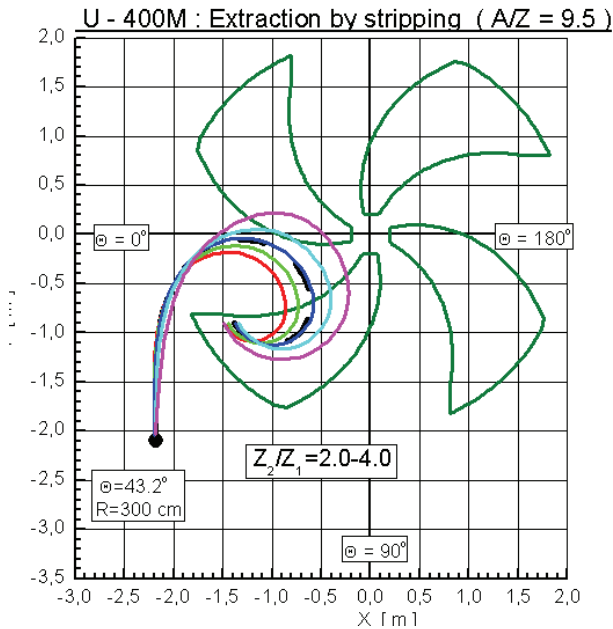


Figure 3: Trajectories of the low energy ion beams extracted from U400M cyclotron by method 1.

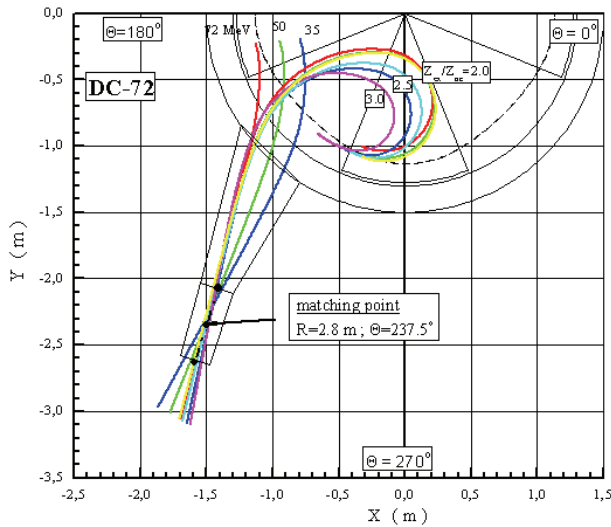


Figure 4: Reference particle trajectories of the ions extracted from DC72 cyclotron.

STRIPPING FOILS

The foils made of Be, C, Al, Al₂O₃, and mylar can be used as the stripping foils.

Choice of the foil material depends on its serviceability, lifetime, and limitation of the foil influence on the beam quality after its stripping. Beryllium would be the best material (maximum charge after stripping under smallest charge dispersion, additional angle scattering, and additional energy spread) but this material is toxic. It is convenient to work with Al and mylar but only when the beams have the high energies and small intensities. We have an experience of work with foils made of C, Al, Al₂O₃, and mylar. In practice the foils made of carbon have the best properties.

Circular Accelerators

For every accelerated ion there is so called “equilibrium thickness” of the foil at which increasing the charge distribution does not change [2]. We use the following formula for evaluation of the foil equilibrium thickness in wide energy range

$$X_{\infty} [\mu\text{g} \cdot \text{cm}^{-2}] \approx 30 \cdot W^{0.6} [\text{MeV}/\text{amu}] \quad (1)$$

Dependence of the ion stripping degree on the ion energy is shown in Fig. 5.

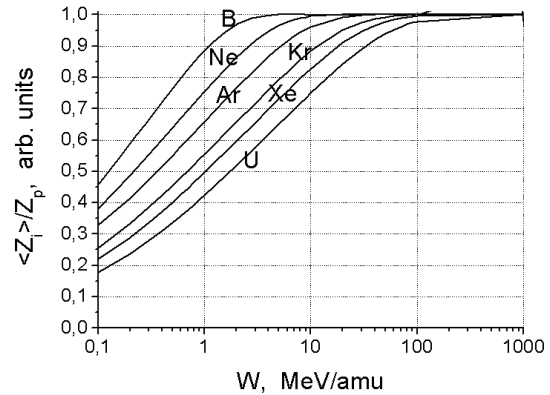


Figure 5: Dependence of the ion stripping degree on the ion energy.

The extraction efficiency by stripping of one charge from the spectrum is defined by the charge dispersion [3].

Dependence of the maximum efficiency of a single charge extraction by stripping versus the ion beam energy is shown in Fig. 6. Here I_{max} is the current of the ions with maximum charge and I_{in} is the common ion current.

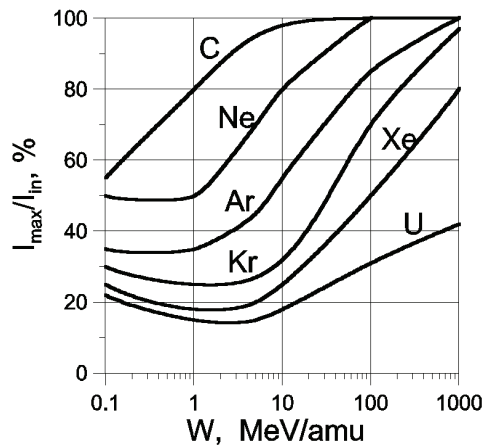


Figure 6: Maximum efficiency of a single charge extraction by stripping.

The ion scattering in the stripping foil causes the growth of the beam emittance (Fig. 7) [4].

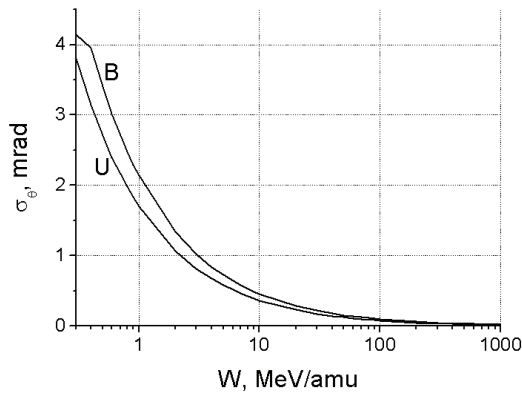


Figure 7: Dependence of the scattering angles for B and U in the carbon foils having the equilibrium thickness.

The stripping foil inserts an additional energy spread in the extracted beam (Fig. 8) [2].

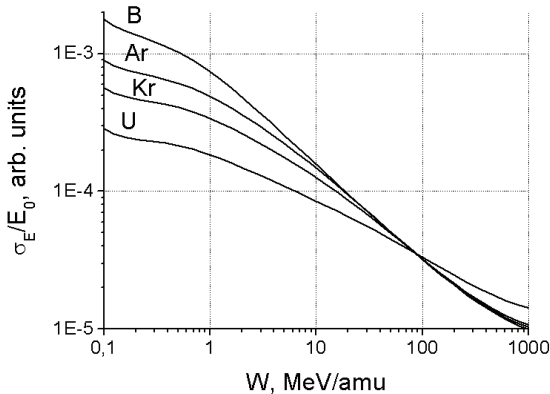


Figure 8: Dependence of the additional energy spread in the extracted beam.

The angle scattering and energy spread in a stripping foil may have a vital importance for cyclotrons with spectroscopic beams.

In evaluations of the carbon foil lifetime one should emphasize above all their radiation damage. Estimation of the foil lifetime is given below:

$$T[\text{hours}] \approx (3 \div 6) \cdot 10^3 \frac{W \left[\frac{\text{MeV}}{\text{amu}} \right]}{Zp^2 \cdot j \left[\frac{\mu\text{A}}{\text{cm}^2} \right]} \quad (2)$$

Here Z_p is the ion element number, W is the ion energy, and j is the beam current density. For B and U beams difference in the radiation lifetime of the foil amounts about 1000 under equal value of W and j .

The technology of foil production has a strong action on the foil lifetime. The pure amorphous or diamond-like foils are the best ones. Contamination, for example by hydrogen, drastically decreases the foil lifetime [5].

Circular Accelerators

Usually the stripping foil intended for the beam extraction is glued on a small frame made of Al, C or Cu.

One internal edge of the foil is free. The frame with the foil is placed on the head of locked probe with radial and azimuthal movement of the head. The probe head may have water cooling, or temperature control or some control of the foil itself. Usually accuracy of the foil positioning is at the level of 0.1 mm.

The energy losses of ions in the foil to a certain degree do not affect on its lifetime. Dissipation of the delivered power occurs actually only owing to the thermal radiation temperature rise. The power losses of the ion beam stripping in a foil versus the energy and type of ions are shown in Fig. 9.

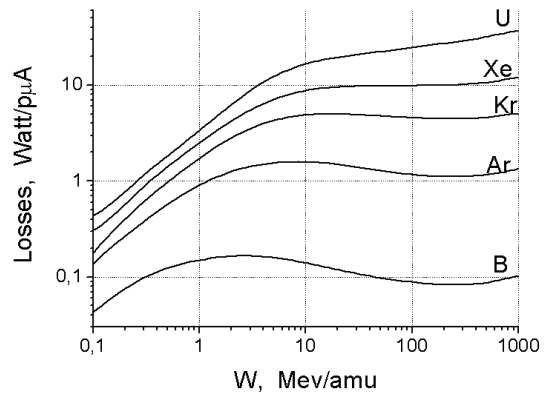


Figure 9: Power losses of the ion beam.

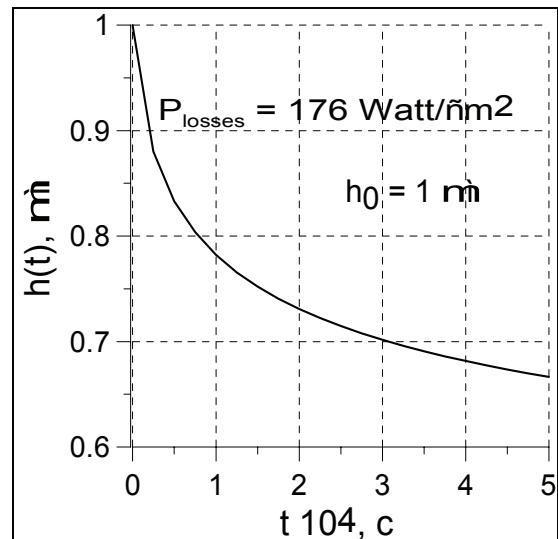


Figure 10: Evolutions of the carbon foil thickness.

In reality the beam density on the foil has some distribution. Evolution of the foil thickness by the beam having Gaussian distribution is shown in Fig. 11.

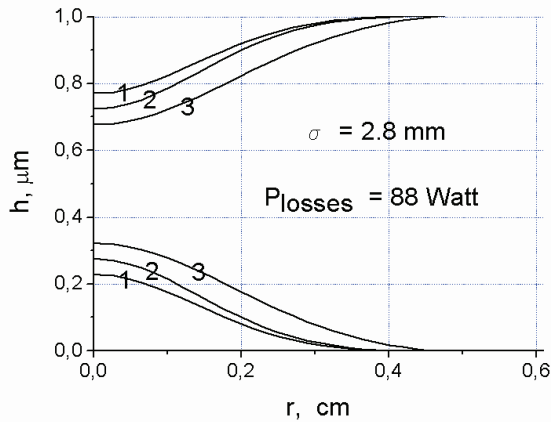


Figure 11: Curves 1, 2 and 3 correspond accordingly to the moment 100 c, 200 c and 2000 c after beginning of irradiation.

The power losses, foil temperature, and pressure of the carbon steam grow when the beam intensity increases. Sublimation of the carbon steam and decrease of the foil thickness intensively occurs. At that the foil thickness stabilizes at a new level (Fig. 10) [6].

As an additional result, the energy spread increases in the extracted beam. The radiation damages also bring to the same effect.

CONCLUSION

Extraction of the heavy ion beams by stripping from AVF cyclotrons is convenient in realization. The extraction efficiency of sum of the charges after stripping is about 100% and for a single charge it is from 20 up to 100% in dependence of the ion type and energy.

The stripping foil weekly affects on the extracting beam quality. The foil lifetime can be well estimated by the radiation damages. Under high power losses ($> 150 \text{ W/cm}^2$) sublimation of carbon defines the foil lifetime.

REFERENCES

- [1] G.N. Vialov, G.N. Flerov, Y.Tz. Oganessian, JINR Preprint 1884, Dubna, 1964.
- [2] E. Baron, IEEE Trans. on Nucl. Sc. 526, (1979), p. 2411.
- [3] V.S. Nikolaev and I.S. Dmitriev, Phys. Letters 28A, (1968), p. 277.
- [4] LISE (version 6.5.5) <http://dnr080.jinr.ru>
- [5] E.A. Koptelov, S.G. Lebedev, V.N. Panchenko, Nucl. Instr. Meth. B, v. 42 (1989), p. 239.
- [6] B.N. Gikal et al., JINR Communication P9-2005-110, Dubna, 2005.

GANIL HIGH INTENSITY TRANSPORT SAFETY SYSTEM

G. Sénécal, C. Jamet, T. André, P. Anger, J.L. Baelde,
 C. Doutressoulles, B. Ducoudret, E. Petit, E. Swartvagher
 GANIL, BP 55027, 14076 Caen Cedex, France

Abstract

In order to provide several kilowatt stable ion beams for radioactive ion beam production, the Grand Accélérateur National d'Ions Lourds (GANIL, Figure 1) upgraded several devices [1]. A High Intensity Transport (THI) safety system has also been studied in 1995 and validated in 1998. By monitoring beam losses all along the cyclotrons and lines and shutting down the beam in case of problem, this system allows accelerating and sending onto targets up to 6kW power beams (instead of 400W in standard mode). Beam losses diagnostics, the associated electronics and software will be depicted (principle, location) as well as the tuning method of the machine to reach step by step the needed power.



Figure 2: Beam loss detectors (examples).

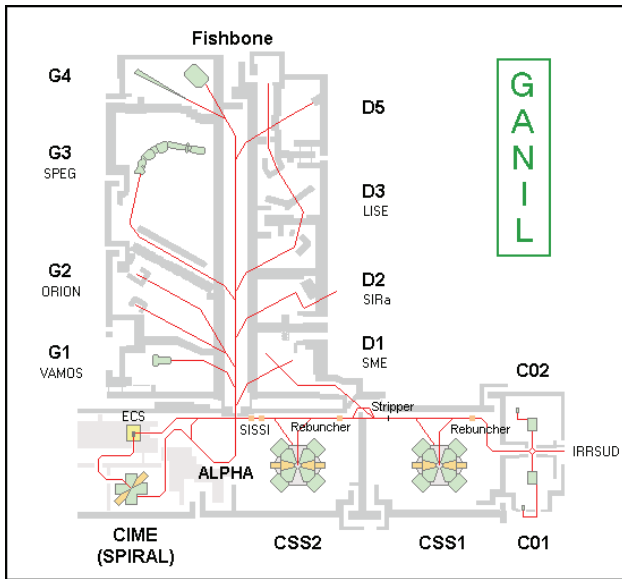


Figure 1: GANIL layout.

BEAM LOSS DIAGNOSTICS

There are two types of diagnostics to monitor beam losses. First of them are interceptive detectors like diaphragms or copper plate (Fig. 2) that measure the part of beam current lost on them. They are located at the input and output of dipoles as well as at the entrance of the inflectors and deflectors inside the cyclotrons. The location of these diagnostics all along the machine is represented in Figure 3.

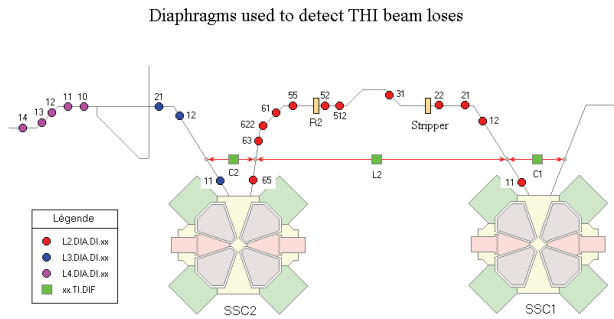


Figure 3: Diaphragm layout.

The second type of diagnostics used to monitor beam losses are alternative current transformer (ACCT, Figure 4). By measuring the beam current at the input and the output of a given section of the machine (cyclotron or beam line), we can determine the transport efficiency and the whole beam losses of the considered section. The differential current transformers layout is given on Figure 5.

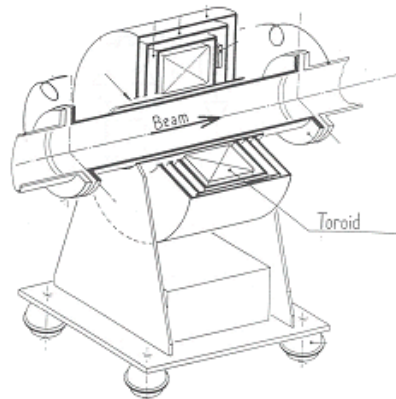


Figure 4: Current transformer.

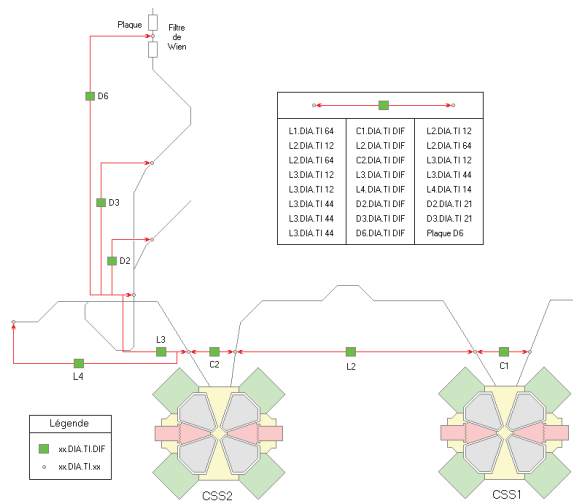


Figure 5: Differential transformers layout.

The two types of diagnostics are complementary. The diaphragms are dedicated to the protection of a given device (for example the vacuum chamber of a dipole). The differential current transformers have to be considered as a second level barrier that deals with all the losses that are not localised and detected on an interceptive detector (for example, the transport efficiency of a cyclotron may be poor without localised losses on the inflector or deflector).

SAFETY SYSTEM

The general layout of the THI safety system is given on Fig. 6.

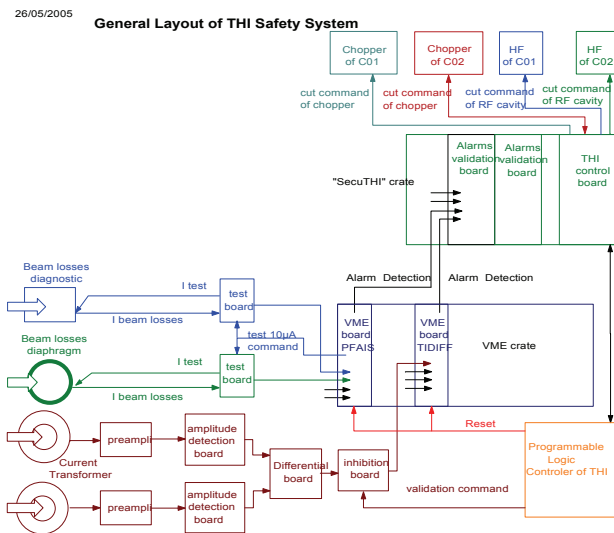


Figure 6: General layout of THI safety system.

The electrical current returned by interceptive diagnostics is measured on a VME board by logarithmic I/V converters, which generate a voltage proportional to the logarithm of the current. This voltage is digitised, compared to a threshold and numerically converted into a current. Each VME board (PFAIS) can deal with 4 diagnostics. In addition, interceptive beam diagnostics are

connected to the test boards which are able to inject a test signal (10µAe) through the diagnostics and filter the return signal. The test process can be remotely controlled by software.

The signals generated by the ACCT are sent through a differential board to a VME board (TIDIFF) which digitises, compares to a threshold and numerically converts to a current.

Each measurement channel of a VME board will generate an alarm signal if the measured current goes over the defined threshold. Depending on the tuning modes, which will be described in the following, the alarm will be taken (or not) into account and the beam intensity will be reduced by setting a chopper on, located in the very low energy line (<1 MeV/A), to a security value. The time response is about 20 ms. In case of a chopper failure, the RF of the C0 injector is shut down. In order to increase the availability of the beam, the safety system allows up to 3 triggers within a 10 s period before reducing the intensity.

TUNING MODE

Principle

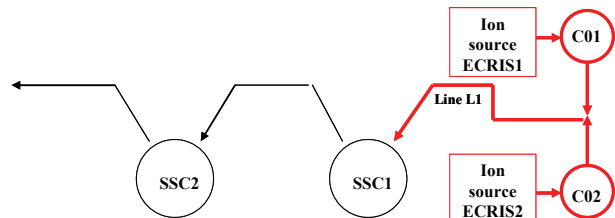
The tuning of the GANIL facility is based on a sequential method, from the ion source to the production target. This sequential tuning is done by keeping the beam power below 400 W at every stage of the machine. At this power level, there is no use of monitor beam losses because GANIL was designed for this value.

In order to take into account the space charge effects, it is also important to tune the cyclotrons and the lines at the crest intensity level that corresponds to the maximum power. That is the reason why we will use a chopper to reduce the mean intensity instead of a pepper pot.

The three following tuning modes have been defined:

Injector Mode

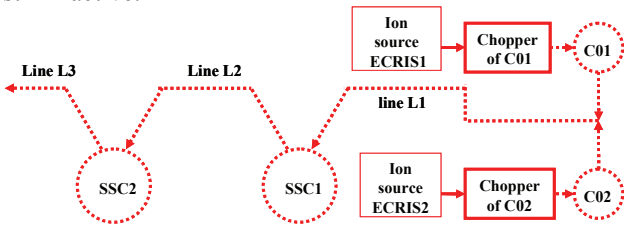
This mode is used to tune the ion beam up to the injection of SSC1. The source is tuned to provide the maximum intensity level needed at the end of the acceleration process. Up to the input of the SSC1, the beam energy is so low that the power cannot exceed 400 W even at the maximum intensity. At the end of this tuning phase, we are sure that the beam intensity available at the input of SSC1 will be high enough.



Tuning Mode

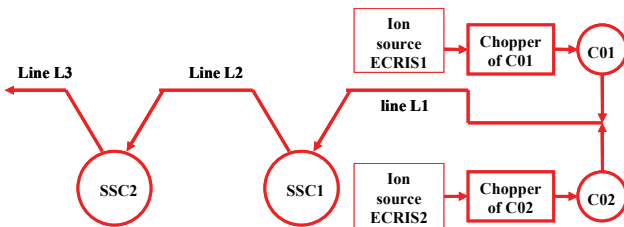
By using a chopper to reduce the mean beam intensity (equipment protection) and keeping the crest intensity identical (space charge limitation) a 400W beam can be

tuned overall the machine. The beam losses can be monitored to ease the tuning but the THI safety system is still inactive.



Watching Mode

The high power beam (up to 6 kW) is reached in this mode, step by step, by reducing the chopping rate and monitoring the beam losses. The alarm signals generated by the THI safety system are now taken into account and in case of overreaching the beam losses limits, the system automatically switches back to the tuning mode.



REMOTE CONTROL

Fig. 7 is a representation of the high level software available in the control room. Operators may choose the running mode (THI or normal) as well as the tuning mode (injector, tuning or watching). Beam intensity, beam power, cyclotrons and lines transport efficiency are displayed. The chopper rate can also be set by the software to reach step by step the maximum intensity.

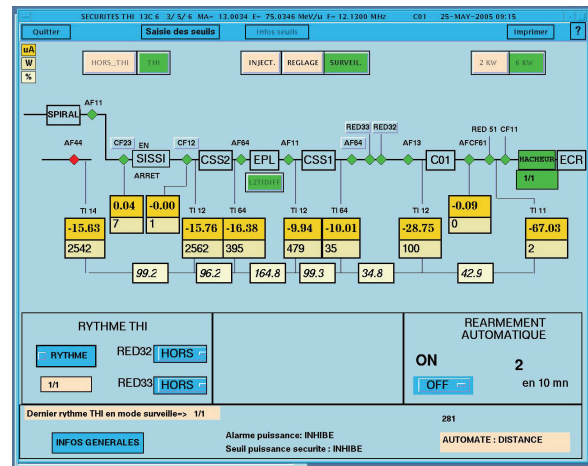


Figure 7: High level software.

CONCLUSIONS

Thanks to the THI safety system a ^{36}Ar (5 kW) for ^{36}Ar at 95 MeV/A has been successfully accelerated in 1998. For safety regulation considerations, the power of the beams sent onto production targets of SPIRAL1 facility has been limited to 3 kW. The ranges of accelerated beams as well as the RIB produced are presented in [2]. The ten years knowledge and experience of the accelerator team in the high intensity transport issue will be useful to extend the high intensity transport up to the target in the LISE experimental room, which is the room at GANIL dedicated to the fragmentation physics.

REFERENCES

[1] E. Baron et al., “High intensity heavy ion beams for exotic nuclei production at GANIL”, 16th Int. Conf. On Cyclotrons and their Applications. Michigan 2001

[2] F. Chautard et al., “Operation status of high intensity ion beams at GANIL”, HIAT 09 (TU07).

ELECTRON COOLING OF Pb⁵⁴⁺ IONS IN LEIR

G. Tranquille, CERN, Geneva, Switzerland

Abstract

Electron cooling is central in the preparation of dense bunches of lead beams for the LHC. Ion beam pulses from the Linac3 are transformed into short high-brightness bunches using multi-turn injection, cooling and accumulation in the Low Energy Ion Ring, LEIR. The LEIR cooler was the first of a new generation of coolers utilising high-perveance variable-density electron beams for the cooling and accumulation of heavy ion beams. It was commissioned in 2006 at the same time as the LEIR ring and has since been used to provide lead ions for the commissioning of the LHC injector chain.

We report briefly on the status of the LHC ion injector chain and present results of measurements made to check and to better understand the influence of the electron beam size, intensity and density profile on the cooling performance. Future plans to improve the performance of the device will also be presented.

IONS FOR LHC

The LHC physics program with heavy ion (lead-lead) collisions at luminosity of $10^{27} \text{ cm}^{-2}\text{s}^{-1}$ will be achieved by upgrading the ion injector chain: Linac3-LEIR-PS-SPS [1]. The main part of the modifications is the conversion of the Low Energy Antiproton Ring (LEAR) to a Low Energy Ion Ring (LEIR), which transforms long pulses from Linac3 to high-density bunches by a multi-turn injection and an accumulation with electron cooling. The conversion of LEIR included new magnets and power converters, high-current electron cooling system produced by INP Novosibirsk, broad-band RF cavities, upgraded beam diagnostics and vacuum equipment to achieve 10^{-12} mbar. The complete accelerator chain for LHC ion operation indicating the major hardware changes that have been made on the different machines is shown in Fig. 1.

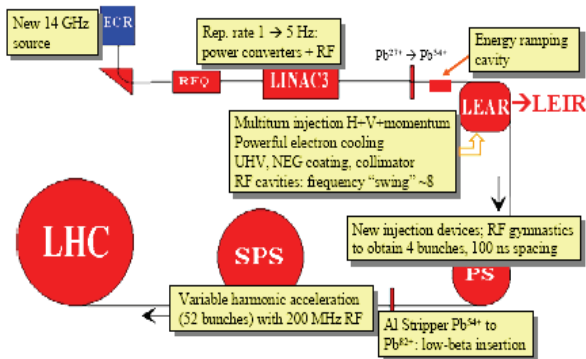


Figure 1: Hardware upgrades in the LHC injector chain.

In the nominal scheme, the injector chain will provide the LHC with 592 bunches of 9×10^7 ions in each ring. This beam may be subject to limitations in the injectors and also in the LHC. These effects are difficult to predict, so it has been decided to start with a beam whose characteristics allow the limitations to be explored with reduced risk. The “early beam” (Table 1) has a reduced number of bunches (60 per LHC ring with $1.35 \mu\text{s}$ bunch spacing) but with the same bunch intensity as in the nominal scheme, yielding a luminosity of $5 \times 10^{25} \text{ cm}^{-2}\text{s}^{-1}$. This beam will allow the study of fundamental limitations in the LHC rings without the risk of damaging the equipment and will also enable early physics discoveries.

Table 1: Beam Parameters along the Injection Chain for “early” LHC Ion Operation

	ECR Source	Linac 3	LEIR	PS	SPS	LHC
Output energy	2.5 KeV/n	4.2 MeV/n	72.2 MeV/n	5.9 GeV/n	177 GeV/n	2.76 TeV/n
²⁰⁸ Pb charge state	27+	27+ → 54+	54+	54+ → 82+	82+	82+
Output Bp [Tm]		2.28 → 1.14	4.80	86.7 → 57.1	1500	23350
number of bunches			1 (1/8 of PS)	1	4, 2	62/ring
ions/pulse ^{1,2}		$9 \cdot 10^8$	$1.15 \cdot 10^9$	$2.25 \cdot 10^8$	$1.2 \cdot 10^8$	$\leq 3.6 \cdot 10^8$
ions/LHC bunch		$9 \cdot 10^8$	$1.15 \cdot 10^9$	$2.25 \cdot 10^8$	$1.2 \cdot 10^8$	$9 \cdot 10^7$
bunch spacing [ns]					1350	1350
ϵ^* (nor. rms) [μm] ³	~0.10	0.25	0.7	1.0	1.2	1.5
ϵ (phys.rms) [μm] ³	50	2.5	1.75	0.14	0.0063	0.0005
Repetition time [s]		2.4	2.4	2.4	18	~5 fill/ring
total bunch length [ns]			200	3.9	1.65	1

¹ $200 \mu\text{A} \times 200 \mu\text{s}$ (Pb^{27+}) from ECR source, $50 \mu\text{A}$, $\times 200 \mu\text{s}$ (Pb^{54+}) from Linac3 after stripping

² Pessimistic assumptions on losses in LEIR. Optimistically LEIR can produce up to $4.5 \cdot 10^8$ Pb ions per cycle with a single Linac3 pulse.

³ Same physical emittance as protons. ϵ^* (normalized) = $\beta \gamma \epsilon$ (physical) invariant if no blow-up

Stripping foil

LEIR beam commissioning started in summer 2005 with a short run with oxygen ions. In 2006 lead ions were used to fully commission the machine and to start delivering beam to the PS ring. This confirmed the ability for LEIR to routinely produce the “early” ion beam for the LHC. 2007 was devoted to sending beam to the SPS and to initiate studies on the “nominal” beam. Unfortunately, the “nominal” LEIR beam has not yet been fully demonstrated; although sufficient intensity could be accumulated on the low energy plateau, the nominal intensity of 4.5×10^8 Pb⁵⁴⁺ ions per bunch was never attained due to losses at the beginning of the ramp. Understanding the reasons for this loss will be the main focus of investigations this year. The performance achieved for the “early” and “nominal” beams in LEIR is summarized in Table 2 and the LEIR cycle showing the evolution of beam intensity can be seen in Fig. 2.

Table 2: Performance of early and nominal LEIR Beams

	Early	Nominal
N [10^8 Pb ⁵⁴⁺ ions/bunch]	2.2	3.7
I [10^{10} charges/bunch]	1.2	2.0
ϵ^*_H [μm]	0.5	0.5
ϵ^*_V [μm]	0.2	0.2
$\epsilon_{//}$ [meVs/u]	40	50
τ_B [ns]	200	200

In the PS ring a number of RF issues were solved before the 2007 run such that the required intensity of 1.2×10^8 Pb⁸²⁺ ions per bunch could be delivered to the SPS. The sensitivity of the head amplifiers of the radial loop was increased by 6 dB curing the beam loss that occurred at the start of the accelerating ramp and a 30 dB attenuation was introduced in the synthesizer signal to reduce the crosstalk with the phase pick-up signal at injection energy.

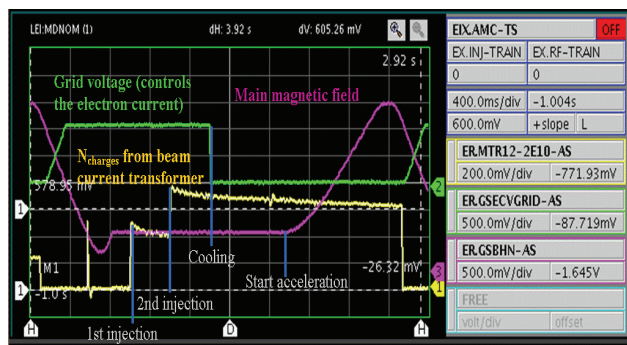


Figure 2: A standard 3.6 s LEIR cycle during which 2 LINAC pulses are cooled-stacked in 800 ms at an energy of 4.2 MeV/n. After bunching the Pb ions are accelerated to 72 MeV/n for extraction and transfer to the PS.

In addition a stand-alone frequency programme was implemented for the ion beam control as the system used for protons was too coarse resulting in the beam being shaken at each B-train pulse at low energy.

An accurate re-matching of the PS to SPS transfer line (TT2) was also necessary in order to take into account the change in the optical functions due to Coulomb scattering of the ions as they pass through the stripping foil.

Much time was devoted in the SPS to study the behaviour of bunches at the injection plateau. This is a source of concern for the “nominal” beam where the bunches will have to wait up to 40 seconds and will be subject to space-charge and intra-beam scattering. The measurements confirmed that, despite a space-charge detuning as high as $\Delta Q_{sc} = 0.092$, there is no transverse blow up of the beam over periods of the order of one minute. Up to 4 single bunch injections were performed into the SPS and they were accelerated to the 450 GeV/c/u flat top required to fill the LHC. After

optimisation of the tunes and the chromaticity, up to 81% transmission was achieved. A short session devoted to the extraction of the ion beam towards the LHC through the TT60 transfer channel was also performed at the end of the 2007 run. Transverse emittances were measured with secondary emission grids and were found to be in agreement with the expected values of 1.2 μm .

THE LEIR ELECTRON COOLER

The LEIR electron cooler (Fig. 3) is based on a design previously used for the construction by BINP of the two electron cooling devices for IMP Lanzhou in China. Taking into account recent improvements tested on various electron coolers during the last decade, it uses a high-perveance, variable-density gun followed by an adiabatic expansion provided by an additional solenoid.

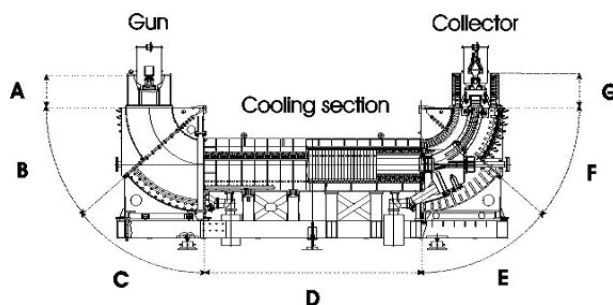


Figure 3: Schematic view of the LIER electron cooler.

The high perveance aims at providing an electron beam with a high density in order to decrease the cooling rate. However, increasing the electron density induces first an increase of the recombination rate (ions may capture an electron from the cooler and, finally be lost hitting the vacuum chamber), which is detrimental to the ion beam lifetime, and secondly increases the electron azimuthal drift velocity and thus increases the cooling time. For these reasons the electron gun has a “control electrode” used to vary the density distribution of the electron beam. In this manner the lifetime of the cooled ion beam will be increased by a reduction of the recombination rate of the ions with the electron beam. The electron beam profile is adjusted in such a way that the density at the centre where the stack sits is smaller and thus the recombination rate is reduced. At larger radii, the density is large and allows efficient cooling of the injected beam executing large betatron oscillations.

The cooling time is influenced by a number of machine and cooler parameters [2]. The electron current, I_e , and the relative angle difference between the ions and the electrons, θ , are two parameters that are easily accessible for experiments. The new electron gun also opens up the possibility to investigate the influence of the electron beam size and density profile on the cooling process.

ELECTRON GUN PERFORMANCE

The high perveance gun provides an intense electron beam in order to reduce the cooling time. However, with

the higher electron density an increase of the recombination rate (capture by the ion of an electron from the cooler) and the electron azimuthal drift velocity is observed. Increased recombination is detrimental to the ion beam lifetime and the larger drift velocity will lengthen the cooling time. To contrast the increase in electron-ion recombination, the electron gun has a “control electrode” used to vary the density distribution of the electron beam. The beam profile is adjusted in such a way that the density at the centre, where the cold stack sits, is smaller and thus the recombination rate is reduced. At larger radii, the density is large and allows efficient cooling of the injected beam executing large betatron oscillations.

Fig. 4 shows the measured electron beam intensity as a function of the control to grid voltage ratio. As the control electrode voltage is increased, the electron beam distribution changes from a parabolic beam ($V_{\text{cont}} < 0.2 V_{\text{grid}}$) to a completely hollow beam ($V_{\text{cont}} = V_{\text{grid}}$). The maximum design current is 600 mA but for the normal operation of the cooler only 200 mA is used.

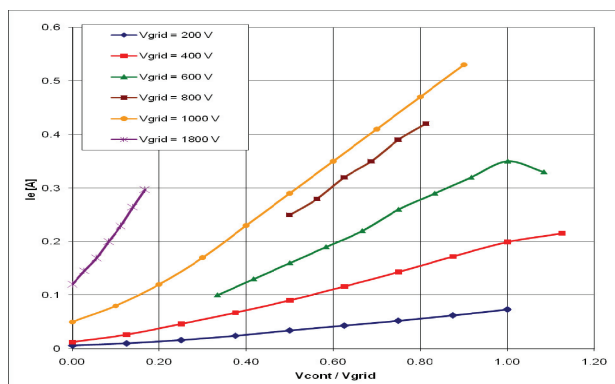


Figure 4: Electron beam current as a function of the ratio $V_{\text{cont}}/V_{\text{grid}}$, for an electron beam energy $E_e = 2.3$ keV.

EXPERIMENTAL SETUP

The cooling of ion beams was studied in parallel with the commissioning of the ions for LHC injector chain [3]. As it was difficult to obtain long cycles dedicated to electron cooling studies, most of our measurements were performed on the standard magnetic cycle lasting 2.4 or 3.6 seconds during which 2 to 5 linac pulses are cooled and stacked at 4.2 MeV/u. Schottky diagnostics, ionisation profile monitors (IPM) and the beam current transformer (BCT) were used to measure the phase-space cooling characteristics and to investigate the ion beam lifetime. The electron beam position was also measured during our measurements to ensure that the two beams were always correctly aligned [4].

COOLING EXPERIMENTS

The short duration of the injection plateau imposed that we used the momentum spread and the transverse beam size after 400 ms as the parameters to characterise the cooling performance. LEIR uses a multi-turn injection in all three planes and the injected beam has a transverse emittance of about $2.5 \mu\text{m}$ and a momentum spread of 4×10^{-3} . After cooling, the beam emittance is reduced by a factor of 10 and the longitudinal momentum is a few 10^{-4} .

Influence of Beam Expansion

The beam size can be varied by applying a stronger longitudinal field in the gun region. A maximum expansion factor, k , of 3 is available thus making it possible to vary the electron beam radius up to 24 mm. Fig. 5 shows the result of a series of measurements made for two electron beam distributions (uniform for $V_c/V_g = 0.2$ and hollow for $V_c/V_g = 0.5$) with similar currents (~ 150 mA) whilst varying k from 0.86 ($r = 13$ mm) to 2.57 ($r = 22.4$ mm).

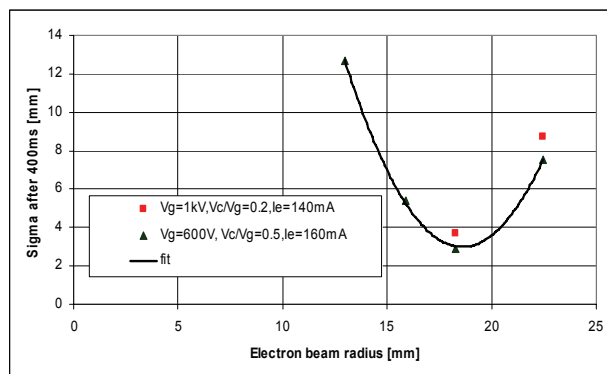


Figure 5: Beam size 400 ms after first injection as a function of the electron beam radius.

What one sees is that beam expansion becomes less useful when the electron beam radius is greater than 20 mm, roughly the size of the injected beam. Another phenomenon that was observed with larger electron beams is the relatively bad cooling of the first injected beam. In all our measurements, regardless of the number of injections, the first beam was never fully cooled to make space for another injection when the electron beam radius was greater than 20 mm. Subsequent injections were cooled to dimensions almost twice smaller than on the first injection.

Influence of the Electron Intensity and Density

As explained earlier, the electron beam intensity and density distribution can be varied by applying voltages to the grid and control electrodes. Roughly speaking, the grid determines the intensity whilst the control electrode changes the density distribution by enhancing the emission from the edge of the cathode.

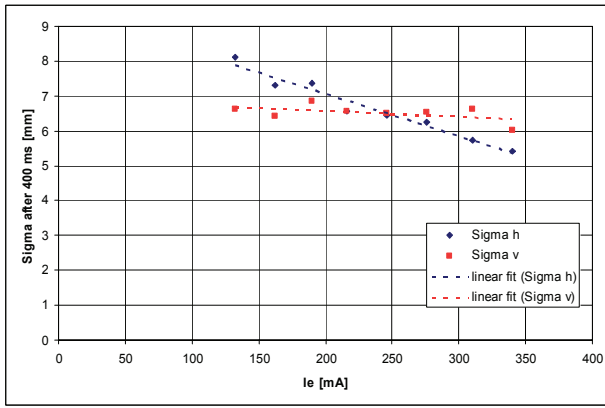


Figure 6: Ion beam size as a function of the electron cooler current ($V_{grid} = 1.1$ kV, $k = 2.57$, $r = 22.4$ mm).

A first set of measurements were made to confirm that the increase in electron current did improve the cooling efficiency. This is shown in Fig. 6 where the ion beam size is plotted as a function of the electron current with a fixed grid voltage of 1.1 kV. The decrease in the beam size as the current is increased is a clear sign of better cooling even though the effect was less pronounced in the vertical plane.

With the grid voltage fixed we were able to explore the influence of the electron beam distribution on the cooling performance by simply increasing the control voltage. Fig. 7 shows the result of one set of measurements where the grid voltage was held at 600 V and the control voltage was increased to 85% of the grid value. The beam size decreases as expected as the current is increased, but as the beam distribution becomes hollower the increase in electron current is no longer beneficial and the cooling is less efficient.

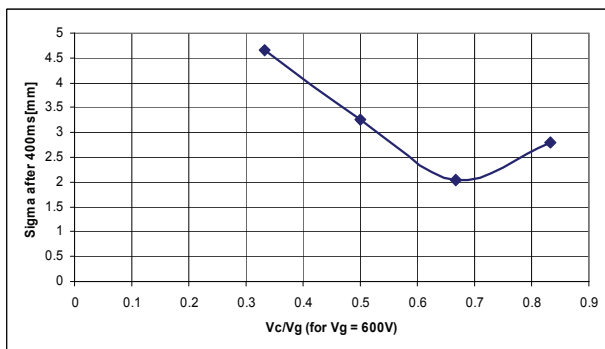


Figure 7: Beam size after 400 ms as a function of the electron beam distribution for a constant value of 600 V on the grid electrode ($k=1.7$, $r=18$ mm).

To further understand the influence of the density distribution, measurements were made where the electron current was kept constant and the density distribution modified. The results (see Fig. 8) clearly show that the determining parameter for obtaining small beam sizes is the electron current and not the density distribution.

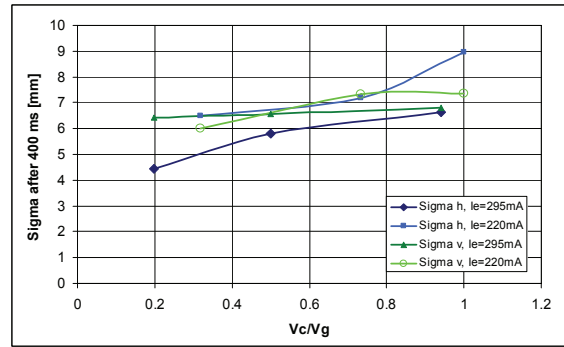


Figure 8: Ion beam size as a function of the density distribution for a constant electron current ($k = 2.57$, $r = 22.4$ mm).

Longitudinal Cooling

The momentum spread after 400 ms of cooling was measured using a down-mixed longitudinal Schottky signal captured with a fast ADC and treated mathematically to produce the spectral density distribution as a function of time. The results show the usual decreasing momentum spread as the electron current is increased.

The influence of the density distribution of the electron beam on the longitudinal cooling was also investigated. The Schottky spectrum was recorded during the cooling/stacking process for three electron density distributions. One sees, from the plots below, that the best cooling is obtained with a uniform electron beam density. As the electron beam becomes hollower the cooling time increases and fewer particles are dragged into the stack.

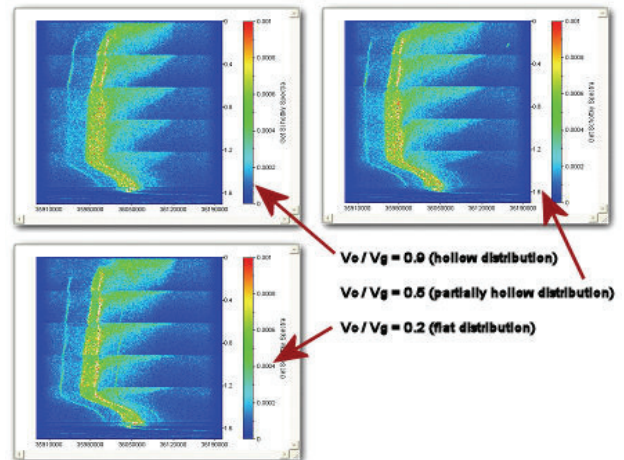


Figure 9: Evolution of the momentum spread during the cooling/stacking process with a constant electron current of 295 mA. The density distribution is changed from a flat distribution ($V_{cont}/V_{grid} = 0.2$) to a completely hollow one ($V_{cont}/V_{grid} = 0.9$).

LIFETIME STUDIES

In previous tests the maximum accumulated intensity was a factor 2 lower than that required for the nominal

LHC ion beam (1.2×10^9 ions). This was in part attributed to a short lifetime due to the recombination of ions with the cooling electrons and also to the limited electron current that could be obtained for effective cooling with the old electron gun.

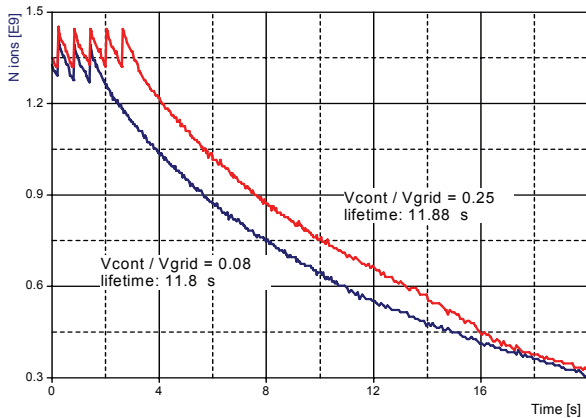


Figure 10: Beam lifetime for a parabolic (blue) and a slightly hollow (red) electron beam distribution.

In our measurements intensities well above 1.2×10^9 ions could easily be accumulated with an injection repetition rate of 1.6 Hz. If the repetition rate is increased, the maximum number of stacked ions decreases proportionally.

The lifetime of the cooled ion beam was measured by recording the evolution of the BCT signal as a function of time. Comparing for a parabolic and a hollow electron beam distribution (Fig. 10), we see that this parameter does not significantly influence the lifetime, indicating that recombination may not be after all the main cause of the short lifetime measured in the 1997 tests [5]. Other processes related to the vacuum conditions or the injection scheme could be more dominant.

A compilation of all our lifetime measurements for different intensities and density distributions is shown in Fig. 11. The slope of the curves gives the lifetime due to the electron beam whilst the intersection with the y-axis gives the vacuum lifetime. Compared with measurements made in 1997, a gain by a factor of 2 in the vacuum lifetime is observed but the lifetime due to the electron beam is only slightly improved and is not influenced by the electron beam distribution.

CONCLUSION

The LHC lead ions injector chain is ready to deliver the “early” beam as soon as it is required. The characteristics of this beam will enable the LHC to explore any limitations in the ring without the risk of damaging any equipment. Despite the lower luminosity, early physics discoveries will also be possible.

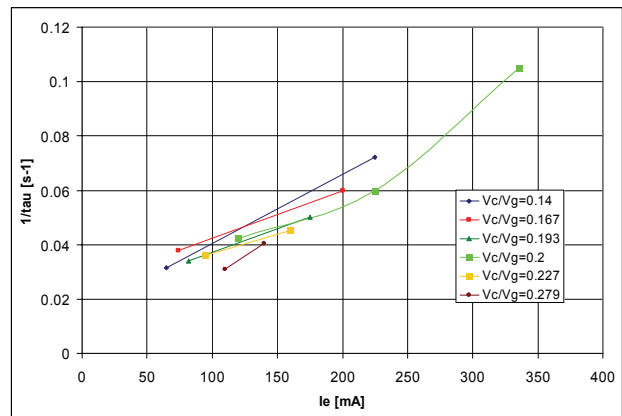


Figure 11: Inverse lifetime of Pb^{54+} ions as a function of electron current and density distribution.

Our cooling experiments on LEIR have shown that the main parameter that enhances the process is the electron beam current. Up to 600 mA of electron current can be obtained with the new gun, but the interplay between the electron beam size, density distribution and intensity is such that the best cooling is obtained with an electron beam having approximately the same size as the injected ion beam, a flat density distribution and an intensity less than 300 mA. It is clear that systematic measurements need to be continued and dedicated machine time is needed to explore the full potential of the device.

After a stop of nearly 18 months, the focus of the next lead ion run (which will start in July) will be the generation of the “nominal” beam for the LHC. In parallel the cooling process will be further investigated in order to optimise the lead ion beam characteristics in LEIR. In particular, it may be necessary to introduce a variation in the electron beam size during the cooling/stacking cycle. This has the potential to obtain faster cooling rates, thus enhancing the total number of ions that can be accumulated.

REFERENCES

- [1] S. Maury et al, “Ions for LHC: Beam Physics and Engineer Challenges”, PAC05, Knoxville, Max 2005.
- [2] G. Tranquille, “Optimum Parameters for Electron Cooling”, COOL01, Bad Honnef, May 2001.
- [3] D. Manglunki et al, “Ions for LHC: Status of the Injector Chain”, APAC’07, Indore, January 2007.
- [4] G. Tranquille et al, “Cooled Beam Diagnostics on LEIR”, EPAC08, Genoa, June 2008.
- [5] J. Bossler et al, “The Production of Dense Lead ion Beams for the CERN LHC”, NIM Phys. Res., A 441(2000) 60-3.

APPROACH TO 2 DIMENSIONAL LASER COOLING AND ITS OPTICAL OBSERVATION SYSTEM*

A. Noda[#], M. Nakao, H. Souda, H. Tongu, ICR, Kyoto University, Uji-city, Kyoto, 611-0011 Japan
 K. Jimbo, IAE, Kyoto University, Uji-city, Kyoto, 611-0011 Japan
 T. Shirai, NIRS, Chiba-city, Chiba, 263-8555, Japan
 M. Grieser, MPI-K, D-69029, Heidelberg, Germany
 A. Smirnov, JINR, Dubna, 141980 Moscow Region, Russia

Abstract

Laser cooling for bunched Mg ion beam with the kinetic energy of 40 keV has been applied with S-LSR at ICR, Kyoto University. Up to now, clear peaking of equilibrium momentum spread after laser cooling has been observed at such a synchrotron tune as resonates with the horizontal betatron tune, which is considered to be due to heat transfer from the horizontal degree of freedom to the longitudinal one. In order to demonstrate transverse cooling by observation of reduction of the horizontal beam size, spontaneous emission from laser induced excited state of the Mg ion, has been observed with the use of CCD camera. Some reduction of horizontal beam size has been observed with a certain synchrotron tune, a little bit smaller compared with the fractional part of the horizontal tune.

OUTLINE OF S-LSR

S-LSR is an ion storage and cooler ring, where electron beam cooling of 7 MeV proton and laser cooling of 40 keV $^{24}\text{Mg}^+$ ion beam have been applied to realize a ultra-low temperature beam. Its circumference and radius of curvature are 22.557 m and 3.57 m, respectively [1]. This ring is designed with a super-periodicity of 6 in order to enable an operation satisfying the so-called ‘‘maintenance condition’’ of beam envelope [2]. In addition, S-LSR has special characteristics to suppress shear heating as described below. In Figs. 1 and 2, the layout of S-LSR and an overall view of S-LSR are shown.

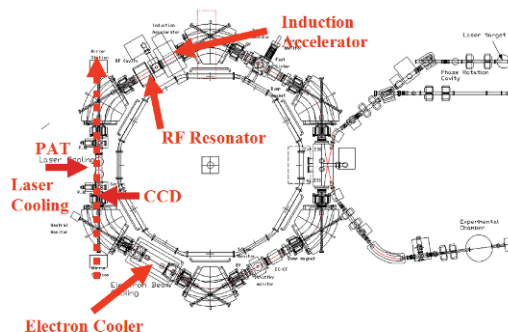


Figure 1: Layout of S-LSR.

*The present work was supported by Advanced Compact Accelerator Development program by MEXT of Japanese Government. Support from Global COE, The Next Generation of Physics, is also greatly appreciated.

[#]noda@kyticr.kuicr.kyoto-u.ac.jp

Circular Accelerators

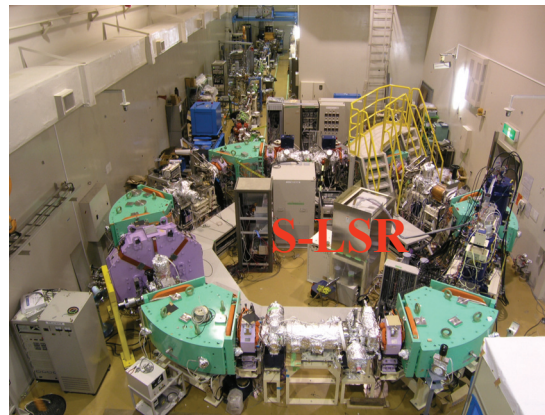


Figure 2: Overall view of S-LSR.

Special Feature of S-LSR Lattice with Use of Electrostatic Deflectors in Dipole Magnets

For the purpose of suppressing a shear heating, we have proposed a doubly achromatic ring lattice with a simultaneous use of an electrostatic field in each dipole magnet as illustrated in Fig. 3 [5, 6].

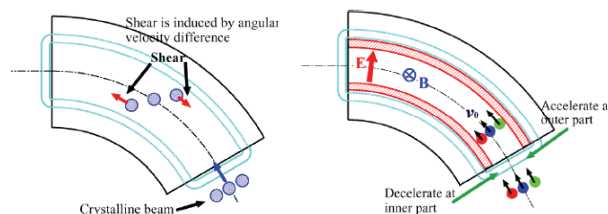


Figure 3: Scheme for suppression of a shear heating with the use of electrostatic field together with a dipole magnetic field.

The orbit dispersions in an electric and magnetic fields are given by the relations

$$\frac{d^2x}{ds^2} + \frac{3-n}{\rho^2}x = \frac{1}{\rho} \frac{\Delta W}{W} \quad (1)$$

and

$$\frac{d^2x}{ds^2} + \frac{1-n}{\rho^2}x = \frac{1}{\rho} \frac{\Delta p}{p} \quad (2)$$

respectively.

In a non-relativistic case where

$$\frac{\Delta W}{W} = 2 \frac{\Delta P}{P} \quad (3)$$

is satisfied, these orbit dispersions cancel out between each other if the following condition,

$$2\vec{E} = -(\vec{v} \times \vec{B}) \quad (4)$$

is satisfied by the electric, \vec{E} , and magnetic, \vec{B} , fields. In the case of the S-LSR lattice as shown in Fig. 1, each dipole magnet deflects the ion beam as much as 120° towards the inside while the electric field deflects it by 60° towards the outside, thus net 60° deflection to inner side is realized. Suppression of a shear heating is possible by realizing the same angular velocity accelerating or decelerating the ions with an electrostatic potential according to their radial positions.

Experimental Results so-far attained

Reflecting such a superiority of S-LSR as is optimized to stabilize ion beam dynamics, one dimensional ordering has been realized by an electron beam cooling with the beam number less than ~ 2000 for the first time for proton beam with 7 MeV as shown in Fig. 4 [3].

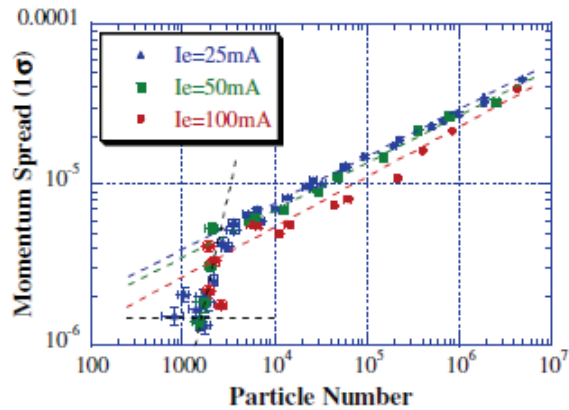


Figure 4: Phase transition to one dimensional ordered state by application of an electron beam cooling for 7 MeV proton at the particle number ~ 2000 .

The cooled proton temperature is ~ 2 K and ~ 12 K for longitudinal and transverse directions, respectively.

In order to extend the cooled beam temperature toward much lower region, application of laser cooling with much stronger cooling force is inevitable and a laser cooling has been applied for coasting beam of $^{24}\text{Mg}^+$ ion beam with a kinetic energy of 40 keV. In Fig. 5, a laser cooling system consisting of a solid state green laser, a ring dye laser and its second harmonics generator, is shown.

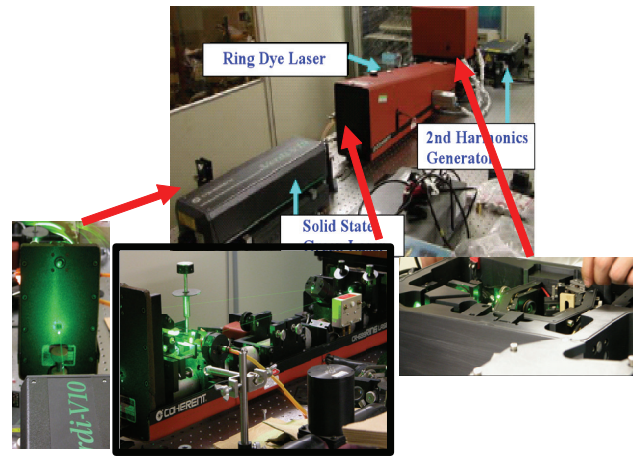


Figure 5: Laser cooling system for $^{24}\text{Mg}^+$ of 40 keV consisting of a solid green laser, a ring dye laser and the second harmonics generator.

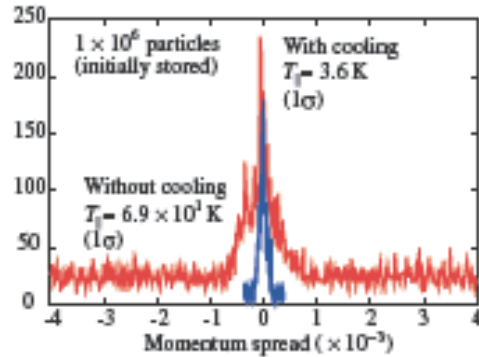


Figure 6: Experimental result of longitudinal laser cooling applied for a coasting beam counter balanced with an induction deceleration voltage.

In this system, the laser light co-propagates with $^{24}\text{Mg}^+$ ion beam and accelerates ion beam as large as $h\nu$ (ν : laser frequency, h : Planck's constant) for excitation by a laser light, which is counterbalanced with deceleration by an induction accelerator. In Fig. 6, the experimental result of laser cooling applied for a coasting beam is shown.

Table 1: Main Parameters of S-LSR and its Laser Cooling

Ring Lattice		
Circumference	22.557 m	
Average radius	3.59 m	
Length of straight section	1.86 m	
Number of periods	6	
Betatron Tune Horizontal	2.07	
Vertical	1.07	
Laser for Beam Cooling		
Type of Laser	Wave Length	Typical Power
Pumping Laser	532 nm	10 W
Dye Laser	560 nm	600 mW
2 nd Harmonics	280 nm	50 mW

Equilibrium longitudinal beam temperature after cooling is estimated to be 3.6 K, which is limited by a heat transfer from transverse degrees of freedom due to intra-beam scattering because transverse temperature of the injected beam is rather high as ~ 500 K [7]. In Table 1, main parameters of S-LSR and its laser cooling system are given.

APPROACH TO 2 DIMENSIONAL LASER COOLING

After the achievement of above mentioned results, our main efforts are oriented to realization of crystalline beam, which is free from variation of inter-particle distance. For such a purpose, the following items need to be carefully investigated.

Resonant Coupling between Longitudinal and Transverse Degrees of Freedom

After laser cooling so far applied, the transverse equilibrium temperature is more than 2 orders of magnitude higher than the longitudinal one, because a laser cooling force is only applied in the longitudinal direction and heat transfer by intra-beam scattering so far observed is too weak. In order to improve such a situation, a scheme to couple the beam motions in longitudinal and transverse directions with the use of a ‘‘Synchro-Betatron Resonance’’ has been proposed [8]. For the purpose of experimental verification of feasibility of such a scheme, bunched beam laser cooling has been applied with the condition satisfying ‘‘Synchro-Betatron Resonance’’ as is given by the formula,

$$\nu_s - \nu_H = m \text{ (integer),}$$

where ν_s and ν_H are synchrotron tune and betatron tune in horizontal direction, respectively, and with application of RF acceleration at the position with a finite dispersion function (~ 1 m).

In order to obtain the evidence of longitudinal and transverse coupling, an equilibrium momentum spread after application of laser cooling has been measured for various synchrotron tunes as shown in Fig. 7.

Existence of local maxima can be seen at the synchrotron tunes almost equal to the fractional part of the horizontal betatron tune, which, we think, is the indication of a coupling between the longitudinal and horizontal degrees of freedoms.

For direct demonstration of transverse laser cooling, observation of reduction of the horizontal beam size by a bunched beam laser cooling at the resonant condition of ‘‘Synchro-Betatron Resonance’’ has been tried. For this purpose, we have observed spontaneous emission from laser excited $^{24}\text{Mg}^+$ ions by an observation system described in the next section. In Fig. 8, preliminary result

of such measurement of the horizontal beam size for various synchrotron tunes is shown.

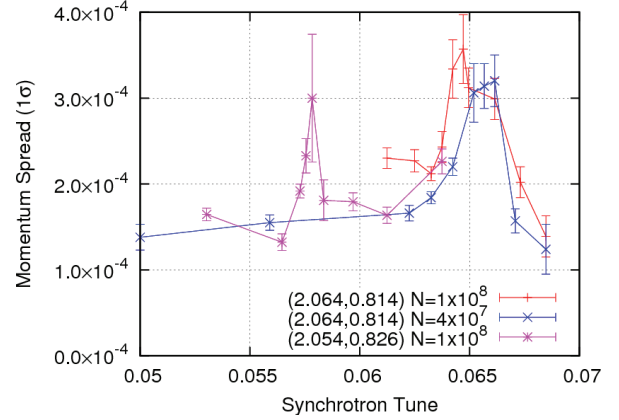


Figure 7: Equilibrium momentum spread after laser cooling for various synchrotron tunes.

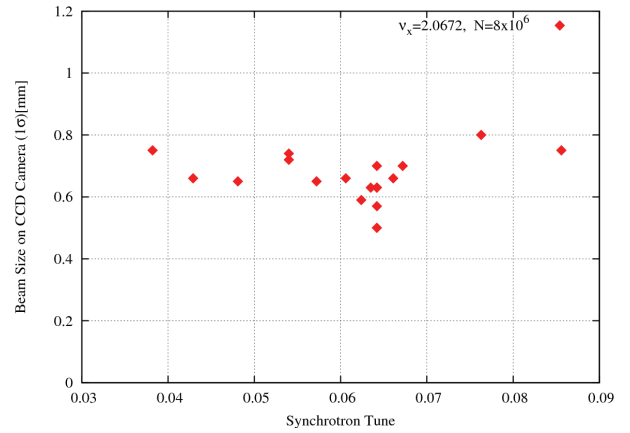


Figure 8: Variation of the horizontal beam size after laser cooling of bunched beam by RF acceleration at a position with the finite dispersion.

It is seen at a certain synchrotron tune, reduction of the horizontal beam size is indicated although this synchrotron tune is somewhat smaller compared with the fractional part of the horizontal betatron tune, which needs further investigation.

Reduction of Initial Transverse Temperature

As the injected $^{24}\text{Mg}^+$ ion beam is directly transported from the ion source after extraction from the ion source by a high voltage of 40 keV, transverse beam size is not yet well reduced, which is the reason of a rather higher transverse temperature of the injected beam. The reached longitudinal temperature after application of laser cooling remains at a rather higher value as 3.6 K for particle numbers of 3×10^4 due to heat transfer from the transverse direction through intra-beam scattering. So as to reach much lower final temperature, pre-cooling of injected beam by an electron beam cooling might be needed, which is to be applied from now on.



Figure 9: PAT (Post Acceleration Tube) for observation of momentum spread of the laser cooled Mg ion beam.

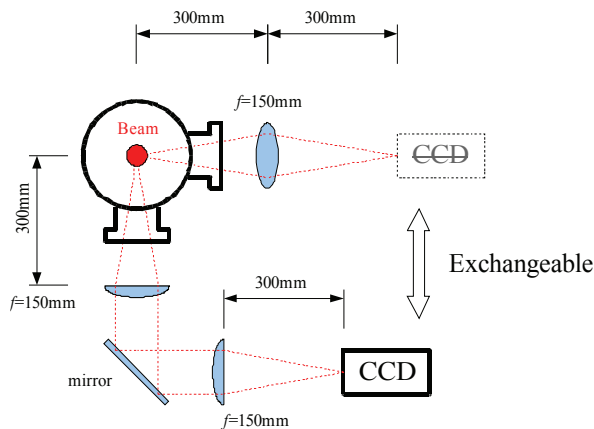


Figure 10: Observation system of the transverse beam profile with the use of CCD.

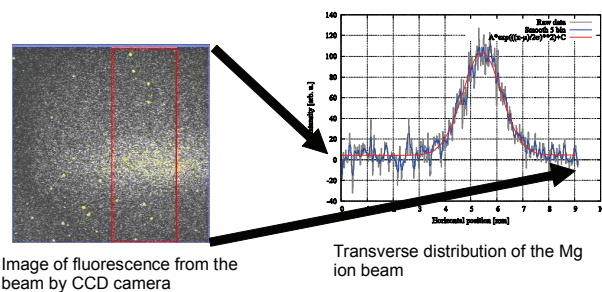


Figure 11: Observation of horizontal beam profile and beam size with the use of CCD.

OPTICAL OBSERVATION SYSTEM AT S-LSR

For observation of momentum spread and transverse beam size after cooling, the following optical observation system has been developed [9, 10].

Observation of Laser Cooled Momentum Spread

The momentum spread of the laser cooled $^{24}\text{Mg}^+$ ion beam has been measured by observing the emitted light from $^{24}\text{Mg}^+$ ions with a photo-multiplier through a hole at the side wall of a PAT (Post Acceleration Tube) as shown in Fig. 9 varying the applied potential to the PAT.

Mg ion can only be excited when their velocities are in a certain range satisfying Doppler Cooling condition and

Circular Accelerators

we can measure the momentum spread after laser cooling with observation of the intensity of emitted light by sweeping the applied voltage to the PAT as shown in Fig. 7.

Observation of Horizontal Beam Size by CCD

The transverse beam profile of the laser cooled $^{24}\text{Mg}^+$ ion beam has been measured by observation of emitted light from Mg ion with the use of CCD camera.

Beam size is obtained by fitting the observed profile after subtracting background as illustrated in Fig. 11.

At the beginning, the CCD was set to observe the vertical beam size, which however, was not efficient to detect coupling between longitudinal and transverse directions, because such a coupling occurs between longitudinal and horizontal directions. So the observation system by CCD has been modified to detect the horizontal beam profile by adding a view port from the bottom in summer 2008 and preliminary results as shown in Fig. 8 have become available.

SUMMARY

Laser cooling has been applied to $^{24}\text{Mg}^+$ ion beam with the kinetic energy of 40 keV at S-LSR. Longitudinal cooling has reduced the longitudinal temperature to 3.6 K, which is limited by heat transfer from transverse motion due to intra-beam scattering. Coupling between longitudinal and horizontal directions on purpose by using “Synchro-Betatron Resonance” has been investigated in these several months. Experimental indications of such a coupling has been obtained by observation of the cooled momentum spread and the horizontal beam size, which, however, needs further refinement in a more quantitative way from now on. Application of pre-electron beam cooling might also be investigated to realize much lower equilibrium temperature needed for creation of crystalline beam, where the special feature of S-LSR lattice will play an essential role.

REFERENCES

- [1] A.Noda, Nucl. Instrum. Meth., A532 (2004) 150.
- [2] J. Wei, XSD.P. Li and A.M. Sessler, Phys. Rev. Lett., 73 (1994) 3089.
- [3] T. Shirai et al., Phys. Rev. Lett., 98 (2007) 204801.
- [4] M. Tanabe et al., Applied Physics Express, 1 (2008) 028001.
- [5] M. Ikegami, A. Noda, M. Tanabe, M. Grieser, H. Okamoto, Phys. Rev. ST-AB, 7 (2004) 120101.
- [6] A. Noda, M. Ikegami and T. Shirai, New Journal of Physics, 8 (2006), pp268-288.
- [7] M. Tanabe et al., Applied Physics Express, 1 (2008) 028001.
- [8] H. Okamoto, A.M. Sessler and D. Möhl, Phys. Rev. Lett., 72 (1994) 3977.
- [9] M. Nakao et al., Contribution to PAC09 (2009), Vancouver.
- [10] H. Souda et al., Contribution to PAC09 (2009), Vancouver.

LATTICE STUDY OF A COMPACT SYNCHROTRON FOR CARBON THERAPY

H. Yim^{*}, D.H. An, G. Hahn, Y.-S. Kim, KIRAMS, Seoul, Korea

Abstract

A magnet lattice of the carbon-ion synchrotron was studied for cancer therapy, which requires maximum 400 MeV/u carbon beam, at KIRAMS. In the study, we optimized the magnet lattice configuration to fit into the therapy purpose. Major requirements for the purpose are (1) long extraction time (about 1 second), (2) compact size, and (3) low cost. For the requirement (1), a slow extraction scheme was adopted by the use of third integer resonance. For (2) and (3), we minimized the circumference as 69.6 m and a number of the magnet elements as 16 and 20 for bending magnet and quadrupole magnet, respectively. The study was carried out by the use of a simulation codes for beam particle dynamics and optics. A detail of the conceptual lattice design of the carbon-ion synchrotron is described in the paper.

INTRODUCTION

The carbon-ion cancer therapy is known as most efficient treatment. The Bragg peak of carbon-ion at the human body is more localized than the proton beam. In addition, the relative biological effect (RBE) is much higher than the established beam treatment. Therefore, in these days, a construction of carbon-ion synchrotron for the cancer therapy is rapidly increasing. The study for the synchrotron has been carried out at the Korea Institute of Radiological And Medical Sciences (KIRAMS).

LATTICE DESIGN

A design study of the compact synchrotron was carried out through a beam dynamics simulation tool, WinAgile [1]. The Fig. 1 shows the designed layout of the synchrotron.

Table 1: Basic Machine Parameters

Specifications	
Particle	C^{6+}
Injection energy	7 MeV/u
Extraction energy	120 – 400 MeV/u
Circumference	69.6m
Super periodicity	2
Max. dipole filed	1.47 T
Max. filed gradient	4.4 T/m
Tune Q_x/Q_y	1.667/1.563
Natural chromaticity ξ_x/ξ_y	-0.024/-0.944

*mouse@kirams.re.kr

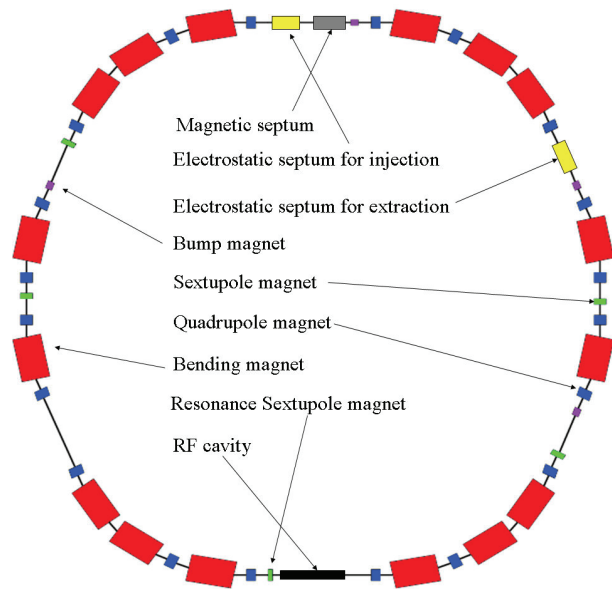


Figure 1: Layout of the synchrotron. Each colour indicates respective category of components. The red block, for example, correspond to the bending dipole magnet.

At the conception stage of the design, we required a compact size, a reasonably small aperture of the ring, and dispersion free region. The compact size of the synchrotron was required to minimize building cost for the facility in which the synchrotron will be placed. The small aperture size is necessary to reduce power consumption of the magnet component of the synchrotron. Lastly, the dispersion free region is required to place a resonance sextupole magnet, RF-cavity, beam injection, and beam extraction components. Thereby, we intended to avoid complex dynamics like a coupling effect between horizontal motion and vertical motion.

The circumference of the designed synchrotron is 69.6 m. The resultant diameter of the ring is 21.25 m. The number of bending dipole magnets and quadrupole magnets are 16 and 20, respectively. The magnetic rigidity of maximum energy (400 MeV/u) is 6.34 T m. The dispersion free region was obtained by adjusting field strength and position of each magnet component.

The resultant Twiss function is shown in Fig. 2.

The ranges of betatron function for horizontal and vertical space are 1.4 – 15.9 m and 5.0 – 15.8 m, respectively. The two dispersion free region of length of 4.2 m could be obtained, and a super periodicity of the synchrotron lattice is 2. To adjust a chromaticity, 4 families of sextupole magnet were implemented to the lattice. 2 families are horizontally acting sextupole magnets, and other 2 families are vertically acting

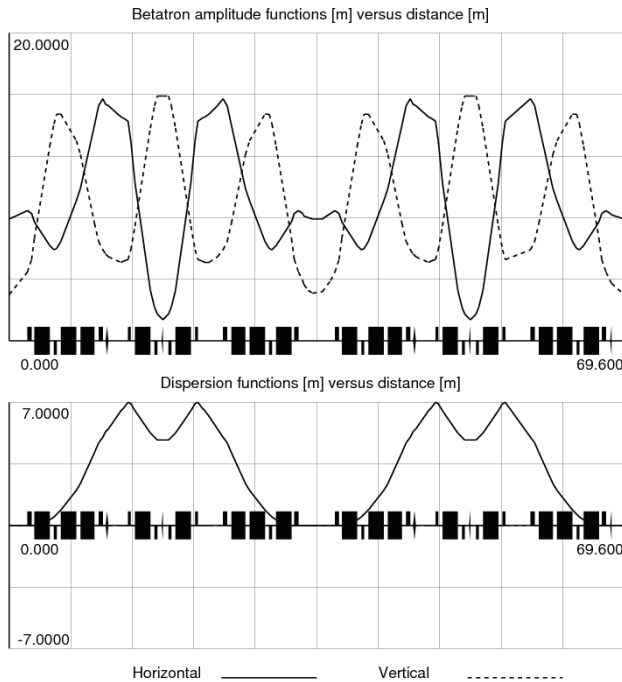


Figure 2: The betatron and dispersion functions. The solid line is for horizontal plane, and the dot line is for vertical plane. The Betatron function vs. distance (top) and the dispersion function vs. distance (bottom).

sextupole magnets. Each sextupole magnet is positioned in a diametrically symmetric way, to avoid the third order resonant excitation that is not desired at the cycle of injection and acceleration.

The basic lattice structure of the synchrotron comprises the bending magnets, the quadrupole magnets, and the sextupole magnets. Through the design study, we could achieve a compact size, reasonable size of betatron function, and implementation of dispersion free region.

INJECTION

The injection system from the linac to the synchrotron is one of most important part in the design of the synchrotron, because the initial beam condition affects the whole beam dynamics.

The system consists of one electrostatic septum, three orbit bump magnets. The beam from the linac is injected through electrostatic septum. A typical kick angle of orbit bump is around 2 mrad. The energy of injection beam is set to 7 MeV/u.

To achieve sufficient amount of beam in the ring, we chose a multi-turn injection scheme. For the horizontal phase space, the injected beam is filled in a desired horizontal total emittance realm by collapsing strength of the injection bump magnet. For vertical phase space, the mismatched injection beam is filled in a vertical total emittance to minimise the size of the vertical emittance. The resultant phase space of injected beam after 16 turns is shown in Fig. 3.

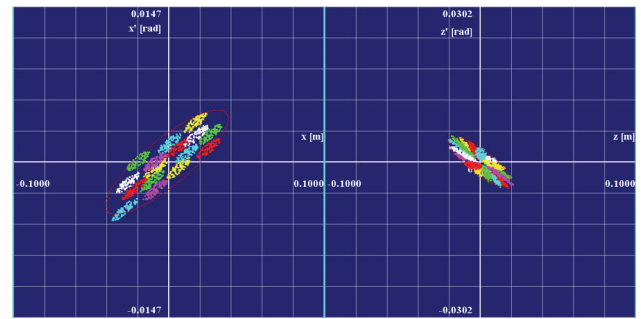


Figure 3: Phase space distribution of injected beam after 16 turn. The horizontal phase space of injected beam (left) and the vertical phase space of injected beam (right).

To optimize the injection efficiency, the working tune was set to 1.728 and 1.563 for a horizontal tune and a vertical tune, respectively. With emittance of 1π mm mrad, the resultant total emittance for 16 turn injection is about 22π mm mrad and 12π mm mrad for horizontal phase space and vertical phase space, respectively.

EXTRACTION

The applied extraction scheme is the third integer resonance driving method. The extraction system consists of one electrostatic septum for beam deflection, three orbit bump magnets for orbit excitation at the electrostatic septum, and one magnetic septum for beam extraction. The extraction energy is 120 MeV/u to 400 MeV/u. The working tune for the extraction is set to 1.667 and 1.563 for a horizontal and a vertical phase space, respectively.

To excite the resonance, a resonance sextupole magnet is implemented. The resonance sextupole magnet is placed on the dispersion free region to avoid an influence on the chromaticity of the synchrotron. When the resonance sextupole is turned on, the separatrix is formed.

The electrostatic septum is located in a dispersion region of ($D_x > 0$, $D'_x < 0$). The first condition for efficient transfer to the electrostatic septum is the phase advance of 225° between the resonance separatrix and the electrostatic septum. The second condition for the transfer to the magnetic septum is the phase advance of 90° since the electrostatic septum. In the present design, the phase advance is 233° and 90° , respectively. The last condition for the extraction is satisfying the Hardt condition, which guarantees minimum beam loss at the septum. Fig. 4 shows the resultant phase space distribution of separatrix and extracting beam.

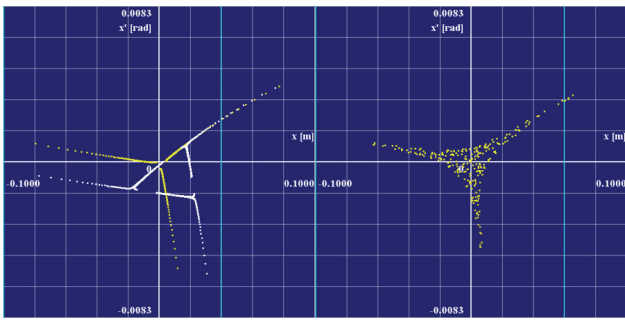


Figure 4: The horizontal phase space distribution of separatrix at extraction mode: the separatrix distribution for on-momentum beam and off-momentum beam (left) (the lines of separatrix at septum occupy same phase space for respective momentum by satisfying the Hardt condition); the phase space distribution of beam at extraction mode (right).

SUMMARY

The conceptual compact synchrotron for carbon-ion cancer therapy is designed and the circumference of the synchrotron is 69.6 m. The third integer resonance scheme, which generates slow beam extraction, was studied.

Further optimization work is in progress.

REFERENCES

- [1] P. J. Bryant, in Proceedings of the European Particle Accelerator Conference 2000, Geneva, Switzerland, p. 1357.

BEAM STABILITY IN SYNCHROTRONS WITH DIGITAL FILTERS IN THE FEEDBACK LOOP OF A TRANSVERSE DAMPER

V.M. Zhabitsky*, Joint Institute for Nuclear Research, Dubna, Russia

Abstract

The stability of an ion beam in synchrotrons with digital filters in the feedback loop of a transverse damper is treated. Solving the characteristic equation allows to calculate the achievable damping rates as a function of instability growth rate, feedback gain and parameters of the signal processing. A transverse feedback system (TFS) is required in synchrotrons to stabilize the high intensity ion beams against transverse instabilities and to damp the beam injection errors. The TFS damper kicker (DK) corrects the transverse momentum of a bunch in proportion to its displacement from the closed orbit at the location of the beam position monitor (BPM). The digital signal processing unit in the feedback loop between BPM and DK ensures a condition to achieve optimal damping. Transverse Feedback Systems commonly use digital FIR (finite impulse response) and IIR (infinite impulse response) filters for the signal processing. A notch filter is required to remove the closed orbit content of the signal and correct for the imperfect electric centre of the BPM. Further processing is required to adjust for the betatron phase advance between the beam pick-up (BPM) and the damper kicker (DK). Damping rates of the feedback systems with digital notch, Hilbert and all-pass filters are analysed in comparison with those in an ideal feedback system.

INTRODUCTION

Heavy ion beams of a high quality are required by many physicists for experimental studies. Gold ion beams are accelerated now in RHIC (BNL) [1], it is planned to accelerate lead ions in LHC [2]. Future accelerator facilities at GSI (FAIR project [3]) and JINR (NICA project [4]) are designed for acceleration of uranium beams. These facilities include a linear accelerator and several synchrotrons. For example, the CERN accelerator chain for ion beams consists of Linac – LEIR – PS – SPS – LHC. In the framework of the FAIR project the existing GSI accelerators serve as injectors for new synchrotrons SIS100 and SIS300. It is planned to build a booster as the injector for the Nuclotron operated now with a linac at JINR and to use the Nuclotron as the injector for a collider designed in the framework of the NICA project. It is clear that injection errors during the beam path from the linac to synchrotrons can lead to the undesirable growth of a beam emittance. It should be emphasised also that high intensity beams will be provided by these accelerators. The ultimate intensities after injection into the LHC will be about $4.8 \cdot 10^{10}$ ions for the $^{208}\text{Pb}^{82+}$ beam with an energy of 177 GeV/u. The peak intensities

of particles after injection into the SIS100 will be about $5 \cdot 10^{11}$ for the $^{238}\text{U}^{28+}$ beam with an energy of 0.2 GeV/u. These intensities can lead to coherent transverse instabilities. Theoretical predictions for the instability rise time τ_{inst} correspond to hundreds revolution periods T_{rev} of particles in the synchrotron. Therefore it is necessary to cure the transverse instabilities as well as to damp the transverse oscillations of the beam due to injection errors.

Transverse feedback systems (TFS) are used widely in synchrotrons for damping of coherent oscillations. The damping time τ_{d} of TFS must be shorter the instability rise time τ_{inst} to suppress instability: $\tau_{\text{d}} < \tau_{\text{inst}}$. In addition to that the damping time must be chosen to limit the emittance growth due to the beam injection errors. If e_{inj} is the maximum assumed amplitude of a beam deviation from the closed orbit due to displacement and angular errors at injection, then the relative emittance growth $\Delta\epsilon/\epsilon$ is [5, 6]:

$$\frac{\Delta\epsilon}{\epsilon} = \frac{e_{\text{inj}}^2}{2\sigma^2} F_{\text{a}}^2; \quad F_{\text{a}} = \left(1 + \frac{\tau_{\text{dec}}}{\tau_{\text{d}}} - \frac{\tau_{\text{dec}}}{\tau_{\text{inst}}}\right)^{-1}, \quad (1)$$

where σ is the initial RMS beam size and τ_{dec} is the beam decoherence time. Dependencies of the form factor F_{a} on

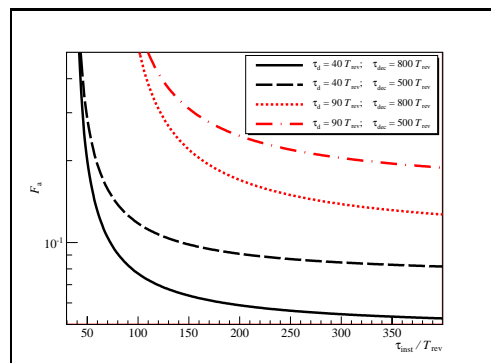


Figure 1: Dependencies of F_{a} on $\tau_{\text{inst}}/T_{\text{rev}}$.

the instability rise time τ_{inst} for several values of the damping time τ_{d} and the beam decoherence time τ_{dec} are shown in Fig. 1. As rule $F_{\text{a}} < 0.1$ is assumed that corresponds to $\tau_{\text{d}} \approx 40T_{\text{rev}}$ for $\tau_{\text{inst}} > 100T_{\text{rev}}$ and $\tau_{\text{dec}} > 500T_{\text{rev}}$. The damping time $\tau_{\text{d}} = 40T_{\text{rev}}$ is used commonly as the design specification of TFS for synchrotrons [7, 8].

BASIC DESCRIPTION

A classical transverse feedback system (see Fig. 2) consists of a beam position monitor (BPM), a damper kicker (DK) and an electronic feedback path with appropriate signal transmission from the BPM to the DK [9]. The damper

* V.Zhabitsky@jinr.ru

kicker corrects the transverse momentum of a bunch in proportion to its displacement $x[n, s_p]$ from the closed orbit at the BPM location s_p of the synchrotron's circumference C_0 at the n -th turn. The digital signal processing ensures the

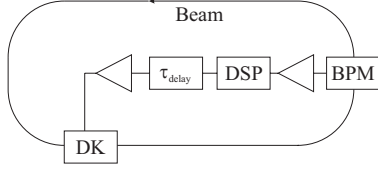


Figure 2: Layout of a classical transverse feedback system.

adjustment of the phase advance and the correction of the time of flight for optimum damping. The total delay τ_{delay} in the signal processing of the feedback loop from BPM to DK is adjusted to be equal to τ_{PK} , the particle flight of time from BPM to DK, plus an additional delay of q turns:

$$\tau_{\text{delay}} = \tau_{\text{PK}} + qT_{\text{rev}}. \quad (2)$$

For the practical realization in a particle accelerator, we note that $q = 0$ or $q = 1$ are used [8].

Following the matrix description of the free oscillation of a particle in synchrotrons, the matrix equation for the bunch states at the BPM location s_p at the $(n+1)$ and n -th turns after a small kick by the DK is given by [10]

$$\begin{aligned} \widehat{X}[n+1, s_p] &= \widehat{X}[n, s_p + C_0] \\ &= \widehat{M}_0 \widehat{X}[n, s_p] + \widehat{B} \widehat{T} \Delta \widehat{X}[n, s_k], \end{aligned} \quad (3)$$

where elements of the column matrix $\widehat{X}[n, s]$ are the bunch displacement $x[n, s]$ and the angle $x'[n, s]$ of its trajectory, \widehat{M}_0 is the revolution matrix, \widehat{B} is an ordinary transfer matrix from the point $[n, s_k]$ on the closed orbit at the DK location to the point $[n, s_p + C_0]$ at the BPM position at the n -th turn, \widehat{T} is the 2×2 matrix in which $T_{21} = 1$ and the other elements are zero. The first element of the column matrix $\Delta \widehat{X}$ in Eq. (3) is equal to the kick value $\Delta x'$

$$\Delta x'[n, s_k] = S_k V_{\text{out}}[n], \quad (4)$$

where S_k is the transfer characteristic of the damper kicker. The second element of the column matrix $\Delta \widehat{X}$ can be an arbitrary value due to the form of the matrix \widehat{T} . The output voltage $V_{\text{out}}[n]$ of the feedback loop depends on the input voltage $V_{\text{in}}[n, s_p]$ at the BPM. In the general case of linear systems the output voltage can be written as follows:

$$V_{\text{out}}[n] = u[n-q] \sum_{m=-\infty}^{n-q} h[n-m] V_{\text{in}}[m, s_p], \quad (5)$$

where elements $h[m]$ are determined by the electronics in the feedback loop, $u[n]$ is the Heaviside step function and q corresponds to the number of turns for delay (see Eq.(2)). For a bunch injected at $n = 0$, the input voltage $V_{\text{in}}[n, s_p]$ depends on the bunch displacement at the BPM location:

$$V_{\text{in}}[n, s_p] = S_p u[n] (x[n, s_p] + \delta x), \quad (6)$$

where S_p is the BPM sensitivity and δx is a deviation of the BPM electric centre from a closed orbit. It should be emphasised that equations (3), (4), (5) and (6) correspond to the bunch-by-bunch feedback where the correction kick for a given bunch is computed based only on the motion of that bunch. Applying the bilateral Z -transform (see [11])

$$y(z) = \sum_{n=-\infty}^{\infty} y[n] z^{-n}$$

in equations (3), (4), (5) and (6) we obtain from (3):

$$\begin{aligned} \widehat{\mathbf{X}}(z) &= \frac{z\widehat{I} - \widehat{\mathbf{M}}^{-1} \det \widehat{\mathbf{M}}}{\det(z\widehat{I} - \widehat{\mathbf{M}})} \begin{pmatrix} z \begin{pmatrix} x[0, s_p] \\ x'[0, s_p] \end{pmatrix} \\ + \frac{z^{-q} \mathbf{K}(z)}{\sqrt{\hat{\beta}_p \hat{\beta}_k}} \widehat{B} \widehat{T} \begin{pmatrix} \delta x / (1 - z^{-1}) \\ 0 \end{pmatrix} \end{pmatrix}, \end{aligned} \quad (7)$$

where \widehat{I} is the identity matrix, the matrix $\widehat{\mathbf{M}}(z)$ is given by

$$\widehat{\mathbf{M}}(z) = \widehat{M}_0 + \frac{z^{-q} \mathbf{K}(z)}{\sqrt{\hat{\beta}_p \hat{\beta}_k}} \widehat{B} \widehat{T}, \quad (8)$$

the betatron amplitude function at the point s_p of the synchrotron's circumference is $\hat{\beta}_p = \hat{\beta}(s_p)$, and $\hat{\beta}_k = \hat{\beta}(s_k)$. The transfer function $\mathbf{K}(z)$ is determined by the system transfer function $H(z)$ of the electronics in the feedback loop in accordance with parameters $h[n]$ in (5):

$$\begin{aligned} \mathbf{K}(z) &= \sqrt{\hat{\beta}_p \hat{\beta}_k} S_p S_k H(z), \\ H(z) &= \sum_{n=-\infty}^{\infty} z^{-n} h[n]. \end{aligned} \quad (9)$$

Consequently the bunch dynamics is determined by the poles z_k of $\widehat{\mathbf{X}}(z)$ which are roots of the characteristic equation:

$$\begin{aligned} \det(z_k \widehat{I} - \widehat{\mathbf{M}}(z_k)) &= z_k^2 - 2z_k \text{Tr} \widehat{\mathbf{M}}(z_k) + \det \widehat{\mathbf{M}}(z_k) \\ &= z_k^2 - \left[2 \cos(2\pi \tilde{Q}) + z_k^{-q} \mathbf{K}(z_k) \sin(2\pi \tilde{Q} - \psi_{\text{PK}}) \right] z_k \\ &\quad + 1 - z_k^{-q} \mathbf{K}(z_k) \sin \psi_{\text{PK}} = 0, \end{aligned} \quad (10)$$

where \tilde{Q} is the beam tune, ψ_{PK} is the betatron oscillation phase advance from BPM to DK.

In the general case, \tilde{Q} is a complex function depending on z [12, 13]. The real part of \tilde{Q} is the number of betatron oscillations per turn: $\text{Re} \tilde{Q} = Q$. The imaginary part of \tilde{Q} is determined by the increment of the transverse instability: $2\pi \text{Im} \tilde{Q} = T_{\text{rev}} / \tau_{\text{inst}}$, where τ_{inst} is the transverse instability rise time.

The beam is stable if eigenvalues z_k from Eq.(10) lie inside the unit circle:

$$|z_k| < 1. \quad (11)$$

Damping rates of the coherent betatron oscillations are defined by the absolute value of z_k :

$$\frac{T_{\text{rev}}}{\tau_k} = -\ln |z_k|, \quad (12)$$

where τ_k is the time constant of the betatron oscillation amplitude decay. Fractional parts $\{\text{Re } \tilde{Q}_k\}$ of the betatron frequency of a particle in presence of the transverse feedback system

$$\{\text{Re } \tilde{Q}_k\} = \frac{1}{2\pi} \arg(z_k) \quad (13)$$

are the fractional tunes ($-0.5 < \{\text{Re } \tilde{Q}_k\} \leq 0.5$).

If $|\mathbf{K}(z)| = 0$ then the solution of the Eq.(10)

$$z_{\pm}^{(0)} = \exp(\pm j2\pi\tilde{Q}) \quad (14)$$

corresponds to the solution for frequencies of the betatron motion equation of a particle in synchrotrons. Let us assume that for small values of $|\mathbf{K}(z)|$ we can write:

$$z^{-q}\mathbf{K}(z) = g \exp(\mp j\varphi) \exp(\mp j2\pi q\tilde{Q}), \quad (15)$$

where the gain $|g| \ll 1$ and the phase shift

$$\varphi = \arg\left(H(z_{\pm}^{(0)})\right) \quad (16)$$

of the feedback loop depend weakly on z , so that we can neglect dependences of g and φ on z in Eq.(10), and zero approximation from (14) can be used for g and φ at betatron frequencies. Let us assume also that the fractional part of the tune is not close to 0 or 0.5. In this case the solutions of Eq.(10) in the linear approximation with $|g| \ll 1$ are expressed by the formula:

$$z_{\pm} \approx \left(1 - \frac{g}{2} \exp(\pm j(\frac{\pi}{2} - \tilde{\Psi}_{\text{PK}}))\right) \exp(\pm j2\pi\tilde{Q}), \quad (17)$$

where

$$\tilde{\Psi}_{\text{PK}} = \psi_{\text{PK}} + 2\pi q\tilde{Q} + \arg\left(H(z = \exp(-j2\pi\tilde{Q}))\right). \quad (18)$$

Using definitions (12) and (13) the damping rates follow as

$$\frac{T_{\text{rev}}}{\tau_{\pm}} \approx \frac{g \exp(\pm \text{Im } \tilde{\Psi}_{\text{PK}})}{2} \sin(\text{Re } \tilde{\Psi}_{\text{PK}}) \pm 2\pi \text{Im } \tilde{Q}, \quad (19)$$

and the fractional parts of tunes are:

$$\begin{aligned} \{\text{Re } \tilde{Q}_{\pm}\} &\approx \pm\{Q\} \\ &\mp \frac{g \exp(\pm \text{Im } \tilde{\Psi}_{\text{PK}})}{4\pi} \cos(\text{Re } \tilde{\Psi}_{\text{PK}}). \end{aligned} \quad (20)$$

Therefore the best damping of coherent transverse oscillations is achieved by optimally choosing the positions of BPM and DK yielding a phase advance of $\text{Re } \tilde{\Psi}_{\text{PK}}$ equal to an odd multiple of $\pi/2$:

$$\text{Re } \tilde{\Psi}_{\text{PK}} = \frac{\pi}{2}(2k + 1), \quad (21)$$

Circular Accelerators

where k is an integer. Hence the overall damping rate is:

$$\begin{aligned} \frac{T_{\text{rev}}}{\tau} &\approx \frac{g \exp(-\text{Im } \tilde{\Psi}_{\text{PK}})}{2} \cos(\pi k) - 2\pi \text{Im } \tilde{Q} \\ &= \frac{T_{\text{rev}}}{\tau_{\text{d}}} - \frac{T_{\text{rev}}}{\tau_{\text{inst}}}, \end{aligned}$$

where τ_{d} is the damping time constant of the TFS without instability.

In the following transverse feedback systems satisfying the optimal conditions (2) and (21) are considered. We call the special case with $\varphi = 0$ and $q = 0$ hereafter the *ideal* transverse feedback system.

If \tilde{Q} depends weakly on z then the characteristic equation (10) with the feedback transfer function

$$z^{-q}\mathbf{K}(z) = ga_0z^{-q}H(z)$$

can be converted to a polynomial. It can be solved with the use of a root-finding algorithm or analytically for a polynomial of degree less than five. However, it is clear from (20) that $\{\text{Re } \tilde{Q}_k\} \approx \{Q\}$ for $|g| \ll 1$ in the case of (21). Therefore dependences of damping rates $|z_k|$ on gain g for the TFS with digital filters can be compared with those for the ideal TFS if a_0 is defined for $z_0 = \exp(-j2\pi Q)$ such that

$$\begin{aligned} |a_0z_0^{-q}H(z_0)| &= 1, \\ a_0 \sin(\arg(z_0^{-q}H(z_0)) + \text{Re } \psi_{\text{PK}}) &> 0. \end{aligned} \quad (22)$$

Hence the damping regime corresponds to $g > 0$. The calibration condition (22) will be used hereafter for all dependences of TFS damping parameters on gain g .

DIGITAL FEEDBACK SYSTEMS

Taking into account the final value theorem [11] and the solution (7) for $\tilde{\mathbf{X}}(z)$ we can conclude that

$$\begin{aligned} \hat{X}[\infty, s_{\text{p}}] &= \lim_{z \rightarrow 1} (1 - z^{-1})\tilde{\mathbf{X}}(z) = 0 \\ &\text{if } \mathbf{K}(z = 1) = 0. \end{aligned} \quad (23)$$

Therefore as minimum a notch filter to suppress all the revolution harmonics (DC included) is required in the feedback loop. The magnitude of the difference signal from the BPM electrodes, after passing through the notch filter, is proportional to the bunch deviation from the closed orbit. The system transfer function of the notch filter is [11]:

$$H(z) = H_{\text{NF}}(z) = 1 - z^{-1}. \quad (24)$$

It is clear from (24) that the notch filter changes the gain g and the phase φ of the open loop transfer characteristics. For example, if $Q = 6.73$ then $\{Q\} = -0.27$ and in accordance with (16) the phase φ is $\arg(H_{\text{NF}}(z_0)) = \varphi_{\text{NF}} = 41.4^\circ$. The gain $|H_{\text{NF}}| = 2|\sin(\{Q\}\pi)| = 1.5$ can be adjusted by an amplifier a_0 in the feedback loop in accordance with (22). However, according to the approximation formula (19), the damping rates for the TFS with the

notch filter still change due to the phase shift φ_{NF} resulting in slower damping than for the case of the ideal TFS.

The unwanted phase-shift φ_{NF} due to the notch filter can be compensated by a Hilbert filter [14] with the system transfer function

$$H_{\text{HF}}(z) = h_0 z^{-3} + h_1 z^{-2}(1 - z^{-2}) + h_3(1 - z^{-6}), \quad (25)$$

where

$$h_0 = \cos(\Delta\varphi), \quad h_1 = -\frac{2}{\pi} \sin(\Delta\varphi), \quad h_3 = -\frac{2}{3\pi} \sin(\Delta\varphi)$$

are the Hilbert transform impulse response coefficients.

The electric circuit of a feedback loop with the notch and Hilbert filters is shown in Fig. 3. The difference signal V_{in}

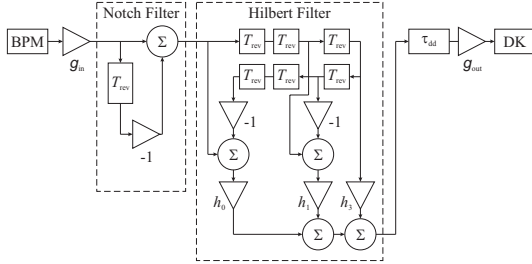


Figure 3: Block diagram of feedback loop with the notch and Hilbert filters.

from the electrodes of the beam position monitor (BPM) is amplified by front electronics with the gain g_{in} . Then the signal proceeds through the notch filter and the Hilbert filter. The synchronisation needed is adjusted by the digital delay τ_{dd} . The output voltage V_{out} on the damper kicker (DK) is supplied by the high power amplifier with the gain g_{out} . The notch filter has the standard configuration. It includes a one turn delay T_{rev} , an inverter and a summator. The Hilbert filter includes six one turn delays, four inverters, two inverting amplifiers and three amplifiers h_0 , h_1 , h_3 . For example, the phase shift needed for compensation of $\varphi_{\text{NF}} = 41.4^\circ$ is obtained by using the Hilbert filter with $\Delta\varphi = -72.8^\circ$.

The unwanted phase-shift φ_{NF} due to the notch filter can be compensated also by an all-pass filter [11] with a frequency-response magnitude that is constant but a phase advance which is variable and adjustable. The notch and Hilbert filters are FIR (finite impulse response) filters but the all-pass filter is IIR (infinite impulse response) filter. The transfer function of the first order an all-pass filter is

$$H_{\text{AF}}(z) = \frac{z^{-1} - a^*}{1 - az^{-1}}, \quad (26)$$

where a is a free filter parameter for the adjustment of the phase, and a^* denotes its complex conjugate. For example, the phase shift needed for compensation of $\varphi_{\text{NF}} = 41.4^\circ$ is obtained by using the all-phase filter with $a = -0.501$.

The electric circuit of a feedback loop with the notch and all-pass filters is shown in Fig. 4. The all-pass filter

includes a one turn delay T_{rev} , an inverting amplifier $(-1/a^*)$ in the non-recursive electric circuit, an amplifier a in the recursive electric circuit and two summators. An additional inverting amplifier $(-a^*)$ in the output electric circuit is ensuring $|H_{\text{AF}}| = 1$ for all frequencies independently on the filter parameter a . It allows to adjust phase shifts in the feedback loop by varying the parameter a but keeping the gain of the TFS constant.

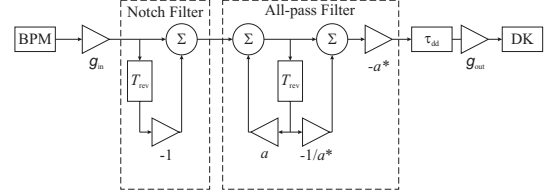


Figure 4: Block diagram of feedback loop with the notch and all-pass filters.

Dependences of damping rates $|z_k|$ on gain g for the ideal TFS, the TFS with notch and the TFS with notch and all-pass filters are shown in Fig. 5 (the tune of $Q = 6.73$ was used [15]). In case of the feedback loop with a notch

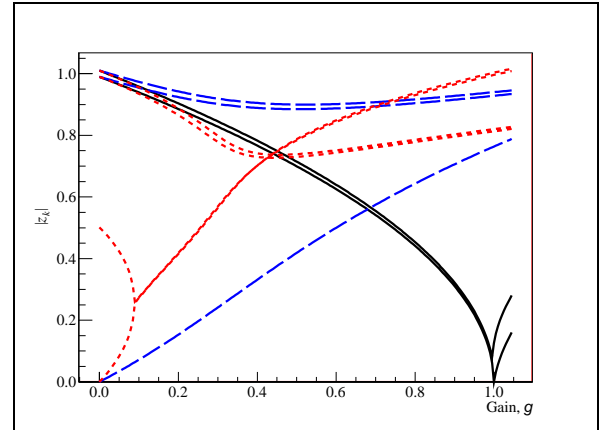


Figure 5: Dependences of damping rates $|z_k|$ on gain g for the ideal TFS (solid curves), for the TFS with the notch filter (dashed curves) and for the TFS with the notch and all-pass filters (dotted curves), parameter $a = -0.501$; shown is the case of the tune of $Q = 6.73$ and an assumed instability rise time of $\tau_{\text{inst}} = 100T_{\text{rev}}$.

filter only the Eq.(10) is a characteristic polynomial of the third degree. The characteristic equation (10) is a characteristic polynomial of the fourth degree in case of TFS with notch and all-pass filters. Therefore all dependences in Fig. 5 correspond to analytical solutions of Eq.(10). It is clear from Fig. 5 that the damping rates of the TFS with the notch filter are worse than the damping rates of the ideal TFS for all magnitudes of the feedback gains. However, for small gains $g \ll 1$ the characteristics of the TFS with the notch and all-pass filters coincide with the corresponding parameters of the ideal transverse feedback system if the phase shift of the notch filter was compensated by the all-pass filter with the parameter $a = -0.501$.

Dependences of overall damping rates T_{rev}/τ on gain g for the ideal TFS and for feedback systems with digital notch, all-pass and Hilbert filters are shown in Fig. 6 in cases of optimal values for a and $\Delta\varphi$. Therefore the

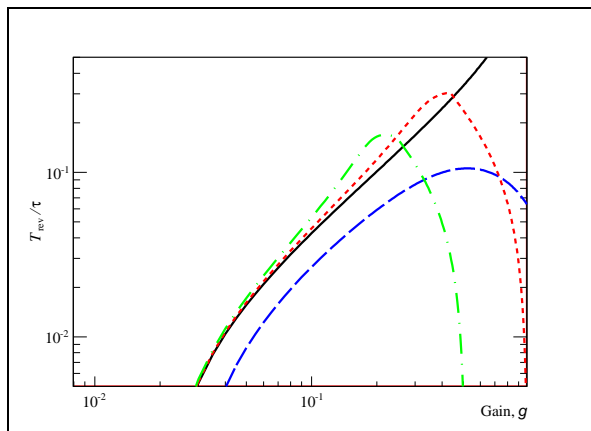


Figure 6: Dependences of overall damping rates T_{rev}/τ on gain g for feedbacks: the ideal TFS (solid curve), with the notch filter (dashed curve), with the notch and all-pass filters for $a = -0.501$ (dotted curve), with the notch and Hilbert filters for $\Delta\varphi = -72.8^\circ$ (dash-dotted curve); shown is the case of the tune of $Q = 6.73$ and an assumed instability rise time of $\tau_{\text{inst}} = 100T_{\text{rev}}$.

damping parameters of the ideal TFS can be obtained in the TFS with notch and all-pass or Hilbert filters for small gains. However the stability range is wider for TFS with the notch and all-pass filters. The gain g of TFS with the notch filter only must be in ≈ 1.3 times higher in the case of $\tau_{\text{d}} = 40T_{\text{rev}}$ than for TFS with the all-pass or Hilbert filter.

CONCLUSION

Following the analysis presented in this paper we can conclude that for small gains of the feedback loop the optimum damping characteristics of the ideal TFS can be restored in presence of a notch filter using a first order all-pass filter or a six order Hilbert filter with optimised parameters. Tuning the phase transfer characteristic of the all-pass or Hilbert filters in order to compensate the phase shift in the feedback loop caused by the notch filter we can obtain the optimal beam damping time. This possibility of tuning is an interesting feature and constitutes an advantage over a transverse damping system with a notch filter only.

ACKNOWLEDGEMENTS

The author thanks E. Gorbachev (JINR), T. Linnecar, W. Höfle, V. Rossi and G. Kotzian (CERN) for the fruitful discussions and the helpful assistance.

REFERENCES

- [1] W. Fischer. “RHIC Operational Status and Upgrade Plans”. Proceedings of the 10th European Particle Accelerator Conference,

- 26–30 June 2006, Edinburgh, pp. 905–909. The European Physical Society Accelerator Group (EPS-AG), 2006.
- [2] John M. Jowett. “Ions in the LHC”. Proceedings of Chamomix 2009 workshop on LHC Performance, pp. 289–297. CERN, Geneva, 2009.
- [3] P. Spiller et al. “Design Status of the FAIR Synchrotrons SIS100 and SIS300 and the High Energy Beam Transport System”. Proceedings of the 11th European Particle Accelerator Conference, 23–27 June 2008, Genoa, pp. 298–300. The European Physical Society Accelerator Group (EPS-AG), 2008.
- [4] G. Trubnikov et al. “Project of the Nuclotron-based Ion Collider Facility (NICA) at JINR”. Proceedings of the 11th European Particle Accelerator Conference, 23–27 June 2008, Genoa, pp. 2581–2583. The European Physical Society Accelerator Group (EPS-AG), 2008.
- [5] L. Vos. “Transverse Emittance Blow-up from Double Errors in Proton Machines”. Proceedings of the Sixth European Particle Accelerator Conference, 22–26 June 1998, Stockholm, Sweden, pp. 1365–1367. Institute of Physics, 1998.
- [6] V.M. Zhabitsky. “Transverse Emittance Blow-Up from Beam Injection Errors in Synchrotrons with Nonlinear Feedback Systems”. Physics of Particles and Nuclei Letters, vol. 5, No.1(143), pp. 49–53, 2008.
- [7] V.M. Zhabitsky et al. “Transverse Damping System at SIS100”. Proceedings of the 10th European Particle Accelerator Conference, 26–30 June 2006, Edinburgh, pp. 3014–3016. The European Physical Society Accelerator Group (EPS-AG), 2006.
- [8] E.V. Gorbachev et al. “LHC Transverse Feedback System: First Results of Commissioning”. XXI Russian Particle Accelerators Conference RuPAC-2008, 28 September–3 October 2008, Zvenigorod, Russia, pp. 97–100. Moscow, 2008.
- [9] L. Vos. “Damping of Coherent Oscillations”. NIM A, 391, pp. 56–63, 1997. CERN-SL-96-066-AP, Geneva, CERN, December 1996.
- [10] V.M. Zhabitsky. “The Z-Transform Application for Solving the Problem of Free Beam Oscillation Damping in the Accelerator”. JINR Communications. P9-91-91, Dubna, 14 February 1991.
- [11] Alan V. Oppenheim and Ronald W. Schaffer, with John R. Buck. “Discrete-Time Signal Processing”. Prentice-Hall, 2nd edition, 1999.
- [12] V.M. Zhabitsky. “Transverse Damper System for LHC”. SL-RFS Note 91-14, LHC Note 175, Geneva, CERN, 13 December 1991.
- [13] V.M. Zhabitsky. “Theory of Multi-Bunch Resistive Wall Instability Damping using Feedback System with a Digital Filter”. Proceedings of the Fourth European Particle Accelerator Conference, 27 June – 1 July 1994, London, England, pp. 1090–1092. World Scientific, 1994.
- [14] V. Rossi. “Digital Signal Processing for 1-Turn Delay Feedback Systems of the CERN Accelerator Chain”. CERN-BE-2009-009, CERN, Geneva, 1 January 2009.
- [15] V. Volkov et al. “Nuclotron Extracted Beam Spill Control”. Proceedings of the 9th European Particle Accelerator Conference, 5–9 July 2004, Lucerne, pp. 2718–2720. The European Physical Society Accelerator Group (EPS-AG), 2004.

SIMULATION AND DESIGN OF THE COMPACT SUPERCONDUCTING CYCLOTRON C400 FOR HADRON THERAPY

Y. Jongen, M. Abs, A. Blondin, W. Kleeven, S. Zaremba, D. Vandeplassche, IBA, Belgium
 V. Aleksandrov, S. Gursky, G. Karamysheva, N. Kazarinov, S. Kostromin, N. Morozov,
 V. Romanov, N. Rybakov, A. Samartsev, E. Samsonov, G. Shirkov, V. Shevtsov, E. Syresin,
 A. Tuzikov, JINR, Russia.

Abstract

Carbon therapy is a most effective method to treat the resistant tumors. A compact superconducting isochronous cyclotron C400 has been designed by IBA-JINR collaboration. This cyclotron will be used for radiotherapy with proton, helium and carbon ions. The $^{12}\text{C}^{6+}$ and $^4\text{He}^{2+}$ ions will be accelerated to the energy of 400 MeV/amu and will be extracted by electrostatic deflector, H_2^+ ions will be accelerated to the energy 265 MeV/amu and protons will be extracted by stripping. The magnet yoke has a diameter of 6.6 m, the total weight of the magnet is about 700 t. The designed magnetic field corresponds to 4.5 T in the hills and 2.45 T in the valleys. Superconducting coils will be enclosed in a cryostat; all other parts will be warm. Three external ion sources will be mounted on the switching magnet on the injection line located below of the cyclotron. The main parameters of the cyclotron, its design, the current status of development work on the cyclotron systems and simulations of beam dynamic will be presented.

INTRODUCTION

Today, cancer is the second highest cause of death in developed countries. Its treatment still presents a real challenge. Protons and light ions allow depositing the radiation dose more precisely in a cancer tumor, reducing greatly the amount of dose received by healthy tissue surrounding the tumor with respect to electrons. But in addition to the ballistic accuracy of protons, light ion beams, like carbon beams have an extra advantage in radiation therapy: they have a different biological interaction with cells and are very effective even against some type of cancerous cells which resist to usual radiations. That is why the last years have seen increasing interest in particle therapy based on $^{12}\text{C}^{6+}$ ions. A C400 dedicated Carbon/Proton therapy cyclotron [1-4] (Fig. 1) has been designed by IBA-JINR collaboration.

Over the last 15 years IBA has designed and equipped over half of the clinical-based Proton Therapy (PT) facilities in the world. The new C400 cyclotron is derived from the design of the current PT C235 cyclotron and will be used for radiotherapy with proton, helium or carbon ions. The $^{12}\text{C}^{6+}$ and $^4\text{He}^{2+}$ ions will be accelerated to the energy 400 MeV/amu and extracted by an electrostatic deflector, H_2^+ ions will be accelerated to the energy 265 MeV/amu and extracted by stripping. All other ions with $Q/M = 0.5$, which can be produced in reasonable amount by current ECR ion sources, can be accelerated as well as for research purposes with unspecified intensity.

Circular Accelerators

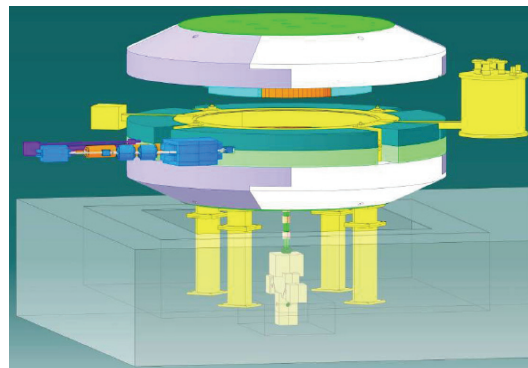


Figure 1: Common view of C400 cyclotron.

Table 1: Main parameters of the C400 Cyclotron

General properties	
Accelerated particles	H_2^+ , $^4\text{He}^{2+}$, $^6\text{Li}^{3+}$, $^{10}\text{B}^{5+}$, $^{12}\text{C}^{6+}$
Injection energy	25 keV/Z
Final energy of ions, protons	400 MeV/amu 265 MeV
Extraction efficiency	~70 % (by deflector)
Number of turns	~1700
Magnetic system	
Total weight	700 tons
Outer diameter	6.6 m
Height	3.4 m
Pole radius	1.87 m
Valley depth	60 cm
Bending limit	$K = 1600$
Hill field	4.5 T
Valley field	2.45 T
RF system	
Radial dimension	187 cm
Vertical dimension	116 cm
Frequency	75 MHz
Operation	4 th harmonic
Number of dees	2
Dee voltage: center extraction	80 kV 170 kV

The C400 design was based on the main cyclotron characteristics: compact design similar to the existing IBA C235 cyclotron; fixed energy, fixed field and fixed RF frequency (small RF frequency change 0.6% for H_2^+ regime set up); bending limit $K=1600$; accelerated particles H_2^+ , $^4He^{2+}$, $^6Li^{3+}$, $^{10}B^{5+}$ and $^{12}C^{6+}$; superconducting coils enclosed in cryostat, all other parts are warm; axial injection using a spiral inflector; extraction of carbon beam with an electrostatic deflector; extraction of H_2^+ beam by stripping. All operating parameters of the C400 cyclotron are fixed now (Table 1).

The required isochronous magnetic field is shaped by axial and azimuth profiling of the sectors. The optimized sector geometry provides vertical focusing $Q_z \sim 0.4$ in the region of extraction. Four-fold symmetry and spiral sectors with an elliptical gap (120 mm at the center decreasing to 12 mm at the extraction) provide stable beam acceleration up to 10 mm from the pole edge. Keeping the last orbit as close as possible to the pole edge facilitates extraction. Detailed dynamic simulations were performed to be sure that resonances crossed during acceleration did not cause significant harmful effect to the beam. The number of turns is expected to be about 1700.

INJECTION

Three external ions sources are mounted on the switching magnet on the injection line located below of the cyclotron. $^{12}C^{6+}$ are produced by a high performance ECR at current $3 \mu A$, alphas and H_2^+ are also produced by a simpler ECR source. All species have a Q/M ratio of 1/2 and all ion sources are at the same potential, so that small retuning of the frequency and a very small magnetic field change achieved by different excitation of 2 parts in the main coil are needed to switch from H_2^+ to alphas or to $^{12}C^{6+}$. We expect that the time to switch species will be not longer than two minutes, like the time needed to retune the beam transport line between different treatment rooms.

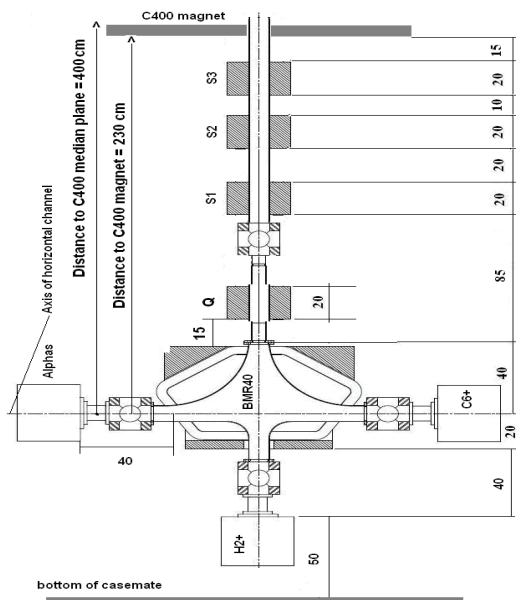


Figure 2: Scheme of the injection beam line.

Focusing in the channel (Fig. 2) is provided by three solenoid lenses (S1 ... S3), the rotational symmetry of the beam is reestablished with the help of one quad Q placed just behind the BMR40 bending magnet. The 90° bending magnet has two horizontal entrances, one vertical one, and one exit for the ion beams. The bending radius of the magnet BMR40 is equal to 40 cm. The maximum magnetic field corresponds to 0.75 kG, gap height is 70 mm. The maximum magnetic field of the solenoids does not exceed 3 kG, a good field region is of 80 mm. The maximum quadrupole lens gradient does not exceed 100 G/cm.

The big values of the magnetic field from the C400 cyclotron in the region of the horizontal part of the channel and inside the BMR40 and the quadrupole lens require an additional shielding.

The simulation of the ion beam transportation has been made. For all types of ions the beam diameters at the entrance into the spiral inflector are smaller than 2 mm.

A model of the dee geometry at the cyclotron center with the inflector housing was developed. Dee tips have the vertical aperture 1.2 cm in the first turn and 2 cm in the second and further turns. In the first turn the gaps were delimited with pillars reducing the transit time. The azimuth extension between the middles of the accelerating gaps was chosen to be 45° . The electric field simulation of the central region was performed. The electric field in the inflector was chosen to be 20 kV/cm. Thus, the height (electric radius) of the inflector (Fig. 3) is 2.5 cm. The gap between electrodes was taken to be 6 mm, tilt parameter is equal to $k'=0.1$. The aspect ratio between the width and the spacing of the electrodes was taken to be 2 to avoid the fringe field effect.

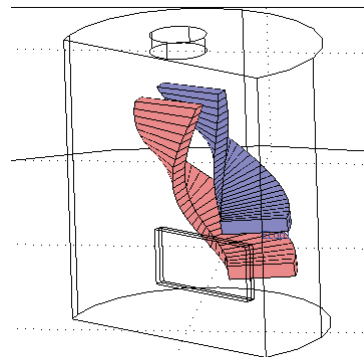


Figure 3: The spiral inflector $k'=0.1$ $E=20$ kV/cm.

Beam dynamics simulations were made for particles with initial distributions in transverse phase planes obtained from the axial injection line. The inflector with tilt $k'=0.1$ can be effectively used for beam intensity modulation. Axial beam motion is given in Fig. 4. Fig. 5 demonstrates turns in the central region for design voltage $U_0 = \pm 5.82$ kV (100% intensity - green lines), for $U=0.95U_0$ (53% intensity - blue lines) and for $U=0.9U_0$ (15% intensity - red lines). The voltage $0.89U_0$ corresponds to the situation when all beam is lost in the diaphragm (situated on the first antidee - 0.2 mm).

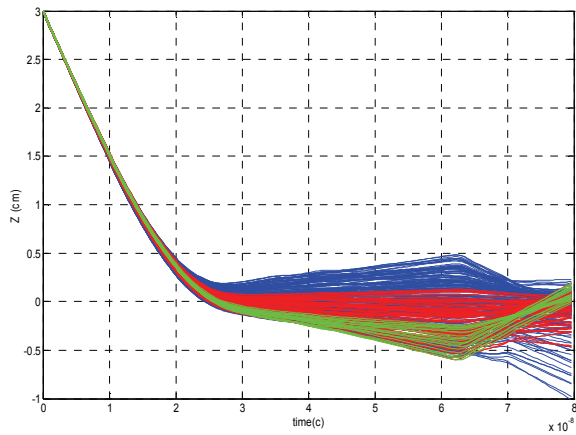


Figure 4: Axial beam motion.

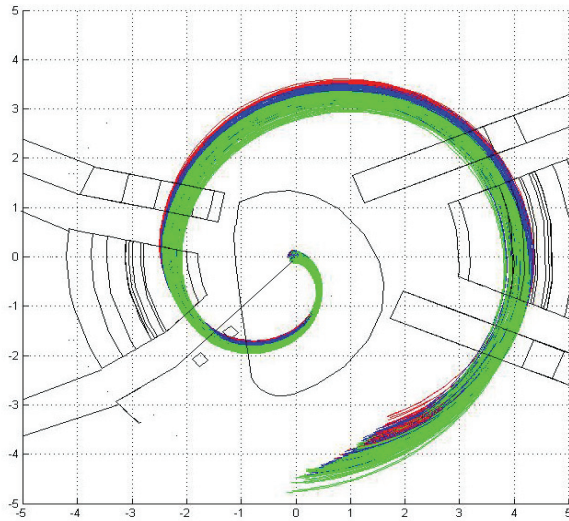


Figure 5: First turns in the center region.

MAGNET SYSTEM

The simulation and design of the C400 magnetic system was based on its main characteristics: four-fold symmetry and spiral sectors; deep-valley concept with RF cavities placed in the valleys; elliptical pole gap is 120 mm at the center decreasing to 12 mm at extraction; accelerate up to 10 mm from the pole edge to facilitate extraction; pole radius is 187 cm; hill field is 4.5 T, valley field is 2.45 T; magnetic induction inside yoke is less 2-2.2 T; the magnet weight is 700 tons and the magnet yoke diameter is 6.6 m; the main coil current is 1.2 MA. The main parameters of the cyclotron magnetic system were estimated and optimized by computer simulation with the 3D TOSCA code (Fig. 6).

The view of the spiral sectors is given in Fig. 6. The sectors are designed by a way with flat top surface and without additional grooves, holes etc. The sectors have the following parameters: the initial spiral law with parameter $N\lambda=77$ cm with increasing spiral angle to the final radius with parameter $N\lambda\sim 55$ cm; the sectors azimuth width is varying from 25° in the cyclotron center to 45° at the sectors edge; axial profile is the ellipse with

60/1874 mm semi-axis, at the final radii the ellipse axial profile is cut by the planes at the distance $z = \pm 6$ mm.

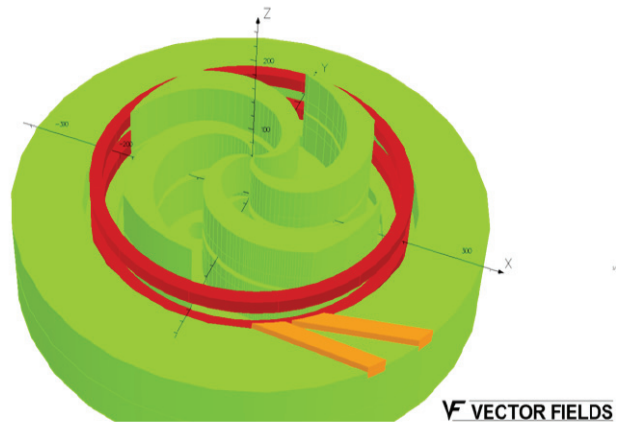


Figure 6: 3D TOSCA simulation of C400 magnetic system.

The accuracy of average magnetic field at shaping simulation is ± 10 G in the middle and end region of the beam acceleration. The required isochronous magnetic field was shaped by azimuth profiling of the sectors. The optimized sector geometry provides vertical focusing $Q_z \sim 0.4$ in the extraction region (Fig. 7).

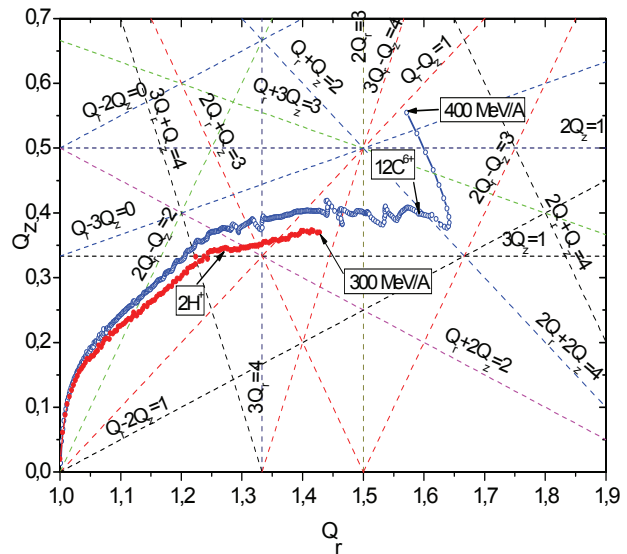


Figure 7: Working diagram of the cyclotron.

ACCELERATING SYSTEM

Acceleration of the beam will occur at the fourth harmonic of the orbital frequency, i.e. at 75 MHz. The acceleration will be obtained through two cavities placed in the opposite valleys. Two 45° dees working at the fourth harmonic will guarantee the maximum acceleration. The dee voltage increases from 80 kV at the center to 170 kV in the extraction region. A geometric model of the double gap delta cavity housed inside the valley of the magnetic system was developed in the Microwave Studio (Fig. 8).

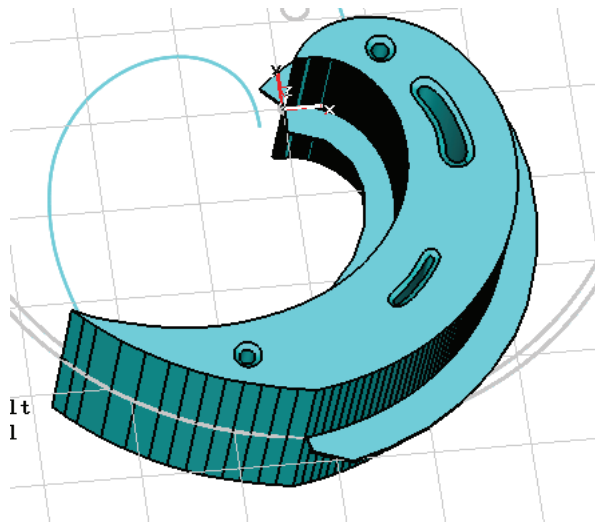


Figure 8: View of RF cavity model.

The depth of the valley permits accommodation of the cavity with total height 116 cm. The vertical dee aperture was equal to 2 cm. The accelerating gap was 6 mm at the center and 80 mm in the extraction region. The distance between the dee and the back side of the cavity was 45 mm. The azimuth extension of the cavity (between the middles of the accelerating gaps) was 45° up to the radius 150 cm. The cavities have a spiral shape similar to the shape of the sectors. We inserted four stems with different transversal dimensions in the model and investigated different positions of the stems to ensure increasing voltage along the radius. The thickness of the dee was 20 mm. Edges of the dees are 10 mm wide. Basing on the 2D electric field simulations we have chosen the optimal form of the dee edges. RF heating simulation was performed to determine the cooling system layout.

Each cavity will be excited with the RF generator through a coupling loop (which should be rotated azimuthally within small limits). For precise resonator adjustment, a tuner (piston) will be provided at radii compatible with the holes in the yoke. Average losses will be about 50 kW. Each cavity will be powered by a 75 MHz 100 kW tetrode-based amplifier (as used in the current C235 cyclotron).

ION DYNAMICS

During a whole range of acceleration the carbon beam crosses the lines of 15 resonances up to 4th order (Table 2). The working diagrams presented in Fig. 7 have been computed via an analysis [3] of the small oscillations around the closed orbits. All resonances can be subdivided into two groups. The first group consists of 6 internal resonances ($nQ_r \pm kQ_z = 4$, $n, k=0, 1, 2, 3, 4$, $n+k \leq 4$) having the main 4th harmonic of the magnetic field as a driving term. The second group includes 11 external resonances ($nQ_r \pm kQ_z = m$, $m=0, 1, 2, 3$) that could be excited by the magnetic field perturbations.

Requirements to the field imperfections imposed by the dangerous resonances will be able to be provided in practice at today's level of cyclotron technology.

Circular Accelerators

Table 2: List of Resonances up to 4th Order

Resonance, (Level of Danger)	Radius (cm) (Driving Term)	Description, tolerances
$Q_r = 1$ (Yes)	2-10 (B_{z1})	Increase in radial amplitudes $B_{z1} < 2-3$ G
$4Q_r = 4$ (Not)	2-10 (B_{z4}, φ_{z4})	Weak influence on radial motion at acceleration
$2Q_r - Q_z = 2$ (Not)	110 (B_{z2}, B_{r2})	Increase in axial amplitudes $B_{z2} < 200$ G, $B_{r2} < 50$ G
$3Q_r + Q_z = 4$ (Not)	131 (B_{z4}, φ_{z4})	No influence up to A_z , $A_r = 5-7$ mm
$Q_r - Q_z = 1$ (Yes)	145 (B_{r1})	Increase in axial amplitudes $B_{r1} < 5-7$ G
$3Q_r = 4$ (Yes)	154 (B_{z4}, φ_{z4})	Increase in radial amplitudes beginning from $A_r = 1.5$ mm. Can be corrected by average field perturbation.
$2Q_r + Q_z = 3$ (Not)	157 (B_{r3})	Increase in axial amplitudes $B_{r3} < 10$ G
$Q_r + 2Q_z = 2$ (Not)	162 (B_{z2})	Increase in axial amplitudes $B_{z2} < 20$ G
$3Q_z = 1$ (Not)	167 (B_{r1})	Increase in axial amplitudes $B_{r1} < 20$ G
$3Q_r - Q_z = 4$ (Not)	167 (B_{z4}, φ_{z4})	Increase in radial amplitudes. No influence if no axial amplitudes increase on resonance $3Q_z = 1$ due to B_{r1}
$2Q_r = 3$ (Not)	172 (B_{z3})	Increase in radial amplitudes $B_{z3} < 10$ G
$Q_r + Q_z = 2$ (Not)	177 (B_{z2}, B_{r2})	Increase in radial and axial amplitudes $B_{r2} < 10$ G
$2Q_r + 2Q_z = 4$ (Not)	177 (B_{z4}, φ_{z4})	No influence
$Q_r + 3Q_z = 3$ (Not)	179 (B_{z3})	Increase in axial amplitudes $B_{z3} < 10$ G
$2Q_r - Q_z = 3$ (Not)	180 (B_{z3})	Increase in axial amplitudes $B_{z3} < 10$ G
$2Q_r + Q_z = 4$ (Not)	181 (B_{z4}, φ_{z4})	Increase in axial amplitudes. Requires proper deflector positioning.
$2Q_z = 1$ (Yes)	181 (B_{z1}, B_{r1})	Increase in axial amplitudes $B_{r1} < 10$ G, $dB_{z1}/dr < 1$ G/cm

EXTRACTION

Extraction of protons is supposed to be done by means of the stripping foil. It was found that 320 MeV is the minimal attainable energy of protons which can be extracted during 1-turn after the stripping foil and 265 MeV is the minimal energy of protons for 2-turns

extraction (Fig. 8). This variant was chosen as optimal one because the energy of the 2-turns extracted protons is essentially closer to the normally used energy for the proton beam treatment. The radius of foil in this case is 161.3 cm, azimuth is 51° .

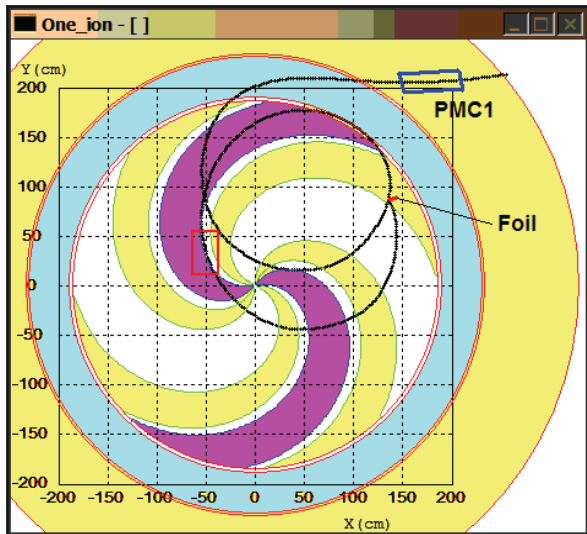


Figure 8: Extraction of proton with energy 265 MeV.

It is possible to extract the carbon beam by means of one electrostatic deflector (which is located in valley between sectors) with a 150 kV/cm field inside. Septum of the deflector was located at the radius 179.7 cm for tracking simulation. The extraction efficiency was estimated as 73% for the septum with increased (0.1 – 2) mm thickness along its length. The extraction of the carbon and proton beams by the separate channels and their further alignment by the bending magnets outside the cyclotron was chosen as the acceptable variant. The passive magnetic elements (correctors) are supposed to be used inside the cyclotron and the active current elements (quadrupole lenses and bending magnets) outside the yoke. A plan view of both lines is shown in Fig. 9. The system for carbon ion extraction consists of the electrostatic deflector, two passive magnetic correctors MC1,2, three quadrupole lenses CQL1–3 and two steering dipole magnets CSM1-2. Proton beam extraction system consists of the stripping foil, magnetic corrector PMC1, two bending magnets BM1-2, two quads PQL1-2 and two steering magnets PSM1-2.

Modeling of the different focusing elements action in both carbon and proton extraction systems was carried out to avoid the beams large divergence during the extraction (Fig. 10). It is possible to align both beams into one direction just before the energy degrader (6750 mm from the cyclotron center). Both beams have a spot with $\sigma_{x,y} < 1$ mm at this point. Transverse emittances are equal to 10π mm-mrad and 4π mm-mrad for the extracted carbon beam.

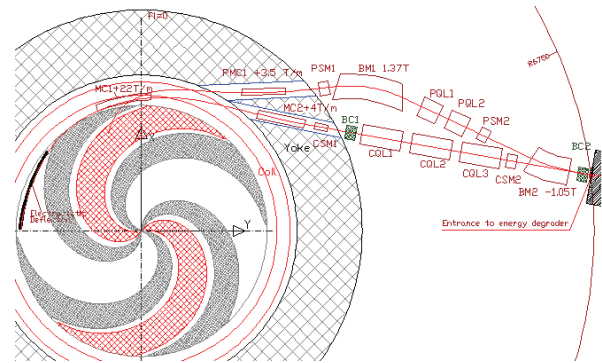


Figure 9: Layout of the cyclotron C400 with two extraction lines.

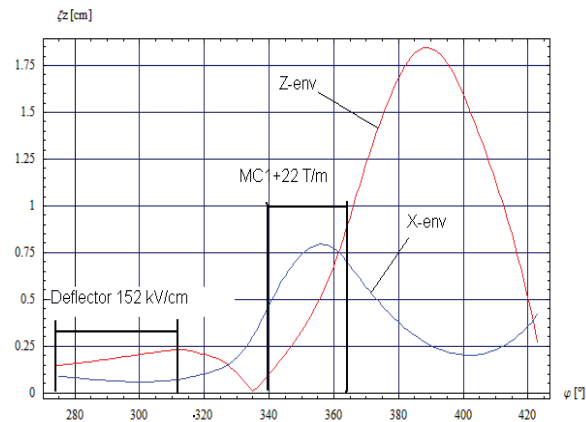


Figure 10: Carbon envelopes (2σ) inside the cyclotron. Deflector with uniform electric field is used.

CONCLUSIONS

The detailed computer simulations of the beam dynamics and the main systems of C400 cyclotron have been performed. The results of the simulations show that the energy range up to 400 MeV/amu ($K = 1600$) can be achieved with the compact design similar to that of the existing IBA C235 cyclotron. The C400 cyclotron will also provide a proton therapy beam with energy 265 MeV.

REFERENCES

- [1] Y. Jongen et al., “Design Studies of the Compact Superconducting Cyclotron for Hadron Therapy”, in Proc. of EPAC 2006, Scotland, p. 1678.
- [2] Y. Jongen et al., “IBA C400 Cyclotron Project for hadron therapy”, in Proc. of Cyclotrons 2007, p. 151.
- [3] Y. Jongen et al., “Numerical study of the resonances in superconducting cyclotron C400”, in Proc. of Cyclotrons 2007, p. 382.
- [4] Y. Jongen et al., “Current status of the IBA C400 cyclotron project for hadron therapy”, in Proc. of EPAC 2008, p. 1806.

FORMATION OF HIGH-INTENSIVE RADIOACTIVE CARBON ION BEAMS IN THE ELECTRON STRING ION SOURCE

D. E. Donets, E. D. Donets, E. E. Donets, V. V. Salnikov, V. B. Shutov, E. M. Syresin
Joint Institute for Nuclear Research, Dubna, Russia

Abstract

Accelerated ^{12}C ion beams are effectively used for cancer treatment at various medical centers, in particular to treat patients with radio resistant tumors. On the other hand, positron emission tomography is the most effective way of tumor diagnostics. The intensive ^{11}C ion beam could allow both these advantages to be combined. It could be used both for cancer treatment and for on-line positron emission tomography. Formation of a primary radioactive $^{11}\text{C}^{6+}$ ion beam with the intensity of 10^{10} - 10^{11} pps from the ion source may allow cancer treatment and on-line dose verification.

^{11}C isotope is produced in the nuclear reaction $^{14}\text{N}(p,\alpha)^{11}\text{C}$ using the gas target chamber irradiated by a proton beam. If the nitrogen target chamber contains about 5% of hydrogen, approximately 10^{14} methane molecules $^{11}\text{CH}_4$ can be produced each 20 minutes. The separated radioactive methane can be loaded into an ion source.

The methodology and technique of formation of high-intensity radioactive carbon beams were tested in the JINR electron string ion source (ESIS) Krion-2 using usual non radioactive methane. The measured conversion efficiency of methane molecules to carbon ions appeared to be rather high, 15 % for C^{6+} ions and 25% for C^{4+} ions. The developed technique of pulsed methane loading and the experimentally obtained conversion efficiency permit obtaining primary radioactive $^{11}\text{C}^{6+}$ beams at the intensity of 10^{10} - 10^{11} pps and performing cancer treatment and on-line dose verification.

FORMATION OF HIGH-INTENSITY RADIOACTIVE CARBON ION BEAMS

Accelerated $^{12}\text{C}^{6+}$ beams at the ion intensity of 10^9 particles per second (pps) are effectively used for cancer treatment at various medical centers, in particular to treat patients with radio resistant tumor targets [1]. On the other hand, positron emission tomography (PET) is the most effective way of tumor diagnostics.

Accelerated ion beams of the positron-emitting ^{11}C isotope (half-lifetime is about 20 min) were first used at NIRS-HIMAC for cancer therapy applications [2]. The use of the ^{11}C ion beam could allow both these advantages to be combined because this beam could be simultaneously used both for cancer treatment and for on-line positron emission tomography. Verification of the radiation dose in the tumor target will be carried out simultaneously with cancer treatment.

In order to produce ^{11}C beam for cancer therapy, the Projectile Fragmentation Method (PFM) was used at HIMAC [2]. In this scheme the ^7Be target was irradiated

by the accelerated primary ^{12}C beam and the maximum ^{11}C production rate was about 1% and the purity was near 93%.

To increase the intensity of radioactive carbon ion beams by two orders of magnitude, the ISOLDE scheme was proposed [3]. An advantage of primary radioactive ^{11}C ion beams is the higher space resolution at PET tomography compare to secondary radioactive beams produced in PFM.

In the ISOLDE scheme ^{11}C isotope is produced through the nuclear reaction $^{14}\text{N}(p,\alpha)^{11}\text{C}$ in the target chamber filled with N_2 gas at the initial pressure of about 20 bars. The proton beam from the 18 MeV cyclotron allows getting the activity of 1.5 Ci (10^{14} atoms of ^{11}C) for 20 min of irradiation with the proton beam current of 20 μA . The nitrogen gas target also contains 5% of H_2 instead of 2% of O_2 gas [3] to produce $^{11}\text{CH}_4$ molecules which are more applicable for our scheme. A Porapac cryogenic trap is used for separation of frozen radioactive methane $^{11}\text{CH}_4$ from N_2 gas pumped away from the trap with a flow rate of about 1.5 l/min. After stopping the flow of the target gas, the cryogenic system raises the temperature and radioactive methane is passed into a tank. In these steps, the ^{11}C collection efficiency is expected to be about 95%. The total separation time is about 3 min. After the separation about $8.5 \cdot 10^{13}$ $^{11}\text{CH}_4$ methane molecules still remain, and they could be loaded into an ion source.

The standard transmission injection-extraction efficiency of the beam at the HIMAC synchrotron is around 10%. Since the HIMAC operation is based on a very low duty factor with a range of 10^3 , it is necessary to provide pulsed gas injection into the working space of the ion source. The Electron String Ion Source [5, 6] is one of the promising ion sources for generation of the positron-emitting $^{11}\text{C}^{4+}$ ion beam at the intensity of 10^{10} pps. The $^{11}\text{C}^{4+}$ ions formed in the ion source could be injected in the linac at the repetition frequency of 1 Hz, where after acceleration up 6 MeV/n, they will be transformed into $^{11}\text{C}^{6+}$ ions on a target and then will be injected in HIMAC. Finally, the ^{11}C ion beam at intensity about 10^9 pps will be extracted from HIMAC on a tumor target.

Realization of such parameters could provide the possibilities of the synchrotron-based cancer treatment and on-line dose verification both on the existing carbon accelerators and on the projected ones. This work is a step towards this goal.

DECAY AND INJECTION OF ^{11}C ISOTOPES

The number of the remaining $^{11}\text{CH}_4$ molecules (Figure 1) decreases with time because of their

radioactive decay and also because of their pulsed injection into the electron string ion trap

$$N(t) = N_0 \cdot \exp(-\lambda t) - (\dot{n}/\lambda\xi) \cdot [1 - \exp\{-\lambda t\}],$$

where $N_0=8.5 \cdot 10^{13}$ is the initial number of $^{11}\text{CH}_4$ molecules loaded in the ion source, $\dot{n} = 10^{10}$ pps is the ion injection rate, $\lambda=1/1200 \text{ s}^{-1}$ is the decay constant, $\xi=0.25$ is the conversion efficiency of the methane molecules to ions.

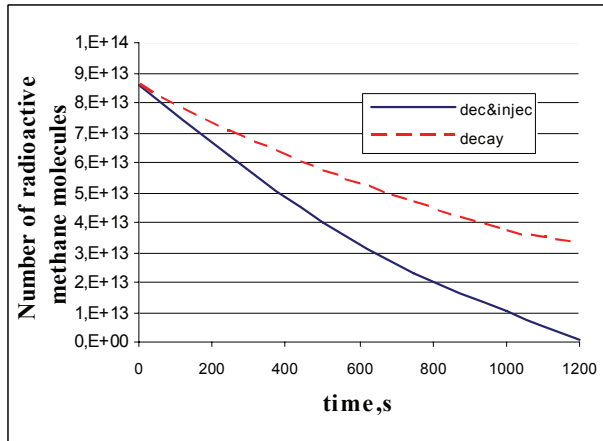


Figure 1: Dependences of the number of remaining $^{11}\text{CH}_4$ molecules on time (upper curve: radioactive decay alone; lower curve: decay and pulsed injection).

The remaining number of $^{11}\text{CH}_4$ molecules after 20 min injection is still large, $N=10^{12}$. The injection efficiency corresponding to the ratio of the number of $^{11}\text{C}^{4+}$ ions injected during the cycle to the number of methane molecules loaded in each cycle is $\eta = \dot{n}/(N_0 \cdot \lambda) = 0.12$ at the parameters given in Fig. 1.

ELECTRON STRING ION SOURCE

The Electron Beam Ion Source (EBIS) [7] usually operates in the “direct beam” mode in order to produce highly charged ions. The dense electron beam of about 1 m long and of about 1 mm in diameter, which is confined in such a source by a strong longitudinal magnetic field of a super conducting solenoid, is used both for confinement of positive ions in the beam electron space charge and for step-by-step electron impact ionization of the ions. The highly charged ions can be extracted from the source and used as required. High power of the electron beams and especially their high power density in the electron collector region are disadvantages of EBIS sources.

The reflex mode of the EBIS operation (ESIS mode) [5, 6, 8] is realized by using the specially designed electron gun and the electron reflector that allows a multiple use of beam electrons. The electrons do not reach the electron collector after one pass through the drift space of the source; instead, they are reflected backwards to the emitter side and then are reflected again in the vicinity of

the emitter and so on. Finally, the reflected electrons can perform, depending on experimental conditions, up to 10^3 oscillations between the electron emitter and the collector. When due to the reflections the electron density reaches a definite value, a phase transition can occur to the so-called electron string state. The string electrons are used for ion production in ESIS (Table 1) similar to the beam electrons in EBIS. And in the ESIS mode it is possible to reduce the power consumption of the ESIS high-voltage system by 1 - 3 orders of magnitude and to obtain a similar effective electron density, which allows improving the source reliability and at the same time increasing the ion output. As a result, the power of the high-voltage system in ESIS corresponds to several tens Watts.

The electron string phenomenon was first discovered at JINR LHE about 10 years ago and after sufficient researches the Krion-2 ESIS was constructed. Now it is successfully used as the ion source producing highly charged ions beams for the JINR relativistic superconducting synchrotron Nuclotron [9]. This source provides a rather high pulse intensity of really highly charged ion beams, for example, Ar^{16+} - 200 μA , Fe^{24+} - 150 μA in 8 μs pulses.



Figure 2: Electron String Ion Source Krion-2.

Table 1: Parameters of Electron String Ion Sources

Ion source	Krion-2 C^{4+}	Krion-5T C^{4+}	TESIS C^{4+}
Electron energy, keV	3-5	5-7	5-7
Number of electrons	$6 \cdot 10^{10}$	$3 \cdot 10^{11}$	$3 \cdot 10^{12}$
Magnetic field, T	3	5	5
Ion current, mA	0.2	1	10
Pulse duration, μs	8	8	8
Number ions extracted per pulse	$2.5 \cdot 10^9$	10^{10}	10^{11}
Injection frequency, Hz	100	100	100
Average current, μA	0.15	0.8	8

The charge capacitance of the Krion-2 ion trap is $6 \cdot 10^{10}$ elementary charges. The trap can be easily half-filled with low charge state (similar to C^{2+}) ions during 1-2 ms pulse injection, and then during about 5 ms confinement in the electron string the ions will increase their charge state by a factor 2, filling the trap and compensating the negative electron space charge. As was shown experimentally, adjusting the electron energy, injection time, and time of ion confinement, one can get up to 50 % of C^{4+} in the total ion beam pulse extracted from the source. It is pertinent to mention that hydrogen ions produced from methane molecules leave the ion trap taking energy from carbon ions which the last ones take from string electrons. This process was also studied earlier and was given the name ion-ion cooling. Increasing the confinement time to about 90 ms, one can get mostly the C^{6+} ion beam, but because of some losses during the longer confinement the number of particles will be slightly smaller than for C^{4+} beam.

So, the existing ion source Krion-2 could produce around $2.5 \cdot 10^9 C^{4+}$ particles per pulse. Another advantage of the source is the quite small emittance of extracted beam (5-10 π -mm-mrad).

MODELING OF FORMATION OF RADIOACTIVE ION BEAM IN ESIS

We used ordinary methane $^{12}CH_4$ for this research since the problem under consideration does not depend on the type of the carbon isotopes incorporated into the methane molecule. According to the HIMAC cancer therapy requirements, the ion source should produce C^{4+} ion beams with the intensity of 10^{10} pps and pulse width of 1 ms. Note that a limited number of methane molecules ($\sim 10^{14}$) is available during each 20 minutes. The problems we faced and solved are the following: 1) pulsed injection (in ms range) of some optimal number of methane molecules into the working space of the ESIS, keeping all the rest molecules for the next ionization cycles; 2) studies of carbon loss, caused by production of neutral radicals (CH_3 , CH_2 , etc) by the electron impact and their subsequent escape; 3) minimization of carbon ion loss during ionization.

CRYOGENIC PULSED GAS INJECTION TECHNOLOGY

The scheme of cryogenic pulsed gas injection [4] is given in Fig. 3: 1 is the injection section drift tube structure at temperature 78 K, 2 are the main ion trap drift tube sections at temperature 4.2 K, 3 are the ion potential barriers during ion injection, 4 and 5 are the ion potential barriers during ion confinement, 6 is the methane freezing-evaporation cell, 7 is the cell road covered by aluminized mylar, 8 and 9 are the junctions of the interior and exterior aluminum layers of mylar, 10 is the copper wire connecting the rod with the terminal at 4.2 K, 11 is the small vessel volume, 12 is the big vessel volume, 13 is the vacuum meter, 14 is the vacuum gauge, V1-V4 are the valves for methane isolation.

Ion Sources

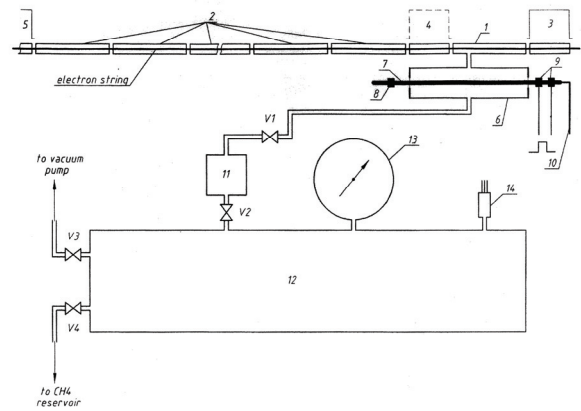


Figure 3: Scheme of Krion 2 cryogenic pulsed injection.

A special cryogenic cell was elaborated and successfully tested [4]. The cell consists of an isolated chamber which is situated in the vicinity of the working space of the ESIS, 1 cm away from the axis. The isolated chamber is arranged at the 78 K cold terminal. The key element of the cell is a copper rod 2.5 mm in diameter and 90 mm in length located in the middle of the chamber. The rod is arranged along the axis of the cell and fixed by its ends to the opposite walls of the chamber. One rod end is connected to the 4.2 K cold terminal, being thermo insulated on the chamber walls. As a result, every portion of the loaded methane molecules is completely frozen at the rod surface, which has temperature 4.2 K. The rod has sandwich-type insulation layers in its outer part and an aluminium conducting layer on its surface, which provides pulsed heating of the surface from 4.2 K to $40 \div 45$ K during a few ms due to pulsed electrical current through the aluminium layer. As a result, all methane molecules leave the rod surface. The resulting methane vapour pressure at this temperature provides penetration of about 10^{10} molecules into the working drift tube of the ESIS. When the electrical current passed through the aluminium layer is switched off, the temperature at the rod surface decreases to 4.2 K during few ms as well and all the rest of the methane molecules are frozen again at the rod surface. Thus, the elaborated cryogenic cell provides pulsed injection of methane molecules with the pulse duration in the ms range, sufficiently reducing the total working gas (methane) consumption. Moreover, the cell works with relatively small pulse power consumption (about 40 W).

CONVERSION EFFICIENCY

The electron strings used in the Krion-2 were formed by injected electrons of energy 4.4 keV and reflection voltages about 6 kV. First, we experimentally studied the initial part of the CH_4 to C^{4+} (C^{6+}) transformation. Figure 4 shows the ion charge state spectrum when the methane injection was 30 μ s long and the produced ions were extracted from the ion source without any additional confinement.

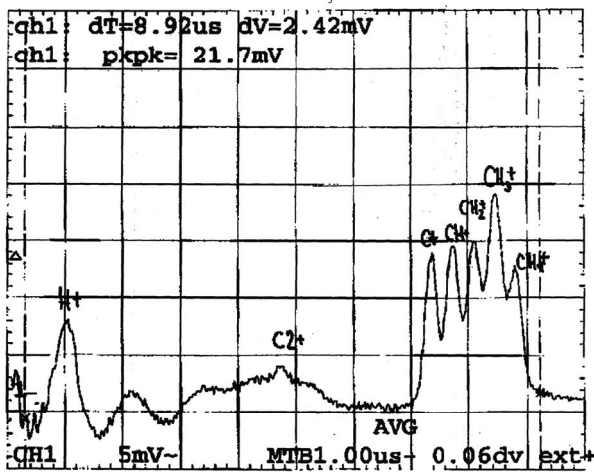


Figure 4: Ion spectra after 30 μ s methane injection into the Krion-2.

One can see that in addition to H^+ it predominantly comprises singly charged methane molecule ions, hydrocarbon radical ions, and atomic carbon ions CH_4^+ , CH_3^+ , CH_2^+ , CH^+ , and C^+ . In fact, neutral hydrocarbon radicals can also be produced during the initial part of the transformation. Some part of the neutrals may leave the source electron string without ionization. Therefore, the total transformation efficiency of the methane molecule to carbon ion can be decreased. It was difficult to estimate a priori the influence of the production of neutrals on the total conversion efficiency; nevertheless, it was done experimentally.

Testing various times of methane injection and ion confinement we found out that the electron string carbon ions reach the charge state C^{4+} approximately in 8 ms and the charge state C^{6+} in 90 ms. The ion charge state spectrum after 6 ms confinement is presented in Fig. 5. The ion charge state spectrum after 90 ms confinement is presented in Figure 6.

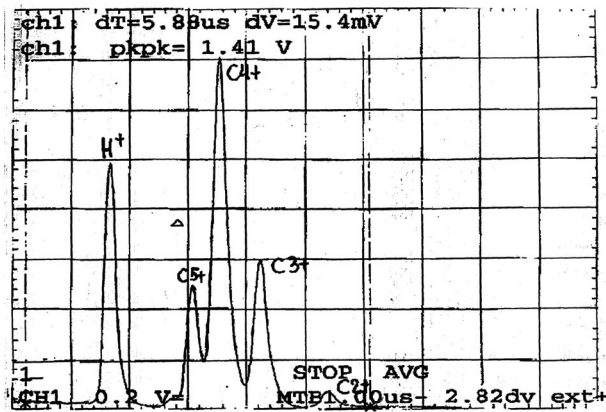


Figure 5: Ion spectra after 6 ms confinement in the electron string of the Krion-2.

Then, injecting methane molecules during 1 ms, we found out that after their confinement in the Krion-2 electron string during 5.8-6.2 ms the percentage of C^{4+} in

the carbon ion charge state distribution is the highest and amounts to 53%. Injecting methane molecules during 5 ms and confining them in the electron string during 90 ms, we obtained 67% of C^{6+} in the carbon ion charge state distribution in the extracted ion beam. We consider this confinement time and percentage to be the optimum ones in production of C^{6+} ion beam. A further increase in the confinement time could increase the percentage, but the total conversion efficiency would decrease because of additional ion losses during the confinement.

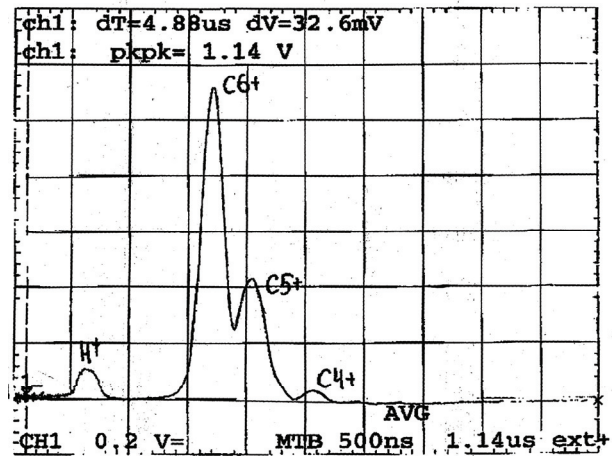


Figure 6: Ion spectra after 90 ms confinement in the electron string of the Krion-2.

As a rule, we introduced about $4 \cdot 10^{14}$ methane molecules into the cell. Then we reached the necessary heating pulse power (36 W) at 1 Hz repetition rate of heating pulses. The maximum repetition rate of accumulation – ionization was 100 Hz. In this regime we usually accumulated 26-30 nC of positive ion charge per second.

The introduced portion of methane evaporated in 2 hours, which means that in $7.2 \cdot 10^3$ seconds we produced $(1.87 \div 2.16) \cdot 10^5$ nC at the repetition rate 100 Hz. Now it is easy to calculate the conversion efficiency of methane molecules to carbon ions considering that 67% of the ion charge is the C^{6+} and 55% of carbon ions are C^{4+} ions. The number of the produced C^{4+} ions was $1.02 \div 1.18 \cdot 10^{14}$. This gives us the conversion efficiency $\xi = 26 \div 29\%$. To measure the conversion efficiency of methane to C^{6+} ions, we had to use 10 Hz repetition rate of 60 ms accumulation and 40 ms ionization process. In this case the conversion efficiency is evaluated to be $\xi = 12 \div 15\%$.

We would like to summarize the conversion efficiency results:

- The cryogenic technology of accumulation and pulsed injection of methane into the electron string has been elaborated and proven experimentally.
- It has been shown experimentally that neutral CH radicals cannot dramatically decrease the conversion efficiency of methane to carbon ion beams in the ESIS.

- The measured conversion efficiencies of methane molecules to carbon ions beams is rather high, 26 – 29% for C⁴⁺ and 12-15 % for C⁶⁺ ion beams.

PERSPECTIVE OF RADIOACTIVE CARBON BEAM FORMATION

An increase up to 10¹⁰ of the total number of the produced C⁴⁺ ions per pulse (Table 1) is expected to be possible with the new Krion-5T ESIS source, which is under construction at JINR now at magnetic field 5T. It was found experimentally [5, 6] that the maximum number of electrons accumulated in a string was proportional to the confined magnetic field B to the third power $Q_e = aB^3$. (Fig. 7). A grows of the magnetic field from 3 T in Krion-2 to 5 T in Krion-5T could permit about 4.5 times increase in the number of stored electrons and their density. The increase in the electron density at 5T reduces the ion confinement time, which determines the injection repetition frequency.

A further increase in the intensity of the radioactive carbon ion beams is connected with the construction of the Tubular Electron String Ion Source (TESIS) [10-11] with a capacitance of the electron string and stored ions 50 times larger of Krion-2 (Table 1). The main point is that the tubular geometry of the drift tube structure allows one to avoid virtual cathode formation for the corresponding number of accumulated electrons. The gain of the highly charged ion input in TESIS compared with ESIS is characterized by the ratio of the tubular beam diameter d to the radial beam thickness a : $N_{TESIS}/N_{ESIS} = 2 \cdot d/a \approx 50$. It is expected that this new TESIS will meet all rigid conceptual and technological requirements and should provide an ion output approaching 10 mA of C⁴⁺ ions in the pulse mode or 10¹¹ ions per pulse and about 10 μA of C⁴⁺ ions in the average current mode.

The high conversion efficiency and the carbon ion beam intensities obtained at ESIS make it uniquely favourable for cancer treatment with ¹¹C ion beams.

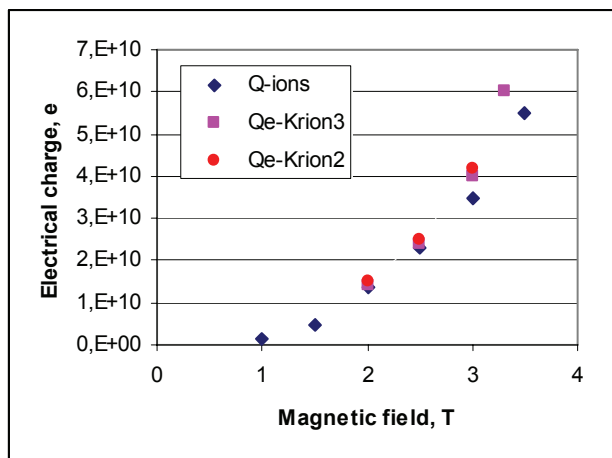


Figure 7: Dependence of the electron and ion space charge capacitances on the confined magnetic field.

ACKNOWLEDGMENTS

The research was supported in part by the International Science and Technology Center, grant № 3454.

REFERENCES

- [1] S. Yamada, PAC95, p.9.
- [2] M. Kanazawa et al., NIM A701 (2002) p.244.
- [3] S. Hojo et al., Production of ¹¹C-beam for particle therapy, Paris, 2004.
- [4] E.E. Donets et al., J. of Phys.: Conf. Series (2008).
- [5] E.D. Donets, Physica Scripta T12 (1996), p.11
- [6] E.D. Donets, Rev. Sci. Instr. 71 (2000), p. 810.
- [7] E.D. Donets, in book: Physics and Technology of Ion Sources, NY, 1989, p. 245.
- [8] E.D. Donets, Rev. Sci. Instr. 71 (2000), p. 810.
- [9] D.E. Donets et al., Rev. Sci. Instr. 75 (2004), p. 1543.
- [10] D.E. Donets, et al., Rev. Sci. Instr. 73 (2002), p. 696.
- [11] E.D. Donets, et al., EPAC08, p. 403.

SIMULATION AND DESIGN OF TUBULAR ELECTRON STRING ION SOURCE

D. E. Donets, E. D. Donets, E. E. Donets, V. M. Drobin, A. V. Shabunov, Yu. A. Shishov,
V. B. Shutov, E. M. Syresin, Joint Institute for Nuclear Research, Dubna, Russia

A. E. Dubinov, R. M. Garipov, I.V. Makarov,

Russian Federal Nuclear Center “All–Russian Institute of Experimental Physics”, Sarov, Russia.

Abstract

The so-called reflex mode of Electron String Ion Source (ESIS) operation has been under intense study, of both experimental and theoretical at JINR during the last decade. The idea of using a tubular electron string ion source (TESIS) has been put forward recently to obtain 1-2 orders of magnitude increase in the ion output as compared with ESIS. The project is aimed at creating TESIS and studying an electron string in tubular geometry. The new tubular source with a superconducting solenoid up to 5 T should be constructed in 2010.

The method of the off-axis TESIS ion extraction will be used to get TESIS beam emittance comparable with ESIS emittance. It is expected that this new TESIS (Krion T1) will meet all rigid conceptual and technological requirements and should provide an ion output approaching 10 mA of Ar^{16+} ions in the pulse mode and about 10 μA of Ar^{16+} ions in the average current mode.

Analytical, numerical study of the tubular electron strings and the design of the TESIS construction are given in this report. The experiments with quasi tubular electron beams performed on the modified ESIS Krion 2 are also discussed there.

TUBULAR ELECTRON STRING ION SOURCE

The Electron String Ion Source is based on a specially designed electron gun and an electron reflector that allows multiple uses of beam electrons [1-3]. At some conditions the electron string is formed with about few hundreds reflections for each electron. The electron string can be used for production of highly charged ions similarly to beam electrons. The interest in the ESIS mode was motivated by the attractive possibility of decreasing the electron beam power by a factor of 100 preserving simultaneously the same ion yield. The Krion-2 ESIS has been used successfully at the injection complex of JINR synchrotron Nuclotron for production of highly charged ion beams: Ar^{16+} - 200 μA , Fe^{24+} - 150 μA in 8 μs pulses (see Table 1) [3].

The idea of using TESIS was proposed in [4] to obtain a considerable increase of ion outputs (Table 1) in comparison with the ESIS and simultaneously a small ion beam emittance, usually provided by ESIS. The method of the off-axis TESIS ion extraction was proposed in [4-5] to get beam emittance comparable with ESIS one.

In fact, the number of produced ions is proportional to the number of the stored electrons and for a given source

length it is proportional to the beam cross-section area. The ratio of the stored electrons/ions in the tubular source N_{TESIS} and in the solid cylindrical beam N_{ESIS} of the same length is $N_{\text{TESIS}}/N_{\text{ESIS}} \approx 4r/a \approx 25 \div 50$, where a is the radial electron beam thickness and r is the main radius for the tubular electron beam. Second crucial point is that the use of tubular geometry of drift tube structure allows avoiding the virtual cathode formation for the corresponding amount of accumulated electrons in comparison to the cylindrical drift tube structure.

It was found experimentally [1-3] that the maximum number of electrons N_e accumulated in a linear string was proportional to a confined magnetic field B to the third power:

$$N_e = \kappa B^3 \quad (1)$$

An increase in the magnetic field from 3 T in Krion-2 to 5 T in Krion-T1 permits 5 times increases of the ion yield.

Table 1: Parameters of Electron String Ion Sources

Ion source	Krion-2	TESIS
Electron energy, keV	3÷5	3÷5
Number of stored electrons	$5 \cdot 10^{10}$	$3 \cdot 10^{12}$
Magnetic field, T	3	5
Ion current, mA	0.15	10
Pulse duration, μs	$8 \div \infty$	$8 \div \infty$
Maximal number of Ar^{16+} extracted ions	$5 \cdot 10^8$	$3 \cdot 10^{10}$
Ion extraction frequency, Hz	1	5
Average ion current, mA	0.15	10

NOTES ON TUBULAR ELECTRON STRING EXPECTED PARAMETERS

The density of the tubular electron string is determined by the initial injected electron current density and by the time of the electron escape from the ion source. It is reasonable to consider electron escape rate based on test electron propagation properties ignoring for a while corresponding contributions from collective effects. The escape of the stored electrons depends on an electron elastic scattering angle α_{gun} , which is produced at a reflection of the electrons from gun and collector potential barriers. As a rule, the electron gun and reflector

are situated in the fringe magnetic field with $B_{\min} = B/20$, where B is a value of the magnetic field in the uniform region. The scattering angle α_{gun} strongly depends on the magnetic field in the gun region $\alpha_{\text{gun}} \approx (r_c/d) \cdot (\rho/d) \approx 10 \text{ mrad}$, where $r_c = 1 \text{ mm}$ is the tubular cathode emitter width, $d = 10 \text{ mm}$ is the cathode-anode gap, $\rho = v/\omega = 1 \text{ mm}$ is the Larmor radius in the gun or collector magnetic field $B_{\min} = 0.25 \text{ T}$, v is the total electron velocity, $\omega = eB_{\min}/mc$ is the cyclotron frequency in the magnetic field B_{\min} , e and m are the electron charge and mass, c is the velocity of light. The gun/collector electron scattering angle is increased to $\alpha = \alpha_{\text{gun}} \cdot R^{1/2} \approx 50 \text{ mrad}$ as electron penetrates into the uniform magnetic field region with $B = 5T$, where $R = B/B_{\min} = 20$ is magnetic trap ratio.

There are two evident channels of electron escape in this scenario without collective effects. Main part of the stored electrons escape the ion source due to the transverse diffusion, caused by the mentioned scattering at gun/reflector regions. The other part of the stored electrons could be captured after $N_{\text{os}} \approx 1/4\alpha^2 \approx 100 \div 300$ oscillations in the magnetic traps formed between edges of solenoid and the gun or collector potential barriers due to electrons entering into the “cone loss” functional space.

The number of string electrons stored in the ion confinement region could be estimated as

$$N_e = (I_e \cdot L / v \cdot e) \cdot (1/4\alpha^2) \approx 3 \cdot 10^{12} \quad (2)$$

where $I_e = 0.2$ is the electron injection current, $L = 1.0 \text{ m}$ is the setup length. Reduction of the confining magnetic field B leads to the corresponding reduction of the stored electrons (2) because of an increase of the scattering angle α . In the high magnetic field the radial half-width of a tubular beam $a/2 = 110 \mu\text{m}$ is twice as large as the Larmor radius $\rho_B = 50 \mu\text{m}$ calculated at full electron energy and B . In this case the electron escape is realized mainly due to capture in the “cone loss”.

The main favourable effect of dense electron string formation is related to energy spread $\Delta E/E_0$ of the stored electrons. The energy spread was experimentally observed with linear electron string and it is caused by the collective interaction of the stored electrons. The large electron energy spread leads to strong reduction of the space charge effects in the gun region at a high string density. The oscillating electrons with low energy practically do not have influence on the operation of the gun since they are reflected from the potential barrier far enough from the emitter surface. The maximal density of stored string electrons in the gun region essentially depends on the electron energy spread (Fig. 1). For example, the density of string electrons n_0 in the gun region increases by the factor $k = n_0/n_{b0} = 11.5$ at $\Delta E/E_0 = 0.3$ (Fig. 1) compared with nominal Child-Langmuir density n_{b0} . The gun perveance $P_{g\text{-st}}$ for a tubular string with a wide electron energy spread is also k times larger $P_{g\text{-st}} = kP_g$, than the gun perveance related to the Child-Langmuir low $I_{b0} = P_g U_{3/2}$. At energy spread $\Delta E/E_0 \approx 1$ the string density increases to $n_0/n_{b0} = 27$, however the yield of

highly charged ions reduces because of a decrease of the ionization cross section caused by the low energy string electrons. These electrons make a small contribution to the deep ionization of highly charged ions. The yield of highly charged ions reduces at a large electron energy spread $\Delta E/E_0 > J/(2J + e\Delta U) \approx 0.3 - 0.4$, where $E_0 = 5 \text{ keV}$ is the electron energy, it corresponds to $E_0 \approx 2J + e\Delta U$ at the optimal ion ionization, $e\Delta U \approx 1.5 \text{ keV}$ is the kinetic electron energy reduction related to the string space charge effects, J is the ionization potential of the highly charged ions, $J \approx 1 - 2 \text{ keV}$ for ions like Ar^{16+} and Fe^{24+} . There is an optimal electron energy spread for production of dense string at which an intensive highly charged ion beam is formed. Below in simulation we consider the uniform energy distribution function in the interval of $2/3E_0 < Ee < E_0$ typical of the experiments with the linear electron strings [1-3]. In fact, it was experimentally observed that there are some amounts of string electrons with kinetic energy larger than injection energy; however, presence of this high energy electron tail works in the enhancement side of the given estimations.

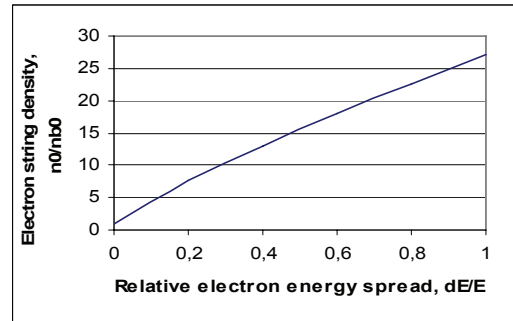


Figure 1: Ratio of string electron density to the Child-Langmuir density n_{b0} versus the electron energy spread.

The tubular geometry of drift tube structure permits a 25÷50 time increase in number of the stored string electrons comparing to the linear one. The drift chamber perveance P_{ch} should be larger the gun perveance $P_{g\text{-st}}$ for tubular string with a wide electron energy spread $P_{\text{ch}} > P_{g\text{-st}}$ to avoid virtual cathode formation. The virtual cathode formation leads necessarily to formation of a low energy electrons and therefore to reduction of yield of the highly charged ions. The number of stored electrons in a high intensity tubular string is

$$N_e = (\Delta U_{an} \cdot L / e) \cdot 2r / h_{ap} \approx (k \cdot I_{b0} / e) \cdot (L / v) \approx 4 \cdot 10^{12} \quad (3)$$

at $P_{\text{ch}} > P_{g\text{-st}}$, here $k \cdot I_{b0} / 2$ is the current of string electrons propagating in one longitudinal direction, $I_{b0} = 1.9 \text{ A}$ is the beam current corresponding to the Child-Langmuir low, $U = 5 \text{ kV}$ is the cathode-anode accelerating voltage, $k = 11.5$ is the gain in the string density for electrons with the energy spread $\Delta E/E_0 = 0.3$, $r = 8.2 \text{ mm}$ is the radius of central beam line in the high magnetic field region, $h_{ap} = 1 \text{ mm}$ is the minimal electron string radial aperture in the uniform magnetic field B , ΔU_{an} is the potential inside of anode diaphragm related to electron string space charge,

$\Delta U_{an}=U/[1+(d^2/1,3Rh_{ap}\alpha)\cdot(1+47\alpha^2)]$. The value $d^2/(1,3Rh_{ap}\alpha)=P_{an}/P_{g-st}$ defines a ratio of the anode diaphragm perveance P_{an} to the gun perveance P_{g-st} , where $P_{an}/P_{ch}=h/h_{ap}=3$, $h=3$ mm is the radial gap between the coaxial tubular drift chambers in the ion confinement region. The coefficient $1+47\alpha^2$ is related to the contribution of the electron scattering effects to formation of a high intensive tubular string. At saturation of the tubular string capacitance the number of stored electrons N_e (3) has more slow dependence on the electron scattering angle α and the magnetic field B compared with (2) and experimental data (1). The potential of the tubular string ΔU in the ion confinement region is defined by the equation $\Delta U\cdot(U-\Delta U)^{1/2}=U^{1/2}\cdot\Delta U_{an}\cdot(h/h_{ap})$ at $h\gg h_{ap}$. The virtual cathode is formed here at $\Delta U=2/3U$. To avoid creation of virtual cathode in the high magnetic field region the potential inside anode diaphragm ΔU_{an} should be lower than $\Delta U_{an}<U\cdot(2h_{ap})/(3^{3/2}h)=0,13U$ or the cathode-anode gap should be larger than $d>d_0=\{(1,3Rha/2)\cdot(3^{3/2}-2h_{ap}/h)\}^{1/2}=6$ mm. The virtual cathode is formed at $d<d_0$ ($P_{ch}<P_{g-s}$) and number of stored string electrons is equal to

$$N_{max}=(2U\cdot L/3e)\cdot 2r/h=1,5\cdot 10^{13} \quad (4)$$

At a high electron scattering angle α (low magnetic field) the electron string is formed with intensity (2). At a high magnetic field and $P_{ch}>P_{g-s}$ the maximum number of string electrons is defined by (3). This regime corresponds to formation of a high intensive tubular string without creation of virtual cathode. In opposite case $P_{ch}<P_{g-s}$ (4) the virtual cathode is formed in the ion source, as result, the string electrons have the large energy spread $\Delta E/E_0 \cong 1$, which leads to reduction of yield of the highly charged ions.

EXPERIMENTS WITH QUASI-TUBULAR ELECTRON BEAMS

Experiments with quasi-tubular electron beams were performed on the modified ion source Krion-2. Eight special electron guns were installed (Fig. 2) on equal radial distance but at different azimuthal angles along the circle in fringe magnetic field region (1/20 B). Each such IrCr emitter of 1 mm diameter injected a separate pencil beam towards uniform magnetic field region where tubular drift tube structure has been installed as well.

Annular repeller ring was installed at opposite side of the source mirror symmetrically to the gun geometry in respect to the center of the solenoid. However only 4 holes in repeller were produced and 4 corresponding electron collectors behind them were installed.

The quasi-tubular electron beam (Fig. 3) has been formed by those 8 pencil azimuthally distinct electron emitters. We planned to fulfil the whole space between distinct pencil beams in the azimuthal direction due to azimuthal electron drift motion. Special electrodes were installed in the modified Krion-2 source to produce radial

electric field leading to the azimuthal electron drift motion in the longitudinal uniform magnetic field.

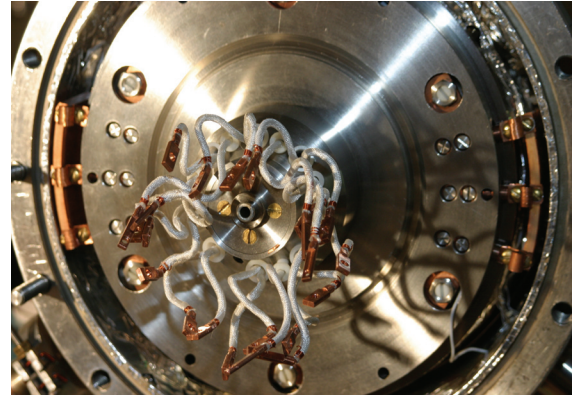


Figure 2: Back side of quasi-tubular electron gun assembly with 8 distinct electron emitters, installed at various azimuthal angles.

The experiments in such set-up allowed to investigate dynamics of separate beams as well as to check effects related to the azimuthal asymmetry of the solenoid magnetic field and the azimuthal imperfection of the ion source mechanical constriction. At variation of the radial electric field the pencil beam from each gun was able to enter the two nearest collectors placed at different azimuthal angles at opposite side of the source (Fig. 3).

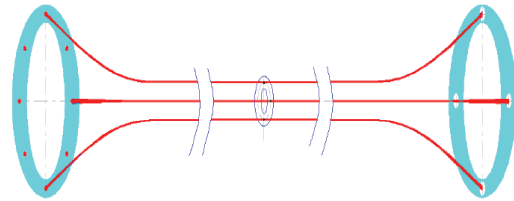


Figure 3: Distinct electron beams and their azimuthal rotation by the applied radial electric field.

The experimental results related to transportation of the pencil electron beams are given in Fig 4. When the pencil electron beam is accepted by the collector the repeller current is became equal to zero. At variation of the radial electric field one can provide a condition when the pencil electron beam is turned on azimuthal angle 90° (Fig. 3) by the drift electrodes and therefore it is collected by second collector (second peak in the Fig 4a).

The electron beam widths are given in Fig. 4b for first and second collectors. They are equal to 4.5 mm in the first collector and 5.2 mm in the second one. The increase in the beam width in the second collector is due to the action of the large radial electric field of the drift electrodes together with the electron angle and energy spreads. The collector current of the pencil electron beam depends on the number of the reflections from repeller electrode and cathode. The collector current without reflection is 20% larger than its value after two reflections from the repeller electrode and the cathode.

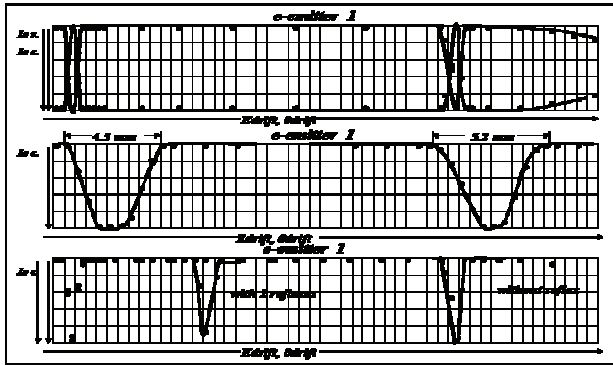


Figure 4: Dependences of collector and repeller currents on the radial electric field.

The performed experiments permit to investigate the azimuthal symmetry of the longitudinal magnetic field and to define a parallelism of the magnetic field axis and the setup axis and showed, that the symmetry in the Krion-2 is not perfect.

DESIGN OF TESIS KRION T1

The tubular electron string ion source [6] (Fig. 5) consists of cryomagnetic, electron-optical, ion-optical and vacuum systems, power supplies, diagnostic and control electronics. The parameters of the superconducting solenoid are given in the Table 2. The superconducting solenoid is fixed by two supports on the vacuum chamber. The cryocooler head is placed at the edge of the cryostat part. The current loads, thermal shielding, superconducting keys, cooled diodes and resistors are placed between the cryocooler and the solenoid. The thermal shielding is connected with the first cryocooler section at the temperature of 4.2 K. The power of the first cryocooler section is 1.5 W. The temperature of the second cryocooler section is of 40 K. The electron gun, reflection electrodes and other elements have temperature from room to cathode temperature.

Ultrahigh vacuum of 10^{-9} – 10^{-10} Pa is the a feature of the tubular electron string ion source. This vacuum should be provided in the space between the internal and external drift tubes. The choice of the vacuum system design is dictated by a small diameter of drift tubes (internal diameter is 0.9 cm, external one is 1.5 cm) which are 120 cm long. The cryo-pumping conception was adopted for TESIS. The external pumping provides preliminary pressure of 10^{-4} Pa and then an ultrahigh vacuum is achieved at cryosorption of surfaces cooled to temperatures of 4.2 K and 40 K. The external drift tube is cooled to 4.2 K, which permits its internal surface to work as a cryopanel on which all gases are frozen (except He, H₂). The internal drift tube is connected to the cryocooler section at 40 K. The surface of the internal drift tube works also as a cryopanel with a smaller sorption efficiency as compared with the external one. Different gases except He, H₂ are also frozen here. Some problems can appear at pumping of hydrogen.

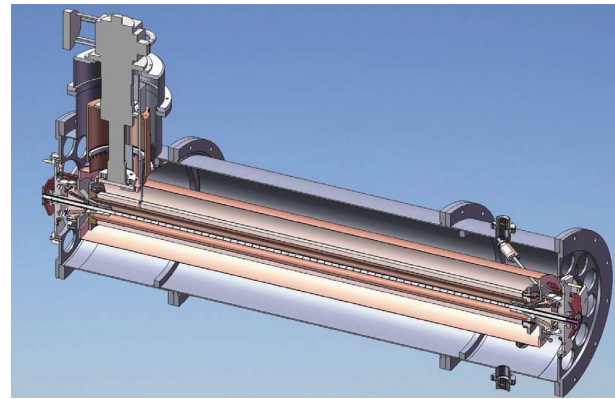


Figure 5: General view of the TESIS.

Table 2: Parameters of Magnetic System

Parameter	Value
Internal solenoid diameter, mm	70
External solenoid diameter, mm	101
Solenoid length, m	1.2
Maximal current, A	95.22
Number of windings per layer	2263
Number of layers	22
Total number of windings	49786
Thickness layer, mm	0.63
Current density, j/mm ²	285.1
Maximal field, T	5.0
Fr, kG/rad	2.46×10^4
$2 \times \pi \times Fz$, kG	5.68×10^3
Induction, Gn	14
Stored energy, kJ	63
Cooled mass at 4.2 K, kg	~ 50

It is connected with high outgassing of hot gun surfaces and the anode reflector. A high level of outgassing is usually realized at the initial work stage and it essentially decreases with increasing operation time. The external pumping is provided only for initial operation time. As the gun and the reflector electrodes are placed near the pumps on both edges of the setup and this reduces the problem at initial pumping of hot surfaces.

Based on the computer simulation we designed the electron-optical (Fig. 6) and ion-optical systems (Fig. 7). The electron gun has three electrodes. The diameter of the cathode emitter is 73.8 mm, its width is 1 mm. The suppressing electrodes are installed to suppress emission by the appropriate voltage, applied to the electrodes, which is necessary for efficient operation in a typical pulsed mode of injection. The gap between the annular emitter and the suppressing electrodes is 0.4 mm, the slit between the suppressing electrodes has radial width

1 mm. The cathode–anode gap corresponds to $d=10$ mm, it defines the electron scattering angle and gun perveance. The chosen gun is an annular version of the Pierce-type gun since the slopes of the focusing electrodes are 22.50 with the central magnetic flux line. The entrance anode diaphragm has a radial size of 4.5 mm that corresponds to an available aperture of the tubular string electrons in the ion confinement region of $h_{ap} = 1$ mm. The anode diaphragm provides collection of the string electrons that leave the system in the radial direction due to electron scattering and diffusion.

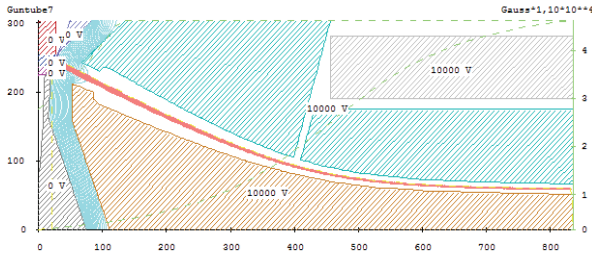


Figure 6: Formation of tubular electron beam in the fringe solenoid field.

The electron reflector was chosen to be mirror symmetrically with respect to the solenoid center. The orifice for ion extraction is foreseen to be arranged instead of the emitter at some azimuthal position of the reflector. The reflection voltage is chosen to be a few kV lower than the cathode voltage in order to ensure total reflection of the whole electron beam.

The drift tube structure (Fig. 7) consists of several electrodes which are used for production of ion traps, formation of a tubular ion beam (Fig. 7), off-axis ion extraction, and observation by means of pick-up electrodes of processes related to the electron string and ion beam formation. The ion extraction channel runs along the magnetic flux line at a definite azimuthal angle. Off-axis ion extraction was simulated with use of the Opera-3D code. On the basis of these simulations the azimuthal width of the extraction channel was optimally chosen to be 10^0 . The extraction channel begins in the uniform magnetic field region and consists of several electrodes which follow the shape and size of the corresponding magnetic flux lines up to B_{min} . Azimuthal ion migration in a uniform field region naturally occurs due to drift motion of ions in the longitudinal magnetic and radial electrical fields. When ions approach the beginning of the extraction channel, they are reflected back to the uniform field region by the applied positive voltage, except those ions which are captured in the extraction channel. Ions in the extraction channel are azimuthally confined due to the potential well created everywhere along the extraction channel in the azimuthal direction. Moreover, ions are accelerated towards the extraction orifice in the weak magnetic field due to the gradual decrease in the applied potentials along the extraction channel. It was proven in various simulations

that ions could be accelerated to $2 \cdot Z$ keV in the extraction channel without disturbing the electron beam. The electron reflector mounted at B_{min} reflects electrons and extracts ions. The extracted ion beam penetrates the orifice in the reflector placed at the same azimuthal position as the ion extraction channel. The extracted ion beam has an ellipsoidal shape with diameter $\Delta r_i=2$ mm in the radial direction and diameter $\Delta y_i=8$ mm in the azimuthal one. This azimuthal size is the minimal one allowed by the voltage applied to the extraction electrodes at the chosen azimuthal size of the extraction channel.

The simulated beam spot sizes permit to define the normalized radial ϵ_{r-n} and azimuthal $\epsilon_{\phi-n}$ emittances of the extracted ion beam: $\epsilon_{r-n} = \beta_i \cdot \Delta r_i^2 / 4 \rho_i = 0.04 \pi \cdot \text{mm} \cdot \text{mrad}$, $\epsilon_{\phi-n} \cong \beta_i \cdot \Delta r_i \cdot \Delta y_i / 4 \rho_i = 0.15 \pi \cdot \text{mm} \cdot \text{mrad}$, where $\beta_i = v_i / c = 3,5 \cdot 10^{-3}$, v_i is the velocity of extracted ions at reflector electrode voltage $U_{ref}=6$ kV, $\rho_i = v_i / \omega_i = 10$ cm is the ion Larmor radius calculated at ion energy ZeU_{ref} , $2\rho_i$ plays a role of β -function, ω_i is the ion cyclotron frequency in the magnetic field B_{min} . We assume that the ion azimuthal angle spread is comparable with the radial one. The radial and azimuthal emittances of the extracted ion beam accelerated to energy of $eU_{ac} = 25 \cdot Z$ keV are $\epsilon_r \cong 5 \pi \cdot \text{mm} \cdot \text{mrad}$ and $\epsilon_{\phi} \cong 20 \pi \cdot \text{mm} \cdot \text{mrad}$.

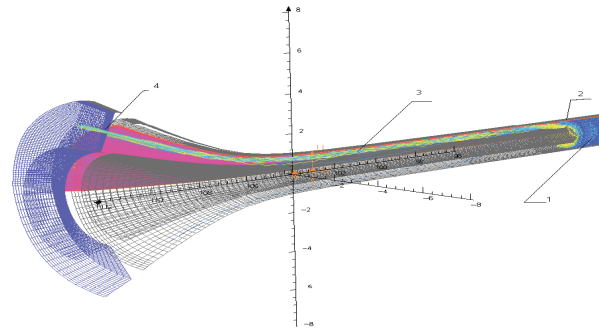


Figure 7: OPERA 3D simulation of the ion optic system and the ion off-axis extraction channel.

ACKNOWLEDGEMENTS

The research was supported by the International Science and Technology Center, grant № 3454. Discussions with L. Liljeby and H. Danared are greatly acknowledged. E.E.D. is grateful to the Manne Siegbahn Laboratory (Stockholm, Sweden) for hospitality where numerical simulations with use of Opera-3D code were performed.

REFERENCES

- [1] E.D. Donets, Physica Scripta T12 (1996), p.11.
- [2]. E.D. Donets, Rev. Sci. Instrum. 71 (2000), p. 810.
- [3] E.D. Donets et al., Rev. Sci. Instr. 75 (2004), p. 1543.
- [4] E.D. Donets, et al., Rev. Sci. Instr. 73 (2002), p. 696.
- [5] E.E. Donets, J. of Phys.: Conf. Series 2, (2004) p. 97.
- [6] E.E. Donets et al, EPAC 08, (2008), p. 403.

LARGE BORE ECR ION SOURCE WITH CYLINDRICALLY COMB-SHAPED MAGNETIC FIELDS CONFIGURATION

Y. Kato, F. Sato, T. Iida

Osaka University, Suita, Osaka 565-0871, Japan

Abstract

Electron Cyclotron Resonance Ion Sources (ECRIS) have been developed for long time and performances are still extended at present. Recently, they are not only used in producing multi-charged ions, but also molecules and cluster ions. A new type of ion source with a wide operation window is expected for various uses. We developed a novel magnetic field configuration ECRIS. The magnetic field configuration is constructed by a pair of comb-shaped magnetic field by all permanent magnets and has opposite polarity each other with ring-magnets. This magnetic configuration suppresses the loss due to $E \times B$ drift, and then plasma confinement is enhanced. We conduct preliminary extracting and forming large bore ion beam from this source. We will make this source a part of tandem type ion source for the first stage. Broad ion beams extracted from the first stage are transferred like a shower to the plasma generated by the second stage. We hope to realize a device which has a very wide range operation window in a single device to produce many kinds of ion beams. We try to control plasma parameters by multiply frequency microwaves for broad ion beam extraction. It is found that plasma and beam can be controllable on spatial profiles beyond wide operation window of plasma parameters. We investigated feasibility of the device which has wide range operation window in a single device to produce many kinds of ion beams as like universal source based on ECRIS.

INTRODUCTION

Electron Cyclotron Resonance Ion Sources (ECRIS) have developed with time [1, 2]. Nowadays the ECRIS is used not only in atomic physics and semi-conductors but also with a wide variety of applications. For example, they are applied to heavy ion cancer therapy [3], investigation for discovery of new elements, and super-heavy nucleus science [4], and so on. Recently, the ion sources are not only used in producing multi-charged ions, but also cluster ions, iron encapsulated fullerenes which are important in the field of bio-nano technology [5]. A new type of ion source with a wide operation window is expected for various uses. We are planning to build the device which gives these required performance features in a single apparatus.

We developed a novel magnetic field configuration ECRIS. The magnetic field configuration is constructed by a pair of comb-shaped magnetic field by all permanent magnets and has opposite polarity each other with ring-magnets. The comb-shaped magnet cylindrically

surrounds the plasma chamber. This magnetic configuration suppresses the loss due to $E \times B$ drift, and then plasma confinement is enhanced. We tried many experiments by this ECRIS [6-8]. We will make this source a part of tandem type ion source for the first stage. We conduct preliminary extracting and forming large bore ion beam from this source [9]. Extraction broad-ion-beam from the first stage plasma are transferred like a shower to the plasma generated by second stage ECRIS. We hope to realize a device which has a very wide range operation window in a single device to produce many kind of ion beams, *e.g.*, from multi-charged ion to cluster ion, nano-tube, fullerenes, including impurities trapping, etc, as a universal source.

In this paper, we try to control plasma parameters and their profiles in an unused way, *i.e.*, by feeding simultaneously 2.45 GHz and 11 to 13 GHz frequency microwaves for broad ion beam from the first stage.

EXPERIMENTAL DEVICE

Outline of Experimental Device

The top view and the side view of the large bore ECRIS as the first stage of tandem ECRIS is shown in Fig. 1. The base pressure is about 10^{-5} Pa. Two frequencies microwaves are supplied to the plasma chamber (200 mm in diameter and 320 mm in length) with the cylindrically comb-shaped magnetic fields. 2.45 GHz microwaves generated by magnetron (max. power: 1.3 kW) are transformed from the waveguide mode to the coaxial mode, and launched to the chamber along z -axis by L-shaped semi-dipole antenna. 11 to 13 GHz microwaves amplified by travelling-wave transformer amplifier (TWTA, max. power: 350 W) from the synthesizer are directly fed to the chamber beyond a quartz window along to z -axis. Incident and reflected microwaves are tuned by the stainless steel meshed plate for the 11 to 13 GHz microwaves. The 2.45 GHz microwaves are tuned by the three stub tuner. The operating pressure is about $10^{-1 \sim -3}$ Pa. The plasma parameters are measured by a Langmuir probe. The measurement position ranges vertically from the chamber wall ($y=100$ mm) to the center of the chamber ($y=0$ mm). Ion beam is preliminarily extracted from this source by the large bore extractor consisting of three electrode plates with multiple holes, and measured by the Faraday cup (20 mm in diameter and 37 mm in length) located at $z=360$ mm, 263 mm apart from the electrode. The position and gap length of these electrodes are not yet optimized, and are now under investigation [9].

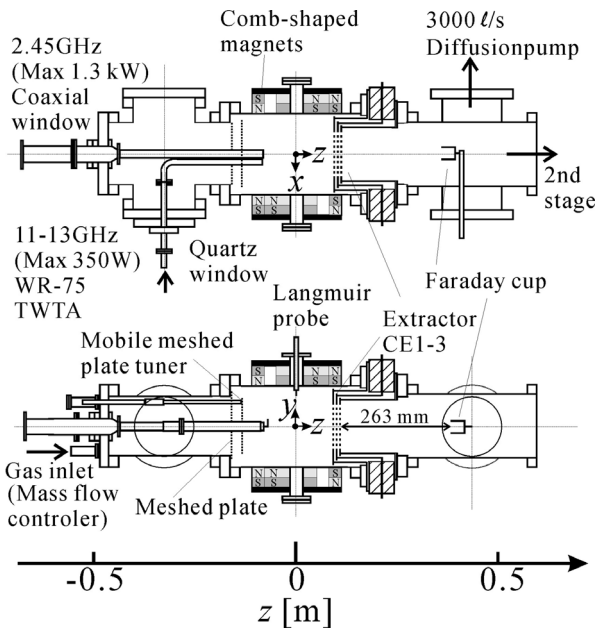


Figure 1: Top and side views of the large bore ECRIS as the first stage of tandem ECRIS.

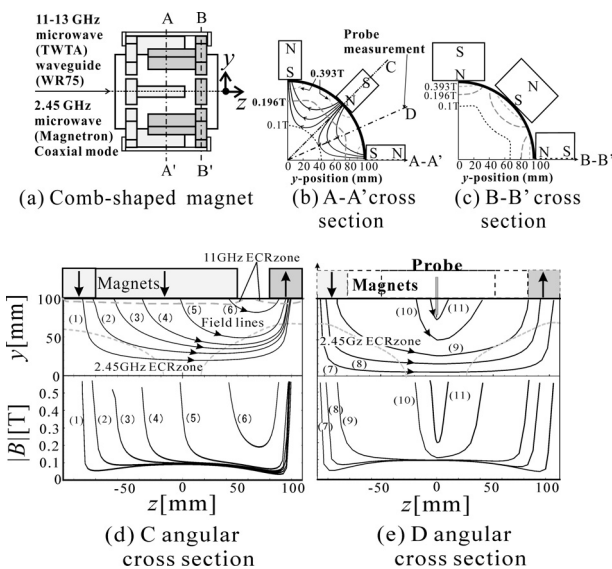


Figure 2: Side view of cylindrically comb-shaped magnets (a). Contour plots of field strength and field lines in A-A' (b) and B-B' cross sections (c), respectively; those in radial-z direction at C (d) and D angular (e).

Configuration of Magnetic Field

Fig. 2 (a) shows side view of the cylindrically comb-shaped magnets surrounding the chamber, *i.e.* octupole magnets with a pair of ring magnets with opposite polarity. Fig. 2 (b) and (c) show contour plot and line forces in the cross section A-A' and B-B' indicated in Fig. 2 (a). The upper figures of Fig. 2 (d) and (e) depict contour plots and field lines in the radial and z direction cross section at the positions indicated by C and D angular cross section in Fig. 2 (b). The field lines in Fig. 2 (e) indicate their projections to the plane. The lower

Ion Sources

figures denotes field strength along the field line labelled by (1)–(11) corresponding to the upper field lines. The positions of resonance zones for 11 GHz microwaves are formed around peripheral region nearby the chamber wall. Those for 2.45 GHz are formed around the center of the chamber, but vanish at the center cross section. The probe measurement conducted along D angular cross section is indicated in Fig. 2 (b).

EXPERIMENTAL RESULTS AND DISCUSSION

By using 2.45 and 11 to 13 GHz microwaves individually, we can conduct experiments for production of ECR plasma and extraction of ion beams. First of all we investigate profiles of plasma parameters and characteristics in feeding each single frequency microwave to the ECRIS. Then we introduce simultaneously two frequency microwaves, measure the profiles, survey the experimental conditions, and confirm the effect of feeding multi-frequencies microwaves on the ECRIS plasma. We conduct preliminary ion beam extraction.

ECR Ion Source Plasma Characteristics in Single Frequency Microwave (11 to 13 GHz)

Fig. 3 shows the experimental results obtained by 11 GHz frequency microwaves. The upper and lower figures depict profiles of the electron density n_e and the electron temperature T_e . The left and right side figures are the cases of microwave power 100 W at 0.03 Pa and 0.016 Pa, and those of pressure 0.03 Pa at microwave powers 100 and 200 W, respectively. Each horizontal axis indicates y directions, where $y=0$ and $y=100$ mm means the center and the inner wall of the chamber. The peak positions of n_e and T_e are observed around the second harmonics resonance zone at $y=80$ mm [8]. These tendencies, *i.e.* peaking in peripheral regions, are caused from the peripheral formations of the fundamental and the second harmonic resonance zones, and are largely-unaltered by variation of microwave powers and pressures.

ECR Ion Source Plasma Characteristics in Single Frequency Microwave (2.45 GHz)

The experimental results obtained by 2.45 GHz frequency microwaves are shown in Fig. 4. The upper and lower figures depict profiles of n_e and T_e . The left and right side figures are the cases of microwave power 200 W at 0.03 Pa and 0.016 Pa, and those of pressure 0.03 Pa at microwave powers 200 and 300 W, respectively. Horizontal axes are the same of Fig. 3. It is found that n_e attains and crosses the cut-off density depicted by dotted lines in Fig. 4 for 2.45 GHz under low microwave powers. The peak positions are observed around the center at $y=0$ mm in contradiction to the case of 11 GHz microwaves. While these facts are the result of the construction of the ECR zone for 2.45 GHz frequency microwaves around the center, these tendencies are also largely unaltered by variation of microwave powers and pressures. It is

considered that the profile controlled by single microwave frequency in fixed magnetic field consisting only of permanent magnets is limited within operating pressure and microwave powers.

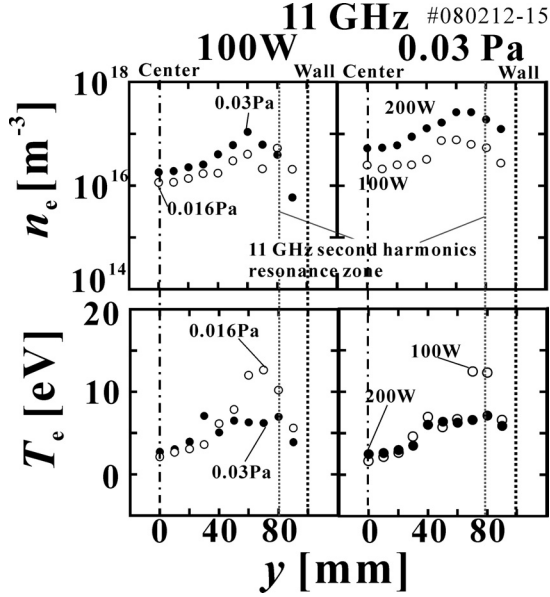


Figure 3: Profiles of n_e and T_e at the center in the cylindrically comb-shaped magnetic field ECRIS in the case of microwave frequency 11 to 13 GHz.

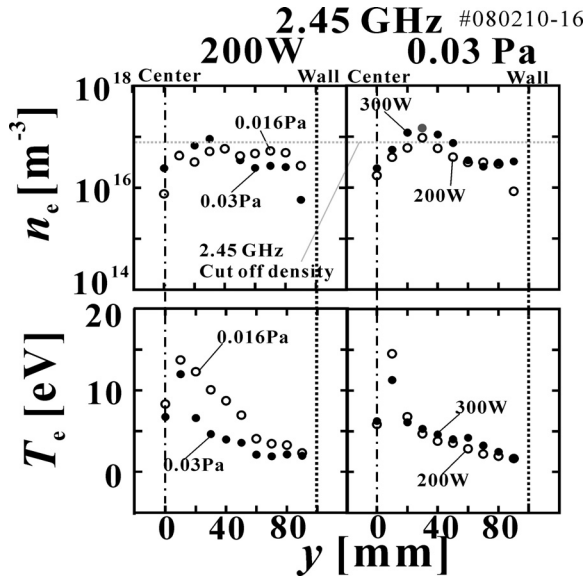


Figure 4: Profiles of n_e and T_e at the center in the cylindrically comb-shaped magnetic field ECRIS in the case of microwave frequency 2.45 GHz.

Efficiency of Comb-Shaped Magnets and Dependence of n_e on Microwave Power

In our experimental procedures, first of all we produced ECR plasma by using simple multipole (octupole) magnets, and measured its plasma parameters briefly. After then we reconstructed them to comb-shaped

Ion Sources

magnets and produced ECR plasma in the same experimental conditions except them [6]. We measured the n_e around their peak position ($r=60$ mm) in the case of 11-13 GHz frequency microwaves, and measured the dependences of the n_e on microwave power and frequency at high pressure (0.3 Pa).

Fig. 5 shows dependence of electron density on microwave powers. Solid lines and dotted lines indicate the case of comb-shaped and that of the simple multipole magnets. It is found clearly that n_e increased in the case of comb-shaped magnets with respect to that in the simple multipole magnets, and that the confinement was improved by constructing comb-shaped magnets. Under the maximum power of the TWTA, the saturation of n_e does not appear yet. When the frequency increased, n_e increased. Furthermore we obtained a 10^{18} m^{-3} density by using 13 GHz frequency microwaves at high pressure (1 Pa) at rather low microwave powers (350 W).

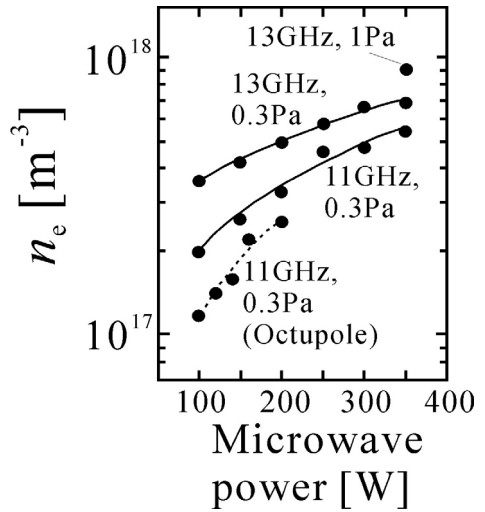


Figure 5: Dependence of n_e on microwave powers, and comparison between simple multipole and comb-shaped magnets.

Profile Controlling by Multi-Frequencies Microwaves

Next we tried to control the n_e and the T_e profiles by feeding simultaneously three microwave frequencies, *i.e.* 11 to 13 GHz and 2.45 GHz. Our experimental procedure is the following: we launch the 2.45 GHz microwaves into the chamber flowing Ar operating gas, ignite, and then sustain the ECR discharge. We superimpose 11 to 13 GHz microwaves to this initial ECR plasma, *i.e.* simultaneous two frequencies microwaves operations. The appearance from the viewing port obviously changes to be more luminous in contrast to the case of single 2.45 GHz frequency microwaves. Finally we turn off 2.45 GHz microwave and hold the ECR plasma by only 11 to 13 GHz microwaves. We recognized the difference in plasma emissions in each case of single 2.45 GHz and 11 to 13 GHz. We conducted measurements of the n_e and the T_e profiles in these steps.

Fig. 6 shows the typical n_e and T_e profiles obtained by these experimental results. The operating pressure is 0.03 Pa. The microwave powers are 200 W and 100 W for 2.45 GHz and 11 GHz, respectively. Fig. 6 (a) shows the peaking profiles around the center and periphery regions for the 2.45 GHz (open circles) and the 11 GHz (open squares) lined by gray lines, respectively. On the other hand, we obtain the flat profiles by launching simultaneous multi-frequencies microwaves as shown by closed circles and solid lines in Fig. 6 (a). The n_e profile can be controlled by varying each frequency microwave power. Fig. 6 (b) shows the T_e profiles corresponding to the n_e profiles as shown in Fig. 6 (a). The T_e profiles has basically the similar tendency to the case of the n_e , but flattening the T_e peaking is a little harder than that of the n_e at the low pressure. The T_e profile can be also controlled by varying each frequency microwave power.

The cylindrically comb-shaped magnetic field configurations are easy to scale up to larger size by selecting the number of multipole and the strength of the ring-like magnets. The disadvantages of fixed magnetic configuration of ECR zone, operation and controllability of the profiles are redeemed by frequency-controllable TWTA, and moreover simultaneously feeding largely different frequency microwaves, as in our experimental results.

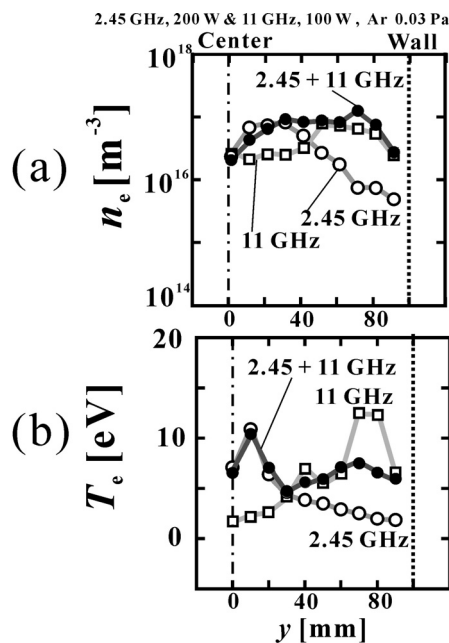


Figure 6: n_e and T_e profiles in the cases of each single and multi-frequencies microwaves.

Preliminary Ion Beam Extractions from ECRIS with Comb-Shaped Magnetic Field

We conduct preliminary ion beam extraction from the cylindrically comb-shaped magnetic field configuration ECR ion source [9]. At present, we are optimizing extraction conditions of ion beams, *i.e.* the position, the gap length, the shape of multi-holes extractor. We are

Ion Sources

investigating the effect of multi-frequencies of microwaves to the ion beams. At present we obtain also different profile ion beams and find a way to control spatial profiles of broad ion beams by these multi-frequencies microwaves; moreover, we are optimizing the ion beam extraction.

FUTURE PLANNING

Construction of Tandem Type ECRIS

We will make this ECRIS consisting of all comb-shaped magnets a part of tandem type ion source for the first stage. Large bore extractor set at the end of this source and extracted broad ion beams under low voltages to the second stage, like shower of ions, are needed. The second stage will also be large bore and ECRIS with long length along the z axis, individually operated by 2.45 GHz microwaves. The magnetic field configuration consists of octupole magnets and a mirror field made of 2 coils and a supplemental coil. At the end plate of the second stage we set the single hole extractor, and set beam lines for handling and analysis of ion charges state distributions.

We investigated feasibility and hope to realize the device which has a wide range operation window in a single device with tandem-type ion source based on ECR to produce many kinds of ion beams from multiply charged, to molecular, cluster ions, nano-tube, fullerenes, including impurities trapping, etc, aiming at a universal source based on ECRIS.

This tandem type ion source and ancillary equipments are now in construction. In the second stage, preliminary plasma production and the extraction have already been conducted under the limited low magnetic mirror field.

Large Bore Ion Extractions

Large bore extractor consisting of three electrodes is set at the opposite side against the microwaves feeds between the first stage and the second stage of the tandem-type ECRIS. We need to optimize the extractor position, the gap length and the shape of electrodes. The profiles of the extracted ion beams are measured by a Faraday cup downstream the extractor.

We will conduct the profile control of these broad ion beams by multiplex frequencies microwaves, and will investigate effects of ion streams from the first stage to the second stage plasma and the ion beams and the charges state distributions from the second stage.

Further Enlarged Operation Window by Pulse Modulated Microwave Feeding

Effects of after glow mode were well-known on conventional ECRIS's for production of multicharged ions and have been conducted in almost all ECRIS's in the world [10-12]. In a first stage, we tried to feed pulse-modulated microwaves to the ECRIS in order to enlarge operation windows for ECR plasma production, and then also to enhance ion beam current adding the after glow mode. Under the constraint of the same time-average

incident microwave, typical duration of pulse mode microwave operations and duty ratios are 50-500 μs and 30-80%, respectively. The maximum currents are obtained in the cases of 100-200 μs duration at 50% duty ratio. It is found that the total beam currents are enlarged by pulse mode operations.

The profiles of n_e and T_e are measured in both cases of CW and pulse mode. It is found that differences of their profiles also appear similar to ion beam profiles. It is found that the peak value of n_e in the pulse mode is larger than that in the CW mode, and that T_e in the pulse mode has tendency to be lower than that in the CW mode operations. These indirect evidences cause to enhance ion beams in the pulse mode operation, and then suggest a spread of operation windows for plasma parameters suitable to production of molecular or cluster ions. At present we are measuring time-dependent behaviors of the n_e and the T_e .

The pulse-modulated microwave operation is one of the powerful candidates to enlarge the operation window of the ECRIS, as well as availability of controlling microwave frequencies by TWTA on magnetic configurations fixed by all magnets.

We will be able to operate also 2.45 GHz frequency microwaves in the second stage by similar pulse-mode launching.

ACKNOWLEDGEMENTS

The authors wish to thank Professor A. G. Drentje, KVI, for helpful discussions and continuous encouragements. The authors would like to thank Professor Y. Yoshida, Toyo University, Dr. A. Kitagawa, NIRS and Dr. S. Biri, ATOMKI for helpful discussions, and Dr T. Asaji, Mr T. Satani, Mr T. Watanabe, Mr Y. Matsui, Osaka University for preparations and construction of devices in these works.

REFERENCES

- [1] R. Geller, Electron Cyclotron Resonance Ion Sources and ECR Plasma, IOP, Bristol, 1996.
 [2] A. G. Drentje, "Techniques and mechanisms applied in electron cyclotron resonance sources for highly

- charged ions", Rev. Sci. Instrum. 74, 2631-2645(2003).
 [3] M. Muramatsu, *et al.*, contribution in IIT2008; A. Kitagawa, M. Muramatsu, M. Sasaki, S. Yamada, T. Sakuma, N. Sasaki, H. Takahashi, W. Takasugi, M. Yamamoto, S. Biri, K. Sudlitz, and A.G. Drentje; "Status Report on ECR Ion Sources at HIMAC", Rev. Sci. Instrum. 75, 1476-1478(2004).
 [4] K. Morita, *et al.*, "Experiment on the Synthesis of Element 113 in the Reaction $208\text{Bi}(70\text{Zn},n)278113$ ", J. Phys. Soc. Jpn. 73, 2593-2596(2004).
 [5] F. Éva, S. Biri, I. Iván, "Investigation of Iron-Fullerene Mixture Plasmas in ECR Discharge", Fullerenes, Nanotubes and Carbon Nanostructures, 15, 249-256(2007); S. Biri, A.Valek, Kenez, A. Janossy, A. Kitagawa, "Production of Multiply Charged Fullerene and Carbon Cluster Beams by a 14.5GHz ECR Ion Source", Rev. Sci. Instrum., 2002, 73, 881-883(2002); K. Tanaka, *et al.*, contribution in IIT2008.
 [6] T. Asaji, Y. Kato, F.Sato, T. Iida and J. Saito, "11-13 GHz Electron Cyclotron Resonance Plasma Source Using Cylindrically Comb-shaped Magnetic-Field Configuration for Broad Ion-Beam Processing", Rev. Sci. Instrum., 77, 113503 1-6 (2006).
 [7] Y. Kato, H. Sasaki, T. Asaji, T. Kubo, F. Sato, and T. Iida, "An Electron Cyclotron Resonance Ion Source with Cylindrically Comb-Shaped Magnetic Field Configuration", AIP Conference Proceedings 866, 373-376(2006).
 [8] Y. Kato, T. Satani, T. Asaji, F. Sato, and T. Iida, "Effects of Fundamental and Second Harmonic Electron Cyclotron Resonances on ECRIS", Rev. Sci. Instrum., 79, 02A323 1-4(2008).
 [9] T. Watanabe, T. Satani, Y. Matsui, F. Sato, Y. Kato, T. Iida, AIP Conference Proceedings, 1066, pp.533-536, 2008.
 [10] G. Melin, F. Boutg, P. Briand, J. Debernardi, M. Delaunay, R. Geller, J. Phys. Colloq. (France), 1989, 50, no.C-1, 673.
 [11] P. Sortais, Rev. Sci. Instrum., 1992, 63, 2801.
 [12] Y. Kato, S. Kobayashi and S. Ishii, Rev. Sci. Instrum., 2000, 71, 657.

NOVEL MODES OF VACUUM DISCHARGE IN MAGNETIC FIELD AS THE BASE FOR EFFECTIVE ION GENERATION

S. A. Cherenshchykov, NSC KIPT, Kharkov 61108, Ukraine

Abstract

New properties of vacuum discharges in magnetic field with unconventional discharge gaps at low pressure up to high vacuum are briefly described. Both single- and multi-charge ion sources may be developed on the basis of such new discharge modes. Such ion sources may have advantages in comparison with conventional ones. The main advantages are the long lifetime due to the absence of filaments and arc spots, high energy and gas efficiency due to high plasma electron temperature. The development of the discharge research and recent results are discussed.

INTRODUCTION

It is known that ion sources have very low power efficiency as compared to energy necessary for ionization. Also in addition powerful ion sources are featured by short lifetime. Such features of ion sources largely depend upon one another. It is related to properties of electric discharges used for ionization. With increase of the discharge power and according to the extracted current, it is necessary to increase pressure of ionized gas or vapour and to apply additional means such as heated cathodes for increasing the current of a discharge (magnetic fields and also high-frequency fields). It is noted at the same time that the most power efficiency of sources without cathode spots is observed in the vicinity of the low bound of pressure of the discharge initiation [1]. Only one type of discharge was known before, the maintenance of which is possible at the lowest pressure. It is a magnetic insulated glow discharge [2]. However, such discharge has relatively high initiation voltage at low pressure ($\sim 10^3$ volts and more), which is unacceptable due to the considerable energy spread of an extracted ion beam. Nevertheless, at relatively high pressure, the sources of this type (gas-magnetron and Penning) found wide enough application.

As a result of long-term researches, discharges were discovered which differ substantially from traditional magnetic insulated discharge. These properties allow hoping to increase power and gas efficiency of sources substantially and to increase their lifetime.

DESCRIPTION OF NEW FORMS OF THE DISCHARGE

Magnetic Insulated Discharge with an Additional High-Frequency Feed

The electrode system of such discharge is like the Penning and differs only by an additional hollow anode.

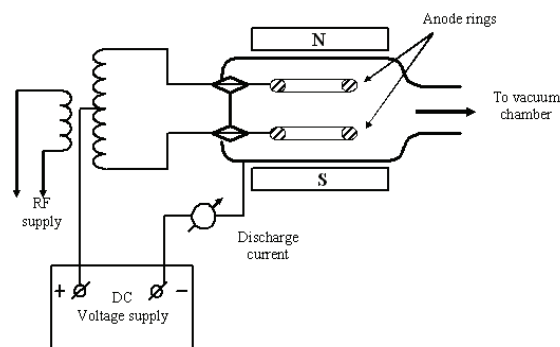


Figure 1: Double Penning vacuum cell with additional RF supply.

An additional anode, which can have the same design as the first one, is placed along direction of the magnetic field axially with the first one. The plot of such discharge gap is shown on Fig. 1.

If both anodes are fed by identical positive potential relatively to flat cathodes then such system has the same properties as the ordinary single-anode Penning cell with the large height of an anode. However, if anodes are fed by relatively small radio-frequency voltage of tens of volts then properties of the discharge are changed substantially [3-5].

- The voltage of the discharge initiation decreases by an order of magnitude.
- The application of alternate voltage to an already initiated discharge increases the discharge current by an order of magnitude.
- The current of the discharge has maximum value depending on pressure.
- The discharge goes out and does not pass to the arc with increasing pressure.

These properties related to high efficiency of ionization processes in such system that has to provide high power efficiency. The possibility of maintenance of the discharge at low voltage will allow decreasing energy spread of extracted beam. Low energy of ions bombarding cathodes will allow increasing the lifetime of the source. Table 1 shows the increase of the discharge current due to the effect of relatively low alternating voltage. It should be noted here that in the gas-discharge ion sources based on the Penning discharge the ion beam current is proportional to the discharge current at high enough extracting voltage. The model of a similar source was developed and tested at low currents. It has a ratio of beam current to discharge current of 2.5 %.

Table 1: Discharge Current Increasing by Applied Radio Frequency

DC voltage, V	RF voltage, V	Frequency, MHz	Pressure of Nitrogen, Pa	Discharge current without RF, mA	Discharge current, mA	Increasing ratio
700	50	5.28	0.01	0.081	0.156	1.9
250	90	13.26	4	4.8	48	10 (!)

Thus, one may hope to achieve ion currents of a milliampere order in the mode corresponding to the bottom line of the table 1.

Secondary-Emission Discharge in Cross Fields

The possibility of maintenance of such discharge is not related with the presence of gas in a discharge gap. An electron cloud hold by a set of electric and magnetic field generates electrons with an excess energy. Bombarding a cathode, these electrons provide considerable secondary emissions [6]. Electrons can be extracted across the magnetic field under application of the high-frequency electric field of a split anode as in a RF magnetron with a cold, secondary-emission cathode providing transformation of energy of a constant field to a high-frequency field. Electrons may also be extracted from a discharge along the magnetic field providing the generation of powerful electron beam as in a magnetron gun with secondary emission [7-9]. There is a deep high-frequency modulation of electron beam at certain conditions [10-12]. Thus, frequencies of generation may be in a frequency range, where the effect of increasing of ionization efficiency under application of the high-frequency field is observed [11]. At the same time, differently from the first discharge type, additional actions are needed for the discharge initiation. The discharge should be initiated by creating, preliminarily, a dense electron cloud in the cross fields.

RESULTS OF RECENT EXPERIMENTS

During first experiments with a magnetron gun in the secondary emission mode the excitation of the self-sustained emission was achieved due to a fall of a voltage pulse [7, 8, 11]. Thus, the amplitude of the pulse should exceed tens of kilovolts for providing the excitation. Beam current at such voltage values achieved tens of amperes. Such high power is unacceptable and such high voltage is uncomfortable for many ion sources. The possibility of excitation of such discharge was recently tested due to the small increase of pressure in a vacuum system [13]. In such conditions, characteristic of ion sources, a self-sustained secondary emission discharge is excited a considerably lower voltage (units of kilovolts). Thus, the electron beam current is $\sim 10^{-1}$ - 10^1 A.

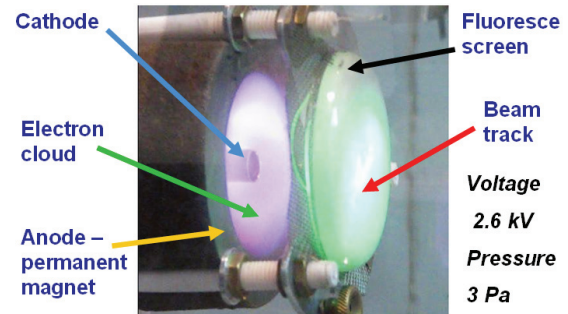


Figure 2: Operating gun.

The picture of operating gun is shown with track of beam on a fluorescence screen in Fig. 2. It should be noted here that, in case of not enough cleared and degassed electrodes, such discharge passes easily to the arc mode when voltage in a discharge gap falls and the generation of electron beam is terminated. This situation is illustrated in Fig. 3,a where oscillograms of collector current and gun voltage, obtained on the upgraded installation «Rassvet» [13], are shown.

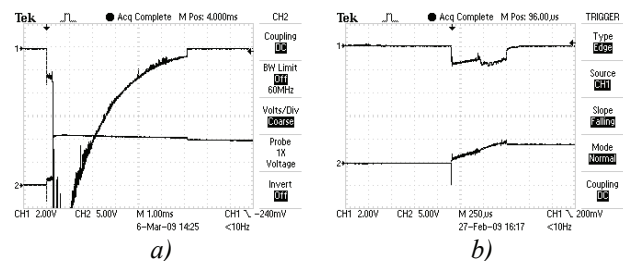


Figure 3: Oscillograms of the operating gun.

One may see in the figure the sharp growth of the collector current determined by the value of a protective resistor. At the same time the gun voltage is decreased sharply. As the current and voltage are negative, the y-axis is directed downwards. Heating up of the cathode by an internal heater to temperatures about 400° C during few hours, with subsequent cooling off and discharge training, results in suppression of an arc mode development. This is shown on the oscillogram (Fig. 3b). The pictures of the hollow beam on the luminescent screen for the same mode were taken on the installation «Rassvet» (Fig. 4a). Since in a number of applications such hollow beam can appear unsuitable, a focusing system, allowing transformation of a hollow beam into continuous one, was used. The spot of the continuous beam is shown in Fig. 4b.

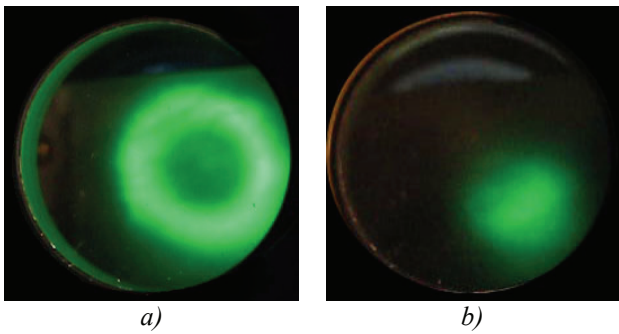


Figure 4: Beam traces.

A storing condenser of small capacity was set to avoid the damage of the luminescent screen by high energy pulses.

For the magnetic field creation, a permanent magnet with a magnetic field strength of 0.03 T was used here, differently from the installation «Rassvet». The gun together with the magnet, was placed in a glass chamber. The insufficient magnetic field did not allow exciting a secondary emission discharge at such low pressures, as in the installation «Rassvet». The pressure was increased approximately up to 3 Pa in order to get discharge excitation. At this point we detected the excitation of intense high-frequency oscillations with frequency about 10 MHz and magnitude up to 5 A in the collector circuit. The corresponding oscillogram is shown on Fig. 5.

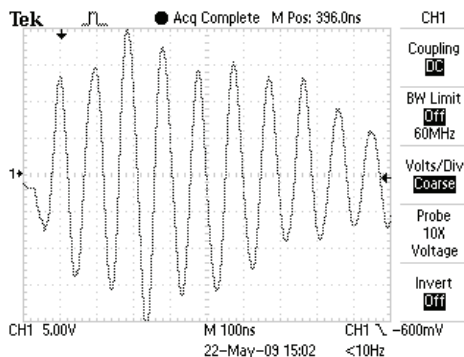


Figure 5: High-frequency oscillations.

The presence of bipolar oscillations on the collector indicates an origin of dense enough plasma in vicinity of the collector. The electron current in similar case must be of single polarity. High-frequency modulation of the beam in a magnetron gun was observed before [10, 12]. Besides, the supposed amplitude of the beam current is substantially lower than the collector current. Therefore, an intense build-up of oscillations takes place in plasma. The frequency of these oscillations corresponds to the mode of excitation of waves, absorbed intensively by plasma. These frequencies are well absorbed by a gas-discharge plasma in a magnetic field. Such phenomenon was noticed both in our experiments [4, 5] and in later works [14-16]. Here one has not only injection of electron beam, ionizing gas, but also the excitation of oscillations of plasma and heating the last one by these oscillations. Thus, transition of the energy from a beam to plasma

becomes considerably more effective. It will allow reducing operating pressure of a filled gas and increasing plasma electron temperature. All of these will increase the degree of ionization and the efficiency of the ion source. By decreasing the pressure and increasing the length of the beam interaction with plasma, with corresponding increase of beam power, and also by increasing the magnetic field, it might be possible to obtain the effective generation of multicharged ions.

PROBLEMS IN REALISATION OF THE PROPOSED CONCEPTION

Structurally, an ion source with such an operation principle can be of the same design as one of the most wide-spread sources with oscillating electrons, or a source with ionization by an electron beam. It is sufficient to apply the corresponding voltage to a device that is similar to the gun test installation. Ions can be extracted along magnetic field direction through holes in a cathode or in a collector. The extraction of ions is possible across the magnetic field direction. A choice will depend on the required parameters and is a function of the source. However, cathode emission in such source will not demand heating up of the cathode and gas or vapour injection into space near the cathode for the neutralization of electron space charge, in to limiting a current. Therefore, the design may provide such admission or pumping-down so that a cathode could be in high vacuum and its dispersion both thermal and ion would be suppressed. All these means will provide the generation of plasma with high temperature of electrons and with desirable elemental composition. For the realization of such source a set of problems should be solved:

- excitation of Secondary Emission Discharge;
- suppression of arc excitation;
- increasing of pulse duration;
- beam compression;
- RF generation control;
- control of gas or vapour input;
- plasma stability.

Part of these problems was successfully solved during the described experiments. Thus, the ways of their solving are outlined in the ion sources under development.

COMPARISON OF EXISTING ION SOURCES AND DISCUSSION

The proposed conception occupies an intermediate position among the types of ion sources. The presence of electron gun moves it to the electron-beam sources [17-18], differing only by the type of electron gun. The possibility of excitation of high-frequency oscillations and transition of their energy into plasma moves it to high-frequency sources [14-16, 19-21]. It will differ by simple design from last ones. Ion sources utilizing gas-discharge plasma, in particular, are difficult for calculations. Therefore, the choice of parameters and sizes of designs is often determined by the operating

experience of ones with similar operation principle and parameters. Therefore, it is necessary to study carefully the experience of the development and operation of both electron-beam and high-frequency sources before the development of ion sources on the indicated principles. Foremost, those high-frequency sources have close parameters of frequency plasma excitation. The so-called gelicon sources [14-16] present one of the most advanced directions in development of ion sources belong to them. The possibility of operation at very low pressures and the cleanness of generated plasma will make than close to other advanced direction of sources on electron-cyclotron resonance [20, 21]. A difference will be the simplicity of design and the absence of rigid reference of operating frequency to magnetic field. The large efficiency due to low efficiency of corresponding microwave sources of high-frequency feed with a very small wavelength may become another difference. All these conditions will provide the cheapness of production and operation of ion sources of the proposed principles. Recent achievements of current level up to several kilo-amperes was reported for the secondary emission mode in cold-cathode magnetron gun [22]. It was at voltage up to several hundred kilovolts. This current and electron energy may be enough for transferring all elements up to the heaviest to pure (single) nuclei.

ACKNOWLEDGEMENTS

The author expresses great thanks to V.N. Kotsubanov and I.K. Nikolskii for their assistance in experiments. I also wish to thank J.G. Alessi from BNL for improvement of English text and discussion. The main part of the research was supported financially by governments of USA and Canada through the intergovernmental fund STCU in frame of the project #1968 "High-current electron gun with secondary emission".

REFERENCES

- [1] N.N. Krasnov. *Pribery i Technika Experimenta*. 2 (1960) 148. (in Russian).
- [2] R.L. Jepsen *J. Appl. Phys.* 32 (1961) 2619.
- [3] S.A. Cherenshchykov and S.A. Vasiliev. Author's Certificate (State Patent USSR) #1150506, Claimed 04/26/84. Pub. 04/15/85. Bul. #14.
- [4] S.A. Cherenshchykov. 4th International Symposium "Vacuum Technologies and Equipment" Kharkov April 23-27, p.102 (2001)
<http://www.kipt.kharkov.ua/conferences/vacuum/sym/en/VTO.html> (in Russian)
- [5] S.A. Cherenshchykov. *Vacuum*. 73 (2004) 285.
- [6] R.L.Jepsen, M.W. Muller. *J.Appl. Phys.* 22 (1951) 1196.
- [7] S.A. Cherenshchykov, B.G. Safronov, V.S. Balagura. "Short-pulses electron guns with no heating cathodes for linac" Abstract of 12-th all-Union seminar of charge particle linear accelerators. Kharkov, May 1991, p.40 (1991).

- [8] S.A. Cherenshchykov, "The Multipactor Emission of Electrons in the Cold-cathode-Magnetron Gun" Proceeding of 13-th. Conference of Charge Particle Accelerators. JINR, Dubna. October 1992. p.142 (1993).
- [9] S.A. Cherenshchykov, A.N. Opanasenko, A.N. Dovbnya, and V.V. Zakutin. "Secondary Emission Magnetron Injection Gun as High Current Durable Electron Source". Pulsed RF Sources for Linear Colliders. AIP Conference Proceeding, Montauk, p.350-359 (1994).
- [10] S. A. Cherenshchykov, B. G. Safronov. "Possibility of Full Operation with Fast-Acting in no Heating Cathode Magnetron Gun" Abstract of 13th. Kharkov Seminar on Linear Accelerators. Kharkov, 1993, p.27. (in Russian).
- [11] Y.M. Saveliev, W. Sibbett, and D.M. Parkes. "Crossed-Field Secondary Emission Electron Source" Proc. of the 11-th Int. Pulsed Power Conference, Baltimore, p. 340 (1997).
- [12] S. Cherenshchykov, A. Opanasenko. "High-Current Electron Gun with Secondary Emission" Brookhaven National Laboratory. Accelerator Physics Seminars. November 14, (2003),
www.agsrhichome.bnl.gov/AP/BNLapSeminar/HighCurrentElectronGun.ppt
- [13] S.A. Cherenshchykov, V.D. Kotsubanov, I.K. Nikolskii. *Problems of Atomic Science and Technology. Series: Plasma Physics*. 1(15) (2009) 162,
http://vant.kipt.kharkov.ua/ARTICLE/VANT_2009_1/article_2009_1_162.pdf
- [14] Y. Lee, R.A. Gough et al. *Rev. Sci. Instrum.* 68 (1997) 1398.
- [15] S.M. Mordyk, V.I. Miroshnichenko, D.A. Nagorny, V.E. Storizhko. *Problems of Atomic Science and technology. Ser.: Plasma electronics and new acceleration methods* 4(6) (2008) 147.
- [16] V.I. Voznyi, V.I. Miroshnichenko, S.N. Mordyk, V.E. Storizhko, D.P. Shulha. *Problems of Atomic Science and Technology. Series: Plasma Physics*. 1(15) (2009) 142.
- [17] J.G. Alessi, E. Beebe, D. Graham et al. "Design of an EBIS for RHIC" Proc. of the 2003 Particle Accelerator Conference EBIS-BNL-MOPB009, p.89 (2003).
- [18] G. Brautti, T. Clauser, A. Rainò et al. "BRIC: an Electron Beam Ion Source as Charge State Breeder for Radioactive Ion Beam Facilities". Proc. of EPAC 2000, Vienna, Austria. THP6B01 p. 1619 (2000);
<http://www.JACoW.org>
- [19] K. N. Leung, D.A. Bachman and D.S. McDonald, "RF Driven Multicusp Ion Source for Particle Accelerator Applications" EPAC'1992, EPAC1992_1038 (1992);
<http://www.JACoW.org>
- [20] M. Leitner, D. Wutte, J. Brandstotter, F. Aumayr, and H.P. Winter. *Rev. Sci. Instrum.* 65 (4), April (1994)1091.

- [21] Claude M. Lyneis, D. Leitner, D. S. Todd et al. Rev. Sci. Instrum. 79 (2008) 02A321_2008_.
- [22] S.A. Chereshchikov. "Cold-cathode Kiloampere Electron Gun with Secondary Emission at Relativistic voltage" PAC09 Vancouver, May 2009, TU6PFP096 in book of abstracts, p.281 (2009); www.triumf.ca/pac09

UPGRADE AND COMMISSIONING OF THE PIAVE-ALPI ECR INJECTOR AT LNL

A. Galatà, M. Sattin, L. Bertazzo, L. Boscagli, S. Contran, A. Dainese, A. Lombardi, D. Maniero,
M. Poggi, F. Scarpa, A. Facco, INFN-LNL, viale dell'Università 2, I-35020 Legnaro, Italy
T. Kulevoy, ITEP, Bolshaja Chermushkinskaja n. 25, Moscow, Russia

Abstract

The positive ion injector for the PIAVE-ALPI complex consists of an ECR ion source placed on a high voltage platform. A 14.4 GHz ECRIS named Alice [1], designed and constructed at LNL in the early '90, reliably delivered gaseous beams to the Superconducting RFQ PIAVE for nuclear physics experiments until 2008 [2]. The requests for heavy ion beams of increased current and energy, needed to perform the experiments planned for the next years with the AGATA demonstrator, prompted us to upgrade our injector with a new ECR source capable of higher output beam currents and higher charge states. This activity started in 2008 and was completed at the beginning of 2009.

A 14.5 GHz, SUPERNANOGAN type ECRIS built by Pantechnik [3], was installed in our refurbished high voltage platform in July 2008. The space available for maintenance in the platform was increased and a new lead shielding for X-rays has been set up. The water cooling circuits have been redesigned to deliver different fluxes and inlet pressures to the equipment mounted on the platform (plasma chamber, extraction electrodes, bending dipole and power supply). A new safety system has been implemented in order to cope with new and more demanding safety rules.

A lot of attention has been paid to the optimisation of the injection line with new diagnostic devices for beam characterisation (movable slits, emittance measurement tools). Commissioning of the new source and injector with beams has started and first results will be reported.

ECR SOURCE AND RELATED EQUIPMENT

The new ECR ion source, named LEGIS (LEGnaro ecrIS) is a full permanent magnet source working at 14.5 GHz. Good performance and low power consumption make it well suited for operation on a high voltage platform.

The source is equipped with a DC Bias tube, which works as a biased disk and coaxial tube for microwave coupling; a 1500° C resistive oven to evaporate solid material like silver or gold; a movable sputtering or direct insertion system to evaporate samples of refractory metals like tantalum.

The maximum microwave power that can be injected into the source is 700W with a water flow for cooling of 200 l/h at an input pressure of 3 bars.

The beam is extracted from the source through a four electrode system: the extraction electrode ($V_{max}=30$ kV), which gives the beam energy; the puller electrode ($V=$

$5000 \div 0$ V); the focus electrode ($V = -5000 \div 5000$ V) to directly couple the extracted beam to the bending dipole; the ground electrode. The source and its beam line are controlled via National Instruments FieldPoint modules that acquire all parameters and display them through a LabView interface.

All the beam line from the source to the accelerating tube has been redesigned in order to have good flexibility and complete beam characterization: to this scope, two independent movable slits (for beam shaping in both horizontal and vertical plane) and transverse emittance measurements device have been installed (see Fig. 1).

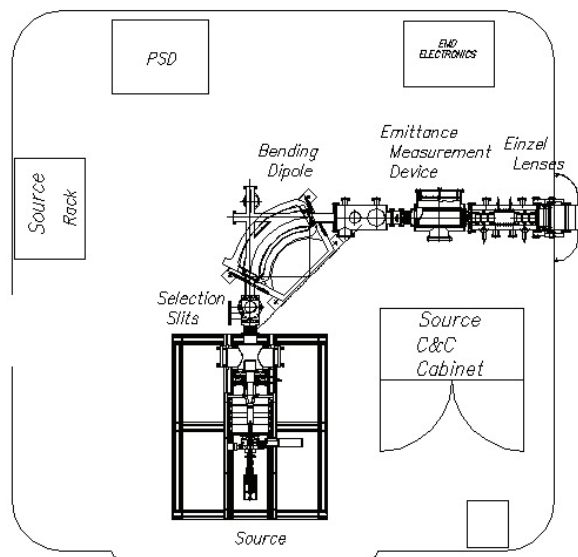


Figure 1: The complete beam line on the high voltage platform and its equipment.

Each slit consists of two water cooled tantalum plates, moved together by a stepper motor. Each plate has a current pickup in order to monitor the beam current lost on it. The plate aperture goes from 37 mm to 2 mm, with steps down to 0.1 mm.

Both slits are software-controlled in a LINUX environment.

The emittance measurement device consists of a slit-grid system (see Fig. 2). A common support holds a 0.12 mm copper slit with a tantalum shield and an 80 wires grid, with 0.5 mm spacing, 280 mm apart. They are centered and moved together by a remotely controlled motor.

The maximum stroke of the system is ± 30 mm while the maximum divergence that can be measured is more than 70 mrad. The resolution of the system (without

considering mechanical errors) is 0.36π mm mrad. The current collected by each wire is preamplified, acquired and processed by a program made in house. The gain of the preamplifiers can be varied in order to characterize beams with different intensities.

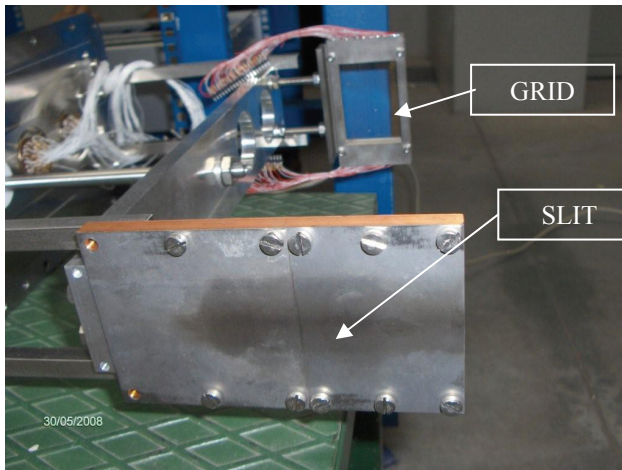


Figure 2: Detail of the slit-grid system for emittance measurement.

Two systems (one for each transverse plane) are mounted on a stainless steel box (Fig. 3) which houses also a Faraday cup and a collimator (an elliptical aperture with vertical axis of 24 mm and horizontal axis of 12 mm) mounted on CF flanges.

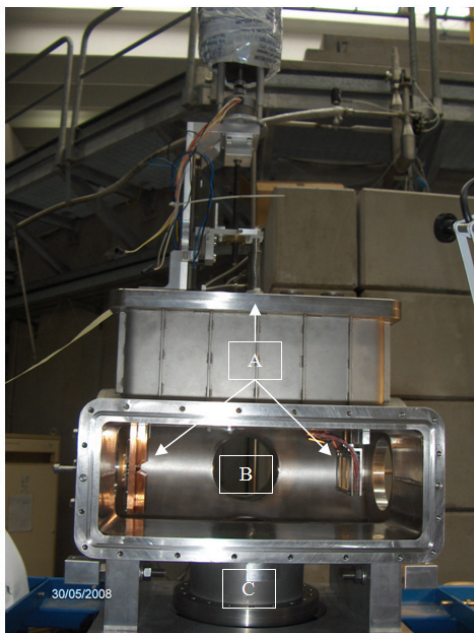


Figure 3: View of the stainless steel box for emittance measurement. A) slit-grid system mounted on a rectangular flange; B) horizontal mounting for Faraday Cup; C) vertical mounting flange for collimator.

In order to protect all the equipment mounted on the platform, a fire-fighting system that uses a mixture of water and nitrogen has been implemented. Sensors and expellers have been positioned close to all the critical

Ion Sources

points. To start the system, two sensors have to be activated but just one is sufficient to switch off the electrical power on the platform.

The vacuum system is now hardware-protected by means of relays: for each turbo pump, dry contacts coming from the vacuum gauge and the controllers have been put in series with +24 V power supply, in order to automatically close all the valves when the vacuum exceeds the operating threshold.

X-rays coming from the source during operation are stopped by a lead shielding (from the ion source to the bending dipole, see Fig. 4) designed at LNL and built by a local company.

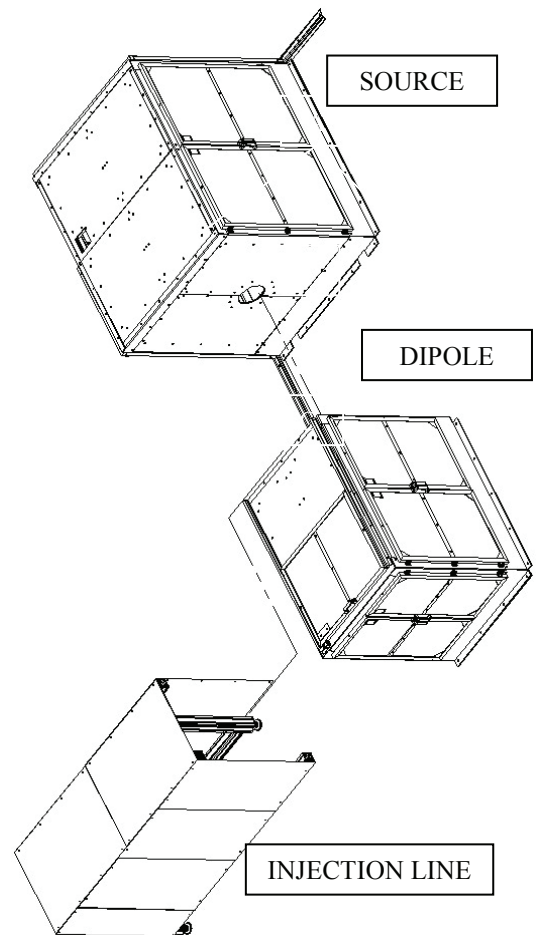


Figure 4: Lead shielding for the source line up to the bending dipole.

The whole beam line has been surrounded by aluminum profiles, creating three boxes. Two of them (one for the source and one for the bending dipole) have been covered with 1 cm thick lead shielding, sandwiched between two steel plates. Each face of the boxes (except for the upper parts) has two extendable shielding plates, forming a sort of window, in order to have easy access to the source for maintenance. The windows have micro switches which allow, when in closed position, high voltage and microwave feeding to the source.

ALIGNMENT [4]

During installation of the new source and its beam line it became necessary to check, and eventually improve, the alignment of the transfer line going from the source to the first dipole (PD1 from now on) which bends the beam towards the injection line of the PIAVE superconducting RFQ.

As a first step, the reference line of PD1 and the two 90° degrees line of the source dipole (LBD from now on) have been defined. Very precise tools (precision ± 0.005 mm) have been machined, controlled on a bench in the LNL workshop, and mounted on the two dipoles.

Two optical levels (model WILD NAK2) have been used: the first one to define the injection axis in LBD, the second one to align the extraction axis from LBD to the reference line of PD1. The tolerance requested by the beam dynamics calculations was ± 0.2 mm and 0.4 mrad at the injection in PD1.

For each optical and beam diagnostic element (source electrodes, emittance measurement device, einzel lenses) special aluminum tools have been machined to house very precise (precision better than 0.1 mm) optical marks for the definition of the alignment axis.

When the use of these tools was not possible, due to mechanical restrictions (selection slits, accelerating tube, electrostatic triplet and first diagnostic box out from the platform), crosses with a 80 μ m tungsten wire have been paced on the flanges.

Independent supports (see Fig. 5) have been mounted at both ends of each beam line component (except for the emittance measurement device and the electrostatic triplet, hold by a single support).

Each support allows a rough regulation in height by means of M10 screws. The beam line component itself is supported by an aluminum plate with a fine regulation in all three directions: three vertical screws for the horizontal plane and 8 more screws for back-forth and left-right regulation. Once centered, the tube is fixed in position by aluminum cover. At the end of the work the precision requested was reached.

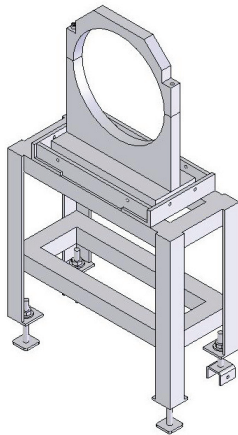


Figure 5: Special support for each part of the beam line.

ACCEPTANCE TESTS

In order to have a proof of good source performances, some requirements for beam intensity and quality have been put in the contract. They regarded the production of two gaseous beams (O^{6+} and Ar^{9+}), three metallic beams from an oven (Ag^{21+} , Au^{26+} and Au^{30+}) and one metallic beam with a sputtering system (Ta^{24+}). Table 1 summarizes the requests for beam intensity.

Table 1: LNL Current Requests

	Ion	Current [$\square A$]
Gaseous beams	O^{6+}	200
	Ar^{9+}	100
Metals with oven	Ag^{21+}	3
	Au^{26+}	10
	Au^{30+}	1
Metals with sputtering	Ta^{24+}	1

For each one of the ions listed in Table 1 a 2 hours test of the beam current stability had to be repeated two times, first at the Pantechnik site and finally at the LNL site after final installation. The current had to stay within $\pm 5\%$ of the reference value for the 98% of testing time. A normalized 4-RMS emittance of less than 0.3 π -mm-mrad for the 90% of the beam was also required for the two gaseous beams.

A brief description of the acceptance tests hold at Pantechnik site will be given in the following. The extraction voltage was fixed at 24 kV for all the beams produced; the test bench used was made by the source directly coupled to a 90° bending dipole and an horizontal emittance measurement device consisting of a slit and a scanning wire.

Gaseous Beams

For both Ar^{9+} and O^{6+} beams the current stability and the emittance test results were satisfactory. Figs. 6 and 7 show spectra acquired during the acceptance test. Even if not so high microwave power was used (about 170 W for both beams) more than 10 μA of O^{7+} and slightly less than 20 μA of Ar^{11+} were recorded. Looking at the emittance measurements (see Fig. 8) we saw that the beam parameters slightly changed during stability tests, showing that the source was still not totally conditioned due to the limited operation time.

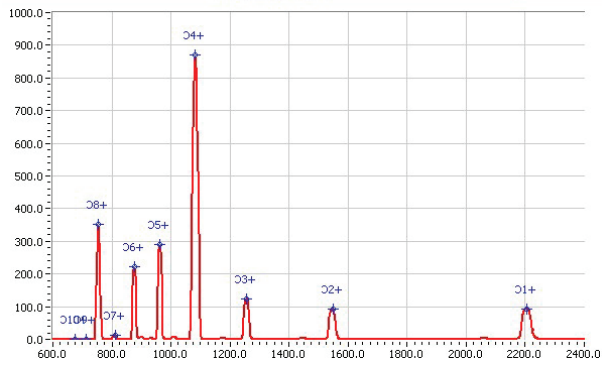


Figure 6: Spectrum acquired at the end of stability test for O^{6+} .

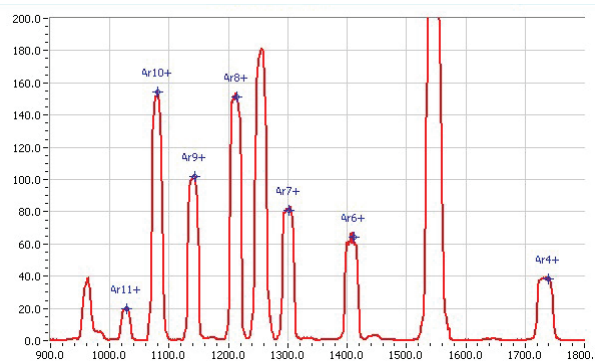


Figure 7: Spectrum acquired at the end of stability test for Ar^{9+} .

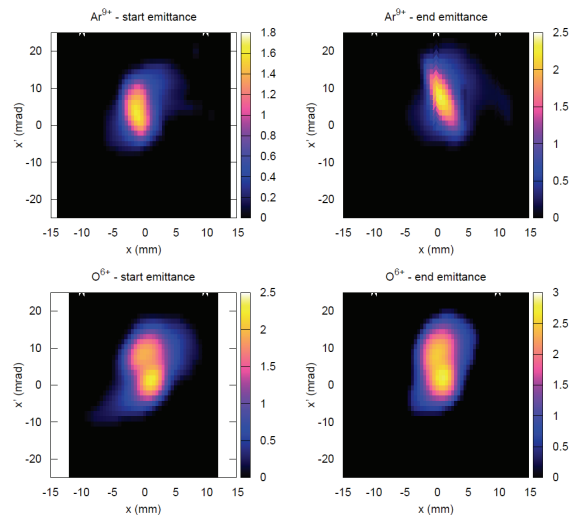


Figure 8: Gaseous beams emittance plots.

Metallic Ion Beams

The new source is equipped with two different systems for production of ion beams from metallic elements:

- A resistive oven, consisting of a tungsten wire heating an alumina crucible containing the sample to be evaporated. Such an oven can produce metallic vapours from elements which reach a vapour pressure of 1 Pa for $T < 1500$ °C.
- A plasma heating or direct insertion method. It consists of a long movable rod which holds at its extremity the sample to be evaporated in the shape of

a cylinder of 1 mm diameter. The sample is carefully placed closer and closer to the plasma until the evaporation starts and metallic ion can be seen in spectra.

The tests with both methods were satisfactory, especially the direct insertion method which proved to be very easy and fast. Fig. 9 shows the spectrum acquired after stability tests for gold: it can be seen that current for both 26+ and 30+ ions are well above the requested ones.

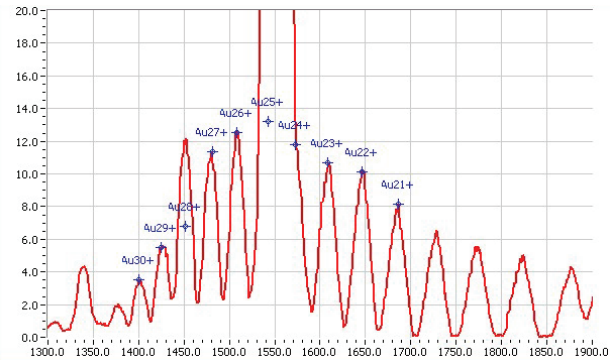


Figure 9: Spectrum acquired after stability tests for gold.

ION SOURCE AND INJECTOR COMMISSIONING [5]

Once the installation was completed, first tests with oxygen beam were performed on the new source. The attention paid on the cleaning of each component put under vacuum played an important role on source conditioning.

Fig. 10 shows an oxygen spectrum acquired in December 2008: it can be seen that more than 270 μA of O^{6+} and 16 μA of O^{7+} have been obtained with 325 W of microwave power. No contaminants are present in the spectra.

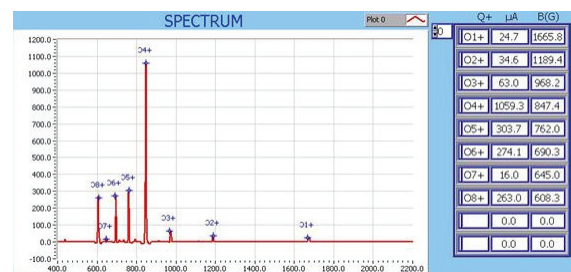


Figure 10: First oxygen beam extracted from the new source mounted on the HV platform.

After source conditioning for some days with oxygen, commissioning of the injector started in March 2009. The chosen beam was Ar^{9+} with a current between 1 and 3 μA ; the voltage applied to the platform was about 140 kV to meet the right velocity for injection into the PIAVE RFQ.

Most part of the work was done during the first days: after fixing the voltages on the lenses to couple the beam to the injection line and on the electrostatic quadrupole, the values of the magnetic lenses and of the phases and amplitudes of accelerating cavities have been optimized.

Thanks to the good emittance coming from the source (about $0.05 \pi \cdot \text{mm} \cdot \text{mrad}$ norm. rms in both transverse planes) and to the good job in improving alignment we had an improvement of 10% in transmission at the entrance of the LINAC ALPI.

Moreover, the beam characteristics were reproducible in the following days: in fact putting exactly the same parameters for source tuning and the same values for the magnetic lenses, the beam was transmitted through the injector exactly with the same transmission as on the previous days, except for a slight adjustment of the field of the dipoles.

The injection and complete acceleration in the ALPI LINAC, together with the production of Xe, Sm, Sn and Ca beams, are foreseen for the next months.

REFERENCES

- [1] M. Cavenago, T. Kulevoy, Rev. Sci. Instrum. 71(2000), 758.
- [2] A. Galatà et al., LNL Annual Report 2007.
- [3] <http://www.pantechnik.fr/joomla/>.
- [4] A. Galatà et al., LNL internal document.
- [5] E. Fagotti et al., these proceedings.

HIGH CURRENT ION SOURCES, BEAM DIAGNOSTICS AND EMITTANCE MEASUREMENT

M. Cavenago*, M. Comunian, E. Fagotti, M. Poggi, INFN-LNL, Legnaro, Italy
T. Kulevoy, S. Petrenko, INFN-LNL, Legnaro, Italy and ITEP, Moscow, Russia

Abstract

Singly charged ion sources can easily surpass the 1 kW beam power, as in TRIPS (H^+ , 60 mA, 80 kV, now installed at LNL) or in NIO1 (H^- , 130 mA distributed into 9 beamlets, 60 kV, a project of RFX and INFN-LNL). Beam diagnostic constitutes an important instrument in the high current source development. Even if calorimetric and optical beam profile monitors become possible, still a phase space plot of the beam will be the most useful tool for validation of extraction simulation and for input of subsequent beam transport optimization. Improvements in extraction beam simulations are briefly reported, and effect of space charge neutralization is discussed. Since preliminary design of the traditional two moving slit beam emittance meter show problems with slit deformations and tolerances and with secondary emission, an Allison scanner was chosen with the following advantages: only one movement is needed; data acquisition is serial and signal can have an adequate suppression of secondary electrons. The design of a compact Allison scanner head is discussed in detail, showing : 1) the parameter optimization; 2) the segmented construction of electrodes. Experimental commissioning at lower power seems advisable.

INTRODUCTION

An ion source extraction system requires careful design, its difficulty generally increasing with the beamlet perveance ($I_b V_b^{-3/2}$) [1] and the nucleon number A of the dominant ion species and the number N of beamlets; here V_b is the source acceleration voltage and I_b the current per beamlet. The worldwide effort to improve ion sources, mainly for fusion application, requires detailed modeling of the plasma depending on several parameters (namely the plasma potential, the negative ion to electron ratio) difficult to measure directly. A high quality emittance measurement will be crucial to validate most code and plasma modeling, and to reliably design the following beam line; it is a topic of the NIO2BEAM experiment (financed by INFN-CSN5). An emittance meter design based on an Allison scanner is described in this paper.

Use of negative ions in high current sources is related to need of having a charge exchange (CX) later, to accumulate more beam in a given phase space or to enter a high magnetic field as a neutral beam; CX cross section (over few hundred keV) favours negative ions over positive ions; in other words, negative ions are more difficult to produce,

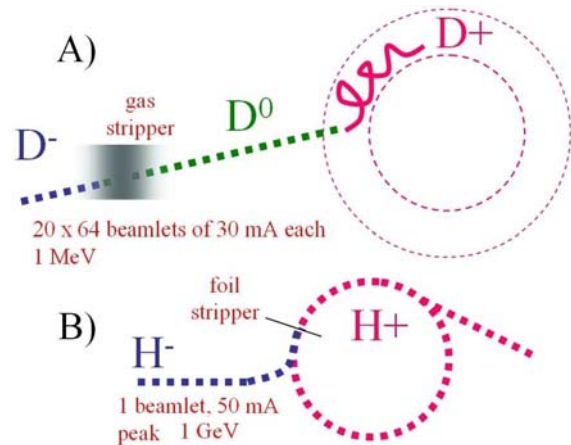


Figure 1: Typical applications of high current negative ion sources: A) Tokamak injection (40 MW average) is a two stage gas stripping: the second stripping happens inside tokamak plasma. A gas target (called the neutralizer) is used for the first stripping. Beam emittance is determined by D^- source; B) Spallation Neutron Source (1.4 MW average).

hence they are easier to dismount. Typical applications (see Fig. 1) are the neutral beam injectors (NBI), featuring 1280 beamlets of 35 mA each of D^- for the ITER project (2 or 3 NBI needed) and the Spallation Neutron Source (single beam, 65 mA of H^-) [2, 3, 4]. In other applications, where no beam accumulation is needed, positive ions are obviously preferred (IFMIF project, two beams of 125 mA each of D^+ [5]). Beam extracted from D^+ sources can be generally contaminated by D^{2+} and D^{3+} molecular ions.

Gas filling pressure of the source p is typically in the range from 0.3 to 3 Pa, while higher pressures are found in industrial ion sources. Negative ion formation inside the source requires two plasma regions, separated by a so called magnetic filter. In the first region, radiowaves with frequency f_1 heat an inductively coupled plasma (ICP) to a temperature $T_{1e} \geq 4$ eV, which is determined from global plasma balance laws [6], to produce a reasonable rate of dissociation of molecular hydrogen. In some prototypes, plasma heating was obtained by an arc discharge with voltage $\cong 100$ V between filaments and the source chassis; in industrial sources, rf voltage is applied to an electrode (so to have a capacitively coupled plasma, CCP). Note that we measure plasma temperature in energy unit, that is to say that T should be read $k_B T_K$ where k_B is the Boltzmann constant and T_K is the standard temperature (in Kelvins).

*cavenago@lnl.infn.it

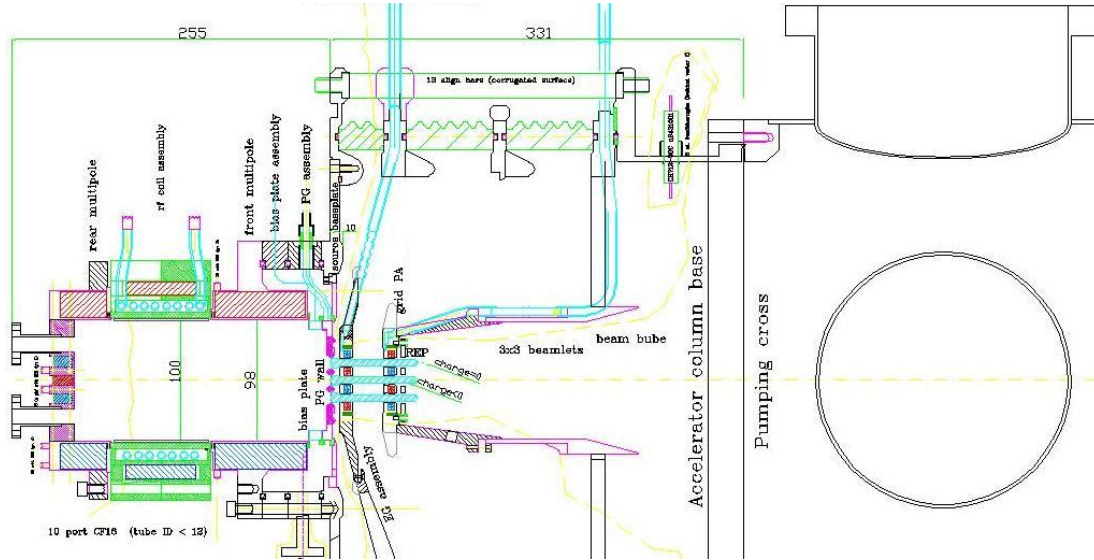


Figure 2: A view of NIO1 design. Scanner(s) can fit into the CF200 ports shown, or in similar ports spaced each 0.5 m.

The second plasma region (near the plasma grid electrode PG) must have a small enough electron temperature T_{2e} to reduce the ionization of H^- , which has an electron affinity of 0.753 eV. To fix ideas $T_{2e} \cong 1$ eV; negative ions can be produced by dissociative attachment to a vibrationally excited H_2 molecule (produced in the first region) or by collisions of fast H atoms (always produced in the first region) with cesium atoms adsorbed on the PG wall. A third production mechanism consider that vibrationally excited H_2 molecule can be also produced efficiently by impact of fast particles on the PG walls [7].

In positive ion sources (based on rf or filament) we still find a magnetic filter, which has the purpose of reducing the fraction of H_3^+ in the extracted beam [8]. Moreover, in both sources most of the metallic walls are covered by magnetic multipoles [1], to reduce plasma energy loss. Other positive ion sources (like TRIPS built at LNS and now installed at LNL [9]) are based on microwaves and higher magnetic fields [10], around the well-known electron cyclotron resonance (ECR)

$$\omega_c(\mathbf{x}) = eB(\mathbf{x})/m_e\gamma = \omega \quad (1)$$

where $\omega = 2\pi f_1$. TRIPS uses a 80 kV extraction voltage for extracting a 50 mA beam from a 6 mm hole; the extraction system is a pentode, with electrode voltages of +80 kV, +35 kV, 0, -2.5 kV, 0 (listed with increasing z) with respect to ground.

Important advantages of ICP sources with an external rf coil and of ECR sources are the absence of arcs inside the plasma and a longer duration. Moreover, it can be speculated that ICP can achieve a larger power efficiency than filament or CCP sources; up to now, the need to use a so called Faraday shield (to protect alumina parts from plasma heat load) has hindered this goal. In the source NIO1 (Negative Ion Optimization phase 1) under development at Consorzio RFX and INFN-LNL, permanent magnets may be

Ion Sources

placed also behind the alumina walls, so to test operation without Faraday shield.

A plan of NIO1 is shown in Fig. 2 [11]. The nine beamlets are arranged into a 3×3 square matrix, so that electrodes can be rotated by 90 degrees during assembly. Source is made from five modules, the rear multipole, the rf coil assembly, the front multipole (with a filter magnet submodule), the bias plate assembly and the PG assembly. The extraction column is basically a triode, made of the PG, the extraction grid EG and the acceleration grid PA; actually PA may be floated by a small positive voltage with respect to the following drift tube at ground potential, to improve the space charge compensation of the drifting beam; nominal voltages are $\phi_{PG} = -60$ kV, $\phi_{EG} = -52$ kV, $\phi_{PA} = 0.15$ kV with respect to the following drift tube at $\phi = \phi_{dr} = 0$. A small repeller electrode REP may be inserted before the drift tube; in that case nominal voltages are $\phi_{REP} = 0.15$ kV and $\phi_{PA} \cong \pm 0.01$ kV.

SPACE CHARGE EFFECTS

The Poisson equation is

$$\Delta\phi = -\rho/\epsilon_0 = -(e/\epsilon_0)[N_p - N_n - N_e] \quad (2)$$

with N_p the density of positive ions (times the their average charge state \bar{i}_p in general), N_n the density of negative ions and N_e the electron density; in our case $\bar{i}_p = 1$. These densities are to be related to ϕ .

Some approximation may be valid in particular plasma or beam regions, like the Maxwellian density $N_p \propto e^{-\phi}$ for ions trapped into the plasma or $N_n \propto (\phi - \phi_{pl})^{-1/2}$ in the so called free fall regimes [12], as in a planar collisionless acceleration; here ϕ_{pl} is the plasma potential (near to ϕ_{PG}) whose exact definition is model dependent. Simulating these regions with standard multiphysics tools [13] is then straightforward.

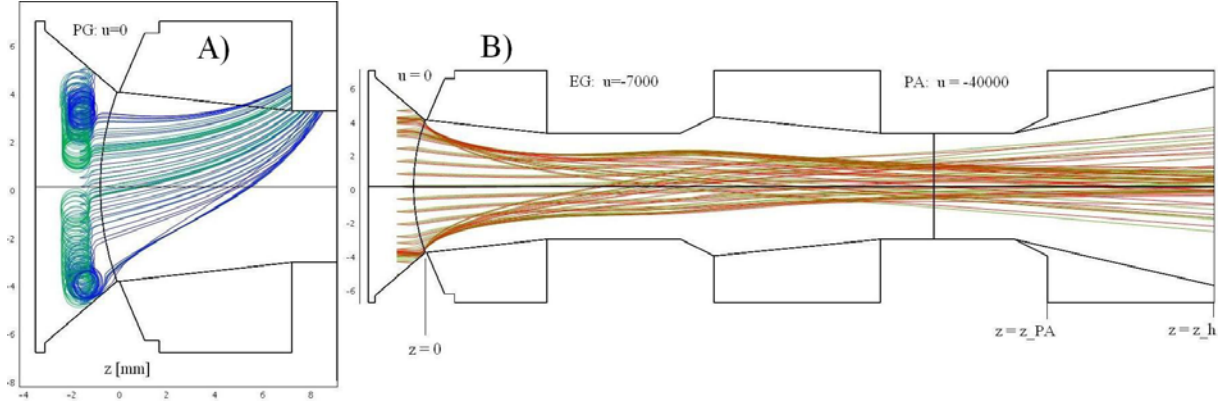


Figure 3: A simulation example (acceleration gap shorter than in NIO1, extraction voltage and bending fields are slightly lower); A) electrons; B) H^- ions; note the crossover of rays starting near the PG edge and the resulting halo.

In general N_n and N_e are complicated functionals of ϕ and the plasma parameters, so that ray tracing seems necessary [4, 14, 15, 16]. Ray map interpolation was used in a self consistent code for Poisson-Vlasov solution, discussed elsewhere [17]. This code still consists of macros in a multiphysics environment [13], so flexibility to incorporate new effects is maximal. It was convenient to scale densities as $n = N/N_0$, with N_0 the plasma density of negative charges much before the extraction, and to scale the potential as $u = -(\phi - \phi_{PG})/(T_c)$, where T_c is the temperature of the extraction plasma. Since $T_e \cong 1$ eV there and $N_0 \cong 3 \times 10^{17} \text{ m}^{-3}$, collisional effects are strong and ion temperature T_p must be of the same order $T_e \cong T_p \cong T_c$. Poisson equation becomes

$$\Delta u = [n_p - n_n - u_e]/\lambda_D^2 \quad (3)$$

where the $\lambda_D = (\epsilon_0 T_e / N_0 e^2)^{1/2}$ is the Debye length.

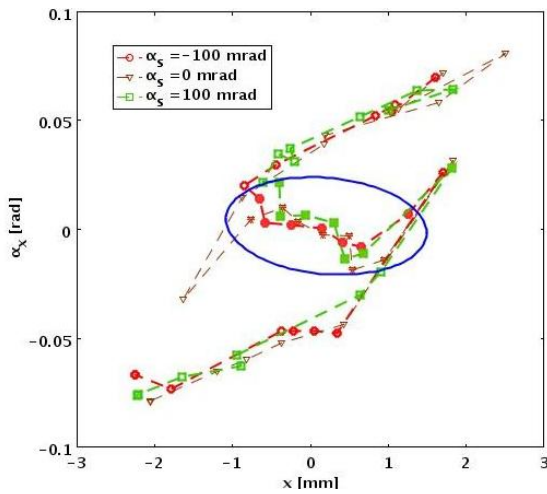


Figure 4: H^- phase space x, α_x at $z = 43$ mm with $u_{EG} = -6900$; α_s is the angular deviation at start. The halo rays (open markers) were started with a much closer spacing, which explains their lower weight in computing the emittance ellipse.

Ion Sources

Expression of n in terms of u and the current modulus $j_\Sigma(z, x)$ determined by ray map interpolation were discussed elsewhere [17]; here z is the beam extraction axis, y is the direction of an externally applied magnetic field, and the electrode structure is assumed periodic in x ; period L_x is the spacing between beamlets.

Sample results are shown in Figs. 3 and 4, with $j(H^-) = 300 \text{ A/m}^2$ at the source. Thus $N_0 = 3 \times 10^{17} \text{ m}^{-3}$. Since $\lambda_D = 0.014$ mm mesh be must be really dense in the plasma and 330000 degrees of freedom were needed in this example. Computer resources usage was reasonable: four ray tracing iterations were completed in 18 minutes, using 4 GB RAM and 7 CPU cores (total CPU time 5500 s). The simulation domain necessarily ends at a given z_h , after the end z_{pa} of the PA electrode; here $z_h = z_{pa} + d_h$ with d_h mm the drift space. It must be discussed how d_h should be chosen: clearly it must be much greater than the length d_c needed to reach a compensation of the negative beam space charge; that is, for $z > z_h$ the beam charge compensation should be at equilibrium.

From 1D equilibrium analysis [18] it is well known that space charge compensation of a negative ion beam is a fast process, which may reach a large fraction f_c of charge compensation; for example at a H_2 pressure of 0.05 Pa and a beam voltage $V_b = 60$ kV, f_c ranges from 0.997 (for a typical beam density $N_b = 10^{15} \text{ m}^{-3}$ and a beam radius $r_b = 4$ mm) to 1.0001 (for a beam density $N_b = 10^{16} \text{ m}^{-3}$ and a beam radius $r_b = 40$ mm). So $d_h = 10$ mm seems provisionally reasonable. Another issue is that boundary conditions at $z = z_h$ affects space charge compensation. To fix ideas, assume that drift tube has a radius $R_{dr} = 50$ mm (much larger than L_x) so that a general solution of Poisson equation for $z > z_h$ is about

$$u(z, r) \cong A + B J_0(kr) e^{-kz} + C g(r/r_b) \quad (4)$$

where $r = (x^2 + y^2)$ and $k = 2.40483/R_{dr}$ and all modes but the fundamental with amplitude B were neglected; moreover C is the effect of the residual space charge and g is a shape function, depending on charge distribution inside the beam and about $g = \ln(r/r_b)$ for $r > r_b$. Neglecting

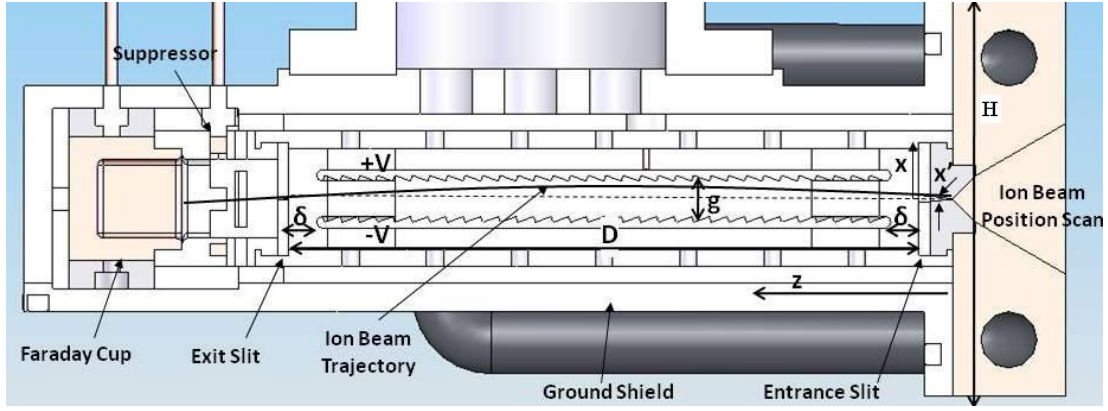


Figure 5: Typical scheme of an Allison meter measuring head, of height H ; secondary emission suppression is used; electrode parameters described in the text.

C since the charge compensation is large, gives $A = u_{dr}$; eliminating B gives the mixed boundary condition

$$u_{,z} = -k(u - u_{dr}) \quad (5)$$

which is easily implemented in the multiphysics solver[13]. In planar geometry, replace with $k = \pi/2/R_{dr}$. The case $R_{dr} \rightarrow \infty$ is more elegant, gives a simple Neumann condition $u_{,z} = 0$ and simplifies further analysis; practically it is often a good approximation (for a reasonable u_{dr}).

FAST EMITTANCE SCANNER

Over the last 20 years, Allison scanners [19, 20] have been introduced in many laboratories to measure the emittance of low-energy ion beams. Allison scanners feature entrance and exit slits that are rigidly mounted on the same support base, thus allowing for their relative alignment within tight tolerances. The space between the slits is occupied by a set of electric deflection plates as shown in Fig. 5. Charged particles that pass both slits are collected in the Faraday cup (FC), which features secondary electron suppression. A grounded shield surrounds the assembly, intercepting any charged particles that could produce ghost signals [21]. A stepper motor moves the entire assembly through the beam to probe the different positions of the beam. At each stop, the beam part that passed the entrance slit is scanned electrically across the exit slit to determine the distribution of the entry angles.

After passing the entrance slits, ions with energy eV_b enter the electric field between the deflection plates, which are charged to opposite voltages $-V$ and $+V$. Before and after the opposite ends of the deflection plate the two selection slits are placed at an equal distance δ ; the first slit selects the ion position, the second the ion angle. Let D be the distance between these slits. The deflection voltage-to-entrance-angle conversion depends primarily on lengths D and δ and the gap g between the deflection plates. Making the assumption that electric field is uniform in the region inside plates of length $D_\delta = D - 2\delta$ and falls to zero outside (hard edge approximation), the entry angle x' is related

Ion Sources

to the voltage difference V_d between the deflection plates by $x' = V_d D_\delta / (4gV_b)$. The space between the deflection plates allows only for trajectories where x never exceeds $g/2$, which geometrically limits the angular acceptance to $x'_M = \pm 2g/(D + 2\delta)$ where we took into account that trajectory is a parabola in the region between plates and a straight line outside. Correspondingly the maximum required voltage difference is

$$V_M = \pm \frac{8g^2 V_b}{D_\delta (D + 2\delta)} = \pm 2 \frac{(D + 2\delta)}{D_\delta} V_b x'_M{}^2 \quad (6)$$

We have chosen the front and rear slit width s to be equal to maximize the scanner current for a given angular resolution. Then the mechanical angular resolution is $\theta_d = \pm s/D$, which corresponds to a rms value (for a parallel beam uniformly illuminating the front slit) $\theta_{rms} = s/(6^{1/2}D)$. The FC signal current i_d is estimated from the ratio of scanner acceptance to the un-normalized phase-space area $\pi\epsilon/\beta$, so that $i_d = I_b s^2 / [D(\pi\epsilon/\beta)]$. Due to the finite bandwidth f of the Faraday cup amplifier, the smaller

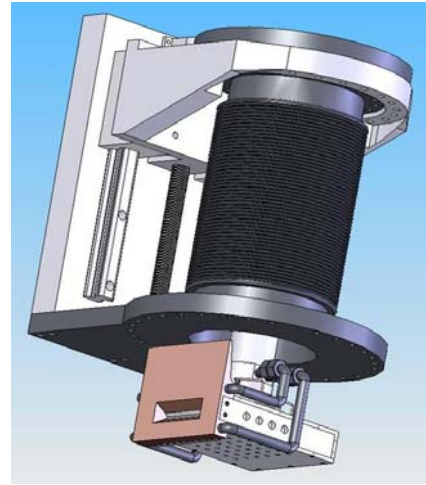


Figure 6: Artist view of the Allison scanner plugin module, in the beam-non-intercepting position.

Table 1: Beam Parameters for Scanner Specifications

	Units	NIO1	TRIPS
Beam ion		H ⁻	H ⁺
Energy eV_b	keV	60	80
Current I_b	mA	130	50
Power density	MW/m ²	20.3	22.6
Beam dimension	mm	±40	±40
Beam divergence	mrad	±40	±130
Power (CW)	kW	7.8	4.0

rms observable is $\theta_{rms} = 2^{1/2}x'_M/(\pi T f)$, where T is the ramp time to analyze angles in the range $\pm x'_M$. By equating the full mechanical resolution with that due to the finite bandwidth, we obtain a criteria for the amplifier bandwidth $f = 12^{1/2}x'_M D/(\pi s T)$.

The beam part selected with the first slit expand itself due to finite emittance and due to space charge effects. It is important that space charge forces do not affect angular resolution; this implies a limit for the slit distance D . Consider a uniform elliptical beam with dimensions R_x and R_y . If we require that expansion due to space charge to be less than $s/2$, then $D^2 < 2\pi\epsilon_0 R_x R_y m v_b^3 / (I_b e)$ with v_b the beam velocity; we get $D < 0.35$ m.

In our work, we want to use the scanner for both NIO1 and TRIPS source. Currents, beam power and maximum beam divergence are different for the two sources (Table 1). Allison scanner has to be designed for the worst parameters. This means that we need a divergence acceptance of more than 130 mrad and dictates a relationship between g , D and δ . For economic reasons we choose a voltage range of ± 2 kV for deflection plates amplifier. Parameters of this new Fast Emittance Scanner (FES) are presented in Table 2. The scanner has 90 mm long deflection plates with a 8 mm gap centered between the slits separated by 100 mm. Accordingly, its geometrical acceptance is 145 mrad. Both deflection plates are powered with bipolar ± 2 kV voltage amplifiers. This limits the voltage acceptance to 188 or 141 mrad for ion source potentials of 60 or 80 kV, respectively.

The scanner is covered with a drilled aluminum shield that should guarantee a sufficient vacuum pumping. Getter pump may also be inserted. A very good heat removal is obtained by using aluminum nitride as electric insulator

Table 2: FES Design Parameters

	Units	NIO1	TRIPS	FES
g	mm	8	8	8
D	mm	100	100	100
δ	mm	5	5	5
s	mm	0.05	0.05	0.05
V_M	kV	±0.43	±1.85	±2
x'_M	mrad	±40	±130	±145
θ_d	mrad	±0.5	±0.5	±0.5
Slew rate	V/μs	300	300	300
v_h	m/s	0.3	0.3	0.3
f bandwidth	MHz	31	23.3	35

material. The suppressor voltage will be tested by tuning the setup for maximum beam current in the Faraday cup of the scanner. For low suppressor voltages the Faraday cup current should change substantially. Then, to assure the suppression of all secondary electrons, the Faraday cup current has to reach a plateau significantly before reaching the intended suppressor voltage. Deflection plates have a sawtooth inner surface, to partly capture the secondary particle emission there produced by the ion impact. Provided that sawtooth depth is small enough, uniform field approximation is adequate, as easily shown by simulations. Some more elaborate machining of the deflection plates which may improve the secondary trapping efficiency is also being evaluated.

FES can work in two different modes: a very fast scan favored by an extremely fast motion (with velocity v_h up to 30 cm/s) of the active box through the beam and a slow scan (this is allowed by the efficient water cooling system) that guarantees a better resolution. An artistic view of the Fast Emittance Scanner is presented in Fig. 6.

REFERENCES

- [1] A. T. Forrester, *Large Ion Beams*, John Wiley, NY, 1996.
- [2] H.P.L. de Esch et al., *Rev. Sci. Instrum.*, **73**, 1045 (2002).
- [3] R. S. Hemsworth, *Nuclear Fusion*, **43**, 851 (2003).
- [4] R. F. Welton et al., *Rev. Sci. Instrum.*, **75**, 1789 (2004).
- [5] P. Garin, Proceedings of EPAC08, Genoa, Italy, p 974 (2008).
- [6] M. A. Lieberman, A. J. Lichtenberg, *Principles of Plasma Discharges and Material Processing*, J. Wiley, NY, 1994.
- [7] M. Bacal, *Rev. Sci. Instrum.*, **79**, 02A516 (2008).
- [8] K. W. Ehlers, K. N. Leung, *Rev. Sci. Instrum.*, **52**, 1452 (1981).
- [9] L. Celona et al. *Rev. Sci. Instrum.*, **75**, 1423 (2004).
- [10] R. Gobin et al. *Rev. Sci. Instrum.*, **73**, 923 (2002).
- [11] M. Cavenago et al., in *Negative ions, Beams and Sources* (eds. E. Surrey, A. Simonin, AIP-CP 925), p 149 (2008)
- [12] L. Tonks, I. Langmuir, *Phys. Rev.*, **34**, 826, (1929).
- [13] *Comsol Multiphysics 3.3*, see also <http://www.comsol.eu>
- [14] P. Spadtke, *Rev. Sci. Instrum.*, **75**, 1643 (2004)
- [15] R. Becker, *Rev. Sci. Instrum.*, **75**, 1723, (2004).
- [16] G. Fubiani, H. P. L. de Esch, A. Simonin, R. Hemsworth, *Phys. Rev. ST-AB*, **11**, 014202 (2008).
- [17] M. Cavenago, P. Veltri, F. Sattin, G. Serianni, V. Antoni, *IEEE Trans. on Plasma Sci.*, **36**, 1581, (2008).
- [18] A. T. Holmes, *Beam Transport*, in *The Physics and Technology of Ion Sources*, (ed. I.G. Brown), J. Wiley, NY, 1989.
- [19] P. W. Allison, J. D. Sherman, and D. B. Holtkamp, *IEEE Trans. Nucl. Sci.*, NS-30, 2204-2206 (1983).
- [20] R. McAdams et al., *Rev. Sci. Instrum.*, **59**, 895 (1988).
- [21] M. P. Stockli et al., in Proc. of the 16th Int. Work. on ECR I. S., (ed. M. Leitner, AIP Conference Proceedings AIP-CP 749, Melville, New York) p 108 (2008).

A SECONDARY RADIOACTIVE BEAM LINE FOR THE SPIRAL 2 PROJECT: FIRST STEP, THE DESIGN STUDY

F. Osswald[#], A. Khouaja, M. Rousseau,

Institut Pluridisciplinaire Hubert Curien, CNRS/IN2P3, Université de Strasbourg, France

Abstract

This second generation RIB radioactive ion beam facility will be constructed at GANIL and be operational in 2012 with stable beams and 2013 with radioactive ion beams. The aim of the installation is to produce high-intensity, high-quality radioactive ion beams of isotopes from large regions of the chart of nuclei in the range of 3 to 240u. Following description corresponds to the conceptual design study of a low energy RIB transport line for the SPIRAL 2 project.

INTRODUCTION

The RIB production cave of the SPIRAL 2 project is based on the ISOL technique and will be composed of a thick target, an ion source (TIS), a beam extraction and an adaptation section followed by a mass separator, see Fig. 1. In order to transport secondary beams special attention has to be taken concerning beam transport, containment of radioactive materials and protection against ionizing radiations. In fact, material activation should be kept as low as possible. Equipment activation during beam processing and matching is difficult to estimate and control. Access to the equipments is usually forbidden or restricted. Therefore discrete modules are designed with quick coupling, reduced and standard operations, and remote handling in order to mitigate the doses during maintenance.

The design has to be specially adapted in this project in regard to radioprotection, mechanics, maintenance and alignment. The key issues are the beam characterization at the source, multi particle and multi component beam optics with space charge, nuclear engineering, mechanical integration and optimization. With conventional beam lines, half the working time is spent for the beam optics design. With RIB lines, only 10-20 % of the time is spent for beam optics design, the remaining investigations are devoted to nuclear engineering, maintenance and infrastructure.

MAIN OBJECTIVES OF THE LEBT

The main objectives are to

- Extract the secondary beams from the TIS and realize a preliminary ion selection;
- Perform a mass separation with a resolution power in the range of 240 to 350;
- Transport the single charged ion beam to exit the production building with elements in the range of 3 to 240u, 1 μ A current, 80 π .mm.mrad emittance, 60 keV electric rigidity, and 0,39 T.m magnetic rigidity.

[#]francis.osswald@ires.in2p3.fr

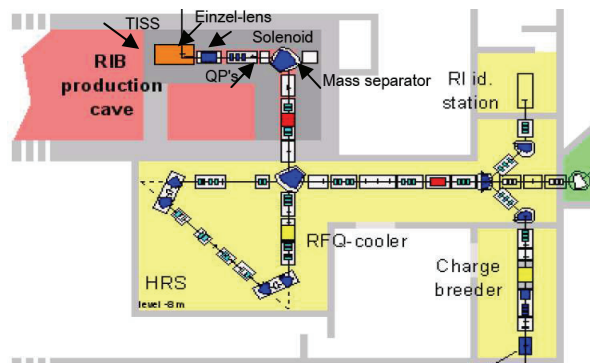


Figure 1: RIB production cave and beam transport line layout with extraction, focusing, and mass separation.

The facility should also:

- Maintain the vacuum level at 10^{-7} mbar;
- Provide the interfaces with all the technical services (vacuum, cooling, magnets, diagnostics, controls, connections, feed throughs, etc.);
- Guaranty the radioprotection and the safety: forbidden access in red class area and controlled access in yellow class area;
- Integer the waste management and the remote operation capacities.

The beam extraction from the TIS is achieved with an extraction potential of 60 keV located in an ECR-ion source, an Einzel-lens and a solenoid focus the beam and contribute to the elimination of the supporting gas. The current of the supporting gas may achieve 1 mA and should be eliminated before the analysing magnet in order to control the transverse dimensions of the extracted beam and the performances of the mass analysis.

BEAM OPTICS DESIGN

At SPIRAL 2, the LEBT system will handle the radioactive beam from the ECR-ion source of the TIS to the identification station (IBE), the low energy area (DESIR) and to the post-acceleration complex (CIME). The RIB production cave and beam transport line are designed with an extraction, focusing, mass separation (low resolution), high resolution separation (HRS), beam transport and switching to charge breeder, beam identification station and experimental area (DESIR).

The extracted beam is fed with a combination of Einzel, solenoid and triplet of magnetic quadrupoles lenses. The former has to purify the beam from contaminants (charge state, space charge, and residual gas) and to focus on the object point for the subsequent part of the design. For this set-up, first order ion optics matrix calculations using TRANSPORT [1] and GALOPR [2] codes were primarily

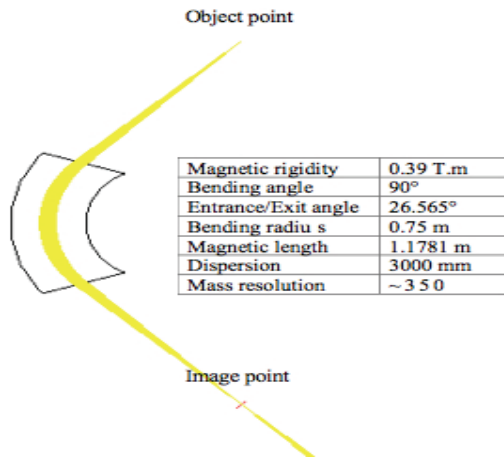


Figure 2: Main parameters of the mass separator. The trajectories correspond to a mass of 122u and magnetic field of 5.213 kG (GEANT4 model).

performed assuming a mass of 122u with kinetic energy of 60 keV for different object sizes at the exit ion source.

The pre-selected species are transported according to their mass/charge ratio and analyzed with an achromatic system of two 90° sector-bending magnets, aperture slits, and two electrostatic quadrupole doublets. The last doublet is used to inject the beam in a cryotrap in order to confine the residual contaminants not stopped by the first separator and then refocus the beam on the object point of the second analysing magnet.

Despite of a large acceptance of the beam line, a transverse space charge due to the supporting gas could

lead to a halo formation increasing the emittance of the beam in interest and then its losses. A model is currently under development with GEANT4, see Fig. 2.

Due to the low rigidity of the beam, the final part of the transport line is designed with electrostatic lenses. The beam envelope along the line is shown in Fig. 3 for an object point of 2.25mm horizontal half-width and 4.35mm vertical half-width leading to a mass resolving power of 333 for the mass 122u. The tuning of the system is evaluated and scaled from the magnetic rigidity and diagnostics along the transport beam line.

SAFETY MANAGEMENT

The production cave is the heart of the process; it delivers 10^{14} Fission/s and generates a neutron dose rate of 10^5 Sv/h. That neutron flux induces an integrated dose of 10^5 Gy/FY at the mass separator. The access to the production cave will be forbidden and the equipments will need remote handling.

The activation of the equipments is generated by beam loss, on-line volatile propagation and contamination (mostly neutral particles), and secondary radiations due the neutron flux and gamma-ray irradiation under service conditions. Containment of volatile radioactivity is obtained by carrying out the principle of double barrier: the first one is a static one and is provided by the vacuum chamber, the second is a dynamic one and is provided by the pumping system.

Safety is provided by correct sizing of the radiological shielding for all ionising radiations: neutrons, β , and γ ,

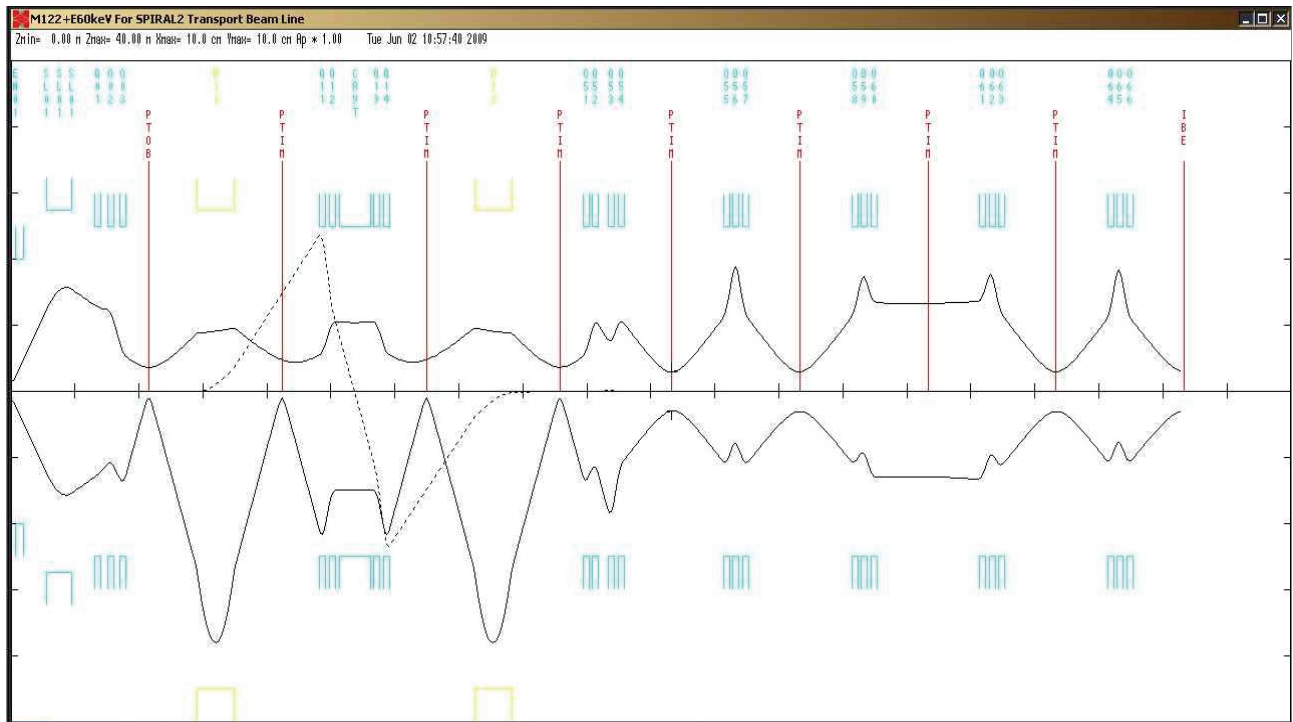


Figure 3: Beam-line optic from the extraction point to the IBE station: Einzel-lens (EN01), solenoid (SL01), magnetic quadrupole triplets (Q01, Q02, Q03), bending magnets (D11, D12), cryotrap (CRYT), electrostatic lenses (Q11-14, Q51-64). The horizontal (negative, 2 cm/unit) and vertical (positive, 2 cm/unit) beam profiles are drawn for an emittance of 80π .mm.mrad along the longitudinal axis (2 m/unit).

Radioactive Ion Beam Facilities

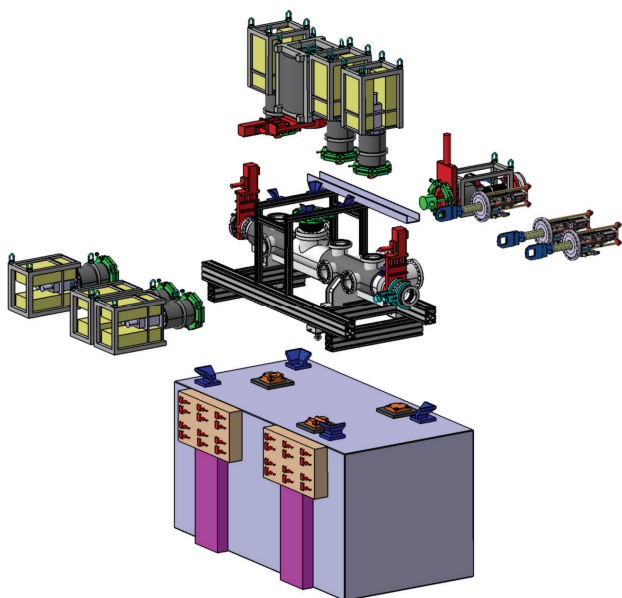


Figure 4: CATIA V5® mock-up of a modular beam line, here different beam diagnostics, vacuum pumping, shielding, connections and mechanical structure.

controlled access to the areas, definition of tolerable levels of accumulated and residual doses at different time delays, use of remote-handling system for the irradiated materials (blinded cell, crane, containment chamber). For correct sizing the design takes into account normal and accidental service conditions. The safety of the process requires hazard and accident analyses to ensure workers, the public, and the environment is protected against hazards such as radioactivity, fire, electric discharge, etc. The process is analyzed in order to determine the vulnerabilities and their treatment, it includes:

- Comprehensive hazard analysis to identify surges and off-normal conditions that require technical or administrative controls;
- Accident analysis to demonstrate effective mitigation of worst-case hazard;
- Additionally, risk analysis to define optional maintenance devices and procedures. In all cases, components with high or adapted radiation durability are selected.

MECHANICAL DESIGN

In addition to their complexity, the beam line equipments have to be accurately positioned and sustain severe operation conditions and requirements: radiation, neutron flux, mechanical rigidity due to the replacement and alignment (0.1 mm tolerance), and must satisfy our safety administration. The transport of radioactive matter is a regulated field of activity in the nuclear industry.

The system should be constructed ab-initio using components with high reliability, long life time and minimizing maintenance duration. Material properties specification requires low out gassing rate, high radiation tolerance, low activation under irradiation, mechanical reliability, and in some cases non-magnetic. The main

Radioactive Ion Beam Facilities

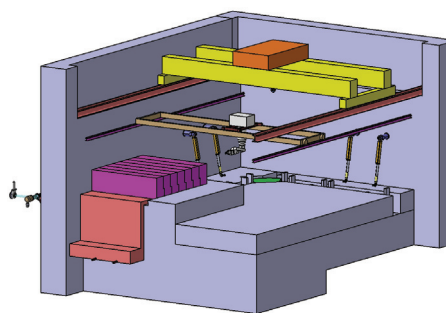


Figure 5: RIB production cave with infrastructure and maintenance tools. Process is installed inside a channel in the concrete and covered by blocks.

cost drivers are maintenance equipments, more expensive than process equipments. Standard components (commercially available) should be used whenever it is possible in order to lower the costs. Due to the nature and characteristics of the beam transport equipments in the RIB production cave the remote handling system should be highly reliable. Virtual mock-ups are built with CATIA V5®, see Fig. 4, and most numerical analysis is performed with COMSOL Multiphysics®. Different modelling and simulation technologies are employed to reduce development cycles and to lower costs instead of with time-consuming, costly and some times less precise physical testing which remain nevertheless indispensable.

MAINTENANCE AND MISCELLANEOUS

Concerning the process: in-situ remote handling is required for the modular equipments of the beam production area, the high vacuum pumping units, and some specific devices of the yellow class area placed in a hot cell. Equipments in yellow class area have partial remote handling abilities and allow hands-on maintenance under controlled conditions. Complex operations resulting in significant maintenance downtimes and high operational risk are avoided. In the case a failed component cannot be repaired in-situ, complete module is therefore replaced. Redundancy may be applied whenever possible taking into account global risk and cost effectiveness.

Concerning the infrastructure: maintenance and monitoring of remote tooling is a significant cost, frequently greater than the operational costs associated with the process due to the use of dexterous and mobile manipulators, see Fig. 5. The preliminary design of the production building and the infrastructure is currently externalized. On some places, conventional components can be used if integrated radiation tolerance is less than 10^5 grays and so must be replaced more frequently.

ACKNOWLEDGEMENT

SPIRAL 2 is one of the few projects in Europe which has been selected for the ESFRI. The ESFRI Roadmap identifies new Research Infrastructure of pan-European interest corresponding to the long term needs of the European research communities under FP7 Capacities

Specific Programme. The project is funded jointly by the CEA and CNRS, with support of the territorial authorities (Région Basse-Normandie, Département Calvados, ville de Caen). Main contributors to the LEBT design are: F. Varenne*, T. Adam, P. Anger*, R. Beunard*, B. Bru*, P. Dolegiewiez*, M. Duval*, G. Gaudiot, T. Goeltenlichter, Y. Huguet*, M. Michel*, M. Ozille*, M. Quiclet*, P. Royet*, C. Ruescas, A. Savalle*, J. Schuler, A. Sellam (* GANIL, Caen France).

REFERENCES

- [1] U. Rohrer, "TRANSPORT, PSI Graphic Transport Framework", 2008, based on a CERN-SLAC-FermiLab version by K.L. Brown, D.C. Carey, Ch. Iselin and F. Rothacker, CERN 73-16, 1973.
- [2] B. Bru, "GALOPR, A beam transport program with space charge and bunching", GANIL report A88-01.
- [3] V.D Elvira, "GEANT4 applications to accelerator physics", G4 Users meeting, Feb. 2002.

HOLLOW CATHODE E-GUN FOR EBIS IN CHARGE BREEDING EXPERIMENT

V. Variale*, V. Valentino, INFN-Bari
M. Batasova, G. I. Kuznetsov, BINP SB RAS, Novosibirsk
T. Clauser, A. C. Rainò, Bari University, and INFN-Bari

Abstract

The charge breeding technique is used for Radioactive Ion Beam (RIB) production in the Isotope Separation On Line (ISOL) method in order of optimizing the reacceleration of the radioactive elements produced by a primary beam in a thick target. In some experiments a continuous RIB of certain energy could be required. The EBIS based charge breeding device cannot reach a real CW operation because the high charge state ions produced are extracted by the same part where the $1+$ ions are injected, that is, from the electron collector. In this paper, an hollow cathode e-gun for an EBIS in charge breeding operation has been presented. Furthermore, a preliminary system design to inject the $1+$ ions from the cathode part will be also shown. In this way, the ions extraction system, placed in the electron beam collector, can be left only to extract the $n+$ ions, and then the CW operation, at least in principle, could be reached.

INTRODUCTION

SPES (Selective Production of Exotic Species) is a project of a new facility for the production of Radioactive Ion Beams accelerated up to several MeV/u [1]. It is in an advanced phase of study at the Legnaro National Laboratory (LNL) (Padua, Italy). Several proposals were made for the SPES project since 2002, with the aim to fulfil the physics goals and the budget constraints, the main objective being to develop a second generation ISOL facility on the way to EURISOL. Reaccelerated beams of neutron rich nuclei produced by Uranium fission with a fission rate on the order of 10^{13} fission s^{-1} in the production target are expected. The actual proposal represents an effective cost project, which fulfils the original requirement for the production of neutron rich radioactive ion beams able to make a breakthrough in studying nuclei far from stability, and takes advantage of proton drivers accelerators and selected exotic species to open up the possibility for application of nuclear physics in other fields as astrophysics, medicine and material science. Also in its last version, the SPES project foresees a charge breeding device in order to optimize the ion post-acceleration efficiency. The ‘charge breeding’ is a technique used to increase the ion charge state of the produced radioactive ions that are extracted from the target-ion source system, usually, only with a single charge. After the action of the ‘charge breeding’ device the produced radioactive ions can increase their charge state up to $n+$. The increase of the radioactive ion charge

state before the post-acceleration can be realised by making use of either an Electron beam Ion Source (EBIS) or an Electron Cyclotron Resonance Ion Source (ECRIS) [2, 3]. During the last past 4 years a large experience has been acquired at ISOLDE facility with both charge breeders. A comparison between those two methods describing advantages and disadvantages in their use can be found in scientific literature [4]. In short, Those systems can handle ion lifetimes down to some 10 ms, with a charge breeding efficiency of around 5%. Each device has its virtues and drawbacks. The clean EBIS is capable of handling low intensity beams, <1 nA, but its setup is relatively complicated. The ECRIS has a large charge capacity, and is the natural choice for beams larger than 1 nA. However, the beam contamination is significantly higher. Neither of the two charge breeders can so far manage very short-lived isotopes. Then, in that case, the technically simpler stripper technique has to be used. Its efficiency is comparable, and very clean high or low current beams can be dealt with, but it requires very big and costly ion pre - post acceleration [4]. The main drawback of a EBIS charge breeder device, which limits the beam intensity of the radioactive ions that can be post-accelerated, is its intrinsic pulsed operation. In a EBIS charge breeder, usually, the $1+$ ions are injected in the EBIS ion trap from the e-collector side where there is also placed the $n+$ ion extraction system. In fact, before the collector ion injection-extraction electrode entrance is located a deflection system that, alternatively, allows the $1+$ ion injection from one direction and the $n+$ ion extraction toward an other direction, in general, transverse to the first direction. That injection system could have a complicate and, further, intrinsically pulsed operation with a relatively low duty cycle. In this paper will be described a charge breeding experiment (TEBREC) with an EBIS having an electron beam generated by a hollow cathode in order to inject the $1+$ ions from the e-gun instead that from the e-collector side of the EBIS trap. In that way, at least in principle, the EBIS could be operated in Continuous Way (CW) avoiding the main drawback of an EBIS charge breeder, the intrinsic pulsed operation.

THE TEBREC EXPERIMENT

Recently at LNL a low cost test EBIS has been designed and built for an experiment on RF selective containment in EBIS [5]. That experiment had the aim to improve the ion charge state breeding efficiency by using a RF quadrupole inside the EBIS trap. The same device (called BRIC) with some modifications could be used for

*vincenzo.variale@ba.infn.it

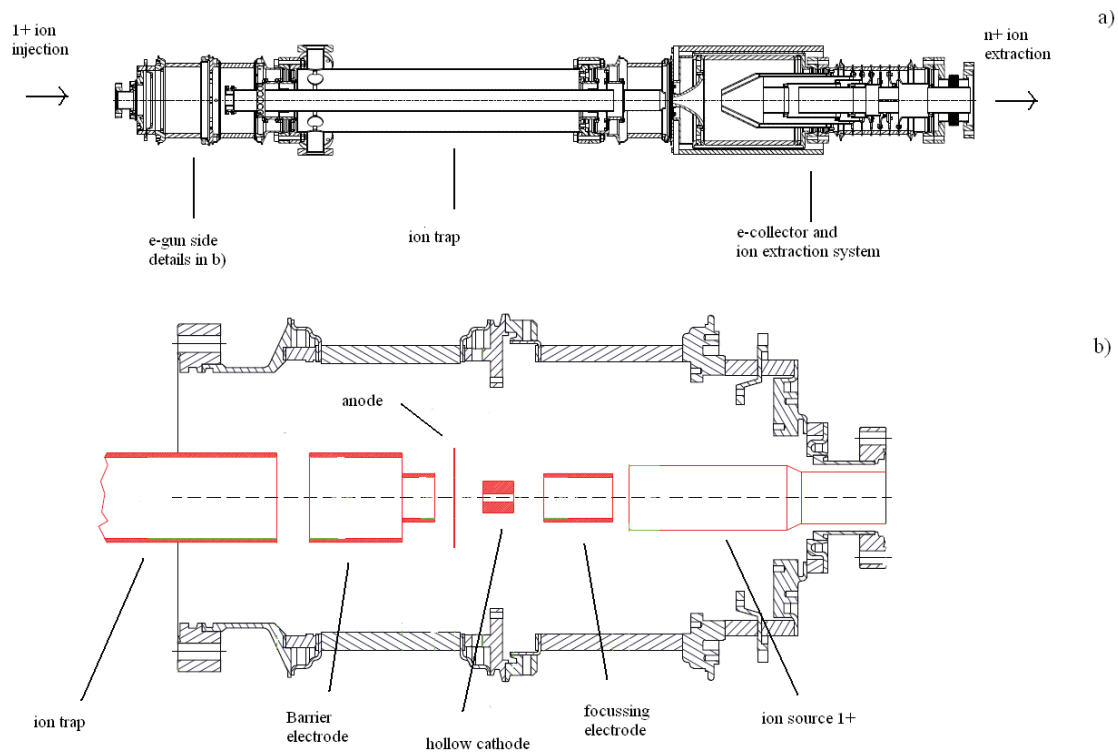


Figure 1: a) EBIS structure, longitudinal mechanical section; b) Details of the e-gun with hollow cathode. The 1+ ion source shown in the figure is a surface ion source.

a further R&D experiment on a EBIS charge breeding in CW operation. Since we have obtained very few funds the same solenoid of the previous experiment will be used and the modifications on the EBIS mechanical structure has been also minimized. The design of the new modified EBIS structure is shown in Fig. 1a) while the details of the new e-gun is shown in Fig. 1b). The main new feature of this charge breeding experiment is that of using an e-gun with hollow cathode in order to allow the 1+ ion injection from the e-gun side and leave in this way the e-collector only for the n+ ion extraction. In this way the duty cycle of the EBIS charge breeding could be sensitively improved and, as we will see, at least in principle the CW operation could be also reached.

In the experiment the 1+ ions that will be injected in the EBIS ion trap through the hollow cathode will be generated by a surface ion source [6].

From Fig. 1b), it can be seen that the surface ion source is very close to the hollow cathode. That solution gives a more compact and cheaper device. A simulation of the ion trajectories from the 1+ ion source up to the EBIS ion trap is shown in Fig. 2. The ion trap and electrode voltages have been chosen to minimize the 1+ ion kinetic energy in the trap. In fact, the 1+ kinetic energy at the end of simulation, that is at the entrance of the ion trap, was about 1 eV. The code used for those simulations has been SIMION.

In first approximation, the initial ion distribution used in carrying out the simulation of Fig. 2 has been not Maxwellian but had a constant distribution in the range of \pm a fraction of eV with initial transverse positions in the range \pm 1.5 mm around zero and with the vector velocities

having a maximum angle of 90° around the symmetry axis. The main problem in our experiment is the electron gun design with a hollow cathode that could generate a beam without hollow in the ion trap region. An e-gun of this type has been proposed studied and tested few years ago for electron cooling application [7, 8, 9]. In Fig. 3d), it is shown the proposed e-gun design with the electron trajectory simulation that close completely the hollow on the e-beam axis. Unfortunately, in designing the hollow e-gun for our experiment we had some constrain that prevented us to get an e-beam with the hollow completely closed as in Fig. 3d). The main constrain was given by the relatively low magnetic field that we could use for the e-beam focussing (about 1.8 kG). In fact, the electron beam compression depends on the square root ratio between the magnetic field on the trap region (B_{max}) and the magnetic field on the cathode (B_c) [10]. In Fig. 3a) the value of that ratio is 4 while in 3c) it is 8. From those figures, it can be seen that for the higher ratio value a greater beam compression can be obtained. However, on the other hand, if the maximum magnetic field value is not enough big to keep the electron beam scallop amplitude low, a high magnetic field ratio could generate scallop with very high amplitude as shown in Fig. 3b). A trade off between these two effect must be found to get a relatively high compression with a minimum electron beam scallop (Fig. 3a). In Fig. 3c) is also shown the simulation of the electron trajectories that starting from the hollow cathode go through the ion trap up to the collector. In the top of that ure is also shown the position of the coils forming the focussing solenoid capable to give a B_{max} of 1.75 kG [5].

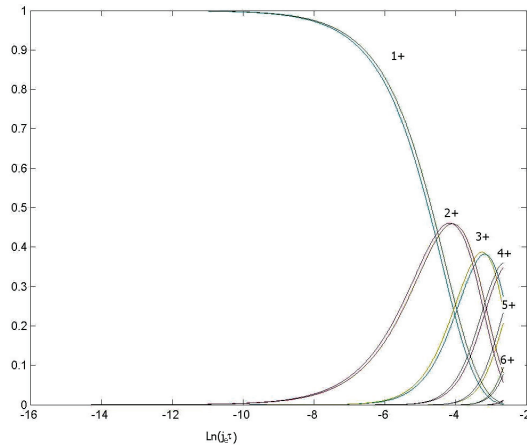


Figure 4: Ion charge state time evolution for Xe. The lower curves refer to an electron beam with hollow radius of 30% with respect to e-beam radius (upper curves).

CONCLUSION

The TEBREC experiment should finish in 2 years. The 1+ ion injection system, the new e-gun with hollow cathode and the EBIS trap has been already designed and the new electrodes are in construction. Meanwhile the surface 1+ ion source has been ordered and soon will be installed and tested. The first high charge state distribution measurement, in which should be used alkali ions as Cs and/or Rb, can be foreseen for the beginning of the next year.

In this experimental scheme a continuous 1+ ion injection should sensitively increase the device 'duty cycle' and, at least in principle, could give the CW operation. The 1+ ions, in fact, can be injected continuously in the ion trap with a kinetic energy just greater than of the trap barrier electrode voltage. The charge breeding time needed to reach the desired ion charge state of the injected ion, essentially, depends on the breeder parameter [14] $j_e \tau_c$, with τ_c indicating the confinement time. For example, the ion charge state foreseen for SPES for Sn should be 18+ then for a j_e of about 300A/cm² a τ_c of about 10 ms should be needed [15]. This means that the ions should stay in the trap for a time of about 10 ms before to be extracted. Usually, that ion trapping time is realized by confining the longitudinal ion motion with an electrostatic longitudinal trap that at the same time can prevent the continuous n+ ion

extraction. However, alternatively, a kind of magnetic longitudinal confinement has been also proposed in ref. [16] where, to allow a continuous ion extraction and in a really CW operation, the ions bombarded by the e-beam are slowed down in such a way they could reach the extraction electrode at the time needed to get the desired ion charge state.

REFERENCES

- [1] SPES Project study, LNL-INFN (REP), 145/99.
- [2] E. Donets, Rev. Sci. Instrum. 69 (1998) 614.
- [3] R.Geller, Annu. Rev. Nucl. Part.Sci. 40 (1990) 15.
- [4] F. Wenander, 'Charge breeding techniques', Nucl. Phys., A 746 (2004) 40c-46c.
- [5] V. Variale, G. Brautti, T. Clauser, A. Rainò, V. Stagno, G. Lamanna, V. Valentino, A. Boggia, Y. Boilmelshtein, P. Logatchov, B. Skarbo and M. Tiunov, "An EBIS for charge state breeding in the SPES project", PRAMANA- journal of physics, Vol. 59 (2002) 765.
- [6] IGS4 surface ion source from KPI.
- [7] N. Sharapa and A. V. Shemiakin, Nucl. Instr. And Meth., A336 (1993) 6.
- [8] V. M. Barbashin et al. Nucl. Instr. And Meth., A366 (1995) 215.
- [9] G. Ciullo et al., Rev. Sci. Instrum. Vol. 68 (1997) 1403.
- [10] G. I. Kuznetsov, M. A. Batasova and M. Tiunov, 'Formation and collection of Electron Beams for EBIS', on EBIS/T 2000 AIP conference proceedings - 572, p. 143.
- [11] V. Variale and M. Claudione, "BRICTEST: a code for charge breeding simulations in RF quadrupolar field", NIM in Phys. res. A 543 (2005) 403-414.
- [12] V. Variale, 'Ion charge state time evolution simulation in a hollow e-beam EBIS', INFN-internal report in preparation.
- [13] V. Variale et al., "Selective containment in EBIS for charge breeding applications", NIM in Phys. res. A, 592 (2008) 9-15. [14].
- [14] R. Becker, on Handbook of ion sources, ed. by B. Wolf CRC press (1995) 157.
- [15] PES Technical Design Report INFN-LNL-223.
- [16] R. Becker, H. Klein and W. Schmidt, 'The Electron Beam Ion Source and Some Possibilities for Improvement', Nucl. Sci. IEEE Transactions on vol. 19 (1972) 125-131.

THE LIGHT ION GUIDE CB-ECRIS PROJECT AT THE TEXAS A&M UNIVERSITY CYCLOTRON INSTITUTE

G. Tabacaru, D. P. May,
Cyclotron Institute, Texas A&M University, College Station, 77843 TX, U.S.A.
J. Ärje, JYFL, Jyväskylä, Finland

Abstract

Texas A&M University is currently configuring a scheme for the production of radioactive-ion beams that incorporates a light-ion guide (LIG) coupled with an ECRIS constructed for charge-boosting (CB-ECRIS). This scheme is part of an upgrade to the Cyclotron Institute and is intended to produce radioactive beams suitable for injection into the K500 superconducting cyclotron. The principle of operation is the following: the primary beam interacts with a production target placed in the gas cell. A continuous flow of helium gas maintains a constant pressure of 500 mbar maximum in the cell. Recoils are thermalized in the helium buffer gas and ejected from the cell within the gas flow through a small exit hole. The positively charged recoil ions (1^+) are guided into a 2.43 m long rf-only hexapole and will be transported in this manner on-axis into the CB-ECRIS (Charge Breeding – ECRIS). The CB-ECRIS will operate at 14.5 GHz and has been specially constructed by Scientific Solutions of San Diego, California for charge-boosting [1]. An overall image of the entire project will be presented with details on different construction phases. Specific measurements and results will be presented as well as future developments.

PROJECT OVERVIEW

In 2005 the Cyclotron Institute at Texas A&M University initiated a facility upgrade project [2]. This project will extend the research capabilities as a stable beam facility with moderate rare beam capabilities. This will be achieved by re-activating the 88" Cyclotron to deliver high intensity light-particle and heavy-ion beams, to be used for production of rare isotopes for acceleration in the existing K500 Cyclotron. The plan is to produce radioactive species for re-acceleration by the existing K500 Cyclotron. The main items of the scientific program that drive this project are summarized as: nuclear astrophysics (the extension of the Asymptotic Normalization Coefficients method and study of the ($^3\text{He},d$) reactions), nuclear structure (study of the Giant Monopole Resonances and the cluster structure of the nuclei using the radioactive beams), fundamental interactions and nuclear thermodynamics (multifragmentation). We are expecting also to gain valuable experience in the development of radioactive ion sources and different methods of diagnosis for weak beams.

The project is divided in three tasks: a) recommission of the existing 88" Cyclotron and install new beam lines; b) construct light-ion and heavy-ion guides and produce

and transport 1^+ radioactive ions; c) charge boost radioactive ions, transport and accelerate in the K500 Cyclotron. Table 1 presents the new beams intended to be developed using the Light Ion Guide (LIG).

Table 1: Projected Beam Intensities from the LIG after K500 Re-acceleration

(p,n) reaction Product $T_{1/2}$	Max Energy [MeV/A]	Intensity [particles/sec]
^{27}Si (4.16s)	57	5.4×10^3
^{50}Mn (0.28s)	45	2.1×10^4
^{54}Co (0.19s)	45	5.4×10^3
^{64}Ga (2.63m)	45	3.5×10^4
^{92}Tc (4.25m)	35	3.5×10^4
^{106}In (6.20m)	28	5.4×10^4
^{108}In (58.0m)	28	2.7×10^4
^{110}In (4.9h)	26	5.4×10^4

PRODUCTION OF RADIOACTIVE IONS

The Light-Ion Guide (LIG) will produce radioactive species mainly from (p,n) reactions. The beam (a proton beam around 30 MeV) interacts with a production target (e.g. ^{27}Al) placed in a gas cell. In the gas cell helium gas is flowing continuously at constant pressure of 500 mbar maximum. The recoil ions (e.g. ^{27}Si from $^{27}\text{Al}(p,n)^{27}\text{Si}$) are trapped in the buffer gas and ejected at a 90° direction (with respect to the beam direction) through a small exit hole [3]. All ions created in the gas cell are collected and transported by a rf-only hexapole: a resonant structure similar to the RFQ in a residual gas analyzer. The large flow of helium gas is evacuated by a differential pumping system. The ions are then injected into a Charge Breeding ECRIS (CB-ECRIS) source which will ionize them to higher charge states. The radioactive species are injected into the K500 Cyclotron and re-accelerated. The primary beam (proton beam) will exit the gas cell and will be stopped in the beam dump. Fig. 1 shows an engineering drawing of the LIG coupled with the CB-ECRIS. The main new feature of the device is the rf-only hexapole with a length of 2.43 m. Extensive calculations performed with SIMION [4] software confirm early theoretical approaches [5] where it was shown that all the particles entering the central region of the hexapole should have almost 100 % transport efficiency. The rf-only hexapole is

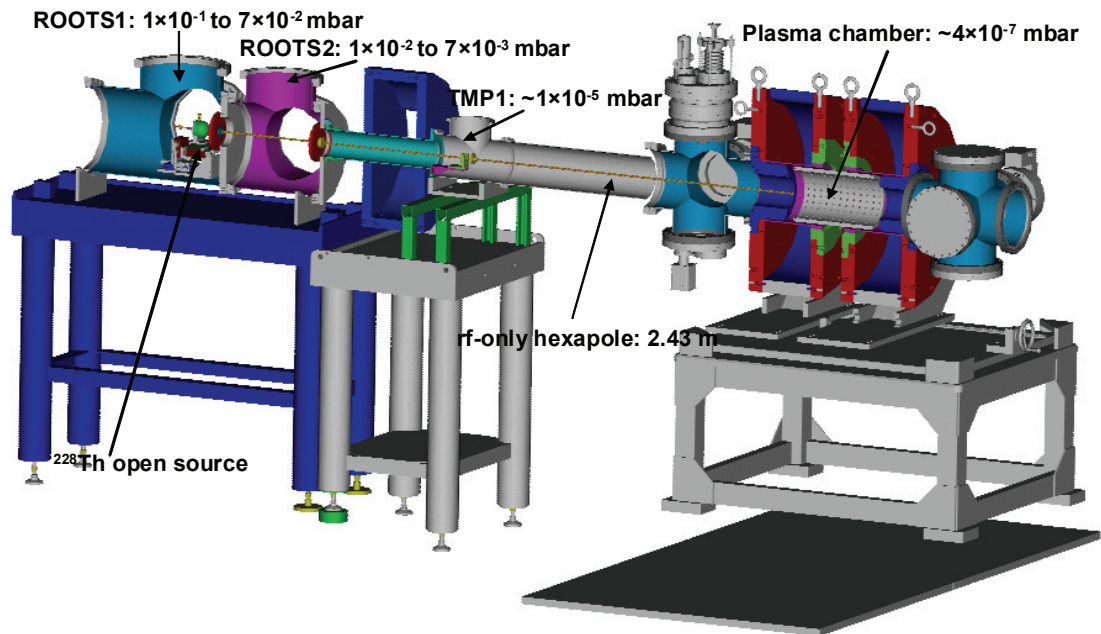


Figure 1: Engineering drawing of the Light Ion Guide coupled with the CB-ECRIS.

non-selective device, meaning that all ions, singly and possibly doubly charged, as well molecular ions, are transported with the same efficiency, independent of their mass-to-charge ratio.

DEVELOPMENT OF THE LIGHT ION GUIDE

At the Cyclotron Institute we developed, built and tested a prototype of the Light Ion Guide that will only suffer minor modifications for future operation. The vacuum system consists of two large chambers and a 2 m long beam tube for connection to the CB-ECRIS. The chambers are pumped with ROOTS blowers (2000 m³/h and 1000 m³/h pumping speed) and the beam tube is pumped with a turbo molecular pump (520 l/s pumping speed). Two similar turbo pumps are coupled also at the injection and extraction side of CB-ECRIS. Fig. 1 indicates the helium pressures in the different sections of the device.

Inside the first vacuum chamber, stands a semispherical gas cell (volume of about 50 cm³) with an exit orifice: 1 and 2 mm in diameters were used. Between the cell exit and the inlet of the CB-ECRIS plasma chamber is a 2.43 m long rf hexapole divided into three sections: two of 1 m and one of 0.43 m. The hexapole is made from 2 mm brass rods placed on a circle pattern with diameter of 6 mm (equivalent with an interior diameter of the hexapole of 4 mm).

The device was initially developed with ionized gas created by two high-voltage spark electrodes inside the gas cell. We were able to produce a few mA of current, mainly ionized helium and ionized impurities. The transported current (a few nA) was measured at the end of the rf hexapole on a Faraday cup. Fig. 2 presents, as an

example, a graph of the transported current at the end of the first 1 m long section rf hexapole as a function of the pressure inside the gas cell. The discharge voltage and current were 227 V and about 3.5 mA, respectively. The production of the ions via the spark method has drawbacks: the high voltage needed to ignite the spark accelerates the ions, and at the end of the rf hexapole the ions gain about 180 eV in energy. This energy is too high for the injection into the CB-ECRIS.

In order to eliminate the described feature, and reproduce more closely the future on-line operation, we decided to use an open radioactive source (228Th) as the recoil-ion source. An effort to use a heated alkali source was unsatisfactory due to the fact that the continuous flow of helium in the gas cell prevents attaining the temperature where the alkali source will start releasing the products.

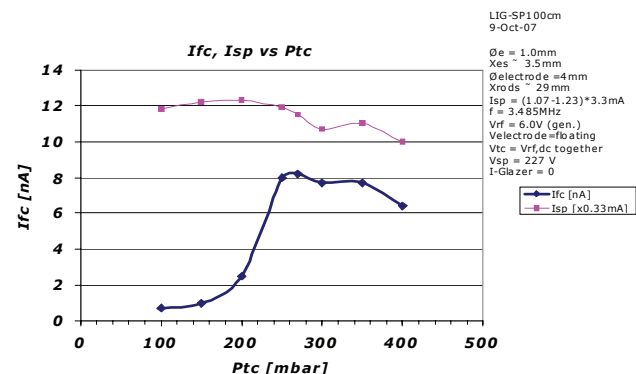


Figure 2: Faraday Cup current (I_{fc}) vs. the pressure in the gas cell (P_{tc}).

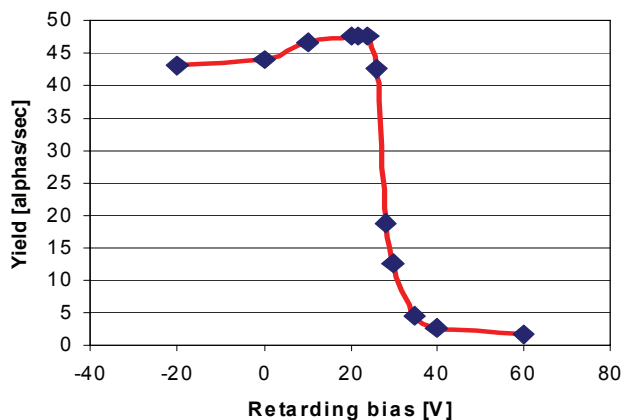


Figure 3: The retarding bias is a measure of the energy of the ions. The radioactive products exhibit an energy of 20-25 eV approximately. The acceleration voltage was 24 V.

Inside the gas cell the daughters from ^{228}Th are released continuously and they are thermalized by the helium gas. In order to have maximum stopping efficiency of the radioactive products, a pressure of 30 mbar of helium was used. The daughters are injected into the rf-only hexapole within helium flow by applying a small (approx. 10 - 50 V) acceleration (guiding) voltage between the cell exit and the hexapole inlet. The same voltage will control the injection energy of the recoil ions into CB-ECRIS plasma chamber. In this preliminary experiment the recoil ions were transported to a collector plate (aluminized mylar), placed at the inlet of the CB-ECRIS plasma chamber. The collector plate is backed by a silicon detector. The alpha particles coming from the products pass through the collector plate and are detected with the Silicon detector. The decay series of ^{228}Th include ^{216}Po with a half life of 145 ms. This is an excellent candidate to test our device: the half-life is short enough to provide a reasonable counting rate and is long enough to be charged boosted in the CB-ECRIS. The first tests, without CB-ECRIS plasma, were successful: we were able to measure about 50 alphas/sec coming from the ^{216}Po . We measured also the energy of the ^{216}Po ions, and found that the energy spread is only around 1 eV (see Fig. 3). This extra energy will have to be taken into account for stopping the products in the plasma of the CB-ECRIS. The extraction of radioactive highly charged ions will be attempted in future experiments when the CB-ECRIS will be operational.

FUTURE PLANS

Much further development of this system is necessary before it can produce a usable beam of highly charged radioactive ions with high efficiency for further re-acceleration in the K500 cyclotron. Two major directions should be followed to achieve the proposed efficiencies. The first is to find optimum parameters in the operation of the gas cell in conjunction with the rf-only hexapole. We need to determine the factors that will lead to high efficiency extraction of the radioactive products from the gas cell and high efficiency transport of the products to the CB-ECRIS. The second direction is to determine the ideal conditions for injection and extraction of the highly charged products from the CB-ECRIS with maximum efficiency. In pursuing these two directions the efficiencies of different sections of this system need to be measured along with finally the efficiency of the entire system.

ACKNOWLEDGMENTS

The authors would like to thank the staff of the Cyclotron Institute Texas A&M University for the commitment to their work. This work is supported by the U.S. Department of Energy under Grant number DE-FG02-93ER40773.

REFERENCES

- [1] W. D. Cornelius, Design of a Charge-Breeder Ion Source for Texas A&M University, ECRIS 2008, 18th International Workshop on ECR Ion Sources, Chicago, Illinois USA, <http://cern.ch/AccelConf/ecris08/papers/wecob01.pdf>.
- [2] "A proposed facility upgrade for the Texas A&M University Cyclotron Institute", http://cyclotron.tamu.edu/facility_upgrade.pdf
- [3] J. Årje et al., Nucl. Instr. and Meth. A247, 431 (1986).
- [4] SIMION: Industry standard charged particle optics simulation software. <http://www.simion.com/>
- [5] C. Hagg and I. Szabo, Intl. Jour. of Mass Spectrometry and Ion Process, 73 (1986) 295-312.

A NEW UNIT ACCESS CONTROL FOR GANIL AND SPIRAL 2

J. L. Baelde, C. Berthe, F. Chautard, F. Lemaire, S. Perret-Gatel, E. Petit, E. Pichot, B. Rannou, J. F. Rozé, G. Sénécal, GANIL, Caen, France

INTRODUCTION

For the GANIL safety reevaluation and the new project of accelerator SPIRAL 2, it was decided to replace the existing access control system for radiological controlled areas. These areas are all cyclotron rooms and experimental areas. The existing system is centralized around VME cards. Updating is becoming very problematic. The new UGA (access control unit) will be composed of a pair of PLC to ensure the safety of each room. It will be supplemented by a system UGB (radiological control unit) that will assure the radiological monitoring of the area concerned.

This package will forbid access to a room where the radiological conditions are not sure and, conversely, will forbid the beam if there is a possibility of presence of a person. The study of the system is finished and the record of safety in preparation. At GANIL, the ions are accelerated by cyclotrons (C01 or C02, CSS1, CSS2, CIME) and are transported through beamlines towards the rooms of experiments (D1-D6, G1-G4). A first named extension SPIRAL was brought into service in 2000. It makes it possible to produce and post-accelerate, via the cyclotron CIME, the radioactive ion beams obtained by fragmentation of stable ions resulting from CSS2 in a carbon target. The project SPIRAL2 will arrive soon and has the same need in safety.

Each room must thus remain confined (without human presence) when potentially dangerous ionizing radiations are present. This protection was identified as an important function for safety and is provided by EIS (Important Equipment for Safety). The EIS of GANIL are referred and described in the RGE (General Rules of Exploitation). It was decided to replace the current systems of security management by four distinct but inter-connected systems.

DESCRIPTION

TCR (Control board of Radiations)

This system controls, visualizes and stores the radiological state of the INB areas via radiation detectors. This system already exists but must be renewed in order to fulfil the current requirements of safety and to upgrade its electronics and its interfaces. This project is in phase of realization. It generates thresholds on its measures. This project is studied at the GANIL.

UGB (Unit of Management of the Radiation detectors)

This system ensures the safety of people in the event of detection of ionizing radiations in the controlled zones. It

is inter-connected with the TCR which informs about measurements and thresholds of the radiation detectors and with the UGA (defined below) which informs on the possibility of presence of people in the rooms. It acts on the possibilities of decreasing or of stopping the radiations in question. This project is studied at the GANIL.

UGA (Unit of Management of the Access)

This project is planned to prevent the possibility that people can be in the presence of ionizing radiations in the controlled areas. That involves two precepts:

- no staff in a room if ionizing radiations exceeds a threshold considered as unacceptable for health;
- stop all accelerated beams which can create an ionizing radiation exceeding the threshold of 25 $\mu\text{Sv/h}$ in a room where remains someone.

Thus, the access should be forbidden:

- to prohibit the entry, the rooms to be supervised will have manual or automatic doors and "security vestibules" with "one by one" passage to count and deduct the number of people in a room;
- to prevent the radiations in a room, this system will command 2 beam-stops by beamline at the origin of the radiation; a second barrier is made up by SAAF;
- information on presence of ionizing radiations will come via the associated system UGB.

This project is studied by industrial companies.

SAAF (Automatic System to Stop the Beam)

If a problem is detected by the UGB or the UGA, this system stops all the beams of the facility before acceleration. This project is studied by industrial companies.

The poster deals with the UGA. This system manages the room status. If someone is in the room, the UGA should stop the beam(s). If a beam can create radiation in a room, the UGA locks the doors and forbids the access.

To do that, the UGA can control:

- all the doors, closing and locking, of a room;
- the 2 doors of a "security vestibule";
- the pair of beam-stops on each way of beam which can create radiations in the room;
- evacuation signals (sound and visual).

It manages the different status of the room and the passage between them.

It dialogues with the UGB, SAAF and the Access Control System (biometric system).

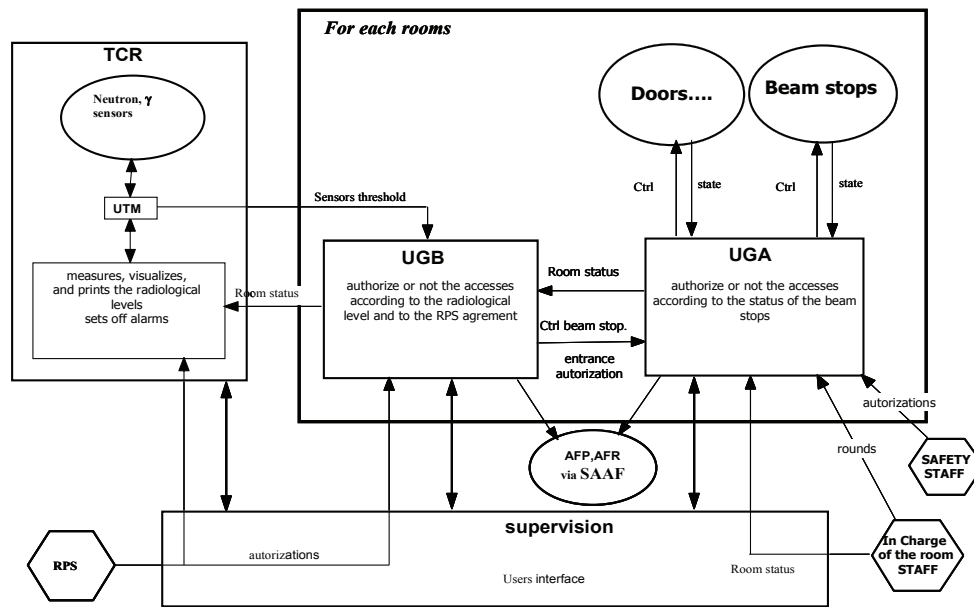


Figure 1: Interconnection between the systems.

STATUS

There are 3 statuses for the standard rooms:

- “PROHIBITED ACCESS”: there is nobody in the room and the entries are prohibited. The doors are locked by the UGA. The “beam stops” can be put OUT.
- “ACCESS CONTROLLED BY UGA”: the doors are locked by the UGA but the accesses are authorized via the “Entrance control” in order to count-deduct the people inside the room. Consequently, the “beam stops” are maintained IN.
- “ACCESS REGULATED”: the access is authorized and not controlled by the UGA. Consequently, the “beam stops” are forced IN. In order to recall this status, these rooms remain radiological controlled areas; all the doors are basically closed but not locked.

Safety Integrity Level	DEMAND MODE (“Low Demand Mode”)		CONTINUOUS MODE (“High Demand Mode”)	CONSEQUENCE OF A FAILURE
	AVAILABILITY	Probability of a failure on demand	Probability of a dangerous failure per hour	
SIL 4	>99.99%	$\geq 10^{-5}$ to $< 10^{-4}$	$\geq 10^{-8}$ to $< 10^{-6}$	Potential for fatalities in the community
SIL 3	99.9%	$\geq 10^{-4}$ to $< 10^{-3}$	$\geq 10^{-7}$ to $< 10^{-5}$	Potential for multiple fatalities
SIL 2	99% - 99.9%	$\geq 10^{-3}$ to $< 10^{-2}$	$\geq 10^{-6}$ to $< 10^{-4}$	Potential for major injuries or one fatality
SIL 1	90% - 99%	$\geq 10^{-2}$ to $< 10^{-1}$	$\geq 10^{-5}$ to $< 10^{-3}$	Potential for minor injuries
SIL 0	No Requirement			N/A

Figure 2: SIL Levels.

Industrials Standard IEC 61508

Given the size of the project, it was decided to subcontract the study and the system realization UGA and SAAF to industrial companies.

To do that, a GANIL working group realized a “functional terms of reference” and the choice of safety

Applications and Ancillary Systems

Standard was naturally the IEC 61508 and the FMECA (Failure Modes, Effects and Criticality Analysis).

IEC 61508 covers all safety-related systems that are electro technical by nature (i.e. electromechanical systems, solid-state electronic systems and computer-based systems). For the UGA, the asked Safety Integrity Level is SIL3 (Fig. 2).

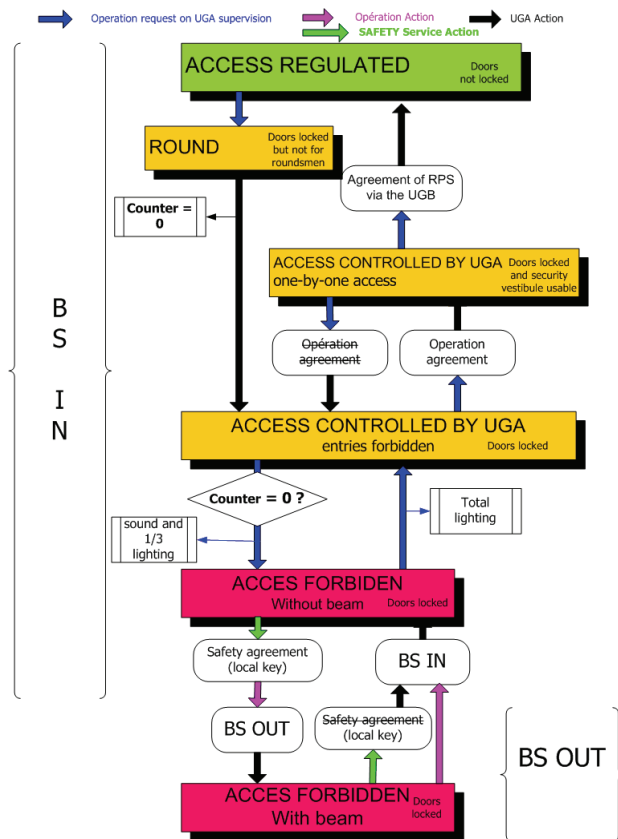


Figure 3: Synoptic of status changes.

This Standard gives recommendations for the development of hardware and software:

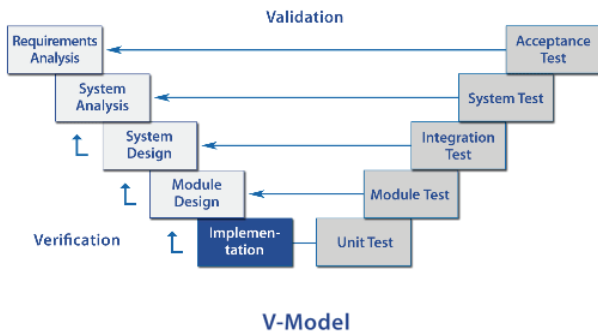


Figure 4: Development V-model.

The redundancy of the hardware is needed to have the SIL3 level.

Materials

The UGA retained structure for each room is:

- Two PLC (1 safety PLC and 1 standard PLC).

- All sensors have three contacts: NO (Normally Open) and NL (Normally Locked) for the safety PLC and NO for the standard PLC.

- Two beam-stops by beam line.

The Access Control System (biometric system) and the supervision are not important for safety. They are centralized systems and they dialog with the PLC via a private network.

CONCLUSION

The test of the prototype will begin at the end of June. The ASN (French Nuclear Safety Agency) will approve the systems within a few months. The UGA, UGB and SAAF will be installed in 2011 for GANIL and later for SPIRAL 2.

REFERENCES

[1] Industrials Standard IEC 61508.

STATUS OF THE CAVIAR DETECTOR AT LISE-GANIL

L. Perrot[#], IPNO-IN2P3-CNRS, Orsay, France
 S. Grévy, C. Houarner, R.Hue, C. Marry, GANIL, Caen, France
 S. M. Lukyanov, Yu. Penionzhkevich, FLNR JINR, Dubna, Russia

Abstract

Physics that motivated the building of the LISE magnetic spectrometer, main ideas exposed in the scientific council of GANIL held on 4th June 1981 by M. Brian and M. Fleury, were: atomic physics studies with stripped ions and the study of new isotopes produced by the fragmentation of beams. The LISE line is a doubly achromatic spectrometer (angle and position), with a resolution better than 10^{-3} . Since the first experiment done in 1984, several improvements of the spectrometer were performed: use of an achromatic degrader (1987, used for the first time in the world), building of the achromatic deviation and the Wien Filter (1990), building of a new selection dipole and associated vertical platform (1994), building of the new LISE2000 line (2001), use of the CAVIAR detector (2002), building of the CLIM target (2007). Despite an extreme international competition, the LISE spectrometer remains a world-leader equipment using more than 50 % and up to 90 % of the beam time available at GANIL. This paper presents the status of CAVIAR detector which consists of a MWPC dedicated to in flight particle position at the first dispersive plane of LISE. Since two years, intensive efforts were done with the objective to make available a “plug and play” detector for nuclear physics experiment. We will describe the system from MWPC up to acquisition system. As example few experimental results will be presented.

INTRODUCTION

In the energy domain of GANIL (from 30 up to 100 MeV/u), a large fraction of the reaction cross section goes into the fragmentation of the projectile. Fragments are emitted around 0° at velocities very close to the one of the incident beam, in a mass range which spreads from the projectile. A physics program with the goals to study exotic nuclei and secondary radioactive beams started in the early eighties [1]. LISE provides two main selection criteria in the identification process of reaction products. The first one is the magnetic rigidity ($B\rho=Av/Q$) given by the first analyzing dipole D31. Dispersion term of the section is typically 16.5mm/% of $\delta p/p$. Slits are placed at the dispersive plane with full aperture of ± 45 mm. The momentum acceptance is equal to $\Delta p/p=2.72\%$. The second selection is the differential energy loss (dE) of the ions in materials, by means of an achromatic degrader located in the intermediate focal plan of the spectrometer (cf. Fig. 1). The combination of Bp and dE measurements provides a selection to A^3/Z^2 (with B the magnetic field, ρ the radius, A the mass number, v the velocity and Z the atomic number). Beam line acceptance is around 1msr. These two previous selections are the selection reference of LISE spectrometer.

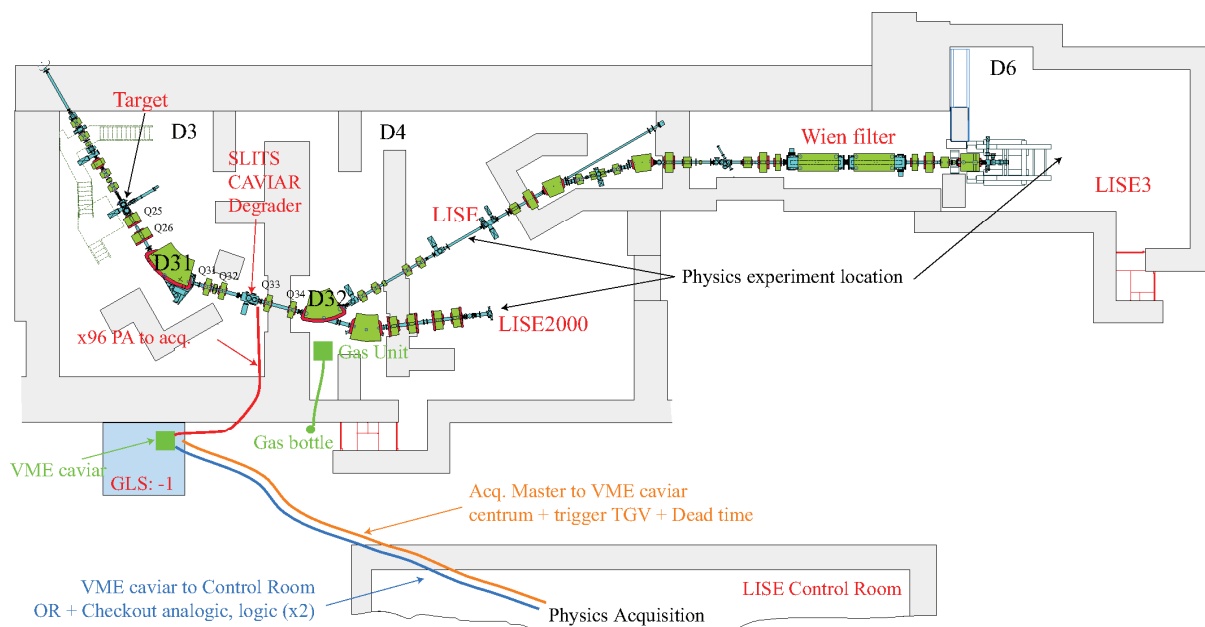


Figure 1: View of the LISE spectrometer. Essential beam lines elements can be located. CAVIAR and physics acquisition location are precise.

[#]perrot@ipno.in2p3.fr

The angle of entry of the primary beam with respect to the axis of the spectrometer has been made variable (from 0° up to 3.5°). This improvement allows the suppression of remaining incompletely stripped beam charge states in experiments with heavy beams ($Z > 30$).

A third selection was added in the early nineties to increase the rejection power. In order to filter out a given velocity, a device has been constructed, in which an electrostatic and a magnetic field are crossed in a "classical" Wien filter [2]. The flight path between the target and the final focus is around 43m. The line was named LISE3.

In 2001, the new line LISE2002 was built for increasing magnetic rigidity (until 4.2 Tm) and beam line acceptance [3]. LISE2002 line is connected to old LISE line after the intermediate focal plane. It imposed quadruples and first dipole changing.

More recently, according the various LISE features, a new rotating target was build. This target can accept beam power up to 2 kW [4].

During an experiment carried out in 2002, a multi-wires proportional detector was placed in the dispersive plane of the spectrometer [5]. This detector named CAVIAR by the GANIL staff allowed measuring the magnetic rigidity of each fragment via its position in the focal plane, improving the mass-to-charge A/Q resolution.

Activities on this detector began again in 2006 with α -source and beam test before a real experiment. During the two last years, various improvements have been done. We will present in this paper the status of the detector. We will first describe the detector. Next, we will give the methodology to tune the system. Finally, few results will be presented.

CAVIAR DETECTOR

To take the maximum benefit of the secondary beam intensity produced in the target, momentum selection slits of the LISE dispersive plane must be opened. The expected counting rate can be increased by a factor 5. But the major difficulty is that heavy nuclides have too close mass-to-charge A/Q ratio and time of flight (which is the case for fragmentation beams). For the full slits aperture, nuclides can not be distinguished. Contaminant rates can largely dominate the very low production rates of the interesting nuclide.

Identification can be provided using a MWPC [6] placed at the dispersive focal point (cf. Fig. 1). Each wire detects the horizontal position of the particle at this point. With a coincidence between CAVIAR and detectors placed at the final focal plane (LISE2000 or LISE3) and a time of flight measurement, we can reconstruct precisely the mass-to-charge ratio event by event. Maximum counting rate per wire is 10 kHz.

FLNR JINR team performs MPWC and preamplifiers R&D according to their great experience [7-8].

CAVIAR is a powerful tool for research and nuclear spectroscopy on nuclides produced with very low cross section. For example, it will concern nuclides close to the proton or the neutron drip-lines. In addition, CAVIAR

Applications and Ancillary Systems

detector can be used during LISE tuning at the beginning of experiment. We obtain nuclides momentum distribution in the first LISE dispersive plane and optimize properly the spectrometer to the nuclide of interest.

Mechanics

The sensitive area of this detector is 96 mm in the horizontal plane and 32 mm in the vertical plane. These sizes are defined by the secondary beam sizes and maximum aperture of the slits in the dispersive plane. CAVIAR is composed by 96 wires of 10 μm in diameter with 1 mm step between each of them. Wires are in gilded Tungsten. Two 1.5 μm thicknesses Aluminum Cathodes are placed 3.4 mm distance from the anode (cf. Fig. 2).

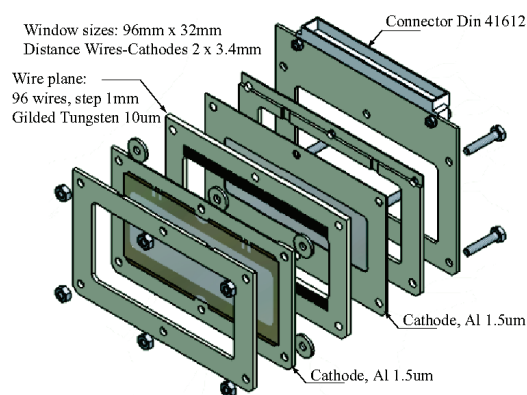


Figure 2: Mechanical view of the sensitive area of CAVIAR.

Detector is filled with variable and less than 50 mbar Isobutene (C_4H_{10}). Two Kapton ($\text{C}_{22}\text{H}_{10}\text{N}_2\text{O}_5$) windows of 8 μm thicknesses are used. They isolate the detector from beam line vacuum [9]. CAVIAR is a low interceptive detector for high energy beams.

CAVIAR detector can be easily inserted in the beam line using a classical gage, which has connections on the top for high voltage, gas circulation and 96 out signals from wires. On the beam axis, CAVIAR is located 45 mm after the selection slits.

Gas System

The Isobutene was chosen for his cost and good properties to nuclides and energy range. For safety reason, gas filling system is located outside the experimental room (cf. Fig. 1). This gas unit, developed at GANIL, is inside the experimental room. We can control it by software. The gas unit system is working in such a way to protect the detector in case of any trouble. Without gas regulation, valve is open to obtain the same vacuum in the detector and in the beam vacuum chamber.

Signal Pre-amplification

Directly fixed to the propeller, 6 boxes of 16 channels of pre-amplification are connected. Each wire is individually read out. Using this type of charge

preamplifiers and due to ECM compatibility, we need short lengths from wires up to the PA entry. Fig. 3 shows signals amplitudes after amplification.

New tension preamplifiers have been recently built at JINR to take into account possible long distance between detector and preamplifiers. Tests with beam have been done in March 2009.

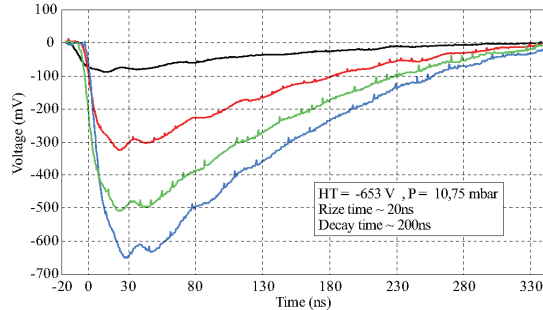


Figure 3: Amplified signals (50Ω adapt.).

CAVIAR Acquisition System

The 96 amplified signals are transported along 16 m cables to the acquisition system. Analog signals process is based on VME standard [10]. 6 DDM16 modules developed at GANIL are inserted [11]. Each DDM16 manage 16 channels. The module provides leading edge triggering, delay time and memorization. Scalers, tests, checkouts of analogical and logical signals are also available.

When a particle passes through CAVIAR detector, a signal can be induced on a wire. Signal is treated by associated DDM16 channel. The particle can be also detected by the detection system placed at the final focus point which is the master. The associated trigger generated by a validated event in the final detection system is transported to a TGV (Trigger Général VME) module with a CENTRUM receptor, which can correlate the event number with the logical signal generated by the DDM16 (cf. Fig. 4).

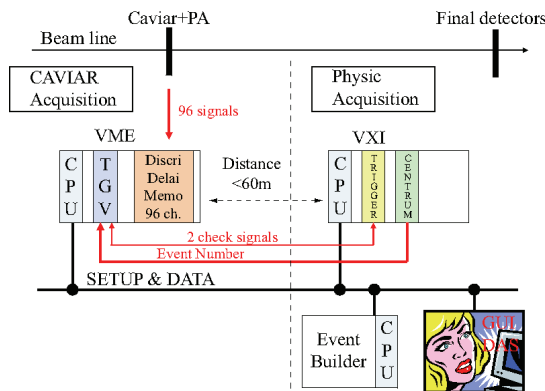


Figure 4: Synoptic adopted for CAVIAR.

Due to beam line flight path, cables lengths and various signals treatments, all CAVIAR logical signals must be delayed to obtain the good memorization (cf. Fig. 5).

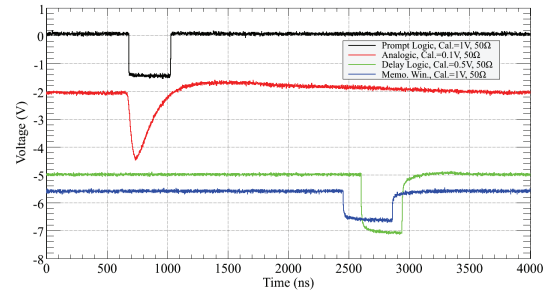


Figure 5: Synoptic adopted for CAVIAR.

CAVIAR memorization pattern is defining in 6 words of 16 bits.

Finally, each DDM16 provides a “Or” of its 16 channels. The 6 resulting Or can be mixed to produce a single one. This “Or” logic can be use for the time measurement during the experiment.

CAVIAR TUNING

We will briefly describe up to now the method to tune the CAVIAR detector.

First of all, the detector must be connected to the line few days before the experiment. Vacuum in both chamber and detector must be in agreement with normal condition (around 10^{-6} mbar). Some tests must be done with gas circulation for ensure that no gas leak occurs with the Kapton windows. At the experiment start, gas pressure must be chosen in agreement with the species and beam energy. At LISE, gas pressure will be typically 10 mbar.

High voltage value for the detector must also be prepared and checked. In order to protect the MWPC, current limit (of few μA) must be fixed for automatic switch-off the voltage. At LISE for 10 mbar isobutene, optimum voltage will around -600 V.

During the experiment, any CAVIAR insertion in line must be done with beam off. With beam, observation of dedicated analogical signal to one wire can be done at oscilloscope. In that way we can increase progressively the high voltage until obtaining signals like the ones in Fig. 3.

Then, a threshold is applied just above the noise (~ 13 mV). Using dedicated CAVIAR scaler, we can flag wires with abnormal counting rate. Threshold can be changed individually wire by wire and observed at the oscilloscope (cf. Fig. 4).

In order to verify if the detector tuning is well optimized, slits just before CAVIAR can be closed at ± 0.1 mm for the primary beam. If more than one wire has signal with a too high statistics, it is an indication that the high voltage and threshold are not satisfactory.

With the closed slits, we can also determine the center of the CAVIAR detector in the beam line.

We have recalled that CAVIAR is a low interceptive detector. However, energy losses can be observed in the refocusing LISE section. Beams have to be re-centered by decreasing the current in the second LISE dipole D32 (cf.

Fig. 1). Typically, with fragments at LISE, Bp correction is around 0.5% (in energy, it is around 1%).

DDM16 delays are the same for all CAVIAR logical signals. They are fixed only when Trigger comes from the acquisition of the experiment (cf. Fig. 4). CAVIAR memorization is valid when the forehead of rise delay logical signal of CAVIAR is within the memorization window (cf. Fig. 4, green and blue curves).

Various parameters have to be known or determined in order to reconstruct the mass-to-charge ratio during the experiment. All the following parameters are used to calculate the nuclide speed and for the nuclide localization on CAVIAR (see appendix for explanation).

- Wire value (W_c) in the beam line center on the horizontal axis. As we have already seen, it is achieved by closing the selection slits at ± 0.1 mm.
- Time of flight (ToF) measurement have to be known from CAVIAR and from the final detection. Absolute calibration must be determined.
- The magnetic rigidity of the first ($B\rho_{D31}$) and the second ($B\rho_{D32}$) sections must be known. At LISE, RMN measurement will provide the field gradients. Magnetic rigidities are determined by multiplication of the field by the radius of the dipole.
- Path length (L) between LISE target and CAVIAR and also LISE target and final detection [9].
- The dispersive transport matrix term T16 at the CAVIAR position has to be known. For LISE3 standard optics, we have $T16=16.1$ mm/% ($\delta p/p$). We can notice that different optics are available for the LISE spectrometer.

Checks must be done during the experiment. In that way, we take advantage of the various checks out of CAVIAR signals (analog, prompt and delayed signals), memorization window and DDM16 scalers. Spectra produced on line during the experiment like CAVIAR profile and his multiplicity will be also some good additional checks.

EXPERIMENTAL RESULTS

Different tests and experiments have been realized since 2006. Few of them are now presented.

α -source Measurements

For detector checks, it can be useful to use radioactive $^3\alpha$ -source emitter (α energies < 6 MeV). CAVIAR detector can be inserted between the radioactive source and a Silicon detector. The Silicon junction detector is used for precise energy deposition measurements and to simulate the physics detector (like in a real experiment). Electronic treatments to Silicon detector is a classical spectrometry electronics.

We can study α energy losses in CAVIAR and detected in the Silicon detector. Fig. 6 presents the α energy spectra measured with the Silicon detector for CAVIAR off line, in line with and without gas. We can observe that α 's lose almost half of their energy in CAVIAR, and contribution of gas is not negligible. Careful calculations

using TRIM code [12] have very well reproduced these experimental results. It is important to well understand the contribution of the energy loss in CAVIAR. In real experiment at LISE, we remind that nuclides energies are very high (more than 30 MeV/u); energies losses in CAVIAR will be around 1%.

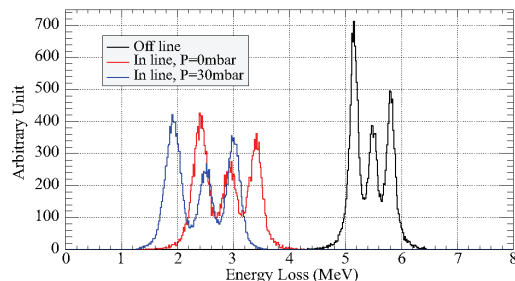


Figure 6: α energy loss in a Silicon detector.

An important parameter is the wires number touched per nuclides pass across CAVIAR. This parameter is the multiplicity. It depends on the beam divergence characteristics, high voltage and threshold. There will also be an impact on the localization accuracy of the nuclide in CAVIAR (cf. Fig. 7).

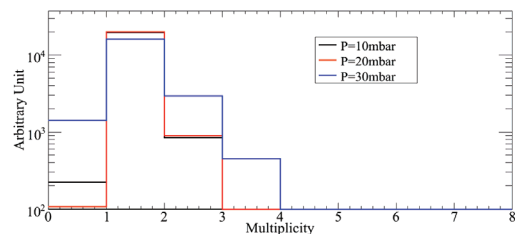


Figure 7: Example of CAVIAR event multiplicity.

Krypton High Energy Beam

An experiment has been realized using a $^{78}\text{Kr}^{33+}$ primary beam at 70 MeV/u. LISE target was a 500 μm Beryllium. Heavy ions of high atomic number (here $Z=36$) impose a low gas pressure to 6 mbar. High voltage apply to CAVIAR was -513 V.

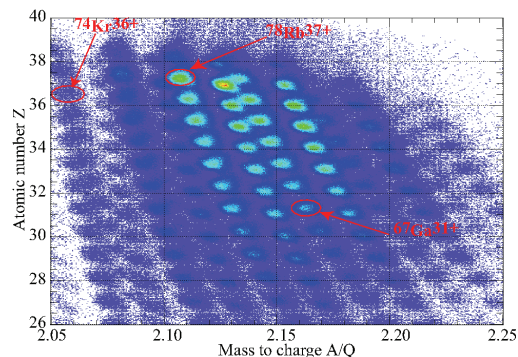


Figure 8: Determination of the atomic number Z as a function of the mass-to-charge ratio A/Q using CAVIAR.

Experiment has been performed using a Silicon junction at the final focus point in LISE D4. This single

detector provides nuclides identification (atomic number Z) by measurements of particles energy losses and time of flight. Selection slits in the dispersive plane was open at ± 42.5 mm. From the CAVIAR mass to charge reconstruction and the atomic number determination from energy loss in the silicon detector, we can obtain a complete identification of particles (cf. Fig. 8). We can observe that nuclides are well separated. Various nuclides charge states are also identified. Case of heavy ions like Krypton area of the nuclides chart is an extreme case of the CAVIAR contribution. Lower mass ions produced with smaller charge states will be more easily separated.

Finally, using contour selection in $Z\%A/Q$ distribution, we can determine the momentum distribution for few nuclides (cf. Fig. 9).

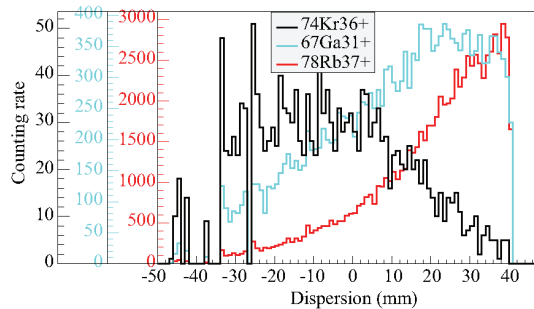


Figure 9: Distribution of selected nuclides in the LISE dispersive plane.

CONCLUSION

In this paper, we have presented the status of the CAVIAR detector at LISE GANIL. This MWPC measures the horizontal position of each fragment in the first dispersive plane of the spectrometer. We can determine precisely the mass to charge ratio of each particle during experiment. Since 2006, various improvements have been done like new preamplifiers, dedicated acquisition system based on VME standard. Some improvements must be done on the cables, connectors and ECM before preamplifiers with the objective of noise reduction. CAVIAR detector offers new possibilities to the LISE spectrometer. It will be certainly an interesting tool for SPIRAL2 beams that will be available in 2013.

APPENDIX

We give here formulas to determine the nuclides mass-to-charge A/Q knowing its position in the dispersive plane and its time of flight (see appendix A in [8]).

For each event, we have to determine the average CAVIAR wire (W_a) touched knowing his multiplicity N_{mult} and wires touched W_i : $W_a = \sum W_i / N_{mult}$.

Knowing the central wire W_c , the dispersion is $X_{disp} = W_a - W_c$.

With the LISE magnetic rigidity of the first section ($B\rho_{D31}$) and the matrix dispersive term T_{16} in the plane of CAVIAR, we can determine the single magnetic rigidity $B\rho_w$ like:

$$B\rho_w = B\rho_{D31} \times \left(1 + \frac{X_{Disp}}{T_{16}} \right) \quad (1)$$

Finally, knowing the path length L and the measured time of flight T , we determine the mass-to-charge ratio:

$$\frac{A}{Q} = \frac{B\rho_w \times c}{M_{UMA} \times \beta\gamma} \quad (2)$$

where c is the speed light, $\beta=L/(cT)$, γ the Lorentz factor and M_{UMA} the atomic mass unit.

REFERENCES

- [1] R. Anne et al., "The achromatic Spectrometer LISE at GANIL", NIM, A257, (1987), 215-232.
- [2] R. Anne, A.C. Mueller, "LISE3: a magnetic spectrometer-Wien Filter combination for the secondary beam production". NIM, B70 (1995), 276-285.
- [3] R. Anne, "LISE2000", Preprint GANIL, P 02 01
- [4] S. Grévy, R. Hue, "CLIM: the new rotating target for exotic nuclei production at LISE spectrometer", 24th World Conference of the International Nuclear Target Development Society - INTDS2008, Caen: France (2008).
- [5] S.M. Lukyanov et al., "Experimental evidence for the particle stability of ^{34}Ne and ^{37}Na ", J. Phys. G: Nucl. Part. Phys. 28 (2008), L41-L45.
- [6] F. Sauli, "Principles of operation of multiwire proportional and drift chambers", Lectures given in the Academic Training Programme of CERN, CERN 77-09, 3 May 1977.
- [7] R.A. Asaturyan et al. "The Multiwire Proportional Chambers Coordinate System of MULTI Set-Up", Instruments and Experimental Techniques, V 42, N3, 1999, pp 342-346.
- [8] R.A. Astabatyán, "Set-Up on the basics of multiwire proportional and ionization chambers for radioactive beam experiments", Preprint JINR, E13-2002-138, Dubna, 2002.
- [9] L. Perrot, "Le détecteur CAVIAR", Preprint GANIL, R 07 04, HAL: in2p3-00178047, version 1
- [10] W. D. Peterson, "Versa Module Eurocard", VMEbus International Trade Association, USA, 1991. <http://www.vita.com/>
- [11] C. Houarner, L. Olivier "Discriminator Delay Memorization 16 Channels" and "CAVIAR Acquisition System Guide", Preprints GANIL, December 2008, <http://wiki.ganil.fr/gap/wiki/Documentation/VME/DDM16>.
- [12] J. F. Ziegler, J. P. Biersack and U. Littmark, "The Stopping and Range of Ions in Solids", Pergamon Press, New York, 1985 (new edition in 2009).

HEBT LINES FOR THE SPIRAL2 FACILITY

L. Perrot[#], J.L. Biarrotte, IPNO-IN2P3-CNRS, Orsay, France

P. Bertrand, G. Normand, GANIL, Caen, France

D. Uriot, SACM/IRFU/DSM/CEA, Saclay, France

Abstract

The SPIRAL2 facility at GANIL-Caen is now in its construction phase, with a project group including the participation of many French laboratories (CNRS, CEA) and international partners. The SPIRAL2 facility will be able to produce various accelerated beams at high intensities: 40 MeV Deuterons, 33 MeV Protons with intensity until 5 mA and heavy ions with $q/A=1/3$ up to 14.5 MeV/u until 1 mA current. We will present the status of the beam dynamics studies recently performed for the high energy beam transport lines of the facility. Various studies were performed on beam-dump concerning beam dynamics, safety and thermo-mechanical aspects. New experimental areas using stable beams and the cave dedicated to radioactive ion production will be presented according the scientific program.

INTRODUCTION

The construction phase of SPIRAL2 is already launched within a consortium formed by CNRS, CEA and the region of Basse-Normandie in collaboration with French, European and international institutions [1, 2]. The facility will deliver high intensity rare isotope beams for fundamental research in nuclear physics, high intensity stable heavy ions beams, and high neutron flux for multidisciplinary applications. SPIRAL 2 will give access to a wide range of experiments on exotic nuclei, which have been impossible up to now. In particular, it will provide intense beams of neutron-rich exotic nuclei (10^6 – 10^{10} pps) created by the ISOL production method. The extracted ion beams will subsequently be accelerated to higher energies (up to 20 MeV/nucleon) by the existing CIME cyclotron, typically 6–7 MeV/nucleon for fission fragments. A low energy branch will be built to transport the beam to the DESIR hall. High intensity stable isotope beams and high power fast neutrons are other major goals of the facility. After two years of preliminary study, and following the decision to launch the construction phase, a complete design of the driver accelerator is presently under way [3]. This paper describes the studies performed on the high energy beam transport lines which deliver stable beams to experimental areas, radioactive production cave and beam dump.

GENERAL LAYOUT OF THE DRIVER ACCELERATOR

The driver accelerator delivers CW beams of deuterons (40 MeV, 5 mA) and heavy ions ($q/A=1/3$, 15 MeV/A, 1 mA). The injector is composed of two ion sources

[#]perrot@ipno.in2p3.fr

(deuterons and heavy ions) and a common RFQ cavity (88 MHz) [4]. The superconducting LINAC is composed of two sections of quarter-wave resonators (QWR), beta 0.07 and 0.12 at the frequency of 88 MHz, with room temperature focusing devices [5, 6]. After the LINAC, ions are transported using various high energy beam transport (HEBT) lines according to experimental programs. Beams can be transported to the beam-dump, to experimental areas like the Neutrons For Science (NFS) area, the Super Separator Spectrometer (S3) or to the converter of the radioactive ions production area.

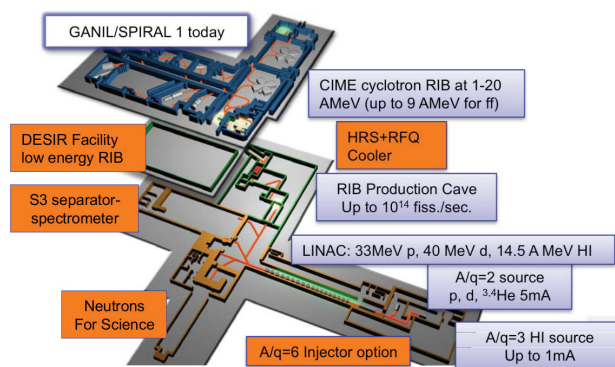


Figure 1: General scheme of the SPIRAL2 facility.

It must be noticed that in a second phase of SPIRAL2, a heavy ion source with $q/A=1/6$ will be built with its associated injector. The LINAC will accelerate these ions up to 8.5 MeV/u. This point must be taken into account for the design of the HEBT lines.

SPIRAL2 HEBT LINES

This paper will only focus on the beam transport description after the superconducting LINAC. In a first subsection we will give a compilation of the beam characteristics at the LINAC exit. In a second subsection, we will give the structure of the HEBT.

The well known TRACEWIN code is used for all beam dynamics calculations [7].

Beams Characteristics after the LINAC

From TRACEWIN, we extract transverse and longitudinal beam characteristics for all species after the LINAC. They are used as inputs for HEBT lines calculations. As an example, we give here a compilation for deuterons at minimum and maximum available energies (cf. Tab. 1).

Table 1: Beam Specifications at the LINAC Exit for Deuteron Beams

Deuterons	E=40 MeV	E=4 MeV
X-X'	$E_{\text{norm}}=0.1797$	$E_{\text{norm}}=0.1733$
	π .mm.mrad	π .mm.mrad
	Beta=1.0691	Beta=1.1194
	mm/ π .mrad	mm/ π .mrad
	Alpha=-0.0729	Alpha=-0.105
Y-Y'	$E_{\text{norm}}=0.2090$	$E_{\text{norm}}=0.1783$
	π .mm.mrad	π .mm.mrad
	Beta=2.5362	Beta=3.6565
	mm/ π .mrad	mm/ π .mrad
	Alpha=-1.1941	Alpha=-1.5975
Z-Z'	$E_{\text{norm}}=0.3301$	$E_{\text{norm}}=0.4415$
	π .mm.mrad	π .mm.mrad
	Beta=7.0461	Beta=30.3660
	mm/ π .mrad	mm/ π .mrad
	Alpha=-0.1228	Alpha=-0.5693
	rms Phase=-1.74 ° rms E=0.04 MeV	rms Phase=-22.6 ° rms E=0.005 MeV

HEBT Structure

Since the preliminary design study phase, various designs have been studied, according to the evolution of physics requirements. In addition, a lot of parameters have to be taken into account: beam dynamics of various ion species at various energies, measurements (beam profiles, position, energy, phase, emittance, current, power loss) using different techniques, quadrupoles, dipoles, and steerers sizes and locations, valves, vacuum pumps. Transport lines cost and building implantation are also some crucial aspects. Finally, a major pressure on the HEBT design is the safety and radioprotection.

Present design takes into account most of these previous listed parameters (cf. Fig. 2).

HEBT lines are designed with a limited number of repeated structures. The basic idea for this type of structure is taken from the existing “arête de poisson” at GANIL:

- matching sections composed of 4 quadrupoles are used at the LINAC exit, for the beam dump, and at the entrance of each experimental room;
- triplet or sextuplet sections are used for transport, with repetitive transverse waists and periodic envelopes;
- achromatic double deviations are used for beam distribution and protection of targets against energy fluctuations.

The HEBT beam dynamics scheme is such that we have always the same radial envelopes, up to an homothetic, according to the type of beam and the final energy.

For the beam transport in the transverse plane, the most important is to properly match the beam with the first section at 4 quadrupoles (cf. Fig. 3). Quadrupoles adjustment is obtained with 3 diagnostics at equal

distances. Same beam size for the two extreme diagnostics (D1 and D3) is required; a central diagnostics (D2) will tune a beam waist with RMS size in both planes verifying relation:

$$Size_{x,y} = \sqrt{\frac{L \epsilon_n}{3 \beta \gamma}} \quad (1)$$

where L is the distance between 2 consecutives diagnostics (L=1863 mm), ϵ_n is the normalized transverse emittance in x and y and β , γ the particle speed and the Lorentz factor. RMS beam size values at the waist diagnostic are from 1.0 mm up to 2.1 mm.

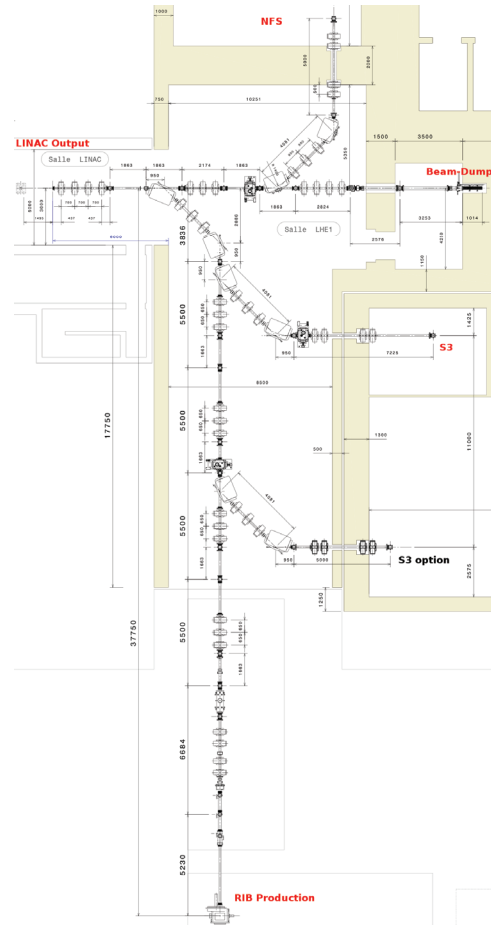


Figure 2: Detailed HEBT lines of SPIRAL2.

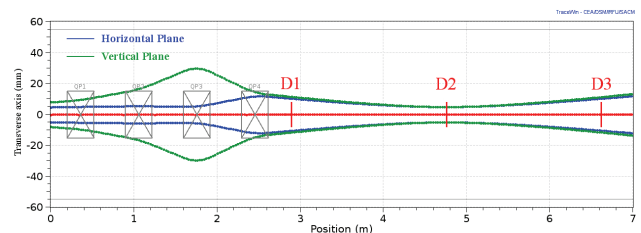


Figure 3: Transverse beam envelopes at 5 RMS for deuterons at 40 MeV in the matching section following the LINAC.

Applications and Ancillary Systems

An important feature will be the measurement precision and reproducibility provided by secondary emission profilers at low intensity. The impact of this type of errors on HEBT lines is presently under study.

Other repeated sections (triplet, sextuplet and deviation sections) are tuned using a magnetic rigidity scale.

Components in connection with the beam dynamics can be summarized:

- 44 quadrupoles with internal diameter 120 mm, $L_m=120$ mm;
- 2 rectangular dipoles at 45° with $\rho=1.4$ m, gap=100 mm;
- 4 rectangular dipoles at 45° with $\rho=1.5$ m, gap=100 mm;
- 2 SC cavities ($\beta=0.07$) used to provide very short bunch time lengths required by NFS and S3;
- 14 steerers (both transverse planes), one per section;
- 27 EMS profilers;
- energy measurement (using diamond detector and/or time of flight method) ;
- phase measurement;
- few beam position monitors, beam loss monitors;
- intensity measurements using ACCT, DCCT.

We can now present beam characteristics requirements for the heavy ions experimental areas, beam dump and radioactive ions production area.

RIB PRODUCTION

As we have already seen, the SPIRAL 2 facility will deliver a high intensity, 40 MeV deuteron beam as well as a variety of heavy-ion beams with mass over charge ratio equal to 3 and energy up to 14.5 MeV/n. Using a carbon converter, fast neutrons from the breakup of the 5 mA of deuterons impinging on a uranium carbide target will induce a rate of up to 10^{14} fissions/s. The RIB intensities in the mass range from $A=60$ to $A=140$ will be of the order of 10^6 to 10^{11} part./s surpassing by one or two orders of magnitude any existing facilities in the world [8]. A direct irradiation of the UC2 target with beams of deuterons, $^3,4\text{He}$, $^6,7\text{Li}$, or ^{12}C may also be used if higher excitation energy leads to a higher production rate for a nucleus of interest.

SPIRAL 2 would allow to perform experiments on a wide range of neutron- and proton-rich nuclei far from the line of stability (cf. Fig 4) using different production mechanisms and techniques to create the beams.

According to the technical risk for the project to start with a 200 kW deuterons beam on the converter, it has been decided to increase the beam current progressively. That is why, in a first step of operation, beam power will be limited at 50 kW. Objectives are in particular the validation of the carbon converter, target system, safety.

In addition, for thermo-mechanical constraints, the converter at 50 kW must be representative to the conditions at 200 kW. It is only in a second step that the beam power will increase until the 200 kW nominal value.

In this context, considering a Gaussian beam in X and Y directions, the maximum beam power for 50 kW at the center must be identical to 200 kW. For the full beam power, size at ± 3 RMS will be 40 mm. Therefore, the beam size for 50 kW will be 10 mm at ± 3 RMS.

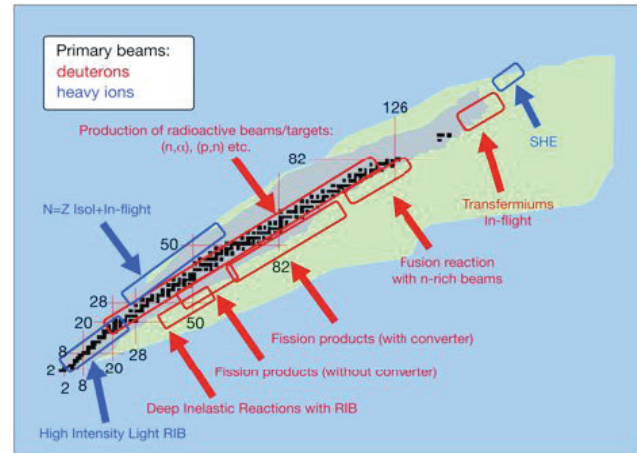


Figure 4: Regions of the chart of nuclei accessible for research on nuclei far from stability at SPIRAL2.

From the HEBT lines point of view, the major constraint comes from the Deuterons beam at 40 MeV and 5 mA current (cf. Fig. 5).

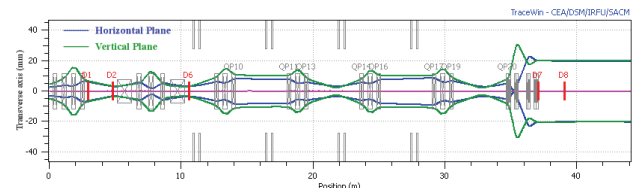


Figure 5: Transverse beam envelopes at ± 3 RMS for deuterons beam at 40 MeV, 5 mA from LINAC exit up to RIB production target.

Careful studies are in progress to choose the most appropriate method to match the beam on the converter. It must also demonstrate the absolute reproducibility of the quadrupoles matching for safety reasons.

BEAM-DUMP

The LINAC Beam dump (BD) is dedicated to the commissioning of the facility. It will be used during the beam tuning, for beam control and qualifications. Beam dump must be able to accept 200 kW beam power (40 MeV, 5 mA Deuterons) on the thermo-mechanical point of view. To restrict BD activation, beam power actual limit is 10 kW during 1 hour per day in normal operation.

The SPIRAL2 beam dump is located at 21 m in the straight line of the LINAC (cf. Fig 2). BD entrance is located 6 m from the last quadrupole which is imposed by a dedicated room. An optimized beam-dump geometry profile has been defined: 20 copper blocs of 50 mm long and 130 mm external diameter. Each bloc is drilling with internal cone shape to accept 10 kW beam power in

normal operation (cf. Fig. 6). From this basic structure, some improvements have been done.

Transverse beam characteristics at BD entrance must be independent of the species and their energy. Using last 4th quadrupoles, we match the beam to obtain transverse beam distributions at the BD entrance around 14 mm and 2.5 mrad RMS. For this condition, no deposited beam power is observed before the beam-dump.

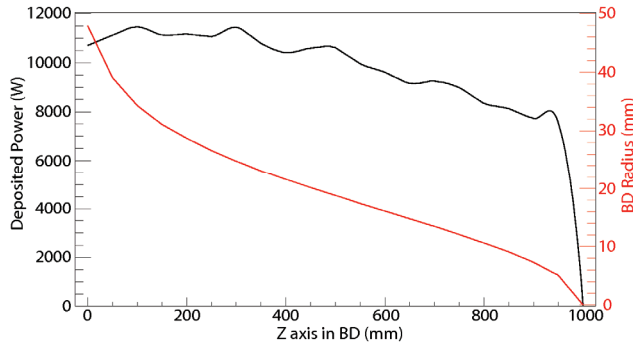


Figure 6: Beam-dump profile and deposited power for initial 200 kW beam power.

NEUTRONS FOR SCIENCE

The deuteron and proton beams delivered by the SPIRAL2 LINAC are particularly well suited to produce high energy neutrons in the 1 MeV – 40 MeV energy range. The NFS area will be composed of mainly two rooms: a converter room where neutrons are produced by the interaction of deuteron or proton beams with thick or thin converters, and an experimental hall with a well collimated pulsed neutron beam. A white neutron source from 1 up to 40 MeV energy range and quasi mono-energetic neutron beam will be available. This facility is of first importance for academic research and applied physics. Several research areas will be covered by NFS, such as the study of the fission process, the transmutation of nuclear waste, the design of future fission and fusion reactors, the nuclear medicine or the test and development of new detectors, etc. In addition, cross-section measurements of neutron- and deuteron- induced reactions could be realized by activation technique in a dedicated irradiation station [9]. This experimental area will be also used to study materials under irradiation (dpa, neutron damage) in atomics physics fields.

As we can see only light particles beam will concern NFS area: deuterons, protons, helium. For safety reason, maximum current will be limited to 50 μ A for D-beam at 40 MeV. Neutrons ToF experiments impose a fast chopper able to select 1/100 beam pulse. The fast chopper is under study, and will take place in the Medium Energy Beam Transport (MEBT) line of SPIRAL2. Beam sizes on targets or converters are 4 mm RMS in X and Y with a variable focal point. Neutrons ToF experiments require a short time pulse length ($\Delta T \sim 1$ ns at ± 3 RMS) which is almost realized using a $\beta=0.07$ cavity place before the achromatic deviation along the HEBT line (cf. Fig. 7).

Applications and Ancillary Systems

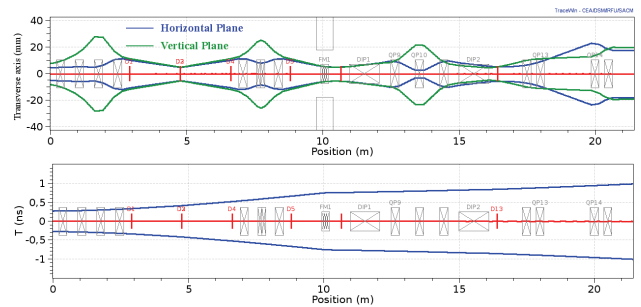


Figure 7: Transverses and longitudinal beam envelopes at ± 5 RMS for Deuterons beam at 40 MeV, 5 mA from LINAC exit up to NFS area.

Additional studies have been done on the dynamic of the primary beam (slow down in the converter, deviation using a dipole and stop with a dedicated system). Complementary calculations will be done to take into account all the processes in the NFS target area.

SUPER SEPARATOR SPECTROMETER

S3 is a device designed for experiments using the very high intensity stable beams of LINAC. These beams, which will be provided in a first phase of SPIRAL2 ions with $A/q=3$ (and in a 2nd step $A/Q=6$), can reach intensities exceeding 100 μ A for light ions ($A < 40-50$). These unprecedented intensities open new opportunities in several physics domains, e.g. super-heavy and very-heavy nuclei, spectroscopy at and beyond the dripline, isomers and ground state properties, multi-nucleon transfer and deep-inelastic reactions. All of the experiments have the common feature of requiring the separation of very rare events from intense backgrounds. S3 will have a large acceptance and clearly must have excellent primary beam suppression.

Primary beam requirements on target are:

- 0.2 ns time pulse length at ± 3 RMS (in a second phase of operation). This feature imposes to use a $b=0.07$ cavity placed after the deviation (cf. Fig. 2);
- $\Delta E/E < 0.5\%$ at ± 3 RMS. This feature will be almost fixed by the LINAC characteristics;
- transverse flat beam, ± 1 mm in X, ± 10 mm in Y.

Transverse beam requirements have been carefully studied. First of all, it is theoretically possible to use some sextupoles [11, 12]. But beam sizes are too small to obtain a stable solution. Otherwise, the variety of beams and energies would impose to have a large set of values for the sextupole tuning. In complement, real transverse distributions present large peak power densities at the extreme positions, and distributions are largely sensitive to the beam position in the line. This solution was eliminated. According to Shafer remarks [13], we proposed to use also a beam raster magnet only in the vertical plane placed after the last quadrupole of the matching line and at a distance of 2.7 m before the S3 target. Beam spot with 2 mm at 3 RMS in X and Y direction can be provided. In this configuration, the field gradient in the raster magnet with a magnetic length of

0.2 m will be less than 500 G, fixed by the heavy ions with $A/q=6$ at 8.5 MeV/u. It can be noticed that the beam will have an oscillation angle on the target of less than ± 4 mrad.

Beam dynamics studies have been done (cf. Fig 8). Impacts on the S3 rotating target and beam dynamic in S3 are not yet available. Technical design for the beam raster magnet is also under study.

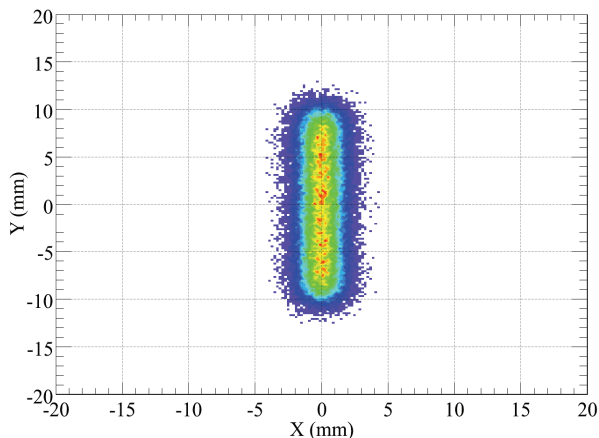


Figure 8: Integrated beam spot at the S3 target position for heavy ions with $A/q=3$ to all energies.

CONCLUSION

In this paper, we introduced the status of the High Energy Beam Transport Lines of the SPIRAL2 facility in connection with target location of the experimental areas NFS and S3. The beam dump has been also presented. RIB production line beam optics has been described. In each case, careful attention is taken to provide the beam characteristics required by each line end.

Various beam dynamics studies have been done in connection with safety aspects. The project objective in this field is to have less than 1 W/m beam power loss.

Up to now, new precise error calculations of the whole machine must be done [14].

Precise mechanical design of the HEBT lines will be available until the end of 2009 which will coincide with the permission for construction grant. First beams will be produced at the beginning of 2012 for stable beams and experimental areas (NFS or S3). RIB production will start for physics experiments at the end of 2013.

REFERENCES

- [1] T. Junquera et al., "Superconducting Driver Linac for the New Spiral 2 Radioactive Ion Beam Facility GANIL".
- [2] The SPIRAL2 Project Reports 2005-2006 <http://www.ganil.fr/research/developments/spiral2>.
- [3] T. Junquera, "Status of the Construction of the SPIRAL2 Accelerator at GANIL", TU102, LINAC 2008, Vancouver, Canada.
- [4] R. Ferdinand, "SPIRAL2 RFQ Prototype – First Results", MOPCH103, EPAC06, Edinburgh, Scotland.
- [5] G. Devanz et al., "Status of the Low Beta Cryomodules For The SPIRAL2 LINAC", THP007, LINAC 2008, Vancouver, Canada.
- [6] Saugnac et al., "RF and Cryogenic Tests fo the First Beta 0.12 SPIRAL2 Cryomodule", THP009, LINAC 2008, Vancouver, Canada.
- [7] <http://irfu.cea.fr/Sacm/logiciels/>
- [8] M-G Saint-Laurent on behalf of the Spiral2 project group, "Future opportunities with Spiral2 at GANIL", AccApp07, Pocatello, Idaho, July 30-August 2nd, 2007.
- [9] X. Ledoux on behalf of the NFS Collaboration, "Status Report of the NFS collaboration", 2008, December.
- [10] H. Savajols on behalf of the S3 Collaboration, "Technical Proposal for the Spiral2 Instrumentation: S3 Spectrometer", 2008, December.
- [11] N. Tsoupas et al., "Uniform Particle Beam Distributions Produced by Octupole Focusing", Nuclear Science and Engineering, 126, 71-79 (1997)
- [12] A. J. Jason et al., "Uniform Ribbon-Beam Generation for Accelerator Production of Tritium", M02-58, LINAC88, Cebaf, USA
- [13] R. E. Shafer, "Comment on Uniformization of the transverse beam profile by means of nonlinear focusing method", Phys. Rev. Spe. Topics – Acc. & Beams, 11, 039001, 2008.
- [14] R. Duperrier, D. Uriot, "Application of the extreme value theory to beam loss estimates in the SPIRAL2 linac based on large scale Monte Carlo computations", Phys. Rev. ST Accel. Beams 9, 044202 (2006).

DEVELOPMENT OF RASTER SCANNING SYSTEM AT NIRS-HIMAC

T. Furukawa[#], T. Inaniwa, S. Sato, N. Saotome, S. Fukuda, T. Shirai, Y. Takei, Y. Iwata, A. Nagano, S. Mori, S. Minohara, T. Murakami, E. Takada and K. Noda
 National Institute of Radiological Sciences, Chiba, JAPAN
 Y. Iseki, K. Hanawa, N. Kakutani, C. Yamazaki, Y. Kanai
 Toshiba, Tokyo, JAPAN
 H. Izumiya and Y. Sano
 Accelerator Engineering Corp., Chiba, JAPAN

Abstract

A new treatment facility project, as an extension of the existing HIMAC facility, has been initiated for the further development of carbon-ion therapy in NIRS. This new treatment facility will be equipped with a 3D irradiation system with pencil beam scanning. The challenge of this project is to realize treatment of a moving target by scanning irradiation. To accomplish practical moving target irradiation and to fix the final design, a prototype of the scanning irradiation system was constructed and installed into existing HIMAC experiment course. The system and the status of the beam test are described.

INTRODUCTION

Heavy-ion beams have attracted growing interest for cancer treatment due to their high dose localization and high biological effect at the Bragg peak. To make optimal use of these characteristics and achieve accurate treatment, 3D pencil beam scanning [1-3] is one of sophisticated techniques, and it has already been utilized for treatment at the PSI [2] and GSI [3]. At HIMAC, a project [4] to construct a new treatment facility was initiated for implementation of this irradiation technique. The challenge of this project is to realize treatment of a moving target by scanning irradiation, because pencil beam scanning is more sensitive to organ motions compared with the conventional broad-beam irradiation. Design study of the scanning system had been started in 2006. One of the most important features of the system is fast scanning to realize moving target irradiation with a relatively large number of rescanning within an acceptable irradiation time. As a result of the conceptual design study [5], we decided to employ the hybrid raster scanning method similar to GSI [3] considering the beam characteristics of the HIMAC synchrotron [6]. Further, we found that the specification of the raster scanning system strongly depends on the specifications of following components: 1) fast scanning magnet and its power supply, 2) high-speed control system and 3) beam monitoring. Thus, we focused on the detailed design and the fabrication of these components. The prototype of the scanning system was constructed and installed in physics experiment course (PH1) of HIMAC in Dec. 2008. Fig. 1 shows the photograph of the prototype.

On the other hand, following developments are carried

out toward fast scanning: 1) Treatment planning for fast scanning and 2) modification of synchrotron control. The technical details of them are referred to [7, 8] and [9]. Our goal is to achieve the irradiation time of moving target to be less than few minutes for 10 times rescanning with gating.

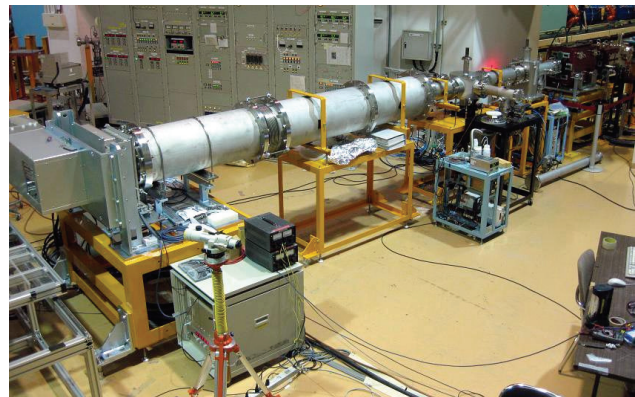


Figure 1: Photograph of the prototype of the raster scanning system.

PROTOTYPE OF SCANNING SYSTEM

Layout of Devices

The raster scanning irradiation system is around 9 m long between the last quadrupole magnet and the iso-center. The distances from both scanning magnets to the iso-center are set to 8.4 and 7.6 m, respectively. After the vacuum window located 1.3 m upstream of the iso-center, flux monitors, a position monitor, a ridge filter, and a range shifter are placed. Details of these components are described below.

Fast Scanning Magnet and its Power Supply

Specifications of the scanning magnets and their power supply are summarized in Table 1. The gap of the magnets and the good field region are defined based on the beam envelope calculation. The maximum magnetic field of both magnets is designed to be less than 0.3 T to decrease the eddy current and the iron losses. In addition, the silicon-steel lamination thickness of 0.35 mm was employed. Vacuum ducts in the scanning magnets are made of 4 mm-thick FRP to suppress the eddy current due to the ramping magnetic field. Consequently, the fast scanning velocity more than 100 mm/ms is realized.

[#] t_furu@nirs.go.jp

In order to check the eddy current effect especially for the magnet edge, measurement of the temperature rise was carried out. Fig. 2 shows the pictures of the horizontal and vertical scanning magnets before the installation and the typical result of the temperature rise measurement for the horizontal scanning magnet. The temperature rise was not severe, even when operating at the maximum field and repetition rate.

Table 1: Specifications of Scanning Magnets and their Power Supply

	unit	SMx	SMy
Deflection angle	mrad	± 18	± 21
Magnet gap width	mm	40	82
Effective length	mm	393.6	681.2
Pole length	mm	360	618
Pole width	mm	90	140
Max. field strength	T	0.286	0.190
Num. of coil-turns	turns/pole	12	15
Coil resistance	m Ω	5.6	10.3
Coil inductance	mH	0.94	2.02
Weight	kg	290	730
Max. current	A	± 410	± 440
Max. voltage	V	420	460
Scan speed	mm/ms	> 100	> 50

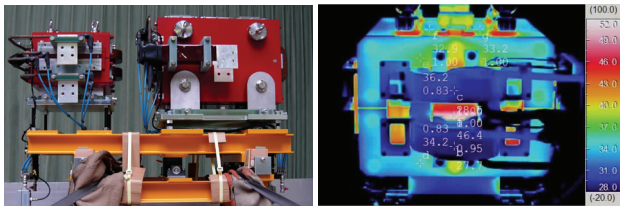


Figure 2: Pictures of the scanning magnets and the result of the temperature-rise measurement.

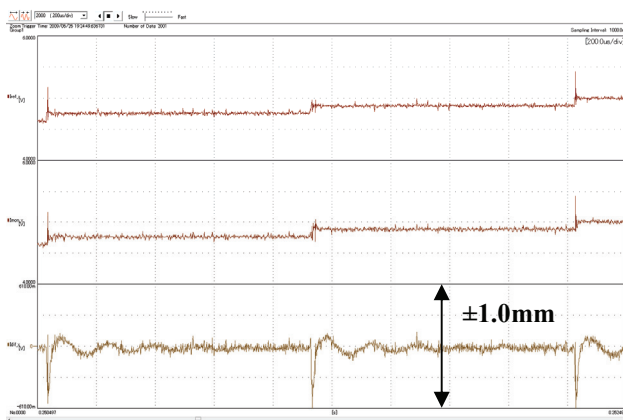


Figure 3: Oscilloscope display in the power supply test. From the upper trace, the reference current, the measured current and the measured deviation. Time scale is 200 μ s/division.

In the power supply, IGBT units and FET units are employed, and separated functionally. The IGBT units are

used to change the current fast, and the FET units are used to keep the current constant with the PID feedback control. The fast control of the IGBT units is the most crucial issue of this power supply. The switching timing precision of around 300 ns is necessary to suppress over/under shoot. As shown in Fig. 3, the overshoot is successfully suppressed within 0.5 A corresponding to the beam-position shift of 0.2 mm. Consequently, FET units can control such over/under shoot within 100 μ s.

Beam Monitors

The beam monitoring is one of the most important components in the scanning delivery. In order to measure and control the dose of each spot, two flux monitors (principal and subordinate) and a beam position monitor will be placed. However, a sub flux monitor and the position monitor are not yet installed in this stage, and will be installed soon. The flux monitors are parallel-plate ionization chambers with an effective area of 240 mm². The beam position and profile are measured with a multi wire proportional counter (MWPC), which will be set just after the main and sub monitors. While the MWPC needs to have controlled gas flow, the flux monitor operates in air. The flux monitor consists of a signal foil, two HV foils and two grounded shielding foils. Each foil is made of 50 μ m-thick polyimide coated by Cu, Ni and Au. The gap between signal and HV foils is 4 mm on both sides of the signal foil. The output current from the flux monitor is digitized by the current-frequency converter having maximum frequency of 2 MHz.

Mini Ridge Filter and Range Shifter

The Bragg peak of the pristine beam is slightly broadened to produce a “mini peak” by using a mini ridge filter (RGF). The shape of bar ridge is designed to make Gaussian shaped mini peak of 3 mm width at 1-sigma. The RGF consists of 160 bar ridges made of aluminium, and has an effective area of 240 mm². The distance between the RGF and the iso-center is set to be 1 m. Considering the RGF structure blurring [10] and the alignment accuracy of bar ridges, each bar ridge has the aluminium base plate of 1 mm thickness.

The range shifter (RSF) is used to precisely change the range slice-by-slice in the target. In order to reduce the beam size expansion by multiple scattering, the RSF is located close to the iso-center. The entrance and exit of RSF are 0.9 and 0.6 m upstream of the iso-center, respectively. This binary type RSF consists of ten acrylic plates. Each plate has the thickness of 0.2 ~ 102.4 mm with an effective area of 240 mm². By using the compressed-air cylinder, it takes around 300 ms to move/remove each plate.

Control System for Scanning Delivery

The scanning beam delivery is realized by the specific controllers that consist of the high-speed control part (order of few hundred ns) and the low-speed control part (order of few ms). The high-speed part consists of the FPGA and memory modules, on the VME board, and

controls the irradiation dose and the position of each spot. Concerning reliability of the system, the CPU on the VME is only used to download the scanning steering data to the memory modules, and not used to control the scanning delivery. Since the memory modules need to memorize the steering data including the rescannings, each memory module has the memory area for 22M spots. The steering data are delivered through the gigabit network. On the other hand, the low-speed part consists of the programmable logic controllers (PLC) and their I/O modules. This part controls and monitors the components having slow response, such as the RSF, the HV, and the monitor gas.

BEAM TEST

Commissioning of the prototype started in December 2008. Cooperating with highly stabilized beam provided by HIMAC, the commissioning is successfully in progress. Since the measured beam property is employed in the treatment planning calculation [7, 8], firstly, pencil beam measurement was carried out by using a cylinder type water column with ionization chambers. The cylinder type water column is a sealed tank of the water for the depth dose curve measurement. The detectors are the large area parallel plate ionization chamber and the 94 channel cross-shaped monitor, not only for the integral depth dose curve measurement, but also for the lateral dose distribution. Both detectors are set in the same case made of aluminum having the grounded shielding window. Fig. 4 shows the typical result of pencil beam measurement and its modelling.

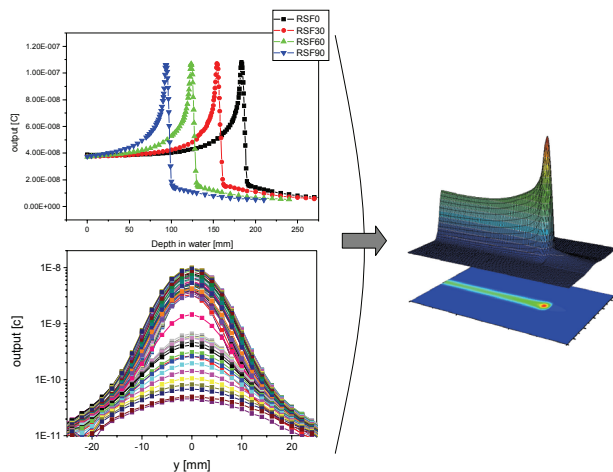


Figure 4: Typical result of pencil beam measurement and its modelling for dose calculation in the treatment planning.

A fluorescent screen with CCD camera [11] is a very useful tool for 2D measurement in the scanning delivery verification. By applying calibration using the film measurement, it was possible to remove artefacts from 2-D images caused by variations in the pixel-to-pixel sensitivity of the detector or screen and by distortions in the optical path between the screen and the detector. We

Applications and Ancillary Systems

employ this device for 1) calibration of the scanning magnet deflection, 2) observation of beam symmetric property and 3) check of lateral uniformity of delivered field. Fig. 5 shows typical results of 1) and 3).

For the verification of 3D delivery, the box shaped target of $60 \times 60 \times 60 \text{ mm}^3$ was planned to generate uniform physical dose field of 1 Gy. As shown in Fig. 6, the dose distributions measured by ionization chamber were in good agreement with the planned one at various penetration depths.

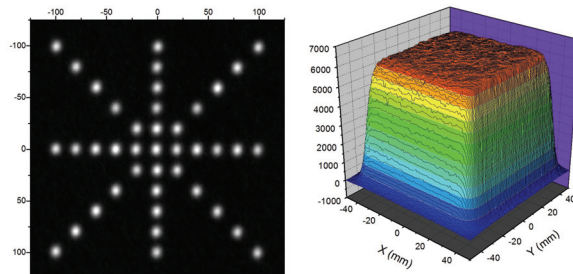


Figure 5: Measured images by the fluorescent screen system.

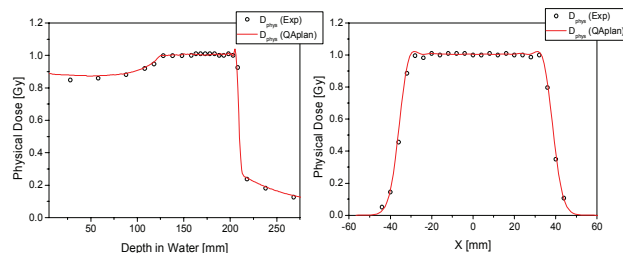


Figure 6: Comparison between measured (open circle) and planned (line) dose distribution.

SUMMARY

The beam tests of the scanning prototype for the HIMAC new treatment facility are well underway. Until end of 2009, the beam test will be continued including the moving phantom irradiation. After the small modification, this prototype will be installed in the new facility.

ACKNOWLEDGEMENTS

We would like to express our thanks to members of Accelerator Engineering Corporation for their skilful operation of the HIMAC accelerator complex. We would also like to express our thanks to other members of Department of Accelerator and Medical Physics at NIRS for useful discussion. This work was carried out as a part of Research Project with Heavy Ions at NIRS-HIMAC.

REFERENCES

- [1] T. Kanai et al, Nucl. Instr. Meth. 214 (1983) 491.
- [2] E. Pedroni et al, Med. Phys. 22 (1995) 37.
- [3] Th. Haberer et al, Nucl. Instr. Meth. A 330 (1993) 296.
- [4] K. Noda et al, Proc. of EPAC 2008, 1818.

- [5] T. Furukawa et al, Med. Phys. 34 (2007) 1085. [9] Y. Iwata et al, Proc. of EPAC 2008, 1800.
- [6] T. Furukawa et al, Nucl. Instr. Meth. A560 (2006) 191. [10] U. Weber, G. Kraft, Phys. Med. Biol. 44 (1999) 2765.
- [7] T. Inaniwa et al, Med. Phys. 34 (2007) 3302. [11] N. Saotome et al, Proc. of EPAC 2008, 1830.
- [8] T. Inaniwa et al, in these proceedings.

STATUS OF ELECTRON BEAM ION SOURCES FOR PARTICLE THERAPY*

G. Zschornack[†], Technische Universität Dresden, Dresden, Germany

F. Grossmann, V. P. Ovsyannikov, A. Schwan, F. Ullmann, DREEBIT GmbH, Dresden, Germany

E. Tanke, P. Urschütz, SIEMENS AG, Erlangen, Germany

Abstract

The technical performance of ion sources of the Electron Beam Ion Source (EBIS) type has substantially improved during the last years. This is demonstrated by proof-of-principle experiments which have been done using a room-temperature EBIS, a so-called Dresden EBIS-A, which has been in use for several years. A new superconducting EBIS, a so-called Dresden EBIS-SC, has been taken into operation. With the expected higher beam intensities the Dresden EBIS-SC will offer a compact and low-cost solution for applications in particle therapy and will be applicable for synchrotron based solutions (single- or multi-turn injection) as well as other accelerator schemes. It is shown that the introduction of the Dresden EBIS-SC will simplify the injection beam line of medical accelerator facilities.

INTRODUCTION

High-energy ionising radiation has proven to be effective in the treatment of cancerous tumours. In particular protons and light ions (e.g. carbon ions) have the advantage of penetrating the body easily and then depositing their energy at a depth determined by their initial energy, referred to as "Bragg peak". Additionally light ions are characterized by an increased relative biological effectiveness. Due to these advantages compared to conventional radiotherapy, hadron therapy facilities are built in an increasing number.

The use of different hadron beams needs the availability of powerful ion sources which are time-stable and provide high-quality beams of different light ions. At the moment ECR ion sources provide the particle beams for hadron therapy. Searching for alternatives, the combination of an electron beam ion source (EBIS) with an RFQ-LINAC facility has been suggested already in the middle of the 1990s [1, 2]. Moreover, recent publications discuss that the use of an EBIS can both simplify the accelerator construction, resulting in a more economical solution for medical accelerators, and provide high-quality hadron beams [3].

In the present paper we will give an overview about recent developments of the EBIS technology for applications in particle therapy. We present experimental data measured with a room-temperature EBIS of the Dresden EBIS-A type (for details see [4]) demonstrating different features which are important for the application in synchrotron based accelerator schemes. In addition, we will present a new EBIS

type, the Dresden EBIS-SC, a superconducting ion source intended to provide beams of light ions which are sufficient for the application at synchrotrons, CYCLINACs [5], and Rapid Cycling Medical Synchrotrons (RCMS) [6].

REQUIREMENTS

Injectors for synchrotron based solutions consist of a number of ion sources, the low energy transport line, a Linac and the medium energy beam transport line. In order to satisfy the requirements of a medical ion beam a set of demands have to be met. In the following a selection of important requirements is given:

- *Particle number per pulse.* Table 1 lists numbers of hydrogen and carbon ions per pulse for different accelerator types. The particle numbers demanded given by different authors differ more than one order of magnitude.
- *Ion species from the source.* The focus here is on the application of H^+ , H_2^+ , C^{4+} , and C^{6+} . In the future this will also concern ions such as helium, oxygen, and others.
- *Beam purity.* Beam impurities should not exceed 0.1 % after the mass spectrometer magnet.
- *Pulse-to-pulse current stability.* The current from the ion source has to be constant within about $\pm 2\%$ at the flat top.
- *General beam stability.* The ion source should provide stable and reproducible beams.
- *Beam emittance.* The RMS beam emittance should be $< 40 \pi$ mm mrad for the applied ion beam.

Table 1: Requirements for the Ion Output for Different Types of Medical Accelerators

Accelerator	Protons	C^{6+}	f/Hz	Ref.
Synchrotron [a] (SIEMENS)	$1 \cdot 10^{11}$	$8 \cdot 10^9$	0.1 ... 1	
Synchrotron [b] (MEDAUSTRON)	$1 \cdot 10^{10}$	$4 \cdot 10^8$	0.1 ... 1	[7]
CYCLINAC [a]	–	$\leq 10^8$	up to 400	[8]
RCMS [a]	$2 \cdot 10^9$	$3 \cdot 10^7$	30	[6]

The particle numbers are given per pulse. [a] – ion source output; [b] – at the patient.

*Work supported by the EFRE fund of the EU and by the Freistaat Sachsen (Project Nos. 12321/2000 and 12184/2000) and Siemens AG.

[†] g.zschornack@fzd.de

THE DRESDEN EBIS ION SOURCES

The basic idea of an EBIS is to generate a high-density electron beam by magnetic beam compression. The magnetic field is produced either by superconducting coils [9] or by room-temperature permanent magnet configurations [10], respectively. Incoming atoms are ionized and trapped by the electron beam and successively ionized by electron-impact ionization. The extraction of the ions is realized by switching the electric axial trap potentials asymmetrically. The time characteristics of the extracted ion pulses depends on the pulsed extraction field along the z-axis of the ion trap.



Figure 1: 3D Drawing of the Dresden EBIS-A (left) and the Dresden EBIS-SC (right). In each case the ion extraction can be seen on the right.

Three generations of high-innovative room temperature EBIS/EBIT ion sources have been developed by the collaboration of the Technische Universität Dresden and the DREEBIT GmbH since 1999 [4]. They differ in the extractable currents of highly charged ions. Fields of application are research, industrial technologies as well as medicine. A new class of high-current ion sources for particle therapy, the so-called Dresden EBIS-SC, is currently under test and the following results have been obtained so far:

- a 6 T magnetic field for electron beam compression,
- an electron beam current of 750 mA,
- extraction of first H^+ and $C^{(4,6)+}$ ion pulses.

The EBIS-SC will feature beam parameters which satisfy the requirements of medical synchrotrons [11]. This leads to a compact and low-cost solution for medical applications in particle therapy. 3D drawings of both ion sources are shown in Fig. 1.

MEASUREMENTS WITH THE DRESDEN EBIS-A

In this section we report on proof-of-principle experiments at the Dresden EBIS-A to demonstrate the general ability of EBIS sources to cope with the demands for particle therapy.

Applications and Ancillary Systems

Particle Numbers per Pulse

Table 2 lists particle numbers per pulse extracted from the Dresden EBIS-A at different operation conditions.

Table 2: Ions per Pulse Extracted from the Dresden EBIS-A. C_{trap} – Electrical Trap Capacity of the EBIS-A

Ion	Ions per pulse	percent C_{trap}
H^+	$2.1 \cdot 10^8$	42
H_2^+	$5.7 \cdot 10^7$	12
C^{4+}	$5.6 \cdot 10^7$	32
C^{6+}	$3.3 \cdot 10^7$	40

For the Dresden EBIS-SC the number of extracted ions will be increased to meet the requirements mentioned in Table 1.

Ion Species

The Dresden EBIS-A as well as the Dresden EBIS-SC can provide any required ionization stage of all relevant elements up to fully stripped ions ($q/A = 0.5$; not valid for heavy ions). For injection into a linac elements with $q/A = 0.5$ are available up to calcium.

Beam Purity

All ion production processes occur in a finite rest gas atmosphere, i.e. slight fractions of oxygen and nitrogen contribute to the q/A -ratio of fully stripped ions which cannot be distinguished by a magnetic analyzer. For direct injection of C^{6+} ions into a synchrotron it is therefore of great importance to produce C^{6+} beams which are as pure as possible. The Dresden EBIS-A has been demonstrated to limit the impurity of C^{6+} beams at a level of $< 1\%$ at standard operation conditions. Measured spectra gave the following ratios

$$\frac{N^{7+}}{C^{6+}} \approx 3 \cdot 10^{-3} \quad \text{and} \quad \frac{O^{8+}}{C^{6+}} \approx 9 \cdot 10^{-3}.$$

The higher contribution of bare oxygen ions arises from embedded oxygen in the construction materials of the source. Selection as well as preprocessing of the used construction materials should further reduce the oxygen fraction.

Pulse-to-Pulse Stability

Fig. 2 pictures the pulse-to-pulse stability of carbon ion pulses. The switching velocity of the ion trap potential (SLEW rate) was $100 \mu s$ while the ion extraction frequency was 77 Hz resulting from 12 ms ionization time and 1 ms duration for switching off of the trap potential. Fig. 2 shows that the pulses are reproducible with only small variation (typically $\Delta Q/Q \approx 1\%$). The widths of

the pulses extracted from the Dresden EBIS-A have been demonstrated to span from about $1 \mu\text{s}$ up to $60 \mu\text{s}$.

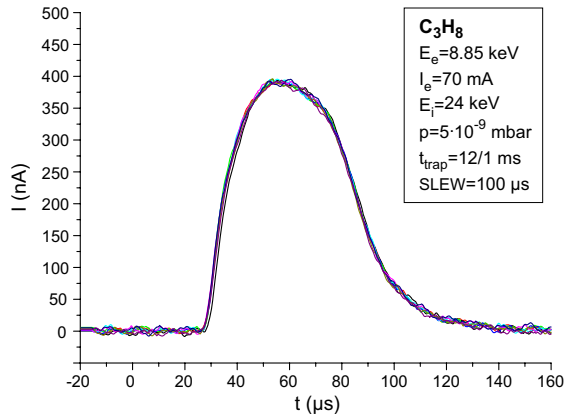


Figure 2: Pulse-to-pulse stability for C^{4+} ion pulses at a propane working gas pressure of $5 \cdot 10^{-9}$ mbar.

General Beam Stability

Fig. 3 pictures the 12 h long-term stability of a C^{4+} ion current. The measurements show that the beam current varies at most by 2% and is correlated with the change of the temperature of the source environment.

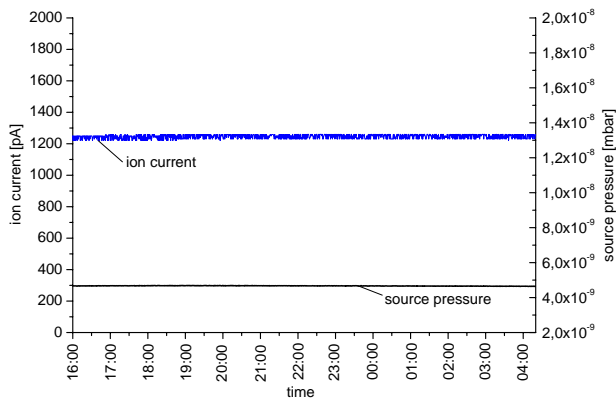


Figure 3: 12 h long-term stability of C^{4+} ion pulses from a propane working gas atmosphere. The source operation parameters are given in Fig. 2. The working gas pressure of the ion source is given supplementary (black line).

Beam Emittance

Measurements using a recently developed pepperpot emittance meter [4] have shown that the RMS emittance of the extracted carbon ion beams is in the range of 2 to 8π mm mrad. In contrast to ECR sources the distribution of the beam cross-section is homogenous and nearly circular compared to the triangular aberrations known from beams

of ECR ion sources (see for instance [12]). Fig. 4 gives an example of an x- and y-RMS-emittance of a carbon beam. The left picture shows a phase space plot of the beam parallelized by an Einzel lens while the right picture gives the beam emittances at different Einzel lens potentials.

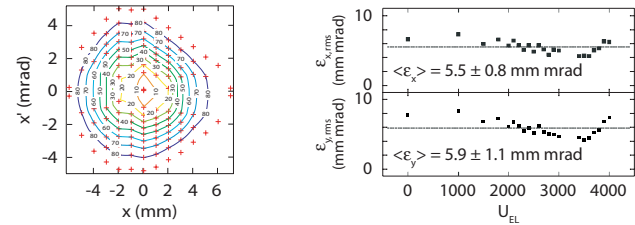


Figure 4: Emittance measurements of a carbon beam extracted from the Dresden EBIS-A. See text for explanation.

DRESDEN EBIS-SC: A NEW ION SOURCE GENERATION FOR MEDICAL PARTICLE THERAPY

The prototype of the Dresden EBIS-SC is a compact superconducting EBIS with a specially designed electron optics. The overall source length is 70 cm while the source body is based on CF350 flanges. The most important design parameters are given in table 3.

Table 3: Design Parameters of the Dresden EBIS-SC

Parameter	Value
Magnetic field	≤ 6 T
Max. electron beam current	1 A
Max. electron energy	30 keV
Eff. electron beam density	> 1000 A/cm ²
Max. electrical trap capacity	$5 \cdot 10^{10}$ e
Distance cathode-anode	variable (controllable from outside)
Trap length	20 cm
Number of drift tubes	8 (individually controlled)

The EBIS SC is designed to meet the demands for the application in particle therapy. The implementation of the Dresden EBIS-SC will allow a redesign of the injector beamline of medical accelerators in order to reduce the complexity and installation costs of the beam line. This is pictured in Fig. 5. The upper part shows the scheme of an ECR-based injection beam line. Here, the production of C^{6+} ions is usually realized by the extraction of C^{4+} ions from an ECR ion source. After following pre-acceleration, the C^{4+} ions are stripped to C^{6+} ions. The ion beam is then chopped into pulses of some tens of microseconds in order to allow multi-turn ion injection into the synchrotron. However, single pulses of C^{6+} ions and protons with appropriate particle numbers are ideal for a therapy irradiation facility.

Applications and Ancillary Systems

The middle part of Fig. 5 pictures the simplification of the injection beam line using an EBIS-SC. In principle, an EBIS-SC directly will provide sufficient and pure pulses of C^{6+} ions with variable time structures needed for single-turn and multi-turn injection, respectively. Moreover, the EBIS-SC also will provide pulses of H^+ and H_2^+ ions as well as a variety of fully stripped ions with $q/A=0.5$ in particular. This favours their application in both clinical and non-clinical research.

A next step to simplify the ion injection scheme of a synchrotron can be the application of a compact Wien filter (EBIS-SC(W); overall filter length of about 20 cm) [13] as shown in the lower part of Fig. 5. The Wien filter which is directly mounted behind the ion extraction lens system replaces the magnetic analyzer.

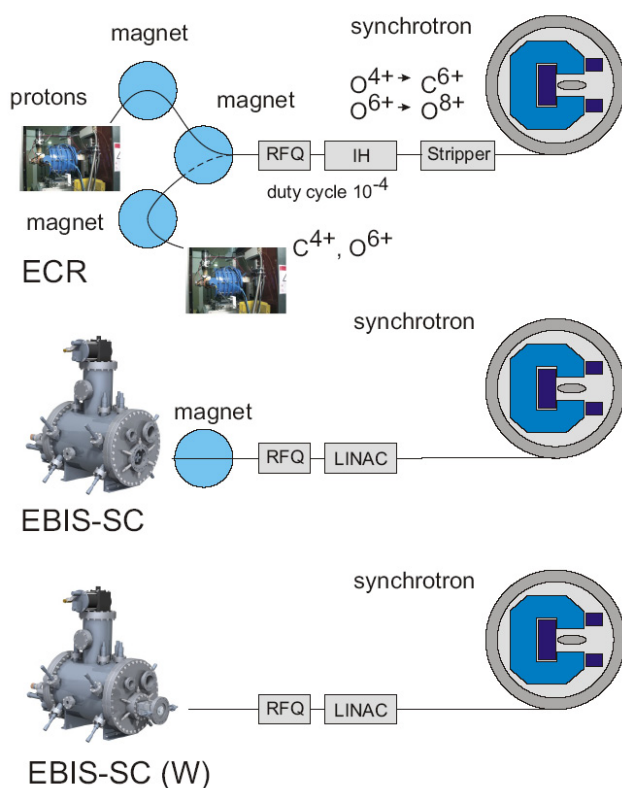


Figure 5: Possible simplification of the ion injection beam line of a synchrotron. The "classical" ion injection scheme using ECR ion sources is shown in the upper part. The injection scheme with a Dresden EBIS-SC is shown in the middle part. The application of a Dresden EBIS-SC(W) is shown in the lower part.

SUMMARY

Experiments at the Dresden EBIS-A have demonstrated that the EBIS technology will be capable of delivering ions meeting the demands of particle therapy in near future. Moreover, it has been shown that an EBIS has a variety of advantages compared to standard sources at present used for beam injection into different accelerator set-ups.

The Dresden EBIS is designed to provide sufficient ion numbers and pulse shapes that are applicable to different solutions of medical accelerator schemes. Finally, the application of an EBIS will simplify the ion injection beam line.

REFERENCES

- [1] R.Becker, M.Kleinod, A.Schempp, E.D.Donets, A.I.Pikin, Review of Scientific Instruments 63 (1992) 2812.
- [2] O.Kester, R.Becker, M.Kleinod, Review of Scientific Instruments 67 (1996) 1165.
- [3] M.Pavlovic, V.Necas, E.Griesmayer, T.Schreiner, International Review of Physics 1 (2007) 251.
- [4] <http://www.dreebit.com>
- [5] U.Amaldi, "CYCLINACS: Novel Fast-Cycling Accelerators for Hadron Therapy", Proc. of the 18th Int. Conf. on Cyclotrons and their Applications, Giardini Naxos, Italy, October 2007, p.166.
- [6] T.Satogata, E.Beebe, S.Peegs, "Ions in Rapid Cycling Medical Synchrotron", Report C-A/AP/#226, Collider-Accelerator Department, Brookhaven NL, May 2006.
- [7] T.Auberger, E.Griesmayer, "Das Projekt Medaustrom - Designstudie", 1.Aufl., fotec GmbH, Wiener Neustadt, 2004.
- [8] A.Garonna, private communication 2009.
- [9] F.J. Currell, "The Physics of Electron Beam Ion Traps", in: Trapping Highly Charged Ions, Fundamentals and Applications, ed. by J. Gillaspay, Science Publishers, Inc., Huntington and New York, 2001.
- [10] V.P. Ovsyannikov, G. Zschornack, Review of Scientific Instruments 70 (1999) 2646.
- [11] J. Debus, K.D. Gross, M. Pavlovic, "Proposal for a dedicated ion-beam facility for cancer therapy", GSI Darmstadt, DKFZ Heidelberg, University of Heidelberg, September 1998.
- [12] T.Winkelmann, R.Cee, T.Haberer, B.Naas, A.Peters, S.Scheloske, P.Spdtke, K.Tinschert, Review of Scientific Instruments 79 (2008) 02A331.
- [13] M.Schmidt, H.Peng, G.Zschornack, S.Sykora, accepted for publication in Review of Scientific Instruments (2009).

DEVELOPMENT OF TREATMENT PLANNING SOFTWARE FOR CARBON-ION SCANNING AT HIMAC

T. Inaniwa, T. Furukawa, S. Sato, S. Mori, N. Kanematsu, K. Noda,
National Institute of Radiological Sciences, Chiba, JAPAN
T. Kanai, Gunma University, Maebashi, JAPAN

Abstract

In order to use an intensity-controlled raster scan method at the new treatment facility in HIMAC, we have developed a code system dedicated to the planning of radiotherapy with the scanned ^{12}C beam. Inverse planning techniques are implemented in the software in order to obtain the uniform biological dose distribution within the planned target volume (PTV) as well as reduce the dose delivered to the organ at risks (OARs) delineated on clinical CT images. The scan trajectory is determined so that the path length will be minimized by applying a fast simulated annealing algorithm for scan trajectory optimisation. Furthermore, the extra dose inevitably delivered to the irradiated site during the beam transition time from one spot to the next spot is integrated into the inverse planning process to shorten the treatment time. The code also copes with the planning for intensity modulated ion therapy (IMIT). The reliability of the developed code has been confirmed through the irradiation experiments at the secondary beam line in HIMAC.

INTRODUCTION

A project to construct a new treatment facility as an extension of the existing Heavy-Ion Medical Accelerator in Chiba (HIMAC) facility has been initiated for further development of carbon-ion therapy at the National Institute of Radiological Sciences (NIRS). The new treatment facility will be equipped with three treatment rooms, two of them will provide the horizontal and vertical fixed beam ports, and another one a rotating gantry [1]. In all rooms, three-dimensional (3D) irradiation with pencil beam scanning will be utilized in order to make full use of the advantages of heavy-ion therapy such as high dose concentration and high relative biological effectiveness (RBE) around the Bragg peak. This method has already been implemented for clinical use at the Paul Scherrer Institute (PSI) with protons [2] and the Gesellschaft für Schwerionenforschung mbH (GSI) with carbon ions [3]. In the new facility, we intend to treat not only static tumors but also moving tumors by using gated irradiation and re-scanning methods. In order to complete the treatment irradiation within a few minutes with these methods, the fast scanning is the key in the development [4]. For this purpose, we developed an inverse planning code dedicated to radiotherapy with the scanned ^{12}C beam which suits for the unique scanning system designed at the new treatment facility in HIMAC. This paper describes the basic principles of the code.

Applications and Ancillary Systems

METHODS AND MATERIALS

Beam Model

In 3D irradiation with pencil beam scanning, the prescribed dose distribution can be achieved by superimposing the dose of the individual pencil beams d with different stopping positions according to the optimized weights w for these beams. The Bragg peak of the pristine beam is slightly broadened to produce a “mini peak” by the ridge filter, and is used as a pencil beam. In the new treatment facility, pristine beams with about 10 individual energies will be prepared between 140 MeV/u to 430 MeV/u. The dose response at a point (x_i, y_i, z_i) delivered by the pencil beam stopped at (x_0, y_0, z_0) can be represented as follows:

$$d(x_i, y_i, z_i; x_0, y_0, z_0) = d_x(x_i; x_0, \sigma_x(z_i; z_0)) d_y(y_i; y_0, \sigma_y(z_i; z_0)) d_z(z_i; z_0) \quad (1)$$

Here, $d_z(z_i; z_0)$ is the integrated dose at a depth of z_i . On the other hand, $d_x(x_i; x_0, \sigma_x(z_i; z_0))$ and $d_y(y_i; y_0, \sigma_y(z_i; z_0))$ are the normalized Gaussian functions with standard deviations $\sigma_x(z_i; z_0)$ and $\sigma_y(z_i; z_0)$ representing the beam spread at a depth z_i . The integrated dose $d_z(z_i; z_0)$ and the lateral beam spread, i.e., $\sigma_x(z_i; z_0)$ and $\sigma_y(z_i; z_0)$, were determined from the measured dose distribution with a large area parallel plate ionisation chamber and the profile monitor, respectively. Then they are fitted to simple formulae and incorporated into the planning software. With this algorithm, the effect of the beam spread due to multiple scattering in range shifter can be incorporated, at least for the primary particles. However, our recent research revealed that the field-size effect of the dose will occur also in carbon ion scanning with range shifter plates [5]. In order to account for this effect, the novel pencil beam model, in which the lateral dose distribution is represented by a superposition of three Gaussians, was incorporated into the software. The beam model can optionally be used in optimization and/or recalculation process to determine the “predicted dose scaling factor” [5].

Clinical Dose Calculation

For scanning irradiation method, we employed the same biophysical model based on the linear quadratic (LQ) model as that for the passive irradiation [6] and the layer-stacking methods [7]. When a biological system is irradiated with scanned pencil beams within a sufficiently

short period of time, the survival at point (x_i, y_i, z_i) is derived by

$$S_{mix,i} = \exp\left[-\alpha_{mix,i} D_{phys,i} - \beta_{mix,i} D_{phys,i}^2\right] \quad (2)$$

In the above equation, $D_{phys,i}$ is the physical dose at the point i delivered by the scanned pencil beams with their weights w . α_{mix} and β_{mix} are the dose averaged values of coefficients α and β in the LQ model at (x_i, y_i, z_i) [6]. The biological RBE at (x_i, y_i, z_i) can be obtained from the ratio between the doses required to obtain a desired level of cell killing, i.e. survival level S , by a reference radiation quality (Co-60) and by the carbon beam. The survival level of 10% for HSG cells is used in the biological RBE calculation independent of the dose levels. Then, the clinical RBE are derived by multiplying the clinical factor 1.43 to the biological RBE in order to account for the difference between *in vivo* and *in vitro*. Finally, the clinical dose in units of GyE at the point, $D_{biol,i}$, can be calculated by

$$D_{biol,i} = D_{phys,i} \times RBE_i(S) \quad (3)$$

Dose Optimization

The goal of dose optimisation in treatment planning software is to find the best particle numbers (weight) and positions of all rasterpoints, i.e. the best weighting matrix, so that the resulting dose distribution is as close as possible to the prescribed dose distribution within the target volume and does not exceed the dose restrictions within the OARs. In determination of the weighting matrix, the dose-based objective function $f(w)$ is minimized through an iterative optimisation process. The objective function can be described as;

$$f(w) = \sum_{i \in T} \left[Q_p^o [D_{biol,i}(w) + U_i - D_p^{\max}]_+^2 + Q_p^u [D_p^{\min} + U_i - D_{biol,i}(w)]_+^2 \right] + \sum_{i \in O} Q_o [D_{biol,i}(w) + U_i - D_o^{\max}]_+^2 \quad (4)$$

where $D_{biol,i}(w)$, D_p^{\max} , D_p^{\min} , Q_p^o , Q_p^u , D_o^{\max} , Q_o are the biological dose at a point i obtained with matrix w , the maximum and minimum doses applied to the target T , the penalties for over- and underdosage specified for the target, the maximum dose allowed for the OAR and the penalty for overdosage in OAR, respectively. In raster scanning irradiation, the beam delivery is not switched off during the transition time from one spot to the next. Therefore, in this scheme, the extra dose is inevitably delivered to the sites between two successive spots during the beam spot transition, along the scan trajectory. The contribution of extra dose is included in the optimization process by adding the term U_i to the objective function representing the amount of the extra dose delivered to a voxel i [8]. The objective function (4) is minimized by applying the iterative minimization algorithm based on

quasi-Newton method, and the best weighting matrix w can be obtained for each rasterpoint.

Flow of Treatment Planning

By using the developed software, the treatment plans are produced according to the following steps. (a) Radio-oncologists delineate the PTV and OARs on the clinical CT images using an external platform, and determine the primary treatment parameters, e.g. isocenter, desired dose level, number of ports, and beam directions. Then, these data are imported to the developed software. (b) The CT images are stored into the dose calculation region by using the tri-linear interpolation. The voxels within the PTV and OARs are identified with different flags within the dose calculation region. (c) The x-ray CT numbers stored into each voxel is converted to the effective density for therapeutic carbon beam based on the polybinary tissue model [9]. (d) The position of all rasterpoints are determined automatically from the PTV so as to account for the dose fall-off at the longitudinal and lateral edges of the PTV due to the finite size of the mini peak and beam width. (e) From the information about the maximum range found in (d), the optimum beam energy is selected among 10 individual energies prepared in the HIMAC synchrotron. (f) In order to minimize the extra dose in raster scanning and shorten the treatment time, we determined the scan trajectory on each slice so that the path length would be minimized by applying a fast simulated annealing algorithm to scan trajectory optimization. (g) The particle numbers (weight) for each raster-point are determined by the dose optimization method described in the previous section. (h) Finally, the beam steering file is produced in which the position of the raster-point x_0, y_0, z_0 , corresponding thickness of the range shifter plates, and the particle numbers (weights) of all pencil beams are written in following the order of the optimized scan trajectory.

RESULTS AND DISCUSSIONS

In order to investigate the clinical applicability of the developed software, treatment plans are produced for data of patients treated at HIMAC. We can produce both a single field plan and an IMIT plan with the software.

Single Field Planning

As an example of single field planning, a patient having bone and soft tissue sarcoma was selected (Fig. 1). The biological dose of 1.0 GyE is delivered from a single port in the anterior to posterior direction. In this plan, only the target volume is specified on the CT images and implemented for dose optimization. The maximum and minimum doses applied to the PTV is 1.0 GyE and the penalties for over- and underdosage are 6 and 8, respectively. The voxel resolution as well as the scanner step sizes, Δx and Δy , and step size of range shifter plate, Δz , were set to 2.0 mm. The beam energy determined for the plan was 350 MeV/u, and the total of 36351 rasterpoints was located within the rasterpoint

region. In Fig. 1 the planned distributions of the biological dose are shown with color-wash display on axial, sagittal and frontal CT images. We can see that highly conformal biological dose distribution can be achieved within the PTV.

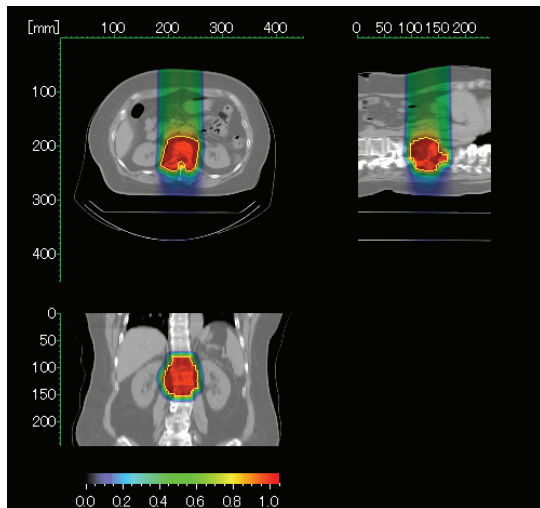


Figure 1: CT images with color-wash display of biological dose distribution. The PTV is identified with yellow curve on each CT image.

In order to verify the developed software, we carried out irradiation experiments at the secondary beam line (SBL) in HIMAC. In the experiments, a carbon pencil beam with an intensity of 6.0×10^6 particles/s was scanned in a water vessel according to the beam steering file obtained for the plan shown in Fig. 1. The physical dose distributions are measured with a beam profile monitor by moving it stepwise along the beam axis in a water vessel. In Fig. 2, the physical dose distributions measured with the monitor (open circles) are compared with the recalculated ones in water according to the derived beam steering file (red curves). Good agreement between them implies that the prescribed biological dose distribution (black curve) is also realized at the PTV.

IMIT Planning

As an example of the intensity modulated ion therapy (IMIT) planning, an RTOG benchmark phantom was selected (see Fig. 3(a)). A five equidistant, coplanar beam setup was chosen for the treatment plan. Two types of plans were generated, a plan that considers each of the five fields separately and an IMIT plan, in order to investigate the effectiveness of an IMIT. For both plans, the maximum and minimum doses to the target and the maximum dose to the OAR were 5.1, 4.9 and 2.0 GyE, respectively. In Fig. 3(b), the clinical dose distribution by a IMIT plan is shown with color-wash display. It can be seen that the OAR could be spared in each beam port. The mean dose delivered to the OAR could be reduced by a factor of three using the IMIT plan without any large deterioration in dose conformation to the PTV as compared to the single-field plan.

Applications and Ancillary Systems

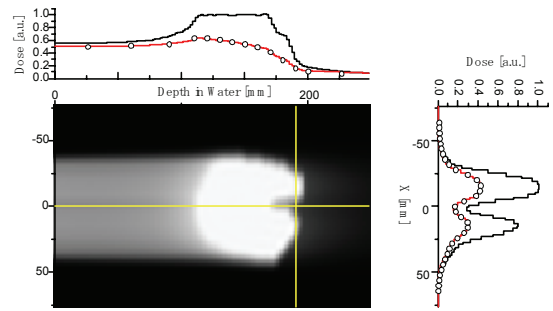


Figure 2: The physical dose distribution measured with the beam profile monitor (open circles) and the recalculated one (red curve) on the x-z plane at $y=0$ mm. In the figure, the black curve indicates the expected biological dose distribution.

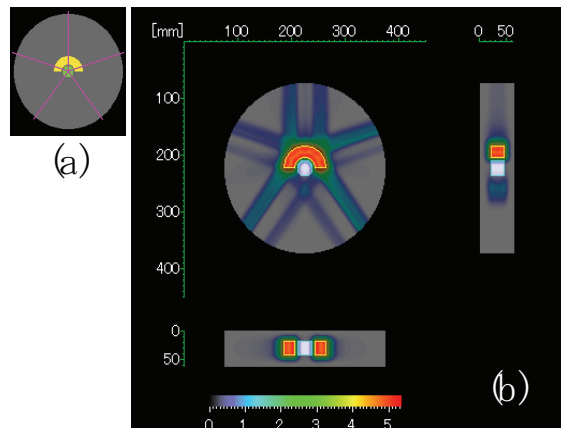


Figure 3: (a) RTOG benchmark phantom. Target and OAR are specified with yellow and green colours, respectively. (b) The color-wash display of clinical dose distribution planned with a five equidistant, coplanar beam setup using IMIT procedure.

SUMMARY

We have developed the inverse planning software for an intensity-controlled raster scan method with carbon ions, which is to be used at the new treatment facility in HIMAC. The reliability of the software was confirmed through the irradiation experiments at the SBL in HIMAC.

REFERENCES

- [1] K. Noda et al., J Radiat Res. 48 (2007) Suppl. A43.
- [2] E. Pedroni et al., Med Phys. 22 (1995) 37.
- [3] G. Kraft, Nucl Instr Meth. A 454 (2000) 1.
- [4] T. Furukawa, Med Phys. 34 (2007) 1085.
- [5] T. Inaniwa et al., Med Phys. (in press).
- [6] T. Kanai et al., Int J Rad Onc Bio Phys. 44 (1999) 201.
- [7] N. Kanematsu et al., Med Phys. 29 (2002) 2823.
- [8] T. Inaniwa et al., Med Phys. 34 (2007) 3302.
- [9] N. Kanematsu et al., Phys Med Biol. 48 (2003) 1053.

RESEARCH ON MEASUREMENT OF ^{126}Sn BY AMS*

H.-T. Shen[#], X.-G Wang, S. Jiang[†], M. He, K.-J. Dong, C.-L. Li,
G.-Z. He, S.-L. Wu, J. Gong, L.-Y. Lu, S.-Y. Wu,

Department of Nuclear Physics, China Institute of Atomic Energy, Beijing 102413, China
S.-Z. Li, D.-W. Zhang, S. Jiang, G.-Z. Shi, C.-T. Huang, College of Physical Science and
Engineering Technology, Guangxi university, Nanning, 530004

Abstract

A new method was developed for AMS measurement of ^{126}Sn . Major features of the method include the use of SnF_2 as target material, the selection of SnF_3^- molecular ions for extraction from the target, and the transmission of ^{126}Sn beam current. A sensitivity of $(1.92 \pm 1.13) \times 10^{-10}$ ($^{126}\text{Sn}/\text{Sn}$) has been reached by measuring a blank sample.

INTRODUCTION

^{126}Sn is a long-lived beta emitting radionuclide with a half-life of $(2.35 \pm 0.07) \times 10^5$ a [1]. Being a fission product, the main natural production mechanism of ^{126}Sn is through spontaneous fission of ^{238}U and the abundance ratio of the $^{126}\text{Sn}/\text{Sn}$ in the earth's crust is less than 10^{-14} [2]. Artificially produced ^{126}Sn has entered our environment through nuclear weapons testing and released from reprocessing plants and may locally lead to strongly enhanced ^{126}Sn concentrations. Although the fission yield of ^{126}Sn is lower by two orders of magnitude as compared to the well-known fission nuclides such as ^{90}Sr ($T_{1/2}=29.1\text{a}$) and ^{137}Cs ($T_{1/2}=30.2\text{a}$), the longer half-life makes it a more nasty nuclide to the environment. Therefore, ^{126}Sn is a very important nucleus to monitor the nuclear contamination and the ultra-high-sensitivity measurement of ^{126}Sn in rocks or soil samples from the fission environment would provide very important information for nuclear safety inspection. However, the concentration of ^{126}Sn in the environmental samples as well as fission products is very low (below the detection limit of the ordinary mass spectrometry) and the interferences from the molecular ions and isobar ^{126}Te are very strong. AMS technology is probably the best method for highly sensitive measurement of ^{126}Sn thanks to its many advantages [3, 4, 5, 6]. However, some difficulties, especially isobaric interference from ^{126}Te , still pose obstacles in AMS measurement of ultratrace ^{126}Sn .

The first AMS measurement of ^{126}Sn was performed at the Argonne ATLAS facility [7]. They claimed that ^{126}Te can be separated from ^{126}Sn at high energies (>400 MeV) using a gas-filled magnet and a gas ionization chamber. However, the transmission efficiency and the optical path of ^{126}Sn were derived from ^{107}Ag simulation and are not very accurate. So it does not allow absolute measurements of $^{126}\text{Sn}/\text{Sn}$. An absolute measurement of $^{126}\text{Sn}/\text{Sn}$ in samples extracted from spent fuel rods of a nuclear power

plant has been carried out by P. Gartenmann at the Zurich AMS facility [8, 9]. The terminal voltage of the tandem they used was comparatively low and the ^{126}Te background was very strong. So the results of their measurements, $^{126}\text{Sn}/\text{Sn}=(9.23 \pm 0.87) \times 10^{-6}$, have relatively large uncertainty. There were two other problems in the above AMS measurements – insufficient accuracy due to the lack of calibration standards; and insufficient sensitivity caused by strong isobaric interference from ^{126}Te introduced mainly by the extraction of Sn^- from the ion source. In this paper, a new method for AMS measurement of $^{126}\text{Sn}/\text{Sn}$ at Beijing HI-13 AMS system is presented. Major features of the method include the usage of SnF_2 target and the extraction of SnF_3^- molecular negative ions. A sensitivity of $(1.92 \pm 1.13) \times 10^{-10}$ ($^{126}\text{Sn}/\text{Sn}$) has been reached by measuring a blank sample.

MEASUREMENTS OF ^{126}Sn WITH AMS BASED ON EXTRACTION OF MOLECULAR IONS

Beam Current Extraction

The electron affinity of each element determines the negative ion yield from a sputter ion source and thus has an important role in any AMS measurements. Many elements or molecules can not form stable negative ions which is very helpful to effectively eliminate them when they are interference isobars of the nuclides of interest. There are two stable isobars for ^{126}Sn , i.e. ^{126}Te and ^{126}Xe . Inert element Xe can not form a stable negative ion, therefore, the main interference for ^{126}Sn AMS measurement is ^{126}Te . We should find an appropriate target material and extracting corresponding molecular negative ions to depress the interference of Tellurium-126 as much as possible. So far, Sn^- ion atoms were extracted from metal target in the measurement of ^{126}Sn at some world-famous AMS laboratory [7, 8]. By extracting Sn^- atom ions, large beam current (about 200 nA) of Sn^- can be obtained. At the same time, however, a considerable beam current (about 2 μA) of Te^- will bring about a very strong background for ^{126}Sn measurements. That is one of the main reasons why the sensitivities for AMS measurements of ^{126}Sn were unsatisfactory in previous studies. In this work, six kinds of molecular negative ions of Sn (Sn^- , SnC_2^- , SnO^- , SnO_2^- , SnF_3^- , SnF_5^-), and correspondingly, the same ion forms of Te (Te^- , TeC_2^- , TeO^- , TeO_2^- , TeF_3^- , TeF_5^-) were tested. the extraction of either SnF_3^- or SnC_2^- molecular negative ions might

*Supported by National Natural Science Foundation of China (10576040)

[#]E-mail: shenht@ciae.ac.cn

[†]E-mail: jiangs@ciae.ac.cn

effectively suppress the interference of Te, and the beam current of SnF_3^- is comparably larger (about 400 nA), while that of TeF_3^- is comparably weaker (<1 nA). So, the extraction of SnF_3^- from ion source is the best choice for AMS measurement of ^{126}Sn .

Background

The ^{126}Te background was measured with our AMS system by using a SnF_2 commercial blank sample. A mixture of SnF_2 and Ag powder with the mass ratio of 2:1 was pressed into aluminium cones, and then the target plate, on which all the aluminium cones were mounted, was baked at 70°C for 24 hours before it was put into the MC-SNICS (Multi-Cathode Source of Negative Ion by Cesium Sputtering) ion source. SnF_3^- negative ions were extracted from the cesium sputter source. $^{126}\text{TeF}_3^-$ ions were selected by an injection magnet and injected into the accelerator. The charge state of 11^+ was selected by analyzing magnet after ^{126}Te was stripped by a carbon foil stripper. The accelerator terminal voltage was chosen at 8.7 MV owing to the limitation of the electrostatic analyzer in our AMS system. ^{126}Te counts were recorded by a multi-anode detector filled with 105 mbar P10 gas. As shown in Fig. 1, a sensitivity of 1.92×10^{-10} can be reached, thanks to the effective suppression of ^{126}Te interference by the extraction of SnF_3^- ions. The transmission of ^{126}Te was previously simulated by the extraction and injection of $^{124}\text{SnF}_3^-$, and the acceleration of $^{124}\text{Sn}^{11+}$ ions.

The procedure of simulation transport of ^{126}Sn (^{126}Te) is expounded as follow. Firstly, the sample material of $^{124}\text{SnF}_2$ was used and $^{124}\text{SnF}_3^-$ ions were extracted from ion source to simulate $^{126}\text{Sn}^{11+}$ beam transport of sample material of $^{126}\text{SnF}_2$. In the simulation transport, the voltage of the terminal was set at 8.70 MV to make $^{124}\text{Sn}^{11+}$ ions having the same energy as that of $^{126}\text{Sn}^{11+}$ ions. The electric parameters of ions optics system were tuned for the optimum state of beam transport. Secondly, the voltage of the terminal was raised to 8.84 MV so that, $^{124}\text{Sn}^{11+}$ ions having the same momentum as that of $^{126}\text{Sn}^{11+}$ ions and the parameters of magnetic elements after analyzing magnet were further tuned for optimal statue of $^{124}\text{Sn}^{11+}$ beam transport. The transmission efficiency from low-energy side Faraday-cup to detector was measured to be about 4.0×10^{-3} for $^{124}\text{SnF}_2$ sample and $^{124}\text{Sn}^{11+}$ ions. Thirdly, the voltage of the terminal was set back to 8.7 MV and the sample material of $^{126}\text{SnF}_2$ was used and $^{126}\text{SnF}_3^-$ ions were extracted from ion source and recorded by the multi-anode detector after passing through injection magnet, accelerator, analyzing magnet, electrostatic analyzer, and a $7 \text{ mm} \times 7 \text{ mm}$ slit. $^{126}\text{Sn}/\text{Sn}$ value would be determined by alternant measurements of $^{124}\text{SnF}_2$ current at low energy side and the count rate of ^{126}Sn on the detector at high energy side. The sensitivity of $^{126}\text{Sn}/\text{Sn}$ is $(1.92 \pm 1.13) \times 10^{-10}$, given by the background from the measurement of a commercial SnO_2 sample.

Applications and Ancillary Systems

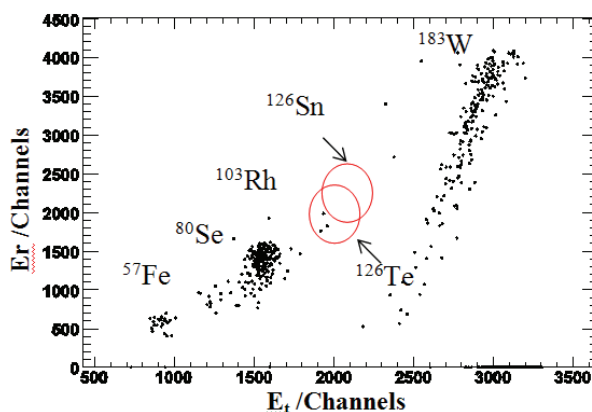


Figure 1: Two-dimensional spectra of a blank.

CONCLUSIONS AND DISCUSSION

By experiments on extracting multiform negative molecular ions, SnF_3^- was found to be the most suitable form of ions in terms of maximizing the beam current of SnF_3^- while minimizing that of TeF_3^- . In addition, SnF_2 was found to be the most suitable chemical form of target samples and the procedures for the preparation of SnF_2 was developed. Finally, the method for measuring ^{126}Sn by AMS was established, including transmission of ^{126}Sn beam current, detection of ^{126}Sn particles and the sensitivity determination by the measurement of blank sample. The sensitivity for $^{126}\text{Sn}/\text{Sn}$ was $(1.92 \pm 1.13) \times 10^{-10}$, 2-3 orders of magnitude better than those reported in previous studies on AMS measurement of ^{126}Sn [7, 8].

There are some interference peaks of different masses in the two-dimensional spectra (as can be seen from Fig. 1), because some ions with the same values of ME/q^2 and M/q as $^{126}\text{Sn}^{11+}$ can pass through the analysis magnet and the electrostatic deflector and be recorded by the multi-anode detector. Thanks to the high resolution of the detector, these peaks do not interfere with the measurement of $^{126}\text{Sn}^{11+}$ peak.

There is still room for further improvement. First of all, chemical procedures of removing Te, such as the ones reported by Catow [10] and Zhang [11], can be added into the preparation of samples. Second, special detection method, such as gas filled magnet combined with time of flight and projectile X-ray detection, can be considered. In addition, the provision of ^{126}Sn samples with high concentration will make it possible to obtain more accurate standard samples determined by TIMS or ICPMS. These and other improvements are being implemented or considered in our lab for the AMS measurement of ^{126}Sn at much lower levels.

REFERENCES

- [1] Oberli F. et al., Int. J. Mass. Spec., 184 (1999) 145.
- [2] Haas P, Gartenmann P T. Nucl. Instr. and Meth., B 114 (1996) 131.
- [3] D. Elmore, F M Phillips. Science 236 (1987) 543.
- [4] W. Wolfli, Nucl. Instr. and Meth. B 29 (1987) 1.

- [5] W. Kutschera, Nucl. Instr. and Meth. A 268 (1988) 552.
- [6] W. Kutschera et al., Nucl. Instr. and Meth. B 50 (1990) 252.
- [7] W. Kutschera and I. Ahmad, Nucl. Instr. and Meth., B. 42 (1989)101.
- [8] P. Gartenmann, R. Golser, Nucl. Instr. and Meth., B 114 (1996) 125.
- [9] P. Haas, P. Gartenmann, Nucl. Instr. and Meth., B 114 (1996) 131.
- [10] S.A. Catlow, "Half life measurement of ^{126}Sn isolated from Hanford nuclear defence waste", Fluor Hanford, Richland, WA 99352, USA.
- [11] Zhang S., "Measuremet of the thermal neutron cross sections of the reaction of $^{126}\text{Sn}(n,\gamma)^{127}\text{Sn}^g,^{127}\text{Sn}^m$ " [Doctoral Thesis], China Institute of Atomic Energy, 2004.

ACCELERATOR MASS SPECTROMETRY FOR LONG-LIVED HEAVY ION ^{236}U AT CIAE*

Wang Xianggao[†], Shen Hongtao, Jiang Shan[#], He Ming, Dong Kejun, Li Chaoli, Wang Wei,
Wu Shaoyong, Bao Yiwen, Guan Xialing, Hu Yueming, You Qubo
China Institute of Atomic Energy, Beijing 102413, China
Zhang Dawei, Shi Guozhu, Huang Chuntang
College of Physics Science and Technology, Guangxi University, Nanning 530004, China

Abstract

^{236}U is a long-lived radioactive isotope with a half-life of $2.342(3) \times 10^7$ a, which produced principally by thermal neutron capture on ^{235}U . ^{236}U is potentially applied in geological research and nuclear safeguards. Accelerator mass spectrometry (AMS) is presently the most sensitive technique for the measurement of ^{236}U . A method for AMS measurement of long-lived heavy ion ^{236}U was developed at CIAE with the set up the AMS dedicated injector and the newly proposed $^{208}\text{Pb}^{16}\text{O}_2^-$ molecular ions for the simulation of ^{236}U ion transport. A sensitivity of lower than 10^{-10} has been achieved for isotopic ratio $^{236}\text{U}/^{238}\text{U}$ in present work.

INTRODUCTION

^{236}U is a long-lived radioactive isotope with a half-life of $2.342(3) \times 10^7$ a, mainly produced by the thermal neutron induced $^{235}\text{U}(n,\gamma)^{236}\text{U}$ reaction. The isotopic ratio of $^{236}\text{U}/^{238}\text{U}$ in nature is about 10^{-14} , depending strongly on the integral thermal neutron flux received by the material. This makes ^{236}U usable as an integrating neutron monitor over the last 100 million years [1], and potentially applicable in geological research [2]. The isotopic ratio of $^{236}\text{U}/^{238}\text{U}$ could also be used as a “fingerprint” for indicating the presence of neutron-irradiated uranium usually originated from nuclear activities [3].

Recently, several efforts have been made to measure ^{236}U in environmental samples using techniques based on mass spectrometry such as high-resolution inductively coupled plasma spectrometry (HR-ICPMS), thermal ionization mass spectrometry (TIMS) and accelerator mass spectrometry (AMS). However, detection limits with conventional mass spectroscopy for $^{236}\text{U}/^{238}\text{U}$ are $\sim 10^{-10}$, leading to errors larger than 50% for uranium ore samples [4, 5]. Therefore the measurement of natural ^{236}U is difficult or even impossible without AMS. AMS offers significant advantages over conventional mass spectroscopic methods in high sensitivity, smaller sample size, relatively free from isomer and molecular-ion interferences, and shorter measurement time. AMS measurement of actinides was presented firstly by IsoTrace facility X.L. Zhao *et al.* of Toronto group [6], in which the $^{236}\text{U}/^{238}\text{U}$ is lower than 5×10^{-10} in a natural

uranium ore from Cigar Lake deposit in Canada. The natural $^{236}\text{U}/^{238}\text{U}$ has also been measured by several other groups, such as: VERA [7], ANU [8], LLNL [9], ANSTO [10], Munich [11], ETH [12] and Israel Weizmann Institute [13].

In this paper, a method for AMS measurement of long-lived heavy ion ^{236}U developed on the HI-13 Accelerator at China Institute of Atomic Energy (CIAE) is reported. The unique features include establishing of the AMS dedicated injector and the newly proposed $^{208}\text{Pb}^{16}\text{O}_2^-$ molecular ions for the simulation of ^{236}U ion transport.

THE AMS DEDICATED INJECTOR

There is a general rule in AMS that a high mass resolution analyzer is needed to separate the neighboring interference and a high energy resolution analyzer is required to clip the tail of the high energy. The original injector setup at CIAE [14] with the mass resolution of $M/\Delta M \sim 220$, could not satisfy the requirement for AMS measurement of heavy isotopes (e.g., ^{236}U , ^{182}Hf , ^{151}Sm). Therefore, a high resolution dedicated injector for AMS was developed, as shown in Fig. 1. The new injector adopts achromatic technique, which consists of a 90° electrostatic analyzer (ESA) and a 112° double-focusing analyzing magnet (MA). A triplet electric quadrupole lens and a single electric quadrupole lens were mounted at the entrance and the exit of the ESA beam line, respectively, for ions focusing. This spherical 90° ESA with 750 mm radius, has maximum electric field strength of 4 kV/cm and provides both horizontal and vertical focusing. The 112° double-focusing MA with a bending radius of 800 mm, has a maximum magnetic field of 1.3 T.

The energy resolution of the electrostatic deflector is $\frac{E}{\Delta E} = \frac{D\rho}{S_2 - MS_1}$. The Mass resolution of the analyzing

magnet is $\frac{M}{\Delta M} = \frac{D\rho}{S_2 - MS_1}$, where $D\rho$ is coefficient of

chromatic dispersion (3000 for ESA, 3360 for MA), M (-1 for ESA, -1.14 for MA) is the coefficient of magnification, S_2 and S_1 are the slits of object and image, respectively. The new injector system was tested by using the sample material of HfO_2 . When the ESA's slits (Slit 1) and MA's object slits (Slit 2) are fully open, the image point slit (Slit 3) of MA is 1 mm, the mass resolution of the injector system is about 430. If the Slit 2 and Slit 3 are respectively set at ± 2.5 mm and ± 1 mm, the

* Work supported by the NSAF (National Nature Science Foundation-China Academy of Engineering Physics Foundation) No.10576040

[†] E-mail: wangxg@ciae.ac.cn

[#] E-mail: jangs@cicae.ac.cn

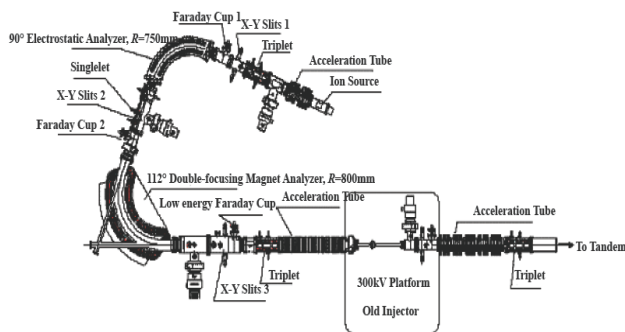


Figure 1: The Layout of the improved Injector System.

mass resolution can be increased to 630, which leads to a decrease of beam current only by 5%, compared with the beam current of slits completely opened up. If the Slit 2 and Slit 3 are respectively set at ± 1 and ± 1 mm, the mass resolution can be increased to ~ 1100 , but the beam transmission efficiency will decrease by 40%. When the Slit 1 is set at ± 5 mm, the $^{238}\text{U}^{11+}$ count rate is 10 times lower than that when the Slit 1 is fully open. The overall transmission efficiency is very low in our AMS system based on our experimental experience, especially for heavy ions, due to the long beam line of the AMS system. During the ^{236}U AMS measurement, the slit 1, slit 2 and slit 3 were set at ± 5 , ± 2.5 and ± 1 mm, respectively. The mass resolution is about 400.

The negative ions are pre-accelerated to the maximum injection energy $E_{inj} = 120$ keV. During the heavy ion ^{236}U measurement, we found that the pre-accelerated voltage must be higher than 90 kV to clip the tails from ^{235}U and ^{238}U . Because the interactions of the ions of interest with residual gas in the accelerator tubes may change the charge state and movement direction, and lead to the unwanted transmission of interfering ions with either the wrong mass or the wrong energy. This is a small effect, but the $^{236}\text{U}/^{238}\text{U}$ is also very small and the effect ultimately becomes the main background in the detection. If the pre-accelerated voltage is lower than 90 kV, the transmission efficiency, and in turn the measurement sensitivity will be very low. During the ^{236}U AMS measurement, 100 kV pre-accelerated voltage is chosen and the vacuum is better than 10^{-6} Pa.

AMS MEASUREMENT

Production and Analysis of Negative Ions

In order to optimize the source performance for ^{236}U measurement, experiments on extracting multiform negative ^{238}U -containing molecular ions (including UO_x^- , UC_x^- , UF_x^-) and different conductor powders (Nb, Al and Ag) were carried out. Considering the overall efficiency (including the yield and transmission of the negative ions of interest), UO^- was found to be the most suitable form of ions to be extracted from the target. As an approximate measure of ionization efficiency, a sample consisting of U_3O_8 Nb=1:1 by weight was measured. The ionization efficiency, calculated from the integrated uranium oxide beam, was at least 0.1%.

Applications and Ancillary Systems

At the settings for ions with a mass of -252 (aiming at $^{236}\text{U}^{16}\text{O}^-$) to be injected into the accelerator, all kinds of ions with mass number of -252, such as $^{235}\text{U}^{17}\text{O}^-$, $^{235}\text{U}^{16}\text{OH}^-$, $^{238}\text{U}^{14}\text{N}^-$, $^{238}\text{U}^{12}\text{CH}_2^-$, etc, will be accompanied. Of these ions, $^{235}\text{U}^{17}\text{O}^-$ is unavoidable. For heavy ion ^{236}U AMS measurement, the isobar problem is not expected to occur, the problem is how to identify the interest ^{236}U ions from isotope background ^{238}U and ^{235}U .

Acceleration and Transmission

The measurement of ^{236}U was performed with a 13-MV tandem accelerator (HI-13) mass spectrometer at CIAE [14]. On the high-energy side, the beam was analyzed by a 90° post-analyzing magnet (maximal 200 MeV·amu) and a 17° AMS ESA. For $^{236}\text{U}^{11+}$ ions, the maximum usable terminal voltage was 7.800 MV, which corresponds to a final energy of 93.2 MeV, with a charge state fraction of about 14%. In the terminal of the HI-13 tandem accelerator, a $7 \mu\text{g cm}^{-2}$ thick carbon foil was used as a stripper. At the high-energy side, $^{236}\text{U}^{11+}$ ions were analyzed.

At the beginning of our work, the ^{236}U beam transport was simulated with the sample material of UO_2 and extracting ions of $^{238}\text{U}^{16}\text{O}^-$. Due to the small beam current (20-100 nA) and the significant scattering induced by the carbon foil and Coulomb explosion, the beam current in high-energy side was too small to be tuned for beam transport simulation. In order to tune the accelerator, the transportation simulation was divided into two steps by using $^{238}\text{UO}_2$ and $^{208}\text{Pb}^{16}\text{O}_2$ pilot beams, respectively. Firstly, in order to optimize the accelerator parameters, a $^{238}\text{U}^{11+}$ beam (7.773 MV) was used to simulate the beam transport from lower energy system to the image of the post-analyzing magnet. Secondly, a $^{208}\text{Pb}^{10+}$ (8.034 MV) ion beam (~ 300 nA) was used to simulate the $^{236}\text{U}^{11+}$ transport from the image of post-analyzing magnet to the AMS detection system, while keeping all the parameters already optimized in the first step unchanged. The experiment showed that the two-step simulation method for the optimization of ^{236}U beam transportation makes the adjustment much easier.

The overall particle transmission between the image of the injection magnet (mass 254) and the detection system ($^{238}\text{U}^{11+}$) is about 8×10^{-4} .

Detector System

The energy difference between the background ^{238}U and ^{235}U ions and the interested ion ^{236}U is only 0.8% and 0.4%, respectively. Only the time of flight (TOF) detector has sufficient resolution to distinguish the isotopes ^{238}U and ^{235}U from ^{236}U . The TOF system consists of a time "start" detector micro-channel plate (MCP) and a time "stop" detector gold-silicon surface barrier detector (SBD), separated by a flight path of 1.8 m. A $7 \mu\text{g cm}^{-2}$ carbon foil was employed to the "start" detector to produce the secondary electrons, which were then reflected by an electrostatic mirror, collected and multiplied by MCP. In order to minimize the scattering when the 93 MeV heavy ions $^{236}\text{U}^{11+}$ pass through the

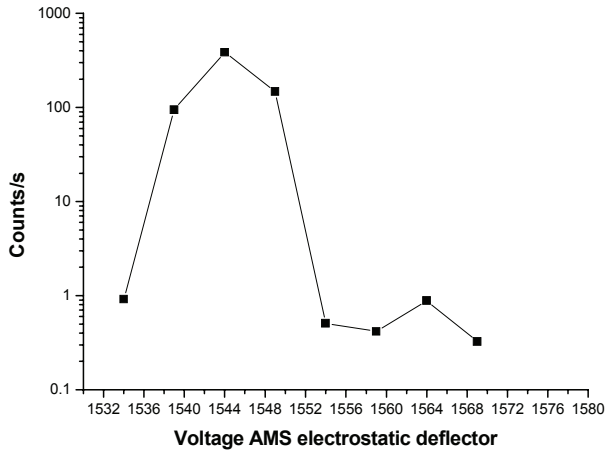


Figure 2: The scan spectrum of the AMS electrostatic deflector.

“start” detector, the carbon foil supported by a copper mesh was designed with a transparency of 95%. The SBD detector is also used as energy detector for mass/charge discrimination, since the nuclide of interest (^{236}U) has an energy gain different from that of interfering isotopes (isobars) in the acceleration process. The detector efficiency was measured to be about 50%.

In order to get a good time resolution of the TOF, the threshold and constant fraction delay were set carefully to optimize the CFD584 (constant fraction discrimination). The length of the 50 Ω -coaxial cable in CFD584 for constant-fraction shaping delay was calculated according

to the formula $L = \frac{t_{d(Ext)}}{\lambda} \approx \frac{1.1t_r - 0.7}{\lambda}$ ($\lambda = 5 \text{ ns}$, delay

time of 1m 50 Ω -coaxial cable; t_r is the rise time). The bias voltage for the “stop” detector SBD was set carefully too. When the bias voltage is 300 V, the time resolution (FWHM) is about 790 ps for 93 MeV $^{236}\text{U}^{11+}$, and the energy resolution is 4.7%. When it is increased to 600 V, the time and energy resolutions are \sim 670 ps and 4.2%, respectively, as shown in Fig. 5(a). As can be seen from Table1, this resolution is sufficient to separate ^{236}U from ^{238}U of the same magnetic rigidity, but still needs further improvement for the separation of ^{235}U .

Table 1: Flight Times over a 1.8 m Flight Path for 11+ Uranium Ions of different Masses with the same Magnetic Rigidity

Ion	Energy (MeV)	Flight time, T (ns)	ΔT (ns)
$^{235}\text{U}^{11+}$	93.167	205.34	0.88
$^{236}\text{U}^{11+}$	93.198	206.22	
$^{238}\text{U}^{11+}$	93.261	207.97	1.75

Calibration and Cross-Checks

The 17 $^\circ$ AMS ESA with 360 mm radius, and the maximal voltage (\pm 200 kV) result in an energy/charge state ratio of $E/q = 10.7 \text{ MeV}$ for $^{236}\text{U}^{11+}$. The vacuum is

about 10^{-5} Pa to reduce charge changing and scattering of the ions inside the ESA. At the beginning of ^{236}U measurement, the AMS ESA was used to scan the spectrum from ^{238}U to ^{235}U to monitor the beam transport and locate the would-be ^{236}U candidate events. A scan spectrum of the AMS electrostatic deflector is depicted in Fig. 2. The isotopes were counted directly with SBD. The image slit of the AMS electrostatic deflector was set to 4 mm \times 7mm for clipping the tails of $^{235}\text{U}^{11+}$ and $^{238}\text{U}^{11+}$ ions. An energy resolution ($\Delta E/E$) of better than 0.4% was achieved. A dilute ^{236}U standard (10^{-8}) was then used to validate the above calibration, as shown in Fig. 3(a).

RESULTS

Fig. 3 shows two-dimensional spectra of TOF vs energy and TOF spectra for a natural uranium ore sample and a ^{236}U dilution standard sample. Taking the advantages of the high terminal voltage of HI-13 accelerator and the relatively small energy straggling of the flying ions, a TOF resolution (FWHM) of about 670 ps has been obtained. However, the rise time of the “stop” SBD detector (bias voltage at 300 V is about 20 ns) and the quality and the thickness of the MCP foils are still the limiting factors for further improvement of TOP resolution. The total transmission of uranium ions at 93.2 MeV from the “start” MCP to the SBD was measured to be \sim 45%, resulting from the angular spread of the heavy-ion beam after the TOF carbon foils and the shadow of the wire grids.

Table 2 shows the suppression factors for ^{235}U and ^{238}U and transmission efficiencies of ^{236}U in various AMS components. The new AMS dedicated Injector has a very high suppression factor when the slit 1, slit 2 and slit 3 are set at \pm 5, \pm 2.5 and \pm 1 mm (about 10^8 for both ^{238}U and ^{235}U). The total suppression factors for ^{238}U and ^{235}U is about 10^{14} and 10^{10} , respectively. ^{235}U is hard to be separated from ^{236}U , due to the small differences in energy and time of flight.

Table 2: The Rejection Power for neighboring Isotopes ^{235}U , ^{238}U and Transmission Efficiency of ^{236}U in the various AMS Components

Components	^{238}U rejection	^{235}U rejection	^{236}U transmission efficiency
Injector system	$\sim 10^8$	$\sim 10^8$	~ 0.9
Accelerator			~ 0.3
Post-analyzing magnet			~ 0.8
Electrostatic deflector	$\sim 10^3$	$\sim 10^1$	~ 0.8
TOF dectector	$\sim 10^3$	$\sim 10^1$	~ 0.4
Total	$\sim 10^{14}$	$\sim 10^{10}$	$\sim 8 \times 10^{-4}$ ($Q=11+$)

Applications and Ancillary Systems

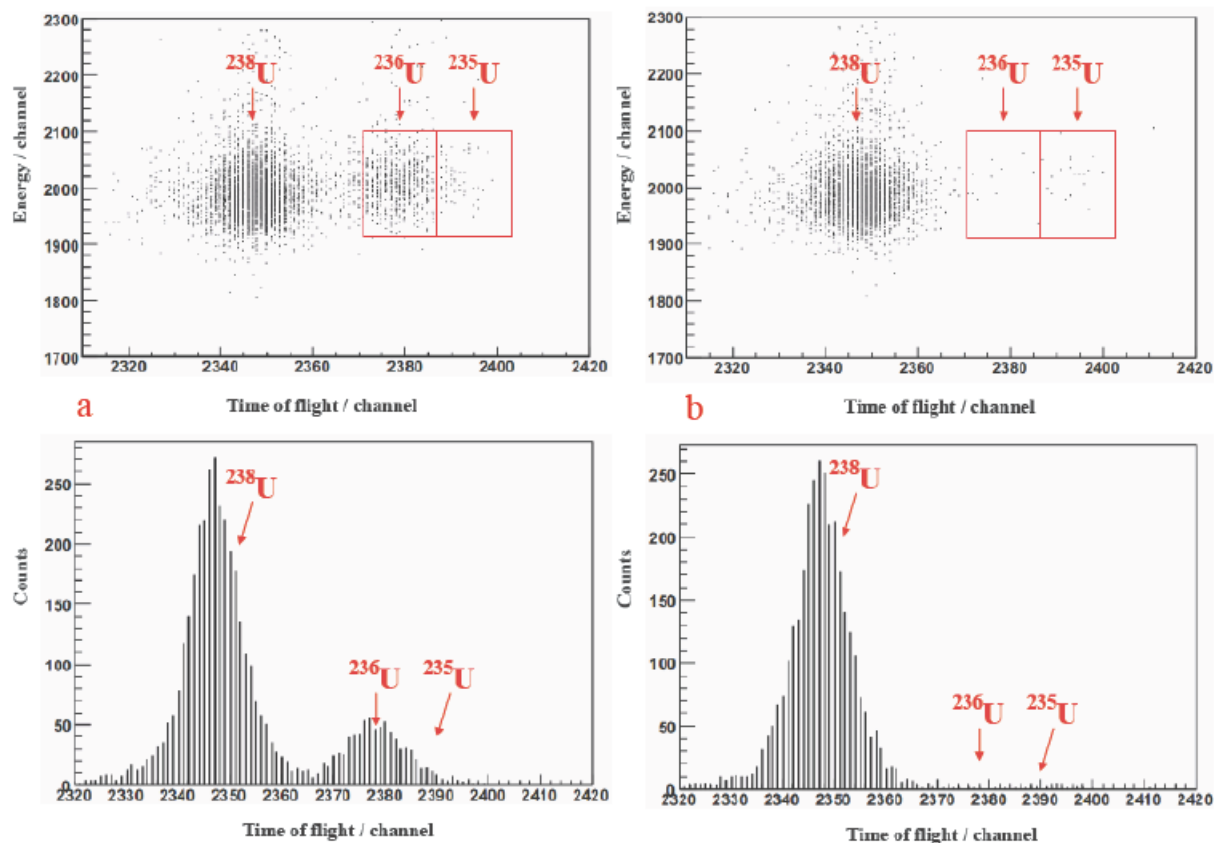


Figure 3: Example of a full-width figure showing the distribution of problems commonly encountered during paper processing. This figure is labeled with a multi-line caption which has to be justified, rather than centred.

Table 2 shows that the overall particle transmission between the image of the injection magnet and the detection system is about 8×10^{-4} , lower than those of most other AMS facilities. The transmission efficiency is especially low inside the accelerator which is about 30%, mainly due to the small diameter (8 mm) and long gas tube (1 m) of the gas stripper tube that is not suitable for the beam optics design. Besides, the carbon foil stripper used in our measurement system would increase the yield for high charge-states (high energy) ions, and deteriorate the beam quality (larger divergence and wider energy distribution) due to Coulomb explosion in the foil, especially for heavy ion $^{236}\text{U}^{11+}$.

Table 3: Results of $^{236}\text{U}/^{238}\text{U}$ ratios for Uranium Ore Sample

Sample	$^{236}\text{U}/^{238}\text{U}$ ratio
Sample 1 ^a	$(2.710 \pm 0.008) \times 10^{-5}$
Sample 2 ^b	$(4.6 \pm 0.4) \times 10^{-8}$
Sample 3	$(4.8 \pm 0.7) \times 10^{-10}$
Sample 4	$(5.9 \pm 0.8) \times 10^{-10}$

^a measured with thermal ionisation mass spectrometry, and used for normalization. ^b Sample 2 is diluted from Sample 1, and used for normalization.

The results for $^{236}\text{U}/^{238}\text{U}$ ratio are shown in Table 3. The $^{236}\text{U}/^{238}\text{U}$ of Sample 1 is $(2.710 \pm 0.008) \times 10^{-5}$, measured with Thermal Ionization Mass Spectrometry (TIMS). Sample 2 was quantitatively diluted from Sample 1, and used for normalization. Sample 3 and Sample 4 were purchased by CIAE in 1960s. The $^{236}\text{U}/^{238}\text{U}$ for sample 3 and sample 4 is $(4.8 \pm 0.7) \times 10^{-10}$ and $(5.9 \pm 0.8) \times 10^{-10}$, respectively. The main contribution to the uncertainties is the poor counting statistics due to the small number of ^{236}U atoms recorded in the detector. The sensitivity is lower than 10^{-10} for $^{236}\text{U}/^{238}\text{U}$ in present work.

SUMMARY

A method for AMS measurement of long-lived heavy ion ^{236}U has been developed at CIAE. Its unique features include the establishing of the AMS dedicated injector and $^{208}\text{Pb}^{16}\text{O}_2^-$ molecular ions for simulation of ^{236}U transportation. A sensitivity of lower than 10^{-10} for $^{236}\text{U}/^{238}\text{U}$ has been achieved in present work.

There is still room for further improvement in the AMS measurement of ^{236}U on our AMS system. Firstly, a new TOF system is being considered with two MCPs, one energy detector, and an ultra-thin diamond-like carbon foil [15] (DLC foils) as the entry window. The new TOF system may have a resolution of ~ 500 ps, sufficient to identify the isotope ^{235}U for ^{236}U AMS measurement. Secondly, a new stripper made of a thinner carbon foil

(such as diamond-like carbon foil) is to be installed in our HI-13 tandem accelerator to increase the transmission efficiency for ^{236}U measurement, so that we can set the AMS dedicated injector at ± 1 mm state to increase the mass resolution (~ 1000) for ^{236}U AMS measurement.

The method can also be applied to other long-lived actinide isotopes, such as ^{210}Pb , ^{237}Np , ^{239}Pu , ^{240}Pu , ^{242}Pu and ^{244}Pu .

ACKNOWLEDGEMENTS

We wish to thank Professor Weizhi Tian from Department of Nuclear Physics, China Institute of Atomic Energy (CIAE) for useful suggestions concerning the experiment.

REFERENCES

- [1] K.H. Purser, L.R. Kilius, A.E. Litherland and X.L. Zhao, *Instr. and Meth. B* 113 (1996) 445.
- [2] Peter Steier et al., 11th International Conference on Accelerator Mass Spectrometry, September 14-19, 2008, Rome, Italy.
- [3] J. Donohue, *Alloys Comp.* 271(1998) 11.
- [4] J. Rokop, D.N. Metta, C.M Stevens, *Int. J. Mass Spectrom. Ion Phys.* 8 (1972) 259.
- [5] S. Richter, A. Alonso, De Bolle, et al. *Int J Mass Spectrom*, 1999, 193: 9.
- [6] X.-L. Zhao, M.-J. Nadeau et al., *Nucl. Instr. and Meth. B* 92 (1994) 249.
- [7] Steier, R. Golser, W. Kutschera et al., *Nucl Instr And Meth.* B188(2002) 283.
- [8] Fifield L.K., *Quaternary Geochronology* 3(2008) 276.
- [9] T. A. Brown, A. A. Marchetti, R. E. Martinelli et al., *Nucl Instr And Meth*, 2004, B223-224 : 788.
- [10] M A C Hotchki, D Child, D Fink et al., *Nucl Instr And Meth*, 2000, B172:659.
- [11] Wallner L., Faestermann T., Gerstman U. , et al. *Nucl Instr And Meth*, 2000, B172:333.
- [12] Fifield L.K., Synal H. A., Suter M. et al., *Nucl Instr And Meth B*223-224 (2004) 802.
- [13] D. Berkovits, H. Feldstein, S. Ghelberg et al., *Nucl Instr And Meth*, 2000, B172:372.
- [14] Shan Jiang, Ming He et al., *Nucl. Instr. and Meth.* B172 (2000) 87.
- [15] V.K. Liechtenstin, T.M. Ivkova, E.D. Olshanski, A.M. Baranov, R. Repnow, R. Hellborg, R.A. Weller, H.L. Wirth, *Nucl. Instr. and Meth.*